META 2018 in Marseille – France

The 9th International Conference on Metamaterials, Photonic Crystals and Plasmonics



Proceedings

ISSN 2429-1390

metaconferences.org

META 2018 in Marseille – France

The 9th International Conference on Metamaterials, Photonic Crystals and Plasmonics

Share your comments, photos & videos !



www.facebook.com/metaconference



@metaconference

Edited by

Said Zouhdi | Paris-Sud University, France

CONTENTS

ABOUT META 5

META 2018 ORGANIZATION 6

PLENARY SPEAKERS 8

KEYNOTE SPEAKERS 10

META 2018 VENUE 11

GUIDELINES FOR PRESENTERS 16

TECHNICAL PROGRAM 17

ABOUT META

The International Conference on Metamaterials, Photonic Crystals and Plasmonics (META) features every year the latest developments in the area of Nanophotonics, Metamaterials and related topics.

The conference program consists of plenary lectures, keynote talks, special sessions of invited talks, general sessions and high-profile poster sessions that typically cover a broad range of exciting physics, such as metamaterials and negative index materials, metatronics and graphene metamaterials, plasmonics and nanophotonics, plasmon-enhanced photovoltaics, photonic and plasmonic crystals and cavities, materials for photonics (Graphene, MoS2, WS2, etc), quantum photonics, nanobiophotonics, structured light, near-field optics and nano-optics, transformational electromagnetics and cloaking, acoustic metamaterials, optomechanics, nanofabrication technologies, etc.

The origin of the conference dates back to 2002 as a NATO Advanced Research Workshop at a time when many of the current topical research areas began to emerge from the field of complex electromagnetic materials.

Following a now well-established tradition META takes place every year in unique locations around the world.

Year	Organizers	Venue
2017	Junsuk Rho, Hakjoo Lee, Said Zouhdi	Incheon, Korea
2016	Manuel Nieto-Vesperinas, Said Zouhdi	Torremolinos, Spain
2015	Vinod Menon, Said Zouhdi	New York, USA
2014	Nikolay Zheludev, Jing Hua Teng, Said Zouhdi	Singapore
2013	Hamid M. K. Al-Naimiy, Said Zouhdi	Sharjah-Dubai, United Arab Emirates
2012	Xavier Begaud, Said Zouhdi	Paris, France
2010	Hadia Elhennawy, Said Zouhdi	Cairo, Egypt
2008	Alexey Vinogradov, Said Zouhdi	Marrakesh, Morocco
2002	Said Zouhdi	Marrakesh, Morocco

META 2018 ORGANIZATION



Said Zouhdi, General Chair
Paris–Sud University, France

INTERNATIONAL ADVISORY COMMITTEE

Harry Atwater, USA
Federico Capasso, USA
Andre de Lustrac, France
Nader Engheta, USA
Teruya Ishihara, Japan
Tatsuo Itoh, USA
Yuri Kivshar, Australia
Graeme W. Milton, USA
Raj Mittra, USA
Manuel Nieto-Vesperinas, Spain
Susumu Noda, Japan
Masaya Notomi, Japan
Vladimir Shalaev, USA
Ari Sihvola, Finland
David R. Smith, USA
Martin Wegener, Germany
Xiang Zhang, USA
Nikolay Zheludev, UK

TECHNICAL PROGRAM COMMITTEE

Pierre-Michel Adam, France
Ishwar Aggarwal, USA
Javier Aizpurua, Spain
Mohamed Bakr, Canada
Xavier Begaud, France
Svetlana V. Boriskina, USA
Alberto Bramati, France
Kurt Busch, Germany
Bernard Casse, USA
Che Ting Chan, Hong Kong
Debashis Chanda, USA
Pai-Yen Chen, USA
Johan Christensen, Spain
Naresh Das, USA
Alfredo De Rossi, France
Mohamed Farhat, Qatar
Michael A. Fiddy, USA
Monika Fleischer, Germany
Wolfgang Fritzsche, Germany
Francisco Garcia-Vidal, Spain
Alexander Govorov, USA
Ortwin Hess, United Kingdom
Joachim Krenn, Austria
Laura M. Lechuga, Spain
Howard (Ho Wai) Lee, USA
Jensen Li, Hong Kong
Jichun Li, USA
Haitao Liu, China
Anatole Lupu, France
Bumki Min, Korea
Fernando Moreno, Spain
Teri Odom, USA
Namkyoo Park, Korea
Dorota Pawlak, Poland
Min Qiu, China
Junsuk Rho, Republic of Korea
Kazuaki Sakoda, Japan
Luca Sapienza, UK
Mohamed Swillam, Egypt
Takuo Tanaka, Japan
Giorgos P. Tsironis, Greece
Augustine Urbas, USA
Hong Wei, China
Joel K. W. Yang, Singapore
Anatoly V Zayats, UK
Lei Zhou, China

SPECIAL SYMPOSIA ORGANIZERS



Alexander Govorov
USA



Xing Yi Ling
Singapore



Jerome Plain
France



Mohamed Swillam
Egypt

SPECIAL SESSIONS ORGANIZERS

Henri Benisty, France
Debashis Chanda, USA
Hongsheng Chen, China
Pai-Yen Chen, USA
Qin Chen, China
Alasdair W. Clark, UK
Kofi Edee, France
Mohamed Farhat, Qatar
Denis Garoli, Italy
Yuri Gorodetski, Israel
Tobias Heindel, Germany
Eugene Kamenetski, Israel
Alina Karabchevsky, Isreal
Howard Lee, USA
Dangyuan Lei, Hong Kong
Guixin Li, China
Qiang Li, China
Xiaofeng Li, China
Chun-Wen Lin, Taiwan
Hui Liu, China
Anatole Lupu, France
Guancong Ma, Hong Kong
Marco Miniaci, France
Dorota Pawlak, Poland
Virginie Ponsinet, France
Stephan Reitzenstein, Germany
Almas Sadreev, Russia
Xiaowei Sun, China
Din Ping Tsai, Taiwan
Jian Wang, China
Hong Wei, China
Tzong-Lin Wu, Taiwan
Jie Zhu, Hong Kong
Xue-Feng Zhu, China
Zakaria Zouhdi, Taiwan

PLENARY SPEAKERS



Federico Capasso

Harvard University, USA

The Present and Future of Flat Optics : from Metalenses to Polarization Metaoptics and Arbitrarily Structured Light

Federico Capasso is the Robert Wallace Professor of Applied Physics at Harvard University, which he joined in 2003 after 27 years at Bell Labs where he was Member of Technical Staff, Department Head and Vice President for Physical Research. He is visiting professor at NTU with both the School of Physical and Mathematical Sciences and Electrical and Electronic Engineering. His research has focused on nanoscale science and technology encompassing a broad range of topics. He pioneered band-structure engineering of semiconductor nanostructures and devices, invented and first demonstrated the quantum cascade laser and investigated QED forces including the first measurement of a repulsive Casimir force. His most recent contributions are new plasmonic devices and flat optics based on metasurfaces. He is a member of the National Academy of Sciences, the National Academy of Engineering, the American Academy of Arts and Sciences. His awards include the King Faisal Prize, the IEEE Edison Medal, the SPIE Gold Medal, the American Physical Society Arthur Schawlow Prize in Laser Science, the Jan Czochralski Award for lifetime achievements in Materials Science, the IEEE Sarnoff Award in Electronics, the Materials Research Society Medal, the Wetherill Medal of the Franklin Institute, the Rank Prize in Optoelectronics, the Optical Society Wood Prize, the Berthold Leibinger Future Prize, the Julius Springer Prize in Applied Physics, the European Physical Society Quantum Electronics Prize.



Nader Engheta

University of Pennsylvania, USA

X-Y-Z-T Metamaterials

Nader Engheta is the H. Nedwill Ramsey Professor at the University of Pennsylvania in Philadelphia, with affiliations in the Departments of Electrical and Systems Engineering, Materials Science and Engineering, Physics and Astronomy, and Bioengineering. He received his B.S. degree from the University of Tehran, and his M.S and Ph.D. degrees from Caltech. His current research activities span a broad range of areas including nanophotonics, metamaterials, nano-scale optics, graphene optics, optical metatronics, imaging and sensing inspired by eyes of animal species, optical nanoengineering, microwave and optical devices, and physics and engineering of fields and waves He has received several awards for his research including the 2017 William Streifer Scientific Achievement Award from the IEEE Photonics Society, the 2015 Gold Medal from SPIE, the 2015 Fellow of US National Academy of Inventors (NAI), the 2015 National Security Science and Engineering Faculty Fellow (NSSEFF) Award (also known as Vannevar Bush Faculty Fellow Award) from US Department of Defense, the 2015 IEEE Antennas and Propagation Society Distinguished Achievement Award, the 2015 Wheatstone Lecture in KingâĂŹs College London, the 2014 Balthasar van der Pol Gold Medal from the International Union of Radio Science (URSI), the 2013 Inaugural SINA Award in Engineering, the 2012 IEEE Electromagnetics Award, 2006 Scientific American Magazine 50 Leaders in Science and Technology, the Guggenheim Fellowship, and the IEEE Third Millennium Medal. He is a Fellow of seven international scientific and technical societies, i.e., IEEE, URSI, OSA, APS, MRS, SPIE, and American Association for the Advancement of Science (AAAS). He has received the honorary doctoral degrees from the Aalto University in Finland in 2016 and from the University of Stuttgart, Germany in 2016.



Andrea Fratalocchi

KAUST, Saudi Arabia

Evolutionary metamaterials : the imitation game of Nature for renewable energy harvesting, artificial intelligent photonics and advanced material engineering

Andrea Fratalocchi is an Associate Professor (from July 2016) in the Computer, Electrical and Mathematical Sciences and Engineering Division at KAUST University. He joined KAUST in January 2011 as Assistant Professor. Prior to joining KAUST, Andrea Fratalocchi was a Research Fellow of Sapienza University of Rome under a KAUST Fellowship Award. From 2007 to 2009, Andrea Fratalocchi worked as a post-doctoral researcher at Sapienza University, under a "New Talent" Award from the research center âĂIJEnrico Fermi.âĂİ In 2012 he was appointed as Editor of Nature Scientific Report. In 2017, he won the middle east GCC enterprise Award as best electrical engineer of the year. Andrea Fratalocchi is the group leader of PRIMALIGHT, which focuses on providing new sustainable and scalable Photonics technologies for renewable energy, nanomedicine and material science.



Michelle L. Povinelli

University of Southern California, USA

Microstructured Materials for Thermal Regulation and Logic

Michelle Lynn Povinelli, is an Associate Professor in the Ming Hsieh Department of Electrical Engineering at the University Southern California. Her research interest is nanophotonics, the study of how light interacts with nano- and microscale structures. Her group studies nanophotonic structures such as photonic crystals„ nanowires, and metamaterials for applications in optical trapping, photovoltaics, and thermal control. She is a recipient of the NSF CAREER Award, the Army Research Office Young Investigator Award, the Presidential Early Career Award for Scientists and Engineers (PECASE), and the TR35 Award for innovators under age 35 from MIT's Technology Review magazine. She received a BA from the University of Chicago, an MPhil from the University of Cambridge, and a PhD from MIT, all in Physics and was a postdoctoral researcher in Electrical Engineering at Stanford University. She has co-authored more than seventy-five journal articles and three US Patents.



Vladimir M. Shalaev

Purdue University, USA

Catching Light with Metamaterials

Vladimir M. Shalaev, Scientific Director for Nanophotonics at Birck Nanotechnology Center and Distinguished Professor of Electrical and Computer Engineering at Purdue University, specializes in nanophotonics, plasmonics, and optical metamaterials. Vladimir M. Shalaev has received several awards for his research in the field of nanophotonics and metamaterials, including the Max Born Award of the Optical Society of America for his pioneering contributions to the field of optical metamaterials, the Willis E. Lamb Award for Laser Science and Quantum Optics, IEEE Photonics Society William Streifer Scientific Achievement Award, Rolf Landauer medal of the ETOPIM (Electrical, Transport and Optical Properties of Inhomogeneous Media) International Association, the UNESCO Medal for the development of nanosciences and nanotechnologies, OSA and SPIE Goodman Book Writing Award. He is a Fellow of the IEEE, APS, SPIE, MRS and OSA. Prof. Shalaev has authored three books, thirty invited book chapters and over 500 research publications.

KEYNOTE SPEAKERS



Renaud Bachelot
University of Technology of Troyes, France
Advanced hybrid plasmonics based on nanoscale photopolymerization



Alexandra Boltasseva
Purdue University, USA
Optical Metamaterials with Emerging MXenes



Andrei Faraon
California Institute of Technology, USA
Optical components and systems based on dielectric metasurfaces



Alexander Govorov
Ohio University, USA
Quantum and Classical Phenomena in Bio-Plasmonic Nanostructures and Assemblies



Philippe Lalanne
Institut Optique Graduate School, France
Nanoresonator : a modal theory of Fano-like resonance



Peter Lodahl
University of Copenhagen, Denmark
Quantum devices based on quantum dots in planar nanophotonic structures



Dongling Ma
Institut National de la Recherche scientifique (INRS), Canada
Enhancing Photon Harvesting with Plasmonic Nanostructures



Willie Padilla
Duke University, USA
Electromagnetic Metamaterials - the First Twenty Years



Mu Wang
Nanjing University, China
Ultrafast pump-probe studies on graphene and graphene-based structures



Xiang Zhang
UC Berkeley, USA
Optical Metasurfaces from classical to quantum regime

META 2018 VENUE

META 2018 will be held aboard the dream-class cruise ship Costa Diadema as a round-trip Marseille cruise from 24 June to 1st July 2018.



GETTING TO THE CRUISE PORT/TERMINAL

The departure port is located :

Porte 4, Port de Marseille, Chemin du Littoral
13015 Marseille
France



Get driving directions and arrange for transfers from your airport or hotel ahead of time. If you are flying in, don't forget to claim your luggage at the airline's baggage claim area.

From ”Marseille Provence” Airport

Marseille Provence Airport is located around 27 km / 17 ml (1/2 hour drive distance) northwest of the cruise port and 9 km (5,6 ml) from the city centre.

☐ **By Taxi**

The easiest way to reach the cruise port is to take a taxi straight from the airport, the price is around €50.

☐ **By Bus and Taxi**

Shuttle bus lines run every 20 min from the airport to the St Charles train station daily (between 5 am - 11 pm). Drive distance is approx 30 min. A taxi from from the train station to the cruise ship terminals costs about €20. Occasionally, the port also provides a free shuttle bus line to the city.

Travelling by Car

To reach terminal car parking, take exit 5 off the A55 if you are heading for the cruise terminal area at Porte 4 (Gate 4). You should find a large cruise passengers' car-park, or parking croisieristes, at the end of the Mole Leon Gourret near the Marseille-Provence Cruise Terminal. Be advised that the charges for this car-park are fairly steep.

CRUISE ITINERARY

7 Days Mediterranean-West

Costa Diadema is setting sail on Sunday, 24 June 2018, for 7 nights departing from Marseille and visiting Palma de Mallorca ; Cagliari ; Civitavecchia ; Savona ; Marseille.



Embarkation Time

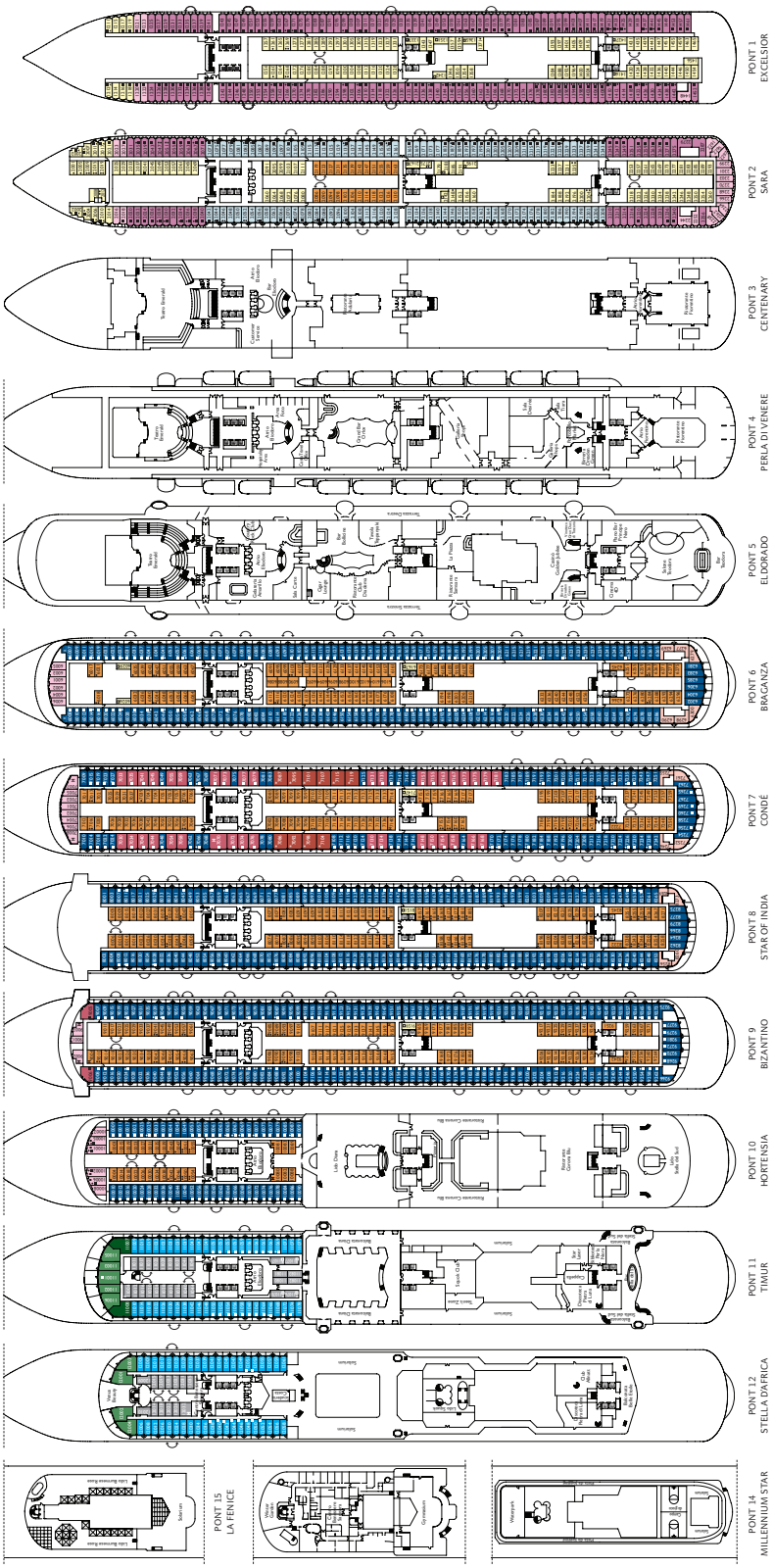
Embarkation time is when you should arrive at the cruise terminal. In Marseille we will procced with the conference registration before embarking (from **12 :00** to **15 :30**). This will give you enough time to complete your check-in at the cruise terminal before boarding.

In the other stopover ports (Barcelona, Palma de Mallorca, Cagliari, Civitavecchia and Savona) we highly encourage you to board no later than one hour prior to the departure time (gates close 30mn before departure).

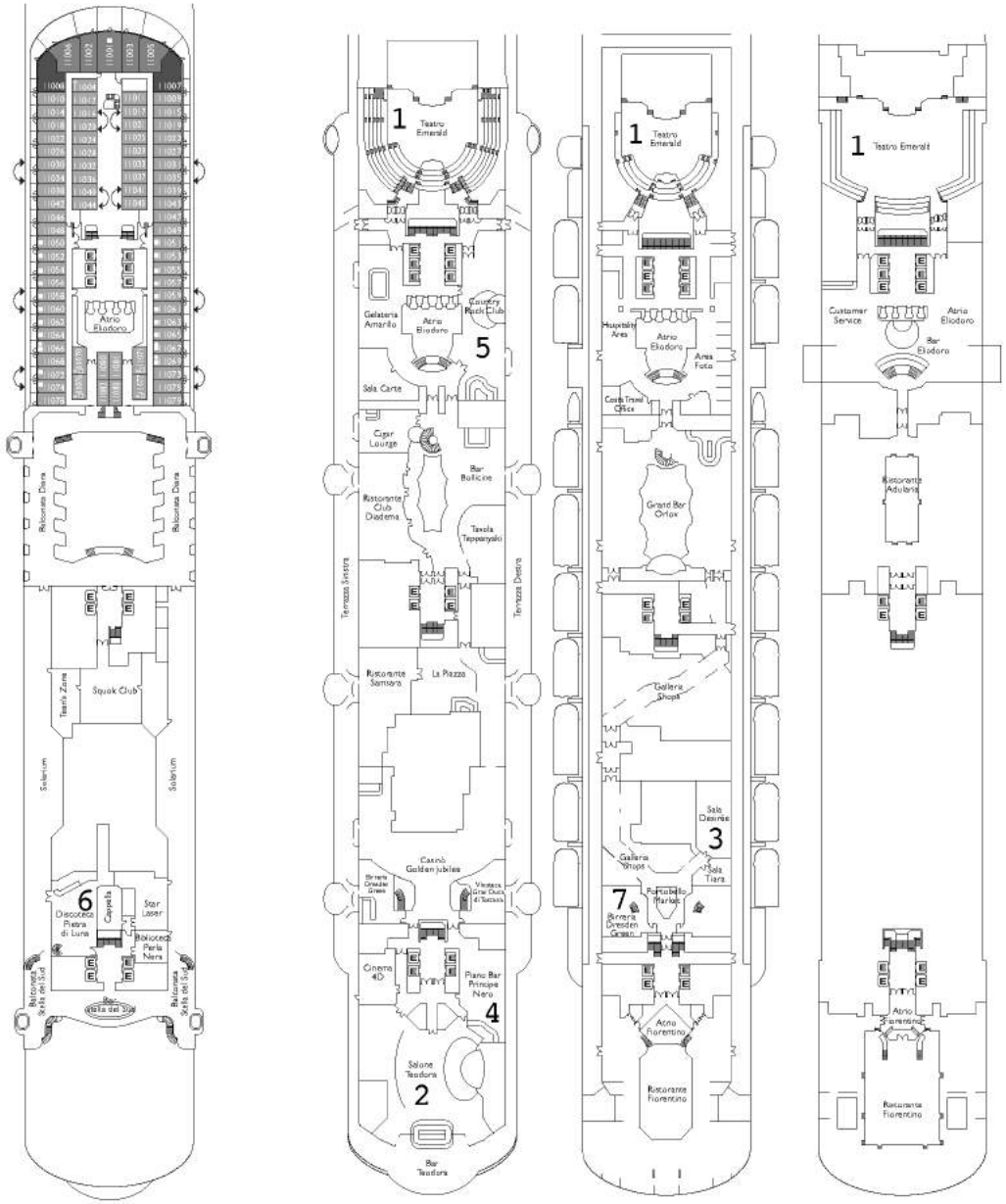
Ports of Call

Day	Port	Arrival	Departure
1	Marseille	-	17:00
2	Barcelona	9:00	19:00
3	Palma de Mallorca	9:00	-
4	Palma de Mallorca	-	1:00
5	Cagliari, Sardinia	8:00	17:00
6	Civitavecchia	8:00	19:00
7	Savona, Italy	7:00	17:00
8	Marseille	8:00	-

COSTA DIADEMA DECK PLANS



FLOOR PLANS



1 : Teatro Emerald
2 : Salone Teodora
3 : Sala Desirée
4 : Piano Bar Principe Nero
5 : Country Rock Club
6 : Discoteca Pietra di Luna
7 : Birreria Dresden Green

GUIDELINES FOR PRESENTERS

ORAL PRESENTATIONS

Each session room is equipped with a stationary computer connected to a LCD projector. Presenters must load their presentation files in advance onto the session computer.

Scheduled time slots for oral presentations are 15 mn for regular, 20 mn for invited presentations, 30 mn for keynote talks and 35 mn for plenary talks, including questions and discussions. Presenters are required to report to their session room and to their session Chair at least 15 minutes prior to the start of their session.

The session chair must be present in the session room at least 15 minutes before the start of the session and must strictly observe the starting time and time limit of each paper.

POSTER PRESENTATIONS

Presenters are requested to stand by their posters during their session. One poster board, A0 size (118.9 x 84.1 cm), in portrait orientation, will be available for each poster. Pins or thumbtacks are provided to mount your posters on the board. All presenters are required to mount their papers before the session and remove them at the end of their session. Posters must prepared using the standard META poster template (available on the conference website).

TABLE OF CONTENTS

Plenary Lectures

Catching Light with Metamaterials (pp. 42)
Vladimir Shalaev,

X-Y-Z-T Metamaterials (pp. 43)
Nader Engheta,

The Present and Future of Flat Optics: from Metalenses to Polarization Metaoptics and Arbitrarily Structured Light (pp. 44)
Federico Capasso,

Evolutionary metamaterials: the imitation game of Nature for renewable energy harvesting, artificial intelligent photonics and advanced material engineering (pp. 45)
Andrea Fratalocchi,

Microstructured Materials for Thermal Heating and Memory (pp. 46)
Michelle L. Povinelli,

Keynote Lectures

Enhancing Photon Harvesting with Plasmonic Nanostructures (pp. 48)
Dongling Ma,

Advanced hybrid plasmonics based on nanoscale photopolymerization (pp. 50)
Renaud Bachelot,

Quantum and Classical Phenomena in Bio-Plasmonic Nanostructures and Assemblies (pp. 51)
Alexander O. Govorov, Lucas V. Besteiro, Xiang-Tian Kong,

Optical Metasurfaces from classical to quantum regime (pp. 52)
Xiang Zhang, Yuan Wang,

Ultrafast pump-probe studies on graphene and graphene-based structures (pp. 53)
Mu Wang, Yingying Zhu, Lianzi Liu, Dongxiang Qi, Renhao Fan, Ruwen Peng,

Optical components and systems based on dielectric metasurfaces (pp. 54)
Adrei Faraon, Ehsan Arbabi, Seyedeh Mahsa Kamali, MohammadSadegh FarajiDana, Yu Horie, Amir Arbabi,

Rigorous modal analysis of plasmonic nanoresonators (pp. 55)
Wei Yan, Philippe Lalanne, Jean Paul Hugonin, Christophe Sauvan,

Exploration of Novel Electromagnetic Scattering with All-Dielectric Metamaterials (pp. 56)
Willie Padilla, Andrew Cardin, Xinyu Liu, Kebin Fan,

Quantum nanophotonics with semiconductor quantum dots (pp. 57)
Leonardo Midolo, Peter Lodhal,

Hybrid and Metastructured Materials for Photonics, Sensors and Energy

Plasmonic Nanostructures for Point-of-Care Sensors (pp. 59)
Nianqiang Wu,

Probing dynamics and controlling ultrafast plasmon via photoemission electron microscopy (pp. 60)
Boyu Ji, Yingping Dou, Haiyan Tao, Xiaowei Song, Xun Gao, Zuoqiang Hao, Jingquan Lin,

Dynamic hot-spots in plasmonic photocatalysis (pp. 62)
Miguel A. Correa-Duarte,

Active control of the photoluminescence emitted by quantum dots using metallic nanoparticles and photochromic molecules (pp. 64)
Gwenaelle Lamri, Jana B. Nieder, Edite Figueiras, Jean Aubard, Pierre-Michel Adam, Christophe Couteau, Nordin Felidj, Anne-Laure Baudrion,

Plasmo-Mechanical Control of Photo-Induced Heat Generation from Au Nanoparticles Immobilized on a Flexible Substrate (pp. 66)
Roberto Caputo, Giovanna Palermo, Antonio Condello, Ugo Cataldi, Thomas Buergi, Cesare Paolo Umeton, Antonio De Luca,

Image multiplexing with laser-controlled plasmonic colors (pp. 68)
Nathalie Destouches, Nipun Sharma, Oleksii Vodorov, Nicolas Dalloz, Christophe Hubert, Francis Vocanson, Mathieu Hebert,

Anisotropic chiroptically active nanomaterials (pp. 70)
Yurii K. Gun'ko, Finn Purcell-Milton, Vera A. Kuznetsova, Natalia Garcia Domenech, Nikita V. Tepliakov, Anvar S. Baimuratov, Ivan D. Rukhlenko, Alexander V. Baranov, Anatoly V. Fedorov,

MoirÃ© Chiral Metamaterials with Tunable Optical Chirality for Ultrasensitive Sensing (pp. 72)
Zilong Wu, Yuebing Zheng,

Towards energy transfer of nanoemitters assisted by surface plasmons (pp. 74)
AurÃ©lie Broussier, Ali Issa, Loic O. Le Cunff, Tien Hoa Nguyen, Dinh Xuan Quyen, Safi Jradi, Christophe Couteau, Renaud Bachelot,

Artificial chirality with fractal aluminum nanostructures (pp. 76)
Dmitry Khlopin, JÃ©rome Martin, Davy GÃ©rard,

Plasmonic Nanomaterials as Infrared-Blocking Radiation Filters and Energy-Saving Glasses (pp. 77)
Lucas V. Besteiro, Xiang-Tian Kong, Zhiming Wang, Federico Rosei, Alexander Govorov,

Plasmon-Enhanced Quantum Dot Solar Cells (pp. 79)
Jiang Wu, Peng Yu, Alexander Govorov, Zhiming Wang,

Ultra-Fine Electrochemical Tuning of the Plasmonic Dimer Structures to Generate Highly Confined Light Field (pp. 81)
Hiro Minamimoto, Shunpei Oikawa, Kei Murakoshi,

Enhanced Terahertz Light - Matter Coupling in Plasmonic Nanocavities (pp. 83)
Xin Jin, Andrea Cerea, Gabriele C. Messina, Andrea Rovere, Riccardo Piccoli, Francesco De Donato, Francisco Palazon, Andrea Perucchi, Paola Di Pietro, Roberto Morandotti, Stefano Lupi, Francesco De Angelis, Mirko Prato, Andrea Toma, Luca Razzari,

Comparative plasmonic waveguide design for nanoscale lasing and four-wave mixing (pp. 85)
Stefano Palomba, Guangyuan Li, Martijn da Sterke,

Tailoring the Resonance Couplings between 2D-Excitons and Nanophotonics Structures (pp. 87)
Jinxiu Wen, Hao Wang, Huanjun Chen,

Molecular Junction-Controlled High-Order Charge Transfer Plasmon and Fano Resonance (pp. 89)

Ximin Cui, Yunhe Lai, Lei Shao, Jianfang Wang,

Anti-Reflective All-Dielectric Metasurfaces Engraved on an Optical Waveguide Facet (pp. 91)
Alina Karabchevsky, Yakov Galutin,

Resonant-state expansion generalized to magnetic, chiral, and bi-anisotropic open optical systems and metamaterials (pp. 93)
Egor Muljarov, Thomas Weiss,

Simulation the Effect of Transparent Conducting Oxides Layer on the Waveguide Reflection (pp. 94)
Hala Jarallah El-Khozondar, Ahmed A. AlShembari, Mohammed M. Shabat,

Hybrid plasmonic-dielectric nonlinear metasurface with tunable quality factors (pp. 96)
Feng Wang, Hayk Harutyunyan,

Modal Design to Control Transient Ultrafast Events in Nanoscale Materials (pp. 98)
Gregory Wurtz,

Optical detection of proteins in complex media (pp. 99)
Ramon A. Alvarez-Puebla,

Strong Light-Matter Interaction in Single Plasmonic Nanocavity and the Photoluminescence Evolution (pp. 101)
Di Zheng, Shunping Zhang, Qian Deng, Meng Kang, Peter Nordlander, Hongxing Xu,

ZnO-Au heterojunction enhanced the photoluminescence of ZnO nanocrystals (pp. 104)
I. Shahine, J-J. Gaumet, A. En-Naciri, P. Miska, B. El-Eulmi, H. Rinnert, Safi Jradi, Suzanna Akil,

3D plasmonic supercrystals: SERS enhancing properties (pp. 105)
Nicolas Pazos-Perez, Ramon Alvarez Puebla,

All Dielectric Metamaterial for MIR Applications (pp. 107)
Mohamed Swillam,

Plasmon-Assisted Selective and Super-Resolving Excitation of Individual Quantum Emitters on a Metal Nanowire (pp. 108)
Hong Wei, Qiang Li, Deng Pan, Hongxing Xu,

Surface enhanced spectroscopies with new plasmonic platforms (pp. 110)
Pierre-Michel Adam,

Self-assembled metamaterials active at optical frequencies (pp. 111)
V. Many, G. Drisko, P. Barois, A. Baron, V. Ponsinet, P. Richetti, S. De Cicco, J. Leng, J-B. Salmon, S. Ravaine, A. Crut, N. Del Fatti, E. Duguet, M. Treguer-Delapierre,

Photopolymerization at the nanoscale triggered by plasmon resonance (pp. 113)
F. Kameche, W. Heni, S. Telitel, X. Zhou, C. Deeb, R. Bachelot, Olivier Soppera,

Novel Design and Applications of Metamaterials, Metasurfaces and Metadevices using Hybrid and New Materials

Metamaterial superconductors (pp. 116)
Vera N. Smolyaninova, Igor I. Smolyaninov,

The silicon dimer array based sensor (pp. 118)
Ziwei Liu, Tanchao Pu, Jiebin Niu, Lina Shi, Changqing Xie,

Negative permeability in magnetostatics: experimental realization and applications (pp. 120)
Rosa Mach-Batlle, Albert Parra, Sergi Laut, Nuria Del-Valle, Carles Navau, Alvaro Sanchez,

Optoelectronic metasurfaces (pp. 122)
Pierre Berini,

Fiber drawn metamaterials: from guidance to sub-resolution imaging, spanning from IR to THz (pp. 124)
Alessio Stefani, Simon C. Fleming, Boris T. Kuhlmey,

Anisotropic Gain/Loss Metasurface for Directive Surface Plasmon-Polaritons Propagation (pp. 126)
Dmitry Kuzmin, Igor Bychkov, Vladimir Shavrov, Vasily Temnov,

Attojoule Modulators for Photonic Neuromorphic Computing (pp. 128)
Rubab Amin, Jonathan George, Jacob Khurgin, Tarek El-Ghazawi, Paul Prucnal, Volker J. Sorger,

Optical rotation effects in nanostructured materials (pp. 130)
Thierry Verbiest, Tom Swusten, Ward Brullot,

Dispersion-tailored metalenses and their applications (pp. 131)
Wei Ting Chen, Alexander Y. Zhu, Jared Sisler, Federico Capasso,

Raman imaging and tip-enhanced Raman scattering for epitaxial graphene grown on SiC (pp. 133)
Yasutaka Kitahama, Shohei Uemura, Sanpon Vantasin, Yoshito Tanaka, Toshiaki Suzuki, Daichi Doujima, Tadaaki Kaneko, Yukihiro Ozaki,

New Type of Switching Cell Based on Optical Metamaterial and Optically Transparent Ferrite (pp. 135)
Konstantin Vytovtov, E. Barabanova, Said Zouhdi ,

Metasurface Pulse Shaping (pp. 138)
Shawn Divitt, Wenqi Zhu, Cheng Zhang, Henri J. Lezec, Amit Agrawal,

Hybrid Graphene Metasurface for High-Speed Mid-Infrared Light Modulation and Single-Pixel Imaging (pp. 139)
Beibei Zeng, Zhiqin Huang, Akhilesh Singh, Yu Yao, Abul Azad, Aditya Mohite, Antoinette Taylor, David Smith, Hou-Tong Chen,

Power generation from thermal radiation: Photon-assisted tunneling in a metasurface-coupled rectifier (pp. 141)
Paul Davids, Josh Shank, Andrew Starbuck, Robert Jarecki, David Peters,

Longitudinally Multi-slotted Taper for Smooth Transition between Conventional Planar Waveguide and Multi-slotted MMI (pp. 143)
Hamdam Nikkhah, Trevor J. Hall,

What we can Learn from Hybrid Metamaterials Composed of Plasmas (pp. 145)
Osamu Sakai, Akinori Iwai, Alexandre Bambina, Yuuki Kabe, Teruki Naito, Shigeyuki Miyagi,

Magneto-plasmonic metamaterials (pp. 147)
Evangelos Papaioannou,

Controlling the directivity, bandwidth and rate of thermal emission with epsilon-near-zero media (pp. 149)
Inigo Liberal, Nader Engheta,

Silicon Ring Resonator Electro-optical Modulator Utilizing Epsilon-near-zero characteristics of Indium Tin Oxide (pp. 151)
Mahmoud Elgarf, Mohamed Badr, Mohamed Swillam,

Light-induced driving of a micron-size metallic plate (pp. 152)
Min Qiu,

Observation of topologically protected helical edge modes in an elastic waveguide (pp. 153)
Marco Miniaci, R. K. Pal, B. Morvan, M. Ruzzene,

Magnetic spin-orbit interaction of light steers Bloch surface waves (pp. 154)
Mengjia Wang, Hongyi Zhang, Tatiana Kovalevich, Roland Salut, Myun-Sik Kim, Miguel-Angel Suarez, Maria-Pilar Bernal, Hans-Peter Herzig, Huihui Lu, Thierry Grosjean,

Party-Time Symmetry in Chiral Metamaterials (pp. 156)
Maria Kafesaki, Ioannis Katsantonis, Sotiris Droulias, Eleftherios Economou, Costas M. Soukoulis,

Quantum nonlinear effects in metal-insulator-metal plasmonic nanostructures (pp. 158)
Imad Agha, Mallik R. Hussain, Andrew Sarangan, Joseph Haus,

Frenkel Exciton-Polaritons in Organic Photonics (pp. 160)
Boris Fainberg,

Hybrid plasmonic-vanadium dioxide electro-optical switch based modulator (pp. 170)
Mohamed Y. Abdelatty, Mohamed A. Swillam,

Light manipulation through plasmonic metasurfaces based on functional patterns (pp. 172)
Mario Miscuglio, Nicholas J. Borys, Davide Spirito, Beatriz Martin-Garcia, Remo Proietti Zaccaria, Alexander Weber-Bargioni, Roman Krahne,

Compact Silicon Nanowire Ring Resonator Sensor (pp. 173)
Sherif Mohamed, Lamees Shahada, Mohamed Swillam,

Golden dodecapods: a promising nanoresonator for the development of metamaterials active at the optical frequencies (pp. 174)
V. Many, J. Majimel, G. Drisko, S. Mornet, P. Barois, A. Baron, P. Richetti, S. De Cicco, J. Leng, J-B. Salmon, S. Ravaine, E. Duguet, M. Treguer-Delapierre,

A bottom-up Approach Towards Metamaterials and Plasmonics

Novel Photonic Architectures by Nanoimprinting Unconventional Materials (pp. 177)
Camilla Dore, Andre Espinha, Pau Molet, Cristiano Matricardi, Juan Luis Garcia-Pomar, Agustin Mihi,

Large area self-assembled split-nanorod metamaterials (pp. 178)
Mazhar E. Nasir, R. Margoth Cordova-Castro, Jean-Sebastien Bouillard, Pan Wang, Alexey V. Krasavin, Anatoly V. Zayats,

Synthesis of silicon nanoparticles for optically active metamaterials (pp. 180)
Sanaa Semlali, Benoit Cormary, Maria De Marco, Philippe Barois, Patrick Rosa, Mathieu Gonidec, Glenna Drisko,

Can optically-active silicon meta-atoms be produced through bottom-up chemistry? (pp. 182)
Glenna L. Drisko, Sanaa Semlali, Benoit Cormary, Maria Letizia De Marco, Cyril Aymonier, Philippe Barois,

Self-Assembled Metasurfaces and Nanostructured Materials for Linear, Non-Linear and Circular Optical Polarization

Manipulation (pp. 184)
Alessandro Belardini, Grigore Leahu, Emilija Petronijevic, Marco Centini, Roberto Li Voti, Joseph W. Haus, Ventsislav K. Valev, Teemu Hakkarainen, Mircea Guina, Dorota A. Pawlak, Concita Sibilia,

Light scattering from randomly rough metasurfaces with embedded nanoparticles: realizations, low grazing incidence and effective medium theory (pp. 186)
Gerard Berginc,

Advanced Passive and Active Metasurfaces

Waveguided modes, nonlinearity and magneto-optics in self-assembled metamaterials (pp. 196)
Mazhar E. Nasir, Pan Wang, Anton Bykov, Alexey V. Krasavin, Bo Fan, Viktor A. Podolskiy, Anatoly V. Zayats,

Numerical Optimisation and Near-Field Phase Transformation in Metasurface Design for Resonant Cavity Antennas (pp. 198)
Karu P. Esselle, Muhammad U. Afzal, Maria Kovaleva, Ali Lalbakhsh,

Enhanced spin-orbit interaction and all-optical modulation by subwavelength near-zero index media (pp. 200)
Andrea Marini, Alessandro Ciattoni, Carlo Rizza,

Optical chiral effects in ENZ ultrathin slabs (pp. 202)
Carlo Rizza, Xin Li, Andrea Di Falco, Elia Palange, Andrea Marini, Alessandro Ciattoni,

Multipole Contribution into Resonant Scattering of Dielectric Nonspherical Nanoparticles (pp. 204)
Yongqian Li, Yueyue Chen, Yujie Yang, Zili Zhou, Xiaoying Li, Ji Wang,

Optical Metamaterials with Emerging Mxenes (pp. 206)
Krishnakali Chaudhuri, Zhuoxian Wang, Mohamed Alhabeb, Xiangeng Meng, Shaimaa Azzam, Alexander Kildishev, Young L. Kim, Vladimir Shalaev, Yury Gogotsi, Alexandra Boltasseva,

Tailorable nanophotonic devices with ultra-thin transition metal nitrides (pp. 208)
Deesha Shah, Alessandra Catellani, Harsha Reddy, Nathaniel Kinsey, Vladimir Shalaev, Arrigo Calzolari, Alexandra Boltasseva,

Highly Nonlinear III-V Semiconductor Metasurfaces (pp. 210)
Polina Vabishchevich, Sheng Liu, Aleksandr Vaskin, John L. Reno, Gordon A. Keeler, Gregory M. Peake, Michael B. Sinclair, Isabelle Staude, Igal Brener,

Active Mid-Infrared Plasmonics in Graphene (pp. 213)
Min Seok Jang,

Multiple-DWDM-channel heralded single-photon source based on a periodically poled lithium niobate waveguide (pp. 214)
Tong Xiang, Yuanhua Li, Yuanlin Zheng, Xianfeng Chen,

Tunable zero-index and metasurface optics in extreme optical platforms (pp. 216)
Jingyi Yang, Aleksei Anopchenko, Long Tao, Sudip Gurung, Subhajit Bej, Catherine Arndt, Khant Minn, Ho Wai Howard Lee,

Fano Resonances in Optics and Microwaves: Physics and Application

Fano resonance generation and application of three dimensional metamaterials (pp. 220)
Shengyan Yang, Zhe Liu, Junjie Li, Changzhi Gu,

Electromagnetically induced transparency in a superconducting qubit (pp. 222)

Tiefu Li,

Magnetostatic resonances in subwavelength particles: Eigenvalue problem and bound states in microwave continuum (pp. 223)
Eugene Kamenetskii,

Bound States in the Continuum in tri-layer Photonic Crystal slab (pp. 225)
Li Liangsheng, Hongcheng Yin,

On bound states in the continuum in dielectric gratings (pp. 227)
Evgeny N. Bulgakov, Dmitrii N. Maksimov,

Localized field control by plasmonic mode interference (pp. 229)
Keiji Sasaki, Hideki Fujiwara,

Fano resonances in photonics (pp. 231)
Mikhail Limonov,

Fano resonances and supercavity modes (pp. 233)
Mikhail Rybin, Kirill Koshelev, Zarina Sadrieva, Kirill Samusev, Andrey Bogdanov, Yuri Kivshar, Mikhail Limonov,

Hematite in the hot spot: trapping surface plasmons in ultrathin semiconductor films for water splitting (pp. 235)
Alberto Naldoni, Aveek Dutta, Stepan Kment, Radek Zboril, Alexandra Boltasseva, Vladimir M. Shalaev,

Quantum state control in single quantum dots and the coupling with photonic crystal cavities (pp. 237)
Chenjiang Qian, Kai Peng, Xiulai Xu,

Bound States in the Continuum Surrounded by Ultra-strong Resonances (pp. 239)
Lijun Yuan, Ya Yan Lu,

Experimental observation of bound state in the continuum in 1D chain of dielectric disks at GHz frequencies (pp. 241)
Mikhail Balyzin, Zarina Sadrieva, Mikhail Belyakov, Polina Kapitanova, Almas Sadreev, Andrey Bogdanov,

Applications of plasmonic near-perfect absorbers in Chemistry (pp. 243)
Timothy Connell, Kevin Q. Xiao, Jasper J. Cadusch, Anthony Chesman, Ann Roberts, Timothy J. Davis, Daniel E. Gomez,

Light scattering treated by the resonant-state expansion (pp. 245)
Sergey Lobanov, Wolfgang Langbein, Egor Muljarov,

Four-wave mixing in Epsilon-Near-Zero Aluminum Zinc Oxide (pp. 247)
Enrico Giuseppe Carnemolla, Vincenzo Bruno, Matteo Clerici, Stefano Vezzoli, Clayton DeVault, Lucia Caspani, Alexandra Boltasseva, Vladimir Shalaev, Daniele Faccio, Marcello Ferrera,

Multichannel Optical Encryption based on Dielectric Metasurface (pp. 249)
Hang Feng, Fengliang Dong, Lihua Xu, Bo Wang, Zhiwei Song, Xianfeng Zhang, Lanqin Yan, Xiaojun Li, Weiguo Chu, Yan Li,

Guiding electromagnetic waves through the bound states in the radiation continuum in novel types of fibers (pp. 250)
Evgeny N. Bulgakov, Almas Sadreev, Evgeny Bulgakov,

Photo/Thermal Conversions and their Applications

Plasmonic Membranes: Control of Fluid Flow through Light (pp. 253)

Ana Sousa-Castillo, Leonardo N. Furini, Brylee David B. Tiu, Peng-Fei Cao, Begum Topcu, Miguel Comesana-Hermo, Benito Rodriguez-Gonzalez, Walid Baaziz, Ovidiu Ersen, Rigoberto C. Advincula, Moises Perez-Lorenzo, Miguel A. Correa-Duarte,

Thermoplasmonic metasurfaces for energy applications - Solar-heated windows and energy harvesting from random light fluctuations (pp. 255)
Magnus Jonsson,

Opto-Thermal Nano-Tools for Advanced Materials and Life Sciences (pp. 256)
Linhan Lin, Yuebing Zheng,

Resonant laser printing of optical metasurfaces (pp. 258)
Xiaolong Zhu, N. Asger Mortensen, Uriel Levy, Anders Kristensen,

Narrow-band thermal emitter by coupling of cavity and Tamm plasmon resonances (pp. 260)
Zhiyu Wang, J. Kenji Clark, Ya-Lun Ho, Bertrand Vilquin, Hirofumi Daiguji, Jean-Jacques Delaunay,

Structural Color for Displays and Imaging

Hybrid organic and plasmonic systems for smart surfaces and energy-efficient displays (pp. 263)
Magnus Jonsson,

Plasmonic Pixel: Progress in nanoimprint lithography (pp. 264)
Faris Shahidan, Jingchao Song, Evgeniy Panchenko, Paul Mulvaney, Timothy D. James, Ann Roberts,

Metal free, X-ray fabricated metamaterials reproduce full CYMK chromaticity system with 80 nm spatial resolution (pp. 266)
Marcella Bonifazi, Valerio Mazzone, Andrea Fratalocchi,

Skin-like Full-Color Angle Independent Plasmonic Reflective Displays (pp. 268)
Daniel Franklin, Debashis Chanda,

Dual-color plasmonic filters (pp. 273)
Esmaeil Heydari, Justin Sperling, Steven Neale, Alasdair W. Clark,

Structural colors for practical applications (pp. 275)
Chengang Ji, L. Jay Guo,

Nanophotonics and Plasmonics Based on Graphene and Related 2D Materials

Actively tuning the topological valley edge states in photonic boron nitride structure via carrier photo-injection (pp. 278)
Zhiwei Guo, Haitao Jiang, Yunhui Li, Hong Chen,

Plasmonically Enhanced Schottky Solar Cell (pp. 280)
Mohamed Farhat, Fahhad Alharbi, Pai-Yen Chen,

Micron-sized phase-matching-free parametric oscillators based on two-dimensional semiconductors (pp. 282)
Andrea Marini, Alessandro Ciattoni, Carlo Rizza, Claudio Conti,

Sensitivity of all dielectric layered metastructures on a scale below the periodicity (pp. 284)
Agnes Maurel, Jean-Jacques Marigo,

2D semiconductors for nanophotonics (pp. 286)
Alberto G. Curto,

Theoretical Study of Resonance Effects in Graphene-Based Double Ring Resonator (pp. 287)
Cristiano Braga, Geraldo Melo, Gianni Portela, Victor Dmitriev,

New graphene-based circulators and switches for THz region (pp. 291)
Victor Dmitriev, Wagner Castro, Samara Matos, Sergio Rabelo,

Strong light-graphene interaction in graphene/hBN heterostructures based electro-optic modulator on silicon photonics (pp. 298)
Binbin Wang, Sylvain Blaize, Jinbong Seok, Sera Kim, Heejun Yang, Rafael Salas-Montiel,

Wave Propagation in Acoustic and Elastic Metamaterials: Novel Design and Practical Applications

Controlling Reverberating Sound with an Acoustic Metasurface (pp. 301)
Guancong Ma,

Lamb wave focusing by a plano-concave aspherical lens: numerical studies (pp. 303)
Pawel Kudela, Wieslaw Ostachowicz,

Losses in gradient acoustic rainbow trapping metamaterials (pp. 305)
Tuo Liu, Shanjun Liang, Fei Chen, Jie Zhu,

Soft Acoustic Metamaterials: from 3D locally resonant metafluids to soft porous gradient index metasurfaces (pp. 307)
Thomas Brunet, Olivier Poncelet, Christophe Aristegui, Jacques Leng, Olivier Mondain-Monval,

Extraordinary wave dynamics in time-Floquet acoustic systems (pp. 308)
Theodoros Koutserimpas, Romain Fleury,

Tunable Perfect Absorbers for Low-Frequency Sound (pp. 310)
Sibo Huang, Xinsheng Fang, Xu Wang, Badreddine M. Assouar, Qian Cheng, Yong Li,

Lossy Acoustic Materials with Independent Control of Phase and Amplitude for High-quality Manipulation of Airborne Sound (pp. 312)
Bin Liang, Yi-Fan Zhu, Xue-Feng Zhu, Jian-Chun Cheng,

Band structures of a 1D tunable piezoelectric phononic crystal coupled to a 2D-periodic dispersive electric circuit (pp. 314)
Olivier Poncelet, Alexander Shuvalov, Anton Kutsenko,

Negative refraction and double negativity for acoustic waves in three-dimensional bubble metamaterials (pp. 316)
John Hilton Page, Maxime Lanoy, Geoffroy Lerosey, Fabrice Lemoult, Arnaud Tourin, Valentin Leroy,

Air-coupled ultrasound manipulation and laser vibrometry for damage detection in plate-like structures (pp. 318)
Maciej Radzienski, Pawel Kudela, Michal Jurek, Wieslaw Ostachowicz,

Conversion of surface waves in a forest of trees (pp. 320)
Kim Pham, Sebastien Guenneau, Agnes Maurel, Jean-Jacques Marigo,

Parity-Time and Related Symmetries in Photonics, Plasmonics, Acoustics

Active plasmonic and PT symmetric structures for broadband amplified non-reciprocity (pp. 323)
Maude Amyot-Bourgeois, Elham Karami Keshmarzi, Choloong Hahn, Youngsun Choi, Jae Woong Yoon, Niall Tait, Seok Ho Song, Pierre Berini,

Broadband time-asymmetric silicon-photonic architecture grounded on non-Hermitian wave dynamics near exceptional points (pp. 324)
Jae Woong Yoon, Youngsun Choi, Choloong Hahn, Ki-Yeon Yang, Jeong Yub Lee, Gunpyo Kim, Jong Kyun Hong, Yeonghwa Ryu, Seok Ho Song, Pierre Berini,

Asymmetric Optical Effects in Hyperbolic Media (pp. 325)
Rair Macedo, Thomas Dumelow, Robert L Stamps,

Three-wave mixing of guided contra-propagating electromagnetic waves in hyperbolic metamaterials: shaping light (pp. 327)
Victor A. Tkachenko, Vitaly V. Slabko, Sergey A. Myslivets, Alexander K. Popov,

PT-symmetry of magnetostatic resonances in subwavelength ferrite particles (pp. 329)
Eugene Kamenetskii,

Exceptional points in non-Hermitian optical system (pp. 331)
Qingjie Liu, Bing Wang, Peixiang Lu,

Extraordinary Topological Effects and Singular Plasmonics

Nanostructured magnetoplasmonic metamaterials: from extreme bio-sensing to active control of light polarization states at the nanoscale (pp. 334)
Nicolo Maccaferri,

Meta-atoms for arbitrary tuning of plasmonic vortex by using geometric and detour phase multiplexing (pp. 335)
Seung-Yeol Lee, Seong-Won Moon, Gun-Yeal Lee, Byoungho Lee,

Far-field Polarization Singularities of a Dipolar Emitter (pp. 337)
Sergey Nechayev, Martin Neugebauer, Martin Vorndran, Gerd Leuchs, Peter Banzer,

Interaction of an Individual Chiral Nanostructure with Light Carrying Orbital Angular Momentum (pp. 339)
Peter Banzer,

Optical momentum, angular momentum, and helicity in plasmonic and dielectric structures (pp. 340)
Konstantin Y. Bliokh, Aleksandr Y. Bekshaev, M. F. Picardi, F. Alpeggiani, F. J. Rodriguez-Fortuno, L. Kuipers, Franco Nori,

High index dielectric nanostructures: From directional scattering to electric/magnetic local density of optical states control (pp. 342)
Peter R. Wiecha, Bruno Masenelli, GÃ©rard Colas des Francs, Franck Fournel, Vincent Larrey, Thierry Baron, AurÃ©lie Lecestre, Guilhem Larrieu, Arnaud Arbouet, Christian Girard, Vincent Paillard, Aurelien Cuche,

Plasmonics: Fundamentals and Applications

One Particle, Three Superlattices: Configuring Particle Superlattice for Enhanced Raman Spectroscopy (pp. 345)
Xing Yi Ling,

On-chip plasmon-induced transparency and device applications (pp. 346)
Xiaoyong Hu,

Atomic-Scale Plasmonic Hot-Spots: A Frequency-Domain Existential Proof and Unusual Photo-Chemical Activities (pp. 347)
Hyun-Hang Shin, Gyu Jin Yeon, Han-Kyu Choi, Sang-Min Park, Kang Sup Lee, Zee Hwan Kim,

Cavity QED based on plasmon nanostructures (pp. 348)
Ying Gu, Juanjuan Ren, Fan Zhang, He Hao, Qihuang Gong,

Plasmonic Anderson localization in correlated disorder (pp. 349)
Ruwen Peng, Wenbo Shi, Renhao Fan, Mu Wang,

Plasmonics for Optical Information Processing (pp. 350)
Lukas Wesemann, Kalpana Singh, Evgeniy Panchenko, Daniel E. Gomez, Timothy J. Davis, Ann Roberts,

Lasing at K-point in plasmonic honeycomb lattice (pp. 352)
Rui Guo, Marek Necada, Aaro Vakevainen, Tommi Hakala, Paivi Torma,

Mapping photoemission and hot-electron emisssion from plasmonic nanoantennas (pp. 353)
Richard Hobbs, William Putnam, Arya Fallahi, Yujia Yang, Franz Kartner, Karl Berggren,

Emerging materials for plasmonics (pp. 355)
Jerome Plain,

Modulation of chiral optical responses in hybrid nanostructures (pp. 357)
Wei Zhang,

Surface-enhanced Circular Dichroism in the Nanostructure/chiral Medium Hybrid System (pp. 359)
SeokJae Yoo, Q-Han Park,

Driving Plasmonic Nanocircuits With Antenna-coupled Tunnel Junctions (pp. 361)
Surya Prakash Gurunarayanan, Jente Vandersmissen, Marc Heyns, Iuliana P. Radu, Pol van Dorpe, Niels Verellen,

Shaping Light with an Inclusion: Contribution of Multipoles in Scattering Effect on Waveguide (pp. 363)
Alina Karabchevsky, Yuriy A. Artemyev, Nikita Volsky, Alexey A. Basharin, Alexander S. Shalin,

Shaping Light Using Photonic Integrated Devices

A phase-shifted Solc-type filter based on periodically poled lithium niobate in a reflective geometry (pp. 366)
Tingting Ding, Yuanlin Zheng, Xianfeng Chen,

Optical Vortices Generation with Metallic Nano-Slit (pp. 368)
Xue Feng, Xuesi Zhao, Yidong Huang,

Nonlinear Metasurface for Simultaneous Control of Spin and Orbital Angular Momentum (pp. 369)
Guixin Li,

Integrated OAM Laser at Telecom Wavelengths (pp. 371)
Changzheng Sun, Juan Zhang, Bing Xiong, Jian Wang, Zhibiao Hao, Lai Wang, Yanjun Han, Hongtao Li, Yi Luo, Takuo Tanemura, Yoshiaki Nakano, Xinlun Cai, Siyuan Yu,

Light wavefront manipulation using dielectric metasurfaces (pp. 373)
Yan Li, Bo Wang, Qitong Li, Dong Yang, Hang Feng, Qihuang Gong,

Advances in Shaping Light Using Photonic Metasurfaces (pp. 375)
Jian Wang,

Flexibly Tunable Valley Polarized Exciton-Plasmon Polaritons in 2-dimensional Semiconductors (pp. 377)
Boyang Ding, Zhepeng Zhang, Yu-Hui Chen, Yanfeng Zhang, Richard John Blaikie, Min Qiu,

3D Printing for Photonics, Metamaterials, and Energy Applications

Three-Dimensional Photonic Devices Functionalized With CdS Quantum Dots (pp. 380)
Ioanna Sakellari, Elmina Kabouraki, Dimitris Karanikolopoulos, Sotiris Droulias, David Gray, Panagiotis Loukakos, Maria Vamvakaki, Maria Farsari,

Nonlinear Metasurfaces and Plasmonics

Second harmonic generation enhancement by Mie resonances in individual barium titanate nanoparticles (pp. 383)
Churong Ma, Jiahao Yan, Yingcong Huang, Guowei Yang,

Broadband Achromatic Optical Metasurface Devices (pp. 385)
Shuming Wang, Pin Chieh Wu, Vin-Cent Su, Yi-Chieh Lai, Cheng Hung Chu, Jia-Wern Chen, Shen-Hung Lu, Ji Chen, Beibei Xu, Chieh-Hsiung Kuan, Tao Li, Shining Zhu, Din Ping Tsai,

Nonlinear Spin-Orbital Angular Momentum Interaction in Plasmonic Nanostructures (pp. 386)
Xiaoyan Y. Z. Xiong, Li-Jun Jiang, Wei E. I. Sha, Ahmed Al-Jarro, Nicolae C. Panoiu, Weng Cho Chew,

Giant Optical Chirality in a Quasi-3D Meta-structure (pp. 388)
Jiafang Li, Ximin Tian, Zhiguang Liu,

Phase control of second harmonic generation from metasurfaces composed of complementary split ring resonators (pp. 390)
Xin Yang, Zhuo Chen, Zhenlin Wang,

Hide and Seek in the Polarization Profile of a Laser Beam (pp. 392)
Xianzhong Chen, Fuyong Yue, Shuang Zhang,

Fano resonance enhancement using fishnet metamaterials (pp. 394)
Jiaxin Bao, Libang Mao, Tun Cao,

Magnetic Hyperbolic Metasurface (pp. 396)
Yihao Yang, Peifei Qin, Bin Zheng, Huaping Wang, Lian Shen, Hongsheng Chen,

Plasmonic enhancement and manipulation of optical nonlinearity in monolayer WS2 (pp. 397)
Jinwei Shi, Wei-Yun Liang, Hyeyoung Ahn, Soniya S. Raja, Yungang Sang, Xin-Quan Zhang, Chun-An Chen, Yanrong Wang, Xinyue Yang, Yi-Hsien Lee, Shangjr Gwo,

Enhancement of nonlinearity at interfaces with discontinuous second-order susceptibility (pp. 399)
Yuanlin Zheng, Xiaohui Zhao, Xianfeng Chen,

Active Plasmonics Based on Liquid Crystals (pp. 401)
Yanjun Liu, Shengtao Yin, Dong Xiao, Guixin Li, Dan Luo, Wei Ji, Shouzhen Jiang, Xiaowei Sun,

Guide Mode Enhanced Third Harmonic Generation in Silicon Metasurfaces (pp. 403)
Shumei Chen, Mohsen Rahmani, King Fai Li, Andrey Miroshnichenko, Thomas Zentgraf, Guixin Li, Dragomir Neshev, Shuang Zhang,

External control of multipolar third harmonic generation from arrays of dielectric-metal core-shell resonators (pp. 405)
Xin Yang, Chi Zhang, Lina Qian, Zhi-Qin Li, Ping Gu, Zhuo Chen, Zhenlin Wang,

Optimal double resonant condition in metallic core-shell nanocavity for third harmonic generation (pp. 407)
Wenbo Zang, Lingling Fan, Guangxu Su, Xin Yang, Mingyu Ma, Peng Zhan, Zhuo Chen, Zhenlin Wang,

Engineering optical responses of plasmonic objects with a hyperbolic coating (pp. 409)
Pan Wang, Alexey Krasavin, Francesco Viscomi, Ali Adawi, Jean-Sebastien Bouillard, Diane Roth, Giovanni Sartorello, Anatoly Zayats,

All-optical dynamic metasurface for terahertz wave-front modulation (pp. 411)
Yan Zhang, Jingying Guo, Teng Wang, Xinke Wang,

Metasurface-assisted plasmonic wavefront modulation with incident polarization (pp. 413)
Luping Du, Chonglei Zhang, Jiao Lin, Xiaocong Yuan,

Wavefront engineering based on complex amplitude modulation with metasurfaces (pp. 415)
Lingling Huang, Xu Song, Ruizhe Zhao, Yongtian Wang, Thomas Zentgraf,

Highly uniform and controllable metasurface structures fabricated by shaped femtosecond laser: Fundamentals and Applications (pp. 417)
Xiaowei Li,

Controlling Light by Metasurfaces in the Linear and Nonlinear Regimes (pp. 419)
Mengxin Ren, Di Zhang, Ninghui Gao, Wei Wu, Jingjun Xu,

Unidirectional Second-Harmonic Generation with Plasmonic Nanoresonator Dimers (pp. 421)
Shao-Ding Liu, Dangyuan Lei,

Refractometric Sensing Using Gradient Plasmonic Nanostructures: Mapping Spectral Information to Spatial Patterns (pp. 423)
Wen-Di Li, Siyi Min, Shijie Li, Zhouyang Zhu, Chuwei Liang, Jingxuan Cai,

Interfacial Solar Steam Generations: Materials, Structures and Applications (pp. 425)
Jia Zhu,

Linear frequency conversion via sudden merging of resonances in time-variant metasurfaces (pp. 426)
Kanghee Lee, Jaehyeon Son, Jagang Park, Byungsoo Kang, Wonju Jeon, Fabian Rotermund, Bumki Min,

Lock-in study of acoustic waves through a lead phononic plate (pp. 428)
Cesar Alejandro Torres-Torres, Carlos Roberto Santillan-Rodriguez, Renee Joselin Saenz- Hernandez, Maria Eugenia Botello-Zubiate, Maria Cristina Grijalva-Castillo, JosÃ© Andres Matutes Aquino,

Electrically Small Resonators-Based Infrared Imaging Pixel Configuration (pp. 430)
Mohammed R. AlShareef, Mohamed Ramy Abdel-Rahman,

Generation and Enhancement of UV-Harmonic Wave at Nonlinear Interfaces (pp. 432)
Xiaohui Zhao, Yuanlin Zheng, Yanqi Gao, Yong Cui, Daxing Rao, Xianfeng Chen,

Direct visualization of momentum conversation through second harmonic Fourier image in 1D waveguide (pp. 434)
Junjun Shi, Yang Li, Meng Kang, Shunping Zhang, Hongxing Xu,

Transformation Optics and Other Waves: Novel Physics and Practical Applications

Magnetic invisible cloak without superconductor (pp. 437)
Wei Jiang, Jianfei Zhu, Yungui Ma,

Optical Spacetime in Self-Assembled Hyperbolic Metamaterials (pp. 438)

Igor I. Smolyaninov, Vera N. Smolyaninova,

Chirality and Cartan's torsion in transformation optics (pp. 440)
Yongliang Zhang, Che Ting Chan, Kin Hung Fung,

Controlling Surface Plasmons by Covariant Curved Spaces in One-dimensional Transformation Optical Nanostructures (pp. 442)
Fan Zhong, Jensen Li, Hui Liu, Shining Zhu,

Optical orbital angular momentum generated in a metamaterial ring by transformation optics (pp. 443)
Mu Wang, Hongwei Wu, Renhao Fan, Ruwen Peng,

Definite Light Deflection of Cosmic Topological Defects Mimicked By Rotational Metasurfaces (pp. 444)
Chong Sheng, Ying Chen, Zhiwei Yan, Lin Xu, Xiangyang Wang, Qing Huo Liu, Shining Zhu, Huanyang Chen, Hui Liu,

Lightcone fluctuations in a metamaterial that mimics a cosmic string (pp. 446)
Jiawei Hu, Hongwei Yu,

Light in Transformed Spaces: Optical Black Holes and Nanofocusing Lenses (pp. 448)
Alexander V. Kildishev, Lian Shen, Hongsheng Chen, Ludmila J. Prokopeva,

A phase space plot of resonances in transformation cavities (pp. 450)
Inbo Kim, Jinhang Cho, Yushin Kim, Bumki Min, Sang-Jun Park, Muhan Choi,

Quantum Nanophotonics for Applications in Quantum Information Science

Near-optimal entangled-photon sources in the solid state? (pp. 453)
Fei Ding,

Nonlinear AlGaAs nanodisks as sources of sum-frequency light and entangled photons (pp. 455)
Giuseppe Marino, Alexander S. Solntsev, Lei Xu, Valerio F. Gili, Luca Carletti, Alexander N. Poddubny, Mohsen Rahmani, Daria Smirnova, Haitao Chen, Guoquan Zhang, Anatoly V. Zayats, Costantino De Angelis, Giuseppe Leo, Yuri S. Kivshar, Andrey A. Sukhorukov, Dragomir N. Neshev,

In(Ga)As quantum dots at the telecom wavelength: single and entangled photons emission (pp. 457)
Simone L. Portalupi, Fabian Olbrich, Marc Sartison, Stephan Hepp, Cornelius Nawrath, Sascha Kolatschek, Michael Jetter, Peter Michler,

Combining Laser 3D Printing with Self-Assembly (pp. 459)
Maria Farsari, Argyro Klini, Argyro N. Giakoumaki, George Kenanakis,

A Bright Triggered Twin-Photon Source in the Solid State (pp. 461)
Tobias Heindel, Alexander Thoma, Martin von Helversen, Marco Schmidt, Alexander Schlehahn, Manuel Gschrey, Peter Schnauber, Jan-Hindrik Schulze, Andre Strittmatter, Jorn Beyer, Sven Rodt, Alexander Carmele, Andreas Knorr, Stephan Reitzenstein,

Quantum Dots in Nanowires Tuned to Atomic Transitions (pp. 463)
Nika Akopian,

Towards practical single-photon sources at telecom wavelengths with GaAs-based deterministic QD-mesas (pp. 464)
Anna Musial, Lukasz Dusanowski, Pawel Holewa, Pawel Mrowinski, Aleksander Marynski, Krzysztof Gawarecki, Tobias Heuser, Nicole Srocka, David Quandt, AndrÃ© Strittmatter, Sven Rodt, Stephan Reitzenstein, Grzegorz Sek,

Advanced Numerical and Theoretical Tools as Applied to Materials for Photonics

Effective-Medium Permittivity of Planar One-Dimensional Gratings of Vertically Invariant and Laterally Arbitrary Permittivity Distribution (pp. 467)
Lifeng Li,

Novel Guided Wave Configurations with Nanostructures for Emerging Applications

Si Nanostrip Optical Waveguide for Molecular Overtone Spectroscopy (pp. 469)
Aviad Katiyi, Alina Karabchevsky,

Metamaterial substrates for optomechanical applications (pp. 471)
Aliaksandra Ivinskaya, Natalia Kostina, Mihail I. Petrov, Andrey A. Bogdanov, Sergei Sukhov, Pavel Ginzburg, Alexander S. Shalin,

Low-contrast photonic hook manipulator for cellular differentiation (pp. 473)
Angeleene Ang, Igor Minin, Oleg Minin, Sergey Sukhov, Alexander Shalin, Alina Karabchevsky,

Coupling of Phononic Cavities in a Corrugated Nanobeam and Control of Transmission (pp. 475)
A. V. Korovin, Y. Pennec, B. Djafari Rouhani,

Residue Number System Arithmetic based on Integrated Nanophotonics (pp. 477)
Jiaxin Peng, Shuai Sun, Vikram K. Narayana, Volker J. Sorger, Tarek El-Ghazawi,

Giant subradiance, strong interactions and positional disorder in metamaterials (pp. 479)
Stewart D. Jenkins, Nikitas Papasimakis, Salvatore Savo, Nikolay I. Zheludev, Janne Ruostekoski,

Bio-Engineered Metamaterials and Plasmonics

Optogenetic, tissue clearing, and viral vector approaches to understand and influence whole-animal physiology and behavior (pp. 482)
Viviana Gradinaru,

Utilising Nature's Biological Toolkit to Control the Enhancement of Raman Scattering through DNA Hybridisation (pp. 484)
Jennifer Gracie, Karen Faulds, Duncan Graham,

Surface Enhanced Raman Scattering-Active Nanoparticle Assemblies for the Probing of Protein-Carbohydrate Interactions and their Applications (pp. 486)
Craig Ward, Karen Faulds, Daniel Bracewell, Duncan Graham,

Fluorous directed facial selectivity of DNA origami structures on surfaces for the assembly of plasmonic nanoparticles (pp. 488)
Sarah Louise Henry, Gabriella Flynn, Andrea Taladriz Sender, Jamie Withers, Nadia Chaher, Glenn Burley, Alasdair Clark,

Functional Materials and Devices for Lighting and Display

Control Photon Dynamics in Circuit Quantum Electrodynamics by Manipulating Qubits through a Phonon Bath (pp. 491)
Fulu Zheng, Yuyu Zhang, Lu Wang, Yadong Wei, Yang Zhao,

Ultra-high sensitive distributed acoustic sensor (DAS) based on distributed micro-structured optical fiber (DMOF) (pp.

493)
Qizhen Sun, Fan Ai, Zhijun Yan, Wei Zhang, Hao Li, Deming Liu,

Dynamically encircling an exceptional point in voltage-controlled LRC resonator circuits (pp. 494)
Youngsun Choi, Jong Kyun Hong, Yeonghwa Ryu, Jae Woong Yoon, Seok Ho Song,

Substrate engineering for super-resolution tip-enhanced Raman spectroscopic imaging (pp. 495)
Evgeniya Sheremet, Ashutosh Mukherjee, Vladimir Kolchuzhin, Alexander Milekhin, Ekaterina Rodyakina, Dietrich R.T. Zahn, Raul D. Rodriguez,

Plasmon-Induced Hot Carrier: Fundamentals and Applications

Broadband hot-electron photodetection based on hotspots-enriched disordered nanosystem (pp. 498)
Qin Chen, Long Wen,

Low Cost Silicon-Based Hot-Electron Photodetector in the Near-Infrared Regime (pp. 500)
Yupei Li, Yusheng Zhai, Guangdian Chen, Zhiyang Qi, Qilong Wang,

Electrical generation of hot electrons in plasmonic nanorod metamaterials (pp. 502)
Pan Wang, Alexey Krasavin, Mazhar Nasir, Wayne Dickson, Anatoly Zayats,

Anisotropic Pt-Au Nanostructure with Plasmonic Hot Electron Transfer for Hydrogen Generation Studied at Single-Particle Level (pp. 504)
Zaizhu Lou,

Plasmon-based nanohybrid structures for SERS and temperature sensing (pp. 506)
Hongxiang Lei,

Plasmon-enhanced electron emission in nano-metallic/semiconductor composites (pp. 508)
Qilong Wang, Zhiyang Qi, Yupei Li, Yusheng Zhai,

Hot-electron generation in plasmonic nanostructures with hot spots: Quantum mechanisms (pp. 510)
Alexander O. Govorov, Lucas V. Besteiro, Xiang-Tian Kong,

Harnessing Acoustic and Elastic Waves via New Materials and Advanced Technologies

Accidental acoustic double Dirac degeneracy emerged by rotating scatterers and the corresponding topological transitions (pp. 512)
Xiang Xie, Honglang Li, Qiuyun Fu, Xuefeng Zhu, Degang Zhao, Wei Luo,

Handed walk of sound in periodically driven systems (pp. 514)
Xue-Feng Zhu, Jie Zhu, Yu-Gui Peng, Ya-Xi Shen,

A Design of Transparent Anisotropic metamaterial for airborne sound (pp. 516)
Weiwei Kan, Menping Guo,

Observation of the Weyl points and Fermi arcs in a chiral phononic crystal (pp. 518)
Feng Li, Xueqin Huang, Jiuyang Lu, Jiahong Ma, Zhengyou Liu,

Valley States and Valley Edge States in Phononic Crystals (pp. 520)
Jiuyang Lu, Chunyin Qiu, Zhengyou Liu,

Soft Metasurface with Gradient Acoustic Index (pp. 522)
Yabin Jin, Raj Kumar, Olivier Poncelet, Olivier Mondain-Monval, Thomas Brunet,

Current Advances in Frequency Selective Surfaces and Metasurfaces

Learning from Nature: Bio-inspired Metasurface Microwave Absorber (pp. 525)
Shubo Wang, C. T. Chan,

Plasmonic components towards photonic-nose (pp. 527)
Yoshiaki Nishijima, Armandas Balcytis, Gediminas Seniutinas, Saulius Juodkazis,

Optical Metasurfaces for Simultaneous Control of Holograms and Twisted Light Beams (pp. 529)
Xianzhong Chen, Chunmei Zhang, Wei Wang,

Surface Acoustic Wave Manipulation by a Phononic Crystal Made of Multilayered Ridges or Pillars (pp. 531)
M. Oudich, Y. Jin, E. H. El Boudouti, B. Bonello, Y. Pennec, F. Sarry, B. Djafari Rouhani,

Metasurfaces: from fundamental ideas of polarization conversion, broadband Huygens' surfaces and topological photonics to applications in magnetic resonance imaging (pp. 533)
Stanislav B. Glybovski, Alena V. Shchelokova, Irina V. Melchakova, Alexey P. Slobozhanyuk, Pavel A. Belov,

Wideband Metamaterial Absorber Made of Composite Materials (pp. 535)
Olivier Rance, Anne-Claire Lepage, Xavier Begaud, Michel Soiron, AndrÃ© Barka, Patrick Parneix,

Advances in Textile (Knitted) Frequency Selective Surfaces (FSS) and Meta-Surfaces (pp. 537)
Alan Tennant, Xiaobin Jia, William Hurley, Tilak Dias,

Plasmonics and Nanophotonics

Optical metasurface based holographic stereogram (pp. 542)
Yun-Seok Choi, Joo-Yun Jung, Min-Kyo Seo,

Optical properties and mid infrared applications of plasmon perfect absorber metasurfaces (pp. 544)
Yoshiaki Nishijima, Armandas Balcytis, Gediminas Seniutinas, Sauliuss Juodkazis,

Frequency discrete diffraction control by photonic gauge potentials (pp. 546)
Chengzhi Qin, Bing Wang, Peixiang Lu,

Active controlled scattering from dielectric nanoantennas in the visible range (pp. 549)
Jiahao Yan, Churong Ma, Yingcong Huang, Guowei Yang,

Realizing Scattering Dark State in a Hybrid System of Germanium Nanogroove and Molecular Excitons (pp. 551)
Yingcong Huang, Churong Ma, Jiahao Yan, Guowei Yang,

Inelastic Relaxation and Thermal Properties in Strongly Coupled Plasmon-Exciton Hybrid Nano Structures (pp. 553)
Martin Claes Wersall, Gulis Zengin, Jorge Cuadra, Tomasz Antosiewicz, Mikael Kall, Timur Shegai,

Local polarization of nano rectangle ring and the spontaneous emission enhancement of a circularly polarized emitter (pp. 555)
Fan Zhang, Juanjuan Ren, Zhao Chen, Xueke Duan, Ying Gu, Qihuang Gong,

Surface electromagnetic waves in a semiconductor with strong magnetic field (pp. 557)
Igor Bychkov, Dmitry Kuzmin, Valentin Tolkachev, Vladimir Shavrov, Vasily Temnov,

Large Enhancement of the Goos-Hanchen shift and Fragmentation of the Reflected Beam due to the Excitation of Surface Plasmons (pp. 559)
Sangbum Kim, Kihong Kim,

Near-field coupling and mode competition in anapole system (pp. 561)
Valerio Mazzone, Juan Sebastian Totero Gongora, Andrea Fratalocchi,

Holographic tracking for real-time spectroscopy of moving nanoparticles (pp. 563)
Minh-Chau Nguyen, Pascal Berto, Fabrice Valentino, Catherine Combellas, Frederic Kanoufi, Gilles Tessier,

Full control of near-field dipolar coupling beyond spin-momentum locking (pp. 565)
Michela F. Picardi, Lei Wei, Jack J. Kingsley-Smith, Anatoly V. Zayats, Francisco J. Rodriguez-Fortuno,

Probing and Controlling Negative Photoconductivity of Plasmonic Nanowire (pp. 567)
Jihye Lee, Jiyoung Yoon, Sang-Heon Park, Jong-Souk Yeo,

Probing Spin-Orbit Interaction via Fano Interference (pp. 569)
Rajesh Desapogu, Dima Cheskis, Shmuel Sternklar, Yuri Gorodetski,

Oscillatory Plasmon-Exciton Coupling and Non-Traditional Plasmonics (pp. 571)
Matthew S. Kirschner, Wendu Ding, Xiao-Min Lin, Lin X. Chen, George C. Schatz, Richard D. Schaller,

Tuning propagation of surface plasmon polariton by geometric phases (pp. 573)
Feng Lin,

Phase resonances in all dielectric compound silicon gratings (pp. 575)
Jian Qiang Liu, Yu Xiu Zhou, Guang Hou Sun, Xia Qin Zeng,

Nanonewton Plasmonic Forces from a 3D Coaxial Nanopillar (pp. 577)
Brandon Terranova, Adam Fontecchio,

Metamaterials and Negative Index Materials

Analysis of solitonic pulse propagation in metamaterials implemented in photonic crystals (pp. 581)
Michelle Savescu, Kaisar Khan,

Multiple toroidal Resonances in Folded Metamaterials (pp. 583)
Shengyan Yang, Zhe Liu, Ling Jin, Wuxia Li, Junjie Li, Shuang Zhang, Changzhi Gu,

Shear Horizontal Wave Propagation in Magnetoelastic Multilayered Plates with Negative-Indexed Piezomagnetic Materials (pp. 585)
Yongqiang Guo, Liangteng Guo,

Negative refraction and negative dispersion due to quadrupole response of finite size particles (pp. 587)
Eugene Fourkal, Andrei Smolyakov,

Plasmon resonances, extraordinary transmission and reflection-less absorption in overdense plasma-diffraction grating structures (pp. 589)
Andrei Smolyakov, N. Sternberg,

Polaritonic light-matter interaction in van der Waals heterostructures (pp. 591)
Itai Epstein,

Double-Epsilon-Near-Zero and Resonant Gain Metal/Dielectric Multilayers (pp. 592)
Vincenzo Caligiuri, Milan Palei, Muhammad Imran, Liberato Manna, Roman Krahne,

Investigation on the optimization of the coding matrix based on the tailor scattering properties of the coding metamaterials (pp. 594)
Shuai Yang, Qun Wu, Yuming Wu, Xumin Ding, Kuang Zhang,

Photonic Crystals, Laser and Cavities

Standing waves with infinite group velocity in temporal photonic crystals (pp. 599)
Juan Sabino Martinez Romero, Peter Halevi,

Ultralow-threshold continuous-wave lasing assisted by a metallic optofluidic resonantor (pp. 601)
Bei Jiang, Hailang Dai, Xianfeng Chen,

Lasing Cavity based on Defect Modes in 2D Groove Metal Array inside MIM Structure (pp. 603)
Seong-Han Kim, Chul-Sik Kee,

An angular study of the diffraction of light from one row of cylinders (pp. 605)
Jesus Daniel Valenzuela-Sau, Raul Garcia-Llamas,

Non-local effect on surface modes of non-reciprocal effective media (pp. 607)
Kai Fung Lee, Raymond Pak Hong Wu, Yong-Liang Zhang, Wang Tat Yau, Kin Hung Fung,

Acoustic Metamaterials

Acoustic Metasurface for Giant Transmission through Water-Air Interface (pp. 610)
Eun Bok, Jong Jin Park, Haejin Choi, Chung Kyu Han, Oliver B. Wright, Sam H. Lee,

Materials for Photonics (Graphene, MoS2, WS2, etc)

Engineering Photon Upconversion with an Optical Cavity (pp. 613)
Ye Yu, Yejing Liu, Joel K. W. Yang, Tobias A. F. Konig, Andreas Fery,

Crystal Growth and optical properties of BaMgF4 single crystal (pp. 615)
Zhuo Wang, Junjie Chen, Yanzhi Ma, Yuanlin Zheng, Xianfeng Chen,

Laser-patterning of graphene oxide beyond the diffraction limit (pp. 617)
Raul D. Rodriguez, Ma Bing, Gennadiy Murastov, Munis Khan, Ashutosh Mukherjee, Zoheb Khan, Suhail Shah, Alexey Ruban, Sergey Pavlov, Anna Lipovka, Ammar Al-Hamry, Olfa Kanoun, Varnika Prakash, Surinder K. Mehta, Evgeniya Sheremet,

Dynamically Tunable Electromagnetically Induced Transparency in Graphene and Split-Ring Hybrid Metamaterial (pp. 619)
Guangxu Su, Zhong Huang, Wenbo Zang, Peng Zhan, Zhenlin Wang,

Highly confined biaxial hyperbolic phonon polaritons in van der Waals crystal of semiconducting transition metal oxides (pp. 621)
Zebo Zheng, Huanjun Chen,

High-efficiency sound collimation with an ultra-thin metastructure (pp. 623)
Jie Hu, Bin Liang, Jun Xiao Qiu,

Direct Observation of Semiconductor-Metal Phase Transition in Bilayer Tungsten Diselenide Induced by Potassium Surface

Functionalization (pp. 625)
Bo Lei, Yuanyuan Pan, Zehua Hu, Jialin Zhang, Du Xiang, Yue Zheng, Rui Guo, Cheng Han, Lianhui Wang, Jing Lu, Li Yang, Wei Chen,

Chiral and Bianisotropic Materials

Metamaterial with magnetism and structural chirality in the deep UV region (pp. 627)
Hiroyuki Kurosawa, Shin-Ichiro Inoue,

Large Area Fabrication of 2D Chiral Plasmonic Nanoparticles (pp. 629)
Vladimir E. Bochenkov,

Broadband and high-efficiency wavefront manipulation based on chiral metamaterials (pp. 631)
Chaoqun Fang, Chao Wu, Zhijie Gong, Song Zhao, Anqi Sun, Zeyong Wei, Hongqiang Li,

Analytical study of the chiral optical potential for dielectric nano-objects (pp. 633)
Hipolito A. Arredondo Champi, Rina H. Bustamante, Walter J. Salcedo,

Plasmonics-Based Devices

Photocurrent transient variation in IGZO phototransistors decorated with Au nanoparticles (pp. 639)
Yusheng Zhai, Guangdian Chen, Yupei Li, Qilong Wang,

Polarization-controlled tunable-focusing of surface plasmon polaritons with nanostructure array (pp. 641)
Mingqian Zhang,

Plasmonic-coupled sensors: from multiphoton-assisted quantum coupling to graphene-coupled subwavelength resonant strain sensors (pp. 642)
Morteza Aramesh, Raphael Tiefenauer, Janos Voros,

Fabrication of plasmonic nanostructure for optical brain imaging (pp. 644)
Ji Suk Kang, Jun Hyun Kim, Zeshan Shoaib, Myung Yung Jeong,

Metamaterial-based devices

Broadband enhancement of light absorption in energy harvesting systems by complex epsilon-near-zero materials (pp. 647)
Marcella Bonifazi, Yi Tian, Andrea Fratalocchi,

Application of Semiconductor into Solar Cells using Lorentzian-Drude Model (pp. 649)
Rifa J. El-Khozondar, Hala Jarallah El-Khozondar, Mohammed M. Shabat,

Quantum Searching with Metamaterials (pp. 651)
Weixuan Zhang, Kaiyang Cheng, Chao Wu, Yi Wang, Hongqiang Li, Xiangdong Zhang,

Plasmonics for Highest-Speed (pp. 653)
Juerg Leuthold, W. Heni, M. Ayata, C. Haffner, A. Messner, U. Koch, C. Hoessbacher, T. Watanabe, Y. Salamin, R. Bonjour, A. Josten, B. Baeuerle, A. Dorodny, P. Ma, Y. Fedoryshyn, M. Burla, D. L. Elder, L. R. Dalton,

Metamaterial based nanobiosensors, nanophotodetectors and perfect absorbers (pp. 655)
Ekmel Ozbay,

Metasurfaces and Flat Optics

Generating of optical vortices by spiral metalenses (pp. 657)
Victor Victorovich Kotlyar, Anton Gennadyevich Nalimov,

High Quality Factor Fano Resonances in All-Dielectric Metasurfaces (pp. 659)
Tanchao Pu, Ziwei Liu, Jiebin Niu, Lina Shi, Changqing Xie,

Correlations of cascaded photons: Two-photon processes in the Mollow regime (pp. 661)
Alexander Carmele, Samir Bounuoar, Max Strauss, Stephan Reitzenstein,

Thin metalens based on subwavelength grating (pp. 663)
Sergey Stafeev, Anton Nalimov, Changyu Hu, Liam O'Faolain, Maria Kotlyar, Desmond Gibson, Shigeng Song, Victor Kotlyar,

Active metasurface for terahertz beam steering (pp. 665)
Sang-Hyeok Mun, Yong-Hoon Lee, Sang-Jun Park, Jinhang Cho, Inbo Kim, Muhan Choi,

3D nanostructuring of functional photopolymers for photonics and sensing (pp. 667)
Safi Jradi, MÃ©lissa Merheb, Ali Issa, Ying Peng, AurÃ©lien Bruyant, Xuan Quyen Dinh, Xiaowei Sun, Renaud Bachelot,

Optical Antennas

Broadband Infrared Refractive Index Measurement Using Plasmonic Antenna Resonance (pp. 670)
Hibiki Kagami, Tomohiro Amemiya, Satoshi Yamasaki, Keisuke Masuda, Zhichen Gu, Nobuhiko Nishiyama, Shigehisa Arai,

Design of plasmonic grating nano structure for enhancing optical imaging system signal (pp. 672)
Junhyun Kim, Jisuk Kang, Zeshan Shoaib, Myung Yung Jeong,

Silicon-based Nanoscale Plasmonic Bowtie Nanoantenna in the Mid-IR (pp. 674)
Hosam Mekawey, Yehea Ismail, Mohamed Swillam,

Strong coupling at SWIR in Photocurrent of Quantum Cascade Infrared Photodetectors Coupled to Metamaterial Nano-antennas (pp. 677)
Matias Katz, Ofir Sorias, Ben Dror, Nicolas Grandjean, Meir Orenstein, Gad Bahir,

Photothermal and Photoelectric Nanophotonics

Biased-modulating photodetector using graphene embedded carbon film/n-Si heterojunction (pp. 680)
Xi Zhang, Luping Du,

Plasmon-Enhanced Photovoltaics, Photocatalysis, and Solar Fuels

3D Multi-scale Nanostructured Plasmonic Materials for Record Efficient Hot-Carriers Based Photocatalysis (pp. 683)
Yi Tian, Francisco Pelayo Garcia de Arquer, Cao-Thang Dinh, Gael Favraud, Marcella Bonifazi, Min Liu, Sjoerd Hoogland, Edward H. Sargent, Andrea Fratalocchi,

Partially-Embedded Plasmonic Nanoparticles within Semiconductors for Enhanced Hot Electrons Extraction (pp. 685)
Charlene Ng, Peng Zeng, Julian Lloyd, Ann Roberts, Trevor A. Smith, Udo Bach, Timothy J. Davis, Andreas Fery, Daniel E. Gomez,

Quantum Photonics

Some electronic transport properties of nanostructure HgTe/CdTetype III superlattice for mid infrared and terahertz detection (pp. 688)
Nassima Benchtaber, Abdelhakim Nafidi, Abderrazak Boutramine, Driss Barkissy, Rachid Ben Koujan, Fatiha Chibane,

Es-SaÃ¯d Es-Salhi,

Bands structure and electro-optical properties in ternary InAs/GaInSb type II superlattice for LWIR photodetection (pp. 694)
Nassima Benchtaber, Abdelhakim Nafidi, Driss Barkissy, Abderrazak Boutramine, Rachid Ben Koujan, Es-SaÃ¯d Es-Salhi, Fatiha Chibane,

Biophotonics

On-Chip Sensing and Multiplexing Platform for miRNA in Cancer Cell based on Nanoplasmonics (pp. 701)
Sang-Heon Park, Jihye Lee, Jong-Souk Yeo,

Transformational Electromagnetics, Cloaking

Cloaking a magnetic sensor (pp. 704)
Rosa Mach-Batlle, Carles Navau, Alvar Sanchez,

CMA-ES based topology optimization for external cloaks (pp. 706)
Garuda Fujii,

FSS, HIS and Extraordinary Transmission

Extraordinary Transmission in Mid-IR through a perforated doped silicon film (pp. 709)
Hosam Mekawey, Yehea Ismail, Mohamed Swillam,

Modeling, Computational Techniques and Verification of Theory

2D-3D coupled spectral element method for modelling of guided waves propagation in a composite plate (pp. 713)
Piotr Fiborek, Pawel Kudela, Wieslaw Ostachowicz,

A Theoretical, Numerical and Experimental Analysis of Adhesive Bond Effect on Lamb Wave Propagation in Sandwich Structure (pp. 715)
Shirsendu Sikdar, Wieslaw Ostachowicz,

Near Optimal Freeform Inverse Design Approach For Future Metastructures (pp. 717)
Mohammad Haghtalab, Federico Capasso, Safieddin Safavi-Naeini,

An asynchronous FDTD solver for efficient simulations in nanophotonics (pp. 719)
Sergei Belousov, Sergey Khilkov, Vadim Levchenko, Anastasia Perepelkina, Ilya Valuev,

Modal Analysis of Cylindrical Waveguides with 2D Metamaterial Wall (pp. 721)
Lucille Kuhler, Gwenn Le Fur, Luc Duchesne, Nathalie Raveu,

Emerging Applications

Artificial Intelligence Based Complex ENZ Network Nanomaterials for Large Scale Microprinting, Broadband Holograms and Bio-imaging (pp. 728)
Gael Favraud, Marcella Bonifazi, Valerio Mazzone, Yi Tian, Andrea Fratalocchi,

Nanofabrication Technology

Spectroscopic Analysis of Structural Colour Reflectors of Helical nanostructures (pp. 731)
Taewoo Ha, Wongi Park, Teun-Teun Kim, Anna Zep, Hyungju Ahn, Tae Joo Shin, Damian Pociecha, Kyung Ik Sim, Taek Sun

Jung, Jae Hoon Kim, Ewa Gorecka, Dong Ki Yoon,

Plenary Lectures

Catching Light with Metamaterials

Vladimir M. Shalaev

[1]School of Electrical and Computer Engineering, Purdue University, West Lafayette IN, USA
*corresponding author, E-mail: shalaev@purdue.edu

Abstract

In this presentation, emerging plasmonic, metamaterial and metasurfaces concepts as well as material platforms will be discussed with the focus on practical photonic technologies for communication, quantum optics, bio-medical and energy applications.

X-Y-Z-T Metamaterials

Nader Engheta

Department of Electrical and Systems Engineering, University of Pennsylvania, Philadelphia, Pennsylvania, 19104, USA
E-mail: engheta@ee.upenn.edu

Abstract

In this talk, I will present an overview of our ongoing efforts in exploring four-dimensional "X-Y-Z-T Metamaterials", i.e., the metastructures in which the material parameters can vary with time as well as with space. We will show how some of the exciting features such as "freezing and growing waves" in combination with the non-Foster circuits, temporal effective parameters, temporal anti-reflection matching, etc. can be obtained by proper combinations of temporal and spatial variations of parameters in metamaterials. We will also show how we can expand this 4D metamaterials concept to higher-dimensional metamaterials using temporal anisotropy, which leads to other exciting features such as "rainbow radiation". I will discuss some of our most recent results from my group and forecast future directions and potentials.

The Present and Future of Flat Optics: from Metalenses to Polarization Metaoptics and Arbitrarily Structured Light

Federico Capasso

John A. Paulson School of Engineering and Applied Sciences
Harvard University, Cambridge, MA 02138
capasso@seas.harvard.edu

Abstract

Metasurfaces enable the redesign of optical components into thin, planar and multifunctional elements, promising a major reduction in footprint and system complexity as well as the introduction of new optical functions including arbitrary wavefront control.[1,2] The planarity of flat optics will lead to the unification of semiconductor manufacturing and lens-making,[3] where the planar technology to manufacture computer chips will be used to make CMOS compatible metasurface-based optical components, ranging from metalenses[4-6] to novel polarization optics[7], areas where I foresee the greatest technological and scientific impact.[8] New polarization optics results on an ultracompact metasurface polarimeter and polarization state generator, will be presented and applications to polarization sensitive imaging for a wide range of applications will be discussed. Finally structured light generation with metasurfaces based on J-Plates for arbitrary spin to orbital angular momentum converter will be discussed [9], along with the general problem of arbitrary vector beam generation.

1. N. Yu et al. *Science* **334**, 333 (2011)
2. N. Yu and F. Capasso *Nature Materials* **13,** 139 (2014)
3. A. She et al. *Optics Express* **26**, 1573 (2018)
4. M. Khorasaninejad et al. *Science* **352**, 1190 (2016)
5. M. Khorasaninejad and F. Capasso, Science ***358*,** 8100 (2017)
6. W-T. Chen et al. *Nature Nanotechnology* **13**, 220 (2018)
7. J. P. B. Mueller et al. *Physical Review Letters* **118**, 113901 (2017)
8. F. Capasso, *Nanophotonics,* **DOI:** 10.1515/nanoph-2018-0004, Feb. 14, 2018
9. R. C. Devlin et al. *Science* **358,** 896 (2017)

Evolutionary metamaterials: the imitation game of Nature for renewable energy harvesting, artificial intelligent photonics and advanced material engineering

Andrea Fratalocchi

King Abdullah University of Science and Technology, Saudi Arabia

Abstract

In this presentation, I summarize recent research in the field, discussing both fundamental and applied aspects. These encompass the exploitation of irreversible chaotic dynamics for energy harvesting, the control of rare catastrophic events at nanoscale, coherent light generation from black-bodies, biomimetic nanomaterials with unique properties, record performing photocatalysis membranes generated by warped spaces, early stage cancer detection, and new types of optical neural networks.

META 2018 CONFERENCE, ROUND-TRIP MARSEILLE CRUISE, JUNE 24 – JULY 1, 2018

Microstructured Materials for Thermal Heating and Memory

Michelle L. Povinelli

University of Southern California, USA

Abstract

We explore the effect of microstructure on regulating the interaction light and heat. In particular, we examine the use of absorptive resonances in photonic crystal slabs. In the first part of the work, we use resonances to create selective on-chip heating for lab-on-chip applications. In the second part, we use an absorptive resonance to encode information in the internal device temperature, forming a hybrid optothermal memory. Such a device may prove useful for operation in highly fluctuating environments.

Keynote Lectures

Enhancing Photon Harvesting with Plasmonic Nanostructures

Dongling Ma[1]

[1]Institut National de la Recherche Scientifique, Center of Energy, Materials and Telecommunications
Quebec, Canada
*corresponding author, E-mail: ma@emt.inrs.ca

Abstract

With unique surface plasmon resonance properties, plasmonic nanostructures are able to enhance photon harvesting of semiconductor materials via near-field effects and/or enhanced light scattering, which has significant implications for the realization of cost-effective high-performance solar technologies. In this talk, I will overview some of our recent progress on the development of plasmonic nanostructures and their beneficial role in solar water splitting, photocatalytic degradation of pollutants and solar cells.

1. Introduction

With unique surface plasmon resonance properties and high potential for many important applications, plasmonic nanostructures are attracting more and more attention in the past decades. In addition to ever increasing research interest in realizing precise control over their structure (such as size, shape, aspect ratio and uniformity), plasmon enhanced photocatalysis and solar cells represent two highly promising and important research areas.

In this context, I will present some of our development in plasmonic nanostructures, such as symmetric silver nanorice, non-symmetric Ag carrots and Au stars synthesized by wet chemical approaches, and Au spherical nanoparticles fabricated by pulsed laser ablation in water, as well as their contributions to photocatalysis and solar cell performance [1-8].

2. Results and Discussion

One example of plasmonic-semiconductor nanohybrids is shown in Figure 1 (top). It illustrates the synthesis of novel, plasmonic Au nanoparticle decorated NaYF4:Yb^{3+}, Er^{3+}, Tm^{3+} (denoted as NYF) – core @ porous-TiO_2-shell microspheres, which can harvest solar photons over a wide spectral range from ultraviolet (UV) to near infrared for efficient photocatalysis, significantly better than the benchmark Degussa P25 [2]. The enhanced activity is attributed to synergistic effects from nanocomponents arranged into the nanostructured architecture in such a way that favors the efficient charge/energy transfer among nanocomponents and largely reduced charge recombination.

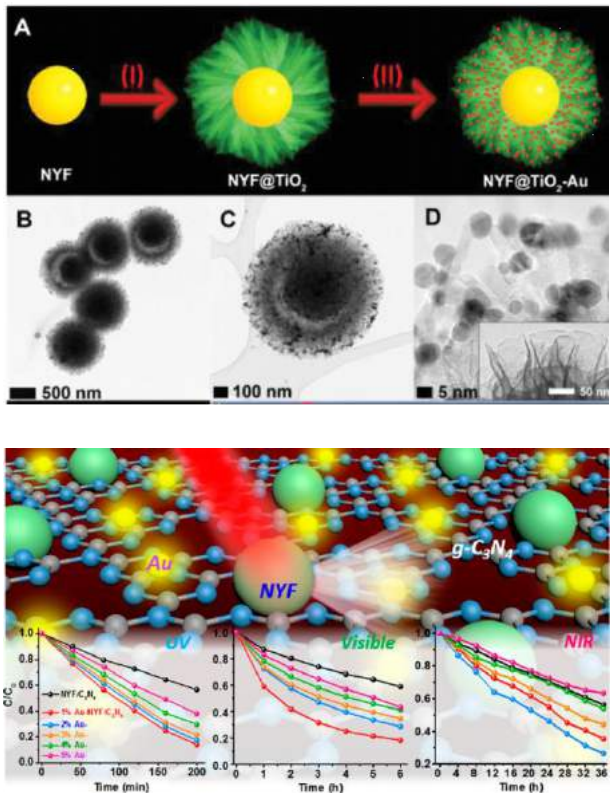


Figure 1. TOP: A) Schematic illustration of the formation process of the NYF@TiO2 - Au core@shell microspheres. B,C) transmission electron microscopy (TEM) images, D) high-resolution TEM images [2]. BOTTOM: Schematic illustration of structure and concepts of Au nanoparticle and NaYF4:Yb^{3+}, Er^{3+}, Tm^{3+} (NYF) microsphere loaded graphitic C_3N_4 (g-C_3N_4) nanosheets and their photocatalytic behavior under UV, visible and near infrared illuminations [4].

Recently, we developed an even simple method for preparing the complex structure of plasmonic nanoparticles and semiconductor catalysts. In this case, we first synthesized NYF microspheres in situ, in the presence of two-dimensional graphitic C_3N_4 (g-C_3N_4) nanosheets and

then loaded Au nanoparticles onto the C_3N_4 nanosheets (Au-NYF/g- C_3N_4) (Figure 1, bottom) [2]. The simple one-step synthesis of NYF in the presence of g-C_3N_4, which was not previously reported in the literature, leads to both high NYF yield and high coupling efficiency between NYF and g-C_3N_4. The Au-NYF/g-C_3N_4 structure exhibits excellent stability, wide photoresponse from the ultraviolet, to visible and near infrared regions, and prominently enhanced photocatalytic activities compared with the plain g-C_3N_4 sample in the degradation of methyl orange.

Very recently, by constructing a complete comparative framework, based on the similar catalysts having alloy synergistic effect or plasmonic effect, or both, we compared the plasmonic and synergistic effects [5]. It helps answer an important, yet not previously addressed question: synergistic and plasmonic effects, which can make more important contribution to solar water splitting?

Plasmonic nanostructures also contribute to solar cell performance. I will briefly present and discuss the role of Au nanostars and nanorods in quantum dot-based solar cells, dye-sensitized solar cells and polymeric solar cells, which led to the increase of power conversion efficiency at varying levels, up to ~30%, depending on the device configuration and the way the plasmonic nanostructures are integrated. The enhancement mechanisms will be discussed.

3. Conclusions

The work demonstrates the significant contribution that plasmonic nanostructures can make to photocatalysis and solar cells. Rational and appropriate design of plasmonic nanostructures and their conjugation with other materials are the key to attain desired performance enhancement.

Acknowledgements

The author would like to acknowledge financial support from the Natural Sciences and Engineering Research Council of Canada, Fonds de la recherche sur la nature et les technologies and CQMF. The author sincerely thanks all co-authors shown below for their contributions.

References

[1] H. Liang, D. Rossouw, H. Zhao, S. K. Cushing, H. Shi, A. Korinek, H. Xu, F. Rosei, W. Wang, N. Wu, G. A. Botton, D. Ma, *J. Am. Chem. Soc*. 135: 9616−9619, 2013.

[2] Z. Xu, M. Quintanilla, F. Vetrone, A. O. Govorov, M. Chaker, D. Ma, *Adv. Funct. Mater*. 25: 2950–2960, 2015 (**Front Cover**).

[3] H. Liang, H. Zhao, D. Rossouw, W. Wang, H. Xu, G. A. Botton, D. Ma, *Chem. Mater*. 24: 2339−2346, 2012.

[4] Q. Zhang, J. Deng, Z. Xu, M. Chaker, D. Ma, *ACS Catalysis* 7: 6225−6234, 2017.

[5] Z. Xu, M. Kibria, B. AlOtaibi, P. N. Duchesne, L. V. Besteiro, Y. Gao, Q. Zhang, Z. Mi, P. Zhang, A. O. Govorov, L. Mai, M. Chaker, D. Ma, *Applied Catalysis B: Environmental* 221: 77–85, 2018.

[6] B. A. Gonfa, M. R. Kim, P. Zheng, S. Cushing, Q. Qiao, N. Wu, M. A. El Khakani, D. Ma, *Journal of Materials Chemistry A* 4: 13071–13080, 2016.

[7] H. Elbohy, M. R. Kim, A. Dubey, K. M. Reza, D. Ma*, J. Zai*, X. Qian*, Q. Qiao*, *Journal of Materials Chemistry A* 4: 545–551, 2016.

[8] S. Li, J. Zhang, M. G. Kibria, Z. Mi, M. Chaker, D. Ma,* R. Nechache*, F. Rosei* *Chem. Commun*. 49: 5856-5858, 2013.

Advanced hybrid plasmonics based on nanoscale photopolymerization

Renaud Bachelot

Light, Nanomaterials and Nanotechnologies (L2N)
Charles Delaunay Institute-CNRS, University of Technology of Troyes, France

renaud.bachelot@utt.fr

Abstract

We review the synthesis, characterization, and applications of new hybrid plasmonic nanomaterials that are created through plasmon-induced photopolymerization. In particular, involved polymer can contain quantum emitters, resulting in advanced anisotropic hybrid nano-emitters.

Context and content of the presentation (Key Note)

Hybrid nanomaterials are targeted by a rapidly growing group of nanooptics researchers, due to the promise of optical behavior that is difficult or even impossible to create with nanostructures of homogeneous composition. Examples of important areas of interest include coherent coupling, Fano resonances, optical gain, solar energy conversion, photocatalysis, and nonlinear optical interactions.

In addition to the coupling interactions, the strong dependence of optical resonances and damping on the size, shape, and composition of the building blocks provides promise that the coupling interactions of hybrid nanomaterials can be controlled and manipulated for a desired outcome. Great challenges remain in reliably synthesizing and characterizing hybrid nanomaterials for nanooptics.

We review a promising original approach of hybrid plasmonic nanoparticles based on plasmon-induced photopolymerization. The plasmonic modes of the metallic nanoparticles are used for triggering a local photochemical reaction. As a result, it is possible to integrate, in an anisotropic way, polymer nanoparts that are located where plasmonic hot spots are susceptible to be activated.

The work is placed within the broader context of hybrid nanomaterials involving plasmonic metal nanoparticles and molecular materials placed, in an anisotropic way, within the length scale of the evanescent field from the metal surface.

We specifically review important applications of this approach: molecular nanoprobing of localized plasmonic fields [1-3], robust molecular trapping [4], local symmetry breaking [5], and photoinduced synthesis of advanced hybrid anisotropic nanoemitters (see Fig. 1 as an illustration) [6]. This approach of hybrid nanostructure opens a way towards control of the local energy transfer in nanophotonics.

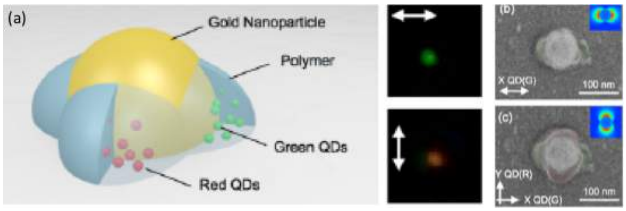


Figure 1: (a) illustration an anisotropic light emitting hybrid nanosystem presenting two tunable colors. The structure was obtained through a two-step approach. (b) step 1: SEM image taken after the first exposure that positions green QDs in X-axis. (c) step 2: SEM image taken after the second exposure that positions red QDs in Y-axis .

Acknowledgements

This approach has been developed over the past decade within the context of a fruitful long term international partnership involving the University of Technology of Troyes (A. Broussier, D. Ge, J. Plain, C. Couteau, S. Jradi, H. Chen), Argonne National Laboratory (G. P. Wiederrecht, S. K Gray), CINTRA&Nanyang Technological University (D. X. Quyen, X. W. Sun, H. V. Demir), UHA (O. Soppera), ICB (G. Colas de Francs, A. Bouhelier), and CEA Saclay (S. Marguet, C. Fiorini, L. Douillard). We thank the Nanomat plateform (UTT), as well as the ANR French agency that funds the HAPPLE and ACTIVE-NANOPHOT projects. The project is developed in the context of the Labex ACTION program (ANR 2011-2010).

References

[1] C. Deeb et al. ACS Nano 4, 4579 (2010)
[2] C. Deeb et al. J. Phys. Chem C. 116, 24734 (2012)
[3] C. Deeb et al. J. Phys. Chem. Lett. 2, 7 (2011).
[4] X. Zhou et al. ACS Photonics 2, 121 (2015)
[5] H. Ibn El Ahrach et al. Phys. Rev. Lett. 98, 107402 (2007)
[6] X. Zhou et al. Nano Letters 15, 7458 (2015).

Quantum and Classical Phenomena in Bio-Plasmonic Nanostructures and Assemblies

Alexander O. Govorov, Lucas V. Besteiro and Xiang-Tian Kong

Department of Physics and Astronomy, Ohio University, Athens, OH, 45701
govorov@ohio.edu

Metal nanocrystals and semiconductor quantum dots have the ability to absorb and scatter light very efficiently. This study concerns special designs of hybrid nanostructures with electromagnetic hot spots, where the electromagnetic field becomes strongly enhanced and concentrated. Overall plasmonic nanostructures with hot spots demonstrate strongly amplified optical and energy-related effects.

(1) Using nanoparticle arrays made of different metals, one can transfer plasmonic signals coherently and with small losses [1].

(2) Plasmonic hot spots efficiently generate energetic electrons, which can be used for photochemistry and photodetection [2,3].

(3) Using nanostructures with hot spots, one can strongly enhance optical generation of heat and also confine high photo-temperatures in small volumes [4,5,6].

(4) Colloidal nanocrystal assemblies and metasurfaces with plasmon resonances allow us to strongly enhance chiral optical responses (circular dichroism) of biomolecules and drugs [7,8,9].

[1] E.-M. Roller, et al., *Nature Physics*, 13, 761 (2017).

[2] A.O. Govorov, H. Zhang, H.V. Demir and Y. K. Gun'ko, *Nano Today* 9, 85 (2014).

[3] H. Harutyunyan, et al., *Nature Nanotech*. 10, 770 (2015).

[4] A. O. Govorov and H. Richardson, *Nano Today* 2, 20 (2007).

[5] C. Jack, et al., *Nat. Commun.* 7, 10946 (2016).

[6] X.-T. Kong, et al., Nano Letters, DOI: 10.1021/acs.nanolett.7b05446

[7] A. O. Govorov, et al., *Nano Letters 10,* 1374–1382 (2010).

[8] A. Kuzyk, et al., *Nature* 483, 311 (2012).

[9] X.-T. Kong, et al., Nano Letters 17, 5099–5105 (2017).

Optical Metasurfaces from classical to quantum regime

Xiang Zhang and Yuan Wang

University of California, Berkeley, CA 94720, USA

Abstract:

Metasurfaces are an important new class of ultrathin materials which has had a profound and far-reaching impact in science and technology. Nature materials derive its properties from the chemical nature of the constituent atoms and molecules. Metasurfaces extend the range of these properties enormously deriving from the carefully designed shapes, sizes and spatial arrangements of unit cells at length scales much smaller than the wavelength of the radiation. Their properties therefore can be designed and tailored at will. These revolutionary structures will profoundly change our human society and accelerate technology innovations in ultra-resolution lithography, medical imaging, and high speed communication. This talk will review our research efforts in optical metasurfaces in the past few years, which ranges from classical to quantum regime.

Ultrafast pump-probe studies on graphene and graphene-based structures

Mu Wang*, Yingying Zhu, Lianzi Liu, Dongxiang Qi, Renhao Fan, and Ruwen Peng

National Laboratory of Solid State Microstructures, School of Physics, and Collaborative Innovation Center of Advanced Microstructures, Nanjing University, Nanjing 210093, China
*corresponding author, E-mail: muwang@nju.edu.cn

Abstract

The request for novel high-speed and ultrathin optoelectronic devices has trigged numerous researches in the ultrafast behavior of two-dimensional materials and their heterostructures, especially graphene-based materials[1-4]. In this work [5], we demonstrate an unexpected saturation behavior happens in the ultrafast systems based on graphene. Ultrafast pump-probe spectroscopy has been used to monitor the carrier dynamics down to femtosecond in our system. The investigations provide a microscopic view on ultrafast multi-channel scattering dynamics in nonlinear physics.

References:

1. F. Xia, T. Mueller, Y.M. Lin, A. Valdes-Garcia, P. Avouris, Ultrafast graphene photodetector, Nat Nanotechnol, 4 (2009) 839-843.
2. F. Ceballos, H. Zhao, Ultrafast Laser Spectroscopy of Two-Dimensional Materials Beyond Graphene, Advanced Functional Materials, 27 (2017) 1604509.
3. F. Bonaccorso, Z. Sun, T. Hasan, A.C. Ferrari, Graphene photonics and optoelectronics, Nature Photonics, 4 (2010) 611-622.
4. D. Sun, G. Aivazian, A.M. Jones, J.S. Ross, W. Yao, D. Cobden, X. Xu, Ultrafast hot-carrier-dominated photocurrent in graphene, Nat Nanotechnol, 7 (2012) 114-118
5. Yingying Zhu, Lianzi Liu, Dongxiang Qi, Ruwen Peng, and Mu Wang, manuscript prepared (2018).

Optical components and systems based on dielectric metasurfaces

Andrei Faraon, Ehsan Arbabi, Seyedeh Mahsa Kamali, MohammadSadegh Faraji-Dana, Yu Horie, Amir Arbabi,

T.J. Watson Laboratory of Applied Physics, California Institute of Technology, Pasadena, CA, USA

*corresponding author: faraon@caltech.edu

Abstract- In this talk I give an overview of our recent work on various optical components and systems based on dielectric metasurfaces

Flat optical devices based on lithographically patterned sub-wavelength dielectric nano-structures provide precise control over optical wavefronts, and thus promise to revolutionize the field of free-space optics. I discuss our work on high contrast transmitarrays and reflectarrays composed of high index nano-posts located on top of low index substrates like silica glass or transparent polymers. Complete control of both phase and polarization is achieved at the level of single nano-post, which enables control of the optical wavefront with sub-wavelength spatial resolution. Using this platform, we demonstrated various optical components including lenses and dichroic phase masks. I focus on applications in holographic imaging, compact spectrometers and two-photon microscopy.

Rigorous modal analysis of plasmonic nanoresonators

Wei Yan and Philippe Lalanne[1], Jean Paul Hugonin and Christophe Sauvan[2]

[1]Laboratoire Photonique Numérique et Nanosciences, Université Bordeaux, IOGS, CNRS, France
[2]Laboratoire Charles Fabry, Université Orsay, IOGS, CNRS, France

*corresponding author, E-mail: philippe.lalanne@institutoptique.fr

Abstract

Because they enhance and localize fields, nanoresonators are key elements for controlling light at the nanoscale. This control is ultimately limited by our capability to engineer electromagnetic near-fields with several nanoresonances, enable energy transfers between them, and model how every individual mode precisely interfere to create new resonant states that overlap in space and energy. We review recent advance in the development of theories for analyzing the response of nanoresonators. See https://onlinelibrary.wiley.com/doi/full/10.1002/lpor.201700113 for details.

Exploration of Novel Electromagnetic Scattering with All-Dielectric Metamaterials

Willie J Padilla[1], Andrew Cardin[1], Xinyu Liu[1], and Kebin Fan[1]

[1]Department of Electrical and Computer Engineering, Duke University, Box 90291, Durham, NC 27708, USA
*corresponding author, E-mail: willie.padilla@duke.edu

Abstract

All-dielectric metasurfaces (DMSs) are a versatile system to investigate a number of unconventional physical scattering responses ranging from Huygens' surface to high absorption and bound-states-in-the-continuum (BIC). We present experimental results from several types of DMSs. DMSs are fabricated with semiconducting materials, and we further demonstrate the ability to control the scattering properties of DMSs in real-time with optical band-gap light. The physics underlying the nature of the electromagnetic responses is described with temporal coupled mode theory and waveguide analysis.

Quantum nanophotonics with semiconductor quantum dots

Leonardo Midolo[1] and Peter Lodahl[1]

[1]Niels Bohr Institute, University of Copenhagen, Blegdamsvej 17, 2100-DK Copenhagen, Denmark.
*corresponding author, E-mail: midolo@nbi.ku.dk

Abstract

In this keynote talk, I will report about the recent progress on developing quantum photonic technologies based on semiconductor quantum dots in Gallium Arsenide membranes. The excellent properties of quantum dots as sources of efficient, pure, and indistinguishable single photons, allows us to build a platform for solid-state quantum optics by combining these emitters with active and passive planar nanophotonic devices. I will present the state-of-the-art techniques for controlling the coherence of quantum dot emitters and recent results on interfacing photons to electron spins in quantum dots. Finally, I will discuss future challenges required to scale single-photon sources for quantum-information processing with multiple photonic qubits, and illustrate the steps which have been taken so far in this direction.

Hybrid and Metastructured Materials for Photonics, Sensors and Energy

Plasmonic Nanostructures for Point-of-Care Sensors

Nianqiang Wu

Department of Mechanical and Aerospace Engineering, West Virginia University, Morgantown, West Virginia 26506-6106,
*corresponding author, E-mail: nick.wu@mail.wvu.edu

Abstract

This talk presents our effort to develop zero-dimensional (0D), one-dimensional (1D) and two-dimensional (2D) plasmonic nanostructures. The plasmonic band and the electromagnetic field of the plasmonic nanostructures have studied and tuned systematically. The plasmonic nanostructures developed are used to construct surface-enhanced Raman scattering (SERS) sensor. This talk will give several examples of the applications of SERS sensor in the point-of-care setting.

Probing dynamics and controlling ultrafast plasmon via photoemission electron microscopy

Boyu Ji, Yingping Dou, Haiyan Tao, Xiaowei Song, Xun Gao, Zuoqiang Hao and Jingquan Lin*

School of Science, Changchun University of Science and Technology, Changchun, China
*corresponding author, E-mail: linjingquan@cust.edu.cn

Abstract

We demonstrate subwavelength imaging plasmon dynamics evolution and control of the localized near-field distribution in gold bow-tie and nanoring nanostructure through photoemission electron microscopy. Different localized near-field dynamics are disclosed within a bow-tie nanostructure. Subwavelength imaging of near field distribution between the structure with sharp corners (bow-tie) and the one without (nanoring) is compared and the underling physics responsible for the difference is discussed.

1. Introduction

In recent years, ultrafast plasmon, which can be realized by concentrating ultrashort femtosecond laser pulses in a subwavelength structure, has been intensively explored[1−2] and it has potentials in fabrication of the plasmonic chip with speed in the Peta–Hertz domain.[3] Also, manipulating the near-field on ever smaller length and ever shorter time scale offers the ability to perform ultrafast optical near-field coherent control and nano-optical switching.[4−5] Coherent control of the near field in a nanostructure could be realized by selectively exciting the localized surface plasmon (LSP) mode. The ability to engineer a plasmonic system providing a desired ultrafast response in a predetermined nanostructure is crucial, thus it is necessary to understand the temporal evolution of ultrafast plasmon mode and to manipulate optical near field in a given nanoscale volume. Obviously, in this direction a technique that is capable of imaging plasmon and characterizing the ultrafast plasmon dynamics with nanometer and femtosecond spatiotemporal resolution is imperative.

2. Experimental description

The experimental set up for direct imaging of plasmon on the tips of nano-prisms in a bowtie structure excited by 7 fs laser pulses and probing of ultrafast plasmon dynamics by combining the pump-probe technology with three-photon photoemission electron microscopy has been published elsewhere[6]. Control of the near-field distribution in the bow-tie and nanoring is realized by polarization rotation of single femtosecond laser pulse and variation of phase delay of two orthogonally polarized femtosecond laser pulses respectively.

3. Results and discussions

Different photoemission patterns induced by the plasmon effect are observed when the bowties are excited by s- and p-polarized femtosecond laser pulses. A series of images of the evolution of local surface plasmon modes on different tips of the bowtie are obtained by the time-resolved three-photon photoemission electron microscopy, and the result discloses that plasmon excitation is dominated by the interference of the pump and probe pulses within the first 13 fs of the delay time, and thereafter the individual plasmon starts to oscillate on its own characteristic resonant frequencies as shown in Fig.1.

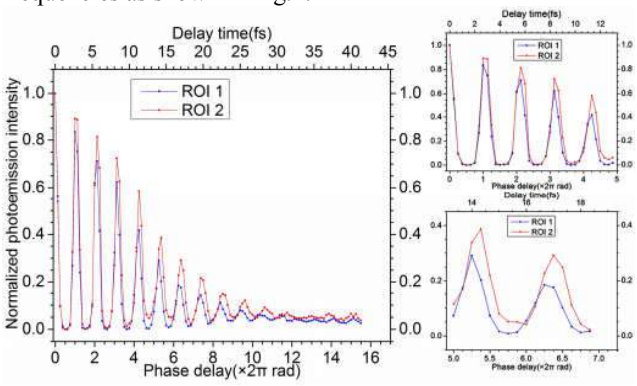


Figure 1 Left panel: Evolution of the photoemission signals with a delay time for different hot spots (ROI 1 and 2) in the bow-tie. Right panel: Two magnified regions

We show that the localized optical near field distribution can be well controlled either among the corners of the nano-prisms in the bow-tie for resonant excitation or the edges for off-resonant excitation, and a better visualization of PEEM image is achieved for the resonant excitation than the case of off-resonant excitation. The experimental results of the optical near field distribution control in the bowtie are well reproduced by finite-difference time-domain simulation and understood by linear combination of electric charge distribution of the bow-tie by s- and p- polarized light illumination. In addition, a shift of the near field excitation position with inverted or unchanged

phase, alternatively un-shift of position but only with inverted phase of the near field can be realized by rotating the polarization angle of single pulse and coherent control of two orthogonally polarized fs laser pulses respectively.

For the case of optical near field distribution control in the nanoring, as shown in Fig.2, it is found that there is discrepancy in hot spot distribution in the nanoring between the observed PEEM images and the simulated photoelectron emission pattern which is attributed to some possible factors such as band structure near Fermi level of the nanoring material and temporal profile of femtosecond laser pulse[7]. In addition, the FDTD simulation of temporal evolution of the near field enhancement regions of the quadrupolar plasmon resonance mode in the nanoring is also given.

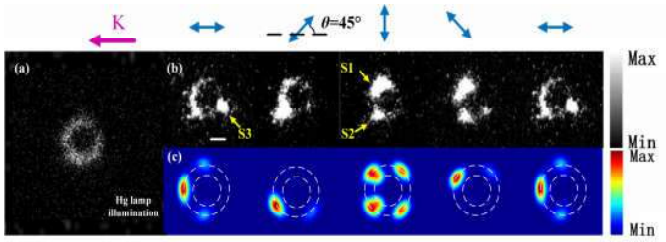


Fig. 2. PEEM image of near field of the nanoring under Hg lampe illumination(a), under femtosecond laser ilumination (b) and simulated photoelectron emission (c) of nanoring with an assumption of 3 photon photoemission process. The polarization direction of light is labeled as blue double-end arrow and light incident direction labeled as megenta arrow. Three excited hot spots are marked with S1,S2, and S3.

4. Conclusions

The femtosecond time-resolved PEEM with few-cycle laser pulses has been employed to map the ultrafast plasmonic near-field temporal evolution in the gold bow-tie nanostructures at femtosecond and nano-sized spatiotemporal resolution. Different localized near-field dynamics are disclosed within a bow-tie nanostructure. Subwavelength imaging of near field distribution between the structure with sharp corners (bow-tie) and the one without (nanoring) is compared and the underling physics responsible for the difference is discussed. Real-space near-field imaging of the plasmonics mode evolution and its control provides a fundamental understanding of the near field and paves the way for further advancing the applications of plasmonic modes in various fields.

Acknowledgements

This project was supported by National Natural Science Foundation of China under Grant Nos. 11474040, 61605017 and 61775021.

References

[1] D.Brinks, M.Castro-Lopez, Hildner R and Hulst N F *Proc. Natl. Acad. Sci. USA* 110:18386, 2013

[2] Rewitz C, Keitzl T, Tuchscherer P, Huang J S, Geisler P, Razinslas G, Hecht B and Brixner T , *Nano Lett.* 12:45, 2012

[3] http://www.bacatec.de/en/gefoerderte_projekte.html

[4] Stockman M I, Sergey V F and David J B Phys. Rev. Lett. 88 : 067402,2002

[5] Brixner T, de Abajo F G J, Schneider J and Pfeiffer WPhys. Rev. Lett. 95:093901, 2005

[6] Ji, B., Qin, J., Tao, H., Hao, Z. & Lin, J. Subwavelength imaging and control of ultrafast optical near-field under resonant- and off-resonant excitation of bowtie nanostructures. New J. Phys. 18:1–10. 2016

[7] Boyu Ji, Qian Wang, Xiaowei Song, Haiyan Tao, Yinping Dou, Xun Gao, Zuoqiang Hao and Jingquan Lin, Disclosing dark mode of femtosecond plasmon with photoemission electron microscopy J. Phys. D: Appl. Phys. 50 : 415309 ,2017

Dynamic hot-spots in plasmonic photocatalysis

Miguel A. Correa-Duarte

Department of Physical Chemistry, Center for Biomedical Research (CINBIO), Southern Galicia Institute of Health Research (IISGS), and CIBERSAM, Universidade de Vigo, 36310 Vigo, Spain.
E-mail: macorrea@uvigo.es

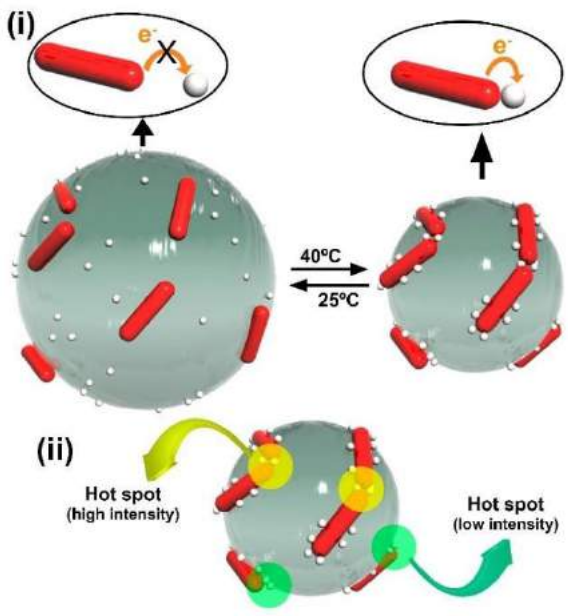
Abstract

Herein, we introduce a novel approach for achieving a real-time control over the hot-electron injection process in metal-semiconductor photocatalysts. Such functionality is attained through the design of a hybrid nanocomposite in which plasmonic Au nanorods and TiO2 nanoparticles are synergistically integrated with a thermoresponsive polymer.

Reconfigurable plasmonic assemblies represent a novel class of nano-entities whose chemical and physical properties can be reversibly controlled.[1–3] More precisely, this family of materials offers the possibility of tuning the unique optical properties of their individual plasmonic units by applying a stimulus such as light, temperature, pH or ionic strength. In this way, the many opportunities afforded by plasmonic assemblies, i.e., formation of hot spots,[4] optical magnetism[5] or Fano resonances,[6] among others, can be oriented to the development of novel optical transducers, biosensors or therapeutic agents. In the present work we extend the outstanding potential of reconfigurable plasmonic assemblies to the emerging field of plasmon-induced photocatalysis.[7]

Noble metal nanoparticles have recently gained relevance as photosensitizers in photocatalytic processes given their ability to extend the optical operational range of large band gap semiconductors, such as TiO2, to a broader range of the electromagnetic spectrum.[8] One of the main mechanisms behind this phenomenon arises from the ability of plasmonic nanomaterials to efficiently harvest visible and near infrared (NIR) photons, thus creating a population of excited "hot" electrons that can be transferred to a nearby semi-conductor when both materials are combined forming a hybrid.[7,9] Along these lines, the extent of such photosensitization process is inversely proportional to the space separating both species.[10] Moreover, the magnitude of the electromagnetic field enhancement created by the plasmonic component at the metal-semiconductor interface is another parameter of paramount importance to increase the efficiency of the hot electron transfer.[11–13] In other possible mechanisms the ability of plasmonic nanoparticles to focalize the incoming light is used as a means to couple the plasmonic near-field to the semiconductor, thus increasing the effective absorption cross-section of the later (antenna effect).[14,15] Nevertheless, in those scenarios the excitation source must comprise a wavelength range in which both the metal and the semiconductor have to be excited simultaneously.

Mastering the coupling efficiency between a plasmonic metal and a photocatalytic semiconductor by simply tuning the interparticle distance created between them may be a simple way to manipulate the efficiency of the electron injection mechanism. Simultaneously, plasmonic hot spots created at the nanometric gap between adjacent plasmonic nanoparticles can be used to additionally induce a significant rise in the photocatalytic activity of the semiconductor. Bearing this in mind, the present work takes advantage of the reconfigurable capabilities given by a third party in order to create a plasmonic photocatalytic hybrid whose activity can be reversibly activated by applying an external stimulus.



Scheme 1. Representation of the collapse-swelling transition experienced by the Au-TiO2/pNIPAM nanohybrids leading to, (i) the control of the electron injection on TiO2 by tuning the interparticle distance between the semiconductor and the plasmonic material, and (ii) the reversible formation of interparticle hot spots.

The formation of these reversible plasmonic photocatalysts is expected to pave the way for the applicability of reconfigurable plasmonic materials, broadening the already exciting opportunities that these architectures hold in the design and fabrication of plasmon-enhanced technologies. In this context, this novel approach may be particularly relevant in those scenarios where the interactions between nanostructures or nanoparticles play a critical role in the operational features of photocatalytic and photovoltaic devices, among others.[16–18]

As a proof of concept of this novel paradigm, we have made use of poly(N-isopropylacrylamide) (pNIPAM), a thermoresponsive polymer that presents an abrupt change in its hydrodynamic diameter. Accordingly, below its lower critical solution temperature or LCST (32–34 °C) the polymer network is in a swollen state, while above this temperature is found in a collapsed state.[19] In this way, when pNIPAM colloids are combined with plasmonic and photocatalytic nanoparticles, the phase transition of the polymer can be used as a transducer to induce a modification in the metal-semiconductor interparticle distance while activating or deactivating the formation of plasmonic hot spots (Scheme 1).[20]

References

[1] Z. Qian, D. S. Ginger, J. Am. Chem. Soc. 2017, 139, 5266–5276.

[2] P. Zhan, P. K. Dutta, P. Wang, G. Song, M. Dai, S.-X. Zhao, Z.-G. Wang, P. Yin, W. Zhang, B. Ding, et al., ACS Nano 2017, 11, 1172–1179.

[3] Q. Liu, Y. Cui, D. Gardner, X. Li, S. He, I. I. Smalyukh, Nano Lett. 2010, 10, 1347–1353.

[4] A. Lee, G. F. S. Andrade, A. Ahmed, M. L. Souza, N. Coombs, E. Tumarkin, K. Liu, R. Gordon, A. G. Brolo, E. Kumacheva, J. Am. Chem. Soc. 2011, 133, 7563–7570.

[5] S. N. Sheikholeslami, H. Alaeian, A. L. Koh, J. A. Dionne, Nano Lett. 2013, 13, 4137.

[6] B. Luk'yanchuk, N. I. Zheludev, S. A. Maier, N. J. Halas, P. Nordlander, H. Giessen, C. T. Chong, Nat. Mater. 2010, 9, 707–715.

[7] T. Tatsuma, H. Nishi, T. Ishida, Chem. Sci. 2017, 8, 3325–3337.

[8] D. B. Ingram, P. Christopher, J. L. Bauer, S. Linic, ACS Catal. 2011, 1, 1441–1447.

[9] A. O. Govorov, H. Zhang, Y. K. Gun'ko, J. Phys. Chem. C 2013, 117, 16616–16631.

[10] S. K. Cushing, J. Li, J. Bright, B. T. Yost, P. Zheng, A. D. Bristow, N. Wu, J. Phys. Chem. C 2015, 119, 16239–16244.

[11] A. Sousa-Castillo, M. Comesaña-Hermo, B. Rodríguez-González, M. Pérez-Lorenzo, Z. Wang, X.-T. Kong, A. O. Govorov, M. A. Correa-Duarte, J. Phys. Chem. C 2016, 120, DOI 10.1021/acs.jpcc.6b02370.

[12] L. V Besteiro, A. O. Govorov, J. Phys. Chem. C 2016, 120, 19329–19339.

[13] X.-T. Kong, Z. Wang, A. O. Govorov, Adv. Opt. Mater. 2017, 5, 1600594.

[14] J. Li, S. K. Cushing, F. Meng, T. R. Senty, A. D. Bristow, N. Wu, Nat. Photonics 2015, 9, 601–607.

[15] H. A. Atwater, A. Polman, Nat. Mater. 2010, 9, 205–213.

[16] C. Jia, X. Li, N. Xin, Y. Gong, J. Guan, L. Meng, S. Meng, X. Guo, Adv. Energy Mater. 2016, 6, 1600431.

[17] R. Jiang, B. Li, C. Fang, J. Wang, Adv. Mater. 2014, 26, 5274–5309.

[18] C. Clavero, Nat. Photonics 2014, 8, 95–103.

[19] M. Karg, T. Hellweg, Curr. Opin. Colloid Interface Sci. 2009, 14, 438–450.

[20] C. Fernández-López, L. Polavarapu, D. M. Solís, J. M. Taboada, F. Obelleiro, R. Contreras-Cáceres, I. Pastoriza-Santos, J. Pérez-Juste, J. Pe, ACS Appl. Mater. Interfaces 2015, 7, 12530–12538.

Active control of the photoluminescence emitted by quantum dots using metallic nanoparticles and photochromic molecules

Gwénaëlle Lamri[1], Jana B. Nieder[2], Edite Figueiras[2], Jean Aubard[3], Pierre-Michel Adam[1], Christophe Couteau[1], Nordin Felidj[3] and Anne-Laure Baudrion[1]

[1]Laboratoire de Nanotechnologies et d'Instrumentation Opitique, Institut Charles Delaunay, UMR CNRS 6281, Université de Technologie de Troyes, 12 rue Marie Curie, 10004 Troyes Cedex, France
[2]QuantaLab, Ultrafast Bio- and Nanophotonics Group, INL – International Iberian Nanotechnology Laboratory, Av. Mestre José Veiga, 4715-310 Braga, Portugal
[3]ITODYS, Université Paris Diderot, 15 rue Jean-Antoine de Baïf, 75205 Paris Cedex 13, France
*corresponding author, E-mail: anne_laure.baudrion@utt.fr

Abstract

In this work, we demonstrate an optical activation of the resonant coupling between quantum dots and metallic nanoparticles due to the photochromic transition. Indeed, the quantum dots photoluminescence is highly enhanced when the plasmon resonance coincides with the quantum dots emission and both are in presence of the colored form of the photochromic molecules. We also show a Förster Resonant Energy Transfer between the quantum dots (donors) and the colored form of the photochromic molecules (acceptors).

1. Introduction

Quantum dots (QDs) can lead either to the enhancement or to the quenching of their photoluminescence [1], provided that they are coupled with metallic nanoparticles (MNPs). Such MNPs, well known to sustain Localized Surface Plasmon (LSP) resonances, may indeed affect the QDs photoluminescence. The distance between QDs and MNPs is one of the switch parameters between both regimes. The goal of this study is to control the coupling distance (different from the physical distance) between QDs and MNPs by changing the refractive index of the surrounding medium using organic photochromic molecules. These molecules are optical switches, which move from a transparent state to a colored one by absorbing UV light. The spectral overlap and the lifetime of each optical phenomenon are the key parameters, since the photochromic molecules can couple to LSP to induce strong coupling [2] or couple to QDs to quench the photoluminescence [3].

2. Discussion

In this study, the Fluorescence Lifetime Imaging Microscopy (FLIM) [4] has been performed to record QDs photoluminescence lifetime and intensity. We fabricated silver nanoparticles arrays covered with a protective 5 nm-thick-SiO_2 layer and we spin-coated on it a solution of QDs and photochromic molecules diluted in a PMMA matrix. Due to their high refractive index change [2], the photochromic molecules we chose were spiropyran molecules (Spy), which absorb UV light to become merocyanine molecules (MC), as we can see in Figure 1. The QDs photoluminescence lifetime and intensity have then been explored before and after the photochromic transition, above and nearby the MNPs arrays.

The Figure 2 summaries the results obtained for silver nanostructures coupled to QDs embedded with PM in a polymer film. The images represent the photoluminescence (PL) intensity when the nanoparticles are in presence of QDs before (in Spy) and after (in MC) the photochromic transition. The nanoparticles arrays are easily located in these images by the squares. Before the photochromic transition (Figure 2a), the photoluminescence of the QDs is quenched above all the arrays regardless of the nanoparticles size. After the photochromic transition (Figure 2b), the PL is enhanced, and we can observe an intensity difference between the arrays. Indeed, there is a maximum of enhancement for the 70 nm-diameter MNPs.

If we plot the normalized PL intensity as a function of the plasmonic resonance recorded above the MNP patterns, before and after the photochromic transition, which means we divided the PL intensity above the MNP patterns by the PL intensity outside them. The PL is quenched when the QDs are coupled with Spy and there is no influence of the MNP size. For QDs coupled with MC, there is a maximum enhancement when the plasmon resonance coincides with the QDs emission wavelength (Figure 3). From fluorescence lifetime measurements, we can deduce that we activated the resonant coupling between silver nanoparticles and QDs thanks to the photochromic transition between Spy and MC.

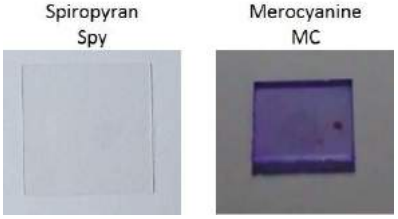


Figure 1 – Sample before (left) and after (right) the photochromic transition

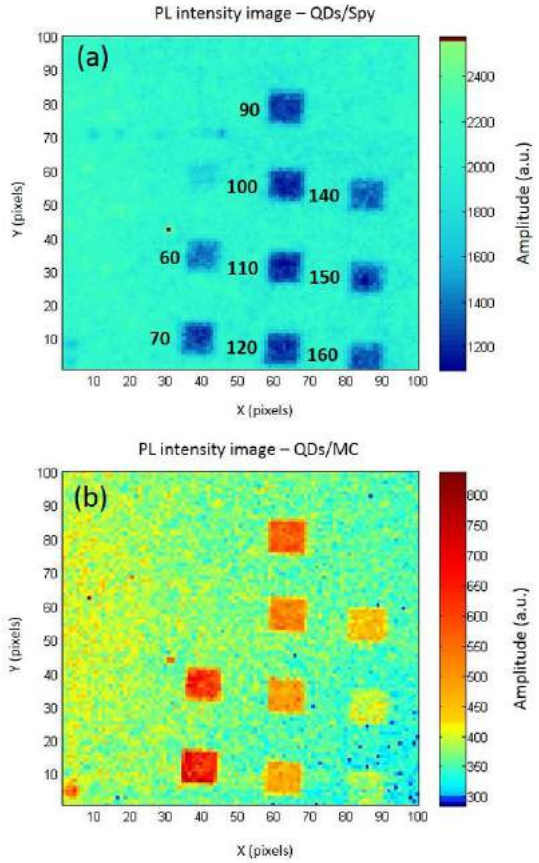


Figure 2 – PL images – (a) PL image recorded on the silver nanoparticles ensembles coupled to QDs and Spy – (b) PL image recorded on the silver nanoparticles ensemble coupled to QDs and MC

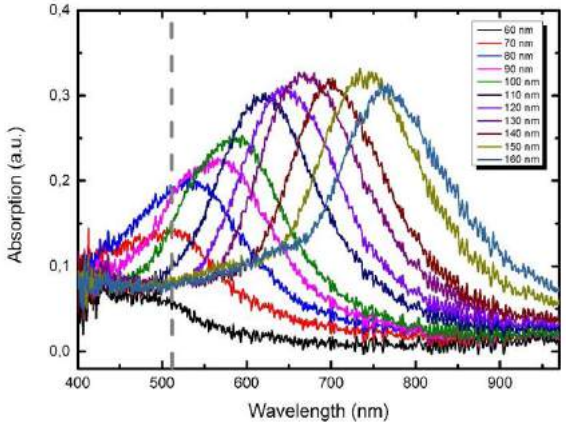


Figure 3 – Silver plasmon resonance recorded in PMMA-PM. The vertical dashed grey line represents the QDs emission maximum.

Moreover, if we were interested at the QDs and PM without metallic nanoparticles, we can show a Förster Resonant Energy Transfer (FRET) between the QDs (donors) and the colored form of the photochromic molecules (acceptors). This result is confirmed by the lifetime of the QDs which decreases from 12,6 ns in absence of PM to 1,3 ns when coupled with MC.

3. Conclusions

To conclude, it was observed that the fluorescence intensity of QDs embedded in a MC doped PMMA matrix presents a maximum value when they are on top of 70 nm-diameter silver particles. This size dependence is expected as theses specific silver nanoparticles present a maximum spectral overlap between its localized surface plasmon resonance and the QDs emission. Moreover, the lifetime analysis and the additional measurements of PL spectra allow us to confirm an energy transfer, as FRET, between QDs and MC. But the more important conclusion of this work is the optical activation of the plasmonic resonant coupling between the QDs and the MNPs. As the plasmonic enhancement of the QDs emission is not observed when QDs and MNPs are embedded in the Spy form of the photochromic molecules, the photochromic transition is definitely responsible of the coupling between QDs and MNPs.

Acknowledgements

The authors acknowledge the Region Champagne-Ardennes for its financiel support in the framework of scholarship for PhDs. This work has been technically supported by Nano'Mat (www.nanomat.eu).

References

[1] Enhancement and quenching regimes in metal-semiconductor hybrid optical nanosources, P. Viste et al., ACS Nano, vol.4, n° 2, p. 759-764 (2010).

[2] Reversible strong coupling in silver nanoparticle arrays using photochromic molecules, A.-L. Baudrion et al., Nano Lett. 13, p. 282−286 (2013).

[3] Reversible Modulation of Quantum Dot Photoluminescence Using a Protein-Bound Photochromic Fluorescence Resonance Energy Transfer Acceptor, I. L. Medintz et al., J. Am. Chem. Soc., 126, p. 30-31 (2004).

[4] Munster, Erik B. van, and Theodorus W. J. Gadella. « Fluorescence Lifetime Imaging Microscopy (FLIM) ». In *Microscopy Techniques*, edited by Jens Rietdorf, 143-75. Berlin, Heidelberg: Springer Berlin Heidelberg, 2005. https://doi.org/10.1007/b102213.

Plasmo-Mechanical Control of Photo-Induced Heat Generation from Au Nanoparticles Immobilized on a Flexible Substrate

Roberto Caputo[1,*], Giovanna Palermo[1], Antonio Condello[1], Ugo Cataldi[2], Thomas Bürgi[2], Cesare P. Umeton[1] and Antonio De Luca[1]

[1]Department of Physics and CNR Nanotec, University of Calabria, 87036 Rende (CS), Italy
[2]Department of Physical Chemistry, University of Geneva, Quai Ernest Ansermet 30, 1211 Geneva 4, Switzerland

*corresponding author, E-mail: roberto.caputo@unical.it

1. Abstract

A new method is presented to mechanically control the photo-induced heat generated by an amorphous arrangement of homogenously distributed gold nanoparticles (AuNPs), immobilized on a flexible elastomeric tape. The macroscopic application of a mechanical strain to the polydimethylsiloxane (PDMS) tape supporting the particles leads to a nanoscale change of the gap between them. As a result, the strong variation of the particles near-field coupling gives rise to a sensitive change of the photo-generated heat. A fine control of the amount of generated heat is thus possible by stretching the initially isotropic sample of only few percents. Due to the anisotropy of the stretching procedure, the plasmon shift and thus the heat generation are strongly polarization-dependent. This system holds promises for sensing and biomedical lab-on-a-chip applications.

2. Introduction

Temperature control at the nanoscale is a quite intriguing possibility and one of the most emerging and fastest growing research field of recent years [1,2]. Based on the use of noble metal nanoparticles (NPs), thermo-plasmonics exploits the localized plasmon resonance (LPR), which occurs when the conduction electrons of NPs oscillate in resonance with the electric field of an impinging light, thus producing a photo-induced heating process in the entire nanostructure. In past, it has been widely demonstrated that plasmon properties are also tunable and several possibilities have been explored. An efficient way for LPR tuning is to involve an "active" host (e.g. liquid crystals) through which it is possible to modify, in a dynamic and reproducible way, the spectral position of the NPs plasmonic resonance [3,4]. On this way, a LPR shift is observed because we are actually changing the refractive index of the environment in which the plasmonic subunits are embedded. Recently, another approach has been explored resulting in a very sensitive spectral shift of the LPR. This has been achieved by mechanically acting on the nanoparticles inter-distance. In this case, the application of a macroscopic strain to the substrate supporting metal nanoparticles, leads to a nanoscale change of the gap between them and thus to the near-field coupling of their spatially localized electric fields [5-8]. This approach results in a drastic shift of the plasmon band and a naked-eye visible color change of the sample (Figure 1).

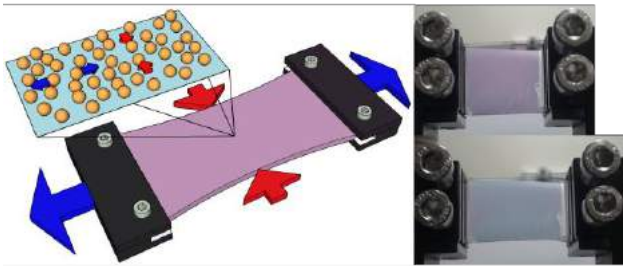


Figure 1. By stretching a PDMS sample coated with a single layer of gold nanoparticles the average distance between them becomes larger in the stretching direction and shorter in the perpendicular one. Stretching of the sample is accompanied by a remarkable change of color from purple-red (b) to blue-violet (c). Images were acquired with a polarizer, mounted to a camera, with direction of polarization perpendicular to the applied strain.

This approach gives rise to the emergence of a new discipline within nanotechnology named Plasmomechanics, with main applications in sensing. However, more fascinating outcomes are expected if Plasmomechanics is efficiently exploited to realize a fine control of the photo-induced plasmon generation of heat. Indeed, it is worth considering that the illumination of metal nanoparticles with a resonant wavelength results in a local temperature variation. The effect can be controlled by fixing the

excitation wavelength and actively shifting the plasmon resonance spectral position.

3. Discussion

The starting point of our work is the numerical simulation of the plasmon response of an ensemble of AuNPs distributed in a centro-symmetrical configuration. In the simulation, particles are excited with different electric-field polarization directions, with or without a mechanical strain applied to their flexible substrate (Figure 2).

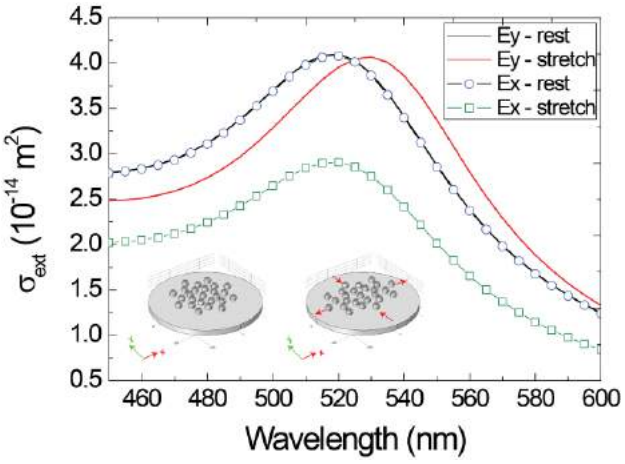


Figure 2. Numerical simulation of the plasmon response of an ensemble of AuNPs when the substrate supporting them is at rest or stretched of few percents. Polarization direction of the exciting electric field along (x) or perpendicular

The numerical result shows that, in case of the sample at rest, a perfect overlap of the plasmon response is obtained. A few-percent elongation of the sample leads instead to a remarkable shift of the plasmon curve, when the polarization direction is perpendicular to the stretching. The excitation with the along-stretching polarization direction produces a limited shift and a considerable decrease of the extinction amplitude. Considering that the amount of photo-induced heat is proportional to the extinction amplitude, we expect a temperature variation in dependence of the wavelength value and polarization direction of the exciting light [9]. In order to experimentally verify this prediction, a large area substrate coated with a monolayer of Au nanoparticle has been characterized by performing extinction spectroscopy and photo-thermal analysis experiments during green laser irradiation (532nm). This wavelength is very close to the resonance value of the involved particles, when the sample is at rest. The measured behavior is in good agreement with the simulated one even if the number of nanoparticles involved in the experiment is much higher than that in the simulation.

4. Conclusions

In this communication, a system is reported comprising AuNPs supported by a flexible substrate. A plasmomechanical approach has been exploited to realize a fine control of the photo-induced generation of heat from the particles when these are excited with resonant-wavelength light. Numerical simulations of a small ensemble of centro-symmetrically distributed particles have provided a quite good agreement with the results of polarized extinction spectroscopy and photo-thermal analysis experiments performed on a large-area sample comprising a much higher number of particles.

Acknowledgements

The research leading to these results has received support and funding from the Italian Project ‘NanoLase’—PRIN 2012, Protocol No. 2012JHFYMC and by the CNR User Facility ‘Materials and processes BEYOND the NANO scale’, Beyond ’Nano, Pole of Cosenza, cod. PONa3-00362.

References

[1] A.O. Govorov and H. Richardson, Generating heat with metal nanoparticles, Nano Today 2, 30–38, 2007.

[2] A.O. Govorov, W. Zhang, T. Skeini, H. Richardson, J. Lee and N.A. Kotov, Gold nanoparticle ensembles as heaters and actuators: melting and collective plasmon resonances, Nanoscale Res. Lett. 1, 84–90, 2006.

[3] L. De Sio , R. Caputo, U. Cataldi and C. Umeton, Broad band tuning of the plasmonic resonance of gold nanoparticles hosted in self-organized soft materials, J. Mater. Chem. 21, 18967–18970, 2011.

[4] L. De Sio, A. Cunningham, V. Verrina, C.M. Tone C, R. Caputo, T. Bürgi and C. Umeton, Double active control of the plasmonic resonance of a gold nanoparticle array, Nanoscale 4, 7619–7623, 2012.

[5] U. Cataldi, R. Caputo, Y. Kurylyak, G. Klein, M. Chekini, C. Umeton and T. Bürgi, J. Mater. Chem. C, 2, 7927, 2014.

[6] T. Maurer, J. Marae-Djouda, U. Cataldi, A. Gontier, G. Montay, Y. Madi, B. Panicaud, D. Macias, P.-M. Adam, G. Lévêque, T. Bürgi and R. Caputo, Front. Mat. Sci. 9, 170, 2015.

[7] C. Burel, A. Alsayed, L. Malassis, C.B. Murray, B. Donnio, B. and R. Dreyfus, Plasmonic-Based Mechanochromic Microcapsules as Strain Sensors, Small, 13 39, 2017.

[8] M. Böhm, T. Uhlig, S. Derenko and L.M. Eng, Mechanical tuning of plasmon resonances in elastic, two-dimensional gold-nanorod arrays, Optical Materials Express, 7(6), 1882-1897, 2017.

[9] L. Pezzi, G. Palermo, A. Veltri, U. Cataldi, T. Bürgi, T. Ritacco, M. Giocondo, C. Umeton and A. De Luca, Photo-thermal study of a layer of randomly distributed gold nanoparticles: from nano-localization to macro-scale effects. Journal of Physics D: Applied Physics, 50(43), 435302, 2017.

Image multiplexing with laser-controlled plasmonic colors

Nathalie Destouches[1*], Nipun Sharma[1], Oleksii Sidorov[2], Nicolas Dalloz[3], Christophe Hubert[1], Francis Vocanson[1], Mathieu Hébert[1]

[1]Univ Lyon, UJM-Saint-Etienne, CNRS, Laboratoire Hubert Curien UMR 5515, F-42023, Saint-Etienne, FranceE
[2]Univ Lyon, UJM-Saint-Etienne, F-42023, Saint-Etienne, FranceE
[3] Institut d Optique Graduate School, Univ Lyon, UJM-Saint-Etienne, CNRS, Laboratoire Hubert Curien UMR 5515, F-42023, Saint-Etienne, FranceE
*corresponding author, E-mail: Nathalie.destouches@univ-st-etienne.fr

Abstract

Anisotropic plasmonic nanostructures have recently had a renewed interest for producing colors with subwavelength resolution and have been used for color image multiplexing owing to the identification of two orthogonal parameters enabling changes in the nanostructures color in specific polarized modes of observation. Here, we extend the concept to multidimensional color image multiplexing and we demonstrate that it can be implemented with a scanning laser technique enabling the control of plasmonic colors.

1. Introduction

Structural colors of plasmonic nanostructures have been largely used in the past decade for manipulating visible light through optical filters or wavefront control metasurfaces. Anisotropic metallic nanopatterns have especially been designed by electron beam lithography to control the spectral polarized reflectivity of surfaces. This led to the production of polarization tunable optical filters, stereoscopic prints and polarization selective image multiplexing. In image multiplexing two images are encoded in the same microprint and displayed independently when observing the sample with two orthogonal polarizations of the incident white light. Using individual anisotropic metallic nanostructures with variable length and width affords two orthogonal parameters to selectively vary the color in each mode of observation with one parameter, the other parameter being without effect.
Here, we demonstrate that the concept of color image multiplexing can be implemented using laser-controlled plasmonic colors and extended to more than two images provided that we are able to produce nanostructures that exhibit specific combinations of colors in different modes of observation and illumination. This approach really opens the route for multiple color image multiplexing and high-density information encoding with versatile, easy-to-implement and fast scanning laser techniques.

2. Overview of the experimental setup

Authors should observe the following rules for page layout. A highly recommended way to meet these requirements is to use a given template (MS-Word or LaTeX) and check details against the corresponding example file.

3. Laser-controlled plasmonic nanostructures

Figure 1: This is the figure caption. Color figures are acceptable.

4. Principle of image multiplexing

4.1. References

References should be numbered in order of appearance, for example [1], [2], and [3,4].

4.2. Submitted files

Authors are requested to submit PDF files of their manuscripts. The PDF file should comply with the following requirements: (a) there must be NO password protection on the PDF file at all; (b) all fonts must be embedded; and (c) the file must be text searchable (do CTRL-F and try to find a common word such as ‘the’).

5. Discussion

xxxxx xxxxx xxxxx

xxxxx xxxxx xxxxx xxxxx xxxxx xxxxx xxxxx xxxxx xxxxx xxxxx

Acknowledgements

Acknowledgements belong here.

References

[1] A.-B. Zhang, C.-D. Kim, E. Yamada, F.G. Smith, The numerical investigation on the turbulent heat transfer, *Int. J. Heat Mass Transfer* 12: 345−365, 2010.

[2] S.V. Patankar, *Numerical Heat Transfer and Fluid Flow*, Hemisphere Publishers, New York, 1980.

[3] W.M. Kays, M.E. Crawford, *Heat transfer*, Wiley, New York, pp.256-258, 1990.

[4] Y. Kawaguchi, T. Tsukahara, M. Motozawa, Experimental and numerical investigations of turbulent drag reduction phenomena by additives, *Proc. ASCHT09*, Jeju, Korea, pp. 23−32, 2009.

Anisotropic chiroptically active nanomaterials

Yurii K. Gun'ko*[1] , Finn Purcell-Milton[1], Vera A. Kuznetsova [1], Natalia Garcia Domenech [1], Nikita V. Tepliakov [2], Anvar S. Baimuratov [2], Ivan D. Rukhlenko [2], Alexander V. Baranov [2], Anatoly V. Fedorov [2]

[1]School of Chemistry, University of Dublin, Trinity College, Dublin 2, Ireland
[2] ITMO University, St. Petersburg, 197101, Russia
*corresponding author, E-mail: igounko@tcd.ie

Abstract

Anisotropic nanostructures have unique physical properties including a high aspect ratio, optical polarization anisotropy, giant birefringence and many others. Here we demonstrate advances in the development of new chiroptically active anisotropic nanostructures such as rods, tetrapods, 2D nanomaterials and others. We present the progress in various colloidal chemistry approaches for the synthesis of these chiral nanostructures. We also discuss structure-property relations as well as the corresponding potential applications of these nanomaterials in sensing, photocatalysis, biology and other areas.

1. Introduction

It is well known that at the nanoscale, properties of semiconducting nanostructures are highly dependent on geometrical factors such as size and shape. Accurate control of size, shape and aspect ratio enables the move from 0-dimentional to 1-, 2, and 3 D systems and generates new types of anisotropic nanostructures. These new anisotropic nanostructures are of great interest for science and technology as they are expected to demonstrate considerable advantages over their 0-D spherical counterparts in various areas, including enhanced energy harvesting, improved charge transport properties, nonlinear optical responses, enhanced optical gain and polarized light absorption and emission. Therefore over recent years there was considerable interest in the synthesis and investigation of new anisotropic quantum nanostructures.

Chirality is a fascinating occurrence of asymmetric structures, giving rise to chiral molecules in the real world with two mirror-image forms, termed enantiomers, which are non-superimposable in three dimensions. Overall, chirality plays an important role in molecular recognition and therefore chiral compounds play a very significant role in chemistry, biology, pharmacology and medicine. Chirality has been studied in a range of nanomaterials including quantum dots [1], transition metal oxides [2] and metal nanoparticles [3], since it has been envisaged to play an important role in inorganic material based nanotechnology [4] due to the range of potential applications offered by these materials including chiral sensors, catalysts and as metamaterials in advanced optical devices.[1, 5-7] Therefore, an understanding and development of the fundamental concepts relevant to chirality in these systems is of paramount importance.

2. Results and Discussion

We have developed a range of new anisotropic chiral nanomaterials including chiral II-VI semiconducting nanostructures and metal oxides (e.g. TiO_2). The new nanomaterials have shown a very interesting optical activity and unusual chiral morphologies which were confirmed by various instrumental techniques. We have found that in some nanocrystals (e.g. CdSe/ZnS quantum rods) the chirality and corresponding optical activity are intrinsic features that can occur even without the presence of chiral ligands. The intrinsic chirality of the nanocrystals is caused by the presence of intrinsically occurring chiral defects such as dislocations or point defects in these nanostructures. The use of chiral ligands enabled us to separate these nanostructures into different phases and enhance their chiroptical activity. Chiral anisotropic nanomaterials have shown very interesting biological behavior. For example, it was found that live cells demonstrate an enantioselective uptake of chiral quantum tetrapodal nanostructures.

We have also demonstrated potential applications of selected anisotropic chiral nanostructures for chiral recognition and luminescent chemo- and bio- sensing.

In addition, we have prepared new chiral 2D nanomaterials by liquid exfoliation of MoS_2 and WS_2 in the presence of appropriate chiral ligands (e.g. cysteine and penicillamine) in water by ultrasonic treatment. These chiral 2D nanomaterials have been characterised by UV-Vis absorption spectroscopy, circular dichroism (CD) spectroscopy, Diffuse Reflectance Infrared Fourier Transform (DRIFT), X-ray photoelectron spectroscopy (XPS), Raman spectroscopy, Transmission electron microscopy (TEM) and Scanning Transmission electron microscopy (STEM). Using theoretical modelling we demonstrated that the chiral nature of MoS_2 nanosheets is related to the presence of chiral ligands causing preferential

folding of the MoS_2 sheets. There was an excellent match between the theoretically calculated and experimental spectra (Figure 1) [8].

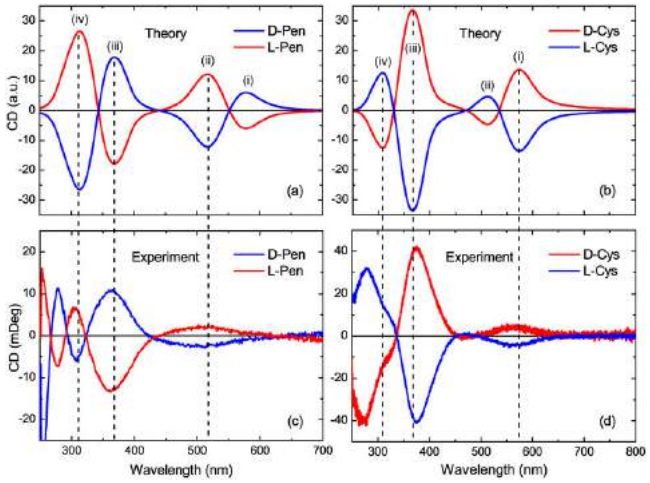


Figure 1: Comparison between [(a) and (b)] theoretical and [(c) and (d)] experimental spectra of MoS_2 nanosheets exfoliated in the presence of penicillamine (left panels) and cysteine (right panels) molecules.

We believe that due to their high aspect ratio planar morphology, chiral 2D nanomaterials could offer great opportunities for the development of chiroptical sensors, materials and devices for valleytronics and other potential applications. Also it is expected that anisotropic chiral nanomaterials will find applications in asymmetric catalysis and as metamaterials in various optical devices

3. Conclusions and outlook

Thus anisotropic chiroptically active nanostructures present a great interest for science and technology as they demonstrate several advantages over their lower dimensional QD counterparts, including enhanced energy harvesting, improved charge transport properties, nonlinear optical responses, enhanced optical gain and unique circular polarized light absorption and emission. However, one of the primary barriers to the effective utilization of anisotropic nanostructures is the need to develop new synthetic approaches enabling to produce new uniform anisotropic nanostructures with narrow size distribution. Further research is required in order to improve synthetic methods and fabrication processes and to provide better control of the structural complexity, composition uniformity, surface chemistry interface electronics, and the yield of anisotropic nanostructures. Another very important aspect is the detailed investigation of biological activity and behavior of chiral anisotropic nanomaterials. The unique shape and small size of semiconductor nanocrystals may lead to unusual and unexpected interactions with biomolecules, live cells and tissues. This should have a pronounced effect on biological activity and toxicity of chiral nanostructures affecting their further production and potential applications in biological imaging, diagnostics and therapy.

Acknowledgements

The authors gratefully acknowledge financial support from the Science Foundation of Ireland (Grant SFI 12/IA/1300) and the Ministry of Education and Science of the Russian Federation (Grant No. 14.B25.31.0002).

References

[1] F.P. Milton, J. Govan, M.V. Mukhina, Y.K. Gun'ko, The chiral nano-world: chiroptically active quantum nanostructures, *Nanoscale Horizons* 1: 14-26, 2016.

[2] O. Cleary, F. Purcell-Milton, A. Vandekerckhove, Y.K. Gun'ko, Chiral and Luminescent TiO_2 Nanoparticles, *Advanced Optical Materials* 5: 1601000, 2017.

[3] M. Farrag, M. Tschurl, U. Heiz, Chiral Gold and Silver Nanoclusters: Preparation, Size Selection, and Chiroptical Properties, *Chemistry of Materials*, 25: 862-870, 2013.

[4] W. Ma, L.G. Xu, A.F. de Moura, X.L. Wu, H. Kuang, C.L. Xu, N.A. Kotov, Chiral Inorganic Nanostructures, *Chemical Reviews*, 117: 8041-8093, 2017.

[5] A. Guerrero-Martinez, J. Lorenzo Alonso-Gomez, B. Auguie, M. Magdalena Cid, L.M. Liz-Marzan, From individual to collective chirality in metal nanoparticles, *Nano Today* 6: 381-400, 2011.

[6] A.O. Govorov, Y.K. Gun'ko, J.M. Slocik, V.A. Gerard, Z. Fan, R.R. Naik, Chiral nanoparticle assemblies: circular dichroism, plasmonic interactions, and exciton effects, *Journal of Materials Chemistry*, 21: 16806-16818, 2011.

[7] A. Ben-Moshe, B.M. Maoz, A.O. Govorov, G. Markovich, Chirality and chiroptical effects in inorganic nanocrystal systems with plasmon and exciton resonances, *Chemical Society Reviews*, 42: 7028-7041, 2013.

[8] F. Purcell-Milton, R. McKenna, L.J. Brennan, C.P. Cullen, L. Guillemeney, N.V. Tepliakov, A.S. Baimuratov, I.D. Rukhlenko, T.S. Perova, G.S. Duesberg, A.V. Baranov, A.V. Fedorov, Y.K. Gun'ko, Induction of Chirality in Two-Dimensional Nanomaterials: Chiral 2D MoS_2 Nanostructures, *ACS Nano*, DOI: 10.1021/acsnano.7b06691, 2018.

Moiré Chiral Metamaterials with Tunable Optical Chirality for Ultrasensitive Sensing

Zilong Wu[2] and Yuebing Zheng[1,2,*]

[1]Department of Mechanical Engineering, The University of Texas at Austin, Austin, TX 78712, USA.
[2]Materials Science & Engineering Program and Texas Materials Institute, The University of Texas at Austin, Austin, TX 78712, USA
*corresponding author, E-mail: zheng@austin.utexas.edu

Abstract

Moiré chiral metamaterials (MCMs) with strong optical chirality and active tunability were developed to achieve enantiodiscrimination of chiral molecules and sensing of solvent contaminants with ultrahigh sensitivity.

1. Introduction

Plasmonic chiral metamaterials with strong optical chirality and high tunability in visible and near-infrared light regimes have emerged as promising candidates for photonic sensors and devices.[1-4] Here, we demonstrate a new type of ultrathin chiral metamaterials, known as MCMs, to overcome limits in current chiral metamaterials that rely on local structural chirality or site-specific symmetry breaking. Moreover, we have exploit Fano coupling as a new mechanism to achieve ultrathin active chiral metamaterials of highly tunable chiroptical responses by adding a dielectric spacer layer in MCMs. We further introduce silk fibroin as spacer to achieve silk-MCMs that are actively tunable by controlling the polarity of surrounding solvents.

2. MCMs and ultrasensitive enantiodiscrimination of chiral molecules

As schematically shown in Figure 1(a), MCMs consisted of two layers of identical achiral Au nanohole arrays stacked into moiré patterns.[5] The patterns and the resulted chiroptical responses can be precisely tuned by controlling the interlayer rotation angle between the top and the bottom Au nanohole arrays. The MCMs can be cost-effectively fabricated by the combination of nanosphere lithography, standard thin film deposition, and a wet-chemical transfer process. Figure 1 (b) and (d) show the scanning electron microscopy (SEM) images of left-handed (LH) and right-handed (RH) MCMs, respectively. The optical chirality was characterized by circular dichroism (CD), which was obtained by the difference between transmission under LH and RH circularly polarized lights. The strong chiroptical effects of MCMs have been applied to detect the chirality of chiral molecules. Figure 1(e) shows the detection of

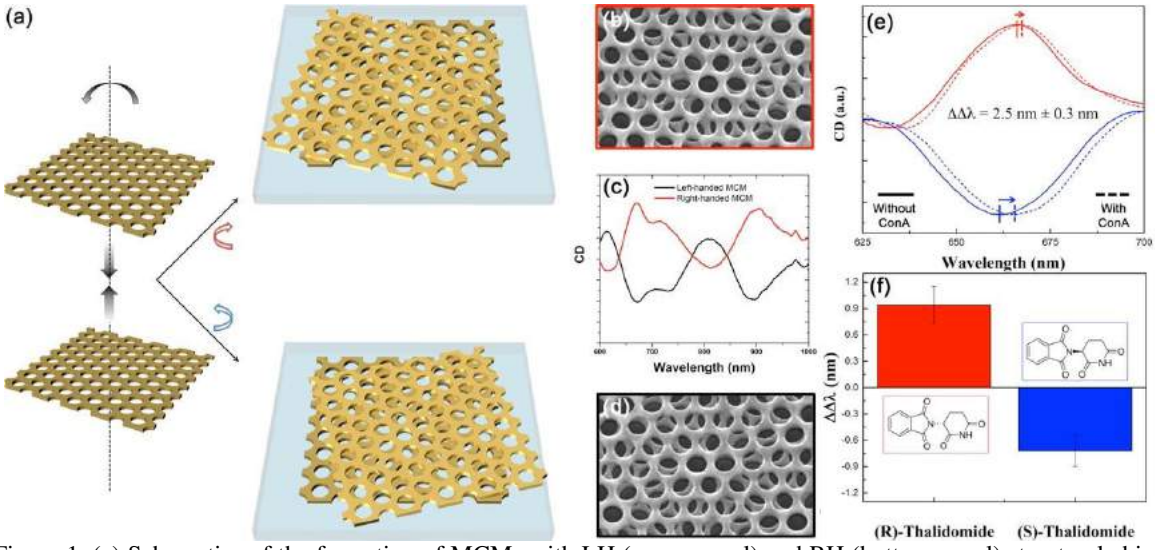


Figure 1. (a) Schematics of the formation of MCMs with LH (upper panel) and RH (bottom panel) structural chirality. (b) and (d) show the SEM images of the LH and RH MCMs, respectively. (c) CD spectra of the LH and RH MCMs. (e) and (f) Enantiodisctimination of ConA (e) and thalidomide (f) based on plasmonic polarimetry.

chirality of concanavalin A (ConA), which is a chiral protein. We have further demonstrated that MCMs can distinguish a therapeutic chiral drug, R-thalidomide, from its medically toxic enantiomer (S-thalidomide) at picogram level in a label-free manner, as shown in Figure 1(f).

3. Active MCMs and ultrasensitive detection of solvent contaminants

We have introduced Fano coupling in MCMs by adding a dielectric spacer between the top and bottom layers of Au nanohole arrays. Our simulations and experiments reveal that spacer-dependent Fano coupling exists in the MCMs, which significantly enhances the spectral shift and line shape change of the CD spectra of the MCMs. We further used a silk fibroin thin film as an active spacer layer in the MCMs, as shown in Figure 2(a). With the solvent-controllable swelling of the silk fibroin thin films, we demonstrated tunable Fano coupling and chiroptical responses of the silk-MCMs using different solvents and their mixtures, as shown in Figure 2(b). Impressively, we have achieved the spectral shift over a wavelength range that is more than one full width at half maximum and the sign inversion of the CD spectra in a single ultrathin (1/5 of wavelength in thickness) MCM. Finally, we applied the silk-MCMs as ultrasensitive sensors to detect trace amount of solvent impurities down to 200 ppm, corresponding to an ultrahigh sensitivity of $>10^5$ nm/refractive index unit (RIU) and a figure of merit of 10^5 /RIU.

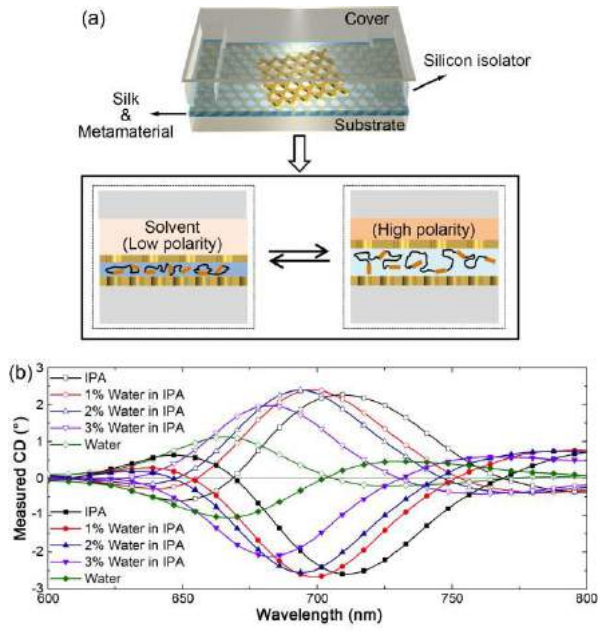


Figure 2. (a) Schematic demonstration of the silk-MCM and the controllable spacer thickness by the solvent polarity. (c) Measured CD spectra of LH and RH silk-MCMs at water-IPA mixtures with different water concentrations.

4. Conclusions

Plasmonic chiral metamaterials based on moiré patterns have been demonstrated. The patterns and the resulted chiroptical responses can be precisely controlled by the interlayer rotation angle between the two Au nanohole arrays. By introducing spacer-dependent Fano coupling and a silk fibroin spacer layer between the Au nanohole arrays, actively tunable chiroptical responses have been achieved. With their strong and tunable optical chirality, in combination with robust cost-effective fabrication, the MCMs will become critical components for chiroptical devices. Our results also pave a way towards active chiral metamaterials of high tunability, ultrathin thickness and large-scale fabrication for a wide range of applications.

References

[1] J. T. Collins, C. Kuppe, D. C. Hooper, C. Sibilia, M. Centini, and V. K. Valev: Chirality and Chiroptical Effects in Metal Nanostructures: Fundamentals and Current Trends. *Advanced Optical Materials*, 1700182 (2017).

[2] L.Zhang, S. Mei, K. Huang, and C.-W. Qiu: Advances in full control of electromagnetic waves with metasurfaces. *Advanced Optical Materials* 4(6), 818 (2016).

[3] M. Hentschel, M. Schäferling, X. Duan, H. Giessen, and N. Liu: Chiral plasmonics. *Science Advances* 3(5), e1602735 (2017).

[4] Z. Wu, and Y. Zheng: Moiré Metamaterials and Metasurfaces. *Advanced Optical Materials*, In press.

[5] Z. Wu, and Y. Zheng: Moiré Chiral Metamaterials. *Advanced Optical Materials* 5(16), 1700034 (2017).

Towards energy transfer of nanoemitters assisted by surface plasmons

Aurélie Broussier[1], Ali Issa[1], Loïc O. Le Cunff[1], Tien Hoa Nguyen[2], Dinh Xuan Quyen[2], Safi Jradi[1], Christophe Couteau[1] and Renaud Bachelot,[1,*]

[1] Institut Charles Delaunay, CNRS, Light, Nanomaterials, Nanotechnologies (L2N).
Université de Technologie de Troyes, 12 rue Marie Curie, 10004 Troyes Cedex, France
[2] CINTRA CNRS, Nanyang Technological University, Nanyang Avenue, Singapore 639798
*corresponding author, E-mail: renaud.bachelot@utt.fr

Abstract

Quantum plasmonic systems require efficient coupling between emitters and plasmonic structures. We present results on energy transfer between a plasmonic system (silver nanowires) and nanocrystals. The nanocrystals have been placed on the nanowires using photopolymerization. We used a confocal microscope to investigate the interactions between nanocrystals and surface plasmons on nanowires. When nanocrystals are in the close vicinity of nanowires, coupling between guided modes and nanocrystals emission can occur.

1. Introduction

The domain of plasmonic has been an area of interest for several years, especially the energy transfer between emitters through surface plasmons (SP) [1]. Nanocrystals (NCs) are well-known as good emitters [2] and their optical properties make them suitable candidates for light-emitting hybrid plasmonic systems. The position of the NCs, however, has to be accurately controlled to obtain an efficient coupling and energy transfer. Furthermore, the effectiveness of this transfer depends on the SP propagation length, which should be optimized. The two-photon photopolymerization (TPP) of a photosensitive material [3] allows one to place in a controlled way the NCs near the plasmonic system. A similar trapping of NCs around metal nanoparticles has previously been demonstrated, using evanescent fields to trigger the photopolymerization [4]. The idea of our work is to couple the CdSe/ZnS NCs emission to propagating SPs supported by silver nanowires (Ag-NWs), considered as SP resonators [5], and observe their scattering at the nanowire ends. The NCs can be placed at different distances from the Ag-NW end to obtain the maximum propagation length.

2. Discussion

In this study, the main challenge is to couple the NCs emission to the nanowire SP. The first step is to study the size, shape and length of the nanowires to see if surface plasmons can be launched. The Ag-NW are diluted in an isopropanol solution with a length dispersion between 5 to 50 µm (Sigma-Aldrich, ref 739448). Scanning electron microscopy (SEM) images showed that the average nanowire diameter is 160 nm. Moreover, the nanowire end geometry is conical in shape as we can see in Fig. 1(a).
First, we illuminated the nanowire tip with a 532 nm laser in order to launch SPs. As can be seen in Fig. 1(b) and (c), we obtain scattering at the other end of the nanowire. In fact, the specific nanowire end geometry allows one to efficiently couple surface plasmons into propagating waves that can be detected in the far field. Fig. 1(d) shows the spectrum characterizing the scattering at the nanowire end when we excite the other end with a laser power of 6.7 µW. As we can expect, there is a decrease between the excitation spot (red curve) and the scattered intensity (blue curve).

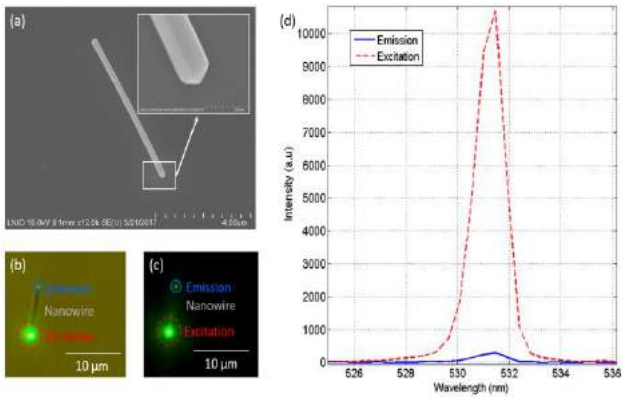


Figure 1: (a) SEM image of a Ag-NW (length around 7 µm), (b) and (c) optical image of a nanowire excited by a laser at 532 nm in bright field and dark field respectively. (d) Spectrum of the scattering (blue curve) and excitation (red curve) spots for a power of 6.70 µW.

The next step is to find NCs with an emission wavelength similar to the laser previously used. CdSe/ZnS NCs have been chosen for their emission wavelength centered around 510 nm, as shown in Fig. 2. Eventually, a parameter that has to be taken into account is the wavelength at which we will excite the NCs, which can be determined through their absorption spectrum as shown on Fig. 2 (dashed line). A 405 nm laser was chosen to excite the NCs. At this wavelength, direct excitation of Ag wire SPs turns out to be impossible (or negligible).

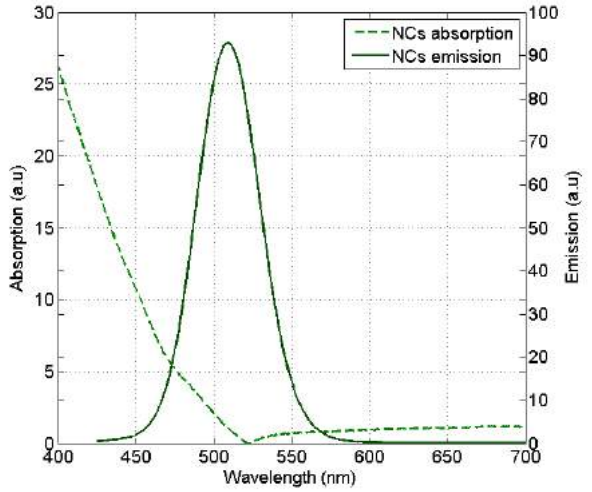


Figure 2: CdSe/ZnS NCs absorption (dashed line) and emission (full line) spectra.

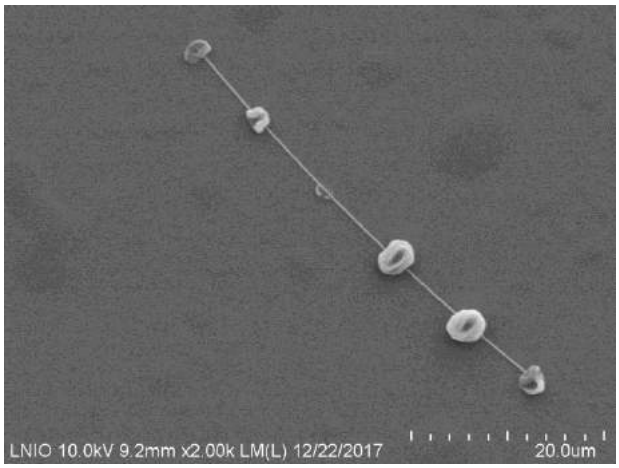


Figure 3: SEM image of Ag-NW with 6 dots of NCs with a 10 µm spacing between each, with different exposure times.

The chosen NCs and Ag-NW make a compatible pair for a promising hybrid plasmonic system. Controlled integration of emitters on the nanowire is needed: good control of size and location of the polymer dots containing the NCs is expected to enable efficient NCs/Ag-NW coupling.

The NCs trapping process is as follows: first, NCs were grafted to a polymer called pentaerythritol triacrylate (PETIA). We then added 1% of Irgacure (IRG 819) which is a photoinitiator allowing efficient TPP in the near infrared. The photopolymerization is done using the Nanoscribe laser writing system (Nanoscribe GmbH) based on the use of a femtosecond pulsed laser (λ_0 = 780 nm) with circular polarization. In a typical TPP process, light induces the polymerization reaction when the exposure dose exceeds a given threshold D_{th}. In our experiment, we used a incident dose D_0 that is lower than D_{th} in order to selectively integrate polymer structures in the close vicinity of the nanostructures through local plamon-induced thermal effects. After the TPP process, the unpolymerized NCs-grafted solution is removed by rinsing in acetone and isopropanol for 10 min each. As can be seen in Fig. 3, NCs-containing polymer dots were successfully integrated to the Ag nanowire. Polymer dot size turns out depends on the TPP exposure time: dots area around the nanowire grows as the exposure time increases, allowing control of location and density of NCs around nanowires.

3. Conclusions and perspectives

In conclusion, we realized a hybrid plasmonic system based on Ag nanowires and NC-containing polymer dots which size and location are controlled.

We hope to excite the NCs with a 405 nm laser and detect their emission through SPP launching, propagation and scattering at the end our silver nanowires. In the near future, this approach will allow for a parametric study of the maximum energy transfer distance in a NC-based donor-acceptor system, assisted by surface plasmons. We find a second NC type with lowest energy. Furthermore, we can reduce the concentration of NCs in the PETIA to move towards a plasmonic system containing single emitters, opening an avenue towards new hybrid quantum photonic nanosystems.

Acknowledgements

The authors would like to thank the platform Nano'mat and the ANR that funds the ACTIVE-NANOPHOT project.
This work is done within the context of the national ACTION Labex project.

References

[1] J. de Torres *et al*., Coupling Emitters and Silver Nanowires to Achieve Long-Range Plasmon-Mediated Fluorescence Energy Transfer, *ACS Nano*, **10**, 3968-3976, 2016.

[2] D. J. Norris and M. G. Bawendi, Measurement and assignment of the size-dependent optical spectrum in CdSe quantum dots, *Phys. Rev. B*, **53**, 16338, 1996.

[3] J. Serbin, *et al*., Femtosecond Laser-Induced Two Photon Polymerization. *Optics letters*, 301, 2003.

[4] X. Zhou, *et al*., Two-Color Single Hybrid Plasmonic Nanoemitters with Real Time Switchable Dominant Emission Wavelength, *Nanoletters*, **15**, 7458-7466, 2015.

[5] H. Ditlbacher, *et al*., Silver Nanowires as Surface Plasmon Resonators, *Phys. Rev. Lett*., 95, 257403, 2005.

Artificial chirality with fractal aluminum nanostructures

Dmitry Khlopin[1], Jérôme Martin[1], and Davy Gérard[1,*]

[1]Light, Nanomaterials, Nanotechnologies (L2N), Institut Charles Delaunay, CNRS, Université de Technologie de Troyes, Troyes, France
*corresponding author, E-mail: davy.gerard@utt.fr

Abstract

We propose, design and characterize aluminum nanostructures based on the Cayley tree fractal geometry. We demonstrate that adding a twist angle in the fractal geometry generates artificial circular dichroism.

1. Introduction

Chirality is a widespread property in the natural world, both at the macroscopic and microscopic scales. Chirality is often probed with optical techniques based on circular dichroism (CD), i.e. the difference in the optical absorption of a chiral object under left- and right-circularly polarized light. Natural CD exists in chiral moelcules, but it can also be observed and engineered in artificial structures such as chiral metamaterials, metasurfaces and metamolecules. In particular, plasmonic nanostructures with chiral shapes have been shown to exhibit high values of artificial CD, linked to the various localized surface plasmon resonances (LSPR) in the nanostructure [1]. In the following, we propose planar aluminum nanostructures based on the Cayley tree fractal to generate artificial circular dichroism.

2. Results

Fractal plasmonics has been recently proposed as a way to obtain scalable plasmonic resonances. Gottheim and co-workers [2] demonstrated broadband and tunable plasmonic resonances using simple fractal geometries (Cayley trees). By playing with the mathematical complexity of the structure, fractal plasmonics allow the creation of complex plasmonic modes with intricate spatial distribution, while keeping a relative ease of fabrication. As aluminum exhibits a broadband plasmonic response, ranging from the ultraviolet to the infrared [3], we fabricated Cayley trees made of aluminum (Figure 1).

However, the fractal structure depicted in Figure 1 is not chiral. In order to impose circular dichroism, it is necessary to twist the fractal geometry. Hence, we introduced a rotation angle between each generation (i.e. branch) of the Cayley tree. The resulting fractal is twisted and cannot be superimposed to its mirror image: it is chiral. In this communication, we will demonstrate that twisted aluminum fractals exhibit CD in the visible range. Furthermore, our numerical calculations evidence the presence of superchiral light around the metallic nanostructures, i.e. spatial regions where the twist of light is locally enhanced.

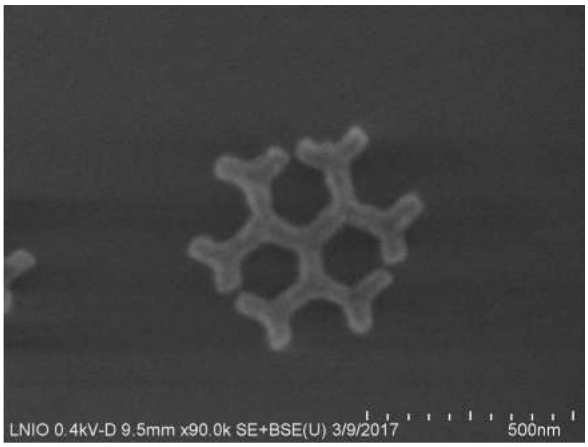


Figure 1: MEB picture of an achiral fractal aluminum nanostructure (Cayley tree).

3. Conclusion

Using twisted Cayley tree fractals, we demonstrated circular dichroism and superchirality in aluminum nanostructures. The structures are fabricated using conventional e-beam lithography and are easily scalable.

References

[1] J.T Collins, C. Kuppe, D.C. Hopper, C. Sibilia, M. Centini and V.K. Valev, Chirality and chiroptical effects in metal nanostructures: fundamentals and current trends, *Adv. Opt. Mater.* 5:1700182 (2017)

[2] S. Gottheim, H. Zhang, A.O. Govorov and N.J. Halas, Fractal Nanoparticle Plasmonics: The Cayley Tree, *ACS Nano* 9:3284-3292 (2015)

[3] D. Gérard and S.K. Gray, Aluminium plasmonics, *J. Phys. D: Appl. Phys.* 48: 184001, 2015.

Plasmonic Nanomaterials as Infrared-Blocking Radiation Filters and Energy-Saving Glasses

Lucas V. Besteiro[1,2,*], Xiang-Tian Kong[1,3], Zhiming Wang[1], Federico Rosei[2], and Alexander O. Govorov[3]

[1]Institute of Fundamental and Frontier Sciences, University of Electronic Science and Technology of China, Chengdu, Sichuan, China
[2]Institut National de la Recherche Scientifique – Énergie, Materiaux Télécommunications, Varennes, Québec, Canada
[3]Department of Physics and Astronomy, Ohio University, Athens, Ohio, USA
*corresponding author, E-mail: lucas.besteiro@emt.inrs.ca

Abstract

Plasmons are collective excitations of charge carriers in nanostructured materials. Using different plasmonic materials to fabricate nanocrystals and controlling their size and geometry allows us to obtain sharp resonances from UV to near IR. By embedding ensembles of nanocrystals in dielectric materials, we can design metamaterials with specific transmission profiles that filter out a broad spectrum while remaining transparent to selected frequency bands. We overview this idea, alongside general design principles and illustrative implementations for applications such as energy-saving windows.

1. Introduction

One key characteristic of plasmonic resonances is their strong coupling with electromagnetic radiation, affording interaction cross sections much larger than the geometrical cross sections of the nanocrystals (NCs). Furthermore, the spectral dependency of plasmonic resonances with the size and geometry of the NC make of plasmonic nanostructures a versatile tool to create miniaturized optical devices and metamaterials [1]. The work summarized here approaches the creation of electromagnetic filters by using a linear combination of the extinction of different plasmonic NCs, either in a colloidal suspension or embedded into a polymer or glass, to efficiently cover the part of the electromagnetic spectrum, while respecting a, potentially narrow, window of frequencies in which the material remains transparent.
Such systems, if adequately deployed, can be used to shield electronic components from external radiation while maintaining a detection channel open, or to create energy-efficient passive cooling glasses, for example.

1.1. Theoretical approach

Computational methods using classical electrodynamics are well suited to predict the spectral response of plasmonic NPs, and they have been extensively used during the last decades to facilitate the design of nanostructures interacting in the optical range. They are a powerful tool to predict the extinction profiles of plasmonic systems, thus allowing to find the right geometrical ensemble that affords specific spectral responses.
The theoretical study and design of the plasmonic nanocomposites mentioned herein have been accomplished using the simple theoretical framework of Beer-Lambert law, which provides an important insight on how to connect the attenuation of light of a macroscopic sample,

$$I/I_0 = 10^{-OD} \quad (1)$$

where I_0 and I are the incident and transmitted light intensity, respectively, to the microscopic characteristics of such sample. According to the B-L law, the optical density, OD, of the sample can be expressed in terms of the extinction cross section of the light-interacting species in it, σ_i, and their corresponding number densities, n_i, through the relationship

$$OD = L/\ln 10 \sum_i \sigma_i n_i \quad (2)$$

which also includes the optical thickness of the sample, L.

2. Plasmonic nanocomposites

Different implementations are possible when using plasmonic nanocomposites as radiation filters.

2.1. Patterned layouts

In an approach that resembles many of the contributions to optical metamaterials on the optical domain, a single layer of plasmonic nanostructures can be deposited on a substrate. This method makes possible the creation of long rods and crosses through lithographic techniques, covering spectra reaching wavelengths up into mid-wavelength IR [2,3]. An example of such system can be seen in Fig. 1. Without considering layer stacking, which represents a major fabrication difficulty, the total extinction achievable with this is strategy is limited by the planar NC density.

2.2. Ensembles in solution and embedded in glass

A different approach would use the dispersion of a heterogeneous ensemble of NC into a dielectric matrix, be it liquid [2-4] or solid [5]. The NC concentration in this kind of systems can be easily increased to fully attenuate selected

wavelength ranges, and the fabrication of the suspended NCs can be performed through scalable methods of colloidal synthesis and gas-phase deposition. We illustrate the expected outcomes of such nanocomposites in Fig. 2, which shows the expected transmission window obtained with a range of sizes of copper nanoshells. Other shapes investigated were nanocups [6] and nanorods. However, we have found that nanoshells are the best candidates for IR-blocking energy-saving glasses.

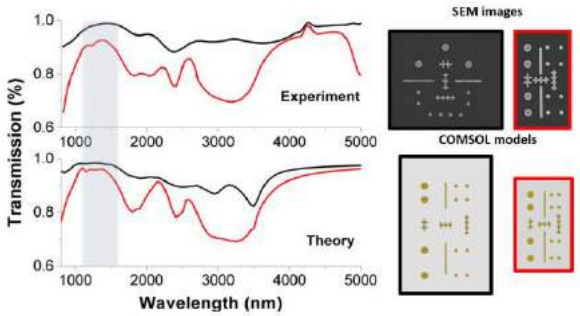


Figure 1. Theoretical and experimental transmission profiles of planar metastructures with different surface densities of individual NCs. Reproduced from Ref. [3].

3. Alternative materials

Much of the research conducted on plasmonics uses gold for of its desirable properties, e.g. narrow optical resonances and chemical stability, but its high price represents an important difficulty when considering realistic industrial applications at scale. A variety of alternative materials for their use in plasmonics have been steadily appearing in the literature, partly to access different spectral ranges, but also to provide cheaper alternatives to the use of noble metals. Adhering to this latter goal, we have examined the viability of several materials (Au, Ag, Cu, Al, TiN) in the design of plasmonic radiation filters [5].

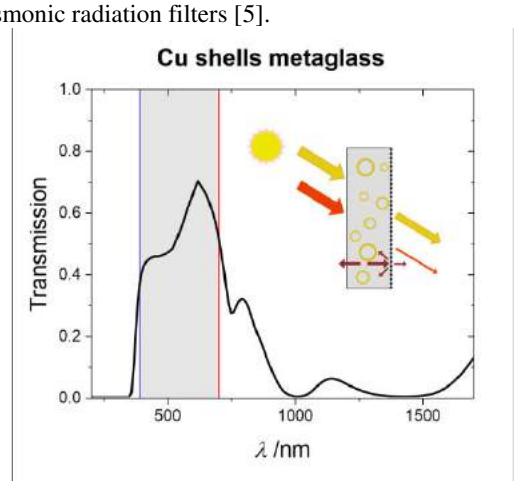


Figure 2. Theoretical transmission profile of an ensemble of differently-sized Cu nanoshells embedded in glass, with the visible spectrum highlighted in grey. Inset: diagram of its possible use within passive cooling windows, filtering out the IR component of solar radiation (red arrows), while remaining transparent to visible light (yellow arrows). Adapted from Ref. [5]

4. Conclusions

We have examined a variety of methods to integrate differentiated plasmonic resonant modes in carefully designed collection of NCs, achieving broadband attenuation of electromagnetic radiation while preserving the transparency of the material in selected spectral ranges.
In particular, this can be done using a variety of different plasmon-supporting materials, so in addition to several geometries we have surveyed a number of promising alternatives to noble metals that can provide comparable results at prices that could allow a wider implementation in commercial applications.

Acknowledgements

L.V.B. was supported by China Postdoctoral Science Foundation (2017M622992). This work was supported by Volkswagen Foundation and by the EU RISE project 734690-SONAR (A.O.G.). Z.W. was supported by National Basic Research Program of China (project 2013CB933301) and National Natural Science Foundation of China (project 51272038). A.O.G. and F.R. are Chang Jiang (Yangtze River) Chair Professors of the Government of China. F.R. is grateful to the Canada Research Chairs program for partial salary support. F.R. also acknowledges Sichuan Province for a 1,000 talent short term award.

References

[1] S.A. Maier, *Plasmonics: fundamentals and applications*, Springer, New York, 2007.

[2] H. Zhang, H.V. Demir, A.O. Govorov, Plasmonic Metamaterials and Nanocomposites with the Narrow Transparency Window Effect in Broad Extinction Spectra, *ACS Photonics* 1: 822–832 (2014).

[3] L.V. Besteiro, K. Gungor, H.V. Demir, A.O. Govorov, Simple and Complex Metafluids and Metastructures with Sharp Spectral Features in a Broad Extinction Spectrum: Particle–Particle Interactions and Testing the Limits of the Beer–Lambert Law, *J. Phys. Chem. C* 121: 2987–2997 (2017).

[4] J. Yang, N.J. Kramer, K.S. Schramke, L.M. Wheeler, L.V. Besteiro, C.J. Hogan Jr., A.O. Govorov, U.R. Kortshagen, Broadband Absorbing Exciton−Plasmon Metafluids with Narrow Transparency Windows, *Nano Lett.* 16: 1472-1477 (2016).

[5] L.V. Besteiro, X.-T. Kong, Z. Wang, F. Rosei, A.O. Govorov, Plasmonic Glasses and Films Based on Alternative Inexpensive Materials for Blocking Infrared Radiation, *Nano Lett.* 18: 3147-3156 (2018).

[6] Y. Qin, X.-T. Kong, Z. Wang, A. O. Govorov, U. R. Kortshagen, Near-infrared plasmonic copper nanocups fabricated by template-assisted magnetron sputtering, *ACS Photonics* 4: 2881-2890 (2017).

Plasmon-Enhanced Quantum Dot Solar Cells

Jiang Wu[1*], Peng Yu[2], Alexander Govorov[2,3], and Zhiming Wang[2]

[1]Department of Electronic and Electrical Engineering, University College London, Torrington Place, London WC1E 7JE, United Kingdom
[2]Institute of Fundamental and Frontier Sciences, University of Electronic Science and Technology of China, Chengdu 610054, PR China
[3]Department of Physics and Astronomy, Ohio University, Athens, OH 45701, USA
*corresponding author, E-mail: jiang.wu@ucl.ac.uk

Abstract

In this paper, plasmon-enhanced InAs/GaAs quantum dot solar cells have been investigated. Detailed optical characterization has been carried out to study the effects of different kinds of plasmonic metal nanoparticles on the performance of quantum dot solar cells. We demonstrate that star-shaped gold nanoparticles can be particularly helpful in enhancing the absorption in the quantum dot solar cells. Finite-difference time-domain method is used to analyze the efficiency enhancement, indicating the broad plasmon resonances of nanostars with different sizes and shapes.

1. Introduction

Quantum dot solar cells (QDSCs) is currently one of the main focuses for implementing intermediate band solar cells, which have a high theoretical efficiency beyond the Shockley-Queisser limit.[1] Since the proposal of intermediate band solar cell concept by Luque and Martì, a lot of efforts, driven by its high theoretical efficiency, have been devoted to quantum dot (QD) intermediate band solar cells.[2]-[5] Over the last decade, much progress has been made in proof-of-concept studies as well as realizing high efficiency quantum dot solar cells, including the demonstration of two photon absorption and enhanced photocurrent in QDSCs.[2], [6], [7] Despite these progresses, QD based intermediate band solar cells still remain challenging.

One of the major challenges to implement the intermediate band concept using QDs is the relatively low absorption volume of QDs.[8] In quantum dot solar cells, the additional photocurrent is generated by absorption of two photons via the intermediate quantized electron states in QDs. Due to the low density of states in QDs compared with bulk materials, the contribution from QDs is rather marginal. The enhancement of optical absorption in QDs plays a key role in realizing intermediate band solar cells.[9] Increasing the density of QDs has been often adopted by a number of methods, but the enhancement in photocurrent is rather limited, and in cases, it compromises the photovoltage.[10], [11]

In this paper, a distinct enhancement of the photon absorption in QDs have been achieved via depositing plasmonic nanostars on the QDSC surface.[8] The multispiked nanostars not only provide broadband forward scattering but also generate localized near field modes, which causes distinct improvement in quantum efficiency in the entire absorption spectrum.

2. Experiment

2.1. Fabrication of quantum dot solar cells

QDSCs were grown by the molecular beam epitaxy. The cell consists of a 300-nm p-type GaAs emitter and a 1.4 μm base. In the base region, 20 periods of InAs QDs were grown by the Stranski–Krastanov (S–K) growth mode and each period of QDs is separated by a 50-nm GaAs spacer. Solar cells were processed by standard photolithography and metallization.

2.2. Synthesis and deposition of gold nanostars

Gold nanostars were synthesized by a solution method using cetyltrimethylammonium bromide as the capping agent and ascorbic acid as the reducing agent. By controlling the reaction time, gold nanostars can be formed with a controllable number of surface protrusions (spikes). A simple and facile “boiling deposition” technique is used to deposit gold nanostars on the QDSC surface.

2.3. FDTD calculation

FDTD method was used to simulate the interaction of gold nanostars and QDSCs. Single gold nanostars with different morphology were simulated in air using perfectly matched layer and periodic boundary condition. The gold nanostars placed on a semi-infinite GaAs layer was simulated to calculate the light absorption enhancement in QDSCs. The influence of nanostar surface density on light absorption in the QDSC was also simulated. All the simulations were done by Lumerical FDTD Solutions software.

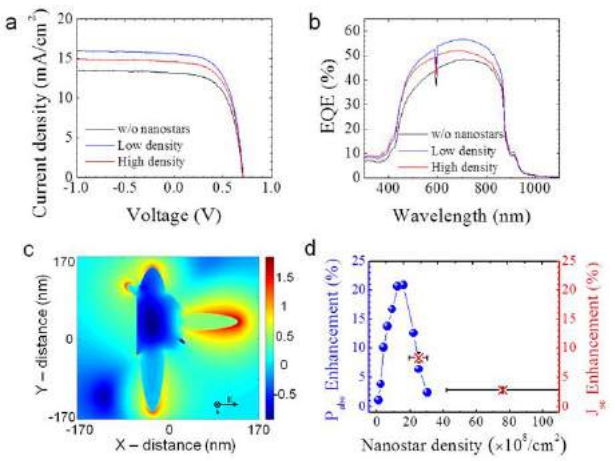


Figure 1: (a) Current-voltage characteristics and (b) external quantum efficiencies of QDSCs solar cells before and after deposition of different densities of gold nanostars. (c) Electrical field distribution near the gold nanostars on a logarithmic scale at the resonant wavelength (993 nm). (d) Simulated enhancement of the absorbed optical power for periodic arrays of gold nanostars at ~800 nm. The red crosses represent the experimentally observed short circuit current enhancement obtained from (a).

3. Discussion

As shown in Fig. 1a, the performance of the QDSCs has notably improved after deposition of gold nanostars. The short circuit current density (J_{sc}) increased to 15.65 mA/cm^2 from 13.15 mA/cm^2 after depositing with gold nanostars with a surface density of 2.9×10^9/cm^2. As shown in Fig. 1b, a maximum increase in power conversion efficiency of ~20% was obtained.

To gain insight into the enhancement of photocurrent, the interaction between the incident electromagnetic wave and multispiked nanostars was analysed the finite-difference time-domain method. Figure 1c shows the calculated electric field distribution near the gold nanostars on a logarithmic scale at the resonant wavelength of 993 nm. The electrical field distribution around the gold nanostar presents a strong electrical field. Therefore, electrical field is significantly enhanced and localised in the close proximity of gold nanostars, particularly at resonance excitation. The local field enhancement at resonance excitation can be as high 20 times compared with that under off-resonance conditions. Therefore, the enhanced light absorption in QDSCs can be attributed to the strong concentration of local electrical field by gold nanostars.

Figure 1d shows that the enhancement percentage of the absorbed light power as a function of nanostar density at a fixed wavelength of ~800 nm. This wavelength is selected to match one of the resonance peaks at long wavelength and to represent a general enhancement ratio in photocurrent. In agreement with the experiment, simulation shows that a gold nanostar array on a 2-μm GaAs thin film can lead to 21% improvement in the absorbed light power at ~800 nm. The nanostars generally have dimensions with a favourable ratio of the scattering to absorption cross-section in the long wavelength region, which cause the photocurrent improvement in the GaAs sub-bandgap region. On the other hand, despite a less favourable scattering/absorption ratio at short wavelength region, both experiment and simulation also shows that the near field of the plasmonic nanostructures may contribute to a significant enhancement of photocurrent up to four-fold.

4. Conclusions

Significant optical concentration by plasmonic nanostars has been demonstrated in QDSCs, which may potentially address the low optical absorption in QDs. Solar cells can particularly benefit from the distinct forward scattering of photons over a broad spectral range. However, the optical enhancement is yet needed to be further enhanced for the QD absorption. This requires design of new nanophotonic structures, e.g. placing the QDs in close proximity of plasmonic nanostars.

References

[1] A. Luque and A. Martí, "Increasing the Efficiency of Ideal Solar Cells by Photon Induced Transitions at Intermediate Levels," Phys. Rev. Lett., vol. 78, (26), pp. 5014, 1997.

[2] A. Martí et al, "Production of Photocurrent due to Intermediate-to-Conduction-Band Transitions: A Demonstration of a Key Operating Principle of the Intermediate-Band Solar Cell," Phys. Rev. Lett., vol. 97, (24), pp. 247701, 2006.

[3] N. López et al, "Experimental Analysis of the Operation of Quantum Dot Intermediate Band Solar Cells," Journal of Solar Energy Engineering, vol. 129, (3), pp. 319, 2007.

[4] G. Wei and S. R. Forrest, "Intermediate-Band Solar Cells Employing Quantum Dots Embedded in an Energy Fence Barrier," Nano Letters, vol. 7, (1), pp. 218-222, 2007.

[5] J. Wu et al, "Surface plasmon enhanced intermediate band based quantum dots solar cell," Solar Energy Mater. Solar Cells, vol. 102, (0), pp. 44-49, 7, 2012.

[6] K. A. Sablon et al, "Strong Enhancement of Solar Cell Efficiency Due to Quantum Dots with Built-In Charge," Nano Lett., vol. 11, (6), pp. 2311-2317, 2011.

[7] F. Tutu et al, "Antimony mediated growth of high-density InAs quantum dots for photovoltaic cells," Appl. Phys. Lett., vol. 103, (4), pp. 043901, 2013.

[8] J. Wu et al, "Broadband efficiency enhancement in quantum dot solar cells coupled with multispiked plasmonic nanostars," Nano Energy, vol. 13, pp. 827-835, 2015.

[9] A. Luque and A. Marti, "The Intermediate Band Solar Cell: Progress Toward the Realization of an Attractive Concept," Adv. Mater., vol. 22, (2), pp. 160-174, 2010.

[10] F. Tutu et al, "Antimony mediated growth of high-density InAs quantum dots for photovoltaic cells," Appl. Phys. Lett., vol. 103, (4), 043901, 2013.

[11] R. Oshima et al, "High - density quantum dot superlattice for application to high - efficiency solar cells," Physica Status Solidi (c), vol. 8, (2), pp. 619-621, 2011.

Ultra-Fine Electrochemical Tuning of the Plasmonic Dimer Structures to Generate Highly Confined Light Field

Hiro Minamimoto, Shunpei Oikawa, and Kei Murakoshi

Department of Chemistry, Faculty of Science, Hokkaido University, North 10 West 8, Kita-ku, Sapporo, Hokkaido 060-0810, Japan.
*corresponding author, E-mail: minamimoto@sci.hokudai.ac.jp

Abstract

The plasmon-active metal nano dimer structure with the gap distance less-than a single nm can confine the energy of light very effectively beyond the diffraction limit. In this study, we have tried to establish a new method by combining electrochemical method with in-situ dark-field microscopy for tuning the optical properties of Au nanodimers. Controlled metal dissolution in the size range below a few nm leads to the successful switching from the charge transfer plasmon (CTP) to the bonding dipolar plasmon (BDP) mode.

1. Introduction

Under illumination of visible or near-infrared light on the metal nanodimer structures, the unique photo response properties, such as polarization anisotropy, generating the hot electron, and light confinement at the gap, can be observed. These characteristics are originated from the excitation of the localized surface plasmon resonance (LSPR). Basically, these specific characteristics strongly depend on the shape, size, and the gap distance of the nanodimer structure. Interestingly, when the gap distance is down to sub-nanometer level, the strength of the excited near-field becomes much stronger due to the dipolar coupling. In addition to the optical polarization, for the case of the gap distance of less than 1 nm, the charge transfer plasmon (CTP) appears derived from the effect of the tunneling electrons [1]. Under the condition of the gap distance of less than 1 nm, the light scattering is extremely suppressed, so the highly concentrated light energy field, which can be applied to various fields can be obtained [2]. Based on these backgrounds, it can be easily expected that the fine tuning technique for these plasmon properties would lead to various nanophotonic applications, such as biological sensors, surface enhanced Raman scattering measurements, or photovoltaic devices. However, although there have been various techniques for the control of the nano-fabrication method, the sub-nm control of the dimer structure is still difficult under the ambient condition. Up to date, we have attempted to establish a novel technique for the ultra-fine tuning of the gap distance and the shape of Au nanodimer structures via the control of the electrochemical oxidation reaction at the surface of nanodimer [3]. In this study, the change in the photo-response property for well-defined Au nanodimer associated with the progress of the electrochemical oxidation reaction was evaluated by the in-situ electrochemical dark-field scattering measurements. Through the detailed analysis of the optical properties depending on the structural changes, atomic scale gap was prepared by the present method with high reproducibility and it shows very strong confinement of LSP filed.

2. Experiment

Individual Au nanodisk dimers with various gap distances (*D*) were fabricated on an indium tin oxide coated glass substrate by electron-beam lithography method. The detail about the structure preparation is reported in our previous report [4]. Electrochemical dissolution of Au nanostructures was performed in the 10 mM KBr solutions. Under dark-field microscopy measurements, the plasmonic property change have been analyzed with the system as depicted in Figure 1. In this system, the bridged Au nanodimer supported substrate, Pt plate, and Ag/AgCl wire were used as the working electrode (WE), counter electrode (CE) and reference electrode (RE), respectively. The electrode potential was set to 0.80 V for the dissolution of Au. The structural changes associated with the electrochemical Au dissolution were examined by scanning electron microscope (SEM) and atomic force microscopy.

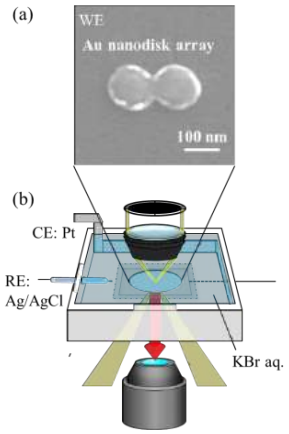


Figure 1: Schematic illustration of the present experimental system

3. Results and Discussion

Figure 2a shows SEM images of each prepared bridged Au nanodisk structures having the different gap distances (from −30 (bottom) to 30 nm (top)). According to the previous report, for the case of the dimer structures which have the enough size as the conductive path, a screened hybridized dipolar plasmon which is called CTP' mode is excited at higher energy region than the CTP mode. By the previous attempts, it was revealed that this CTP' mode shifts to lower energy correlated with the decrease of the size for the conductive path. In the present results, by the separation of two particles with the gap within the atomic scale, CTP' transfers to bonding dipolar plasmon (BDP) mode, resulting in the shift to the higher energy region. It is important that this mode transition was only confirmed under the polarized light illumination parallel to the long axis of the metal nanostructure (Figure 2c). Consequently, each plasmonic property depending on the change of the gap or the conductive path have been confirmed.

In order to tune the plasmonic properties by the change in the size of the conductive path or the gap distance, the electrode potential of the structure was set to 0.80 V for inducing the dissolution reaction of Au. The electrode potential was applied for 1200 s. SEM images were obtained before and after the dissolution. The images indicate the formation of the well-defined gap between Au nanoparticles. From the collection of time series scattering spectra of Au nanodimer, the transition from CTP' mode to BDP mode was observed. These experimental results would indicate that our electrochemical method can tune the structure of Au nanodimer very precisely with the sub-nm level. As one of the advantage for our technique, the rate for the optical property change can be easily tuned by the change in the electrode potential and the electrode polarized time. This result would strongly suggest that we have achieved the formation of the highly concentrated light energy fields via the electrochemical method. In addition to these experiments, we have succeeded in the assignment of each plasmon mode through the theoretical calculations.

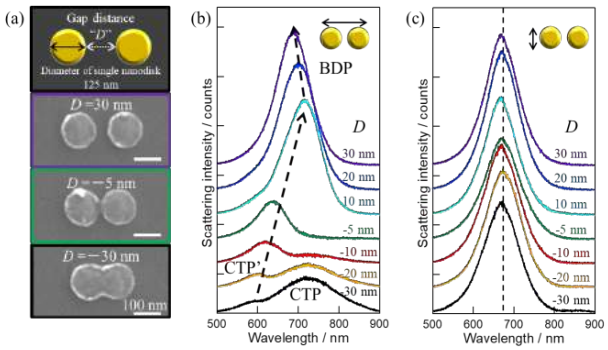


Fig. 2 Single particle dark-field scattering properties of bridged Au nanodisk dimers in the visible and NIR regimes. Thickness is 50 nm and radius of single Au nanodisk is 75 nm. (a) SEM images of individual bridged Au nanodisk dimers with a gap distance increasing from -30 (black) to 30 nm (violet). (b) Experimentally measured optical scattering spectra of individual Au nanodisk dimers by longitudinal polarization, (c) by transverse polarization.

4. Conclusions

From present results, it can be concluded that our method would be a useful tool for controlling the shape and the gap distance of Au dimer in a single nanometer scale. Now we strongly believe that our present method can be applied to novel technique of highly efficient light confinement for future.

References

[1] K. J. Savage and M. M. Hawkeye, *et al*., Revealing the quantum regime in tunneling plasmonics, *Nature*, 491, 574-577, 2012.

[2] H. Minamimoto. S. Oikawa, X. Li, and K. Murakoshi, Plasmonic Fields Focused to Molecular Size, ChemNanoMat, 3, 843-856, 2017.

[3] S. Oikawa, H. Minamimoto, X. Li, and K. Murakoshi, Nanoscale Control of Plasmon-Active Metal Nanodimer Structures via Electrochemical Metal Dissolution Reaction, *Nanotechnol*. 29(4), 045702, 2018.

[4] S. Oikawa, H. Minamimoto, and K. Murakoshi, Reversible Electrochemical Tuning of Optical Property of Single Au Nano-bridged Structure via Electrochemical under Potential Deposition, *Chem. Lett*. 46, 1148-1150, 2017.

Enhanced Terahertz Light – Matter Coupling in Plasmonic Nanocavities

Xin Jin[1], Andrea Cerea[2,3], Gabriele C. Messina[2], Andrea Rovere[1], Riccardo Piccoli[1], Francesco De Donato[2], Francisco Palazon[2], Andrea Perucchi[4], Paola Di Pietro[4], Roberto Morandotti[1,5,6], Stefano Lupi[7], Francesco De Angelis[2], Mirko Prato[2], Andrea Toma[2], and Luca Razzari[1,*]

[1]INRS Énergie, Matériaux et Télécommunications, 1650 Blvd Lionel Boulet, J3X 1S2 Varennes (Québec), Canada.
[2]Istituto Italiano di Tecnologia, via Morego 30, 16163 Genova, Italy.
[3]Dipartimento di Informatica, Bioingegneria, Robotica e Ingegneria dei Sistemi (DIBRIS), Università degli Studi di Genova, via Balbi 5, 16126, Genova, Italy.
[4]Elettra - Sincrotrone Trieste S.C.p.A, AREA Science Park, S.S. 14 km163.5, Trieste, Italy.
[5]National Research University of Information Technologies, Mechanics and Optics, 199034 St. Petersburg, Russia.
[6]Institute of Fundamental and Frontier Sciences, University of Electronic Science and Technology of China, Chengdu 610054, Sichuan, China.
[7]CNR-IOM and Dipartimento di Fisica, Università di Roma "La Sapienza", Piazzale A. Moro 2, I-00185, Roma, Italy.
*corresponding author, E-mail: razzari@emt.inrs.ca

Abstract

We report on our recent findings regarding the coupling of the resonance of terahertz nanoantennas with phonons in nanomaterials.

1. Introduction

Nanoantennas guarantee a strong enhancement of the local electric field, beyond the diffraction limit, which has been widely exploited, for example, in Raman and direct infrared absorption spectroscopies.

During the last years, we have investigated the properties of resonant nanoantennas for applications in terahertz (THz) science [1,2]. Such nanostructures can confine THz radiation on a deeply sub-wavelength scale and show high electric field values close to their extremities. The local field can be further increased by means of antenna nanocavities, which are obtained through the end-to-end coupling of THz nanoantennas in extremely narrow gaps (few tens of nanometers in width). The effective absorption of an object scales with the square of the local electric field and can thus be significantly increased within nanocavities. This can be employed to enhance the interaction of THz radiation with nanomaterials. In our investigation, we have explored the coupling between the phonon resonance of polar nanocrystals and the plasmon resonance of nanoantenna arrays. When the two resonances are matched, the combined system presents a clear destructive interference feature in its THz far-field response. This effect has been first used to perform enhanced THz spectroscopy of a single layer of quantum dots [3,4]. Recently, we have also found that, under proper conditions, such coupling can lead to significant modifications of the nanomaterial properties.

2. Experimental Results

We prepared arrays (200x200 μm^2) of 200-nm wide gold nanoantenna chains coupled through gaps of 30 nm along their long-axis direction and featuring a spacing 8.5 μm along their short-axis direction. Arrays with different nanoantenna length, ranging from 4 to 7 μm, were fabricated on the same silicon substrate, to tune their plasmonic resonance within a THz band comprising the Fröhlich (FR) optical phonon mode [5] of CdS nanocrystals (10 nm in diameter) at about 7.85 THz. A monolayer of nanocrystals was then spin-coated over the arrays and THz transmission measurements were performed on the sample. When the THz polarization was set parallel to the nanoantenna long axis, evidence of the onset of a plasmon-phonon hybridization was retrieved, as shown by the characteristic anti-crossing behavior that can be seen in the THz extinction map presented in Fig. 1.

Matter systems coupled to optical cavities can form new hybrid entities with peculiar properties that no longer belong to either the cavity or the matter element separately [6]. To investigate this at the scale of individual nanocavities, we have characterized our system by means of micro-Raman spectroscopy, exploiting the fact that the nanocrystal FR resonance is both THz and Raman active and can thus also be observed through Raman measurements. The Raman characterization performed on individual nanocavities has shown that the phonon spectrum of the nano-objects is profoundly modified, even in the absence of any THz illumination (i.e. with no direct excitation of the plasmonic cavities), triggered only by THz vacuum fluctuations. Indeed, two new "polariton" peaks (i.e. the result of the light-matter mixing) were observed in the Raman spectrum

at the two sides of the FR resonance. As expected, the separation between these peaks was found to increase with the number of nanocrystals in the cavity. More details regarding this investigation will be presented on site.

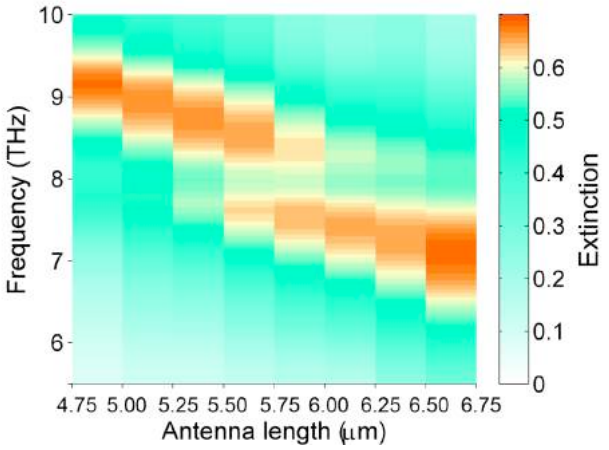


Figure 1: Experimental map of the plasmon-phonon polariton branches dispersion. The color bar corresponds to the values of the extinction E = 1 – T, where T is the array transmission.

3. Conclusions

In the last two decades, the combination of electronic transitions resonantly coupled to optical cavities has led to discoveries of paramount importance. Recently, vibrational transitions of molecules placed in infrared microcavities were also shown to strongly couple to the vacuum electric field [7,8], and this was found to significantly modify their structural and chemical properties [9]. Being inspired by these findings, we have applied this concept to phonons in nanosystems. We have shown that the phonon response of nanomaterials can be modified when the nano-objects are positioned inside a properly nano-engineered electromagnetic environment. This can have implications in our capacity to tailor the functional properties of nanomatter.

Acknowledgements

The authors are grateful for financial support from the Natural Sciences and Engineering Research Council of Canada (NSERC), PRIMA Quebec, Compagnia di San Paolo (ID ROL 10262), Fonds de Recherche du Québec - Nature et Technologies (FRQNT), Government of the Russian Federation (grant 074-U 01), and 1000 Talents Sichuan Program.

References

[1] L. Razzari, et al., *Opt. Express* 19: 26088, 2011.

[2] L. Razzari, et al., *Plasmonics* 8: 133, 2013.

[3] A. Toma, et al., *Nano Lett.* 15: 386, 2015.

[4] R. Piccoli, et al., Terahertz Nanoantennas for Enhanced Spectroscopy, in *Terahertz Spectroscopy - A Cutting Edge Technology*, ed. J. Uddin, InTech, 2017.

[5] G. Irmer et al., *Encyclopedia of Nanoscience and Nanotechnology* 4: 561, 2004.

[6] Y. Yamamoto, F. Tassone, H. Cao, *Semiconductor Cavity Quantum Electrodynamics*, Springer, Berlin Heidelberg, 2000.

[7] A. Shalabney et al., *Nat. Commun.* 6: 5981, 2015.

[8] A. Shalabney et al., *Angew. Chem. Int. Ed.* 54: 7971, 2015.

[9] A. Thomas et al., *Angew. Chem. Int. Ed.* 55: 11462, 2016.

Comparative plasmonic waveguide design for nanoscale lasing and four-wave mixing

S. Palomba[1,2,3*], G. Li[2,3], and C. M. de Sterke [2,3]

[1] The University of Sydney Nano Institute, the University of Sydney, NSW 2006, Australia
[2] Centre for Ultrahigh bandwidth Devices for Optical Systems (CUDOS), the University of Sydney, NSW 2006, Australia
[3] Institute of Photonics and Optical Science (IPOS), School of Physics, the University of Sydney, NSW 2006, Australia

*Corresponding author: Email stefano.palomba @sydney.edu.au

Abstract Summary: Nanolasers and nano-sized nonlinear optical devices are the two fundamental building blocks of any modern optical integrated circuit. In order to operate beyond the diffraction limit, these devices implement plasmonic waveguide-based platforms. However, both classes of devices are currently at an impasse. In this presentation we show how a unified theoretical framework can lead to novel and superior performing plasmonic waveguide configurations, in spite of the fact that the underlying physics is totally different.

Introduction: Modern optical integrated devices are limited by the diffraction of light, which can be overcome by implementing structures based on plasmonic waveguide platforms. Plasmonic nanolasing and nonlinear optical generations, such as four-wave mixing, developed separately due to their different physics, although both used metal-based configurations. Both fields are currently at an impasse. In order to break this impasse, we developed a unified theoretical approach.

Section Title: We find that the waveguide design for both lasing and degenerate four-wave mixing in lossless and in plasmonic waveguides can be described by a single theoretical framework, in spite of the distinct physics. We perform a global comparison of plasmonic waveguide configurations and show that the results to be essentially the same, though nanolasers require an additional buffer layer to eliminate quenching. Not only do we confirm the performance of configurations in the literature but also we exploit innovative designs with even better performance, and that may also solve the long-standing objective of low-threshold electrically pumped plasmonic nanolasers.

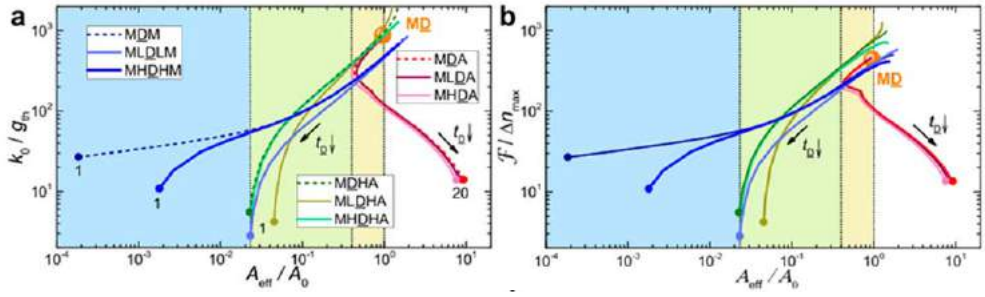


Fig. 1. (a) The ratio of the electric energy in the gain medium and in the lossy metal versus the normalized effective area for various nanolasing configurations. The continuous curves indicate configurations with a buffer layer in order to avoid quenching effects. (b) Figure of merit for four-wave mixing processes using the same plasmonic configurations as in (a). The graph represents the plot between the ratio between the electric energy in the nonlinear medium and in the lossy metal versus the normalized effective area. In both plots, t_D represents the thickness of the D layer.

Figure 1 shows the best performing plasmonic waveguide configurations, such as MDM, MLDLM, MHDHM, etc. where M stands for Metal, D for the active medium (for nanolasing) or the nonlinear medium (for four-wave mixing), L stands for low refractive index, H for high refractive index and A for air. Figure 1a shows the figure of merit for nanolasing, represented by the ratio k_0/g_{th} and the normalized effective area of the propagating plasmonic mode, where g_{th} is the gain threshold and $k_0 = 2\pi/\lambda$. The continuous lines represent configurations that include a buffer layer which is necessary for obtaining lasing action by avoid quenching effects. Figure 1b plots the ratio $\mathcal{F}/\Delta n_{max}$ versus the normalized effective area by comparing the same plasmonic configurations as per Figure 1a. $\mathcal{F}$ is the figure of merit for four-wave mixing based plasmonic devices [1,2], which quantifies the maximum conversion efficiency via $\eta_{max} = 4\mathcal{F}^2/27$, and Δn_{max} is the maximum index change sustainable by a nonlinear material. As is clear from Figure 1 both phenomena can be described by the same theoretical frameworks giving the same results, although the physics is totally different.

[1] Li, G.; de Sterke, C. M.; Palomba, S. “Figure of merit for Kerr nonlinear plasmonic waveguides”, Laser & Photonics Reviews, 10, (4), 639-646, 2016.

[2] Li, G.; de Sterke, C. M.; Palomba, “Fundamental limitations of Kerr nonlinear plasmonic waveguides” Accepted in ACS Photonics, 2018.

Tailoring the Resonance Couplings between 2D-Excitons and Nanophotonics Structures

Jinxiu Wen[1,2], Hao Wang[1,2], Huanjun Chen[1]

[1]State Key Laboratory of Optoelectronic Materials and Technologies, Guangdong Province Key Laboratory of Display Material and Technology, and School of Electronic and Information Technology, Sun Yat-sen University, Guangzhou 510275, China
[2]School of Physics, Sun Yat-sen University, Guangzhou 510275, China
*corresponding author: chenhj8@mail.sysu.edu.cn

Abstract

Resonance coupling between excitons and nanophotonics structures occurs when the excitons are placed in a nano-microcavity with spectrally overlapped optical modes. In this talk I will review our recent results on resonance couplings between 2D excitons in monolayer semiconductors and nanophotonic structures, including the plasmonic nanorods and dielectric Si nanospheres. The tailoring strategy for these couplings will be discussed in detail.

1. Introduction

The resonance coupling phenomenon, where the excitons are placed closely to a nanostructure with spectrally-overlapped optical resonances, has attracted much attention in the research field of nanophotonics. In this scenario, the excitons can interact coherently with the optical resonances and form hybrid modes with intriguing optical properties. In the past decades the resonance coupling has been extensively cultivated in heterostructures composed of molecular J-aggregates and metal nanostructures,[1] atoms and dielectric microcavities,[2] as well as quantum wells and microcavities.[3] From an application point of view, a robust, all-solid-state system exhibiting room-temperature resonance coupling with active control is strongly desired. Furthermore, from the operation point of view, it is also important that the system where the resonance coupling takes place is easy access.

On the other hand, two-dimensional transition-metal dichalcogenides (TMDs) have attracted much attention in recent years due to the exotic optical and optoelectronic responses associated with their atomically thin thicknesses.[4] The TMDs exhibit large exciton binding energies (0.3−0.9 eV), strong exciton transition dipole moments, and tunable exciton characteristics.[4,5] These merits can greatly favor the resonance coupling if the TMDs were integrated with the optical cavities.

In this talk I will review our recent works on resonance coupling between the 2D excitons in the TMDs with the plasmonic and dielectric nanocavities. The large mode splittings upto ~ 100 meV were observed at room temperature. The active control on such coupling processes were achieved with temperature scanning and electrostatic gating approaches.

2. Results and discussions

2.1. Resonance coupling between plasmonic nanorods and 2D excitons in monolayer WS_2

Metallic plasmonic nanocavities have been well-known as excellent platforms for the resonance couplings to occur. By integrating the gold nanorods with tunable plasmon resonance wavelengths with the 2D WS_2, strong resonance coupling can be observed at room temperature. The anti-crossing behaviors can be observed from the couping energy diagram (Fig. 1). The extracted mode splitting energy from an individual hybrid structure can reach upto 106 meV, which has entered the strong coupling regime. We furthermore demonstrated the active control on the resonance coupling by applying temperature scanning or electrostatic gating to the hybrid nanostructure. The modulation depth of the electric approach can be upto 17%.

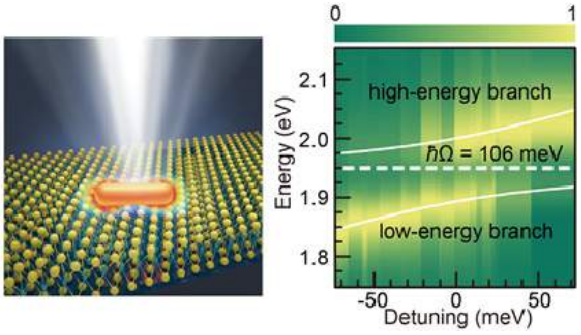


Fig. 1. Room-temperature strong coupling observed in individual plasmonic nanorod coupled with monolayer WS_2.

2.2. Resonance couplings between Si nanospheres and 2D excitons in monolayer WS_2

High-refractive-index dielectric nanostructures are another type of nanocavities capable of confining the free-space light into nanoscale volumes.[6] In comparison with the metals, the dielectrics usually exhibit a very small imaginary part of their dielectric functions across a broad spectral range. Furthermore, the dielectric nanostructures can exhibit intriguing optical magnetic and electric resonance modes which are amenable to the sizes and compositions of the nanostructures.[7] As a result, the dielectric nanostructures will endow the resonance coupling with additional virtues that cannot be accessed using individual pristine plasmonic nanostructures.

In our study, we demonstrated the resonance coupling between the magnetic dipole mode and two-dimensional excitons by integrating an individual silicon nanosphere with the monolayer WS_2 (ML-WS_2). A distinct mode splitting and anticrossing behavior with a mode splitting of 77 meV can be observed, which can be attributed to the coherent energy transfer between the magnetic dipole resonance and exciton transitions. In comparison with the plasmon−exciton coupling, resonance coupling in this all-dielectric heterostructure is much stronger and less sensitive to the separations between the nanosphere core and ML-WS_2. In particular, the hybrid modes induced by resonance coupling exhibit distinct light scattering directionality. We also explored the active control on the resonance coupling effect by temperature scanning technique.

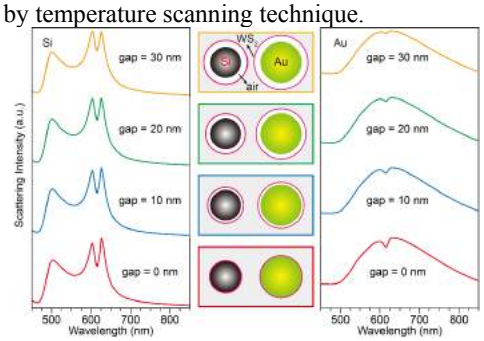


Fig. 2. Resonance coupling between an individual silicon (left) and gold (right) nanospheres coupled to ML-WS_2.

3. Conclusions

To sum up, I have reviewed our recent studies on resonance couplings between 2D excitons in monolayer WS_2 and nanophotonic structures. Evident anticrossing and mod splittings were observed. Active control on the resonance couplings was demonstrated. These results can pave the way for design of novel nanophotonic platforms for studying light–matter interactions at the nanoscale.

Acknowledgements

This work was financially supported by the National Natural Science Foundation of China (Grant Nos. 51290271, 11474364), the National Key Basic Research Program of China (Grant Nos. 2013CB933601, 2013YQ12034506), the Guangdong Natural Science Funds for Distinguished Young Scholars (Grant No. 2014A030306017), the Guangdong Special Support Program, and the Fundamental Research Funds for the Central Universities.

References

[1] H. J. Chen, T. Ming, L. Zhao, F. Wang, L.-D. Sun, J. F. Wang, C.-H. Yan, Plasmon—molecule interactions. *Nano Today* 5: 494−505, 2010.

[2] T. Yoshie, A. Scherer, J. Hendrickson, G. Khitrova, H. M. Gibbs, G. Rupper, C. Ell, O. B. Shchekin, D. G. Deppe, Vacuum Rabi splitting with a single quantum dot in a photonic crystal nanocavity. *Nature* 432: 200−203, 2004.

[3] J. M. Raimond, M. Brune, S. Haroche, Manipulating quantum entanglement with atoms and photons in a cavity. *Rev. Mod. Phys.* 73: 565−582, 2001.

[4] Q. H. Wang, K. Kalantar-Zadeh, A. Kis, J. N. Coleman, M. S. Strano, Electronics and optoelectronics of two-dimensional transition metal dichalcogenides. *Nat. Nanotechnol.* 7: 699−712, 2012.

[5] H. Zeng, J. Dai, W. Yao, D. Xiao, X. D. Cui, Valley polarization in MoS_2 monolayers by optical pumping. *Nat. Nanotechnol.* 7: 490−493, 2012.

[6] A. I. Kuznetsov, A. E. Miroshnichenko, M. L. Brongersma, Y. S. Kivshar, B. Luk'yanchuk, Optically resonant dielectric nanostructures. *Science* 354: aag2472, 2016.

[7] A. B. Evlyukhin, S. M. Novikov, U. Zywietz, R. L. Eriksen, C. Reinhardt, S. I. Bozhevolnyi, B. N. Chichkov, Demonstration of magnetic dipole resonances of dielectric nanospheres in the visible region. *Nano Lett.* 12: 3749–3755, 2012.

Molecular Junction-Controlled High-Order Charge Transfer Plasmon and Fano Resonance

Ximin Cui[1], Yunhe Lai[1], Lei Shao[1]
Jianfang Wang[1]

[1]Department of Physics, The Chinese University of Hong Kong, Hong Kong, China

*corresponding author, E-mail: shaolei@cuhk.edu.hk

Abstract

We report the fabrication of molecular-tunnel-junctions-bridged plasmonic nanocavities with high quality from single-crystalline metal nanostructures and use them as a platform for quantum plasmonics study. Specifically, we observed the excitation of high-order charge transfer plasmon modes. We also found the effect of quantum tunneling on the peak shift of other plasmon resonances and the Fano interference between different plasmon modes. Furthermore, the experimental results can be well reproduced by a theoretical model.

1. Introduction

Plasmonic cavities formed by noble metal nanostructures and with ultra-small gap distances, where quantum mechanical behaviors of both the electromagnetic fields and matter emerge, are an important type of plasmonic devices. Such plasmonic cavities provide a powerful material platform for interesting applications such as surface-enhanced molecular spectroscopy [1], plasmon–exciton strong coupling [2] and ultimate miniaturization of photonic components for quantum optics [3–5]. Bridging a plasmonic gap with conductive molecular junctions has recently been shown to increase the electron tunneling rate significantly at both DC and optical frequencies and allow for the excitation of charge-transfer plasmons at moderate gap distances [6,7]. The molecular tunnel junctions thus help to address the fabrication challenges of quantum plasmonic devices. The tunneling barrier width and height of molecular tunnel junctions can further be tuned by varying the molecular type, structure and functional groups. The molecular tunnel junctions provide solutions to controlling plasmons by molecular electronic means [7,8], therefore opening up a promising route towards molecular plasmonic devices and ultrafast on-chip integrated plasmonic electronic circuits [9,10].

Although the feasibility of using molecular junctions to modulate the quantum plasmonic properties, including the first-order tunneling CTP mode, has been clearly demonstrated in very recent works, many challenges remain, including large-scale and reproducible fabrication of molecular tunnel junctions, active control of quantum plasmons *via* adjusting the molecular properties, and theoretical modeling of quantum plasmons in molecular tunnel junctions [10].

2. Result

In this study, we developed a large-scale bottom-up fabrication of molecular-tunnel-junctions-bridged plasmonic nanocavities with high quality from single-crystalline metal nanostructures and use them as a platform for quantum plasmonics study. Specifically, we observed the excitation of high-order charge transfer plasmon modes. We also found the effect of quantum tunneling on the peak shift of other plasmon resonances and the Fano interference between different plasmon modes. The experimental results can be well reproduced by a theoretical model. We believe that our results will be very useful for the design of molecular quantum plasmonic devices and the study of quantum plasmonics of molecular-tunnel-junctions-bridged nanocavities.

Acknowledgements

This work is supported by the Hong Kong General Research Fund.

References

[1] W. Q. Zhu, K. B. Crozier, Quantum mechanical limit to plasmonic enhancement as observed by surface-enhanced Raman scattering. *Nat. Commun.*5: 5228, 2014.

[2] R. Chikkaraddy, B. de Nijs, F. Benz, S. J. Barrow, O. A. Scherman, E. Rosta, A. Demetriadou, P. Fox, O. Hess, J. J. Baumberg, Single-molecule strong coupling at room temperature in plasmonic nanocavities. *Nature* 535: 127–130, 2016.

[3] S. I. Bozhevolnyi, N. A. Mortensen, Plasmonics for emerging quantum technologies. *Nanophotonics* 6: 1185–1188, 2017.

[4] W. Q. Zhu, R. Esteban, A. G. Borisov, J. J. Baumberg, P. Nordlander, H. J. Lezec, J. Aizpurua, K. B. Crozier, Quantum mechanical effects in plasmonic structures with subnanometre gaps. *Nat. Commun.* 7: 11495, 2016.

[5] M. S. Tame, K. R. McEnery, S. K. Özdemir, J. Lee, S. A. Maier, M. S. Kim, Quantum plasmonics. *Nat. Phys.*, 9: 329–340, 2013.

[6] K. J. Savage, M. M. Hawkeye, R. Esteban, A. G. Borisov, J. Aizpurua, J. J. Baumberg, Revealing the quantum regime in tunnelling plasmonics. *Nature* 491: 574–577, 2012.

[7] S. F. Tan, L. Wu, J. K. W. Yang, P. Bai, M. Bosman, C. A. Nijhuis, Quantum plasmon resonances controlled by molecular tunnel junctions. *Science* 343: 1496–1499, 2014.

[8] W. Du, T. Wang, H.-S. Chu, L. Wu, R. R. Liu, S. Sun, W. K. Phua, L. J. Wang, N. Tomczak, C. A. Nijhuis, On-chip molecular electronic plasmon sources based on self-assembled monolayer tunnel junctions. *Nat. Photonics* 10: 274–280, 2016.

[9] A. J. Wilson, K. A. Willets, Molecular plasmonics. *Annu. Rev. Anal. Chem.* 9: 27–43, 2016.

[10] T. Wang, C. A. Nijhuis, Molecular electronic plasmonics. *Appl. Mater. Today* 3: 73–86, 2016.

Anti-Reflective All-Dielectric Metasurfaces Engraved on an Optical Waveguide Facet

Alina Karabchevsky*, Yakov Galutin

Electrooptical Engineering Unit, Ben-Gurion University, Israel
Ilse Katz Institute for Nanoscale Science & Technology, Ben-Gurion University, Israel
Center for Quantum Information Science and Technology, Ben-Gurion University, Israel
*corresponding author, E-mail: alinak@bgu.ac.il

Abstract

For each value of refractive index n, there exists an optimum shape of the particle that produces a minimum back-scattering together with a maximum forward scattering. This effect can be metasurface-engineered. Here we show, that randomly-distributed anti-reflective structures (RAS) have a superior anti-reflective (far-field back-scattering) properties compared to the periodic anti-reflective surfaces - both engraved on the optical waveguide facet.

1. Introduction

In our previous work [1], we investigated the scattering effect of high-index silicon nanoparticles, for which the third-order multipoles contribute considerably to the light-scattering process reported in ref. [1]. Here, we study periodic and random arrays of silicon nanoparticles of truncated conical shape engraved in a silicon rib waveguide facet. In ref. [2], we showed that the Kerker effect (i.e., the strong suppression of the back-scattering and, simultaneously, the resonant forward scattering) can be associated with the resonant excitation of a toroidal dipole moment in the system. Here, we show the metasurface-engineered suppression of back-reflection (suppression of far-field backward scattering). Figure 1a shows schematics of the silicon rib waveguide with smooth facet. Figure 1b shows the schematics of the silicon rib waveguide with periodic structure on the facet. Figure 1c shows the schematics of the silicon rib waveguide with random structure on the facet. Figure 1c shows the geometry of the unit cells which is the truncated cone.

2. Periodic metasurface

We evaluated the feasibility of studying silicon metasurface (periodic array of truncated cones) contribution to wide-band transmission in optical waveguides. Figure 2b shows the 25x2 array of periodically arranged truncated cones compared to the smooth facet shown in Figure 2a (purple). The period is Λ=463 nm and the cones are as high as h=400 nm with lower diameter of d_2=450 nm and the upper diameter d_1=290 nm as shown on Figure 2.

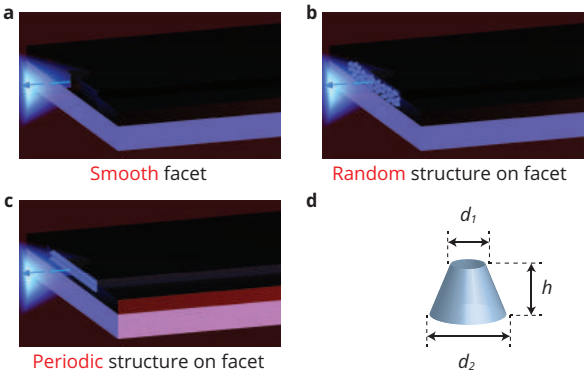


Figure 1: Render of the silicon rib waveguide with (a) smooth facet, (b) periodic metasurface engraved on the facet, (c) random metasurface engraved on the facet, (d) unit cell.

3. Engineering of random metasurfaces

To generate the spatial distribution, we set a bounded area as large as the waveguide facet and assigned randomly placed single point on it. Then we added another point, while each location is completely random within the bounded region. We excluded points if an area defined as a circle with radius d_2 around the point overlaps with an adjacent one. The process is repeated until we reach a predefined amount of points. This property is known as Poisson process in other words, there is a lack of interaction between different regions and the points in general.

4. Results and discussion

Figure 3 shows the reflection spectrum from the silicon waveguide facet. Random metasurface exhibits about 3% from 1-2 μm reflection compared to the periodic structure which exhibits about 5% and compared to the smooth surface which exhibits about 13%. Figure 3 shows the transmission spectrum of silicon waveguide. The transmission in case of the random surface is as high as about 94% while in case of the periodic structure it 91% compared to 83% in case of the smooth facet.

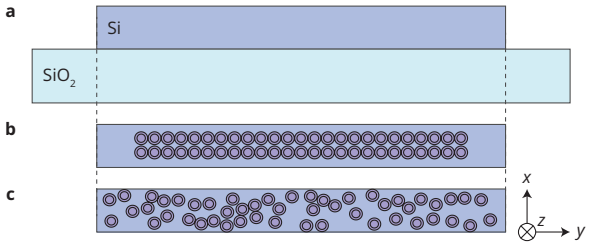


Figure 2: (a) Schematics of the silicon waveguide with smooth (purple) facet, (b) periodic metasurface on facet which includes array of 25x2 truncated cones, (c) randomly distributed 50 truncated cones.

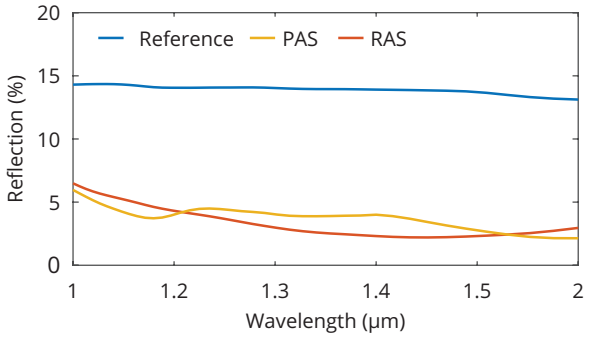


Figure 3: Calculated reflection spectrum from the facet of silicon rib waveguide with (blue) smooth facet, (orange) periodic structure on the facet and (red) random structure on the facet.

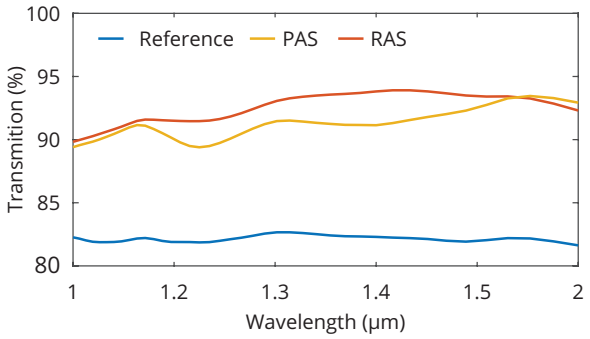


Figure 4: Calculated transmission spectrum from the facet of silicon rib waveguide with (blue) smooth facet, (orange) periodic structure on the facet and (red) random structure on the facet.

5. Conclusions

Antireflective properties of optical waveguide facet can be tuned by carefully designed metamaterial pattern engraved on the waveguide facet. We show that, random metasurfaces exhibit superior anti-reflection properties and improve the waveguide overall transmission. These textures can be directly fabricated on an optical waveguide facet and result in improved spectral transmission. The results indicate that random antireflective structures can present better performance than a periodic structure and offer great potential to applications requiring minimization of back reflections and enhanced transmission.

Acknowledgment

The work was supported by the Israel Innovation Authority Kamin Program (Grant No. 96717).

References

[1] P. D. Terekhov, K. V. Baryshnikova, A. S. Shalin, A. Karabchevsky, and A. B. Evlyukhin, "Resonant forward scattering of light by high-refractive-index dielectric nanoparticles with toroidal dipole contribution," *Optics letters*, vol. 42, no. 4, pp. 835–838, 2017.

[2] P. D. Terekhov, K. V. Baryshnikova, Y. A. Artemyev, A. Karabchevsky, A. S. Shalin, and A. B. Evlyukhin, "Multipolar response of nonspherical silicon nanoparticles in the visible and near-infrared spectral ranges," *Physical Review B*, vol. 96, no. 3, p. 035443, 2017.

Resonant-state expansion generalized to magnetic, chiral, and bi-anisotropic open optical systems and metamaterials

Egor Muljarov[1*] **and T. Weiss**[2]

[1]School of Physics and Astronomy, Cardiff University, Cardiff CF24 3AA, United Kingdom
[2]4th Physics Institute and Research Center SCoPE, University of Stuttgart, Pfaffenwaldring 57, D-70550 Stuttgart, Germany
*corresponding author, E-mail: Egor.Muljarov@astro.cf.ac.uk

Abstract

We have generalized the resonant-state expansion for open optical systems containing arbitrary reciprocal bi-anisotropic materials or metamaterials, including those having magnetic and chiral optical activity, as well as circular dichroism. The resonant-state expansion is the most efficient and intuitive computational approach for treating open optical systems, as demonstrated in numerous publications. The present theory has the widest spectrum of applications, ranging from modeling and optimization of chirality sensors to accurate description of the optics of magnetic and metamaterial systems.

References

[1] E. A. Muljarov and T. Weiss, arXiv:1801.08883v1 (2018).

Simulation the Effect of Transparent Conducting Oxides Layer on the Waveguide Reflection

Hala J. El-Khozondar[1], Ahmed A. AlShembari [2], Mohammed M. Shabat[2],

[1]Electrical Engineering Department, Engineering Faculty, Islamic University of Gaza, Gaza, Palestine
[2]Physics Department, Islamic University of Gaza, Gaza, Palestine
*corresponding author, E-mail: hkhozondar@iugaza.edu.ps

Abstract

A four layer waveguide structure is proposed. It consists of transparent conducting oxide (TCO) substrate made of ITO, topped by two layers of Silicon monoxide (SiO) and Fe-InGaAsP that are covered by air. The Transfer Matrix Method is used to investigate the properties of the structure. The reflectance in the visible light are derived and plotted versus the operating wavelength for different physical parameters for TM mode. The results indicates that the waveguide is suitable for solar cell fabrication.

1. Introduction

Wave guide is a common structure for Solar cell. Solar Cell (PV) is used in the solar system to absorb sun light and converted to electrical energy. The higher the efficiency of the PV the more output energy is obtained. Several researches are conducted to enhance the PV efficiency by adding single antireflection coating (ARC) [1] or double ARC [2-3]. Recently, low loss ARC is produced using transparent conducting oxide layer (TCO) made of ITO [4].

A new waveguide structure containing 4 layers is proposed, the first layer is Silicon monoxide (SiO) covered with air, the third layer is Fe-InGaAsP sitting above the substrate layer which is TCO made of ITO as in Fig. 1. The thickness of SiO layer is l_1 and the thickness of Fe-InGaAsP is l_2. The air layer and the TCO layer are assumed to be semi-infinite layer.

TM light polarizations through the proposed structure have been extracted using Hybrid Transfer Matrix Method (TMM) [5]. Hybrid TMM is used to investigate the efficiency of waveguide solar cells. The transmitted, reflected and absorbed spectra versus the operating wavelength for several physical parameters have been computed numerically using MAPLE software. The effect of substrate TCO is analyzed and discussed. Section 2 presents the numerical results, followed by conclusion in section 4.

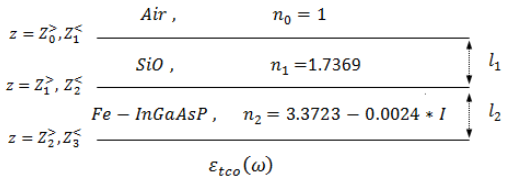


Figure 1: The proposed four layer waveguide structure.

2. Numerical Results

In the calculations, the refractive index for each layer is considered as follows:
The refractive index for the air layer n_0=1. The refractive index for SiO, n_1=1.7369. The refractive index for Fe-InGaAsP, n_2=3.3723-0.0024I. The refractive index for TCO layer is written in terms of the permittivity ε_{tco} as follows $n_{tco} = \sqrt{\varepsilon_{tco}}$, where

$$\varepsilon_{tco} = \varepsilon_b - \frac{\omega_p^2}{\omega\left(\omega + i\,\gamma_p\right)} + \frac{f_1\omega_1^2}{\left(\omega_1^2 - \omega^2 - i\,\omega\gamma_1\right)} \quad , \quad \text{where}$$

the values of each parameter is indicated in Table 1.

Table 1: Drude-Lorentz parameters for TCO layer [4].

parameter	value
ε_b	3.528
ω_p[J]	696.54
γ_p[J]	7.999×10^3
f_1	0.3884
ω_1[J]	294.5
γ_1[J]	1.3491×10^4

The thickness of SiO (l_1) is taken to be fixed and equals 90nm, while the thickness Fe-InGaAsP (l_2) can assume the following values 5nm, 10nm, and 15 nm respectively. The wavelength (λ) varies from 300nm to 1200 nm and the frequency ω=2πc/ λ, where c is the speed of light and equals 3×10^8 m/s.

Fig. 2 displays the reflection power (R) as function of λ at different values of l_2. The red, blue and black curves corresponds to l_2=5nm, 10nm and 15nm respectively.

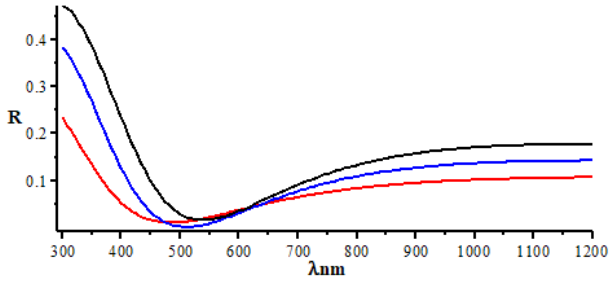


Figure 2: displays the reflection power (R) as function of wavelength (λ) at different values of l_2

Fig. 3 displays the tansmission power (T) as function of λ at different values of l_2. The red, blue and black curves corresponds to l_2=5nm, 10nm and 15nm respectively.

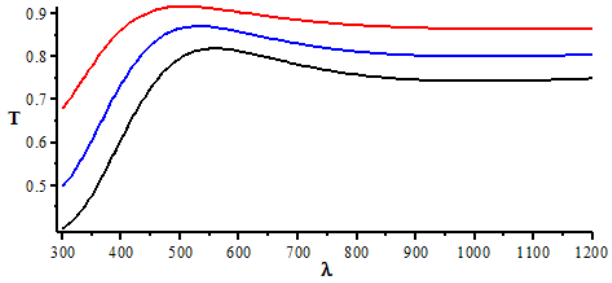


Figure 3: displays the Transmission power (T) as function of wavelength (λ) at different values of l_2

The absorption power is plotted for the same condition at fig. 4.

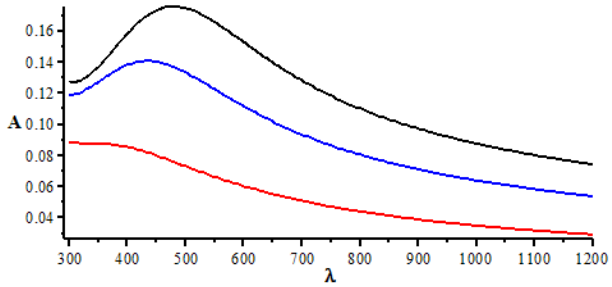


Figure 4: displays the Absorption power (T) as function of wavelength (λ) at different values of l_2

Figure 3 indicates that the structure has a low reflection in the region around 500nm. The values at which exact minimum occurs depends on l_2. These minimum corresponds to the maximum in the transmission curve (Figure 3). Moreover, we can see that the loss is very small as exhibited by Figure 4.

3. Conclusions

This work has shown excellent results for high transmission of the incident waves for certain frequency bands. Hence, the studied structure would be promising to be utilized in the field of solar cells.

References

[1] D. Bouhafs, A. Moussi, A. Chikouche and J. M. Ruiz, Design and simulation of antireflection coating systems for optoelectronic devices: Application to silicon solar cells, *Sol. Energ. Mat. Sol. C*. 52: 79-93, 1998.

[2] K. Choi, and K.J. Kim, Antireflection coating of a SiO/SiN double layer on silicon fabricated by magnetron sputtering. *J. Ceram. Process. Res*. 11(3): 341-343, 2010.

[3] S. K. Dhungel, J. Yoo, K. Kim, S. Jung, S. Ghosh and J. Yi, Double-layer antireflection coating of MgF_2/SiN_x for crystalline silicon solar cells. *J. Korean Phys. Soc*. 49(3): 885-889, 2006.

[4] T. Gric, Spoof plasmons in corrugated transparent conducting oxides, *Journal of Electromagnetic Waves and Applications* 30(6):721–727, 2017.

[5] H. J. El-Khozondar, M. M. Shabat and A. N. AlShembari, Characteristics of Si-Solar Cell (PV) Waveguide Structure Using Transfer Matrix Method, IEEE 2017 International Conference on Promising Electronic Technologies (ICPET), Deir El-Balah, Palestine, 2017, pp. 99-102.

Hybrid plasmonic-dielectric nonlinear metasurface with tunable quality factors

Feng Wang[1] and Hayk Harutyunyan[1,*]

[1]Department of Physics, Emory University, Atlanta, GA 30322, USA
*corresponding author, E-mail: hayk.harutyunyan@emory.edu

Abstract

We develop a hybrid plasmonic/dielectric metasurface that can simultaneously achieve high quality factors and large field enhancement values. The optical response of the designed nano-architecture is dominated by the formation of a tunable hybridized plasmonic-photonic mode. By tuning the Q factors of the system we demonstrate that optimized conditions for nonlinear signal generation can be achieved.

1. Introduction

Plasmonic nano-antennas and metamaterials concentrate optical energy into nanometric volumes strongly enhancing the light-matter interaction [1]. This makes them promising platforms for optical sensing, nonlinear effects and quantum optics [2-3]. However, absorption losses and radiative damping result in broad, low quality factor (Q) resonances of plasmonic systems that significantly limit their performance. Here we demonstrate hybrid plasmonic/dielectric metasurfaces that can achieve high Q and large field enhancement values.

2. Results and discussion

The nonlinear metasurface design is shown in Fig. 1. The metasurface comprises of arrays of gold dimer nano-antennas fabricated on top of a silicon – on – insulator (SOI) wafer. A hybridized mode with a tunable Q factor is formed between nano-antenna's plasmonic mode and the photonic waveguide mode of Si device layer.

As it can be seen in simulations shown in Fig. 1a, strongly localized E-fields with small mode volumes can be excited inside the dimer gap and the SiO_2 cladding layer. In the Si device layer, a resonant vortex electric field is excited through the near field coupling from the Au antennas. The coupling between the localized plasmonic modes and the device layer wafer mode plays a key role in improving the Q factor the optical resonance. First, most of the electromagnetic energy scattered by the plasmonic dimer can be trapped in the Si waveguide so that the leakage or the radiation loss can be effectively reduced. Second, because of the negligible absorption of Si in the infrared, the Ohmic loss of the trapped electromagnetic energy can be minimized. The coupling strength between the plasmonic and photonic modes can be tuned by controlling the gap width of the gold dimer thus resulting in tunable Q factor of the resonance, Fig. 1c. The field enhancement observed in the SiO_2 cladding layer between the plasmonic particles and Si is remarkably large and comparable to the enhancement factors observed between two plasmonic elementsAs a result, our metasurfaces can support extreme light localization and field enhancement that is only limited by the thickness of the SiO_2 cladding layer. At the same time, the quality factors achieved in this design are more than an order of magnitude larger compared to pure plasmonic systems. Similar tunability of the resonances can be achieved by tuning the periodicities of the dimer arrays.

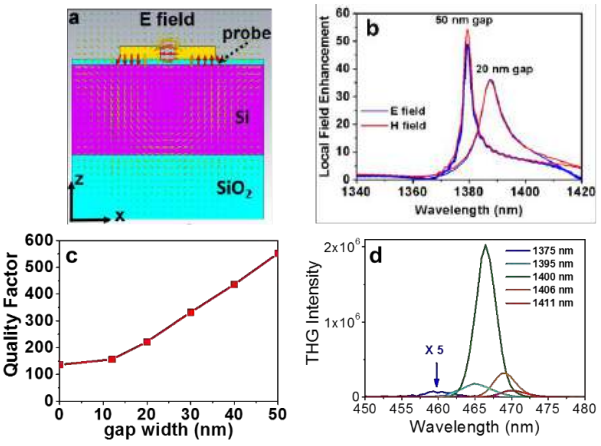


Figure 1: Hybrid plasmonic-dielectric metasurfaces. **a)** Schematic of one unit of metasurfaces showing local E-field enhancement at the resonant wavelength of the hybridized mode. **b)** Local E and H-field enhancement at the probe position indicated in a). **c)** Quality factor of the resonance as a function of plasmonic dimer width. **d)** Measured THG of the metasurfaces around its resonant wavelength.

To probe the near-field enhancement of the metasurfaces we performed nonlinear high-harmonic generation experiments. We observe strong enhancement of Third Harmonic Generation (THG) at the resonance wavelength

of the hybridized mode, Fig. 1d. The narrow width of the resonance enhancement confirms the simultaneous realization of high Q factor and strong field-enhancement.

3. Conclusions

In conclusion, we have developed a hybrid plasmonic/dielectric cavity that can sustain strong field confinement with electromagnetic field enhancement of >30, and a high Q factor of ~100. While these achieved quality factors are lower than some pure dielectric waveguides or nanoresonator arrays with experimental Q values of several hundreds and theoretical Q values of more than 1000, our metasurface exhibits stronger nanometer-scale field confinement and exposed near fields in the plasmonic dimer gap. These properties make our platform promising for applications including nonlinear optics, Purcell factor enhancement, optical sensing and quantum optics.

Acknowledgements

This work was supported by NSF EFMA – 1741691 and startup funds from Emory University.

References

[1] J. A. Schuller, E. Barnard, W. Cai, Y. C. Jun, J. White, and M. L. Brongersma, Plasmonics for extreme light concentration and manipulation, Nature Mat. 9, 193–204 (2010).

[2] F. Wang, A. B. F. Martinson, and H. Harutyunyan, Efficient nonlinear metasurface based on non-planar plasmonic nanocavities," ACS Photonics 4(5), 1188–1194 (2017).

[3] N. Liu, M. L. Tang, M. Hentschel, H. Giessen, and A. P. Alivisatos, Nanoantenna-enhanced gas sensing in a single tailored nanofocus, Nat. Mater. 10(8), 631–636 (2011).

MODAL DESIGN TO CONTROL TRANSIENT ULTRAFAST EVENTS IN NANOSCALE MATERIALS .

Gregory Wurtz
Department of Physics, King's College London, Strand, London WC2R 2LS, United Kingdom
Department of Physics, University of North Florida, 1
UNF Drive, Jacksonville, FL 32224, United States of America
g.wurtz@unf.edu

Optical metamaterials have stimulated an increasing interest from scientists over the past decade expanding our ability to manipulate electromagnetic fields in nanostructured systems for the design of selected functionalities with a degree of control never experienced before. The core of metamaterial design is in the crafting of their dispersion through careful geometrical nanostructuring. This has lead to the practical development of superlenses, sub-diffraction imaging systems, cloaking, and other enhanced optical nonlinearity design.

In this work we focus our attention on 2D plasmonic metamaterials and metasurfaces, which development provides both passive and active optical functionalities. In particular we studied the ultrafast transient response of multi-resonant plasmonic systems, including nonlinear coherent emitters, and demonstrate the ability to modulate both their linear and nonlinear properties at the sub-ps timescales. The results are rationalized on the basis of the temporal response of the electron density in the metal through both time-resolved transient extinction measurements and numerical simulations. The unique ability offered by nanostructured systems through their modal response to provide control over the dynamics of the nonlinear optical response is also discussed.

Optical detection of proteins in complex media

Ramón A. Alvarez-Puebla

Departamento de Quimica Fisica e Inorganica; Universitat Rovira i Virgili, Avda. Països Catalans 26, 43007 Tarragona, Spain
*corresponding author, E-mail: ramon.alvarez@urv.cat

Abstract

Changes in protein expression levels and protein structure may indicate genomic mutations and may be related to some diseases. Therefore, the precise quantification and characterization of proteins can be used for disease diagnosis. Compared with several other alternative methods, surface-enhanced Raman scattering (SERS) spectroscopy is regarded as an excellent choice for the quantification and structural characterization of proteins. Herein, we review the main advance of using plasmonic nanostructures as SERS sensing platform for this purpose. Three design approaches, including direct SERS, indirect SERS, and SERS-encoded nanoparticles, are discussed in the direction of developing new precise approaches of quantification and characterization of proteins.

1. Introduction

Proteins are large biopolymers with molecular weights ranging from some thousands (aprotinin) to nearly one million (α2-macroglobulin) daltons. These macromolecules are formed by one or more chains of linearly aligned amino acids bonded through peptide bonds. Proteins are responsible for a large variety of biological functions including structural, immunological, metabolic, or catalytic activity, signaling, or transporting.

Surface-enhanced Raman scattering (SERS) spectroscopy has emerged as an excellent choice for the detection, quantification, and characterization of proteins. Herein, we will discuss the late developments in SERS technology with special emphasis on the quantification and characterization of proteins as well potential application. To outline conceptual highlights however also the detection of other biological molecules will be described in the form of selected examples.

2. Results and discussion

The application of nanostructured materials toward the development of novel detection techniques with improved sensitivity and/or simplified and faster applicability has rapidly become an appealing alternative to other technologies. Among them, SERS is a powerful analytical technique that has already proven to be particularly effective in chemical biology and medicine. Essentially, SERS can be described as amplified Raman scattering by the presence of a plasmonic structure (most often metallic nanostructures) in the close vicinity of the target analyte. In such a case, the main cause of the excitation of the molecular vibrational levels is the collective oscillation of the conduction electrons in the metal, upon excitation with the appropriate light, which generates an ultrastrong electromagnetic near-field in the proximity of the nanostructure surface (known as localized surface plasmon resonances, LSPRs). As Raman scattering, SERS provides a complex spectral pattern that contains all the compositional and structural characteristics of the target analyte with an extreme experimental flexibility. SERS can be carried out over a wide spectral range, is insensitive to water, and, in many cases, requires no sample preparation. Recent spectacular advances in nanofabrication techniques fueled the development of a large variety of rationally designed SERS substrates with optimized, uniform, and reproducible response. This successfully translated the spectacular analytical potential of SERS to reliable, widely accepted, and commercially viable sensing applications. The dependence of LSPRs with parameters such as size, shape, composition, and surrounding medium provides multiple possibilities for tuning the optical response and thus optimizing the SERS performance of the plasmonic nanostructure for a specific application. In conjunction with the control of the signal amplification provided by the optical enhancer, a key step in the practical implementation to sensing applications (including SERS) is the appropriate chemical functionalization of the "bare" metallic (i.e., plasmonic) surface necessary to impart the required selectivity and/or sensitivity toward the target analyte, especially in complex media. Three design approaches are commonly used to devise plasmonic nanostructures as SERS sensing platforms: (i) direct SERS; (ii) indirect SERS; and (iii) SERS-encoded particles.

3. Conclusions

SERS technology provides a novel emerging chance for the quantification and characterization of proteins, speeding up their exploration of structure and function, while developing novel nonlabeled medical diagnosis technology. Nanostructures such as gold or silver colloids, 2D nanosheets, etc. can markedly enhance the Raman scattering signal of proteins, down to the single molecule detection level in some cases. The potential molecular mechanism is associated with LSPR and the formation of hotspots. To date, novel strategies such as direct SERS detection,

indirect SERS detection, and SERS-encoded nanoparticle-based detection have been reported. Their potential in applications such as SERS imaging of in vivo tumor biomarkers and SERS quantification detection of protein biomarkers has been positively explored. Much of the existing literature still demonstrates concepts in lab samples with few reports associated with the SERS detection of proteins in biological conditions. However, although the single and multiplex detection of relevant proteins in real biofluids and solid samples (tissues) is still challenging, field advances are happening quickly, with many new discoveries almost at a daily basis. In summary, although SERS technology for protein quantification and characterization faces many challenges, SERS combined with nanotechnology has exhibited attracting technological prospects, and will dramatically advance our ability to understand the chemical biology of proteins while developing novel series of SERS-based technology, which will eventually help to promote the application of SERS in other fields.

Strong Light-Matter Interaction in Single Plasmonic Nanocavity and the Photoluminescence Evolution

Di Zheng[1], Shunping Zhang*,[1], Qian Deng[1], Meng Kang[1], Peter Nordlander[3], and Hongxing Xu*,[1,2]

[1]School of Physics and Technology, Center for Nanoscience and Nanotechnology, and Key Laboratory of Artificial Micro- and Nano-structures of Ministry of Education, Wuhan University, Wuhan 430072, China.
[2]The Institute for Advanced Studies, Wuhan University, Wuhan 430072, China.
[3]Department of Physics and Astronomy, Department of Electrical and Computer Engineering and Laboratory for Nanophotonics, Rice University, Houston, Texas 77005, USA.
*corresponding author, E-mail: spzhang@whu.edu.cn, hxxu@whu.edu.cn

Abstract

Strong light-matter interaction between plasmons and excitons in nanocavities can result in the formation of hybrid plexcitonic states. Understanding the dispersion relation in the plexcitonic states is important both for fundamental quantum science and for applications including optoelectronics and nonlinear optics devices. Here we realize strong light-matter interaction in single nanocavity with excitons in a monolayer tungsten diselenide [1]. The plexciton dispersion along with photoluminescence (PL) spectrum evolution is measured by in-situ redshifting the plasmon energy via successive deposition of dielectric layers.

1. Introduction

The realization of strong coupling relies on increasing the coupling strength while reducing the dissipation and decoherence rates. In this study, we realize strong coupling of surface plasmons (SPs) on an individual nanoparticle with excitons in a monolayer tungsten diselenide, one type of transition metal dichacogenides (TMDs) that is promising for optical and optoelectronic applications. Deterministic spectral coincidence is achieved by successively tuning the energy of the SP by depositing a thin dielectric layer onto the nanoparticle. Deterministic spatial coincidence is accomplished by the near-field interaction between the in-plane 2D Wannier type excitons and the nanoparticle plasmon. The dispersion curves of the hybrid plexcitonic states are mapped out *in-situ* in the nanorod system, giving a definite plasmon-exciton Rabi splitting of 49.5 meV. Free of any uncertainty associated with the inhomogeneities of different samples.

2. Experiment results

Our plexciton system is fabricated by dropping cast and spinning a metal nanoparticle onto a monolayer WSe_2. We choose the n = 3 mode in single silver nanorod system. It satisfies the high-Q-low-V criterion in that its Q is about three times higher than for the dipolar plasmon resonance (n = 1) on the nanorod [2]. In the single silver nanoplate system, we choose the dipolar plasmon mode (n = 1), since the dipolar mode is much more emissive. WSe_2 was chosen due to its giant excitonic effect in a single atomic layer. Single particle dark-field spectroscopy was used to measure the scattering spectra of the individual nanoparticles. Then PL spectrum of hybrid system compare with the nearby monolayer WSe_2 was measured by 532 nm laser excitation, followed by a correlated scanning electronic microscopy (SEM) characterization of their morphologies.

2.1. Single silver nanorod on monolayer WSe_2

Tuning the SP energy is an efficient way of varying plasmon-exciton detuning. As the SP energy E_{pl} shifts across the exciton E_0, clear evidence of strong coupling – spectral splitting – is manifest in the scattering spectra (Figure 1).

We consider the system as two classical dissipative harmonic oscillators, coupled to each other with a strength g. To obtain the energy of the plasmon and the coupling strength, we fit the scattering spectra in Figure 1 using the following formula [3]

$$\sigma_{scat}(E) = AE^4 \left| \frac{(E^2 - E_0^2 + iE\Gamma_0)}{(E^2 - E_0^2 + iE\Gamma_0)(E^2 - E_{pl}^2 + iE\Gamma_{pl}) - 4E^2 g^2} \right|^2 \quad (1)$$

where A is the scattering amplitude, E_{pl} and E_0 are the resonant energies of the nanocavity and the X^0 exciton, respectively. The excitonic resonance is restricted around $E_0 = 1.659$ eV. The dissipation rates are denoted as Γ_{pl} and Γ_0.

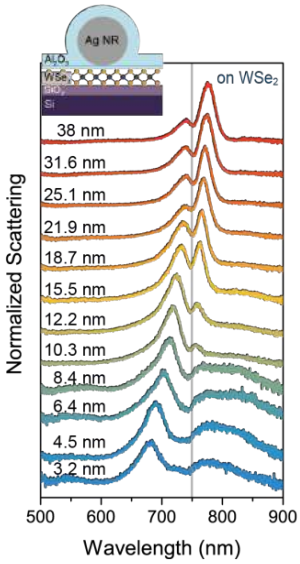


Figure 1: A set of dark-field scattering spectra of the silver nanorod with increased alumina coating. The inset is the schematic cross section of the silver nanorod on monolayer WSe_2 system.

By fitting the scattering spectra in Figure 1 to the coupled osicllator model (COM), see equation 1, we extracted E_{pl} and g (assuming $E_0 = 1.659$ eV which was determined from the X^0 absorption peak). The energy of the upper plexciton branches (UPB) and lower plexciton branches (LPB) exhibits a clear anti-crossing behavior (Figure 2). A vacuum Rabi splitting of $\Omega = 2g|_{\delta=0} = 49.5$ meV is obtained at zero detuning.

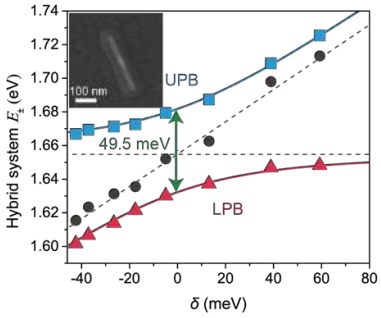


Figure 2: The energy of the UPB (E_+, blue square) and LPB (E_-, magenta triangle) as a function of detuning. The solid lines are fit to the COM Eq. (1), giving a splitting of 49.5 meV. The extracted energy of the plasmon (E_{pl}, gray dot) is included for comparison. The gray dashed lines are guide to the eyes showing the dispersion of the uncoupled exciton and plasmon. The inset is the corresponding SEM image of the silver nanorod.

2.2. Single silver nanoplate on monolayer WSe_2

Single particle dark-field spectroscopy was used to measure the scattering spectra of the nanoplate on monolayer WSe_2. Two different coatings are shown in Figure 3.

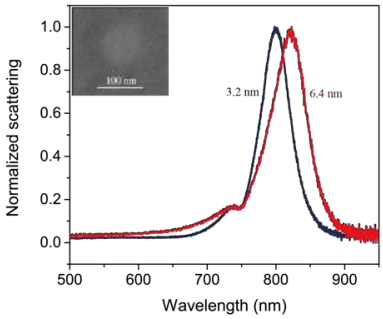


Figure 3: Dark-field scattering spectra of single silver nanoplate on WSe_2 with two different alumina coating (The navy blue is 3.2 nm, and the red is 6.4 nm).

Since the dipolar mode in nanoplate is much more emissive, the PL spectra shape in the hybrid system shows an extra shoulder compare with the monolayer WSe_2 PL, when the system is in the negative detuning regime (Figure 4).

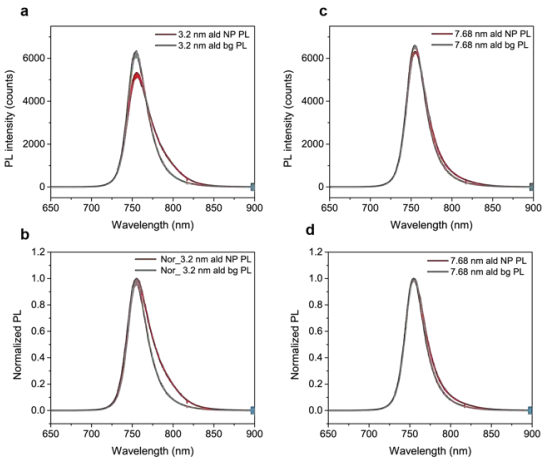


Figure 4: (a) PL spectrum of single silver nanoplate on monolayer WSe_2 hybrid system with 3.2 nm alumina coating (red line) compare with the nearby PL from monolayer WSe_2 (gray line). (b) Normalized PL spectra in

(a). (c) PL spectrum of single silver nanoplate on monolayer WSe_2 hybrid system with 7.68 nm alumina coating (red line) compare with the nearby PL from monolayer WSe_2 (gray line). (d) Normalized PL spectra in (c).

Acknowledgements

We thank Rachel Lee Siew Tanb and Prof. Hongyu Chen for preparation of the silver nanorods, and Xiaoguang Li, Pengfei Suo for helpful discussions. This work was supported by the Ministry of Science and Technology (Grant No. 2015CB932400), the National Natural Science Foundation of China (Grants Nos. 11304233, 11134013, and 11227407) and the China Postdoctoral Science Foundation (Grant No. 2014T70727).

References

[1] D. Zheng, S.P. Zhang, Q. Deng, M. Kang, P. Nordlander, H.X. Xu, Manipulating coherent plasmon-exciton interaction in single silver nanorod on monolayer WSe_2, *Nano Letters* 17:3809−3814, 2017.

[2] S.P. Zhang, L. Chen, Y.Z. Huang, H.X. Xu, Reduced linewidth multipolar plasmon resonances in metal nanorods and related applications, *Nanoscale* 5:6985-6991, 2013.

[3] X.H. Wu, S.K. Gray, M. Pelton, Quantum dot induced transparency in a nanoscale plasmonic resonator, *Optics Express* 18: 23633−23645, 2010.

ZnO-Au heterojunction enhanced the photoluminescence of ZnO nanocrystals

I. Shahine[1], J-J. Gaumet[1], A. En-Naciri[1], P. Miska[2], B. El-Eulmi[2], H. Rinnert[2], S. Jradi[3] and S. Akil[1]

[1] Laboratoire de Chimie et Physique ; Université de Lorraine
1 Bd. Arago, 57070 Metz, France
[2] Université de Lorraine, UMR CNRS 7198, Institut Jean Lamour, BP 70239, 54506 Vandœuvre-lès-Nancy, France
[3] Laboratoire de Nanotechnologie et d'Instrumentation Optique (LNIO), Institut Charles Delaunay, CNRS UMR 6281, Université de Technologie of Troyes (UTT), Troyes, France

Corresponding author: suzanna.akil@univ-lorraine.fr

Abstract

The construction of a semiconductor heterojunction has attracted a lot of attention due to its perfect effectiveness in improving the sensing, luminescence and photocatalytic activity of a wide range of nanomaterials. [1,2] In particular, hybrid nanostructures composed of semiconductor (SC) and metallic nanoparticles (MNP) have received growing interest due to the high confinement associated to the plasmonic resonances of MNP. This phenomenon enables strong interactions with other photonic elements such as quantum emitters. [3]
The resulting plasmon-exciton interaction gave benefits to a wide range of applications such as gas and vapor sensing, hydrogen storage, electro-optics, and catalysis. [4]
In this context, we develop a metal-semiconductor nanomaterial (Au-ZnO and Ag-ZnO) using a new synthesis method which is green, simple and exhibiting high quantum yield and good stability nanomaterials.
First, ZnO nanocrystals were fabricated by a hydrothermal method based on an advanced synthesis study in order to tune their photoluminescence properties. We are particularly interested by the fabrication of pure and small nanoparticles (diameter < 3 nm) to favor a strong coupling with Au NPs. Then, another chemical process was adapted to prepare ZnO-Au nanosystems. Subsequently, photoluminescence measurements were performed on ZnO-Au nanoparticles of different characteristics. More precisely, the role of both the size of ZnO and Au NPs, and the ZnO-Au mass ratio in the coupling was investigated to determine the quenching and enhancement conditions of ZnO photoluminescence. In this communication, we show results about the synthesis of ZnO nanocrystals and the optical properties of the hybrid nanoparticles.

References

[1] Jiang, R., Li, B., Fang, C., & Wang, J. (2014). Advanced Materials, 26(31), 5274-5309.

[2] Wang, X., Chen, X., Thomas, A., Fu, X., & Antonietti, M. (2009). Advanced Materials, 21(16), 1609-1612.

[3] Zhang, L., Wong, K. H., Chen, Z., Jimmy, C. Y., Zhao, J., Hu, C. & Wong, P. K. (2009). Applied Catalysis A: General, 363(1), 221-229.

[4] Alvarez-Puebla, R., Liz-Marzan, L. M., & Garcia de Abajo, F. J. (2010). The Journal of Physical Chemistry Letters, 1(16), 2428-2434.

3D plasmonic supercrystals: SERS enhancing properties

Nicolas Pazos-Perez[1], and Ramon Alvarez-Puebla[1,2]

[1]Department of Physical Chemistry and Inorganic and EMaS, Universitat Rovira i Virgili, Spain
[2]Institució Catalana de Recerca i Estudis Avançats (ICREA), Spain
*corresponding author, E-mail: nicolas.pazos@urv.cat

Abstract

In this work, we report novel methods to produce arrays of nanoparticles, either as continuous or as isolated super-crystals made with plasmonic nanoparticles. These macroscale organizations are created via confinement controlled drying and spin coating. SERS studies on the super-crystals shape and size were conducted. Moreover, the produced structures were effectively use for SERS sensing showing very good reproducibility among big areas.

1. Introduction

Nowadays, it is possible to control quite well the wet chemical synthesis of plasmonic nanoparticles and thus, controlling their individual plasmonic response in solution. However, to use them in many technological applications, such as microelectronics, wave guiding, sensing or metamaterials, it is required their controlled organization over extended areas.[1-8] In the last decade, special attention has been drown to the fabrication of long-ranged ordering of metal nanoparticles (NPs) as building blocks to generate macro scale materials with plasmonic properties.[5] These materials, preserve their nanoscale properties, meanwhile new properties are generated due to the interaction between their individual constituents.[9] However, the fabrication of such structures is not trivial due to the small size of the building blocks. And till recent, it was restricted to expensive and time-consuming lithographic techniques.[10-11] Nowadays, bottom-up approaches based on the self-assembly of colloidal particles[12-13] are gaining relevance arising as a promising alternative to produce such structures. These large organized structures made of nanoparticles as building blocks, are known as supercrystals.[6, 8, 14] In this work, we report a new fast and inexpensive template-assisted method based on the drying confinement of colloidal particles to produce periodical arrays of organized nanoparticles in large-areas forming macro structured super-crystals. Moreover, since the building blocks of these structures are plasmonic nanoparticles, the extraordinary optical properties exhibited by, the crystals, can be used as platforms for the design of cheap ultrasensitive and ultrafast sensors based on surface-enhanced Raman scattering (SERS) spectroscopy.[15]

2. Results and discussion

2.1. Super-crystals fabrication

The successful NP assembly into densely packed and well-ordered three-dimensional super-crystals requires the simultaneous control of different experimental parameters. Therefore, the process can be divided in four main different steps: 1) Synthesis purification and concentration of Au nanoparticles; 2) Template production and hydrophilization; 3) Nanoparticles confinement and sedimentation; 4) Solvent removal and surface cleaning. Figure 1 shows a schematic representation of the process.[15]

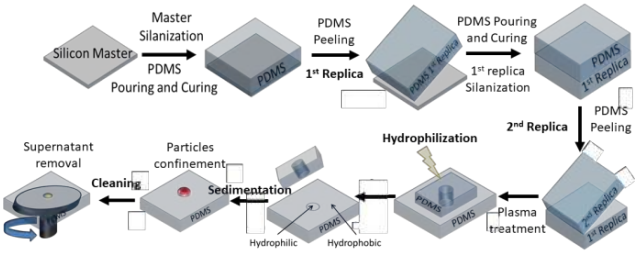


Figure 1: Schematic representation of the process.

2.1.1. Synthesis purification and concentration of Au nanoparticles

One of the crucial steps to organize Au NPs into super-crystals achieving dense packed and clean three-dimensional structures is the right preparation and processing of the Au NPs used. Three main requirements are essential, first, the Au NP dispersion needs to be highly pure and monodisperse to produce well-ordered crystals. Second, since many particles are required to form the crystals, the Au NPs have to be highly concentrated keeping their stability avoiding particle aggregation. Third, the NPs should also sediment with time.

2.1.2. Template production and hydrophilization

Si-masters with various topographies were used. Replica molding was used to duplicate these surfaces topographically. PDMS was chosen because their surface properties can be easily changed from hydrophobic to hydrophilic by plasma treatment. To exactly replicate the Si-masters, two replica molding processes were performed. The first molds, named 1st replicas, were prepared by

casting PDMS on the Si-masters and curing them. After that, the relief stamps exhibit the opposite structures as the Si-masters. Thus, to achieve the exact same structures as the masters, a 2nd replica molding step was performed using the 1st PDMS molds as templates and using again PDMS for molding. The 2nd replicas have the exact same pattern as the masters. To avoid that the reactive vinyl-groups from the first PDMS replica cross-link with the second replica and bond irreversibly together during the curing process, the 1st PDMS replica needs to be silanized before performing the second replication step.

2.1.3. Nanoparticles confinement and sedimentation

The different wetting properties were achieved via plasma treatment. A PDMS piece with a hole in the middle was placed on the structured surface of the PDMS replica. Afterwards the system was treated with O_2 plasma rendering to the hydrophobic PDMS surface a temporally hydrophilicity meanwhile the PDMS stamp on top, prevents the PDMS replica underneath to become hydrophilic. After that, the PDMS stamp was removed leaving and hydrophilic region on the hydrophilic PDMS surface. Because of the wetting contrast, the GNPs droplet remains confined in the hydrophilic region without spreading. After that, the GNPs sediment driven by gravitational force and capillary forces. During this process, the GNPs spontaneously assemble into organized supercrystals. To avoid solvent evaporation during the assembly process a humidity chambers was used.

2.1.4. Solvent removal and surface cleaning

After sedimentation of the GNP the residual water containing CTAB was removed via spin-coating. Doing this, the overall surfactant concentration was decreased, leading to cleaner supercrystals. Afterwards two additional cleaning steps were performed using Millipore water to further remove excess of surfactant and GNP. Once the crystals were formed, they were transfer to glass slides (or any surface) using adhesive tape. In Figure 2 well controlled assemblies of NPs (prepared super-crystals) are shown.

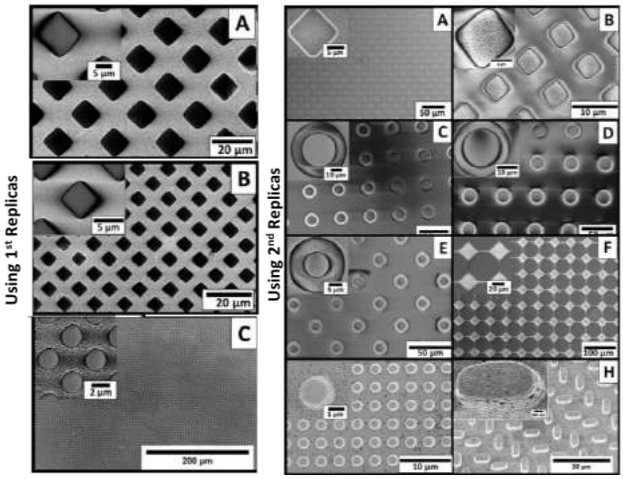


Figure 2: SEM images of various supercrystals.

2.2. SERS enhancing properties

To test the SERS enhancing properties, the colloidal crystals were first cleaned with O_2 plasma to remove all residual organics from the metallic surfaces, including CTAB.[16] Benzenethiol (BT), selected as the Raman probe, was deposited on the substrates through gas phase. Crystals with different morphological features were characterized by SERS. Remarkably, two major features arise from the SERS analysis of the crystals. First, all the patterned substrates provide a consistent larger intensity than that sustained by the continuous film. Second, regardless the crystal geometry, the absolute intensity increases as the side of the structures increases, giving rise to similar enhancements for similar values.

3. Conclusions

In summary, we have developed an innovative cheap, easy, and fast process to produce homogeneous discrete microstructured supercrystals arrays with complex geometries over very large areas using Au nanoparticles as building blocks. The proposed process, the plasma drop confinement is very convenient and innovative, because of its simplicity. The obtained plasmonic supercrystals provide high and uniform SERS enhancement over extended areas.

References

[1] R. F. Aroca, R. A. Alvarez-Puebla, N. Pieczonka, S. Sanchez-Cortez, J. V. Garcia-Ramos, *Advances in Colloid and Interface Science* **2005**, *116*, 45-61.

[2] S. Lal, S. Link, N. J. Halas, *Nat Photon* **2007**, *1*, 641-648.

[3] O. D. Velev, S. Gupta, *Advanced Materials* **2009**, *21*, 1897-1905.

[4] M. L. Brongersma, V. M. Shalaev, *Science* **2010**, *328*, 440-441.

[5] N. Pazos-Perez, W. Ni, A. Schweikart, R. A. Alvarez-Puebla, A. Fery, L. M. Liz-Marzan, *Chemical Science* **2010**, *1*, 174-178.

[6] R. A. Alvarez-Puebla, A. Agarwal, P. Manna, B. P. Khanal, P. Aldeanueva-Potel, E. Carbó-Argibay, N. Pazos-Pérez, L. Vigderman, E. R. Zubarev, N. A. Kotov, L. M. Liz-Marzán, *Proceedings of the National Academy of Sciences* **2011**, *108*, 8157-8161.

[7] R. A. Álvarez-Puebla, *The Journal of Physical Chemistry Letters* **2012**, *3*, 857-866.

[8] M. Alba, N. Pazos-Perez, B. Vaz, P. Formentin, M. Tebbe, M. A. Correa-Duarte, P. Granero, J. Ferré-Borrull, R. Alvarez, J. Pallares, A. Fery, A. R. de Lera, L. F. Marsal, R. A. Alvarez-Puebla, *Angewandte Chemie International Edition* **2013**, *52*, 6459-6463.

[9] O. Hess, J. B. Pendry, S. A. Maier, R. F. Oulton, J. M. Hamm, K. L. Tsakmakidis, *Nat Mater* **2012**, *11*, 573-584.

[10] C. M. Soukoulis, M. Wegener, *Nat Photon* **2011**, *5*, 523-530.

[11] O. Benson, *Nature* **2011**, *480*, 193-199.

[12] O. D. Velev, A. M. Lenhoff, *Current Opinion in Colloid & Interface Science* **2000**, *5*, 56-63.

[13] C. Burda, X. Chen, R. Narayanan, M. A. El-Sayed, *Chemical Reviews* **2005**, *105*, 1025-1102.

[14] N. Pazos-Perez, F. J. Garcia de Abajo, A. Fery, R. A. Alvarez-Puebla, *Langmuir* **2012**, *28*, 8909-8914.

[15] M. Tebbe, S. Lentz, L. Guerrini, A. Fery, R. A. Alvarez-Puebla, N. Pazos-Perez, *Nanoscale* **2016**, *8*, 12702-12709.

[16] M. Tebbe, M. Maennel, A. Fery, N. Pazos-Perez, R. A. Alvarez-Puebla, *The Journal of Physical Chemistry C* **2014**, *118*, 28095-28100.

All Dielectric Metamaterial for MIR Applications

M. A. Swillam

[1]Department of Physics, School of Sciences and Engineering, New Cairo, Egypt, 11835
*corresponding author, E-mail: m.swillam@aucegypt.edu

Abstract

Metamaterials have the ability to focus and absorb light at different wavelengths. These characteristics are highly useful for harvesting thermal radiation in the Mid infrared range. They are also important for sensing and absorption spectroscopy application. In the work we discuss different designs for metamaterials in the Mid infrared using all dielectrics to reduce the losses and the fabrication complexity.

Plasmon-Assisted Selective and Super-Resolving Excitation of Individual Quantum Emitters on a Metal Nanowire

Hong Wei[1]*, Qiang Li[2], Deng Pan[3], and Hongxing Xu[3,4]

[1]Institute of Physics, Chinese Academy of Sciences, Beijing 100190, China
[2]School of Information and Optoelectronic Science and Engineering, South China Normal University, Guangzhou 510006, China
[3]School of Physics and Technology, Wuhan University, Wuhan 430072, China
[4]Institute for Advanced Studies, Wuhan University, Wuhan 430072, China
*corresponding author, E-mail: weihong@iphy.ac.cn

Abstract

We show that multiple quantum dots coupled with a silver nanowire can be controllably excited by tuning the interference field of surface plasmons on the nanowire. We demonstrate the selective excitation of two quantum dots separated by a distance as short as 100 nm. We also numerically demonstrate a new kind of super-resolution imaging method that combines the tunable surface plasmon interference pattern on the nanowire with the structured illumination microscopy technique.

The ability to control the single photon emission from single solid state quantum emitters is essential for various quantum information processing applications. Metal nanostructures supporting surface plasmon (SP) modes have been proposed to exquisitely tailor the photoluminescence properties of single quantum emitters. The propagating SPs on metal nanowires (NWs) are particularly attractive due to their nanoscale field confinement and microscale propagation length, and hold promise for a wide range of applications in the fields such as enhanced light-matter interactions, and integrated nanophotonic circuits [1]. As a result of the potentially large Purcell effect, the propagating SP modes of the metal NW can efficiently harvest the photons emitted from single quantum emitters, resulting in an enhancement of the emitter's spontaneous decay rate as well as the generation of single SPs guided on the NW [2, 3].

In addition to single quantum emitters, the interaction of multiple quantum emitters mediated through the strong interaction with the SP modes on the plasmonic waveguide has been explored theoretically. However, there are challenges in experimentally studying the hybrid system of multiple quantum emitters coupled with the plasmonic waveguide. One is the super-resolution imaging of these quantum emitters along the waveguide. Although a recent experiment has demonstrated the imaging for two closely spaced quantum dots (QDs) on a silver NW using the single molecule fluorescence localization method [4], for quantum emitters with temporally stabilized fluorescence, such as color centers, multiple quantum emitters in diffraction limited area cannot be resolved. Another challenge is to selectively control the excitation conditions of the quantum emitters in diffraction limited area, which cannot be achieved by using the conventional focused laser beam excitation method.

In this paper, we show that multiple QDs coupled with a Ag NW can be controllably excited by tuning the interference pattern of the localized and propagating SPs, or two counter-propagating SP waves on the Ag NW [5]. Figure 1a shows the fluorescence image of the coupled system of a silver NW and four QDs. When two laser beams are focused onto the two ends of the NW, two counter-propagating SP waves are excited, which interfere and form a standing wave on the NW. By tuning the phase difference of the two laser beams, the standing wave pattern moves along the NW and the electric field experienced by the QDs on the NW is changed, which modulates the emission intensity of the QDs. Figure 1b shows the emission intensity of the four QDs excited by focusing the laser beams onto the two ends of the NW with the phase of one laser beam monotonically increased. The emission intensities of the QDs exhibit distinct phase dependent oscillations with different peak positions, which can be attributed to the varying near-field intensity on the NW during the moving of the standing wave. With this method we demonstrated the selective excitation of two QDs separated by 100 nm, a distance much smaller than the diffraction limit. In addition, we numerically demonstrated a new kind of super-resolution imaging method by applying the tunable SP interference pattern on the NW to the structured illumination microscopy technique. Our work provides a novel high-resolution optical excitation and imaging method for the coupled systems of multiple quantum emitters and plasmonic waveguides, which adds a new tool for studying and manipulating single quantum emitters and single plasmons for quantum plasmonic circuitry applications.

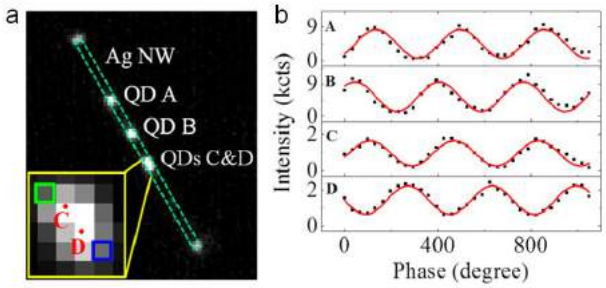


Figure 1: (a) Fluorescence image of the investigated QDs-NW system under wide-field excitation. The bright spots A and B correspond to the fluorescence of two separated QDs A and B, while the elongated spot C&D corresponds to two QDs (QDs C and D) near each other. The spots E and F correspond to the two ends of the NW. The inset at the lower left corner is a magnified view of the spot C&D. The fitted positions of QDs C and D are marked with red dots. The green and blue squares indicate the pixels used to track the intensities of QDs C and D, respectively. (b) Emission intensities of the four QDs as a function of the phase increment of one laser beam. The red solid lines represent sinusoidal fitting of the data.

Acknowledgements

This work was supported by The Ministry of Science and Technology of China (Grant No. 2015CB932400), National Natural Science Foundation of China (Grant Nos. 11422436, 11374012 and 11674256), the Prominent Young Scientist Program and the "Strategic Priority Research Program (B)" (Grant No. XDB07030100) of Chinese Academy of Sciences, and the New Star of Science and Technology Program of Beijing Municipal Science and Technology Commission.

References

[1] H. Wei, D. Pan, S.P. Zhang, Z.P. Li, Q. Li, N. Liu, W.H. Wang, H.X. Xu, Plasmon Waveguiding in Nanowires, *Chem. Rev.* http://dx.doi.org/10.1021/acs.chemrev.7b00441

[2] H. Wei, D. Ratchford, X.Q. Li, H.X. Xu, C.K. Shih, Propagating Surface Plasmon Induced Photon Emission from Quantum Dots, *Nano Lett.* 9: 4168−4171, 2009.

[3] Q. Li, H. Wei, H.X. Xu, Quantum Yield of Single Surface Plasmons Generated by a Quantum Dot Coupled with a Silver Nanowire, *Nano Lett.* 15: 8181−8187, 2015.

[4] Q. Li, H. Wei, H.X. Xu, Resolving Single Plasmons Generated by Multiquantum-Emitters on a Silver Nanowire, *Nano Lett.* 14: 3358−3363, 2014.

[5] Q. Li, D. Pan, H. Wei, H.X. Xu, Plasmon-Assisted Selective and Super-Resolving Excitation of Individual Quantum Emitters on a Metal Nanowire, *Nano Lett.* http://dx.doi.org/10.1021/acs.nanolett.7b05448.

Surface enhanced spectroscopies with new plasmonic platforms

Pierre-Michel Adam[1]

[1]*Laboratoire de Nanotechnologie et d'Instrumentation Optique, ICD, CNRS UMR 6281, Université de Technologie de Troyes, 12 Rue Marie Curie, CS42060, 10004 Troyes Cedex, France*

[*]*corresponding author: adam@utt.fr*

ABSTRACT

Plasmonics concerns the excitation, manipulation and detection of the surface plasmons at the subwavelength scale. It has highly potential applications for nanoscale and ultrafast photonics. Understanding the coupling properties between quantum emitters and plasmons resonances and/or nanonantennas is a key step towards realistic applications in the near future. We will present in this paper our latest experimental and theoretical results on surface enhanced spectroscopies, consisting in emitters coupled to different types of surface plasmons excitations, localized plasmons on bimetallic nanoparticles and surface plasmons polaritons on waveguides.

MAIN

Plasmonics is a now well-established field finding numerous applications in pharmacology, biology, optoelectronics and metamaterials among others. For the sensitive detection of molecules or markers Surface Enhanced Spectroscopies, such as Surface Enhanced Raman Spectroscopy (SERS) and Surface Enhanced Fluorescence (SEF), are widespread and the most used for applications. Both these enhanced spectroscopies rely on local field enhancements in the near vicinity of resonant metallic nanoparticles when Surface Plasmon oscillations are driven for a specific optical wavelength. SERS can achieve single molecule detection when two or more metallic nanoparticles are coupled through their near-fields, resulting in enhancements usually ranging from 4 up to 10 orders of magnitude, even if the way to evaluate such an absolute magnitude of enhancement is still a subject of debate. A drawback is that these highly sensitive SERS substrates are difficult to reproduce and control.

Less enhancement is obtained with SEF but usually the intrinsic fluorescence cross section of a molecule is more than 10 orders of magnitude more important than that of its non-resonant Raman cross-section. In SEF one has to take into account the finite lifetime of the excited levels of the molecule of interest, which results in quantum yield modifications in the presence of the metallic nanoparticles. Quantum yield can be enhanced or even reduced, leading in the latter case to a competition with local field excitation enhancement and thus the possibility of quenched fluorescence from the emitters.

This contribution will show our recent progress towards the understanding of SERS and SEF effects with a variety of coupled plasmonic systems [1-4].

REFERENCES

[1] M. Yehia Khaywah, S. Jradi, G. Louarn, Y. Lacroute, J. Toufaily, Tayssir Hamieh and P.-M. Adam, "Ultra Stable, Uniform, Reproducible and Highly Sensitive Random Arrays of Bimetallic Nanoparticles as Reliable Large Scale SERS Substrates, *The Journal of Physical Chemistry C*., 119 (46), 26091–26100, 2015

[2] A. Muravitskaya, A. Rumyantseva, S. Kostcheev, V. Dzhagan, O. Stroyuk and P.-M. Adam, "Enhanced Raman scattering of ZnO nanocrystals in the vicinity of gold and silver nanostructured surfaces", *Optics Express*, 24 (2), A168-A173, 2016

[3] S. Ashraf, A. Konrad, H. Lokstein, M. Skandary, , M. Metzger, J.M. Djouda, T. Maurer, P.-M. Adam, A. J. Meixner, and M. Brecht, "Temperature Dependence of Metal-Enhanced Fluorescence of Photosystem I from Thermosynechococcus elongatus", *Nanoscale,* 9(12), 2017

[4] F. Tang, P.-M. Adam, and S. Boutami, "Theoretical investigation of SERS nanosensors based on hybrid waveguides made of metallic slots and dielectric strips", *Optics Express,* 24 (19), 21244-21255, 2016.

Self-assembled metamaterials active at optical frequencies

V. Many[1,2], G. Drisko[1], P. Barois[2], A. Baron[2], V.Ponsinet[2], P. Richetti[2], S. De Cicco[3], J. Leng[3], J-B Salmon[3], S. Ravaine[2], A.Crut[4], N. Del Fatti[4], E. Duguet[1], M. Treguer-Delapierre*[1]

[1]ICMCB-CNRS, UPR 9048, France, Pessac
[2] CRPP-CNRS, UPR9048, France, Pessac
[3]LOF-CNRS, UMR 5258, France, Pessac
[4]ILM-CNRS, UMR 5306, France, Villeurbanne
*treguer@icmcb-bordeaux.cnrs.fr

Abstract

Self-assembled metamaterials constitute a promising platform to achieving bulk and homogenous optical materials that exhibit unusual effective medium properties. For many years now, the research community has contemplated lithographically fabricated metasurfaces, with extraordinary optical features. However, achieving large volumes at low cost is still a challenge by top-down fabrication. Bottom-up fabrication, that relies both on nanochemistry and self-assembly, is capable of building such materials while greatly reducing the energy footprint in the formulation of the metamaterial. Self-assembled metamaterials have shown that they are capable of reaching unprecedented values of bulkiness and homogeneity figures of merit. This feat is achieved by synthesizing plasmonic nanoresonators and assembling them into a fully three-dimensional matrix. Furthermore it has been shown that a wide range of material parameters can be tailored by controlling the geometry and composition of the meta-atoms as well as the volume fraction of the nano-objects in the metamaterial. In this talk, we will review some of the self-assembled optical metamaterials active in the visible range that we recently developed.

1. Introduction

Metamaterials are ensembles of resonators - meta-atoms - that exhibit unsual optical properties that are otherwise unattainable with natural materials. The first metamaterial was realized by Smith et al. in 1999 who produced a composite medium that had simultaneously negative electric permittivity and magnetic permeability [1], which constitutes a negative index material. Such a material have only been thought of purely theoretically by Veselago in 1968 and many pro- found physical implications had been predicted such as the reversal of the Cherenkov radiation [2]. Since then the metamaterials concept has been used to produce extraordinary devices ranging from invisibility cloaks to hyperlenses that enable imaging beyond the diffraction [3,4]. Today, metamaterials have moved beyond electromagnetic waves and now include acoustic, mechanical, thermal and seismic waves. Where optics are concerned, most metamaterials produced thus far have been fabricated using energy-intensive top-down lithographic approaches, which severely limits the total amount of resonators that can be build (~ 10^6). As result, the total surface area that metamaterials typically cover rarely exceeds (100 μm)^2. The bottom-up approach offers a serious alternative to tackle this hurdle, because it allows considering the meta-atom and the metamaterial separately, in a way that we may refer to as hierarchical self-assembly [5]. Indeed, nanochemistry tackles the problem of synthesizing complex nanoparticles with desired dispersions of the electric and magnetic polarizabilities, while soft-matter self-assembly focuses on producing materials made of large volumes of these meta-atoms. In recent years, we have developped different complex nanoparticles and develop an efficient approach for the fabrication of hierarchically self-assembled metamaterials. We show, in this contribution, some of the complex systems explored.

2. Results and discussion

We produced, for example, meta-atoms made of clusters of metallic satellites surrounding a dielectric core (so-called plasmonic "raspberries"): $SiO_2@Ag_n$ or $SiO_2@Au_n$, (Figure 1), at the gram scale [6,7].

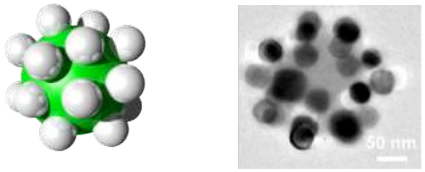


Figure 1: Example of basic magnetic units with a raspberry-like architecture synthesized to produce self-assembled metamaterials

Their optical characteristics have been investigated at single particle level using the spatial modulation spectroscopy technique as well as for a collection of nano-objects using polarized resolved static light scattering at variable angle.

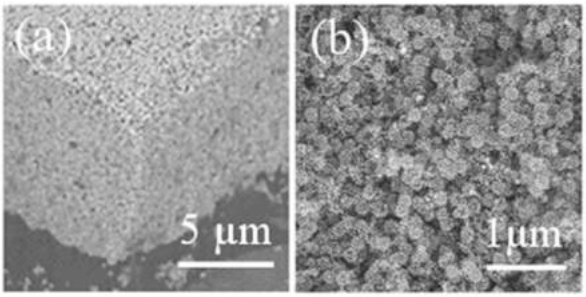


Figure 2: SEM images of the metamaterials formed by self-assembly of plasmonic nanoraspberries

These engineered meta-atoms have tailored magnetic polarizabilities in the visible regime. Their assembly using microfluidics allows to get truely bulk isotropic optically magnetic metamaterials active in the visible (Figures 2 & 3).

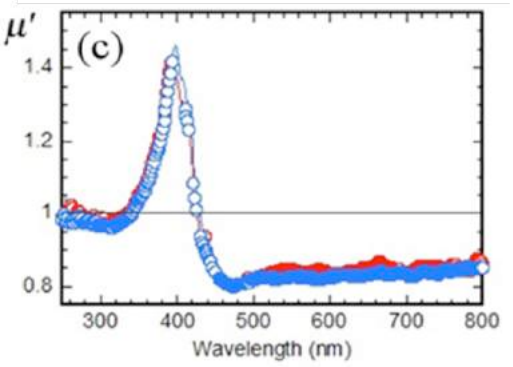


Figure 3. Real part of the magnetic permeability extracted from spectroscopic elllipsometry. Red and blue colors correspond to two different samples. Natural materials lie on the black line at $\mu' = 1$.

Since the refractive index of the assembled metaatoms depends on governing parameters like the size (core & satellites) as well as the number of satellites, we further explore the possibility to control simultaneously the composition, the number of plasmonic satellites surrounding the dielectric core. Some of the most interesting structures are the Platonic solids, for example, tetrapods (tetrahedra), hexapods (octahedra) and dodecapods (icosahedra (Figure 4)) because these morphologies have isotropic optical properties. These nano-objets with a well-controlled morphology were elaborated by using the concept of patchy particles, i.e. shape-isotropic particles with precisely controlled patches of varying surface and sticking properties. Exploiting the surface properties of patchy colloidal particles with a well-controlled number of patches at their surface, the metaatoms with the symmetries of Platonic solid were fabricated on a large scale.

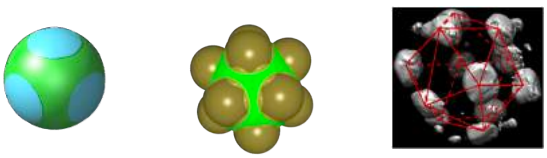


Figure 4: scheme and electron tomography image of another magnetic unit consisting of 12 gold satellites onto a silica core. Their synthesis is initiated from a patchy silica particle.

These basic units of sub-wavelength size offer unique optical properties and a magnetic polarization of high magnitude in visible or near-IR light.

3.Conclusion

This work reported the realization of optical magnetism based on the bottom-up approach of material chemistry. The major objectives of this approach are a large-scale cost effective production of nano-sized meta-atoms exhibiting magnetic and electric response of high magnitude in visible or near-IR light, the possibility to tune the overlap the electric and magnetic responses of such meta-atoms and an easy processing of the nano-objects to produced optical functional devices of large area.

Acknowledgements

We acknowledges the LABEX project (under the Contract ANR-10-LABX-42) in the framework of IdEx Bordeaux (ANR-10-IDEX-03-02).

References

1. Smith R., Padilla W., Vier DC, Nemat-Nasser S., Schultz S., Composite medium with simultaneous negative permeability and permittivity *Phys. Rev. Lett.* **84,** 4181 (2000).
2. Veselago V., The electrodynamics of substances with simultaneously negative values of and m. *Soviet physics uspekhi* **10,** 509 (1968).
3. Schurig D., Mock J., Justice B., Cummer S., Pendry J., Starr A, SMith D, metamaterial electromagnetic cloak at microwave frequencies, *Science,* **314,** 977 (2006).
4. Liu Z., Lee H., Xiong Y., SUn C., Zhang X., Far-field optical hyperlens magnifying sub-diffraction-limited objects, *Science,* **315,** 1686 (2007).
5. Ponsinet, V., Barois P., Gali Manoj, Richetti P., Salmon JB, Vallechi A., Albani M., Le Beulze A., Gomez-Grana S. Duguet E., Tréguer-Delapierre M. Resonant isotropic optical magnetism of plasmonic nanoclusters in visible light. *Phys. Rev. B* **92,** 220414 (2015).
6. Gomez-Grana, S., Le Beulze A., Treguer-Delapierre M., Duguet E., Grana E., Cloutet E. Hadzzioannou G., Leng J., Salmon JB, Barois P. Hierarchical self-assembly of a bulk metamaterial enables isotropic magnetic permeability at optical frequencies. *Mater. Horizons* **3,** 596–601 (2016).
7. Le Beulze, A., Gomez-Grana S., Mornet S., Ravaine S., Correa-Duerte M, Guerrini L., Alvarez-Puebla, Crut A., Del Fatti N., Vallee F., Tréguer-Delapierre M. Robust raspberry-like metallo-dielectric nanoclusters of critical sizes as SERS substrates. *Nanoscale* **9,** 5725–5736 (2017).
8. Chomette, C., Tréguer-Delapierre, M., Schade N., Manoharan V., Taveau JC, Ravaine S., Duguet E., Colloidal Alchemy: Conversion of Polystyrene Nanoclusters into Gold. *ChemNanoMat* **3,** 160–163 (2017).

Photopolymerization at the nanoscale triggered by plasmon resonance

F. Kameche[1], W. Heni[1], S. Telitel[1], X. Zhou[2], C. Deeb[2], R. Bachelot[2], O. Soppera*[1]

[1] Institut de Science des Matériaux de Mulhouse (IS2M), CNRS UMR 7361, Université de Haute-Alsace, Mulhouse, France
[2] Laboratoire de Nanotechnologie et d'Instrumentation Optique (LNIO), ICD CNRS UMR 6281, Université de Technologie de Troyes, Troyes, France
*corresponding author, E-mail: olivier.soppera@uha.fr

Abstract

We report on the physicochemical and optical parameters controlling the photopolymerization process in near-field at the vicinity of metal nanoparticles. Kinetic parameters were shown to be of paramount importance to control the polymerization in highly confined space. Different photopolymers were used in this context to investigate the process at the molecular scale and finely tune the final properties of the nanoparticles.

1. Introduction

Over the past ten years, localized surface plasmons have been exploited for triggering and controlling photochemical and photophysical reactions. Achieving hybrid nanosystems coupling metal nanostructures with enhanced effect is a major challenge for applications in nanophotonics, sensors or spectroscopy. [1]

In our case, surface plasmon resonance of individual metal nanoparticles was used as an optical near-field source to locally trigger free radical polymerization of an acrylic monomer: metal nanoparticles embedded in a photopolymer sensitive at the resonance wavelength are irradiated under the polymerization threshold but close enough to this threshold to initiate the free-radical polymerization thanks to electromagnetic near-field enhancement.

We will report on the physicochemical and optical parameters controlling the photopolymerization process in near-field. Kinetic parameters were shown to be of paramount importance to control the polymerization in highly confined space. Different photopolymers were used in this context to finely tune the final properties of the nanoparticles.

2. Principle

The principle of our approach is schematized in Figure 1.

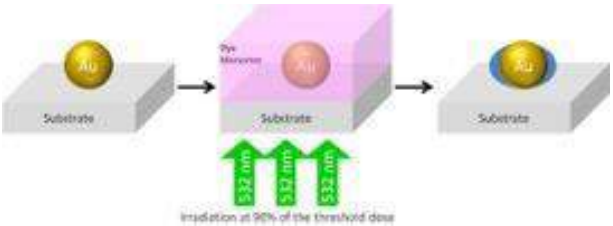


Figure 1. Schematic of the preparation of the hybrid metal-polymer nanoparticles by free-radical photopolymerization

The fabrication of the hybrid nanoparticles is described in details in [2]. Briefly, metal nanoparticles are deposited in a substrate and covered by a photopolymer. The photopolymer is prepared with the suitable photoinitiator system with absorption spectrum overlapping the soectrum of the metal nanoparticles. The system is irradiated at a wavelength corresponding to both systems. The irradiation conditions are chosen to avoid any polymerization in far-field, using a non-linear response of the photopolymer. The electro-magnetic field enhancement at the vicinity of the metal nanoparticles allows starting the crosslinking of the photopolymer by free-radical polymerization. The non-reacted monomer can be washed out by a solvent and the hybrid nanoparticles remain on the substrate.

Gold nanoparticles were used here and a photopolymer composed of EosinY, MDEA and a triacrylate monomer (PETA) was used as a reference system. [3]

The analysis of the hybrid nanoparticles was obtained so far by Atomic Force Microscopy. We developed a new procedure based on Transmission Electronic Microscopy to allow a more precise analysis of the hybrid nanoparticles. This method makes it possible to finely localize the polymer part in the nanoparticle.

3. Influence of the irradiation parameters on the shape

The influence of the photonic parameters (light intensity, dose) is first discussed. The analysis of the spatial extend of

the polymer lobes vs the laser intensity reveals the important role of the diffusion of the dye and the inhibitor to the near-field zone. [3]

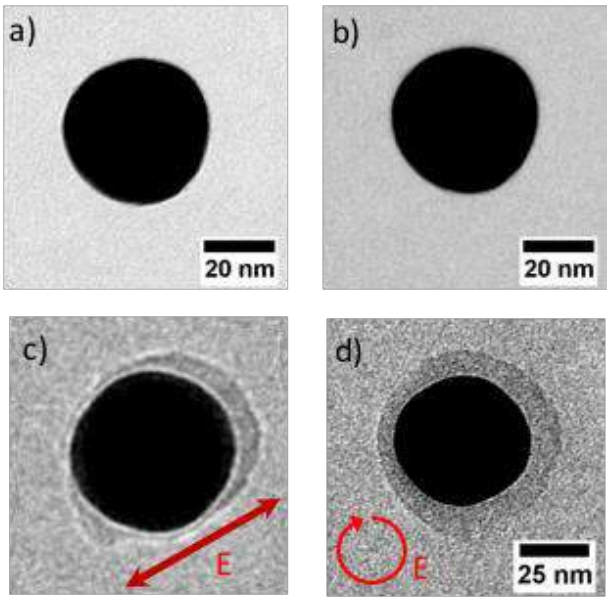


Figure 2 : Typical TEM images of the nanoparticles. a) is a Au nanoparticles as deposited. b) shows a control experiment with addition of the photopolymer without any irradiation. c) shows a typical particle fabricated in linear incident polarization. In d) a circular polarization was used.

Typical TEM images are presented in Figure 2. Control experiments were first done to validate the procedure (Figures 1a and 1b). TEM imaging allows a precise characterization of the structure of the hybrid particle. It was shown that in linear incident polarization, polymers parts in the direction of polarization could be obtained (Figure 2c). However, in numerous nanoparticles, we could not find this directional behavior.
Circular polarization gives rise to a more efficient polymerization, homogeneously distributed around the nanoparticle. Interestingly, the analysis on a large number of particles shows a better yield of the polymerization with such polarization state.

4. Extending to new photopolymers

Modification of the photopolymer composition was also proposed in order to further investigate the photoinduced physico-chemical phenomena.
It also allowed extending the properties of the hybrid nanoparticles.

5. Conclusion

Plasmon resonance can be efficiently used to fabricate advanced functional hybrid nanoparticles. This configuration also constitutes a unique experimental configuration to investigate free-radical photopolymerization at the nanoscale.

Acknowledgements

The authors thank the French Agence Nationale de la Recherche (ANR) for fundings (projects HAPPLE and SAMIRE).

References

[1] Zhou, X.; Soppera, O.; Plain, J.; Jradi, S.; Sun, X. W.; Demir, H. V.; Yang, X.; Deeb, C.; Gray, S. K.; Wiederrecht, G. P.; Bachelot, R., *J Optics* **2014**, 16, 114002.

[2] Deeb, C.; Bachelot, R.; Plain, J.; Baudrion, A. L.; Jradi, S.; Bouhelier, A.; Soppera, O.; Jain, P. K.; Huang, L. B.; Ecoffet, C.; Balan, L.; Royer, P., *Acs Nano* **2010**, 4 (8), 4579-4586.

[3] Deeb, C.; Ecoffet, C.; Bachelot, R.; Plain, J.; Bouhelier, A.; Soppera, O., *Journal of the American Chemical Society* **2011**, 133 (27), 10535-10542.

Novel Design and Applications of Metamaterials, Metasurfaces and Metadevices using Hybrid and New Materia

Metamaterial Superconductors

Vera N. Smolyaninova[1], Igor I. Smolyaninov[2,3]

[1]Department of Physics Astronomy and Geosciences, Towson University,
8000 York Rd., Towson, MD 21252, USA
[2]Department of Electrical and Computer Engineering, University of Maryland, College Park, MD 20742, USA
[3]Saltenna LLC, 1751 Pinnacle Drive, McLean, VA 22102,USA

*corresponding author, E-mail: vsmolyaninova@towson.edu

Abstract

Searching for natural materials exhibiting larger electron-electron interactions constitutes a traditional approach to high temperature superconductivity research. Very recently we pointed out that the newly developed field of electromagnetic metamaterials deals with the somewhat related task of dielectric response engineering on a sub-100 nm scale. Considerable enhancement of the electron-electron interaction may be expected in such metamaterial scenarios as in epsilon near zero (ENZ) and hyperbolic metamaterials. This approach has been verified in experiments with aluminium-based metamaterials.

1. Introduction

One of the most important goals of condensed matter physics is reliably designing new materials with enhanced superconducting properties. Recently, an electromagnetic metamaterial strategy, consisting of deliberately engineering the dielectric properties of a nanostructured "metamaterial superconductor" that results in an enhanced electron pairing interaction that increases the value of the superconducting energy gap and the critical temperature, Tc, was suggested to achieve this goal [1, 2]. Our recent experimental work [3-5] has conclusively demonstrated that this approach can indeed be used to increase the critical temperature of a composite superconductor-dielectric metamaterial. For example, we have demonstrated the use of Al_2O_3-coated aluminum nanoparticles to form epsilon near zero (ENZ) core-shell metamaterial superconductors with a Tc that is three times that of pure aluminum [4]. This deep and non-trivial connection between the fields of electromagnetic metamaterials and superconductivity research stems from the fact that superconducting properties of a material, such as electron-electron pairing interaction, the superconducting critical temperature Tc, etc. may be expressed via the effective dielectric response function $\varepsilon_{eff}(q,\omega)$ of the material [6]. For example, considerable enhancement of attractive electron-electron interaction may be expected in such actively studied metamaterial scenarios as epsilon near zero (ENZ) and hyperbolic metamaterials, since in both cases $\varepsilon_{eff}(q,\omega)$ may become small and negative in substantial portions or the four-momentum (q,ω) space. Such a dielectric response-based macroscopic electrodynamics description is valid if the material may be considered as a homogeneous medium on the spatial scales below the superconducting coherence length. Electromagnetic properties are known to play a very important role in the pairing mechanism of superconductors [6]. According to the BCS theory, a Cooper pair is formed from two electrons with opposite spins and momenta that are loosely bound. This mechanism may be described as an attractive interaction of electrons that results from the polarization of the ionic lattice which these electrons create as they move through the lattice. Based on this interpretation, Kirzhnits *et al*. formulated their description of superconductivity in terms of the dielectric response function of the superconductor [6]. They demonstrated that the electron-electron interaction in a superconductor may be expressed in the form of an effective Coulomb potential

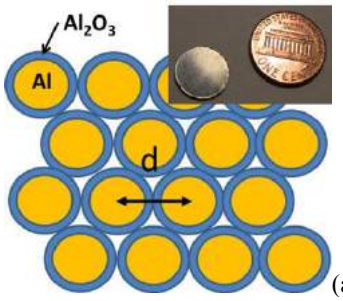
$$V(\vec{q},\omega)=\frac{4\pi e^2}{q^2\varepsilon_{eff}(\vec{q},\omega)}=V_C\frac{1}{\varepsilon_{eff}(\vec{q},\omega)} \quad (1)$$

where V_C is the Fourier-transformed Coulomb potential in vacuum, and $\varepsilon_{eff}(q,\omega)$ is the linear dielectric response function of the superconductor treated as an effective medium.

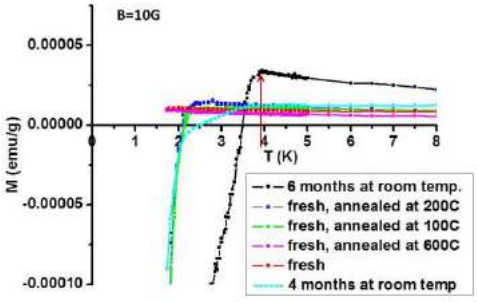
The key observation made in Refs. [1,2] was that the "homogeneous medium" approximation may remain valid even if the basic structural elements of the material are not simple atoms or molecules. It was suggested that artificial "metamaterials" may be created from much bigger building blocks, and the electromagnetic properties of these fundamental building blocks may be engineered in such a way that the attractive pairing interaction described by Eq. (1) is maximized. The two potential solutions described in [1,2] require minimization of $\varepsilon_{eff}(q,\omega)$ within a substantial portion of the relevant four-momentum spectrum, while keeping the real part of $\varepsilon_{eff}(q,\omega)$ negative. These solutions involve either the epsilon-near-zero (ENZ), or hyperbolic metamaterial scenarios, which naturally lead to broadband small and negative $\varepsilon_{eff}(q,\omega)$ behaviour in substantial portions of the relevant four-momentum spectrum.

2. Discussion

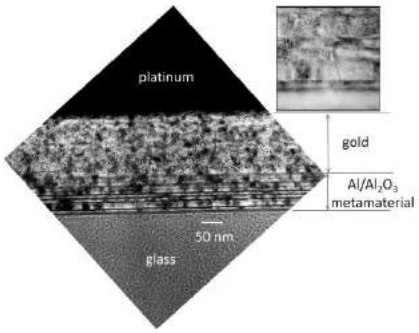
Fig.1 demonstrates that tuning electron-electron interaction is indeed possible using the epsilon-near-zero (ENZ) metamaterial approach, which is based on intermixing metal and dielectric components in the right proportions.



(a)



(b)



(c)

Figure 1: (a) Schematic geometry of the ENZ metamaterial superconductor based on the core-shell nanoparticle geometry. The nanoparticle diameter is d=18 nm. The inset shows typical dimensions of the fabricated bulk aluminum-based core-shell metamaterial. (b) Temperature dependence of zero field cooled magnetization per unit mass for several Al-Al_2O_3 core-shell metamaterial samples with increasing degree of oxidation measured in magnetic field of 10 G. The highest onset of superconductivity at ~3.9K is marked by an arrow. This temperature is 3.25 times larger than Tc=1.2K of bulk aluminum. (c) Transmission electron microscope (TEM) image of a 16 layer Al-Al_2O_3 hyperbolic metamaterial sample.

Aluminum is ideal for the proof of principle experiments because the critical temperature of bulk aluminum is quite low (TcAl=1.2K), leading to a very large superconducting coherence length ξ=1600 nm. The 18 nm diameter Al nanoparticles for these experiments were acquired from the US Research Nanomaterials, Inc. Upon exposure to the ambient conditions a ~ 2 nm thick Al_2O_3 shell is known to form on the aluminum nanoparticle surface, which is comparable to the 9 nm radius of the original Al nanoparticle. Further aluminum oxidation may also be achieved by heating the nanoparticles in air. The resulting core-shell Al_2O_3-Al nanoparticles were compressed into macroscopic, ~1cm diameter, ~0.5 mm thick test pellets using a hydraulic press, as illustrated in the inset in Fig.1(a). Al-Al_2O_3 hyperbolic metamaterial samples shown in Fig.1(c) demonstrated similar Tc enhancement while having superior transport properties compared to the core-shell metamaterials. The developed technology enables efficient nanofabrication of bulk aluminum-based metamaterial superconductors with a Tc that is three times that of pure aluminum and with virtually unlimited shapes and dimensions. These results open up numerous new possibilities of considerable Tc increase in other simple superconductors.

3. Conclusions

Taking advantage of the demonstrated success of the metamaterial approach, the critical temperature of hypothetic niobium, MgB_2 and H_2S-based metamaterial superconductors may be evaluated. The MgB_2-based metamaterial superconductors are projected to reach the liquid nitrogen temperature range. In the case of an H_2S-based metamaterial projected Tc appears to be as high as ~250 K, which almost reaches the room temperature range.

Acknowledgements

This work was supported in part by the DARPA Award No: W911NF-17-1-0348 “Metamaterial Superconductors”.

References

[1] I.I. Smolyaninov, V.N. Smolyaninova, Is there a metamaterial route to high temperature superconductivity? *Adv. Cond. Matt. Phys.* 2014: 479635, 2014.

[2] I.I. Smolyaninov, V.N. Smolyaninova, Metamaterial superconductors, *Phys. Rev. B* 91: 094501, 2015.

[3] V.N. Smolyaninova, *et al*. Experimental demonstration of superconducting critical temperature increase in electromagnetic metamaterials, *Scientific Reports* 4: 7321, 2014.

[4] V.N. Smolyaninova, *et al*. Using metamaterial nanoengineering to triple the superconducting critical temperature of bulk aluminum, *Scientific Reports* 5: 15777, 2015.

[5] V.N. Smolyaninova, *et al*. Enhanced superconductivity in aluminum-based hyperbolic metamaterials, *Scientific Reports* 6: 34140, 2016.

[6] D.A. Kirzhnits, E.G. Maksimov, D.I. Khomskii, The description of superconductivity in terms of dielectric response function, *J. Low Temp. Phys.* 10: 79, 1973.

The silicon dimer array based sensor

Ziwei Liu[1,2,3], Tanchao Pu[1,2,3], Jiebin Niu[1], Lina Shi[1,3,*] and Changqing Xie[1,3,*]

[1]Key Laboratory of Microelectronic Devices & Integrated Technology, Institute of Microelectronics, Chinese Academy of Sciences, Beijing, China
[2]University of Chinese Academy of Sciences, Beijing, China
[3]Jiangsu National Synergetic Innovation Center for Advanced Materials, Nanjing, China
*corresponding author, E-mail: shilina@ime.ac.cn; xiechangqing@ime.ac.cn

Abstract

We propose a sensor structure of silicon dimer array based on magnetic resonances. The refractive index sensing capability is investigated numerically. We obtained the sensitivity of 559nm/RIU and FOM of 52.8 for Y-polarization incident and the structure with Px=600 nm and Py=340 nm. We also investigate the effects of periods and polarizations on the sensitivity and find the larger period Px and Y-polarization incident light will benefit the sensitivity. Our results offer opportunities for designing sensors with low loss.

Keywords: Dimer arrays, sensor, magnetic resonance

1. Introduction

Recently high-refractive-index dielectric particles have been paid much attention due to their unique optical properties compared with plasmonic nanoparticles [1, 2]. The dielectric nanoparticles such as Si offer a number of advantages, including lower intrinsic loss, apparent non-toxicity and compatibility with the mature complementary metal–oxide–semiconductor (CMOS) process. Moreover, both the electric and magnetic resonant modes can be simultaneously induced in dielectric nanoparticles, and thus enabling an additional freedom to manipulate the optical properties of nanoparticles. Especially, a silicon nanosphere dimer supports magnetic-based Fano scattering [2, 3]. Sensing based on Fano resonance have been demonstrated very recently [4, 5]. Therefore, the dimer array can be a promising optical sensing structure.

In this work, we investigate the refractive index sensing capability of low-loss silicon dimer arrays by using the finite-difference time-domain (FDTD) method. The transmittance spectra of the dimer arrays exhibit a deep narrow dip, whose wavelength is very sensitive to the background refractive index. Then, we show the feature of transmittance spectra with the refractive index increasing. And we obtain the sensitivity of 559 nm RIU^{-1} and FOM of 52.8. In addition, we discuss the effects of the periods and polarizations on the sensitivity of our structure. Our structures will find the promising applications in biosensor and gas sensor.

2. Simulations and discussion

The structure in Fig. 1 we propose, comprises the square array of dimers of two silicon cylinders with the diameter d=140 nm and the height h=220 nm. The gap between two silicon cylinders is g=20 nm. The periods of the square array are Px=600 nm and Py=340 nm. The dimer nanostructures are illuminated by normal incident plane-waves polarized along the x or y axis in the visible spectral range (λ=730-960nm). Unless stated otherwise, the background refractive index is n=1.33.

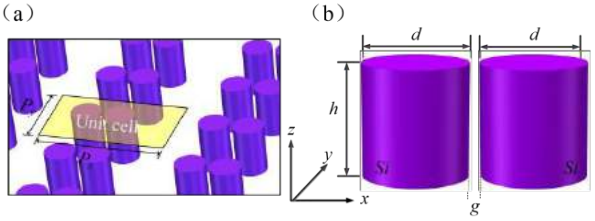


Figure 1: (a) The schematic of the square array of dimers of two silicon cylinders. Px=600 nm, Py=340 nm. (b) The silicon dimer. The height h=220 nm, the diameter d=140 nm, the gap g=20 nm.

2.1. Magnetic resonance in dimer arrays

We begin with the spectra feature of the square array of silicon dimers in Fig. 2. There exists a distinct dip at the transmittance spectrum for both polarizations. And also the absorption under the X-polarization is a little higher than that under Y-polarization. Insets of Fig. 2 are the electric and magnetic distributions at dip wavelengths for both polarizations, which denote that both resonances at 833 nm and 913 nm are mainly dominated by the magnetic dipole. The black arrows clearly show the loop induced in the electric field (see Insets of Fig. 2). The strong electric field outside the silicon cylinders promises the resonances will be affected by the background refractive index.

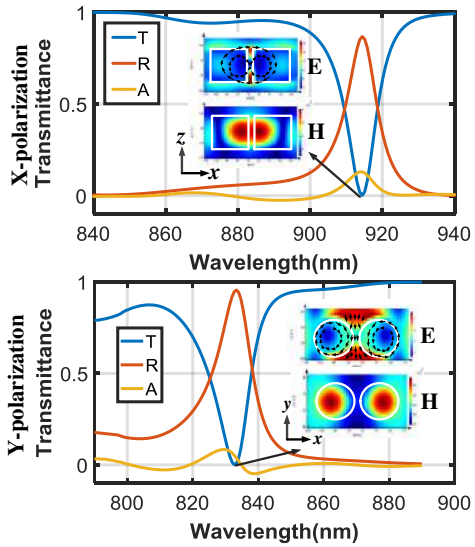


Figure 2: Transmittance (blue curve), reflectance (green curve) and absorption (red curve) spectra of silicon dimer arrays. (a) For the X-polarized incident light. Inset: The magnetic and electric field distributions of the magnetic dipole resonance at the dip wavelength for the X-polarized light. White lines indicate the substrate and particle position. (b) The same as (a) except for the Y-polarized incident light.

2.2. Refractive-index sensing

Then we discuss the sensitivity of the structure with Px= 600 nm and Py=340 nm for the Y-polarization. The background refractive index ranges from 1.40 to 1.45. Figure 4 shows that the dip position shifts to longer wavelengths with the refractive index increasing. The sensitivity attains 559 nm/RIU and the FOM is 52.8.

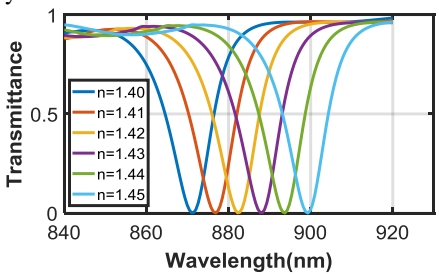


Figure 3: Transmittance spectra of the silicon dimer arrays for the different refractive index n=1.40, 1.41…1.45.

2.3. The influences of periods and polarizations

At last, we investigate the influences of the array periods and polarizations on the sensitivity of the sensor. Figure 4 presents that the sensitivity increases with the period along x axis for both polarizations. Moreover, the sensitivity for the Y-polarization increases much faster than that for the X-polarization. We can understand this from the field distributions in Insets of Fig.2. The electric field outside silicon cylinders for Y-polarization is much stronger than that for X-polarization. Therefore, the magnetic resonance for Y-polarization is much sensitive to the surrounding refractive index.

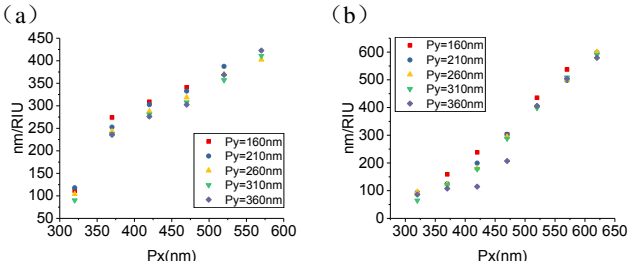


Figure 4: The sensitivities for different periods Px and Py. (a) For X-polarization incident light. (b) For Y-polarization incident light.

3. Conclusion

We have numerically investigated the spectrum features of the silicon dimer arrays. We obtained the sensitivity of 559 nm/RIU and FOM of 52.8. The larger period Px and Y-polarization incident light will benefit the sensitivity. Our structure provides a choice for biosensor and chemical sensor towards detecting the background21 refractive index variations besides traditional plasmonic resonance sensor.

Acknowledgements

This work was partially supported by National Key Research and Development Program of China (2017YFA0206002), Major National Scientific Instruments Developed Special Project (2013YQ1508290602), National Natural Science Foundation of China (NSFC) (61107032, 61275170), Research and Development of Major Research Equipment of Chinese Academy of Sciences (YZ201446) and Opening Project of Key Laboratory of Microelectronic Devices and Integrated Technology, Institute of Microelectronics of Chinese Academy of Sciences.

References

[1] A. I. Kuznetsov, A. E. Miroshnichenko, M. L. Brongersma, Y. S. Kivshar, B. Luk'yanchuk, Optically Resonant Dielectric Nanostructures. *Science* 6314: 2472, 2016.

[2] B. Luk'yanchuk, N. I. Zheludev, S. A. Maier, N. J. Halas, P. Nordlander, H. Giessen, C.-T. Chong, The Fano resonance in plasmonic nanostructures and metamaterials. *Nat. Mater*., 9: 707–715, 2010.

[3] J.-H. Yan, P. Liu, Z.-Y. Lin, H. Wang, H. J. Chen, C. X. Wang, G. W. Yang, Directional Fano Resonance in a Silicon Nanosphere Dimer *ACS Nano* 9: 2968–2980, 2015.

[4] E. Semouchkina, R. Duan, G. Semouchkin, R. Pandey, Sensing Based on Fano-Type Resonance Response of All-Dielectric Metamaterials. *Sensors*, 9344-9359, 2015.

[5] J.-H. Yan, P. Liu, Z.-Y. Lin, G.-W. Yang, New type high-index dielectric nanosensors based on the scattering intensity shift. *Nanoscale*, 8: 5996, 2016.

Negative permeability in magnetostatics: experimental realization and applications

Rosa Mach-Batlle, Albert Parra, Sergi Laut, Nuria Del-Valle, Carles Navau, and Alvaro Sanchez*

Departament de Física, Universitat Autonoma de Barcelona, 08193 Bellaterra, Barcelona, Catalonia, Spain
*corresponding author, E-mail: alvar.sanchez@uab.cat

Abstract

Negative permeability is presented as a useful novel tool to control magnetostatic fields. In a way analogous to the role that negative refraction has in optics, we show how negative permeability can yield new phenomena in magnetostatics. To overcome the fact that passive materials with static negative permeability do not exist we demonstrate how their effective behavior can be emulated by tailored sets of currents. The experimental realization of magnetic illusion is presented as an example of the possibilities opened by negative permeability in magnetostatics.

1. Introduction

New possibilities for controlling electromagnetic waves arise from the theoretical consideration and, later, experimental realization, of negative refraction [1, 2]. Negative values of either permeability μ or permittivity ε, or both (negative refraction index), have allowed, for example, perfect lenses [3]. These negative values are achieved by resonances in materials or metamaterials appearing at some frequency values, typically in the microwave region.

The control of static magnetic fields, essential in many technologies, is carried out by materials -and recently metamaterials [4]- involving positive values of μ. Actually, in the strict static limit, passive materials cannot have negative permeability, since they would violate fundamental magnetostatic laws [5].

We show here how the consideration of negative permeability in magnetostatics, as active materials, is not only possible from the point of view of the consistency of the magnetostatic theory, but it also brings new tools to control magnetic fields.

2. Negative permeability in magnetostatics

To demonstrate the feasibility of negative permeability in magnetostatics, we explore solutions of Maxwell magnetostatic equations assuming that such materials exist [5]. One of the new properties that arise when considering negative μ values is that at some particular negative values of μ all magnetic fields diverge. These values, which are analytically obtained, depend on the geometry - solid or hollow bodies, cylinders or spheres, for instance. Another interesting property is that negative μ values bring in new solutions for cloaking magnetic fields. For the example of hollow isotropic cylinders and spheres with negative μ, an extra solution for cloaking magnetic fields, apart from the trivial solution of no material, $\mu = 1$, appears from the equations.

3. Experimental demonstration of magnetic illusion

One of the most interesting new features that negative μ materials can provide is the realization of magnetic illusion. For electromagnetic waves, it was theoretically predicted [6] that the response of an object to impinging electromagnetic waves could be transformed into the response of a different object. After this work, some experimental demonstrations of illusion for waves were carried out, albeit in reduced schemes [7, 8, 9].

We present here the realization of magnetic illusion, which consists on transforming the magnetic signature of a 3D magnetic object into that of another object of different magnetic nature [10]. In our case, the response of a ferromagnetic ($\mu \to \infty$) sphere is transformed into that of a superconducting ($\mu \to 0$) one (as shown in Fig. 1a). Our theory provides the necessary (negative) value of μ that a spherical shell surrounding an actual ferromagnetic sphere should have in order to transform the overall response into that of a superconducting sphere. The required material with negative μ is effectively realized in practice by substituting it by its magnetization currents. In Fig. 1b we show the experimental setup: a ferromagnetic sphere is covered by a set of currents (in red) simulating the negative μ material, and both are immersed in a uniform magnetic field created by a pair of Helmholtz coils. The initial ferromagnetic response of the sphere only (blue points in Fig. 1c) is transformed into that of a superconducting sphere (red points in Fig. 1c). The agreement between analytic and experimental results (lines and symbols, respectively in Fig. 1c) is very good.

4. Conclusion

We have presented negative permeability materials in magnetostatics as a powerful new tool to control magnetic fields. Such materials can be realized in practice by tailored sets of electric currents. The experimental realization of the magnetic illusion of transforming the response of a

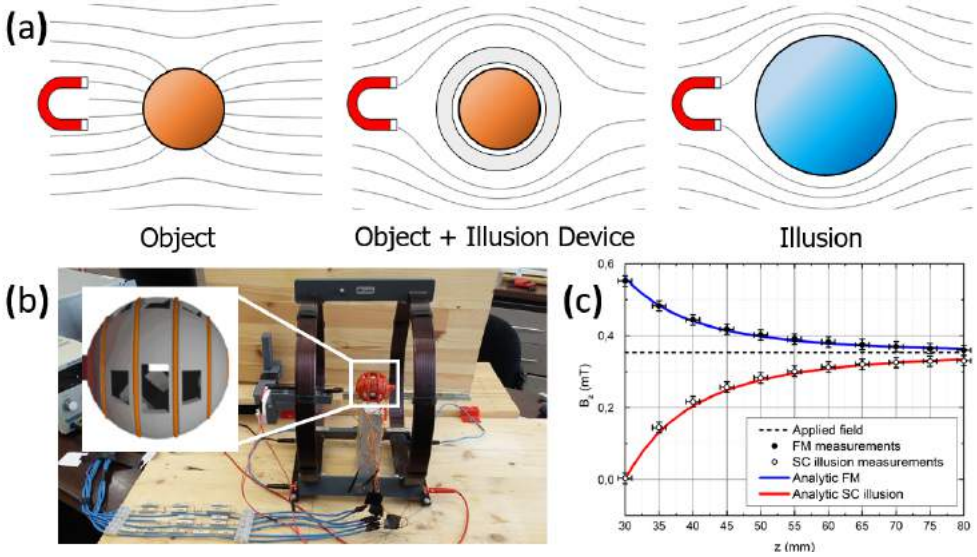


Figure 1: (a) Illusion of transforming a ferromagnetic material into a diamagnetic one. (b) Experimental setup for magnetic illusion. (c) Experimental (symbols) and analytic (solid lines) results for the magnetic response of the original object (FM) and the illusion (SC).

ferromagnet into that of its antagonistic, a superconductor, is presented as a striking example of the possibilities enabled by negative permeability.

Acknowledgement

We thank European Union Horizon 2020 Project FET-OPEN MaQSens (grant agreement 736943), and project MAT2016-79426-P (Agencia Estatal de Investigacion / Fondo Europeo de Desarrollo Regional) for financial support. A. S. acknowledges a grant from ICREA Academia, funded by the Generalitat de Catalunya.

References

[1] V. G. Veselago, The electrodynamics of substances with simultaneously negative values of ϵ and μ, *Sov. Phys.Usp.*, 10:509, 1968.

[2] J. B. Pendry, A. J. Holden, D. J. Robbins, and W. J. Stewart, Magnetism from conductors and enhanced nonlinear phenomena, *IEEE Trans. Microw. Theory Tech.*, 47:2075, 1999.

[3] J. B. Pendry, Negative refraction makes perfect lens, *Phys. Rev. Lett.*, 85:3966, 2000.

[4] B. Wood and and J. B. Pendry, Metamaterials at zero frequency, *J. Phys. Condens. Matter*, 19:076208, 2007.

[5] R. Mach-Batlle, A. Parra, J. Prat-Camps, S. Laut, C. Navau, and A. Sanchez, Negative permeability in magnetostatics and its experimental demonstration, *Phys. Rev. B.*, 96:094422, 2017.

[6] Y. Lai, J. Ng, H. Chen, D. Han, J. Xiao, Z.-Q. Zhang, and C. T. Chan, Illusion Optics: The Optical Transformation of an Object into Another Object, *Phys. Rev. Lett.*, 102:253902, 2009.

[7] C. Li, X. Meng, X. Liu, F. Li, G. Fang, H. Chen, and C. T. Chan, Experimental Realization of a Circuit-Based Broadband Illusion-Optics Analogue, *Phys. Rev. Lett.*, 105:233906, 2010.

[8] W. X. Jiang and T. J. Cui, Radar illusion via metamaterials, *Phys. Rev. E*, 83:026601, 2011.

[9] Q. Ma, Z. L. Mei, S. K. Zhu, T. Y. Jin, and T. J. Cui, Experiments on Active Cloaking and Illusion for Laplace Equation, *Phys. Rev. Lett.*, 111:173901, 2013.

[10] R. Mach-Batlle, A. Parra, S. Laut, N. Del-Valle, C. Navau, and A. Sanchez, Magnetic illusion: transforming a magnetic object into another object by negative permeability, to be published in *Phys. Rev. Appl.*, 2018.

Optoelectronic metasurfaces

Pierre Berini
School of Electrical Engineering and Computer Science, University of Ottawa, Canada
Centre for Research in Photonics, University of Ottawa, Canada
Department of Physics, University of Ottawa, Canada
corresponding author: berini@eecs.uottawa.ca

Abstract- Metasurfaces constructed from metal nanostructures can operate as efficient coupling structures for incident optical beams to surface plasmons. On a semiconductor, metallic metasurfaces can act simultaneously as a device electrode while ensuring strong plasmon field overlap with the active region. Additionally, plasmon fields can be confined to sub-wavelength dimensions and significantly enhanced relative to the exciting field. These features are very attractive for nanoscale optoelectronic device applications, such as photodetectors and modulators.

Metallic nanostructures, *e.g.*, antennas [1,2] and grating couplers [3-5] can operate efficiently as structures for coupling incident light to surface plasmon polaritons (SPPs) resonating or propagating thereon. Such nanostructures can act simultaneously as a device electrode on a semiconductor, while ensuring strong SPP field overlap with the active region. Furthermore, SPP fields can be confined to volumes that are deeply sub-wavelength in dimensions and can be significantly enhanced compared to the excitation.

Attributes such as these are very attractive for applications such as plasmonic optoelectronic devices, particularly, photodetectors [6-13] and modulators [14-17]. The involvement of SPPs results in altered trade-offs between responsivity and speed, or modulation and speed. This is because the deep sub-wavelength confinement of SPPs enables active regions to be scaled (down to nanoscale sizes) while maintaining compelling optoelectronic performance through SPP field enhancement.

In this paper we review progress on device concepts for SPP-enhanced photodetectors and modulators, particularly, recent proposals for photodetectors exhibiting very broad electrical bandwidths (THz) [8,9], photodetectors on Si that operate below the Si bandgap [12,13], high-speed reflection modulators operating as a MOS capacitor and exploiting the carrier refraction effect in Si under accumulation [15,16], and on plasmonic structures for the enhancement of high-harmonic generation [17].

REFERENCES

[1] Bharadwaj, P., Deutsch B., and Novotny, L., "Optical antennas," Adv. Opt. Photon. **1**, 438–483 (2009).
[2] Siadat Mousavi, S., Berini, P., and McNamara, D., "Periodic plasmonic nanoantennas in a piecewise homogeneous background," Opt. Express **20**, 18044-18065 (2012).
[3] Lévêque, G., and Martin, O. J. F., "Optimization of finite diffraction gratings for the excitation of surface plasmons," J. Appl. Phys. **100**, 124301 (2006).
[4] Radko, I. P., Bozhevolnyi, S. I., Brucoli, G., Martín-Moreno, L., García-Vidal, F. J., and Boltasseva, A., "Efficient unidirectional ridge excitation of surface plasmons," Opt. Express **17**, 7228–7232 (2009).
[5] Fong, N., Berini, P., and Tait, R. N., "Characterization of Grating-Coupled Long Range Surface Plasmon Polariton Membrane Waveguides," Opt. Express **23**, 17421-17430 (2015).
[6] Berini, P., "Surface Plasmon Photodetectors and their Applications," Lasers & Photonics Reviews **8**, 197-220 (2014).
[7] Brongersma, M. L., Halas, N. J., and Nordlander, P., "Plasmon-induced hot carrier science and technology," Nature Nanotechnol. **10**, 25–34 (2015).
[8] Siadat Mousavi, S., Stöhr A., and Berini, P., "Plasmonic photodetector with terahertz electrical bandwidth," Appl. Phys. Lett. **104**, 143112 (2014).
[9] Siadat Mousavi, S., Stöhr, A., and Berini, P., "Ultra-fast Surface Plasmon III-V Photodetectors Based on Nanomonopoles," J. Lightw. Technol. **34**, 4682-4687 (2016).
[10] Knight, M. W., Sobhani, H., Nordlander, P., and Halas, N. J., "Photodetection with active optical antennas," Science **332**, 702–704 (2011).
[11] Goykhman, I., Desiatov, B., Khurgin, J., Shappir, J., and Levy, U., "Waveguide based compact silicon Schottky photodetector with enhanced responsivity in the telecom spectral band," Opt. Express **20**, 28594–28602 (2012).
[12] Othman, N., and Berini, P., "Nanoscale Schottky contact surface plasmon point detectors for optical beam scanning applications," Appl. Opt. **56**, 3329-3334 (2017).

[13] Alavirad, M., Olivieri, A., Roy, L., and Berini, P., "High-responsivity sub-bandgap hot-hole plasmonic Schottky detectors," Opt. Express **24**, 22544-22554 (2016).
[14] Dionne, J. A., Diest, K., Sweatlock, L. A., and Atwater, H. A., "A metal–oxide–Si field effect plasmonic modulator," Nano Lett. **9**, 897-902 (2009).
[15] Hassan, S., Lisicka-Skrzek, E., Olivieri, A., Tait, R. N., and Berini, P., "Fabrication of a plasmonic modulator incorporating an overlaid grating coupler," Nanotechnology **25**, 495202 (2014).
[16] Olivieri, A., Chen, C., Hassan, S., Lisicka-Skrzek, E., Tait, R. N., and Berini, P., "Plasmonic Nanostructured Metal−Oxide−Semiconductor Reflection Modulators," Nano Lett. **15**, 2304-2311 (2015).
[17] Vampa, G., Ghamsari, B. G., Siadat Mousavi, S., Hammond, T. J., Olivieri, A., Lisicka-Skrek, E., Yu Naumov, A., Villeneuve, D. M., Staudte, A., Berini, P., Corkum, P. B. "Plasmon-enhanced high-harmonic generation from silicon," Nat. Phys. **13**, 659-662 (2017).

Fiber drawn metamaterials: from guidance to sub-resolution imaging, spanning from IR to THz

Alessio Stefani[1,2,*], Simon C. Fleming[1], and Boris T. Kuhlmey[1]

[1]Institute of Photonics and Optical Science (IPOS), School of Physics, The University of Sydney, NSW 2006, Australia
[2]DTU Fotonik, Department of Photonics Engineering, Technical University of Denmark, 2800, Kgs. Lyngby, Denmark
*corresponding author, E-mail: alessio.stefani@sydney.edu.au

Abstract

Fiber drawing is used to realize extended and scalable metamaterials. Such metamaterials are used for light guidance and sub-resolution imaging. The scalability of the process allows fabrication of structures sized for frequencies between the THz and the IR.

1. Introduction

The ability to co-process different materials at the same time in a thermal process opens up the possibility of realizing metamaterials in large sizes and volumes. In particular, we have exploited the fiber drawing technique combined with the Taylor wire method to realize large volumes of microstructured metal-dielectric composites [1]. The structures produced are invariant in one direction and therefore lead to wire array and slotted cylinders array metamaterials. Such metamaterials are used for guiding radiation in hollow structures [1-3] and to realize hyperlenses for sub-resolution imaging [4-8]. The nature of the fiber drawing process allows us to easily scale the structures with features from hundreds of microns to hundreds of nanometers, allowing operation from the THz to the IR [9]. Moreover, by carefully choosing the dielectric, we are able to fabricate deformable structures allowing tunability of the metamaterial properties [10].

We present approaches to single mode TM [3] and low loss THz waveguides [1], hyperlenses that can focus radiation to 1/176 of the wavelength [5] and can operate across three orders of magnitude in wavelength [9], metamaterials that can be used to excite high spatial frequencies [8] and metamaterials the permeability of which can be tuned more than 50% [10].

Acknowledgements

This work was supported by the Marie Sklodowska-Curie grant of the European Union's Horizon 2020 research and innovation programme (708860). The work was supported in part by Australian Research Council (ARC) Discovery Projects DP140104116 and DP170103537. This work was performed in part at the Optofab node of the Australian National Fabrication Facility (ANFF), using NCIRS and NSW State Government funding.

References

[1] S. Atakaramians, A. Stefani, H. Li, Md. S. Habib, J. G. Hayashi, A. Tuniz, X. Tang, J. Anthony, R. Lwin, A. Argyros, S. C. Fleming, B. T. Kuhlmey., "Fiber-Drawn Metamaterial for THz Waveguiding and Imaging," J. Infrared, Millimeter, Terahertz Waves, vol. 38, no. 9, pp. 1162–1178, 2017.

[2] X. Tang, B. T. Kuhlmey, A. Stefani, A. Tuniz, S. C. Fleming, and A. Argyros, "Electromagnetic Wave Propagation Through Air-Core Waveguide with Metamaterial Cladding," J. Light. Technol., vol. 34, no. 22, pp. 5317–5324, 2016.

[3] H. Li, S. Atakaramians, R. Lwin, X. Tang, Z. Yu, A. Argyros, B. T. Kuhlmey, "Flexible single-mode hollow-core terahertz fiber with metamaterial cladding," Optica, vol. 3, no. 9, pp. 941–947, 2016.

[4] A. Tuniz, K. J. Kaltenecker, B. M. Fischer, M. Walther, S. C. Fleming, A. Argyros, B. T. Kuhlmey, "Metamaterial fibres for subdiffraction imaging and focusing at terahertz frequencies over optically long distances," Nat. Commun., vol. 4, pp. 2706, 2013.

[5] J. G. Hayashi, R. Lwin, A. Argyros, S. Fleming, B. T. Kuhlmey, A. Stefani, "Extreme sub-diffraction focusing of THz radiation with magnifying metamaterial hyperlenses," The 3rd Australia New Zealand Conference on Optics and Photonics (ANZCOP), Paper 37, 2017.

[6] A. Stefani, J. G. Hayashi, S. Fleming, A. Argyros, B. T. Kuhlmey, "Split-ring resonators hyperlens for undistorted sub-wavelength imaging," in *2017 European Conference on Lasers and Electro-Optics and European Quantum Electronics Conference*, (Optical Society of America, 2017), paper EH_P_22.

[7] Md. S. Habib, A. Stefani, S. Atakaramians, S. C. Fleming, A. Argyros, B. T. Kuhlmey, "A prism based magnifying hyperlens with broad-band imaging," Appl. Phys. Lett., vol. 110, no. 10, pp. 101106, 2017.

[8] Md. S. Habib, "Sub-diffraction Imaging with Wire Array Metamaterial Fibres: Novel Geometries and Mitigation of Artefacts," PhD Thesis, The University of Sydney.

[9] J. G. Hayashi, “Wire array Infrared Metamaterial Fibers: Fabrication and Applications” PhD Thesis, The University of Sydney, http://hdl.handle.net/2123/17790.

[10] S. Fleming, A. Stefani, X. Tang, A. Argyros, D. Kemsley, J. Cordi, R. Lwin, “Tunable metamaterials fabricated by fiber drawing,” J. Opt. Soc. Am. B, vol. 34, no. 7, p. D81, 2017.

Anisotropic Gain/Loss Metasurface for Directive Surface Plasmon-Polaritons Propagation

Dmitry A. Kuzmin[1,2,*], Igor V. Bychkov[1,2], Vladimir G. Shavrov[3] and Vasily V. Temnov[4,5]

[1]South Ural State University (National Research University), 76 Lenin Prospekt, Chelyabinsk 454080, Russian Federation
[2]Chelyabinsk State University, Br. Kashirinykh Street 129, 454001 Chelyabinsk, Russian Federation
[3]Kotelnikov Institute of Radio-engeneering and Electronics of RAS, 11/7 Mokhovaya Str., Moscow 125009, Russian Federation
[4]Institut des Molécules et Matériaux du Mans, CNRS UMR 6283, Université du Maine, 72085 Le Mans cedex, France
[5]Groupe d'Etude de la Matiere Condensée (GEMaC), Université de Versailles-Saint Quentin en Yvelines, CNRS UMR 8635, Université Paris-Sacley, 45 avenue des Etats-Unis, 78035 Versailles Cedex, France
*corresponding author, E-mail: kuzminda@csu.ru

Abstract

In this work we propose new concept of directive surface plasmon propagation in gain-loss metasurfaces. We show analytically the possibility of propagation of surface plasmon-polaritons, which have a hyperbolic isofrequency contour, along an anisotropic metasurface with gain in one direction and loss in the orthogonal one. We propose the simple realization of such a metasurface based on array of gain and loss stripes.

1. Introduction

Nowadays, hyperbolic plasmonics attracts researchers' attention by its exciting optical properties [1-4]. Hyperbolic metasurfaces (HMTSs) support highly localized low-loss surface plasmon-polaritons (SPPs), providing drastic increase of the light-matter interactions near the surface. Moreover, HMTSs allow the very effective manipulation by SPPs varying from routing them towards specific directions within the sheet, dispersion-free propagation (canalization), and to the negative refraction.

The usual realization of HMTSs is constructing the surface which behaves as a dielectric in one direction and as a metal in the orthogonal one. Here, we propose the new class of HMTSs based on the gain-loss metasurface consisting of the array of gain and loss stripes.

2. Results

Let us consider an anisotropic metasurface with the diagonal conductivity tensor

$$\hat{\sigma} = \begin{pmatrix} \sigma_{xx} & 0 \\ 0 & \sigma_{yy} \end{pmatrix}. \quad (1)$$

SPPs propagating along such a metasurface have the following dispersion relation [4]:

$$\left(q_x^2 - k_0^2\right)\sigma_{xx} + (q_y^2 - k_0^2)\sigma_{yy} = 2i\gamma\omega\left(\varepsilon_0 + \mu_0\sigma_{xx}\sigma_{yy}/4\right), \quad (2)$$

where $\gamma^2 = q_x^2 + q_y^2 - k_0^2$, $k_0 = \omega/c$. Let us suppose that conductivity is mainly real with small (but non-zero) imaginary part $\sigma_{ii} = \mathrm{Re}[\sigma_{ii}] + i\mathrm{Im}[\sigma_{ii}]$, $\mathrm{Im}[\sigma_{ii}] \ll \mathrm{Re}[\sigma_{ii}]$. This means that gain/loss plays a crucial role in the electrodynamical behavior of the surface. We will also looking for a well localized SPPs with $q_x, q_y \gg k_0$. In the linear approximation with respect to $\mathrm{Im}[\sigma_{ii}]$ one may calculate

$$\begin{aligned} &\mathrm{Re}\left[\sigma_{xx}\right]q_x^2 + \mathrm{Re}\left[\sigma_{yy}\right]q_y^2 \\ &= -\gamma\omega\mu_0\left\{\mathrm{Re}[\sigma_{xx}]\mathrm{Im}[\sigma_{yy}] + \mathrm{Re}[\sigma_{yy}]\mathrm{Im}[\sigma_{xx}]\right\}/2 \end{aligned} \quad (3)$$

It's easy to see, that if $\mathrm{Re}[\sigma_{xx}]\mathrm{Re}[\sigma_{yy}] < 0$, and the right-hand-side of the Eq. (2) is positive, the isofrequency contour will form a hyperbola. Assuming the x-axis to be a gain axis (i.e. $\mathrm{Re}[\sigma_{xx}] = -|\mathrm{Re}[\sigma_{xx}]| < 0$), the gain should satisfy to the relation $|\mathrm{Re}[\sigma_{xx}]| > \mathrm{Re}[\sigma_{yy}]\mathrm{Im}[\sigma_{xx}]/\mathrm{Im}[\sigma_{yy}]$, which means that constructing the metasurface with high anisotropy $\mathrm{Im}[\sigma_{xx}]/\mathrm{Im}[\sigma_{yy}] \ll 1$ may allow to achieve a hyperbolic SPPs even at relatively low gain.

3. Discussion

Let us discuss some possible practical realization of the gain-loss metasurface supporting hyperbolic SPPs. We will consider an array of gain and loss stripes with the conductivities σ_g and σ_l and stripe width W_g and W_l (see Fig. 1a for detailes). Using an effective medium approach which is valid for $\lambda_{SPP} \gg W_g + W_l$, one may calculate an effective conductivities of the surface $\sigma_{xx} = \sigma_g\sigma_l(W_g+W_l)/(W_l\sigma_g + W_g\sigma_l)$ and $\sigma_{yy} = (\sigma_g W_g + \sigma_l W_l)/(W_g + W_l)$. When $\sigma_g\sigma_l < 0$ and $\sigma_g > -\sigma_l W_g/W_l$ the metasurface will satisfy the abovementioned conditions and propagation of the hyperbolic SPPs is possible (see Fig. 1b). We should note that hyperbolic surface plasmon-polaritons supported by the metasurface propagate along hyperbolae's asymptotes without attenuation (see Fig. 1c).

A lot of 2D conductive materials at the frequencies above the resonant intraband transition may be used for the loss stripes. For example, graphene at the frequencies of visible

range which are higher that $2E_F/h$ (E_F is a Fermi energy, h is Plank's constant) has a conductivity σ_{gr} with $\mathrm{Re}[\sigma_{gr}] >> \mathrm{Im}[\sigma_{gr}]$ [5,6] and even small gain between the graphene stripes will lead to the hyperbolic regime of the metasurface.

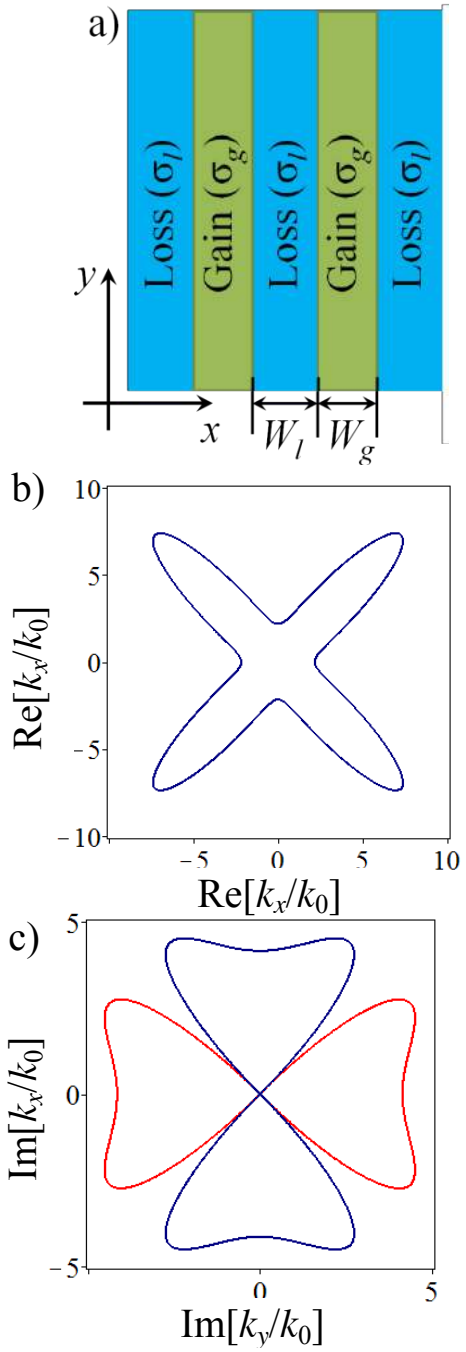


Figure 1: Scheme of the anisotropic gain-loss metasurface (a). Isofrequency contour (b) and attenuation (c) of the gain-loss metasurface calculated for the conductivities σ_{xx} = -0.001+0.0005 S and σ_{yy} = 0.001+0.0005 S. Blue and red curves in (c) correspond to $\mathrm{Im}[k] > 0$ (attenuation) and $\mathrm{Im}[k] > 0$ (amplification), respectively.

4. Conclusions

We have shown that the metasurface constructed from the loss and gain stripes may support highly directive surface plasmon-polaritons propagation. Such surface plasmon-polaritons have a hyperbolic isofrequency contour. For practical realization of such a metasurface at the visible light frequencies graphene is a good candidate for obtain desired low loss, while some optically active elements (such as quantum dots, for example) arranged into the stripes near graphene may induce the gain in the structure.

The effects proposed here may be useful for numerous plasmonic applications ranging from plasmon manipulation for flatland optics to directive spaser design.

Acknowledgements

The work was financially supported in part by RFBR (16-07-00751, 16-29-14045, 17-57-150001), RScF (14-22-00279), Grant of the President of the RF (MK-1653.2017.2), Act 211 Government of the Russian Federation (contract № 02.A03.21.0011), Stratégie internationale NNN-Telecom de la Région Pays de La Loire, PRC CNRS-RFBR "Acousto-magneto-plasmonics".

References

[1] J. S. Gomez-Diaz, M. Tymchenko, A. Alù, Hyperbolic plasmons and topological transitions over uniaxial metasurfaces, *Phys. Rev. Lett.* 114: 233901, 2015.

[2] J. S. Gomez-Diaz, M. Tymchenko, A. Alù, Hyperbolic metasurfaces: surface plasmons, light-matter interactions, and physical implementation using graphene strips, *Optical Materials Express* 5: 2313-2329, 2015.

[3] J. S. Gomez-Diaz, A. Alù, Flatland Optics with Hyperbolic Metasurfaces, *ACS Photonics* 3: 2211–2224, 2016.

[4] A. Nemilentsau, T. Low, G. Hanson, Anisotropic 2D materials for tunable hyperbolic plasmonics, *Phys. Rev. Lett.* 116: 066804, 2016.

[5] G. W. Hanson, Dyadic Green's functions and guided surface waves for a surface conductivity model of graphene, *Journal of Applied Physics* 103: 064302, 2008.

[6] L. A. Falkovsky, A. A. Varlamov, Space-time dispersion of graphene conductivity, *The European Physical Journal B* 56: 281–284, 2007.

Attojoule Modulators for Photonic Neuromorphic Computing

Rubab Amin[1], Jonathan George[1], Jacob Khurgin[2], Tarek El-Ghazawi[1], Paul R. Prucnal[3], Volker J. Sorger[1,*]

[1]Department of Electrical and Computer Engineering, George Washington University, Washington, DC 20052, USA
[2]Department of Electrical and Computer Engineering, Johns Hopkins University, Baltimore, Maryland 21218, USA
[3]Department of Electrical Engineering, Princeton University, Princeton, New Jersey, 08544, USA
*Author email address: sorger@gwu.edu

Abstract

We show how the nonlinear transfer function of electrooptic modulators enables vector matrix multiplications of photonic neural networks. Here the modulators energy-per-bit function and signal-to-noise ratio are critical factors impacting system performance.

1. Introduction

Neuromorphic networks are computational algorithms and network models inspired by signal processing in the brain with societal-relevant applications in machine-learning such as speech and image recognition, non-linear optimization, and real-time simulation [1]. Recent progress by both industry and academia has demonstrated compute efficiencies surpassing the digital efficiency wall set by von-Neuman compute architectures (**Fig. 1a**). An artificial neural network consists of a set of input artificial neurons connected to both the hidden- and the output layer. Within each layer, information propagates by a linear combination such as matrix multiplication followed by the application of a nonlinear activation function **(Fig. 1b)**. Optical neural network (ONN) implementations offer unique advantages over microelectronics because the linear transformation (e.g. matrix multiplication) can be executed in the optically with temporal response times <10ps.

2. Nanophotonic Perceptrons

Here we discuss how the nonlinear activation function can be mapped onto the transfer function of an electro-optic modulator. Then, given a bit-resolution of the ONN, the question then becomes how to optimize the transfer function to minimize the systems energy overhead, and maximize the computational speed. Here the former is given by the multiply and accumulate (MAC)-per-joule metric, while the latter by the MAC-per-second-area (Fig. 1a).

We borrow the neuron model of the perceptron, which is a non-spiking analogue processor depicted schematically in Figure 1b. For our analysis, we start with a simplified network by just considering two stages, namely the signal summation (i.e. balanced photodetector), and the nonlinearity (i.e. electro-optic modulator). It is straightforward to see that the systems energy consumption is reduced when the E/bit of the modulator is reduced.

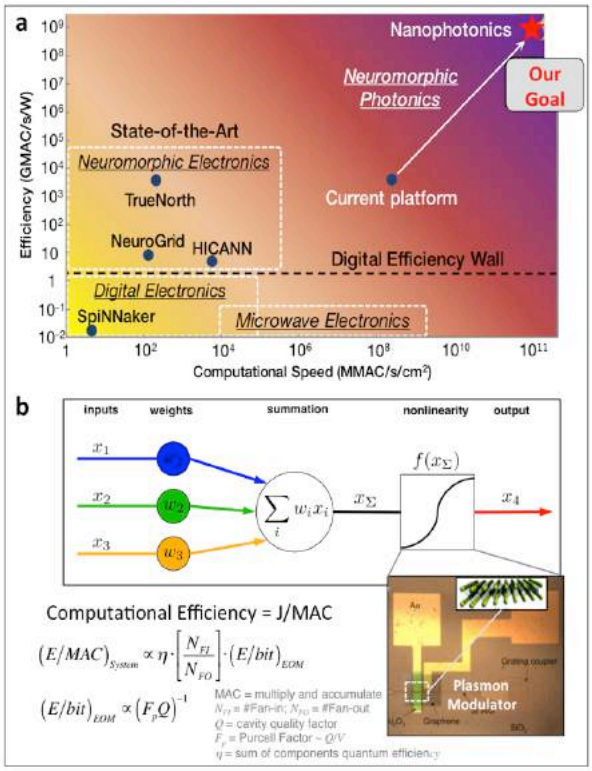


Figure 1. **a**, Performance vectors for compute systems. Neuromorphic (= brain inspired) systems break the digital efficiency wall set by CMOS and von-Neuman architectures [1]. **b**, Model of an optical perceptron neuron inside a artificial neural network. The nonlinear activation function is provided by the transfer function of the plasmonic electrooptic modulator. The computational system efficiency scales with the modulator efficiency, which in turn scales inversely with device the physical volume, *V*, and material broadening [1,2]. Our plasmon modulators are micrometer-compact consuming 100's aJ [3,4].

3. Discussion

In order to understand a modulators energy consumption, we show scaling vectors for this (nano)photonic-based perceptron neurons model, and share our recent demonstrations of plasmonic attojoule per bit efficient modulators on a silicon photonics platform (**Fig. 1b**) [2].

The modulator's efficiency scales inversely with the physical device volume, V, and underlying cavity quality Q-factor, thus inversely with the Purcell factor, F_p. Thus, increasing the weak light-matter-interaction and using Graphene's Pauli blocking mechanism, we demonstrated a modulator with a record-high performance (1 dB/V-μm) while being micrometer compact [3,4].

Secondly, we discuss how the shape of the modulator's transfer function helps to improve the ONN node's signal-to-noise ratio (SNR); in brief, the transfer function can be represented by a Sigmoid function, (i.e. S-like curve). Here the slope-difference (i.e. derivative) between the two saturation parts and the nonlinear steep raise enables to improve the SNR at each node. However, making the input noise (voltage from the detector) too sharp would also result in reduced bit resolution. Thus this simple single-node network of detector input gating a modulator has an optimized operating point given a certain transfer function and bit-density of the system. Detailed results will be shared in the talk. However, a SNR clean-up at each node of the ONN enables for higher cascadability of the network, and thus a higher complexity-density.

4. Conclusions

In conclusion, we show how the transfer function of an electro-optic modulator can provide the nonlinear activation function in optical neural networks. The shape of this transfer function directly impacts not only the modulators performance, but more importantly the networks energy-per-MAC and cascadability.

Acknowledgements

V.S. and T.E. are supported by NSF and SCR under the E2CDA program.

References

[1] P. B. Prucnal, B. J. Shastri, Neuromorphic Photonics ***CRC Press*** (2017).

[2] K. Liu, S. Sun, A. Majumdar, V. J. Sorger, Fundamental Scaling Laws in Nanophotonics ***Sci. Rep.*** 6, 37419 (2016).

[3] R. Amin, C. Suer, Z. Ma, J. Khurgin, R. Agarwal, V. J. Sorger, Active Material, Optical Mode and Cavity Impact on electro-optic Modulation Performance, ***Nanophotonics*** (2017).

[4] V. J. Sorger, R. Amin, J. B. Khurgin, et al. Scaling Vectors for Attojoule per Bit Modulators ***J. Opt.*** (2017).

Optical rotation effects in nanostructured materials

Thierry Verbiest*, Tom Swusten, Ward Brullot

Department of chemistry, University of Leuven, Leuven, Belgium
*corresponding author, E-mail: Thierry.verbiest@fys.kuleuven.be

Abstract

We will discuss optical rotation effects that we have observed in (chiral) nanostructured materials composed of Au and Fe_3O_4 nanoparticles.

1. Introduction

Hybrid nanomaterials that combine different functionalities are currently of great interest. We recently developed a self-assembly method to prepare multi-layered nanostructures composed of Ag, Au and Fe_3O_4 nanoparticles that are linked together by organic molecules. Such structures combine plasmonic and (superpara)magnetic properties and they can show unusual optical properties that cannot be observed in classical materials [1,2,3].

2. Results

We are particularly interested in nonreciprocal optical effects such as Faraday rotation. In this case an external magnetic field is used to induce optical rotation. The optical rotation angle is given by $\theta = VBL$ with V the Verdet constant, B the external magnetic field and L the path length. The effect is non-reciprocal since the optical rotation adds up when the light travels back and forth through the sample. Faraday rotation has been applied in optical isolators and magnetic field sensors.

In our experiments we used a hybrid material composed of alternating layers of gold nanoparticles (10 nm diameter) and iron oxide nanoparticles (8 nm diameter). Faraday rotation spectra (Fig. 1) of this hybrid material show a linear increase in Faraday rotation with layer thickness (or number of layers). Furthermore we calculated the maximum Verdet constant to be on the order of 10^7 °/Tm which is among the highest ever observed. The reason for this extremely strong Faraday rotation is the presence of the superparamagnetic iron oxide and the plasmonic enhancement due to gold.

Faraday rotation is not the only interesting optical rotation effect that can be observed. Upon doping the the hybrid structures with chiral molecules an extremely high natural optical rotation is observed, on the order of 1000 °/mm. Interestingly, in addition to natural optical rotation (which is reciprocal) we also observed a nonreciprocal optical rotation component that is of the same order of magnitude as the natural optical rotation. We speculate that the origin of the nonreciprocal natural optical rotation is the existence of strong quadrupolar interactions in the material.

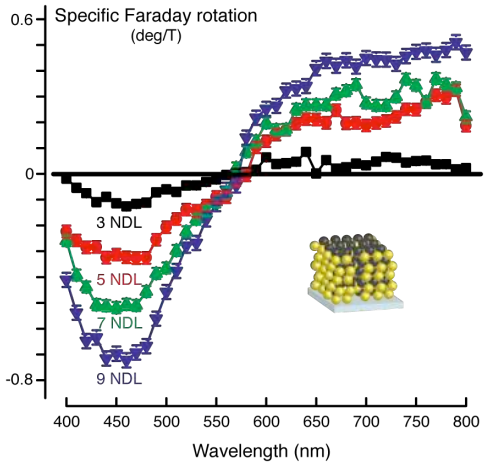


Figure 1: Specific Faraday rotation *vs* wavelength for different sample thicknesses. NDL refers to a nanoparticles double layer, ie 1 layer of gold nanoparticles and 1 layer of iron oxide nanoparticles. The inset is a graphical representation of the sample composed of layers of gold and iron oxide nanoparticles.

References

[1] Brullot W., Swusten T., Verbiest T., Broadband Nonreciprocal Quadrupolarization-Induced Asymmetric Transmission (Q-AT) in Plasmonic Nanoparticle Aggregates., *Advanced Materials* 27, art.nr. adma.201405409, 2015.

[2] Brullot W, Strobbe R, Bynens M, Bloemen M, Demeyer PJ, Vanderlinden W, De Feyter S, Valev VK, Verbiest T, Layer-by-layer synthesis and tunable optical properties of hybrid magnetic-plasmonic nanocomposites using short bifunctional molecular linkers, *Materials Letters,* **118**, 99-102, 2014.

[3] Brullot W, Vanbel MK, Swusten T, Verbiest T, Resolving enantiomers using the optical angular momentum of twisted light, *Science Advances*, **2**, e1501349, 2016.

Dispersion-tailored metalenses and their applications

Wei Ting Chen[1,*], Alexander Y. Zhu[1], Jared Sisler[1,2] and Federico Capasso[1]

[1]Harvard John A. Paulson School of Engineering and Applied Sciences, Harvard University, Cambridge, Massachusetts 02138, USA
[2]University of Waterloo, Waterloo, ON N2L 3G1, Canada
*corresponding author, E-mail: weitingchen@seas.harvard.edu

Abstract

Metalenses are planar lenses comprised of sub-wavelength spaced nanostructures that have been demonstrated with many promising applications. However, the control of their dispersion over a large bandwidth has been a challenge. Here, we show that it is possible to realize metalenses with tailored dispersion, including achromatic metalenses over almost the entire visible bandwidth from wavelength 470 to 670 nm. In addition, applications related to these dispersion-engineered metalenses will be introduced.

1. Introduction

Conventional refractive optical components such as prisms and lenses are mainly manufactured by glass polishing techniques and impart their phases via volumetric propagation of light. As a result, these traditional optical components have considerable bulk, weight and are time-consuming to manufacture for realizing high precision. This greatly limits their applications, particularly in portable systems and conformal/wearable devices.

In recent years, metasurfaces consisting of subwavelength structures have been demonstrated to be a versatile platform for modulating the phase of an incident wavefront from 0 to 2π radians. This enables many compact optical devices, such as lenses [1], spectro-polarimeters [2] and axicons [3]. However, controlling the dispersion of these metasurface-enabled devices remains a challenge. Some related works have addressed this challenge by alternately using multiple coupled resonances to tailor phase profiles at several discrete frequencies [4] and engineering the dispersion [5-7]. Here, we adopt a fundamentally distinct approach of engineering higher order derivatives of phase as a function of frequency [8]. By tailoring the group delay (first order derivative of phase with respect to frequency) and group delay dispersion (second order derivative) while simultaneously and independently varying the phase mask from 0 to 2π, one can precisely control the dispersion of a metasurface in transmission across a large bandwidth in the visible. As a proof of concept, we demonstrate an achromatic metalens with numerical aperture NA = 0.2 at 530 nm capable of focusing white light. We also demonstrate achromatic imaging over 200 nm bandwidth using a metalens.

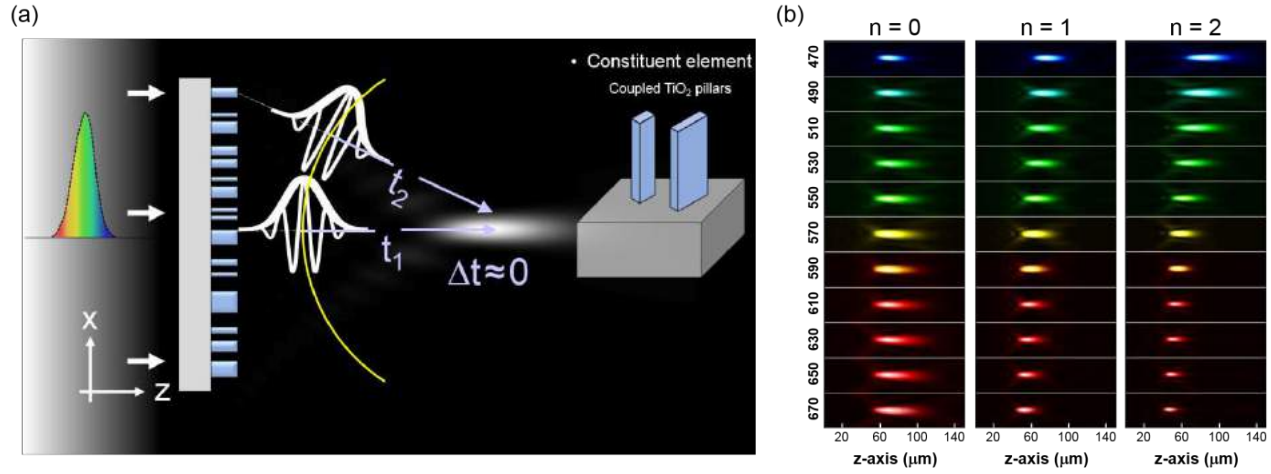


Figure 1: Metalenses with various dispersion. (a) Schematic diagram for illustrating achromatic focusing. The inset shows a constituent element of achromatic metalens. (b) Experimental results of point spread functions for metalenses. The case of $n = 0$ corresponds to achromatic metalens, while $n = 2$ shows larger chromatic focal length shift compared to that of $n = 1$. The case of n = 1 has a focal length shift similar to conventional Fresnel lenses and is referred as diffractive metalenses.

2. Results and Discussion

Figure 1(a) illustrates the principle of how to focus broadband light. The achromatic metalens needs to impart a frequency-dependent phase profile:

$$\varphi(r,\omega) = -\frac{\omega}{c}(\sqrt{r^2+F^2} - F) \quad (1)$$

where r and F are radial coordinate and focal length, respectively. The group delay (first order derivative of Eq. 1) shows that a metalens element (shown in the inset of Fig. 1(a)) placed at a given position r needs to slow a wavepacket by a given value. In addition, the group delay dispersion (second order derivative of Eq. 1) ensures the outgoing wavepackets from different metalens elements are identical. The net effect is the minimization of the spread in the arrival times of wavepackets at the focus to ensure they constructively interfere. We place two 600-nm-height TiO_2 nanofins in close proximity (60 nm apart) to have more degrees of freedom for controlling group delay and group delay dispersion. The focal length F in Eq. 1 can be generalized as $F(\omega) = k\omega^n$, where k is a positive constant and n is a real number. A metalens with n = 1 possesses a focal length shift similar to Fresnel/diffractive lenses and is referred to as a diffractive metalens hereinafter. By satisfying the required group delay and group delay dispersion of different n values, one can control metalens focal length shift from achromatic to chromatic. In Fig. 1(b), we show three metalenses of different focal length shifts. These metalenses are designed at wavelength λ = 530 nm with a numerical aperture of 0.2 and a diameter of approximately 25 μm. In the case of n = 0, the focal length is maintained almost a constant, showing achromatic focusing, while in n = 1 and n = 2, the focal spot positions change with wavelength.

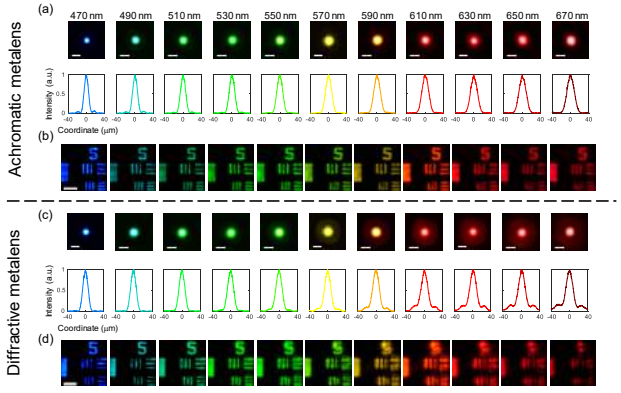


Figure 2: A comparison for the measured focal spot profiles and images of the USAF resolution target using achromatic and diffractive metalenses.

We also fabricated larger sized diffractive and achromatic metalenses (NA = 0.02, diameter = 220 μm) and compared their imaging quality. Their respective focal spot profiles are shown in Fig. 2(a) and 2(c). Figure 2(b) and 2(d) show the images of a standard USAF resolution target obtained from the achromatic and diffractive metalenses, respectively, under various laser illumination wavelengths with a bandwidth of 40 nm. The test target was fixed at the focal plane corresponding to illumination at λ = 470 nm. We observe that the images from the diffractive metalens become significantly blurred due to chromatic aberration for wavelengths beyond 550 nm. In comparison, the images from the achromatic metalens are well focused. Note that a slight decrease of contrast in the images at red wavelengths is because the feature size of the target (~ 15 μm) is close to the diffraction limit of the achromatic metalens.

3. Conclusions

By simultaneously controlling the phase, group delay and group delay dispersion of an incident wavefront, we have demonstrated dispersion-tailored metalenses in transmission configuration over a large continuous bandwidth in the visible region. We have shown an achromatic planar metalens (NA = 0.2) capable of focusing light to the diffraction-limit from 470 to 670 nm, and an achromatic metalens (NA = 0.02) for white light imaging. The fabrication process is based on lithography instead of grinding and polishing in conventional lens manufacturing. This can enable mass-producible high-end optics. Our tailorable metalens can find numerous applications across industry and scientific research, such as in lithography, microscopy, endoscopy and virtual/augmented reality.

Acknowledgements

This work was supported by the Air Force Office of Scientific Research (MURI, grant no. FA9550-14-1-0389 and grant no. FA9550-16-1-0156). This work was performed in part at Harvard CNS, which is supported by the National Science Foundation under NSF award no. 1541959.

References

[1] W. T. Chen, A. Y. Zhu, M. Khorasaninejad, Z. Shi, V. Sanjeev, and F. Capasso, "Immersion Meta-Lenses at Visible Wavelengths for Nanoscale Imaging," *Nano Lett.* **17**, 3188-3194 (2017).

[2] W. T. Chen, P. Török, M. Foreman, C. Y. Liao, W.-Y. Tsai, P. R. Wu, and D. P. Tsai, "Integrated plasmonic metasurfaces for spectropolarimetry," *Nanotechnology* **27**, 224002 (2016).

[3] W. T. Chen, M. Khorasaninejad, A. Y. Zhu, J. Oh, R. C. Devlin, A. Zaidi, and F. Capasso, "Generation of wavelength-independent subwavelength Bessel beams using metasurfaces," *Light Sci. Appl.* **6**, e16259 (2017).

[4] F. Aieta, M. A. Kats, P. Genevet, and F. Capasso, "Multiwavelength achromatic metasurfaces by dispersive phase compensation," *Science* **347**, 1342-1345 (2015).

[5] Y. Li, X. Li, M. Pu, Z. Zhao, X. Ma, Y. Wang, and X. Luo, "Achromatic flat optical components via compensation between structure and material dispersions," *Sci. Rep.* **6**, 19885 (2016).

[6] E. Arbabi, A. Arbabi, S. M. Kamali, Y. Horie, and A. Faraon, "Controlling the sign of chromatic dispersion in diffractive optics with dielectric metasurfaces," *Optica* **4**, 625-632 (2017).

[7] S. Wang, et al., "A broadband achromatic metalens in the visible," *Nat. Nanotechnol.* (2018).

[8] W. T. Chen, A. Y. Zhu, V. Sanjeev, M. Khorasaninejad, Z. Shi, E. Lee, and F. Capasso, "A broadband achromatic metalens for focusing and imaging in the visible," *Nat. Nanotechnol.* (2018).

Raman imaging and tip-enhanced Raman scattering for epitaxial graphene grown on SiC

Yasutaka Kitahama[1], Shohei Uemura[1], Sanpon Vantasin[1], Yoshito Tanaka[1], Toshiaki Suzuki[2], Yasunori Kutsuma[1], Daichi Doujima[1], Tadaaki Kaneko[1], Yukihiro Ozaki[1]

[1]School of Science and Technology, Kwansei Gakuin University, Sanda, Hyogo, Japan
[2]UNISOKU Co. Ltd., Hirakata, Osaka, Japan
*corresponding author, E-mail: kitahama@kwansei.ac.jp

Abstract

Epitaxial graphene grown on 4H-SiC was measured by Raman imaging and tip-enhanced Raman scattering (TERS). On a ridge-like nanostructure of the graphene on the C-face, G' band in the TERS spectrum was shifted via different strain and doping between the ridge and the plain. D band was observed on the edge of the graphene on the Si-face, while it disappears on that on the C-face. The reason is a combination between C and SiC on the C-face.

1. Introduction

Graphene is an interesting material with unique useful properties. In particular, epitaxial graphene grown on SiC provides large sheet with low defect on the substrate, which is a hard, transparent, and electrical insulator. Therefore, it can be applied to electronic circuits without substrate transfer processes. The epitaxial graphene grown on either face of SiC have different properties; the graphene on the C(000$\bar{1}$)- and Si(0001)-face attaches weakly and strongly to the SiC substrate, respectively. On the graphene on the C-face, nanosctructures, which can affect band gap, electron mobility, and internal strain, are formed [1,2].

From graphene sheet, prominent Raman bands are observed such as G, D, and G' (2D) band. They can provide various information such as the number of layers, strain, doping, defects in terms of the peak-shift, the bandwidth, and the intensity ratio. Moreover, Raman imaging can visualize the distribution of the number of layers, strain, doping, and defects. However, the spatial resolution of Raman imaging is limited by the diffraction of light.

Tip-enhanced Raman scattering (TERS) spectrum is measured by a scanning probe microscope (SPM) whose probe is a sharp noble metal tip combined with a Raman microscope. At the apex of the tip, electromagnetic field is enhanced by surface plasmon resonance, and then highly sensitive Raman spectrum can be observed. Moreover, morphological and Raman spectral imaging with high spatial resolution can be observed by the sharp tip. In this study, the nanostructure and edge on the epitaxial graphene grown on 4H-SiC were measured by Raman imaging and TERS.

2. Experiments

The epitaxial graphene was prepared by annealing 4H-SiC in ultrahigh vacuum at 1800 °C for 15 min using semiclosed TaC containers. The sublimation of Si from SiC was regulated by an adjustment of Si vapor pressure inside the container, resulting in precise control of graphene growth rate, number of layers, and domain size. The synthesis details have been written in our previous paper [1–3].

Raman measurement was performed by a reflection mode Raman microscope (Photon design, Nanostar NFRSM800). The sample was excited using a diode-pumped solid-state laser (Cobolt, Fandango; λ = 514 nm), which was focused by an objective lens with a long working distance (90×, NA 0.71). The Raman signal was collected through the same objective lens. The spatial resolution of the Raman measurement was evaluate to be 500 nm. The resolution of the motorized stage for the Raman imaging was 200 nm in both X and Y direction [3–5].

TERS measurement was performed by an atomic force microscope (AFM) setup combined with the reflection mode Raman microscope. An etched bulk silver tip (made by UNISOKU) was attached to a quartz tuning fork on a shear-force-based AFM at an angle of 30–45º from the sample plane and was controlled in non-contact mode [3–5]. The apex of the tip is 50–75 nm in diameter, which corresponds to the spatial resolution of the TERS measurement.

3. Results and Discussion

In the TERS spectra from the ridge nanostructure, the G' (2D) bands and their bandwidths were shifted to lower wavenumber and became broader than those in the Raman spectra. From the plane of the graphene, the band-shift and broadening were not observed. The band-shift originates from different strain on the graphene [5]. The epitaxial graphene on SiC is compressed by a difference in a coefficient of thermal expansion [5]. On the ridge nanostructure, the situation is similar to free-standing graphene, and then the G' (2D) band from the ridge

nanostructure appears at the similar wavenumber to that of the free-standing graphene [6]. The band-shift was observed even in the case of that the direction of strain was perpendicular to the long axis of the tip. TERS shows strong polarization dependence; namely, TERS signal is enhanced by excitation with the parallel polarization to the tip [7]. Therefore, the band-shift can be hardly explained only by the strain.

From the Raman imaging for the epitaxial graphene, Ramanshifts of the G' (2D) bands are plotted against those of the G bands as shown in Figure 1. It suggests a free strain on graphene that the distribution shows gently sloped line, while the steeply sloped line indicates a neutral charge on graphene [8]. In the present case, the distribution in Figure 1 is in the shape of a rhombus; namely, this epitaxial graphene is influenced by both charge, which is influenced by doping, and strain.

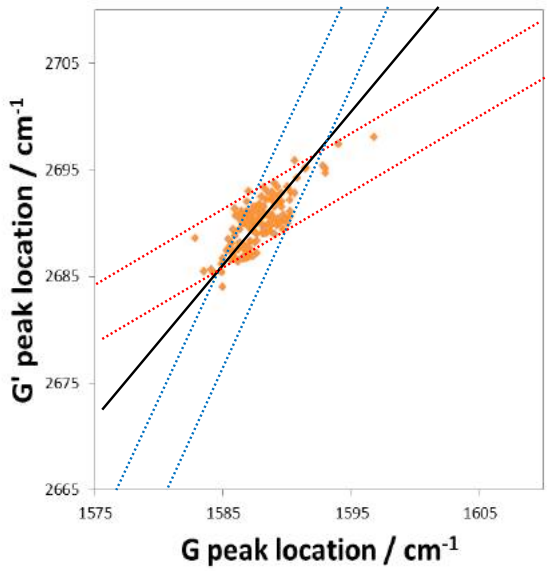


Figure 1: G' (2D) and G band positions observed from the epitaxial graphene grown on 4H-SiC.

On the edge of graphene where C atoms are arranged as armchair, D band appears [9]. Indeed, the D band was observed from our epitaxial graphene on the Si-face. By the TERS measurement, it was confirmed that the D band originates from the edge rather than the defect. However, the D band was not observed from our epitaxial graphene on the C-face, while edges of epitaxial graphene island show an armchair-edge configuration [10]. On the edge of our epitaxial graphene on the C-face, the C atoms may be combined with the SiC, then the chirality disappears, and thus the D band is not observed.

4. Conclusions

Raman imaging and TERS were used for analysis of the epitaxial graphene grown on 4H-SiC. The shift of the G' band in the TERS spectrum suggests the different strain and doping between the ridge and the plain. The disappearance of the D band on the edge of the graphene on the C(000$\bar{1}$)-face indicates the combination of SiC and C atoms.

Acknowledgements

This work was supported by an A-STEP (Grant No. AS2525017J) from the Japan Science and Technology Agency (JST).

References

[1] S. Ushio, A. Yoshii, N. Tamai, N. Ohtani, T. Kaneko, Epitaxial graphene growth on 4H-SiC(0001) with precisely controlled step- terrace surface by high temperature annealing above 2000 °C in UHV, *Phys. Status Solidi C* 8: 580–582, 2011.

[2] S. Ushio, Y. Kutsuma, A. Yoshii, N. Tamai, N. Ohtani, T. Kaneko, 4H-SiC(0001) Basal Plane Stability during the Growth of Epitaxial Graphene on Inverted-Mesa Structures, *Jpn. J. Appl. Phys*. 50: 70104, 2011.

[3] T. Suzuki, T. Itoh, S. Vantasin, S. Minami, Y. Kutsuma, K. Ashida, T. Kaneko, Y. Morisawa, T. Miura, Y. Ozaki, Tip-enhanced Raman spectroscopic measurement of stress change in the local domain of epitaxial graphene on the carbon face of 4H-SiC (000$\bar{1}$), *Phys. Chem. Chem. Phys.* 16: 20236–20240, 2014

[4] S. Vantasin, I. Tanabe, Y. Tanaka, T. Itoh, T. Suzuki, Y. Kutsuma, K. Ashida, T. Kaneko, Y. Ozaki, Tip-Enhanced Raman Scattering of the Local Nanostructure of Epitaxial Graphene Grown on 4H-SiC(000$\bar{1}$), *J. Phys. Chem. C* 118: 25809–25815, 2014.

[5] S. Vantasin, Y. Tanaka, S. Uemura, T. Suzuki, Y. Kutsuma, D. Doujima, T. Kaneko, Y. Ozaki, Characterization of SiC-grown epitaxial graphene microislands using tip-enhanced Raman spectroscopy, *Phys. Chem. Chem. Phys.* 17: 28993–28999, 2015.

[6] S. Berciaud, S. Ryu, L. E. Brus, T. F. Heinz, Probing the Intrinsic Properties of Exfoliated Graphene: Raman Spectroscopy of Free-Standing Monolayers, *Nano Lett.* 9: 346–352, 2009

[7] Y. Kitahama, S. Uemura, R. Katayama, T. Suzuki, T. Itoh, Y. Ozaki, Polarization dependence of tip-enhanced Raman and plasmon-resonance Rayleigh scattering spectra, *Appl. Phys. Lett.* 110: 233104, 2017

[8] J. E. Lee, G. Ahn, J. Shim, Y. S. Lee, S. Ryu, Optical separation of mechanical strain from charge doping in graphene, *Nat. Commun.* 3: 1024, 2012

[9] Y. M. You, Z. H. Ni, T. Yu, Z. X. Shen, Edge chirality determination of graphene by Raman spectroscopy, *Appl. Phys. Lett.* 93: 163112, 2008

[10] G. M. Rutter, N. P. Guisinger, J. N. Crain, P. N. First, J. A. Stroscio, Edge structure of epitaxial graphene islands, *Phys. Rev. B* 81: 245408, 2010

NEW TYPE OF SWITCHING CELL BASED ON OPTICAL METAMATERIAL AND OPTICALLY TRANSPARENT FERRITE

K.Vytovtov [1], E.Barabanova [1], S.Zouhdi [2]

[1] *Astrakhan State Technical University, Astrakhan, Russia, vytovtov_konstan@mail.ru*
[2] *Paris-Sud University, Orsay, France, said.zouhdi@centralesupelec.fr*

***Abstract*. In this work we offer the brand new type of switching cell with four inputs and four outputs. The operation principle is based on spatial deviation of the optical beam due to a change in the magnetic permeability of the transparent ferrite garnet. Additional the spatial diversity of the rays is achieved through the use of metamaterial.**

Keywords: switching cell, photonic crystal, metamaterial, optically transparent ferrite film.

Introduction

Fiber-optic communication lines are possible to transmit information flows at the speed of several tens and even hundreds of terabits per a second. However today, the bandwidth of the most productive switch matrixes does not exceed several hundred Gbit/s [1,2]. At the same time, electronic switchers with low speed and large sizes are most often used today. They do not allow us processing large amounts of data and do not have prospects for further development. While all-optical switches are promising devices in large data processing systems [2]. They have significant advantages such as high speed, smaller geometric dimensions, lower power consumption, lower losses, etc. In this regard the problem of developing all-optical switching systems with high speed for processing large amounts of data is relevant for the design of optical communication systems and it has a great practical importance.

Note that the existing optical cells have two inputs and two outputs. As the results large switching systems is multistage with a large number of cascades. The two-stage optical switching system has been proposed for the first time [3]. It has 256 inputs and 256 outputs and it can be used to process large amounts of data. The system contains 16x16 switching blocks based on the 4x4 all-optical sells.

Here we present the new type of the 4x4-switching cell for the developed system. The cell includes the control optically transparent ferrite films and the metamaterial layers that allow us to increase the spatial diversity of the outputs and therefore to reduce cross-talk and intermodulation noise. It also has been offered the input optical integrated device contains the optical transformer and multiplexer.

Structure and operation principle of the switching sell

The switching cell is based on the two-dimensional photonic crystal of complex shape with the layers of the optically transparent ferromagnet film [4] and the layers including both the optical metamaterial with a negative refractive index [5] and the usual dielectric. In the general case, any material in which the Kerr or Pockels effect is observed must be used.

In the considered case, the cell is the four-layer structure (Fig.1a). The layers I and IV are the optically transparent ferrite ($Fe_9Co_5Al_{19}F_{67}$) [4], the layers II, V, VII are the metamaterial ones, the layers III, VI, VIII are the ordinary dielectric ones, IX are the matching dielectric layers. The arrows show the possible transmission ways of the information signal. Control of the direction of the information signal in this case is carried out by a magnetic field created by external applied voltages U_1 and U_2. The material parameters of each of the dielectric layers and metamaterial layers must be different and provide the necessary spatial diversity of the information signal.

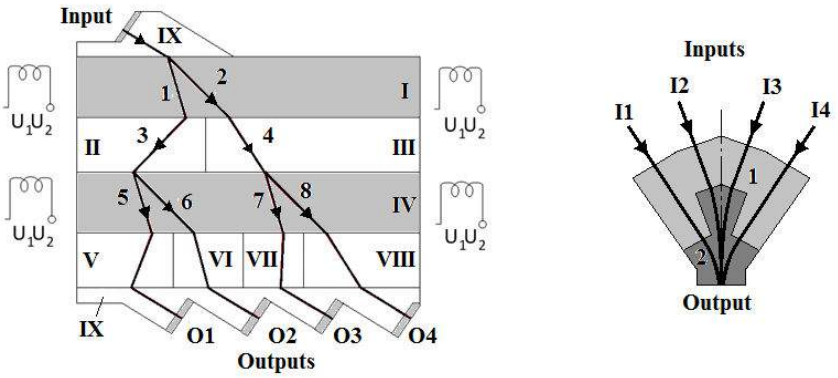
The operation principle of the cell is based on the Kerr effect for anisotropic material and the effect of negative refraction angle in metamaterials.

If there is a voltage U_1 on the coil of the layer I, it has a refractive index n_1 the beam passes in the direction 1 due to the nonlinear Kerr effect, and in the presence of the voltage U_2, it has a refractive index n_2 and the beam passes in the direction 2. The nonlinear dependence of the refractive index on the electric field allows to increase the spatial diversity of the rays. However, for real materials, the separation of rays 1 and 2 is still insignificant at low layer thicknesses, which makes practical use of such a commutation method difficult [patent]. First of all, the limitation is connected with the diameter of the output optical fiber (the diameter of the core is about 100 nm) and with the mutual penetration of signals into the adjacent channel.

The optical integrated device (Fig.1b) includes the optical transformer and multiplexer of the four input information signals. This device is the inhomogeneous optical structure with complex geometry based on dielectric isotropic materials. The layer 1 is a matching and it serves to reduce losses, the layer 2 is an inhomogeneous isotropic and it serves to multiplex four input beams.

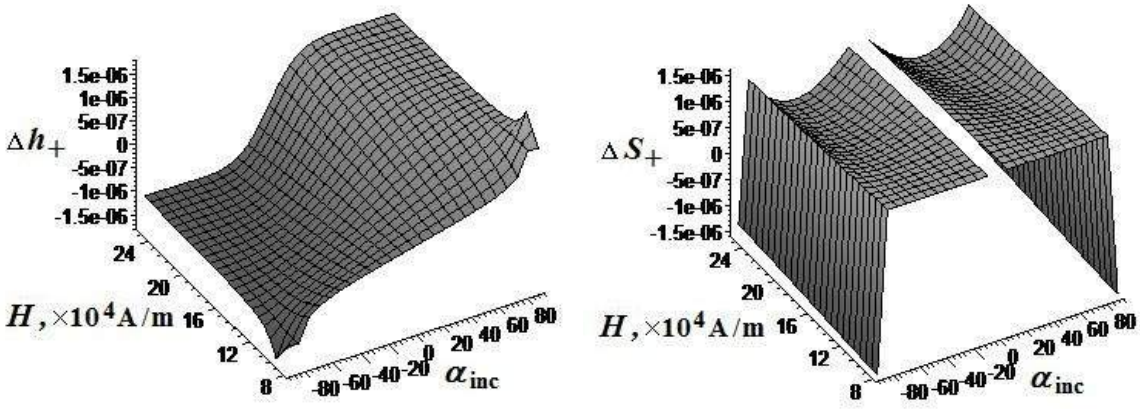
The dependence of the wave front shift for one micrometer of the ferrite layer thickness on the incidence angle and the magnetic field strength is presented in Fig.2a. The dependence of the Poyting vector shift for one micrometer of the ferrite layer thickness on the incidence angle and the magnetic field strength is shown in Fig.2b. The calculations

are carried out for wavelength 1550 nm. It is seen that there is the linear dependence of the Poyting vector shift on the magnetic field strength for α_{inc} from 10° to 60°.



a) b)

Fig.1. Structure of the switching cell (a); and the input device containing optical transformer and the multiplier (b)



a) b)

Fig.2. The dependences on an incidence angle and magnetic field: a) wave front the displacement; b) the ray power

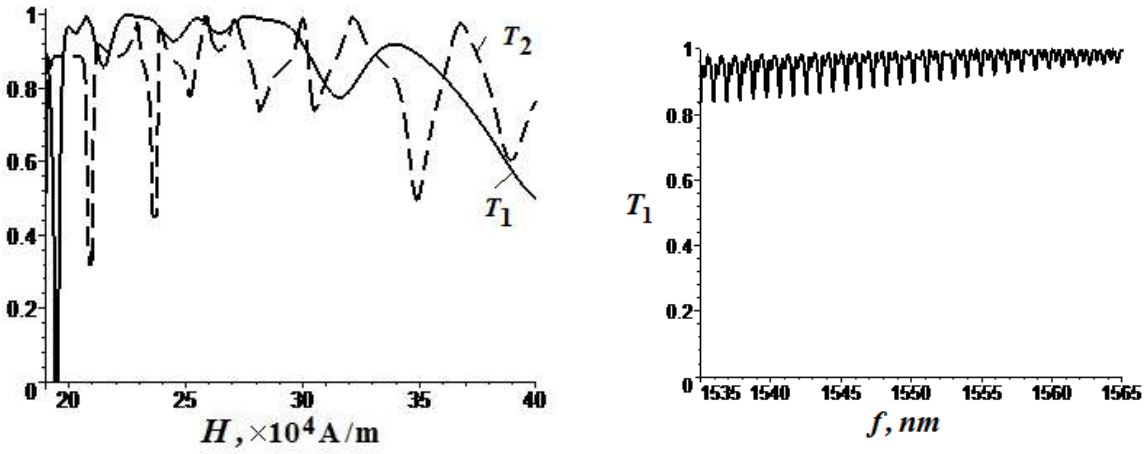
Additionally we study the dependence of the transmission coefficient of the structure on the external magnetic field (Fig.3a) and frequency (Fig. 3b).

For calculation we used well-known translation matrix method [6,7].The method is accurate analytical and it is applicable to solving the given problem without any restrictions on the frequency and thickness of the layers. However, it does not allow us to take into account the influence of the boundaries between metamaterial and isotropic material.

The results of the calculations show that the presented structure can be effectively used for the production of switching cells. The thickness of ferrite film is $d_{ferrite} = 10\mu m$, the thickness of the isotropic and metamaterial layers are $d_{isotropic} = 1mm$, the permittivity's of the isotropic and metamaterial layers are $\varepsilon = 5$ and $\varepsilon = -2$. The incidence angle is chosen $\alpha_{inc} = 20°$. The structure gives us the displacement about $200\mu m$.

Conclussions

In this work we offer the 4x4 switching cell based on the photon crystal containing the optical transparent layers and the layers with the metamaterial and the usual isotropic material. The proposed geometry allows us to increase the spatial diversity of the information beams up to the double diameter of the core of the fiber optic cable. The developed cell, in turn, makes it possible to create 256x256 two-stage switching systems [3] instead of existing multi-stage ones.



a) b)

Fig.3. The dependences of the transmission coefficients a) on the magnetic field; b) on the frequency

References

1. Z. Chai, X.Hu, F. Wang, X. Niu, J. Xie, Q. Gong, Ultrafast all-optical switching, Rev. paper, Advanced Advanced Optical Materials , 2017 21P.
2. El Bawab, Optical switching, Springer Science and Business inc. 2006, 451P.
3.Patent №2017128161/28 (7.08.17) (In Russian)
4. Nobukiyo Kobayashi, Hiroshi Masumoto, Saburo Takahashi, Sadamichi Maekawa, Optically Transparent Ferromagnetic Nanogranular Films with Tunable Transmittance, *Scientific Reports* V 6, Article number: 34227 (2016), doi:10.1038/srep34227
5. Zhi Hao Jiang, Seokho Yun, Lan Lin, Jeremy A. Bossard, Douglas H. Werner, Theresa S. Mayer, Tailoring Dispersion for Broadband Low-loss Optical Metamaterials Using Deep-subwavelength Inclusions *Scientific Reports* V 3, Article number: 1571 (2013),doi:10.1038/srep01571
6. S. Teitler and B. W. Henvis, Refraction in Stratified, Anisotropic Media, *JOSA A*,V.60 (6), pp. 830-834 (1970)
7. K. Vytovtov Analytical investigation of stratified isotropic media *JOSA A*, V. 22 (4), pp.689-696 (2005)

Metasurface Pulse Shaping

Shawn Divitt[1,2], **Wenqi Zhu**[1,2], **Cheng Zhang**[1,2], **Henri J. Lezec**[1], **Amit Agrawal**[1,2]

[1] *Center for Nanoscale Science and Technology, National Institute of Standards and Technology, 100 Bureau Dr., Gaithersburg, MD 20899, USA*

[2] *Institute for Research in Electronics and Applied Physics, University of Maryland, College Park, MD 20742, USA*
amit.agrawal@nist.gov

Abstract: Optical pulse shaping is an integral part of ultrafast optical technology and serves to compliment pulse generation and characterization methods. In general, changing the shape of an optical pulse requires a change in the amplitude and/or phase of its spectral components. Metasurfaces provide extremely fine spatial control over the amplitude and phase of incident light and are natural candidates for use in optical pulse shaping. Here, we demonstrate shaping of $<$15 femtosecond ultrafast laser pulses using a silicon-metasurface acting as both spectral amplitude and phase mask.

Recently, dielectric metasurfaces have emerged as a powerful technology for arbitrary control over the amplitude, phase, or polarization of light in a single, compact optical element [1,2]. Here, we offer the first experimental demonstration of femtosecond pulse shaping using a centimeter-scale metasurface composed of an array of polycrystalline silicon pillars acting as both amplitude and phase modulation mask. Masks of this type offer a lower cost, larger size, higher resolution, high diffraction efficiency and high damage threshold method for controlling ultrafast pulses.

In our experiments, light is angularly dispersed by a grating, focused onto the metasurface mask by a parabolic mirror, and recombined by a second mirror and grating to form the shaped pulse. The characteristics of the shaped pulse are measured using the SPIDER technique [3]. The metasurface masks are composed of an array of 600 nm tall rectangular silicon pillars resting on a fused-silica substrate. The cross-section of each pillar is chosen via an optimization algorithm to achieve the designed spectral phase shift while maintaining a large transmittance. The pillars provide a phase depth of 2π radians such that phase wrapping is necessary to impart the given phase function.

In this talk, we will discuss our recent results in design, fabrication and testing of an optical pulse shaper that uses a metasurface for spectral amplitude and phase modulation. Precision metasurfaces offer a new route toward previously unrealizable applications in optical pulse shaping.

References

1. N. Yu and F. Capasso, "Flat optics with designer metasurfaces," Nat. Mater. **13**, 139–150 (2014).
2. A. Arbabi, Y. Horie, M. Bagheri, and A. Faraon, "Dielectric metasurfaces for complete control of phase and polarization with subwavelength spatial resolution and high transmission," Nat. Nanotechnol. **10**, 937–943 (2015).
3. C. Iaconis and I. A. Walmsley, "Spectral phase interferometry for direct electric-field reconstruction of ultrashort optical pulses," Opt. Lett. **23**, 792–794 (1998).

Hybrid Graphene Metasurface for High-Speed Mid-Infrared Light Modulation and Single-Pixel Imaging

Beibei Zeng[1], Zhiqin Huang[2], Akhilesh Singh[3], Yu Yao[4], Abul K. Azad[1], Aditya D. Mohite[3], Antoinette J. Taylor[5], David R. Smith[2], and Hou-Tong Chen[1*]

[1] Center for Integrated Nanotechnologies, Los Alamos National Laboratory, Los Alamos, USA
[2] Department of Electrical and Computer Engineering, Duke University, Durham, USA
[3] MPA-11, Los Alamos National Laboratory, Los Alamos, USA
[4] School of Electrical, Computer and Energy Engineering, Arizona State University, Tempe, USA
[5] Chemistry, Life, and Earth Sciences Directorate, Los Alamos National Laboratory, Los Alamos, USA
*corresponding author, E-mail: chenht@lanl.gov

Abstract

By leveraging graphene and metasurfaces we demonstrate a high-performance free space mid-infrared modulator operating at gigahertz speeds, low gate voltage and room temperature. We further pixelize the hybrid graphene metasurface to form a prototype spatial light modulator for high frame-rate single-pixel imaging, suggesting orders of magnitude improvement over conventional liquid crystal or micro-mirrors based spatial light modulators. This work opens up the possibility of exploring wavefront engineering for infrared technologies where fast temporal and spatial modulations are indispensable.

1. Introduction

Free space infrared light modulation is essential for many applications but its development remains to be elusive. Prevailing methods reported so far have suffered from drawbacks particularly in the modulation depth and speed. In this context, active metamaterials/metasurfaces composed of planar subwavelength resonators and reconfigurable functional materials have provided an alternative approach [1, 2]. In contrast to conventional semiconductors which provide very limited tunability at mid-infrared wavelengths, graphene has demonstrated exceptional electrical and optical properties and widely tunable electro-optical response through the entire infrared region [3, 4]. Recently, hybrid graphene metasurfaces have shown unprecedented capabilities in developing electrically reconfigurable infrared optoelectronic devices [5, 7, 9], although in these designs the modulation relies on high voltage bias and the modulation speed is limited, and many works have been focusing on a waveguide configuration. Here we show the experimental demonstration of hybrid graphene metasurface free space mid-infrared modulators that enable a large intensity modulation depth up to 90% and a high modulation speed exceeding 1 GHz over a broad bandwidth by applying only a low voltage bias. Furthermore, a prototype mid-infrared spatial light modulator is demonstrated to function as an electrically encoded aperture or mask, realizing single-pixel imaging with a high frame-rate.

2. Results

Figure 1(a) illustrates the device schematic of our hybrid graphene metasurface modulator operating in reflection mode, which is based on a modified metamaterial perfect absorber design. It consists of a 150 nm thick e-beam evaporated Au ground plane, a 400 nm thick e-beam evaporated amorphous silicon (a-Si) with 1 nm thick Ti adhesion layer, a 6 nm thick ultrathin Al_2O_3 gate dielectric grown by atomic layer deposition (ALD), a top electrode defined using standard photolithographic methods followed by e-beam deposition of a 750 nm thick Al_2O_3 insulating layer and 3 nm/30 nm Ti/Au layers and a lift-off process, a transferred monolayer graphene grown by low-pressure chemical vapor deposition (LPCVD), and an array of 150 nm thick 'I'-shaped Au nano-antennas with 5 nm thick Ti adhesion layer fabricated using standard e-beam lithography methods, metal deposition, and a lift-off process, with a scanning electron microscopy (SEM) image shown in Fig. 1(b).

In Fig. 1(c) we plot the measured reflection spectra when applying different gate voltages. They all show a deep reflection dip that suggests high absorption as the transmission is zero. Upon applying the gate voltage bias, the resonance shifts from $\lambda = 7.3\,\mu$m (reflection minimum $\sim$16%) to $8.3\,\mu$m (reflection minimum $\sim$5%) when the low gate voltage changes from $+7\,$V to $-3\,$V. The corresponding change of reflection $\Delta R(\lambda) = R_{+7\,V}(\lambda) - R_{-3\,V}(\lambda)$, and modulation depth $M = |\Delta R(\lambda)|/\max[R_{+7\,V}(\lambda), R_{-3\,V}(\lambda)]$ are plotted in Fig. 1(d) as functions of wavelength, revealing the maximum reflection change of 46.7% (from 53.1% at $+7\,$V to 6.4% at $-3\,V$) at $\lambda = 8.5\,\mu$m and a modulation depth as high as $\sim$90% in this wavelength range. In addition to the high modulation depth, the hybrid graphene metasurface modulator enables ultra-high modulation speed, with measured modulation signal not showing any significant decay up to 1 GHz. We further pixelize the hybrid graphene metasurface to form a prototype 6×6 spatial light modulator, and successfully demonstrate its single-pixel imaging capability.

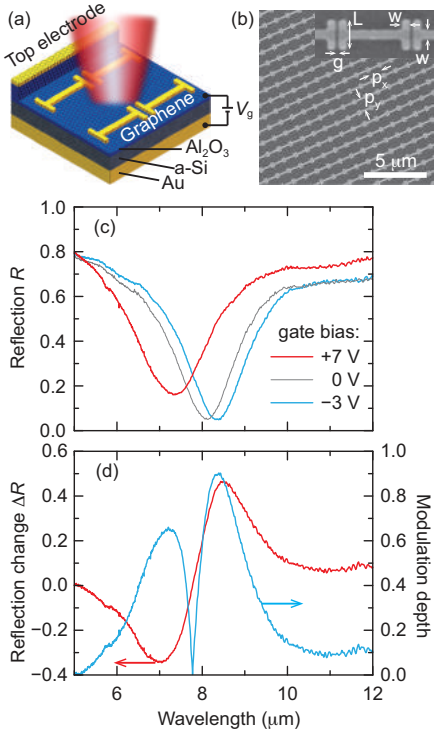


Figure 1: (a) Schematic of the hybrid graphene metasurface mid-infrared modulator. (b) Top-view SEM image of the fabricated device. (c) Reflection spectra under different gate voltage biases. (d) The corresponding change of reflection and modulation depth.

3. Discussion

The metamaterial absorber can be considered as a subwavelength cavity formed between the nano-antenna array and the ground plane, where the dispersion of nano-antenna resonant response results in a phase condition so that the multireflection experiences destructive interference, leading to the cancellation of the overall reflection and inducing high absorption over a narrow wavelength range [10]. That is, the incident light is trapped within the metamaterial cavity and eventually absorbed by either the metallic structure or the lossy dielectric spacer, or both. As the optical loss of a-Si is negligible in the mid-infrared region, the absorption then mainly occurs by ohmic dissipation at the metallic resonator array integrated with graphene. These two facts give rise to the possibility of tuning the resonant dispersion of the nano-antenna array thereby the absorption frequency at a different wavelength, through tuning the conductivity of the integrated graphene by applying a gate voltage. On the other hand, the semiconducting a-Si serves as part of the gate electrode, and the ultrathin Al_2O_3 gate dielectric results in the low gate voltage to tune the graphene conductivity. Together with the low-voltage operation, the thick dielectric layer under the top electrode reduces significantly the parasitic capacitance, allowing for the high-speed modulation which is promising for high frame-rate single-pixel imaging when forming a spatial light modulator.

4. Conclusions

In conclusion, we have demonstrated a hybrid graphene metasurface modulator for free space mid-infrared light based on a tunable metamaterial absorber design. Upon a gate voltage to tune the graphene conductivity, the room temperature device achieves high modulation depth up to 90% and modulation speed exceeding 1 GHz, which is the fastest free space mid-infrared modulator to the best of our knowledge. Our device design enables the low-voltage and high-speed operation, which is promising for mid-infrared spatial light modulator and its use for single-pixel imaging with orders of magnitude faster than using traditional liquid crystal and micro-mirror spatial light modulators.

Acknowledgement

We acknowledge support in part from the Los Alamos National Laboratory LDRD Program. This work was performed, in part, at the Center for Integrated Nanotechnologies, a U.S. Department of Energy, Office of Basic Energy Sciences Nanoscale Science Research Center operated jointly by Los Alamos and Sandia National Laboratories. Los Alamos National Laboratory, an affirmative action/equal opportunity employer, is operated by Los Alamos National Security, LLC, for the National Nuclear Security Administration of the U.S. Department of Energy under Contract No. DEAC52-06NA25396.

References

[1] H.-T. Chen, A. J. Taylor, N. Yu, A review of metasurfaces: Physics and applications, *Rep. Prog. Phys.* 79: 076401, 2016.

[2] H.-T. Chen *et al.*, Active terahertz metamaterial devices, *Nature* 444: 597–600, 2006.

[3] F. Wang *et al.*, Gate-variable optical transitions in graphene, *Science* 320: 206–209, 2008.

[4] M. Liu *et al.*, A graphene-based broadband optical modulator, *Nature* 474: 64–67, 2011.

[5] S. H. Lee *et al.*, Switching terahertz waves with gate-controlled active graphene metamaterials, *Nature Mater.* 11: 936–941, 2012.

[7] Y. Yao *et al.*, Electrically tunable metasurface perfect absorbers for ultrathin mid-infrared optical modulators, *Nano Lett.* 14: 6526–6532, 2014.

[9] K. Fan, J. Y. Suen, W. J. Padilla, Graphene metamaterial spatial light modulator for infrared single pixel imaging, *Opt. Express* 25: 25318–25325, 2017.

[10] H.-T. Chen, Interference theory of metamaterial perfect absorbers, *Opt. Express* 20: 7165–7172, 2012.

Power generation from thermal radiation: Photon-assisted tunneling in a metasurface-coupled rectifier

Paul S. Davids[1*], Joshua Shank[1], Andrew Starbuck[1], Robert L. Jarecki[1], and David Peters[1]

[1]Sandia National Laboratories, Albuquerque, New Mexico, USA
*corresponding author, E-mail: pdavids@sandia.gov

Abstract

Electrical power generation from a thermal source is demonstrated using a large-area metasurface-coupled tunnel diode rectifier. Transverse electric field confinement in the tunnel gap due to epsilon-near-zero (ENZ) material dispersion from the oxide longitudinal optical phonon mode is shown to enhance the gap field and leads to photon-assisted tunneling. A general model for photo-assisted tunneling is developed and shown to accurately model the short-circuit current in the device. The electrical power generated from the thermal source is measured across a load resistance and the peak power is shown to correspond to the impedance matching condition for a rectifier.

1. Introduction

Energy recovery from a low-grade thermal source requires large-area efficient conversion of infrared radiation into electrical power. Direct rectification of infrared radiation by means of an metasurface-coupled tunnel diode, called a rectenna, has been proposed for energy harvesting applications[1, 2].

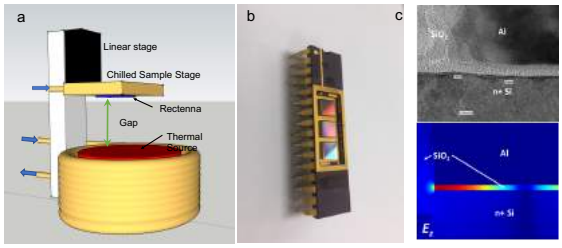


Figure 1: (a) Experimental radiometric power measurement experimental setup (b) Packaged large-area devices for vacuum radiometric testing. (c) SEM image of MOS tunnel diode and EM simulation showing transverse field concentration in the gap. See reference [3].

In this paper, we demonstrate electric power generation from a thermal source in a large-area metasurface rectenna. The rectenna is irradiated with broadband incoherent infrared radiation from a thermal source in a vacuum radiometry setup shown in fig. 1(a)-(b). Previously, we have shown that large photocurrent at zero bias can be observed for metasurface photonic resonances in the region near the LO phonon mode of the oxide[1, 2]. Large transverse electric field enhancement in the tunnel gap leads to large short-circuit photocurrent due to photon-assisted tunneling[3]. (see figure 1 (c)) Photon-assisted tunneling is examined in the transfer matrix Hamiltonian approach and image barrier lowering effects can be observed[3].

2. Results

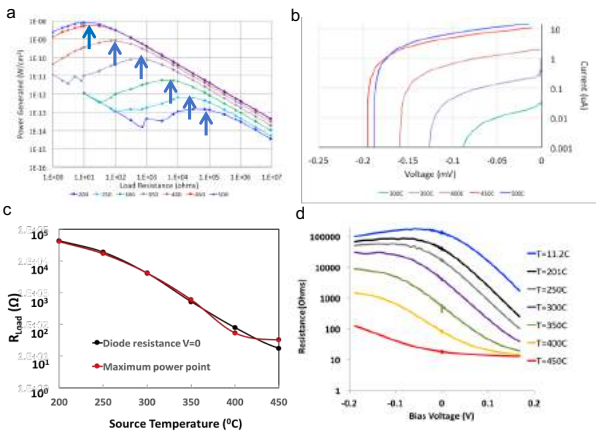


Figure 2: (a) Electrical power generation as a function of the load resistance. Each curve represents a different source temperature. (b) Load diagram in 2nd quadrant. (c) Load resistance at peak power compared to diode resistance at V=0. (d) Diode resistance for various source temperatures.

Power generation from a rectifying antenna requires a load impedance to generate a voltage. Typically, the maximum power point occurs when the load impedance is matched to the coupled-antenna tunnel diode impedance. Power generation from thermal sources occurs due to blackbody emission that depends on the surface temperature and acts like the ac source for our dc power supply. Figure 2(a) shows the measured electrical power over a load resistor as a function of the source temperature. The load line in figure 2(b) shows power generation in the 2nd quadrant indicative of direct rectification The maximum electrical power increases as the temperature is varied from 25C to 500C,

peaking at approximately 10nW/cm^2. The load resistance and peak power tracks the tunnel diode resistance at zero bias (see figure 2(c)-(d)) and the tunnel diode resistance decreases with increasing temperature.

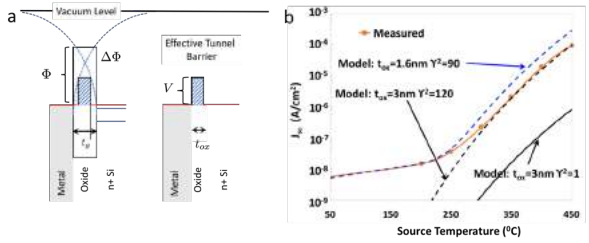


Figure 3: (a) Uniform tunnel barrier model for nMOS tunnel diode including image barrier lowering (b) Comparison of modeled and measured short-circuit photocurrent for various barrier heights, widths and field concentrations. Taken from reference [4]

The measured short-circuit current as a function of the source temperature can be compared to the photon-assisted tunneling model assuming a uniform barrier height for the Al/SiO_2/n+ Si tunnel diode and field enhancement factors estimated from simulation[4]. (see figure 3 (a)-(b)) The incoherent incident transverse electric field is obtained from the blackbody spectral exitance and is dependent on the source temperature. In the model, the photon energy acts as as an effective bias across the device giving rise to large differences between photon emission and photon absorption in the device. The large tunneling current asymmetry is result of the difference in density of states on each side of the barriers.

3. Conclusions

We have demonstrated direct conversion of radiated heat into dc electrical power using a large-area metasurface-coupled tunnel diode. By designing the metasurface photonic resonance near the insulating tunnel barrier material ENZ point, we obtain large transverse electric field confinement in the barrier. This enhanced electric field leads to photon-assisted tunneling and results in large measurable photocurrents as a function of the source temperature. A many-body transfer Hamiltonian approach to photon-assisted tunneling has been developed and is in good agreement with experimentally observed short-circuit currents. Nonlinear optical effects due to the ultrafast photon-assisted tunneling current could be a new source of interesting phenomena in the thermal infrared.

Acknowledgement

Funding for this work was provided by Sandia Laboratory Directed Research and Development (LDRD) program. Sandia National Laboratories is a multi-mission laboratory managed and operated by National Technology and Engineering Solutions of Sandia, a wholly owned subsidiary of Honeywell International Inc., for the United States Department of Energy's National Nuclear Security Administration under contract DE-NA0003525.

References

[1] P. S. Davids, R. L. Jarecki, A. Starbuck, D. B. Burckel, E. A. Kadlec, T. Ribaudo, E. A. Shaner, and D. W. Peters, "Infrared rectification in a nanoantenna-coupled metal-oxide-semiconductor tunnel diode," *Nature nanotechnology*, vol. 10, no. 12, p. 1033, 2015.

[2] E. A. Kadlec, R. L. Jarecki, A. Starbuck, D. W. Peters, and P. S. Davids, "Photon-phonon-enhanced infrared rectification in a two-dimensional nanoantenna-coupled tunnel diode," *Phys. Rev. Applied*, vol. 6, p. 064019, Dec 2016. [Online]. Available: https://link.aps.org/doi/10.1103/PhysRevApplied.6.064019

[3] P. S. Davids and J. Shank, "Density matrix approach to photon-assisted tunneling in the transfer hamiltonian formalism," *Phys. Rev. B*, vol. 97, p. 075411, Feb 2018. [Online]. Available: https://link.aps.org/doi/10.1103/PhysRevB.97.075411

[4] J. Shank, E. A. Kadlec, R. L. Jarecki, A. Starbuck, S. Howell, D. W. Peters, and P. S. Davids, "Power generation from a radiative thermal source using a large-area infrared rectenna," *arXiv preprint arXiv:1801.02544*, 2018.

Longitudinally Multi-slotted Taper for Smooth Transition between Conventional Planar Waveguide and Multi-slotted MMI

Hamdam Nikkhah*, Trevor J. Hall

[1]School of Electrical Engineering and Computer Science, University of Ottawa, Ottawa, Canada
*corresponding author, E-mail: hnikk057@uottawa.ca

Abstract

Longitudinal multi-slotted metamaterial structure has shown an improvement in the accuracy of the paraxial approximation required by the Talbot effect and consequently a reduction in the deviation from perfect imaging of an MMI quantified by the modal phase error. An adiabatic longitudinal multi-slotted waveguide taper is introduced to provide a smooth transition between a conventional waveguide and the longitudinal subwavelength structure that provides an Ex transmission of 92% and Ey transmission of 99%. The taper matches the effective index and geometry of the access waveguides to the ports of the multimode region of the multi-slotted MMI.

1. Introduction

Current minimum feature size limitations of microfabrication processes highly constrains the attainable performance of subwavelength structures. The metamaterial can be described by its local anisotropic response in the deep subwavelength regime, but at optical frequencies this requires feature sizes that are beyond current volume fabrication processes. The spatial and temporal dispersion of structures meeting current fabrication constraints is consequently an important consideration [1]. Conversely, subwavelength structuring enables the engineering of spatial and temporal dispersion, for example to improve the accuracy of the paraxial approximation fundamental to the Talbot that is at the heart of the operating principal of multimode interference couplers (MMIs). An MMI is a component widely used in photonic integrated circuits for coherent optical applications. Dispersion engineering can reduce the error of the modal phase and consequently the departure from perfect imaging in MMIs. On the basis of findings on modal phase error correction, a novel silicon integrated polarisation beam splitter (PBS) based on a longitudinal metamaterial has been proposed [2].

One of the critical challenges of subwavelength structures is their interfacing to conventional waveguides and the remainder of the circuit due to the mismatch between their geometry and effective indices. Without care the mismatch results in reflection at the interfaces and high insertion loss. Adiabatic geometrical tapers have been widely used in photonic integrated circuits (PICs), but in subwavelength structures the tapers must also make a smooth transition in the effective index. In this paper an adiabatic taper for interfacing a conventional single mode waveguide to the multimode waveguide region of a 2 × 2 MMI PBS based on an 18 ridge multi-slotted waveguide.

The taper consists of concatenated sections the number of which depends on the number of ridges in the multimode region. In this paper, the number of ridges was optimized to 18 with a pitch of 0.455 µm for 0.355 µm wide 0.35 µm thick ridges seperated by an air-gap of 0.1µm with air over-cladding. Figure 1 shows a top view and cross- section of the multimode region with two initial ports at the input and output depicted as yellow triangles.

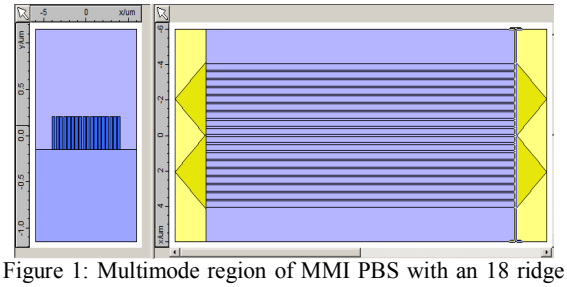


Figure 1: Multimode region of MMI PBS with an 18 ridge multi- slotted waveguide with a pitch of 0.455 µm for 0.355 µm wide and 0.35 µm thick silicon ridges seperated by an air-gap of 0.1µm with air over-cladding; (left), the cross section view, (right) the top view with four ports shown as yellow triangles.

For this structure, the taper contains of 5 stages of which the first stage contains a single access waveguide. The length of each section is 50 µm. At each subsequent stage a pair of waveguides is placed symmetrically about the continuation of the waveguides of the previous stage which converts a single mode access waveguide to three, five, seven and nine ridge multi-slotted waveguides in succession. Figure 2 shows the five stages of the taper.

An exponential function of weight -4 is used on the waveguides to introduce coupling adiabatically between the existing and additional waveguides for an effective index match at the interface between sections and to assist mode expansion. The positions of the waveguides added to each successive stage was chosen carefully to avoid a sudden

change in effective index and hence reflection at the section interfaces.

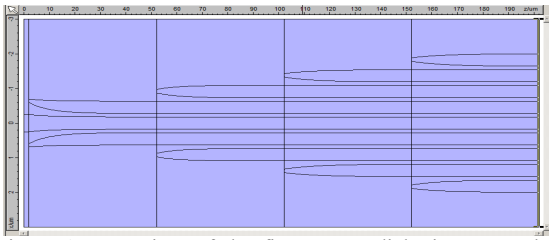


Figure 2: Top view of the five stage adiabatic taper. The first section at the left contains a single access waveguide.

In the second stage the central ridge is tapered down from the 0.5 µm width of the incoming access waveguide is reduced to a 0.355 µm width ridge using an exponential taper. In the following sections all ridges are straight and parallel with a gap of 0.1 µm between adjacent side walls except the additional outer pair of tapered ridges.

2. Simulation and analysis

The design was validated by simulation using the Fimmwave and Fimmprop tools of the Photon Design suite. Figure 3 and 4 show the Ex and Ey profile at the input and output ports of taper respectively.

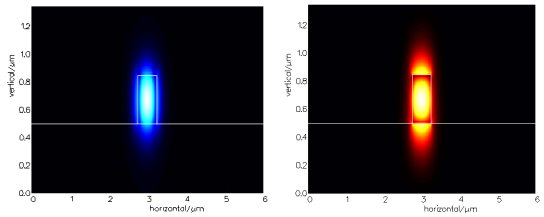


Figure 3: (left) Ex mode profile at the left-end taper (right) Ey mode profile at the left-end taper; at the interface with an access waveguide with ridge width of 0.5 µm.

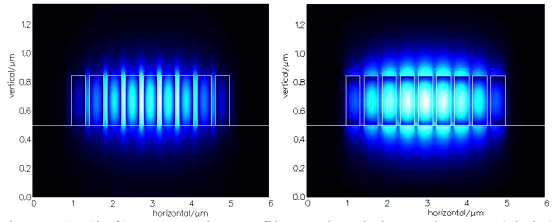


Figure 4: (left) Ex mode profile at the right-end taper (right) Ey mode profile at the right-end taper; on multi-slotted waveguides with ridges of width of 0.355 µm and air-gaps of 0.1 µm width.

A 3D simulation of the whole multi-slotted waveguide taper is shown in figure 5 (for the intensity profile) with a transmission of 92% for Ex mode (-0.36 dB loss) and a transmission of 99% for Ey mode (-0.043 dB loss). A full-scale 3D simulation in FimmProp of a multi-slotted waveguide MMI complete with tapers demands excessive computer resources as the structure contains multiple parallel tapered waveguides which requires a progressive refinement of a partition of each section of the tapers in the computation. The longitudinal patterning seen in the visualization is due to the presence of residual higher-order supermodes interfering with the fundamental supermode. The visual effect is amplified by the coherent interference despite the overwhelming majority of the power being transported by the fundamental supermode.

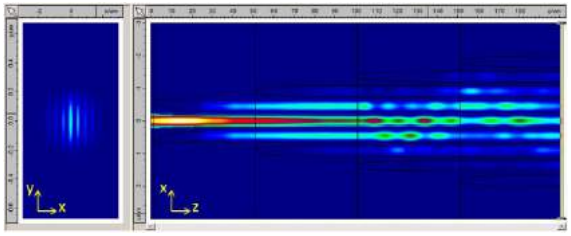


Figure 5: A 3D propagation simulation of the slotted waveguide taper; (left) a cross section of the right end mode, (right) top view of field intensity profile.

3. Discussion and conclusions

Subwavelength engineering can help to modify the dispersion relation to improve the accuracy of the paraxial approximation for modal phase error reduction in MMIs towards perfect imaging. Subwavelength MMIs based on multi-slotted waveguides must be adiabatically connected to the conventional waveguides. An adiabatic multi-slotted taper with Ex transmission of 92% and Ey transmission of 99% has been proposed in this paper for the first time to match the effective index and geometry of the access waveguides to the ports of the multimode region of the multi-slotted MMI.

References

[1] H. Nikkhah, '*Enhancing the performance of Si photonics: structure-property relations and engineered dispersion relations*', PhD thesis, University of Ottawa, 2018.

[2] H. Nikkhah, M. Hasan, T.J. Hall, *The Talbot effect in a metamaterial,* Applied Physics A, 124:106, 2018. https://doi.org/10.1007/s00339-017-1521-1.

What We Can Learn from Hybrid Metamaterials Composed of Plasmas

Osamu Sakai[1*], Akinori Iwai[1,2,3], Alexandre Bambina[1], Yuuki Kabe[1], Teruki Naito[3], and Shigeyuki Miyagi[1]

[1]Department of Electronic Systems Engineering, The University of Shiga Prefecture, Hikone, Japan
[2]Research Institute for Sustainable Humanosphere, Kyoto University, Uji, Japan
[3]Department of Electronic Science and Engineering, Kyoto University, Kyoto, Japan
*corresponding author, E-mail: sakai.o@e.usp.ac.jp

Abstract

After several theoretical, numerical and experimental results from metamaterials of plasma-solid hybrid material, we can derive several common principles in metamaterials, as shown in the following. We successfully observed negative-refractive-index states using this hybrid material with different sizes of meta-atoms, which indicates invariance of parameter identification widely-used in metamaterial science. Cloaking devices can be designed using inherent permittivity gradient in plasma, and the minimum size of cloaking devices based on transformation optics is estimated to be around the scheme of Rayleigh-scattering mode. Energy stored in plasma-metamaterial composites is approximately by 3 orders of magnitude larger than solid-state metamaterials, which means that devices of plasma-metamaterial composites are robust for high-energy microwaves and that nonlinear effects like second-harmonic-wave generation are enhanced. These results are applicable for other materials in metamateials whose permittivity is in the Drude model, and open possibilities for novel energy and imaging devices.

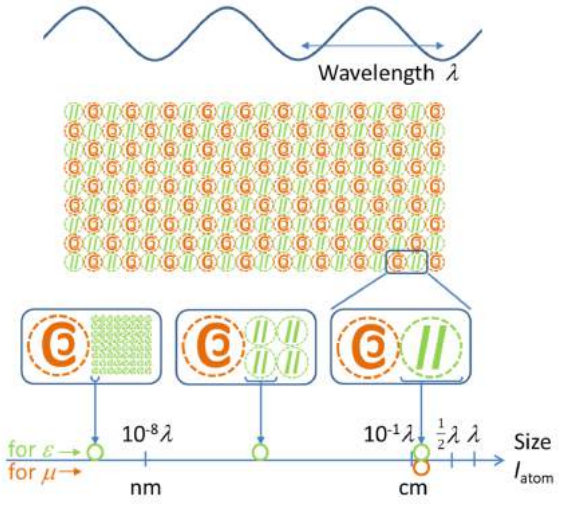


Figure 1: Schematic view of different sizes of meta-atoms l_{atom}. Modified from Ref. [5].

1. Introduction

After the proposal of array of double split ring resonators (DSRRs) for negative permeability μ [1], which are composed of metallic patterns, the concept and the applicable fields of metamaterials have been expanding to many scientific and technological categories, frequently achieved using novel materials.

One example of such metamaterials with novelty of materials is plasma metamaterials [2], which contain discharge plasma inside their configurations. Obviously they have tunable parameters since electron density, which determines permittivity ε in the Drude model, is variable by control of input electric power for ionization. However, the scientific and technological merits and suggestions to other metamaterial researches are not limited to their tunability.

In this report, we summarize the findings in the previous reports on plasma metamaterials [2], and point out potential devices that are achievable by their applications.

2. Theoretical, numerical and experimental results and discussion

2.1. Invariance of parameter identification for refractive index

The refractive index N is controllable in metamaterials; not only in its positive polarity, N can be negative when both ε and μ are negative. As well known in the literature, N is given as

$$N = \sqrt{\varepsilon}\sqrt{\mu}. \tag{1}$$

In the first experimental verification [3], negative N was achieved using the same spatial periodic length of meta-atoms l_{atom} for both ε and μ in a spatial synchronous configuration, partly because of the convenience of fabrication processes. However, in cases of plasma metamaterials, l_{atom} can differ, as shown in Fig. 1. In the experiment using one-dimensional microwave waveguide [2], l_{atom} of microplasma array was spatially synchronized with that of the double metal helix structure. However, the experimental setup of plasma metamaterial in three-dimensional waveguide includes different values of l_{atom} [4]; one is for ε, which is in atomic scales since the plasma is in a bulk state homogeneously distributed in the space, and the other is for μ, which is a array of conventional DSRRs [1]. In both

experiments, negative N was confirmed by several diagnostic methods. The numerical results reinforced these experimental results, and we can conclude [5] that N is identified using Eq. (1), with the upper limit arising from the maximum value of $l_{\rm atom}$ in the structure.

2.2. Estimation of minimum size of cloaking device

In a cloaking device with the design based on transformation optics, N should be anisotropic and have a spatial gradient in its profile [6, 7]. When one designs a cloaking layer by metamaterials, sufficient spatial steps with a gradual change of parameters requires a number of sub-layers with slight variation of N [8]. However, if we use plasma that includes inherent spatial gradient of electron density leading to those of ε and N, smooth variation is possible and may contribute to achievement of a thin cloaking layer.

We performed numerical calculation based on the finite-difference time-domain method [9], where the numerical model includes the naturally-obtained electron density profile in a circular column of discharge plasma; the electron density is in the zeroth Bessel function of the first kind. To induce an anisotropic property in the parameters, we used μ by introduction of one-directional hypothetical magnetic current in the numerical code. As decreasing the size of the corresponding device, we estimate the scattering property by intensity of scattering waves normalized by cross section (or by *cross length* in our two-dimensional model). In various sets of object sizes and wavelengths, the results are along the universal law in which the scattering rate is abruptly increases when the size is down to the Rayleigh-scattering regime (where the factors of the sizes are 0.1-0.2 of the wavelength). This result is reasonable since, in the mode of Rayleigh scattering, the phase element of propagating waves is almost constant and cannot afford deformation of spatial coordinates required in transformation optics.

2.3. Stored wave energy in metamaterial structure

When electromagnetic waves propagate with high intensity, they induce several phase changes of wave media. One of them is breakdown ionization or plasma generation by high-power propagating waves, in which wave energy converts into excited states of ion-electron pairs; in other words, the wave energy is stored in space. Thus, the energy in the space increases from the level of the wave propagation in vacuum approximate by two orders. Furthermore, when we set μ in the negative polarity, we can expect increment of its level since negative ε, which is required for wave propagation in the space with real (negative) values of N, corresponds to high electron density with high energy states.

Such a high-energy metamaterial induces strong nonlinear phenomena [4]. As an event of nonlinear dynamics, we observed saddle-node bifurcations. We also detected enhanced second harmonic waves as an event of nonlinear optics. The observed bifurcation with hysteresis is applicable for high-power microwave switches in tens of Watts or hundreds of Watts, and possibly in optical lasers by similar wave media to discharge plasma.

3. Conclusion

Metamterials composed of plasmas and solids exhibit various novel features that would not be available if we configured metamaterials only by solids. The experimental results verified that N values in metamaterials are in the similar formula even if the sizes of meta-atoms differ. As scientific and technological merits, one can expect minimized size of cloaking devices and enhancement of nonlinearity. Several similar schemes are possible in other metamaterials working at higher frequency ranges, in which ε is in the Drude model and favorably tunable.

Acknowledgement

This study was supported by Grant-in-Aid for Scientific Research from the Japanese Ministry of Education, Culture, Sports, Science and Technology, Japan.

References

[1] J.B. Pendry, A.J. Holden, D.J. Robbins, W.J. Stewart, Magnetism from conductors and enhanced nonlinear phenomena, *IEEE Trans. Microw. Theory Tech.* 47: 2075–2084, 1999.

[2] O. Sakai, K. Tachibana, Plasmas as metamaterials: a review, *Plasma Sources Sci. Technol.* 21: 013001-1-18, 2012.

[3] R.A. Shelby, D.R. Smith, S. Schultz, Experimental verification of a negative index of refraction, *Science* 292: 77–79, 2001.

[4] Y. Nakamura, A. Iwai, O. Sakai, Nonlinear properties of negative-permittivity microwave plasmas embedded in metamaterial of macroscopic negative permeability, *Plasma Sources Sci. Technol.* 23: 064009-1-8, 2014.

[5] O. Sakai, A. Iwai, Y. Omura, Invariance of parameter identification in multiscales of meta-atoms in metamaterials, *Advances Phys.: X* 3: 338–355, 2018.

[6] J.B. Pendry, D. Schurig, D.R. Smith, Controlling electromagnetic fields, *Science* 312: 1780-1782, 2006.

[7] U. Leonhardt, Optical conformal mapping, *Science* 312: 1777-1780, 2006.

[8] D. Schurig, J.J. Mock, B.J. Justice, S.A. Cummer, J.B. Pendry, A.F. Starr, D.R. Smith, Metamaterial electromagnetic cloak at microwave frequencies, *Science* 314: 977–980, 2006.

[9] A. Bambina, S. Yamaguchi, A. Iwai, S. Miyagi, O. Sakai, Valid size of plasma-metamaterial cloaking monitored by scattering wave in finite-difference time-domain code, *AIP Advances* 8: 015309-1-10, 2018.

Magneto-plasmonic metamaterials

E. Th. Papaioannou[1, *]

[1]Department of Physics and Research Center OPTIMAS, TU Kaiserslautern,
Erwin-Schrödinger-Str. 56, 67663 Kaiserslautern, Germany

*corresponding author, E-mail: papaio@rhrk.uni-kl.de

Abstract

Strong localization of light, enabled by surface plasmons, increases the magneto-optical response of ferromagnetic materials. In this work, we define the strategy to design the magneto-optic response of a magneto-plasmonic crystal by correlating near- and far-fields effects. The engineering of the magneto-optic response based on the plasmon-induced modification of the optical properties introduces the concept of a magneto-plasmonic meta-structure. Furthermore, we present how magneto-plasmonic metamaterials can connect the field of plasmonics with magnonics and spintronics.

1. Introduction

The field of magneto-plasmonics is an emergent research field that aims to explore the combination of magnetic and plasmonic functionalities in patterned nanostructures [1, 2].
Strong localization of light due to the presence of surface plasmons, increases the magneto-optical response of ferromagnetic materials [3]. Furthermore, the presence of magnetic materials in plasmonic structures offers the possibility to influence plasmonic resonances with the magnetization and an external magnetic field [4].
In this work, we define the strategy to design the magneto-optic response of a magneto-plasmonic crystal by correlating near- and far-fields effects. The engineering of the magneto-optic response based on the plasmon-induced modification of the optical properties introduces the concept of a magneto-plasmonic meta-structure. In addition, we discuss how such a metamaterial can connect the field of plasmonics with the field of magnonics and spintronics.

2. Magneto-plasmonic enhancement in BiYIG/Au nanostructures

2.1. Experimental Details

The samples are composed of Au nanoparticles (0-Dimension magneto-plasmonic crystal) and Au gratings (1-D) structures in combination with magnetic films. As magnetic films, Bismuth Yttrium Iron Garnet (BiYIG) are used. The evolution of the magneto-optic enhancement in 0-D and 1-D magneto-plasmonic structures is studied optically with Reflectance and Transmittance measurements and magneto-optically with the help of spectroscopic magneto-optical Kerr effect (MOKE) setup operating in the longitudinal and polar mode. Equally important, to investigate the role of the shape of the Au particles and Au stripes on the enhanced electromagnetic field distribution induced by the surface plasmons, we show numerical calculations. These calculations were based on the Finite Integration Technique (FIT) method, by using the Computer Simulation Technology(CST) software. Moreover, Brillouin light scattering (BLS) experiments are employed to reveal the influence of plasmons on the magnetization dynamics of the magnetic layer.

2.2. Discussion

The magneto-optic response is examined in the presence of (i) localized surface plasmons, (ii) of propagating surface plasmons and (iii) in the geometrical percolation limit. The role of the thickness of the magnetic layer is discussed [5]. Finally, the influence of surface plasmons on the magnetization dynamics is examined.
We first reveal the enhancement of the longitudinal magneto-optical effect in the ferromagnetic dielectric bismuth substituted yttrium iron garnet (Bi-YIG), induced by localized surface plasmons (LSPs) in gold nanoparticles (AuNPs), Fig.1. Afterward, we show how the geometrical transition from plasmonic nanoparticles to gratings influences the magneto-plasmonic interaction. We clarify that around the dimensionality crossover between isolated nanoparticles and connected structures localized surface plasmons (LSPs) as well as propagating surface plasmons (SPPs) are excited. The transition from LSPs to SPPs greatly influences the magneto-optic interaction [6]. The thickness of the magnetic layer allows for the coexistence of both LSPs to SPPs on the same pattern that leads to big enhancement of the magneto-optic response.
We furthermore explore how the presence of LSPs is modifying the magnetization dynamics of the magnetic layer. The excitation of localized surface plasmons under visible light illumination maximizes the absorption of light in the magnetic system. We show with BLS measurements how the

plasmonic-induced temperature gradient influences the excitation of spin waves (magnons) in the magnetic layer.

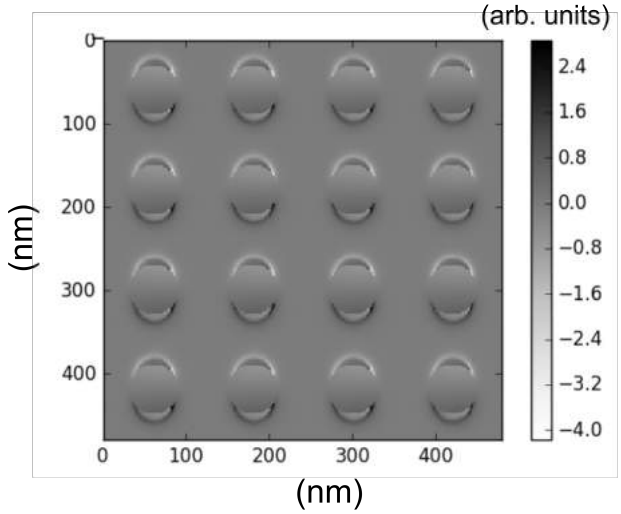


Figure 1: Simulated Near-Field image showing the polarizability rotation around the Au nanoparticles embedded in BiYIG (0-D magneto-plasmonic crystal). The grey scale is proportional to the strength of the magneto-optical rotation. The magneto-optic enhancement in BiYIG is confined around the localized plasmon modes of Au.

3. Conclusions

Tuning the magneto-optical enhancement with the optical properties of plasmonic excitations introduces the concept of a magneto- plasmonic meta-structure and opens new routes for tailoring the functionality of patterned magneto-plasmonic systems. The latter can be extended in the field of spintronics. Plasmonic-induced magnetization dynamics and photo-induced spin currents can pave the way for new devices based on light-spin interaction.

Acknowledgements

The transregional Collaborative Research Center SFB/TRR 173: SPIN+X, Project B07 is gratefully acknowledged.

References

[1] Armelles, G., Cebollada, A., García-Martín, A. and M. U. Gonzalez, Magnetoplasmonics: Combining Magnetic and Plasmonic Functionalities, *Adv. Opt. Mater.* Vol 1, 10−35, 2013.

[2] Bossini D., Belotelov V. I., Zvezdin A. K., Kalish A. N. and A. V. Kimel, Magnetoplasmonics and Femtosecond Optomagnetism at the Nanoscale, *ACS Photonics* Vol 3, 1385–1400, 2016.

[3] Rollinger, M, Thielen P., Melander E., Östman E., Kapaklis V., Obry B., Cinchetti M., García Martín A., Aeschlimann M. and E. Th. Papaioannou, Light Localization and Magneto-Optic Enhancement in Ni Antidot Arrays, *Nano Letters* Vol. 36, 2432–2438, 2016.

[4] E. Melander, E. Östman, J. Keller, J. Schmidt, E. T. Papaioannou, V. Kapaklis, U. B. Arnalds, B. Caballero, A. García-Martín, J. C. Cuevas, and B. Hjörvarsson, Influence of the magnetic field on the plasmonic properties of transparent Ni anti-dot arrays, *Appl. Phys. Lett.* 101, 063107 (2012).

[5] Melander, E., George S., Caballero B., Garcia-Martin A., Hjörvarsson B., Kapaklis V. and E. Th. Papaioannou, Thickness dependent enhancement of the polar magneto-optic Kerr effect in Co magnetoplasmonic nanostructures, http://arxiv.org/abs/1611.00078, 2017.

[6] Evangelos Th. Papaioannou, Hui Fang, Blanca Caballero, Eser Metin Akinoglu, Michael Giersig, Antonio García-Martín, and Paul Fumagalli, Role of interactions in the magneto-plasmonic response at the geometrical threshold of surface continuity, *Optics Express* Vol. 25, No. 26, 32793-32799, 2017.

Controlling the directivity, bandwidth and rate of thermal emission with epsilon-near-zero media

Iñigo Liberal[1,2] and Nader Engheta[2]

[1] Department of Electrical and Electronic Engineering, Public University of Navarre, Pamplona, 31006, Spain
[2] Department of Electrical and Systems Engineering, University of Pennsylvania, Philadelphia, Pennsylvania 19104, USA

Abstract

Epsilon-near-zero (ENZ) media provides the essential ingredients for the design of directive and narrowband thermal emitters. In particular, directivity and emission rate scale along with the size of an ENZ body, while the bandwidth is inversely proportional to it. In addition, ENZ thermal emitters exhibit exotic properties, such as geometry invariance and dopant-position independence. Here, we investigate these theoretical aspects as well as the trade-offs involved in the practical implementation of these concepts in silicon carbide (SiC).

1. Introduction

Black-body radiation is characterized for being intrinsically broadband, isotropic, unpolarized and temporally incoherent. However, photonic nanostructures modify the spatial coherence of thermal fields, thus offering the possibility of designing partially coherent (narrowband) and directive thermal emitters [1]. In turn, this opens a range of applications for thermal sources, including thermophotovoltaics, spectroscopy, communications, bioengineering and near-field heat transfer. For this reason, in recent years a large number of photonic nanostructures have been applied to the design of thermal radiators, including corrugated surfaces, metamaterials, photonic crystals, etc [2].

In a recent work [3], we have investigated the possibility of utilizing epsilon-near-zero (ENZ) media (i.e., continuous media with a near-zero permittivity in a given frequency range) to enable the control of thermal fields, facilitating the design of directive thermal emitters. It is based on our analysis that ENZ media provide unique opportunities for the design of thermal sources. Specifically, it provides an intrinsic enhancement of the spatial coherence of thermal fields, fundamentally based on its material properties. This material-based approach is in stark contrast with all aforementioned techniques based on photonic nanostructures, where their nanoscale geometrical features are utilized to harness thermal fields and enhance spatial coherence. The unique properties of ENZ media in controlling thermal fields stem from its unusual wave dynamics [4]. In essence, as the refractive index goes to zero, the wavelength gets effectively stretched and the field distributions become spatially static [5]. This forms the basis for a number of pathological phenomena, which can be directly applied to the design of thermal emitters. In particular, we theoretically demonstrated an ENZ bodies containing dielectric rods exhibits three distinct features [3]: (i) They show resonant spectral features independently of the geometry of their external boundary. (ii) Thermal emission from these bodies is also independent of the position of the dielectric rods (i.e., "photonic dopants") immersed within them. (iii) These bodies naturally exhibit highly directive thermal beam, which can be straightforwardly design by changing the geometry of the external boundary.

In our talk, we will discuss these results and the different possibilities of engineering thermal emission with ENZ media. In the remaining of the abstract, we provide additional theoretical details on the design of thermal radiators based on realistic implementations of ENZ media, as well as the different design trade-offs.

2. Thermal emitter design

In order to illustrate the thermal emission properties of ENZ bodies containing dielectric rods we numerically investigate the geometry schematically illustrated in Fig. 1. It consist of a two-dimensional (2D) silicon carbide (SiC) rod with a right triangle cross-section (with rounded corners) with catheti of length $L_x = s \times 10$ μm and $L_y = s \times 20$ μm, where s is a generic scaling factor. SiC is a polar dielectric known to exhibit a near-zero permittivity at mid-IR frequencies (λ_p = 10.3 μm) [6]. In addition, this body contains a germanium rod (with relative permittivity $\varepsilon_p = 16$ and radius r_p = 0.992 μm).

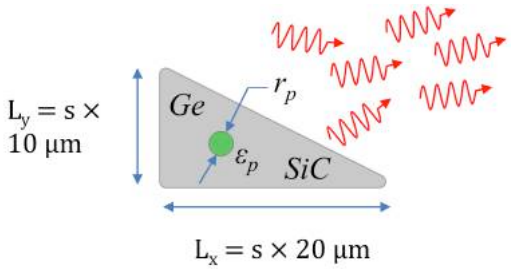


Figure 1: Sketch of the geometry.

In the theoretical ENZ limit, the fields excited by thermal fluctuating currents become spatially static distributions dynamically oscillating in time [3]. In addition, the

properties (radius and dielectric constant) of the rod, can be chosen so as to resonantly excite a geometry-invariant mode, characterized by a uniform magnetic field in the ENZ host [3]. This mode provides an obvious synergy with the design of directive thermal sources. Since the magnetic field at the boundary of the body is uniform, increasing the size of the body results in an increasingly directive emission pattern. Similarly, the emission rate also becomes proportional to the perimeter, as one increases the body size. At the same time, the uniform field results in stored energy that scales proportional to the area, thus leading to a smaller emission bandwidth. In theory, this provides the essential ingredients for the design of a directive and narrowband thermal source: a simultaneous enhancement of directivity and emission rate, while narrowing the bandwidth. Intriguingly, thermal emission properties are also independent of the position of the rod within the ENZ host.

Eventually, this theoretical picture must break down in practice at a given body size for realistic material parameters. The reason for this behavior is that second-order effects associated with the fact that the permittivity is never exactly zero become more prominent as the size of body increases, deviating its response from the theoretical ENZ limit. To illustrate this point, Fig. 2(a) gathers a set of numerical simulations of the emission spectrum as a function of the scaling factor s. As expected, the bandwidth initially shrinks as the scaling factor increases, providing the means for designing a narrowband emitter. However, this narrowing effect breaks down for the scaling factor s = 1.5 (corresponding to L_x = 30 μm ≈ 3 λ_{ENZ}). Thus, these simulations demonstrate that the theoretical ENZ limit can be applied to bodies spanning several (free-space) wavelengths. However, when the second-order nonuniformity of the field becomes comparable to the size of the body, the emission spectra starts to broaden, indicating the range of applicability of the theoretical ENZ limit.

A similar behavior can be observed when analyzing the emission pattern at the ENZ wavelength (see Fig. 2(b)). Since the magnetic field of the resonant mode in the ENZ region is theoretically uniform, increasing the size of the body results in a more directive emission, where the emission pattern simply exhibits one lobe per side of the body. Again, our numerical simulations demonstrate that this effect persists in SiC even for bodies whose size is of several (free-space) wavelengths. However, this effect is ultimately truncated in our numerical simulations at L_x = 30 μm, indicating the practical limits of implementing ENZ thermal emission theory in SiC.

3. Conclusions

Our numerical results demonstrate that the theoretical ENZ limit can be applied in practice to SiC bodies of several (free-space) wavelengths. This result suggests that ENZ concepts can be applied in the design of directive and narrowband thermal emitters, also providing access to beamforming capabilities and geometry-invariant characteristics.

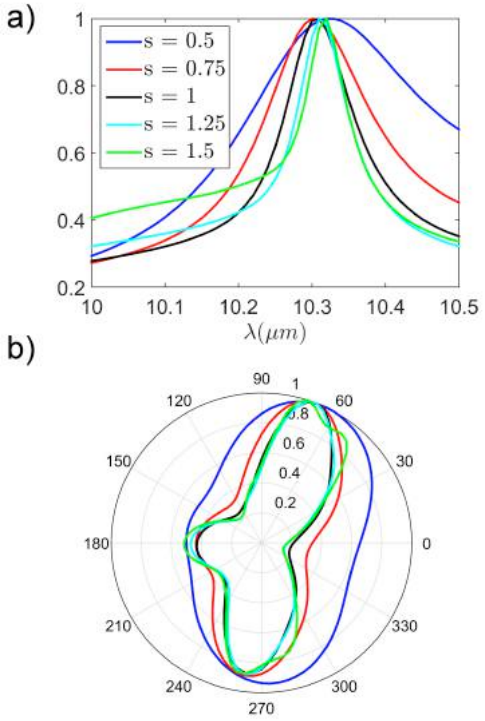


Figure 2: (a) Normalized absorption cross-section for an incident plane-wave along the Y-axis, corresponding to thermal emission along the (-Y) axis, as a function of the scaling factor s (b) Normalized emission pattern at the ENZ wavelength.

Acknowledgements

I.L. acknowledges support from Juan de la Cierva – Incorporación Fellowship and Dotación adicional Caixa.

References

[1] K. Joulain et. al, Surface electromagnetic waves thermally excited: Radiative heat transfer, coherence properties and Casimir forces revisited in the near field. *Surf. Sci. Rep.* 57: 59–112, 2005.

[2] Boriskina et. al, Heat is the new light, Optics & Photonics News 11:26-33, 2017.

[3] I. Liberal and N. Engheta, Manipulating thermal emission with spatially static fluctuating fields in arbitrarily-shaped epsilon-near-zero bodies, *Proc. Nat. Acad. Sci. Accepted for publication*, 2018.

[4] I. Liberal and N. Engheta, Near-zero refractive index photonics. *Nat Photonics* 11(3): 149–158, 2017.

[5] R.W. Ziolkowski, Propagation in and scattering from a matched metamaterial having a zero index of refraction. *Phys. Rev. E* 70(4):46608, 2004.

[6] Caldwell JD, et al. Low-loss, infrared and terahertz nanophotonics using surface phonon polaritons. *Nanophotonics* 4(1):44–68, 2015.

Silicon Ring Resonator Electro-optical Modulator Utilizing Epsilon-near-zero characteristics of Indium Tin Oxide

Mahmoud Elgarf[1], Mohamed Badr[2], Mohamed Swillam[1*],

[1]Department of Physics, School of Sciences and Engineering, The American University in Cairo, Cairo, Egypt
*corresponding author, E-mail: m.swillam@aucegypt.edu

Abstract

One crucial component in optical communication systems is the optical modulator. It links between the electric and optical domains as it transforms the electric signal into an optical stream. Electro-optical modulation is a very popular scheme. Recently, indium tin oxide has been intensively used in optical modulators due to its epsilon-near-zero characteristics. A silicon ring resonator modulator based on ITO is proposed. Insertion loss of 0.075 dB and extinction ratio of 14 dB are achieved at 1550 nm.

Light-induced driving of a micron-size metallic plate

Min Qiu[1,*]

[1]State Key Laboratory of Modern Optical Instrumentation, College of Optical Science and Engineering, Zhejiang University, 310027, Hangzhou, China
*corresponding author, E-mail: minqiu@zju.edu.cn

Abstract

By employing the synergy of optical force and photophoretic force, we propose and experimentally demonstrate a configuration which can drive a micron-size metallic plate moving back and forth on a tapered fiber with supercontinuum light in ambient air. The results might open exhilarating possibilities in applications of optical driving and energy conversion.

1. Introduction

Light-induced forces stem from momentum transfer directly between photons and objects, or indirectly between surrounding media and objects when light interacts with objects. The force comes from the direct way is the well-known optical force, which has been widely used to manipulate microscopic objects in the fields of physics, biochemistry and clinical medicine. Photophoretic force, originating from the indirect way with the light-induced thermal effect, provides an alternative and effective way to transport light-absorbing particles in ambient gases.

2. Results

The schematic of the driving system in Figs. 1(a,b) describes a gold plate (side length, 5.4 μm; thickness, 30 nm) being pulled from the tapered fiber end (cone angle, 6°), and then pushed back after the gold plate is pulled to the middle section of the tapered fiber. The above discussions are confirmed experimentally. The effect of light-induced pulling and pushing is shown in Fig. 2. Figure 2 presents sequencing images of the gold plate being pulled and pushed by a tapered fiber guided with supercontinuum light in ambient air. The gold plate (side length, 5.4 μm; thickness, 30 nm) is placed on the tapered fiber end. After the supercontinuum light being guided into the tapered fiber (power, 1.3 mW), the gold plate is pulled back at an average speed of 35.6 μm/s at first, then is pushed forward at about 28.52 μm/s, then is pulled back again at around 37.11 μm/s, and finally stops in a location 43 μm away from the tapered fiber end.

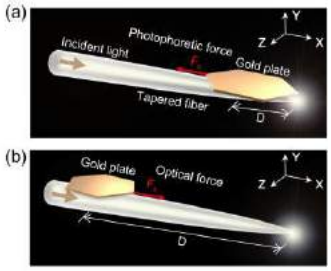


Figure 1: Numerical modelling of light-induced driving by synergy effect of optical force and photophoretic force.

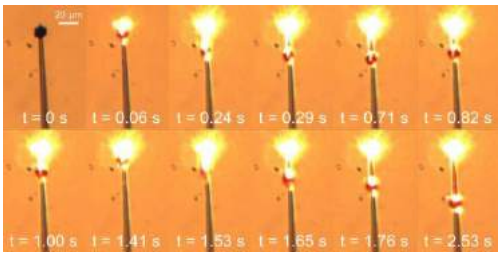


Figure 2: Sequencing optical microscopy images of a back-and-forth moving gold plate driven by unpolarized supercontinuum light on a tapered fiber in ambient air.

3. Conclusions

In conclusion, we have shown that optical force and photophoretic force can be used synergistically to drive a gold plate moving back and forth on a tapered fiber. Our studies could offer a deeper understanding of a diversified light-matter interaction, opening up new avenues for pluralistic optical manipulation including optical control and sensing, and inspiring many researches on optical driving (e.g. light-driven motor).

References

1 J. S. Lu, H. B. Yang, L. N. Zhou, Y. Y. Yang, S. Luo, Q. Li, and M. Qiu Light-Induced Pulling and Pushing by the Synergic Effect of Optical Force and Photophoretic Force. Physical Review Letters, 118: 043601 (2017).

Observation of topologically protected helical edge modes in an elastic waveguide

M. Miniaci[1,2], **R. K. Pal**[1], **B. Morvan**[2], **and M. Ruzzene**[2]

[1]Daniel Guggenheim School of Aerospace Engineering, Georgia Institute of Technology, 270 Ferst Dr, Atlanta, GA 30332 (USA)

[2]Laboratoire Ondes et Milieux Complexes, UMR CNRS 6294, University of Le Havre, 75 Rue Bellot, 76600 Le Havre, France

marco.miniaci@gmail.com

Abstract— In this work we propose the first experimental observation of topologically protected helical edge modes in a Kagome elastic plate. We achieved this by means of a novel and simple approach based on a rational metamaterial design that produces an isolated accidental degeneracy of two overlapped Dirac cones and subsequently lifts it through careful manipulation of geometrical symmetries.

The investigation of topologically protected waves in classical media [1] has opened unique opportunities to achieve exotic properties like one-way phonon transport [2], protection from backscattering and immunity to imperfections [3]. While a number of experimental observations in acoustic [4] and electromagnetic [5] domains has appeared so far, their observation in elastic solids has so far been elusive due to the presence of both shear and longitudinal modes and their modal conversion at interfaces and free surfaces.

Here we report the experimental observation of topologically protected helical edge waves in an elastic plate patterned according to a Kagome lattice with an accidental degeneracy of two Dirac cones induced by drilling blind holes through the waveguide thickness. The careful breaking of symmetries couples the corresponding elastic modes which effectively emulates spin orbital coupling in the quantum spin Hall effect [6, 7].

The experimental full wavefield reconstruction by means of a scanning laser Doppler vibrometer clearly provides the demonstration of topological robustness and the ability to guide waves along channels with sharp corners in elastic structures.

The results may open up new avenues in the fields where vibrations play a crucial role, such as civil engineering, energy harvesting and the aerospace industry, opening avenues for the practical realization of compact, passive and cost-effective elastic topological waveguides.

ACKNOWLEDGMENT

M.M. has received funding from the European Union's Horizon 2020 research and innovation programme under the Marie Sklodowska-Curie grant agreement N. 658483. R.K.P. and M.R. acknowledge the support of the EFRI Award 1741685 from the National Science Foundation.

REFERENCES

1. Huber, S. "Topological mechanics," *Nat. Phyis.*, Vol. 12, 621, 2016.
2. He, C. *et al.* "Acoustic topological insulator and roboust one-way sound transport," *Nat. Phyis.*, Vol. 12, 3867, 2016.
3. Mousavi, S. H., Khanikaev, A. B. & Wang, Z. "Topologically protected elastic waves in phononic metamaterials," *Nat. Comm.*, Vol. 6, 8682, 2015.
4. Yang, Z. *et al.* "Topological acoustics," *Phys. Rev. Lett.*, Vol. 114, 114301, 2015.
5. Lu, L. *et al.* "Topological photonics," *Nat. Phot.*, Vol 8, No. 11, 821–829, 2014.
6. Kane, C. L. and Mele, E. J. "Quantum spin Hall effect in graphene," *Phys. Rev. Lett.*, Vol. 95, No. 22, 226801, 2005.
7. Hasan, M. Z. and Kane, C. L. "Colloquium: topological insulators," *Rev. Mod. Phys.*, Vol. 82, No. 4, 3045, 2010.

Magnetic spin-orbit interaction of light steers Bloch surface waves

Mengjia Wang[1], Hongyi Zhang[1], Tatiana Kovalevich[1], Roland Salut[1], Myun-Sik Kim[2], Miguel Angel Suarez[1], Maria-Pilar Bernal[1], Hans-Peter Herzig[2], Huihui Lu[3], and Thierry Grosjean[1]*

[1] FEMTO-ST Institute, Université Bourgogne Franche-Comté, UMR CNRS 6174 15B Av. des Montboucons, 25030 Besancon cedex, France

[2] Optics & Photonics Technology Laboratory, Ecole Polytechnique Fédérale de Lausanne (EPFL), Rue de la Maladière 71b, Neuchâtel, CH-2000, Switzerland

[3] Guangdong Provincial Key Laboratory of Optical Fiber Sensing and Communications, Jinan University, Guangzhou 510632, China

* Corresponding author, E-mail: thierry.grosjean@univ-fcomte.fr,

Abstract

We show the directional excitation of Bloch surface waves controlled by the magnetic field of light. The phenomenon in play is the first magnetic spin-orbit interaction of light. It opens new degrees of freedom in the manipulation of light and offers appealing novel opportunities in the detection of the spin density of the magnetic optical field.

1. Introduction

The magnetic field of light is often considered to be a negligible contributor to light-matter interaction. However, with the advent of the left-handed metamaterials [1], nanophotonics has recently investigated magnetic response in nanostructures to reveal the hidden magnetic part of the light-matter interaction to achieve new scientific prospects [1,2]. In this paper, we show that the magnetic field of light has also the appealing ability to control the light coupling into optical surface waves.

Optical angular momenta are manifestations of polarization and spatial degrees of freedom of light. Remarkably, spin and orbital momenta are not independent quantities, the spin angular momentum (SAM) can be converted into orbital angular momentum (OAM), and vice versa [3]. Such a spin-orbit interaction (SOI) has recently drawn much interest in applications involving light manipulation. For example, SOI has demonstrated the remarkable property of controlling the propagation direction of guided modes, such as surface plasmons, fiber and waveguide modes, leading to the concept of a spin-controlled unidirectional waveguiding [4-7]. With the help of a subwavelength (dipolar) coupler, the longitudinal SAM of an impinging wave can be transferred into the transverse SAM of the evanescent tail of a guided mode, leading to a spin-directional coupling of the guided mode [4-6]. So far, such investigations mainly focused on the rotating electric component of light as the source of SAM originating the transverse spin-direction coupling.

Here, we introduce the concept of a spin-direction locking mediated solely by a rotating magnetic light field. We study the directional coupling of light in Bloch surface waves (BSW) [8] by projecting circularly polarized light onto a subwavelength scatterer used as a near-field coupler.

2. TE-polarized Bloch surface waves

BSWs are surface modes on top of a 1D photonic crystal [8]. Importantly, when the BSW is TE-polarized, its evanescent tail in the surrounding medium is described by a rotating magnetic field (Fig. 1(a)), instead of a rotating electric field as for the (TM-polarized) surface plasmons or the guided mode of a nanofiber [4,5]. The SAM of the surface wave is thus carried solely by its rotating magnetic field, the electric field shows no helicity.

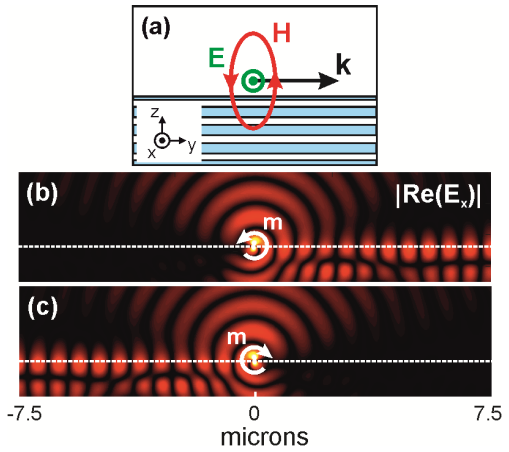


Figure 1: (a) Schematic diagram of the electromagnetic field distribution of a TE-polarized BSW. (b) and (c): FDTD simulations of the coupling of a spinning MD source to a TE-polarized BSW. The absolute value of the real part of the electric field ($|Re(E_x)|$) is represented in false colors. The MD rotates either (b) anti-clockwise or (c) clockwise.

3. Simulations

We numerically studied (by a 2D-FDTD method) the coupling of a single magnetic dipole (MD) to such TE-polarized BSW [7,9]. To this end, the dipole is positioned 10 nm above the top surface of the 1D photonic crystal described above, which radiates light in continuous wave regime at λ = 1.55 μm. The MD rotates in the (yz) plane perpendicular to the surface, i.e., in the helicity plane of the rotating magnetic field of the TE-polarized BSW. Figs. 1(b, c) show the snapshots of the resulting electric field amplitude along the (yz) plane. The MD, whose dipole moment is $\vec{m} \propto \vec{e}_y \pm j * 0.53\vec{e}_z$ ($j = \sqrt{-1}$), rotates either anti-clockwise (Fig. 1(b)) or clockwise (Fig. 1(c)). The portion of the incoupled power that propagates in one of the two possible directions becomes larger than 99,9% of the total incoupled power. These results reveal a tunable unidirectional optical coupling controlled by the magnetic field of light.

4. Experiments

The BSWs are produced on a 1D photonic crystal made of thin layers of silicon oxide and silicon nitride deposited alternately onto a glass wafer. A 600-nm wide and deep groove, used as a light-to-BSW coupler, is milled by FIB over a length of 20 μm. The structure is characterized in the far-field by projecting a slightly focused beam of controlled polarization onto the subwavelength groove, at an incidence angle of about 80° (λ=1.55 μm). The structure is imaged with an objective coupled to an infrared camera. Owing to the light scattering at the free surface of the 1D photonic crystal, a direct measurement of the relative intensities of the surfaces waves excited on both sides of the groove is possible.

We studied the distribution of incoupled power between the two surface waves, as a function of the incident polarization. The polarization is defined by the angle θ between the fast axis of a quarter-wave plate and the transmission axis of a polarizer. When $\theta = k\,90°$, the polarization is linear whereas a circular polarization is achieved for $\theta = 45° + k\,90°$, $k = 0,1,2,3$. For intermediate angles, the polarization is elliptical. We plotted the intensities on both the right and left BSWs (noted S_r and S_l, respectively) as a function of the angle θ (Fig. 2(a)). The experimental plots are represented with circles together with the simulation results obtained with the 3D FDTD method (solid curves).

5. Discussions

Because subwavelength scatterers are optically governed by an electric dipole moment, one may consider that a subwavelength groove on top a 1D photonic crystal interacts with the electric field of an incoming wave to transfer energy to the BSWs. Following this pure electric model, and assuming an incident plane wave, coefficients S_r and S_l defined previously become proportional to the coupling rates:

$$R_i = \alpha \left| \vec{e}_i \cdot \vec{E}_{inc}(\vec{r}_0) \right|^2, \qquad (1)$$

where $i = r, l$ denotes the right and left sides of the groove and α is a constant. $\vec{E}_{inc}(\vec{r}_0)$ is the incident electric field at a single point of coordinate $\vec{r}_0$ along the subwavelength groove. $\vec{e}_i$ is the unit vector in the directions of the electric field of the emerging right and left BSWs.

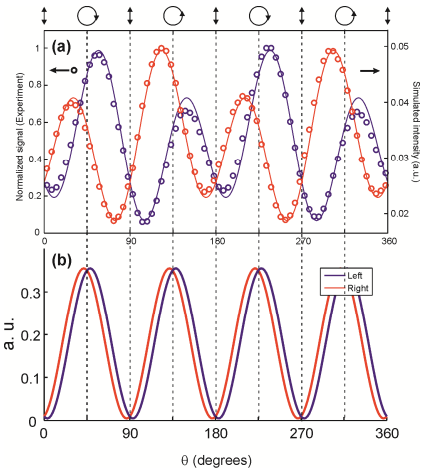


Figure 2: (a) Detected signals (circles) and simulated intensities (FDTD method, dashed lines) on the right (blue) and left (red) BSWs, as a function of the angle. (b) Plots of the coupling rates R_r (blue) and R_l (red) (electric coupling) as a function of the angle θ.

R_r and R_l are described by two 4θ-dependent sinusoids with a relative shift of 8°. The experimental results show two sinusoids, shifted by 30°, whose amplitudes are modulated. We have shown that this helicity-dependent modulation (not predicted with our model of a pure electric coupling) is due to a magnetic spin-orbit interaction of light.

This work is funded by the Collegium SMYLE, the Labex ACTION and the Région BFC. It is supported by the French RENATECH network / FEMTO-ST technological facility.

6. References

[1] Pendry JB. *Phys. Rev. Lett.* 2000; **85**: 3966–3969

[2] Burresi M, *et al. Phys. Rev. Lett.* 2010; **105**: 1–4.

[3] Bliokh KY, *et al*, *Nat. Photonics* 2015; **9**: 796–808.

[4] Petersen J, *et al, Science* 2014; **346**: 67–71.

[5] Rodriguez-Fortuno FJ, *et al, Science* 2013; **340**: 328.

[6] Bliokh KY, Nori F. *Phys. Rev. A* 2012; **85**: 061801.

[7] le Feber B, *et al, Nat. Commun.* 2015; **6**: 6695.

[8] Descrovi E, *et al. Opt. Express* 2008; **16**: 5453–64.

[9] Picardi MF, et al, *Phys. Rev. B* 2017; **95**: 245416

Party-Time Symmetry in Chiral Metamaterials

Maria Kafesaki[1,2], Ioannis Katsantonis[1,2], Sotiris Droulias[1], Eleftherios N. Economou[1,3], Costas M. Soukoulis[1,4]

[1] Institute of Electronic Structure and Laser (IESL), Foundation for Research and Technology Hellas (FORTH), Heraklion, Crete, Greece
[2] Dept. of Materials Science and Technology, University of Crete, Heraklion, Crete, Greece
[3]Department of Physics, University of Crete, Heraklion, Crete, Greece
[4]Ames Lab and Department of Physics and Astronomy, Iowa State, Ames, Iowa, USA
*corresponding author, E-mail: kafesaki@iesl.forth.gr

Abstract

We explore and present the possibility, the conditions and the novel physical phenomena that become possible by combining the quite new concept of Party-Time symmetry with the advanced polarization control capabilities offered by chiral metamaterials. Phenomena like unidirectional invisibility and anisotropic transmission resonances, in general, are demonstrated and analyzed.

1. Introduction

The quite new concept of Parity-Time (PT) symmetry, which was originally introduced in connection with quantum physics [1], denoting systems with PT-symmetric Hamiltonian, i.e. non-Hermitian Hamiltonian commuting with the combined action of Parity and Time operators (such Hamiltonian has the potential, although non-hermitian to have real eigenvalues), was very quickly transferred in optics, where PT-symmetric systems can be more easily realized, by properly combining loss and gain media. Many novel physical phenomena were discovered in optical PT-symmetric systems (and PT-symmetric metamaterials [2]) such as unidirectional transparency, coherent perfect absorption, lasing etc. (see the recent reviews [3,4]).

The combination though of PT-symmetry and chiral metamaterials (i.e. metamaterials lacking any mirror symmetry plane) has been up to recently almost totally unexplored. In this work we (a) explore the possibilities and derive the conditions to achieve PT-symmetric chiral metamaterials, (b) investigate numerically the wave propagation in PT-symmetric chiral systems and identify novel physical phenomena and capabilities that become possible in such systems, (c) properly combine PT-symmetric non-chiral systems with chiral metamaterials, as to achieve novel propagation characteristics, such as direction-dependent optical activity and/or wave ellipticity, offering thus direction-dependent polarization control of an electromagnetic wave.

2. Conditions for PT-symmetric chiral systems

Taking into account the one-dimensional wave equation in chiral metamaterials, transforming it into a form analogous to Schrodinger equation and requiring the corresponding Hamiltonian to commute with the PT operator, we derived the material parameters conditions as to have a PT-symmetric chiral system. These conditions, for wave propagating along z-direction, read as follows:

$$\begin{aligned} \varepsilon(z) &= \varepsilon^*(-z) \\ \mu(z) &= \mu^*(-z) \\ \kappa(z) &= -\kappa^*(-z) \end{aligned} \qquad (1)$$

In Eqs. (1) ε is the electrical permittivity, μ the magnetic permeability and κ the chirality parameter, which connects the electric and magnetic fields in the chiral constitutive equations (see e.g. Ref. [5]). The conditions (1) can be realized in practice by combining loss and gain media of the same thickness (d), as shown Fig. 1.

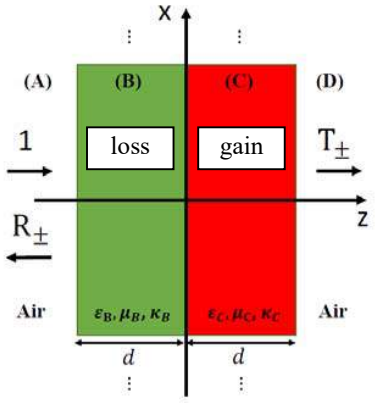
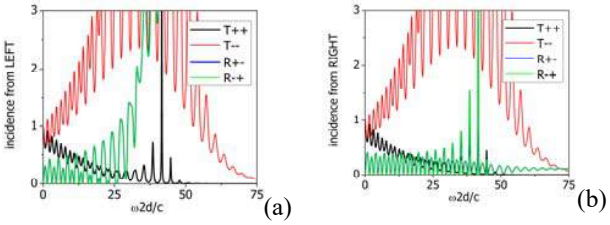


Figure 1: A system for the realization of PT-symmetric chiral structure. The material parameters should obey: $\varepsilon_B = \varepsilon_C^*$, $\mu_B = \mu_C^*$, $\kappa_B = -\kappa_C^*$. The subscripts + and – in the reflection (R) and transmission (T) coefficients denote

respectively right-handed and left-handed circularly polarized waves; these waves are the eigensolutions of the chiral wave equation.

3. Wave transmission through PT-symmetric chiral systems

In PT-symmetric systems, below a critical value of the "potential" of the wave equation, the so-called Exceptional Point (EP), the eigenstates of non-chiral PT-systems are known to be unimodular, despite the presence of gain and loss (above the EP the system is not unitary anymore) [6]. Here, we find that in the presence of chirality the EP is preserved, unaffected by chirality. Hence, phenomena related to the EP location, such as unidirectional invisibility, can be tailored independently of chirality and can be expanded to account for circularly polarized waves. In Fig. 2, the response of a non-magnetic ($\mu_B = \mu_C = 1$) system with $\varepsilon_B = 4+i\,0.4$, $\varepsilon_C = 4-i\,0.4$ and $\kappa_B = -1-i\,0.03$, $\kappa_C = 1-i\,0.03$ is shown (positive/negative imaginary part in the permittivity accounts for loss/gain). The transmission T and reflection R coefficients are shown for circularly polarized input waves, where +/– accounts for Right/Left Circularly Polarized (RCP/LCP) waves. The subscript j in T_{ij}, R_{ij} (i, j: +,–) indicates the incident polarization and the subscript i indicates the output polarization. (For our system $T_{+-} = T_{-+} = R_{++} = R_{--} = 0$.) Depending on the side from which the system is illuminated, different transmitted and reflected powers can be achieved.



(a) (b)

Figure 2: Non-vanishing transmission (T) and reflection (R) coefficients for the system shown in Fig. 1. The first subscript in R and T denotes the handedness of the output wave and the second subscript that of the incident wave. Panel (a) is for incidence from the left (gain) medium and panel (b) from the right (loss) medium. The material parameters of the two media are $\varepsilon_B = 4+i\,0.4$, $\varepsilon_C = 4-i\,0.4$, $\kappa_B = -1-i\,0.03$, $\kappa_C = 1-i\,0.03$ and $\mu_B = \mu_C = 1$.

Due to the symmetries imposed by Eq. (1) on the chirality parameter κ, the real part of κ changes sign across the system. Hence, optical rotation occurring in the first slab is subsequently cancelled out when the wave passes through the second slab, resulting in zero optical activity, regardless of the location of the EP. On the other hand the imaginary part of κ preserves its sign across the system, resulting in circular dichroism (CD) across the whole PT-tunable range, as shown in Figure 3. Since the reflections from both RCP. LCP waves are the same, the CD is expressed via the ellipticity η, which is defined from the difference in transmitted power of the two polarizations as:

$$\eta = \frac{1}{2}\sin^{-1}\left(\frac{|T_{++}|^2 - |T_{--}|^2}{|T_{++}|^2 + |T_{--}|^2}\right) \qquad (2)$$

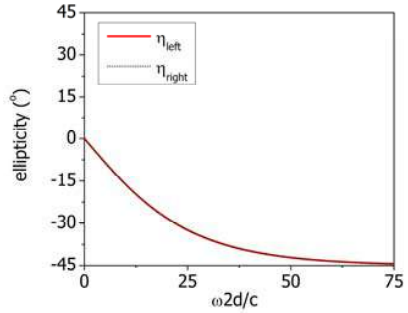


Figure 3: Ellipticity of a wave transmitted through the system described in Figs. 1 and 2.

4. Conclusions

We have examined the concept of Parity Time symmetry in chiral photonic systems. Here, the additional degrees of freedom offered by the chirality parameter expand the interesting phenomena observed in such non-hermitian structures, enabling new possibilities for the wave propagation and polarization control.

Acknowledgements

Authors acknowledge financial support by the EU grants Ultrachiral, Photometa, Visorsurf, as well as by the ELIDEK Foundation via the grant Metamaterials.

References

[1] M. Bender and Boettcher, Real spectra in non-Hermitian Hamiltonians having PT Symmetry, *Phys. Rev. Lett.* 80:5243, 1998.

[2] G. Castaldi, S. Savoia, V. Galdi, A. Alu`, and N. Engheta, PT metamaterials via complex-coordinate transformation optics, *Phys. Rev. Lett.* 110: 173901, 2013.

[3] L. Feng, R. El-Ganainy and L. Ge, Non-Hermitian photonics based on parity–time symmetry, *Nat. Phot.* 11:752, 2017.

[4] R. El-Ganainy, K. G. Makris, M. Khajavikhan, Z. H. Musslimani, S. Rotter and D. N. Christodoulides, Non-Hermitian physics and PT symmetry, *Nat. Phys.* 14:11, 2018.

[5] B. N. Wang, J. F. Zhou, Th. Koschny, M. Kafesaki, and C. M. Soukoulis, Chiral metamaterials: simulations and experiments, *J. Opt. A: Pure and Appl. Opt.* 11: 114003, 2009.

[6] Li Ge, Y. D. Chong and A. D. Stone, Conservation relations and anisotropic transmission resonances in one-dimensional PT-symmetric photonic heterostructures, *Phys. Rev. A* 85: 023802, 2012.

Quantum nonlinear effects in metal-insulator-metal plasmonic nanostructures

Imad Agha[1,2,*], Mallik R. Hussain[1], Andrew Sarangan[1], and Joseph Haus[1,2]

[1]Department of Physics, University of Dayton, Dayton OH 45469
[2]Department of Electro-Optics and Photonics, University of Dayton, Dayton OH 45469
*corresponding author, E-mail: iagha1@udayton.edu

Abstract

In our recent experiments, nonlinear optical harmonics of scattered light from metal-insulator-metal systems were measured to expose an underlying quantum signatures of the electron quantum process. Using atomic layer deposition and self-assembled nanoparticles, we show enhancement, saturation, and quenching of the third harmonic efficiencies, in agreement with the quantum theory. While fundamental in nature, these experiments could potentially lead to new techniques for probing nonlinearities and surface properties of novel materials.

1. Introduction

Current understanding of materials on the nanometer scale has benefitted from an initmate connection between theory and experiment. Intense coherent light interacting with conducting free electron systems has given rise to the field of nonlinaer plasmonics, which has many branches [1]. Recent studies use nonlinear interactions to expose the essential physics at the sub-nanometer scale, which provides further challenges to our understanding of the underlying physics. For instance, the role of nonlocal interactions derived from the hydrodynamics model for free electrons [2-7] and of quantum tunneling effects provide specific predictions of behaviour at new scales. Additionally, the spillout of the electron density at the surface of metals has been exposed as a significant effect.

Our recent studies have concentrated on nonlinear harmonic generation in metal-insulator-metal (MIM) nanostructures as a key phenomenon both at the basic and applied levels. On the fundamental level, the second and third harmonic signals can be used for studying the optical nonlinearity beyond the bulk crystal and classical models, where geometric and quantum effects can play a crucial role. Moreover, in a field where multiple models have been proposed for the efficiency of nonlinear generation, it is crucial to study the efficiency of nonlinear harmonic generation in MIMs as a function of disparate parameters, such as pump power, insulator thickness, particle size, incidence angle, etc. On the applied level, there is a growing interest in MIM nanostructures for broadband detection, nonlinear imaging, as well as photovoltaics. For these applications, nonlinear generation is either directly employed (imaging), or can be used as a tool for indirectly predicting performance (photovoltaics and photodetectors). Therefore, there is a strong interest in measuring and characterizing nonlinear interactions in MIM structures at the nanoscale and under various conditions.

2. Basic principles

A simple, readily achievable geometry is a device with an insulator region sandwiched between two metal plates. This device suffices to illustrate the quantum nature of nanoscale systems. Assume, w is the insulator thickness which possesses both linear and nonlinear conductance terms. Classically, for the case of DC driving E-field, $\sigma \alpha 1/w$ and as $w \rightarrow 0$, $\sigma \rightarrow \infty$ and current density, $J \rightarrow \infty$ (short circuit). For an AC driving field, σ at a certain driving frequency can be estimated using the Drude free electron model. These classical conductances, along with susceptibilities, can be used to explain SH and TH generated due to the surface and bulk nonlinearities. Meanwhile, 'MIM tunnel junctions' are the special kind of capacitors with insulator thickness, w in the nanometer to sub-nanometer range. Quantum mechanically, in this range of w , current density (for both AC and DC driving E-field) is limited by the on-set of tunneling current and, thus, the insulator region acquires new linear and nonlinear conductance terms. These terms we derive are strongly influenced by quantum tunneling, and, as such, formally pertain to the domain of quantum nonlinear plasmonics.

To reconcile theory and experiment, we have implemented an experimental setup that relies on state-of-the art nanofabrication as well as low-light level photodetection. The experimental setup is schematically illustrated in Figure 1. It contains a half-wave plate for polarization control and a focusing lens in the 'input section' before the sample. As well as two lenses (to collimate and refocus the beam), two prisms and a short-pass filter in the 'output'. The SH and TH signals from the bare Au surface were collected and their efficiencies were compared against the values found in the

literature. Then, sets of MI samples with Al_2O_3 or ZnO were fabricated using atomic layer deposition (ALD) on top of planar Au substrates. The SH and TH signals from the MI samples (background signal) are attributed to the surface and bulk nonlinearities. A solution containing Au nanoparticles (AuNPs) was then placed on the MI sample and distributed evenly over the surface by spin coating to produce MIM samples. The samples were dried using N_2 gas. The experiment to extract SH and TH signal from MIM samples repeated the same process used for the MI samples, as described above.

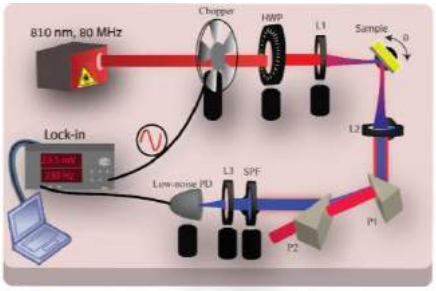
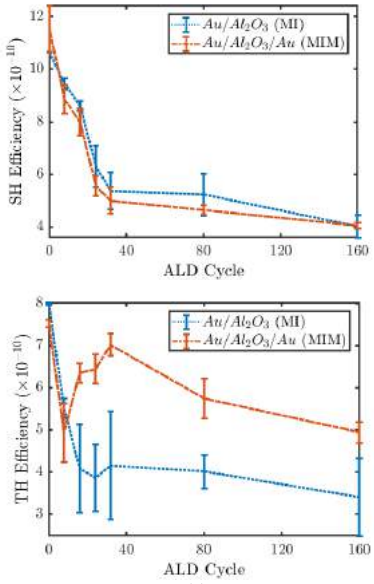


Fig. 1. Experimental setup: HWP: half-wave plate; L1, L2 focusing/collimating lens; (P1, P2): filtering prisms; SPF: short-pass filter; L3: detector lens; PD: photodiode.

3. Discussion



(a)

Figure 2: (top) SH and (bottom) TH efficiencies of Al_2O_3-Au (MI) and $AuAl_2O_3$-Au (MIM) samples.

The results of these recent experiments are in excellent agreement with theory. As shown in Fig. 2 (top), coating the metal substrate with an insulating layer leads to an immediate drop in the SH, due to the metal-dielectric boundary. On the other hand, adding the nanoparticles does not affect the signal, as SH generation is dominated by surface nonlinearities. The TH signal, on the other hand, shows strong enhancements due to the MIM structure, with a maximum near ~ 1 nm thickness of the intermediate insulating layer, after which quenching due ot quantum tunneling rapidly leads to loss of conversion efficiency. The enhancement, taking into accout surface coverage is about 3 orders of magnitude. The result, again, is consistent with our quantum conductivity theory.

Beyond the fundamental question of understanding the role of quantum conductivity in the efficiency of harmonic generation, these experiments yield information of highly applied nature: The SH signal is highly dependent on the interface, and by fitting the data to our model, useful information can be extracted about the quality of the atomic-layer-deposited thin films, that otherwise would be inaccessible. The TH signal, on the other hand, can be used to extract the optical nonlinearity in the limit of quantum tunneling, as well as other useful auxiliary information, such as electron affinities, work functions, and even the film thickness.

4. Conclusions

Our recent experimental results open the window to new studies in both fundamental and applied nonlinear quantum plasmonics. While fairly straightforward in nature, these experiments allow for extracting critical information on metal-insulater thin films in a non-destructive and in-situ fashion.

Acknowledgements

Full support from U.S. Army RDECOM Acquisition Grant No. W911NF-15-1-0178 is acknowledged.

References

[1] M. Kauranen and A. V. Zayats, "Nonlinear Plasmonics," Nature Phot. 6, 737 (2012).

[2] F. J. Garcia de Abajo, "Nonlocal effects in the plasmons of strongly interacting nanoparticles, dimers, and waveguides," J. Phys. Chem. B **112**, 17983 (2008).

[3] J. M. McMahon, S. K. Gray and G. C. Schatz, "Optical Properties of Nanowire Dimers with a Spatially Nonlocal Dielectric Function" Nano Lett. 10, 3473 (2010).

[4] C. Ciraci, R. T. Hill, J. J. Mock, Y. Urzhumov, A. I. Fernandez-Dominguez, S. A. Maier, J. B. Pendry, A. Chilkoti and D. R. Smith, "Probing the ultimate limits of plasmonic enhancement," Science **337**, 1072 (2012).

[5] Y. Luo, A. I. Fernandez-Dominguez, A. Wiener, S. A. Maier, and J. B. Pendry, "Surface Plasmons and Nonlocality: A Simple Model," Phys. Rev. Lett. 111, 93901 (2013).

[6] M. Scalora, D. de Ceglia, M. A. Vincenti and J. W. Haus, "Nonlocal and Quantum Tunneling Contributions to Harmonic Generation in Nanostructures: Electron Cloud Screening Effects," Phys. Rev. A**90**, 013831 (2014).

[7] N. A. Mortensen, S. Raza, M. Wubs, T. Søndergaard and S. I. Bozhevolnyi, "A generalized non-local optical response theory for plasmonic nanostructures," Nature Commun. 5, 3809 (2014).

Frenkel Exciton-Polaritons in Organic Photonics

Boris Fainberg

Faculty of Sciences, Holon Institute of Technology, Holon, Israel
Tel Aviv University, School of Chemistry, Tel Aviv, Israel
*corresponding author, E-mail: fainberg@hit.ac.il

Abstract

We develop a mean-field electron-vibrational theory of Frenkel exciton polaritons in organic dye structures. The theory contains experimentally measured quantities that make it closely related to experiment, and provides a possibility of generalization to a nonlinear regime. Between other things, we explain the additional red shift of the H-aggregate absorption spectra (that are blue-shifted as a whole). We apply the theory to experiment on fraction of a millimeter propagation of Frenkel exciton polaritons in photoexcited organic nanofibers made of thiacyanine dye. A good agreement between theory and experiment is obtained.

1. Introduction

Recently organic dye nanofibers demonstrated long-range Frenkel exciton polariton (EP) propagation at room temperature [1, 2]. EPs are new quasi-particles formed when the coupling between excitons and photons in condensed matter is strong. They combine exciton and photon properties.

The long-range Frenkel EPs are formed in organic dye nanofibers at room temperatures owing to a considerably larger oscillator strength compared to inorganic semiconductors [1]. To realize such long-range propagation, the Frenkel EPs should be stable. Their stability is governed by splitting between two branches of the polariton dispersion, the correct calculation of which is of decisive importance. The latter necessitates the proper description of the Frenkel exciton line shape that is impossible without taking the electron-vibrational interaction into account (especially for H-aggregates, as it took place in experiment [1]). In other words, we needs in an EP theory that takes electron-vibrational interaction into account in a simple way and provides a possibility of generalization to a nonlinear regime.

In this work we develop a mean-field electron-vibrational theory of Frenkel EPs in organic dye structures and apply it to experiment [1]. Our consideration is based on the model of the interaction of strong shaped laser pulse with organic molecules, Refs.[3, 4, 5], extended to the dipole-dipole intermolecular interactions in the condensed matter. These latters results in two options: one mother - two daughters. The first option correctly describes the behaviour of the first moment of molecular spectra in condensed matter, and specifically, the red shift, according to the Clausius-Mossotti Lorentz-Lorentz (CMLL) mechanism [6]. The second option is related to the dramatic modification of molecular spectra in condensed matter due to aggregation of molecules into J- or H-aggregates. The theory contains experimentally measured quantities that makes it closely related to experiment. Between other things, using the first option, we explain the additional red shift of the H-aggregate experimental absorption spectra [7] (that are blue-shifted as a whole, and the lineshape of which is described by the second option).

2. Derivation of equations for dipole-dipole intermolecular interactions in condensed matter

In this section we shall extend equations for vibrationally non-equilibrium populations of molecular electronic states of Refs. [3, 4, 5] to a condensed matter. In this picture we considered a molecule with two electronic states $n = 1$ (ground) and 2 (excited) in a solvent described by the Hamiltonian

$$H_0 = \sum_{n=1}^{2} |n\rangle \left[E_n + W_n(\mathbf{Q})\right] \langle n| \tag{1}$$

where $E_2 > E_1, E_n$ is the energy of state $n, W_n(\mathbf{Q})$ is the adiabatic Hamiltonian of reservoir R (the vibrational subsystems of a molecule and a solvent interacting with the two-level electron system under consideration in state n). The molecule is affected by electromagnetic field $\mathbf{E}(t)$

$$\mathbf{E}(t) = \frac{1}{2}\mathbf{e}\mathcal{E}(t)\exp(-i\omega t) + \text{c.c.} \tag{2}$$

the frequency of which is close to that of the transition $1 \to 2$. Here $\mathcal{E}(t)$ describes the change of the pulse amplitude in time, $\mathbf{e}$ is unit polarization vector.

Since an absorption spectrum of a large molecule in condensed matter consists from overlapping vibronic transitions, we shall single out the contribution from the low frequency (LF) optically active (OA) vibrations $\{\omega_s\}$ to $W_n(\mathbf{Q})$: $W_n(\mathbf{Q}) = W_{nM} + W_{ns}$ where W_{ns} is the sum of the Hamiltonian governing the nuclear degrees of freedom of the solvent in the absence of the solute and LFOA intramolecular vibrations, and the part which describes interactions between the solute and the nuclear degrees of freedom of the solvent; W_{nM} is the Hamiltonian representing

the nuclear degrees of freedom of the high frequency (HF) OA vibrations of the solute molecule.

The influence of the vibrational subsystems of a molecule and a solvent on the electronic transition within the range of definite vibronic transition related to HFOA vibration ($\approx 1000-1500cm^{-1}$) can be described as a modulation of this transition by LFOA vibrations $\{\omega_s\}$ [8]. We suppose that $\hbar\omega_s \ll k_BT$. Thus $\{\omega_s\}$ is an almost classical system. In accordance with the Franck-Condon principle, an optical electronic transition takes place at a fixed nuclear configuration. Therefore, the quantity $u_{1s}(\mathbf{Q}) = W_{2s}(\mathbf{Q}) - W_{1s}(\mathbf{Q}) - \langle W_{2s}(\mathbf{Q}) - W_{1s}(\mathbf{Q})\rangle_1$ representing electron-vibration coupling is the disturbance of nuclear motion under electronic transition where $\langle\rangle_n$ stands for the trace operation over the reservoir variables in the electronic state n. Electronic transition relaxation stimulated by LFOA vibrations is described by the correlation function $K(t) = \langle\alpha(0)\alpha(t)\rangle$ of the corresponding vibrational disturbance with characteristic attenuation time τ_s [9, 10, 11] where $\alpha \equiv -u_{1s}/\hbar$. The analytic solution of the problem under consideration has been obtained due to the presence of a small parameter. For broad vibronic spectra satisfying the "slow modulation" limit, we have $\sigma_{2s}\tau_s^2 \gg 1$ where $\sigma_{2s} = K(0)$ is the LFOA vibration contribution to a second central moment of an absorption spectrum, the half bandwidth of which is related to σ_{2s} as $\Delta\omega_{abs} = 2\sqrt{2\sigma_{2s}\ln 2}$. According to Refs. [10, 11], the following times are characteristic for the time evolution of the system under consideration: $\sigma_{2s}^{-1/2} < T' << \tau_s$, where $\sigma_{2s}^{-1/2}$ and $T' = (\tau_s/\sigma_{2s})^{1/3}$ are the times of reversible and irreversible dephasing of the electronic transition, respectively. The characteristic frequency range of changing the optical transition probability can be evaluated as the inverse T', i.e. $(T')^{-1}$. Thus, one can consider T' as a time of the optical electronic transition. Therefore, the inequality $\tau_s \gg T'$ implies that the optical transition is instantaneous where relation $T'/\tau_s << 1$ plays the role of a small parameter. This made it possible to describe vibrationally non-equilibrium populations in electronic states 1 and 2 $\rho_{jj}(\alpha,t)$ $(j = 1, 2)$ by balance equations for the intense pulse excitation (pulse duration $t_p > T'$) and solve the problem [12, 3, 4, 5]. For brevity, we consider here only one vibronic transition related to a HFOA vibration. Generalization to the case of a number of vibronic transitions will be made below.

The equation under discussion were written for the partial density matrix of the system $\rho_{jj}(\alpha,t)$ that described the system distribution in states 1 and 2 with a given value of α at time t. The complete density matrix averaged over the stochastic process which modulates the system energy levels, is obtained by integration of $\rho_{ij}(\alpha,t)$ over α, $\langle\rho\rangle_{ij}(t) = \int\rho_{ij}(\alpha,t)\,d\alpha$, where quantities $\langle\rho\rangle_{jj}(t)$ are the normalized populations of the corresponding electronic states: $\langle\rho\rangle_{jj}(t) \equiv n_j$, $n_1 + n_2 = 1$. Knowing $\rho_{jj}(\alpha,t)$, one can calculate the positive frequency component of the polarization $\mathbf{P}^{(+)}(t) = N\mathbf{D}_{12}\langle\rho\rangle_{21}(t)$, and the susceptibility $\chi(\Omega,t)$ [3] that enables us to obtain the dielectric function ε due to relation $\varepsilon(\Omega,t) = 1 + 4\pi\chi(\Omega,t)$. Here N is the density of molecules, and $\mathbf{D}_{12}$ is the electronic matrix element of the dipole moment operator. It is worthy to note that magnitude $\varepsilon(\Omega,t)$ does make sense, since it changes in time slowly with respect to dephasing. In other words, $\varepsilon(\Omega,t)$ changes in time slowly with respect to reciprocal characteristic frequency domain of changing $\varepsilon(\Omega)$.

Let us include now the dipole-dipole intermolecular interactions in the condensed matter that are described by Hamiltonian [13, 9] $H_{int} = \hbar\sum\limits_{m\neq n} J_{mn}b_m^\dagger b_n$ where J_{mn} is the resonant exciton coupling. Let us discuss the contribution of Hamiltonian $\hat{H}_{int}$ to the change of $\rho_{ij}(\alpha,t)$ in time. In other words, we shall generalize Eq.(11) of Ref.[3] to the dipole-dipole intermolecular interactions in the condensed matter. Using the Heisenberg equations of motion, one obtains that $\hat{H}_{int}$ gives the following contribution to the change of the expectation value of excitonic operator b_k in time

$$\begin{aligned}\frac{d}{dt}\langle b_k\rangle &\sim \frac{i}{\hbar}\langle[\hat{H}_{int}, b_k]\rangle \equiv \frac{i}{\hbar}Tr([\hat{H}_{int}, b_k]\rho) \\ &= -i\sum_{n\neq k} J_{kn}\langle(\hat{n}_{k1} - \hat{n}_{k2})b_n\rangle \qquad (3)\end{aligned}$$

where $\hat{n}_{k1} = b_kb_k^\dagger$, and $\hat{n}_{k2} = b_k^\dagger b_k$ is the exciton population operator. Considering an assembly of identical molecules, one can write $\langle b_k\rangle = \rho_{21}(\alpha,t)$ [14] if averaging in Eq.(3) is carried out using density matrix $\rho(\alpha,t)$. Consider the expectation value $\langle(\hat{n}_{k1} - \hat{n}_{k21})b_n\rangle = Tr[(\hat{n}_{k1} - \hat{n}_{k2})b_n\rho(\alpha_k,\alpha_n,t)]$ for $n \neq k$ where α_m is the effective vibrational coordinate of a molecule m $(m = k, n)$. Due to fast dephasing (see above), it makes sense to neglect all correlations among different molecules [9], and set $\langle(\hat{n}_{k1} - \hat{n}_{k2})b_n\rangle = \langle\hat{n}_{k1} - \hat{n}_{k2}\rangle\langle b_n\rangle$ and correspondingly $\rho(\alpha_k,\alpha_n,t) \simeq \rho(\alpha_k,t)\,\rho(\alpha_n,t)$, i.e. density matrix $\rho(\alpha_k,\alpha_n,t)$ is factorized. Here from dimension consideration one expectation value should be calculated using density matrix $\rho(\alpha,t)$, and another one - using $\langle\rho\rangle(t) = \int\rho(\alpha,t)\,d\alpha$. Since we sum with respect to n, it would appear reasonable to integrate with respect to α_n. However, this issue is not so simple. The point is that in addition to intramolecular vibrations, there is a contribution of low-frequency intermolecular and solvent coordinates into effective coordinate α. Because of this, partitioning the vibrations into α_k and α_n groups is ambiguous, and the mean-field approximation gives two options

$$p\langle b\rangle\langle\hat{n}_1 - \hat{n}_2\rangle = \begin{pmatrix} p\rho_{21}(\alpha,t)\,\Delta n \\ p\langle\rho_{21}\rangle(t)\Delta'(\alpha,t)\end{pmatrix} \qquad (4)$$

where $\Delta'(\alpha,t) = \rho_{11}(\alpha,t) - \rho_{22}(\alpha,t)$, $p \equiv -\sum_{n\neq k} J_{kn}$, $\Delta n \equiv n_1 - n_2$. Below we shall discuss which option better corresponds to a specific experimental situation. Consideration based on non-equilibrium Green functions (GF) shows that the terms $p\rho_{21}(\alpha,t)$ and $p\langle\rho_{21}\rangle(t)$ on the right-hand-side of Eq.(4) represent the self-energy, $i\Sigma_{21}(t)$, and the terms Δn and $\Delta'(\alpha,t)$ - the difference of the "lesser" GFs for equal time arguments, $\frac{i\hbar}{N}[G_{11}^<(t,t) -$

$G^<_{22}(t,t)]$, that are the density matrix, i.e. $p\langle b\rangle\langle\hat{n}_1-\hat{n}_2\rangle = -\frac{\hbar}{N}\Sigma_{21}(t)[G^<_{11}(t,t)-G^<_{22}(t,t)]$, respectively. In other words, for the first line on the right-hand-side of Eq.(4), the self-energy depends on α and the "lesser" GFs $G^<_{11}(t,t)-G^<_{22}(t,t)$ do not. In contrast, for the second line on the right-hand-side of Eq.(4), the self-energy does not depend on α and the "lesser" GFs $G^<_{11}(\alpha;t,t)-G^<_{22}(\alpha;t,t)$ do depend. This yields $\partial\rho_{21}(\alpha,t)/\partial t \sim -\frac{i\hbar}{N}\Sigma_{21}(t)[G^<_{11}(t,t)-G^<_{22}(t,t)]$. Adding term "$-\frac{i\hbar}{N}\Sigma_{21}(t)[G^<_{11}(t,t)-G^<_{22}(t,t)]$" to the right-hand side of Eq.(9) of Ref.[3] for the non-diagonal density matrix $\tilde{\rho}_{21}(\alpha,t)$

$$\begin{aligned}&\frac{\partial}{\partial t}\tilde{\rho}_{21}(\alpha,t)+i(\omega_{21}-\omega-\alpha)\tilde{\rho}_{21}(\alpha,t)\\ \approx\ &\frac{i}{2\hbar}\mathbf{D}_{21}\cdot\mathbf{E}(t)\Delta'(\alpha,t)-i\frac{\hbar}{N}\tilde{\Sigma}_{21}(t)[G^<_{11}(t,t)\\ &-G^<_{22}(t,t)]\end{aligned}\tag{5}$$

where ω_{21} is the frequency of Franck-Condon transition $1\to 2$, $\tilde{\rho}_{21}=\rho_{21}\exp(i\omega t)$, $\tilde{\Sigma}_{21}=\Sigma_{21}\exp(i\omega t)$, and using the procedure described there, we get the extensions of Eq.(11) of Ref.[3] to the dipole-dipole intermolecular interactions in the condensed matter.

Consider first the case of self-energy depending on effective vibrational coordinate α (the first line on the right-hand-side of Eq.(4)) when the main contribution to α is due to low-frequency intermolecular vibrations and solvent coordinates. Then we obtain Eq.(1) of Ref.[15] (see Appendix 1). In that case, as one can see from Eq.(27) of Appendix 1, the self-energy $i\Sigma_{21}(t)=p\rho_{21}(\alpha,t)$ results in the frequency shift of spectra "$-p\Delta n$" without changing the line shapes. One can show that this approach correctly describes the change of the first moment of optical spectra in the condensed matter. Calculations of p for isotropic medium give $p=\frac{4\pi}{3\hbar}|D_{12}|^2N>0$ [9, 15] that corresponds to a red shift, according to the Clausius-Mossotti Lorentz-Lorentz (CMLL) mechanism [6].

Let us consider the particular case of fast vibrational relaxation. Physically it means that the equilibrium distributions into the electronic states have had time to be set during changing the pulse parameters. In that case one gets the equations for the populations of electronic states $n_{1,2}$ (see Appendix 1)

$$\begin{aligned}\frac{dn_j}{dt} &= (-1)^j\sigma_a(\omega_{21})\tilde{J}(t)\mathrm{Re}[n_1\bar{W}_a(\omega+p\Delta n)-\\ &-n_2\bar{W}_f(\omega+p\Delta n)]-(-1)^j\frac{n_2}{T_1}\end{aligned}\tag{6}$$

where $n_1+n_2=1$, σ_a is the cross section at the maximum of the absorption band, $\tilde{J}(t)$ is the power density of exciting radiation, $\bar{W}_{a(f)}(\omega)=W_{a(f)}(\omega)/F_{a,\max}$, $F_{a,\max}$ is the maximum of the absorption line (see below), and we added term "$(-1)^j n_2/T_1$" taking the lifetime T_1 of the excited state into account. Here "$-iW_{a(f)}(\omega)$" is the line-shape function of a monomer molecule for the absorption (fluorescence) for fast vibronic relaxation. In the case under consideration, it is related to the line-shape function, $\int d\alpha\Delta'(\alpha,t)\zeta(\omega-\omega_{21}+\alpha)/\pi$, by formula

$$\begin{aligned}&\int_{-\infty}^{\infty}d\alpha\Delta'(\alpha,t)\zeta(\omega-\omega_{21}+\alpha)/\pi\\ =\ &-i[n_1(t)W_a(\omega)-n_2(t)W_f(\omega)]\end{aligned}\tag{7}$$

where $\zeta(\omega-\omega_{21}+\alpha)=\frac{P}{\omega-\omega_{21}+\alpha}-i\pi\delta(\omega-\omega_{21}+\alpha)$, P is the symbol of the principal value.

The imaginary part of "$-iW_{a(f)}(\omega)$" with sign minus, $-\mathrm{Im}[-iW_{a(f)}(\omega)]=\mathrm{Re}W_{a(f)}(\omega)\equiv F_{a(f)}(\omega)$, describes the absorption (fluorescence) lineshapes of a monomer molecule, and the real part, $\mathrm{Re}[-iW_{a(f)}(\omega)]=\mathrm{Im}W_{a(f)}(\omega)$, describes the corresponding refraction spectra. For the "slow modulation" limit considered in the beginning of this section, quantities $W_{a(f)}(\omega)$ and $F_{a(f)}(\omega)$ are given by Eqs. (30) and (31), respectively, of Appendix 1.

2.1. Population difference ("lesser" GFs) depending on effective vibrational coordinate α

Consider now the case when the population difference depends on effective vibrational coordinate α (the second line on the right-hand-side of Eq.(4); the main contribution to α is due to intramolecular vibrations). Then using Eq.(24) of Appendix 1 and Eq.(5), we arrive to equation

$$\begin{aligned}\frac{\partial\rho_{jj}(\alpha,t)}{\partial t} &= L_{jj}\rho_{jj}(\alpha,t)+\frac{(-1)^j\pi}{2}\Delta'(\alpha,t)\\ &\times\delta(\omega_{21}-\omega-\alpha)|\Omega_{eff}(t)|^2\end{aligned}\tag{8}$$

where $\Omega_{eff}(t)=\Omega_R(t)+2p\langle\rho_{21}\rangle(t)=\Omega_R(t)+2\Sigma_{21}(t)$ is the effective Rabi frequency that can be written as

$$\Omega_{eff}(t)=\frac{\Omega_R(t)}{1+p\int d\alpha\Delta'(\alpha,t)\zeta(\omega-\omega_{21}+\alpha)},\tag{9}$$

Here $\Omega_R(t)=(\mathbf{D}_{12}\cdot\mathbf{e})\mathcal{E}(t)/\hbar$ is the Rabi frequency, operator L_{jj} describes the diffusion with respect to the coordinate α in the corresponding effective parabolic potential, Eq.(25) of Appendix 1.

One can see that in contrast to the self-energy depending on effective vibrational coordinate α (see above), here the self-energy $\Sigma_{21}(t)=-ip\langle\rho_{21}\rangle(t)$ (the second line on the right-hand-side of Eq.(4)) results in the change of both the frequency shift of spectra and their lineshapes. In that case considering the dense collection of molecules under the action of one more (weak) field $\tilde{\mathbf{E}}(t)=\frac{1}{2}\mathbf{e}\tilde{\mathcal{E}}(t)\exp(-i\Omega t)+\text{c.c.}$, one can calculate the susceptibility $\chi(\Omega,t)=P^+(\Omega,t)/(\tilde{\mathcal{E}}(t)/2)$ related to the positive frequency component of the polarization $\mathbf{P}^+=N\mathbf{D}_{12}\langle\rho_{21}\rangle(t)$, and the dielectric function $\varepsilon(\Omega)=\varepsilon_0(1+4\pi\chi(\Omega))$ [16] that in our case is given by

$$\varepsilon(\Omega,t)=\varepsilon_0[1-\frac{q\int d\alpha\Delta'(\alpha,t)\zeta(\Omega-\omega_{21}+\alpha)}{1+p\int d\alpha\Delta'(\alpha,t)\zeta(\Omega-\omega_{21}+\alpha)}]\tag{10}$$

Here $\varepsilon_0 = n_0^2$, n_0 is the background refractive index of the medium, $q \equiv 4\pi\eta\frac{N|\mathbf{D}_{12}|^2}{\hbar}$, $\eta = 1/3$ for randomly oriented molecules, and $\eta = 1$ for the molecules of the same orientation.

2.1.1. Line-shape in the fast vibrational relaxation limit

Below we shall see that the approximation based on the self-energy integrated on the effective vibrational coordinate (the second line on the right-hand-side of Eq.(4)) correctly describe the exciton spectra. In that case the fast vibrational relaxation limit should be based on the equilibrium state of the collective system (molecules coupled by the dipole-dipole interaction). However, the exciton wave function in the ground state is the product of the wave functions of monomers [13] (no intermolecular interactions). Because of this, for the absorption of weak radiation, one should put $j = 1$ and $\Delta'(\alpha, t) = \Delta'^{(0)}(\alpha)$ in Eqs. (8) and (9) where $\Delta'^{(0)}(\alpha) = \rho_{11}^{(0)}(\alpha) = (2\pi\sigma_{2s})^{-1/2}\exp[-\alpha^2/(2\sigma_{2s})]$ is the equilibrium value of $\Delta'(\alpha, t)$ corresponding to the equilibrium value for a monomer in the ground state, and we retained only terms that are proportional to $|\Omega_R(t)|^2$ on the right-hand side of Eq.(8). The next procedure is similar to that used for obtaining Eq.(6) (see Appendix 1). Integrating Eq.(8) using Green function [12], we obtain an integral equation. Then integrating both sides of the obtained integral equation with respect to α, and bearing in mind Eq.(7), we get

$$\frac{dn_1}{dt} = -\sigma_a(\omega_{21})\tilde{J}(t)\mathrm{Re}\frac{\bar{W}_a(\omega)}{1 - ip\pi W_a(\omega)} + \frac{n_2}{T_1} \qquad (11)$$

where the term $\mathrm{Re}\{\bar{W}_a(\omega)/[1 - ip\pi W_a(\omega)]\}$ describes the absorption spectrum of molecules susceptible to the dipole-dipole intermolecular interactions expressed through their monomer spectra W_a. The calculation results of the absorption spectra of J-aggregates according to the expression $\mathrm{Re}\{W_a(\omega)/[1 - ip\pi W_a(\omega)]\}$ are given in Appendix 2.

Touching on how Eq.(11) can be extended to stronger radiation, one should recognize two limit cases. In the first case an optical transitions occur near zero quasi-momentum $\mathbf{k} \approx 0$. After the light absorption a quasi-equilibrium is established. However, the luminescence should be resonant to the absorption line due to the quasi-momentum conservation [13]. This case is realized for J-aggregates [17]. The second case is characterized by a strong electron-vibrational interaction when the relaxation to the equilibrium vibrational configuration in the excited state occurs before the excitation transfers to the neighboring molecule [18]. It seems such a case is realized for the H-aggregates of thiacyanine (TC) dye molecules where a large Stokes shift between absorption and photoluminescence spectra of the TC aggregates was observed in the aqueous solution [19, 20]. Since the description of the H-aggregate spectra necessitates including also the HFOA vibrations and the mechanism described by Eq.(6) (see Section 3), the extension to stronger radiation for H-aggregates will be carried out elsewhere.

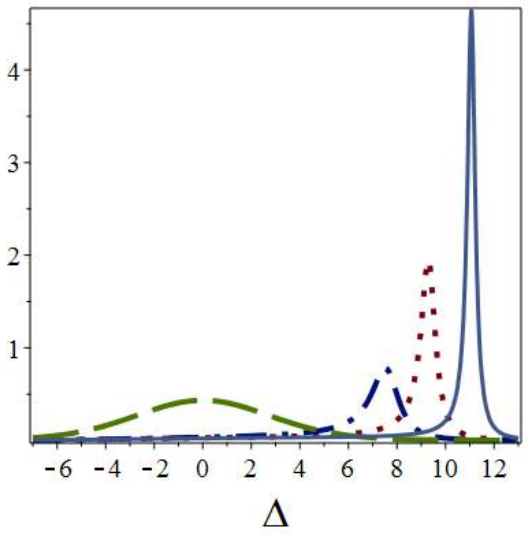


Figure 1: Nonlinear absorption spectra (in terms of τ_s/π) of the J-aggregate for $\Delta n = 1$ (solid line), $\Delta n = 0.8$ (dotted line), $\Delta n = 0.6$ (dash dotted line), and the corresponding monomer absorption spectrum (dashed line) for $\sqrt{\sigma_{2s}}\tau_s = 3.16$ and $p\tau_s = 10$. Dimensionless parameter is $\Delta = \tau_s(\omega_{21} - \omega)$, $\tau_s/(2T_1) << 1$.

For the first case one can put $\Delta'(\alpha, t) = \Delta n\,(2\pi\sigma_{2s})^{-1/2}\exp[-\alpha^2/(2\sigma_{2s})]$ in Eqs. (8) and (9), and we obtain the extension of Eq.(11) to stronger radiation

$$\frac{dn_1}{dt} = -\sigma_a(\omega_{21})\tilde{J}(t)\mathrm{Re}\frac{\Delta n\bar{W}_a(\omega)}{1 - ip\pi\Delta n W_a(\omega)} + \frac{n_2}{T_1} \qquad (12)$$

In Eq.(12) the probability of the light induced transitions may be of the same order of magnitude as T_1^{-1}, however, the first should be smaller than the reciprocal dephasing time.

The term "$\mathrm{Re}\frac{\Delta n\bar{W}_a(\omega)}{1-ip\pi\Delta n W_a(\omega)}$" on the right-hand-side of Eq.(12) describes a nonlinear absorption. In particular case of weak radiation when $\Delta n = 1$, this term recovers the coherent exciton scattering (CES) approximation [21, 7, 22]. The latter is well suited to describing the absorption spectrum lineshape for J-aggregates using their monomer spectra and the intermolecular interaction strength that is a fitting parameter. As to the absorption spectra of H-aggregates, the CES approximation describes correctly only their lineshapes. The positions of the H-aggregate spectra calculated in the CES approximation should be corrected [7]. This issue will be considered in more details in Section 3, since we apply our theory to the EPs in H-aggregates of TC dye molecules below.

Fig.1 shows the calculation results of the nonlinear absorption spectra of J-aggregates according to the expression $\mathrm{Re}\{\Delta n W_a(\omega)/[1 - ip\pi\Delta n W_a(\omega)]\}$ on the right-hand-side

of Eq.(12) for different values of the population difference Δn. The vibrationally equilibrium monomer absorption spectrum $W_a(\omega)$ was calculated using Eq.(36) of Appendix 2. The spectra of Fig.1 demonstrate the saturation effect accompanied by the blue shift of the spectra when the population difference Δn diminishes. Such a frequency shift arises also in the many-body theory of 1D Frenkel excitons [23] that does not consider the vibrations. In contrast, our theory does take the vibrations into account that enables us to correctly describe the lineshape of J-aggregates.

3. Proper description of the lineshape and the frequency shift of absorption spectra of H-aggregates

Applying expression $\mathrm{Re}\{W_a(\omega)/[1-ip\pi W_a(\omega)]\}$ (see Section 2.1.1) to the description of the absorption of H-aggregates, one should take into account also HFOA intramolecular vibrations, in addition to the LFOA vibrations $\{\omega_s\}$ under consideration in our paper. The intramolecular relaxation related to the OAHF vibrations takes place in a time shorter than intermolecular relaxation of the low frequency system $\{\omega_s\}$ [4, 24, 5]. Therefore, we can consider the density matrix averaged with respect to the intramolecular OAHF vibrations: $\rho_{ns}(t) = Tr_M \rho_{nn}(t)$ where the total density matrix $\rho_{nn}(t)$ is factorized, $\rho_{nn}(t) = \rho_{nM}\rho_{ns}(t)$, and $\rho_{nM} = \exp(-\beta W_{nM})/Tr_M \exp(-\beta W_{nM})$ is the equilibrium density matrix of the intramolecular OAHF vibrations. Here Tr_M denotes the operation of taking a trace over the variables of the intramolecular OAHF vibrations, $\beta = 1/(k_B T)$. Using density matrix ρ_{ns}, one can obtain an equation akin to Eq.(11) where the monomer spectrum is given by

$$W_a(\omega) = \frac{\tau_s}{\pi}\exp(-S_0)\sum_{k=0}^{\infty}\frac{S_0^k}{k!}\frac{\Phi(1,1+x_{ak};\sigma_{2s}\tau_s^2)}{x_{ak}} \tag{13}$$

where $x_{ak} = \tau_s/(2T_1) + \sigma_{2s}\tau_s^2 + i\tau_s(\omega_{21} - \omega + k\omega_0)$. Eq.(13) is derived in Appendix 3 for the model of one normal high frequency intramolecular oscillator of frequency ω_0 whose equilibrium position is shifted under electronic transition (S_0 is the dimensionless parameter of the shift). Here $\Phi(1,1+x_a;\sigma_{2s}\tau_s^2)$ is a confluent hypergeometric function [25] the parameters of which are defined in Appendix 2.

As we mentioned above, expression $\mathrm{Re}\{W_a(\omega)/[1-ip\pi W_a(\omega)]\}$ corresponds to the CES approximation that describes well the shape of the absorption spectra of H-aggregates. However, the spectra calculated in the CES approximation are blue shifted with respect to experimental ones [7]. To resolve the problem, the authors of Ref.[7] empirically introduced additional red shift that can be substantiated in our more general theory. Indeed, let us write down Eq.(5) when both the self-energy ($\sim \tilde{\rho}_{21}$) and the population difference depend on the effective vibrational coordinate

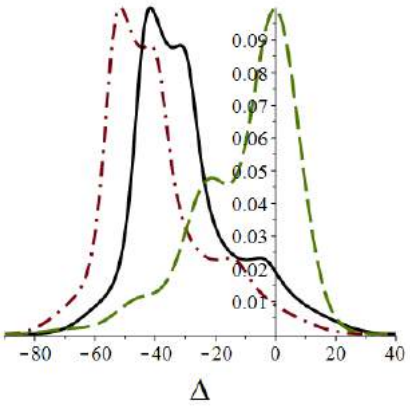


Figure 2: Absorption spectra (in terms of τ_s/π) of the H-aggregate (solid line), the corresponding monomer (dash line) and the H-aggregate without the contribution of the CMLL mechanism (dash dot line) for $p_1 = 500\ cm^{-1}$ and $p_2 = -1500\ cm^{-1}$ Dimensionless parameter is $\Delta = \tau_s(\omega_{21} - \omega)$.

$$\begin{aligned}&\frac{\partial}{\partial t}\tilde{\rho}_{21}(\alpha,t) + i(\omega_{21} - \omega - p_1 - \alpha)\tilde{\rho}_{21}(\alpha,t)\\ &= i[\frac{\mathbf{D}_{21}\cdot\mathbf{E}(t)}{2\hbar} + p_2\int d\alpha\tilde{\rho}_{21}(\alpha,t)]\rho_{11}^{(0)}(\alpha)\end{aligned} \tag{14}$$

Using the procedure described in Ref.[3], we get an equation similar to Eq. (8) (together with Eq.(9)) with the only difference that ω_{21} should be replaced by $\omega_{21} - p_1$, and p - by p_2

$$\begin{aligned}\frac{\partial\rho_{11}(\alpha,t)}{\partial t} &= \frac{-\frac{\pi}{2}\rho_{11}^{(0)}(\alpha)|\Omega_R(t)|^2\delta(\omega_{21} - \omega - p_1 - \alpha)}{\left|1 + p_2\int d\alpha\rho_{11}^{(0)}(\alpha)\zeta(\omega + p_1 - \omega_{21} + \alpha)\right|^2}\\ &\quad + L_{11}\rho_{11}(\alpha,t)\end{aligned} \tag{15}$$

Then similar to Eq.(11), we obtain

$$\frac{dn_1}{dt} = -\sigma_a(\omega_{21})\tilde{J}(t)\mathrm{Re}\frac{\bar{W}_a(\omega + p_1)}{1 - ip_2\pi W_a(\omega + p_1)} + \frac{n_2}{T_1} \tag{16}$$

where the term $\mathrm{Re}\{\bar{W}_a(\omega + p_1)/[1 - ip_2\pi W_a(\omega + p_1)]\}$ describes the absorption spectrum of molecules susceptible to the dipole-dipole intermolecular interactions expressed through their monomer spectra $W_a(\omega + p_1)$, Eq.(13). Fig.2 shows the calculation results of the absorption spectrum of an H-aggregate according to the expression $\mathrm{Re}\{W_a(\omega + p_1)/[1 - ip_2\pi W_a(\omega + p_1)]\}$ on the right-hand side of Eq.(16) and Eq.(13) (solid line), and its comparison with the monomer spectrum $\mathrm{Re}W_a(\omega)$ (dash line) and the spectrum of H-aggregate, $\mathrm{Re}\{W_a(\omega)/[1 - ip_2\pi W_a(\omega)]\}$, calculated without the contribution of the CMLL mechanism (dash dot line). The values of parameters are found by fitting the experimental spectrum of the linear absorption of

LD690 in methanol [5]: $\tau_s = 10^{-13}s$, $k_BT = 210\ cm^{-1}$, $\hbar\omega_{st}/(2k_BT) = 1.99$, $S_0 = 0.454$, $\omega_0 = 1130\ cm^{-1}$, $\sigma_{2s} = \omega_{st}k_BT/\hbar$. The spectra presented in Fig.2 manifest that though the shape of the H-aggregate spectrum is fully described by the self-energy not depending on the effective vibrational coordinate, its position (including the additional red shift of the experimental spectra of H-aggregates [7]) may be correctly described only taking the CMLL mechanism into account. In other words, our more general theory enables us to describe both the shape and the position of the experimental spectra of H-aggregates due to the self-energy and the population difference ("lesser" GFs) both depending on the effective vibrational coordinate that leads to their frequency dependence. This can be understood as follows. The frequency dependent "lesser" GFs corresponding to the CES approximation describe well the spectral shapes of H-aggregates. The latters can interact with each other by the dipole-dipole interaction leading to the CMLL red shift that is described by the frequency dependent self-energy.

In the case under consideration Eq.(10) for the dielectric function becomes

$$\varepsilon(\omega) = \varepsilon_0[1 + \frac{iq\pi W_a(\omega + p_1)}{1 - i\pi p_2 W_a(\omega + p_1)}] \qquad (17)$$

where we put $\int_{-\infty}^{\infty} d\alpha \Delta'^{(0)}(\alpha)\,\zeta(\omega - \omega_{21} + p_1 + \alpha) = -i\pi W_a(\omega + p_1)$ for the vibrational equilibrium in the ground state.

4. Application to the exciton-polariton experiment

The theory developed in Section 3 properly describes both the lineshape and the frequency shift of the absorption spectra of H-aggregates. Therefore, it can be applied to the experiment on fraction of a millimeter propagation of EPs in photoexcited fiber-shaped H-aggregates of TC dye at room temperature [1].

The transverse eigenmodes of the medium are obtained from the dispersion equation [16]

$$c^2k^2(\omega) = \omega^2\varepsilon(\omega) \qquad (18)$$

where dielectric function $\varepsilon(\omega)$ is given by Eq.(17) and depends on the monomer spectra W_a.

Fig. 3 shows the experimental absorption lineshape of TC monomer solution prepared by dissolving TC dye in methanol [19] (top), and its theoretical description by ReW_a, Eq.(13), (bottom). Good agreement is observed with the values of parameters $\omega_{21} = 23810\ cm^{-1}$, $1/\tau_s = 75\ cm^{-1}$, $\omega_0\tau_s = 20$, $S_0 = 0.454$, $\sigma_{2s}\tau_s^2 = 80$ obtained by comparison between experimental and theoretical curves.

The monomer spectrum found, W_a, enables us to calculate the aggregate absorption spectrum according to the formula Re$\{W_a(\omega+p_1)/[1-ip_2\pi W_a(\omega+p_1)]\}$ (see Eqs.(16) and (17)) shown in Fig.4. Again good agreement between theoretical and experimental spectra is observed with the values of parameters $p_1\tau_s = 4$, $p_2\tau_s = -7$ obtained by comparison between experimental and theoretical curves.

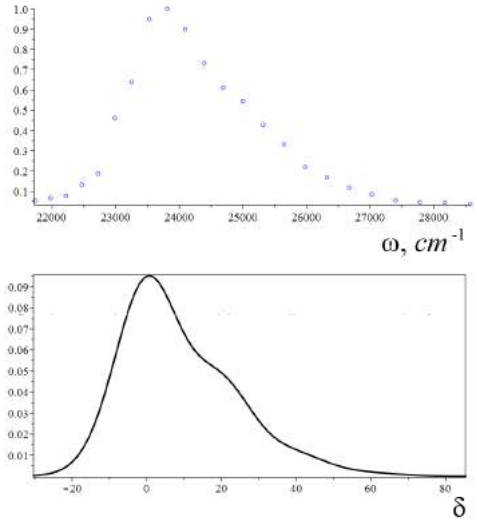


Figure 3: Experimental absorption lineshape of TC monomer solution prepared by dissolving TC dye in methanol [19] (top), and its theoretical description (in terms of τ_s/π) by ReW_a, Eq.(13), (bottom). Dimensionless parameter is $\delta = -\Delta = \tau_s(\omega - \omega_{21})$.

We did not make additional fitting since experimental absorption spectra of TC aggregates and monomers were measured in different solvents [19] (see caption to Fig.4).

4.1. Polariton dispersion

Let us analyze Eq.(18) where the dielectric function is determined by Eq.(17) and depends on the aggregate spectrum, $W_a(\omega + p_1)/[1 - ip_2\pi W_a(\omega + p_1)]$. The parameters of the aggregate spectrum were found above. In order to satisfy Eq.(18), the wave number k should be complex $k = k' + ik''$. Then using Eq.(18), we get for the real and imaginary part of k

$$k'\frac{c}{n_0} = \omega\mathrm{Re}\sqrt{1 + i\pi q\frac{W_a(\omega + p_1)}{1 - i\pi p_2 W_a(\omega + p_1)}} \qquad (19)$$

and

$$k''\frac{c}{n_0} = \omega\mathrm{Im}\sqrt{1 + i\pi q\frac{W_a(\omega + p_1)}{1 - i\pi p_2 W_a(\omega + p_1)}}, \qquad (20)$$

respectively. Fig.5 shows the Frenkel EP dispersion calculated using Eqs.(19) and (20).

To give physical insight into the Frenkel EP dispersion, we shall calculate also the dispersion outside the resonance when $k'' \approx 0$. In that case Eq.(18) leads to the undamped polariton modes

$$k'\frac{c}{n_0} \approx \omega\sqrt{1 - \pi q\mathrm{Im}\frac{W_a(\omega + p_1)}{1 - i\pi p_2 W_a(\omega + p_1)}} \qquad (21)$$

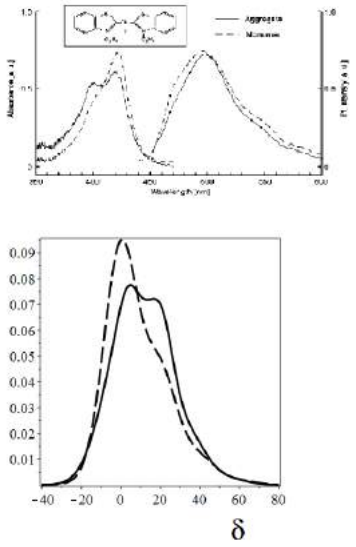


Figure 4: Experimental absorption and photoluminescence spectra of TC aggregates and monomers [19] (top), and theoretical description of aggregate absorption (in terms of τ_s/π) (bottom). In the top solid curve represents spectra of the aqueous solution containing TC aggregates; dashed curve, spectra of a monomer solution prepared by dissolving TC dye in methanol. In the bottom solid curve represents the spectrum of an aggregate; dashed curve - spectrum of a monomer. Dimensionless parameter $\delta = -\Delta = \tau_s(\omega - \omega_{21})$ increases when the wavelength decreases.

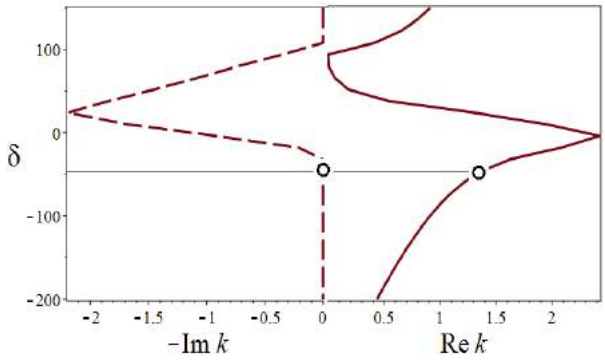


Figure 5: Frenkel EP dispersion for real (solid line) and imaginary (dashed line) part of the wave number k calculated with Eqs.(19) and (20), respectively, when $q\tau_s = 84$. Other parameters are identical to those of the bottom of Fig.3. k is in units of $c/(\omega_{21}n_0)$. Dimensionless parameter is $\delta = \tau_s(\omega - \omega_{21})$. Circles show the position of the fluorescence spectrum of a nanofiber.

Taking spectrum $W_a(\omega)$ to be centered on $\omega = \omega_a$ and to have a finite width Γ, it is clear from the dispersion relation [22] that $W_a(\omega) \sim (i/\pi)/(\omega - \omega_a)$ for $|\omega - \omega_a| >> \Gamma$, and we get

$$k'\frac{c}{n_0} \approx \omega\sqrt{\frac{\omega - (\omega_a - p_1 - p_2) - q}{\omega - (\omega_a - p_1 - p_2)}} \qquad (22)$$

Eq.(22) leads to two branches of the polariton dispersion shown in Fig.5, namely, the lower branch for $\omega < \omega_a - p_1 - p_2$, and the upper branch for $\omega > \omega_a - p_1 - p_2$. For $\omega \to \omega_a - p_1 - p_2$ the wavenumber diverges, $k' \to \infty$. No solution of Eq.(22) exists for frequences between $\omega_a - p_1 - p_2$ and $(\omega_a - p_1 - p_2) + q$. In other words, there is a forbidden gap between $\omega_a - p_1 - p_2$ and $(\omega_a - p_1 - p_2) + q$ separating the lower and upper polariton branch. However, in the gap range more precise formulas, Eqs.(19) and (20), should be used, and the polariton dispersion shows the leaky part in the splitting range between two branches, Fig.5.

From Eq.(22) we get for low frequencies, $\omega << \omega_a - p_1 - p_2$, a photon-like dispersion

$$\omega \simeq \frac{ck'}{n_0\sqrt{1 + q/(\omega_a - p_1 - p_2)}} \qquad (23)$$

with a light velocity smaller than c/n_0.

From the above discussion, it is evident that parameter $q = \frac{4\pi}{\hbar}\eta N|\mathbf{D}_{12}|^2$ defines the separation between the lower and upper polariton branch. For the molecules of the same orientation ($\eta = 1$) that corresponds to experiment [1], and $D_{12} \sim 10^{-17} CGSE$, $N = 10^{21}\ cm^{-3}$, one obtains the evaluation $q \simeq 6322\ cm^{-1}$. This value agrees with the measurements of Ref.[1]. The position of the fluorescence spectrum of a nanofiber that is in the range of ~ 2.5 eV is shown as circles in Fig.5. One can see that it is located in the range where $\mathrm{Im}k \approx 0$, and it is out of the splitting range under discussion. That is why the fluorescence was amplified well in experiment [1].

Fig.6 shows the real part of the group refraction index $n_g(\omega) = n(\omega) + \omega dn(\omega)/d\omega$ as a function of frequency where $n(\omega) = (c/\omega)k(\omega)$ is the phase refraction index. The curve of Fig.6 agrees with the experimental curve of Fig.2a of Ref.[1]. Both curves give the same value $\mathrm{Re}n_g \approx 7$ at the position of the fluorescence spectrum of a nanofiber (~ 2.5 eV).

5. Conclusion

In this work we have developed a mean-field electron-vibrational theory of Frenkel EPs in organic dye structures. Our consideration is based on the model of the interaction of strong shaped laser pulse with organic molecules, Refs.[3, 4, 5], extended to the dipole-dipole intermolecular interactions in the condensed matter. We show that such a generalization can describe both a red shift of the resonance frequency of isolated molecules, according to the CMLL mechanism [6], and the wide variations of their spectra related to the aggregation of molecules into J- or H-aggregates. In particular case of weak radiation we recover

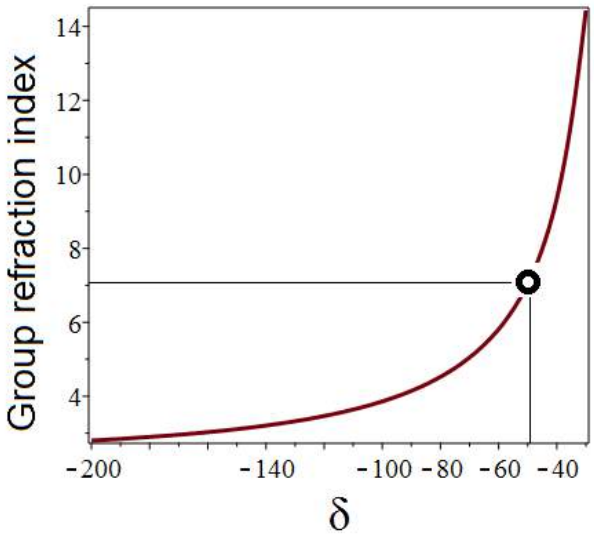


Figure 6: Real part of the group refraction index n_g for $n_0 = 1.5$. Other parameters are identical to those of Figs. 3 and 5. Circle shows the position of the fluorescence spectrum of a nanofiber. Parameter $\delta = \tau_s(\omega - \omega_{21})$.

the CES approximation [21, 7, 22]. We show that the experimental absorption spectra of H-aggregates may be correctly described only if one takes both mechanisms into account. Our theory contains experimentally measured quantities that makes it closely related to experiment, and provides a possibility of generalization to a nonlinear regime.

We have applied the theory to experiment on fraction of a millimeter propagation of Frenkel EPs in photoexcited organic nanofibers made of thiacyanine dye [1]. A good agreement between theory and experiment is obtained. The theory can be also applied to Frenkel EPs in organic microcavities [26] and to plexcitonics [27].

Acknowledgement

I thank G. Rosenman and B. Apter who attracted my attention to Ref. [1].

6. Appendix 1

In the presence of the dipole-dipole intermolecular interactions in the condensed matter Eq.(6) of Ref. [3] describing vibrationally non-equilibrium populations in electronic states $j = 1, 2$ for the exponential correlation function $K(t)/K(0) \equiv S(t) = \exp(-|t|/\tau_s)$ can be written as

$$\frac{\partial}{\partial t}\rho_{jj}(\alpha,t) = \frac{-i}{\hbar}[H_0(\alpha) + H_{int} - \mathbf{D}\cdot\mathbf{E}(t), \rho(\alpha,t)]_{jj} + L_{jj}\rho_{jj}(\alpha,t) \quad (24)$$

where $j = 1, 2$, and we added the term H_{int} into the Hamiltonian; the operator L_{jj} is determined by the equation:

$$L_{jj} = \tau_s^{-1}[1 + (\alpha - \delta_{j2}\omega_{st})\frac{\partial}{\partial(\alpha - \delta_{j2}\omega_{st})} + \sigma_{2s}\frac{\partial^2}{\partial(\alpha - \delta_{j2}\omega_{st})^2}], \quad (25)$$

describes the diffusion with respect to the coordinate α in the corresponding effective parabolic potential $U_j(\alpha)$, δ_{ij} is the Kronecker delta, $\omega_{st} = \beta\hbar\sigma_{2s}$ is the Stokes shift of the equilibrium absorption and luminescence spectra, $\beta = 1/k_BT$. In the absence of the dipole-dipole intermolecular interactions in the condensed matter, H_{int}, Eq.(24) is reduced to Eq.(11) of Ref.[3].

Consider first the case of self-energy depending on effective vibrational coordinate α (the first line on the right-hand-side of Eq.(4)) when the main contribution to α is due to low-frequency intermolecular vibrations and solvent coordinates. Then Eq.(5) becomes

$$\frac{\partial}{\partial t}\tilde{\rho}_{21}(\alpha,t) + i(\omega_{21} - \omega - p\Delta n - \alpha)\tilde{\rho}_{21}(\alpha,t) \approx \frac{i}{2\hbar}\mathbf{D}_{21}\cdot\mathbf{E}(t)\Delta'(\alpha,t) \quad (26)$$

Solving Eq.(26) for $\tilde{\rho}_{21}(\alpha,t)$ and substituting for the corresponding expression in Eq.(24), we we arrive to equation

$$\frac{\partial\rho_{jj}(\alpha,t)}{\partial t} = L_{jj}\rho_{jj}(\alpha,t) + \frac{(-1)^j\pi}{2}\Delta'(\alpha,t)|\Omega_R(t)|^2 \times \times\delta[\omega_{21} - p\Delta n - \omega - \alpha] \quad (27)$$

that was obtained in Ref.[15]. Here ω_{21} is the frequency of Franck-Condon transition $1 \to 2$, $\Omega_R(t) = (\mathbf{D}_{12}\cdot\mathbf{e})\mathcal{E}(t)/\hbar$ is the Rabi frequency, $\mathbf{D}_{12}$ is the electronic matrix element of the dipole moment operator. Integration of Eq.(27) is achieved by the Green's function [12]. Then integrating both sides of the obtained integral equation with respect to α, we get

$$\frac{dn_j}{dt} = (-1)^j\frac{\pi}{2}|\Omega_R(t)|^2\Delta'(\omega_{21} - p\Delta n - \omega, t) \quad (28)$$

Let us consider the particular case of fast vibrational relaxation when one can put the normalized correlation function $S(t-t') \equiv K(t-t')/K(0)$ equal to zero. Physically it means that the equilibrium distributions into the electronic states have had time to be set during changing the pulse parameters. Bearing in mind that for fast vibronic relaxation

$$\Delta'(\alpha,t) = \frac{n_1(t)}{(2\pi\sigma_{2s})^{1/2}}\exp(-\frac{\alpha^2}{2\sigma_{2s}}) - \frac{n_2(t)}{(2\pi\sigma_{2s})^{1/2}}\exp[-\frac{(\alpha-\omega_{st})^2}{2\sigma_{2s}}], \quad (29)$$

substituting the last equation into Eq.(28), one gets Eq.(6) of the main text. The latter contains the line-shape functions

of a monomer molecule for the absorption (fluorescence) for fast vibronic relaxation, "$-iW_{a(f)}(\omega)$". For the "slow modulation" limit considered in the beginning of Section 2, these quantities are given by [15]

$$W_{a(f)}(\omega) = \sqrt{\frac{1}{2\pi\sigma_{2s}}} w(\frac{\omega - \omega_{21} + \delta_{a(f),f}\omega_{st}}{\sqrt{2\sigma_{2s}}}) \quad (30)$$

where $w(z) = \exp(-z^2)[1 + i\mathrm{erfi}(z)]$ is the probability integral of a complex argument [25], and the absorption (fluorescence) lineshapes $\mathrm{Re}W_{a(f)}(\omega) \equiv F_{a(f)}(\omega)$ are given by

$$F_{a(f)}(\omega) = \sqrt{\frac{1}{2\pi\sigma_{2s}}} \exp[-\frac{\left(\omega_{21} - \omega - \delta_{a(f),f}\omega_{st}\right)^2}{2\sigma_{2s}}] \quad (31)$$

In the case of the Gaussian modulation of the electronic transition by the vibrations the absorption lineshape is given by [28, 9, 8]

$$F_a(\omega) = \frac{1}{\pi}\mathrm{Re}\int_0^\infty \exp[i(\omega - \omega_{21})t + g(t)]dt \quad (32)$$

where

$$g(t) = -\int_0^t dt'(t - t')K(t') \quad (33)$$

is the logarithm of the characteristic function of the spectrum of single-photon absorption after substraction of a term which is linear with respect to t and determines the first moment of the spectrum, $K(t)$ is the correlation function. Eq.(32) can be used in general case when the "slow modulation" limit is not realized. Then the monomer spectrum is given by

$$W_a(\omega) = \frac{1}{\pi}\int_0^\infty \exp[i(\omega - \omega_{21})t + g(t)]dt \quad (34)$$

For the exponential correlation function $K_s(t) = \sigma_{2s}\exp(-|t|/\tau_s)$, we get

$$g_s(t) = -\sigma_{2s}\tau_s^2[\exp(-t/\tau_s) + \frac{t}{\tau_s} - 1] \quad (35)$$

that leads to Eq.(36) of Appendix 2.

7. Appendix 2. Description of the absorption of J-aggregates

Applying expression $\mathrm{Re}\{\bar{W}_a(\omega)/[1 - ip\pi W_a(\omega)]\}$ on the right-hand-side of Eq.(11) to the description of the absorption of J-aggregates, one should take into account that the Gaussian shape of the monomer absorption spectrum obtained in the "slow modulation" limit, Eq.(31), is correct only near the absorption maximum. The wings decline much slower as $(\omega_{21} - \omega)^{-4}$ [29]. At the same time, the expression under discussion has a pole, giving strong absorption, when $1/(p\pi) = -\mathrm{Im}W_a(\omega)$. If parameter of the dipole-dipole intermolecular interaction p is rather large, the pole may be at a large distance from the absorption band maximum where the "slow modulation" limit breaks down. This means one should use exact expression for the monomer spectrum W_a that is not limited by the "slow modulation" approximation, and properly describes both the central spectrum region and its wings. The exact calculation of the vibrationally equilibrium monomer spectrum for the Gaussian-Markovian modulation with the exponential correlation function $S(t) = \exp(-|t|/\tau_s)$ gives [29, 28] (see Eqs.(34) and (35))

$$W_a(\omega) = \frac{\tau_s}{\pi}\frac{\Phi(1, 1 + x_a; \sigma_{2s}\tau_s^2)}{x_a} \quad (36)$$

where $x_a = \tau_s/(2T_1) + \sigma_{2s}\tau_s^2 + i\tau_s(\omega_{21} - \omega)$, $\Phi(1, 1 + x_a; \sigma_{2s}\tau_s^2)$ is a confluent hypergeometric function [25]. Eq.(36) is used for calculating the nonlinear absorption spectra of J-aggregates in Section 2.1.1.

8. Appendix 3. Description of the absorption of H-aggregates

To describe the absorption of H-aggregates, one should take also HFOA intramolecular vibrations into account, in addition to the LFOA vibrations $\{\omega_s\}$. The extension of Eq.(11) to the presence of the HFOA vibrations carried out in Section 3, enables us to use previous expression $\mathrm{Re}\{W_a(\omega)/[1 - ip\pi W_a(\omega)]\}$ (see Section2.1.1) for the description of the absorption of H-aggregates where the monomer spectrum W_a should include the contribution from the HFOA intramolecular vibrations. We will consider one normal high frequency intramolecular oscillator of frequency ω_0 whose equilibrium position is shifted under electronic transition. Its characteristic function $f_{\alpha M}(t)$ is determined by the following expression [4]:

$$\begin{aligned} f_{\alpha M}(t) &= \exp(-S_0\coth\theta_0)\sum_{k=-\infty}^{\infty} I_k(S_0/\sinh\theta_0) \\ &\quad \times \exp[k(\theta_0 + i\omega_0 t)] \end{aligned} \quad (37)$$

where S_0 is the dimensionless parameter of the shift, $\theta_0 = \hbar\omega_0/(2k_BT)$, $I_n(x)$ is the modified Bessel function of first kind [25]. Then $W_a(\omega)$ can be written as

$$\begin{aligned} W_a(\omega) &= \frac{1}{\pi}\int_0^\infty f^*_{\alpha M}(t)\exp[i(\omega - \omega_{21})t + g_s(t)]dt \\ &= \sum_{k=-\infty}^{\infty}\frac{\exp(-S_0\coth\theta_0 + k\theta_0)}{\pi} I_k(\frac{S_0}{\sinh\theta_0}) \\ &\quad \times \int_0^\infty \exp[i(\omega - k\omega_0 - \omega_{21})t + g_s(t)]dt \end{aligned}$$

where $g_s(t)$ is given by Eq.(35) of Appendix 1. Integrating with respect to t, one gets Eq.(13) of the main text for $\theta_0 >> 1$.

References

[1] K. Takazawa, J. Inoue, K. Mitsuishi, and T. Takamasu, "Fraction of a millimeter propagation of exciton polaritons in photoexcited nanofibers of organic dye," *Phys. Rev. Letters*, vol. 105, p. 067401, 2010.

[2] K. Takazawa, J. Inoue, K. Mitsuishi, and T. Kuroda, "Ultracompact asymmetric mach-zehnder interferometers with high visibility constructed from exciton polariton waveguides of organic dye nanofibers," *Advanced Functional Materials*, vol. 23, no. 7, pp. 839–845, 2013.

[3] B. D. Fainberg, "Nonperturbative analytic approach to interaction of intense ultrashort chirped pulses with molecules in solution: Picture of "moving" potentials," *J. Chem. Phys.*, vol. 109, no. 11, pp. 4523–4532, 1998.

[4] B. D. Fainberg and V. Narbaev, "Chirped pulse excitation in condensed phase involving intramolecular modes studied by double-sided Feynman diagrams for fast electronic dephasing," *J. Chem. Phys.*, vol. 113, no. 18, pp. 8113–8124, 2000.

[5] ——, "Chirped pulse excitation in condensed phase involving intramolecular modes. ii. absorption spectrum," *J. Chem. Phys.*, vol. 116, no. 11, pp. 4530–4541, 2002.

[6] M. V. Klein and T. E. Furtak, *Optics*. New York: Willey, 1988.

[7] A. Eisfeld and J. S. Briggs, "The j- and h-bands of organic dye aggregates," *Chem. Phys.*, vol. 324, pp. 376–384, 2006.

[8] B. D. Fainberg, in *Advances in Multiphoton Processes and Spectroscopy*, S. H. Lin, A. A. Villaeys, and Y. Fujimura, Eds. Singapore, New Jersey, London: World Scientific, 2003, vol. 15, pp. 215–374.

[9] S. Mukamel, *Principles of Nonlinear Optical Spectroscopy*. New York: Oxford University Press, 1995.

[10] B. D. Fainberg, *Opt. Spectrosc.*, vol. 68, p. 305, 1990, [Opt. Spektrosk., vol. 68, 525, 1990].

[11] B. Fainberg, *Phys. Rev. A*, vol. 48, p. 849, 1993.

[12] B. D. Fainberg, "Non-linear polarization and spectroscopy of vibronic transitions in the field of intensive ultrashort pulses," *Chem. Phys.*, vol. 148, pp. 33–45, 1990.

[13] A. S. Davydov, *Theory of Molecular Excitons*. New York: Plenum, 1971.

[14] B. D. Fainberg and B. Levinsky, "Stimulated raman adiabatic passage in a dense medium," *Adv. Phys. Chem.*, vol. 2010, p. 798419, 2010.

[15] B. D. Fainberg and G. Li, "Nonlinear organic plasmonics: Applications to optical control of coulomb blocking in nanojunctions," *Applied Phys. Lett.*, vol. 107, no. 5, p. 053302, 2015, [Erratum, v. 107, 109902 (2015)].

[16] H. Haug and S. W. Koch, *Quantum theory of the optical and electronic properties of semiconductors*. Singapore: World Scientific, 2001.

[17] K. Minoshima, M. Taiji, K. Misawa, and T. Kobayashi, "Femtosecond nonlinear optical dynamics of excitons in j-aggregates," *Chem. Phys. Lett.*, vol. 218, pp. 67–72, 1994.

[18] Y. Toyozawa, "On the dynamical behavior of an exciton," *Progr. Theor. Phys. Suppl.*, vol. 12, pp. 111–140, 1958.

[19] K. Takazawa, Y. Kitahama, Y. Kimura, and G. Kido, "Optical waveguide self-assembled from organic dye molecules in solution," *Nano Letters*, vol. 5, no. 7, pp. 1293–1296, 2005.

[20] K. Takazawa, "Waveguiding properties of fiber-shaped aggregates self-assembled from thiacyanine dye molecules," *J. Phys. Chem. C*, vol. 111, pp. 8671–8676, 2007.

[21] A. Eisfeld and J. S. Briggs, "The j-band of organic dyes: lineshape and coherence length," *Chem. Phys.*, vol. 281, pp. 61–70, 2002.

[22] ——, "Absorption spectra of quantum aggregates interacting via long-range forces," *Phys. Rev. Lett.*, vol. 96, p. 113003, 2006.

[23] V. A. Malyshev and P. Moreno, "Mirrorless optical bistability of linear molecular aggregates," *Phys. Rev. A*, vol. 53, no. 1, pp. 416–423, 1996.

[24] B. D. Fainberg and D. Huppert, *Adv. Chem. Phys.*, vol. 107 (Chapter 3), pp. 191–261, 1999.

[25] M. Abramowitz and I. Stegun, *Handbook on Mathematical Functions*. New York: Dover, 1964.

[26] M. Litinskaya, P. Reineker, and V. M. Agranovich, "Exciton polaritons in organic microcavities," *Journal of Luminescence*, vol. 119–120, pp. 277–282, 2006.

[27] N. J. Halas, S. Lal, W.-S. Chang, S. Link, and P. Nordlander, "Plasmons in strongly coupled metallic nanostructures," *Chem. Rev.*, vol. 111, pp. 3913–3961, 2011.

[28] B. D. Fainberg, *Opt. Spectrosc.*, vol. 58, p. 323, 1985, [Opt. Spektrosk. v. 58, 533 (1985)].

[29] S. G. Rautian and I. I. Sobel'man, "The effect of collisions on the doppler broadening of spectral lines," *SOVIET PHYSICS USPEKHI*, vol. 9, no. 5, pp. 701–716, 1967, [Usp. Fiz. Nauk 90, 209-238 (1966)].

Hybrid plasmonic-vanadium dioxide electro-optical switch based modulator

M. Y. Abdelatty[1,2], and M. A. Swillam[*1]

[1]Dept. of Physics, School of Science and Engineering, American University in Cairo, New Cairo, 11835, Cairo
[2]Basic Sciences Dept., Faculty of Engineering, The British University in Egypt, El-Sherouk City, 11837, Cairo
*corresponding author: m.swillam@aucegypt.edu

Abstract

This work presents the study and the design of optical switch based on a hybrid plasmonic-vanadium dioxide based waveguide, with a power-attenuating mechanism that takes the advantage of the phase change properties of vanadium dioxide that exhibits a change in the real and complex refractive indices upon switching from the dielectric phase to the metallic phase. The proposed switch designed to operate under the telecommunication wavelength. The switch was analyzed by 3D full electro-magnetic simulations.

1. Introduction

The main operations in digital signal processing are modulation and switching. The growing demand for high capacity signal processing systems made the assimilation of photonic circuitries into electronic circuitries [1]. Optical signal processing systems and components concerned a lot of research [2]. Switches are among the fundamental components in optical systems since they can be used as modulators [3].

A lot of designs and configurations for Si-based electro-absorption modulators have been studded and developed. Electro-absorption effect has a very weak impact in silicon which raised the demand for investigating new plasmonic materials with larger linear and non-linear optical properties. Silicon-germanium, organic polymers, graphene, transparent conducting oxides, and vanadium dioxide are among the materials investigated for modulation applications [4], [5].

Vanadium dioxide (VO_2), a phase change material, alters the real and complex refractive indices upon switching from the dielectric phase to the metallic phase [6]. This feature enables designing optical modulators with high extinction ratio (ER) and small foot-print; however, the high absorption of VO_2 results in high insertion loss (IL) [7].

The proposed switch is based on silicon-on-insulator rib waveguide coated with VO_2 and metal layers. The optical wave is guided in the silicon layer. The refractive index of VO_2 changes with the applied electric field; that results in changes in the mode profile which affects the power transmission. Due to the high field confinement in the silicon layer, the change in the VO_2 refractive index significantly changes the effective refractive index of the propagating mode. Designing a hybrid plasmonic-vanadium dioxide electro-optical modulator with high ER, low IL, and small footprint is very challenging.

2. Design

The proposed plasmonic absorption switch is based on silicon-on-insulator (SOI) rib waveguide. To modulate the optical power, the modulation section is formed by coating the SOI rib waveguide with VO_2 and metal layers as shown in figure 1. The optical wave is guided in the Si-rib.

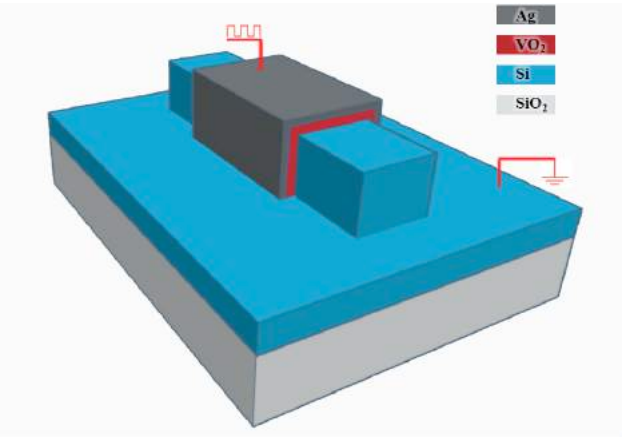


Figure 1: Bird-eye view of the proposed optical switch.

3. Principle of operation

The optical wave is excited through the SOI-rib waveguide. In the off-state, when there is no external electric field applied to the modulation section is applied, the optical wave propagates through plasmonic modulation section with minor losses. When an external electric field is applied to the metal layer, the VO_2 layer switches from the dielectric phase to the metallic phase. Thus, the effective refractive index of the propagating mode changes; as well as, the losses upturns. This results in perturbing the propagating power. An Eigen mode finite difference solver is used to analyze the modes and calculate the losses. The field distribution ($|E_z|$) of the modulation sections modes, off-state and on-state, are shown in figure 2.

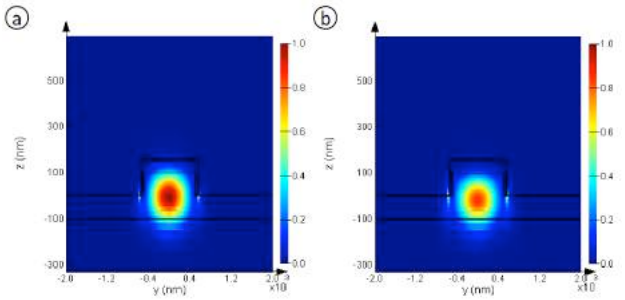


Figure 2: Field distribution for the propagating modes of the plasmonic modulation section: (a) off-state and (b) on-state.

Finite difference time domain simulations were conducted to simulate and study this design. Figure 3 shows the normalized intensity at the center of the Si layer along the device for the off- and on-states for 2 μm long modulation section at wavelength of 1.55 μm.

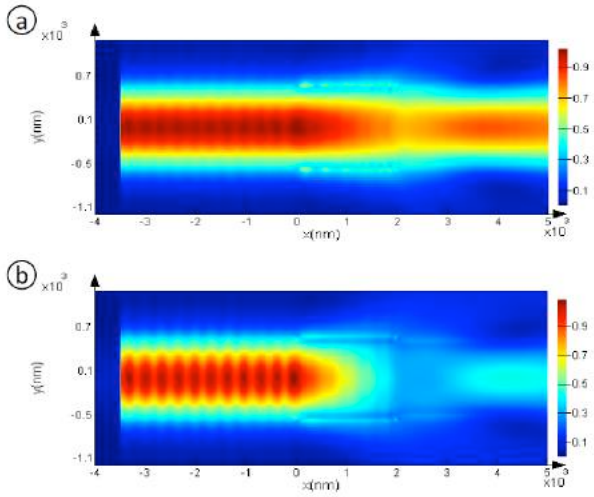


Figure 3: The normalized intensity, with respect to the input, of the guided mode the center of the Si layer as a function of the propagation length for the (a) off- and (b) on-states.

4. Conclusions

An optical plasmonic electro-absorption switch based on VO2's phase change effect studied. The structure and principles are described. Modal analysis and FDTD analysis are used to verify and simulate the design. An extinction ratio of 7.74 dB and insertion loss of 1.84 dB can be achieved at 2 μm length of the modulation section. Different devices, such as ring resonator and directional coupler, can be utilized based on this configuration.

Acknowledgements

This work was made possible by a NPRP award [NPRP7-456- 1- 085] from the Qatar National Research Fund (member of the Qatar Foundation). The statements made herein are solely the responsibility of the authors.

References

[1] D. C. Zografopoulos, M. A. Swillam, L. A. Shahada, and R. Beccherelli, "Hybrid electro-optic plasmonic modulators based on directional coupler switches," *Appl. Phys. A*, vol. 122, no. 4, pp. 1–6, Mar. 2016.

[2] H. Zhao, X. G. Guang, and J. Huang, "Novel optical directional coupler based on surface plasmon polaritons," *Phys. E Low-Dimens. Syst. Nanostructures*, vol. 40, no. 10, pp. 3025–3029, Sep. 2008.

[3] J. T. Kim, "CMOS-compatible hybrid plasmonic modulator based on vanadium dioxide insulator-metal phase transition," *Opt. Lett.*, vol. 39, no. 13, pp. 3997–4000, Jul. 2014.

[4] Z. Lu, W. Zhao, and K. Shi, "Ultracompact Electroabsorption Modulators Based on Tunable Epsilon-Near-Zero-Slot Waveguides," *IEEE Photonics J.*, vol. 4, no. 3, pp. 735–740, Jun. 2012.

[5] M. Y. Abdelatty, A. O. Zaki, and M. A. Swillam, "Hybrid silicon plasmonic organic directional coupler-based modulator," *Appl. Phys. A*, vol. 123, no. 1, p. 11, Jan. 2017.

[6] H. M. K. Wong and A. S. Helmy, "Performance Enhancement of Nanoscale VO2 Modulators Using Hybrid Plasmonics," *J. Light. Technol.*, vol. 36, no. 3, pp. 797–808, Feb. 2018.

[7] M. Sun, W. Shieh, and R. R. Unnithan, "Design of plasmonic modulators with vanadium dioxide on silicon-on-insulator," in *2017 IEEE Photonics Conference (IPC)*, 2017, pp. 77–85.

Light manipulation through plasmonic metasurfaces based on functional patterns

Mario Miscuglio[1], Nicholas J Borys[2], Davide Spirito[1], Beatriz Martin-Garcia[1], Remo Proietti Zaccaria[1], Alexander Weber-Bargioni[2], Roman Krahne[1]

[1]Istituto Italiano di Tecnologia, Via Morego 30 Genova Italy
[2]Molecular Foundry, Lawrence Berkeley National Lab, 1 Cyclotron Road, Berkeley, California 94720, USA

*corresponding author, E-mail: roman.krahne@iit.it

Abstract

We investigate the plasmonic effects in gold functional patterns using numerical simulations, near field and two-photon spectroscopy. These patterns consist of gold rhomboidal elements whose size and position is defined according to a grating function. By a proper choose of this function, the near field intensity in the pattern can be redistributed in non-trivial ways, by exploiting multiple localized surface resonances and near field coupling between the elements.
Our experimental data, which are in good agreement with the numerical simulations, highlights that the flat patterns focus light between 750 and 900 nm, below diffraction limit, and convert the imping linear polarization to radial. We verify the possibility to use our structures as polarized light-emitting devices by tailoring the interactions between the emitted light of a PbS nano-crystals film and the plasmonic resonances from the functional patterns. The proposed design and novel approach could allow to engineer useful devices in optical communication, energy harvesting, near field spectroscopy and sensing.

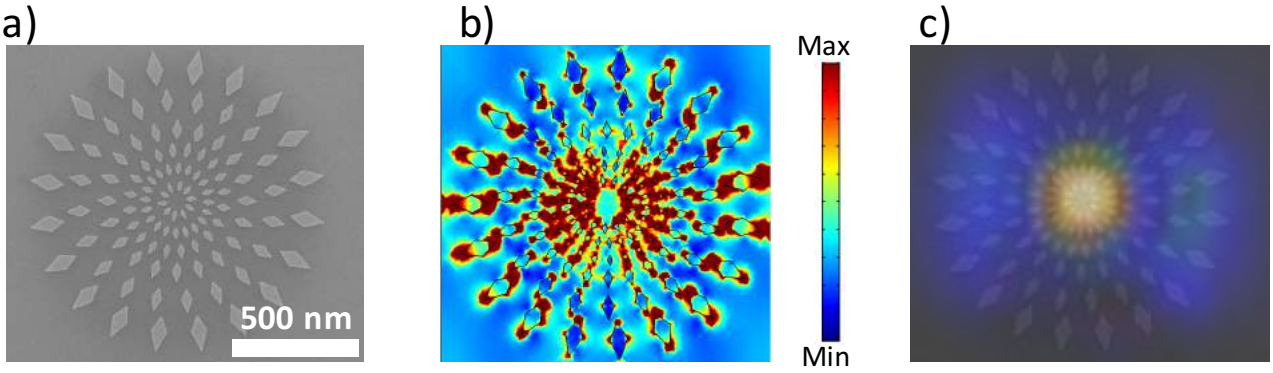


Figure 1 ***Radial Polarizer****. SEM image of the functional pattern (a)* ***Optical response of the radial polarizer:*** *Near field distribution (b) and two-photon photoluminescence map for a linearly polarized impinging radiation at 800 nm.*

Compact Silicon Nanowire Ring Resonator Sensor

Sherif Mohamed,[1] Lamees Shahada,[1] Mohamed Swillam[2,*]

[1]*Department of Chemistry and Earth Sciences, College of Arts and Sciences, Qatar University, P.O. Box 2713, Doha, Qatar*
[2]*Department of Physics, School of Sciences and Engineering, The American University in Cairo, New Cairo 11835, Egypt*
**m.swillam@aucegypt.edu*

Abstract—**We propose a highly sensitive ring resonator sensor. The structure of the sensor utilizes the silicon nanowires platform. The gas to be sensed dominates the spacings between the silicon nanowires. The proposed device is characterized by its small footprint, low insertion losses, and high sensitivity. Full 3D Finite Difference Time Domain simulations were employed for designing and simulating the operation of the sensor at the telecommunication wavelength, while characterizing the device performance.**

Keywords—Silicon Photonics; Silicon Nanowires; Ring Resonator; Optical Sensors

I. INTRODUCTION

Optical waveguides based on the silicon on insulator platforms are the most commonly used in the field of silicon photonics. Silicon photonics have been successful in producing a wide variety of applications such as sensors, filters, splitters, combiners, and modulators.

There is an increasing demand in achieving higher sensitivity sensors with lower losses and compact designs. The conventional silicon on insulator design allows only the cladding surrounding the waveguide to be detected. However, using silicon nanowires instead of bulk silicon is expected to result in higher sensitivities. This is mainly due to the existence of spacings between the silicon nanowires, these spacings are filled with the surrounding gas. So, there is a larger overlap between the effective mode and the surrounding gas. In this work, we demonstrate a compact high sensitive sensor based on the silicon nanowires platform.

II. RING RESONATOR SENSOR

The sensor device consists of a bus waveguide and a ring resonator. The bus waveguide transports the electromagnetic power to the ring resonator, and also serves as the output port after the resonator. The bus waveguide is a conventional silicon on insulator waveguide, while the ring resonator is built from silicon nanowires on a SiO_2 substrate. Fig. 1 shows the design of the silicon nanowires ring resonator sensor.

The ring resonator is designed such that to resonate at the 1.55mm wavelength, this wavelength is the most commonly used in telecommunication applications.

The silicon nanowires guide the electromagnetic power while the spacings between them are filled with the surrounding gas, thereby, the surrounding gas can be sensed by the guided mode. When there is a change in the surrounding gases, the effective index of the mode changes leading to a shift of the resonant wavelength. This resonant wavelength shift leads to a change of the power level detected at the 1.55μm.

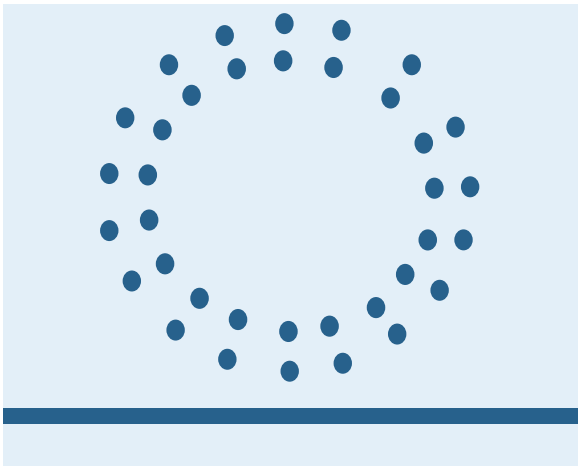


Fig. 1. Layout of the silicon nanowires ring resonator sensor.

III. RESULTS AND DISCUSSION

The sensor presented in this work was designed and simulated using 3D FDTD tools. The device parameters were investigated and its dimensions were optimized for the device operation at the telecom wavelength of 1.55 μm, results show that the insertion losses can be limited to 0.6 dB, and the sensitivity can reach 300 nm/RIU.

IV. ACKNOWLEGEMENT

This work was made possible by a NPRP award [NPRP7456-1-085] from the Qatar National Research Fund (member of the Qatar Foundation). The statements made herein are solely the responsibility of the authors.

Golden dodecapods: a promising nanoresonator for the development of metamaterials active at the optical frequencies

V. Many[1,2], J. Majimel[1], G. Drisko[1], S. Mornet[1], P. Barois[2], A. Baron[2], P. Richetti[2], S. De Cicco[3], J. Leng[3], J-B Salmon[3], S. Ravaine[2], E. Duguet[1], M. Treguer-Delapierre[1]

[1]ICMCB-CNRS, UPR 9048, France, Pessac
[2] CRPP-CNRS, UPR9048, France, Pessac
[3]LOF-CNRS, UMR 5258, France, Pessac
*veronique.many@icmcb.cnrs.fr

Abstract

Making metamaterials for optical frequencies is a nanotechnological challenge because the resonators must be on the order of 100 nm or smaller. The resonator should be composed of subwavelength structures that show electric and magnetic dipole resonances. One of the optimal geometry for isotropic resonances is symmetric three-dimensional structures such as tetrapods (tetrahedral), hexapods (octahedral), dodecapods (icosahedra) like nanoclusters. The challenge is to produce these structures in high yield and with high precision. We show in this communication that the use of patchy particles enables to produce isotropic plasmonic clusters consisting of a controlled number of gold satellites around a silica core. This versatile chemical approach offers the possibility to produce dodecapods nanoclusters on a large scale i.e. in gram quantities. These clusters exhibit magnetic and electric responses of high magnitude in visible or near-IR light and offer the possibility to tune and overlap the electric and magnetic responses (Huyghens' sources).

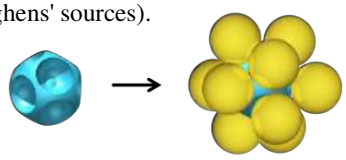


Figure 1: Well-defined SiO_2/Au dodecapods produced from silica patchy particles. Dodecahedral clusters of metal nanospheres are isotropic electromagnetic dipole resonators. A metamaterial active at optical frequencies is a dense, disordered assembly of these clusters.

1. Introduction

Metamaterials are artificial substances designed to exhibit physical properties that are not found in naturally occurring materials. No materials are known to exhibit $\mu < 0$ naturally at optical frequencies and thus there are no known substances that exhibit a negative index of refraction. The design of metamaterials with negative index requires a deep understanding of how the electric permittivity and magnetic permeability of a given material are determined and how they can be manipulated. Urzhumov et *al.* used plasmon hybridization theory which relates the electromagnetic resonances of various structures to their symmetries, to show that some regular polyhedral clusters of metal nanoparticles exhibit isotropic electric and magnetic dipole resonances. Examples include Platonic solids such as tetrahedron, octahedron and icosahedron. No matter how the three-dimensional structures is oriented with respect to incoming light, a magnetic dipole can be excited in at least one face of the structure. Thus, to make a metamaterial active at optical frequency, one needs only a dense material made of icosahedral clusters made of metal nanospheres. Negative index of refraction requires than the electric and magnetic dipole resonances overlap and these resonances are sensitive to the symmetry and the gap between the particles. Since the building blocks for metamaterials are three-dimensional structures, they have to be made by colloidal routes, from the 'bottom-up' using self-assembly. In this report, we report a route to develop isotropic plasmonic clusters. Their synthesis, in high yield, allowed the fabrication of a material exhibiting isotropic negative refraction at optical frequencies by self-assembly approach.

2. Results and discussion

Patchy particles were synthesized from Polystyrene/Silica dodecapods obtained by an emulsion polymerization strategy (Figure 2).

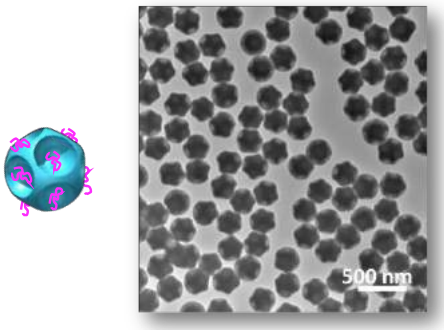


Figure 2: TEM image of the silica patchy particles.

The patches were made sticky to tiny gold seeds. The growth of the gold satellites from these attached seeds yielded to the

formation of highly symmetric SiO_2/Au dodecapods (Figure 3). The synthesis strategy could be extended to tetrapods and hexapods. Their morphology, size, and chemical composition can be varied independently.

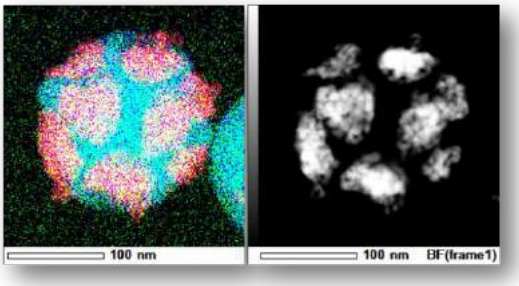


Figure 3: EDX and dark field image of golden dodecapods fabricated from patchy silica particles.

These symmetrical clusters can be produced in gram quantities. Their optical properties and the electromagnetic coupling between satellites were observed using polarization resolved static light scattering technique and interpreted through a numerical model. The clusters exhibit strong coupling in between the satellites and an intense multipolar response in visible whatever the angle of incidence. The magnetic response is higher than the one reported for raspberries-like nanoclusters consisting of a random number of satellites (Figure 4).

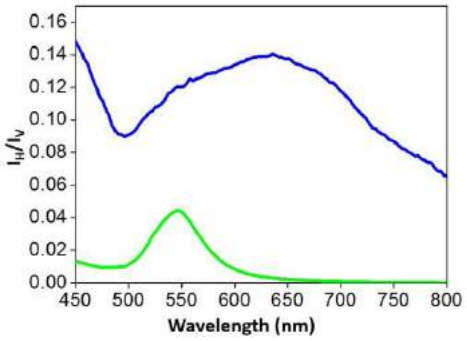


Figure 4: Magnetic resonance of a colloidal suspension of golden dodecapods (blue) and of raspberries like nanostructures (green). The efficiency of the dipolar magnetic scattering for the dodecapods is found to be 3.5 times higher than the one for nanostructures of similar morphology but made with a random number of gold satellites.

Numerical simulations evidence that the electric and the magnetic responses of the clusters are highly dependent on the gap in between the satellites as well as their state of condensation. In the case of the clusters shown in Figure 3, the simulations demonstrate that the electric and magnetic responses overlap offering the possibility to produce Huygens 'sources (Figure 5). They can scatter light in the forward direction due to the interference of the scattering from both an electric and a magnetic dipole response to incoming radiation at the same frequency.

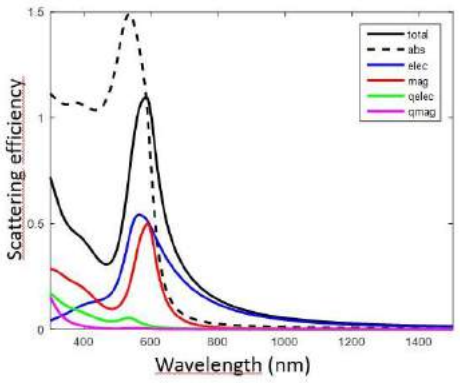


Figure 4: Electric (blue curve) and magnetic (red) responses of the gold dodecapods.

3. Conclusion

This work reported the synthesis of isotropic, reproducible, electromagnetic resonators exhibiting a strong isotropic artificial optical magnetism at visible or near-IR frequencies. The nanoresonators consists of a controlled number of gold satellites around a silica core and were produced by exploiting the concept of patchy particles. Polarized resolved static light scattering at variable angle was used to evidence experimentally the multipolar response of the engineered nanoresonators. Their production in high yield allows to fabricate optical functional devices of large area.

Acknowledgements

We acknowledge the LABEX project (under the Contract ANR-10-LABX-42) in the framework of IdEx Bordeaux (ANR-10-IDEX-03-02).

References

Urzhumov Y. *et al.*, "Plasmonic nanoclusters: a path towards negative-index metafluid" Opt. Express, **15**, 14129 (2007).

Ponsinet, V. *et al.* Resonant isotropic optical magnetism of plasmonic nanoclusters in visible light. *Phys. Rev. B* **92,** 220414 (2015).

Gomez-Grana, S. *et al.* Hierarchical self-assembly of a bulk metamaterial enables isotropic magnetic permeability at optical frequencies. *Mater. Horizons* **3,** 596–601 (2016).

Le Beulze, A. *et al.* Robust raspberry-like metallo-dielectric nanoclusters of critical sizes as SERS substrates. *Nanoscale* **9,** 5725–5736 (2017).

Hubert, C. *et al.* Regioselective functionalization of dimpled silica particles. *Colloids Surfaces A Physicochem. Eng. Asp.* **510,** 239–244 (2016).

Fontana, J. *et al.* Nanoclusters: Virus-Templated Plasmonic Nanoclusters with Icosahedral Symmetry via Directed Self-Assembly (Small 15/2014). *Small* **10,** 3196 (2014).

Désert, A. *et al.* Multipod-like silica/polystyrene clusters. *Nanoscale* **8,** 5454–5469 (2016).

Chomette, C. *et al.* Colloidal Alchemy: Conversion of Polystyrene Nanoclusters into Gold. *ChemNanoMat* **3,** 160–163 (2017).

Dezert, R., Richetti, P. & Baron, A. Isotropic Huygens dipoles and multipoles with colloidal particles. *Phys. Rev. B* **96,** 180201 (2017).

A bottom-up Approach Towards Metamaterials and Plasmonics

Novel Photonic Architectures by Nanoimprinting Unconventional Materials

Camilla Dore, André Espinha, Pau Molet, Cristiano Matricardi , Juan Luís García-Pomar and Agustín Mihi*

[1]Institut de Ciència de Materials de Barcelona (ICMAB-CSIC), Campus de la UAB, 08193 Bellaterra, Spain

*corresponding author, E-mail: amihi@icmab.es

Abstract

In this presentation, I will demonstrate how to use soft nanoimprinting lithography to mold unconventional materials such as cellulose derivatives to fabricate a variety of photonic architectures exhibiting exciting optical properties with tremendous applications as inexpensive disposable photonic components and sensors.

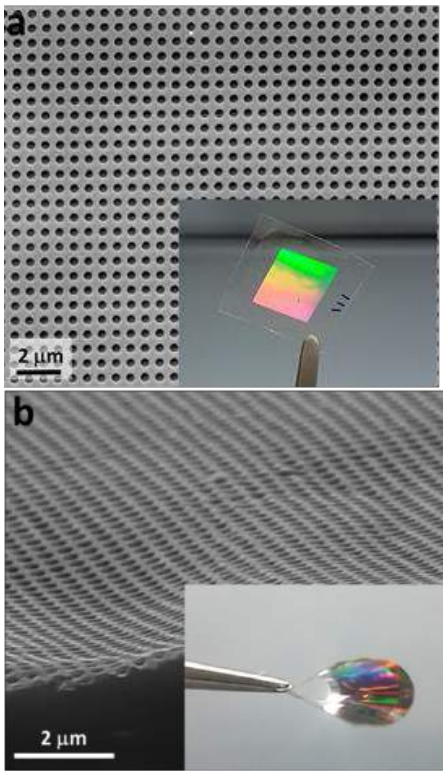


Figure 1: Cellulose based Photonic (a) and Plasmonic (b) architectures fabricated via nanoimprint lithography

Cellulose is the most abundant polymer on Earth and for centuries has had a wide technological impact in areas such as textile, packaging or knowledge storage. It is biodegradable, biocompatible and possesses excellent mechanical characteristics that have raised the interest of many engineering fields. The versatility of cellulose has opened new venues in advanced materials in electronics, energy or biological applications. In particular, its biocompatibility paves the way for new implantable photonic devices to improve health monitoring, diagnostics and light-activated therapies.

To the extraordinary properties of the cellulose, we incorporate enhanced photonic functionality by shaping it into photonic and plasmonic crystal structures via nanoimprinting lithography (Fig 1 and 2), the most promising method for mass-produced nanostructures. [1] This combination opens up new venues in the field of cellulose based photonic architectures, offering a smart opportunity for the ecofriendly production of color in packaging systems or in photonic papers, anti-counterfeiting technology, washable and edible detectors or labels for the food industry. In addition, I will demonstrate further uses of the cellulose derivatives as water processable and environmentally friendly nanoimprinting resists. I will demonstrate the patterning of silicon wafers and the fabrication of metal nanoparticles with the aid of cellulose and water as only chemicals. [2]

To conclude, I will demonstrate a metasurface capable of sustaining a wide variety of photonic resonant modes, from strong interference effects to Mie and Bragg modes. The interplay between these resonances results in a broadband enhancement in the optical absorption of thin films of germanium with thicknesses below 100 nm from VIS until NIR frequencies. Such a broadband enhancement in Ge thin films has tremendous implications in many optoelectronic devices such as solar cells or photodetectors. [3]

Acknowledgements

We thank the Spanish Ministry of Economy and Competitiveness (MINECO) for its support through Grant MAT2016-79053-P. and the auspices of the Spanish Severo Ochoa Centre of Excellence programme (grant SEV-2015-0496). This project has received funding from the European Research Council (ERC ENLIGHTMENT grant agreement No 637116).

References

[1] A. Espinha et al., Cellulose-based biodegradable and multifunctional photonic architectures, *Submitted* 2018.

[2] C. Dore et al., Water-processable cellulose-based resist for green nanofabrication, *Submitted* 2018.

[3] P. Molet et al. Ultrathin Semiconductor Superabsorbers from the Visible to the Near-Infrared, *Advanced Materials* 2018. 1705876

Large area self-assembled split-nanorod metamaterials

Mazhar E. Nasir[1], R. Margoth Córdova-Castro[1], J-S Bouillard[2], Pan Wang[1], Alexey V. Krasavin[1] and Anatoly V Zayats[1]

[1]Department of Physics, King's College London, Strand, London WC2R 2LS, UK

[2]Physics, School of Mathematics and Physical Sciences, University of Hull, Cottingham Road Hull, HU6 7RX, UK

**corresponding author: mazhar.nasir@kcl.ac.uk*

Abstract:

Plasmonic metamaterials have gained great attention due to their unique optical properties and have already achieved a significant impact in a variety of photonic, data processing, and sensing applications. Here, we report the design and fabrication technique of periodic arrays of split nanorods Au/ZnO/Au using highly ordered porous alumina templates. Nanoscale confinement of light between two Au segments opens up new possibilities for a variety of applications in the field of nanophotonics. These metamaterials can be used in optically-controlled memristive devices.

Introduction:

Light can be coupled between two plasmon surfaces leading to nanoscale confinement that shows high sensitivity to the surrounding medium. This effect can be used for a variety of applications in the fields of biochemical sensing[4, 5], enhanced nonlinear optical effects[1-3], as well as for localised light sources for imaging[6]. The resonant wavelengths in self-assembled Au nanorod metamaterials modified by interaction between the nanorods, can be tuned throughout the visible and into the infra-red spectral range by varying the geometry of the nanorod arrays and the permittivity of the surrounding medium. In case of split nanorods, the resonant wavelength depends on the nanoscale confinement of light between two segments and the coupling between the nanorods. Zinc oxide is deposited between two segments of nanorods as it is a transparent and wide-bandgap semiconductor with refractive index 2.004. The resistance of ZnO between the Au nanorods can be changed from semiconductor to insulator during electrodeposition and post-treatment.

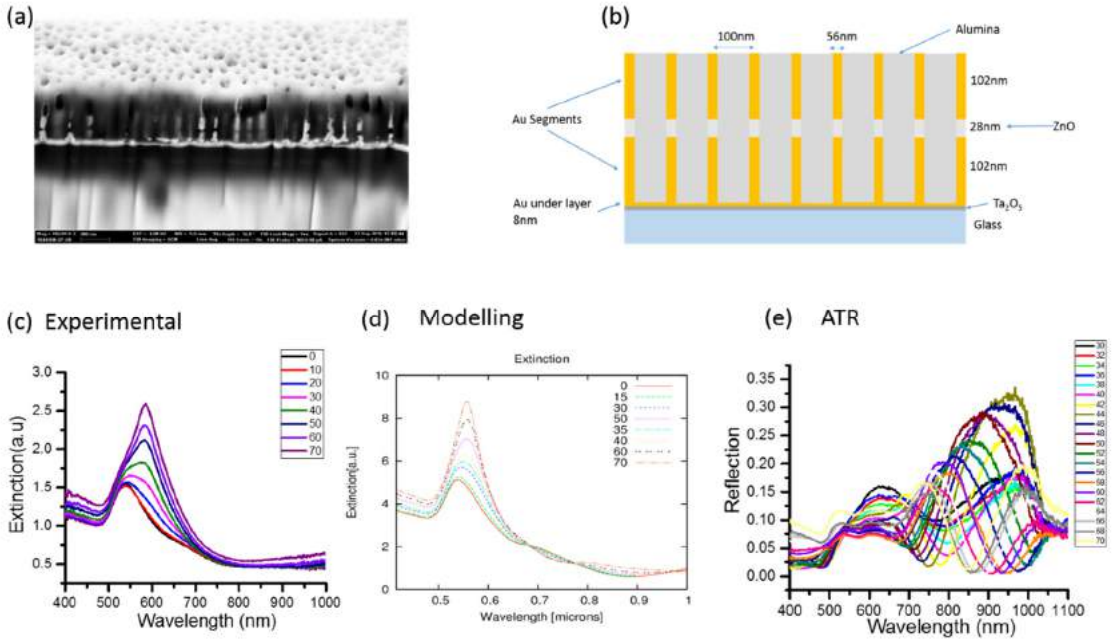


Figure 1: (a) SEM cross-section of split nanorods. (b) Schematic of the split metamaterials with geometrical parameters. (c–d) Experimentally measured and simulated extinction spectra. (e) Reflection spectra of the split nanorod metamaterials measured in an ATR geometry.

Memristive devices comprised of conductor/insulator/conductor structures are electrical resistance switches that can retain a memory of the applied voltage and current[7]. The split plasmonic nanorod metamaterials comprised of Au-ZnO-Au structure can be utilised for potential applications in memristive devices.

Experimental Section:
The split plasmonic nanorod metamaterials consist of two Au segments separated by ZnO, electrochemically grown into perfectly ordered nanoporous alumina membranes, having large domain areas (~square microns) obtained by employing two-step anodization. The pore geometry and spacing can be controlled over a wide range with nanoscale precision by a choice of anodization conditions and chemical post processing. Samples were annealed at 350°C to tune the composition of ZnO. The resonant wavelength can be tuned by changing thickness of ZnO between the two Au segments during electrodeposition.

Discussion:
SEM cross-section of the sample is shown in Fig. 1a and its structural parameters are shown in Fig. 1b. The extinction spectra of the split nanorods embedded in alumina show strong coupling between the two segments of the nanorods shown in Fig 1c. The origin of the peak can be traced to the field enhancement in the gap between the two segments of nanorods, modified by their interaction in the assembly. These results are validated by finite element modelling shown in Fig 1d. It has been observed that increasing the gap between the nanorod segments results in weak coupling and the nanorod metamaterial slab behave like two separate assembly of nanorods, where plasmonic resonances interfere with each other. The split nanorod system with a large gap also shows two weak resonances in the near infrared different from the strong confinement observed in the visible spectral range for a smaller gap shown in Fig 1c.

When excited with p-polarized light, the same nanorod metamaterials in the ATR geometry reveal a waveguided mode in the near-infrared spectral range that shows a shift with the incident angle, as shown in Fig. 1e. This behaviour is different from Au nanorod assembly without gap with the same geometry. Cathodoluminescence microscopy was carried out to investigate ZnO luminescence. Plasmoelectronic effects are investigated by applying voltage across the bi-segment nanorods in transmission measurements.

Conclusions:
We have investigated the plasmonic resonances in split nanorod metamaterials and observed a combined effect of nanoscale confinement between two segments of nanorods and coupling between the nanorods.

References:

1. N. Vasilantonakis, M. E. Nasir, W. Dickson, G. A. Wurtz and A. V. Zayats, *Laser Photonics Rev.* **9** (3), 345 (2015).
2. M. Nasir, S. Peruch, N. Vasilantonakis, W. Wardley, W. Dickson, G. Wurtz and A. Zayats, *Appl. Phys. Lett.* **107** (12), 121110 (2015).
3. A. V. Krasavin, P. Ginzburg and A. V. Zayats, *Laser Photonics Rev.* **12**, 24 (2018).
4. A. V. Kabashin, P. Evans, S. Pastkovsky, W. Hendren, G. Wurtz, R. Atkinson, R. Pollard, V. Podolskiy and A. Zayats, *Nat Mater* **8**, 867 (2009).
5. M. E. Nasir, W. Dickson, G. A. Wurtz, W. P. Wardley and A. V. Zayats, *Adv. Mater.* **26** (21), 3532 (2014).
6. A. V. Zayats and I. I. Smolyaninov, *J. Opt. A: Pure Appl. Opt.* **5** (4), S16 (2003).
7. J. J. Yang, D. B. Strukov and D. R. Stewart, *Nat. Nanotechnol.* **8** (1), 13 (2013).

Synthesis of silicon nanoparticles for optically active metamaterials

Sanaa Semlali[1*], Benoit Cormary[1], Maria L. De Marco[1], Philippe Barois[2], Patrick Rosa[1], Mathieu Gonidec[1], Glenna L. Drisko[1]

[1] CNRS, Univ. Bordeaux, ICMCB, UPR 9048, 33600 PESSAC, France.
[2] CNRS, Univ. Bordeaux, CRPP, UPR 8641, 33600 PESSAC, France
*corresponding author, E-mail: sanaa.semlali@icmcb.cnrs.fr

Abstract

Due to its high refractive index, silicon is considered promising for the next generation of optically active metamaterial. Large Si particles could conceivably be produced via wet chemistry. However, wet chemistry methods typically generate fluorescent quantum dots. We successfully synthesize Si nanoparticles with sizes above 50 nm, by changing the solvent at room temperature and by changing the experimental conditions in microwave. We have begun preliminary optical measurements on these large dielectric resonators.

1. Introduction

Colloidal silicon nanoparticles have become attractive materials due to their high refractive index, high chemical stability and optical properties. Depending on the size, shape and crystallinity of the Si particle, a number of applications could be explored. Small particles favor a strong photoluminescence response [1]. Larger particles present good candidates for optically active metamaterials [2]. In the case of metamaterials applications; particles larger than 80 nm are needed to enhance the electric and magnetic response. Not only does the size matter, but also crystallinity, dispersity, shape and density. So choosing the appropriate preparation methods become necessary to control all these features (size, shape and dispersity) [3].
Silicon nanoparticles have been largely produced by diverse synthetic methods going from top-down to bottom-up approaches. Top-down methods (etching bulk silicon, laser pyrolysis, etc.) permits the production of large Si particles, but they are often amorphous, porous and polydisperse in size. In addition, these approaches need an excess use of hazardous acid, HF. For bottom-up methods, the common techniques to produce silicon are the metallothermic reduction of silica, aerosol synthesis, chemical vapor deposition, synthesis in supercritical fluids, thermal decomposition in molten salts. These methods produce a large range of silicon particle sizes from sub-nanometeric to micrometers. The common drawbacks of these methods are polydispersity, porosity and obtaining a low yield [1].

Particle coalescence is a typical technique used in wet-chemistry to make larger nanoparticles in Au, Ag and SiO_2. Ostwald ripening is used to advantage for systems that can dissolve and reprecipitate, which unfortunately is not the case for silicon. Other coalescence techniques can be used for silicon, stimulated by the use of pressure, heat or by using non-solvents/solvent mixtures to encourage particle agglomeration without flocculation. Despite the large interest in obtaining large diameter silicon particles for optical applications, coalescence techniques have not previously been reported for this material.
Metal reduction permits a good control over silicon particle size and crystallinity. In this work, magnesium was used to reduce silicon precursors at room temperature and led to the production of large Si particles up to 50 nm in diameter, simply by changing the solvent. To increase particle diameter further, brief microwave treatment was performed.

2. Results and discussion

2.1. Effect of solvent on Si particle size

Silicon nanoparticles were synthesized by mixing silicon tetrachloride with magnesium grit in one of the following solvents: diethyl ether, THF, 1, 2-dimethoxyethane (glyme), diethylene glycol dimethyl ether (diglyme), Tetraethylene glycol dimethyl ether (tetraglyme). The solution was then stirred at room temperature for 20 h before being centrifuged to remove magnesium salt precipitate. No Si nanoparticles were obtained in diethyl ether or dioxane while in glyme and tetraglyme a brown solution was obtained. Si nanoparticles suspended in THF appear blood red and in diglyme they are yellow, indicating a diameter of several nanometers. Transmission electron microscopy (TEM) revealed the size difference of silicon nanoparticles synthesized in THF, glyme and tetraglyme (Figure 1). The average particle size was calculated using ImageJ software on TEM images. In THF, the mean size of Si particles was 7.5 nm with size distribution of 2.5 nm while in diglyme, the mean size was 3.5 ± 2.5 nm. Otherwise, glyme and tetraglyme produces nanoparticles of a larger diameter, even though a broad size distribution was obtained. Using glyme, two particle populations exist: the majority of counted particles have sizes ranging from 5 to 10 nm and the residual particles ranged between 10 to 50 nm. In tetraglyme, silicon particles had a size between 10 and 15 nm in general, with a few

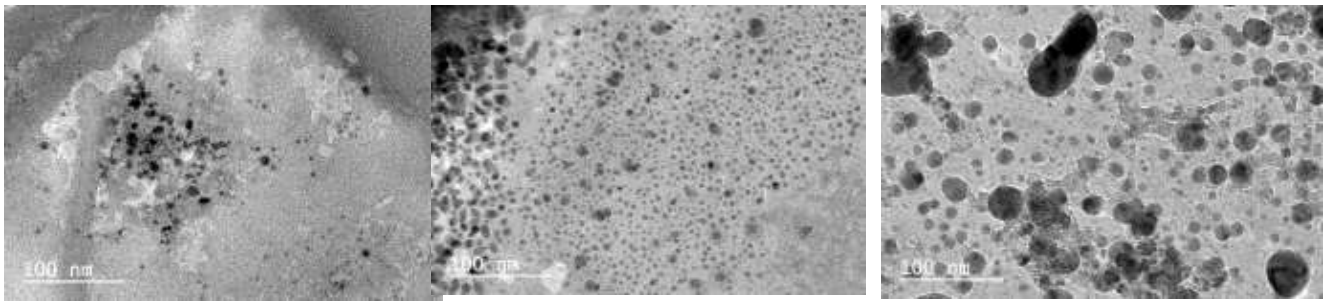


Figure 1: TEM images of silicon nanoparticles synthesized at room temperature in a) THF b) glyme and c) tetraglyme

particles having diameters between 20 and 40 nm. It was obvious that solvent did affect the size of silicon nanoparticles. The redox potential of the reagents in each solvent have been tested to understand the mechanism.

2.2. Coalescence of Si particles

Small particles of silicon have never been processed to grow or coalesce larger particles from seeds. In this work, we used silicon nanoparticles synthesized in glyme at room temperature as seeds (with size ranging from 5-10 nm) Figure 1-b. After centrifugation, the solution was placed in the microwave in a Teflon flask. The temperature was then set to 150 °C at a pressure of 5 bars. Figure 2 shows a TEM image of silicon particles heated in the microwave for 10 min and their particle size distribution. Compared to Figure 1b, which represents silicon nanoparticles before the microwave treatment, we see that small Si nanoparticles with a size of 10 nm or less disappear. Presumably they have coalesced into larger particles, producing particles up to 70 nm in diameter. These particles were crystalline, and thus have low losses for optical frequencies. This process is currently being optimized to obtain more monodisperse and larger particles. For this purpose, reaction time and temperature are keys factors.

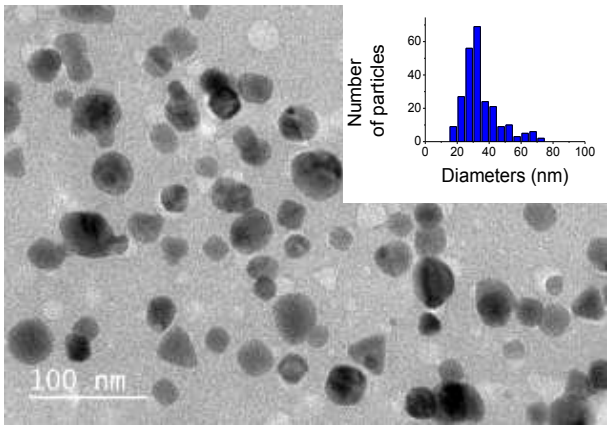


Figure 2: TEM image of silicon nanoparticles aged in microwave in glyme at 150°C and 5 bars for 10 min. Insert figure represents histogram of Si particles size distribution

3. Conclusions

The magnesium reduction of $SiCl_4$ at room temperature was not only possible, but also led to the formation of silicon nanoparticles with sizes ranging from 2 to 70 nm. The difference in the size was due to changing solvent, coming from differences in the kinetics of nucleation and growth in different solvents and differences in reduction potential. Preliminary results of particles treated with microwaves led to large increases in particle diameters, as well as crystallization and a decrease in polydispersity. By optimizing the microwave treatment, silicon nanoparticles large enough to act as resonators for optical frequencies can be obtained in bulk via a simple and efficient synthesis method.

Acknowledgements

This work is supported by AMADEUS/ LABEX (ANR-10-LABX-42) in the framework of IdEx Bordeaux (ANR-10-IDEX-03-02), administrated by University of Bordeaux and CNRS. Thanks to all technical support provided within ICMCB institute and PLACAMAT platform.

References

[1] Q. Li, T. Y. Luo, M. Zhou, H. Abroshan, J. Huang, H. J. Kim, N. L. Rosi, Z. Shao, R. Jin, Silicon Nanoparticles with Surface Nitrogen: 90% Quantum Yield with Narrow Luminescence Bandwidth and the Ligand Structure Based Energy Law, *ACS Nano*, *10, 8385−8393*, 2016.

[2] S. Jahani, Z. Jacob, All-dielectric metamaterials, *Nature Nanotechnology, 11, 23-36,* 2016.

[3] M. L. De Marco, S. Semlali, B. A. Korgel, P. Barois, G. L. Drisko, C. Aymonier, Silicon-Based Dielectric Metamaterials: Focus on the Current Synthetic Challenges, *Angew. Chem. Int. Ed., 57, pp. 2 – 22,* 2018.

Can optically-active silicon meta-atoms be produced through bottom-up chemistry?

Glenna L. Drisko[1], Sanaa Semlali[1], Benoit Cormary,[1] Maria Letizia De Marco[1], Cyril Aymonier[1], Philippe Barois[2]

[1] CNRS, Univ. Bordeaux, ICMCB, UPR 5026, 33600 PESSAC, France.
[2] CNRS, Univ. Bordeaux, CRPP, UPR 8641, 33600 PESSAC, France
*corresponding author, E-mail: glenna.drisko@icmcb.cnrs.fr

Abstract

Semiconductors boast the highest refractive index across the visible spectrum among naturally occurring materials. Silicon is generally favored for optical applications due to its natural abundance and *relatively* easy synthesis compared to other semiconductors. However, even silicon is extremely difficult to fabricate using bottom-up chemistry. It is relatively easy to produce 10 nm silicon particles, however these are too small for optically-active meta-atoms and such small particles oxidize completely to low-refractive index SiO_2. This begs asking, what silicon forms can we realistically expect to produce?

1. Introduction

Silicon meta-atoms have been theoretically modelled and experimentally demonstrated to have strong electric and magnetic resonances at optical frequencies [1,2]. Contrary to plasmonic-based meta-atoms, dielectric resonators show low losses and low heat generation. However, many constraints exist for silicon meta-atoms: they should be between 75-200 nm in diameter, they should be composed of pure silicon, crystalline, non-porous and ideally spherical [3]. If a metamaterial is desired, the meta-atoms should be monodisperse in size and non-aggregated to facilitate particle assembly into a material. To date, no synthetic chemist has been able to generate silicon particles that meet all of these criteria.

But there is hope. Firstly, some deviation from the ideal silicon meta-atom is apt to diminish the intensity of the electric and magnetic resonances, but not eliminate them entirely. For example, up to 30% porosity is predicted to be acceptable although the electric and magnetic resonance will be less intense and blue-shifted [3]. Secondly, there is a large array of available synthetic techniques that can provide bulk quantities of meta-atoms, including implementation of an aerosol, supercritical or solvothermal reactors, chemical vapor deposition, metallothermic reduction, molten salt media, and traditional wet-chemistry [3]. By optimizing these methods or by using a combinatorial approach, we may obtain nearly ideal meta-atoms.

2. Discussion

The synthetic conditions determine several properties of the obtained silicon properties: the purity of the particle, the diameter, the crystallinity and even the form. Thus the solvent, reducing agent, silicon precursor, and synthetic conditions (concentration, temperature, pressure, reaction time, etc.) must be chosen with care.

We focused on studying the effects of reducing agent and solvent, as these have not been systematically studied, with the exception of one report on reducing agent strength using complex metal hydrides [4]. Because complex metal hydrides are such powerful reducing agents, and because the authors were using surfactants to encourage monodispersity, silicon quantum dots were obtained between 1-3.5 nm in diameter. By changing the reducing agent the mean diameter only changed from 1.5 to 2.5 nm. As meta-atoms require much larger sizes, a much gentler reducing agent should be employed to encourage nanoparticle growth. We broadened the study of complex metal hydrides to include naphthalene, magnesium, hydrogen gas and zinc as reducing agents (Fig. 1). Gentler reducing agents take longer to initiate nucleation, thus once seeds are generated, nucleation and growth reactions compete, yielding larger, but more disperse, nanoparticle diameters. As weaker reducing agents are less reactive, we needed to use a more reactive precursor. Thus we synthesized silicon bis(amidinate), which was more reactive than commercially available silicon precursors.

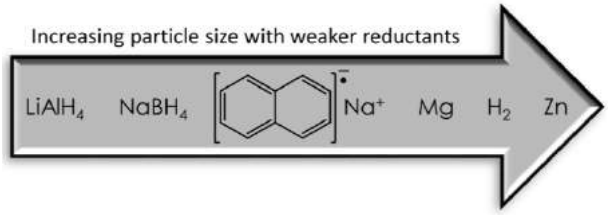


Figure 1: Stronger reducing agents produce small silicon nanoparticles, while gentle reducing agents produce larger silicon particles.

Solvent had a large impact on nanoparticle size, dispersion and also the yield of the reaction. Using magnesium as a reducing agent and a suit of glycol ethers and heterocyclic ethers as solvents, we found that many ethers were incapable of producing nanoparticles, while others produced nanoparticles up to 65 nm in diameter. Amongst the solvents tested, tetrahydrofuran produced the most monodisperse particles. However the largest particles were produced using glyme. Seeing as the chemical nature of these solvents is very similar, the huge changes in nanoparticle size and dispersity is surprising. It seems the solvent plays a role in the reaction mechanism.

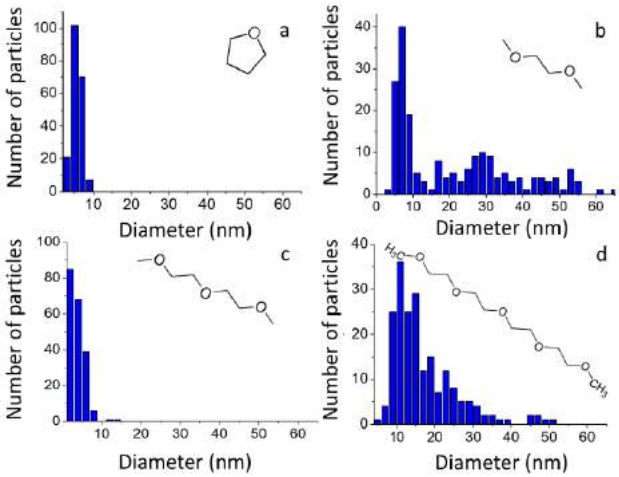


Figure 2: Nanoparticle distribution is dependent on the solvent used, *e.g.* (a) tetrahydrofuran, (b) glyme, (c) diglyme, and (d) tetraglyme. All other parameters were equivalent.

We have found that nanoparticle size can be dramatically increased, while decreasing polydispersity, by heating the nanoparticles under pressure (Fig. 3). Silicon, unlike silica, cannot grow via Ostwald ripening. This is because silicon cannot spontaneously dissolve, the uncoordinated element is too unstable. Thus, it seems that the particles grow via coalescence. Coalescence kinetics have been studied using simulations and experiments [5,6], showing that when temperature alone is used, the nanoparticles must be heated to 1000 °C for coalescence to occur.

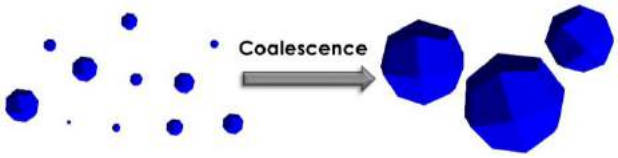


Figure 3: Silicon nanoparticles can be coalesced into larger and more monodisperse nanoparticles using pressure and heat.

Finally, silicon nanoparticles, far from ideal meta-atoms, have been assembled using dip-coating. Large particles suspended in a volatile solvent can be deposited using dip-coating. By varying the temperature, the solvent and the withdrawal rate, the density of deposited silicon nanoparticles can be adjusted. These films will be used for preliminary optical scattering measurements.

3. Conclusions

The most promising synthetic methods come from supercritical, aerosol and more traditional solution chemistry synthetic strategies. Bottom-up methods deliver large quantities of meta-atoms, which then can be incorporated into devices to test theoretical predictions of dielectric meta-atom assemblies.

We have focused on studying the nature of the solvent and the reducing agent. Both the solvent and the reducing agent affect the kinetics of nucleation and growth, and thus determine ultimate particle dimensions. The solvent seems to play an important role regarding stabilizing either the product or intermediate species during reaction. The degree of silicon crystallinity is also dependent on the solvent used. Silicon nanoparticle diameter can be increased using post-synthetic coalescence techniques, such as using pressure and heat. Preliminary attempts to assemble non-ideal silicon meta-atoms have begun. Through combinations of synthetic chemistry techniques, we advance slowly, but surely towards ideal dielectric resonators.

Acknowledgements

GLD, SS, BC and MLDM were supported by the LabEx AMADEus (ANR-10-LABX-42) in the framework of IdEx Bordeaux (ANR-10-IDEX-03-02), *i.e.* the Investissements d'Avenir program of the French government managed by the Agence Nationale de la Recherche.

References

[1] A. B. Evlyukhin, C. Reinhardt, A. Seidel, B. S. Luk´yanchuk, B. N. Chichkov, Optical response features of Si-nanoparticle arrays, *Phys. Rev. B* 82: 045404, 2010.

[2] U. Zywietz, A. B. Evlyukhin, C. Reinhardt, B. N. Chichkov, Laser printing of silicon nanoparticles with resonant optical electric and magnetic responses, *Nat. Commun.* 5: 3402, 2014.

[3] M. L. De Marco, S. Semlali, B. A. Korgel, P. Barois, G. L. Drisko, C. Aymonier, Silicon-based dielectric metamaterials: Focus on the current synthetic challenges, *Angew. Chem. Int. Ed.* DOI: 10.1002/anie.201709044.

[4] A. Shiohara, S. Prabakar, A. Faramus, C.-Y. Hsu, P.-S. Lai, P. T. Northcote, R. D. Tilley, Sized controlled synthesis, purification, and cell studies with silicon quantum dots, *Nanoscale* 3: 3364, 2011.

[5] T. Hawa, M. R. Zachariah, Coalescence kinetics of bare and hydrogen-coated silicon nanoparticles: A molecular dynamics study, *Phys. Rev. B* 71: 165434, 2005.

J. Holm, J. T. Roberts, Sintering, Coalescence, and Compositional Changes of Hydrogne-terminated silicon nanoparticles as a function of temperature, *J. Phys. Chem. C*, 113: 15955-15963, 2009.

Self-Assembled Metasurfaces and Nanostructured Materials for Linear, Non-Linear and Circular Optical Polarization Manipulation

Alessandro Belardini[1,*], Grigore Leahu[1], Emilija Petronijevic[1], Marco Centini[1], Roberto Li Voti[1], Joseph W. Haus[2], Ventsislav K. Valev[3], Teemu Hakkarainen[4], Mircea Guina[4], Dorota A. Pawlak[5], and Concita Sibilia[1]

[1]SBAI Department, Sapienza University of Rome, 00161 Rome, Italy
[2]Department of Electro-Optics and Photonics, University of Dayton, Dayton, Ohio, USA
[3]Department of Physics, University of Bath, Bath, BA2 7AY, United Kingdom
[4]Optoelectronics Research Centre, Tampere University of Technology, 33720 Tampere, Finland
[5]Institute of Electronic Materials Technology, ul. Wólczyńska 133, 01-919 Warsaw, Poland
*corresponding author, E-mail: alessandro.belardini@uniroma1.it

Abstract

A self-assembly approach in the fabrication of nanostructured metasurfaces can lead to high reproducible, low cost, large area samples that can exploit different optical functionalities, like polarization manipulation or optical filtering. Usually these effects are gotten with more complex processes. Here we investigate different self-assembled structures by using linear and nonlinear optical techniques such as photothermal and photoacoustic spectroscopy, second harmonic generation circular dichroism among others. The results show the wide range of possibilities offered by a bottom-up approach.

1. Introduction

The peculiar optical properties of metamaterials and metasurfaces arise from the proper design of the inclusions in the host material, in order to obtain electromagnetic responses that are not achievable in homogeneous materials [1]. In plasmonic metamaterials the proper geometry of the metallic inclusions (nanoantennas) that guides the free-electrons motion are responsible for interesting behavior such as anomalous refraction [2], second harmonic generation (SHG) enhancement [3], chiral light polarization manipulation [4]. One drawback of using metal inclusions are ohmic losses introduced by free electrons. An alternative approach uses dielectric compounds with different anisotropic refractive indices. In these cases, it is possible to create a surface, which can modulate the optical wavefront and control light polarization [5].

2. Nanostructured materials

Here we present examples of both metallic-based and all-dielectric-based nanostructured materials realized by different self-assembled approach. The studies were carried out by a variety of optical techniques in linear and nonlinear regime.

2.1. Dielectric based nanostructures

The dielectric based structures are composed of the eutectic mixture of zinc tungstate (ZnWO4) [6] and zinc oxide (ZnO). The material was obtained by directional solidification via a micro-pulling-down (μ-PD) method realizing lamellar structure of ZnO embedded in $ZnWO_4$ matrix in which the thickness of ZnO lamellas was ~250 nm separated by 2μm thick $ZnWO_4$. The ZnO-$ZnWO_4$ eutectic mixture shows a sharp and very intense (60%) peak of transmitted light at the central wavelength of 397 nm with high degree of polarization (see Fig.1).

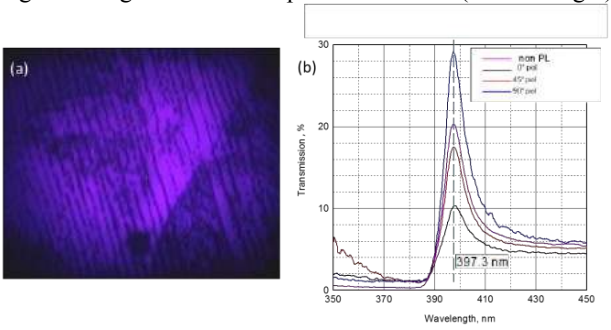


Figure 1: (a) ZnO-ZnWO4 lamellar structure; (b) transmission for different polarizations.

Absorption measurements obtained by photothermal deflection spectroscopy (PDS) confirms that light is partially absorbed only in the short wavelength spectral region (<380nm) due to ZnO absorption band and that the transmission peak is the result of proper indices matching between the two eutectic phases.

2.2. Plasmonic nanostructures

2.2.1. Gold Nanowires

By depositing gold at grazing incidence on a silicon substrate maintained at a temperature of ~300 K (Glancing Angle Deposition-GLAD) we realized a self-ordered forest of tilt Au 300nm long nanowires (NWs), as shown in Fig.2.

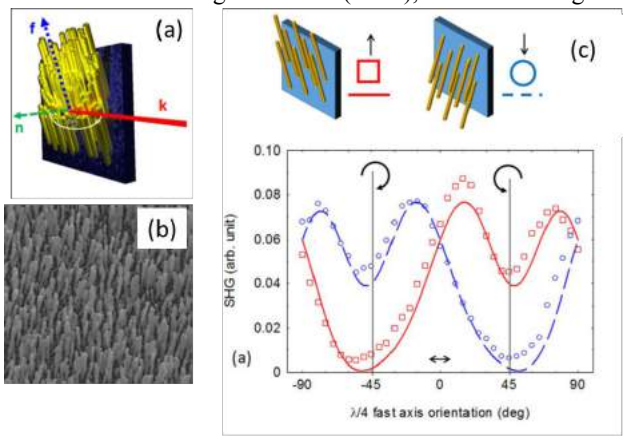


Figure 2: (a) scheme of the NWs structures; (b) SEM image; (c) SHG measurements.

The asymmetric orientation of the gold wires with respect to the pumping light orientation (Fig.2a) leads to the excitation of extrinsic chiral response [7] in the SHG response [8] that can be evaluated by using circular polarized pump light (Fig.2c).

2.2.2. GaAs Nanowires with asymmetric gold capping

Here we present the photoacoustic (PA) measurements on Au partially covered GaAs nanowires 5 microns long fabricated on Si substrate by a by a self-catalyzed approach (Fig.3). Comparison with the same sample without asymmetric gold covering gives rise to a dramatic circular dichroism enhancement [9].

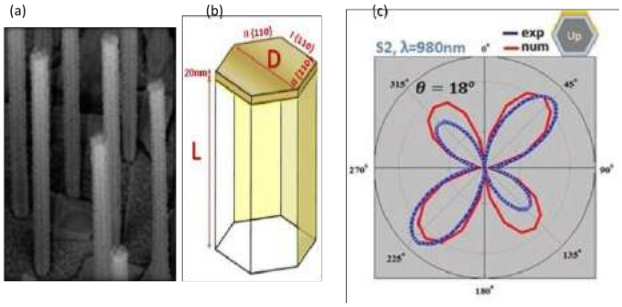


Figure 3: (a) SEM image of the Au-coated GaAs wires; (b) scheme of the NWs structures with gold; (c) PA measurements.

The measurements where performed at different incident angles with circular and elliptical polarized light in order to put in evidence the extrinsic chiral response of the samples.

3. Discussion

All discussed samples possess peculiar optical properties such as polarization filtering and manipulation that were induced by the proper design of single component materials that constitute the metasurface itself. In the dielectric case the orientation of the optical axes and the indices matching between the two compounds leads to extraordinary optical properties. While in the plasmonic cases it is the geometrical arrangement of the metal clusters to induce symmetry breaking and chiral response.

4. Conclusions

The potentiality of the self-assembled approach in the fabrication of low-cost nanostructured materials for photonics applications are here demonstrated and illustrated in some real cases. Different optical techniques, such as linear spectroscopy, nonlinear circular dichroism, photothermal deflection and photoacoustic absorbance, are used in order to put into evidence the peculiar optical behavior of such metamaterials, which can be utilized in different potential applications.

References

[1] J. B. Pendry, A. J. Holden, D. J. Robbins, and W. J. Stewart, IEEE Trans. Microwave Theory Tech. 47, 2075 (1999)

[2] A. Belardini, F. Pannone, G. Leahu, M.C. Larciprete, M. Centini, C. Sibilia, C. Martella, M.C. Giordano, D. Chiappe, F. Buatier de Mongeot, J. Europ. Opt. Soc. Rap. Public. 7, 12051 (2012).

[3] A. Belardini, M. C. Larciprete, M. Centini, E. Fazio, C. Sibilia, M. Bertolotti, A. Toma, D. Chiappe, F. Buatier de Mongeot, Opt. Express 17, 3603 (2009).

[4] A. Belardini, Benedetti, A., Centini, M., Leahu, G., Mura, F., Sennato, S., Sibilia, C., Robbiano, V., Giordano, M. C., Martella, C., Comoretto, D. and de Mongeot, F. B. Advanced Optical Materials 2, 208–213 (2014).

[5] Aieta, F., Kats, M. A., Genevet, P. & Capasso, F., Science 347, 1342–1345 (2015).

[6] P. Osewski, A. Belardini, E. Petronijevic, M. Centini, G. Leahu, R. Diduszko, D. A. Pawlak, C. Sibilia. Scientific Reports 7, 45247 (2017).

[7] A. Belardini, M. C. Larciprete, M. Centini, E. Fazio, C. Sibilia, D. Chiappe, C. Martella, A. Toma, M. Giordano, and F. Buatier de Mongeot, Phys. Rev. Lett. 107, 257401 (2011).

[8] A. Belardini, M. Centini, G. Leahu, D.C. Hooper, R. Li Voti, E. Fazio, J. W. Haus, A. Sarangan, V. K. Valev, C. Sibilia, Scientific Reports 6, 31796 (2016).

[9] G. Leahu, E. Petronijevic, A. Belardini, M. Centini, C. Sibilia, T. Hakkarainen, E. Koivusalo, M. Rizzo Piton, S. Suomalainen, and M. Guina, Adv. Optical Mater. 2017, 1601063 (2017).

Light scattering from randomly rough metasurfaces with embedded nanoparticles: realizations, low grazing incidence and effective medium

Gerard Berginc[1]

[1]THALES, Elancourt, France
*corresponding author, E-mail: Gerard.berginc@fr.thalesgroup.com

Abstract

In this paper, we present designs and realizations of randomly rough metasurfaces or thin films with metallic nanoparticle inclusions demonstrating antireflective or absorption properties in the visible or near-infrared band. Then we discuss the theoretical aspects of multiple scattering in random media, the scattering field at grazing angle for randomly rough metafilms and the multiple scattering of surface waves upon the rough interface. Finally, we give the expression of the effective permittivity of inhomogeneous nano-films.

1. Introduction

Controlling the scattered light is crucial in many areas of science and technology. We can modify the perception of an object by tailoring its scattering properties. Artificial materials with nanoscale random modulations of the surface and including nanoparticles can exercise such control and have opened new possibilities for light manipulation by an optimized definition of their properties. In the first part of the paper, two examples are discussed, the nano-structuration of silicon surface and metafilms with nano-inclusions. The nanostructuration of silicon surfaces is a well-known method to improve, for example, solar cells efficiencies by controlling reflectivity in the visible and near-infrared bands. Several methods have been developed to produce Black Silicon (BS). RIE (Reactive Ion Etching) is a low-cost, mask-less process working on large areas. In the first part of the paper, we present results of BS realizations with reactive ion etching at room temperature. And we discuss reflectivity of BS sample in the visible and near-infrared bands. We give another example of metasurface, which can be considered as a perfect absorber in the visible band. The considered metasurfaces are composite structures made of small metallic particles. These particles play the same role as atoms or molecules in ordinary materials, which make metamaterials, considered as « artificial materials ».This metamaterial is a thin film based upon silver nanoparticles dispersed inside a matrix. This kind of metasurfaces can be considered as inhomogeneous thin films with absorbing or anti-reflective properties. The embedded nanostructures support the excitation of surface plasmon resonances, and absorption of light is dependent of the size and shape of the metal nanoparticles, but also, of the spacing of the nanostructures, which can create collective behaviors and new absorbing frequencies. We propose, in this part of the paper, to discuss the realization and the performance of these metasurfaces. In the second part of the paper we discuss light scattering of arbitrary polarization incident upon a three-dimensional thin film bounded by a randomly rough interface and containing metallic resonant or non-resonant nanostructures. For classical waves, the most interesting case is that of three-dimensional disorder. The quantity that obeys the disordered wave equation – the electric field – is a vector and not a scalar as in the Schrödinger equation. If many theoretical and numerical approaches have been developed to model transport of scalar light in random media, few or even no method at all nowadays can deal with ensembles of complex nanoparticles in interaction between themselves and randomly rough boundaries. This aspect of the problem was never considered in detail up to now. In mesoscopic physics, multiple light scattering in disordered potentials gives rise to complex wave interference phenomena, like speckle correlations or Anderson localization of light, and to applications like imaging through opaque biological tissues or perfect absorbers. The model is based upon a multiple scattering theory to describe the diffusion of polarized light in disordered media with randomly rough interfaces. This electromagnetic model of this random thin film can predict and interpret the electromagnetic properties of the metasurfaces we have realized. And we, theoretically, analyze the diffuse reflection of the realized sample and we present an effective medium theory, with which we can compute the interaction of the incident polarized light with the random thin film. In the last paragraph of this paper, we will discuss scattering theory at grazing angles, and we will focus our attention on scattering of polarized light from randomly rough interfaces.

2. Randomly rough surfaces and metafilms

2.1. Nanostructured silicon

The high reflectance of silicon, about 40%, limits the applications of optoelectronic devices. The silicon surface texturing minimizes the optical reflectance of this semiconductor in many optoelectronic applications, photovoltaics, and CCD or CMOS imagers. The use of randomly rough surfaces improves antireflection function and angular acceptance [1]. These properties are related to the height of roughness of the random surface. Silicon with nanostructured surface has a strong light absorption due to the light-trapping effect. Silicon appears dark if the roughness height is sufficient. E. Mazur showed that Black Silicon surfaces possess higher absorptance in short-infrared wavelength (SWIR) range when irradiated with 500 femtosecond laser pulses in SF6 [2-3]. This phenomenon is due to the sulfur-doping effect in silicon. We explore the possibility of fabricating Black Silicon by a novel patented method [4]. It is a Reactive Ion Etching (RIE) process without photolithographic mask. We develop RIE at room temperature using SF_6/O_2 gases. As shown in Figure 1, the surface covers with micro-nano spikes after RIE process and has a low reflectivity (Fig.2). Black Silicon is absorbent for visible and near-infrared wavelengths (Fig.3), and for large angles of incidence up to 50 ° (Fig.4).

We observe high absorptance in visible and infrared wavelengths and the reflectivity is below 1%. BS can be used in visible and infrared photodetectors for night vision cameras, solar cells, and near-infrared (near-IR) avalanche photodiode (APD). The energy band structures of black silicon have been changed, we observe [Fig.3] a better absorptance in near-infrared and short-wave infrared bands for BS than for a silicon wafer. In our process [4], Black Silicon was etched though a room temperature inductively coupled plasma reactive ion etching process (ICP-RIE) using sulfur hexafluoride (SF_6) and dioxygen (O_2) as etching gases. Before the etching process, a standard RCA cleaning is done and a vacuum higher than 10^{-5} Torr is achieved to ensure reproducibility. Samples were etched during several tens of minutes depending of their doping level. The ratio SF6/O2 is within the range of 1 to 10. As can be seen in Figure 1, the BS results in a morphology consisting of pillars densely and randomly distributed on the silicon surface with heights of about 800nm.

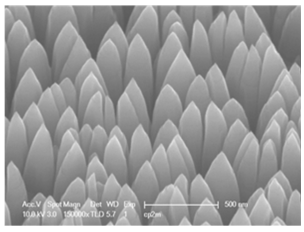


Figure 1: MEB image of Black Silicon (BS) obtained by reactive ion etching at room temperature. The surface covers with micro-nano spikes after RIE process.

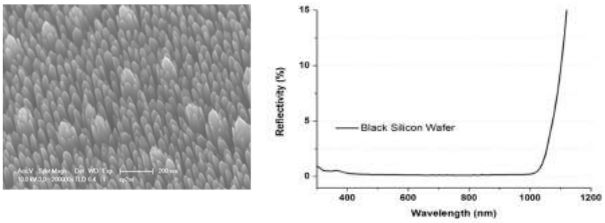


Figure 2: Black Silicon (BS) obtained by reactive ion etching at room temperature and reflectivity of the BS sample in the visible and near-infrared bands.

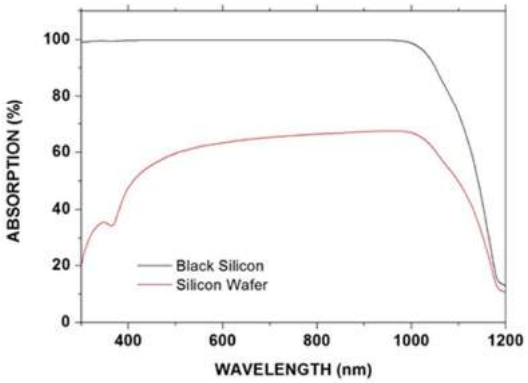


Figure 3: Comparison of the absorption of Black Silicon (BS) obtained by reactive ion etching at room temperature and traditional silicon wafer. Optical properties of the samples were also measured in NIR and SWIR bands.

The shape and the density of the nano-structures are modified by small variations of these parameters because of the sensitive competition between etching and passivation mechanisms. Increasing the chemical or physical etching will lead to smaller and sharper structures due to the lack of passivation. On the other hand, a too strong passivation will block the etching mechanism and structures become smaller and rounder.

A remarkable combined effect of doping and surface structuring obtained by F. Atteia [5] is observed for the reflection of Black Silicon. When the sulfur concentration is high enough, the discrete states broaden and become a band, allowing absorption of less energetic photon. The sample can be annealed to strengthen the diffusion of the sulfur into the silicon.

Random structuration of silicon surfaces has demonstrated a strong efficiency due to light scattering and light trapping along the rough surface. It is a perfect example of tailoring light scattering with randomly rough surfaces.

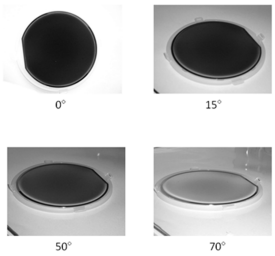


Figure 4: Backscattering increases for incidence angle larger than 50°.

2.2. Metafilms

In this section we consider metafilms composed of silver nanoparticles. With the help of these nanoparticles we can control the light-matter interaction. The use of nanoparticles allows us a precise control of the optical properties. The optical properties of the nanoparticles are size and shape dependent (Fig. 5), therefore a precise control of the optical properties is achieved by controlling the morphology of the nanoparticles. And through recent progress in chemistry, differently sized and shaped nanoparticles can be produced. In this part, we focus on silver nanoparticles with a control of the optical properties in the visible spectrum and near infrared spectrum. The interest in silver nanoparticles originates in their plasmonic properties, which result from the interaction of an electromagnetic wave with the electron cloud of the nanoparticles. Optical properties of the silver nanoparticles are driven by ability to support localized surface plasmon resonances, which gives an enhanced absorption of the incident electromagnetic waves if the frequency of this electromagnetic wave corresponds to the resonance frequency of the silver nanoparticles.

To demonstrate the control of the absorption of the incident wave and the control of the color, we consider silver nano-particles of different shapes (prism, spheres, and cubes) synthetized by easy wet chemistry methods [6-8]. The silver nanoparticles are synthesized by a modified polyol process and successfully embedded in a polymer thin film as discussed in the following. We consider, firstly, colloidal solutions of nanospheres (yellow colloidal solution) and differently sized nanoprisms (from orange to blue colloidal solutions) (Fig.5). In the visible wavelength range, the optical control is linked to a controlled-absorption of the metamaterial composed of nanoparticles. In Figure 5, we see the impact of shapes and sizes of silver nanoparticles on absorption of light. The sizes of the prisms are less than 100nm.

The next step consists in obtaining efficient and tunable absorption for a quasi-two-dimensional structure that is to say a metafilm. These structures are essential for a variety of applications, such as designing controlled-reflectance surfaces for stealth specifications, photovoltaic devices or detector elements for imaging. We will demonstrate that metamaterials based upon metallic elements are particularly efficient as absorbing media, because of the excitation of localized surface plasmon resonances. The excitation wavelength of these resonances can be tuned by structuring the design of the nanoparticles. Wet chemistry synthesis yields high concentration of nanoparticles with a small size disparity. Nanospheres and nanocubes are produced by a modified polyol process in ethylenglycol. In a first step of the synthesis, nanospheres are produced. These nanospheres then grow into nanocubes with time. By stopping the reaction prior to the nanocube growth, 20 nm diameter nanospheres are obtained. In the following, we will use nanocubes measuring about 40 nm edge length. The size of the produced nanoparticles is determined by transmission electron microscopy. Increasing the reaction time produces larger nanocubes. Excess polyvinylpyrrolidone (PVP) is added to the colloidal solution to protect the nanoparticles. The PVP forms a 1 nm thick shell around the nanoparticles as confirmed by the TEM image (Fig.6). Several centrifugation steps increase the concentration of nanoparticles. At first we consider silver nanocubes as the smallest component part (nanocrystal) of the silver nanoparticles used in our absorber. The PVP solution is mixed together with the colloidal solution to be deposited. The PVP-nanoparticle solution is deposited by spin coating on previously cleaned microscopic glass substrates. The thin film thickness deposited by spin coating depends on the rotation speed and time and ranges from a few tens of nanometers up to 1 micrometer. The sizes of the deposited nanoparticles do to not vary during the deposition. PVP is a flexible polymer which could open applications on flexible devices. The embedded nanoparticles support the excitation of surface plasmon resonances when light interacts with the metal nanoparticle and couples to its free electrons. The nanoparticles are randomly dispersed in the layer. Elaborating these composite films is not straightforward as nanoparticles have a general tendency to aggregate into clusters rather than dispersing in the polymer host We consider two metafilms: in the first example, the nanoparticles are only composed of silver nanocubes, the nanocrystal building blocks (Fig.7 and 8); in the second example, we have one-dimensional (1D) chains of nanocubes dispersed randomly in the PVP (Fig.9 and 10). The length of the different 1D chains are randomly produced and the 1D chains of nanocubes support different resonance wavelengths, which can broaden the absorption band. In this paper, we demonstrate a simple method to create a metafilm absorber by randomly chemically synthesized 1D chains of silver nanocubes embedded in a PVP film, making no effort to control the spatial arrangement of the cubes in the film. This makes them easy to produce over large areas. The thickness of the metafilm is about 300nm (Fig.9). The appeal of these metafilm lies in their ability to exhibit electromagnetic properties of absorption that are not available from natural materials. Nano-cubes present, in the thin film layer, several absorption peaks associated to the localized surface plasmon resonance, as shown in Figure 8.

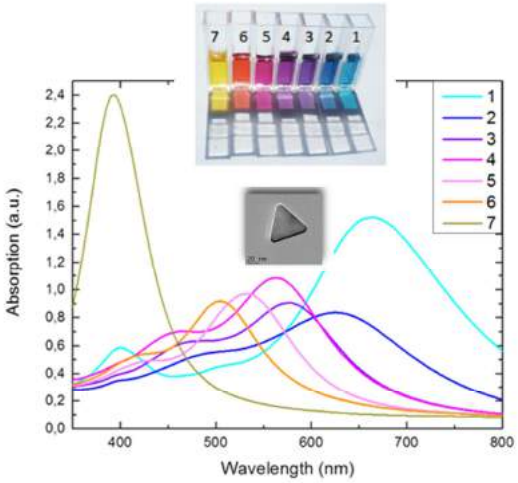


Figure 5: Impact of shapes and sizes of silver nanoparticles on absorption of light.

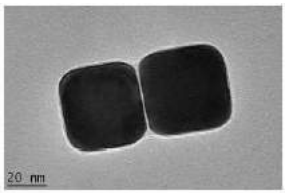


Figure 6: TEM image of the nanocubes.

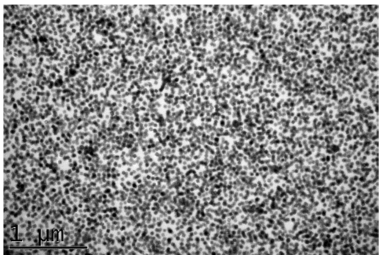


Figure 7: TEM images of the PVP thin films with dispersed nanocubes. In this film, we have only single building blocks of nanocubes.

The total reflectance (Fig.8) of the PVP thin films with dispersed nanocubes deposited on glass was measured by collecting signal in an integration sphere, at near-normal incidence angle of 6°. The total reflection is the sum of the diffuse reflection and the specular reflection. The absorption peak around 450 nm is associated to the dipolar resonance of the nanocubes. The peaks around 393nm and 355nm correspond respectively to the quadrupolar resonances of the nanocubes and the resonance associated with the cubic shape of the nanoparticles, this peak is linked to the sharp corners of the nanocube.

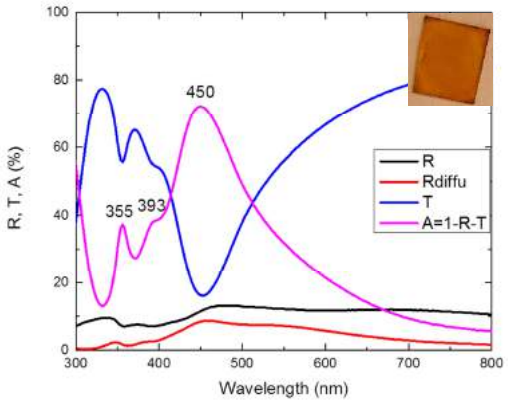


Figure 8: Total reflection (R), diffuse reflection (Rdiffu), absorption (A) and transmission (T) measured for the film on glass.

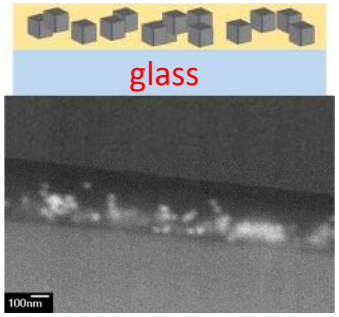


Figure 9: Example of SEM image of the film cross-section for aggregated nanocubes, i.e. one-dimensional chains of silver nanocubes dispersed in the PVP film.

We now consider the electromagnetic properties of a thin film with one-dimensional aggregated chains of silver nanocubes (Fig.9 and 10) deposited on glass.

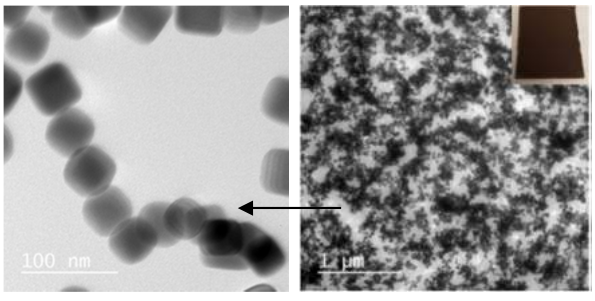


Figure 10: TEM images of the PVP thin films with embedded one-dimensional chains of silver aggregated nanocubes. In the upper right side, we can notice the black color of this nanofilm.

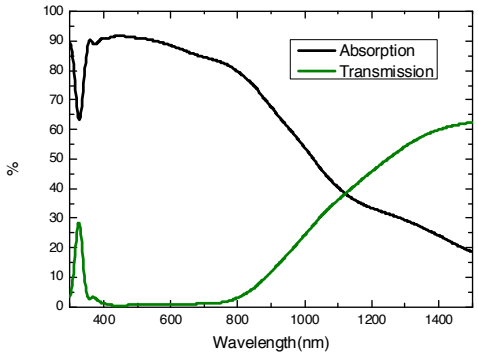


Figure 11: Absorption and transmission of the thin film of Figure 8 in the visible, near-infrared (NIR) and short-infrared band (SWIR).

We show that the film-coupled chains of nanocubes provide an absorption spectrum close to 0.9 and a transmission close to 0 in the visible band. The film has a thickness of 300nm. The absorption properties of this nanofilm can be tailored by varying the size of the aggregated chains of nanocubes where the electromagnetic response of the whole arises from the individual properties of the different chains, or the collective responses of the different constituent elements of the thin film.

We study (Fig.11) the reflectance of the film of Figure 9. We give the total reflectance, the diffuse reflectance and the specular reflectance. To determine the specular reflection, the diffuse reflectance was subtracted from the total reflectance in the integrated sphere.

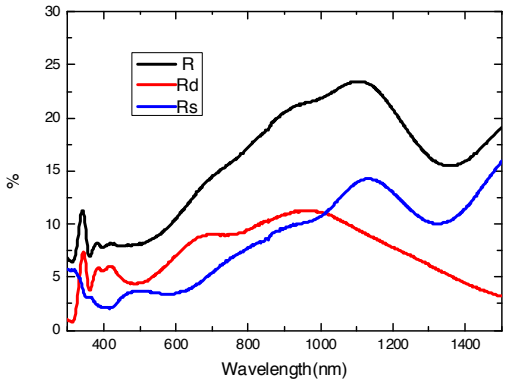


Figure 12: Total reflectance, diffuse reflectance and specular reflectance of the sample described in Figure 10.

The total reflectance (Fig.12) measured in the integrated sphere is the total hemispherical intensity scattered by the sample at an incidence of 6°. Depositions on glass yield highly homogeneous layers. This sample can be considered as a homogeneous material characterized by an effective medium. The following part introduces the theoretical analysis of the diffuse scattering from this kind of metafilm and the effective medium theory taking into account the multiple scattering of the particles in the layer and the polarization of the light.

3. Effective medium theory and scattering at low grazing incidence

3.1. Effective medium theory and multiple scattering theory

In this section we try to interpret the different results for the diffuse or total reflectance of the two metafilms that we obtained in the previous chapter. To understand the different scattering events that take place in the structure of the metafilms, we rapidly present a theory of transport based on an equation for the second statistical moment of the scattered electromagnetic field, i.e. the Bethe-Salpeter equation in which the vectorial character of electromagnetic wave is taken into account. We can derive the radiative transfer equation from the Maxwell equations. The procedure is to write the Maxwell equations in an integral form with the help of Green tensors and to apply the Wigner transform to the considered equation. The main advantage to starting from wave equations is that we are able to take into account new contributions to the scattered intensity such as the enhanced backscattering and the correlations between the scatterers of the slab that cannot be obtained from phenomenological radiometric considerations. We do not aim at developing the complete theory, which is described in [9-11] We are going to model our sample of section 2 by a three-dimensional slab, which is composed of an incident medium of permittivity ε_0, a first randomly rough boundary, a random medium defined by a permittivity ε_1 which contains nanoparticles, a second randomly rough boundary and a semi-infinite homogeneous medium with a permittivity ε_2. The N nanoscatterers of the random slab are defined by their positions $r_1,..,r_N$ and the probability density function of finding the N particles at position $r_1,..,r_N$ in the layer. The main characteristic, we must study for the scattering from a random slab is the specific intensity $\boldsymbol{I(R,k)}$. The specific intensity can be deduced from the Wigner function of the electrical field [9].

If we take into account the polarization of the wave, the specific intensity is defined as a Stokes vector or a tensor which gives the power flux per unit area and solid angle at the point $\boldsymbol{R}$ in the direction $\boldsymbol{k}$. The relation between the specific intensity and the incoherent cross-section is given by a product of two tensors. For a random layer with rough interfaces, the incoherent specific intensity can be decomposed into four parts (see [9-10] for the detailed formulas):

$$\overline{\boldsymbol{I}}^{incoh} = \overline{\boldsymbol{I}}^{incoh}_{L=0} + \overline{\boldsymbol{I}}^{incoh}_{L=1} + \overline{\boldsymbol{I}}^{incoh}_{Ladder} + \overline{\boldsymbol{I}}^{incoh}_{Crossed}$$

The first term $\boldsymbol{I}^{incoh}_{L=0}$ gives the scattering by the slab with rough boundaries and defined by an effective permittivity ε_e

given by the QC-CPA approximation. We have introduced [11] a formulation for the effective permittivity for different classes of Rayleigh scatterers. In the following formula, we take the example of two classes of scatterers *a* and *b*. The expression of the effective permittivity is given by:

$$\epsilon_e(\omega) = \epsilon_1 + \frac{1}{K_{vac}^2} \frac{n_a \bar{t}_a^1(\omega) + n_b \bar{t}_b^1(\omega)}{1 - \left(\frac{1}{3K_e^2} (n_a \bar{t}_a^1(\omega) + n_b \bar{t}_b^1(\omega)) + \frac{iK_e}{6\pi} [(w_a - 1)\bar{t}_a^1(\omega) + (w_b - 1)\bar{t}_b^1(\omega)] \right)}$$

Where the transition operator $\bar{t}_i^1(\omega)$ is written in the following form ($i = a$ or b):

$$\bar{t}_i^1(\omega) = \frac{3\, K_{vac}^2 \epsilon_e\, v_i\, (\epsilon_i - \epsilon_1)}{(\epsilon_i - \epsilon_1)[1 - \frac{\mathrm{i}\, 3K_e K_{vac}^2}{6\,\pi} \epsilon_e v_i] + 3\epsilon_e} .$$

and,

$$w_i = \frac{(1 - f_{vol}^i)^4}{(1 + 2\, f_{vol}^i)^2} .$$

In these equations, n_i is the number of particles of type i, v_i their volume.

$f_{vol}^i = n_i\, v_i$ is the volume fraction, and we have:

$$K_e^2 = \epsilon_e K_{vac}^2$$

$K_{vac} = \omega/c$, c is the speed of light in vacuum. The equation related to the effective permittivity is a non-linear equation connecting the effective permittivity ε_e and the permittivities ε_1 of the layer, and ε_a, ε_b of the scatterers. Its derivation is obtained with the assumptions (QC-CPA, "the Quasi-Crystalline and Coherent Potentiel Approximation") and gives a tractable formula for the effective permittivity. This formula for the effective permittivity is a generalization of the usual Maxwell-Garnett formula or the Keller approximation. We can notice that metallic nanoparticles with a size of a few nanometers exhibit behaviors different than that of the bulk due to confinement effects which change the electronic properties. The treatment of the permittivity of such nanoparticles cannot be considered without taking into account quantum effects related to the behavior of electrons in the atom cloud. The permittivity of a nanoparticle whose dimension is less than 10 nm is given by a quantum expression where conduction electrons are modeled as a gas of free electrons constrained by infinite potential three-dimensional barriers at the boundary of the particle.

The second term $\mathcal{I}_{L=1}^{incoh}$ of the incoherent scattered specific intensity is related to the approximation where only one process of interaction (scattering, absorption) by a nanoparticle is taken into account. In this process, there is no multiple scattering between the different nanoparticles.

The third term $\mathcal{I}_{Ladder}^{incoh}$ corresponds to the ladder approximation.

The ladder approximation describes the transport of intensity as an incoherent process. This approximation contains the multiple scattering process in the slab.

The fourth term $\mathcal{I}_{Crossed}^{incoh}$ of the specific intensity corresponds to the most-crossed approximation. The most-crossed approximation is responsible for coherent backscattering enhancement (weak localization) producing an intensity peak in the backscattering direction due to the interference of waves following the same path but in opposite directions.

For our two examples of metafilms, i.e. (1) nanocubes dispersed in PVP films and (2) aggregated nanocubes dispersed in PVP films, the absorption diagrams are different. For these two types of metafilm, the boundaries of the slab are quasi-plane. The diffuse field intensity scattered by the surfaces is negligible. The random distribution of the nanoparticles in the thin films should result in metafilms whose optical properties are not polarization dependent. For the first metafilm, the structure is a resonant one, and the process of interaction is dominated by the resonant absorption of the nanocubes. The second metafilm contains different chains of nanocubes, its structure is more inhomogeneous and the process of interaction between the scatterers is more important. The resonance wavelength is then redshifted for long chain of nanocubes. The second and third terms of the specific intensity gives the diffuse reflection of the film and the multiple scattering between chains of aggregated nanocubes (the third term of the specific intensity) helps controlling the absorption of the slab, therefore the transmission through the metafilm is quasi-null.

The most important contribution of the specular reflection is given by the first term of the specific intensity which depends on the effective permittivity.

For the slab (1), we observe a diffuse reflection, which increases after 400nm and decreases slowly after 450nm. The specular reflection becomes more important after 600nm, the metafilm can be considered as homogeneous for the incident wavelength in the waveband after 700nm (Fig.5).

For the slab (2), the diffuse reflection increases from 400nm to 1000nm and decreases from 1000nm to 1500nm. The transmission of the film is null between 400nm and 800nm (Fig.8). The slab (2) is a better absorber but the scattering events are more important and the diffuse reflection is more important.

3.2. Light scattering at grazing incidence

In this last section, we are going to take an interest in the theoretical expression of the light scattering on randomly rough surfaces at grazing angles. It is particularly of interest for randomly rough metasurfaces with small reflectivity.

When materials are structured at the scale of light wavelength or a fraction of the wavelength, optical waves are diffracted, scattered and, the multiple waves obtained can interfere together. In this work we consider an electromagnetic plane wave of arbitrary polarization incident at low grazing angles upon a three-dimensional inhomogeneous medium bounded by a randomly rough interface (Fig.13). The subject of our interest concerns a

random medium, consisting of a statistical ensemble of different scattering species and artificial material structures developed on base of dielectric or metallic resonant nanoparticles. As we have previously seen, the expression of the effective permittivity of the random volume, developed in this paper, is extended to random media with different types of particles and bounded by rough surfaces [11].

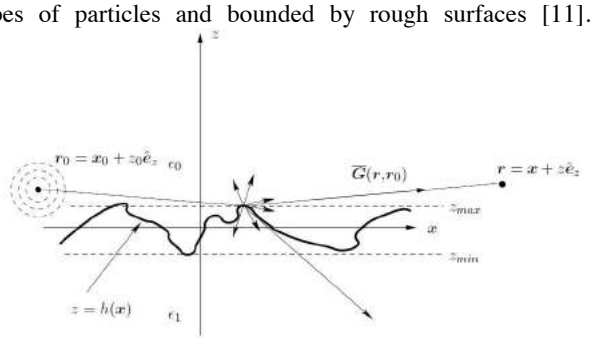


Figure 13: Representation of the Green function.

The randomly rough surface is defined by the correlation function:

$$W(\boldsymbol{x}_1 - \boldsymbol{x}_2) = < h(\boldsymbol{x}_1)\, h(\boldsymbol{x}_2) >$$

ε_1 can be an effective permittivity. Mathematically, the scattering process is decomposed in introducing two Green functions.

$\overline{\boldsymbol{G}}(\boldsymbol{r},\boldsymbol{r}_0)$ gives the electrical field at the point $\boldsymbol{r}$ which is produced by a point source of spherical wave at the point $\boldsymbol{r_0}$. The spherical wave is scattered by a randomly rough surface. Then we introduce the Green function for a plane surface: $\overline{\boldsymbol{G}}_0(\boldsymbol{r},\boldsymbol{r}_0)$

The two Green functions are related by a Lipman-Schwinger equation:

$$\overline{\boldsymbol{G}}(\boldsymbol{r},\boldsymbol{r}_0) = \overline{\boldsymbol{G}}_0(\boldsymbol{r},\boldsymbol{r}_0) + \int \mathrm{d}^3\boldsymbol{r}_1\, \mathrm{d}^3\boldsymbol{r}_2\, \overline{\boldsymbol{G}}_0(\boldsymbol{r},\boldsymbol{r}_1) \cdot \overline{\boldsymbol{V}}(\boldsymbol{r}_1,\boldsymbol{r}_2) \cdot \overline{\boldsymbol{G}}(\boldsymbol{r}_2,\boldsymbol{r}_0)$$

$\overline{\boldsymbol{V}}$ is the potential describing the interaction of the wave with the rough surface

This equation can be written as:

$$\overline{\boldsymbol{G}} = \overline{\boldsymbol{G}}_0 + \overline{\boldsymbol{G}}_0 \cdot \overline{\boldsymbol{V}} \cdot \overline{\boldsymbol{G}}$$

We can obtain the following equation:

$$\overline{\boldsymbol{G}} = \overline{\boldsymbol{G}}_0 + \overline{\boldsymbol{G}}_0 \cdot \overline{\boldsymbol{V}} \cdot \overline{\boldsymbol{G}}_0 + \overline{\boldsymbol{G}}_0 \cdot \overline{\boldsymbol{V}} \cdot \overline{\boldsymbol{G}}_0 \cdot \overline{\boldsymbol{V}} \cdot \overline{\boldsymbol{G}}_0 + \ldots$$

In this equation, the different multiple scattering events on the randomly rough surface are clearly given. With a perturbative development of the boundary conditions on the surface and using the Reduced Rayleigh Equations [12], we can express the potential in function of the surface profile:

$$z = h(\boldsymbol{x})$$

With the following definition $(K_i)^2 = \varepsilon_i(\omega/c)^2$, $i = 0$ or 1, we obtain for the mean value of the Green function, which gives the coherent field:

$$< \overline{\boldsymbol{G}}(\boldsymbol{r},\boldsymbol{r}_0) >= \frac{\mathrm{i}}{2} \iint \frac{\mathrm{d}^2\boldsymbol{p}}{(2\pi)^2}\, \mathrm{e}^{\mathrm{i}\,\boldsymbol{p}\cdot(\boldsymbol{x}-\boldsymbol{x}_0)} \left[\overline{\boldsymbol{I}}\, \mathrm{e}^{\mathrm{i}\,\alpha_0(\boldsymbol{p})|z-z_0|} + \overline{\boldsymbol{R}}^{moy}(\boldsymbol{p})\, \mathrm{e}^{\mathrm{i}\alpha_0(\boldsymbol{p})(z+z_0)} \right]$$

with:

$$\boldsymbol{r} = \boldsymbol{x} + z\,\hat{\boldsymbol{e}}_z,\ \boldsymbol{r}_0 = \boldsymbol{x}_0 + z_0\,\hat{\boldsymbol{e}}_z,$$

we have:

$$\alpha_0^2(\boldsymbol{p}) \equiv K_0^2 - \boldsymbol{p}^2$$
$$\alpha_1^2(\boldsymbol{p}) \equiv K_1^2 - \boldsymbol{p}^2$$

and:

$$\overline{\boldsymbol{R}}^{moy}(\boldsymbol{p}) = \begin{pmatrix} \frac{\epsilon_1\,\alpha_0(\boldsymbol{p}) - \epsilon_0\,\alpha_1(\boldsymbol{p}) + \mathrm{i}\,\epsilon_1\,M_V(\boldsymbol{p})}{\epsilon_1\,\alpha_0(\boldsymbol{p}) + \epsilon_0\,\alpha_1(\boldsymbol{p}) - \mathrm{i}\,\epsilon_1\,M_V(\boldsymbol{p})} & \\ 0 & \frac{\alpha_0(\boldsymbol{p}) - \alpha_1(\boldsymbol{p}) + \mathrm{i}\,M_H(\boldsymbol{p})}{\alpha_0(\boldsymbol{p}) + \alpha_1(\boldsymbol{p}) - \mathrm{i}\,M_H(\boldsymbol{p})} \end{pmatrix}.$$

with:

$$\overline{\boldsymbol{M}} = \begin{pmatrix} M_V & 0 \\ 0 & M_H \end{pmatrix} = < \overline{\boldsymbol{V}} \cdot \overline{\boldsymbol{G}}_0 \cdot \overline{\boldsymbol{V}} >$$

$\overline{\boldsymbol{M}}(\boldsymbol{p})$ is expressed in function of $\overline{\boldsymbol{V}}$.

The incoherent intensity is given by the following formula:

$$\delta I = < \overline{\boldsymbol{G}}\overline{\boldsymbol{G}}^* > - < \overline{\boldsymbol{G}} >< \overline{\boldsymbol{G}}^* > = < \overline{\boldsymbol{G}} >< \overline{\boldsymbol{G}}^* > : < \overline{\boldsymbol{V}}\overline{\boldsymbol{V}}^* > : < \overline{\boldsymbol{G}} >< \overline{\boldsymbol{G}}^* >$$

A good approximation of $< \overline{\boldsymbol{G}} >$ is necessary to calculate the incoherent intensity. We can notice that the roughness do not modify the general form of the Green function but only the Fresnel coefficients. So we can use the asymptotical development of the Sommerfeld theory by replacing the Fresnel coefficients by the coefficients of the matrix $\boldsymbol{R}^{moy}$. The coefficients M_H and M_V describe the attenuation of the mean Green function due the roughness of the surface. This attenuation corresponds to the transfer of energy of the coherent part to the incoherent part of the scattered signal.
If the positions of the source point and the observation point are far from the surface, we can use the steepest descent method and we have:

$$< G(\boldsymbol{r},\boldsymbol{r}_0) > \simeq \left(\overline{\boldsymbol{I}} + \frac{\nabla\nabla}{K_0^2} \right) \frac{\mathrm{e}^{\mathrm{i}\,K_0\,||\boldsymbol{r}-\boldsymbol{r}_0||}}{4\pi\,||\boldsymbol{r}-\boldsymbol{r}_0||} + \overline{\boldsymbol{R}}^{moy}(\boldsymbol{p}_{asym}) \frac{\mathrm{e}^{\mathrm{i}\,K_0\,||\boldsymbol{r}-\boldsymbol{r}_0^s||}}{4\pi\,||\boldsymbol{r}-\boldsymbol{r}_0^s||}$$

with:

$$\boldsymbol{p}_{asym} = K_0 \frac{\boldsymbol{x}-\boldsymbol{x}_0}{||\boldsymbol{r}-\boldsymbol{r}_0^s||}$$

The first term corresponds to the direct propagation between the source point and the observation point without interaction with the rough surface. The different parameters of the previous equation are defined in Fig.12. For grazing

angles, we can easily verify that the two terms of the equation cancel each other out for $\theta = \pi/2$.

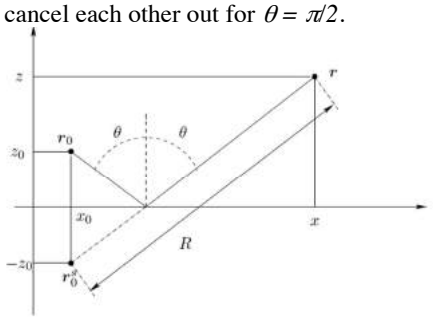


Figure 14: Definition of the parameters.

For grazing angles, we modify the steepest descent method by taking into account the singularities of the integrant of the mean Green function. These singularities represent the different surface waves excited by the incident wave.
To simplify the mathematical problem of scattering, we pose $\varepsilon_0 = 1$, and we consider a 1D randomly rough surface. The surface is defined by the following permittivity:

$$\mathrm{Re}(\epsilon_1) < -1$$
$$\mathrm{Re}(\epsilon_1) \gg \mathrm{Im}(\epsilon_1)$$

For this medium, the reflection coefficient R_V has a pole corresponding to plasmon polariton surface wave for the TM polarization. The principal contribution for the mean Green function is given by:

$$< G(\boldsymbol{r},\boldsymbol{r}_0) > \simeq \mathrm{e}^{\mathrm{i}\, p_r\,(x-x_0)+\mathrm{i}\alpha_0(p_r)\,(z+z_0)}\; Res_{p=p_r}\{\, R_V(p)\}$$

p_r is the root of the following equation:

$$\epsilon_1\,\alpha_0(p_r) + \epsilon_0\,\alpha_1(p_r) - \mathrm{i}\,\epsilon_1\,M_V(p_r) = 0$$

$Res_{p=p_r}\{\, R_V(p)\}$ is the residue of the function $R_{V(p)}$.
The Green function decreases when the distance from the randomly rough surface becomes larger.
We have:

$$\alpha_0(p_r) = \alpha_0' + \mathrm{i}\,\alpha_0''$$

with

$$\alpha_0'' > 0$$

And the mean Green function is given by:

$$< G(\boldsymbol{r},\boldsymbol{r}_0) > \simeq \frac{\mathrm{i}}{2}\,\mathrm{e}^{\mathrm{i}\,p_r\,(x-x_0)+\mathrm{i}\alpha_0'\,(z+z_0)}\,\mathrm{e}^{-\,\alpha_0''(z+z_0)}\; Res_{p=p_r}\{\, R_V(p)\}$$

We have the same behavior for the incoherent intensity (exponential decreasing) at grazing incidence.
The incoherent intensity is given by:

$$\delta I(\boldsymbol{r}) = < G(\boldsymbol{r},\boldsymbol{r}_0)G^*(\boldsymbol{r},\boldsymbol{r}_0) > - < G(\boldsymbol{r},\boldsymbol{r}_0) >< G^*(\boldsymbol{r},\boldsymbol{r}_0) >$$
$$\propto \sigma^2\,\exp\left[-2\,\alpha_0''\,(z+z_0)\right],$$

the root mean square of the randomly rough surface is :

$$\sigma = \sqrt{< h(x)^2 >}$$

We have introduced the asymptotic development of the Green function in the integral equation to take into account the different surface waves and we generalize the multiple scattering theory at grazing angles. And we have obtained the expressions for the coherent field and incoherent intensity at grazing incidence.

4. Conclusions

In this paper, we have described a Black Silicon surface which presents very low reflectance in the visible and near infrared domains. We have discussed the absorption of silver cubic nanoparticles embedded in a thin film. Two metafilms were analyzed, nanocubes embedded in PVP, random chains of nanocubes embedded in PVP. The last one presents a remarkable absorption higher than 80% in the entire visible band. For the first time, we have shown that high density of randomly distributed chains of silver nanocubes within the polymer host allows almost perfect visible light absorption Control of the aggregation of nanoparticles to further tune the optical properties shows promising results. In the last theoretical part of the paper, we have described a multiple scattering theory in the ladder approximation to interpret the phenomenology of the wave scattering in the different realized metafilm. And we have obtained the expressions of the scattered coherent field and the scattered incoherent intensity at grazing incidence and we discuss the multiple scattering for surface waves. These formulations contribute to understand the light scattering process at very low grazing angles for the metasurfaces.

References

[1] G. Berginc, Periodic or random nanostructures for light scattering control, *Applied Physics A*, 122: 318, 2016.
[2] J. Lv et al., Review application of nanostructured Black Silicon, *Nanoscale Research Letters* 13:110, 2018.
[3] T.H. Her, R.J. Finlay, C. Wu, S. Deliwala, E. Mazur Microstructuring of silicon with femtosecond laser pulses, *Appl Phys Lett,* 73:1673, 1998.
[4] L. Escoubas, V. Brissonneau, G. Berginc, J.-J Simon, Method for the random texturing of a semiconductor substrate, WO 2015186064 A1, 2014.
[5] F. Atteia and al., Properties of black silicon obtained by reactive ion etching (RIE) at room temperature, to be submitted.
[6] M. Carlberg, F. Pourcin et al, Optical response of heterogeneous polymer layers containing silver nanostructures, *Beilstein J. Nanotechnol.* 8: 1065–1072, 2017.
[7] M. Carlberg, Modeling, realization and optical characterization of heterogeneous layers containing nanoparticles, *PhD thesis, Aix-Marseille University* 2017.

[8] F. Pourcin et al, Solution-processed thin films using silver nanocubes embedded polymer with controlled reflectance and high substrate tolerance, submitted.
[9] G. Berginc and A.A.Maradudin, Scattering properties of random structures in thin films, *in Optical Thin Films and Coatings* Ed. A Piegari and F Flory, Oxford: Woodhead Publishing Limited, pp 177-289, 2013.
[10] G. Berginc, Electromagnetic coherent effects in metamaterials with randomly rough surfaces, *J. Phys.*: 633 012043, 2015.
[11] G. Berginc, Coherent light scattering of heterogeneous randomly rough films and effective medium in the theory of electromagnetic wave multiple scattering, *Quantum Electronics* 43: 1055-1064, 2013.
[12] A. Soubret, G. Berginc and C. Bourrely, Application of reduced Rayleigh equations to electromagnetic wave scattering by two-dimensional randomly rough surfaces, *Phys Rev B* 63: 245411, 2001.

Advanced Passive and Active Metasurfaces

Waveguided modes, nonlinearity and magneto-optics in self-assembled metamaterials

Mazhar E. Nasir[1,], Pan Wang[1], Anton Bykov[1], Alexey V. Krasavin[1], Bo Fan[2], Viktor A. Podolskiy[2] and Anatoly V. Zayats[1]*

[1]Department of Physics, King's College London, Strand, London, WC2R 2LS, UK

[2]Department of Physics and Applied Physics, University of Massachusetts Lowell, Lowell, MA, 01854, USA

**corresponding author: mazhar.nasir@kcl.ac.uk*

Abstract:

Hyperbolic metamaterials are playing a key role in the design of integrated deep-subwavelength biochemical sensors, nonlinear nanophotonic devices and magneto-optical applications. Here we discuss a waveguided mode structure of nanorod hyperbolic metamaterials and its effects on various optical properties, such as magneto-optical and nonlinear responses. The mode structure variation with nanorod length will be discussed. Nonlinear response of these metamaterials will be presented, focusing on the second-harmonic generation. We also describe the design and magneto-optical response of core-shell plasmonic nanorod metamaterials.

Introduction:

Plasmonic nanorod metamaterials with hyperbolic dispersion are emerging as a novel platform for applications in sensing[1, 2], ultrasound detection[3], controlling quantum optical processes[4], ultrafast switching of light polarization[5] and quantum mechanical tunnelling[6]. These anisotropic metamaterials exhibit hyperbolic dispersion in the spectral range determined by the electromagnetic interaction between the rods forming the array and can be described within the effective medium theory via the effective permittivity tensor components $\varepsilon_x = \varepsilon_y \neq \varepsilon_z$, corresponding to the directions perpendicular to (x,y) and along (z) nanorod axes[7-9]. A large nonlinear optical response has been observed in plasmonic nanorod metamaterials over a broad spectral range[10-14]. The hyperbolic dispersion in Au nanorod metamaterials exhibit various unusual modes, which are interesting for nonlinear nanophotonic devices and quantum information processing.

.

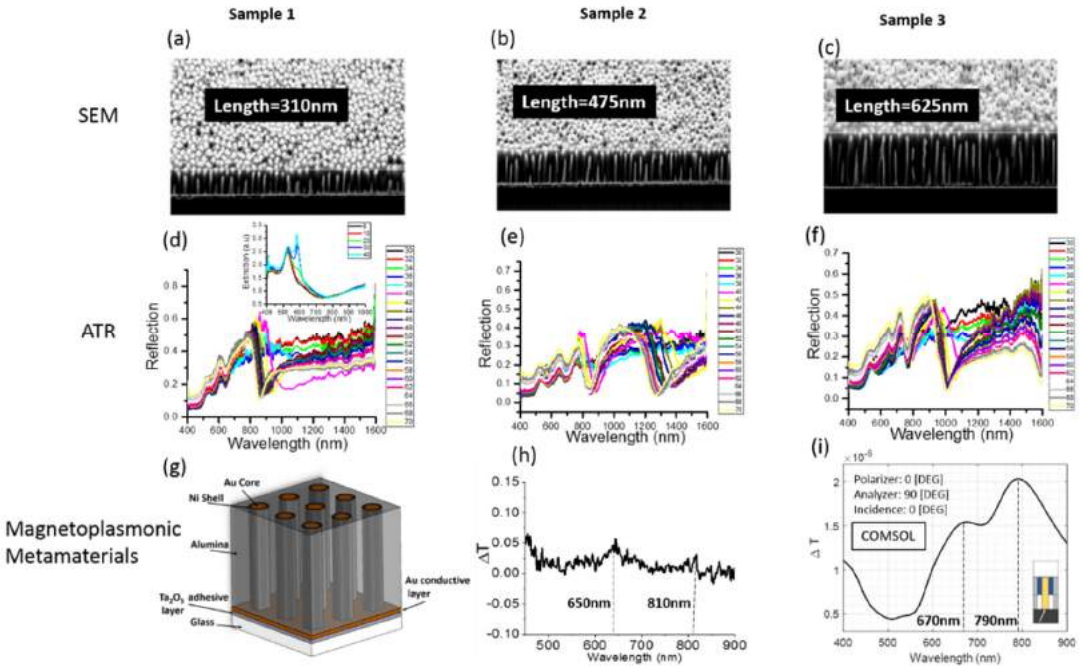


Figure 1: (a–c) SEM cross-sections of samples 1, 2 and 3, respectively. (d–f) Corresponding reflection spectra of the metamaterials measured in an ATR geometry. (g) Schematic of magnetoplasmonic metamaterials. (h–i) Experimentally measured and simulated transmission spectra in cross-polarization configuration with **B** along the direction of the incident light.

Magnetoplasmonics combine magnetism and plasmonics for the development of novel metamaterials to both enhance magneto-optical effects and control plasmonic response. The enhancement of magneto-optical activity in magnetic metamaterials can be utilised for potential

applications in many fields such as bio-sensing, data storage, and nonlinear optics.

Experimental Section:

The metamaterials consist of an assembly of Au nanorods electrochemically grown into a highly ordered porous aluminium oxide template. The structural parameters can be controlled by altering the fabrication conditions with typical dimensions being in the range of rod lengths between 150 and 700 nm, rod diameter 55nm and separation 100 nm.

Magnetoplasmonic metamaterial comprises an array shelled plasmonic nanorods with Au cores of 30 nm in diameter and magneto-optic Ni shells of about 8 nm thickness embedded into a alumina substrate.

Discussion:

SEM images of three samples are shown in Figs. 1a, 1b and 1c. The extinction spectra of the nanorod array in alumina show two pronounced peaks at 525 and 590 nm, as shown in Fig. 1d (inset). The origin of these resonances can be traced to different plasmonic modes of the individual nanorods, modified by the interaction in the assembly. The transverse mode is related to the electron motion perpendicular to the nanorod long axes and can be excited with the light having an electric-field component perpendicular to it, whereas the longitudinal mode is related to the electron oscillations along the nanorod axes and requires p-polarized light to be excited with a component of the incident electric field along the nanorods.

When excited with p-polarized light, the same nanorod metamaterials in the ATR geometry reveals a waveguided mode in the near-infrared spectral range, as shown in Fig. 1d. When the length of nanorods is increased, more waveguided modes emerge as shown in Figs. 1e and 1f. It has been observed that there is strong absorption with increasing length of nanorods but position of transverse and longitudinal modes remains same. Fig. 1g shows geometrical structure of magnetoplasmonic metamaterials and Fig 1h shows the MO spectra measured in cross polarization configuration with incident light at 0° and magnetic field along the direction of the incident light. Two peaks observed at 650 nm and 810 nm are validated with modelling shown in Fig. 1i.

The waveguided mode structure strongly influences second-harmonic generation from the metamaterial and its magneto-optical properties.

Conclusions:

We have investigated the mode structures of long range nanorod metamaterials and observed multiple waveguided modes. The waveguided modes of plasmonic nanorods metamaterials can be tailored by the length of nanorods while keeping the diameter and separation same. Magnetoplasmonic metamaterials have showed an enhanced magneto-optics response both in transmission and reflection.

References:

1. A. V. Kabashin, P. Evans, S. Pastkovsky, W. Hendren, G. Wurtz, R. Atkinson, R. Pollard, V. Podolskiy and A. Zayats, *Nat Mater* **8**, 867 (2009).
2. M. E. Nasir, W. Dickson, G. A. Wurtz, W. P. Wardley and A. V. Zayats, *Adv. Mater.* **26** (21), 3532 (2014).
3. V. V. Yakovlev, W. Dickson, A. Murphy, J. McPhillips, R. J. Pollard, V. A. Podolskiy and A. V. Zayats, *Adv Mater* **25** (16), 2351 (2013).
4. G. A. Wurtz, R. Pollard, W. Hendren, G. Wiederrecht, D. Gosztola, V. A. Podolskiy and A. V. Zayats, *Nat Nanotechnol* **6**, 107 (2011).
5. L. H. Nicholls, F. J. Rodríguez-Fortuño, M. E. Nasir, R. M. Córdova-Castro, N. Olivier, G. A. Wurtz and A. V. Zayats, *Nat. Photonics* **11** (10), 628 (2017).
6. P. Wang, A. V. Krasavin, M. E. Nasir, W. Dickson and A. V. Zayats, *Nat. Nanotechnol.*, https://doi.org/10.1038/s41565-017-0017-7 (2017).
7. N. Vasilantonakis, M. E. Nasir, W. Dickson, G. A. Wurtz and A. V. Zayats, *Laser Photonics Rev.* **9** (3), 345 (2015).
8. M. Nasir, S. Peruch, N. Vasilantonakis, W. Wardley, W. Dickson, G. Wurtz and A. Zayats, *Appl. Phys. Lett.* **107** (12), 121110 (2015).
9. W. Dickson, S. Beckett, C. McClatchey, A. Murphy, D. O'Connor, G. A. Wurtz, R. Pollard and A. V. Zayats, *Adv. Mater.* **27** (39), 5974-5980 (2015).
10. A. V. Krasavin, P. Ginzburg and A. V. Zayats, *Laser Photonics Rev.* **12**, 24 (2018).
11. B. Wells, A. Y. Bykov, G. Marino, M. Nasir, A. Zayats and V. Podolskiy, *arXiv preprint arXiv:1801.00069* (2017).
12. D. J. Roth, A. V. Krasavin, A. Wade, W. Dickson, A. Murphy, S. p. Kéna-Cohen, R. Pollard, G. A. Wurtz, D. Richards and S. A. Maier, *ACS Photonics* **4** (10), 2513-2521 (2017).
13. P. Ginzburg, D. J. Roth, M. E. Nasir, P. Segovia, A. V. Krasavin, J. Levitt, L. M. Hirvonen, B. Wells, K. Suhling and D. Richards, *Light: Science & Applications* **6** (6), e16273 (2017).
14. S. Peruch, A. Neira, G. A. Wurtz, B. Wells, V. A. Podolskiy and A. V. Zayats, *Advanced Optical Materials* **5** (15) (2017).

Numerical Optimisation and Near-Field Phase Transformation in Metasurface Design for Resonant Cavity Antennas

Invited Paper

Karu P. Esselle, Muhammad U. Afzal, Maria Kovaleva and Ali Lalbakhsh

School of Engineering, Macquarie University
Sydney, Australia
karu@ieee.org, muhammad.afzal@mq.edu.au, ali.lalbakhsh@mq.edu.au

Abstract

This paper reviews two of the latest techniques used to improve radiation performance of resonant cavity antennas (RCAs) by means of metasurfaces. The first technique employs numerical optimisation to find the optimal set of design parameters of a metasurface that produces the desired performance. The second technique is based on near-field phase transformation. Application of these techniques has led to a significant improvement in the performance of resonant cavity antennas compared to the classical design approaches.

Keywords — beam focusing; beam steering; near-field pahse trasnforamtion; numerical optimisation; phase correction

1. INTRODUCTION

Resonant cavity antennas (RCAs) are excellent for feeding large reflector dishes and can also replace antenna arrays for high-gain applications. RCAs have attracted considerable attention of the research community owing to their unique characteristics and superior radiation performance. RCAs are typically comprised of a cavity that extends in transverse direction and resonates in the longitudinal direction [1]. Several methods have been investigated to enhance their radiation performance with the latest being focused on metasurface design. This paper gives an overview of the RCA advances based on two techniques: numerical optimisation and near-field phase transformation.

Numerical optimisation is a powerful mathematical tool that can obtain the optimal design parameters much faster than the traditional trial-and-error approaches. Survival of the fittest is the basic idea of evolutionary optimisation algorithms, which were successfully applied to many electromagnetic (EM) designs. One of the algorithms that gained significant popularity in EM community is extremely simple yet powerful Particle Swarm Optimisation (PSO) [2]. In its classical form, it is ideal for continuous problems, but it has also been adapted for binary [3] and mixed-integer problems [4]. Recently, we have implemented PSO on the optimisation of all-dielectric [6,7] and printed RCAs.

The concept of phase transformation originated from the field of optics where it has been utilized to develop lenses for focusing a beam of light. Lenses achieve beam focusing by transforming a spherical wave front of an optical source to a planar wave front. The objective of near-field phase transformation is similar to lenses, however, the phase transformation here is performed in the near-field region at subwavelength spacing from the radiating antennas such as RCAs. There are several challenges in the realization of near-field phase transformation in metasurface design. Firstly, it is highly critical to have the accurate phase distribution on the surface of a RCA. Secondly, the phase transformation is to be done in such a way that it does not affect the base RCA.

The paper is organized such that Section 2 describes the optimisation method and its applications, and Section 3 presents the near-field phase transformation technique for RCAs performance enhancement.

2. USE OF NUMERICAL OPTIMISATION

PSO concept is based on swarm intelligence, and its distinctive characteristics are knowledge sharing between the agents and personal memory of the best observed positions in a search space. Over iterations, the agents move across the predefined region searching for the best possible fitness value. It is the responsibility of a designer to define such boundaries for each design parameter that the device could be feasible and the goals are realizable. Taking into account that the fitness of each potential design is calculated by simulation, it is highly desirable to reduce the number of function evaluations required for optimisation. It means that fast optimisation methods are preferable for EM problems. One of such methods is PSO with inertia weight [5].

We have shown in [6, 7] that by optimising the permittivity profiles of partially reflective surfaces of RCAs, non-intuitive permittivity distributions have been generated which result in high-gain (≈ 20 dB) and extremely wideband (70%) performance. In [6], the objective was to maximize the boresight directivity at the specified frequencies without taking into account the bandwidth, while in [7], the objective was to maximize the directivity-bandwidth product. The same optimization technique has been

successfully implemented on the design of phase-correcting metasurfaces.

3. NEAR-FIELD PHASE TRANSFORMATION

On the contrary to numerical optimisation, which relies on the mathematics, the near-field phase transformation technique aims to improve RCA far-field performance by engineering near-field phase distribution. The basic idea of near-field phase transformation is to manipulate and transform a given phase distribution to a desired phase distribution. It is similar to a transfer function that relates the two phase distributions. The transfer function is then is implemented by designing a metasurface. The near-field phase transformation method has been used: to enhance broadside directivity of RCAs and to achieve beam steering. It is worth mentioning that the detailed methodology has been reported in our earlier publications [8-11]; the purpose of this article is to summarize the advancements in RCAs' performance.

The directivity is enhanced by transforming a non-uniform near-field phase distribution of RCAs to a nearly uniform phase distribution [8, 10]. The phase transformation is being implemented using three different designs of phase transforming structure: stepped dielectric, continuous dielectric and a metasurface. The directive radiation characteristics of RCA were significantly improved by the application of three structures/surface. The application of stepped dielectric design reported in [8] improved the peak directivity by ~9 dB with a considerable 3dB radiation bandwidth. The phase transformation obtained from the metasurface in [10] resulted in ~8 dB increase in peak directivity and a radiation bandwidth of ~6.4%. It has also been shown that near-field transformation can be achieved by simulation-driven optimisation techniques to increase the peak directivity of RCAs [12, 13]. Performance comparison of the designs obtained by the aforementioned methods is given in Table 1.

Table 1. Performance comparison of RCAs designed using numerical optimisation and near-field phase transformation.

	Design Technique	Peak Directivity (dBi)	Bandwidth (%)
[6]	Optimisation	19.1	24
[7]	Optimisation	17.6	70
[8]	Phase Transformation	21.6	8
[9]	Phase Transformation	22.8 (dBic)	11.7
[10]	Phase Transformation	20.2	6.4
[12]	Optimisation	21.1	11.8

Recently, the beam steering of resonant cavity antennas has been demonstrated by two metasurfaces [11]. For the beam steering, an arbitrary phase distribution above an RCA is transformed into a linearly increasing phase distribution. A prototype developed at X-band frequencies demonstrated beam steering within a conical region having an apex angle of 102°. The unique and striking feature is that the total height of the antennas is only $1.3\lambda_0$, which became possible due to the near-field phase transformation.

Although the near-field phase transformation has been demonstrated for beam focusing and beam steering of RCAs, the method can be easily extended to other antennas. Also, the technique is applicable for beam shaping, beam forming, or for the design of multi-beam antennas.

4. CONCLUSION

Numerical optimisation and near-field phase transformation applied to design the metasurfaces for the enhancement of radiation performance in RCAs have been described and compared. Numerical optimisation resulted in RCAs with ~20dB gain and ~70% radiation bandwidth. The near-field phase-transforming metasurfaces have been focused on high-gain and narrow-band applications and beam steering techniques.

References

[1] G. V. Trentini, "Partially reflecting sheet arrays," *Antennas and Propagation, IRE Transactions on,* vol. 4, pp. 666-671, 1956.

[2] J. K. a. R. Eberhart, "Particle swarm optimization," presented at the IEEE International Conference on Neural Network, Perth, WA.

[3] J. Kennedy and R. C. Eberhart, "A discrete binary version of the particle swarm algorithm," in *1997 IEEE International Conference on Systems, Man, and Cybernetics. Computational Cybernetics and Simulation*, 1997, pp. 4104-4108 vol.5.

[4] N. Jin and Y. Rahmat-Samii, "Hybrid Real-Binary Particle Swarm Optimization (HPSO) in Engineering Electromagnetics," *IEEE Transactions on Antennas and Propagation,* vol. 58, pp. 3786-3794, 2010.

[5] J. Liu, Y. Mei, and X. Li, "An Analysis of the Inertia Weight Parameter for Binary Particle Swarm Optimization," *IEEE Transactions on Evolutionary Computation,* vol. 20, pp. 666-681, 2016.

[6] M. Kovaleva, B. A. Zeb, D. Bulger, and K. P. Esselle, "Radiation performance enhancement of a compact Fabry-Perot cavity antenna using particle swarm optimization," in *2015 International Symposium on Antennas and Propagation (ISAP)*, 2015, pp. 1-3.

[7] M. Kovaleva, B. A. Zeb, D. Bulger, and K. P. Esselle, "An extremely wideband Fabry-Perot cavity antenna for superfast wireless backhaul applications," in *2016 17th International Symposium on Antenna Technology and Applied Electromagnetics (ANTEM)*, 2016, pp. 1-2.

[8] M. Afzal, K. Esselle, and B. Zeb, "Dielectric Phase Correcting Structures for Electromagnetic Band Gap Resonator Antennas," *IEEE Trans. Antennas Propagat.,* vol. 63, pp. 3390-3399, 2015.

[9] M. U. Afzal and K. P. Esselle, "Quasi-analytical synthesis of continuous phase correcting structures to increase the directivity of circularly polarized Fabry-Perot resonator antennas," *Journal of Applied Physics,* vol. 117, p. 214902, 2015.

[10] M. U. Afzal and K. P. Esselle, "A Low-Profile Printed Planar Phase Correcting Surface to Improve Directive Radiation Characteristics of Electromagnetic Band Gap Resonator Antennas," *IEEE Trans. Antennas Propagat.,* vol. 64, pp. 276-280, 2016.

[11] M. U. Afzal and K. P. Esselle, "Steering the Beam of Medium-to-High Gain Antennas Using Near-Field Phase Transformation," *IEEE Transactions on Antennas and Propagation,* vol. 65, pp. 1680-1690, 2017.

[12] A. Lalbakhsh, M. U. Afzal, and K. P. Esselle, "Multiobjective Particle Swarm Optimization to Design a Time-Delay Equalizer Metasurface for an Electromagnetic Band-Gap Resonator Antenna," *IEEE Antennas and Wireless Propagation Letters,* vol. 16, pp. 912-915, 2017.

[13] A. Lalbakhsh, M. U. Afzal, B. A. Zeb, and K. P. Esselle, "Design of a dielectric phase-correcting structure for an EBG resonator antenna using particle swarm optimization," in *2015 International Symposium on Antennas and Propagation (ISAP)*, 2015, pp. 1-3

Enhanced spin-orbit interaction and all-optical modulation by subwavelength near-zero index media

Andrea Marini[1*], Alessandro Ciattoni[2], and Carlo Rizza[2]

[1]Department of Physical and Chemical Sciences, University of L'Aquila, Via Vetoio 10, 67100 L'Aquila, Italy
[2]Consiglio Nazionale delle Ricerche, CNR-SPIN, Via Vetoio 10, 67100 L'Aquila, Italy
*corresponding author, E-mail: andrea.marini@aquila.infn.it

Abstract

We demonstrate that a homogeneous and isotropic subwavelength near-zero index film enables efficient polarization control, phase manipulation and amplitude modulation at the nanoscale. When illuminated by a circularly polarized paraxial beam with axial symmetry, the near-zero index film acts as a vortex generator thanks to the enhanced spin-orbit interaction triggered by the medium. In addition, the near-zero index medium enhances nonlinearity thus enabling efficient all-optical modulation of a probe beam.

1. Introduction

Spin-orbit interaction (SOI) of light provides a tool for manipulating the spatial degrees of freedom of the radiation by acting on its circular polarization state. A remarkable SOI effect is the generation of optical vortices from circularly polarized beams, a process accompanied by spin to orbital angular momentum conversion. Standard procedures to achieve vortex generation are: focusing by high-numerical aperture lenses, scattering by small particles, propagation along the optical axis of a homogeneous uniaxial crystal, interaction with inhomogeneous anisotropic media and propagation through semiconductor microcavities. Similar SOI effects involving Bessel beams have been considered in uniaxial crystals and at reflection and transmission by a planar interface between two homogeneous media. Optical vortex beams have a lot of potential applications such as trapping of particles, propagation through atmospheric turbulence and optical communications. The advent of metamaterials has further increased the SOI research effort, mostly in the use of ultra-thin metasurfaces for manipulating the angular momentum of light and for vortex generation. Epsilon near zero (ENZ) media are nowadays attracting an increasing research interest due to the very unconventional way they affect the electromagnetic radiation. The effective wavelength in ENZ media is much larger than the vacuum wavelength and this entails a regime quite opposite to geometrical optics where the field is slowly-varying over relatively large portions of the bulk. Such feature has been exploited for squeezing electromagnetic waves at will, for tailoring the antenna radiation pattern and for enhancing the nonlinear response of matter.

Here we show that a homogeneous, isotropic and ultrathin (sub-wavelength thick) slab can support vortex generation [1]. We prove that such phenomenon is physically due to the mutual difference between the dynamics of transverse magnetic (TM) and transverse electric (TE) fields upon reflection and transmission. As the majority of radiation spin-orbit interaction phenomena, the slab vortex generation is mainly a nonparaxial effect.

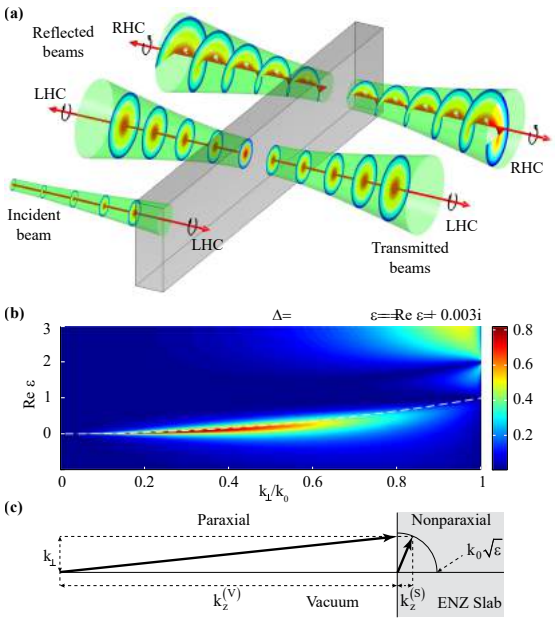


Figure 1: (a) Geometry of the vortex generation process. The incident beam is left-handed circularly (LHC) polarized with no topological charge. Both the reflected and the transmitted beams have a LHC component with no topological charge and a RHC component containing a second-order vortex. (The beams in the figure are spatially separated for clarity purposes). (b) TM-TE transmissivity asymmetry $\Delta = |t_{TM} - t_{TE}|$ versus $k_\perp/k_0$ and $\mathrm{Re}\,\varepsilon$. The white dashed line is the curve $k_\perp = k_0\sqrt{\mathrm{Re}\,\varepsilon}$. (c) Excitation of nonparaxial waves within the ENZ slab by vacuum paraxial waves.

However, we prove that slab vortex generation in the ENZ regime is remarkably efficient even for incident paraxial beams in spite of the very small slab thickness. Such phenomenology is unprecedent since, to the best of our

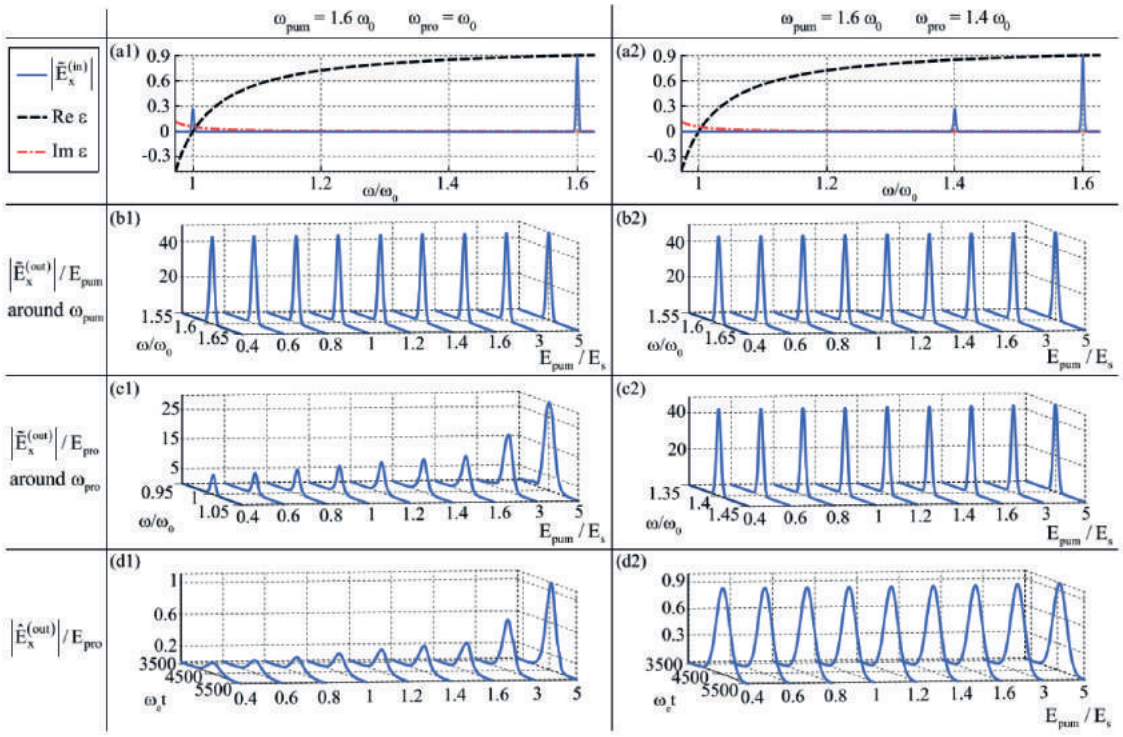


Figure 2: Left and right columns refer to the situations where the probe is in and out of the ENZ regime, respectively. (a1) and (a2) Spectra (arbitrary units) of the launched pump and probe at the plane $z_{\rm in}$ superimposed to real and imaginary parts of the slab dielectric permittivity. (b1) and (b2) Transmitted pump spectra normalized to the pump amplitude. (c1) and (c2) Transmitted probe spectra normalized to the probe amplitude. (d1) and (d2) Transmitted probe analytic signals normalized to the probe amplitude.

knowledge, paraxial vortex generation in homogenous media (i.e. through lenses and uniaxial crystals) requires samples whose thickness is much larger than wavelength. Here, the crucial role is played by the physical ability of an ENZ slab to turn a paraxial wave, incoming from vacuum, into a nonparaxial one within the bulk, its nonparaxiality triggering the predicted slab vortex generation. The vortex generation method proposed can have important nanophotonic applications since, unlike the one based on metasurfaces, it does not require microfabrication (the ENZ slab is homogenous) and it is scalable down to very small wavelengths (exploiting the ultraviolet ENZ point of metals) where metamaterials are not available. It is also worth noting that our method, unlike the one based on inhomogeneous anisotropic media (q-plates), is based on a very simple setup that does require neither preparation nor external biasing by electric field, it operates in sub-wavelength thick slabs and it can be used even up to the ultraviolet frequencies. In addition, we consider the nonlinear interaction of two pulses occurring in a very thin ENZ slab. The two quasi-monochromatic pulses, pump and probe with well separated spectral profiles, have very different powers and are launched simultaneously into the slab. Our full-wave simulations show that the transmission of the weak probe is affected by the pump, only if it is spectrally located at the ENZ frequency [2]. Such a marked all-optical pulse modulation is due to the fact that the pump produces an effective intensity dependent nonlinear shift of ENZ point, so that the probe in the ENZ regime experiences dielectric-like and metallic-like slab behaviors at different pump intensities.

2. Conclusions

In conclusion a homogeneous and isotropic subwavelength near-zero index film acts as an efficient, compact, and ultrafast metadevice for polarization and phase control and for all-optical light modulation. Near-zero index devices are expected to become a viable alternative to traditional semiconductor, photonic crystal, and plasmonic devices for fully controlling light at the nanoscale.

References

[1] A. Ciattoni, A. Marini and C. Rizza, Efficient Vortex Generation in Subwavelength Epsilon-Near-Zero Slabs, *Phys. Rev. Lett.* 118: 104301, 2017.

[2] A. Ciattoni, A. Marini and C. Rizza, All-optical modulation in wavelength-sized epsilon-near-zero media, *Opt. Lett.* 41: 3102–3105, 2016.

Optical chiral effects in ENZ ultrathin slabs

C. Rizza[1], **X. Li**[2], **A. Di Falco**[2], **E. Palange**[3], **A. Marini**[4], **and A. Ciattoni**[1]

[1]Institute for superconductors, oxides and other innovative materials and devices, National Research Council (CNR-SPIN), L'Aquila, Italy
[2]SUPA, School of Physics and Astronomy, University of St. Andrews, North Haugh, St Andrews, UK
[3]Department of Industrial and Information Engineering and Economics, Via G. Gronchi 18, University of L'Aquila, L'Aquila, Italy
[4]Department Physical and Chemical Sciences, Via Vetoio 1, University of L'Aquila, L'Aquila, Italy
carlo.rizza@aquila.infn.it

Abstract— Epsilon-near-zero (ENZ) media have attracted a great deal of interest since ENZ regime is able to trigger secondary light-matter interactions such as nonlinear and nonlocal effects. Here, we show the boosting of asymmetric transmission for forward and backward propagation of tilted circular polarized optical waves in ultrathin epsilon-near-zero hyperbolic slabs. Remarkably, this effect is solely triggered by anisotropy without resorting to any breaking of reciprocity and chiral symmetries or spatial nonlocal effects. The ENZ enhancement is due to the fact that the hyperbolic dispersion activates etalon resonances where extraordinary waves accumulate propagation phase even though the slab is ultrathin.

ENZ Media host a regime where field amplitude and phase are slowly-varying and this feature has been exploited to realize nanophotonics setups where the electromagnetic response can be driven by nonlinearity and/or nonlocality [1]. In addition, a relevant consequence of the ENZ regime is the enhancement of asymmetric response between the transverse magnetic (TM) and transverse electric (TE) fields in a slab and this asymmetry supports several intriguing effects like as vortex generation, efficient ultrathin waveplate. Here, we show that this asymmetry can become huge in a ultrathin ENZ hyperbolic slab and it provides an unusual diode-like asymmetric transmission. We consider a slab of thickness L illuminated by a monochromatic plane wave of wavelength λ whose electric field is $\mathrm{Re}\left[\mathbf{E}(z)\exp\left(-i2\pi ct/\lambda+ik_y y+ik_x x\right)\right]$ and impinging from vacuum with incident angles θ and φ, as reported in Fig.1(a), so that its wave vector is $\mathbf{k}^{(i)}=\mathbf{k}_\perp+k_z^{(i)}\hat{\mathbf{e}}_z=k_0\left(\sin\theta\cos\varphi\hat{\mathbf{e}}_x+\sin\theta\sin\varphi\hat{\mathbf{e}}_y+\cos\theta\hat{\mathbf{e}}_z\right)$ ($k_0=2\pi/\lambda$, $\mathbf{k}_\perp=k_x\hat{\mathbf{e}}_x+k_y\hat{\mathbf{e}}_y$). The considered slab is a homogeneous uniaxially anisotropic medium (a natural homogeneous material or a metamaterial), where the optical axis is oriented along the x-axis so that the electromagnetic response is described by the permittivity tensor $\varepsilon=\mathrm{diag}(\varepsilon_{||},\varepsilon_\perp,\varepsilon_\perp)$. Imposing the transverse momentum conservation across the slab interfaces for a given transversal wave vector $\mathbf{k}_\perp$, there are two forward waves excited within the slab, i.e., the ordinary and extraordinary plane waves, whose their longitudinal wave vectors are

$$k_z^{(o)}=\sqrt{k_0^2\epsilon_\perp-k_\perp^2},\quad k_z^{(e)}=\sqrt{k_0^2\epsilon_{||}-\left(k_x^2\frac{\varepsilon_{||}}{\varepsilon_\perp}+k_y^2\right)}. \tag{1}$$

In order to demonstrate the asymmetric transmission of circularly polarized waves as described in Fig.1 (b) and (c), we consider at first the the forward scattering in the TM (p) and TE (s) linear polarization basis $\hat{\mathbf{e}}_p=\cos\theta\cos\varphi\hat{\mathbf{e}}_x+\cos\theta\sin\varphi\hat{\mathbf{e}}_y-\sin\theta\hat{\mathbf{e}}_z$, $\hat{\mathbf{e}}_s=-\sin\varphi\hat{\mathbf{e}}_x+\cos\varphi\hat{\mathbf{e}}_y$. After matching the fields at the slab interfaces, we obtain the forward transmission matrix, $\overrightarrow{\mathbf{T}}_l$, connecting the components of the incident $\mathbf{E}^{(i)}$ and the transmitted $\mathbf{E}^{(t)}$ electric fields, namely

$$\begin{pmatrix}E_p^{(t)}\\E_s^{(t)}\end{pmatrix}=\begin{pmatrix}\overrightarrow{t}_{pp} & \overrightarrow{t}_{ps}\\ \overrightarrow{t}_{sp} & \overrightarrow{t}_{ss}\end{pmatrix}\begin{pmatrix}E_p^{(i)}\\E_s^{(i)}\end{pmatrix}=\overrightarrow{\mathbf{T}}_l\begin{pmatrix}E_p^{(i)}\\E_s^{(i)}\end{pmatrix}. \tag{2}$$

Note that, for the considered slab, anisotropy yields to polarization conversion where the cross-polarization transmission coefficient are identical and non-vanishing, viz. $\overrightarrow{t}_{ps}=\overrightarrow{t}_{sp}\neq 0$. On the other hand, in the circular polarization basis $\hat{\mathbf{e}}_+=1/\sqrt{2}\left(\hat{\mathbf{e}}_p+i\hat{\mathbf{e}}_s\right)$, $\hat{\mathbf{e}}_-=1/\sqrt{2}\left(\hat{\mathbf{e}}_p-i\hat{\mathbf{e}}_s\right)$, the

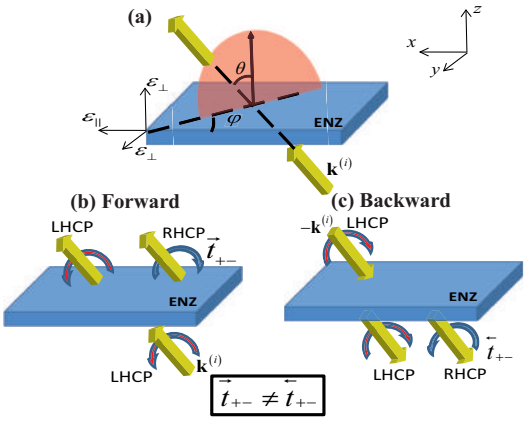


Figure 1: Geometry of the asymmetric transmission process. (a) Schematic view of the considered setup. Propagation direction is defined as forward for the $\mathbf{k}^{(i)}$ direction (b) and backward for the $-\mathbf{k}^{(i)}$ direction (c).

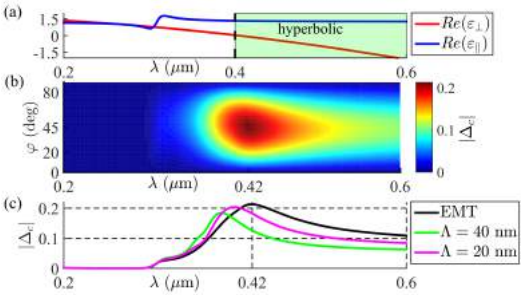


Figure 2: (a) Real part of the metamaterial effective permittivity as a function of λ (the shadow area indicates hyperbolic region). (b) Δ_c parameter as a function of φ and λ for $\theta = 60$ deg and $L = 30$ nm. (c) Comparison between the asymmetric transmission evaluated with EMT (black solid line) and those predicted by the rigorous coupled-wave analysis for different values of the spatial period Λ.

forward transmission matrix $\overrightarrow{\mathbf{T}}_c$ has the entries

$$\overrightarrow{t}_{++} = \frac{1}{2}\left(\overrightarrow{t}_{pp} + \overrightarrow{t}_{ss}\right), \qquad \overrightarrow{t}_{+-} = \frac{1}{2}\left(\overrightarrow{t}_{pp} - \overrightarrow{t}_{ss} - i2\overrightarrow{t}_{ps}\right),$$
$$\overrightarrow{t}_{-+} = \frac{1}{2}\left(\overrightarrow{t}_{pp} - \overrightarrow{t}_{ss} + i2\overrightarrow{t}_{ps}\right), \qquad \overrightarrow{t}_{--} = \frac{1}{2}\left(\overrightarrow{t}_{pp} + \overrightarrow{t}_{ss}\right), \tag{3}$$

Now, we consider the backward excitation as depicted in Fig.1(c) where the backward incident wave propagates along $-\mathbf{k}^{(i)}$. According to the reciprocal theorem, asymmetric transmissions in the circularly polarized bases is characterized by the parameters $\Delta_c = |\overrightarrow{t}_{+-}|^2 - |\overleftarrow{t}_{+-}|^2 = |\overrightarrow{t}_{+-}|^2 - |\overrightarrow{t}_{-+}|^2$. Using the above expressions for entries of the transmission matrices in the linear basis we obtain

$$\Delta_c = 2|\Delta t||\overrightarrow{t}_{sp}|\sin(\Delta\psi), \tag{4}$$

where we define $\Delta t = \overrightarrow{t}_{pp} - \overrightarrow{t}_{ss}$ and $\Delta\psi = Arg\left(\Delta t\,\overrightarrow{t}^{*}_{ps}\right)$. From Eq.(4), it is evident that the asymmetric transmission for tilted plane waves is a consequence of both the transverse electric and transverse magnetic polarization asymmetric response $\Delta t \neq 0$ and the presence of the linear cross-polarization conversion $\overrightarrow{t}_{sp} \neq 0$, two ingredients naturally offered by an uni-axial medium. Next, we focus our attention on a subwavelength binary grating, made of silver and air whose filling fraction are $f_{Ag} = 0.5$,$f_{Air} = 0.5$, respectively, and whose stacking direction is along the x-axis. The silver dielectric permittivity is described by the Drude model where $\epsilon_b = 5$, $\omega_p = 14 \cdot 10^{15}$ Hz and $\alpha = 0.32 \cdot 10^{15}$ Hz). In the homogenized regime, the effective electromagnetic response is described by the permittivity tensor $diag\left(\varepsilon_{||}, \varepsilon_\perp, \varepsilon_\perp\right)$, where $\varepsilon_\perp = f_{Ag}\varepsilon_{Ag} + f_{Air}$ and $\varepsilon_{||} = \left(f_{Ag}/\varepsilon_{Ag} + 1/f_{Air}\right)^{-1}$, so that the metamaterial response is characterized by the ENZ crossing point $\mathrm{Re}(\varepsilon_\perp) = 0$ at $\lambda = 0.4$ μm as reported in Fig.4(a). In Fig.4(b), we plot the Δ_c parameter evaluated for $\theta = 60$ deg and $L = 30$ nm. The asymmetric transmission attains its maximum $\Delta_c \simeq 0.2$ at $\lambda = 0.42$ μm and $\varphi = 45$ deg where $\varepsilon_{||} = 1.32 + i0.01$ and $\varepsilon_\perp = -0.14 + i0.14$. For completeness, in the Fig.4(c), we report the comparison between the asymmetric transmission evaluated with EMT (black solid line) and those predicted by the rigorous coupled-wave analysis technique for different values of the spatial period Λ.

REFERENCES

1. I. Liberal, and N. Engheta, **11**, 149-158 (2017).
2. A. Ciattoni, C. Rizza, and E. Palange, Phys. Rev. A **81**, 043839 (2010).

Multipole Contribution into Resonant Scattering of Dielectric Nonspherical Nanoparticles

Yongqian Li[1*], Yueyue Chen[2], Yujie Yang[2], Zili Zhou[3], Xiaoying Li[2], Ji Wang[4]

[1]Research & Development Institute of Northwestern Polytechnical University in Shenzhen, Shenzhen, China
[2]Key Laboratory of Micro/Nano Systems for Aerospace of Ministry of Education, Northwestern Polytechnical University, Xi'an, China
[3] Chinese Aeronautical Establishment, Chaoyang District, Beijing, China
[4]Science and Technology on Metrology and Calibration Laboratory, Beijing, China
*corresponding author, E-mail: liyq@nwpu.edu.cn

Abstract

Dielectric cylindrical nanoparticles with resonant responses are elemental blocks for building metasurfaces. Here, the scattering effects of high-dielectric silicon cylindrical particles are investigated by the discrete-dipole approximation (DDA), which calculates the multipole contribution into the resonant responses of nanoparticles. Resonant electric and magnetic multipole responses up to the electric octupole moment have been analyzed in theory and calculated by our self-written DDA toolbox. The numerical results help to understand the resonant scattering process of the metasurface devices made of dielectric cylindrical particles.

1. Introduction

Dielectric cylindrical nanoparticles with resonant responses are elemental blocks for building metasurfaces, which can efficiently control the phase, amplitude, and directivity of reflected or transmitted light[1]. However, the multipole contribution of magnetic and electric dipole moments to the light scattering effects of nonspherical nanoparticles is ambiguous. The discrete-dipole approximation (DDA) is a powerful method for calculating absorption and scattering effects of nonspherical nanoparticles that have sizes smaller than or comparable to the wavelength of the incident radiation[1]. In theory, the DDA provides the multipole contribution of nanoparticles, including the magnetic dipole (MD), electric dipole (ED), and higher order response, including the electric quadrupole moment (EQ), the magnetic quadrupole moment (MQ), and the electric octupole moment (OCT), and even the toroidal dipole (TD) moments [2].

In our work, the DDA solution has been used to separate the interesting magnetic dipole (MD) and electric dipole (ED) for resonant responses in silicon cylindrical nanoparticles. Spectral positions of electric and magnetic multipole resonances of dielectric nanoparticles are calculated by self-written DDA programs. The dependence of spectral positions on their size and aspect ratio has indicated that the spectral overlap of electric and magnetic dipole responses will result in the backward light scattering, or forward light scattering, which provide very useful applications for nanophotonics, like light nanoantennas, and metasurfaces, like ultrathin metadevices.

2. General Light Scattering by Silicon Nanoparticles

We consider the plane wave scattering of cylindrical nanoparticles with different aspect ratios, as shown in Fig. 1. The cylinders diameter equals to a fixed value, and their height H varies between 100 and 300 nm. We use the DDA method to learn about the contribution information of multipole modes into the spatial distribution of the scattered fields.

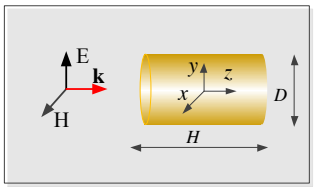


Figure 1: Dielectric cylindrical nanoparticles irradiated by a plane wave, which propagates along the particle's axis. D and H are the diameter and the height of the cylinder, respectively.

3. Multipole Decomposition of Scattering Fields in DDA theory

The theoretical investigation comes from the multipole decomposition method presented in previous work[3]. Briefly, when considering multipole moments up to the electric octupole moment, the scattering power can be calculated by,

$$P_{sca} = \frac{k_0^4}{12\pi\varepsilon_0^2 v_d \mu_0}\left|\boldsymbol{p} + \frac{ik_d}{v_d}\boldsymbol{T}\right|^2 + \frac{k_0^4\varepsilon_d}{12\pi\varepsilon_0 v_d}|\boldsymbol{m}|^2 + \frac{k_0^6\varepsilon_d}{144\pi\varepsilon_0^2 v_d \mu_0}\sum_{\alpha\beta}|Q_{\alpha\beta}|^2 + \frac{k_0^6\varepsilon_d^2}{160\pi\varepsilon_0 v_d}\sum_{\alpha\beta}|M_{\alpha\beta}|^2 + \frac{k_0^8\varepsilon_d^2}{3780\pi\varepsilon_0^2 v_d \mu_0}\sum_{\alpha\beta\gamma}|O_{\alpha\beta\gamma}|^2 \quad (1)$$

which describes the superposition of the scattering fields generated by all dipoles of the nanoparticle, which covers the magnetic quadrupole moment (MQ), and the electric octupole moment (OCT), and even the toroidal dipole (TD) moments.

The total scattering cross section is obtained through the dividing the scattering power by the radiation energy flux of the incident wave. The scattering cross sections are,

$$\sigma_{sca} \cong \frac{k_0^4}{6\pi\varepsilon_0^2|E_{inc}|^2}\left|\mathbf{p}+\frac{ik_d}{v_d}\mathbf{T}\right|^2+\frac{k_0^4\varepsilon_d\mu_0}{6\pi\varepsilon_0|E_{inc}|^2}|\mathbf{m}|^2 + \frac{k_0^6\varepsilon_d}{720\pi\varepsilon_0^2|E_{inc}|^2}\sum_{\alpha\beta}|Q_{\alpha\beta}|^2+\frac{k_0^6\varepsilon_d^2\mu_0}{80\pi\varepsilon_0|E_{inc}|^2}\sum_{\alpha\beta}|M_{\alpha\beta}|^2+\frac{k_0^8\varepsilon_d^2}{1890\pi\varepsilon_0^2|E_{inc}|^2}\sum_{\alpha\beta\gamma}|O_{\alpha\beta\gamma}|^2 \quad (2)$$

The total exciting spectra, the corresponding scattering spectra and absorption coefficients can also be calculated numerically using finite element method (FEM) by commend commercial softwares.

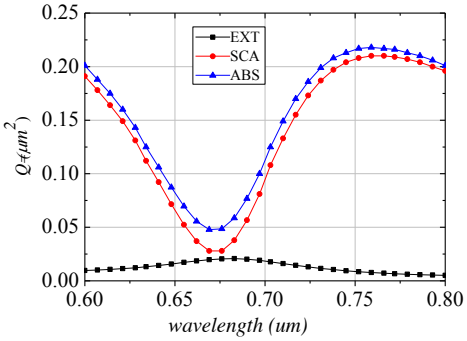


Figure 2: Spectra responses of a silicon cylindrical nanoparticle located in air, including extinction, scattering, and absorption spectra, are calculated using the DDA method.

4. Numerical results and discussion

In our investigation, the multipole decomposition of total scattering and their contributions into resonant scattering cross sections are calculated by Eq. (2). The extinction spectrum, scattering, and absorption spectral responses of a silicon cylindrical nanoparticle are calculated, as shown in Fig.2. There are slight deviations from the results obtained by finite-difference time-domain (FDTD) software, which are not show here. The higher order more than octupole moments are ignored in our investigation, which rise to such small difference. The scattering spectra of a silicon cylindrical nanoparticle with a fixed height of 100 nm and varying diameter of 10 nm to 30 nm are calculated as shown in Fig. 3.

The contributions of different multipole modes excited in a silicon cylindrical nanoparticle are presented in Fig.4. The multipole decomposition of the scattering cross sections includes the contribution of the third-order multipole moments. The results can be used for investigations of the role of different multipole moments in light scattering. The multipole decompositions also could be expected to provide useful information about multipole contributions in light extinction and absorption.

It can be expected that the reciprocal interference among the multipole moments basically determine the forward scattering and strong suppression of the back forward scattering, which are interesting for the investigation of metasurfaces with novel features, like ultrathin metadevices.

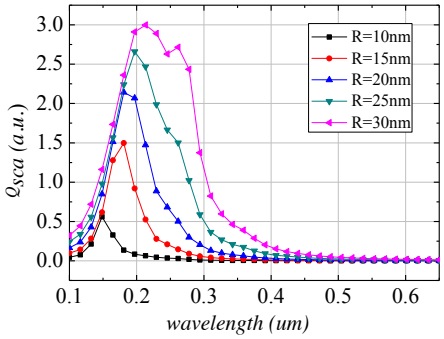


Figure 3. Scattering cross sections spectra for a silicon cylindrical nanoparticle with a height of 100nm, and varying diameter of 10 nm to 30 nm are calculated using the DDA method.

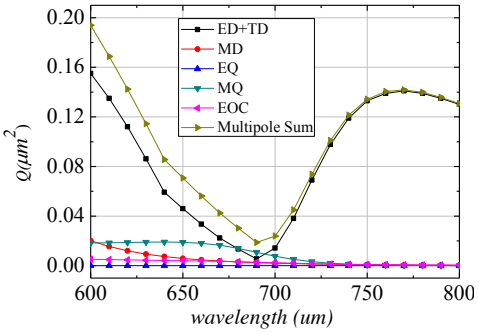


Figure 4: The multipole decomposition spectra of the electric dipole (ED), magnetic dipole (MD), electric quadrupole (EQ), magnetic quadrupole (MQ), and electric octupole moment (EOC) calculated for the cylindrical nanoparticles. The total multipole is summarized by the decomposed multipole moments.

Acknowledgements

This work has been supported by the Foundation for Basic Research from Science and Innovation Commission of Shenzhen Municipality(JCYJ20170306153605871), and from National Natural Science Foundation of China (NSFC) (51575455).

References

[1] Pavel D. Terekhov, Kseniia V. Baryshnikova, Yuriy A. Artemyev, A. Karabchevsky, A. S. Shalin, and A. B. Evlyukh, Multipolar response of nonspherical silicon nanoparticles in the visible and near-infrared spectral ranges. *Phy. Rev. B*, 96, 035443, 2017.

[2] N. Papasimakis, V. A. Fedotov1, V. Savinov, T. A. Raybould1 and N. I. Zheludev, Electromagnetic toroidal excitations in matter and free space. *Nature Materials* 15,264,2016

[3] Andrey B. Evlyukhin, C. Reinhardt, E. Evlyukhin, B. Chichkov Chichkov. Multipole analysis of light scattering by arbitrary-shaped nanoparticles on a plane surface. *J. Opt. Soc. Am. B* 30, 2013.

Optical Metamaterials with Emerging MXenes

Krishnakali Chaudhuri,[1] Zhuoxian Wang,[1] Mohamed Alhabeb,[2] Xiangeng Meng,[1] Shaimaa I Azzam,[1] Alexander Kildishev,[1] Young L. Kim,[3] Vladimir M. Shalaev,[1] Yury Gogotsi,[2] and Alexandra Boltasseva[1]

[1]School of Electrical and Computer Engineering, and Birck Nanotechnology Center, Purdue University, West Lafayette, IN 47907, USA

[2]Department of Materials Science and Engineering, and A. J. Drexel Nanomaterials Institute, Drexel University, Philadelphia, PA 19104, USA

[3]Weldon School of Biomedical Engineering, Purdue University, West Lafayette, IN 47907, USA

Author e-mail address: aeb@purdue.edu

Summary We report on an emerging two-dimensional material class MXenes as a potential material platform for plasmonic metamaterials. Application as a broadband plasmonic metamaterial absorber and a random laser device have been discussed.

1. Introduction

An emerging class of two-dimensional (2D) nanomaterials formed of transition metal carbides and carbon nitrides are known as MXenes. They have the general chemical form $M_{n+1}X_nT_x$, where 'M' is a transitional metal, 'X' is either C or N, and 'T' represents a surface functional group (O, -OH or -F).[1] MXenes are chemically synthesized from a corresponding layered ternary carbides or nitrides phase known as MAX ($M_{n+1}AX_n$) phases by selective chemical etching of the 'A' layers and addition of surface functional groups 'T'.[2] Until now, MXenes have been widely explored in a variety of applications e.g. electromagnetic shielding, SERS, energy harvesting, sensing, battery and fuel cells etc.[3–6] However, investigations of MXenes in the context of nanophotonics and plasmonics have been limited leading to this current exploration of MXenes as building blocks for plasmonic and metamaterial devices.

2. Results and Discussions

For our work with this material class, we've focused on one of the most well studied MXene, titanium carbide ($Ti_3C_2T_x$). Single to few layer sheets of $Ti_3C_2T_x$ (in a solution dispersed form) is spin coated create a continuous film on a desired substrate, followed by drying in an inert ambient. A dielectric to metallic crossover of the real part of dielectric permittivity (ε) at ~1.07 μm indicates the existence of surface plasmons (SP) at the MXene interface in the near- and mid- infrared (IR) frequencies (Figure 1 (a)). Losses inherent to the bulk MXene and existence of strong localized SP resonances in $Ti_3C_2T_x$ disks/pillar-like nanostructures (Figure 1 (b)) at near-IR frequencies are optimized to design an efficient broadband absorber. In a simple $Ti_3C_2T_x$ MXene disk array, ~80% absorption across ~0.5-1.6 μm is observed experimentally.[7] To further increase the performance, a metal/ dielectric stack of Au/Al_2O_3 are added underneath the disk array. This geometrical configuration supports gap surface plasmon resonance that is optimized to achieve high efficiency (>90%) absorption across a ~1.55 μm bandwidth spanning visible and near-IR (Figure 1 (c)).[7]

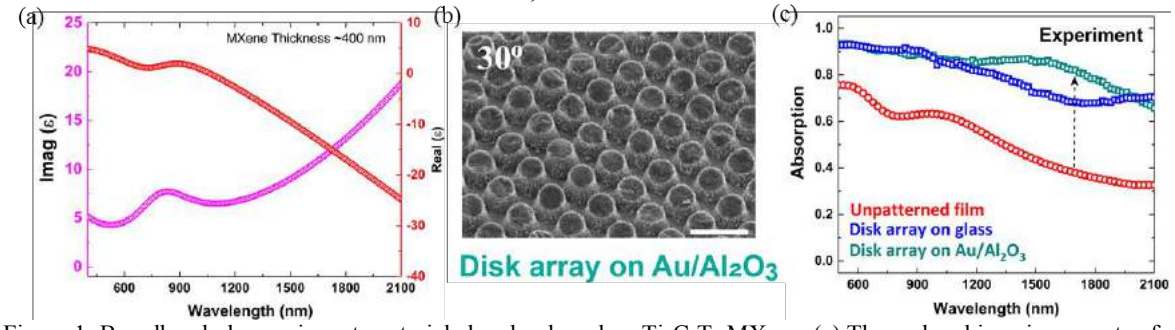


Figure 1: Broadband plasmonic metamaterial absorber based on $Ti_3C_2T_x$ MXene. (a) The real and imaginary parts of the dielectric permittivity. (b) The scanning electron microscope image of the fabricated disk array on Au/alumina substrate (the scale bar indicates 1 μm). (c) Measured absorption spectra comparison for the two types of disk arrays and unpatterned MXene film (incident light is TE polarized, angle of incidence is 20°).

In another work, random lasing behavior in a disordered metamaterial composed of 2D $Ti_3C_2T_x$ MXene is experimentally illustrated. Our metamaterial is constructed by randomly dispersing single layer nanosheets of $Ti_3C_2T_x$ into a gain medium (rhodamine 101, R101) (Figure 2 (a)). To study lasing properties, a 532 nm picosecond laser is used to pump the device. Sharp peaks begin to emerge from the broad-band background when the pump energy reaches the threshold value of ~ 0.70 μJ/pulse. When the pump energy is further increased, other sharp peaks subsequently appear which is consistent with the behavior of random lasing achieved through coherent feedback (Figure 2 (b)).[8] The lasing threshold in this metamaterial is controlled by changing the density of the $Ti_3C_2T_x$ in solution. (Figure 2 (c)) This is the first experimental demonstration of random lasing behavior in metamaterials made from 2D materials. The extraordinarily low threshold for saturable absorption of 2D materials suggests that 2D materials have great potential to controlling the feedback and emission properties of lasing which is currently under investigation. [9]

3. Conclusion

A member of the emerging class of two dimensional MXenes and its nanostructures have been explored in the realm of nanophotonics and plasmonics. A broadband plasmonic metamaterial absorber and a random laser device have thus been demonstrated. As the material class and its synthesis techniques continue to mature, applicability in optics along with device performances are also expected to improve further.

4. Acknowledgement

This work is financially supported by ONR MURI Grant N00014–13–0649, AFOSR MURI Grant FA9550-12-1-0389, ARO grant W911NF-13-1-0226, and NSF grant DMR-1120923.

5. References

[1] M. Naguib, M. Kurtoglu, V. Presser, J. Lu, J. Niu, M. Heon, L. Hultman, Y. Gogotsi, M. W. Barsoum, *Adv. Mater.* **2011**, *23*, 4248.

[2] B. Anasori, M. R. Lukatskaya, Y. Gogotsi, *Nat. Rev. Mater.* **2017**, *2*, 16098.

[3] F. Shahzad, M. Alhabeb, C. B. Hatter, B. Anasori, S. Man Hong, C. M. Koo, Y. Gogotsi, *Science* **2016**, *353*, 1137.

[4] A. Sarycheva, T. Makaryan, K. Maleski, E. Satheeshkumar, A. Melikyan, H. Minassian, M. Yoshimura, Y. Gogotsi, *J. Phys. Chem. C* **2017**, *121*, 19983.

[5] R. Li, L. Zhang, L. Shi, P. Wang, *ACS Nano* **2017**, *11*, 3752.

[6] M. R. Lukatskaya, O. Mashtalir, C. E. Ren, Y. Dall'Agnese, P. Rozier, P. L. Taberna, M. Naguib, P. Simon, M. W. Barsoum, Y. Gogotsi, *Science* **2013**, *341*, 1502.

[7] K. Chaudhuri, M. Alhabeb, Z. Wang, V. M. Shalaev, Y. Gogotsi, A. Boltasseva, **n.d.**, DOI 10.1021/acsphotonics.7b01439.

[8] D. S. Wiersma, *Nat. Phys.* **2008**, *4*, 359.

[9] A.Marini, F. J. Garcia de Abajo, Phys. Rev. Lett. **2016**, 116, 217401.

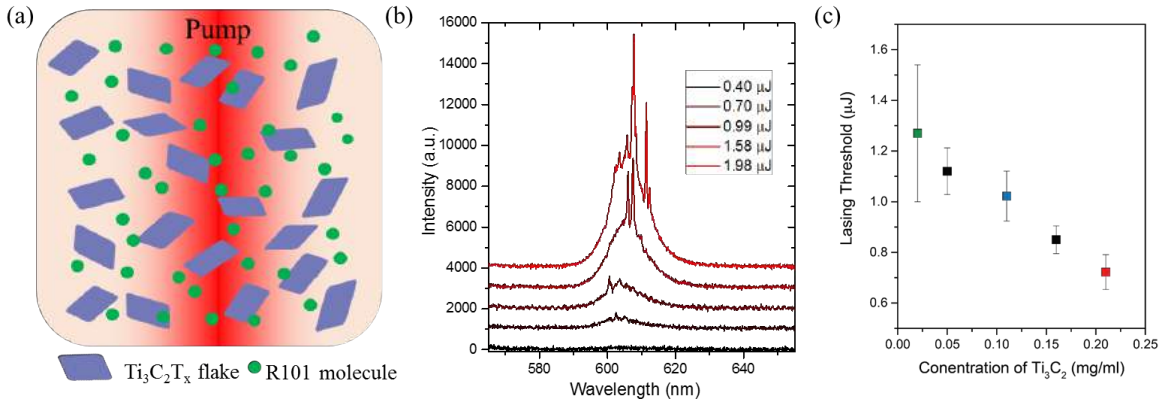


Figure 2: Random Laser based on $Ti_3C_2T_x$ nanoflakes. (a) Schematic illustration of the RL device, which consists of a mixture of monolayer $Ti_3C_2T_x$ nanoflakes and R101 molecules. (b) Emission spectra recorded under various pump energies. An offset is applied when plotting the spectra. (c) Pump threshold as a function of the concentration of $Ti_3C_2T_x$.

Tailorable nanophotonic devices with ultra-thin transition metal nitrides

Deesha Shah[1], Alessandra Catellani[2], Harsha Reddy[1], Nathaniel Kinsey[3], Vladimir M. Shalaev[1], Arrigo Calzolari[2] and Alexandra Boltasseva[1]*

[1]School of Electrical & Computer Engineering and Birck Nanotechnology Center, Purdue University, 1205 West State St., West Lafayette, IN 47907, USA
[2]CNR-NANO Istituto Nanoscienze, Centro S3, I-41125 Modena, IT
[3]Department of Electrical and Computer Engineering, Virginia Commonwealth University, 601 West Main St., Richmond, VA 23284-3072, USA
*corresponding author, E-mail: aeb@purdue.edu

Abstract

In this study, we present a joint theoretical and experimental study on the dielectric permittivity of ultra-thin TiN films of varying thicknesses. Our results indicate a remarkably persistent metallic character as the thickness is reduced. The effects of oxidation and strain on the plasmonic properties of the thin films emerge as fundamental parameters to optimize their response. Due to their increased sensitivity to structural parameters, atomically thin plasmonic materials display great potential for the realization of tailorable and dynamically switchable metasurfaces.

1. Introduction

As a result of recent developments in nanofabrication techniques, the dimensions of metallic building blocks of plasmonic devices continue to shrink down to nanometer range thicknesses. The strong spatial confinement in atomically thin films is expected to lead to quantum and nonlocal effects, making ultra-thin films an ideal material platform to study light-matter interactions at the nanoscale. Most importantly, the optical and electronic properties of ultra-thin plasmonic films are expected to have a strong dependence on the film thickness, composition, strain, and local dielectric environment, as well as an increased sensitivity to external optical and electrical perturbations. Consequently, unlike their bulk counterparts which have properties that are challenging to tailor, the optical responses of atomically thin plasmonic materials can be engineered by precise control of their thickness, composition, and the electronic and structural properties of the substrate and superstrate. This unique tailorability establishes ultra-thin plasmonic films as an attractive material for the design of tailorable and dynamically switchable metasurfaces.

While continuous ultra-thin films are very challenging to grow with noble metals [5], the epitaxial growth of TiN on lattice matched substrates such as MgO allows for the growth of smooth, continuous films down to 2 nm. To move towards the realization of practical devices utilizing ultra-thin plasmonics, additional studies are needed to understand the optical behavior of ultrathin films and the different factors contributing to their thickness dependent properties. In this study, we present both a theoretical and an experimental study on the dielectric function of ultrathin TiN films of varying thicknesses. we demonstrate that the optical response can be engineered by controlling the thickness, strain, and oxidation. The observed plasmonic properties in combination with confinement effects introduce the potential of TiN ultra-thin films as a material platform for tailorable plasmonic metasurfaces.

2. Results

Ultrathin TiN films with thicknesses of 2, 4, 6, 8, and 10 nm were grown on MgO using DC reactive magnetron sputtering. The linear optical properties measured using variable angle spectroscopic ellipsometry show that the films become less metallic as the thickness decreases (Figure 1a). This trend is corroborated by first principles density functional (DFT) calculations for films containing 1 to 10 layers of TiN(001) (Figure 1b), where the metallic character is also decreased as a result of quantum confinement effects which increase the contribution from under-coordinated surface atoms leading to electron localization. While the theoretical results show good qualitative agreement with experimental findings, the atomistic analysis of the experimental samples indicates a non-negligible deviation from the ideal TiN structure. Two different factors resulting in this difference between experiment and theory are considered here: (i) surface oxidation and (ii) interface strain.

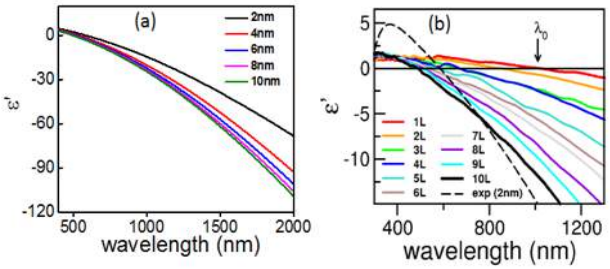


Figure 1: Dielectric function retrieved from (a) ellipsometry for thicknesses 2 to 10nm and (b) DFT for 1 to 10 monolayers of TiN

X-ray photoelectron spectroscopy reveals that the films are a combination of three different phases: titanium nitride, titanium oxynitride, and titanium dioxide (Figure 2a). This oxidation reduces the overall effective thickness of the TiN films, which causes a slower blue shift of the crossover wavelengths in thinner films (Figure 2b). On the other hand, the induced strain in the film due to the MgO would only result in a 0.7% compressive strain. While the substrate induced strain would affect the optical properties of ultrathin TiN films (Figure 2c), oxidation is the primary cause of the differences between the ideal TiN model and experimental results.

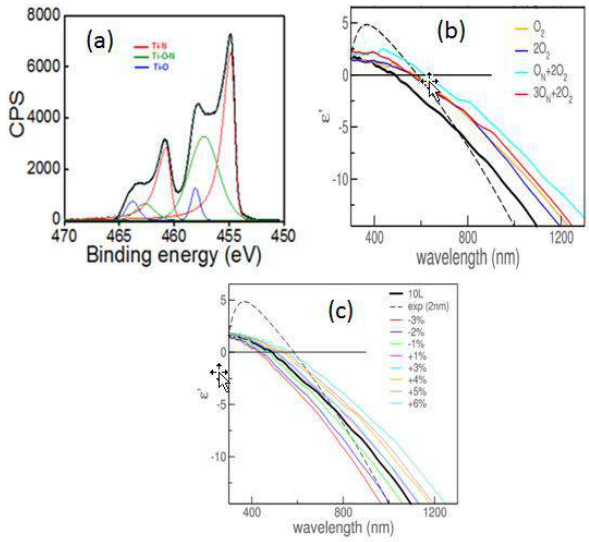


Figure 2: (a) The XPS spectrum reveals the chemical environment of the TiN film surface. Effects of (b) oxidation and (c) strain on the optical properties calculated using DFT

3. Conclusions

The characterized ultra-thin films remain highly metallic and can be largely tuned by controlling structural and chemical properties, such as the thickness, strain, and oxidation during growth. These tunable plasmonic properties, in combination with confinement effects, make TiN a promising material for the realization of tailorable ultra-thin metasurfaces.

Acknowledgements

The authors acknowledge financial support from the NSF OP grant DMR-1506775

References

[1] D. Shah, H. Reddy, N. Kinsey, V. M. Shalaev, and A. Boltasseva, "Optical Properties of Plasmonic Ultrathin TiN Films," Advanced Optical Materials, vol. 5, no. 13, (2017).

[2] N. Rivera, I. Kaminer, B. Zhen, J. D. Joannopoulos, and M. Soljačić, "Shrinking light to allow forbidden transitions on the atomic scale," Science, vol. 353, no. 6296, pp. 263–269, (2016).

[3] I. V. Bondarev and V. M. Shalaev, "Universal features of the optical properties of ultrathin plasmonic films," Opt. Mater. Express, OME, vol. 7, no. 10, pp. 3731–3740, (2017).

[4] A. Manjavacas and F. J. G. de Abajo, "Tunable plasmons in atomically thin gold nanodisks," Nature Communications, vol. 5, p. 3548, (2014).

[5] A. Kossoy, V. Merk, D. Simakov, K. Leosson, S. Kéna-Cohen, and S. A. Maier, "Optical and Structural Properties of Ultra-thin Gold Films," Advanced Optical Materials, vol. 3, no. 1, pp. 71–77, (2015).

Highly Nonlinear III-V Semiconductor Metasurfaces

P. P. Vabishchevich,[1,3]* S. Liu,[1,3] A. Vaskin,[2] J. L. Reno,[1,3] G. A. Keeler[1], G. M. Peake,[1] M. B. Sinclair[1], I. Staude,[2] I. Brener[1,3]

[1]Sandia National Laboratories, Albuquerque, NM, USA
[2]Institute of Applied Physics, Abbe Center of Photonics, Friedrich Schiller University Jena, Jena, German
[3]Center for Integrated Nanotechnologies, Sandia National Laboratories, Albuquerque, NM, USA
*corresponding author, E-mail: pvabish@sandia.gov

Abstract

Optical metasurfaces are quasi-planar nanostructured materials that have the ability to tailor local fields, providing new opportunities for light control and manipulation. In this talk I will show our recent results in the nonlinear optical response of III-V semiconductor metasurfaces, starting from the second harmonic generation and strategies for increasing its efficiency by applying broken symmetry designs. Then I will present results of nonlinear frequency mixing in the GaAs metasurface, pumped with two femtosecond near-IR laser pulses.

1. Introduction

Dielectric metasurfaces are one of the most promising candidates for the ultra-thin optical devices that allow the possibility to develop a mixer at optical frequencies. Recent studies show that dielectric nanostructured materials enable nonlinear frequency conversion in thin films with high efficiencies and high damage threshold. Moreover, in comparison with bulk materials, metasurfaces don't require any phase matching: comparable to the wavelength, element dimensions remove constraints and allow the simultaneous generation of multiple nonlinear processes. For the past decade, the harmonics generation, as well as frequency mixing processes, have been widely explored in Si, Ge, GaAs, AlGaAs metasurfaces that support the excitation of the Mie resonances [1]. This work will focus on the nonlinear response of metasurfaces when they are made of direct bandgap semiconductors. First, I will discuss the second-harmonic generation (SHG) in III-V semiconductors and ways to substantially improve the efficiency by implementing Fano resonances. Second, I will show the simultaneous generation of eleven new frequencies in the dielectric metasurfaces within the spectral range from the UV to the near-IR.

2. Results and discussion

2.1. Second harmonic generation in Fano metasurfaces

One of the most common designs that are used to excite the Mie resonances in the visible and near-IR range of spectrum consists of an array of nanodiscs with nanoscale dimensions. For example, Fig.1a shows the III-V semiconductor metasurface: a square array of pillars that has three layers: the top one is a SiOx mask with low n = 1.4 refractive index, the middle one is a GaAs layer, and the bottom one is the $(Al_xGa_{1-x})_2O_3$. The top and the bottom layers have low refractive indexes, to separate the GaAs nanodisk from the GaAs substrate. Such design of metasurfaces allows the excitation of the first-order Mie-resonances. Moreover, since GaAs possesses a large intristinc second-order nonlinearity, GaAs metasurfaces show SHG enhancement factors as large as 10^4 relative to unpatterned GaAs [2]. However, nonlinear optical processes can be further enhanced by utilizing high-Q resonances, since the efficiencies of nonlinear processes strongly depend on the electromagnetic field localization inside the nanoresonator. By applying the broken symmetry nanoresonators design, shown in Fig. 1b, it is possible to achieve multifold SHG efficiency enhancement (Fig.1c) in comparison with a GaAs nanodisc metasurface.

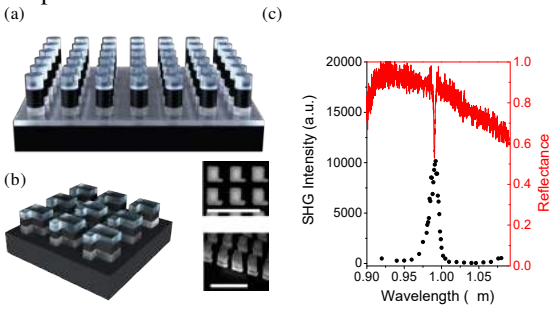


Figure 1: (a) Schematic of the GaAs metasurface. (b) Schematic of a broken symmetry Fano metasurface. The insets show a top-view, and a side-view SEM images of sample. The scale bar corresponds to 1 μm. (c) Black dots – spectral dependence of the SHG intensity enhanced at Fano resonance. Red line – linear reflectivity spectrum of the broken symmetry metasurface.

2.2. Nonlinear frequency mixing in dielectric metasurfaces

To further study the nonlinear processes generation in GaAs metasurfaces we used two ~45 fs laser pulses to simultaneously pump the sample with an array of nanocylinders, shown in Fig. 2a. Arrows in Fig. 2b indicate the laser wavelengths that coincide with the maxima of the

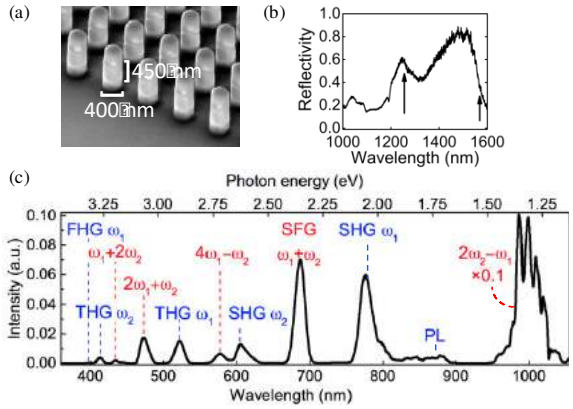


Figure 2: (a) SEM image of the GaAs nanocylinder metasurface. (b) Linear reflectivity spectrum of the GaAs metasurface. Arrows indicate the pumping wavelengths. (c) Nonlinear frequency mixing spectrum generated by the GaAs metasurface.

electromagnetic field enhancements inside the nanoresonator due to the excitation of the Mie resonances. Figure 2c shows the frequency-mixing spectrum of the GaAs metasurface, that was obtained when the two near-IR pumping pulses spatially and temporarily overlap at the surface of the sample. Eleven new peaks with wavelengths that span from UV to near IR were generated. They can be divided into two groups. The first one is the processes that are supported only by one of the pumping beams, such as SHG, third-harmonic generation (THG), fourth-harmonic generation (FHG) and induced by two-photon absorption photoluminescence (PL), noted in blue in Fig.2c. Another group of peaks, noted in red, corresponds to the processes that rely on two pumping beams: sum-frequency generation (SFG), three four-wave mixing (FWM) processes $2\omega_1+\omega_2$, $2\omega_1-\omega_2$, and $\omega_1+2\omega_2$, and a six-wave mixing process. The nature of the newly generated frequencies was verified by the power-dependence measurements, as well as by comparing the expected and measured wavelengths of the frequency mixing processes when the pumping wavelengths were tuned.

Fig. 3a shows the nonlinear frequency mixing spectra of the GaAs metasurface obtained when we varied the time-delay between the pumping pulses. The single-beam processes, such as SHG, THG, FHG are observed regardless of the delay. Two-beam processes, SFG, three FWM processes, are generated only when two pumping pulses coincide at the surface of the sample. Moreover, not only frequency-mixing processes are influenced by the two pump beams: both SHG intensities drastically drop at zero-time delay when another pulse starts pumping the sample, as shown in the Fig. 3b for ω_1 pulse. At negative time-delay SHG ω_1 intensity slowly recovers with ~3.7 ps time constant determined by the free carriers relaxation process. This dynamic of the second harmonics reflects the behaviour of the electric and magnetic resonances [3].

The optimization of the frequency mixing processes can be done in a few ways. First, the wavelengths of the generated nonlinear processes lie above the bandgap of GaAs and are suppressed by the absorption of the material. The adjustments of the dimensions of the nanoresonators, resulting in a red-shifting of the Mie resonances to the IR, will allow generation of frequencies below the band gap of GaAs, thus achieving higher conversion efficiencies. Another way is to use high-Q resonances, as was shown earlier as well as to optimize the mode structure and mode overlap that can significantly improve the performance of the GaAs metasurface.

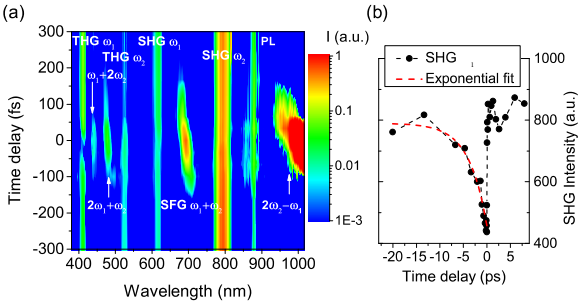


Figure 3: (a) Transient nonlinear frequency mixing spectra. (b) The SHG intensity time-dependence fitted by the exponential function.

3. Conclusions

In this work, we showed new developments in the nonlinear optical response of metasurfaces made from III-V semiconductors. Such metasurfaces support the simultaneous generation of multiple nonlinear processes in the wavelength range from UV to the near-IR. Moreover, the efficiencies of the nonlinear processes can be increased further by applying the broken symmetry designs. These results bring new insights into the nonlinear optical generation in nanostructures, opening the possibility to realize the ultra-compact universal mixer at optical frequencies.

Acknowledgements

This work was supported by the U.S. Department of Energy, Office of Basic Energy Sciences, Division of Materials Sciences and Engineering and performed, in part, at the Center for Integrated Nanotechnologies, an Office of Science User Facility operated for the U.S. Department of Energy (DOE) Office of Science. Sandia National Laboratories is a multi mission laboratory managed and operated by National Technology and Engineering Solutions of Sandia, LLC, a wholly owned subsidiary of Honeywell International, Inc., for the U.S. Department of Energy's National Nuclear Security Administration under contract DE-NA0003525.

References

[1] A. Krasnok, M. Tymchenko, and A. Alù, Nonlinear metasurfaces: a paradigm shift in nonlinear optics, *Materials Today*, 2017.

[2] S. Liu et. al., Resonantly Enhanced Second-Harmonic Generation Using III–V Semiconductor All-Dielectric Metasurfaces, *Nano Lett.*, 16 (9):

5426–5432, 2016.

[3] M. R. Shcherbakov et. al., Ultrafast all-optical tuning of direct-gap semiconductor metasurfaces, *Nature Communications*, 8(1): 17, 2017.

Active Mid-Infrared Plasmonics in Graphene

Min Seok Jang[1, *]

[1]School of Electrical Engineering, Korea Advanced Institute of Science and Technology (KAIST), Daejeon, Korea
*corresponding author, E-mail: jang.minseok@kaist.ac.kr

Abstract

Graphene is an interesting material for mid-infrared active nanophotonics. Recent studies have shown that the effective optical index of graphene depends on the local Fermi level, which can be varied greatly via electrostatic gating techniques. More interestingly, the low carrier concentration and the atomic thinness of graphene allows for highly confined plasmonic modes whose properties are also widely tunable as a function of doping density. We showed that these plasmonic modes can play a dominant role in controlling the optical properties of periodically patterned graphene at mid-infrared frequencies [1-3]. We showed that the energy-momentum dispersion relation of graphene plasmons are fundamentally different from the conventional noble metal surface plasmons and that the wavelength of graphene plasmons is more than 100 times shorter than the free space wavelength [1]. As a consequence of such extreme field confinement, we further demonstrated that graphene plasmons strongly interact with substrate phonons, forming hybrid modes called surface phonon plasmon polaritons [1, 2]. By placing a reflector to block transmission channels and engineering the spacing between the reflector and the graphene resonators, we demonstrated that the absorption in a single layer of graphene resonators can be dynamically tuned from 0 to 25% by electrostatic gating [3]. We also showed that the absorption modulation by graphene resonators can be 2.67 fold enhanced by incorporating EOT(extra-ordinary transmission) metallic resonant structures [4]. By further advancing the idea of overlapping various scales of resonances in a narrow spectral and spatial window, we recently demonstrated that it is possible to achieve perfect mid-infrared absorption modulation based on graphene plasmonic metasurfaces [5]. Finally, Kirchhoff's law of thermal radiation, which states the absorptivity and the emissivity of an object are equal, also allows for dynamic control of thermal radiation from heated graphene plasmonic nanoresonators [6]. These tunable plasmonic modes offered by graphene and other 2D materials provide new opportunities to create electo-optically active devices with novel functionalities that have thus far been impossible to be realized by using conventional media.

References

[1] Brar, V. W.[#], Jang, M. S.[#], Sherrott, M., Lopez, J. J., and Atwater, H. A.[*], "Highly confined tunable mid-infrared plasmonics in graphene nanoresonators," Nano Letters 13, 2541 (2013).

[2] Brar, V. W.[#], Jang, M. S.[#], Sherrott, M., Kim, S., Lopez, J. J., Kim, L. B., Choi, M., and Atwater, H. A.[*], "Hybrid surface-phonon-plasmon polariton modes in graphene/monolayer h-BN heterostructures," Nano Letters 14, 3876 (2014).

[3] Jang, M. S.[#], Brar, V. W.[#], Sherrott, M. C., Lopez, J. J., Kim, L., Kim, S., Choi, M., and Atwater, H. A.[*], "Tunable large resonant absorption in a midinfrared graphene Salisbury screen," Physical Review B 90, 165409 (2014).

[4] Kim, S.[#], Jang, M. S. [#], Brar, V. W. [#], Tolstova, Y., Mauser, K. W., and Atwater, H. A.[*], "Electronically tunable extraordinary optical transmission in graphene plasmonic ribbons coupled to subwavelength metallic slit arrays," Nature Communications 7, 12323 (2016).

[5] Kim, S.[#], Jang, M. S. [#], Brar, V. W. [#], Mauser, K. W., Atwater, H. A.[*], "Electronically Tunable Perfect Absorption in Graphene," Nano Letters 18, 971 (2018).

[6] Brar, V. W., Sherrott, M. C., Jang, M. S., Kim, S., Kim, L., Choi, M., Sweatlock, L. A., and Atwater, H. A.[*], "Electronic modulation of infrared radiation in graphene plasmonic resonators," Nature Communications 6, 7032 (2015).

Multiple-DWDM-channel heralded single-photon source based on a periodically poled lithium niobate waveguide

Tong Xiang,[1,2] Yuanhua Li,[1,2] Yuanlin Zheng,[1,2] and Xianfeng Chen[1,2,*]

[1]State Key Laboratory of Advanced Optical Communication Systems and Networks, School of Physics and Astronomy, Shanghai Jiao Tong University, Shanghai 200240, China
[2]Key Laboratory for Laser plasma (Ministry of Education), Collaborative Innovation Center of IFSA (CICIFSA), Shanghai Jiao Tong University, Shanghai 200240, China
*corresponding author, E-mail: xfchen@sjtu.edu.cn

Abstract

We report on the experimental realization of a multiple-DWDM-channel heralded single-photon source in a periodically poled lithium niobate waveguide. Our single photon at the telecom wavelength covers more than 40 channels of the ITU grid. All channels have virtually identical efficiencies, and the multi-photon emission probability is reduced by a factor up to more than 150 compared to a Poissonian light source. The pump with a 50MHz pulsed laser has potential applications in practical quantum communication. Together with the all-fiber structure, all these advantages make our heralded single-photon source compatible with real-world quantum networks.

1. Introduction

The single-photon source (SPS) plays a key role in hot research fields such as quantum computing and communication, especially in quantum key distribution (QKD). Multi-photon can compromise the security of the communication by allowing eavesdroppers to steal information. In principle, for the same secure communication rate, single-emitter-based QKD systems can achieve longer key transmission distances than faint laser pulse systems. So far, several schemes for SPS have been proposed, which are mainly divided into two categories: 1. Color centers, quantum dots, single atoms, single ions and atomic ensembles are considered as deterministic SPS; 2. Photons created in pairs via four-wave mixing in fibers and spontaneous parametric down conversion (SPDC) in bulk crystals and waveguides are described probabilistic one, which is called heralded single-photon source (HSPS). SPS have been continuously improved in purity, efficiency, repetition rate and usability in the past decade. However, some drawbacks make the deterministic SPS unsuitable for practical applications. For instance, the emitted photons are in visible spectrum, which is not compatible with existing telecommunication networks. Furthermore, the operating temperature of current available SPS is quite low. Therefore, the HSPS by SPDC can be more widely used in the field of quantum communication. Considering the excellent security of the quantum networks, it will be great significance to build the quantum networks in communication. In a real multipoint-to-multipoint quantum networks, the point-to-multipoint SPS is an essential component.

Here, we report on the realization of a high efficiency multiple-channel HSPS at telecom wavelength through SPDC with a periodically poled lithium niobate (PPLN) waveguide. In brief, it is a point-to-multipoint HSPS. The efficiency of SPDC in waveguide is several times higher than the one in bulk, which ensures high repetition rate in each channel. Our source covers over forty 100-GHz dense wavelength division multiplexer (DWDM) ITU grid channels and each channel contains almost the same brightness and high quality. In addition, all fiber setup makes our source a good choice for quantum networks.

2. Theory

By definition, the SPS can be characterized with the $g^{(2)}(\tau)$ parameter of second-order correlation function. For an ideal SPS, the parameter $g^{(2)}(0)=0$, with $g^{(2)}(\tau)>g^{(2)}(0)$ $(\tau\neq 0)$. In our setup, the $g^{(2)}(\tau)$ is equal to:

$$g^{(2)}(\tau)\cong\frac{p(2)}{p(1)^2}=\frac{p_{BC}}{p_B\cdot p_C}, \qquad (1)$$

$P(1)$ is the probability of generating exactly one photon per heralding signal, while $P(2)$ is the probability of generating more than one photon. $P(1)$ and $P(2)$ are two other crucial parameters for the HSPS, which are relevant to $g^{(2)}(\tau)$. In our HSPS experiment, The high efficient process of SPDC should meet the quasi-phase matching (QPM) condition:

$$\vec{k}_p=\vec{k}_s+\vec{k}_i+\vec{k}_\Lambda, \qquad \omega_p=\omega_s+\omega_i. \qquad (2)$$

where p, s, i denote pump, signal and idler waves, respectively. k and ω are the wavevector and the frequency of the waves. The result in Figure 1 shows an ultra-wide QPM bandwidth with a full width at half maximum (FWHM) of approximate 70 nm. This special property is basic to our multiple-channel source.

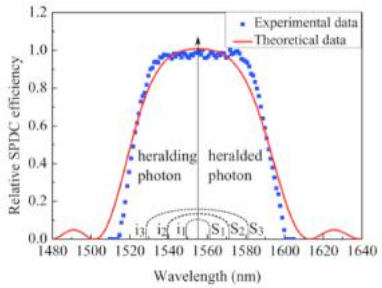


Figure 1: The red curve is the simulation of SPDC efficiency of our PPLN waveguide. s_n and i_n are daughter photon pairs, which represent CH26-CH24 and CH28-CH30 in the experiment, respectively.

3. Experiment and results

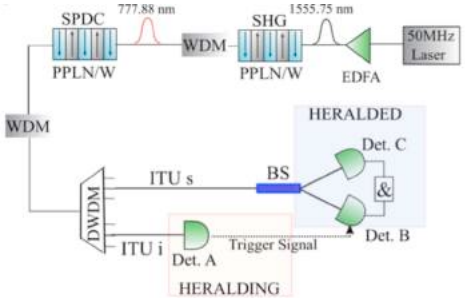


Figure 2: Schematic of multi-channel heralded single-photon source.

The experimental setup is shown in Figure 2. The laser at telecom wavelength with a repetition rate of 50MHz is first amplified to 120 mW by an EDFA, and then it's wavelength is converted to near infrared region by second harmonic generation (SHG) in the first PPLN waveguide, which is used as a pump for spontaneous parametric down conversion through the second PPLN waveguide. Both of the processes take place in PPLN waveguides with type-0 phase-matching condition. At the output of SPDC, a high-isolation WDM is used to filter the pump laser. The photon pairs are then split by a 100-GHz DWDM, which has seven channels within the ITU grid (CH24-30). The short-wavelength photon is defined as heralding photon and detected by Det. A directly. The long-wavelength one propagating through a 50/50 fiber optical beam splitter is considered the heralded single photon and is detected by Det. B and Det. C, which are trigged by Det. A. Two output ports of the detectors are connected to a photon correlator to measure the coincidence.

$P(1)$ and $g^{(2)}(0)$ are shown in Fig. 3. We figure out $P_{24}(1)$=0.23, $P_{25}(1)$=0.22, and $P_{26}(1)$=0.21. At the highest heralding rate of 67 kHz, the $g^{(2)}(0)$ is around 0.13. The $g^{(2)}(0)$ falls to lower than 6.7×10^{-3} at 1.06 μW pump power (heralding rate 5 kHz). We compare these results to a Poissonian light source [$g^{(2)}(0)=1$] featuring the same value for $P(1)$. Mainly the multi-photon emission probability $P(2)$ of each channel is reduced by the factor $1/g^{(2)}(0)$ ranging from around 7.5 to over 150.

$P(2)$ and $g^{(2)}(0)$ can also be expressed as:

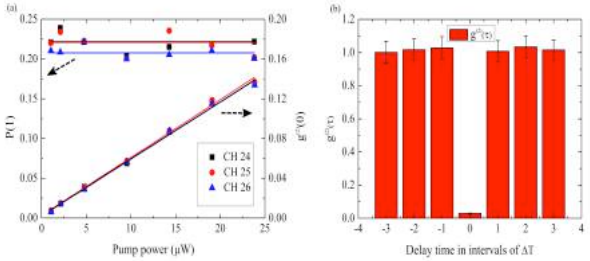


Figure 3: (a) Measured the relationship between $P(1)$ and pump power; Measured $g^{(2)}(0)$ as a linear function of the pump power. (b) The relationship between $g^{(2)}(\tau)$ and delay time.

$$P(2)=\frac{1}{2}\cdot P(1)^2\cdot\Delta t\cdot\eta_p\cdot\overline{P}_p,\qquad g^{(2)}(0)\approx\Delta t\cdot\eta_p\cdot\overline{P}_p,\quad(3)$$

where Δt is the duration of the detector gate, η_p is the pair creation efficiency of the PPLN waveguide and $\overline{P}_p$ is the pump power. Fig. 3(a) shows that $g^{(2)}(0)$ is proportional to $\overline{P}_p$, which is in accordance with theoretical results. Beyond that, the three channels behave almost identically under the same pump power, such as heralding rate, $P(1)$, $P(2)$ and $g^{(2)}(0)$. This unique property makes our source a stable and controllable point-to-multipoint HSPS. Figure 3(b) shows the relationship between $g^{(2)}(\tau)$ and delay time. Evidently, $g^{(2)}(\tau)$ reaches 1 directly when τ is equal to mT, where T is the periodic time of the pump 20 ns and m is nonzero integer.

4. Conclusions

In conclusion, we have demonstrated and characterized a multi-DWDM-channel HSPS with high quality. Each heralded channel has nearly constant $P(1)$ about 0.22. The measured second-order correlation function $g^{(2)}(0)$ ranges from 6.7×10^{-3} to 0.13. For the best $g^{(2)}(0)$, it is suppressed by a factor of more than 150 relative to the classical light. In a practical application, good tradeoffs between low $g^{(2)}(0)$ and high brightness can be guaranteed. Furthermore, our source is all fiber structure at room temperature without cooling. It is therefore an ideal candidate for real-world quantum networks.

Acknowledgements

This work is supported by the National Natural Science Foundation of China under Grant No. 61235009.

References

[1] L. Ngah, O. Alibart, L. Labonte, V. D'Auria, S. Tanzilli, "Ultra-fast heralded single photon source based on telecom technology," Laser & Photonics Rev. **9**, 2 (2015).

[2] M. Bock, A. Lenhard, C. Chunnilall, and C. Bechwe, "Highly efficient heralded single-photon source for telecom wavelengths based on a PPLN waveguide," Opt. Express **24** (21), 23992 (2016).

Tunable zero-index and metasurface optics in extreme optical platforms

Jingyi Yang[1], Aleksei Anopchenko[1], Long Tao[1], Sudip Gurung[1], Subhajit Bej[1], Catherine Arndt[1], Khant, Minn[1], and Ho Wai Howard Lee[1,2,*]

[1]*Department of Physics and Baylor Research and Innovation Collaborative, Baylor University, Waco, United States*

[2]*The Institute for Quantum Science and Engineering, Texas A&M University, College Station, United States*

[*]Howard_Lee@Baylor.edu

Abstract- We present our recent development on the use of tunable transparent conducting oxides to demonstrate electrically tunable epsilon-near-zero (ENZ) optical devices and to develop ENZ/metasurface nanostructured optical fibers.

Light harvesting and high-resolution optical technologies demand optical coatings with strong light absorption. Recent studies suggest that epsilon-near-zero (ENZ) materials can be useful to make perfect ultrathin film absorbers [1-3]. The ultrathin ENZ layers support radiative Berreman and bound ENZ modes [2, 4]. Excitation of these modes in two different incident light configurations leads to resonant absorption. In this work, a broadband perfect absorber has been demonstrated by using a stack of Transparent conducting oxide (TCO) nanolayers with gradually varying electron concentration and hence ENZ frequency. The light absorption dependence on the ENZ layer thickness in the multilayer stack was optimized so that absorption >95% was achieved at deep subwavelength ENZ thicknesses. Electronically tunable absorption via formation of electron accumulation/depletion layer in the field-effect devices was studied.

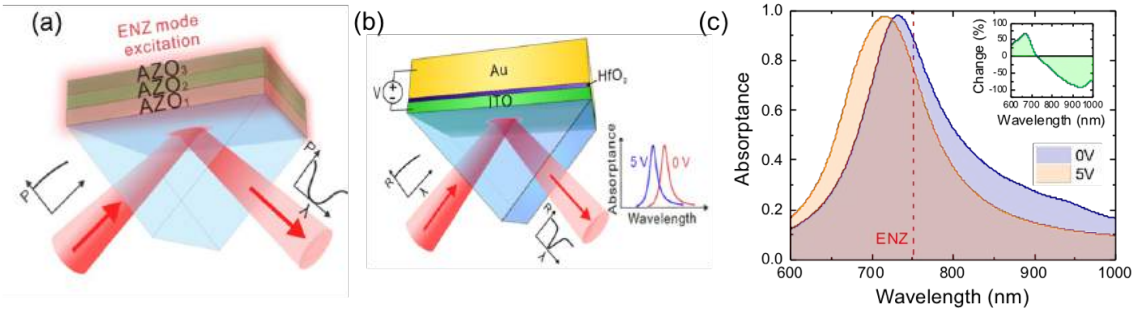


Fig.1 Schematic of (a) broadband and (b) field-effect tunable metal-oxide-semiconductor (MOS) ENZ perfect absorbers. Perfect absorption tuning: absorptance of the unbiased and 5V-biased MOS field-effect perfect absorber at the incidence angle of 60°.

The ENZ multilayers are composed of 3 AZO nanolayers (Fig. 1a). The optical properties of the AZO are modelled using free electron Drude model. We found that the highest absorption can be achieved with the AZO thickness of ~ 10-30 nm in the ENZ multilayers. The absorptance is attributed to the excitation of the radiative Berreman mode. The ENZ multilayer is supported by a thick gold reflector [5]. The electron concentration decreases, and ENZ wavelength increases, from the top to the bottom of the multilayer stack. Broadband maximum absorption >95% and field enhancement are observed at the ENZ wavelengths by exciting Berreman mode. Excitation of the bound ENZ mode in the Kretschmann-Raether configuration) results in resonant light absorption with much borader bandwidth than the

Berreman mode. The absorptance of >95% for more than 400 nm wavelength range is observed for the multilayer stack with 8-nm thin AZO layers [6].

Tunable absorption can be enabled by the field-effect dynamic in metal-oxide-semiconductor (MOS) configuration (Fig. 1b). The MOS device consists of a metal substrate, single 8-nm thin ITO layer, and 5-nm-thin HfO_2 layer between them. Electron accumulation occurs in ITO at the ITO-HfO_2 interface when bias is applied between metal and ITO, thus modifying the complex dielectric constant of the ITO. Electron accumulation increases plasma and ENZ frequency and therefore leads to a blue shift of the absorption peak in wavelength (Fig. 1c) [7]. The larger absorptance change (> 300%) is observed at shorter wavelengths due to larger field enhancement in the accumulation layer. These results open the path to develop ultrathin tunable ENZ absorbers and thin-film modulators.

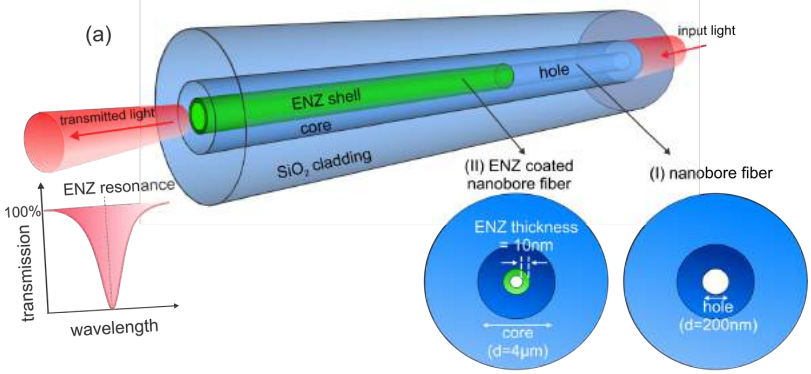


Fig.2. Schematic of the proposed ENZ fiber waveguide design. The inserts are cross-sections of the ENZ fiber (coated with ITO ENZ nano-shell) and hollow nanobore fiber (without ITO ENZ nano-shell).

We also report a novel optical waveguide design of a hollow step index fiber modified with a thin layer of indium tin oxide (ITO) (Fig. 2). We show an excitation of highly confined waveguide mode in the proposed fiber near the wavelength where permittivity of ITO approaches zero [8]. Due to the high field confinement within thin ITO shell inside the fiber, the ENZ mode can be characterized by a peak in modal loss of the hybrid waveguide. Our results show that such in-fiber excitation of ENZ mode is due to the coupling of the guided core mode to the thin-film ENZ mode. We also show that the phase matching wavelength, where the coupling takes place, varies depending on the refractive index of the constituents inside the central bore of the fiber. These ENZ nanostructured optical fibers have many potential applications, for example, in ENZ nonlinear and magneto-optics, as in-fiber wavelength-dependent filters, and as subwavelength fluid channel for optical and bio-photonic sensing.

Acknowledgement

This work was supported in part by the Young Faculty Award Program from Defense Advanced Research Projects Agency (grant number N66001-17-1-4047), CAREER Award Program from National Science Foundation (grant number: 1752295), the Young Investigator Development Program, the Undergraduate Research and Scholarly Achievement (URSA), and the Vice Provost for Research at Baylor University.

References

[1] M. A. Badsha, Y. C. Jun, and C. K. Hwangbo, Opt. Commun. 332, 206-213, 2014.

[2] S. Campione, I. Kim, D. de Ceglia, G. A. Keeler, and T. S. Luk, Opt. Express 24, 18782-18789, 2016.

[3] J. Yoon, M. Zhou, M. A. Badsha, T. Y. Kim, Y. C. Jun, and C. K. Hwangbo, Sci. Rep. 5, 12788, 2015.

[4] S. Vassant, J.-P. Hugonin, F. Marquier, and J.-J. Greffet, *Opt. Express* **20**, 23971-23977, 2012.

[5] A. Anopchenko, S. Gurung, L. Tao, C. Arndt, H. W. Lee, *Materials Research Express* **5**, 014012 (2018).

[6] A. Anopchenko, L. Tao, C. Arndt, H. W. Lee, “Gate tunable and broadband Epsilon-near-zero perfect absorbers with deep subwavelength thickness,” *ACS Photonics* (submitted) (2018).

[7] Y. W. Huang *et al.*, "Gate-tunable conducting oxide metasurfaces," *Nano Lett*. **16**, 5319-5325, 2016.

[8] K. Minn, A. Anopchenko, J. Yang, H. W. Lee, “Excitation of epsilon-near-zero resonance in ultra-thin indium tin oxide shell embedded nanostructured optical fiber,” *Nature Scientific Reports* **8**, 2342(2018).

Fano Resonances in Optics and Microwaves: Physics and Application

Fano resonance generation and application of three dimensional metamaterials

Shengyan Yang[1,2], Zhe Liu[1], Junjie Li[1,2], and Changzhi Gu[1,2*]

[1]Beijing National Laboratory for Condensed Matter Physics, Institute of Physics, Chinese Academy of Sciences, Beijing 100190, China

[2]School of Physical Sciences, CAS Key Laboratory of Vacuum Physics, University of Chinese Academy of Sciences, Beijing 100190, China

[*]corresponding author: czgu@iphy.ac.cn

Abstract- We report the generation of high-quality-factor Fano resonances in substrate-free 3D metamaterials. The unique 3D configurations lead to the excitation of otherwise inaccessible out-of-plane dark modes, which strongly couple with the surface-plasmon-polaritons mode in the square apertures, and results in the emergence of the sharp Fano resonance with pronounced electromagnetic field enhancement. The spectral properties of the Fano resonances can be drastically manipulate by tailoring the geometric parameters of the 3D metamaterial. The 3D metamaterials possessing multiple high-Q-factor Fano resonances provide a remarkable versatile platform for multispectral filtering, ultrasensitive sensing, lasing spasers and nonlinear optics.

Fano resonances in plasmonic nanostructures and metamaterials have attracted extensive interest in recent years due to their promising applications in ultrasensitive sensing, high-contrast optical imaging, high-quality optical waveguide, high-performance nonlinear devices and switching[1,2]. Although a wide variety of approaches and geometries have been explored to generate Fano resonances in plasmonic materials and metamaterials, the realization of Fano resonance in most of the reported systems are based on planar metallic configurations on a substrate[1], which usually suffer from low Q factor and compromise the device performance due to large radiative and non-radiative losses. Moreover, the high-order dark resonance modes, usually necessary for Fano resonance, were normally weak and not easily accessible.

Here, we experimentally demonstrate a series of substrate-free 3D metamaterials that support prominent high-Q-factor Fano resonances with enormous spatial electromagnetic field enhancement, which can be exploited for ultrasensitive sensing and SERS detection. This 3D metamaterials, composed of out-of-plane gold nanostructures standing along one edge of square apertures, were fabricated using Focused ion beam induced deformation technique[3-5], and characterized by Fourier transform infrared (FTIR) spectrometer. The unique Fano resonances in the 3D metamaterials are induced by the destructive interference between the super-radiant surface-plasmon-polariton mode supported by the apertures and out-of-plane dark modes in the vertical structures. The resonant properties of the Fano resonance can be engineered by modulating the geometric parameters of the 3D metamaterials. The 3D metamaterial sustaining multiple high-Q-factor Fano resonances are highly promising for potential applications, such as high-performance sensors, lasing, switching, and nonlinear and slow-light devices.

Acknowledgements: This work is supported by the National Key Research and Development Program of

China under Grant No. 2016YFA0200400, and No. 2016YFA0200800; the National Natural Science Foundation of China under Grants Nos. 91323304, 11674387, 11504414, 11574369, 11574385, 11574368, and 61390503; Strategic Priority Research Program and Key Research Program of Frontier Sciences, CAS, Grant No.XDB07020200 and No.QYZDJ-SSW-SLH042.

REFERENCES

1. Luk'yanchuk, B., Zheludev, N. I., A. Maier, Stefan., Halas, N. J., Nordlander, P., Giessen, H., and Chong, C. T., "The Fano resonance in plasmonic nanostructures and metamaterials," *Nature Mater.*, Vol. 9, 707-715, 2010.
2. Singh, R., Cao, W., Al-Naib, I., Cong, L., Withayachumnankul, W., and Zhang, W., "Ultrasensitive terahertz sensing with high-Q Fano resonances in metasurfaces," *Appl. Phys. Lett*., Vol. 105, No. 171101, 2014.
3. Liu, Z. G., Liu, Z., Li, J. F., Li, W. X., Li, J.J., Gu C. Z., Li, Z.Y., "3D conductive coupling for efficient generation of prominent Fano resonances in metamaterials," *Scientific Reports* Vol. 6, No. 27817, 2016.
4. Yang, S. Y., Liu, Z., Jin, L., Li, W. X., Zhang, S., Li, J. J., and Gu, C. Z., "Surface plasmon polariton mediated multiple toroidal resonances in 3D folding metamaterials," *ACS Photonics*, Vol. 4, 2650-2658, 2017.
5. Cui, A. J., Liu, Z., Li, J. F., Shen, T. H., Xia, X. X., Li, Z. Y., Gong, Z. J., Li, H. Q., Wang, B. L., Li, J. J., Yang, H. F., Li, W. X., and Gu, C. Z., "Directly patterned substrate-free plasmonic "nanograter" structures with unusual Fano resonances," *Light: Science & Applications*, Vol. 4, No. e308, 2015.

Electromagnetically induced transparency in a superconducting qubit

Tiefu Li

Institute of Microelectronics, Tsinghua University, 100084 Beijing, China

Electromagnetically induced transparency (EIT) has been realized in atomic systems, but fulfilling the EIT conditions for artificial atoms made from superconducting circuits is a more difficult task. Here we report an experimental observation of the EIT in a tunable three-dimensional transmon by probing the cavity transmission. We tune the transmon to adjust its damping rates to fulfill the EIT conditions. From the experimental observations, we clearly identify the EIT and Autler-Townes splitting (ATS) regimes as well as the transition regime in between. Also, the experimental data demonstrate that the threshold \Omega_{AIC} determined by the Akaike information criterion can describe the EIT-ATS transition better than the threshold \Omega_{EIT} given by the EIT theory.

Magnetostatic resonances in subwavelength particles: Eigenvalue problem and bound states in microwave continuum

E. O. Kamenetskii

Microwave Magnetic Laboratory,
Department of Electrical and Computer Engineering,
Ben Gurion University of the Negev, Beer Sheva, Israel
*Email: kmntsk@bgu.ac.il

Abstract-We make a comparative analysis of quasistatic eigenvalue problems for plasmon and magnon oscillations in subwavelength particles. We show that in a case of magnetostatic resonances one observes non-Maxwellian propagation-wave behaviors. We show that a case of a quasi-2D ferrite-disk particle, the problem for magnetostatic-potential wave function is Hermitian. We analyze bound states in a microwave-field continuum with an embedded magnetostatic-resonance ferrite particle.

Magnetostatic (or magnetic-dipolar) resonances in ferrite samples with dimensions much smaller than the wavelength of microwave radiation has its origin in magnetic-potential theory, which describes systems of magnetic dipoles and the magnetostatic potentials produced by these dipoles. To a certain extent, this can be considered as a situation dual to the electrostatic theory describing the localized surface plasmons in nanoparticles with dimensions much smaller than the wavelength of light, which describes systems of electric dipoles and the electrostatic potentials they produce. When the material linear response is described by a bulk dielectric scalar function, the electrostatic resonances can be found as solutions of the equation for an electrostatic potential. It was pointed out that for electrostatic resonances in nanoparticles one has a non-Hermitian eigenvalue problem with bi-orthogonal (instead of regular-orthogonal) eigenfunctions. The spectral solutions for eigenvalue problem for magnetic-dipolar resonances in a small ferrite sample can be obtained based on Walker equation for magnetostatic wave function. As an appropriate approach for description of quasistatic oscillations in small particles, one uses a classical formalism where the material linear response at frequency ω is described by a local bulk dielectric function the permittivity tensor $\ddot{\varepsilon}(\omega)$ or by a local bulk magnetic function the permeability tensor $\ddot{\mu}(\omega)$. For a case of plasmonic (electrostatic) resonances in small metallic samples, one neglects a magnetic displacement current and has quasistationary electric fields. A dual situation is demonstrated for magnetic-dipolar (magnetostatic) resonances in small ferrite samples, where one neglects an electric displacement current. It is evident that these potentials do not have the same physical meaning as in the problems of “pure" (non-time-varying) electrostatic and magnetostatic fields. Fundamentally, subwavelength sizes should eliminate any effects of the electromagnetic retardation. When one neglects the displacement currents (magnetic or electric) and considers scalar functions $\phi(\vec{r},t)$ or $\psi(\vec{r},t)$ as the wave functions, one becomes faced with important questions, whether there could be the propagation behaviors inherent for the quasistatic wave processes and, if any, what is the nature of these retardation effects. From classical electrodynamics, the eigenvalue problem formulated *exceptionally* for the electrostatic-potential wave function $\phi(\vec{r},t)$ do not presume an involvement of alternative magnetic fields in a resonance process and, similarly, the eigenvalue problem formulated *exceptionally* for the magnetostatic-potential function wave $\psi(\vec{r},t)$ do not presume an involvement of alternative electric fields in magnetic-dipolar resonances. The curl magnetic field appearing in plasmonic oscillations

due to the Ampere-Maxwell law, does not affect the electrostatic result. Similarly, the curl electric field appearing in magnonic oscillations due to the Faraday law does not affect the magnetostatic result. The fact that the retardation effects in the plasmonic or magnonic oscillations appear only when the particle sizes are comparable with the free-space electromagnetic wavelength raises the question on the possibility of existence of non-Maxwellian propagation-wave behaviors for the quasistatic-resonance processes. In electromagnetically subwavelength particles, there can be, for example, space-charge waves in semiconductors and waves of magnetization (spin waves) in ferrites.

Solutions of the spectral problem for magnetostatic-potential wave function give evidence for two distinctive features on magnetic-dipolar-modes (MDMs) in a ferrite samples. Firstly, there is the existence of non-Maxwellian propagation-wave behaviors for the magnetostatic resonances. Secondly, one can show that in a case of a quasi-2D ferrite-disk particle, the problem for magnetostatic-potential wave function $\psi(\vec{r},t)$ is Hermitian. In such a ferrite particle, the function $\psi(\vec{r},t)$ appear as orthonormal complex eigenfunction. The adjoint of this function is equal to its complex conjugate quantity. This differs from the resonances in metal nanoparticles where one has a non-Hermitian eigenvalue problem for electrostatic-potential wave function $\phi(\vec{r},t)$.

One of the main reasons for appearance of the bound states in a microwave-field continuum with an embedded magnetostatic-resonance ferrite particle is a symmetry mismatch. Modes of different symmetry classes (such as reflection or rotation) are completely decoupled. MDM oscillations do not exhibit a rotational symmetry, while a regular waveguide structure is rotationally symmetric. With such a condition, the MDM bound states observed in microwave structures can be classified as the symmetry-protected BICs. The MDM bound states are embedded in the microwave continuum but not coupled to it. If a bound state of one symmetry class is embedded in the continuous spectrum of another symmetry class their coupling is forbidden. Moreover, the near fields, originated from a MDM ferrite disk, and electromagnetic fields in a microwave structure are described by different types of equations. At any stable state, MDMs cannot radiate because there is no way to assign a far-field electromagnetic-wave polarization that is consistent with vortex fields near a MDM ferrite disk. In a short-range interaction, an important aspect concerns the topological nature of the MDM BICs. These topological properties can be understood through eigen power-flow vortices with corresponding topological charges. Quantized topological charges cannot suddenly disappear. They are protected by special boundary conditions in a quasi-2D ferrite disk. The MDM BICs cannot be removed unless MDM topological charges are cancelled with another structure carrying the opposite topological charges. Such opposite topological charges appear on metal walls of a microwave waveguide. The probing of these BICs is due to topological-phase properties of MDMs resulting in appearance of spiral electric currents induced on metal parts of a microwave structure. The coupling is possible via the continuum of decay channels at the condition that phases of the MDM bound states are strongly determined phases.

Bound States in the Continuum in tri-layer Photonic Crystal slab

Liangsheng Li[1] Hongcheng Yin[1]

1 Science and Technology on Electromagnetic Scattering Laboratory, Beijing 100854, China

*corresponding author, E-mail: liliangshengbititp@163.com

Abstract

We have investigated the Fano resonances in the tri-layer photonic crystal (PhC) structures by tuning the hole size and displacement of the middle PhC slab along the y axis. It is found that a new kind of bound states in the continuum (BIC) in this systems without C2 rotational symmetry for the z axis. These new BIC phenomena can be understood by the two band coupled model, which has different resonance frequencies and different radiation rates.

1. Introduction

Photonic crystal slabs with a periodic modulation of refractive index are used in many applications. Fano resonances can be observed and originates from the coupling between the guided modes supported by the slab and external plane waves. When the linewidth of Fano resonaces tends to zero, BICs emerges due to the existence of topological charges defined by the winding number of the polarization vectors around the BIC[1]. This specific resonance state has a high quality factor making it potentially useful for filters, antennas, chemical sensing, or single-photon sources[2-4]. However, all reported PhC systems have BICs with C2 rotational symmetry for the z axis [5-7]. A fundamental question is thus to know whether there exist structures in which BICs can be exhibited without C2 symmetry.

2. Page layout and style

We consider a tri-layer PhC system, where a PhC slab with finite thickness L has a square lattice of square air holes. This single layer PhC slab structure has an inversion geometric symmetry and a mirror geometric symmetry in the z direction. The middle layer of tri-layer PhC system can move along the y axis. Light incident on the tri-layer PhC slab can excite the Fano resonances observed in the reflectivity spectrum due to interference between in-plane waveguide modes and out-of-plane far-field radiation. Figure 1 shows that Fano resonances are characterized by the asymmetric profile consisted of blue and red branches corresponding to the reflectivity of zero and one, respectively. When the displacement of middle layer (y_0) is changed, four BICs (p1,p2,p3,p4) are observed because the geometric symmetry forbids coupling to any far-field radiation.

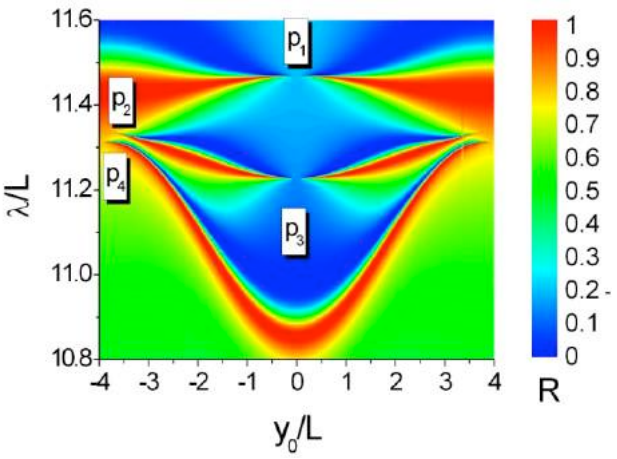


Figure 1: Numerical reflectivity spectra (R) for the p-polarized as a function of displacement and wavelength.

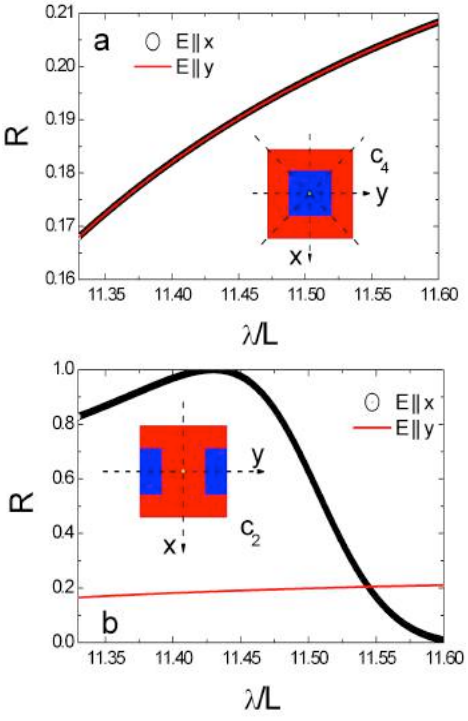


Figure 2: Numerical reflectivity spectra for the p-polarized and s-polarized as a function wavelength. (a) $y_0/L=0$. (b) $y_0/L=4$.

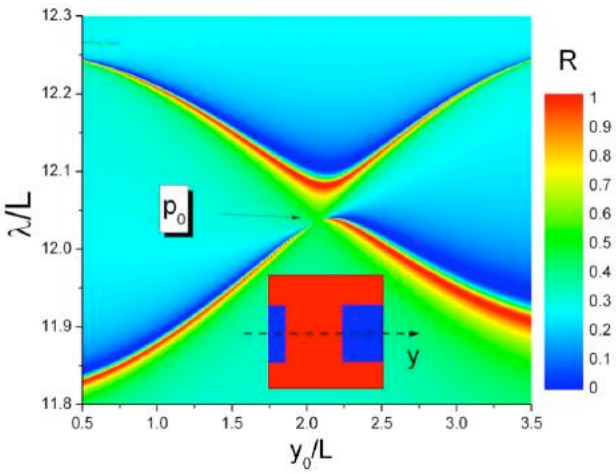


Figure 3: Numerical reflectivity spectra for the p-polarized as a function of displacement and wavelength.

However, p_1 and p_3 are protected by C_4 symmetry, and p_2 and p_4 are protected by C_2 symmetry. When the BICs are protected by C_4 symmetry, the reflectivity of p-polarized and s-polarized are identical results as shown in Figure 2 (a). For the BICs protected by C_2 symmetry, the reflectivity of p- and s-polarized are different shown in Figure 2 (b).

When the size of square hole decrease, a new BIC without C_2 symmetry is observed in Figure 3. Zhen *et al.* shown that a BIC can be only found in PhC slabs with C_2, C_3, C_4, and C_6 symmetries [2]. However, they only consider a single degenerate band, and bands in the system do not cross with each other. Then, the symmetry requirements can be changed by introducing the coupling between original bands. The coupling here can be adjusted by changing the supercell of PhC structures. This results can be understood by using the effective Hamiltonian

$$H = \begin{bmatrix} w_1 & k \\ k & w_2 \end{bmatrix} - i \begin{bmatrix} g_1 & \sqrt{g_1 g_2} \\ \sqrt{g_1 g_2} & g_2 \end{bmatrix} \quad (1)$$

which has complex eigenvalues

$$w_{\pm} = \frac{w_1 + w_2}{2} - i\frac{g_1 + g_2}{2} \pm \sqrt{\left(k - i\sqrt{g_1 g_2}\right)^2 - \left(\frac{g_1 - g_2}{2} + i\frac{w_1 - w_2}{2}\right)^2} \quad (2)$$

In the absence of inter resonance couplings $k = 0$, when g_1 and g_2 become zero the system can exhibit two decoupled BICs. Then, the complex eigenvalues become two pure real frequencies,

$$w_{\pm} = \frac{w_1 + w_2}{2} \pm \sqrt{k^2 + \left(\frac{w_1 - w_2}{2}\right)^2}. \quad (3)$$

By tuning system parameters (here, size of hole and displacement of middle layer), one can achieve accidental degeneracy between a quadrupole mode and two degenerate dipole modes at the special point, leading to a BIC state due to the anti-crossing between two bands without C_2 symmetry. The condition is given by

$$k\left(g_1 - g_2\right) = \sqrt{g_1 g_2}\left(w_1 - w_2\right) \quad (4)$$

Then, one of complex eigenvalues become pure real number, but the other still are complex number as following

$$w_+ = w_- + k\frac{g_1 + g_2}{\sqrt{g_1 g_2}} - i\frac{g_1^2 - g_2^2}{g_1 - g_2}, \qquad w_- = \frac{w_2 g_1 - w_1 g_2}{g_1 - g_2} \quad (5)$$

3. Conclusions

The Fano resonances are investigated in the tri-layer photonic crystal structures by tuning the hole size and displacement of the middle PhC slab along the y axis. A new BIC is observed in this systems without C2 symmetry. These new BIC phenomena can be understood by the effective Hamiltonian, which the eigenvalues can point out the different types of BIC.

Acknowledgements

The work was supported by the Chinese National Science Foundation, Project No. 6149069502.

References

[1] B. Zhen, C. W. Hsu, L. Lu, A. D. Stone, and M. Solja cic, Topological Nature of Optical Bound States in the Continuum, Phys. Rev. Lett. 113, 257401, 2014.

[2] Shen, Y. et al. Optical broadband angular selectivity. *Science* 343, 1499, 2014 .

[3] Granier, C. H. et al. Optimized aperiodic multilayer structures for use as narrow-angular absorbers. J. *Appl. Phys* 116, 243101, 2014.

[4] Lepetit, T. & Kante, B. Controlling multipolar radiation with symmetries for electromagnetic bound states in the continuum. *Phys. Rev. B* 90, 241103(R) , 2014.

[5] LiangSheng Li & Hongcheng Yin Bound States in the Continuum in double layer structures. *Scientific Reports*, srep26988, 2016.

[6] Yang, Y., Peng, C., Liang, Y., Li, Z. & Noda, S. Analytical perspective for bound states in the continuum in photonic crystal slabs. *Phys. Rev. Lett* 113, 037401, 2014.

[7] Lee, J. et al. Observation and differentiation of unique high-Q optical resonances near zero wave Vector in macroscopic photonic crystal slabs. *Phys. Rev. Lett* 109, 067401, 2012.

On bound states in the continuum in dielectric gratings

E.N. Bulgakov[1,2],D.N. Maksimov[1,2,*], P.N. Semina[1], S.A. Skorobogatov[1]

[1]Reshetnev Siberian State University of Science and Technology, 660037, Krasnoyarsk, Russia
[2]Kirensky Institute of Physics, Federal Research Center KSC SB RAS, 660036, Krasnoyarsk, Russia
[*]Corresponding author: mdn@tnp.krasn.ru

February 15, 2018

Abstract

Bound states in the continuum (BICs) in dielectric gratings are considered. We found the geometries of the gratings supporting propagating BICs . It is demonstrated that if a two-sided grating possesses either mirror or glide symmetry the propagating BICs are stable to variation of parameters. The formation of the BICs is explained via the Friedrich-Wintgen mechanism in the spectral vicinity of avoided crossings. The concurrent phenomenon of collapsing Fano resonances is discussed.

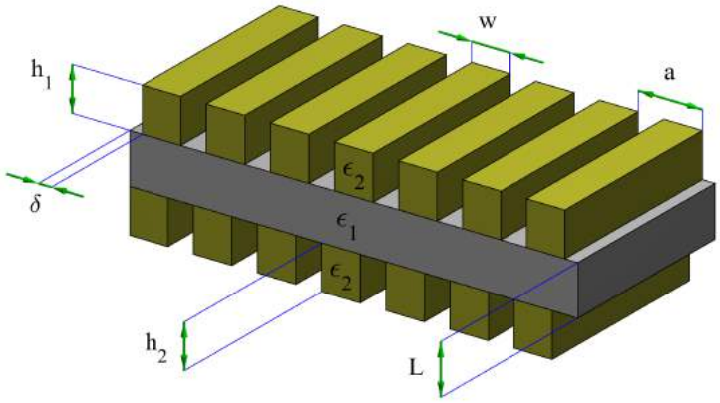


Figure 1: Dielectric grating.

We consider bound states in the continuum (BICs), i.e. localized eigenmodes of Maxwell's equations embedded into continuous spectrum of scattering states [1], in dielectric gratings. The gratings consist of a dielectric slab with permittivity ϵ_1 in air with dielectric ridges with permittivity ϵ_2 periodically placed on the slab as shown in Fig 1. Using the Fourier modal approach [2, 3] we recover the leaky zones above the line of light to identify the geometries of the gratings supporting BICs. In general the system under scrutiny can support two types of BICs. The first type are standing wave eigenmodes symmetrically mismatched to the outgoing waves in the surrounding medium. Such a BIC is shown in Fig. 2 (a). Notice that the grating in Fig. 2 (a) is asymmetric with respect to its central plane. The second type are propagating or Bloch BICs which are localized waves travelling along the axis of periodicity. A BIC of this type is shown in Fig. 2 (b).

In this presentation we address Bloch BICs propagating in the direction perpendicular to the ridges. We demonstrate that if a two-side grating shown in Fig. 1 possesses either mirror or glide symmetry, the Bloch bound states are stable to variation of parameters as far as the symmetries are preserved. This feature of Bloch BICs in dielectric gratings is explained via topological properties of the BICs. One the other hand it can be shown that Bloch BICs in asymmetric gratings are purely accidental in nature and, thus, are easily destroyed by variation of the system's parameters.

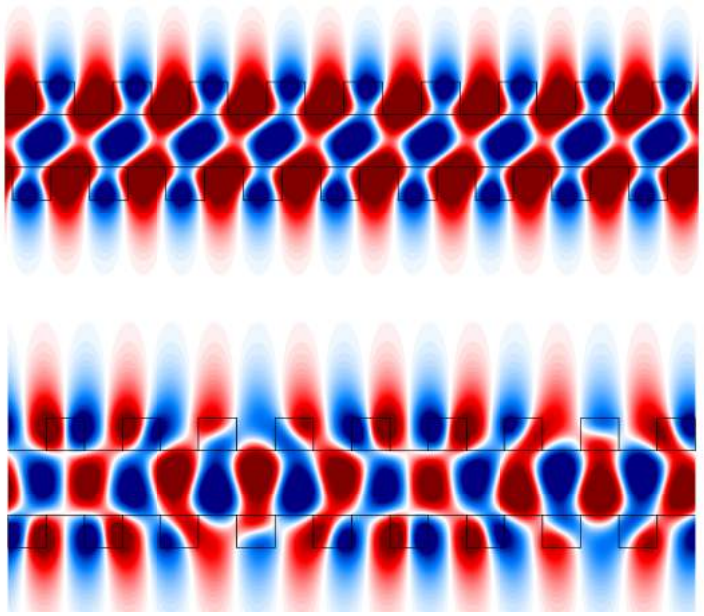


Figure 2: TM BICs mode profiles in form of the real part of the electric field component aligned with the ridges in the dielectric grating shown in Fig. 1: (a) Standing wave BIC, $\epsilon_1 = 1.5$, $\epsilon_2 = 3$, $L = 0.7982a$, $w = a$, $h_1 = h_2 = 0.5a$, $\delta = 0.15a$; (b) Propagating wave BIC $\epsilon_1 = 1.5$, $\epsilon_2 = 3$, $L = a$, $w = a$, $h_1 = h_2 = 0.5a$,$\delta = 0.5a$

At the same time the leaky-zone dispersion picture is descrybed through three-wave interference mechanism. In particular, a perturabtive approach is used to explain the formation of the BICs via the Friedrich-Wintgen [4] mechanism in the spectral vicinity of avoided crossings. The concurrent phenomenon of collapsing Fano resonances is explained.

In summary, we report BICs robust against possible fabrication inaccuracies at the same time allowing for a certain freedom in choosing the geometric parameters of the gratings. We speculate that our finding might be useful in design of multifunction optical elements which steer the flow of light harvested from the ambient medium.

Funding: Ministry of Education and Science of Russian Federation (state contract N3.1845.2017/4.6)

References

[1] Chia Wei Hsu, Bo Zhen, A. Douglas Stone, John D. Joannopoulos, and Marin Soljačić. Bound states in the continuum. *Nature Reviews Materials*, 1(9):16048, Jul 2016.

[2] Maxim Pisarenco, Joseph Maubach, Irwan Setija, and Robert Mattheij. Aperiodic fourier modal method in contrast-field formulation for simulation of scattering from finite structures. *Journal of the Optical Society of America A*, 27(11):2423, oct 2010.

[3] Maxim Pisarenco, Joseph Maubach, Irwan Setija, and Robert Mattheij. Modified s-matrix algorithm for the aperiodic fourier modal method in contrast-field formulation. *Journal of the Optical Society of America A*, 28(7):1364, jun 2011.

[4] H. Friedrich and D. Wintgen. Interfering resonances and bound states in the continuum. *Physical Review A*, 32(6):3231–3242, dec 1985.

Localized field control by plasmonic mode interference

Keiji Sasaki and Hideki Fujiwara

Research Institute for Electronic Science, Hokkaido University, N20W10, Kitaku, Sapporo, Hokkaido 001-0020, Japan
*corresponding author, E-mail: sasaki@es.hokudai.ac.jp

Abstract

We investigate the wavelength dependence of localized plasmonic field distributions in a gold nanodimer structure under total internal reflection illumination condition. Although the gold dimer structure is well known to induce strong localized field at a nanogap, we find that the higher-order plasmonic modes are excited by the oblique light incidence and their interference effect enables the localized spot control at the nano-scale.

1. Introduction

In recent years, localized surface plasmons induced in noble-metal nanostructures have been attracted much attention, which enables enhanced fluorescence, enhanced Raman scattering [1], and efficient nanoparticle trapping [2], because it can concentrate light field to a nano-scale region and greatly enhance the localized field. Their optical properties of plasmons such as resonant frequencies and field distributions can be determined by the size and shape of the metal nanostructures [3], which knowledge are essential for the design of plasmonic nanodevices, especially for the nanoparticle/molecule manipulation at the nano-scale. In this presentation, we will introduce our recent study concerning the spatially mapping of localized field enhancements in the metal nanostructures by using the scattering-type near-field optical microscope [4-6]. By using this method, we also find the modification of localized fields due to the multi-mode interference induced in the nanostructure by the total internal reflection (TIR) illumination.

2. Sample and optical setup

Figure 1 shows a schematic of our scattering-type near-field microscope system using a TIR white light illumination for measuring the local field distribution in a metal nanostructure. A collimated white light was used as an excitation light. By optimally setting a knife-edge and a polarizer, we select a well-defined direction and polarization of the white light, and focused the white light onto a sample under total internal reflection condition via an oil immersion objective lens (100×, N.A.=1.35). The scattering spectra were measured by collecting the scattered light from a gold nano-dimer structure via the same objective, which was introduced into a spectrometer. From the scattering spectra, we determined the detection wavelengths of localized filed distributions. By scanning a silicon probe tip of an atomic force microscope on the sample surface, the confined plasmonic fields are scattered by the sharp tip and detected by a photo-multiplier tube equipped with spectrometer. The detected signal was demodulated at the driving resonant frequency of the AFM tip (~300 kHz) by a lock-in amplifier, which could suppress the signals of scattered light except from the tip apex. Thus, the localized field and the topography images are obtained simultaneously.

Figure 2(a) shows a scanning electron microscopy (SEM) image of a gold nanodimer structure. This structure consisted of a pair of 100 × 100 × 30 nm^3 blocks separated by a nanogap of about 10 nm, which are fabricated on a glass substrate by electron-beam lithography and lift-off technique [7]. Figure 2(b) shows the scattering spectra when the white light is incident along the dimer axis with S- or P-polarizations, in which the peak wavelengths are around 660 and 740 nm, respectively for S- and P-polarized light.

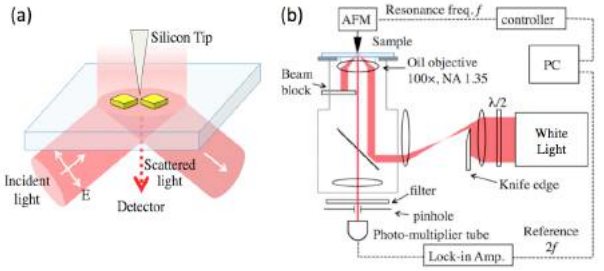


Figure 1: (a) Schematic of near-field imaging of a nanodimer structure with a scattering-type NSOM and (b) experimental setup.

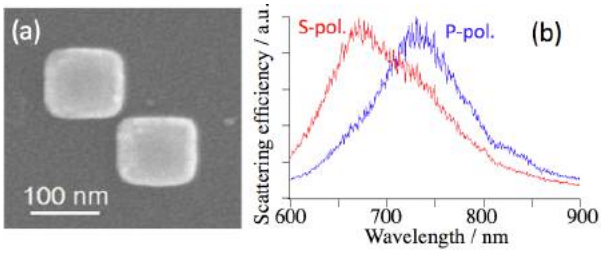


Figure 2: (a) SEM image of a gold nanodimer structure and (b) its scattering spectra for S- and P-polarized illumination.

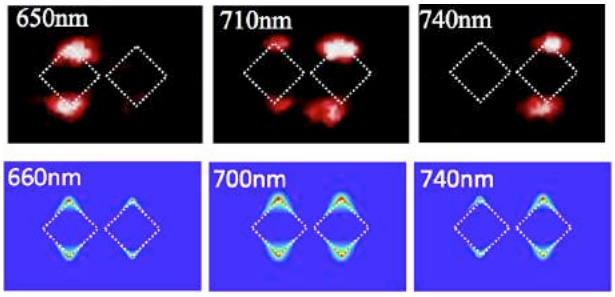


Figure 3: Detection wavelength dependence of scattered near-field images of a gold dimer structure. Experimental results (upper row) and numerical simulations (lower row). The white light is incident along the dimer axis (from left to right under the total internal reflection condition) with the polarization direction perpendicular to the dimer axis (S-polarized light). The numbers in figures indicate the detection wavelengths.

3. Results and discussions

Figure 3 shows the scattered near-filed images of a gold nanodimer structure. Upper and lower rows show the experimental and numerical results. The white light under the total internal reflection condition is incident along the dimer axis (from left to right) with S-polarization. Images from left to right indicate the scattered near-field images with the different detection wavelengths (750, 710, and 740 nm, respectively). Conventionally, the gold nanodimer structure has been known to support strong localized fields at the edges of each block, when the incident light polarization is perpendicular to the dimer axis (like the numerical image at 700 nm). However, we observe the changes in the localized fields depending on the detection wavelength. Especially, when the detection wavelength is shifted to shorter wavelength region, the spots appeared at the corners of the light incident side becomes stronger, while the intense spots at the far-side corners stronger when the detection wavelength set at longer wavelength region.

To confirm the detection wavelength dependence, we performed numerical simulations of localized field distributions, in which the plane wave is incident into the structure under the total internal reflection condition (incident angle 55 degree, from left to right in the figure). Lower row in Fig. 3 shows the numerical results and well corresponds to the experimental results. These results could be explained by higher-order modes induced by the oblique light incidence at the shorter wavelength side, which could not be excited by the normal incidence of light. The interference effect between excited plasmonic modes (dipole and quadrupole modes) would modify the localized field distribution depending on the superposition of these plasmonic modes with different phases and amplitudes. From the results, we confirmed that at the wavelength of 700 nm, the phase difference between dipole and quadrupole modes is $\pi/2$ so that the four corners became stronger similar to the case with the normal incidence of the light, and this phase condition is disturbed against the detection wavelength change. Thus, we conclude that the change in the localized field distribution can be observed under the TIR condition.

4. Conclusions

Using our spectroscopic nanoimaging system, we demonstrate the change in the localized field distribution under the total internal reflection excitation in a simple gold nanodimer structure. From the results, when the white light is incident along the dimer axis with S-polarization, we observed that the intense localized fields at the four corners are observed and their distributions change depending on the detection wavelengths. In addition, when the polarization is changed to the P-polarization, not only the gap mode but also the intense spot at the far-side corner is observed at the shorter wavelength region (not shown). These changes in the localized field distributions at the nano-scale could be explained by the induction of higher-order plasmonic modes by the total internal reflection illumination, which would be interfered with the fundamental plasmonic mode and strongly affected on the field distributions. We believe that our findings will provide important knowledge for the design of plasmonic device applications.

Acknowledgements

This work was supported by JSPS KAKENHI (16H0650607, 16K13647, 26246028), SEM images of samples were measured using a field emission scanning electron microscope system (JEOL, JSM-6700FT) and the fabrication of gold nanodimers were carried out with an electron-beam lithography system (Elionix, ELS-7000HM) at the Open Facility, Hokkaido University Sousei Hall.

References

[1] Y. Tanaka *et al.*, Surface Enhanced Raman Scattering from Pseudoisocyanine on Ag Nanoaggregates Produced by Optical Trapping with a Linearly Polarized Laser Beam, *J. Phys. Chem. C* 113: 11856-11860, 2009.

[2] Y. Tanaka and K. Sasaki, Optical trapping through the localized surface-plasmon resonance of engineered gold nanoblock pairs, *Opt. Express* 19: 17462-17468, 2011.

[3] E. Hao and G. C. Schatz, Electromagnetic fields around silver nanoparticles and dimers, *J. Chem. Phys.* 120: 357-366, 2004.

[4] Y. Tanaka, H. Fujiwara, K. Sasaki *et al.*, Direct imaging of nanogap-mode plasmon-resonant fields, *Opt. Express* 19: 7726-7733, 2011.

[5] H. Fujiwara, K. Sasaki *et al.*, Direct Observation of Localized Fields in Nanogaps between Metal Particles Using a Scattering-Type Near-Field Microscope, *Appl. Phys. Express* 2: 102002, 2009.

[6] Y. Tanaka, H. Fujiwara, K. Sasaki *et al.*, Nanoscale Color Sorting of Surface Plasmons in a Double-Nanogap Structure with Multipolar Plasmon Excitation, *Nano Lett.* 15: 7086-7090, 2015.

[7] K. Ueno, K. Sasaki *et al.* Nanoparticle Plasmon-Assisted Two-Photon Polymerization Induced by Incoherent Excitation Source, *J. Am. Chem. Soc.* 130: 6928-6929, 2008.

Fano resonances in photonics

Mikhail Limonov

ITMO University, St. Petersburg 197101, Russia
Ioffe Institute, St. Petersburg 194021, Russia
M.Limonov@mail.ioffe.ru

Abstract

Fano resonance has a long and interesting history in photonics. However, it continues to surprise with new insights and applications [1]. Here we review the fundamental aspects of Fano resonance and a broad range of resonant electromagnetic effects using a clear two coupled oscillators model and demonstrate a phase diagram of different photonic regimes [2]. That includes Fano resonance as such together with electromagnetically induced transparency, Kerker and Borrmann effects, as well as parity-time symmetry breaking and Rabi splitting.

1. Introduction

In general case, for the interaction of a discrete quantum state with a background of continuum of states when both states are excited by some external source, the absorption spectrum has the Fano profile

$$\sigma(\Omega) = |D|^2 \frac{(q+\Omega)^2}{1+\Omega^2}, \qquad (1)$$

where $q = \cot\delta$ is the Fano parameter, δ is the phase shift of the background continuum, $\Omega = 2(E-E_0)/\Gamma$, where Γ and E_0 are the resonance width and energy respectively, and $|D|^2 = 4\sin^2\delta$ is the amplitude of the spectrum for the continuum states.

2. Model of two coupled oscillators

We illustrate the physics of Fano resonance and a broad range of resonant electromagnetic effects using the simple model [2]. We consider two coupled driven oscillators, described by the following matrix equation:

$$\begin{pmatrix} \omega_1 - \omega - i\gamma_1 & g \\ g & \omega_2 - \omega - i\gamma_2 \end{pmatrix} \begin{pmatrix} x_1 \\ x_2 \end{pmatrix} = i \begin{pmatrix} f_1 \\ f_2 \end{pmatrix}. \qquad (2)$$

Here, x_1 and x_2 are the oscillator amplitudes, ω_1 and ω_2 are the resonant frequencies, γ_1 and γ_2 are the damping terms and f_1, f_2 are the external forces with the frequency ω. The coupling constant g describes the interaction between the oscillators. The considered effects are distinguished by the relative values of g and γ constants, the external forces. We notice that the versatility of the Fano resonances extends far beyond the two-oscillator model (2). For instance, scattering from complex structures such as dielectric oligomers characterized by Fano effect can be analyzed conveniently

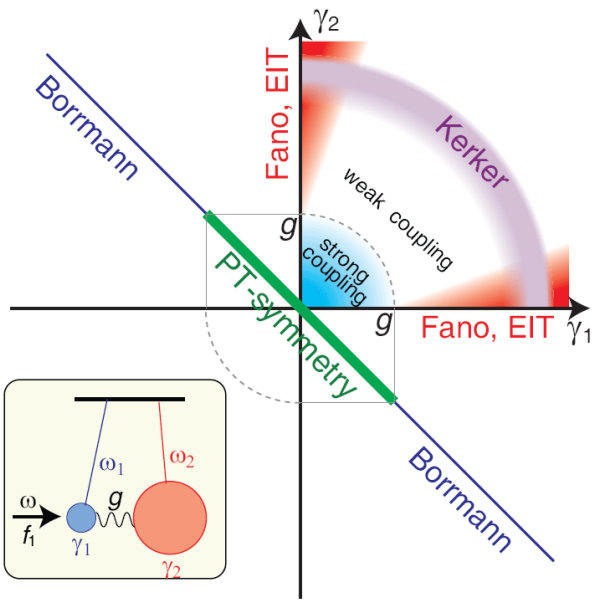


Figure 1: Phase diagram of different photonic regimes in the damping constants (γ_1, γ_2) plane. Insert: schematic view of two coupled damped oscillators with a driving force f_1 applied to one of them.

in terms of the interference between the collective eigenmodes of particles, rather than resonances of individual particles. However, the model of two-oscillators provides a deep insight into the physics of the mode interacting.

We will analyse different resonant electromagnetic effects in a unified manner by comparing the values of the damping constants γ_1 and γ_2 as shown by the phase diagram in Fig. 1. The damping constants are normalized with respect to the absolute value of the coupling between the oscillators g. Both the Fano regime and the optical EIT regime require the dampings strongly different by the absolute values and at least one of them larger than g (weak coupling). This corresponds to the two regions in the first quadrant of the phase diagram, constrained near the abscissa and ordinate axes. The Kerker regime requires both dampings larger than the coupling constant but does not impose special restrictions upon their ratio, it occupies the whole area $\gamma_1 >> g$ and $\gamma_2 >> g$. Contrary to the Fano and EIT case, this region is

not restricted to the sectors near the axes $\gamma_1=0$ and $\gamma_2=0$. The parity-time symmetry regime and the Borrmann regime lie in the quadrants where γ_1 and γ_2 have different signs. Moreover, these effects satisfy the same additional symmetry condition $\gamma_1=-\gamma_2$. This is because the spatial evolution of the waves inside the photonic crystal at the given frequency ω, evanescent in the opposite directions, mimics the time evolution of the solutions in the parity-time symmetric system. The Borrmann effect can be realized for arbitrary ratio between the (complex) coupling parameter g and the decay rates. As such it occupies the whole line $\gamma_1=-\gamma_2$ on the phase diagram. On the other hand, the PT symmetry breaking takes place only when the coupling is stronger than the dampings, i.e. it is constrained to the line $|\gamma_1|<g$. In the case when $|\gamma_1|>g$, the PT symmetry is restored.

3. Purcell effect, Lamb shift, and Fano resonance as closely linked interference phenomena

Recently it was shown that in the weak coupling regime when a narrow-band mode (a system characterized by a discrete state) is superimposed with a broadband background radiation (a continuum spectrum of states), we can expect the existence of three distinct interference effects: a change of the narrow mode lifetime caused by the Purcell effect, a change of the resonance frequency associated with the Lamb shift, and an asymmetric line-shape explained by the physics of the Fano resonances [3]. All of these effect are different sides of a whole interference phenomenon. Therefore the Fano asymmetry parameter q indicates the changes in the mode lifetime. At the same time all of these effects are governed by the equation (2) that describes both weak and strong coupling regimes. Since the study of Fano-type features in different regimes including strong coupling may pave the way for a deeper understanding of other interference phenomena.

4. Conclusions

The Fano formula, first discovered in the studies of the Rydberg series for auto-ionization, has been applied to various spectroscopic problems and for different objects, practically without limitations. Owing to the deep insight it provides for spectroscopic data and its appearance in a broad range of nanophotonics studies, the Fano formula will continue to be a vital tool for optical design and analysis.
The number of citation of the seminal Ugo Fano's paper [4] has grown exponentially in recent years and we are confident that over the coming years it will remain one of the most-cited paper in physics being an influential source of concepts for technologists, experimentalists and theoreticians.

Acknowledgements

It is my pleasure to thank M.V. Rybin, A.N. Poddubny, and Y.S. Kivshar for fruitful cooperation. This work was supported by the Presidium of RAS (Program I.7 "Modern problems of photonics, the probing of inhomogeneous media and materials").

References

[1] Editorial, Fano still resonating, *Nat. Photon.* 11: 529, 2017.

[2] M.F. Limonov, M.V. Rybin, A.N. Poddubny, Y.S. Kivshar, Fano resonances in photonics, *Nat. Photon*. 11: 543–554, 2017.

[3] M.V. Rybin, S.F. Mingaleev, M.F. Limonov, Y.S. Kivshar, Purcell effect and Lamb shift as interference phenomena, *Sci. Rep*. 6: 20599, 2016.

[4] U. Fano, Effects of configuration interaction on intensities and phase shifts, *Phys. Rev*. 124: 1866–1878, 1961.

Fano resonances and supercavity modes

Mikhail Rybin[1,2]*, Kirill Koshelev[1], Zarina Sadrieva[1], Kirill Samusev[1,2], Andrey Bogdanov[1,2], Yuri Kivshar[1,3], and Mikhail Limonov[1,2]

[1]ITMO University, St. Petersburg 197101, Russia
[2]Ioffe Institute, St. Petersburg 194021, Russia
[3]Nonlinear Physics Center, Australian National University, Canberra ACT 2601, Australia
M.Rybin@mail.ioffe.ru

Abstract

We reveal strong mode coupling and Fano resonances in the simplest object – a single homogeneous cylindrical subwavelength dielectric resonator resulting in high-Q factors at the nanoscale. We found that the features of Fano parameter repeat with pinpoint accuracy the behavior of the quality factor Q. Thus, the Fano resonance can be considered as a precursor of bound states in the continuum and high-index dielectric resonators represent the simplest example of nanophotonic supercavities.

1. Introduction

Recently, the physics of bound states in the continuum (BIC) with potentially infinite Q factor attracted a lot of attentions [1]. Although for any structure to support BICs, it should extend to infinity in at least at one of spatial dimensions, finite-size samples can support their analogue in the form of supercavity modes [2]. For a supercavity, the Q factor growing rapidly before reaching a maximum value limited by the finite-size effects. In accord with the Fridrich-Wintgen theory of BIC, the radiating tails of leaky modes can cancel out each other via destructive interference resulting in a rapid growth of Q factor [3]. In compact photonic structures, a trapped state can manifest itself in the scattering spectrum as a sharp Fano resonance [4,5].

2. Strong-coupling regime in the subwavelength dielectric resonators

We study strong coupling between eigenmodes of a simplest object – a single subwavelength high-index dielectric resonator and analyze the mode transformation and Fano resonances by varying resonator's aspect ratio r/l. The low-frequency spectrum of the dielectric cylinder under consideration consists of two types of modes. The first type of modes demonstrates a small frequency shift with changing r/l. They are formed mainly due to reflection from a side wall of the cylinder and could be associated with the Mie resonances of an infinite cylinder. The second type of modes demonstrates a strong shift to higher frequencies with increasing aspect ratio r/l. They are formed mainly due to reflection from the faces of the cylinder and could be associated with the Fabry-Perot modes. Due to different r/l - dependencies of the Mie-like and Fabry-Perot-like modes, the bands can intersect at certain spectral points. Note that only the modes with the same azimuthal index could interact, and they undergo coupling each other with the avoid crossing scenario at special values of the aspect ratio r/l with nearly complete disappearance of one spectral line. The avoided crossing point is the characteristic feature of the strong coupling regime.

3. Supercavity modes and the Fano formula

For the finite cylindrical resonator, we found and analyzed the strong coupling regime between the Mie-like and Fabry-Perot-like modes that manifested itself in the scattering spectra as avoided crossing point [6]. Figure 1 shows the spectra corresponding to the avoided crossing that occurs for TE_{020} (Mie-like) and TM_{012} (Fabry-Perot-like) modes of the dielectric nanoresonator. The resonant Mie scattering from the infinite cylinder can be represented through cascades of Fano resonances and each individual resonance is described by the conventional Fano formula [7]. In the scattering spectra of the finite cylinder [see Fig. 1(a)], both Mie-like and Fabry-Perot-like modes are manifested by an asymmetrical Fano-line shape. We analyze scattering spectra by fitting both resonances with the Fano formula. We study the spectra in detail through the line characteristics such as the frequencies of modes $\omega_{1,2}$, their damping rates $\gamma_{1,2}$ (proportional to the inverse value of the Q factor) and the Fano asymmetry parameters $q_{1,2}$ calculated with the help of the classical Fano formula [8].

We find that the features of Fano parameter q_2 repeat the behavior of the damping coefficients or quality factor Q_2 (Fig. 1) [6]. One can see that in the vicinity of the avoided crossing point, the Q factor of one the coupled mode becomes very high that corresponds to the appearance of a quasi-BIC.

It is important that for a true BIC, the Fano resonance should completely collapse. In out case, due to a finite size of cylinder the width of the Fano resonance remains finite.

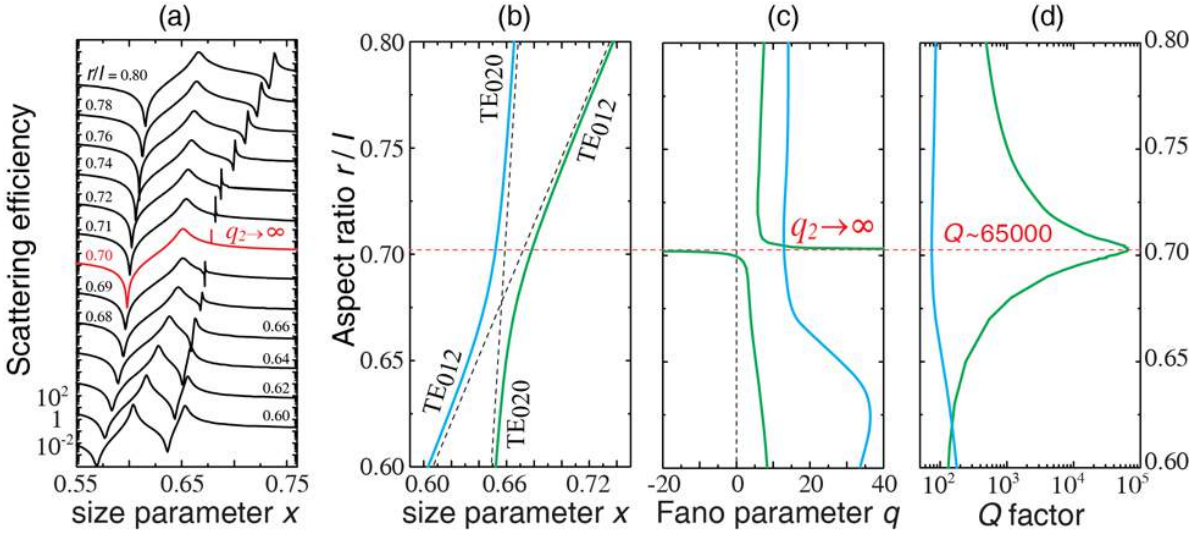


Figure 1: Characterization of the supercavity modes supported by a dielectric resonator. (a) Scattering spectra of a nanorod with ε=80 under the condition of the supercavity mode (m=0). The supercavity mode occurs at r/l = 0.701 (shown in red). Spectra are relatively shifted by 100 dB. (b) Frequencies of the Mie-type TE_{020} and Fabry-Pérot-type TE_{012} modes in the avoided crossing regime for the modes with the azimuthal number m = 0. (c) Fano parameter for both modes. (d) Calculated Q factor for a supercavity with the maximum close to $Q = 65 \times 10^3$. Data in (b)–(d) are obtained by fitting to the Fano formula. Cyan and green mark low- and high-frequency modes, respectively.

It means that the mode is not completely decouple from the continuum and the Fano resonance does not collapse (Fig. 1a). This could be explained by incomplete destructive interference of the coupled modes in far-field and by leakage through the channels corresponding to other cavity modes.

4. Conclusions

We have demonstrated that subwavelength high-index dielectric resonators can support the supercavity modes with high Q factors. We shown that the avoided crossing point is accompanied by the formation of a quasi-BIC when the radiative losses are suppressed due to the Friedrich-Wintgen destructive interference. At the quasi-BIC point, the Fano asymmetry parameter demonstrates an abrupt change from minus to plus infinity with a symmetric Lorentzian shape of the scattering spectra at $q \to \pm\infty$.

Acknowledgements

This work was supported by the Russian Science Foundation (17-12-01581) and by the Presidium of RAS (Program 32).

References

[1] C.W. Hsu, B. Zhen, A.D. Stone J.D. Joannopoulos, M. Soljačić, Bound states in the continuum, *Nat. Rev. Mater.* 1: 16048, 2016.

[2] M.V. Rybin, Y.S. Kivshar, Supercavity lasing, *Nature* 541: 164-165, 2017.

[3] H. Friedrich, D. Wintgen, Interfering resonances and bound states in the continuum, *Phys. Rev. A* 32: 3231-3242, 1985.

[4] C.W. Hsu, B. Zhen, J. Lee, S.-L. Chua, S.G. Johnson, J.D. Joannopoulos, M. Soljačić, Observation of trapped light within the radiation continuum, *Nature* 499: 188-191, 2013.

[5] F. Monticone, A. Alu, Embedded photonic eigenvalues in 3D nanostructures, *Phys. Rev. Lett.* 112: 213903, 2014.

[6] M.V. Rybin, K.L. Koshelev, Z.F. Sadrieva, K.B. Samusev, A.A. Bogdanov, M.F. Limonov, Y.S. Kivshar, High-Q supercavity modes in subwavelength dielectric resonators, *Phys. Rev. Lett.* 119: 243901, 2017.

[7] M.V. Rybin, K.B. Samusev, I.S. Sinev, G. Semouchkin, E. Semouchkina, Yu.S. Kivshar, M.F. Limonov, Mie scattering as a cascade of Fano resonances, *Optics Express* 21: 30107–30113, 2013.

[8] M.F. Limonov, M.V. Rybin, A.N. Poddubny, Y.S. Kivshar, Fano resonances in photonics, *Nat. Photon*. 11: 543–554, 2017.

Hematite in the hot spot: trapping surface plasmons in ultrathin semiconductor films for water splitting

Alberto Naldoni[1,2,*], Aveek Dutta[1], Stepan Kment[2], RadekŕZbořil[2], Alexandra Boltasseva[1,], Vladimir M. Shalaev[1]

[1] School of Electrical & Computer Engineering and Birck Nanotechnology Center, Purdue University, West Lafayette, IN-47907, USA

[2] Regional Centre of Advanced Technologies and Materials, Faculty of Science, Palacky University, Šlechtitelů 27, 78371 Olomouc, Czech Republic

*corresponding author: alberto.naldoni@upol.cz

Abstract

The use of plasmonic nanoantennas in solar energy conversion has recently focused much attention on processes that generate hot carriers through the metal-semiconductor interface. Here, we will present our recent results on ultrathin hematite films for water splitting used as dielectric layer in gap plasmon structures. Several designs including metallic and high index nanoresonators will be analyzed and results will be discussed in terms of physics of electric field enhancement, hot electron generation, and chemical reactivity of plasmonic metamaterials.

1. Introduction

Semiconductor-based solar photoelectrochemical (PEC) water splitting for sustainable hydrogen production has attracted considerable interest in the past decades. Since the first report demonstrating photo-induced water splitting in a TiO_2 photoanode, many materials have been studied. Among them, hematite (alpha-Fe_2O_3) is one of the most promising ones due to a 2.1 eV band-gap, low cost and high stability in PEC conditions [1,2].

Hematite efficiency has been so far limited by two major material limitations such as short hole diffusion length (4 nm) and large light penetration depth (100 nm with wavelength of 500 nm) [1].

Focusing light from the far-field to the near-field and producing highly intense electromagnetic fields region (hot spots), plasmonic nanostructures offer a powerful solution to hematite problems on absorption efficiency and charge carrier transport [3].

Several designs that use mirror – semiconductor –antenna geometry have been proposed showing increase in photocurrent generation due to light trapping and hot electron injection in TiO_2 by using film having thickness higher than 30-50 nm [4,5].

Here we present our recent results on ultrathin hematite films (12 nm) placed as dielectric in gap plasmon structures and their corresponding photocurrent density for water splitting. We present a rational design to control wavelength position of surface plasmon resonances as well as how to tune role of light trapping, E-field enhancement and hot electron injection in the increase of hematite PEC activity.

2. Experimental

Fabrication. Our films were grown on a silicon substrate. Underlayers of Alumina (Al_2O_3) and Au/Pt were deposited as the back metal mirror using e-beam lithography. Hematite layers were deposited by pulsed-laser deposition (PLD) at 550°C and 30mTorr O_2 pressure using a hematite target of 99.5% purity. Nanodisk arrays of Au/Pt/Ge were fabricated by e-beam lithography using lift-off technique.

Characterization. Optical properties of all films were retrieved from ellipsometry measurements. Photoelectrochemical water splitting experiments were carried out in a three-electrode cell and in a HEKA scanning electrochemical microscope.

3. Discussion

Figure 1a show the schematic of our multilayer stacked films. We have a 200 nm metallic under-layer (Au or Pt) as the mirror or metallic support. On top of that we grew a 12 nm hematite film with PLD. After deposition, films were characterized by x-ray diffraction and reflection to determine phase composition and to confirm the thickness of the different layers. Hematite films prepared through PLD exhibits a strong orientation along the 104 crystallographic direction. Finally, nanodisks of 50 nm height (Au/Pt/Ge) of varying diameter and period were fabricated on top of hematite.

Optical response and E-field distribution were simulated with COMSOL software and a typical field plot of the E-field of light for Pt(bottom)/hematite/Ge nanodisks structure at resonance is reported in Figure 1b. It is to be noted that when the top nanodisks is made of Au/Pt we have gap plasmon resonances in the structure [6] whereas for Ge nanodisks on top we have a hybrid plasmon resonance as shown in Fig. 1b. Nevertheless, irrespective of the nature of the resonance, we achieve a strong confinement of the E-

field, i.e. hot spot, inside the hematite layer. In Fig. 1c, we

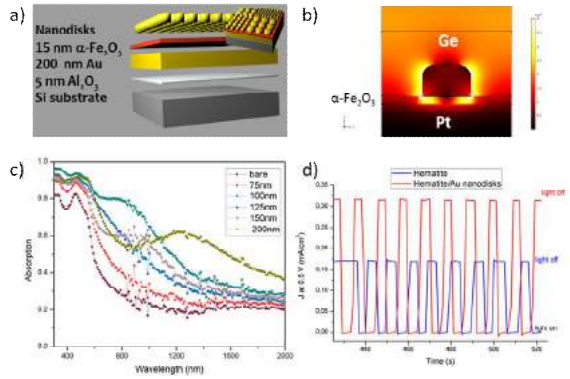


Figure 1: (a) Schematics of hematite-based gap plasmon geometry. (b) E-field distribution for a Ge nanodisk array (75 nm diameter, 200 nm period) on hematite (alpha-Fe_2O_3)/Pt resonating at 600 nm wavelength. (c) Absorption spectra of Pt(bottom)/hematite/Pt nanostructures, and (d) photoelectrochemical water splitting photocurrent in 1 M NaOH and under 1 sun illumination for bare hematite and Au(bottom)/hematite/Au nanodisk array.

Pt(bottom)/hematite/Pt nanodisk arrays of varying diameter and periodicity. The peaks correspond to gap plasmon resonance. Similar spectra with peaks are observed when the Pt nanodisks are replaced by Au, albeit a shift in the peak positions.

We start discussing the properties of Au/hematite/Au films having 100(200)-125(200)-150(300)-200(300) nm diameter (period). Absorption spectra (not reported) show gap plasmon resonances that peak at 800, 1000, 1100 and 1500 nm with increasing nanodisks diameter.

Gold nanodisks samples were tested in PEC water splitting under 1 sun (100mW cm^{-2}) illumination. Bare hematite film produces a steady-state photocurrent of 0.15 mA cm^{-2} at 0.5V vs Ag/AgCl, while the Au gap plasmon structure produces two times that value (See Figure 1d). To investigate the reason behind this observation we discuss wavelength dependent photocurrent measurements (IPCE) and simulated E-field intensity. The IPCE response shows that the doubling of photocurrent in Au gap plasmon structure compared to bare hematite is mainly due to off-resonant scattering due to the nanodisks at wavelengths above the hematite bandgap.

Driven by these observations, we develop others gap plasmon nanostructures such as Pt/hematite/Pt and Pt/hematite/Ge nanodisks. The use of Platinum underneath layer ensures a higher thermal stability (no degradation of the metal under-layer during hematite deposition) than that of gold at the temperature (550°C) of hematite deposition. In addition, platinum exhibits highly negative real part of permittivity in the visible range enabling resonances more shifted to the hematite band-edge region (600 nm) than Au (see Figure 1c). The resonances of our gap plasmon structures can be further shifted to strongly overlap with show the measured absorption spectra for a hematite interband transitions when using Ge nanodisks on top of the stacked layers.

Photocurrent data for PEC water splitting will be discussed for both Pt and Ge stacks. We will discuss the results in terms of hot electron and E-field enhancement effects taking in consideration experimental photocurrents measured though a scanning electrochemical microscope over each nanoantennas array.

4. Conclusions

Trapping surface plasmons in ultrathin semiconductor films is a powerful approach to increase the photoelectrochemical water splitting current and study the physics of hot spots and hot electron generation at the metal-semiconductor interface. Our results show an approach to fabricate plasmonic hybrids that can channel light from the visible to the near field electromagnetic, while exploiting hot spots and hot electron generation to enhance chemical reactions.

Acknowledgements

A.N. acknowledges the support by the Operational Programme Research, Development and Education - European Regional Development Fund, project no. CZ.02.1.01/0.0/0.0/15_003/0000416 of the Ministry of Education, Youth and Sports of the Czech Republic.

References

[1] K. Sivula, F. Le Formal, M. Grätzel, Solar water splitting: progress using hematite (α-Fe_2O_3) photoelectrodes, *ChemSusChem* 4:432−449, 2011.

[2] S. D. Tilley, M. Cornuz, K. Sivula, M. Grätzel, Light-induced water splitting with hematite: improved nanostructure and iridium oxide catalysis, *Angew. Chem. Int. Ed.* 49:6405−6408, 2010.

[3] J. Li, S.K. Cushing, P. Zheng, F. Meng, D. Chu, N. Wu, Plasmon-induced photonic and energy-transfer enhancement of solar water splitting by a hematite nanorod array, *Nat. Commun.* 4:2651, 2013.

[4] Y. Fang, Y. Jiao, K. Xiong, R. Ogier, Z.-J. Yang, S. Gao, A. B. Dahlin, M. Käll, Plasmon Enhanced Internal Photoemission in Antenna-Spacer-Mirror Based Au/TiO2 Nanostructures, *Nano Lett.* 15:4059−4065, 2015.

[5] C. Ng, J. J. Cadusch, S. Dligatch, A. Roberts, T. J. Davis, P. Mulvaney, D. E. Gómez, Hot Carrier Extraction with Plasmonic Broadband Absorbers, *ACS Nano* 10:4704–4711, 2016.

[6] M. G. Nielsen, D. K. Gramotnev, A. Pors, O. Albrektsen, S. I. Bozhevolnyi, Continuous layer gap plasmon resonators, *Optics Express* 19:19310-19322, 2011.

Quantum state control in single quantum dots and the coupling with photonic crystal cavities

Chenjiang Qian, Kai Peng, Xiulai Xu*

Institute of Physics, Chinese Academy of Sciences, Beijing 100190, China

*corresponding author, E-mail: xlxu@iphy.ac.cn

Abstract

Due to the three-dimensional confinement, semiconductor quantum dots (QDs) have atom-like discrete energy levels, which makes QDs a good candidate of quantum information processing. In-plane magnetic field has always been used to construct the energy level structure as a platform to manipulate the single spins in QDs by mixing bright and dark exciton states. Additionally, an applied magnetic field on QDs lifts the degeneracy of electron and hole by Zeeman splitting, and shrinks the carrier wavefunctions by diamagnetic effect. By embedding QDs in a diode structure, photocurrent (PC) spectroscopy, as an effective way to detect the energy level and carriers information in a single QD, has been used to observe Rabi oscillations of a two-level system in single QDs, which can be utilized to build QD-based spin qubit. We report on high-resolution photocurrent (PC) spectroscopies of a single self-assembled InAs/GaAs quantum dot (QD) embedded in an n-i-Schottky device with an applied magnetic field. When the magnetic field is applied in Voigt geometry, the mixture of bright and dark states results in an observation of dark exciton states, which are confirmed by the polarization-resolved PL and PC spectra, as shown in Figure 1.

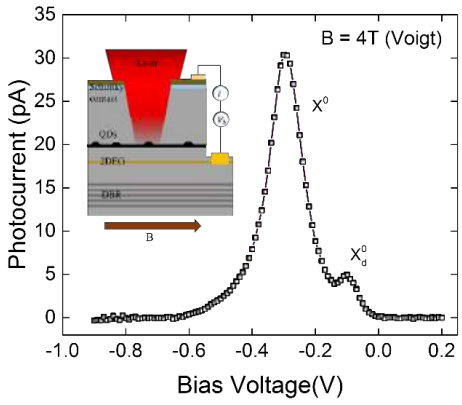


Figure 1 Single quantum dot photocurrent with magnetic field at 4T with Voigt geometry.

In addition, To scale up the quantum dot-based quantum photonic network, photonic crystal cavities with high quality factors around 10000 are fabricated with single quantum dots located in antinode position of the cavity. Selective spin enhancement from single quantum dots in the cavity are observed for each branch in Zeeman splitting because of the Purcell effect, particularly can be precisely controlled with a vector magnetic field. Strong coupling for cavity QED between different excitonic states in a single quantum dot and the cavity will be presented, two-photon Rabi splitting in a strongly coupled cavity-dot system is demonstrated. The quantum dot was grown intentionally large in size for large oscillation strength and small biexciton binding energy. Both exciton and biexciton transitions couple to a high quality factor photonic crystal cavity with large coupling strengths over 130 μeV. When the cavity to simultaneously couple with two exciton states, two-photon Rabi splitting between biexciton and cavity is achieved, which can be well reproduced by theoretical calculations with quantum master equations.

Finally, many-body exciton states in a coupled system with a single self-assembled quantum dot and a wetting layer will be discussed by strong anomalous diamagnetic shifts. A tremendous positive diamagnetic coefficient is observed when an electron in the wetting layer combines with a hole in quantum dot, which is nearly one order of magnitude larger than that of the excitonic states confined in quantum dots. When the electrons recombine with holes within quantum dot in the coupled system, a peculiar negative diamagnetic effect is observed, which can be potentially applicable for enhance the energy tunability of quantum dots for strong coupling.

Acknowledgements

This work was supported by the National Basic Research Program of China under Grant No.2014CB921003; the National Natural Science Foundation of China under Grant No. 11721404, 51761145104 and 61675228; the Strategic Priority Research Program of the Chinese Academy of Sciences under Grant No. XDB07030200 and XDPB0803, and CAS Interdisciplinary Innovation Team.

References

[1] Kai Peng, Shiyao Wu, Jing Tang, Feilong Song, Chenjiang Qian, Sibai Sun, Shan Xiao, Meng Wang, Hassan Ali, David A. Williams, and Xiulai Xu*. Probing the Dark-Exciton States of a Single Quantum Dot Using Photocurrent Spectroscopy in a Magnetic Field. Phys. Rev. Applied 8, 064018, 2017

[2] Chenjiang Qian, Shiyao Wu, Feilong Song, Kai Peng, Xin Xie, Jingnan Yang, Shan Xiao, Matthew J. Steer, Iain G. Thayne, Chengchun Tang, Zhanchun Zuo, Kuijuan Jin, Changzhi Gu, and Xiulai Xu*, Two-Photon Rabi Splitting in a Coupled System of a Nanocavity and Exciton Complexes, submitted.

[3] Shuo Cao, Jing Tang, Yue Sun, Kai Peng, Yunan Gao, Yanhui Zhao, Chenjiang Qian, Sibai Sun, Hassan Ali, Yuting Shao, Shiyao Wu, Feilong Song, David A. Williams, Weidong Sheng, Kuijuan Jin, and Xiulai Xu*. Observation of coupling between zero- and two-dimensional semiconductor systems based on anomalous diamagnetic effects. Nano Research, 9, 306 (2016)

Bound States in the Continuum Surrounded by Ultra-strong Resonances

Lijun Yuan[1] **and Ya Yan Lu**[2,*]

[1]College of Mathematics and Statistics, Chongqing Technology and Business University, Chongqing, China
[2]Department of Mathematics, City University of Hong Kong, Hong Kong
*corresponding author, E-mail: mayylu@cityu.edu.hk

Abstract

On periodic structures sandwiched between two homogeneous media, a bound state in the continuum (BIC) is a guided mode above the light line, and it is always surrounded by a family of resonant modes with quality factors tending to infinity. The quality factors typically blow up quadratically. We present a condition on the BIC, such that the quality factors of the resonant modes have a fourth power blowup.

1. Introduction

Bound states in the continuum (BICs) are trapped or guided modes with their frequencies in the frequency intervals of radiating waves that carry power to or from infinity. For light waves, BICs have been analyzed and observed for many different structures, including waveguides with local distortions, waveguides with lateral leaky structures, and periodic structures sandwiched between or surrounded by homogeneous media. The BICs on periodic structures are particularly interesting, because they are surrounded by families of resonant modes (depending on the Bloch wavevector) with quality factors (Q-factors) tending to infinity, and they give rise to collapsing Fano resonances corresponding to discontinuities in the transmission and reflection spectra. The high-Q resonances and the related strongly enhanced local fields have applications in lasing, nonlinear optics, etc. Collapsing Fano resonances can be exploited in filtering, sensing, and switching applications.

Typically, the Q-factors of the resonant modes tend to infinity quadratically. In [1] and [2], it was realized that for some BICs, the Q-factors of the nearby resonant modes can blow up more rapidly following a fourth power relation. In this paper, we derive a general condition for those special BICs and present numerical examples involving a periodic array of cylinders.

2. Theory

We consider 2D structures which are invariant in z, periodic in y with period L, bounded in the x direction, and surrounded by air. The dielectric function ϵ satisfies $\epsilon(x, y + L) = \epsilon(x, y)$ for all (x, y), and $\epsilon(x, y) = 1$ for $|x| > D$. The structure may have guided and resonant modes which can be written as $\phi(x, y)e^{i\beta y}$, where ϕ is periodic in y with period L, and β is the Bloch wavenumber. A guided mode has a real β and a real angular frequency ω, and $\phi \to 0$ as $x \to \pm\infty$. A resonant mode has a real β and a complex ω, and ϕ satisfies outgoing radiation conditions as $x \to \pm\infty$.

Most guided modes exist below the light line, i.e., $k_0 < |\beta|$, where k_0 is the free space wavenumber. BICs on periodic structures are special guided modes above the light line, i.e., $k_0 > |\beta|$. For a given structure, BICs can only exist as isolated points in the $\beta\omega$ plane. If there is a BIC ϕ_* with frequency ω_* and Bloch wavenumber β_*, then there must be a family of resonant modes for all β near β_*. The complex frequency ω of this family of resonant modes depends on β. As $\beta \to \beta_*$, we have $\mathrm{Re}(\omega) \to \omega_*$, $\mathrm{Im}(\omega) \to 0$, and the Q-factor $Q = -0.5\mathrm{Re}(\omega)/\mathrm{Im}(\omega) \to \infty$. Typically, $Q \sim (\beta - \beta_*)^{-2}$ for β near β_*. However, as shown in [1] and [2], for some BICs, it is possible to have $Q \sim (\beta - \beta_*)^{-4}$.

Using a perturbation method, we show that if a BIC $\{\phi_*, \omega_*, \beta_*\}$ satisfies

$$\int \overline{\varphi}_l G d\mathbf{r} = \int \overline{\varphi}_r G d\mathbf{r} = 0, \tag{1}$$

then $Q \sim (\beta - \beta_*)^{-4}$. In the above, G is related to ϕ_*, β_*, ω_* and ϵ; φ_l and φ_r are diffraction solutions (for the same ω_* and β_*) for incident plane waves given in the left ($x < -D$) and right ($x > D$) media, respectively; and the integrals are evaluated on one peroid of the structure given by $|y| < L/2$ and $-\infty < x < \infty$. For the E polarization, $G = -i\partial_y\phi_* + (\beta_* - \gamma\epsilon)\phi_*$, where

$$\gamma = \frac{\beta_* \int |\phi_*|^2 d\mathbf{r} - i \int \overline{\phi}_* \partial_y \phi_* \, d\mathbf{r}}{\int \epsilon |\phi_*|^2 \, d\mathbf{r}}.$$

Condition (1) can be further simplified if the structure and the BIC have symmetries.

3. Numerical examples

We consider a single periodic array of dielectric circular cylinders surrounded by air. The cylinders are parallel to the z axis, and their centers are located on the y axis periodically with period L. The radius and the dielectric constant of the cylinders are a and ϵ_1, respectively. BICs on such a periodic array have been extensively studied [3, 4, 5, 6]. Assuming the origin is located at the center of one cylinder, the dielectric function $\epsilon(x, y)$ is even in x and even in

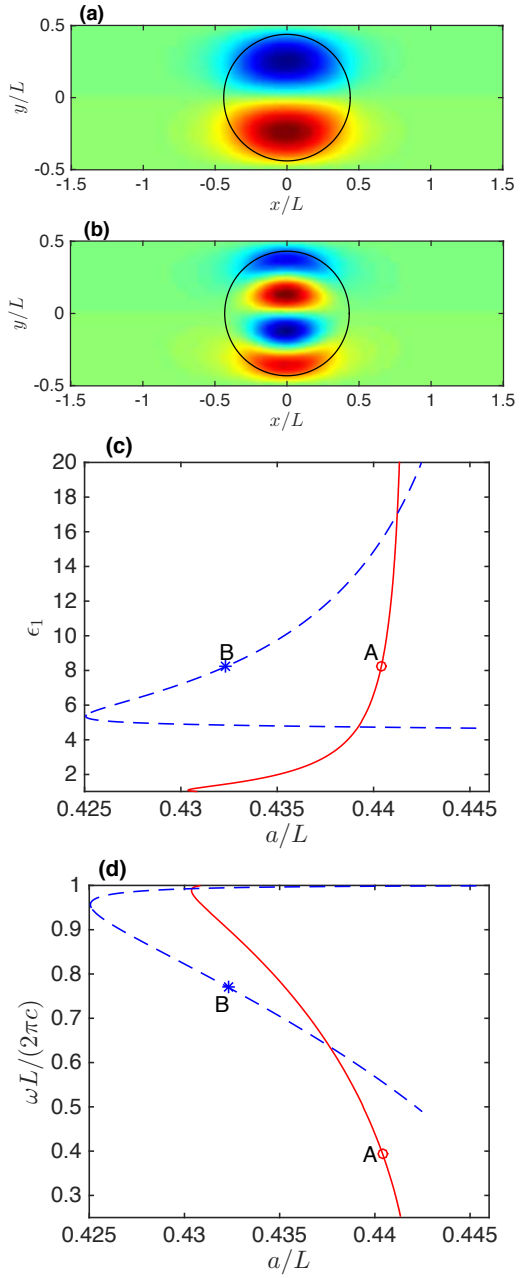


Figure 1: Special ASWs on a periodic array of circular cylinders with nearby resonant modes having $Q \sim 1/\beta^4$.

y. The BICs on the periodic array include antisymmetric standing waves (ASWs, $\beta_* = 0$, ϕ_* is odd in y), propagating BICs ($\beta_* \neq 0$), and symmetric standing waves ($\beta_* = 0$, ϕ_* is even in y).

In [1], it is shown that $Q \sim 1/\beta^4$ for the symmetric standing waves. In [2], numerical results are presented which indicate that $Q \sim 1/\beta^4$ is possible for ASWs. Based on the general condition (1), we perform an extensive search for the special ASWs with the property $Q \sim 1/\beta^4$. Our results are shown in Fig. 1. Panel (a) shows the wave field pattern of a special ASW with frequency $\omega_* L/(2\pi c) = 0.3950$ and it is obtained for $\epsilon_1 = 8.2$ and $a = 0.4404L$. Panel (b) shows another special ASW with frequency $\omega_* L/(2\pi c) = 0.7701$, and it is obtained for $\epsilon_1 = 8.2$ and $a = 0.4323L$. Panel (c) shows the continuous dependence of these two special ASWs on parameters ϵ_1 and a. The two points marked by A and B correspond to the ASWs shown in panels (a) and (b), respectively. Panel (d) shows the frequencies of these two special ASWs.

4. Conclusion

Using a perturbation method, we derived an analytic condition for special BICs on 2D periodic structures, such that the Q-factors of the nearby resonant modes satisfy $Q \sim (\beta - \beta_*)^{-4}$. Based on the obtained general condition, we found two such special BICs (which are ASWs) on a periodic array of dielectric circular cylinders, and studied their dependence on the radius a and dielectric constant ϵ_1 of the cylinders.

Acknowledgement

The work is partially supported by Basic and Advanced Research Project of CQ CSTC (cstc2016jcyjA0491); Scientific and Technological Research Program of Chongqing Municipal Education Commission (KJ1706155); Program for University Innovation Team of Chongqing (CXTDX201601026); and Research Grants Council of Hong Kong Special Administrative Region, China (Grant No. CityU 11304117).

References

[1] L. Yuan and Y. Y. Lu, Strong resonances on periodic arrays of cylinders and optical bistability with weak incident waves, *Phys. Rev. A* 95: 023834, 2017.

[2] E. N. Bulgakov and D. N. Maksimov, Light enhancement by quasi-bound states in the continuum in dielectric arrays, *Opt. Express* 25: 14134-14147, 2017.

[3] S. P. Shipman and S. Venakides, Resonance and bound states in photonic crystal slabs, *SIAM J. Appl. Math.* 64: 322-342, 2003.

[4] E. N. Bulgakov and A. F. Sadreev, Bloch bound states in the radiation continuum in a periodic array of dielectric rods, *Phys. Rev. A* 90: 053801, 2014.

[5] Z. Hu and Y. Y. Lu, Standing waves on two-dimensional periodic dielectric waveguides, *Journal of Optics* 17: 065601, 2015.

[6] L. Yuan and Y. Y. Lu, Propagating Bloch modes above the lightline on a periodic array of cylinders, *J. Phys. B: Atomic, Mol. and Opt. Phys.* 50: 05LT01, 2017.

Experimental observation of bound state in the continuum in 1D chain of dielectric disks at GHz frequencies

Mikhail Balyzin[1], Zarina Sadrieva[1], Mikhail Belyakov[1], Polina Kapitanova[1], Almas Sadreev[2], and Andrey Bogdanov[*1]

[1]Department of Nanophotonics and Metamaterials, ITMO University, Saint-Petersburg, Russia
[2]Kirensky Institute of Physics, Federal Research Center KSC SB RAS, Krasnoyarsk, Russia
*corresponding author, E-mail: a.bogdanov@metalab.ifmo.ru

Abstract

In this work we experimentally observe a symmetry protected optical bound state in the continuum (BIC) with zero angular momentum in 1D array of ceramic disks at GHz frequencies. We analyze the dependence of Q factor of BIC on the number of the disks and the level of the material losses. We confirmed theoretical prediction about quadratic growth of the Q factor with the number of the disks and its following saturation due to material losses.

1. Introduction

It is well known that the spectrum of a dielectric waveguide consists of the guided and leaky modes. Usually, the leaky modes are unwanted since they result in considerable losses and, therefore, hinder the operation of optical devices. However, the radiation losses can be totally canceled. In this case, we have a bound state embedded in the radiation continuum. The simplest way to cancel the radiation losses and get *bound state in the continuum* in a slab or cylindrical waveguide is to periodically modulate their permittivity along the direction of the translation symmetry. The periodicity discretises the number of open (diffraction) channels and makes them finite at each frequency. By choice of the proper design of the unit cell it is possible to make all amplitudes of (diffraction channels) outgoing waves equal to zero. This mechanism is analyzed in details in [4, 5, 6].

First, the concept of BIC was proposed in quantum mechanics in 1929 by E. Wigner and J. von Neuman [1]. In optics, it has been actively studied over the last 10 years. The significant results were achieved for this short period. It was shown that BICs are very prospective for many applications from lasing [2, 3], and filtering [4, 5] and biosensing [6, 7]. The latest achievements in physics of BIC are reviewed in [6].

To date, BICs in 1D periodic arrays were considered only theoretically in spite of these system are very prospective for generation of light with orbital angular momentum. In this work, we demonstrate first experimental observation and provide detailed analysis of BICs in 1D axially symmetric finite array of dielectric scatterers.

2. Sample and Setup

As an experimental sample we use an array of disks fabricated from BaO-TiO_2 microwave ceramic with the permittivity of ε=40 at GHz frequencies. The radius and the height of the disks are D=10.2 mm and h=10.1 mm, respectively. The period of the array is L=15.1 mm. To fix the disks a custom holder with groves was fabricated from a styrofoam material with a permittivity close to 1.1 at the microwave frequencies. The refractive indexes of the holder is close to the refractive index of air that justifies a neglecting of effect of substrate onto the BIC. The fabricated prototype is shown in the inset of Fig. 1(b).

To analyse the resonances of the system, we measure its transmission spectra S_{12}. Here we focus on BIC with zero angular momentum. Thus, to avoid excitation of the states with nonzero angular momentum we use two identical shielded-loop antennas placed concentric with the axis of the array [see Fig. 1(a)]. Both antennas were connected to the ports of the vector network analyser (VNA). The shielded-loop antennas with the outer diameter of 10 mm have been fabricated from 086 Semi-rigid Coax Cable. The antennas have been placed at the distance 5 mm away from the edges. This distance is enough to provide a weak coupling with the array and not distort Q factors of the resonances.

3. Results

The transmission spectra $|S_{12}|$ of the array consisting of 20 disks placed between two loop antenna is shown in Fig. 1(b). The vertical dashed line separates regions of true leaky resonances and quasi-guided modes, which turn into guided modes as number of disks N tends to infinity. One can see that amplitude of the leaky resonances is much less that one of the quasi-guided modes. Figure 1(c) shows zoomed part of Fig. 1(b). The red dotted line shows the results of the simulation carried out in Comsol Multiphysics. The last peak in the series (with the highest frequency) corresponds to quasi-BIC, which turns into symmetry protected BIC as $N \to \infty$. The simulated dependence of its Q factor on the N in absence of material losses is shown in Fig. 2 by black dotted lines. We found that $Q \sim N^2$ at small number of disks and then Q saturates

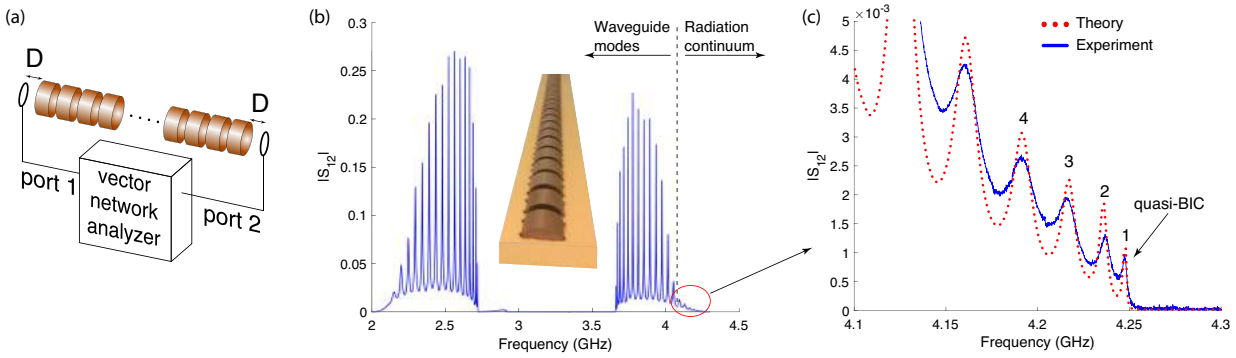


Figure 1: (a) Experimental setup for measurements of transmission spectra through the 1D array of dielectric disks. (b) Spectrum of S_{12} amplitude. The insets shows the experimental sample. (c) Zoomed part of panel (b) showing the resonances in the transmission spectra corresponding to leaky modes.

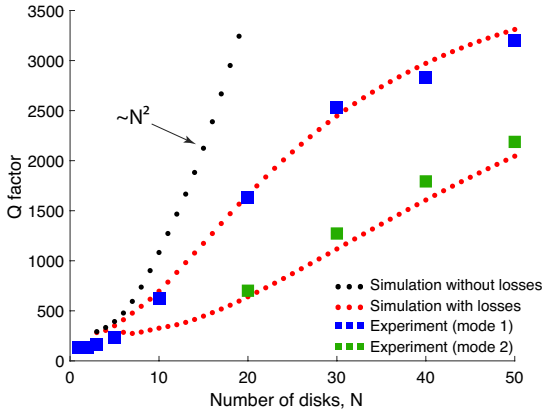


Figure 2: Experimental and simulated dependence of Q factor of the quasi-BIC on the number of the disks in the array. Numeration of the resonances is shown in Fig. 1(c).

due to material losses. The maximal Q factor can be estimated as $\mathrm{Re}(\varepsilon)/\mathrm{Im}(2\varepsilon)$. The dependance of Q factor on N for two last resonances extracted form the experimental spectra is shown in Fig. 2 by green and blue squares. The experimental results are in good agreement with the results of the simulations.

4. Conclusions

We report the first experimental observation of the symmetry protected BIC in 1D periodic array of dielectric scatterers. We analyze the dependence of Q factor of quasi-BIC on the number of the disks in the array. We observe quadratic growth of Q with N at small number of the disks and following saturation at the level $Q_{\max} = \mathrm{Re}(\varepsilon)/\mathrm{Im}(2\varepsilon)$ at N of several tens.

Acknowledgement

This work is supported by RSF (17-12-01581).

References

[1] J. von Neumann, E. P. Wigner, *Phys. Z.* 30: 465–467, 1929.

[2] A. Kodigala, T. Lepetit, Qing Gu, B. Bahari, Y. Fainman and B. Kanté, *Nature*, 541: 196–199 2017.

[3] B. Bahari, F. Vallini, T. Lepetit, R. Tellez-Limon, J. H. Park, A. Kodigala, Y. Fainman, and B. Kante,

[4] E. N. Bulgakov and A. F. Sadreev, *Phys. Rev. A* 92: 023816, 2015.

[5] E. N. Bulgakov and A. F. Sadreev, *Phys. Rev. A* 96: 013841. 2017.

[6] Z. F. Sadrieva, I. S. Sinev, K. L. Koshelev, A. K. Samusev, I. V. Iorsh, O. Takayama, R. Malureanu, A. A. Bogdanov, and A. V. Lavrinenko *ACS Photonics* 4: 723–727, 2017.

[6] C. W. Hsu, B. Zhen, A. D. Stone, J. D. Joannopoulos, and M. Soljacic, *Nat. Rev. Mater* 1: 16048, 2016.

[4] J. M. Foley, S.M. Young, and J. D. Phillips, *Phys. Rev. B* 89: 165111,2014.

[5] X. Cui, H. Tian, Y. Du, G. Shi, and Z. Zhou, *Sci.Rep.* 6: 36066, 2016.

[6] S. Romano, S. Torino, G, Coppola, S. Cabrini, and V. Mocella, *Proc. of SPIE* 10231: 102312J, 2017.

[7] Y. Liu, W. Zhou, and Y. Sun, *Sensors*, 17: 1861, 2017.

Applications of plasmonic near-perfect absorbers in Chemistry

Timothy Connell[1], Kevin Q. Xiao[2], Jasper J. Cadusch[3], Anthony Chesman[2], Ann Roberts[3], Timothy J. Davis[3] and Daniel E. Gomez*[1]

[1]RMIT University, Melbourne, Victoria 3000, Australia
[2]Manufacturing, CSIRO, Private Bag 33, Clayton, Victoria 3168, Australia
[3]School of Physics, The University of Melbourne, Parkville, Victoria 3010, Australia
*corresponding author, E-mail: Daniel.gomez@rmit.edu.au

Abstract

Hot charge carrier extraction from metallic nanostructures is a very promising approach for applications in photocatalysis, photovoltaics, and photo-detection. Here we demonstrate that a monolayer of Au nanoparticles can be assembled on a multi-stack layered configuration to achieve broadband, near-unity light absorption. We show that this enhanced light absorption leads to a 40-fold increase in the photon-to-electron conversion efficiency in photo-electrochemical cells. The measured data is interpreted with a model that enables us to establish that efficient hot carrier extraction is limited to spectral regions where (i) the photons have energies higher than the Schottky barrier at the gold-semiconductor junction and (ii) the absorption of light is localized on the metal nanoparticles..

Organic synthesis via photo-redox processes is a fast growing field with great potential for transforming the fine chemicals industry [1,2]. Almost exclusively, all demonstrations of photo-driven chemical transformations have been enabled by the use of transition-metal organometallic complexes [2], materials that are difficult to synthesize and which have low optical absorption cross-sections, requiring thus high illumination power-densities. On the contrary, metal nanostructures are emerging as an alternative class of photocatalysts that exhibit much greater cross-sections for interaction with light. This is a consequence of the excitation of surface-charge oscillations known as surface plasmon resonances. The resonance frequency of these resonances can be tuned across the entire visible spectrum by changing the geometry of the nanostructures, enabling the prospect for solar photochemistry with plasmonic structures.

One mechanism by which surface plasmon resonances can sensitise a chemical reaction consists on the excitation and emission of (plasmon-derived) hot charge-carriers. Hot-carriers can result from the non-radiative relaxation of surface plasmons, and consist of a transient electron population with an average energy higher than that of a thermally-equilibrated electron population at room temperature. These hot-carriers can be extracted from the metal nanostructure prior to their equilibration with the atomic lattice for the initiation of physical and chemical processes.

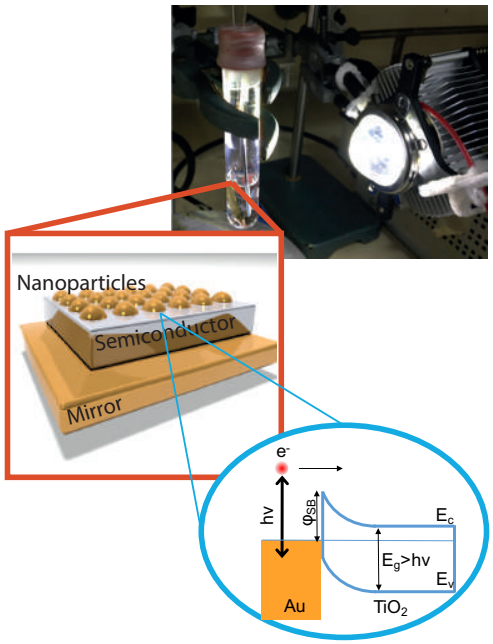


Figure 1: Super-absorber photo-chemical diode for organic synthesis (A) A reaction is driven using a white-light LED as the only source of power and a photocatalyst (B) comprised of a monolayer of Au nanoparticles separated by a thin semiconductor layer from a mirror. (C) The Nanoparticle-semiconductor contact energy diagram

One approach to charge-carrier extraction consist on creating metal-semiconductor diodes (Schottky contacts), where the hot-carriers can be emitted across the material interface and yield charge-separated states with sufficient electrochemical potential to drive chemical transformations. The concept of Photochemical diodes was introduced decades ago [3] and the first chemical product obtained by a hot-carrier reaction was reported by Koval and Segar [4]. Since then, hot electron surface photochemistry has been an

ever growing field that recently has seen some applications in organic synthesis.

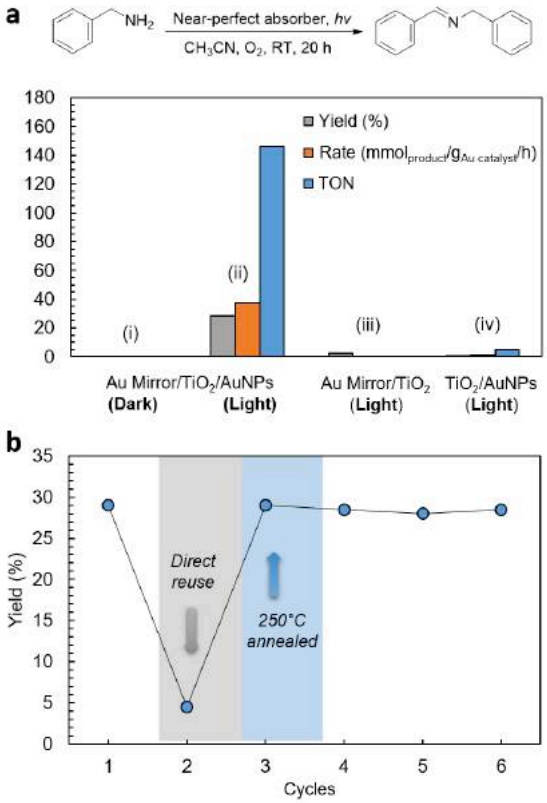


Figure 2. (a) Photocatalytic oxidation of benzylamine with near-perfect absorber: reaction yield, calculated reaction rate and TON for the photocatalytic reaction under control conditions: (i) the reaction with the near-perfect absorber in the dark, (ii) the reaction with the near-perfect absorber under illumination, (iii) a thin film of TiO_2 supported by an Au mirror, and (iv) a thin film of TiO_2 with Au NPs. Reaction conditions: photocatalyst (size 10 × 25 mm, containing 19.3 μg Au); benzylamine, 0.05 mmol; solvent, 4 mL of acetonitrile; 1 atm of O_2; room temperature; reaction time, 20 h; and LED light intensity, 100 mW/cm^2. (b) Photocatalyst recyclability, the heat treatment of catalyst after the reaction to regenerate the photocatalytic surface.

An emerging class of plasmonic photo-catalysts are super-absorber metamaterials (Figure 1). Super-absorbers for hot-carrier photochemistry have been employed (indirectly) for water splitting and the oxidation of simple alcohols [5]. More interestingly, complex chemical reactions can also be initiated and accelerated using these metamaterials. Imines are an important class of intermediates for the synthesis of fine chemicals and pharmaceuticals. Industrially, imines are synthesized by direct oxidation of amines or the condensation of amines with aldehydes, processes that require stoichiometric amounts of harmful or explosive reagents, often in a homogeneous phase, which later require complex separation and purification strategies. Imines can also be synthesised via plasmonic photochemistry, but the current demonstration of this process has lead to modest conversion yields.

Here we demonstrate that a photochemical diode capable of absorbing up to 90% of incident light can transform primary amines into imines with a conversion yield of up to 50% and a selectivity of 99%, at room temperature, atmospheric pressure and without additional power sources. The diode operates by the excitation of plasmonic hot carriers in a monolayer of Au nanoparticles deposited on top of a TiO2/mirror support. The increased capability for light absorption is correlated to the conversion yield of the reaction. Our results indicate that these photodiodes hold great promise in the conversion of visible light into chemical energy.

Acknowledgements

This work was performed in part at the Melbourne Centre for Nanofabrication (MCN) in the Victorian Node of the Australian National Fabrication Facility (ANFF). K.X. acknowledges CSIRO for an OCE Fellowship. We acknowledge the ARC for support through a Discovery Project (DP160100983) and a Future Fellowship (FT140100514).

References

[1] C. K. Prier, D. A. Rankic, and D. W. C. MacMillan Visible Light Photoredox Catalysis With Transition Metal Complexes: Applications In Organic Synthesis Chemical Reviews 113, 5322--5363 (2013)

[2] M. H. Shaw, J. Twilton, and D. W. C. MacMillan Photoredox Catalysis In Organic Chemistry The Journal of Organic Chemistry 81, 6898-6926 (2016)

[3] Nozik, A. J. Photochemical diodes. Applied Physics Letters, 30, 567 (1977)

[4] Koval, C. A.; Segar, P. R. Photoelectrochemical reduction of a Copper(I) complex to Copper metal by hot electrons at p-InP. Journal of the American Chemical Society, 111, 2004 (1989).

[5] Ng, C.; Cadusch, J.; Dligatch, S.; Roberts, A.; Davis, T. J.; Mulvaney, P.; Gomez, D. E. Hot Carrier Extraction with Plasmonic Broadband Absorbers. ACS Nano, 10, 4704 (2016)

Light scattering treated by the resonant-state expansion

Sergey Lobanov, Wolfgang Langbein, and Egor Muljarov*

School of Physics and Astronomy, Cardiff University, Cardiff CF24 3AA, United Kingdom
*corresponding author, E-mail: Egor.Muljarov@astro.cf.ac.uk

Abstract

We present a new rigorous approach to the general problem of light scattering from an arbitrary finite optical system. This approach is based on explicit use of the resonant states of the optical system. These are in turn calculated using the resonant-state expansion, which is a novel powerful method in electrodynamics. We verify and illustrate the developed approach on an example of a dielectric sphere in vacuum which allows an exact analytic solution known as Mie theory.

1. Introduction

Resonances are at the heart of many optical phenomena. In particular, they determine features in optical spectra such as the scattering and extinction cross-sections. Mathematically, resonances themselves and their contribution to physical observables can be elegantly and rigorously described using the concept of resonant states (RSs). A core quantity which contains the full information about the optical system is its dyadic Green's function (GF). The GF provides access to all the observables, including the optical scattering matrix (S-matrix) and the scattering cross-section.

It has been recently shown [1, 2] that using properly normalized RSs, the GF inside any optical system can be constructed efficiently using its spectral representation, also known as the Mittag-Leffler (ML) expansion. Furthermore, based on the ML expansion of the GF, a resonant-state expansion (RSE), capable of treating accurately both small and large perturbations of an optical system, has been developed [1, 2] for dielectrics, and extended [3] to systems with an arbitrary frequency dispersion of the permittivity described by a generalized Drude-Lorentz model. Using this property of the GF, the Purcell factor of a finite three-dimensional (3D) optical system, an important observable, has been expressed as an expansion over RSs [4].

It has been also demonstrated in numerous publications that the S-matrix of an optical system has properties similar to those of the GF, namely, the poles of the S-matrix in the complex frequency plane are also determined by RSs. While the information on the GF contained in the S-matrix is partial, being limited to external excitation, it describes the light scattered by the system completely. Therefore the problem of expressing the S-matrix in terms of RSs reduces to establishing the link between the S-matrix and the GF.

In this paper, we present a rigorous scattering theory based on the concept of RSs, which allows us to calculate precisely the S-matrix and any scattering properties of an arbitrary finite 3D open optical system. The method is based on the following key steps: (i) establishing the link between the S-matrix and the dyadic GF of an arbitrary 3D system and expressing them in the basis of vector spherical harmonics; (ii) using the ML expansion of the GF to represent the S-matrix in terms of RSs of the system; (iii) calculating RSs via the RSE using a spherically symmetric basis system. We verify this approach by comparing results with the exact analytic solution known as Mie theory [5] and demonstrate its convergence in calculating the scattering cross sections.

2. Results: Comparison with exact solution

In this section we verify the developed theory, and in particular the established link between the GF and the S-matrix, by applying it to a dielectric sphere in vacuum. The exact analytic solution for this system is known as the Mie scattering [5] which we compare with (i) the ML result, using the ML expansion of the GF in which the RSs are deter-

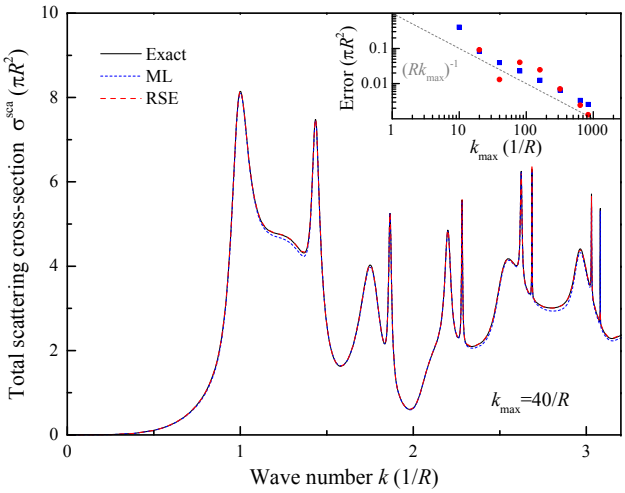


Figure 1: Total scattering cross-section σ^{sca} for a dielectric sphere of radius R and permittivity $\varepsilon = 9$ in vacuum. Exact: the analytic result (Mie scattering [5]). ML: present theory using the analytic RSs of the system. RSE: present theory using the RSs found via the RSE with the basis system having the permittivity $\epsilon = 4$. Inset: absolute error averaged over $0 \leqslant kR \leqslant 10$, as a function of the maximum wave number $k_{\max}$ of the basis RSs.

mined analytically, and (ii) the RSE result, again using ML expansion in which the RSs are found from the RSE treating a sphere with a different refractive index as a basis system.

Figure 1 shows the total scattering cross-section, which is obtained from the S-matrix by summing over all scattering channels l, m and p (l and m are, respectively, the orbital and magnetic quantum numbers and p is the polarization, transverse electric or transverse magnetic). The spectrum shows contribution of RSs of different kind, namely narrow peaks due to the whispering gallery modes on top of much broader Fabry-Pérot resonances, complemented with a background owing to leaky modes. Both the ML and the RSE are close to the exact solution as quantified by the relative error scaling as the inverse maximum wave number $k_{\max}$ of the basis RSs. The error due to this truncation and missing RSs is even partly compensated in the RSE by the error in the calculation of the RSs, making the RSE result presented in Figure 1 more accurate.

In conclusion, the combination of the Mittag-Leffler expansion of the dyadic Green's function and the resonant-state expansion presents an accurate and efficient method to calculate the scattering properties of arbitrary finite three-dimensional systems, which we demonstrate in the present work on exactly solvable examples.

References

[1] E. A. Muljarov, W. Langbein, and R. Zimmermann, Europhys. Lett. **92**, 50010 (2010).

[2] M. B. Doost, W. Langbein, and E. A. Muljarov, Phys. Rev. A **90**, 013834 (2014).

[3] E. A. Muljarov and W. Langbein, Phys. Rev. B **93**, 075417 (2016).

[4] E. A. Muljarov and W. Langbein, Phys. Rev. B **94**, 235438 (2016).

[5] C. Bohren and D. R. Huffman, *Absorption and Scattering of Light by Small Particles* (Wiley Science Paperback Series, 1998).

Four-wave mixing in Epsilon-Near-Zero Aluminum Zinc Oxide

Enrico G. Carnemolla[1], Vincenzo Bruno[1,2], Matteo Clerici[3], Stefano Vezzoli[1], Clayton DeVault[4], Lucia Caspani[5], Alexandra Boltasseva[4], Vladimir M. Shalaev[4], Daniele Faccio[2] and Marcello Ferrera[1,*]

[1] Institute of Photonics and Quantum Sciences, Heriot-Watt University, SUPA, Edinburgh, Scotland, EH14 4AS, UK
[2]School of Physics and Astronomy, University of Glasgow, Glasgow, G12 8QQ, UK
[3]School of Engineering, University of Glasgow, Glasgow, G12 8LT, UK
[4] University of Purdue, Birck Nanotechnology Center and Department of Physics, 1501 West State St., 47907, West Lafayette, Indiana, USA
[5] Institute of Photonics, Department of Physics, University of Strathclyde, Glasgow G1 1RD, UK
*corresponding author, E-mail: m.ferrera@hw.ac.uk

Abstract

Transparent Conductive Oxides (TCOs) are at the center of a tremendous scientific and technological interest. At relevant telecom wavelengths, TCOs allow to operate in the epsilon-near-zero regime where the material transparency is still high, and the optical nonlinear response is enormously enhanced. After a general introduction about nonlinear optics in TCOs, experiments of semi-degenerate four-wave mixing (FWM) in aluminum zinc oxide thin films will be reported where photons were generated in the visible window with a measured efficiency reaching 2%.

1. Introduction

Research on alternative nonlinear materials have produced remarkable findings which raised the bar of the maximum attainable third order susceptibility by several orders of magnitude. In particular, a huge effort has been devoted towards nonlinearities in bulk materials, which from many extents are more suitable for standard integrated photonics than structured and 2D materials. In this direction outstanding results have been attained exploiting transparent conducting oxides, a class of wide band gap compounds which undergo a heavy doping process for enhancing the carrier concentration (typically of the order of $10^{21}cm^{-3}$) and pushing the Fermi level up into the conduction band. This effectively widens the natural energy gap of the intrinsic material which sees its electrical conductivity enhanced without scarifying the optical transparency. In addition to this, the cross-over wavelength in TCOs (i.e. the wavelength at which the real part of the dielectric permittivity crosses zero) is typically located in the NIR and can be arbitrary engineered by changing the material stoichiometry and the deposition conditions. This allows to statically "tune" the so-called epsilon-near-zero window to relevant telecom wavelengths. The fundamental advantage of doing so is that the material nonlinearities are enormously enhanced when the material permittivity approaches zero [1-4]. Here we report nonlinear frequency conversion in aluminum zinc oxide thin films exploiting semi-degenerate FWM.

2. Experiments

The experiments were carried out by using an apparatus which is schematically represented in Fig.1. Here a Ti:Sapphire laser emits ultra-fast pulses of about 100fs at λ=787nm with a repetition rate of 100Hz. This train of pulses is split into two optical paths dedicated to a signal and a pump wave, respectively. The signal is attained by feeding an OPA providing an output which is tunable in the range 1.1-1.5μm while the pump corresponds to the second part of the initial source which goes through a delay line before being focused and overlapped with the signal beam on top of the sample surface. The sample under test was a 900nm thick film of aluminum zinc oxide (AZO) deposited on top of a glass substrate. Our AZO films were grown using Pulsed Laser Deposition (PLD) in an oxygen deprived atmosphere [5]. Our peculiar fabrication strategy allows for pushing the ENZ region to longer wavelengths up to 1.9μm, but for this specific case the cross-over wavelength was set at 1.35μm. By using this system, we performed an experiment of stimulated degenerate four-wave mixing where two degenerate pump photons mix with a signal photon to

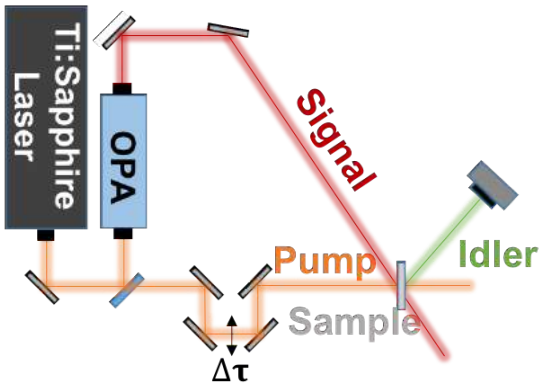


Figure 1: Experimental set-up for the semi-degenerate four-wave mixing experiments.

generate the idler photon according to the energy conservation principle described by:

$$2\omega_{Pump} = \omega_{Signal} + \omega_{Idler} \quad (1)$$

Where the subscript on the angular frequencies refers to the corresponding wave. The efficiency of the process fundamentally depends on the momentum conservation which is related to the condition of phase matching.

The efficiency of the process is reported in Fig.2 as a function of the signal wavelength and for a pump power of 0.6mW. For this set of experiments the waist of the beams was about 90µm while the signal power was approximately 2.5mW. To verify that the correct nonlinear process was identified, the idler power versus the square of the pump power was evaluated and the results are plotted in Fig.3.

3. Results and discussion

We chose this specific FWM configuration because of its fundamental technological relevance. In fact, it allows to produce visible photons within the spectral window of maximum transparency and tune their frequency on a broad range thanks to the action of the signal wave. This functionality is of course of key importance for the design of all-optical signal routers. As evident from Fig. 2, the efficiency of the nonlinear process increases for decreasing signal wavelength, first slowly and then rapidly right after λ_{Signal}<1150nm. This is expected since the phase matching condition is relaxed as the wavelength distance between pump and signal waves is reduced. The maximum measured conversion efficiency was about 2% and limited by the wavelength tunability of our OPA. However, it is evident from the steep gradient of Fig.2 that a considerably higher efficiency is expected at shorter wavelengths. Finally, from Fig.3, we see that even though the general trend of the reported curve can be well fit with a straight line, the beginning of competitive nonlinear processes is visible for the highest values of pump power.

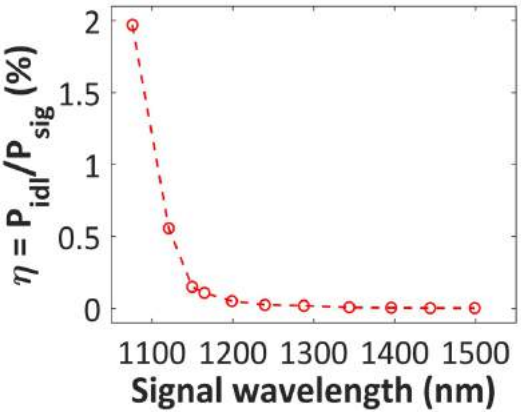


Figure 2: Nonlinear conversion efficiency as a function of the signal wavelength.

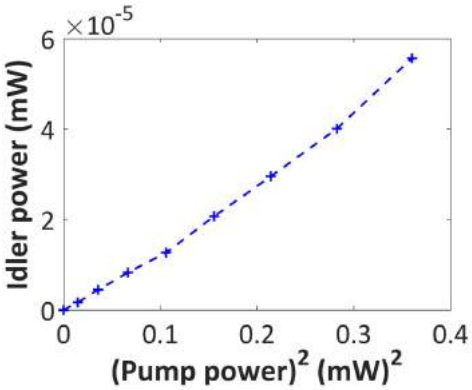


Figure 3: Idler power versus the square of the pump power for the FWM process.

4. Conclusions

In conclusion, we report experiments of degenerate four-wave mixing where the pump signal is located at 787nm and the signal wave is tuned around the ENZ wavelength of our AZO thin films. The nonlinear frequency conversion starts being efficient for pump to signal detuning < 360nm and reaches 2% of efficiency within our experimental capability.

Acknowledgements

D.F. acknowledges financial support from the European Research Council under the European Union Seventh Framework Programme (FP/2007-2013)/ERC GA 306559 and EPSRC (UK, Grant No. EP/M009122/1). M.C. acknowledges support from EPSRC (Grants No. EP/P0096971/1 and No. EP/R511705/1). M.F. acknowledges economic support from EPSRC (UK, Grant EP/P019994/1) and from The Royal Society (Project No. RG2017R1). V.M.S. and A.B. acknowledge support by the U.S. Department of Energy, Office of Basic Energy Sciences, Division of Materials Sciences and Engineering under Award No. DE- SC0017717 (sample fabrication), and Air Force Office of Scientific Research (AFOSR) Grant No. FA9550-18-0002 (far-field characterization).

References

[1] L. Caspani, et al., Enhanced Nonlinear Refractive Index in ε-Near-Zero Materials, Phys. Rev. Lett. 116: 233901-5, 2016.

[2] M. Clerici, et al., Controlling hybrid nonlinearities in transparent conducting oxides via two-colour excitation, Nat. Commun. 2: doi:10.1038/ncomms15829, 2017.

[3] M. Z. Alam, et al., Large optical nonlinearity of indium tin oxide in its epsilon-near-zero region, Science 352: 795-797, 2016.

[4] J. Kim, et al., Dynamic Control of Nanocavities with Tunable Metal Oxides, Nano letters 18: 740-746, 2018.

[5] N. Kinsey, et al., Epsilon-near-zero Al-doped ZnO for ultrafast switching at telecom wavelengths, 2: 616-622, 2015.

Multichannel Optical Encryption based on Dielectric Metasurface

Hang Feng, [1, #] Fengliang Dong, [2, #] Lihua Xu, [2, #] Bo Wang, [1] Zhiwei Song, [2] Xianfeng Zhang, [2] Lanqin Yan, [2] Xiaojun Li, [2] Weiguo Chu, [2, *] and Yan Li [1, 3, *]

ABSTRACT: Amplitude, phase, wavelength and polarization are all intrinsic characteristics of light. Through different combinations of them, optical encryption can be realized, which is effective, flexible and steady. Optical metasurface, consisting of plasmonic or dielectric resonant antennas, can manipulate the wavefront of incident light in variable ways. Here we demonstrate an optical encryption based on dielectric metasurface that information can be encoded into different channels according to different wavelengths and polarizations. The encoded image can be extracted only when the light with designed wavelength and polarization irradiates on the metasurface, or it remains hidden. Furthermore, we realize 63 information encoding combinations through 6 independent channels, including two circular polarization states (RCP, LCP) and the RGB wavelengths (633nm, 532nm and 473nm). This work greatly enhances encryption security, and opens a new avenue for information encoding, data storage and optical communication.

[1]State Key Laboratory for Mesoscopic Physics, Department of Physics, Peking University and Collaborative Innovation Center of Quantum Matter, Beijing 100871, China. [2]Nanofabrication Laboratory, CAS Key Laboratory of Nanosystem and Hierarchical Fabrication, CAS Center for Excellence in Nanoscience, National Center for Nanoscience and Technology, Beijing 100190, China. [3]Collaborative Innovation Center of Extreme Optics, Shanxi University, Taiyuan, Shanxi 030006, China. [#]These authors contributed equally to this work. [*]Correspondence and requests for materials should be addressed to Y. L. (email: li@pku.edu.cn) and W.C. (email: wgchu@nanoctr.cn)

Guiding electromagnetic waves through the bound states in the radiation continuum in novel types of fibers

Evgeny Bulgakov and Almas Sadreev

Kirensky Institute of Physics, Federal Research Center KSC SB RAS, 660036 Krasnoyarsk, Russia
*corresponding author, E-mail: almas@tnp.krasn.ru

Abstract

We consider propagation of electromagnetic waves through the Bloch bound states in the radiation continuum (BICs) in two novel types of fibers. The first type is a single dielectric rod of circular cross-section with refraction index periodically modulated along the rod [Phys. Rev. A 96, 013841 (2017)]. The second type of the fiber consists of N dielectric rods arranged in circular way [arXiv:1711.05965 (2017)]. Each true BIC which occurs in an infinite linear array has its counterpart in the circular array as a near-BIC with extremely large quality factor. These near-BICs are localized with exponential accuracy outside the circular array but can fill the whole inner space of the array. The guiding modes can be excited by plane excited by oblique plane wave with tuned frequency, polarization and angle of incidence. Because of axial symmetry of the fibers the BICs can carry also angular orbital momentum.

1. Introduction

Recently confined electromagnetic modes above the light line, bound states in the continuum (BICs) were shown to exist in different periodic dielectric structures (i) arrays of long dielectric rods, (ii) photonic crystal slabs, and (iii) two-dimensional periodical structures on the surface of material (see the review [1] and references in [2]). Physically occurrence of the BICs in the infinite array of rods is a result of periodicity of the array that quantizes the radiation continua in the form of diffraction continua [3]. We emphasize the BICs which can propagate either along the axis of periodicity of the system [3, 4, 5] or along the rods [6, 7] that introduces new family of the waveguide modes. The subject of this summary is to introduce a new generation of fibers based on similar BIC propagating modes in two kinds of the one-dimensional periodical structures. The first type is single dielectric rod with the refractive index modulated along the rod axis [2, 8]. The utmost case is the stack of dielectric disks as shown in Fig. 1. The second type of the fiber consists of N dielectric rods with constant refractive index which however rolled up into circular periodical array of rods [9, 9] as shown in Fig. 2.

2. BICs in the stack of disks

Similar to the periodic array of dielectric rods [3, 4, 5] the array of disks supports as symmetry protected BICs with the Bloch vector $k_z = 0$ as well as the Bloch BICs with $k_z \neq 0$ of both polarizations demonstrated in Fig. 3. However because of axial symmetry of the rod there are multiple BICs with OAM shown in Fig. 4. These BICs have no definite polarization with all six components of electromagnetic field.



Figure 1: Infinite circular dielectric rod with periodically alternating permittivity ϵ_1 (dark red) and ϵ_2 (light gray).



Figure 2: N infinitely long circular dielectric rods are stacked parallel each other in the circular way.

3. Near BICs

The system shown in Fig. 2 is periodical in the azimuthal direction and therefore preserves properties of linear periodical array of the dielectric rods. We present analytical consideration of that the Q factor of such a system behaves as $Q \sim \exp(\lambda N)$ where the material parameter λ is of order of unit [9, 10]. That allows us to consider these BICs as near BICS. Each true BIC which exists in the linear array of rods finds its counterpart in the circular array. One of this correspondence is demonstrated in Fig. 5.

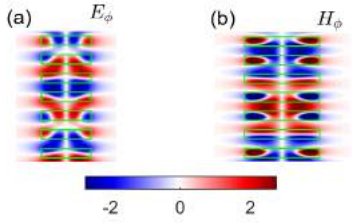


Figure 3: Pattern of the TE BIC with OAM $m = 0$, Bloch vector $k_z = 2.374$ and frequency $\omega = 3.157$ (a) and TM BIC with $m = 0, k_z = 1.087, \omega = 3.884$. The parameters of disks are $\epsilon_2 = 5, R = 1, d = 0.5$.

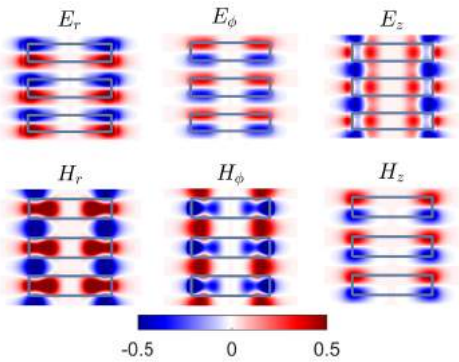


Figure 4: Pattern of the BSC with $m = 5$ and frequency $\omega = 5.144$ for tuned radius $R = 1.876$.

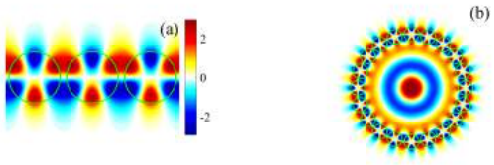


Figure 5: Pattern of the non-symmetry protected BICs in a linear infinite array of rods (a) and its counterpart in the circular array of 20 rods with Q factor $Q = 1.5 \cdot 10^8$

4. Conclusions

The most striking result is related to excitation of Bloch BICs running along the one-dimensional arrays shown in Figs. 1 and 2 above the light line. This process is turned out to be very sensitive to the angle of incidence of plane wave in respect to the axis of the arrays. Thus, that system brings new generation of fibers with extremely high Q factor provided that the parameters of trapped running mode is close to the BIC point [6, 4, 7]. The next interesting result of scattering of oblique plane wave with mixed polarization by the arrays is a possibility to vary the profile of Fano resonance by only rotation of the polarization of the wave not addressing to tuning of material parameters. The phenomenon becomes especially sensitive to variation of external parameters in a vicinity of the BIC frequency.

Acknowledgement

This work was supported by Russian Science Foundation 18–12–00097 and RFBR Grants 16–02–00314 and 17–52–45072.

References

[1] C.W. Hsu, B. Zhen, A.D. Stone, J.D. Joannopoulos, and M. Soljačić, Bound states in the continuum, *Nature Reviews Materials* **1**, 16048 (2016).

[2] E.N. Bulgakov and A.F. Sadreev, "Bound states in the continuum with high orbital angular momentum in a dielectric rod with periodically modulated permittivity", *Phys. Rev. A* **96**, 013841 (2017).

[3] E.N. Bulgakov and A.F. Sadreev, "Bloch bound states in the radiation continuum in a periodic array of dielectric rods", *Phys. Rev. A* **90**, 053801 (2014).

[4] E.N. Bulgakov and D.N. Maksimov, Light guiding above the light line in arrays of dielectric nanospheres, *Opt.Lett.* **41**, 3888 (2016).

[5] Zhen Hu and Ya Yan Lu, "Propagating bound states in the continuum at the surface of a photonic crystal", *J. Opt. Soc. Am.* B **34**, 1878–1883 (2017).

[6] Chia Wei Hsu, Bo Zhen, Song-Liang Chua, S.G. Johnson, J.D.Joannopoulos, and M. Soljačić, "Bloch surface eigen states with in the radiation continuum", *Light: Science and Applications* **2**, 1 (2013).

[7] E.N. Bulgakov and D.N. Maksimov, "Bound states in the continuum and polarization singularities in periodic arrays of dielectric rods", *Phys. Rev.* A **96**, 063833 (2017).

[8] Xingwei Gao, Chia Wei Hsu, Bo Zhen, Marin Soljacic, and Hongsheng Chen, "Bound states in the continuum in low-contrast fiber Bragg gratings", arXiv: 1707.01247 (2017).

[9] Hai-bin Lü and Xiaoping Liu, "Trapped modes with extremely high quality factor in the subwavelength ring resonator composed of dielectric nanorods", arXiv:1709.08006 (2017).

[10] E.N. Bulgakov and A.F. Sadreev, "Near-bound states in the radiation continuum in circular array of dielectric rods", arXiv:1711.05965 (2017).

Photo/Thermal Conversions and their Applications

Plasmonic Membranes: Control of Fluid Flow through Light

Ana Sousa-Castillo[1], Leonardo N. Furini[1], Brylee David B. Tiu[2], Peng-Fei Cao[3], Begüm Topçu[1], Miguel Comesaña-Hermo[1], Benito Rodríguez-González[1], Walid Baaziz[4], Ovidiu Ersen[4], Rigoberto C. Advincula[3], Moisés Pérez-Lorenzo[1], and Miguel A. Correa-Duarte[1]

[1]Department of Physical Chemistry, Biomedical Research Center (CINBIO), Southern Galicia Institute of Health Research (IISGS), and Biomedical Research Networking Center for Mental Health (CIBERSAM), Universidade de Vigo, 36310 Vigo, Spain
[2]Department of Bioengineering, University of California Berkeley, Hearst Memorial Mining Building, Berkeley, CA 94720-1760, USA
[3]Department of Macromolecular Science and Engineering, Case Western Reserve University School of Engineering, Cleveland, Ohio 44106, USA
[4]Institut de Physique et Chimie des Matériaux de Strasbourg (IPCMS), UMR 7504 CNRS-Université de Strasbourg, 67037 Strasbourg Cedex 08, France
*corresponding author, E-mail: moisespl@uvigo.es

Abstract

A novel generation of porous substrates endowed with synergistic sensing and actuating capabilities opens the door to a paradigm shift in membrane technology. Through this synthetic approach, commercial membranes can be easily retrofitted allowing for an unprecedented control over fluid flow in response to an external light stimulus.

Introduction

In the last years, Nanotechnology has afforded many innovative and flexible approaches to fabricate self-regulated membranes by incorporating stimuli-responsive materials as functional gates onto/into traditional porous substrates.[1–5] This rising interest has been fueled by the accessible diversity of functional units that serve as both recognition elements and reversible actuators when incorporated into the channels of porous substrates. Examples of these units include synthetic polymers endowed with macrocyclic structures (such as cyclodextrins,[6] or crown ethers[7]), antibodies,[8] enzymes,[9] aptamers,[10] peptides,[11] or boronic acids.[12] As a result, membrane technology has established itself as a key tool in a myriad of fields such as pharmaceutical industry, food sciences, environmental remediation, biomedicine or biotechnology, among others. In all these cases, the paradigm through which these "smart" membranes control their permeability is well-established, and it consists in an uninterrupted and autonomous operation, where the presence or removal of a given analyte prompts the opening/closing of the pores and thus, an increased/decreased permeability. Unfortunately, this biomimetic behavior does not provide solutions further than that pre-set by the stimuli-responsive material. Thus, the nature and amount of ions/molecules in solution become the only factors determining the membrane behavior through an automated cascade of events involving sensing, transduction and response, in the end leaving no room for the necessary adaptability to the ever-changing requirements of modern industry.[13]

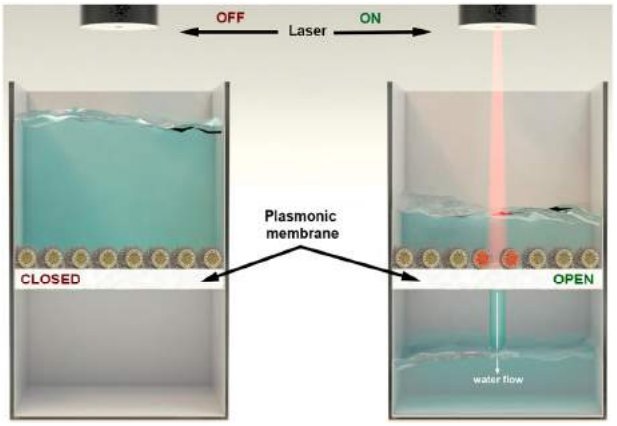


Figure 1: Illustration depicting the operational capabilities of the proposed retrofitted membranes in which a light-mediated spatiotemporal control of permeability can be achieved.

In the present work we propose the reformulation of this deep-rooted paradigm so as to shift the "gating" process from a self-regulated regime to an "on-command" control mode. This will be accomplished through an out-of-the-box approach where plasmonic and thermoresponsive factors are synergistically integrated in carefully engineered nanoarchitectures. Through this strategy, commercial microfiltration substrates can be easily retrofitted becoming capable of providing "real-time" information on the analytes

that diffuse across them. More importantly, once a given wanted signal is detected, these retrofitted membranes can be turned permeable/impermeable at will upon irradiation with a light beam. In this line, the spatial distribution of the laser spot on the porous substrate allows the opening/closing of selected areas of the membrane, thus affording an unprecedented degree of control over the fluid flow. In view of the above, one may envisage the potential of implementing these multifunctional materials as both sensing and actuating films in biomedical microdevices, microfluidic circuits, or lab-on-a-chip systems, among others.

Acknowledgements

This work was funded by MINECO-Spain (CTM2014-58481-R), Xunta de Galicia (Centro Singular de Investigación de Galicia - Accreditation 2016-2019 and EM2014/035), European Union (European Regional Development Fund-ERDF), and Fundación Tatiana Pérez de Guzmán el Bueno.

References

[1] Kowalczyk, S. W.; Blosser, T. R.; Dekker, C. Biomimetic Nanopores: Learning from and about Nature. *Trends Biotechnol.* **2011**, *29* (12), 607–614.

[2] Zhang, H.; Tian, Y.; Jiang, L. Fundamental Studies and Practical Applications of Bio-Inspired Smart Solid-State Nanopores and Nanochannels. *Nano Today* **2016**, *11* (1), 61–81.

[3] Hou, X.; Guo, W.; Jiang, L. Biomimetic Smart Nanopores and Nanochannels. *Chem. Soc. Rev.* **2011**, *40* (5), 2385–2401.

[4] Hou, X.; Jiang, L. Learning from Nature: Building Bio-Inspired Smart Nanochannels. *ACS Nano* **2009**, *3* (11), 3339–3342.

[5] Shen, Y.; Saboe, P. O.; Sines, I. T.; Erbakan, M.; Kumar, M. Biomimetic Membranes: A Review. *J. Memb. Sci.* **2014**, *454*, 359–381.

[6] Yang, M.; Xie, R.; Wang, J.-Y.; Ju, X.-J.; Yang, L.; Chu, L.-Y. Gating Characteristics of Thermo-Responsive and Molecular-Recognizable Membranes Based on poly(N-Isopropylacrylamide) and β-Cyclodextrin. *J. Memb. Sci.* **2010**, *355* (1–2), 142–150.

[7] Liu, Z.; Luo, F.; Ju, X.-J.; Xie, R.; Luo, T.; Sun, Y.-M.; Chu, L.-Y. Positively K^+-Responsive Membranes with Functional Gates Driven by Host–Guest Molecular Recognition. *Adv. Funct. Mater.* **2012**, *22* (22), 4742–4750.

[8] Lee, S. B.; Mitchell, D. T.; Trofin, L.; Nevanen, T. K.; Söderlund, H.; Martin, C. R. Antibody-Based Bio-Nanotube Membranes for Enantiomeric Drug Separations. *Science* **2002**, *296* (5576), 2198 LP-2200.

[9] Ali, M.; Ramirez, P.; Tahir, M. N.; Mafe, S.; Siwy, Z.; Neumann, R.; Tremel, W.; Ensinger, W. Biomolecular Conjugation inside Synthetic Polymer Nanopores Viaglycoprotein-Lectin Interactions. *Nanoscale* **2011**, *3* (4), 1894–1903.

[10] Jiang, Y.; Liu, N.; Guo, W.; Xia, F.; Jiang, L. Highly-Efficient Gating of Solid-State Nanochannels by DNA Supersandwich Structure Containing ATP Aptamers: A Nanofluidic IMPLICATION Logic Device. *J. Am. Chem. Soc.* **2012**, *134* (37), 15395–15401.

[11] Ali, M.; Neumann, R.; Ensinger, W. Sequence-Specific Recognition of DNA Oligomer Using Peptide Nucleic Acid (PNA)-Modified Synthetic Ion Channels: PNA/DNA Hybridization in Nanoconfined Environment. *ACS Nano* **2010**, *4* (12), 7267–7274.

[12] Liu, Q.; Xiao, K.; Wen, L.; Dong, Y.; Xie, G.; Zhang, Z.; Bo, Z.; Jiang, L. A Fluoride-Driven Ionic Gate Based on a 4-Aminophenylboronic Acid-Functionalized Asymmetric Single Nanochannel. *ACS Nano* **2014**, *8* (12), 12292–12299.

[13] Charcosset, C. *Membrane Processes in Biotechnology and Pharmaceutics, 1st Ed.*, Elsevier, Amsterdam, **2012**.

Thermoplasmonic metasurfaces for energy applications – Solar-heated windows and energy harvesting from random light fluctuations

Magnus P Jonsson

Laboratory of Organic Electronics, Department of Science and Technology, Linköping University, Sweden
E-mail: magnus.jonsson@liu.se

Abstract

I will present our recent research on utilizing plasmonic heat generation for passive thermal management and active energy harvesting.

Metallic nanostructures shine in bright colours due to excitation of plasmons, which are collective charge oscillations induced by light. This strong light-matter interaction leads to absorption and heat generation, which makes plasmonic systems suitable as light-induced nanoscale heat sources. In this presentation, I will focus on our recent work on utilizing this effect for energy management and energy conversion. First, I will discuss the use of directional nanoantennas to create transparent surfaces with built-in control of solar heat absorption and energy transmission.[1] These surfaces have particular promise for use in energy-efficient windows. Second, I will discuss means to harvest plasmon-induced thermal energy. This includes the combination of plasmonic nanohole systems, as found particularly efficient as plasmonic heat generators, with thermoelectric systems based on high-Seebeck ionic polymers.[2] Finally, I will demonstrate energy harvesting of random light fluctuations, by combining plasmonic metasurfaces with thin layers of organic pyroelectric materials.[3]

Acknowledgements

Part of this research was performed in collaboration with Alexandre Dmitriev's group at Gothenburg University, Sweden, and with other research groups at the Laboratory of Organic Electronics at Linköping University. We acknowledge financial support from particularly the Wenner-Gren Foundations, the Swedish Research Council, the Swedish Foundation for Strategic Research, the Royal Swedish Academy of Sciences, the ÅForsk Foundation, and the Swedish Government Strategic Research Area in Materials Science on Functional Materials at Linköping University (Faculty Grant SFO-Mat-LiU no. 2009 00971).

References

[1] G. Jönsson, D. Tordera, T. Pakizeh, M. Jaysankar, V. Miljkovic, L. Tong, M.P. Jonsson, and A. Dmitriev, Solar transparent radiators by optical nanoantennas, *Nano Letters* 2017, 17 (11), 6766–6772

[2] D. Tordera, D. Zhao, A.V. Volkov, X. Crispin, and M.P. Jonsson, Thermoplasmonic semitransparent nanohole electrodes *Nano Letters* 2017, 7 (5), 3145–3151

[3] M. Chaharsoughi, D. Tordera, A. Grimoldi, I. Engquist, M. Berggren, Simone Fabiano, and M.P. Jonsson, Hybrid Plasmonic and Pyroelectric Harvesting of Light Fluctuations, *in revision*

Opto-Thermal Nano-Tools for Advanced Materials and Life Sciences

Linhan Lin[1,2] and Yuebing Zheng[1,2,*]

[1]Department of Mechanical Engineering, The University of Texas at Austin, Austin, TX 78712, USA.
[2]Materials Science & Engineering Program and Texas Materials Institute, The University of Texas at Austin, Austin, TX 78712, USA
*corresponding author, E-mail: zheng@austin.utexas.edu

Abstract

Through turning disadvantages to advantages, we develop various low-power opto-thermal nano-tools based on the plasmon-enhanced opto-thermal effect, including bubble printer, opto-thermal tweezers, and opto-thermal scissors. With their simple optics, low operation power, and wide applicability, these opto-thermal nano-tools will find applications in materials science and life sciences such as fabrication of colloidal metamolecules, bio-sensing, and early disease diagnosis.

1. Introduction

The light-to-heat conversion has been considered as the major loss in metal nanoparticles, which prevents signal propagation and causes energy waste in plasmonic devices. A lot of efforts, including the incorporation of photonic modes for photonic-plasmonic coupling, the exploration of semiconductor plasmonics, and the development of all-dielectric metamaterials, have been carried out to overcome this intrinsic loss in metals. However, the generation of Joule heat in metals can also be turned into advantages. Herein, we propose several strategies to develop various opto-thermal nano-tools for optical trapping, optical printing, colloidal assembly, and low-dimensional materials processing. Specifically, the high-efficiency light-to-heat conversion in metal nanoparticles is well explored to reduce the operation power of these nano-tools, opening new doors for versatile and non-invasive all-optical platforms for applications in life sciences and materials science.

2. Underlying physics

Besides the Joule heat generated from the metal nanoparticles under laser radiation, we further explore multiple underlying physics based on the light-induced temperature field, including Marangoni convection,

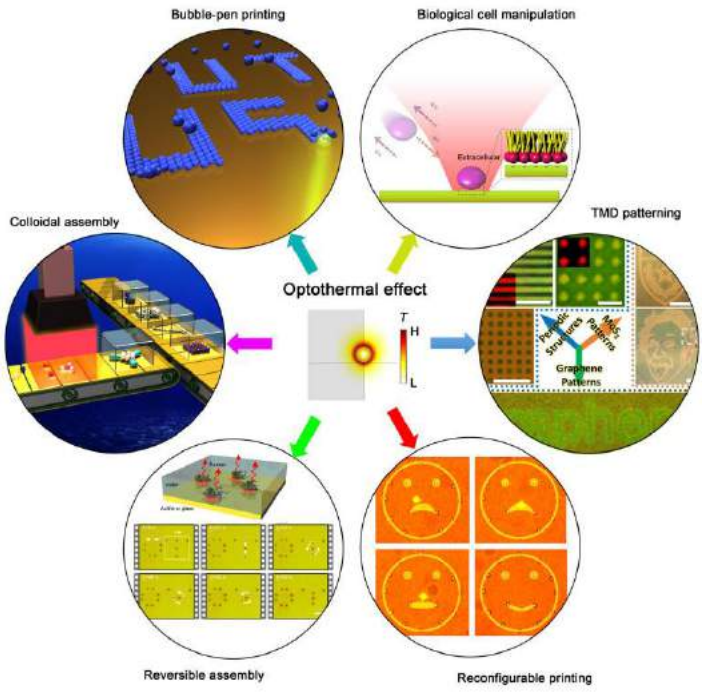


Figure 1: Various opto-thermal nano-tools based on opto-thermal effect in gold plasmonic nanoparticles.

thermophoresis, thermoelectricity, and depletion to enable multiple functionalities in our opto-thermal nano-tools.

3. Results and discussion

3.1. Bubble printer

Firstly, we develop an all-optical bubble-printer through generating a light-directed microbubble at the solid-liquid interface [1]. Upon optical heating, the temperature gradient along the bubble surface induces a strong Marangoni convective flow, which delivers the suspended colloidal particles to the solid state substrate. The colloidal particles are further printed on the surface through coordinated effect of convective drag force, surface tension, gas pressure, and van der Waals interaction. Both single-particle printing and colloidal assembly can be achieved. We further achieve programmable and haptic-interfaced quantum dots printing for semiconductor micro-display [2, 3].

3.2. Opto-thermal tweezers based on thermophoresis

Secondly, we propose and develop a low-power thermophoretic tweezers for non-invasive manipulation of colloidal particles and biological cells [4, 5]. With the heat induced interfacial entropy gradient and structured water molecules in the electric double layer at the particle-liquid interface, we enable the cold-to-hot thermophoretic migration of colloidal particles and the confinement of particles at the light-directed thermal hot spots. Specifically, taking advantage of the low operation power (two orders lower than optical tweezers), we further achieve the thermophoretic manipulation of biological cells with multiple functions such as parallel manipulation, cell assembly, cell alignment and rotation.

3.3. Opto-thermal tweezers based on thermoelectricity

Besides thermophoresis, thermoelectricity can also lead to colloidal migration under the externally applied temperature gradient. To create the thermoelectric field, we introduce ionic micelles as macro ions, which, together with its counter ions, provide a light-controlled thermoelectric field due to their different Soret coefficient and therefore spatial separation along the temperature gradient. We demonstrate that the light-directed thermoelectric field can rapidly assemble various plasmonic nanoparticles in a low-power and reversible manner [6]. The multiple plasmonic "hot spots" in the assembly were explored for in-situ surface-enhanced Raman scattering and molecules sensing. We further incorporate depletion attraction interaction as a bonding force for inter-particle locking to fabricate colloidal matter for a wide range of colloidal atoms in different materials, shapes, and sizes [7]. The colloidal matter, with the sizes at wavelength scale, can be explored as optical matter for different optical devices. Besides inter-particle depletion attraction for colloidal bonding, the particle-substrate depletion attraction provides another dimensionality to lock colloidal particles on the substrate. Specifically, through engineering and management of printing force and repulsive force, we further achieve reconfigurable printing of colloidal particles [8].

3.4. Opto-thermal scissors

Finally, we develop an opto-thermal scissor for on-demand optical patterning of two-dimensional materials, including graphene and different semiconductor atomic layers. Versatile patterns can be optically created with both high throughput and submicron resolution. Specifically, the high-resolution patterning of graphene provides opportunities in the development of terahertz plasmonic devices.

4. Conclusions

We have developed multiple opto-thermal nano-tools for printing and assembly of colloidal particles, non-invasive manipulation of biological cells, and low-dimensional materials processing. The low operation power, on-demand and versatile manipulation of light, and precise control with high resolution in these nano-tools will leads to a new way for both fundamental understanding and applications in advanced materials fabrication and life science.

References

[1] L. Lin, X. Peng, Z. Mao, W. Li, M. N. Yogeesh, B. B. Rajeeva, E. P. Perillo, A. K. Dunn, D. Akinwande, and Y. Zheng, Bubble-Pen Lithography, *Nano Lett.* 16: 701-708, 2016.

[2] B. Bangalore Rajeeva, L. Lin, E. P. Perillo, X. Peng, W. W. Yu, A. Dunn, and Y. Zheng, High-Resolution Bubble Printing of Quantum Dots, *ACS Applied Materials & Interfaces* 9: 16725-16733, 2017.

[3] B. B. Rajeeva, M. A. Alabandi, L. Lin, E. P. Perillo, A. K. Dunn, and Y. Zheng, Patterning and Fluorescence Tuning of Quantum Dots with Haptic-Interfaced Bubble Printing, *Journal of Materials Chemistry C* 5: 5693-5699 2017.

[4] L. Lin, X. Peng, X. Wei, Z. Mao, C. Xie, and Y. Zheng, Thermophoretic Tweezers for Low-Power and Versatile Manipulation of Biological Cells, *ACS Nano* 11: 3147-3154, 2017.

[5] L. Lin, X. Peng, Z. Mao, X. Wei, C. Xie, and Y. Zheng, Interfacial-entropy-driven thermophoretic tweezers, *Lab Chip* 17: 3061-3070, 2017.

[6] L. Lin, X. Peng, M. Wang, L. Scarabelli, Z. Mao, L. M. Liz-Marzán, M. F. Becker, and Y. Zheng, Light-Directed Reversible Assembly of Plasmonic Nanoparticles Using Plasmon-Enhanced Thermophoresis, *ACS Nano* 10: 9659-9668, 2016.

[7] L. Lin, J. Zhang, X. Peng, Z. Wu, A. C. H. Coughlan, Z. Mao, M. A. Bevan, and Y. Zheng, Opto-thermophoretic assembly of colloidal matter, *Science Advances* 3: E1700458, 2017.

[8] L. Lin, X. Peng, and Y. Zheng, Reconfigurable opto-thermoelectric printing of colloidal particles, *Chem. Commun.* 53: 7357-7360, 2017.

Resonant laser printing of optical metasurfaces

Xiaolong Zhu[1], N Asger Mortensen[2], Uriel Levy[3], Anders Kristensen[1]

[1]DTU Nanotech, Department of Micro and Nanotechnology, Technical University of Denmark, DK-2800 Kongens Lyngby
[2]Center for Nano Optics & Danish Institute for Advanced Study, University of Southern Denmark, Campusvej 55, DK-5230 Odense M, Denmark
[3]Department of Applied Physics, The Benin School of Engineering and Computer Science, The Center for Nanoscience and Nanotechnology, The Hebrew University of Jerusalem, Jerusalem, 91904, Israel

*Presenting author, E-mail: xizhu@nanotech.dtu.dk

Abstract

Optical metasurfaces realized by the state-of-the-art nanofabrication technologies have offered the control of light with nanoscale metallic or dielectric elements. Most of them rely on the ability to precisely control its individual meta-elements within the subwavelength scale. The absorption in metallic or dielectric elements provides a new route for photo-to-thermal conversions and processing. Here, we introduce a resonant laser printing (RLP) technique as a flexible photo-thermal post-writing technology for mass-customization of optical metasurfaces.

1. Introduction

Optical metasurfaces are designed photonic surface textures which have the capability of manipulating the amplitude, phase, polarization, activity, spin and quantum-entanglement of light. Metasurfaces can be made on metallic as well as dielectric or hybrid materials with the state-of-the-art nanofabrication facilities. Optical properties of metasurfaces are defined by the material composition, geometry, arrangement, orientation, topology and environment of each meta-element. The absorption in metallic or dielectric meta-elements provides an avenue for photo-to-thermal conversions. We developed a resonant laser printing (RLP) technique as a flexible post-writing technology for mass-customization of optical metasurfaces. Strong on-resonance energy absorption under pulsed laser irradiation locally elevates the lattice temperature of individual optical meta-elements in an ultra-short time scale. In the RLP process, rapid melting allows for surface-energy-driven morphology changes and sintering or annealing of individual meta-elements with associated modification of amplitude, phase, polarization, activity, spin and quantum-entanglement of the reflected and transmitted light from the metasurface. By controlling of the RLP process, we can manipulate the material composition, geometry, arrangement, orientation, topology and environment of the meta-elements on demand and with a very high precision. Combined with the use of prefabricated large-area metasurface templates, RLP is a promising approach for next-generation low-cost optical metasurfaces for advanced applications.

2. Result and discussion

Photonic materials including metamaterials, photonic crystals and plasmonic materials drive our colorful world from medieval stained glass, strong lasers, and fast communications to interactive smart screens. Current technological breakthroughs in this information age, such as virtual reality, internet of things and quantum computers, extensively rely on sensing and manipulating photons in a desired fashion. Enabled by nano and microfabrication technologies, nanophotonics research offers the ultimate control of light with the help of nanoscale metallic or dielectric nanostructures. For instance, optical metasurfaces rely on the ability to precisely control its individual meta-elements, including material and morphology composition, geometry, orientation, and the mutual position of them. The common realization of metasurfaces by complex and expensive nanofabrication techniques is an obstacle to reach consumer products.

The heat generated in the nanoscale meta-elements by photo-to-thermal conversions and processing can be significantly enhanced by the confinement of the photon energy. A resonant laser printing (RLP) technique was recently developed and implemented as a flexible photo-to-thermal post-writing technology for mass-customization of optical meta-surfaces (Figure 1A). This was demonstrated for both metallic [1], and high-index dielectric metasurfaces [2]. Combined with the use of large-area metasurface templates, RLP can be used as a promising approach in the future for low-cost customized photonic devices with subwavelength elements for applications in areas such as color generations, holograms, anti-counterfeit and virtual reality [3].

One example is RLP post-processed Al metasurfaces with morphology-dependent resonances, where rapid photo-thermal melting of the metallic nanostructure allows for their morphology changes with associated spatially

modification of transmittance. With the excitation of the surface plasmon resonances, the plasmon-enhanced photothermal melting ensures that the writing process only takes place at the plasmonic metasurface within the focal plane, causing a strong heat power confined at the interface and thus decreases the power consumption and increases the printing resolution. Figure 1B shows the concept of laser printed flat optics, illustrated by the writing of a Fresnel zone plate (FZP) in a plasmonic template constituted by hybridized nanodisk and nanohole arrays [4].

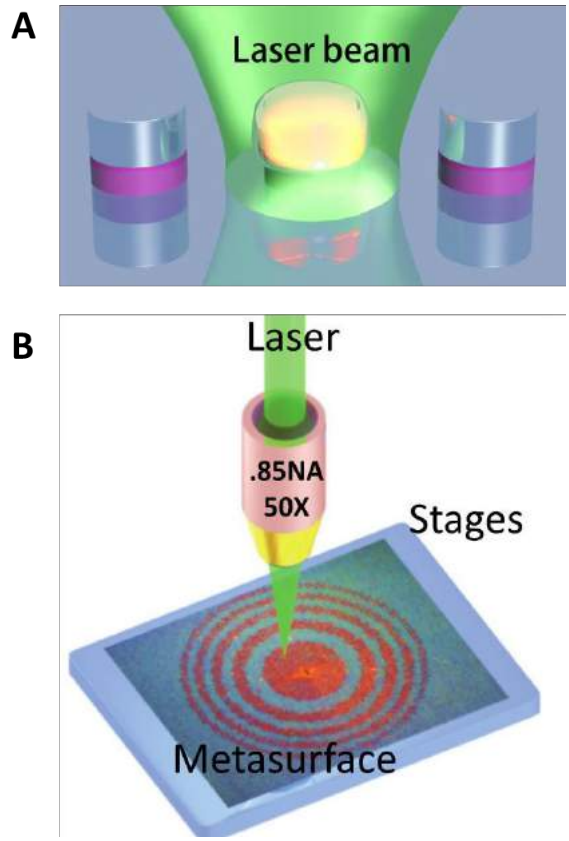


Figure 1: A. The concept of RLP, which is enforced by photo-to-thermal conversions and processing. B. Schematic setup and laser printing of the ultrathin metalens onto plasmonic metasurface templates.

3. Conclusions

In conclusion, as an alternative process to using state-of-the-art and expensive fabrication methods, we demonstrate that RLP is a powerful tool for the fabrication of ultrathin multi-functional metasurfaces. The concept of RLP makes the meta-optics closer to reality by providing a path for mass-production and ready-for-applications processes. This may pave the way of ultrathin flat optics into consumer products in the near future.

Acknowledgements

This work was supported by the European Commission project CHROMAVISION (Grant Agreement No. 665233) and IZADI-NANO2INDUSTRY (Grant Agreement No. 686165), and by the International Network Programme of the Danish Agency for Science, Technology and Innovation (1370-00124Band 4070-00158B). N.A.M. is a VILLUM Investigator (grant No. 16498) and X.Z. is funded by VILLUM Experiment (grant No. 17400), both supported by VILLUM FONDEN.

References

[1] Zhu, X.; Vannahme, C.; Højlund-Nielsen, E.; Mortensen, N. A.; Kristensen, A. Plasmonic colour laser printing. Nat. Nanotechnol. 2015, 11, 325−329.

[2] Zhu, X.; Yan, W.; Levy, U.; Mortensen, N. A.; Kristensen, A. Resonant-laser-printing of structural colors on high-index dielectric metasurfaces. Sci. Adv. 2017, 3, e1602487.

[3] Zhu, X.; Hedayati, M. K.; Raza, S.; Levy, U.; Mortensen, N. A.; Kristensen, A. Digital resonant laser printing: Bridging nanophotonic science and consumer products. Nano Today 2018, 18.

[4] Carstensen, M. S.; Zhu, X.; E. I., Oseze; Levy, U.; Mortensen, N. A.; Kristensen, A. Holographic resonant laser printing of flat optics using template plasmonic metasurfaces. ACS Photonics 2018, 5, in press.

Narrow-band thermal emitter by coupling of cavity and Tamm plasmon resonances

Zhiyu Wang[1], J. Kenji Clark[1], Ya-Lun Ho[1], Bertrand Vilquin[2], Hirofumi Daiguji[1], Jean-Jacques Delaunay[1]

[1]School of Engineering, The University of Tokyo, Tokyo, Japan
[2]Université de Lyon, École centrale de Lyon, Institut des nanotechnologies de Lyon, Ecully, France
*corresponding author, E-mail: jean@mech.t.u-tokyo.ac.jp

Abstract

By coupling an optical cavity mode to a Tamm plasmon mode, an efficient and spectrally selective thermal emitter is realized. The proposed structure, which can be fabricated without the need for patterning steps, produces narrow-band thermal emission with both low angular dependence and low background emission. A thermally induced emittance peak is produced with a maximum peak emittance of ~0.90 and a full width at half maximum of 54 nm.

1. Introduction

Narrow-band light sources covering the mid-infrared fingerprint region have received considerable attention due to their potential in sensing and spectrometry applications [1]. In particular, nano-patterned structures taking advantage of the properties of surface plasmons have been used to design thermal emitter with narrow-band emission [1-4]. However, it is still a challenge to realize efficient narrow-band emission with little angular dependence and high spectral selectivity (low background emission). Additionally, the requirement for the patterning of highly controlled nanostructures is detrimental for the development of practical devices. In contrast to conventional surface plasmons, Tamm plasmons can sustain strong and spectrally selective absorption in multilayer structures without the need for any momentum matching structures (periodicity, edges, trenches, etc.) [5]. Recently, a Tamm plasmons (TP) structure was demonstrated as a narrow-band thermal emitter in the mid-infrared range [4] and it had a resonance quality factor (Q-factor) approximately double the best localized surface plasmons-based thermal emitters [6]. Here, we investigate a novel structure for use in narrow-band thermal emission by incorporating an optical cavity into a TP structure [7]. This hybrid structure is designed to couple a cavity mode to a Tamm plasmon mode with the purpose of improving the spectral selectivity and wavelength controllability of the thermal emission peak. At the resonance wavelength of this TP-cavity coupled mode, incident light is trapped in the optical cavity and absorbed by the metal layer of the TP, resulting in near unity absorptance. The optical cavity sustains a large electric field enhancement (i.e., a large stored energy), thus contributing to the hybrid structure having a higher Q-factor than a pure TP structure (without cavity). Additionally, the hybrid structure enables the design of a wide range of resonance wavelengths simply by adjusting the optical cavity thickness. Finally, the fabrication of the proposed hybrid structure does not require any lithography or patterning steps, and therefore, practical thermal emitters can be designed and fabricated using the proposed hybrid structure.

2. Results and Discussion

The hybrid structure consists of an optical cavity incorporated within a Tamm plasmon structure (distributed Bragg reflector with a bottom mirror), as shown in Figure 1. The distributed Bragg reflector is placed at the top of the structure and provides a high reflectance with a wide stop band. An opaque metal mirror is used at the bottom of the structure. The optical cavity is therefore sandwiched between the metal mirror and the distributed Bragg reflector. The thicknesses of the hybrid structure are optimized to allow the coupling of the optical cavity mode and the Tamm plasmon mode, thus creating a coupled resonance with a strong and sharp absorption peak. At the resonance wavelength of this coupled mode, incident light from the distributed Bragg reflector of the TP is stored in the optical cavity without leakage and absorbed by the bottom metal of the TP, resulting in near unity absorptance. As seen in Figure 1 (b), the optical cavity sustains a large electric field enhancement (i.e., a large stored energy), which contributes to the hybrid mode having a higher Q-factor than a pure TP mode (without cavity). Additionally, the hybrid structure enables the design of a wide range of resonance wavelengths simply by adjusting the optical cavity thickness.

Upon thermal excitation of the hybrid structure at a temperature of 150°C, the hybrid structure shows an emittance peak of ~0.90 with a Q-factor as large as 88. The performance of the proposed hybrid structure exceeds that of reported plasmon-based structures. The Q-factor of 88 is larger than that of pure Tamm plasmon thermal emitters (Q-factor = 30 at 4 μm) [6] by a factor of approximately

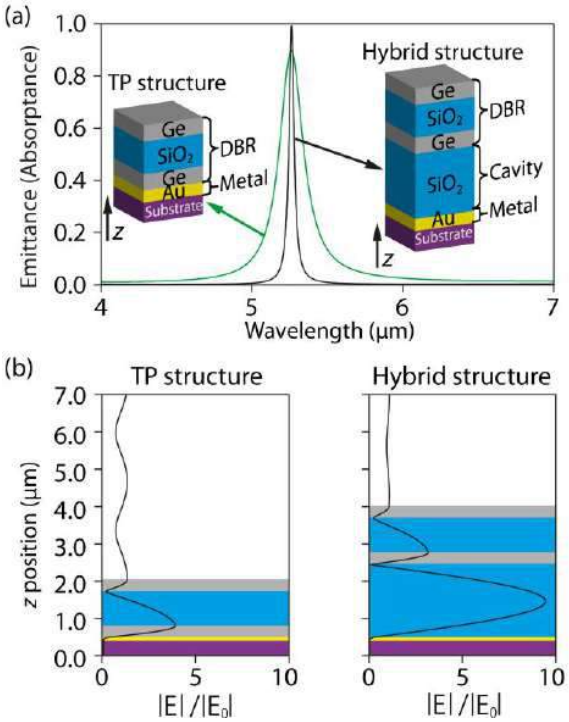


Figure 1: (a) Emittance of the proposed structure together with the emittance of a pure plasmon structure. (b) Distribution of the electric field for the pure Tamm plasmon structure (left) and the proposed hybrid structure (right).

three, and is also larger than that of conventional surface plasmon-based thermal emitters [1-4]. Experimental results will be discussed at the conference.

3. Conclusions

A narrow-band thermal emitter made of an optical cavity inserted between a distributed Bragg reflector and a Au film was studied numerically and experimentally. The proposed structure realized the coupling between the Tamm plasmons mode sustained by the Au film and the distributed Bragg reflector and the cavity modes of the optical cavity. The coupled mode of the proposed structure produced a sharp and large reflectance dip in the mid-infrared region. The fabricated structure realized a narrow-band and high-emittance thermal emitter with low angular and polarization dependence. The emittance of the structure was as high as 0.90 at 4.731 μm with a *Q*-factor of ~88.

Acknowledgements

This work was supported through Japan Society for the Promotion of Science (JSPS) KAKENHI Grant Numbers (17H03229, 17K18867), and JSPS Core-to-Core Program (Advanced Research Networks type A).

References

[1] A. Lochbaum, Y. Fedoryshyn, A. Dorodnyy, U. Koch, C. Hafner, J. Leuthold, On-chip narrowband thermal emitter for mid-IR optical gas sensing, *ACS Photonics* 4: 1371−1380, 2017.

[2] D. Costantini, A. Lefebvre, A.-L. Coutrot, I. Moldovan-Doyen, J.-P. Hugonin, S. Boutami, F. Marquier, H. Benisty, J.-J. Greffet, Plasmonic metasurface for directional and frequency-selective thermal emission, *Phys*. *Rev*. *Appl*. 4: 014023, 2015.

[3] Z. Wang, J. K. Clark, L.-C. Huang, Y.-L. Ho, J.-J. Delaunay, Plasmonic nanochannel structure for narrow-band selective thermal emitter, *Appl*. *Phys*. *Lett*. 110: 251102, 2017.

[4] T. D. Dao, K. Chen, S. Ishii, A. Ohi, T. Nabatame, M. Kitajima, T. Nagao, Infrared perfect absorbers Fabricated by colloidal mask etching of Al−Al2O3−Al trilayers, *ACS Photonics* 2: 964−970, 2015.

[5] M. Kaliteevski, I. Iorsh, S. Brand, R. A. Abram, J. M. Chamberlain, A. V. Kavokin, I. A. Shelykh, Tamm plasmon-polaritons: Possible electromagnetic states at the interface of a metal and a dielectric Bragg mirror. *Appl*. *Phys*. *B* 76: 165415, 2007.

[6] Z.-Y. Yang, S. Ishii, T. Yokoyama, T. D. Dao, M.-G. Sun, P. S. Pankin, I. V. Timofeev, T. Nagao, K.-P. Chen, Narrowband wavelength selective thermal emitters by confined Tamm plasmon polaritons, *ACS Photonics* 4: 2212−2219, 2017.

[7] Z. Wang, J. K. Clark, Y.-L. Ho, B. Vilquin, H. Daiguji, J.-J. Delaunay, Narrow-band thermal emission realized through the coupling of cavity and Tamm plasmon resonances," submitted in *ACS Photonics*, February 2018.

Structural Color for Displays and Imaging

Hybrid organic and plasmonic systems for smart surfaces and energy-efficient displays

Magnus P Jonsson

Laboratory of Organic Electronics, Department of Science and Technology, Linköping University, Sweden
E-mail: magnus.jonsson@liu.se

Abstract

In this presentation, I will focus on our recent development of switchable plasmonic surfaces for reflective-based electronic paper in colour.

Nanostructured metallic surfaces interact strongly with light through excitation of charge oscillations known as plasmons. In our work, we have utilized this for applications such as biosensors,[1,2] optothermal management,[3,4] and smart surfaces with switchable colored reflection.[5] I will focus on the latter in this presentation, based on the possibility of plasmonic systems to provide highly reflective surfaces with distinct colors. However, while suitable for high-resolution color printing, these plasmonic metasurface are typically static and not possible to modulate after fabrication. By contrast, electrochromic polymers such as PEDOT:PSS (poly[3,4-ethylenedioxythiophene] polystyrene sulfonate) provides optical transparency that can be modulated *in situ*. By combining the intense colors of plasmonic surfaces and the dynamic transparency of electrochromic polymers, it is possible to create hybrid devices with dynamic control of the plasmonic colors. In this work, we show that the plasmonic metasurfaces can be produced entirely based on abundant metals instead of the commonly used metals gold and silver.[5] For this, we use an aluminum mirror, a dielectric spacer and a thin copper film perforated with an array of plasmonic nanoholes. The generated colour could be controlled by changing the thickness of the dielectric spacer, leading to a wide gamut covering 27% of the standard RGB. Patterning the metasurfaces into RGB pixels enabled high quality reproductions of famous as well as less famous color photographs. Finally, we used screen-printing to coat the metasurfaces with a thin layer of PEDOT:PSS. This made it possible to dynamically control the reflection *in situ*. The concept opens up for sustainable energy-efficient reflective displays in color.

Acknowledgements

The presented research on plasmonic displays was performed in collaboration with Andreas Dahlin's group at Chalmers University of Technology, rdot AB, and RISE Acreo. We acknowledge financial support by the Swedish Foundation for Strategic Research, the Wenner-Gren Foundations, the Chalmers Nanoscience and Nanotechnology Area of Advance, and the Swedish Government Strategic Research Area in Materials Science on Functional Materials at Linköping University (Faculty Grant SFO-Mat-LiU No 2009 00971).

References

[1] DNA translocations through solid-state plasmonic nanopores, F. Nicoli, D. Verschueren, M. Klein, C. Dekker and M.P. Jonsson, *Nano Letters* 2014, 14, 6917–6925

[2] MP Jonsson, P Jönsson, AB Dahlin and F Höök, F, Supported Lipid Bilayer Formation and Lipid-Membrane-Mediated Biorecognition Reactions studied with a new Nanoplasmonic Sensor Template, *Nano Letters* 2007, 7, 3462-3468

[3] D. Tordera, D. Zhao, A.V. Volkov, X. Crispin, and M.P. Jonsson, Thermoplasmonic semitransparent nanohole electrodes, *Nano Letters* 2017, 7 (5), 3145–3151

[4] M. Chaharsoughi, D. Tordera, A. Grimoldi, I. Engquist, M. Berggren, and M.P. Jonsson, Hybrid Plasmonic and Pyroelectric Harvesting of Light Fluctuations, *in revision*

[5] K. Xiong, D. Tordera, G. Emilsson, O. Olsson, U. Linderhed, M.P. Jonsson, and A.B. Dahlin, Switchable Plasmonic Metasurfaces with High Chromaticity Containing Only Abundant Metals, *Nano Letters* 2017, 17 (11), 7033–7039

Plasmonic Pixel: Progress in nanoimprint lithography

Faris Shahidan[1], Jingchao Song[1], Evgeniy Panchenko[1], Paul Mulvaney[2], Timothy D James[1], and Ann Roberts[1*]

[1]School of Physics, The University of Melbourne, 3010, Australia
[2]ARC Centre of Excellence in Exciton Science, Bio21 and School of Chemistry, The University of Melbourne, 3010, Australia
*corresponding author, E-mail: ann.roberts@unimelb.edu.au

Abstract

The use of plasmonics to generate structural color has attracted considerable recent attention. Her we demonstrate the use of nanoimprint lithography to produce 'plasmonic pixels' producing non-diffractive color. Both polarization-sensitive and polarization-insensitive designs are presented. The extension of the plasmonic pixel concept to semiconductor devices will also be discussed.

1. Introduction

The use of color is widespread in signage, consumer goods, clothing and in various chemical and other sensors. Objects are generally colored by using pigments producing a diverse, controllable color palette that can be incorporated through coatings, printing, paints and dyeing into and onto various materials. The use of pigments, however, adds to fabrication complexity through the introduction of additional chemical components. Pigments can also be 'fugitive' – their appearance changes on exposure to various environmental conditions such as light, temperature, humidity, temperature and pollution. Finally, the use of multiple colors in standard printing processes can lead to registration defects. As a result, there is an ongoing interest in structural approaches to surface coloration for applications ranging from use in consumer goods, through to new types of colorimetric sensors.

2. Non-diffractive structural color

There is considerable interest, therefore, in new methods for producing color through structuring the material. Saturated colors produced by diffraction gratings are very familiar and form the basis of widely used security features on credit cards and banknotes. The vivid colors of butterflies and beetles stimulated initial research into the use of nano- and microstructures to generate color [1]. This initially involved the production of three-dimensional photonic crystals composed of dielectric materials. Not only are these structures challenging to fabricate, photonic crystals and one- and two-dimensional gratings exhibit a strong angular dependence. It is well known, on the other hand, that metallic nanoparticles can produce strongly wavelength-dependent scattering [2,3]. In the case of asymmetric particles such as rods, this scattering also depends on polarization. The use of these localized, rather than collective, resonances of metallic particles and holes provides an avenue for the production of non-diffractive, angle-robust color [4]. We have recently demonstrated [5] the production of polarization dependent, but angle-insensitive, color. This involved using a top-down nanofabrication approach to produce colored 'plasmonic pixels' composed of varying numbers of smaller elements containing characteristic nanoscale features. The fundamental building block is a metallic nanorod 'floating' (although supported by a surrounding dielectric) above its complementary metallic screen. Reference [5] demonstrated a prototype device fabricated using electron beam lithography to define the nanostructures. As pointed out in [5], however, the approach is compatible with nanoimprint lithography and here we present progress toward scalable fabrication of the plasmonic pixel.

3. Fabrication

The resist, PMMA A4 in anisol, was spin-coated onto a 4" Si wafer to a thickness of 200 nm which was then baked for 5 minutes at 180˚C. Electron Beam Lithography to a dose of 850 μC/cm^2 was used to pattern the resists to produce 20 ×20 μm arrays of rods and squares of various lengths and pairs of nanorods. The nominal lengths of rods fabricated ranged from 100 to 250 nm, along with squares of nominal side length from 60 to 180 nm. The periodicity of the fabricated structures was designed to vary from 100 nm to 300 nm. A hard mask produced by deposition of 5nm Cr and 60 nm Al was etched with a pseudo-Bosch process to maintain smooth sidewall structures for 14-20 s. The metal masks were subsequently stripped. Different regions of the master are shown in Figure 1 (a), (c) and (e). The Si masters were then used to create imprints into PMMA via Thermal Nanoimprint Lithography using a Nanonex NX-B200 at a temperature of 130˚C and pressure of 300 psi for 120 s. A 50 nm film of Ag was then evaporated onto the imprinted structures.

4. Results and Discussion

The resulting structure was assessed by cutting a profile using focused ion beam milling and analyzing the resulting

structure using SEM. This verified a 'plasmonic pixel' floating dipole geometry of the metallized structure and an imprint depth of around 130 nm. The results showing typical scanning electron microscope images of one region of the master and corresponding imprint are shown in Fig. 1.

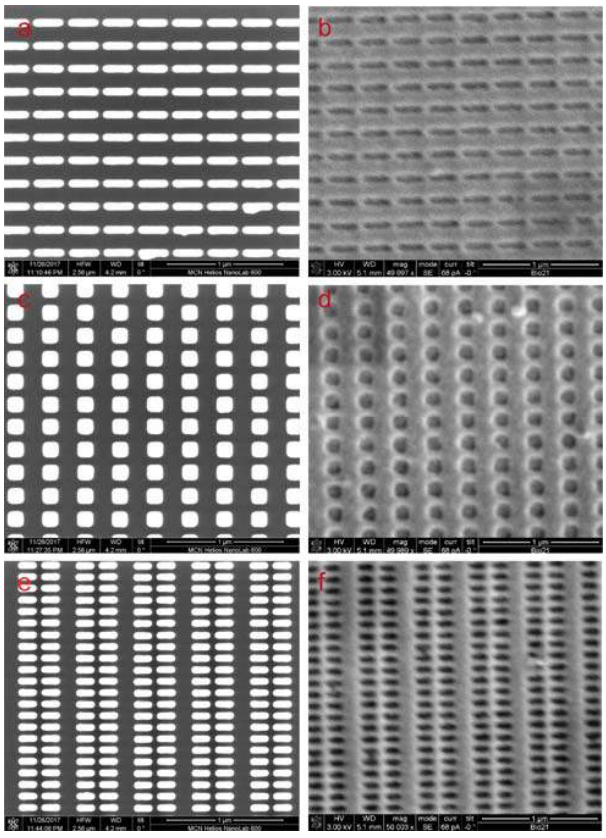


Figure 1: SEM images showing example Si masters (a), (c) and (e) produced using EBL and resulting nanostructures (b), (d) and (f) in PMMA imprinted using nanoimprint lithography. (Scale bars 1 μm).

Images of the Ag coated imprinted structures were obtained using a bright field microscope with polarized light. The results are shown in Fig. 2. The palettes at the top and bottom consist of rods and pairs of rods, respectively. The differences in color are a result of different rod lengths and spacings as well as periodicity. In the upper palette, the rod dimensions varied from 100 nm to 250 nm in length and 100 nm to 300 nm in periodicity with fixed width of 50 nm. Dimer separations down to 20 nm could be resolved. A color palette can be easily seen when the rod structures are viewed with light polarized parallel to the long axis of the rods. As the polarization is rotated, however, the colors are no longer apparent, consistent with the observations of reference [5]. Similarly, a polarization-tunable color palette associated with the dimer arrays can also be seen in Fig. 2 in the lower region. The central palette of Fig. 2 corresponds to squares. As expected, the symmetry of the structure produces results with little apparent sensitivity to polarization.

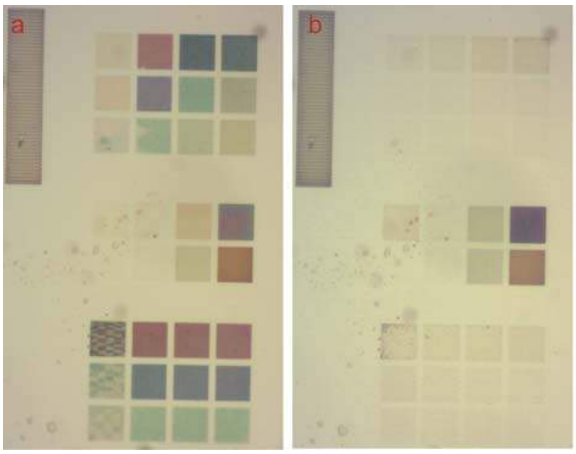


Figure 2: Bright field images of the structures shown at right obtained with horizontally (left) and vertically (right) polarized light. The palette at the top corresponds to the imprinted and metalized rods similar to those shown in Figure 1(b), center to squares similar to Figure 1(d) and bottom rod dimers similar to Figure 1(f). Squares are 20μm on a side.

5. Conclusion

The results of Fig. 2 demonstrate that nanoimprint lithography can be used to produce plasmonic pixel structures using scalable embossing approaches. Current research is aimed at quantifying these promising preliminary results. We will also discuss research aimed at integrating the plasmonic pixel design into semiconductor devices.

Acknowledgements

This work was performed in part at the Melbourne Centre for Nanofabrication (MCN) in the Victorian Node of the Australian National Fabrication Facility (ANFF). The authors acknowledge the financial support of the Australian Research Council Linkage Projects scheme (LP160100054).

References

[1] A. R. Parker, 515 million years of structural colour, *J. Opt. A: Pure Appl. Opt.* **2:** R15-R28 (2000).

[2] I. Freestone, N. Meeks, M. Sax and C. Higgitt, The Lycurgus Cup — A Roman nanotechnology, *Gold Bulletin*, 40: 270- 277 (2007).

[3] T. Huang, X.-H. N. Xu, Synthesis and characterization of tunable rainbow colored colloidal silver nanoparticles using single-nanoparticle plasmonic microscopy and spectroscopy, *J. Mater. Chem*., 20: 9867-9876 (2010).

[4] A. Kristensen, J. K. W. Yang, S. I. Bozhevolnyi, S. Link, P. Nordlander, N. J. Halas and N. A. Mortensen, Plasmonic colour generation, *Nature Reviews Materials,* 2: 16088(2017).

[5] T.D. James, P. Mulvaney and A. Roberts, The Plasmonic Pixel: Large Area, Wide Gamut Reproduction using Aluminum Nanostructures, *Nano Lett*., 16: 3817-3823 (2016).

Metal free, X-ray fabricated metamaterials reproduce full CYMK chromaticity system with 80 nm spatial resolution.

M. Bonifazi[1], **V. Mazzone**[1], **A. Fratalocchi**[1]

[1]PRIMALIGHT, Faculty of Electrical Engineering; Applied Mathematics and Computational Science, King Abdullah University of Science and Technology (KAUST), Thuwal, Saudi Arabia
andrea.fratalocchi@kaust.edu.sa

Abstract— We present new types of complex metamaterials obtained by suitably processing a transparent dielectric with high fluency hard X-rays. We investigated their properties both experimentally and by means of FDTD analysis. We discuss experimental applications for creating structural colors, reproducing the full spectrum of Cyan, Yellow, Magenta, Black (CYMK) with a resolution down to 80 nm. This approach opens an innovative way to engineer nanomaterials with advanced functionalities that can be exploited for several applications in many different fields of research.

X-ray interaction with matter is a subject that fascinates scientists since the first x-ray image was captured by chance on a photographic plate in 1895 [1]. Today, the large part of applications of X-rays is still dominated by imaging, ranging from bio-medical diagnostics to the investigation of atomic structures in crystallography [2, 3, 4, 5]. The study of how X-rays can change matter, on the contrary, is still at an embryonic stage of development despite its huge potential [6, 7].
In this contribution we illustrate how to use hard X-rays with high energy to create new types of nanomaterials, which are based on strong X-ray-matter interactions. We will discuss here the first application of this technology in the field of structural coloration, which is today an intense field of research due to the many possible applications that can be enabled by this technology, such as high resolution micro/nano printing, anti-counterfeiting stamps and biomimetic devices [8, 9, 10]. The current state of art in this field of research is dominated my two-dimensional metallic plasmonic metasurfaces, with diffraction limited resolution (140nm) [11]. These structures are based on combinations of noble expensive metals arranged in periodic patterns that are very challenging to scale up and still do not show a complete spectrum of colors.
On the contrary, we will here present experiments showing new X-rays created metamaterials capable of displaying a full spectrum of CYMK colors with a sub diffraction limited resolution as low as 80 nm. As it is possible to notice in Figure 1a, the colors we obtained experimentally form a circle around the white point. This is becouse our approach enables the possibility to reproduce all the chromaticity of the visible spectrum, including black, red and other colors that are normally created in Nature by pigments and not structures.
These colors are also based on fully random three dimensional nanostructures realized in metal-free cheap materials, and at such are easily scaled up.
Figure 1b-c show some experimental results of this technology. To illustrate the capabilities of this technique we printed the letters α and β varying the exposure and design parameters both outside and inside the designs, spanning a wide range of colors, from magenta to black on the left column and from cyan to orange on the right one. It is clear from the SEM images of details provided (Figure 1b, central panels) that the pattern we reproduce follows precisely the profile of the printed image and due to its intrinsic disorder it is not affecting the overall resolution. As a further example of the color and tonal control achieved we printed the word "light" (Figure 1c). The edges of the shapes are neat and sharp and the colors are uniform all over the image.
These features make this technology ideal for real-world applications of structural colors, ranging from nano-imprinting to anti-counterfeiting. Not limited to structural coloration, this approach opens also a compete new way to create nanomaterials with advanced functionalities by exploiting X-Rays and strong light-matter interactions at the Angstrom scale level.

REFERENCES

1. Bertin, E. P., "Principles and practice of X-ray spectrometric analysis", *Springer*,2012.
2. Momose, A., et al, "Phase contrast x-ray computed tomography for observing biological soft tissues", *Nat. Medicine*, Vol. 2, 473-475, 1996.

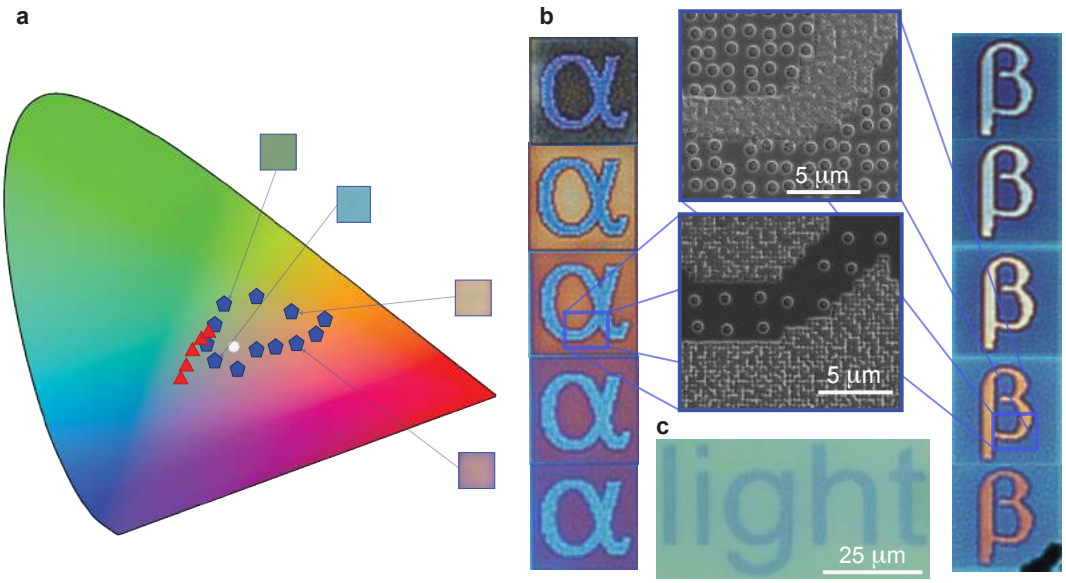


Figure 1: **a** Chromaticity diagram showing the colors obtained from experimental results. **b** Top view images of two letters from the greek alphabet. The sample is nanostructured with two different patterns for the letter and for the background in order to obtain different colors . Results are shown for different doses in the columns on both sides of the panel. SEM details of the sample are shown in the central part of the panel. **c** Top image of the word "light" printed in light blue color.

3. Paunesku, T., et al, "X-ray fluorescence microprobe imaging in biology and medicine", *Juornal of cellular biochemistry*, Vol. 99, 1489-1502, 2006.
4. Bragg, L., "X-ray cristallography" *Scientific American*, Vol. 219, 58-74, 1968.
5. Labelle, J., et al. "Extending the methodology of x-ray crystallography to allow imaging of micrometre-sized non-crystalline specimens", *Nature*, Vol. 400, 342-344, 1999.
6. Koyama, T., et al. "Investigation of ablation thresholds of optical materials using 1-mm-focusing beam at hard x-ray free electron laser", *Optic Express*, Vol. 21, 15,382-15,388, 2013.
7. Hau-Riege, S. P, et al. "Nonequilibrium electron dynamics in materials driven by high-intensity x-ray pulses", *Physical Review*, E 87, 053, 102, 2013.
8. Kats, M. A, et al. "Ultra-thin optical interference coatings on rough and flexible substrates", *Appl. Phys. Lett.*, 105, 131,108, 2014.
9. Shen, Y, et al. "Structural colors from Fano resonances", *ACS Photonics*, Vol. 2, 27-32, 2015.
10. Galinski, H, et al. "Scalable, ultra-resistant structural colors based on network metamaterials", *Light: Science and Applications*, 6, e 16, 233 , 2017.
11. Kristensen, A., et al. "Plasmonic color generation", *Nature Review Materials*, 2, 16,088, 2016.

Skin-like Full-Color Angle Independent Plasmonic Reflective Displays

Daniel Franklin, Debashis Chanda

Physics
NanoScience Technology Center
CREOL, College of Optics and Photonics
University of Central Florida, Florida, USA

Keywords: Full-color, Plasmonics, Reflective displays

Abstract

Tuning plasmonic light absorption with liquid crystal (LC), the color reflected from a nanostructured surface can be changed as a function of voltage. The engineered plasmonic surface allows complete LC reorientation and maximum overlap between plasmonic fields and LC, enabling large tunability across the entire visible spectrum.

1. Introduction

The range of colors and hues in the natural world are amazing, but perhaps even more astonishing is the ability of certain species to actively mimic. The underlying mechanisms are as varied as the species, but can be broken into two main categories: pigmentation and structural color. In pigment producing cells, molecules absorb part of the visible spectrum while leaving the rest to be scattered back to the viewer. Structural color, on the other hand, is produced through combinations of reflection, scattering and interference within a single or system of cells. Of these two classes, structural color serves as the primary color generating mechanism in several extremely dynamic species. Cephalopods, for example, cover vast swaths of color within milliseconds as can be observed. The key aspect of these color displays in nature is color generation on a thin, flexible, stretchable, conformally mapped curvilinear surface. In contrast, state-of-the-art manmade displays are still vastly rigid, brittle and bulky in nature. It's with cephalopods in mind that we propose a flexible reflective metasurface display in which each pixel can be tuned across the visible spectrum.

The majority of current reflective display technologies are based on absorption, employing polymeric color filters or charged pigmented beads. However, these pigment based color technologies are susceptible to high intensity light exposure, require multilayer processing for individual pixels, and are limited in resolution due to macroscopic pixel size. In response, structural color from engineered plasmonic surfaces is a durable and high resolution candidate for future display technologies[1-4]. A key aspect of these devices is scalability of the optical response with structure dimensions. However, the ability to actively tune (post-fabrication) the optical response with the surrounding media's index truly sets plasmonic color apart from typical pigmented color. One popular technique is to utilize the anisotropy and reconfigurability of liquid crystals (LC) to change the dielectric constant surrounding the metallic nanostructure, thereby shifting the plasmonic resonance's spectral location[5-11]. Till date, many of these examples deal with infrared or terahertz frequencies[7,10,12], and those that are in the visible regime remain limited to a small range of color tunability due to modest shifts (~10-40 nm) in plasmon resonance, making them unsuitable for display applications [6,8,11]. Also, creation of black (dark state), needed for any display, remained outside of plasmonic color generation scheme due to inherent narrowband plasmon resonances.

In our preliminary work, we demonstrate a LC tunable plasmonic reflective pixel where color of a nanostructured metasurface is changed continuously as a function of applied voltage. Using nano imprint lithography (NIL) and flexible polymer substrates, the engineered metasurface allows complete LC reorientation and maximum overlap between the plasmonic fields and LC, enabling large tunability across the entire visible spectrum for the first time [13]. Using NIL to produce the plasmonic structure over large areas, we can bypass expensive and tedious electron-beam (EBL) or deep-UV lithography techniques used in fabricating many previously reported plasmonic devices[4,14-16] as well as achieve flexible displays which so far reamined outside of conventional display technologies. This in combination with ultrafast direct laser writing (DLW), we can incorporate multiple features at varying size scales

into our master patterns. A single device master can include arbitrarily pixelated plasmonic metasurface, microscopic LC cell spacers, and nanoscale alignment gratings.

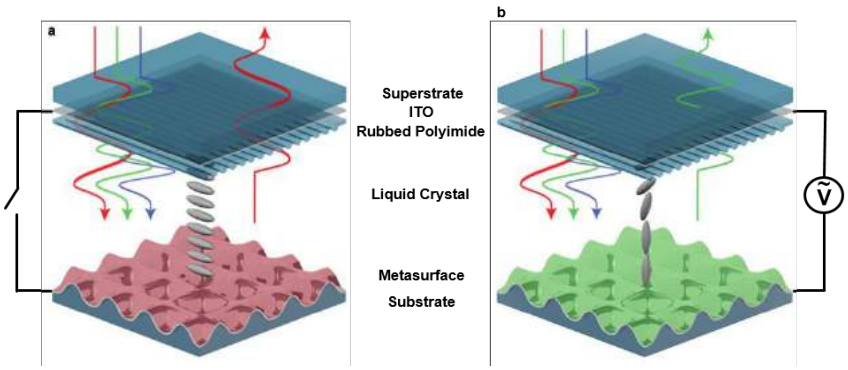


Figure 1 | Liquid Crystal Tunable Imprinted Plasmonic Surface. a, Schematic of metasurface-liquid crystal cell with impinging white light. Light transmits through the superstrate and liquid crystal layers to interact with the reflective plasmonic surface. The metasurface selectively absorbs light while reflecting the rest back out of the device. The wavelength of this absorption depends on the liquid crystal orientation near the interface which in turn depends on the voltage applied across the cell. **b,** Voltage across the cell reorients the liquid crystal and changes the wavelengths of absorbed light. Copyright: *Nature Communications (Vol. 6, pp. 7337, 2015)*

One such master can produce 100's of polymeric imprinting stamps, and one such stamp can produce 1000's of imprints without any noticeable pattern degradation. NIL has also been translated to roll-to-roll processing which shows the entire fabrication process can be scaled to factory norms.

2. Fundamental Principles

Plasmonics offer unique properties which are not present in natural materials. Electromagnetic properties of these artificial materials composed of metal/dielectric composites are governed by their complex electric permittivity and magnetic permeability. When excited with incident light at a resonant frequency, such plasmonic surfaces produce localized and/or propagating surface plasmons, the fields of which penetrate tens of nanometers into the surrounding medium. The tightly focused evanescent fields of the surface plasmon resonance (SPR) are extremely sensitive to the surrounding medium's dielectric constant. By using nematic LCs, the dielectric constant in the region of the plasmonic field can be modulated by the LC's order parameter, which in turn is controlled through an external electric field. This changes the effective index experienced by the metasurface and shifts the spectral location of the plasmonic absorption. If performed in the visible spectrum, this results in a voltage controlled, color tunable reflective surface.

2.1 Preliminary Device

Figure 1 shows an illustration of the preliminary LC-plasmonic coulpled system. The metasurface consists of a shallow periodic array of nanowells which is coated with a continuous layer of aluminum.

The plasmonic suface is then used to complete a LC cell, in which the nanostructured aluminum serves as a bottom electrode. The other half of the LC cell consists of an indium tin oxide (ITO) coated glass substrate, a polyimide alignment layer rubbed parallel to metasurface grating vector, and chopped silica spacers. A high birefringence (Hi-Bi) LC is placed inside the cell in direct contact with the aluminum metasurface. Unpolarized white light is transmittted through the top glass and LC layers and coupled to plasmonic modes on the aluminum metasurface. The spectral location of these surface plasmon resonances (SPR) is dependent on the surrounding dielectric constant and is determined by the LC's orientation, which in turn, is controlled through an applied voltage. Light which is not absorbed by the metasurface is reflected back out of the LC cell to create a visible color. Figures 1a-b illustrate a single pixel as the LC is reoriented between its two extrema and the resulting reflective color change. The range of the plasmonic tunability is proportional to the LC's birefringence, hence we use a commercially available Hi-Bi LC (LCM1107, LC Matter Corp.) with n_e=1.97 and n_o=1.55, with a resultant high birefringence of 0.45. The vertical electrode configuration allows for the plasmonic metasurface to serve as an electrode. This also increases the ability of an applied voltage to reorient the LC near the metasurface as compared to the fringe fields generated by an in-plane-switching device. With

this electrode configuration, the voltage OFF-state LC alignment must be parallel (homogeneous) to the plasmonic surface, allowing reorientation to occur with an applied field. This, therefore, places constraints on the nanostructure dimensions and materials. It has been shown that the orientation of LC around a nanostructure is highly dependent on the space in which it is confined, i.e., if the well depth-to-diameter ratio is too large, the LC align vertically (homeotropic alignment) inside the holes which inhibits re-alignement and tunability with an applied field[17]. Various low loss plasmonic metals, such as silver[18], exhibit homeotropic alignment due to surface energy, prohibiting reorienation and tunability with an applied field. Also, the intrinsic intraband absorption of gold in visible spectral domain makes it unsuitable for visible color. For these reasons, aluminum is preferred as the tunable plasmonic metasurface, which has been shown to have degenerate planar alignment[19] without intrinsic visible domain absorption.

2.2 Color Tunable Images

To emphasize the display potential of these metasurfaces, the resultant color palette is exploited to form color tunable images. Figure 2 (a-d) shows 0.75 mm x 1 mm reflective optical images of the Afghan Girl (National Geographic Society), taken with a 4x objective, while the singular sample is tuned through 0-10 V/μm of applied voltage. From the Afghan Girl image, it is evident that the color from nanostructures with different periodicity saturate at different voltages. For example, the background saturates to its final color (green) at 2.5 V/μm where the shawl saturates (to red/pink) at 10 V/μm. This can be attributed to the surface anchoring force dependence on topography, which varies with the periodicity of the metasurface. Inset 6(e) shows an enlarged image using a 10x objective where 10 μm x 10 μm pixels can be seen in the following SEM subfigures (Fig. 2(f-h)) as 2D gratings of varing periods. In this example, the pixelated surface is singulary addressed and therefore limited to display one image. Further addressing of each pixel based on a standard addressing scheme will enable the display of video. Liquid crystals offer the added benefit of millisecond-scale response times needed for high temporal resolution video. While Hi-Bi liquid crystals tend to have increased viscosities and decreased reorientation times compared to standard liquid crystals, the system in question can complete voltage cycles under 90 ms. Other systems for active structural color, such as electroactive polymers[20] and electric/magnetic ink[21], often require seconds to tens of seconds to change colors, severely limiting their use in displays and other electro-optic devices.

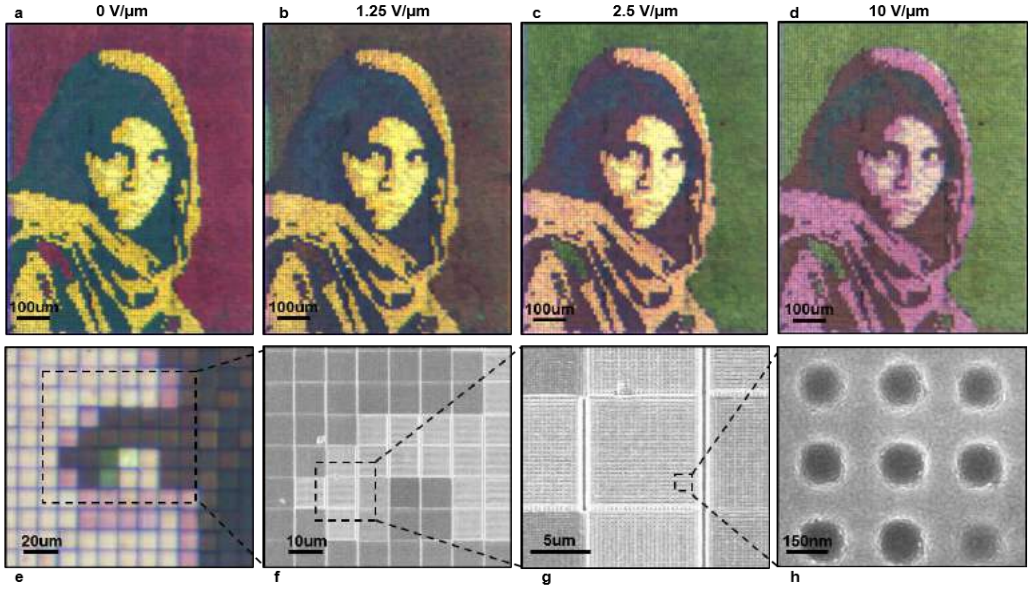


Figure 2 | Dynamic color tuning of arbitrary images. a-d, Optical micrographs of a singular Afghan Girl image (National Geographic Society) as a function of applied electric field. Nanostructure periods are chosen so colors match the original photograph at color tuning saturation, 10 V/μm. Defects due to fabrication errors have been replaced by nearest neighbors. **e,** Optical micrograph at 10 V/μm with 10x objective shows pixilation of the image. **f-h,** SEM images of the sample before fabrication into a liquid crystal cell. The series shows the constituent nanostructure of individual pixels. Copyright: *Nature Communications (Vol. 6, pp. 7337, 2015)*

3. Conclusions

Imagine improving a display's resolution

three-fold with the same back panel technology already in mass production. By implementing state-of-the-art liquid crystal and plasmonics research, the color reflected from the nanostructured surface can be tuned across the visible spectrum as a function of voltage. By using nanoimprint lithography (NIL) and flexible polymer substrates, the engineered plasmonic surface allows complete LC reorientation and maximum overlap between plasmonic fields and LC, enabling large tunability across the entire visible spectrum for the first time. This eliminates the need for static color filters and the standard subpixel display architecture. Along with pixels close in size to the optical resolving limit, the display has demonstrated an astonishing 1,814 dots per inch (DPI) as compared the 401 DPI of the iPhone 6s Plus retina display, a 452% improvement**.**

REFERENCES

1 Chanda, D. *et al.* Coupling of plasmonic and optical cavity modes in quasi-three-dimensional plasmonic crystals. *Nature communications* **2**, 479, doi:10.1038/ncomms1487 (2011).

2 Kumar, K. *et al.* Printing colour at the optical diffraction limit. *Nat Nanotechnol* **7**, 557-561, doi:10.1038/Nnano.2012.128 (2012).

3 Gordon, J. A. & Ziolkowski, R. W. Colors generated by tunable plasmon resonances and their potential application to ambiently illuminated color displays. *Solid State Commun* **146**, 228-238, doi:DOI 10.1016/j.ssc.2007.08.046 (2008).

4 Ellenbogen, T., Seo, K. & Crozier, K. B. Chromatic plasmonic polarizers for active visible color filtering and polarimetry. *Nano letters* **12**, 1026-1031, doi:10.1021/nl204257g (2012).

5 Khoo, I. D., A ; Liou, J; Stinger, MV ; Huang, JB; Ma, Y. Liquid Crystals Tunable Optical Metamaterials. *IEEE JOURNAL OF SELECTED TOPICS IN QUANTUM ELECTRONICS* **16**, 410-417, doi:10.1109/JSTQE.2009.2032246 (2010).

6 Hao, Q. Z. *et al.* Frequency-addressed tunable transmission in optically thin metallic nanohole arrays with dual-frequency liquid crystals. *J Appl Phys* **109**, doi:10.1063/1.3581037 (2011).

7 Shrekenhamer, D., Chen, W. C. & Padilla, W. J. Liquid crystal tunable metamaterial absorber. *Physical review letters* **110**, 177403 (2013).

8 Kossyrev, P. A. *et al.* Electric field tuning of plasmonic response of nanodot array in liquid crystal matrix. *Nano letters* **5**, 1978-1981, doi:10.1021/nl0513535 (2005).

9 Zhang, F. *et al.* Electrically controllable fishnet metamaterial based on nematic liquid crystal. *Optics express* **19**, 1563-1568, doi:10.1364/OE.19.001563 (2011).

10 Bossard, J. A. *et al.* Tunable frequency selective surfaces and negative-zero-positive index metamaterials based on liquid crystals. *Ieee T Antenn Propag* **56**, 1308-1320, doi:10.1109/Tap.2008.922174 (2008).

11 Chu, K. C., Chao, C. Y., Chen, Y. F., Wu, Y. C. & Chen, C. C. Electrically controlled surface plasmon resonance frequency of gold nanorods. *Appl Phys Lett* **89**, doi:10.1063/1.2335812 (2006).

12 Minovich, A., Neshev, D. N., Powell, D. A., Shadrivov, I. V. & Kivshar, Y. S. Tunable fishnet metamaterials infiltrated by liquid crystals. *Appl Phys Lett* **96**, doi:10.1063/1.3427429 (2010).

13 Daniel Franklin *et al.* Polarization Independent, Actively Tunable Color Generation on Imprinted Plasmonic Surfaces. *Nature Communications* **6**, 7337 (2015).

14 Wu, Y. K., Hollowell, A. E., Zhang, C. & Guo, L. J. Angle-insensitive structural colours based on metallic nanocavities and coloured pixels beyond the diffraction limit. *Scientific reports* **3**, 1194, doi:10.1038/srep01194 (2013).

15 Aydin, K., Ferry, V. E., Briggs, R. M. & Atwater, H. A. Broadband polarization-independent resonant light absorption using ultrathin plasmonic super absorbers. *Nature communications* **2**, doi:Doi 10.1038/Ncomms1528 (2011).

16 Inoue, D. *et al.* Polarization independent visible color filter comprising an aluminum film with surface-plasmon enhanced transmission through a subwavelength array of holes. *Appl Phys Lett* **98**, doi:10.1063/1.3560467 (2011).

17 Willman, E. *et al.* Liquid crystal alignment induced by micron-scale patterned surfaces. *Phys Rev E* **89**, doi:10.1103/Physreve.89.052501 (2014).

18 Garbovskiy, Y., Reisman, L., Celinski, Z., Camley, R. E. & Glushchenko, A. Metallic surfaces as alignment layers for nondisplay applications of liquid crystals. *Appl Phys Lett* **98**, doi:10.1063/1.3552674 (2011).

19 Ong, H. L., Hurd, A. J. & Meyer, R. B. Alignment of Nematic Liquid-Crystals by Inhomogeneous Surfaces. *J Appl Phys* **57**, 186-192, doi:10.1063/1.334841 (1985).

20 Arsenault, A. C., Puzzo, D. P., Manners, I. & Ozin, G. A. Photonic-crystal full-colour displays. *Nat Photonics* **1**, 468-472, doi:10.1038/nphoton.2007.140 (2007).

21 Kim, H. *et al.* Structural colour printing using a magnetically tunable and lithographically fixable photonic crystal. *Nat Photonics* **3**, 534-540, doi:10.1038/Nphoton.2009.141 (2009).

Dual-color plasmonic filters

E. Heydari, [1] **J. Sperling,** [1] **S. Neale**[1] **and A.W. Clark**[1*]
[1]School of Engineering, University of Glasgow, UK
[*]corresponding author: Alasdair.clark@glasgow.ac.uk

Abstract- We demonstrate a new plasmonic approach to high-density optical data storage; using dual-color plasmonic nano-pixels to encode two information sets into the same unit area using single arrays of two-state metal nano-apertures.

The ability to effectively separate discrete colors from white-light lies at the heart of how we record and view optical information; whether that be the arrangement of colored inks in painting and printing applications, or the spectral filters that enable many modern image display and recording technologies. In each case, color separation is typically provided by organic compounds; dyes and pigments that absorb and scatter particular wavelengths of light, leading to their distinct color profiles. Recently, structural color systems based on engineered nanophotonic materials have emerged as an appealing alternative to absorptive dyes [1]. Among these examples are color filters based on plasmonics; filters which rely on the resonant interaction between incident photons and the free-electrons of nano-scale metal structures. Plasmonic filters hold several dimensional and stability advantages over their micro-scale, dye-based counterparts. As a result, they have been positioned as new technological solutions for sub-wavelength color printing [1], RGB splitting for image sensors [2], anti-counterfeiting measures [3], and optical data storage [4]; thus representing one of the most promising, commercially relevant areas of current plasmonic research activity.

Here, we demonstrate a method for patterning full-color images and codes, at subwavelength resolutions, that exhibit dual, polarization-dependent information states. Our individual pixels are comprised of asymmetric cross-shaped nano-apertures in a thin film of aluminum; each aperture engineered to exhibit 2 independent plasmonic color resonances that can be individually tuned across the sRGB spectrum. This enables us to encode 2 arbitrary information sets into the same unit area using the same array of nano-pixels. We show that using a standard optical microscope, color separation can be controlled down to 2x2 nano-pixels (approximately 370 x 370 nm), while retaining polarization selectivity. This, in turn, defines our maximum data storage capability; each 2x2 pixel area acting as a 2-state data bit that can be read optically. The maximum data density we can achieve using this technique is approximately 1.46 Gb/cm^2, with the added ability to further encode each of those pixels using the full visible-color spectrum.

Acknowledgements. The work was supported by the Royal Academy of Engineering (grant 10216/103) and the EPSRC (grants EP/P51133X/1 and EP/N016874/1).

References

[1] K. Kumar, H. Duan, R. S. Hegde, S. C. W. Koh, J. 6N. Wei, and J. K. W.Yang, "Printing Colour at the Optical Diffraction Limit", *Nature Nanotechnology*, 7, 557-561 (2012).

[2] S. P. Burgos, S. Yokogawa, H. A. Atwater, "Color Imaging Via Nearest Neighbor Hole Coupling in Plasmonic Color Filters Integrated onto a Complementary Metal-Oxide Semiconductor Image Sensor", *ACS Nano*, 7, 10038-10047 (2013).

[3] Y. H. Zheng, C. Jiang, S.H. Ng, Y. Lu, F. Han, U. Bach, J. J. Gooding, “Unclonable Plasmonic Security Labels Achieved by Shadow-Mask-Lithography-Assisted Self-Assembly”, *Advanced Materials*, 28, 2330-2336 (2016).
[4] M. Gu, X.P. Li, Y. Y. Cao, “Optical Storage Arrays: A Perspective for Future Big Data Storage”, *Light-Science & Applications,* 3 (2014).

Structural colors for practical applications

Chengang Ji and L. Jay Guo

Department of Electrical Engineering and Computer Science
The University of Michigan, Ann Arbor, MI, 48109, USA

Structural colors have shown great promise as an alternative for the existing colorant-based filters owing to their noticeable advantages, which may find potential applications in energy-efficient displays, high-resolution imaging, special effect coatings, and building-integrated photovoltaics. The structural colors can be produced by exploiting optical resonances in various resonators, which can be either 3D, 2D or 1D structures, and can be measured in transmission, reflection or scattering from the designed structures. Some examples include surface plasmon resonances in plasmonic nanoresonators, guided-mode resonances in slab waveguide gratings, and optical resonances in thin-film structures. We have investigated several types of 3D periodic array structural colors in the past.

Thin film structures have been exploited in the past to produce various light filtering functions. For example, filters based on light interference effect in multilayer structures are commercially available and have been used in many applications. Recently thin-film based structural blue developed by Toyota has been used in commercial application, in the form of specially made color pigments, and applied as vehicle coating on the latest Lexus LC500h model.

Simpler structures, e.g. in the form of planar Fabry-Perot (F-P) cavities, have also been exploited extensively for color generations. To address the strong angle-dependent resonance, one can use high-index dielectric (e.g. a semiconductor layer) to produce relative angle-insensitive colors, by taking the advantage of the reduced refraction angle dictated by the Snell's law as light enters the F-P resonator (Fig. 1a-b). Similar principle has been adopted in a 1D photonic crystal structure to produce pure red reflection while preserving angle-robustness up to 70 degrees (Fig. 1c-e).

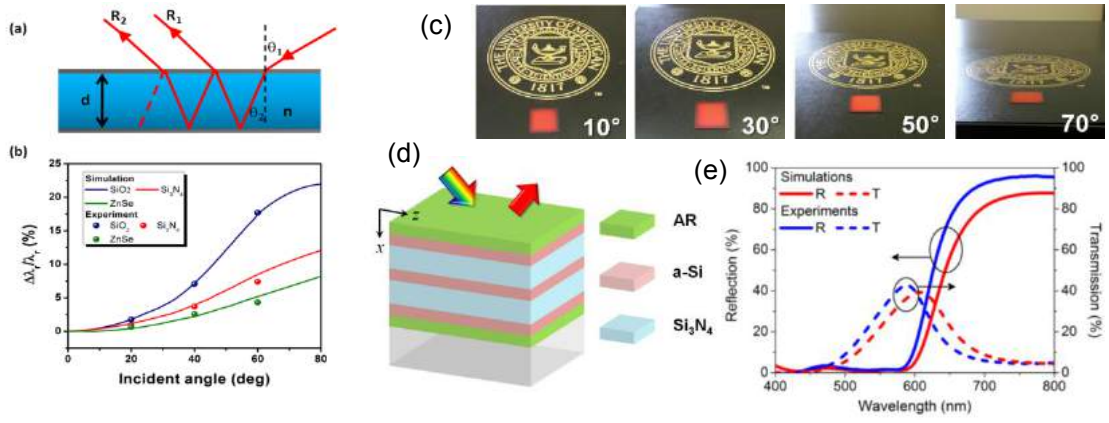


Fig. 1. *(a) Schematic of the F-P etalon structure, showing the incident and refractive angle.(b) Simulation (curve) and experiment (dot) results showing the reduced angle-sensitivity by using higher index dielectric in the F-P cavity. (c-e) A 1-D photonic crystal structure employing high-index dielectrics to produce angle-robust reflection spectra (red color), showing good match between the simulation and experiment.*

One extreme example of the thin-film based resonance structure is shown in Fig. 2 where three optical resonances are formed by using three different materials. The resonance effect and the absorption of the materials result in enhanced absorptions. The three resonances were designed to overlap with each other, leading to an ultra-broad absorption band spanning the visible and near-IR range. A graded index structure is incorporated in the design to reduce the reflection of light, producing close-to-perfect black color.

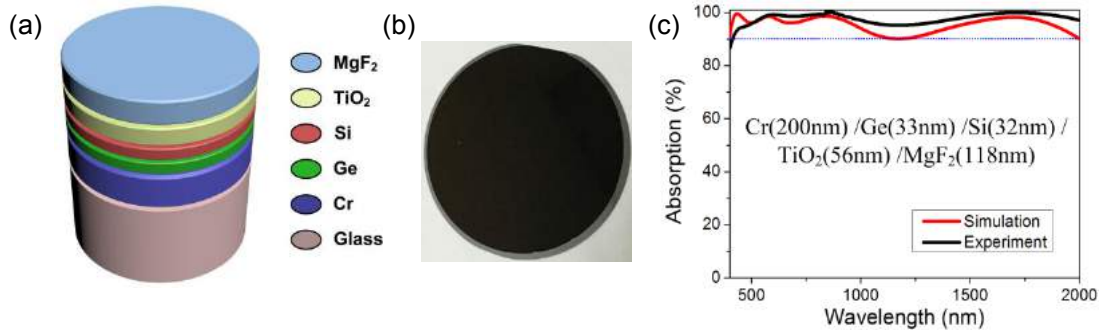


Fig. 2. *(a) Schematic of an ultra-broadband absorber featuring graded refractive index profile and overlapped resonances. (b) photography showing the perfect black color (c) Simulated and measured absorption spectra of this design, showing an average absorption >97% from 400 nm to 2 μm*

Metal thin films have been used as reflectors in the F-P resonators. They can also be used simultaneously as electrodes in active optoelectronic devices. For example, we have created colored solar cells by incorporating a F-P resonator into an amorphous-Si (a-Si) based solar cell structure, producing dual functional devices for energy energy harvesting and colors generation. We further developed an efficient colored solar cell with the power conversion efficiency (PCE) >15% employing a tandem configuration comprising a crystalline silicon (c-Si) PV panel and a reflective color filter. The passive filter consists of a-Si sandwiched between two stacks of transparent dielectrics, which can transmit a large portion of solar spectrum to be harvested by the c-Si module beneath. Meanwhile, the filter renders the tandem structure a distinctive color of ~55% peak reflection and angular insensitivity up to ±60°. Recently we have experimentally demonstrated new optimizations employing materials of high refractive indices, thus successfully extending our designs to all red, green, and blue colors.

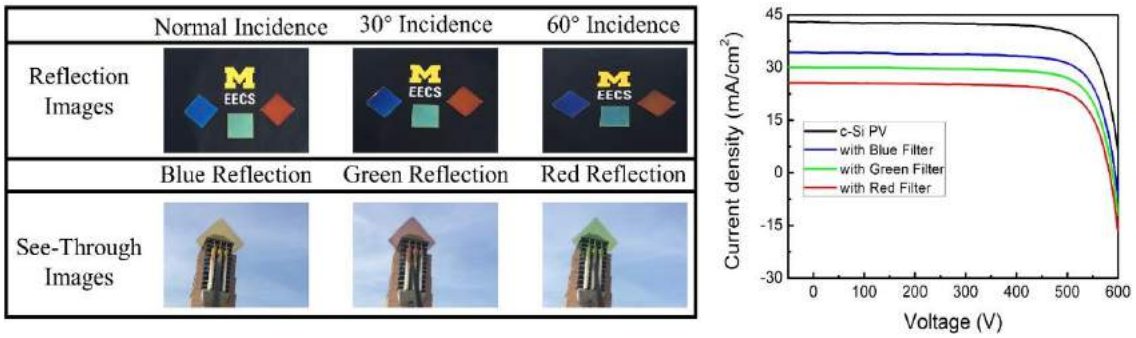


Fig. 3. *Photographs of the passive filters in the reflection and transmission modes; and measured current density-voltage (J–V) characteristics of the colored solar cells under AM1.5 illumination (100mWcm^{-2}) compared to that of the original c-Si cell*

Nanophotonics and Plasmonics Based on Graphene and Related 2D Materials

Actively tuning the topological valley edge states in photonic “boron nitride” structure via carrier photo-injection

Zhiwei Guo, Haitao Jiang*, Yunhui Li, and Hong Chen
MOE Key Laboratory of Advanced Micro-Structured Materials, School of Physics Science and Engineering, Tongji University, Shanghai, 200092, ChinaE
*corresponding author: jiang-haitao@tongji.edu.cn

Abstract-We reveal that topological valley edge states can be actively tuned in photonic “boron nitride” structure by changing the carrier density of InP via photo injecting. Our work provides a direct avenue towards the realization of actively tunable topological valley transport and the related nano-photonic devices.

The generation and control of valley pseudospin lead to a number of profound phenomena such as valley filters and valley Hall effect, which may open up new possibilities for using the valley degree of freedom (DOF) as an information carrier in next-generation electronics [1]. Analogous to the electronic case, the valley DOF in artificial crystals also serves as a good candidate for manipulating the electromagnetic wave [2]. Very recently, it is interesting that there will be very plentiful physical phenomena when the valley DOF is combined with the topological DOF, such as the valley edge states in photonic systems [3,4]. However, the ability to actively tune these effects remains elusive. In this work, we construct a photonic “boron nitride (BN)” structure (Fig. 1(a)) which utilizes the change of permittivity by photo-injecting carriers into InP [5]. Different from the Dirac point in photonic “graphene” structure, a gap will be opened at the corner point K and K’ of the first Brillouin zone in the photonic “BN” structure (Fig. 1(b)). Valley contrasting chiral orbital angular momentum and the phase distributions at K and K’ are shown in Fig. 1(c). The phase chirality will reverse due to the time-reversal symmetry at K and K’. Moreover, the chirality of valley can be changed when the carrier density exchanged in two different positions (A and B).

Figures:

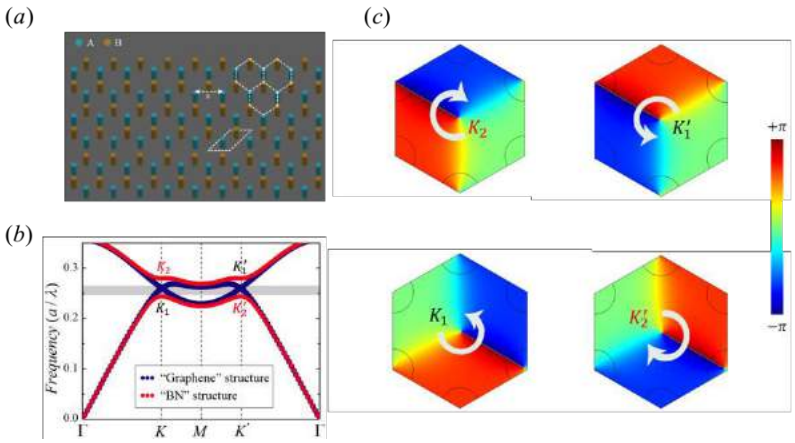


Fig. 1 (a) Schematic of the photonic "BN" structure. The unit cell has two InP rods with different carrier densities embedded in the air (marked by the dashed hexagon). (b) Gapless and gapped bulk dispersions for the photonic "graphene" and "BN" structures, respectively. (c) Phase distributions for different valley states.

Note that, another photonic "BN" structure with different topological property can be formed by a mirror operation. The dispersion of the valley edge states (modes in the gap in Fig. 1(b)) at the interface of two "BN" structures with different topological properties is shown in Fig. 2(a). The electric field distributions of the valley edge states for P1 and P2 in Fig. 2(a) at the normalized frequency $0.25a/\lambda$ are shown in Fig. 2(b), where the white lines indicate the interface.

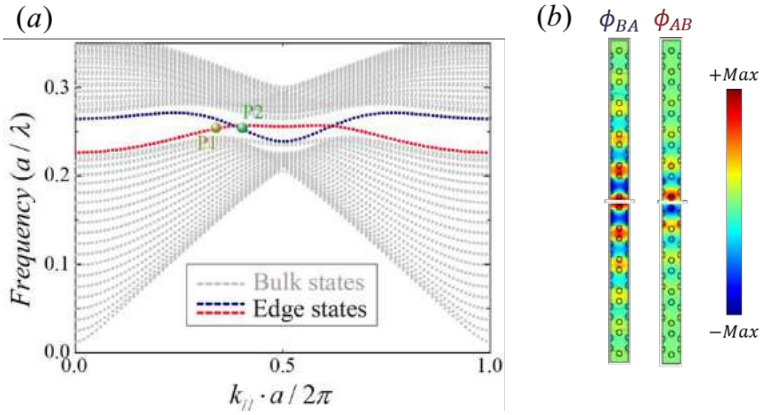


Fig. 2 (a) Dispersion of the valley edge states at the interface of two photonic "BN" structures. (b) The electric field distributions of the valley edge states for P1 and P2 in (a).

Acknowledgements, This work is supported by the National Key Research Program of China (No. 2016YFA0301101), the NSFC (Nos. 11774261, 11474220, 11234010 and 61621001).

REFERENCES

1. Mak, K. F., McGill. K. L, Park. J and McEuen. P. L, "The valley Hall effect in MoS2 transistors," Science, Vol. 344, No. 6191, 1489-1492, 2014.
2. Deng, F., Li. Y, Sun. Y, Wang. X, Guo. Z, Shi. Y, Jiang. H, Chang. K and Chen. H, "Valley-dependent beams controlled by pseudomagnetic field in distorted photonic graphene," Optics Letters Vol. 40, No. 14, 3380-3383, 2015.
3. Dong, J. W., Chen. X. D, Zhu. H, Wang. Y and Zhang. X, "Valley photonic crystals for control of spin and topology," Nature Materials Vol. 16, No. 3, 298–302, 2017.
4. Gao, F., Xue. H, Yang. Z, Lai. K, Yu. Y, Lin. X, Chong. Y, Shvets. G and Zhang. B, "Topologically protected refraction of robust kink states in valley photonic crystals," Nature Physics Vol. 4304, 1-5, 2017.
5. Dunkelberger, A. D., Ellis. C. T, Ratchford. D. C, Giles. A. J, Kim. M, Kim. C. S, Spann. B. T, Vurgaftman. I, Tischler. J. G, Long. J. P, Glembocki. O. G, Owrutsky. J. C and Caldwell. J. D, "Active tuning of surface phonon polariton resonances via carrier photo injection," Nature photonics Vol. 12, 50-56, 2017.

Plasmonically Enhanced Schottky Solar Cell

Mohamed Farhat[1] Pai-Yen Chen[2], and Fahhad H. Alharbi[1,3]

[1]Qatar Environment and Energy Research Institute (QEERI), Hamad Bin Khalifa University, Qatar Foundation, Doha, Qatar

[2]Department of Electrical and Computer Engineering, Wayne State University, Detroit, USA

[3]College of Science and Engineering, Hamad Bin Khalifa University, Doha, Qatar

Plasmonics is an emerging broad area of research, which studies the exceptional optical properties of metallic 2D and 3D nano-structures, i.e. confinement of electromagnetic waves (surface plasmon polaritons) [1]. During the past years, there has been a huge interest in employing plasmonic structures for sunlight harvesting [2], i.e. for example in thermal photovoltaics, thin-film solar cells, or solar thermoelectrics, etc. All these applications exploit the exceptional capabilities of plasmonic structures to concentrate electromagnetic energy and generate "hot" electrons. In this proposal, we aim to use plasmonic light confinement to build Schottky solar cells. The photovoltaic effect in these cells is induced by the metal (insulator) semiconductor interface (see figure below). And the presence of the plasmonic metal will increase the generated current in the active silicon layer and thus increase the overall efficiency of the cell. We will discuss limitations and potentials of this kind of solar cells, in particular ease of fabrication [3].

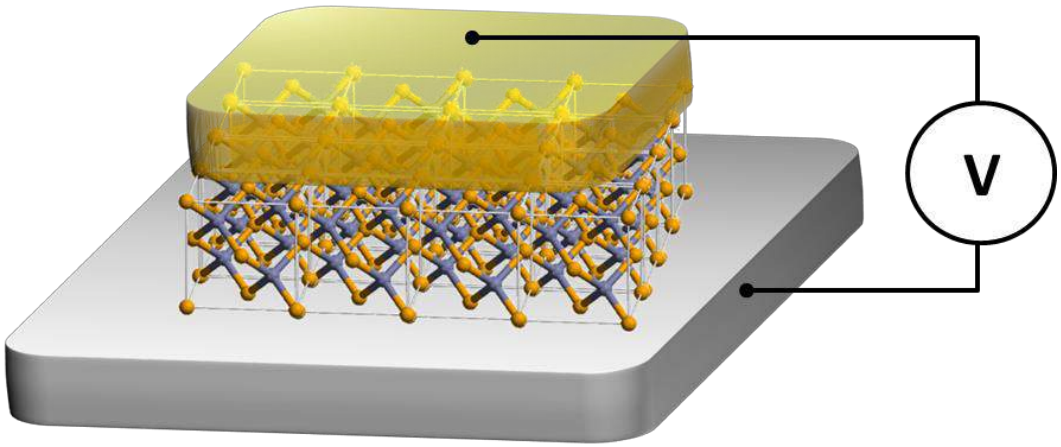


Figure: Scheme of a prototype of a Schottky solar cell showing a patterned gold layer (acting as plasmonic resonator) and a silicon layer between gold and a back contact (Ag for example).

Acknowledgements. This work was funded by the Qatar National Research Fund (QNRF) through a National Priorities Research Program (NPRP) Exceptional grant, NPRP X-107-1-027.

References

[1] Maier, S. A., Plasmonics: fundamentals and applications, Springer Science & Business Media (2007).

[2] Atwater, H. A. and Polman, A., Plasmonics for improved photovoltaic devices, *Nature materials*, **9**, 205-213 (2010).

[3] Farhat, M., Kais, S., and Alharbi, F. H., Plasmonically Enhanced Schottky Photovoltaic Devices, *Scientific Reports*, **7**, 14253 (2017).

Micron-sized phase-matching-free parametric oscillators based on two-dimensional semiconductors

Andrea Marini[1*], **Alessandro Ciattoni**[2], **Carlo Rizza**[2], **Claudio Conti**[3,4]

[1]Department of Physical and Chemical Sciences, University of L'Aquila, Via Vetoio 10, 67100 L'Aquila, Italy
[2]Consiglio Nazionale delle Ricerche, CNR-SPIN, Via Vetoio 10, 67100 L'Aquila, Italy
[3]Institute for Complex Systems (ISC-CNR), Via dei Taurini 19, 00185, Rome, Italy
[4]Department of Physics, University Sapienza, Piazzale Aldo Moro 5, 00185, Rome, Italy
*corresponding author, E-mail: andrea.marini@aquila.infn.it

Abstract

By the exact solution of nonlinear Maxwell equations and first-principle calculations of the semiconductor nonlinear response, we devise a novel kind of parametric micro-resonators adopting monolayer transition-metal dichalcogenides as quadratic nonlinear materials, showing that they are free of phase-matching requirements owing to their surface-like nonlinear interaction.

1. Introduction

The interaction of photons mediated by nonlinear materials, although inherently weak, is key for innumerable photonic applications such as frequency conversion, all-optical signal processing, and non-classical sources of coherent radiation. In particular, parametric down-conversion (PDC) has enabled the development of tunable sources of coherent radiation and generators of entangled photons and squeezed states of light. In traditional configurations a parametric oscillator is composed by an externally pumped optical cavity embedding a nonlinear crystal with broken centrosymmetry, which thus undergoes second-order nonlinear processes sustaining PDC. Because three-wave parametric coupling is an inherently weak nonlinear process, low oscillation thresholds are achieved only by means of doubly or triply resonant optical cavities. A further obstacle hampering this resonant process is represented by the material dispersion imposing a phase-matching (PM) condition among the three waves, which is generally achieved by a complex setup design, thus hindering tunability and miniaturization. Indeed parametric effects are severely hampered by the destructive interference among the three waves propagating with different wavenumbers $k_{1,2,3}$ in the dispersive nonlinear medium because the wavevector mismatch $\Delta k = k_3 - k_2 - k_1$ does not generally vanish.

Here we theoretically demonstrate that two-dimensional (2D) materials with high quadratic nonlinearity, nowadays emerging as important nonlinear photonic elements [1], open an hitherto unexplored ground for the development of tunable parametric micro-sources. Indeed, when illuminated by different visible and infrared waves, these novel 2D materials provide a negligible dispersive dephasing $\Delta\phi$ owing to their atomic-scale thickness $\ell \ll \lambda$, where λ is the optical wavelength. In turn, the three waves interacting within the 2D material do not undergo destructive interference thanks to the surface-like nonlinear interaction and the PM requirement is here removed. Furthermore, these "phase-matching-free" devices turn out to be very versatile and compact, with the additional tunability offered by electrical gating of 2D materials, which provides ultrafast electrical-modulation functionality. The most famous 2D material, graphene, is not the best candidate for PDC owing to the centrosymmetric structure. In principle, a static external field may break

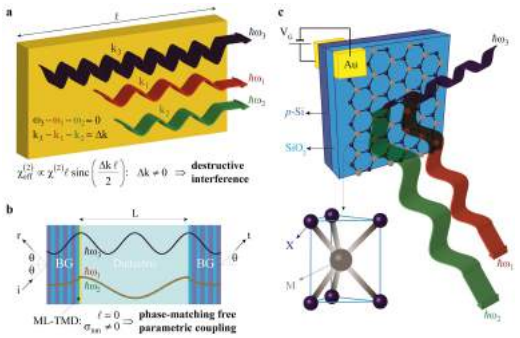


Figure 1: **a.** Three-wave parametric coupling in bulk nonlinear crystals; the effective quadratic susceptibility $\chi^{(2)}_{\rm eff}$ is heavily affected by the mismatch Δk among the wavevectors $k_m = n_m\omega_m/c$ of the pump (3), signal (1) and idler (2). **b.** ML-TMD based parametric micro-oscillator: the cavity is assembled by two Bragg mirrors separated by a dielectric layer and the ML-TMD is placed on the left mirror. The incident (i) pump field produces both reflected (r) and transmitted (t) pump, signal and idler fields by means of the ML-TMD quadratic surface conductivity $\sigma_{nm} \neq 0$. The mutual dephasing $\Delta\phi = \Delta k\ell$ among these three waves becomes negligible within the atomic thickness of the nonlinear ML-TMD ($\Delta\phi \approx 10^{-2}$) because $\ell \ll \lambda$, thus enabling phase-matching free parametric coupling. **c.** Structural geometry of MX_2 ML-TMDs.

centrosymmetry and induce a $\chi^{(2)}_{\rm eff}$, but the spectrally-flat absorption of graphene is severely detrimental for PDC.

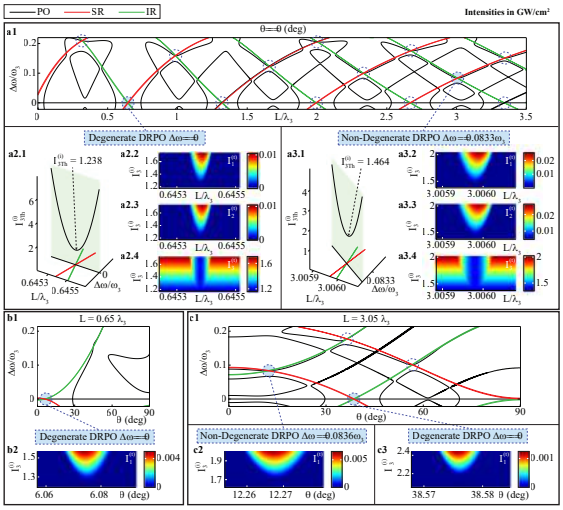


Figure 2: Analysis of the doubly resonant parametric oscillations (DRPOs) of a cavity (with PMMA as cavity dielectric) illuminated by a $\lambda_3 = 780$ nm pump with micron-sized Bragg Mirrors whose stop band is centered at 1560 nm. In subfigure **a** the cavity length is used as a tuning parameter for normal incidence $\theta = 0$ whereas in **b** and **c** the incidence angle θ is the tuning parameter for two assigned cavity lengths. **a1.** Identification of DRPOs as intersection among the parametric oscillation (PO) curve and the signal resonance (SR) and idler resonance (IR) curves in the $(L/\lambda_3, \Delta\omega/\omega_3)$ plane. **a2** Intensity analysis of the degenerate ($\Delta\omega = 0$) DRPO located at $L \simeq 0.645\lambda_3$ comprising the plots of (**a2.1**) the intensity threshold $I^{(i)}_{3\rm Th}$ versus L/λ_3 and $\Delta\omega/\omega_3$ and (**a2.2-4**) the intensities $I^{(t)}_1, I^{(t)}_2, I^{(t)}_3$ of the transmitted signal, idler and pump fields as functions of the scaled cavity length L/λ_3 and the incident pump intensity $I^{(i)}_3$. **a3** Intensity analysis of the non-degenerate ($\Delta\omega \neq 0$) DRPO located at $L \simeq 3\lambda_3$ (the panels are the analogous of those of **a2**). **b1.** DRPOs analysis on the $(\theta, \Delta\omega/\omega_3)$ plane for L as in **a2**. Note that the degenerate DRPO occurs at a small angle θ. **b2.** Signal intensity analysis of the DRPO showing a feasible θ range. **c1.** DRPOs analysis on the $(\theta, \Delta\omega/\omega_3)$ plane for L as in **a3** revealing a variety of DRPOs ad different angles θ. **c2,c3** signal intensity analysis of two DRPOs identified in **c1**.

Recent years have witnessed the rise of transition metal dichalcogenides (TMDs) as promising photonic 2D materials. TMDs possess several unusual optical properties dependent on the number of layers. Bulk TMDs are semiconductors with an indirect bandgap, but the optical properties of their monolayer (ML) counterpart are characterized by a direct bandgap ranging from ~ 1.55 eV to ~ 1.9 eV that is beneficial for several optoelectronic applications [2]. In addition, ML-TMDs have broken centrosymmetry and thus undergo second-order nonlinear processes [3]. We find that the design of parametric oscillators based on micro-cavities embedding ML-TMDs is extremely flexible if compared to standard setups thanks to their phase-matching-free operation. We demonstrate that, at conventional infrared pump intensity, parametric oscillation occurs in wavelength-sized micro-cavities with ML-TMDs. We show that the output signal and idler frequencies can be engineered thanks to the mode selectivity of doubly-resonant cavities; these frequencies are tuned by the pump incidence angle and can be modulated electrically by an external gate voltage.

2. Conclusions

In conclusion, parametric oscillations can be excited in micron-sized cavities embedding ML-TMDs as nonlinear media at conventional pump intensities in a PM-free regime. The cavity design remains inherently free of the complexity imposed by the need for PM and may result into doubly resonant PDC of signal and idler waves. The flexibility offered by such a novel oscillator design enables the engineering of selective degenerate or non-degenerate down-converted excitations by simply modifying the incident angle of the pump field. Our results pave the way for new ultra-fast tunable micron-sized sources of entangled photons, a key device underpinning any quantum protocol. Highly-miniaturized optical parametric oscillators may also be employed in lab-on-chip technologies for biophysics, environmental pollution detection and security.

References

[1] S. Yu, X. Wu, Y. Wang, X. Guo, and L. Tong, 2D Materials for Optical Modulation: Challenges and Opportunities, *Adv. Mater.* 29: 1606128, 2017.

[2] Z. Sun, A. Martinez, and F. Wang, Optical modulators with 2D layered materials, *Nat. Photon.* 10: 227–238, 2016.

[3] N. Kumar, S. Najmaei, Q. Cui, F. Ceballos, P. M. Ajayan, J. Lou, and H. Zhao, Second harmonic microscopy of monolayer MoS_2, *Phys. Rev. B* 87: 161403(R), 2013.

Sensitivity of all dielectric layered metastructures on a scale below the periodicity

Agnès Maurel[1], **Jean-Jacques Marigo**[2],

[1] Institut Langevin, ESPCI, CNRS, 1 rue Jussieu, Paris 75005 - France,
[2]Lab. de Mécanique du Solide, Ecole Polytechnique, Route de Saclay, Palaiseau 91120 - France.
*corresponding author, E-mail: agnes.maurel@espci.fr

Abstract

The unusual scattering properties of multilayered dielectric metamaterial near the critical angle for total reflection are revisited. Our findings are twofolds: (i) we shows that in TE polarization, a fully local model accurately reproduces them, (ii) the sensitivity of these structures is much higher than that reported in previous studies.

1. Introduction

Multilayered metamaterials are one-dimensional structures alternating layers with subwavelength thicknesses. Recently, it has been shown that dielectric multilayered metamaterials exhibit scattering properties highly sensitive to the thickness and arrangement of the layers in the vicinity of the critical angle of total reflection [1]. The effective medium approximation (EMA) fails to explain this sensitivity, a fact which has been often attributable to non local effects. In TE polarization, we show that this is not the case. Using homogenization of finite extent structures at high orders, we derive a fully local model which reproduces the spectra with an accuracy of less than 1%. Besides, we show that the discrete description of the spectra using the layer thickness d as unit of measure misses the complexity of a pattern of point lace within the scale d. This ultra-sensitivity to variations below d is attributable to strong boundary layer effects and for large structures to a cooperation between the boundaries and the phase accumulation during wave propagation.

2. Up to third order homogenized model

For an incident wave in the plane (x, z) in TE, the Maxwell equations simplify to the Helmholtz equation applying to the electric field $\mathbf{E} = E(x, z)\mathbf{e}_y$, namely the scalar field E satisfies

$$\Delta E(x, z) + k^2 \varepsilon(z) E(x, z) = 0, \qquad (1)$$

with in the present case $\varepsilon(z) = \varepsilon_{\text{in}}, \varepsilon_a, \varepsilon_b, \varepsilon_{\text{out}}$, varying along the z-axis (Fig. 1). If the incident wave is a plane wave at incidence θ, the problem reduces to a one-dimensional problem along z which can be solved easily, *e.g.* with the transfer matrix formalism [1]. Our effective model is derived using two-scale homogenization technique detailed in [2]. At the dominant order (order 1), the model HM_1 is that of the classical homogenization and coincides with the effective medium approximation (EMA). The layered material is replaced by an equivalent homogeneous medium with an effective permittivity $\langle\varepsilon\rangle = \frac{d_a\varepsilon_a + d_b\varepsilon_b}{d_a + d_b}$. At this order, the transmission conditions at the boundaries of the structure are the usual continuities of the electric field and of its normal derivative. Conducting the analysis at the order 2 leaves us with a model termed HM_2 where the effective medium in the bulk is the same than in EMA, but with modified transmission conditions, see (2) involving a parameter $\hat{\varepsilon}$ depending only on the arrangement of the layers terminating the structure. Eventually, going up to the order 3 enables the correction in the effective permeability to be obtained. Specifically, our homogenized problem HM_3 reads as

$$\begin{cases} \Delta E + k^2 \varepsilon_{\text{eff}}(k) E = 0, \\ \dfrac{\partial E}{\partial z}(x, 0^+) - \dfrac{\partial E}{\partial z}(x, 0^-) = k^2 d\, \hat{\varepsilon}_{\text{in}}\, E(x, 0), \\ \dfrac{\partial E}{\partial z}(x, L^+) - \dfrac{\partial E}{\partial z}(x, L^-) = k^2 d\, \hat{\varepsilon}_{\text{out}}\, E(x, L), \end{cases} \qquad (2)$$

where L is the structure extent. Closed forms of the coefficients are given in [2]. It is worth noting that (2) is a fully local model, because ε_{eff} depends only on the wavenumber and because the transmission conditions does not involved tangential derivative of the fields.

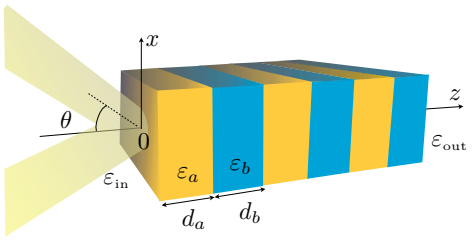


Figure 1: Multilayer structure illuminated by a plane wave.

3. Classical discrete description of the spectra

We consider $k = 2\pi/(500\text{ nm})$, $\varepsilon_{\text{in}} = 4$, $\varepsilon_a = 5$, $\varepsilon_b = 1$ and $d = 20$ nm with $d_a = d_b = d/2$. We consider the transmission spectra in the critical conditions reported in [1] that is in the vicinity of $\varepsilon_{\text{out}} \simeq \langle\varepsilon\rangle = 3$ and $\theta \simeq \theta_c = 60°$. Note that $\varepsilon_{\text{eff}} = 3.053$ and $\arcsin\sqrt{\varepsilon_{\text{eff}}(k)/\varepsilon_{\text{in}}} = 60.09°$ at this frequency. Following [1], we term regular (reverse) order configuration that of a structure with $L = Nd$ (N

integer) starting with an entire layer of material a (material b). We report in Fig. 3 the transmission spectra against the incidence angle close to the critical angle and the extent $L = Nd$, N integer, that is in a d-incremented version of L. Each spectrum resembles the classical spectrum of a homogeneous slab; however the regular or reversed order cases are different, exchanging the locations of their maximum transmissions and reflections. Obviously, the EMA fails in

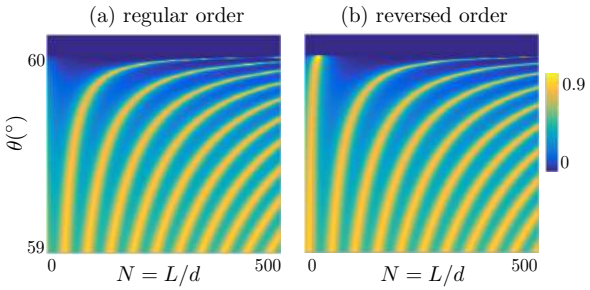


Figure 2: Discrete transmission spectra; $L = Nd$ varies with d-increment, $\varepsilon_{\text{out}} = \varepsilon_{\text{eff}}$.

predicting these transmission properties, see Fig. 3. The critical angle is underestimated ($\theta = 60^\circ$ in Fig. 3), and below the critical angle, the periodicity is overestimated. Capturing the boundary layer effects in HM_2 is the first necessary improvement and it is sufficient for small structures. Eventually, HM_3 recovering in addition the right, small, value of the wavenumber corrects the two drawbacks.

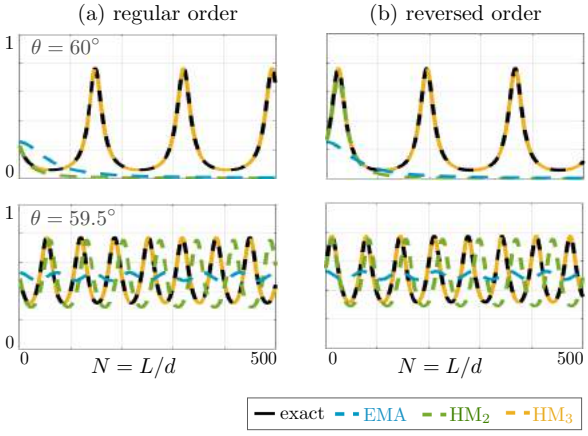


Figure 3: Transmission against N at $\theta = 60^\circ$ and 59.5°, from Figs. 2.

4. Continuous variation of L – a complex cooperation between the bulk and the boundaries

We shall now see that the aspect of the pattern observed in Fig. 2 is deeply modified when the increment ΔL in L is decreased. The result is reported in Fig. 4; we focus on a tiny region of the Fig. 2 corresponding to $L/d \in (490, 500)$

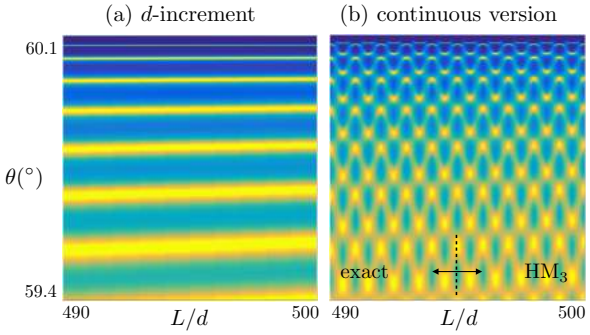


Figure 4: Transmission spectra (a) for the d-increment in L and for continuously varying L ($\Delta L = d/50$); same representation as in Fig. 2 for the regular order. In (b), the numerical solution is reported for $L/d < 495$ and the HM_3 prediction is reported for $L/d > 495$; the discrepancy is 0.4% on average.

and small variations of the angle near the critical angle. The difference between both patterns is impressive, the tiny pixelization revealing a structuration with point lace design due to strong fluctuations in the transmission within the scale d. For these large extents, the observed pattern results from a cooperation between the bulk of the structure and its boundaries. On one hand, interferences of the Fabry-Perot type take place, which are possible since the wave can accumulate phase. Next, $\hat{\varepsilon}_{\text{out}}$ being sensitive to any small change in the layer terminating the structure affects the values of θ realizing these maxima. For ε_{out} far from ε_{eff}, these changes are incidental; for ε_{out} close to ε_{eff}, their are sufficient to structure the spectrum below the size d. It is worth noting that our model HM_3 reproduces the pattern with an accuracy of 0.5% (see Fig. 4(b) and the figure caption).

5. Conclusion

In some critical conditions, simple multilayered structures may be extremely sensitive to changes of the structures at the subwavelength scale and even at a scale beyond that of their basic pattern, here the spacing d. Accurate models are particularly useful to interpret and to anticipate such sensitivity; we have show here that conducting the homogenization of finite extent structures at high order provides such accurate models. Extensions to metal -dielectric structures and to TM polarization will be discussed.

References

[1] H.H. Sheinfux, I. Kaminer, Y. Plotnik, G. Bartal and M. Segev, Phys. Rev. Lett. 113(24), 243901 (2014).

[2] Maurel A, Marigo JJM, 2017 Sensitivity of dielectric layered structure on a scale below the periodicity - a fully local homogenized model, submitted

2D semiconductors for nanophotonics

Alberto G. Curto[1,2]

[1] Department of Applied Physics and Institute for Photonic Integration,
TU/e - Eindhoven University of Technology P.O. Box 513 5600 MB Eindhoven - The Netherlands,
[2] Geballe Laboratory for Advanced Materials, Stanford University, Stanford, California, USA

E-mail: A.G.Curto@tue.nl

Abstract

Layered 2D semiconductors are ideal sources and detectors for nanophotonics and optoelectronics. They exhibit a strong optical response from the UV to the IR, can be incorporated into the very near field of devices without the need for epitaxial growth, are easy to position and pattern, and give access to exciting electronic degrees of freedom like the spin, valley and layer numbers.
Here we present two experimental examples of the advantages and flexibility of 2D semiconductors as light sources for nanophotonics.

1. Directional monolayer MoS_2 emission with silicon nanoantennas

Exploiting a MoS_2 monolayer, we demonstrate directional light emission using a silicon nanowire antenna [1]. The mechanism of operation of this antenna shares similarities with Kerker's conditions of plane wave scattering but, for electric dipole sources, two different paths are available to obtain directionality. We pattern the 2D semiconductor using the antenna as a shadow mask for etching, which allows us to probe its ultimate performance thanks to efficient coupling.

2. Linearly and circularly polarized sources for nanophotonics

Whereas MoS_2 monolayers with a hexagonal crystal symmetry can be used as a source of circularly polarized photons due to spin-valley polarization, crystals with a lower symmetry like black phosphorus [2] can offer atomically thin sources of linearly polarized photons. In the second part of this presentation, we will show how different 2D materials exhibit linearly or circularly polarized excitonic light emission, which are necessary to develop nanophotonic and optoelectronic devices that use polarization.

References

[1] A. F. Cihan, A. G. Curto, S. Raza, P. G. Kik, M. L. Brongersma, Silicon Mie Resonators for Highly Directional Light Emission from monolayer MoS_2, arXiv:1709.04999, to appear in *Nature Photonics*, 2018

[2] Hongtao Yuan, Xiaoge Liu, Farzaneh Afshinmanesh, Wei Li, Gang Xu, Jie Sun, Biao Lian, Alberto G. Curto, Guojun Ye, Yasuyuki Hikita, Zhixun Shen, Shou-Cheng Zhang, Xianhui Chen, Mark Brongersma, Harold Y. Hwang and Yi Cui, Polarization-sensitive broadband photodetector using a black phosphorus vertical p–n junction, *Nature Nanotech.* 10, 707 (2015)

Theoretical Study of Resonance Effects in Graphene-Based Double Ring Resonator

Cristiano Braga[1], Geraldo Melo[2], Gianni Portela[1], and Victor Dmitriev[1*]

[1]Faculty of Electrical Engineering, Federal University of Para, Belem, Brazil
[2]Federal Rural University of Amazonia, Capanema, Brazil
*corresponding author, E-mail: victor@ufpa.br

Abstract

We investigate in this paper a graphene-based double ring resonator with unit cell formed by two coaxial graphene rings placed on the opposite sides of a thin dielectric substrate. The two rings are electromagnetically coupled and resonate with dipole plasmon modes. We have calculated the transmission and reflection coefficients of the structure by means of computational simulations based on finite element method and by employing a Temporal Coupled-Mode Theory approach. A good agreement between the analytical and simulational results are shown. We discuss some properties and possible applications of the structure.

1. Introduction

In the last decade, it has been shown a feasibility of the use of materials whose structure is two-dimensional (2D). Graphene, the first known 2D structure [1, 2], has atomic order thickness and unique properties such as excellent optical and electrical properties, high rigidity, flexibility, good thermal and electrical conductivity, high mobility of electrons, quantum Hall effect and presence of plasmon resonances [3-6].

Strong interaction of graphene with electromagnetic radiation in terahertz (THz) region opens the way for the development of FETs, photodetectors, nanoantennas, etc. Graphene resonators in the form of discs, ribbons, squares, rings and crosses are used to increase plasmon resonance, thus enhancing parameters such as absorption, transmission and reflection of the devices [7-9] in the presence of the Fano resonances, which are related to the interaction of the electromagnetic fields scattered from different resonators in the form of graphene rings [10]. These structures demonstrate band-pass and band-stop filter behavior in the infrared and THz bands. These filters select certain frequency bands that will be blocked and other frequency bands that will propagate through the components, respectively, being very important devices for application in optical communication systems [11,12].

In this work, we investigate numerically resonances in the periodic structure where the unit cell is formed by two graphene-based resonant elements in the form of rings of different radii deposited at the top and bottom of a dielectric substrate. Besides, Temporal Coupled-Mode Theory (TCMT) is used to analytically calculate the transmission and reflection coefficients of the structure.

2. Geometry and Theoretical Model

Figure 1 shows schematically the unit cell of the array composed by rings 1 and 2 of graphene with radius r_1 =4 μm, R_1 = 15 μm, r_2 = 6 μm, and R_2 = 27 μm, respectively. The resonator rings are placed on the opposite sides of a dielectric substrate with permittivity ε = 3.75, length A = 100 μm, and height h = 10 μm.

The surface conductivity of graphene in this analysis was modeled according to the intraband contribution given by Kubo formalism [13]:

$$\sigma_{intra} = -i\frac{e^2 k_B T}{\pi\hbar^2(\omega - 2i\Gamma)}\left[\frac{E_F}{k_B T} + 2\ln\left(e^{-\frac{E_F}{k_B T}} + 1\right)\right] \qquad (1)$$

where ω is the angular frequency, e is the charge of electron, k_B is the Boltzmann constant, T = 300 K, h is the reduced Planck constant, Γ = 0.1 meV, and E_F is the Fermi energy (chemical potential).

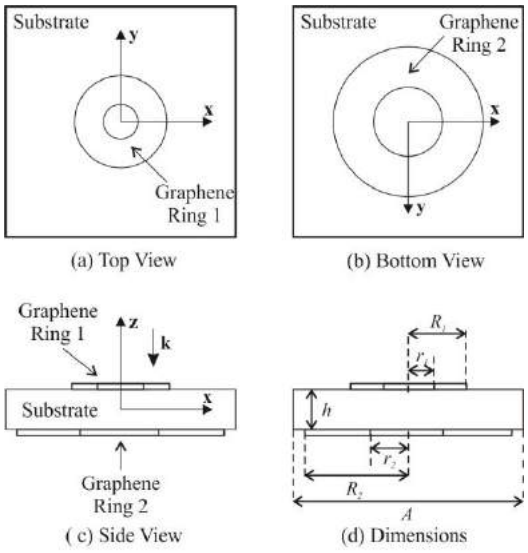


Figure 1: Top view (a) and bottom view (b) of unit cell formed by two rings on dielectric substrate, (c) and (d) represent the side view and dimensions.

In Figure 2, it is shown the frequency dependence of real and imaginary parts of the graphene conductivity for different Fermi energy.

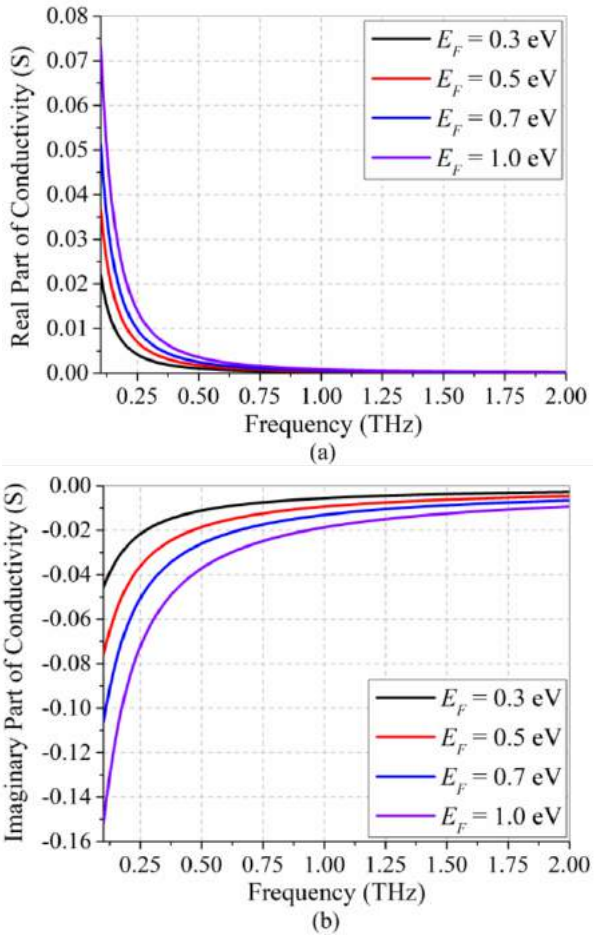


Figure 2: Surface conductivity of graphene as a function of frequency for different chemical potentials: (a) real part and (b) imaginary part.

3 . Transmission and Reflection Coefficients

By using the formalism presented in [15], the equations of TCMT describing evolution of the electromagnetic field in two ring resonators can be written as follows:

$$\frac{da_1}{dt} = \left(i\omega_1 - \frac{1}{\tau_{i,1}} - \frac{1}{\tau_{w,1}} \right) a_1 + \sqrt{\frac{1}{\tau_{w,1}}} s_i - i\mu a_2 \tag{2}$$

$$\frac{da_2}{dt} = \left(i\omega_2 - \frac{1}{\tau_{i,2}} - \frac{1}{\tau_{w,2}} \right) a_2 + \sqrt{\frac{1}{\tau_{w,2}}} s_i - i\mu a_1 \tag{3}$$

$$s_t = s_i - \sqrt{\frac{1}{\tau_{w,1}}} a_1 - \sqrt{\frac{1}{\tau_{w,2}}} a_2 \tag{4}$$

where a_n is the amplitude of the resonant mode in the nth ring (n = 1, 2), ω_n is the resonant frequency of the mode in the nth ring, $\tau_{w,n}$ is the decay rate of the mode in the nth ring to the input/output, $\tau_{i,n}$ is the decay rate of the mode in the nth ring due to intrinsic losses, μ is the coupling coefficient between the two modes, s_i is the amplitude of the incident wave, and s_t is the amplitude of the transmitted wave. From (2) – (5), one can define the transmission and reflection coefficients of the component as follows:

$$t(\omega) = 1 - \sqrt{\frac{1}{\tau_{w,1}}} \frac{A_1}{B_1} - \sqrt{\frac{1}{\tau_{w,2}}} \frac{A_2}{B_2} \tag{5}$$

$$r(\omega) = \sqrt{\frac{1}{\tau_{w,1}}} \frac{A_1}{B_1} + \sqrt{\frac{1}{\tau_{w,2}}} \frac{A_2}{B_2} \tag{6}$$

where

$$A_1 = \sqrt{\frac{1}{\tau_{w,1}}} - \frac{i\mu \sqrt{\frac{1}{\tau_{w,2}}}}{i(\omega - \omega_2) + \frac{1}{\tau_{i,2}} + \frac{1}{\tau_{w,2}}} \tag{7}$$

$$B_1 = i(\omega - \omega_1) + \frac{1}{\tau_{i,1}} + \frac{1}{\tau_{w,1}} + \frac{\mu^2}{i(\omega - \omega_2) + \frac{1}{\tau_{i,2}} + \frac{1}{\tau_{w,2}}} \tag{8}$$

$$A_2 = \sqrt{\frac{1}{\tau_{w,2}}} - \frac{i\mu \sqrt{\frac{1}{\tau_{w,1}}}}{i(\omega - \omega_1) + \frac{1}{\tau_{i,1}} + \frac{1}{\tau_{w,1}}} \tag{9}$$

$$B_2 = i(\omega - \omega_2) + \frac{1}{\tau_{i,2}} + \frac{1}{\tau_{w,2}} + \frac{\mu^2}{i(\omega - \omega_1) + \frac{1}{\tau_{i,1}} + \frac{1}{\tau_{w,1}}} \tag{10}$$

4. Results and Discussion

In Figure 3, one can see that the computational results obtained by finite element method (commercial program ANSYS HFSS [14]) are in good concordance with those provided by TCMT. The parameters of the TCMT equations are: f_1 = 1.41 THz, $\tau_{w,1}$ = 1.2 ps; $\tau_{i,1}$ = 20 ps, f_2 = 0.93 THz, $\tau_{w,2}$ = 5 ps, $\tau_{i,2}$ = 7 ps, and $\mu = 2\text{x}10^{11}$ s^{-1}.

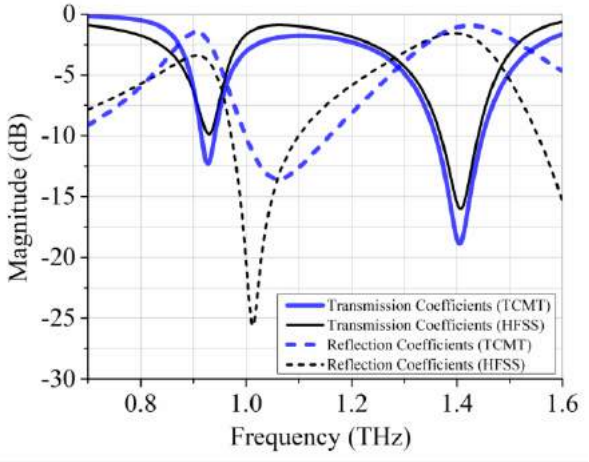
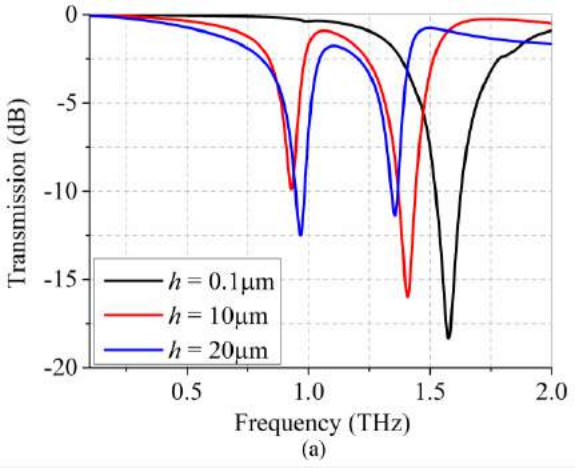
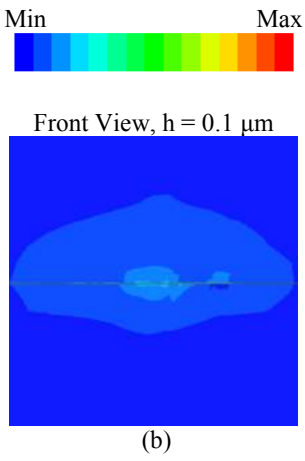


Figure 3: Frequency response of device.

A. *Influence of the TCMT parameter μ*

The frequency response of the structure, considering the substrate thickness h equal to 0.1, 10, and 20 μm, is shown in Figure 4 (a). It can be verified that the transmission levels and bandwidth of the Fano peaks resonance [10] decrease with the increase of h, i. e. with decreasing the coupling μ between the graphene resonators. For h = 10 μm and h = 20 μm, the transmission spectrum has two minimum points corresponding to the resonant frequencies of the two rings. We have calculated also the electric field component E_Z at the resonance frequencies for both rings (see Figures 4 (b)-(f)) and for all the considered values of the parameter h. The thickness of the substrate directly influences the coupling strength between the rings, which in turn influences the transmission levels at the resonance frequencies of the coupled rings. When the substrate thickness is very small, h=0.1 μm, the two resonance frequencies transforms into only one.





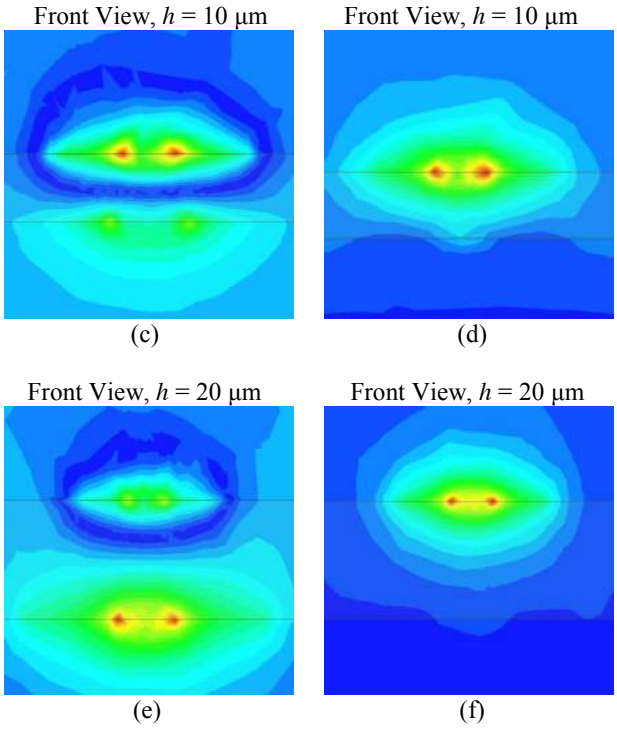


Figure 4: (a) Transmission spectra for h = 0.1, 10 and 20 μm. (b)-(f) Distribution of the electric field component E_z in the two rings at the resonance frequencies as for h = 0.1 μm at the frequency of 1.57 THz, h = 10 μm at the frequencies of 0.93 and 1.41 THz and for h = 20 μm in the frequencies of 0.97 and 1.35 THz, respectively.

In order to relate the computational results concerning the variation of the substrate thickness (or, equivalently, the coupling that takes place between the rings) with the analytical TCMT approach, we have also calculated the transmission coefficient as a function of the parameter μ by using formula (5) (see Figure 5).

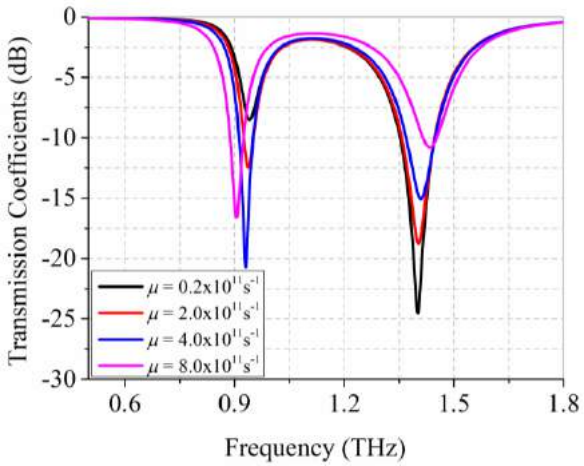


Figure 5: Frequency dependence of transmission coefficients as a function of parameter μ.

B. Control by chemical potential.

Figure 6 shows the transmission curves for different values of Fermi energy E_F of graphene. The transmission curve for E_F = 0.5 eV corresponds to the curves in Fig. 4. One can verify that, by reducing the Fermi energy to E_F = 0.3 eV, there is a shift in transmission levels and in the resonant frequencies that are displaced for smaller values in comparison to the case where E_F = 0.5 eV. On the other hand, increasing the Fermi energy value to 0.7 eV, it is observed an increase of both the minimum transmission levels and the resonance frequencies as compared with the Fermi energy of 0.5 eV. These results show that changing the Fermi energy, it is possible to shift the the transparency window of the possible electromagnetic filter. It can be shown, that this feature enables one the use of the structure as a switch.

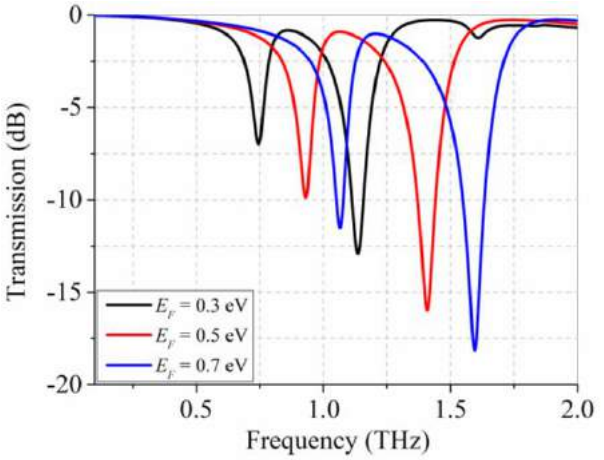


Figure 6: Frequency dependence of transmission coefficient for different Fermi energy.

5. Conclusions

We have investigated a graphene-based structure that can be used as an electromagnetic filter in the THz region, as well as we have developed a TCMT-based approach for the analysis and design of the proposed device. The analytical results provided by the TCMT equations are in good agreement with the numerical ones, so that one can use the presented formulas to analyze and improve the performance of the concerned device. We have also shown that the coupling between two rings and Fermi energy can be used effectively for adjustment of resonance properties of the component.

Acknowledgements

This work was supported by the National Council for Scientific and Technological Development (CNPq), Coordination for the Improvement of Higher Education Personnel (CAPES).

References

[1] Geim, A. K. Novoselov, K. S, The Rise Of Graphene, *Nature Materials* 6, 183-191, 2007.

[2] Andrew J. Mannix, Brian Kiraly, Mark C. Hersam and Nathan P. Guisinger, Synthesis and chemistry of elemental 2D materials, *Nature Reviews|Chemistry* 0014, 2017.

[3] Shiwei Sheng, Kang Li, Fanmin Kong, Huawei Zhuang, Analysis of a tunable band-pass plasmonic filter based on graphene nanodisk resonator, *Optics Communications* 336, 189–196, 2015.

[4] Dmitriev, Victor, Nascimento, Clerisson Lima, Planar THz electromagnetic graphene pass-band filter with low polarization and angle of incidence dependencies, *Appl. Opt. 54,* 1515-1520, 2015.

[5] Ali Akhavan, Hassan Ghafoori Fard, Vali Varmazyari, Dynamically-Tunable Terahertz Band-Stop Filter Based on Multilayer Graphene Metamaterial, International, *Journal of Optics and Applications* 7, 7-12, 2017.

[6] Minjie Wang, Eui-Hyeok Yang, THz applications of 2D materials: Graphene and beyond, Nano-Structures & Nano-Objects, 2017.

[7] Shaolin Ke, Bing Wang, He Huang, Hua Long, Kai Wang, and Peixiang Lu, Plasmonic absorption enhancement in periodic cross-shaped graphene arrays, *Optical Materials Express* 7: 8888-8900, 2015.

[8] Chen Liu, Peiguo Liu, Cheng Yang and Lian Bian, Terahertz metamaterial based on dual-band graphene ring resonator for modulating and sensing applications, *Journal of Optics* 19: 115102, 2017.

[9] Dmitriev Victor, Nascimento Clerisson, Planar THz electromagnetic graphene pass-band filter with low polarization and angle of incidence dependencies, *Appl. Opt. 54:* 1515-1520, 2015.

[10] Boris Luk'yanchuk, Nikolay Zheludev, Stefan Maier, Naomi Halas, Peter Nordlander, Harald Giessen and Chong Tow Chong, The Fano resonance in plasmonic nanostructures and metamaterials, *Nature Materials* vol. 9, 707-715, 2010.

[11] Amir Setayesh, Sayyed Reza Mirnaziry, and Mohammad Sadegh Abrishamian, Numerical Investigation of Tunable Band-pass\band-stop Plasmonic Filters with Hollow-core Circular Ring Resonator, *Journal of the Optical Society of Korea* 15, 82-89, 2011.

[12] Hua Lu, Xueming Liu, Dong Mao, Leiran Wang, and Yongkang Gong, Tunable band-pass plasmonic waveguide filters with nanodisk resonators, *Opt. Express* 18, 17922-17927, 2010.

[13] Hanson, George W. "Dyadic Green's functions and guide surface waves for a surface conductivity model of graphee." *Journal of Applied Physics* 103: 064302, 2008.

[14] https://www.ansys.com

[15] Qiang Li, Tao Wang, Yikai Su, Min Yan, and Min Qiu, Coupled mode theory analysis of mode-splitting in coupled cavity system, *Optics Express* 8: 8367- 8382, 2010.

New graphene-based circulators and switches for THz region

Victor Dmitriev[1], Wagner Castro[1,2], Samara Matos[1,3], and Sergio Rabelo[1]

[1]Department of Electrical Engineering, Federal University of Para, Para, Brazil
[2]Federal Rural University of Amazonia, Para, Brazil
[3]Federal University of Tocantins, Brazil
*corresponding author, E-mail: wagner.ormanes@ufra.edu.br

Abstract

In this work we suggest and analyze five new graphene-based components operating in THz region. They are Y, W and edge guided mode circulators and two switches with different geometries. The graphene elements are magnetized normally to their plane by a modest DC magnetic field. Numerical simulations demonstrate a high level of isolation, low insertion losses and a large bandwidth of circulators. The switches are characterized by high ON-OFF ratio and relatively low insertion losses.

1. Introduction

The THz spectrum of electromagnetic radiation $(0.1 \div 10)$ THz is still little explored scientifically and technologically, but potentially has many applications in such areas as telecommunications, biomedical images, security, remote sensing and civil engineering, among others. The frequency of graphene plasma waves (SPP-surface plasmon-polaritons) lies in this region. These waves, which are collective excitation of electrons in graphene, can be used in projects of many electromagnetic components, including nonreciprocal and control ones. The first experimental graphene THz isolator is described in [1].

2. Problem description

The geometry of the Y-, W-, the edge guided mode circulator and the switches with 90° bend and without bend are shown in Fig. 1a, 1b, 1c, 1d and 1e, respectively. These devices consist of graphene waveguides connected to a central graphene element magnetized normally by a DC magnetic field $\mathbf{B_0}$. The graphene elements are placed on a two-layer dielectric substrate made of silica (SiO_2) and silicon (Si).

The components have the following dimensions: Y and W circulator resonator radius R = 320nm, waveguide width w = 120nm, waveguide length L = 900nm. In the edge guided mode circulator, the side of the triangular element is L_T = 4000nm, waveguide width w = 1500nm and its length L_G = 3500nm. The switches with 90° bend and without bend have the resonator radius R = 600nm, waveguide width w = 200nm, waveguide length L = 1500nm. The gap d in Fig. 1a, 1b, 1d, 1e is 5nm. The thicknesses and electric

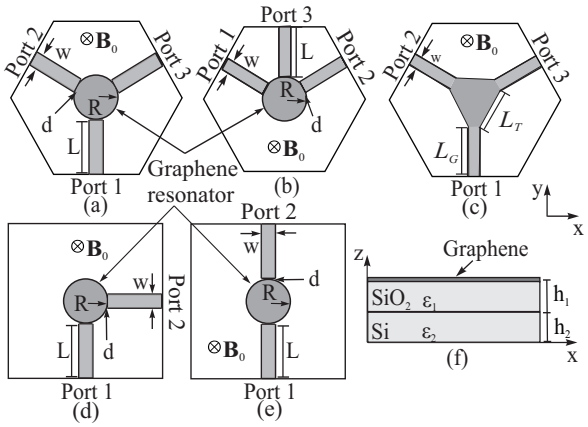


Figure 1: Schematic representation of the devices: top view a) Y-type circulator; b) W-type circulator; c) circulator with edge guided mode; d) switch with 90° bend; e) switch without bend, f) side view of the structures. $\mathbf{B}_0$ is bias DC magnetic field.

permittivities of the dielectric substrate are $h_1 = 5000$nm, $h_2 = 4000$nm, $\varepsilon_1 = 2.09$ and $\varepsilon_2 = 11.9$.

The tensor of graphene conductivity is as follows:

$$[\sigma_s] = \begin{pmatrix} \sigma_{xx} & -\sigma_{xy} \\ \sigma_{xy} & \sigma_{xx} \end{pmatrix}, \tag{1}$$

and the parameters of the tensor are [2]:

$$\sigma_{xx} = \frac{2D}{\pi} \frac{1/\tau - i\omega}{\omega_c^2 - (\omega + i/\tau)^2}, \tag{2}$$

$$\sigma_{xy} = -\frac{2D}{\pi} \frac{\omega_c}{\omega_c^2 - (\omega + i/\tau)^2}. \tag{3}$$

where $D = 2\sigma_0\epsilon_F/\hbar$ is the Drude weight, σ_0 is the conductivity of graphene, ϵ_F is the Fermi energy of graphene $\omega_c = eB_0v_F^2/\epsilon_F$ is the cyclotron frequency, $\hbar$ is the reduced Planck's constant, e is the electron charge, $\tau = 0.9$ps is the relaxation time, ω is the frequency of the incident wave, v_F is the Fermi velocity and $\mathbf{B}_0$ is DC magnetic field. The numerical simulations were fulfilled by software COMSOL Multiphysics [3].

3. Simulation results, circulators

3.1. General Characteristics

The principle of operation of the circulators with the circular elements (Fig. 1a, 1b) is based on guided plasmonic waves in the graphene waveguides, which excite the dipole resonances of the surface plasmon-polariton (SPP) in the central element. In the triangular element of Fig. 1c the edge guided mode is used. Thus, the wave injected into port 1 will be transmitted to port 3 and port 2 is isolated in Fig. 2a (Y-circulator), 2b (W-circulator), 2c and 2d (edge guided mode circulator).

It is well known that the infinite graphene placed on an air-dielectric interface supports transverse-magnetic (TM) SPP waves with a dispersion relation given by [4]:

$$\beta_{spp} = \frac{(1+\varepsilon_1)(\omega\hbar)^2}{4\alpha\epsilon_F\hbar c}, \tag{4}$$

where β_{spp} is plasmons propagation constant, $\alpha = e^2/(4\pi\varepsilon_0\hbar c) \approx 0.01$ is the fine-structure constant and ε_1 is the dielectric constant of the substrate. Thus, one can define the radius R of the resonator with dipole TM mode from the condition $2\pi R = \lambda_{spp}$, where λ_{spp} is the wavelength of the TM SPP mode. From the relations $\beta_{spp} = 2\pi/\lambda_{spp}$ and $R = \lambda_{spp}/2\pi$, it is possible to obtain an approximate expression for the radius of the resonator:

$$R \approx A\frac{\epsilon_F}{(1+\varepsilon_1)(\omega_c^2 - \omega_B^2)}, \tag{5}$$

where $A = 8.3 \times 10^{40}(kg.m)^{-1}$, ϵ_F is Fermi energy given in (J). One can see that the radius of the resonator R in (m) depends on the central frequency of the circulator ω_c and on cyclotron frequency of graphene ω_B given in (Hz) and also on ϵ_F and ε_1. Formula (5) will be used below for the calculus of the resonance structures.

The frequency characteristics of Y- and W-circulators are shown in Fig. 3a,b with the central frequencies 7.3THz and 7.51THz and the bandwidths of 6.3% and 9.1%, respectively. The insertion losses are less than -2 dB and the isolation level better than -15dB for DC magnetic field B_0 = 0.56T. From Fig. 3b, one can see that in the frequency band $(1.76 \div 3.76)$ THz, the isolation of the edge guided ultra-wideband circulator is $-(15 \div 40)$ dB and the fractional bandwidth is BW = 3.76THz / 1.76THz = 2.14 for DC magnetic bias of 0.8T.

3.2. Temporal coupled mode theory of Y-circulator

The temporal coupled mode theory (TCMT) [5] is used here to calculate the characteristics of the Y-circulator. This method is based on some general assumption such as weak coupling of the resonator with external world, linearity of the system and energy conservation. The reflection, transmission and isolation spectrum of the device can be described and given by equations (6), (7) and (8), respectively,

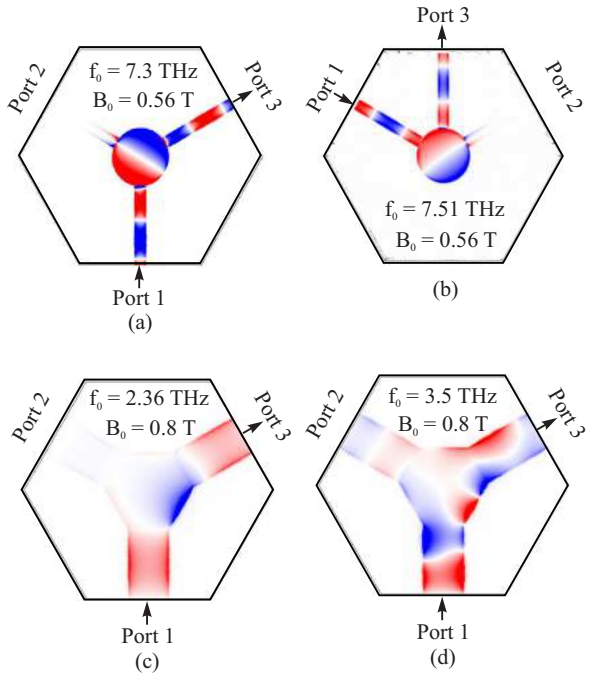


Figure 2: $|E_z|$ field distribution: a), b) Y-circulator (f = 7.3 THz) and W - circulator (f = 7.51 THz), $B_0 = 0.56$T, $\epsilon_F = 0.15$eV for both cases, c), d) Edge guide mode circulator, f = 2.36 THz, f = 3.5 THz; $B_0 = 0.8$T and $\epsilon_F = 0.10$eV for both cases.

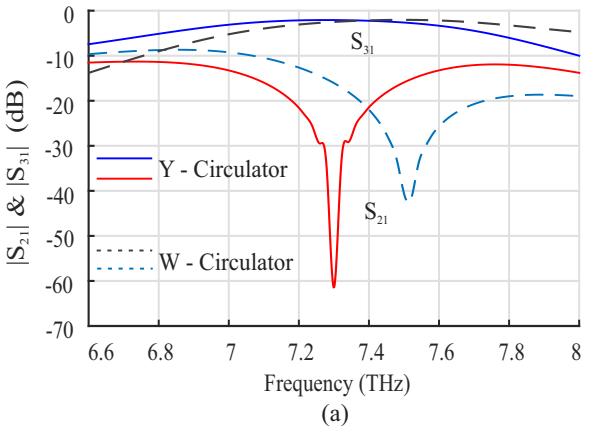
[6]:

$$S_{11} = -1 + \frac{2}{3}\left(\frac{\gamma_{+w}}{1+i(\omega-\omega_+)/\gamma_+} + \frac{\gamma_{-w}}{1+i(\omega-\omega_-)/\gamma_-}\right), \tag{6}$$

$$S_{31} = \frac{2}{3}\left(\frac{e^{i2\pi/3}\gamma_{+w}}{1+i(\omega-\omega_+)/\gamma_+} + \frac{e^{-i2\pi/3}\gamma_{-w}}{1+i(\omega-\omega_-)/\gamma_-}\right), \tag{7}$$

$$S_{21} = \frac{2}{3}\left(\frac{e^{-i2\pi/3}\gamma_{+w}}{1+i(\omega-\omega_+)/\gamma_+} + \frac{e^{i2\pi/3}\gamma_{-w}}{1+i(\omega-\omega_-)/\gamma_-}\right). \tag{8}$$

where ω_+, ω_- are the resonance frequencies and $\gamma_+ = \gamma_{+w} + \gamma_{+i}$ and $\gamma_- = \gamma_{-w} + \gamma_{-i}$ are the decay rates, which γ_{+w} and γ_{-w} are related the decay rates due to coupling of the resonator with waveguides, while γ_{+i} and γ_{-i} are the internal losses of the resonator. The resonance frequencies and the decay rates induced from the waveguide were obtained from the Comsol simulations. The calculated parameters are as follows: $\omega_+ = 47.12 \times 10^{12}$ rad/s, $\omega_- = 44.23 \times 10^{12}$ rad/s, $\gamma_{+w} \cong 1.6 \times 10^{12}$ 1/s, $\gamma_{-w} \cong 2.12 \times 10^{12}$ 1/s, respectively. The internal losses of the resonator are taken into account by the decay rates $\gamma_{+i} \cong 0.57 \times 10^{12}$ 1/s and $\gamma_{-i} \cong 0.6 \times 10^{12}$ 1/s. The frequency responses calculated by equations (6), (7) and (8) are in a good agreement with the results obtained by the Comsol full-wave simulations of the circulator (see Fig. 4).



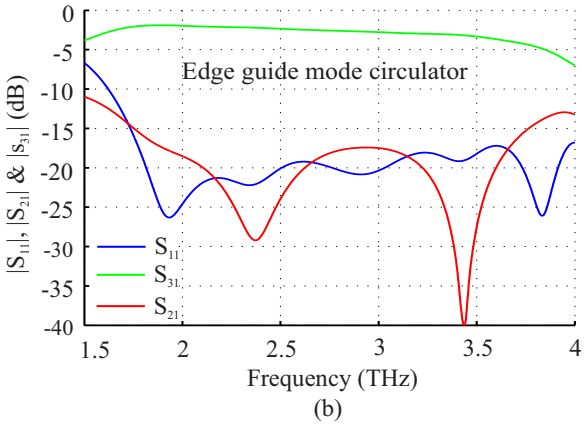


Figure 3: Frequency responses: a) Y- and W-circulator ($B_0 = 0.56$T, $\epsilon_F = 0.15$eV), b) edge guide mode circulator ($B_0 = 0.8$T, $\epsilon_F = 0.10$eV).

3.3. Fermi energy ϵ_F of W-circulator

Varying Fermi energy of graphene by an external electric field, one can change the carrier density of the material. In this way, it is possible to control dynamically the central frequency of the device. The influence of the Fermi energy on the resonance frequencies for the W-circulator was investigated. We consider the case of a fixed value of DC magnetic field $B_0 = 0.56$ T. An increase of ϵ_F shifts the central frequency of operation to the higher frequencies as shown in Fig. 5. With a small change of ϵ_F between 0.13 eV and 0.20 eV, the central frequency varies from 7THz to 8.63THz. However changing ϵ_F from its optimum value $\epsilon_F = 0.15$ eV deteriorates the isolation and narrows down the bandwidth of the device.

4. Simulation results, switches

The switches shown in Fig. 1d and 1e, work on the dipole resonance of the circular resonator. The wave injected into port 1, will be transmitted to port 2 (Fig. 6b and 6c), with DC magnetic bias which is of 0.71T and 0T (ON state) and it will be reflected to port 1 (Fig. 6a and 6d), with magnetic field of 0T and 1.6T (OFF state), respectively. The frequency characteristics of the switches with 90° bend and without bend in ON and OFF states are shown in Fig. 7a and Fig. 7b, presenting the bandwidth of 8.2% and 11.1%, respectively. Below, we present some results concerning the switches with 90° bend.

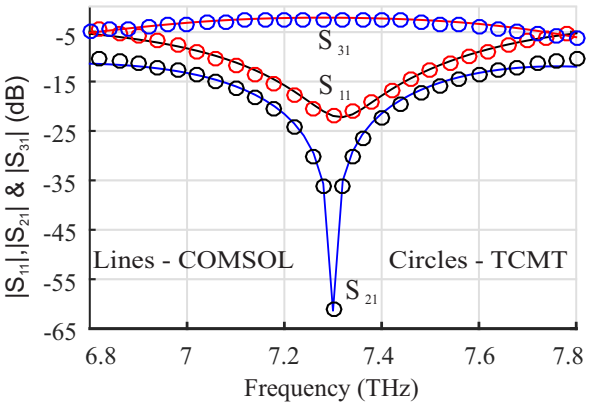


Figure 4: Simulated by Comsol (line), ($B_0 = 0.56$T, $\epsilon_F = 0.15$eV) and by TCMT (circles).

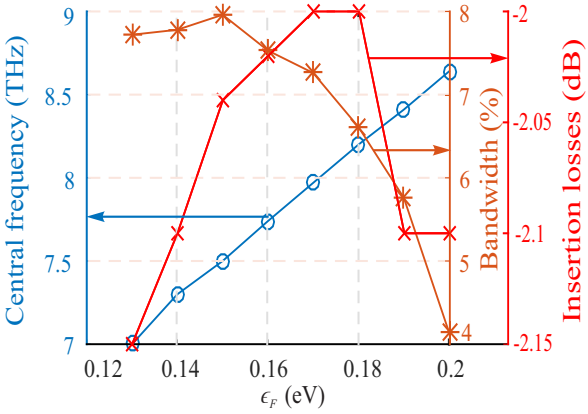


Figure 5: W-circulator, Fermi energy dependence of central frequency (circle marks), bandwidth (asterisk marks) and of insertion losses (x marks), $B_0 = 0.56$ T.

4.1. Influence of gap between resonator and waveguides

The influence of the gaps between the resonator and the waveguides for switch with 90° bend was investigated. The gap was varied from 2.5 nm to 10 nm and the frequency characteristics of the device with different values of the gap d are very similar (see Fig. 8). From Fig. 9 one can see that the central frequency decreases with the increase of the gap. Fig. 10 shows how the necessary magnetic field varies with the gap, presenting an decrease of the magnetic field with the increase of the gap.

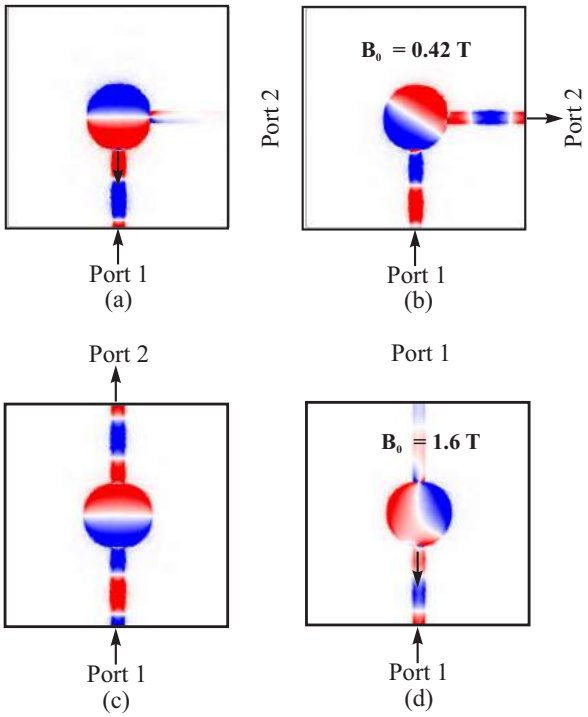


Figure 6: $|E_z|$ field distribution: a) ON state, b) OFF state (switch 90° bend - $B_0 = 0.71$T); c) ON state, d) OFF state (switch without bend - $B_0 = 1.6$T).

4.2. Central frequency versus radius

The radius of the resonator of switch with 90° bend was varied between the values of 350-600 nm. The parameters $w = 200$ nm, $d = 5$ nm and $\epsilon_F = 0.15$ eV were fixed. The frequency responses of the switch for different radii are plotted in Fig. 11. One can see that the characteristics of the device with different values of R are similar. With the increase of the radius of the resonator shifts the resonance frequency to lower values (Fig. 12).

The magnetic field B_0 for every R was optimized to obtain the maximum of transmission. The optimal DC magnetic field B_0 (Fig. 13) decreases with increasing the radius (R) of the resonator.

4.3. Influence of width of graphene waveguide

The influence of the width w of the graphene nano-ribbon of switch with 90° bend on the resonance frequency of the resonator was also analyzed. The frequency responses of the device for the widths of 150 nm, 200 nm, 300 nm and 400 nm, is shown in Fig. 14, maintaining all other parameters fixed, i.e. $R = 600$ nm, $d = 5$ nm and $\epsilon_F = 0.15$ eV. One can see that the characteristics of the switch with different values of w are similar, but for higher w the frequency shifted to lower values and the required magnetic field increases with the width of the nano-ribbon. This is due to the fact that, as we increase the width of the waveguides, the coupling between the guides and the resonator also increases, as can be seen in Fig. 15 and Fig. 16, respectively.

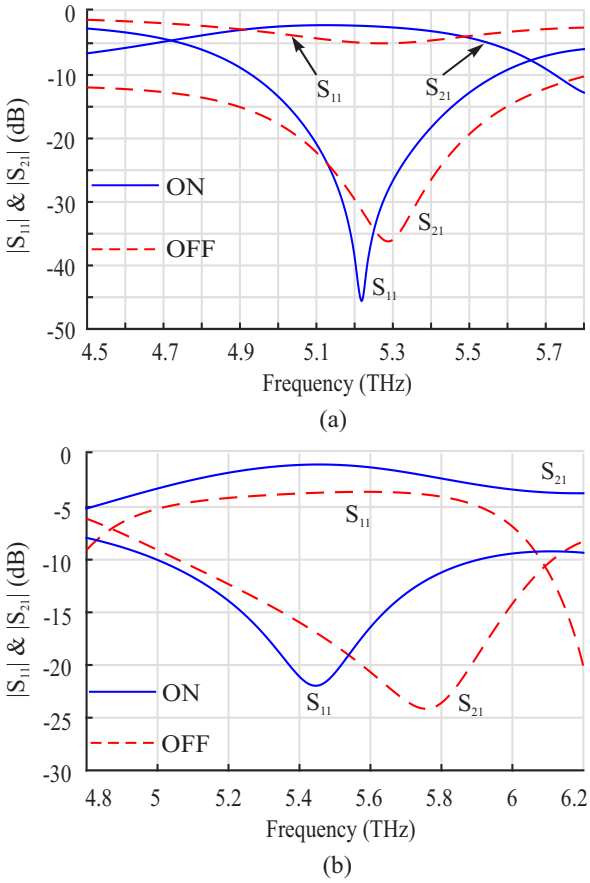


Figure 7: Frequency responses of a) switch with 90° bend and b) switch without bend (ON and OFF states), $\epsilon_F = 0.15$eV.

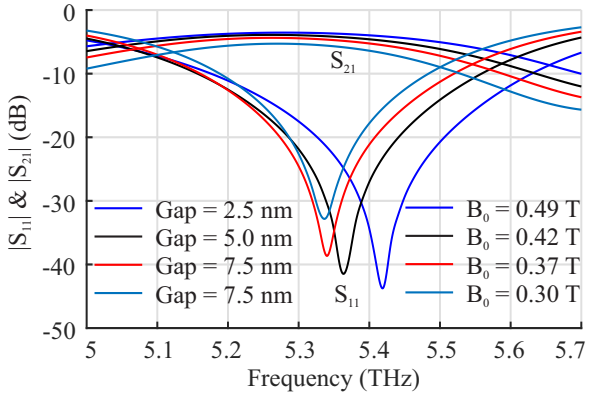


Figure 8: Frequency responses of switch with 90° bend for different values of gap d, w = 200 nm, $R = 600$ nm and $\epsilon_F = 0.15$ eV.

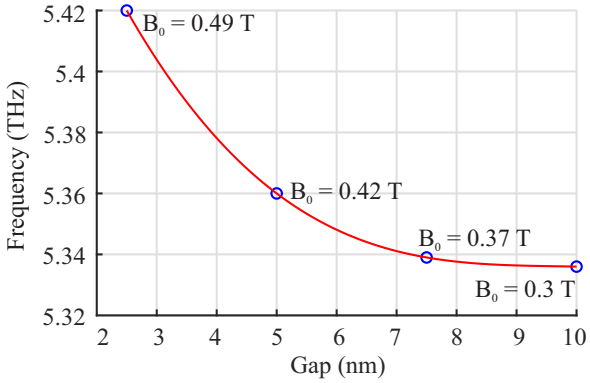


Figure 9: Central frequency of switch with 90° bend for different values of gap d, w = 200 nm, R = 600 nm and ϵ_F = 0.15 eV. Numbers on the curve are magnetic field B_0.

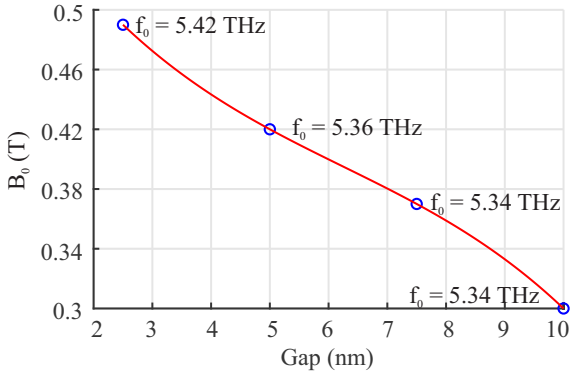


Figure 10: Magnetic field of switch with 90° bend for different values of gap d, w = 200 nm, R = 600 nm and ϵ_F = 0.15 eV. Numbers on the curve are central frequency f_0.

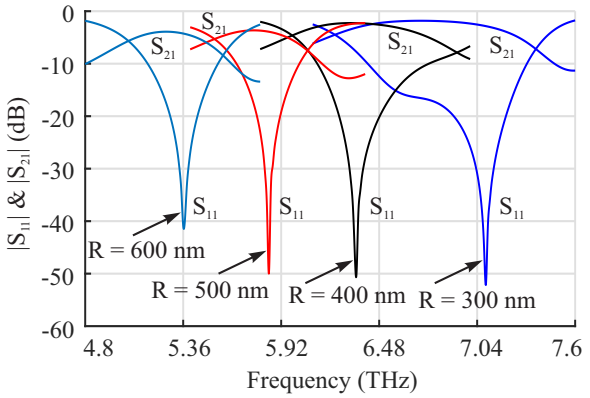


Figure 11: Frequency responses of of switch with 90° bend for different radii R, d = 5 nm, w = 200 nm and ϵ_F = 0.15 eV.

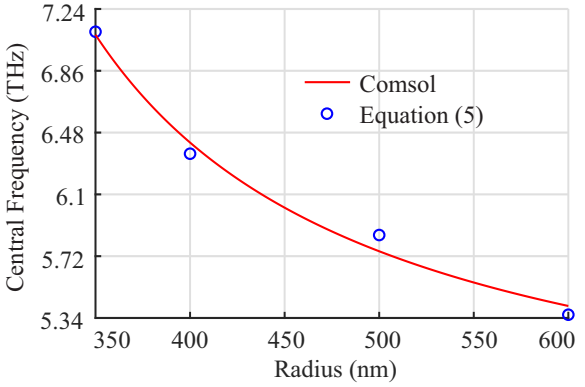


Figure 12: Central frequency of filter versus radii R, d = 5 nm, w = 200 nm, ϵ_F = 0.15 eV.

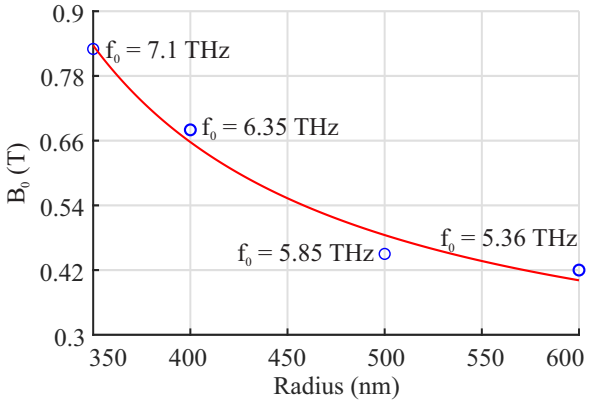


Figure 13: Variation of optimal magnetic field of circulator with radii R, d = 5 nm, w = 200 nm, ϵ_F = 0.15 eV. Numbers on the curve are central frequency f_0.

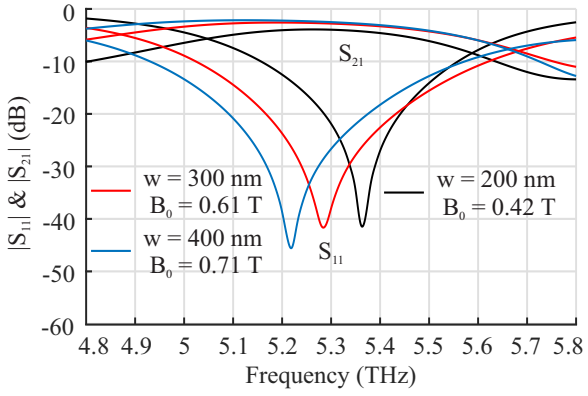


Figure 14: Frequency responses of switch with 90° bend for different widths w, d = 5 nm, R = 600 nm and ϵ_F = 0.15 eV.

4.4. Influence of Fermi energy

Varying Fermi energy of graphene by an external electric field, one can change the carrier density of the material.

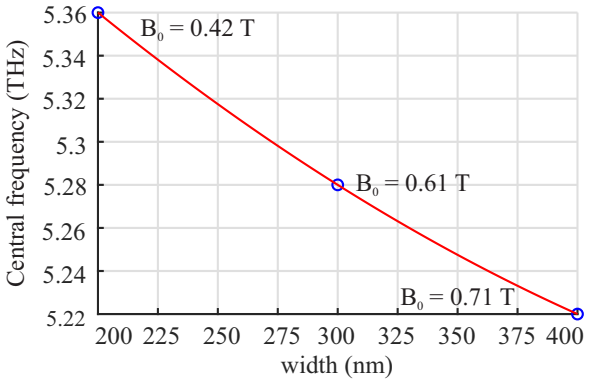


Figure 15: Central frequency of switch with 90° bend for different widths w, d = 2.5 nm, $\epsilon_F = 0.15$ eV. Numbers on the curve are DC magnetic field B_0.

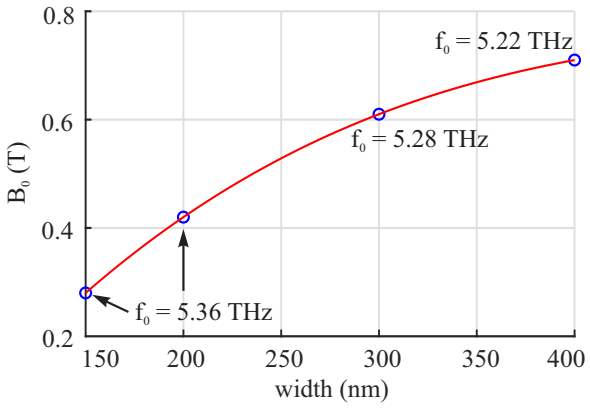


Figure 16: Optimal magnetic field of circulator versus w, d = 5 nm, $\epsilon_F = 0.15$ eV. Numbers on the curve are central frequency f_0.

In this way, it is possible to control dynamically the central frequency of the device. The influence of the Fermi energy on the resonance frequencies for the structure with 5 nm gap, 200 nm width and 600 nm radius was investigated. The Fermi energy was varied from 0.1 eV to 0.3 eV and the corresponding frequency responses are plotted in in Fig. 17. It can be observed that the increase of the Fermi energy shifts the resonance frequency to higher values, between 4.34 THz to 7.67 THz (see Fig. 18). With increasing Fermi energy, the optimal magnetic field B_0 grows almost linearly, as it can be seen in Fig. 19.

5. Conclusions

In this work we have suggested, analysed and conrmed by numerical and TCMT simulations a possibility of realization of five new graphene-based components. Among them three circulators and two switches operating in THz region. The simulations demonstrated that the devices possesses good frequency characteristics, low insertion losses and high bandwidth with a relatively low DC magnetic bias.

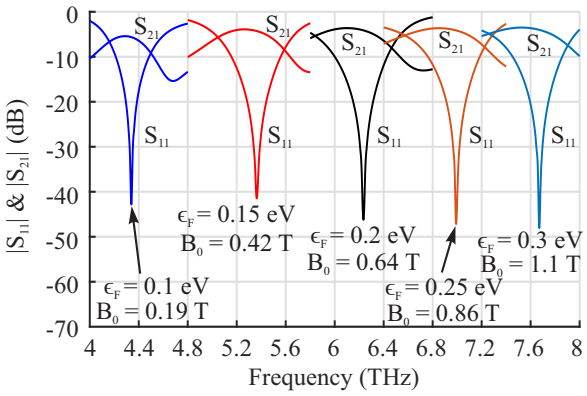


Figure 17: Frequency responses of switch with 90° bend for different values of ϵ_F, $d = 5$ nm, w = 200 nm and $R = 600$ nm.

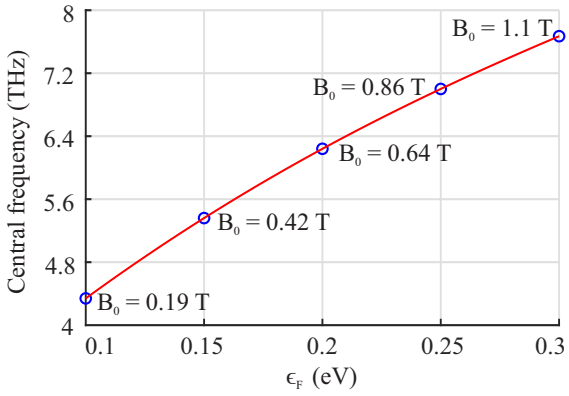


Figure 18: Frequency responses of switch with 90° bend for different values of ϵ_F, $d = 5$ nm, w = 200 nm and $R = 600$ nm. Numbers on the curve are magnetic field B_0.

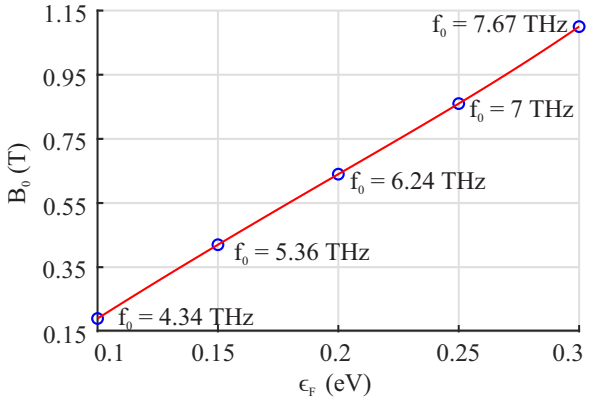


Figure 19: Optimal magnetic field B_0 of switch with 90° bend for d = 5 nm and w = 200 nm and $R = 600$ nm. Numbers on the curve are central frequency f_0.

Acknowledgement

This work was supported by Brazilian agency CNPq.

References

[1] M. Tamagnone, C. Moldovan, J. M. Poumirol, A. B. Kuzmenko, A. M. Ionescu, J. R. Mosig, and J. P. Carrier, Near optimal graphene terahertz non-reciprocal isolator, *Nature communications*, v. 7, pp. 1–6, 2016.

[2] I. Crassee, J. Levallois, A. L. Walter, M. Ostler, A. Bostwick, E. Rotenberg, T. Seyller, D. Van Der Marel, and A. B. Kuzmenko, Giant Faraday rotation in single-and multilayer graphene, *Nature Physics*, v. 7, pp. 48–51, 2011.

[3] http://www.comsol.com.br

[4] P. A. D. Gonalves, and N. M. R. Peres, "An introduction to graphene plasmonics", *World Scientific, New Jersey, 2016*.

[5] J. D. Joannopolus, S. G. Johnson, J. N. Winn, and R. D. Meade "Photonic Crystals", *Princeton University Press, pp. 198, New Jersey, 2007*.

[6] Z. Wang, and S. Fan, "Optical circulators in two-dimensional magneto-optical photonic crystals", *Opt. Letters, vol. **30**, no. 15, pp. 1989-1991, 2005*.

Strong light-graphene interaction in graphene/hBN heterostructures based electro-optic modulator on silicon photonics

Binbin Wang[1], Sylvain Blaize[1], Jinbong Seok[2,3], Sera Kim[2], Heejun Yang[2], and Rafael Salas-Montiel*[1]

[1] Department of Physics, Mechanics, Materials, and Nanotechnologies, ICD/L2n CNRS - Université de technologie de Troyes, 12 rue Marie Curie, 10004, Troyes, France
[2] Department of Energy Science, Sungkyunkwan University, Suwon 440-746, Korea
[3]Center for Integrated Nanostructure Physics (CINAP), Institute for Basic Science, Sungkyunkwan University, Suwon 440-746, Korea
*corresponding author, E-mail: rafael.salas@utt.fr

Abstract

We propose the integration of a plasmonic crystal into graphene/hBN based modulator on silicon photonics. Strong in-plane electric field confinement of the plasmonic Bloch mode enhances the overlap with graphene and hence their light absorption, which reduces device footprint and energy consumption. Here, we also report our current experimental results towards the fabrication and characterization of the nanomodulator with the use of near-field scanning optical microscopy. Optical confinement and absorption of graphene is found for encapsulated graphene on hBN compare to hBN-graphene-SiO_2 heterostructure on silicon photonic waveguides.

1. Introduction

Graphene/hBN based electro-optic devices, such as electro-optic modulators [1,2], photodetectors [3], have been proposed due to remarkable optical properties of graphene/hBN heterostructure. A challenge of high performances graphene/hBN based electro-optic devices is the enhancement of the interaction between light and graphene (ILG). As a 2D material, graphene has strong electric field component selectivity, which means that only in-plane components, parallel to graphene layer, contribute to light absorption within graphene layer (OAG) [4], namely, only in-plane components of light contribute to the enhancement of ILG. Such a selectivity requires special configurations which have strong overlap of in-plane electric field components within graphene layer (OIPG).

2. Enhancement of light-graphene interaction

Here, we propose the integration of a plasmonic crystal into graphene-on-hBN based electro-optic modulator on silicon photonics at communication wavelengths (Fig. 1a). The unit cell is an elliptical metallic cylinder of semi-major axis d_1. To quantify the overlap of light with graphene, we define the in-plane confinement ratio $\gamma = \rho_{xy}/\rho_{xyz}$, where ρ_{xy} and ρ_{xyz} are the in-plane and total electric field densities. Compare to the in-plane confinement ratio γ of a structure without plasmonic waveguide, more than 1000 times higher values are calculated (Fig. 1c, d). Ultra-high overlap is achieved in this configuration due to high in-plane confinement of the plasmonic crystal and high coupling efficiency between the plasmonic crystal waveguide and silicon waveguide. OAG can be expressed by $Q_S = 0.5\iint\sigma|E_{\|}|^2 dS$, where σ is the surface conductivity tensor expressed as diag (σ_{xx}, σ_{yy},0), $E_{\|}$ is the in-plane electric field component [4].

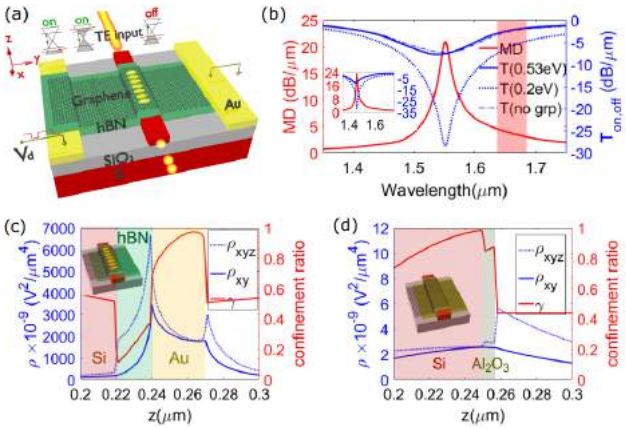


Figure 1: (a) 3D illustration of the nanomodulator. (b) Modulation depth (MD) and transmission spectra (T) with plasmonic crystal width d_1 = 250 nm. Red area highlights the range for transmission loss less than 3 dB/μm and a modulation depth higher than 3 dB/μm. Inset: modulation depth and transmission spectra with d_1 = 235 nm. Calculated electric field density ρ and in-plane confinement ratio γ of graphene-based modulator with (c) the plasmonic crystal waveguide (this work), and (d) without plasmonic waveguide (Ref. [2]). Insets present schematically the respective configurations.

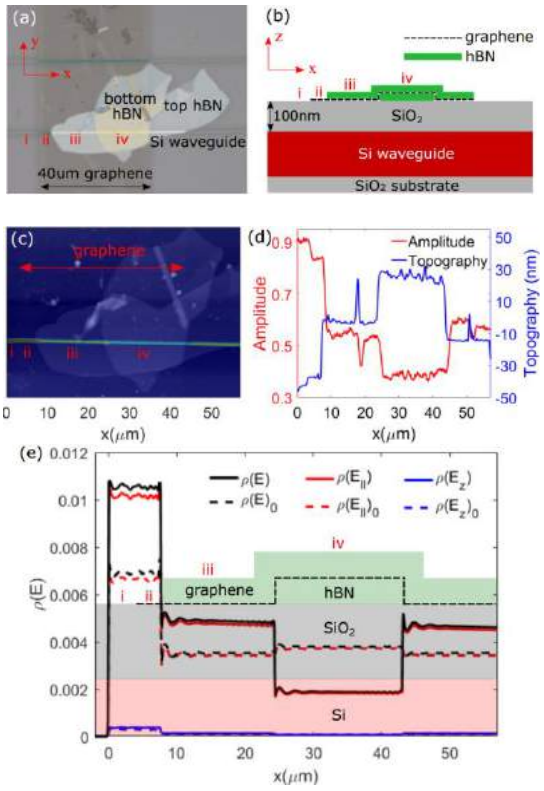


Figure 2: Micrograph of the graphene/hBN heterostructures on a Si photonic waveguide (a) and cross section along Si waveguide (b). i, ii, iii and iv indicate Si waveguide, graphene, hBN-graphene, and hBN-graphene-hBN region, respectively. (c) AFM topography and NSOM image. (d) NSOM signal profile along the propagation direction at the excitation wavelengths at 1.55 μm. (e) Electric field density profiles of the in- and out- of plane components with graphene (solid line) and without graphene (dashed line) above 20 nm from the surface of the sample.

Numerical results of the device present a modulation depth of 4 dB/μm at non-resonant wavelength 1.65 μm while the transmission loss is 2.5 dB/μm (Fig. 1b). Ultra-small footprint of 0.5 μm^2 allows ultra-fast modulation speed of up to 885 GHz and ultra-low energy consumption of 12 fJ/bit. This CMOS-compatible electro-optic modulator is a promising candidate for applications in optical communication integrated and neuromorphic computing circuits.

In our preliminary experimental results towards the plasmonic-enhanced nanomodulator, we have fabricated and characterized by near-field scanning optical microscopy three different graphene structure namely, graphene-on-SiO_2, hBN-graphene-SiO_2, and hBN-graphene-hBN-SiO_2 on a Si photonic waveguide (Fig. 2a). The thickness of the SiO_2 layer is 100 nm (Fig. 2b). The optical near-field image shows a decrease of the signal intensity in the hBN-graphene-hBN-SiO_2 heterostructure region compare to that in the hBN-graphene-SiO_2 region. This results can be explained by the higher electron mobility on encapsulated graphene [5,6] and reduced charges impurities [7]. Those results provide important guide for the design and optimization of electro-optic devices based on graphene-hBN heterostructure.

Acknowledgements

We thank Campus France (PHC Star project No. 34316PG), the French Région Grand-Est (HPC Center ROMEO) and the CSC scholarship (No. 201504490062) for partial support. We also thank M. Fevrier for fruitful discussion.

References

[1] Y. Gao, R.-J. Shiue, X. Gan, L. Li, C. Peng, I. Meric, L. Wang, A. Szep, D. Walker Jr, J. Hone et al., High-speed electro-optic modulator integrated with graphene-boron nitride heterostructure and photonic crystal nanocavity, *Nano letters* 15(3): 2001-2005, 2015.

[2] M. Liu, X. Yin, E. Ulin-Avila, B. Geng, T. Zentgraf, L. Ju, F. Wang, and X. Zhang, A graphene-based broadband optical modulator, *Nature* 474: 64–67, 2011.

[3] R.-J. Shiue, Y. Gao, Y. Wang, C. Peng, A. D. Robertson, D. K. Efetov, S. Assefa, F. H. Koppens, J. Hone, and D. Englund, High-responsivity graphene–boron nitride photodetector and autocorrelator in a silicon photonic integrated circuit, *Nano letters* 15(3): 7288–7293, 2015.

[4] H. Li, Y. Anugrah, S. J. Koester, and M. Li, Optical absorption in graphene integrated on silicon waveguides, *Appl. Phys. Lett* 101: 111110, 2012.

[5] D. H. Tien, J.-Y. Park, K. B. Kim, N. Lee, T. Choi, P. Kim, T. Taniguchi, K. Watanabe, and Y. Seo, Study of graphene-based 2D-heterostructure device fabricated by all-dry transfer process, *ACS Applied Materials & Interfaces* 8(5): 3072–3078, 2016.

[6] L. Banszerus, M. Schmitz, S. Engels, J. Dauber, M. Oellers, F. Haupt, K. Watanabe, T. Taniguchi, B. Beschoten, and C. Stampfer, Ultrahigh-mobility graphene devices from chemical vapor deposition on reusable copper, *Science Advances* 1(6): e1500222, 2015.

[7] K. Chattrakun, S. Huang, K. Watanabe, T. Taniguchi, A. Sandhu, and B. J. LeRoy, Gate dependent Raman spectroscopy of graphene on hexagonal boron nitride, *Journal of Physics: Condensed Matter* 25(50): 505304, 2013.

Wave Propagation in Acoustic and Elastic Metamaterials: Novel Design and Practical Applications

Controlling Reverberating Sound with an Acoustic Metasurface

Guancong Ma[1]

[1]Department of Physics, Hong Kong Baptist University, Kowloon Tong, Hong Kong

E-mail: phgcma@hkbu.edu.hk

Abstract

We show with experiments in a very complex reverberating room, we are able to achieve versatile control of sound fields by only modifying the room reverberating properties using a "spatial sound modulator" (SSM), which is an actively tunable metasurface for acoustic sound. We show the on-demand creation "quiet zones" or "hot spots", which shows the potential to improve quality of life in everyday situations.

Introduction

Reverberating cavity is an important and commonplace complex medium in acoustics. A room can be regarded as such a medium once the frequency is high enough (above the Schroeder frequency [1]). Familiar examples include classrooms, theaters, music halls, etc. In practice, reverberation is an important factor that impacts the usage of any indoor environment. However, so far the complexity and disordered nature of reverberating sound field has hindered its effective control [1]. This is why to alter the "acoustics" of a room usually end up in an overhaul of interior or even structural redesign. These options lack flexibility, and are difficult to implement. A new concept known as "wavefront shaping" [2, 3] has recently emerged in the field of optics. It shows unprecedented capability that control the propagation of light through diffusive media. This is an approach that inspired the current work.

Here, we treat the set of eigenmodes that constitutes the total reverberating sound field as controllable degrees of freedom. By altering the phase of a sufficient number of eigenmodes, we can indeed obtain control over the total sound field that is the consequence of the interference of these eigenmodes.

However, to effective control the modes' phases is no easy task, especially considering the relatively large wavelength of airborne sound in audible regime. To do so, we have designed and realized the first "spatial sound modulator" (SSM) that is based on the membrane-type acoustic metamaterials [4]. The SSM, which is shown in Fig. 1, is essentially an actively controllable metasurface, consisting an array of identical membrane metamaterial units each with 2 switchable states. These states can give the transmitted waves with a phase factor of either 0 or π. The state of each membrane unit is electrically controlled by a PC program through off-the-shelf electronics. The SSM must communicate with a sensor (a microphone placed at a certain position in the room) which acts as a feedback to guide it to reach the desirable state. We use an iterative optimization scheme to decide the best state for each unit on the SSM. By doing so, we demonstrate with experiments the creation of "zones of silence", as well as "acoustic hotspots" in a common reverberating environment. This means that the reverberation of a room is no longer a frigid constraint, but rather becomes a tunable property.

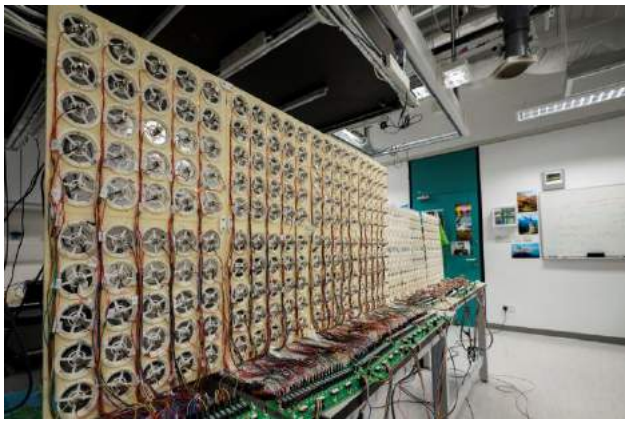


Figure 1: An reconfigurable acoustic metasurface is placed in the laboratory. It functions as a binary-phased spatial sound modulator (SSM).

The capability afforded by this SSM goes far beyond traditional wisdom, which regards sound reverberation as an intrinsic, permanent property of the room. Instead, reverberation now becomes a flexible property that is tunable to suit the function of the room. Our approach is based on the concept of wavefield shaping. To get this result, we build a reconfigurable acoustic metasurface, controllable by programmed electronics, acting as an array of binary phase modulator. This is the first "spatial sound modulator" (SSM) that extend to sound waves the concept of wavefront shaping which has recently been demonstrated in optics. These spatial sound modulators open new avenues to study and to control wave propagation in complex and chaotic media.

Acknowledgement

This work is the result of a collaboration with Xiying Fan, Ping Sheng, and Mathias Fink. The author thanks the support

of Innovation and Technology Commission of Hong Kong Government through Project No. ITF/203/15, and the Hong Kong Research Grants Council (Grant No. AoE/P-02/12).

References

[1] H. Kuttruff, *Room acoustics*, CRC Press (2009).

[2] A. P. Mosk, A. Lagendijk, G. Lerosey, M. Fink, 2012 Controlling waves in space and time for imaging and focusing in complex media, *Nat*. *Photon*. **6**, 283 (2012).

[3] S. Rotter and S. Gigan, Light fields in complex media: Mesoscopic scattering meets wave control, *Rev*. *Mod*. *Phys*. **89**, 015005 (2017).

[4] G. Ma, P. Sheng, Acoustic metamaterials: From local resonances to broad horizons, *Sci*. *Adv*. **2**, e1501595 (2016).

Lamb wave focusing by a plano-concave aspherical lens: numerical studies

Pawel Kudela[1*], Wieslaw Ostachowicz[1]

[1]Institute of Fluid Flow Machinery, Polish Academy of Sciences, Gdansk, Poland
*corresponding author, E-mail: pk@imp.gda.pl

Abstract

Lamb waves are often used for damage detection in structures. Hot-spot monitoring by wave focusing is considered here. It can be achieved by using a plano-concave aspherical lens. Once attached to the plate, the lens modifies the effective plate thickness, and therefore change the Lamb wave characteristics such as the wavenumber and phase velocity, providing a convenient way of controlling Lamb waves. We conducted numerical simulations and demonstrated that a planar A0 mode can be focused on the desired focal point.

1. Introduction

Lamb waves are elastic waves propagating in plate-like structures guided between two parallel free surfaces. There is growing interest in controlling Lamb waves in order to increase the performance of damage detection based on anomalies in propagating waves. Lamb waves are usually excited and registered by piezoelectric transducers of various configurations. However, sometimes it is required to monitor a particular area of a structure (e.g. hot spot) due to high stress concentration or high temperatures. But piezoelectric transducers cannot be placed very close to the hot spot area because they can be destroyed by the harsh conditions. In such case it is better to place transducer farther away and send Lamb waves in such a way that during propagation waves form a beam concentrated on hot spot (focusing). Lamb wave mode focusing can be achieved by using gradient-index phononic crystal [1]. Jin et al. proposed gradient-index phononic plates for simultaneous control of both A0 and S0 modes in a broadband frequency range [2]. Yan et al. [3] proposed surface bonded elastic metamaterials made of planar arrays of lead discs with varying thickness to focus A0 mode Lamb waves. A simple method of creating engineered lenses by locally reducing the plate thickness has been proposed by Climente et al. for controlling flexural waves [4, 5]. Thickness change has also been applied to achieve negative refraction and focusing of Lamb waves [6, 7]. In this paper, we present studies which follows the design of simple slice lens to control Lamb waves by modulating the wavefronts which was presented by Tian et al. [8]. We modified their approach so that piezoelectric transducer is bonded directly to the lens instead of the host structure. The lenses are slices with designed shapes made of the same material as the host plate, and can be easily added to the host plate using a coupling fluid. In this way a lens can be relocated to another area of the plate or removed and attached to another plate along with piezoelectric transducer.

2. Plano-concave aspherical lens design

The principle of focusing Lamb waves using a plano-concave aspherical lens is presented in Fig. 1. The shape of the lens is calculated by solving the following equation:

$$\frac{|D_1E_1|}{c_{PL}}+\frac{|E_1F|}{c_P}=\frac{|D_2E_2|}{c_{PL}}+\frac{|E_2F|}{c_P}, \qquad (1)$$

where c_{PL} and c_P are the phase velocities of A0 Lamb wave mode in the plate with and without the lens, respectively. It was assumed that the plate is made of 1 mm thick aluminium and the lens was made from the same material. Once the shape of the lens is designed, we created a mesh consisting of 3D spectral elements [9] and performed numerical simulations.

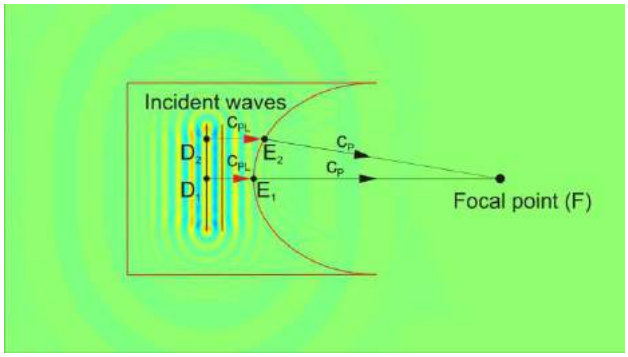


Figure 1: The principle of focusing Lamb waves using a plano-concave aspherical lens. D_1 and D_2 are two locations on the incident wavefront. The waves from the two locations exit the lens at E_1 and E_2, respectively, eventually arriving at the lens' focal point F at the same time.

3. Results and discussion

The Lamb waves were excited by a single piezoelectric transducer. The excitation signal was Hanning windowed toneburst with 10 cycles. Two carrier frequencies were considered: 100 kHz and 200 kHz and two focal points. Appropriate lenses were design for each case. Selected results of emanating waves from the lens are presented in Fig. 2 in which planar waves are propagating to the left whereas focusing waves are propagating to the right. The focusing performance in terms of wave energy (Root Mean Square) is shown in Figs. 3-4. The performance of the lens is frequency dependent, due to the dispersion of Lamb waves. Hence, the design requires narrow band excitations.

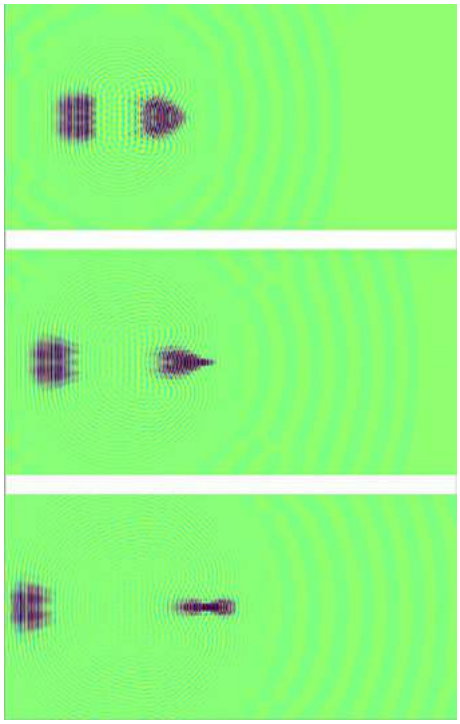


Figure 2: Selected time instances of wavefield of out-of-plane displacements showing focusing of A0 mode (100 kHz).

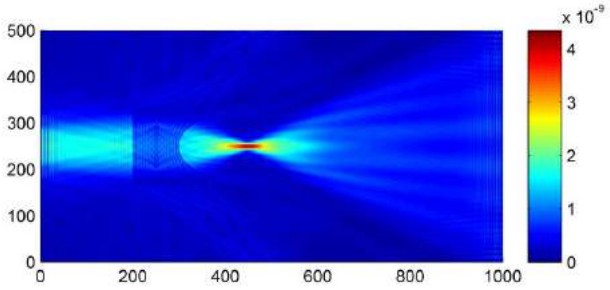


Figure 3: Distribution of the wave energy at 100 kHz and focal point F(450, 250).

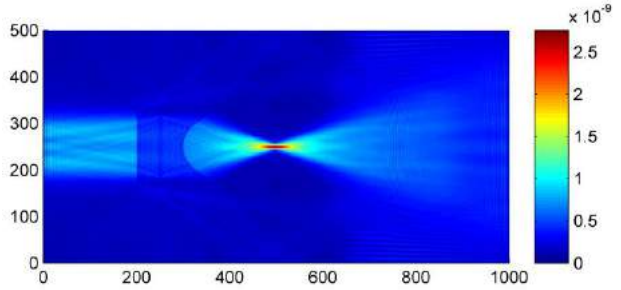


Figure 4: Distribution of the wave energy at 200 kHz and focal point F(500, 250)

Acknowledgements

The research was funded by the Polish National Science Center under grant agreement no DEC-2013/10/A/ST8/00071 in the frame of MAESTRO project entitled: Excitation and control of mechanical waves in nonlinear media.

References

[1] T.T. Wu, Y.T. Chen, J.H. Sun, S.C.S. Lin, T.J. Huang, Focusing of the lowest antisymmetric Lamb wave in a gradient-index phononic crystal plate, *Appl. Phys. Lett.* 98: 171911, 2011.

[2] Y.B. Jin, D. Torrent, Y. Pennec, Y.D. Pan, B. Djafari-Rouhani, Simultaneous control of the S0 and A0 Lamb modes by graded phononic crystal plates, *J. Appl. Phys.* 117: 244904, 2015.

[3] X. Yan, R. Zhu, G.L. Huang, F.G. Yuan, Focusing guided waves using surface bonded elastic metamaterials, *Appl. Phys. Lett.* 103: 121901, 2013.

[4] A. Climente, D. Torrent, J. Sanchez-Dehesa, Omnidirectional broadband insulating device for flexural waves in thin plates, *J. Appl. Phys.* 114: 214903, 2013.

[5] A. Climente, D. Torrent, J. Sanchez-Dehesa, Gradient index lenses for flexural waves based on thickness variations, *Appl. Phys. Lett.* 105: 064101, 2014.

[6] S. Bramhavar, C. Prada, A.A. Maznev, A.G. Every, T.B. Norris, T.W. Murray, Negative refraction and focusing of elastic Lamb waves at an interface, Phys. Rev. B 83: 014106, 2011.

[7] F. D. Philippe, T. W. Murray, C. Prada, Focusing on Plates: Controlling Guided Waves using Negative Refraction, *Sci. Rep.* 5: 11112, 2015.

[8] Z. Tian, L. Yu, Wavefront modulation and controlling for Lamb waves using surface bonded slice lenses, *J. Appl. Phys.* 122: 234902, 2017.

[9] P. Kudela, Parallel implementation of spectral element method for Lamb wave propagation modeling, *Int. J. Numer. Meth. Eng.* 106(6): 413-429, 2016.

Losses in gradient acoustic rainbow trapping metamaterials

Tuo Liu[1], Shanjun Liang[1], Fei Chen[1], Jie Zhu[1]

[1] Department of Mechanical Engineering, The Hong Kong Polytechnic University, Hung Hom, Hong Kong SAR, China
*corresponding author, E-mail: jiezhu@polyu.edu.hk

Abstract

Acoustic rainbow trapping metamaterials allows spatial-spectral modulation and broadband trapping of sound, by providing strong dispersion which normally is absent in natural materials. However, previous studies about the acoustic rainbow trapping metamaterials did not include the effect of intrinsic losses. In this talk, we will introduce a model of acoustic rainbow trapping metamaterial with gradient metasurfaces. We consider the inherent thermal and viscous losses inside the holes. It will be shown that the gradually diminished group velocity of the structure-induced surface acoustic waves becomes anomalous at the trapping position, induced by the existence of the inherent losses. In addition to the progressively increased attenuation of the structure-induced surface acoustic waves along the sound propagation direction, other phenomena such as reflectionless spatial-spectral modulation and sound enhancement can be achieved. Such absorptive trapped rainbow is the result of the balanced interplay among the local resonance inside individual holes, the mutual coupling of adjacent unit cells, and the inherent losses due to thermal conductivity and viscosity.

1. Introduction

The concept of "rainbow trapping" or "trapped rainbow"[1,2] originated from the studies in quantum optics and nonlinear optics3 on how to slow down and trap light. Acoustic rainbow trapping [3-8] also received considerable interests. However, the absence of materials with strong dispersion for sound in natural makes it more difficult to realize the trapped rainbow in acoustic system. Acoustic rainbow trapping metamaterials have been theoretically and experimentally investigated. Yet, the effects of inherent losses on the performance of acoustic rainbow trapping metamaterials have not been studied in previous studies, which hampers their development for practical applications. In this talk, we would like to take the intrinsic viscosity and thermal conductivity into consideration, to study a gradient index acoustic rainbow trapping metamaterial. In this case, incident sound components parallel and close to the gradient structure can be effectively converted into the structure-induced surface acoustic mode with not only gradually compressed waveform but also progressively varied attenuation. At the trapping position, the inherent thermal and viscous losses dominate, playing an important role to balance the interplay between the local oscillation inside individual holes and the mutual coupling among neighboring units. The resultant dissipation helps to mitigate the backscattering so that a so-called absorptive trapped rainbow phenomenon can be observed.

2. Results

Consider a rigid surface perforated with subwavelength square holes that are infinitely extended in two-dimensional space. The background medium has density ρ_0 and sound speed c_0. The side length and depth of the holes are a and h, respectively, with the period of the unit cell being d. The dispersion relation of the structure-induced surface acoustic waves can be obtained by analyzing the divergences of the $(0,0)$-th order reflection coefficient, namely, the zeros of the denominator of

$$1-k_h \tan(k_h h)\frac{\rho_0 a^2}{\rho_h d^2}\cdot\sum_{r,s=-\infty}^{+\infty}\frac{S_{rs}^2}{\sqrt{(q^{(r,s)})^2-k_0^2}}=0 \qquad (1)$$

where $(q^{(r,s)})^2=(k_x^{(r)})^2+(k_y^{(s)})^2$.

By arranging the hole depth distribution in a gradient fashion along the sound propagation direction, we construct the metamaterial now consisting of square holes with linear depth variation ranging from 0.5 mm to 25 mm. The variation of hole depth between neighboring units is much smaller than the lattice constant, to guarantee the gradually changed wavenumber of the structure-induced surface acoustic waves along the propagation direction. The propagation of the structure-induced surface acoustic waves from one unit to next unit has thus very little mismatch of group velocity and attenuation. In our case, $\Delta h/d=1/20$ is designed. Such arrangement is equivalent to the so-called gradient-index design. As shown in Figure 1, the dispersion curves corresponding to a series of uniform infinite metasurfaces constructed with different types of unit cells (different hole depths) are combined to obtain the spatial distributions of group velocity and attenuation. Each calculated group velocity of the structure-induced surface acoustic waves (solid lines) is equal to that of the background medium at and gradually decreases to a non-zero minimum with the increase of horizontal position. It then abruptly turns to infinity, suggesting that a cutoff corresponding to the trapping point exists and the absorption reaches maximum within this lossy system. Such

group velocity distribution is frequency dependent so that the reflectionless spatial-spectral separation becomes possible. Along with the strong attenuation of the structure-induced surface acoustic waves, the metamaterial can act as an absorptive structure to mimic the "permanently" trapped rainbow.

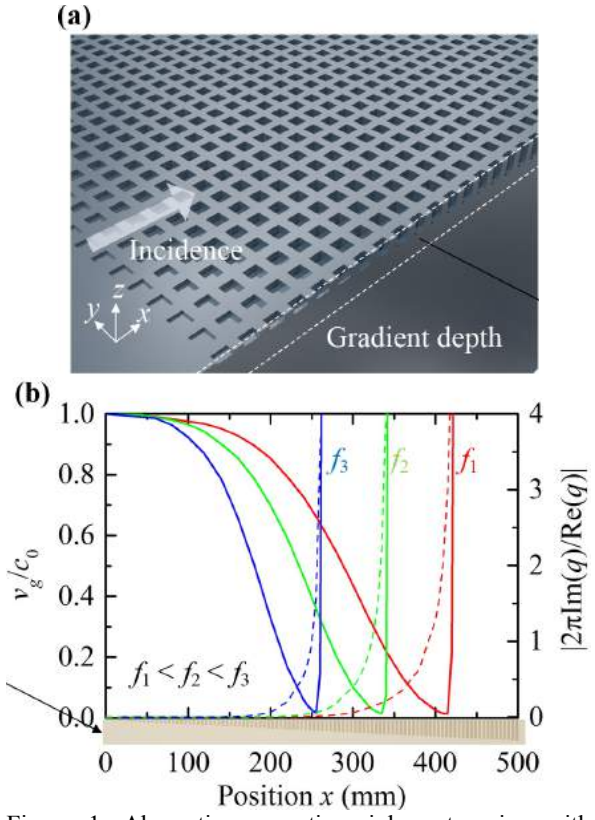


Figure 1: Absorptive acoustic rainbow trapping with gradient metamaterial. (a) Schematic illustration of the gradient design. (b) Group velocity and specific attenuation of the structure-induced surface acoustic wave along the gradient structure. The solid lines denote the group velocity and the dashed lines denote the absolute value of the specific attenuation (attenuation per wavelength). The group velocity anomaly (infinite) along with the attenuation implies the maximum absorption in the lossy system.

3. Discussion

From the physics point of view, the structure-induced surface acoustic wave is a result of the interplay between the local oscillation inside individual holes and the mutual coupling among adjacent units. The interplay forces the acoustic wave to travel in and out among the holes through diffractions. For lossless case, the local oscillation experiences a dynamic process of periodic storage and release of energy subject to the operating frequency, and strikes a balance with the mutual coupling at the resonance frequency. For the lossy case, the losses within the holes participates in the process and dissipate energy into heat. Such dissipation effect slowly becomes stronger along the direction where hole depth increases. At the trapping position, the local oscillation reaches resonance and the dissipation dominates, resulting in strong absorption of the surface mode. Therefore, the fundamental reason of energy absorption is the resonance behavior change of the units due to the inherent losses, together with the spatial modulation offered by the gradient distribution of unit cells in space.

4. Conclusions

In this talk, we introduce a lossy gradient acoustic rainbow trapping metamaterial model to study the absorptive acoustic rainbow trapping. The gradient index is realized by arranging subwavelength square holes with gradually increased depth along the wave propagation direction on a rigid surface. The effects of inherent losses that originate from viscosity and thermal conductivity within the holes are considered. Slowly diminished group velocity and progressively increased attenuation simultaneously happen along the acoustic rainbow trapping metamaterial. The group velocity becomes anomalous at the trapping position, leading to spatial-spectrally modulated and intensively enhanced sound field with vanished reflection. The absorptive trapped rainbow is thus realized. The presented model can be used to design more practical devices for high performance sensing and detection. It may also contribute to the study of hypersonic boundary layer.

Acknowledgements

The work was supported by the Early Career Scheme (ECS) of Hong Kong RGC (Grant No. 25208115) and the Departmental Internal Competitive Research Grant G-UA8T from the Hong Kong Polytechnic University.

References

[1] Tsakmakidis, K. L., Boardman, A. D., & Hess, O., *Nature*, 450(7168), 397-401, 2007.

[2] Gan, Q., Ding, Y. J., & Bartoli, F. J., *Physical Review Letters*, 102(5), 056801, 2009.

[3] Zhu, J., Chen, Y., Zhu, X., Garcia-Vidal, F. J., Yin, X., Zhang, W., & Zhang, X., *Scientific reports*, 3, 2013.

[4] Romero-Garcia, V., Picó, R., Cebrecos, A., Sanchez-Morcillo, V. J., & Staliunas, K., *Applied Physics Letters*, 102(9), 091906, 2013.

[5] Chen, Y., Liu, H., Reilly, M., Bae, H., & Yu, M., *Nature communications*, 5, 5247, 2014.

[6] Ni, X., Wu, Y., Chen, Z. G., Zheng, L. Y., Xu, Y. L., Nayar, P., ... & Chen, Y. F., *Scientific reports*, 4, 2014.

[7] Jiang, X., Liang, B., Li, R. Q., Zou, X. Y., Yin, L. L., & Cheng, J. C., *Applied Physics Letters*, 105(24), 243505, 2014.

[8] Zhou, C., Yuan, B., Cheng, Y., & Liu, X., Applied Physics Letters, 108(6), 063501, 2016.

Soft Acoustic Metamaterials: from 3D locally resonant metafluids to soft porous gradient index metasurfaces

Thomas Brunet[1], Olivier Poncelet[1], Christophe Aristégui[1], Jacques Leng[2], and Olivier Mondain-Monval[3]

[1]Université de Bordeaux – CNRS – Bordeaux INP, I2M, Talence, France
[2]Université de Bordeaux – CNRS – Solvay, LOF, Talence, France
[3]Université de Bordeaux – CNRS, CRPP, Talence, France
*corresponding author, E-mail: thomas.brunet@u-bordeaux.fr

Abstract

Soft acoustic metamaterials are classes of functional materials for acoustics achieved by means of soft matter techniques such as microfluidics, chemical formulation or self-assembly [1]. In this talk, I will review our recent advances in that field that allowed us to achieve the first soft 3D acoustic metamaterials with a negative index [2,3]. This was done by taking benefit from the low frequency Mie-type resonances (monopolar and dipolar) of "ultra-slow" micro-beads randomly dispersed in a water-based gel. The soft porous silicone rubber that we used to make these soft particles, not only has ultra-low sound speeds (~40m/s), but also exhibits a strong dependence of its sound speed on the porosity [4], providing thus materials with acoustic index ranging over a wide range of values (from 1.5 for non-porous materials up to 25 for porosities of about 30%). By assembling several thin rectangular stripes made of these soft porous silicone rubbers with different porosities, we have successfully fabricated soft gradient index metasurfaces with various index profiles that turned out to be very efficient for acoustic beam steering and focusing of ultrasound [5].

Acknowledgements

This work was funded and performed within the framework of the Labex AMADEUS ANR-10-LABEX-0042-AMADEUS with the help of the French state Initiative d'Excellence IdEx ANR-10-IDEX-003-02. This work was also supported by Agence Nationale pour la Recherche, and the Cluster Aerospace Valley (Grant ANR-15-CE08-0024 BRENNUS).

References

[1] T. Brunet, J. Leng, O. Mondain Monval, Soft Acoustic Metamaterials, *Science* 342: 323−324, 2013.

[2] T. Brunet *et al.*, Soft 3D Acoustic Metamaterial with Negative Index, *Nature Materials* 14: 384-388, 2015.

[3] S. Raffy *et al.*, A Soft 3D Acoustic Metafluid with Dual-Band Negative Refractive Index, *Advanced Materials* 28: 1760-1764, 2016.

[4] A. Ba *et al.*, Soft Porous Silicone Rubbers with Ultra-Low Sound Speeds in Acoustic Metamaterials, *Scientific Reports* 7: 40106, 2017.

[5] Y. Jin, R. Kumar, O. Poncelet, O. Mondain-Monval, and T. Brunet, *to be submitted*.

Extraordinary wave dynamics in time-Floquet acoustic systems

Theodoros T. Koutserimpas* **and Romain Fleury**

Laboratory of Wave Engineering, Ecole Polytechnique Fédérale de Lausanne (EPFL), 1007 Lausanne, Switzerland
*corresponding author, E-mail: theodoros.koutserimpas@epfl.ch

Abstract

In this talk, we discuss our recent research advances about wave control and manipulation using periodic temporal modulation of a system's properties. We show that by using the unique properties of so-called time-Floquet systems, we can construct acoustic metamaterials with extreme effective properties, such as with zero index of refraction. In addition, we show that the interaction with a periodic drive can lead to power exchange with the wave, providing a unique route to non-Hermiticity. We demonstrate examples of non-Hermitian acoustic systems based on time modulation, such as Parity-Time symmetric parametric amplifiers.

1. Introduction

Time-Floquet systems have been initially introduced in quantum and solid-state physics, but in recent years, they have been of great interest to research regarding devices operating under classical wave mechanisms [1], [2], [3]. Such systems are in general active and provide a time-periodic modulation to a physical parameter of the physical system. It is well known that when these time-Floquet dynamics are enabled, the frequency is not conserved and time-Floquet harmonics are created, in full agreement with the Floquet theorem [4]. Here, we explore two distinct consequences of these effects: (i) the possibility to break time-reversal symmetry in a space-periodic system (crystal), and use this to shape its band structure [2]; and (ii), the possibility to amplify wave signals, providing gain distributions of parametric nature that can exhibit, for instance, Parity-Time symmetry systems [3].

2. Zero refractive index in time-Floquet acoustic metamaterial

Based on time-Floquet dynamics, we demonstrate a new form of metamaterial with zero refractive index, i.e. in which time-harmonic fields have infinite wavelength and do not exhibit any spatial variations in their phase distribution. This unique feature is achieved by forcing the Floquet band structure to exhibit a Dirac cone at the center of the spatial Brillouin zone (Γ point). The conical dispersion at Γ with twofold degeneracy is confirmed numerically via stroboscopic analysis, and fullwave finite elements simulations (Fig. 1) [2]. The use of this medium for phase front manipulation will be discussed.

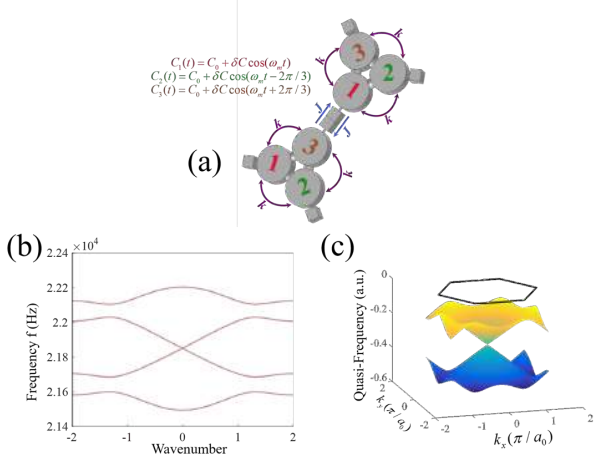


Fig. 1: a) Graphic representation of the unit cell of the examined acoustic spatiotemporal crystal, b) observation of conical dispersion of the band structure, and c) 3-D graphics of the conical dispersion at Γ. *C* is the acoustic capacitance of the cavity.

3. Parity-Time symmetric Parametric Amplifier

Time-Floquet dynamics are also relevant in the case of parametric systems which can amplify the wave signal, providing an interesting platform to implement gain distributions of parametric nature. We show here that simple modulation schemes can lead to distributions obeying Parity-Time ($\mathcal{PT}$) symmetry, which induce interesting scattering features. In particular, the scattering from a simple parametric slab, whose dynamics follow

Mathieu equation, can be described by a $\mathcal{PT}$-symmetric scattering matrix, whose $\mathcal{PT}$-breaking threshold corresponds to the Mathieu instability threshold. We will highlight the link between $\mathcal{PT}$ symmetry and time-Floquet systems, which will explain some unusual scattering phenomena like lasing, CPA, and anisotropic transmission resonances [3]. Our findings are confirmed by FDTD simulations.

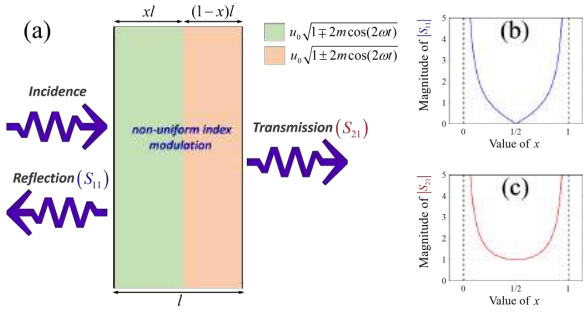


Fig. 2: a) Graphic representation of the non-uniform out-of-phase time-modulated slabs, b) the reflection coefficient diagram, and c) the transmission coefficient.

4. Conclusions

Our findings demonstrate that the physics of time-Floquet systems are very rich and markedly different than the ones of static systems. In particular, the non-conservation of frequency can be used to induce unique wave propagation features like anomalous values of the index of refraction, time-reversal symmetry breaking, or $\mathcal{PT}$ parametric amplification. Our results demonstrate the possibility for a novel class of devices benefitting from the tunability of time-Floquet systems. In acoustics, these systems may be obtained by using electronically controlled acoustic resonators or externally biased smart materials such as piezoelectric or magnetostrictive ceramics.

Acknowledgements

This work was supported by the Swiss National Science Foundation (SNSF) under Grant No.172487.

References

[1] T. T. Koutserimpas and R. Fleury, "Nonreciprocal gain in non-Hermitian time-Floquet Systems," to appear in *Physical Review Letters*.

[2] T. T. Koutserimpas and R. Fleury, "Zero refractive index in time-Floquet acoustic metamaterials," *J. Appl. Phys.*, vol. 123, no. 9, p. 91709, Mar. 2018.

[3] T. T. Koutserimpas, A. Alù, and R. Fleury, "Parametric amplification and bidirectional invisibility in PT-symmetric time-Floquet systems," *Phys. Rev. A*, vol. 97, no. 1, p. 13839, Jan. 2018.

[4] G. Floquet, "Sur les équations différentielles linéaires à coefficients périodiques," *Ann. Sci. l'École Norm. Supérieure*, vol. 12, pp. 47–88, 1883.

Tunable Perfect Absorbers for Low-Frequency Sound

Sibo Huang[1,2], Xinsheng Fang[1,2], Xu Wang[1,2]
Badreddine M. Assouar[3,4], Qian Cheng[1,2], and Yong Li[1,2*]

[1]Institute of Acoustics, Tongji University, Shanghai 200092, China
[2]Shanghai Key Laboratory of Special Artificial Microstructure Materials and Technology, Tongji University, Shanghai 200092, China
[3]CNRS, Institut Jean Lamour,Vandœuvre-lès-Nancy F-54500, France
[4]Université de Lorraine, Institut Jean Lamour, Boulevard des Aiguillettes, BP: 70239, Vandœuvre-lès-Nancy 54506, France
*corresponding author, E-mail: yongli@tongji.edu.cn

Abstract

Metasurface-based acoustic absorbers possessing the ability of perfect absorption with ultra-thin thickness have attracted comprehensive attention. Here, we present theoretical analysis and experimental verification of perfect absorbers via acoustic spiral metasurfaces consisting of coiled channels and further an innovative configuration with embedded-apertures. Due to their superior acoustic impedance manipulation, great tunability and capability in acoustic absorption performance is demonstrated. Our research would benefit to reveal the absorption mechanism and pave a way to design optimal acoustic absorbers.

1. Introduction

Conventional acoustic absorbers [1] generally require a structural thickness comparable to the working wavelength, which results in bulky configurations in low-frequency range. Micro-perforated panels with a backed cavity, as a resonant structure, is able to absorb sound energy more efficiently in low-frequency region, yet still suffers from the large thickness of its back cavity [2]. The emergence of acoustic metamaterials [3] and metasurfaces [4], has significantly broaden the acoustic research fields. Metamaterials and metasurfaces usually contain locally resonant units, which would provide an efficient and intrinsic way to increase the dissipation leading to a high absorption. One impressive type of design is that an efficient perfect absorber can be achieved by an ultra-thin decorated membrane [5]. Considering the fact that acoustic wave is scalar wave, the propagating path is extremely enlarged by coiling up space with labyrinthine configuration [6]. Introducing the concept of coiling up space into acoustic absorption system could realize perfect absorbers with deep sub-wavelength thickness capable of totally absorbing of the acoustic energy [7, 8]. Yet the absorption mechanism of the space-coiling acoustic absorbers and the superior feasibility of perfect absorption have not been systematically investigated, which are crucial for optimized designs of practical applications.

In this work, we theoretically and experimentally investigate and demonstrate ultra-thin acoustic perfect absorbers in low-frequency regime. To enhance the capability of acoustic impedance manipulation, an innovative design combining the coiled channels and an embedded-aperture is presented. The latter, indeed, offer an additional degree of freedom to tune the acoustic impedance providing, therefore, perform a great capability and tunability for achieving perfect absorption.

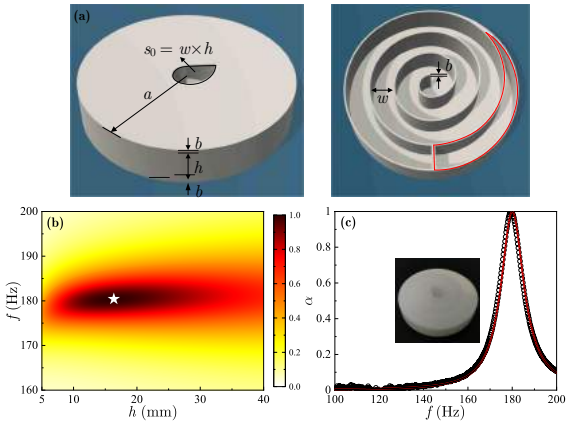


Figure 1: (a) Schematics of a spiral metasurface consisting of a covering panel with an opening, a backed panel and a coplanar coiled channel. (b) The absorption spectrum as functions of the height h and the frequency f. The white pentagram marks the perfect absorption. (c) The corresponding theoretical (lines) and experimental (dots) absorption coefficients, α, of a presented metasurface. The inset photo is the fabricated sample.

2. Results

Acoustic basic spiral metasurfaces with coiled channels are able to dissipate completely the incident energy with a compact thickness [Fig. 1(a)]. The left and right sketches illustrate the exterior and interior of the structure. The part marked by red line is cut down by an inserted thick panel. Herein, the absorption coefficient of the metasurface is

$$\alpha = 1 - \left| \frac{Z - \rho c}{Z + \rho c} \right|^2 . \qquad (1)$$

where ρ is the air density, c is the the sound speed, and the impedance of the basic spiral metasurface, Z, is

$$Z = -j\rho_c c_c A/s_0 \cot(k_c L) + A/s_0(j\omega\rho 0.48\sqrt{s_0} + \sqrt{2\omega\rho\eta}). \quad (2)$$

Here ω is the angular frequency, k_c, ρ_c and c_c refers to the complex wave number, complex air density and complex sound speed in the coiled channel respectively, $A = \pi a^2$ is the area of the integral metasurface, and the items of $j\omega\rho 0.48\sqrt{s_0}$ and $\sqrt{2\omega\rho\eta}$ are the end corrections that come from sound radiation of the channels' openings and the frication of air flow along the metasurfaces respectively. Eq. (1) implies that perfect absorption requires the impedance matching between the air and the metasurface, i.e., $\mathrm{Re}(Z) = \rho c$ and $\mathrm{Im}(Z) = 0$. To realize these conditions, the minimum value of $k_c L$ should be close to $\pi/2$ from the formula of Z [Eq. (2)], which implies that the length of the channel L has to approach to quarter of the wavelength. From the acoustic absorption spectrum, it is observed that total absorption is achieved at $f = 180$ Hz with $h = 16.5$ mm [Fig. 1(b)]. Perfect absorption is realized at $f = 180$ Hz with a deep sub-wavelength thickness of around $\lambda/104$, and the experimental results ($\alpha > 0.999$) exhibit remarkable accordance with the theoretical ones [Fig. 1(c)].

To pursue a improved manipulation of acoustic impedance, we introduce a novel configuration of spiral metasurface with an embedded-aperture (diameter d, and length l) appended at the opening of the coiled channels [Fig. 2(a)]. Compared to the previous configurations equipped apertures by a front panel [**?**], the embedded-aperture could manipulate acoustic impedance more efficient and avoid direct increased thickness. The acoustic impedance of the append aperture contributed to the spiral metasurface can be calculated by

$$Z_a = \frac{4A}{\pi d^2}\left[-j\frac{l\rho\omega J_0(\kappa d/2))}{J_2(\kappa d/2)} + 2\sqrt{2\omega\rho\eta} + j\omega\rho\delta_i)\right], \quad (3)$$

where J_n is Bessel function of the first kind of order n. As a result, the total impedance of the spiral metasurface can be express as $Z = Z_c + Z_a$ where Z_c referring to the acoustic impedance of the coiled channel without the end corrections [Eq. (2)].

With suitably selected geometrical parameters, a perfect absorber can be constructed at 148.5 Hz with a thickness of $h = 24$ mm Fig. 2(b)]. The experimental curve of absorption coefficient validates the occurrence of the perfect absorption [olive line and dots]. Following the same design strategy, perfect absorbers are also constructed exhibiting total absorption at other frequencies by suitable chosen structural parameters [Fig 2(b)]. Apparently, after introducing the appended embedded-apertures to the basic spiral metasurfaces, a more feasible and powerful manipulation of acoustic impedance is realized, resulting in a more tunable methodology in designing thinner acoustic perfect absorbers.

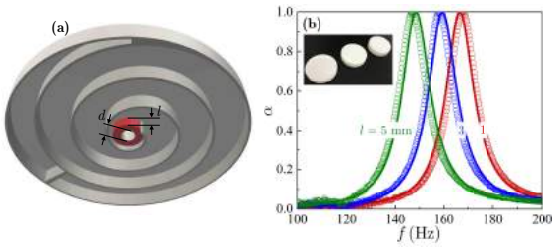


Figure 2: (a) The schematic of a short embedded-aperture with a length of l and a diameter of d (red region) appended to the basic spiral metasurface. (b) Absorption coefficient, α, of the presented metasurfaces.

3. Conclusions

We have investigated both theoretically and experimentally the spiral metasurfaces composed of a coplanar coiled channel and future improved one with appended embedded-apertures, which are capable of absorbing acoustic energy in low-frequency range with a deep sub-wavelength thickness. To resolve the disadvantage in basic spiral metasurfaces, where the working frequency is restricted to the length of the coiled channel, we presented spiral metasurfaces with appended embedded-apertures, which provide a more feasible and powerful way to tune the acoustic absorption performance.

References

[1] J. H. B. Zarek, Sound absorption in flexible porous materials, *J. Sound Vib.* 61: 205, 1978.

[2] D.-Y. Maa, Potential of microperforated panel absorber *J. Acoust. Soc. Am.*, 104: 2861, 1998.

[3] Z. Liu, X. Zhang, Y. Mao, Y. Y. Zhu, Z. Yang, C. T. Chan, P. Sheng, Locally Resonant Sonic Materials, *Science*, 289: 1734, 2000.

[4] Y. Li, B. Liang, Z. M. Gu, X. Y. Zou, J. C. Cheng, Reflected wavefront manipulation based on ultrathin planar acoustic metasurfaces, *Sci. Rep.*, 3: 2546, 2013.

[5] G. Ma, M. Yang, S. Xiao, Z. Yang, P. Sheng, Acoustic metasurface with hybrid resonances *Nat. Mater.*, 13: 873, 2014.

[6] Z. Liang, J. Li, Extreme acoustic metamaterial by coiling up space *Phys. Rev. Lett.*, 108: 114301, 2012.

[7] X. B. Cai, Q. Q. Guo, G. K. Hu, J. Yang, Ultrathin low-frequency sound absorbing panels based on coplanar spiral tubes or coplanar Helmholtz resonators, *Appl. Phys. Lett.*, 105: 121901, 2014.

[8] Y. Li, B. A. Assouar, Acoustic metasurface-based perfect absorber with deep subwavelength thickness, *Appl. Phys. Lett.*, 108: 063502, 2016.

Lossy Acoustic Materials with Independent Control of Phase and Amplitude for High-quality Manipulation of Airborne Sound

Bin Liang[1], Yi-fan Zhu[1], Xue-feng Zhu[2], and Jian-chun Cheng[1]

[1]Institute of Acoustics, Department of Physics, Nanjing University, Nanjing, China
[2]School of Physics, Huazhong University of Science and Technology, Wuhan, China
*corresponding author, E-mail: jccheng@nju.edu.cn

Abstract

The existing wave-steering metamaterials can only modulate the propagation phase, exerting a fundamental limitation on the quality of the resulting acoustic fields. Here we show, both theoretically and experimentally, that by judiciously tailoring the inherent loss, the phase and amplitude of reflected acoustic wave can be tuned independently, which breaks through this barrier and ensures fine manipulation of acoustic field. We experimentally demonstrate the effectiveness of our mechanism via projection of a high-quality acoustic hologram. Our design with capability and flexibility may open a new degree of freedom for realizing the complete control of sound.

1. Introduction

It is of paramount significance in acoustics to mold the wavefront of acoustic waves to form the desired acoustic field, which, however, are usually constrained by the acoustical response of naturally available materials. The recent advances in acoustic metamaterials that offer exotic acoustical properties and make it possible to realize fascinating phenomena of acoustic manipulation in ways unattainable in the nature [1-4]. More recently, acoustic metasurfaces, a class of metamaterials with a reduced dimensionality, empower new physics and lead to extended functionalities different from their three dimensional counterparts, enabling controlling transmitted or reflected acoustic waves in ways that was not possible before [5-11]. However the previous metamaterials only modulate the propagation phase of acoustic waves, posing a fundamental limitation on the wave-steering functionality which indeed calls for a simultaneous and independent control of both the amplitude and phase to achieve a perfect effect.

2. Theory of phase-modulating metamaterials

By introducing abrupt phase shift as acoustic waves traverses the interface between two media, we can revisit the classic law of reflection and refraction and attain a new degree of freedom for controlling the wavefront. In practice, such interfaces capable of imprinting phase discontinuities on propagating acoustic waves can be implemented by using a monolayer of unit cells of artificial structures, dubbed acoustic "metasurface", as schematically illustrated in Fig. 1. The acoustic reflection and refraction on metasurface is governed by the following generalized Snell's law which gives a nonlinear relationship between the incidence angle ϑ_i and reflection (refraction) angle ϑ_r (ϑ_t):

$$\sin\vartheta_r - \sin\vartheta_i = \frac{\lambda_0}{2\pi}\frac{\mathrm{d}\Phi(x)}{\mathrm{d}x},$$

$$\frac{1}{\lambda_1}\sin\vartheta_t - \frac{1}{\lambda_0}\sin\vartheta_i = \frac{1}{2\pi}\frac{\mathrm{d}\Phi(x)}{\mathrm{d}x},$$

where $\lambda_0 = c_0 / f$ is the wavelength in medium 0 with c_0 and f being the sound speed and working frequency respectively. Apparently, when $\Phi(x)$ is designed to be a nonlinear function of x, it is possible to manipulate the reflected and transmitted acoustic beams by controlling the nonlinear function such that the local acoustic response at each point can be engineered differently.

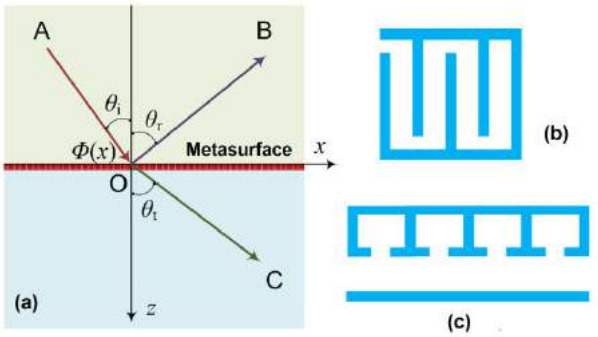


Figure 1: (a) Schematic of generalized Snell's law. (b,c) Schematics of typical designs of (b) reflection-type and (c) transmission-type metasurfaces.

However, the existing mechanisms for acoustic manipulation only rely on modulation of propagation phase, on the basis of the assumption that the amplitude of reflected/transmitted wave is always unity, which can be observerd from the above theoretical analysis.

3. Design of lossy acoustic metamterials for independent control of phase and amplitude

The fundamental limitation in the previous wave-steering metamterials makes it difficult for producing acoustic fields with complicated pattern. A representative example is the generation of acoustic hologram that would have many potential applications such as particle manipulations, ultrasonic therapy, and imaging, etc. Based on time-reversal symmetry, we can deduce the amplitude and phase profiles at the hologram plane conveniently. However the generation of complicated hologram images is very challenging for conventional methoes that use only phase modulation and rely on complex optimization process with the amplitude being assumed to be uniform throughout the hologram plane. The designed metmaterial for independent modulation of phase and amplitude at the surface under the illumination of sound on the front side is a holey structure schematically shown in Fig. 2(a). The leakage of sound through the aperture introduces the effective loss in the metamaterial, indicated by the blue arrow. Via analytical derivation and numerical simulations, we prove that that by changing the parameter w , the amplitude of reflection can be controlled to cover the range from ~0 to 1 without much affecting the phase of reflection ; similarly, by changing the parameter h_1, the phase of reflection can be tuned within a full range from 0 to 2π while the amplitude of reflection is almost unchanged.

By using the designed lossy metamaterials, we can break such limitation, thanks to the ability of independently modulating the amplitude and phase of reflection for all possible profiles. As a result, we can project high quality holographic images with a much simplified design process. A typical example is shown in Figs. 2(b) and (c). A predesigned image (e.g., the capital "N") can be generated by the reflection from lossy metamaterial at the given frequency and incidence angle. The arrows represent incidence and reflection directions of sound, respectively.

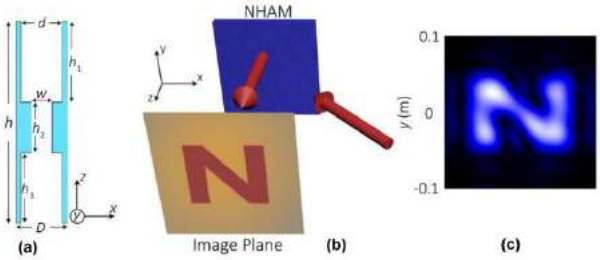


Figure 2: (a) A 3D illustration of a unit-cell of the proposed lossy metamaterial. (b) A 3D schematic diagram of an acoustic hologram. (c) Produced holographic patterns (the capital letters "N") on the image plane. The operating frequency f=17150Hz .

4. Conclusions

We have proposed a new class of metamaterial with judiciously designed loss distribution and employed it to achieve the complete control of sound, viz., modulating both amplitude and phase of sound in a precise, continuous and decoupled manner. An experimental demonstration of a high-quality acoustic hologram with large throughput, fine resolution, and low background noise is reported for verify the effectiveness of our mechanism. The independent control of phase and amplitude makes the proposed lossy metamaterial a very promising candidate for breaking the limitation of wave manipulation in the existing approaches, enabling construction of a required radiation pattern regardless of the complexity. This is impossible by using the previously proposed metasurfaces and may have fundamental significance in a great variety of important applications, such as the realization of arbitrarily shaped focusing for HIFU treatments or complicated 3D holographic images, which is intriguing in particle manipulations, architectural acoustics, and so forth. We believe our findings will provide a capacious platform for the fundamental exploration of wave-manipulation physics as well as various acoustic-wave-based applications.

Acknowledgements

This work was supported by National Key R&D Program of China (Grant No. 2017YFA0303700), the National Natural Science Foundation of China (Grant Nos 11634006, 11374157 and 81127901).

References

[1] J. Li and C. T. Chan, C. T. Double-negative acoustic metamaterial. *Phys. Rev. E* 70, 055602 (2004)

[2] N. X. Fang, et al. Ultrasonic metamaterials with negative modulus, *Nature Mater.* 5, 452-456 (2006)

[3] Z. Liang and J. Li. Extreme Acoustic Metamaterial by Coiling Up Space. *Phys. Rev. Lett.* 108, 114301 (2012).

[4] Z. Liang, et al. Space-coiling metamaterials with double negativity and conical dispersion, *Sci. Rep.* 3, 1614 (2013)

[5] Y. Li, B. Liang, Z. M. Gu, X. Y. Zou, and J. C. Cheng, Reflected wavefront manipulation based on ultrathin planar acoustic metasurfaces. *Sci. Rep.* 3, 2546 (2013).

[6] Y. Li, et al. Experimental realization of full control of reflected waves with subwavelength acoustic metasurfaces, *Phys. Rev. Appl.* 2, 064002 (2014).

[7] Zhao, J. J., Li, B. W., Chen, Z. N. and Qiu, C. W. Manipulating Acoustic Wavefront by Inhomogeneous Impedance and Steerable Extraordinary Reflection. *Sci. Rep.* 3 (2013).

[8] Li, Y., Jiang, X., Liang, B., Cheng, J.-c. & Zhang, L. Metascreen-based acoustic passive phased array. *Phys. Rev. Appl.* 4, 024003 (2015).

[9] Tang, K. et al. Anomalous refraction of airborne sound through ultrathin metasurfaces. *Sci. Rep*. 4 (2014).

[10] Xie, Y. B. et al. Wavefront modulation and subwavelength diffractive acoustics with an acoustic metasurface. *Nature Commun.* 5 (2014).

[11] Zhu, X. F. et al. Implementation of dispersion-free slow acoustic wave propagation and phase engineering with helical-structured metamaterials. *Nature Commun.* 7 (2016).

Band structures of a 1D tunable piezoelectric phononic crystal coupled to a 2D-periodic dispersive electric circuit

Olivier Poncelet[1], Alexander Shuvalov[1], Anton Kutsenko[2]

[1]Université de Bordeaux – CNRS, I2M, Talence, France
[2]Jacobs University, 28759 Bremen, Germany
*corresponding author, E-mail: olivier.poncelet@u-bordeaux.fr

Abstract

The need to confer tunable features to phononic crystals (PC) has prompted the community to invent different types of approaches to modify (online) their band structure (for instance variable frequency ranges of forbidden bands, modification of apparent velocity/elasticity under the quasi-static regime or long-wave conditions etc).

One way is the use of external stimuli (mechanical, thermal, magneto-electrics...) in order to modify the rheology and/or the geometry of some compounds of the PC, and thus alter to a certain extent the initial band diagrams [1-4]. Another approach, more efficient and versatile, is the coupling of the PC incorporating piezoelectric elements to an external electrical circuit [5]. The combination of piezoelectricity with well-chosen electrical/electronic components (piezoelectric patches over elastic structures or internal electrodes in piezo-active materials) not only allows significant quantitative variations of the dispersion curves but also the appearance of new types of band structures [6,7].

The purpose of this communication is to present a new way of tuning a (materially) one-dimensional PC structure with internal electrodes. The PC consists of a (mechanically) homogeneous, fully piezoelectric structure in which electrodes are inserted periodically [8]. The latter are coupled to a 2D-periodic network of electrical capacitors. In addition to some effects already known for the coupling of this type of PC with a 1D-periodic electrical network of capacitors (tunable forbidden bands for example), we theoretically observe new band structures with very peculiar behaviors for the context of 1D PCs, such as: non-monotonic branches, a spectrum of continuous bands, and a new form of acousto-electrical hybridization around specific values of the Floquet wave-numbers [9]. All these new effects are intimately related to the second dimension of the electrical network considered (the "orthogonal" one to the PC) which induces an intrinsic dispersion of the electrical part of the system and the notion of localization of the electric potential close to the mechanical part following the example of surface waves in elasticity.

Acknowledgements

This work was funded and performed within the framework of the Labex AMADEUS ANR-10-LABEX-0042-AMADEUS with the help of the French state Initiative d'Excellence IdEx ANR-10-IDEX-003-02. This work was also supported by Agence Nationale de la Recherche, Fondation de Recherche pour l'Aéronautique et l'Espace and the Cluster Aerospace Valley (Grant ANR-15-CE08-0024 BRENNUS).

References

[1] K.L. Jim, C.W. Leung, S.T. Lau, S.H. Choy, and H.L. W. Chan, Thermal tuning of phononic bandstructure in ferroelectric ceramic/epoxy phononic crystal, *Applied Physics Letters* 94, 193501, 2009.

[2] K. Bertoldi and M. C. Boyce, Mechanically triggered transformations of phononic band gaps in periodic elastomeric structures, *Physical Review B* 77, 052105, 2008.

[3] J.-Y. Yeh, Control analysis of the tunable phononic crystal with electro- rheological material, *Physica B* 400, 137, 2007.

[4] O. B. Matar, J.-F. Robillard, J. O. Vasseur, A.-C. Hladky-Hennion, P. A. Deymier, P. Pernod, and V. Preobrazhensky, Band gap tunability of magneto-elastic phononic crystal, *Journal of Applied Physics* 111, 054901, 2012.

[5] S. Degraeve, C. Granger, B. Dubus, J. O. Vasseur, M.P. Thi, and A.-C. Hladky-Hennion, Bragg band gaps tunability in an homogeneous piezo-electric rod with periodic electrical boundary conditions, *Journal of Applied Physics* 115, 194508, 2014.

[6] G. Trainiti and M. Ruzzene, Non-reciprocal elastic wave propagation in spatiotemporal periodic structures, *New Journal of Physics* 18, 083047, 2016.

[7] C. Croënne, J. O. Vasseur, O. B. Matar, M.-F. Ponge, P. A. Deymier, A.- C. Hladky-Hennion, and B. Dubus, Brillouin scattering-like effect and non-reciprocal propagation of elastic waves due to spatio-temporal

modulation of electrical boundary conditions in piezoelectric media, *Applied Physics Letters* 110, 061901, 2017.

[8] A.A. Kutsenko, A.L. Shuvalov, O. Poncelet and A.N. Darinskii, Quasistatic stopband and other unusual features of the spectrum of a one-dimensional piezoelectric phononic crystal controlled by negative capacitance, *Comptes Rendus Mecanique* 343, 680–688, 2015.

[9] A.A. Kutsenko, A.L. Shuvalov and O. Poncelet, Dispersion spectrum of acoustoelectric waves in 1D piezoelectric crystal coupled with 2D infinite network of capacitors, *Journal of Applied Physics* 123, 044902, 2018.

Negative refraction and double negativity for acoustic waves in three-dimensional bubble metamaterials

John H. Page[1*], Maxime Lanoy[1,2,3], Geoffroy Lerosey[2], Fabrice Lemoult[2], Arnaud Tourin[2] and Valentin Leroy[3]

[1]Department of Physics and Astronomy, University of Manitoba, Winnipeg, Manitoba, Canada R3T 2N2
[2] Institut Langevin, ESPCI Paris, CNRS, PSL Research University, Paris 75005, France
[3]Laboratoire Matière et Systèmes Complexes, Université Paris-Diderot, CNRS (UMR 7057), Paris 75013, France

*corresponding author, E-mail: john.page@umanitoba.ca

Abstract

Bubble metamaterials are created by exploiting the low-frequency Minnaert resonance of bubbles, and can radically modify acoustic wave behaviour. Here we show how three-dimensional structures with pair-wise spatial correlations between the bubbles can exhibit doubly negative behaviour. This can occur when the bubble pairs are arranged in either random or periodic configurations. Predictions for both types of structure will be presented and the influence of dissipation on doubly negative behaviour discussed.

1. Introduction

For more than a decade, negative refraction and its impact on focusing of acoustic waves have been the subject of great interest. These phenomena for acoustic waves were first observed in phononic crystals, where negative refraction is due to a band-folding mechanism (see Ref. [1] for a review). Metamaterials, whose properties result from low-frequency resonances, have the advantage that their subwavelength internal structure enables an effective medium description. As was established in the pioneering work of Li and Chan [2], negative refraction can be achieved when both the dynamic effective compressibility, associated with a monopolar resonance, and the dynamic mass density, associated with a dipolar resonance, are simultaneously negative – hence the term double negativity. Since then, there have been several experimental demonstrations of negative refractive index behaviour for metamaterials with either a single type of resonant inclusion, which exhibits both monopolar and dipolar resonances at overlapping frequencies [3], or two types of resonant inclusions, one of which has a monopolar resonance and the other a dipolar one [4,5]. For bubbles, on the other hand, the only strong resonance is monopolar. How, then, can doubly negative behaviour be realized in bubble metamaterials?

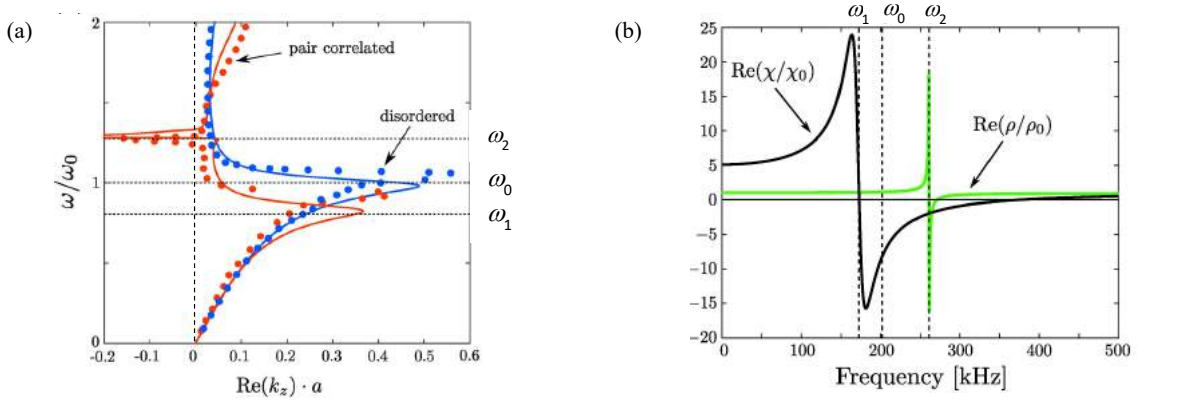


Figure 1: (a) Dispersion relations (frequency, normalized by the monopolar resonant frequency of a single bubble ω_0, versus the real part of the wavevector k_z along the propagation axis, normalized by bubble radius a), comparing pair-correlated disordered (red) and uncorrelated (blue) disordered samples. (b) Effective compressibility χ and density ρ for the pair-correlated case, normalized by their values in the host medium. Here a = 100 μm, the volume fraction is 1%, and ω_1 and ω_2 are monopolar and dipolar resonant frequencies of the bubble pairs. The bubbles in each pair are separated by d = 250 μm and the pairs are aligned along z. Symbols and solid curves represent predictions of multiple scattering theory and effective medium theory, respectively.

2. Results and Discussion

In this presentation, we show that when the bubbles are arranged in pairs at a fixed separation (d), multiple scattering coupling within each pair creates a dipolar response that overlaps the broader monopolar resonance [6]. These spatial correlations lead to a transparency window in which both the effective compressibility and density are negative. Remarkably, our numerical and analytic calculations both show that this behaviour is observed when the bubble pairs are randomly distributed in the metamaterial – see the results in Fig. 1. Near the frequency of the dipolar resonance, the medium is doubly negative [Fig. 1(b)] and the real part of the wave vector is also negative [Fig. 1(a)], indicating a negative index of refraction. Additional numerical calculations were carried out to confirm that when a wave is incident from water on the pair-correlated bubbly material, the waves are negatively refracted.

In Fig. 1, the basic effect of imposing pair-wise spatial correlations is illustrated without accounting for losses. However, including losses in the models, with realistic parameters that are appropriate for bubbles in a yield stress fluid, simply increases the minimum concentration of bubble pairs needed to induce double negativity (to approximately 2.3%), but does not eliminate the negative index behaviour [3,7] seen at the lower concentration chosen for illustrative purposes in Fig. 1.

These results on disordered bubble metamaterials emphasize that all that is needed to achieve double negativity is spatial correlations between pairs of these monopolar scatterers – a completely ordered structure is not required. Having identified this key ingredient, it is nonetheless interesting to also ask what kind of periodic structures naturally incorporate this feature. Our numerical calculations for bubbles arranged on a diamond lattice, which is the three-dimensional counterpart of the honeycomb arrangement used in Ref. [8], demonstrate that this bi-periodic structure is ideal, with a fully isotropic negative band. Figure 2 shows that this metamaterial can be used to focus a point-like source with subwavelength resolution.

3. Conclusions

These results on 3D bubble metamaterials with pair-wise spatial correlations demonstrate how deeply-subwavelength spatial patterning of inclusions in metamaterials can play a crucial role in determining material properties and functionality.

Acknowledgements

We are grateful for support from LABEX WIFI (references ANR-10-LABX-24 and ANR10-IDEX-0001-02 PSL*), Direction Générale de l'Armement (DGA) and NSERC.

References

[1] J.H. Page, Focusing of ultrasonic waves by negative refraction in phononic crystals, *AIP Advances* 6: 121606, 2016.

[2] J. Li and C. T. Chan, Double-negative acoustic meta-material, *Phys. Rev. E* 70: 055602, 2004.

[3] T. Brunet et al., Soft 3D acoustic metamaterial with negative index, *Nat. Mater*. 14: 384-9, 2015.

[4] Y. Ding, Z. Liu, C. Qiu, and J. Shi, Metamaterial with simultaneously negative bulk modulus and mass density, *Phys. Rev. Lett*. 99:093904, 2007.

[5] S. Lee et al., Composite acoustic medium with simultaneously negative density and modulus, *Phys. Rev. Lett.* 104: 054301, 2010.

[6] M. Lanoy et al., Acoustic double negativity induced by position correlations within a disordered set of mono-polar resonators, *Phys. Rev. B* 96:220201(R), 2017.

[7] J. Dubois, C. Aristégui, and O. Poncelet, Spaces of electromagnetic and mechanical constitutive parameters for dissipative media with either positive or negative index, *J. Appl. Phys.* 115:024902, 2014.

[8] N. Kaina, F. Lemoult, M. Fink, and G. Lerosey, Negative refractive index and acoustic superlens from multiple scattering in single negative metamaterials, *Nature* 525:77-81, 2015.

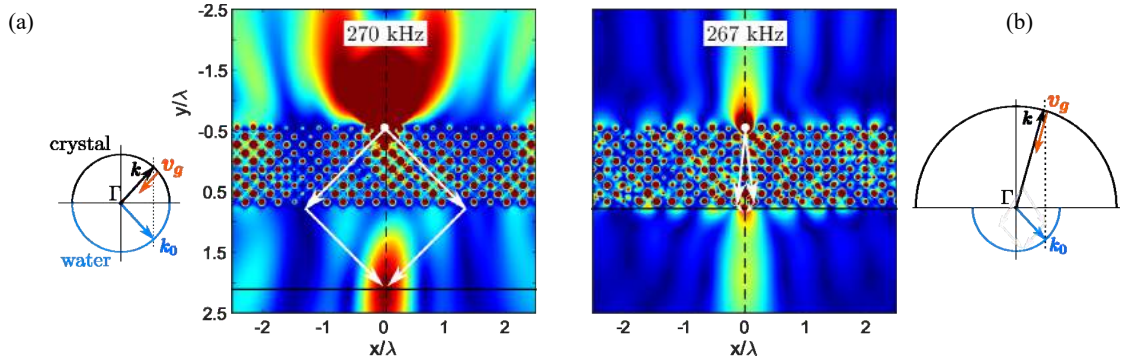


Figure 2: Equifrequency contours and focusing patterns determined numerically in the isotropic negative band of a bubble metamaterial with the diamond structure. In (a), the refractive index $n = -1$ and the resolution of the focal spot (according to the Rayleigh criterion) is $\lambda/1.5$. In (b), $n = -2.2$ and the resolution is $\lambda/6$.

Air-coupled ultrasound manipulation and laser vibrometry for damage detection in plate-like structures

Maciej Radzieński[1,*], Paweł Kudela[1], Michał Jurek[1,2], Wiesław Ostachowicz[1]

[1]Institute of Fluid Flow Machinery, Polish Academy of Sciences, Gdansk, Poland
[2] Department of Structural Mechanics, Rzeszow University of Technology, Rzeszów, Poland
*corresponding author, E-mail: maciej.radzienski@imp.gda.pl

Abstract

In this studies, we presented an approach for ultrasonic, air-coupled excitation of guided waves in thin composite plate for damage detection purposes. An array of ultrasound transmitters was prepared. Scanning laser vibrometer measurements and full wavefield analysis were used to create a damage map of the specimen.

1. Introduction

Guided waves have been utilized in Structural Health Monitoring (SHM) and Non-Destructive Testing (NDT) for decades. Most of the applications are based on a group of PZT transducers attached to specimen surface for excitation and sensing of guided waves. Various damage detection methods in such a setup were developed, like: pulse-echo, pitch-catch and phase-array [1]. In recent decades scanning laser vibrometry was developed and used for full wavefield measurements of guided waves. This allowed for new approaches based on processing full field data [2]. However, in some cases like large objects testing or high-temperature applications, there is a need to use a fully non-contact damage detection system. For this purpose, laser-thermoelastically excited guided waves [3] or excited by laser ablation [4] were proposed. However, those devices can generate only pulse excitation (wide frequency range), need a special surface treatment and are very expensive. An alternative solution to create non-contact excitation system is to use ultrasonic air coupled transmitters. In this research, experimental verification of guided wave based damage detection system with proposed air-coupled excitation, composed of ultrasound transmitter array (UTA) is presented.

2. Air-coupled guided wave excitation

2.1. Ultrasound transmitter array

An array of 36 ultrasonic transmitters (40ST-16) was prepared in circular configuration presented in Figure 1. The resonant frequency of those transmitters is 40 kHz, capacity is 2000 pF, and they are able to produce 115dB sound pressure 300 mm from its front cover.

The focusing point was designed to be 100 mm away from the UTA center point. The focusing point was aligned with the geometrical center of specimens back surface.
Ultrasonic transmitters were divided into four groups, with various distance to the focal point (marked with different colors in Figure 1a). Each transducer was generating the same signal (10 sine cycles modulated by Hanning window) with varying time delay, what is listed in Table 1.
For comparison purposes, a test with PZT transducer, exciting the same signal, attached to the specimen geometrical center was performed.

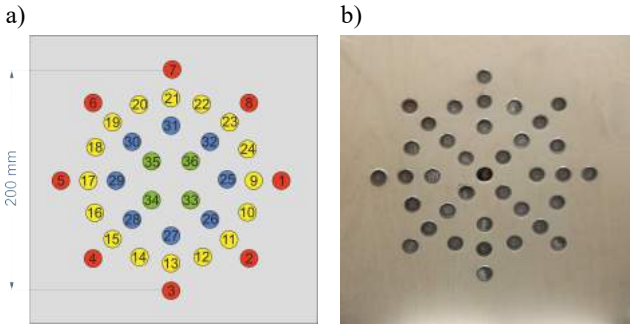


Figure 1: Ultrasonic transmitter array a) scheme b) picture.

Table 1: Ultrasonic transmitters array.

Transmitter number	Color	Time delay [μs]
1- 8	red	0
9-24	yellow	47.85
25-32	blue	86.30
33-36	green	111.72

2.2. Specimen

Carbon fiber reinforced polymer plate with dimension 500 x 500 x 1.5 mm was used for experimental verification of proposed approach. Its diagram is presented in Figure 2. Delamination in a form of 15 x 15 mm Teflon tape insert between layers was introduced during manufacturing process.

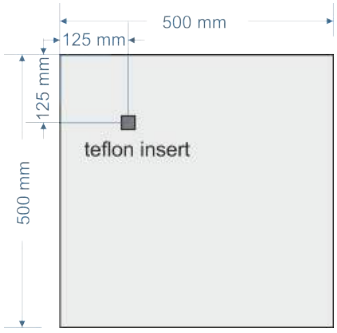


Figure 2: Specimen diagram.

2.3. Experimental setup

Scanning laser Doppler vibrometer was used to measure full field of propagating guided waves in 375 x 375 equally spaced points. Ultrasonic transmitters were supplied from multichannel waveform generator thought amplifier.

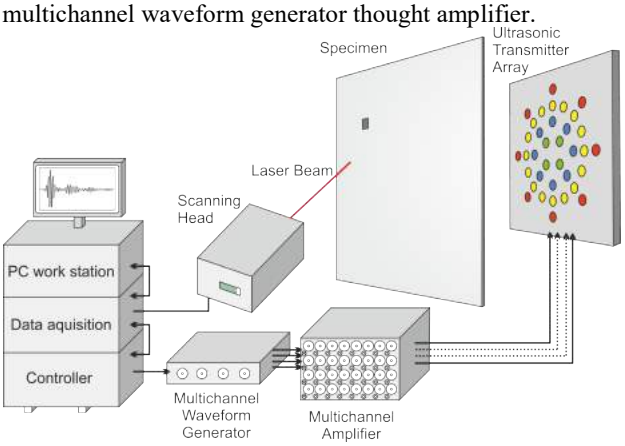


Figure 3: Experimental setup diagram.

3. Damage detection - wavenumber filtering

Damage detection algorithm based on full wavefield processing in wavenumber domain was used. Details of the method may be found in [4].

4. Results

Full wavefield images comparison for both excitations is presented in Figure 4.

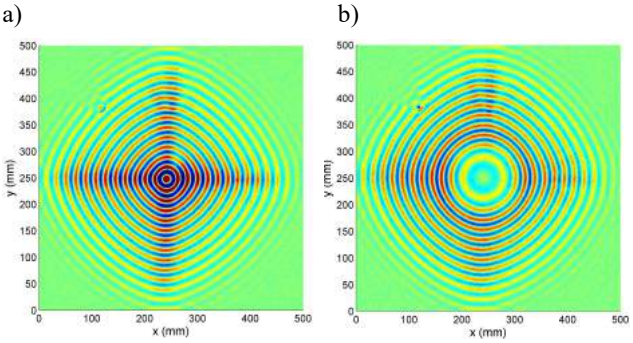


Figure 4: Wave image: a) PZT excitation b) UTA excitation.

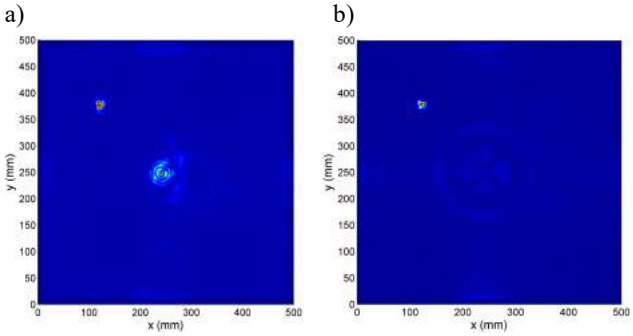


Figure 5: Damage map: a) PZT excitation b) UTA excitation

In both damage maps, presented in Figure 5, exact position of Teflon insert in clearly visible as a high-value region. When PZT excitation was used, also the transducer in the center is visible (Figure 5a).

5. Conclusions

This study aims to realize a non-contact damage detection system using ultrasonic transmitter array for excitation and scanning laser vibrometer for measuring. The results are compared to the contact excitation with PZT transducer. From the obtained results it may be concluded that ATU is a valid alternative to contact excitation and may be used as a replacement for non-contact laser guided waves excitation.

Acknowledgements

The research was funded by the Polish National Science Center under grant agreement no DEC-2013/10/A/ST8/00071 in the frame of MAESTRO project entitled: Excitation and control of mechanical waves in nonlinear media.

References

[1] V. Giurgiutiu, C. Soutis, 2010. *Guided Wave Methods for Structural Health Monitoring*. *Encyclopedia of Aerospace Engineering.* Wiley and Sons Ltd, New York, pp. 2010

[2] W. Ostachowicz, M. Radzieński, P. Kudela, 50th Anniversary Article: Comparison Studies of Full Wavefield Signal Processing for Crack Detection, *Strain* 50: 275–291, 2014.

[3] A. Balvantín, A. Baltazar, P. Rodriguez, P. Characterization of Laser Generated Lamb Wave Modes after Interaction with a Thickness Reduction Discontinuity Using Ray Tracing Theory, Experimental Mechanics 54: 743, 2014

[4] N. Hosoya, R. Umino, A. Kanda, I. Kajiwara, A. Yoshinaga, Lamb wave generation using nanosecond laser ablation to detect damage, *Journal of Vibration and Control,* 1-12, 2017

[5] P. Kudela, M. Radzieński, W. Ostachowicz, Identification of cracks in thin-walled structures by means of wavenumber filtering, *Mechanical Systems and Signal Processing* 50–51: 456-466, 2015.

Conversion of surface waves in a forest of trees

Kim Pham[1], **Sébastien Guenneau** [2],
Agnès Maurel[3], **Jean-Jacques Marigo**[4],

[1]IMSIA, ENSTA, Palaiseau, France,
[2]Aix-Marseille Univ., CNRS, Centrale Marseille, Institut Fresnel, 13013 Marseille, France
[3] Institut Langevin, ESPCI, CNRS, 1 rue Jussieu, Paris 75005 - France,
[4]Lab. de Mécanique du Solide, Ecole Polytechnique, Route de Saclay, Palaiseau 91120 - France.
*corresponding author, E-mail: kim.pham@ensta-paristech.fr

Abstract

We inspect the propagation of surface waves through a forest of trees atop a guiding layer on a soil substrate. We show that these waves behave like spoof plasmons in the limit of a vanishing guiding layer, and like Love waves in the limit of trees with a vanishing height. When we consider a forest with trees of increasing or decreasing height, this hybrid wave is either reflected backwards or converted into a downward bulk wave.

1. Introduction

Seismic metasurfaces have been realized and in the context of Rayleigh waves, it has been shown recently that a so-called meta-wedge is capable of mode-converting destructive seismic surface waves into mainly harmless downward propagating bulk shear waves, see *e.g.* [1]. Here, we show that such seismic metasurfaces can be designed for Love waves. Love waves are shear polarized surface seismic waves, which produce a horizontal shaking particularly deleterious for the foundations of infrastructures. Unlike for Rayleigh waves, they require a guiding layer to propagate at the air-soil surface and we shall see that these surface waves are particularly sensitive to the shape of structural elements above the soil, in the present case, a forest of trees with some foliage (Fig. 1). As a result a forest of trees with varying height can reflect, localize or convert a Love wave.

2. Local analysis - dispersion relation of the Spoof-Love wave

We consider the two-dimensional configuration of a forest of trees periodically spaced by a distance ℓ; the ground is composed of a layer with a lower velocity than that of the soil substrate (Fig. 1). In the absence of trees, this low velocity layer can support Love waves, which propagate within the layer and vanish when moving far from it in the substrate. Using homogenization tools, the region of the trees can be replaced by an equivalent slab filled with a homogeneous highly anisotropic medium and associated boundary conditions (i) at the interface with the guiding layer and (ii) at the top of the trees [2]. This allows us to deeply simplify the problem, resulting in the explicit dispersion relation of guided waves in the form

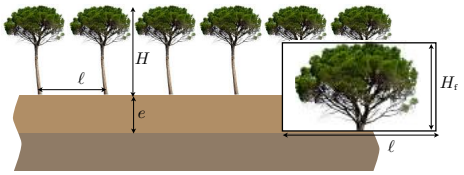


Figure 1: Periodic array of trees with spacing ℓ and total height H; the ground region is surmounted by a guiding layer able to support Love waves. The tree trunks have a diameter d and filling fraction φ and the foliage of height H_f a surface filling fraction φ_f.

$$F_1\left[1-\frac{\mu_2 k_2}{\mu_1\alpha_1}\tan k_2 e\right]-F_2\,\frac{\mu_3 k_3}{\mu_2 k_2}\varphi\left(\tan k_2 e+\frac{\mu_2 k_2}{\mu_1\alpha_1}\right)=0, \tag{1}$$

with

$$\begin{cases} F_1 = 1 - k_3 L_e \tan k_3 H, \\ F_2 = \tan k_3 H + k_3 L_e, \end{cases} \tag{2}$$

and the vertical wavenumbers $\alpha_1 = \sqrt{\beta^2 - \omega^2/c_1^2}$, $k_2 = \sqrt{\omega^2/c_2^2 - \beta^2}$, $k_3 = \omega/c_3$ with the indices 1, 2, 3 denoting the soil, the guiding layer material and the three wood respectively, and we use $\rho_1 = 1300$ kg.m^{-3}, $c_1 = 495$ m.s^{-1} for the ground, $\rho_2 = 2600$ kg.m^{-3}, $c_2 = 350$ ms^{-1} for the guiding layer, and $\rho_3 = 450$ kg.m^{-3}, $c_3 = 1200$ m.s^{-1} for the wood. The dimensions are $e = 2$ m, $H = 10$ m, $d = 0.3$ m, $\ell = 2$ m ($\varphi = 0.15$); when the foliage is considered, we use $d_f = 1.5$ m ($\varphi_f = 0.75$) and $H_f = 1$ m, thus the height of trunk is 9 m in this case.

The Figs. 2 reveal the dispersion relations computed numerically by means of the divergence of the reflection coefficient (red regions) for $H \in (2; 18)$ m; we considered the frequency 70 Hz. At this frequency, resonances occur for trees of heights $H \simeq 4$ m and 13 m, resulting in two bandgaps for $H \in (3.5, 4)$ m and $H \in (12.3, 13)$ m respectively. With the foliage, the first gap is significantly shifted to $H \in (10, 10.5)$ m (and the second to $H \in (1.5, 1.9)$ m). Besides the dispersion relation reveals an interesting feature which may impact significantly the propagation of guided waves through a forest of trees with increasing or decreasing heights, as we shall see below.

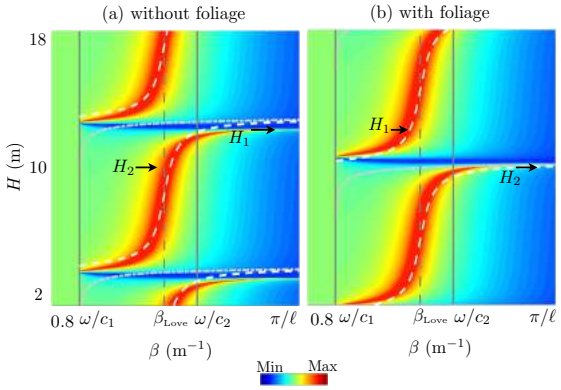


Figure 2: Dispersion relation of the spoof Love waves in the plane (β, H) at $f = 70$ Hz; (a) without and (b) with foliage. $\omega/c_1 = 0.89$ m^{-1}, $\beta_{\text{Love}} = 1.15$ m^{-1}, $\omega/c_2 = 1.25$ m^{-1}, π/ℓ=1.57 m^{-1}.

3. Wedge and anti wedge effects

Let us assume that a local analysis can be done, which means that the wavenumber $\beta(H)$ in a forest of trees with varying heights can be estimated from the above analysis, and consider the cut-off frequency for $H = 4$ m in Fig. 2(a). When the wave propagates from shorter $H <$ 4 m towards higher trees, $\beta(H)$ increases along the branch $\beta(H < 4$ m). Eventually, it reaches the value π/ℓ where the confinement in the trees is maximum (the wave is already evanescent in the guiding layer). On the contrary, if the wave propagates from higher to shorter height trees, $\beta(H)$ is decreasing along the branch $\beta(4 < H < 13$ m). In this case, it reaches the wavenumber $\beta_1 = \omega/c_1$ of the shear wave in the bulk where the confinement vanishes. Owing to this analysis, it seems not too hazardous to state that a wave propagating along trees with decreasing height becomes more and more adapted to be converted into a shear wave in the bulk.

This non symmetric behavior of the spoof Love wave is illustrated in Fig. 3. We considered a point source outside a forest of 29 trees with heights varying from 16 to 2 m (with a decrement of 0.5 m) which generates a Love wave in the guiding layer. When the Love wave is incident from the taller edge of the forest (a,b), it is converted into a Spoof Love wave that propagates within the forest until it reaches a resonant tree; there, it is converted into a downward propagating shear-polarized bulk wave. These "turning points" coincide fairly well with the upper limits of the bandgaps reported in Figs. 2, at 13 and 4 m for trees without foliage and at 10.5 m for trees with foliage. In contrast, when the Love wave is incident from the shorter edge of the forest, it is converted into a spoof Love wave which is eventually trapped for some tree height, resulting in a significant back-reflection (we reported the heights corresponding to the upper limits of the bandgaps in Figs. 2). The "aspiration" effect of the wave by the trees near the turning points is visible; it is consistent with our findings that the spoof Love

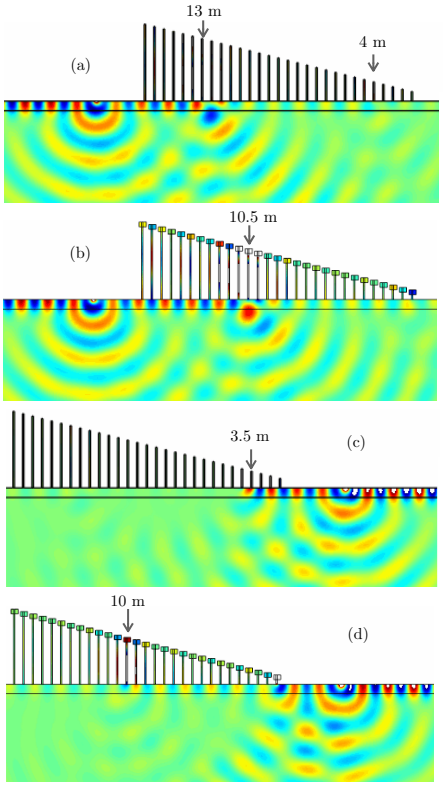


Figure 3: Interaction of a Love wave with a forest consisting of 29 trees (from 16m to 2m); Linear color range is in arbitrary units. Wedge and anti-wedge with (b,d) and without (a,c) foliage.

wave becomes evanescent in the guiding layer near the upper limit of the bandgap ($\beta > \omega/c_2$).

4. Conclusion

Our findings show that spoof Love waves propagate following the same scenario than the one analyzed for Rayleigh waves. When propagating in a forest with decreasing height, they are converted into a downward bulk wave, while when propagating in a forest with increasing tree height, they are eventually aspired within the trees resulting in a strong backscattering due to a rainbow effect. Additional results on Rayleigh waves coupling with the flexural modes of the tree will be presented.

References

[1] Colquitt DJ, Colombi A, Craster RV, Roux P, Guenneau S 2017 J Mech Phys Solids 99, 379-393.

[2] Maurel A, Marigo JJ, Guenneau S 2017 arXiv:1712.08175.

Parity-Time and Related Symmetries in Photonics, Plasmonics, Acoustics

Active plasmonic and PT symmetric structures for broadband amplified non-reciprocity

Maude Amyot-Bourgeois,[1,2] Elham Karami Keshmarzi,[2,3] Choloong Hahn,[2,4] Youngsun Choi,[5] Jae Woong Yoon,[5] R. Niall Tait,[3] Seok Ho Song,[5] and Pierre Berini[1,2,4*]

[1]Department of Physics, University of Ottawa, Canada
[2]Centre for Research in Photonics, University of Ottawa, Canada
[3]Department of Electronics, Carleton University, Ottawa, Canada
[4]School of Electrical Engineering and Computer Science, University of Ottawa, Canada
[2]Department of Physics, Hanyang University, Seoul, Korea
[*]corresponding author: berini@eecs.uottawa.ca

Abstract- We discuss amplified and lasing plasmonic systems and amplified waveguide isolators based on exceptional-point optical structures.

Synthetic optical materials having a carefully-structured complex refractive index distribution, following non-Hermitian Hamiltonian analogs, have attracted significant attention because of their non-orthogonal eigensystems. Such materials enable functions such as uni-directionality, non-reciprocity, and unconventional beam dynamics. The interplay between gain and loss, especially in low-loss (long-range) plasmonic systems is interesting because parity-time (PT) symmetric and exceptional point systems become readily-accessible, leading to practical experimental demonstrations.

Recent progress on the optimisation of a dye-doped polymeric gain medium, specifically IR-140 doped PMMA, has led to an optically-pumped medium that provides 80 to 300 cm^{-1} of gain at 880 nm [1]. This medium can provide long-term (low-bleaching) gain as long as the pump repetition period is greater that the thermal characteristic time (cooling time) of the medium. The medium can also be structured by e-beam lithography and will retain much of its gain as long as the e-beam dosage is not too high.

The ability to easily integrate IR-140 doped PMMA [1] with other structures has been exploited to realise plasmonic distributed feedback (DFB) lasers producing a single-mode outputs of very small linewidth [2]. The structures were realised as step-in-width Ag or Au Bragg waveguide gratings on SiO_2 and over-coated with the gain medium. Threshold pump power densities in the range of 1 MW/cm^2 were required for the onset of lasing (in unoptimised structures).

We show that interactions based on encircling-an-exceptional-point, which are reciprocal in the linear regime, may become nonreciprocal in the nonlinear regime over a very broad optical bandwidth (limited mainly by the bandwidth of the nonlinearity). We describe a coupled-waveguide structure that supports an encircling-an-exceptional-point parametric evolution based on a gain saturation nonlinearity [2]. The structure is capable of low-loss nonreciprocal optical transmission with an isolation greater than 10 dB over an optical bandwidth approaching 100 THz. We describe progress on the experimental realization of the proposed concept, aiming towards an integrated on-chip amplified optical isolator.

REFERENCES

1. M. Amyot-Bourgeois, E. Karami Keshmarzi, C. Hahn, R. N. Tait, and P. Berini, “Gain optimization, bleaching, and e-beam structuring of IR-140 doped PMMA and integration with plasmonic waveguides,” Opt. Mat. Express, Vol. 7, 3963, 2017.
2. E. Karami Keshmarzi, R. N. Tait, and P. Berini, “Single-mode surface plasmon distributed feedback lasers,” submitted
3. Y. Choi, C. Hahn, J. W. Yoon, S. H. Song and P. Berini, “Extremely broadband, on-chip optical nonreciprocity enabled by mimicking nonlinear anti-adiabatic quantum jumps near exceptional points,” Nature Communications, Vol. 8, 14154, 2017.

Broadband time-asymmetric silicon-photonic architecture grounded on non-Hermitian wave dynamics near exceptional points

Jae Woong Yoon,[1,2] Youngsun Choi,[1] Choloong Hahn,[3,4] Ki-Yeon Yang,[5] Jeong Yub Lee,[5] Gunpyo Kim,[1] Jong Kyun Hong,[1] Yeonghwa Ryu,[1] Seok Ho Song,[1*] and Pierre Berini[3,4,5]

[1] Department of Physics, Hanyang University, Seoul, Korea

[2]Electronics and Telecommunications Research Institute (ETRI), Daejeon, Korea

[3]Centre for Research in Photonics, University of Ottawa, Canada

[4]School of Electrical Engineering and Computer Science, University of Ottawa, Canada

[5]Department of Physics, University of Ottawa, Canada

[*]corresponding author: shsong@hanyang.ac.kr

Abstract- We discuss a promising silicon-photonic architecture that creates dynamically encircling an exceptional point and consequent time-asymmetric transmission of broadband optical signals in the technologically important optical telecommunications window.

Wave propagation properties associated with non-Hermitian Hamiltonians, symmetries, and singularities are presently of great interest in optics for generating innovative photonic systems based on carefully configured optical gain and losses [1]. Among various novel properties and unusual effects, encircling an exceptional-point (EP) singularity provides a unique opportunity to create a topological time asymmetry which is in principle parametrically robust and spectrally broad [2-5] in stark contrast to the previous methods using resonances, photonic band gaps, and magnetic thin films.

In this paper, we demonstrate silicon-photonic waveguide devices that function as a broadband asymmetric transmission mode converter while dynamically encircling an EP (EEP) in the optical domain. The proposed device consists of two coupled channel waveguides with complex propagation-index profiles configured such that excited photonic modes undergo time-asymmetric EEP parametric evolutions. Real and imaginary propagation-index profiles required for the EEP evolution are realized by tuning waveguide width and photonic tunnel-gap size, respectively [5,6]. Importantly, a delicate EEP evolution is created in a lithographically generated silicon-photonic waveguide architecture that does not involve any complicated time-varying mechanisms, absorbing components, or noise isolation schemes included in the previous approaches [3,4]. We explain the underlying design principle, theoretical analyses, fabrication, and measurement of the proposed photonic EEP device. Comprehensive theoretical and experimental analyses show robust time-asymmetry in the optical transmission over a broad spectral domain from 1,250 nm to 1,650 nm. Therefore, we establish robust EEP device in the optical domain and an important step toward realization of on-chip optical isolators taking advantages of the unique non-Hermitian wave dynamics. We further discuss nonlinear properties for broadband optical non-reciprocity in the transmission and additional miniaturization schemes associated with our experimental results.

REFERENCES

[1] R. El-Ganainy, K. G. Makris, M. Khajavikhan, Z. H. Musslimani, S. Rotter, and D. N. Christodoulides, "Non-Hermitian physics and PT symmetry," *Nat. Phys.* **14**, 11-19 (2018).

[2] I. Gilary, A. A. Mailybaev, and N. Moiseyev, "Time-asymmetric quantum-state-exchange mechanism," *Phys. Rev. A* **88**, 010102(R) (2013).

[3] J. Doppler, A. A. Mailybaev, J. Böm, U. Kuhl, A. Girschik, F. Libisch, T. J. Milburn, P. Rabl, N. Moiseyev, and S. Rotter, "Dynamically encircling an exceptional point for asymmetric mode switching," *Nature* **537**, 76-79 (2016).

[4] H. Xu, D. Mason, L. Jiang, and J. G. E. Harris, "Topological energy transfer in an optomechanical system with exceptional points," *Nature* **537**, 80-83 (2016).

[5] Y. Choi, C. Hahn, J. W. Yoon, S. H. Song and P. Berini, "Extremely broadband, on-chip optical nonreciprocity enabled by mimicking nonlinear anti-adiabatic quantum jumps near exceptional points," *Nat. Commun.* **8**, 14154 (2017).

[6] J. W. Yoon, Y. Choi, C. Hahn, G. Kim, S. H. Song, K.-Y. Yang, J. Y. Lee, Y. Kim, C. S. Lee, J. K. Shin, H.-S. Lee, and P. Berini, "Broadband time-asymmetry of light through a topological loop around an exceptional point," submitted (Feb. 2018).

Asymmetric Optical Effects in Hyperbolic Media

R. Macêdo[1], T. Dumelow[2] and Robert L. Stamps[1,3]

[1]SUPA School of Physics and Astronomy, University of Glasgow, Glasgow G12 8QQ, United Kingdom
[2]Departamento de Física, Universidade do Estado do Rio Grande do Norte, Costa e Silva, 59625-620 Mossoró RN, Brazil
[3]Department of Physics and Astronomy, University of Manitoba, Winnipeg, MB R3T 2N2, Canada
*corresponding author, E-mail: Rair.Macedo@glasgow.ac.uk

Abstract

Metamaterials have attracted significant attention in recent years due to their many unusual optical properties. These are often artificial structures with negative permeability and negative permittivity. However, a class of strongly anisotropic media has gained in attention as subclass of metamaterials, the so-called hyperbolic media. Here, we show how by rotating the optical axis of crystals, the hyperbolic dispersion and its properties are also rotated. Therefore, the properties of waves propagating in hyperbolic media are also modified and become extremely asymmetric.

1. Introduction

Hyperbolic media and hyperbolic metamaterials are of particular interest due to their capabilities to shape and guide electromagnetic waves in unexpected ways with relatively simple geometry [1,2]. Even though these are often regarded as metamaterials, natural crystals have been shown to be hyperbolic without any tampering with the crystal's internal structures. For instance, negative refraction has been demonstrated in crystal quartz [3], MgF_2 [4] and Sapphire [5]. Some attention has also been paid to the case of natural hyperbolic magnetic media, in which case optical effects such Goos-Hanchen shifts [6] and negative reflection [7] can be tuned by simply applying external magnetic fields.

Hyperbolic media are usually highly anisotropic and the anisotropy has often been set to be either parallel or perpendicular to the materials surface (see Fig. 1(a)) [1]. In this work, we show how electromagnetic waves propagates through a medium in which the anisotropy may be polarized along an arbitrary direction (as shown in Figure 1(b)). We show that, by rotating the easy axis of the crystal, the hyperbolic dispersion (Figure 1(b)) properties are also rotated and therefore the angle of refraction is modified and cannot be defined as simply negative and positive as it is done in conventional hyperbolic media. The optical properties derived from the hyperbolic behaviour are also modified.

2. Crystal's geometry

Here, we start by considering the geometry of incidence shown in Fig. 1. The plane of incidence is xz, z being normal to the interface, and the principal axes of the crystals dielectric tensor lie along the Cartesian axes x, y and z. The anisotropic medium considered in the present work is uniaxial, with the uniaxis (the extraordinary or optic axis) lying along z when $\phi = 0$. In this case we have $\varepsilon_{xx} = \varepsilon_{yy} = \varepsilon_\perp$ and $\varepsilon_{zz} = \varepsilon_\parallel$.

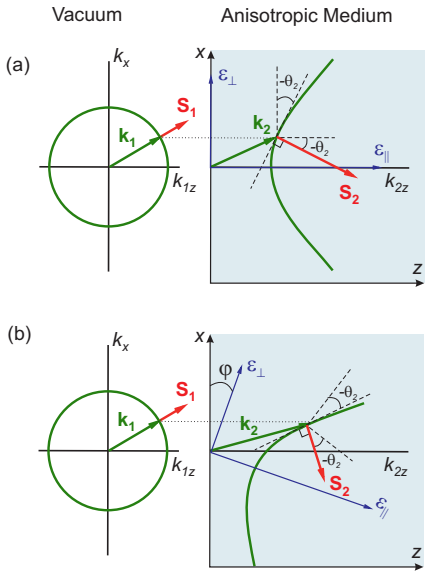


Figure 1: Geometry of incidence and refraction considered in this work where (a) the crystal's main axis lie along the Cartesian x and y axis and (b) where the easy axis is rotated in the xz plane.

If $\phi \neq 0$ the permittivity tensor has to be rewritten and is now given by

$$\overleftrightarrow{\varepsilon}(\omega) = \begin{bmatrix} \varepsilon_{xx} & 0 & \varepsilon_{xz} \\ 0 & \varepsilon_{yy} & 0 \\ \varepsilon_{xz} & 0 & \varepsilon_{zz} \end{bmatrix}. \quad (1)$$

where each component is given as a function of ϕ and these can be written as

$$\varepsilon_{xx} = \varepsilon_\perp \cos^2\varphi + \varepsilon_\parallel \sin^2\varphi \quad (2a)$$

$$\varepsilon_{zz} = \varepsilon_\perp \sin^2\varphi + \varepsilon_\parallel \cos^2\varphi \quad (2b)$$

$$\varepsilon_{xz} = (\varepsilon_\parallel - \varepsilon_\perp)\sin\varphi\cos\varphi \quad (2c)$$

In this geometry the in-plane wave-vector component k_x is then given by $k_x = k_0 \sin\theta$, where $k_0 = \omega/c$ and θ is the angle of incidence. Boundary conditions dictate that this k_x value holds both sides of the interface. Maxwells equations may be applied in the two layers to find the z components of the wave vector. In the first (vacuum) layer, this gives

$$k_{z1}^2 = k_0^2 - k_x^2 \quad (3)$$

In the second layer, however, it is necessary to differentiate between the behaviour of differently polarized waves. For TM-polarised waves (**H** field along y) we have

$$k_{(a,b)z2} = \frac{\varepsilon_{xz}k_x \pm \sqrt{(\varepsilon_{xz}^2 - \varepsilon_{xx}\varepsilon_{zz})(k_x^2 - k_0^2\varepsilon_{zz})}}{\varepsilon_{zz}} \quad (4)$$

Note that k_{z2} has two solutions, a and b. These are defined by the $+$ or $-$ sign in Eq. (4), respectively.

3. Propagation in Simple Anisotropic Media

We now apply the above concepts to a triglycine sulphate (TGS) slab lying in the half space $z > 0$, as shown in Fig. 1. We assume that the crystal's phonon polarization direction lies initially along z, but no corresponding excitation along the other directions. Therefore the dielectric tensor component $\varepsilon_\parallel$ can be written as a damped harmonic oscillation expressed in the form

$$\varepsilon_\parallel = \varepsilon_\infty + \frac{\rho\omega_{TO}^2}{\omega_{TO}^2 - \omega^2 + i\omega\Gamma} \quad (5)$$

where ε_∞ represents the high frequency dielectric constant along the easy axis direction, ω_{TO} is the transverse optical (TO) frequency, ρ is its oscillator strength and Γ is a phenomenological damping parameter.

For this type of medium, the angle of refraction is usually given in terms of the power flow and it is given by [3-7]

$$\tan\theta_2 = \frac{\langle S_{x2}\rangle}{\langle S_{z2}\rangle} \quad (6)$$

When $\phi = 0$, θ_2 simply depends on the signs of $\varepsilon_\perp$ and $\varepsilon_\parallel$ so that when $\varepsilon_{xx} > 0$ and $\varepsilon_{zz} < 0$ negative refraction is possible (shown in Fig. 1(a)). In this case, the angle of refraction has the same magnitude for positive and negative incident angles so that $|\theta_2(+\theta_1)| = |\theta_2(-\theta_1)|$. However, when $\phi \neq 0$, θ_2 also depends on the off diagonal components of Eq. 1, ε_{xz}. In Fig. 2 we show the behaviour of a beam incident on a TGS surface where $\phi = 10^o$ and $\theta_1 = \pm 45^o$. It is clear that, even though there are extraordinary levels of transmission, the magnitude of θ_2 differs accordingly to the sign of θ_1 so that so that $|\theta_2(+\theta_1)| \neq |\theta_2(-\theta_1)|$.

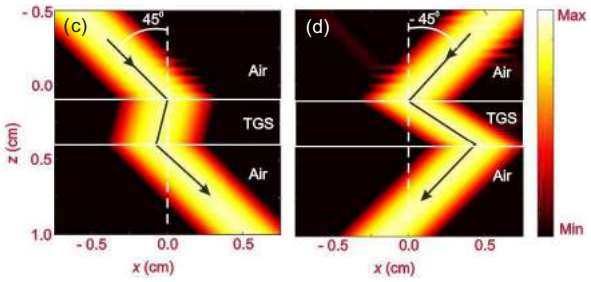


Figure 2: Calculated profile of the overall intensities (in terms of the magnitude of the time-averaged Poynting vector) in the xz plane for $\phi = 10^o$ for incident angles of $\pm 45^o$ and frequency ω = 39 cm^{-1}.

4. Conclusions

We showed how hyperbolic media are extremely dependent on the crystal orientation. When the crystal's axes are rotated the permittivity tensor, which is usually diagonal [4], is replaced by a new tensor with off-diagonal elements. These elements directly affect the wave propagation so that the magnitude of the angle of refraction depends on the the direction of the incident beam. We stress here that our results can be applied to any hyperbolic system, artificial or natural. Thus, while we have presented the above discussion on phonon-polaritons resonance in dielectric media with μ = constant, these could be equally applied to magnetic crystals using its permeability tensor [6,7].

Acknowledgement

This work was supported by the Leverhulme Trust and the University of Glasgow. The work of TD was supported by the Brazilian research agency CNPq.

References

[1] A. Poddubny, I. Iorsh, P. Belov, Y. Kivshar, *Nature Photonics* 7: 948–957, 2013.

[2] D. R. Smith and D. Schurig: *Phys. Rev. Lett.* 90 077405, 2003.

[3] R. R. Silva, R. Macedo, T. Dumelow, J. A. P. Costa, S. B. Honorato and A. P. Ayala, *Phys. Rev. Lett.* 105: 16, 163903, 2010.

[4] R. Macêdo, R. R. da Silva, T. Dumelow, J. A. P. da Costa *Optics Communications* 310: 94-99, 2014.

[5] R. Wang, J. Sun, and J. Zhou, *Appl. Phys. Lett.* 97: 031912, 2010.

[6] R. Macêdo, T. Dumelow, R. L. Stamps, *Optics Express*, 22: 23, 28467–28478, 2014.

[7] R. Macêdo, T. Dumelow, R. L. Stamps, *ACS Photonics*, 3: 9, 1670–1677, 2016.

Three-wave mixing of guided contra-propagating electromagnetic waves in hyperbolic metamaterials: shaping light

Victor A. Tkachenko[1], Vitaly V. Slabko[1], Sergey A. Myslivets[1,2], and Alexander K. Popov[3,*]

[1]Siberian Federal University, Krasnoyarsk 660041, Russian Federation
[2]Kirensky Institute of Physics, Federal Research Center KSC SB RAS, Krasnoyarsk 660036, Russian Federation
[3]Birck Nanotechnology Center, Purdue University, West Lafayette, IN 47907, USA
*corresponding author, E-mail: popov@purdue.edu

Abstract

Three-wave mixing of the phase matched contra-propagating electromagnetic waves enables extraordinary greatly enhanced amplification, frequency and propagation direction conversion as well as control of shape of the light pulses. We present numerical simulation of the plasmonic metamaterials, which provide phase matching of guided ordinary and backward electromagnetic waves, and demonstrate extraordinary transient processes that emerge in such metamaterials.

1. Introduction

The concept of electromagnetic waves (EMWs) with *co-directed* phase velocity and energy flux is commonly accepted in optics as it is true for natural isotropic materials. All optical devices, which we use in every-day life, exploit this concept. However, the advent of the nanotechnology made possible the creation of the metamaterials (MMs) which enable the appearance of the EMWs with *contra-directed* energy flux and phase velocity. They are referred to as *backward* EMWs (BEMWs). Such extraordinary property has opened novel avenues in linear physical optics. Nonlinear optics (NLO) significantly extends the methods of shaping light. Most important among them are the possibilities to convert light frequencies. Phase matching of coupled light waves, i.e., equality of their phase velocities, is a paramount requirement for the *coherent*, i.e., phase-dependent NLO coupling of light waves which paves a way to efficient frequency conversion and pulse shaping. However, phase matching imposes severe limitations on the choice of practical NLO materials. It has been shown that coherent coupling of normal *and BEMWs* opens novel avenues for *extraordinary* NLO processes which hold promise for great benefits in manipulating light. For example, in the case of parametric amplification at ω_1 accompanied by the difference-frequency generation at ω_2 ($\omega_2 = \omega_3 - \omega_1$) in a transparent material slab of thickness L, exponential growth of the output amplitudes at ω_1 and ω_2, $a_{1,2}(L) \sim \exp(gL)$, would dramatically change to $a_{1,2} \sim 1/\cos(gL)$ for the case of coupled normal signal wave a_1 and contra-propagating BLW a_2 exiting the slab from the entrance edge in the *reflection* direction [1, 2]. Here, factor g is proportional to the product of nonlinear susceptibility and amplitude of the pump wave a_3 at ω_3. The *uncommon* "geometrical," i.e. slab thickness dependent, pump *intensity* resonance emerges at $gL \to \pi/2$ which allows for huge enhancements in the NLO coupling, for miniaturization of corresponding photonic devices and for *exotic* pulse regimes [3].

2. Hyperbolic MM which provides phase matching of guided coupled contra-propagating EM modes

Common approach to generating BEMWs is based on MMs that possess simultaneously negative electric permittivity ϵ and magnetic permeability μ and commonly referred to as *negative-index* MMs (NIMs). Here, we employ a *different approach* which *does NOT* rely on optical magnetism. It grounds itself on the more general relationship:

$$\mathbf{S} = \mathbf{v}_g U, \quad \mathbf{v}_g = (\mathbf{k}/k)[\partial\omega/\partial k], \tag{1}$$

where $\mathbf{S}$, is a Poynting vector, U is energy density, and $\mathbf{v}_g$ is group velocity of light waves. It is seen that $\mathbf{S}$ and $\mathbf{k}$ become contra-directed if *spatial* dispersion is negative: $\partial\omega/\partial k < 0$. Such approach opens novel avenue in nanoengineering the MMs that could support both forward (FEMWs) and BEMWs based on different spatial dispersion at different frequencies. The challenge is to determine such sub-wavelength building blocks of the MM and to space them in such a way that their overall EM response cause so significant phase shift of the propagating EMWs that the normal FEMWs would convert into BEMWs. However, the indicated problem is not the sole and the major one. In the context of the stated goal, most restrictive is the requirement to ensure a *set* of EMWs at different frequencies satisfying photon energy conservation law (e.g., $\omega_1 + \omega_2 = \omega_3$) which consists of *both* of FEMWs and BEMWs travelling with *one and the same* phase velocity (phase matching). Proof-of-principle demonstration of such a possibility by using the MM made of carbon nanotubes standing on the metal surface was presented in [4]. Such a MM possesses hyperbolic dispersion properties [5].

Herewith, we present a model that enables phase matching of three FW and BEMWs. Figure 1(a) depicts a "nanoforest" – the MM made of conducting carbon nanotubes of lengths h at subwavelength spacing standing on a

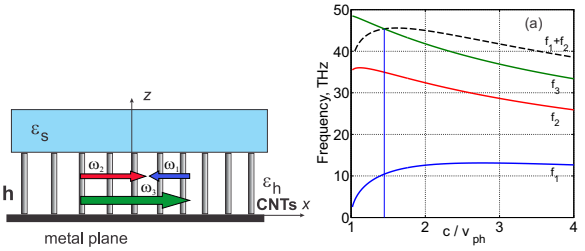


Figure 1: (a) Spatially dispersive metamaterial composed of carbon nanotubes standing on the metalic surface. (b) Dispersion of three lowest modes at $h = 3.5\,\mu$m. v_{ph} is the phase velocity. Vertical line marks the waves travelling with the same phase velocity while satisfying to the frequency requirement $f_1 + f_2 = f_3$. The dashed line represents the sum of two lowest modes.

conducting surface and bounded by a dielectric with electric permittivity ϵ_s. The nanoforest is plunged in dielectric with electric permittivity ϵ_h. The metaslab can be viewed as a tampered waveguide. Its eigenmodes and losses depend both on the properties of the constituent materials, geometry of the nanoblocks as well as on the projection of the electric and magnetic fields on the nanorods. Figure 1(b) presents frequencies of the allowed EM modes and corresponding phase velocities v_{ph}. Details can be found in [6].

3. Extraordinary TWM: parametric amplification, transients and pulse shaping

We found that the opposite direction of phase velocity and energy flux in BEMWs gives rise to *extraordinary transient* processes. The major outcomes are as follows. In the vicinity of the outlined resonance intensity, transient processes develop which cause a change in the output pulse shapes and a significant delay in formation of their maximums. The closer maximum in the pump intensity approaches the resonance value, the longer becomes the transient period. The delay of the output maximum relative to the input one may occur up to *several hundred* times longer than the travel time through the metaslab of the forefront of the semi-infinite fundamental pulse. Similar transients emerge in the oppositely directed idler (in the frequency up or down shifted NLO reflectivity). It appears, that changes in the output pulse shapes are strongly dependent on the ratio of the pump and signal pulse lengths, of the pulse lengths and the metaslab thickness, and on the ratio of the pulse group velocities. Figure 2 demonstrates one of the possible scenarios. Here, continuous wave pump $a_3(t) = a_{30}$ travels through a loss-free slab. Input co-directed FW signal is a rectangular pulse, which is approximately 5 times longer than the metaslab length L, is shown in Fig.2(a) (for $gL = 0$). Because the BW idler is first generated at the forefront of the signal pulse, their output maximums are shifted. At lower pump intensity, amplification of the rear edge of the signal is greater than the forefront one. As its intensity approaches the critical value $gL = \pi/2$, amplification growth, and enhanced idler contributes back to amplification of the signal tail which leads to significant broadening of the pulses.

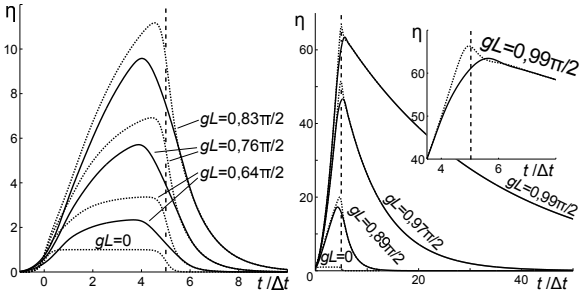


Figure 2: The output normalized signal $\eta_1 = |a_{2L}/a_{20}|^2$ at $z = L$ (gray lines) co-directed with a rectangular pump pulse and the output contra-directed idler $T_2 = |a_{10}/a_{20}|^2$ at $z = 0$ (black lines) for different values of pump amplitude gL. Input signal value is $|a_{20}/a_{30}|^2 = 10^{-8}$. Δt is the pump pulse travel time through the slab. (a): $gL \leq 0.83\pi/2$. (b): $0.83\pi/2 < gL \leq \pi/2$. Inset: blow up of the peak tip. Dashed lines mark exit time for the signal pulse rear edge if the pump is not turned on.

Acknowledgement

AKP acknowledges grant W911NF1410619 by the ARO.

References

[1] A.K. Popov and V.M. Shalaev, Negative-index metamaterials: second harmonic generation, Manley - Rowe relations and parametric amplification, *Appl. Phys. B, Lasers Opt.* 84: 131-137, 2006.

[2] A.K. Popov and V.M. Shalaev, Compensating losses in negative-index metamaterials by optical parametric amplification, *Opt. Lett.* 31: 2169-2171, 2006.

[3] V. V. Slabko, A. K. Popov, V. A. Tkachenko and S. A. Myslivets, Three-wave mixing of ordinary and backward electromagnetic waves: extraordinary transients, *Opt. Lett.* 41: 3976–3979, 2016.

[4] Alexander K. Popov, Mikhail I. Shalaev, Sergey A. Myslivets, Vitaly V. Slabko and Igor S. Nefedov, Enhancing coherent nonlinear-optical processes in nonmagnetic backward-wave materials, *Applied Physics A* 109, 835-840, 2012, DOI 10.1007/s00339-012-7390-8 (*Proc. META12*, 19-22 April 2012, Paris, France, p. 66).

[5] A. Poddubny, I. Iorsh, P. Belov, and Yu. Kivshar, Hyperbolic metamaterials, *Nat. Phot.* 7: 948957, 2013.

[6] A. K. Popov and S. A. Myslivets, Generation, amplification, frequency conversion and reversal of propagation of THz photons in nonlinear hyperbolic metamaterial, *Opt. Lett.*42: 1241-1244, 2017.

PT-symmetry of magnetostatic resonances in subwavelength ferrite particles

E. O. Kamenetskii

Microwave Magnetic Laboratory,
Department of Electrical and Computer Engineering,
Ben Gurion University of the Negev, Beer Sheva, Israel
*Email: kmntsk@bgu.ac.il

Abstract - Magnetostatic resonances in magnetized subwavelength ferrite-disk particles are macroscopically quantized states. In this structure, long-range dipole-dipole correlation in positions of electron spins can be treated in terms of collective excitations of a system as a whole. The spectra of the magnetostatic oscillations, well described by scalar MS-potential wave functions, have property of *PT* symmetry. The near fields in the proximity of the particle are with space and time symmetry breakings.

Long-range magneto-dipole interactions in confined magnetic structures are not in the scope of classical electromagnetic problems and, at the same time, have properties essentially different from the effects of exchange ferromagnetism. The MS-mode spectral properties in confined magnetic structures are based on postulates about the physical meaning of the MS-potential function as a complex scalar wavefunction, which presumes long-range phase coherence. An important feature of the MS-mode oscillations in a ferrite disk concerns the fact that a structure with symmetric parameters and symmetric basic equations goes into eigenstates that are not space–time symmetric.

The time direction in the structure is defined by the direction of the spin and orbital rotations of the fields in a ferrite disk. Depending on a direction of a bias magnetic field, we can distinguish the clockwise and counterclockwise topological-phase rotation of the fields. The direction of an orbital angular-momentum (correlated with the direction of a bias magnetic field $\vec{H}_0$) determines the time direction in our "topological clock". Both directions of rotation are equivalent and thus the biorthogonality relations for can be used. Importantly, magnetostatic resonances in magnetized subwavelength ferrite-disk particles can reveal the properties analogous to the effect of spectral singularities of complex scattering potentials in *PT*-symmetric gain/loss structures. The wave incident on a ferrite disk induces outgoing (transmitted and reflected) waves of considerably enhanced amplitude. The disk then uses a part of the energy of the magnetized ferrite sample to produce and emit a more intensive electromagnetic wave. This spectral singularity-related resonance effect relies on the existence of a localized region with a *PT*-symmetric complex scattering potential. Because this is a characteristic property of resonance states, spectral singularities correspond to the resonance states having a real energy. The near fields in the proximity of the MS-resonance particle are characterized by the helicity factor. This factor is a pseudoscalar. It changes a sign under inversions (also known as parity transformations). On the other hand, the helicity factor changes its sign when one changes the direction of a bias magnetic field, that is, the direction of time. One observes the time-space symmetry properties of the helicity factor.

There can be different types of the microwave structures where *PT*-symmetry of MS-resonances in a ferrite disk are broken. The effect of the *PT*-symmetry breaking can be observed when, for example, a ferrite disk is placed in a rectangular waveguide non-symmetrically with respect to its

walls. Other cases are related to microwave waveguiding structures with inserted special chiral objects.

Exceptional points in non-Hermitian optical system

Qingjie Liu[1], Bing Wang[1,*], Peixiang Lu[1,2]

[1]Wuhan National Laboratory for Optoelectronics and School of Physics, Huazhong University of Science and Technology, Wuhan, 430074, China
[2]Laboratory for Optical Information Technology, Wuhan Institute of Technology, Wuhan, 430205, China
*corresponding author, E-mail: wangbing@hust.edu.cn

Abstract

We investigate the optical exceptional points (EPs) in the graphene incorporated multilayer metamaterial manifesting Fano resonance. The system is non-Hermitian and possesses EPs where both the eigenvalues and eigenvectors of the Hamiltonian coalesce. In the aid of Fano resonance, the reflection may reach zero, resulting in the EPs. The most important property of EPs lies in the topological structure. In our later work, we will design a silicon structure easier to realize in experiment to explore the topological structure.

1. Introduction

In an open quantum system with parity-time symmetry, the Hamiltonian is non-Hermitian but possesses purely real eigenvalues. Once the parity-time (PT) symmetry is broken, the eigenvalues are no longer real and become complex. Subsequently, the eigenvalues and eigenfunctions of the Hamiltonian coalesce and the exceptional points (EPs) may emerge. Therefore EPs are also known as PT symmetry breaking points. In fact, the formation of EPs requires only non-Hermiticity and the PT symmetry is not necessary [1-3]. In our work, by employing the unique tunability of graphene and the merits of Fano resonance, we exploit the EPs in graphene metamaterials under Fano resonance.

2. Fano resonance and EPs in graphene metamaterials

The metamaterial structure considered to realize EPs is shown in Fig. 1. For the structure shown in Fig. 1, the amplitudes of incident and scattered waves can be connected by the scattering matrix in the form

$$\begin{pmatrix} b_1 \\ b_2 \end{pmatrix} = S \begin{pmatrix} a_2 \\ a_1 \end{pmatrix} = \begin{pmatrix} t & r_1 \\ r_2 & t \end{pmatrix} \begin{pmatrix} a_2 \\ a_1 \end{pmatrix}, \quad (1)$$

where a_1 and a_2 are amplitudes of incoming waves from positive and negative directions, and b_1 and b_2 are amplitudes of outgoing wave from negative and positive directions, respectively, as shown in the inset of Fig. 1. The eigenvalues of Eq. (1) are $s_{1,2} = t \pm (r_1 r_2)^{1/2}$, and the corresponding eigenvectors are $(r_1^{1/2}, \pm r_2^{1/2})$. Based on the fact that eigenvalues and eigenvectors coalesce at EPs, the EPs are therefore located at $(r_1 r_2)^{1/2} = 0$. As a result, EPs appear when either r_1 or r_2 is zero. The reflection coefficients at the two sides of the metamaterial can be written as $r_{1,2} = |r_{1,2}|\exp(i\varphi_{1,2})$, where φ_1 and φ_2 are the reflection phases corresponding to reflection coefficients r_1 and r_2. Then we have the reflections $R_{1,2} = |r_{1,2}|^2$. The condition for realizing EPs becomes making R_1 or R_2 be zero.

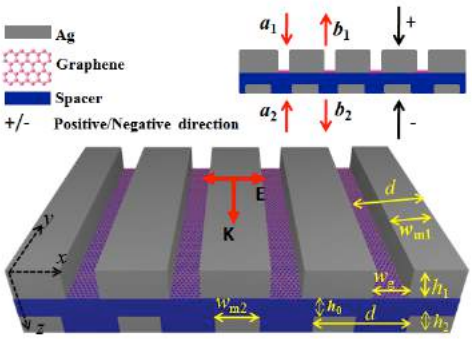


Figure 1. Schematic of the Ag-graphene hybrid structure. The graphene nanoribbons are deposited on the slits of the upper Ag strips. The structure is excited by TM-polarized incident light with the magnetic field parallel to the grating.

We now focus on the transmission and reflection properties of the metamaterial. The green curve in Fig. 2(a) shows the transmission spectrum of the hybrid metamaterial. There is obviously a sharp drop at λ = 5.346 μm, which is cause by the Fano resonance generated by the interaction between the surface plasmon resonance mode of graphene and the waveguide-resonance mode. Figure 2(b) shows the reflection spectra of the hybrid metamaterial with both metals and graphene, from which we can see clearly that the reflections R_1 and R_2 are not identical. Both the spectra R_1 and R_2 have two valleys with one nearly approaching to zero. The EPs should locate at the valleys due to the zero reflection.

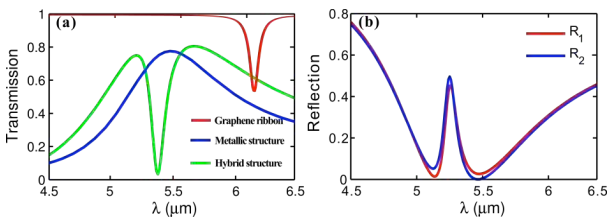


Figure 2. (a) Transmission for the graphene ribbon arrays suspended in air (the red curve), metallic structure without graphene (the blue curve), and the hybrid structure (the green curve). (b) Reflection spectra of the hybrid structure.

Next we show how to find the EPs. Figure 3(a) plots the reflection spectra R_1 as a function of the incident wavelength and graphene chemical potential. A nadir can be observed at μ_c = 0.428 eV and λ = 5.346 μm. The reflection arrives at $R_1 = 4.6\times10^{-7}$ which is fairly equal to zero within the calculation accuracy. Moreover, as shown in Fig. 3(b), the dislocation of phase φ_1 around the nadir point implies that a sharp change of the phase in the vicinity of the EP as the wavelength and chemical potential undergoes a slight variation. In case the light is impinging from the bottom, the reflection spectra R_2 as a function of the wavelength and chemical potential is shown in Fig. 3(c). A nadir at μ_c = 0.479 eV and λ = 5.53 μm is also found, where reflection R_2 equals 2.75×10^{-7} in our calculation. And the phase dislocation of φ_2 (Fig. 3(d)) at the nadir point indicates another EP. Thus two EPs are identified at different incident wavelength and chemical potential of graphene, denoted by $\mu_{c1,2}$ and $\lambda_{1,2}$.

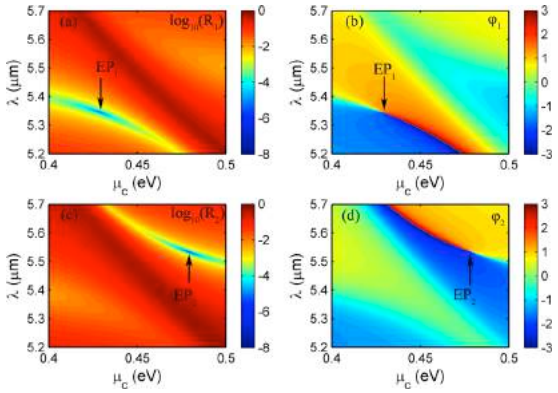


Figure 3. Reflection spectra R_1 and (c) reflection spectra R_2 as a function of the incident wavelength λ and chemical potential of graphene μ_c. (b) and (d) show the reflection phase φ_1 and φ_2. The black arrows point to the positions of EPs

To further verify the EPs, the topological structure has also been investigated. Figures 4(a) and 4(b) illustrate the real and imaginary parts of eigenvalues as a function of the incident wavelength λ and chemical potential of graphene μc in the vicinity of EP₁ and EP₂. At EPs, as indicated by black arrows, the real and imaginary parts of two eigenvalues coalesce simultaneously. The topological structure is examined when encircling the EPs in the parameter space. While only one EP is encircled within a loop in the parameter space, after a whole loop, the real and imaginary parts of the eigenvalues exchange to each other. While two EPs are encircled, after a loop, the two eigenvalues return to their original values. The results indicate that this metamaterial structure may find applications in optical switches by encircling one EP or two in the parameter space

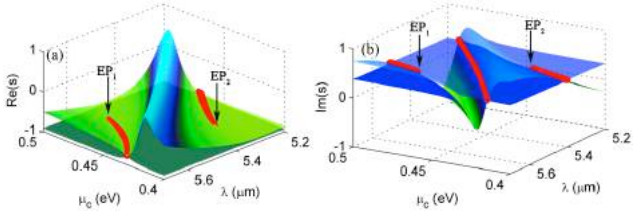


Figure 4. Eigenvalues $s_{1,2}$ as a function of incident wavelength λ and chemical potential of graphene μ_c. Re(s) indicates the real parts of $s_{1,2}$, and Im(s) indicates the imaginary parts of $s_{1,2}$. The red curves indicate the intersection of two surfaces. The black arrows point to the positions of EP_1 and EP_2.

3. Conclusions

In conclusion, we have studied the optical EPs in the hybrid metal and graphene metamaterials. The EPs are located at the valley of Fano-type reflection spectrum. The realization of the EP is implied by unidirectional reflectionless light transport and the corresponding phase dislocation. Moreover, the topological structure of EP is studied. Two eigenvalues of the scattering matrix are interchanged while encircling an EP in parameter space. In our later work, we will design a silicon structure easier to realize in experiment to explore the topological structure of EPs.

Acknowledgements

The work is supported by the 973 Program (No. 2014CB 921301), the National Natural Science Foundation of China (No. 11304108, 11674117, 61622502) and Natural Science Foundation of Hubei Province (No. 2015CFA040).

References

[1] M. Lawrence, N. Xu, X. Zhang, L. Cong, J. Han, W. Zhang, and S. Zhang, Manifestation of PT symmetry breaking in polarization space with terahertz metasurfaces, Phys. Rev. Lett. **113**, 093901 (2014).

[2] L. Feng, Y. Xu, W. S. Fegadolli, M. Lu, J. E. B. Oliveira, V. R. Almeida, Y. Chen and A. Scherer, Experimental demonstration of a unidirectional reflectionless parity-time metamaterial at optical frequencies, Nature Mater. **12**, 108-113 (2013).

[3] M. Kang, H. Cui, T. Li, J. Chen, W. Zhu, and M. Premaratne, Unidirectional phase singularity in ultrathin metamaterials at exceptional points, Phys. Rev. A **89**, 065801 (2014).

Extraordinary Topological Effects and Singular Plasmonics

Nanostructured magnetoplasmonic metamaterials: from extreme bio-sensing to active control of light polarization states at the nanoscale

Nicolò Maccaferri[1*]

[1] Italian Institute of Technology, Genoa, Italy
*corresponding author, E-mail: nicolo.maccaferri@iit.it

Abstract

Plasmonics, where light is squeezed up to the nanometer scale, have revolutionized the way we control light-matter interaction, stimulating new research directions towards light-based nanotechnologies. However, a major challenge facing plasmon-based nanophotonics is the poor dynamic tunability. Several approaches have been explored so far, including mechanical deformation, thermal or refractive index effects, and all-optical switching. In this framework, the rapidly developing field of magnetoplasmonics merges the concepts from plasmonics and magnetism to realize novel and unexpected phenomena for the active manipulation of light properties at the nanoscale. The fundamentals aspects of the physics underlying the optical behavior of magnetoplasmonic nanostructures arising from their intertwined optical and magneto-optical properties have been in large part clarified [1-3]. Moreover, we show how near field interactions between closely spaced nanoantennas [4] or diffractive coupling leading to collective plasmonic surface lattice resonances in arrays [5], induce large and controllable modifications of the magneto-optic response of such metamaterials. Such multifunctional magnetoplasmonic systems may open new views towards applications to variety of emerging technologies such as magnetoplasmonic rulers [4] and ultrasensitive molecular sensing [6]. Furthermore, magnetoplasmonics might have also a huge impact in the field of chiral plasmonics. In particular, we study two archetypical magnetoplasmonic chiral systems. First, we introduce the concept of ultra-thin chiroptical surfaces, where the chiral light transmission is controlled by the externally applied magnetic field. The magnetic field-induced modulation of the far-field chirooptical response exceeds 100% in the visible and near-infrared spectral ranges [7]. Finally, we study chiral nanostructured plasmonic vortex-induced optical beams carrying well-defined optical orbital and spin (helicity) angular momentum. In particular, we focus on a novel architecture where a plasmonic vortex is excited in a gold surface and propagates on an adiabatically tapered magnetoplasmonic tip. We show that both the helicity and the transmission of the emitted beam can be tuned by applying an external magnetic field, providing optimistic opportunities towards a magnetic control of chiral nanostructured optical beams [8].

References

[1] N. Maccaferri et al., *Phys. Rev. Lett.* 111: 167401, 2013.

[2] K. Lodewijks et al., *Nano Lett.* 14: 7207-7214, 2014.

[3] N. Maccaferri et al., *ACS Photonics* 2: 1769-1779, 2015.

[4] I. Zubritskaya et al., *Nano Lett.* 15: 3204-3211, 2015.

[5] N. Maccaferri et al., *Nano Lett.* 16: 2533-2542, 2016.

[6] N. Maccaferri et al., *Nature Commun.* 6: 6150, 2015.

[7] I. Zubritskaya et al., *Nano Lett.*, 2017.

[8] N. Maccaferri et al., *Appl. Phys. Lett.*, 2017.

Meta-atoms for arbitrary tuning of plasmonic vortex by using geometric and detour phase multiplexing

Seung-Yeol Lee[1*], Seong-Won Moon[1], Gun-Yeal Lee[2], and Byoungho Lee[2]
[1]School of Electronics Engineering, Kyungpook National University, Daegu, Republic of Korea
[2]School of Electrical and Computer Engineering, Seoul National University, Seoul, Republic of Korea
*corresponding author, E-mail: seungyeol@knu.ac.kr

Abstract

Various methods for utilizing a meta-atom to the generation of plasmonic vortex and far-field vortex beam are discussed. The concept of multiplexing geometric and detour phase of meta-atoms is introduced in order to provide a polarization-multiplexed plasmonic vortex with arbitrary topological charge. Moreover, the proposed concept also verified that the polarization insensitive plasmonic hot spot or vortex can be manipulated using the geometric phase, by compensating the role of conventional spin-orbitral interaction occurred by circular slit distribution

1. Introduction

Motivated by the recent improvement of a nano-fabrication techniques, tailored surface plasmon polaritons (SPPs) field carrying orbital angular momentum (OAM) has been greatly interested due to the high potentials in designing polarization-dependent ultra-thin optical components [1-4]. Especially, utilizing extraordinary optical phenomenon such as Pancharatnam-Berry phase or spin-Hall effects highly fascinates for designing various kinds of nanostructures which can exhibit a novel functionalities in subwavelength scale optics [5-7].

In order to generalize the topological effects in plasmonic structure, there has been numerous efforts since the early stage of Archimedean spiral-shaped plasmonic vortex lens has been proposed [8], which firstly couples the spin-state of incident light into the topological charge (TC) of plasmonic vortex. One of the most significant improvements for generation of arbitrary TC in plasmonic vortex was achieved when rectangular-shaped nanoaperture is applied as a meta-atom of plasmonic vortex lens (PVL) [9]. A miscellaneous usage of meta-atom instead of continuous curved slit may extend the degree of freedom in designing PVL, especially for higher-order changes of TC without geometrical detuning [10].

The segmentation of curved slit into the set of nanoapertures makes possible to separately design the geometric and detour phases, which leads to the arbitrary polarization-multiplexing of plasmonic field [11]. Moreover, the concept of multiplexing geometric and detour phase can also be applied to metasurfaces designed for far-field focusing or holographic applications [12].

In this presentation, methods for using nanoslit or nanorod-based meta-atom to form the arbitrary TC in plasmonic vortex will be introduced. It is shown that the multiplexing of spin-assisted geometric phase and spin-invariant detour phase may not only used for arbitrary control of vortex size, but also for simultaneous control of amplitude and phase of transmitted light, and image multiplexing. A concept for designing polarization-invariant plasmonic hot spot and vortex are also discussed by using the degenerated spin-orbital interaction, which can be achieved only if geometric phase of meta-atoms perfectly compensate the role of conventional spin-orbitral interaction occurred by circular slit distribution.

2. Design of PVL using meta-atoms

Plasmonic vortices can be generated when SPPs are merged to a specific spot with uniform amplitude and helically changing phase profile, which has a general expression of,

$$E_z(\rho,\phi,z) = E_{z0} J_{l_{TC}}(k_{SPP}\rho) e^{jl_{TC}\phi} e^{-\gamma z}, \quad (1)$$

where E_{z0} indicates an initial amplitude of SPP field, γ indicates an attenuation constant of SPP mode, and the parameter l_{TC} indicates the TC of the plasmonic vortex, which has a generalized relation of,

$$l_{TC} = m + l_{\text{in}} + s(2n-1), \quad (2)$$

where the parameter m represents the OAM number generated by detour phase formed by shifting of PVL, l_{in} is an OAM number of incident light, s is a spin angular momentum number, and the parameter n indicates the factor affected by rotation of normal vector of each meta-atom.

For the case of conventional continuous slit, the normal vector of the slit usually directs to the center of PVL, therefore rotation number of normal vector is fixed to n = 1, which definitely results to ±1 TC change when the optical handedness is changed. However, by adapting nano-slit meta-atom into PVL designing, rotation number of normal vector can be arbitrary designed, which makes possible to multiplex the arbitrary TC of plasmonic vortex for each optical handedness of incident light.

Figure 1(a) shows the schematic of meta-atom based PVL structure designed at freespace wavelength of 980 nm, m = 3, and n = 2. Here, we adapt a multiple-folded envelope for nearly-uniform SPP amplitude along the one circular loop. For the case of left-handed circular polarized

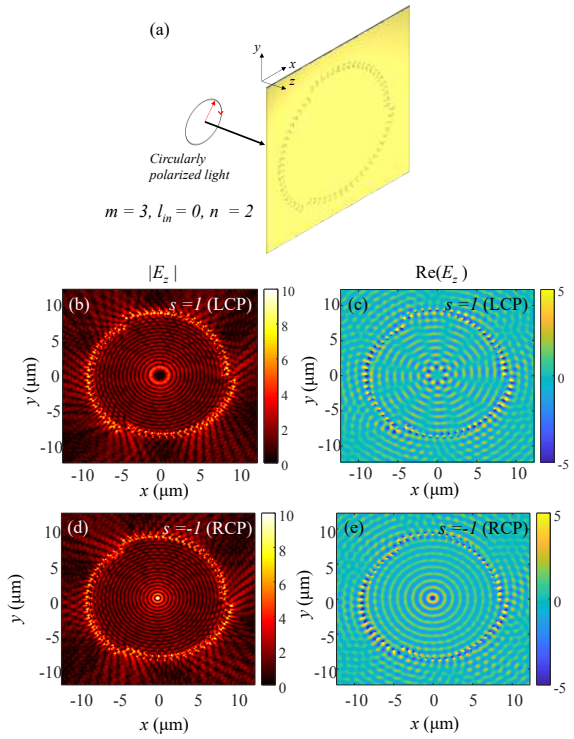


Figure 1: (a) Schematic for designing PVL with nanoslit based meta-atoms which has detour phase OAM of m = 3 and geometric phase OAM of n = 2 is shown. Generated plasmonic vortex with LCP incidence ((b) and (c)) and RCP incidence ((d) and (e)) are shown respectively.

(LCP) incidence (s = +1), therefore TC of plasmonic vortex is given as l_{TC} = 3+3 = 6. The size of plasmonic vortex follows sixth order of Bessel function, and total phase change of 12π appears as depicted in Figs. 1(b) and 1(c). On the other hand, l_{TC} = 3–3 = 0 may predicted for right-handed circular polarized (RCP) incidence, which will show bright hot spot at the center of PVL. The amplitude and real part of E_z field for that case is also shown in Figs. 1(d) and 1(e).

Moreover, according to the Eq. (2), it can be shown that the effect of spin-orbital interaction can be vanished when the rotation number of normal vector become n = 0.5, In this case, the field distribution of plasmonic vortex do not have any change for RCP or LCP incidences, and even for arbitrary linear polarization. For linear polarization incidence, only the relative amplitude can be changed, but the spatial distribution is always fixed. Such degeneracy of spin-orbital interaction can have the significant role for designing polarization-insensitive plasmonic devices.

3. Conclusions

Although this summary only show the use of meta-atom for the generation of arbitrary topological number of plasmonic vortex, the concept of combining detour and geometric phase of meta-atom can also be applied to various applications such as metasurface-based holographic image generation, metalens manufacturing, and plasmonic switching. Further discussions for combining detour and geometric phase of meta-atoms into the various nano-photonic applications will be presented.

Acknowledgements

This work was supported by the National Research Foundation of Korea (NRF) grant funded by the Korea government Ministry of Science and ICT. (No. 2017R1C1B2003585, No. 2017R1A4A1015565)

References

[1] E. Karimi, S. A. Schulz, I. De Leon, H. Qassim, J. Upham, and R. W. Boyd, Generating optical orbital angular momentum at visible wavelengths using a plasmonic metasurface, *Light Sci. Appl.* 3: e167, 2014.

[2] Y. Wang, P. Zhao, X. Feng, Y. Xu, F. Liu, K. Cui, W. Zhang, and Y. Huang, Dynamically sculpturing plasmonic vortices-from integer to fractional orbital angular momentum, *Sci. Rep.* 6: 36269, 2016.

[3] G. Spektor, D. Kilbane, A. K. Mahro, B. Frank, S. Ristok, L. Gal, P. Kahl, D. Podbiel, S. Mathias, H. Giessen, F.-J. Meyer zu Heringdorf, M. Orenstein, and M. Aeschlimann, Revealing the subfemtosecond dynamics of orbital angular momentum in nanoplasmonic vortices, *Science* 355: 1187−1191, 2017.

[4] D. Garoli, P. Zilio, F. De Angelis, and Y. Gorodetski, Helicity locking of chiral light emitted from a plasmonic nanotaper, *Nanoscale* 9: 6965−6969, 2017.

[5] N. Shitrit, I. Bretner, Y. Gorodetski, V. Kleiner, and E. Hasman, Optical spin Hall effects in plasmonic chains, *Nano Lett. 11: 2038*−2042, 2011.

[6] H. Kim, J. Park, S.-W. Cho, S.-Y. Lee, M. Kang, and B. Lee, Synthesis and dynamic switching of surface plasmon vortices with plasmonic vortex lens, *Nano Lett.* 10: 529-536, 2010

[7] G. Rui, Q. Zhan, and Y. Cui, Tailoring optical complex field with spiral blade plasmonic vortex lens, *Sci. Rep.* 5: 13732, 2015.

[8] Y. Gorodetski, A. Niv, V. Kleiner, and E. Hasman, Observation of the spin-based plasmonic effect in nanoscale structures, *Phys. Rev. Lett.* 101: 043903, 2008.

[9] S.-Y. Lee, S.-J. Kim, H. Kwon, and B. Lee, Spin-direction control of high-order plasmonic vortex with double-ring distributed nanoslits, *IEEE Photonic Tech. L.* 27: 705−708, 2015.

[10] H. Kim, J. Park, S.-W. Cho, S.-Y. Lee, M. Kang, and B. Lee, Synthesis and dynamic switching of surface plasmon vortices with plasmonic vortex lens, *Nano Lett.* 10: 529−536, 2010.

[11] S.-Y. Lee, K. Kim, G.-Y. Lee, and B. Lee, Polarization-multiplexed plasmonic phase generation with distributed nanoslits, *Opt. Express* 23: 15598−15607, 2015.

[12] G.-Y. Lee, G. Yoon, S.-Y. Lee, H. Yun, J. Cho, K. Lee, H. Kim, J. Rho, and B. Lee, Complete amplitude and phase control of light using broadband holographic metasurfaces, *Nanoscale*, DOI: 10.1039/C7NR07154J, 2018.

Far-field Polarization Singularities of a Dipolar Emitter

Sergey Nechayev[1,2], Martin Neugebauer[1,2], Martin Vordran[1,2], Gerd Leuchs[1,2] and Peter Banzer[1,2]

[1]Max Planck Institute for the Science of Light, Staudtstr. 2, D-91058 Erlangen, Germany
[2]Institute of Optics, Information and Photonics,
University Erlangen-Nuremberg, Staudtstr. 7/B2, D-91058 Erlangen, Germany
*corresponding author, E-mail: peter.banzer@mpl.mpg.de

Abstract

We investigate the far-field emission of an elliptically polarized dipole, exhibiting in general four points of purely circular polarization (C points). We reveal that the C point locations and helicities bare information on the spin and ellipticity of the dipole. For an almost linear dipole, the C points are barely separated and obscured by the low intensity in the corresponding angular region. However, they can be resolved via weak measurement. Our results link the polarization state of the dipolar emitters and their far-field polarization singularities.

1. Introduction and Theory

A linearly polarized dipole emits linearly polarized light with a donut-like radiation pattern (Fig. 1a and 1b). Thus, a circularly polarized dipole with dipole moment $\boldsymbol{q} = q_\perp \boldsymbol{e}_\perp \pm i q_z \boldsymbol{e_z}$; $q_\perp = q_z \in \mathbb{R}$, where $\boldsymbol{e}_\perp$ is a unit vector in the XY plane, emits circularly polarized light in the direction of its spinning axis $\pm\boldsymbol{e_s} = \pm\boldsymbol{e}_\perp \times \boldsymbol{e_z}$. The circularly polarized emission in the specific direction $\pm\boldsymbol{e_s}$ originates from the phase delay preservation of the emitted field by both dipolar components $q_\perp, q_z$, their mutual orthogonality and equal amplitudes (Fig. 1c). These opposite directions $\pm\boldsymbol{e_s}$ correspond to the far-field "C points", points of purely circular polarization. The plane normal to $\boldsymbol{e_s}$ and intersecting the location of the dipole splits the space into two halves. The dipole $\boldsymbol{q}$ emits predominantly left or right circular polarization in each of these half spaces [1]. Once the dipole $\boldsymbol{q}$ attains ellipticity, $|q_\perp| < |q_z|$, the two C points split to four, and their direction tilts in the plane normal to $\boldsymbol{e}_\perp$ towards the major axis $\pm\boldsymbol{e_z}$ of the dipole polarization ellipse (Fig. 1d). The tilt towards $\pm\boldsymbol{e_z}$ in the plane normal to $\boldsymbol{e}_\perp$ effectively decreases the amplitude of the q_z component and preserves the amplitude of the $q_\perp$ component (compare Fig 1a. and 1b, $\boldsymbol{e}_\perp$ corresponds to the x-axis). In the limit of an almost linear dipole $q_\perp \ll q_z$ the wave-vectors describing the directions of C point singularities are almost aligned with $\pm\boldsymbol{e_z}$. Notably, not only the angular separation of the C point singularities approaches zero as $\propto \left|\frac{q_\perp}{q_z}\right|$, but the four C points are also hidden in the low intensity region of the dipolar emission along z-axis. The low intensity region in the $\pm\boldsymbol{e_z}$ direction originates from the zero emission of the $q_z\boldsymbol{e_z}$ dipolar component in $\pm\boldsymbol{e_z}$ direction and the overall weak $q_\perp$.

In this contribution we show that the far-field polarization singularities, i.e. C points, contain the full information on the dipolar emitter polarization state. To resolve the C points for almost linearly polarized dipoles, we implement a far-field polarization projection, similar to quantum weak measurements [2,3]. This is the first time, to the best of our knowledge, that the polarization basis for optical weak-measurements is spatially varying – TM (radial) and TE (azimuthal).

We consider a dipolar emitter positioned in air (half-space $z < 0$) at subwavelength distance d above a dielectric interface ($z = 0$) with the refractive index n. The far-field intensity pattern $I(k_x, k_y)$ of the dipole in forward direction $+\boldsymbol{e}_z$ (half-space $z > 0$) is given by [4]:

(1) $I(k_x, k_y) \propto \left|\begin{pmatrix} E_{TE} \\ E_{TM} \end{pmatrix}\right|^2 \propto \left|A\hat{T}\hat{M} \cdot \boldsymbol{q}\right|$

(2) $A(k_x, k_y) = (k_0^2 n^2 - k_\perp^2)^2 / k_z \exp(i k_z d)$

(3) $\hat{T}(k_x, k_y) = \begin{pmatrix} t_{TE} & 0 \\ 0 & t_{TM} \end{pmatrix}$

(4) $\hat{M}(k_x, k_y) = \begin{pmatrix} -\frac{k_y}{k_\perp} & \frac{k_x}{k_\perp} & 0 \\ \frac{k_z k_x}{k_\perp k_0} & \frac{k_z k_y}{k_\perp k_0} & -\frac{k_\perp}{k_0} \end{pmatrix}$.

Here, the far-field wave-vector is $\boldsymbol{k} = (k_x, k_y, k_z)$, $k_\perp = \sqrt{k_x^2 + k_y^2} \leq n k_0$, $k_z = \sqrt{k_0^2 - k_\perp^2}$, k_0 is the freespace wavenumber and $t_{TE}(k_x, k_y)$, $t_{TM}(k_x, k_y)$ are the Fresnel coefficients. Imposing the condition of equal far-field amplitudes and phase preservation

(5) $E_{TE}(k_x, k_y) = \pm i E_{TM}(k_x, k_y)$

we find the transverse wave-vectors of the C points:

(6) $\boldsymbol{k}_\perp \cdot \boldsymbol{q}_\perp = 0$; $\boldsymbol{k}_\perp = (k_x, k_y)$; $\boldsymbol{q}_\perp = q_\perp \boldsymbol{e}_\perp = (q_x, q_y)$

(7) $(k_x + \sigma_x)^2 + (k_y - \sigma_y)^2 = \sigma_x^2 + \sigma_y^2$

(8) $\sigma_x = \pm\frac{1}{2}\frac{q_y k_0}{q_z}\frac{t_{TE}}{t_{TM}}$; $\sigma_y = \pm\frac{1}{2}\frac{q_x k_0}{q_z}\frac{t_{TE}}{t_{TM}}$

Equations (5)-(8) define the C points. For instance if the dipole is polarized in the XZ plane ($q_y = 0$) it follows that $k_x = 0, \sigma_x = 0$ and the C points are located at $k_y^c = 2\sigma_y$. From now we restrict ourselves to $q_y = 0$ and $k_x = 0$. Note, the helicity of a C point is a signature of the dipole spin, while the location of the C point dictates the dipole ellipticity. Hence, we have established that the far-field C points bare full information about the dipole helicity and ellipticity. Fig. 1e and 1f show the C points for different dipoles.

For an almost linear dipole, the C points are practically unresolvable, since the two C points of opposite helicity are found in near-to-normal direction where power scales as $|q_x/q_z|^2$ [5] (compare Fig1a and 1f). Yet, it is possible to resolve the C points by projecting the far-field on a post-selection polarization state that takes advantage of the different symmetries of E_{TE} and E_{TM} with respect to the y-axis ($k_x = 0, q_y = 0$):

$$(9)\quad E_{TE}(0,k_y) = -t_{TE}\frac{k_y}{k_\perp}q_x$$

$$(10)\quad E_{TM}(0,k_y) = -it_{TM}\frac{|k_y|}{k_0}q_z.$$

This basis is naturally given by the expected C points locations as $\boldsymbol{u} = \begin{pmatrix} u_{TE} \\ u_{TM} \end{pmatrix} \propto \begin{pmatrix} 1 \\ ik_y^c/k_0 \end{pmatrix}$. The projected intensity pattern is:

$$(11)\quad I_{proj}(k_y) \propto |\boldsymbol{E}\cdot\boldsymbol{u}^*|^2 \propto |k_0^{-1}t_{TE}q_x|^2|k_y + k_0|^2$$

The projected intensity pattern shows an extremum (minimum) at the critical angle $k_y = -k_0$. The helicity of the C point is given by $sign(k_y)$, and its location is encoded in $|k_y|$.

2. Experiment

Our setup consists of confocally aligned microscope objectives with a piezo stage positioning the sample in the focal plane [6]. Such configuration allows to image the Fourier space (far-field) of the sample by imaging the back focal plane of the collecting objective. To induce an elliptical transversely spinning dipole moment $\boldsymbol{q}$, we use a focused radially polarized beam and a gold particle positioned in the focal plane several tenth to several hundreds of nanometers away from the optical axis [7,8]. The projection on the specific spatially varying far-field polarization basis is experimentally realized via transformation of the cylindrically symmetric radial and azimuthal polarization basis to the Cartesian basis by a q-plate [9]. We have measured the far-field C points of a circularly polarized dipole directly, and of an almost linearly polarized dipole applying the weak measurement discussed before. Fig. 1g and 1h show the predicted and the obtained polarization pattern for a general elliptical dipole, polarized in a plane parallel to the z-axis.

3. Discussion and Conclusions

We have established a link between a dipolar emitter and far-field[10] polarization singularities of its radiation. Our scheme is extendable to dipoles polarized in arbitrary planes. In this case, Eq. (5) will be substituted with a more general condition. Experimentally we have measured the C points of almost linear dipoles by applying a novel polarization basis in optical weak measurements. Our results may be of interest for the fundamental experimental physics, as well as for practical implementation such as localization and position sensing [11].

Acknowledgements

Fig. 1a-1d were obtained by freely available software [12].

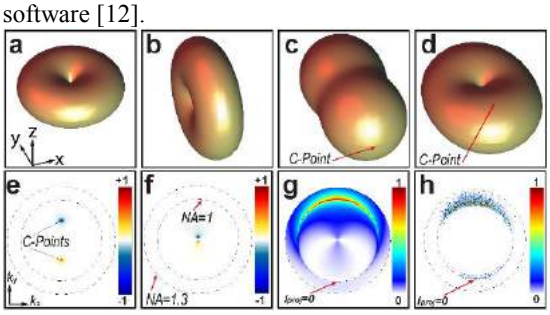


Figure 1. (a) - (d) Radiation patterns of dipoles with dipole moments $\boldsymbol{q_a} = q_0\boldsymbol{e_z}$, $\boldsymbol{q_b} = q_0\boldsymbol{e_x}$, $\boldsymbol{q_c} = q_0[\boldsymbol{e_x} + i\boldsymbol{e_z}]$, $\boldsymbol{q_d} = q_0\left[\frac{1}{2}\boldsymbol{e_x} + i\boldsymbol{e_z}\right]$, respectively. Points of circular polarization (C points) are marked with arrows in (c) and (d). (e), (f) Far-field C points for dipoles $\boldsymbol{q_e} = q_0\left[\frac{1}{2}\boldsymbol{e_x} + i\boldsymbol{e_z}\right]$ and $\boldsymbol{q_f} = q_0\left[\frac{1}{20}\boldsymbol{e_x} + i\boldsymbol{e_z}\right]$ positioned in air above a dielectric with the refractive index $n = 1.5$. The inner and the outer dashed rings mark the critical angle ($NA = 1$) and the maximal collection NA of our objective ($NA = 1.3$). (g) Theoretical polarization projected far-field intensity according to Eq (11) of any elliptical dipole of the form $\boldsymbol{q_g} = q_0[a\boldsymbol{e_x} + ib\boldsymbol{e_z}]$, where a, b are real constants. (h) Experimental camera image for the polarization projection of a dipole $\boldsymbol{q_h} \approx q_0\left[\frac{1}{5}\boldsymbol{e_x} + i\boldsymbol{e_z}\right]$.

References

[1] O. G. Rodríguez-Herrera, D. Lara, K. Y. Bliokh, E. A. Ostrovskaya, and C. Dainty, Phys. Rev. Lett. **104**, 253601 (2010).

[2] Y. Aharonov, D. Z. Albert, and L. Vaidman, Phys. Rev. Lett. **60**, 1351 (1988).

[3] Y. Gorodetski, K. Y. Bliokh, B. Stein, C. Genet, N. Shitrit, V. Kleiner, E. Hasman, and T. W. Ebbesen, Phys. Rev. Lett. **109**, 013901 (2012).

[4] L. Novotny and B. Hecht, *Principles of Nano-Optics* (Cambridge University Press, 2006).

[5] W. Lukosz and R. E. Kunz, JOSA **67**, 1607 (1977).

[6] P. Banzer, U. Peschel, S. Quabis, and G. Leuchs, Opt. Express **18**, 10905 (2010).

[7] M. Neugebauer, T. Bauer, P. Banzer, and G. Leuchs, Nano Lett. **14**, 2546 (2014).

[8] M. Neugebauer, T. Bauer, A. Aiello, and P. Banzer, Phys. Rev. Lett. **114**, 063901 (2015).

[9] S. Slussarenko, A. Murauski, T. Du, V. Chigrinov, L. Marrucci, and E. Santamato, Opt. Express **19**, 4085 (2011).

[10] M. A. Lieb, J. M. Zavislan, and L. Novotny, JOSA B **21**, 1210 (2004).

[11] M. Neugebauer, P. Woźniak, A. Bag, G. Leuchs, and P. Banzer, Nat. Commun. **7**, ncomms11286 (2016).

[12] J. Yang, J.-P. Hugonin, and P. Lalanne, ACS Photonics **3**, 395 (2016).

Interaction of an Individual Chiral Nanostructure with Light Carrying Orbital Angular Momentum

Peter Banzer

Max Planck Institute for the Science of Light, Staudtstr. 2, D-91058 Erlangen, Germany
Institute of Optics, Information and Photonics, University Erlangen-Nuremberg, Staudtstr. 7/B2, D-91058 Erlangen, Germany
E-mail: peter.banzer@mpl.mpg.de

Abstract

We discuss the interaction of an individual chiral nanostructure with light beams carrying orbital angular momentum (OAM). We show that the twisting sense of a Laguerre-Gaussian beam (the sign of the OAM) can be imprinted on the relative phase between longitudinal electric and magnetic fields created by tight focusing, matching and efficiently exciting, for one sign only, the chiral mode of a helical nanostructure exposed to such fields. The chiral scatterer is hence capable of indirectly distinguishing the sign of the original phase charge.

1. Introduction

Light can carry two inherent types of angular momenta. First of all, the spin angular momentum (SAM), which is a result of the spinning electric field of circularly or elliptically polarized light. This property is linked to the polarization of a light beam and its handedness, and is therefore a local property. In addition, light may also exhibit orbital angular momentum (OAM). In contrast to SAM, OAM is a direct consequence of the spatial structure of the beam's phase front and, thus, a spatial/nonlocal property. Both SAM and OAM are equally important from a fundamental and an applied point of view [1], especially when they engage in light-matter interaction schemes [2].

In chiral light-matter interactions, it is known, on the one hand, that an intrinsic property of chiral molecules or nanostructures is their capability of distinguishing the handedness, or SAM, of circularly polarized light. The strength of the interaction depends on the structural handedness of the scatterer, giving rise to effects such as differential absorption (circular dichroism) or polarization rotation (circular birefringence). On the other hand, it is a long-standing debate, whether such chiral objects can also interact with OAM of a light beam (see, for instance, [3-5]). Here, we now approach this intriguing, yet very fundamental question from a different perspective. We show in a proof-of-principle study that an individual nanohelix can be indeed capable of probing the sign of the phase charge of light beams.

2. Discussion and Conclusions

In our theoretical and experimental study we interface a single chiral nanostructure with Laguerre-Gaussian (LG) beams carrying OAM of positive and negative charge. We show that via simple and direct conversion of the twisting sense of the linearly polarized LG beam's phase front (sign of the phase charge) to a well-defined phase difference between longitudinal electric and magnetic fields generated by tight focusing, the chiral nanostructure is indeed capable of distinguishing the sign of OAM. This is an immediate consequence of the fact that only for one phase difference, the created longitudinal fields match the required phase relation between coupled electric and magnetic dipole moments – the fundamental chiral eigenmode – of the excited helical nanostructure. This phenomenon is manifested in the differential absorption, which can be observed for incoming light beams with originally opposite sign of the OAM.

We present experimental and theoretical proof together with a fundamental investigation of the resonant properties of an individual nanohelix used for the aforementioned study.

Acknowledgements

PB acknowledges financial support by the Alexander von Humboldt Foundation.

References

[1] H. Rubinsztein-Dunlop et al., Roadmap on structured light, *Journal of Optics 19*, 013001, 2017.

[2] L. D. Barron, *Molecular Light Scattering and Optical Activity*, Cambridge University Press, Cambridge, 2004.

[3] K. A. Forbes and D. L. Andrews, Optical orbital angular momentum: twisted light and chirality, *Optics Letters 43*, 435-438, 2018.

[4] M. Babiker et al., Orbital Angular Momentum Exchange in the Interaction of Twisted Light with Molecules, *Physical Review Letters 89*, 143601, 2002.

[5] W. Löffler et al., Circular dichroism of cholesteric polymers and the orbital angular momentum of light, *Physical Review A 83*, 065801, 2011.

Optical momentum, angular momentum, and helicity in plasmonic and dielectric structures

Konstantin Y. Bliokh[1,2*], Aleksandr Y. Bekshaev[3], M. F. Picardi[4], F. Alpeggiani[5], F. J. Rodríguez-Fortuño[4], L. Kuipers[5], and Franco Nori[1,6]

[1]CEMS, RIKEN, 2-1 Hirosawa, Wako-shi, Saitama 351-0198, Japan
[2]Nonlinear Physics Centre, RSPE, The Australian National University, Canberra, ACT 0200, Australia
[3]I I. Mechnikov National University, Dvorianska 2, Odessa 65082, Ukraine
[4]Department of Physics, King's College London, London WC2R 2LC, UK
[5]Department of Quantum Nanoscience and Kavli Institute of Nanoscience, Delft University of Technology, The Netherlands
[6]Physics Department, University of Michigan, Ann Arbor, Michigan 48109-1040, USA
*corresponding author, E-mail: k.bliokh@gmail.com

Abstract

We introduce a novel approach efficiently describing the canonical properties – momentum, spin and orbital angular momenta, and helicity – of structured optical fields in structured media. The general theory is applied to examples of surface plasmon-polaritons at metal-dielectric interfaces, guided modes of dielectric and plasmonics cylindrical waveguides, and other systems.

Results

We consider monochromatic optical fields, characterized by complex electric and magnetic field amplitudes $\mathbf{E}(\mathbf{r})$ and $\mathbf{H}(\mathbf{r})$ in isotropic lossless media characterized by real-valued permittivity $(\ ,\mathbf{r})$ and permeability $(\ ,\mathbf{r})$. Here, is the wave frequency, and the medium is allowed to be dispersive as well as inhomogeneous.

The energy density of light in such a medium is given by the well-known *Brillouin formula*:

$$W = \frac{g\omega}{2}\left(\tilde{\varepsilon}|\mathbf{E}|^2 + \tilde{\mu}|\mathbf{H}|^2\right), \qquad (1)$$

where we use Gaussian units with $g=(8\ )^{1}$, and $\tilde{\varepsilon} = \varepsilon + \omega\, d\varepsilon/d\omega$, $\tilde{\mu} = \varepsilon + \omega\, d\mu/d\omega$. The energy flux density is given by the *Poynting vector*, which is also known as the *Abraham momentum density*:

$$\mathbf{\Pi} = g k_0 \,\mathrm{Re}\left(\mathbf{E}^* \times \mathbf{H}\right), \qquad (2)$$

where $k_0 = \ /c$.

However, the Poynting vector is not able to describe the canonical momentum and angular momentum properties of light. Furthermore, the so-called Minkowski momentum density can be considered as the canonical momentum only in the simplest case of plane waves in homogeneous dispersionless media. Recently, we showed [1,2] that the *canonical momentum* ($\mathbf{P}$)*, spin* ($\mathbf{S}$)*, and orbital angular momentum* ($\mathbf{L}$) densities for generic optical fields in dispersive inhomogeneous media are described by the following expressions:

$$\mathbf{P} = \frac{g}{2}\,\mathrm{Im}\left[\tilde{\varepsilon}\,\mathbf{E}^*\cdot(\nabla)\mathbf{E} + \tilde{\mu}\,\mathbf{H}^*\cdot(\nabla)\mathbf{H}\right], \qquad (3)$$

$$\mathbf{S} = \frac{g}{2}\,\mathrm{Im}\left(\tilde{\varepsilon}\,\mathbf{E}^*\times\mathbf{E} + \tilde{\mu}\,\mathbf{H}^*\times\mathbf{H}\right), \quad \mathbf{L} = \mathbf{r} \quad \mathbf{P}. \qquad (4)$$

The momentum density (3) agrees with the Minkowski momentum in the simplest case, but it has much wider range of applicability, including structured light in structured dispersive media. In particular, together with the Brillouin energy density (1) (quantized as $\hbar\omega$ per photon) it provides the momentum density of $\hbar\mathbf{k}$ per photon in all cases, where the real wavevector (phase gradient) is well defined. This includes plane waves in homogeneous dispersive media, surface plasmon-polaritons at planar metal-dielectric interfaces [1,2], eigenmodes of cylindrical dielectric and metallic waveguides [3], etc. Furthermore, the spin angular momentum density (4) yields the value $\hbar\sigma\mathbf{k}/k$, where $[\ 1,1]$ is the polarization helicity (the degree of circular polarization) for plane waves in homogeneous dispersive media. Remarkably, none of the previous approaches provides these simple and fundamental results. This allows one to calculate the spin and orbital angular momentum properties in more sophisticated cases, such as transverse spin and orbital angular momenta of surface plasmon-polaritons [1,2], as well as longitudinal angular momenta of cylindrical-waveguide modes [3]. In particular, our approach for the first time shows that the total angular momentum $\mathbf{J} = \mathbf{L} + \mathbf{S}$ of cylindrical guided modes corresponds to the quantized value $\langle J_z \rangle = \hbar\ell$ (ℓ » , $\langle ... \rangle$ denotes the integration over the cross-section). Again, none of the

previous approaches to the angular momentum in a medium yields this fundamental result. For instance, the Poynting (Abraham) total angular momentum $\mathbf{r}\times\mathbf{\Pi}$ yields a non-integer value without clear physical meaning.

We also derive the physically-consistent definition of the *helicity density* in a dispersive inhomogeneous medium [4]. It is given by:

$$\mathfrak{S} = g\,\mathrm{Re}\left(v\tilde{n}\right)\mathrm{Im}\left(\mathbf{H}^{*}\cdot\mathbf{E}\right), \qquad (5)$$

where $=n/|n|$, n is the phase refractive index of the medium, and $\tilde{n}=n+\omega\,dn/d\omega$ is the group refractive index of the medium. The definition (5) provides meaningful helicity density of $\hbar\sigma$ per photon for plane waves in dispersive homogeneous media [4].

In addition to the macroscopic electromagnetic consideration, we performed microscopic calculations of the energy, momentum, and angular-momentum quantities for surface plasmon-polariton fields in metals [2]. This fully confirmed our macroscopic theory and allowed us to determine the microscopic field and matter (electron) contributions to the quantities (1)–(4). In particular, we found that electron contribution to the spin density (4) describes the *inverse Faraday effect*, i.e., the magnetization of the medium induced by an elliptically-polarized wave. For surface plasmon-polaritons, this means that each polariton carries non-zero *transverse magnetic moment* [1,2]. Its Zeeman interaction with an external magnetic field perfectly describes the nonreciprocal magnetooptical effects (including one-way propagation) with surface plasmon-polaritons [5].

Thus, our theory provides a complete and consistent description of the canonical dynamical properties – momentum, spin and orbital angular momenta, as well as helicity – of monochromatic optical fields in complex (dispersive and inhomogeneous, but locally-isotropic) media. Considering various examples involving structured fields in inhomogeneous dispersive media, we show that our definitions (3)–(5) are fully consistent with physical intuition and notion of a "photon in a medium", in contrast to previous approaches.

Acknowledgements

This work was supported by the MURI Center for Dynamic Magneto-Optics via the AFOSR Award No. FA9550-14-1-0040, the Japan Society for the Promotion of Science (KAKENHI), the IMPACT program of JST, CREST Grant No. JPMJCR1676, RIKEN-AIST Challenge Research Fund, JSPS-RFBR Grant No. 17-52-50023, the Sir John Templeton Foundation, H2020 European Research Council (ERC Advanced Grant No. 340438-CONSTANS and ERC-2016-STG-714151-PSINFONI), Marie Skłodowska-Curie individual fellowship BISTRO-LIGHT (No. 748950), and the Australian Research Council.

References

[1] K. Y. Bliokh, A. Y. Bekshaev, and F. Nori, Optical momentum, spin, and angular momentum in dispersive media, *Phys. Rev. Lett.* 119: 073901, 2017.

[2] K. Y. Bliokh, A. Y. Bekshaev, and F. Nori, Optical momentum and angular momentum in complex media: from the Abraham–Minkowski debate to unusual properties of surface plasmon-polaritons, *New J. Phys.* 19: 123014, 2017.

[3] M. F. Picardi, K. Y. Bliokh, F. J. Rodríguez-Fortuño, F. Alpeggiani, and F. Nori, Angular momenta and helicity of optical fiber and nanowire modes, 2018, in preparation.

[4] F. Alpeggiani, K. Y. Bliokh, F. Nori, and L. Kuipers, Electromagnetic helicity in complex media, *arXiv:1802.09392*, 2018.

[5] K. Y. Bliokh, F. J. Rodríguez-Fortuño, A. Y. Bekshaev, Y. S. Kivshar, and F. Nori, Electric-current-induced unidirectional propagation of surface plasmon-polaritons, *Opt. Lett.* 43: 963−966, 2018.

High index dielectric nanostructures: From directional scattering to electric/magnetic local density of optical states control

Peter R. Wiecha[1], Bruno Masenelli[2], Gérard Colas des Francs[3], Franck Fournel[4], Vincent Larrey[4], Thierry Baron[5], Aurélie Lecestre[6], Guilhem Larrieu[6], Arnaud Arbouet[1], Christian Girard[1], Vincent Paillard[1], and Aurélien Cuche[1]

[1]CEMES-CNRS, Université de Toulouse, CNRS, UPS, Toulouse, France
[2]Université de Lyon, INSA-Lyon, ECL, UCBL, CPE, CNRS, INL-UMR5270, Villeurbanne, France
[3]ICB, UMR 6303 CNRS, Université Bourgogne-Franche Comté, Dijon, France
[4]Université Grenoble Alpes, CNRS, CEA-Leti Minatec, Grenoble, France
[5]Université Grenoble Alpes, CNRS, CEA-Leti Minatec, LTM, Grenoble, France
[6]LAAS-CNRS, Université de Toulouse, CNRS, INP, Toulouse, France
*corresponding author, E-mail: aurelien.cuche@cemes.fr

Abstract

We show both experimentally and theoretically that dielectric nanowires (Si) are able to scatter very efficiently visible light. Furthermore, due to a Fano-like process, we demonstrate that the direction of light scattering can be controlled (forward or backward scattering). Then, we show the effect of a high index dielectric nanoantenna (dimers) on the spontaneous emission of electric and magnetic emitters placed in its vicinity. Our approach allowed us to simultaneously map the electric and magnetic LDOS of individual Si nanostructures.

1. Introduction

For a couple of decades, nanoscale optics has mainly been driven by plasmonics since noble metal nanostructures sustain strong localized resonances (LSPR) that can be used to manipulate, concentrate or redirect visible light. Such properties have led to numerous actual or potential applications in integrated optics, sensors, nonlinear optics, field-enhanced spectroscopies, or photovoltaics. Recently, an alternative to plasmonics emerged with high refractive index dielectric nanostructures, which offer the same range of applications as plasmonics by manipulating Mie optical resonances instead of LSPRs [1].

These resonances can be efficiently tuned by modifying the size, shape, and material of those nanostructures (e.g. silicon, n4). Furthermore, high index dielectric nanostructures offer several key advantages when compared to their metallic counterparts: absorption losses are far weaker for wavelengths longer than the direct band gap, access to semiconductor (CMOS) technology for nanostructure fabrication, and presence of intrinsic strong magnetic resonances, providing an unique opportunity to spatially separate and redistribute the energy of the magnetic and electric parts of the electromagnetic field in the near field, otherwise inextricably connected in the far field.

2. Discussion

We discuss here two optical phenomena associated to dielectric nanostructures: enhancement and directionality control of light scattering, and modification of the photodynamics of electric and magnetic quantum emitters placed in the vicinity of Si nanostructures.

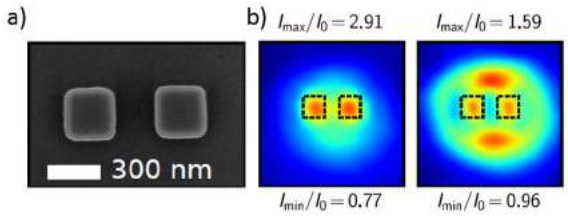


Figure 1: (a) SEM image of a silicon dimer. (b) Photoluminescence maps of Europium-doped clusters deposited on top of a silicon dimer. The left (right) image corresponds to the magnetic (electric) dipole transition.

First, we show that Si nanowires are able to scatter very efficiently visible light. The interference between a broad resonance and a sharp higher mode simultaneously excited in the wire makes possible the control of the direction of light scattering (forward or backward scattering) [2]. Then, we discuss the effect of a high index dielectric nanoantenna on the spontaneous emission of quantum emitters placed in its optical near field. Since the emission rate of the emitters, and therefore the local density of photonic states (LDOS), are modified by the nanostructure, we show that the photodynamics of electric and magnetic dipoles can be controlled (enhancement or quenching) by properly designing the nanoantenna [3]. We then discuss experimental

results of photoluminescence enhancement of Eu3+-doped clusters deposited on top of Si nanostructures (nanowires, dimers) (see Fig.2). We show that these rare earth ions, which exhibit both electric dipole (ED) and magnetic dipole (MD) transitions of nearly equal strength in the same spectral range, allow for a mapping of the electric and magnetic LDOS, respectively, in good agreement with our numerical simulations (Green Dyadic Method - GDM) [4].

Acknowledgement

This work was supported by Programme Investissements d Avenir under the program ANR-11-IDEX-0002-02, reference ANR-10-LABX-0037-NEXT, by LAAS-CNRS micro and nanotechnologies platform member of the French Renatech network, by the Région Midi-Pyrénées and by the computing facility center CALMIP of the University of Toulouse under grant P12167.

References

[1] H. Kallel, A. Arbouet, G. Benassayag, A. Chehaidar, A. Poti, B. Salem, T. Baron, V. Paillard, Tunable enhancement of light absorption and scattering in $Si_{1x}Ge_x$ nanowires, *Phys. Rev. B* 12: 085318, 2012.

[2] P.R. Wiecha, A. Cuche, A. Arbouet, C. Girard, G. Colas des Francs, A. Lecestre, G. Larrieu, F. Fournel, V. Larrey, T. Baron, V. Paillard, Strongly directional scattering from dielectric nanowires, *ACS Photonics* 4: pp 2036–2046, 2017.

[3] P.R. Wiecha, A. Arbouet, A. Cuche, V. Paillard, C. Girard, Decay rate of magnetic dipoles near nonmagnetic nanostructures, *Phys. Rev. B* 97: 085411, 2018.

[4] P.R. Wiecha, C. Majorel, C. Girard, A. Arbouet, B. Masenelli, O. Boisron, A. Lecestre, G. Larrieu, V. Paillard, A. Cuche, Simultaneous mapping of the electric and magnetic photonic local density of states above dielectric nanostructures using rare-earth doped films, *In preparation*, 2018.

Plasmonics: Fundamentals and Applications

‘One Particle, Three Superlattices’: Configuring Particle Superlattice for Enhanced Raman Spectroscopy

Xing Yi Ling

Division of Chemistry and Biological Chemistry, School of Physical and Mathematical Sciences, Nanyang Technological University, 21 Nanyang Link, Singapore 637371
*corresponding author, E-mail: xyling@ntu.edu.sg

Abstract

The structural design on nanoparticle superlattice can significantly impact the resulting macroscopic optical behaviors owing to the nanoscale unique and structure specific light–matter interactions. In this talk, I will discuss how nanoscale surface chemistry is used to direct the self-assembly of shape-controlled silver nanoparticles into three distinct two-dimensional plasmonic superlattices. Systematically tuning the surface chemistry of the silver octahedral nanoparticles leads to a continuous superlattice structural evolution, from close-packed to progressively open structures, and finally silver octahedra standing on vertices arranged in a square lattice. Our ability to constructing different superlattices without changing nanoparticle morphology allows us to single out the influence of superlattice structure on the corresponding SERS performance. The structure-to-function characterization reveals that the nanoparticle assembly with the least packing density generates plasmonic ‘hotstrips’, leading to nearly 10-fold more efficient surface-enhanced Raman scattering compared with the other more densely packed configurations.

References

[1] Y. H. Lee, W. Shi, H. K. Lee, R. Jiang, I. Y. Phang, Y. Cui, L. Isa, Y. Yang, J. Wang, S. Li, X. Y. Ling, Chemically Directed Tunable Assembly of Three Distinct Plasmonic Superlattices from Silver Octahedra *Nat. Commun.* 6: 6990, 2015.

[2] Y. Yang, Y. H. Lee, C. L. Lay, X. Y. Ling, Tuning Molecular-level Polymer Conformations Enables Dynamic Control Over Both The Interfacial Behaviors of Ag Nanocubes and Their Assembled Metacrystals *Chem. Mater.* 29: 6137 – 6144, 2017.

On-chip plasmon-induced transparency and device applications

Xiaoyong Hu[1]*

[1]Department of Physics, Peking University, Beijing, China
*corresponding author, E-mail: xiaoyonghu@pku.edu.cn

Abstract

We realized on-chip plasmon-induced transparency directly in plasmonic circuits. Several nanoscale integrated devices, including all-optical switching, all-optical diode, and all-optical logic devices were realized based on on-chip plasmon-induced transparency.

1. Introduction

Plasmonic circuits provide an essential platform for the large-scale on-chip integration applications due to their extremely strong field confinement effect. plasmon-induced transparency originates from the strong destructive interference coupling between wide-band superradiant plasmonic resonances and narrow-band subradiant plasmonic resonances. plasmon-induced transparency had an unique properties of reduction of the group velocity of light and strong field confinement of light into subwavelength scale regions, which makes plasmo-induced transparency an essential basis of integrated photonic devices. Although phase-coupled mechanisms and and coupled-microcavity mechanisms have been proposed to construct chip-integrated plasmon-induced transparency, very little experimental progress has been made to date due to the great challenge in the sample fabrication. Up to now, it is still a great challenge to realize an ultracompact chip-integrated plasmon-induced transparency nanostructure directly in plasmonic circuits.

We adopted a single plasmonic composite nanocavity to realize on-chip plasmon-induced transparency directly in plasmonic circuits. The plasmonic composite nanocavity was composed of two crossed nanogrooves side-coupled to a bus plasmonic waveguide. The lateral dimension of the plasmonic composite anocavity was only 600 nm, and one transparency window was obtained in the near-infrared range. Moreover, two transparency windows were obtained in the near-infrared range and the optical communication range when the plasmonic composite nanocavity was covered with an 80-nm-thick PMMA layer. Using the thermo-optic effect of PMMA, the transparency windows could be tuned when adjusting the sample temperature.

Using third-order nonlinear optical Kerr effect, several nanoscale integrated devices, including all-optical switching, all-optical diode, and all-optical logic devices were realized based on on-chip plasmon-induced transparency. Through adopting the advantage of light field confinement enhancing nonlinearity of plasmonic circuits and slow-light effect of plasmon-induced transparency windows, the operating threshold light intensity of these nanoscale photonic devices was reduced greatly. Meanwhile, an ultrafast response time was also maintained. For example, ultrafast all-optical switching with the threshold control intensity as low as 560 kW/cm^2, which is reduced by four orders of magnitude, while maintaining ultrafast switching time of 15 ps, were achieved simultaneously.

2. Conclusions

We realized on-chip plasmon-induced transparency directly in plasmonic circuits. Several nanoscale integrated devices, including all-optical switching, all-optical diode, and all-optical logic devices were realized based on on-chip plasmon-induced transparency.

References

[1] Zhen Chai, Xiaoyong Hu, Feifan Wang, Chong Li, Yutian Ao, You Wu, Kebin Shi, Hong Yang, Qihuang Gong, Ultrafast on-chip remotely-triggered all-optical switching based on epsilon-near-zero nanocomposites, *Laser & Photonics Reviews* 11: 1700042, 2017

[2] Feifan Wang, Xiaoyong Hu, Hanfa Song, Chong Li, Hong Yang, Qihuang Gong, Ultralow-power all-optical logic data-distributor based on resonant excitation enhancing nonlinearity via up-conversion radiative-transfer, *Advanced Optical Materials* 5: 1700360, 2017.

[3] Zhen Chai, Xiaoyong Hu, Chong Li, Hong Yang, Qihuang Gong, On-Chip Multiple Electromagnetically Induced Transparencies in Photon−Plasmon Composite Nanocavities, *ACS Photonics* 3: 2068-2073, 2016.

[4] Cuicui Lu, Xiaoyong Hu, Kebin Shi, Qin Hu, Rui Zhu, Hong Yang, Qihuang Gong, An actively ultrafast tunable giant slow-light effect in ultrathin nonlinear metasurfaces, *Light-Science & Applications* 4: e302, 2015.

Atomic-Scale Plasmonic Hot-Spots: A Frequency-Domain Existential Proof and Unusual Photo-Chemical Activities

Hyun-Hang Shin, Gyu Jin Yeon, Han-Kyu Choi, Sang-Min Park, Kang Sup Lee and Zee Hwan Kim*

Department of Chemistry, Seoul National University, Seoul 08826, Korea

E-mail: zhkim@snu.ac.kr

The existence of sub-nm plasmonic hot-spots and its relevance in spectroscopy, microscopy, and photo-chemical applications remain elusive despite a few recent theoretical and experimental evidences. I will present new spectroscopic evidences that angstrom-sized hot-spots do exist on the surfaces of plasmon-excited nanostructures, and that these hot-spots enhances metal - molecule charge-transfer rates. Surface-enhanced Raman scattering (SERS) spectra of 4, 4'-biphenyl dithiols placed in metallic junctions reveal simultaneously blinking Stokes and anti-Stokes spectra, some of which exhibit only one prominent vibrational peak. The activated vibrational modes are found to vary widely between junction-sites. Such site-specific, single-peak spectra could be successfully modelled using single-molecule SERS induced by a hot-spot with a diameter no larger than 3.5 Å, located at specific molecular sites. The model, which assumes the stochastic creation of hot-spots on locally flat metallic surfaces, consistently reproduces the intensity distributions and occurrence statistics of the blinking SERS peaks. We also observe time-resolved Stokes and anti-Stokes SERS spectra of nitrobenzenethiols placed at plasmonic junctions strongly suggesting that such atomic-scale hotspots accelerate the hot-electron transfer between metallic surface and the adsorbed molecules.

Cavity QED based on plasmon nanostructures

Ying Gu[1, 2], Juanjuan Ren[1], Fan Zhang[1], He Hao[1], and Qihuang Gong[1, 2]

[1]State Key Laboratory for Mesoscopic Physics, Collaborative Innovation Center of Quantum Matter, Department of Physics, Peking University, Beijing 100871, China

[2]Collaborative Innovation Center of Extreme Optics, Shanxi University, Taiyuan, Shanxi 030006, China

Requirements for handling on-chip quantum information and building scalable quantum networks are prompting the development of nanostructure-based cavity quantum electrodynamics (CQED) characterized as strong light confinement. Combining the advantages of ultrahigh photon emission rates achievable in the gap surface plasmon polaritons with high extraction decay rates into low-loss nanofibers, we demonstrate theoretically the efficient photon emission of a single dipole emitter and one-dimensional nanoscale guiding in metallic nanorod-coupled nanofilm structures coupled to dielectric nanofibers [1]. The proposed mechanism promises to have an important impact on metal-based optical cavities, on-chip bright single photon sources and plasmon-based nanolasers.

Electromagnetic vacuum engineering plays a fundamental role in controlling light-matter interaction in quantum optics, CQED, and quantum information devices. In previous studies, evanescent optical modes are thought of as cavity modes rather than providing an electromagnetic vacuum environment that the cavity resides in. Here, taking the evanescent vacuum provided by a metallic or dielectric single-mode nanowire as the electromagnetic environment, in which a resonant Ag nanorod (AgNR) is embeded, we theoretically demonstrated the enhanced photon-exciton coupling and the increased fluorescence collection efficiency through the careful optical mode design [2]. This CQED in subwavelength-confined quantum vacuum holds promise for exploring the fundamental physics as well as the applications related to on-chip quantum information and scalable quantum networks.

References

[1] H. Lian, Y. Gu, et al. “Efficient single photon emission and collection based on excitation of gap surface plasmons,” *Phys. Rev. Lett.* 114, 193002 (2015).

[2] JJ. Ren, Y.Gu, et al. “Evanescent-vacuum-enhanced photon-exciton coupling and fluorescence collection ”, *Phys. Rev. Lett.* 118, 073604 (2017).

Plasmonic Anderson localization in correlated disorder

Ruwen Peng*, Wenbo Shi, Renhao Fan, and Mu Wang

National Laboratory of Solid State Microstructures, School of Physics, and Collaborative Innovation Center of Advanced Microstructures, Nanjing University, Nanjing 210093, China
*corresponding author, E-mail: rwpeng@nju.edu.cn

Abstract

The localization of waves in disordered systems is an important effect in condensed matter physics, which was initially investigated by Anderson in 1958 [1]. The absence of electron propagation was predicted because of Anderson localization in disordered systems, eventually causing conductive materials to be insulating [2, 3]. Since it originates from the interference of coherent waves [4], Anderson localization can be extended from electron to other waves [5-6], such as electromagnetic waves, acoustic waves, and matter waves. In this work, we experimentally demonstrate Anderson localization of surface plasmon polaritons (SPPs) at visible regime in metallic nanogratings with short-range correlated disorder. By increasing the degree of disorder, the confinement of SPPs is significantly enhanced, and the effective SPP propagation length dramatically shrinks. Strong localization of SPPs eventually emerges at visible regime, which is verified by the exponentially-decayed fields and the vanishing auto-correlation function of the SPPs. Physically the short-range correlated disorder induces strong interference among multiple scattered SPPs and provides adequate fluctuation to effective permittivity, which leads to the localization effect. Our study demonstrates a unique opportunity for disorder engineering to manipulate light on nanoscale, and may achieve various applications in random nanolasing, solar energy, and strong light-matter interactions.

References:

1. Anderson, P. W. Phys. Rev. 1958, 109, 1492-1505.
2. Lee, P. A.; Ramakrishnan T. V. Rev. Mod. Phys. 1985, 57, 287-337. Byczuk, K.; Hofstetter, W.; Yu, U.; Vollhardt, D. Eur. Phys. J. Spec. Top. 2010, 180, 135-151.
3. Pixley, J. H.; Goswami, P.; Sarma, S. D. Phys. Rev. Lett. 2015, 115, 076601.
4. Sheng, P. Introduction to wave scattering, localisation and mesoscopic phenomena; Springer, 2006.
5. John, S. Phys. Rev. Lett. 1987, 58, 2486-2489.
6. Wenbo, Shi; Lianzi, Liu; Ruwen, Peng; and Mu, Wang; manuscript submitted (2018).

Plasmonics for Optical Information Processing

Lukas Wesemann[1], Kalpana Singh[1], Evgeniy Panchenko[1], Daniel E Gomez[2], Timothy J Davis[1], and Ann Roberts[1*]

[1]School of Physics, The University of Melbourne, 3010, Australia
[2]RMIT University, Melbourne, VIC 3001 Australia
*corresponding author, E-mail: ann.roberts@unimelb.edu.au

Abstract

Optical antennas and metasurfaces can be tailored to modify the intensity, polarization and phase of a scattered electromagnetic wave. These planar devices have considerable potential for integration into photodetectors with enhanced functionality. Resonances of nanoscale plasmonic particles and thin metallic films can also modify the spatial Fourier spectrum of an optical field suggesting their potential as devices for real-time image processing. Here the use of plasmonics in compact optical information processing and imaging systems is discussed and recent progress into the integration of optical antennas into photodetectors presented.

1. Introduction

Light carries a wealth of information about the source of the illumination and objects with which it has interacted. As well as the intensity of the light, the spectral, polarimetric and phase content of an optical field provides considerable insight into emission of light and the nature of matter. Alternatively, information can be explicitly encoded onto an optical field and transmitted as part of a communication system. The capacity for an optical field to carry information on multiple channels underpins the broad approach to using light for sensing, imaging and communication. Although conventional photodetectors essentially measure the intensity of incident light, various strategies can be used to convert 'invisible' properties of light to intensity permitting their measurement, or intensity measurements can be used to reconstruct, for example, phase gradients in the field. Although widely used, these approaches, however, generally require bulky and expensive optical components and/or considerable computational post-processing.

2. Optical antennas and metasurfaces

It is well-known that resonant nanostructures, including plasmonic systems, can modify the amplitude, phase and polarization of scattered fields presenting the possibility of new ways to extract information from optical fields. Here we discuss the use of optical antennas to directly convert amplitude and phase gradient information in an optical field into intensity and the incorporation of plasmonic metasurfaces and antennas into photodetectors. These devices provide an avenue for the development of ultracompact devices that will perform on-chip, real-time, single-shot conversion of wavefield information to readily measured intensity distributions. These devices, compatible with standard CMOS fabrication processes, demonstrate the capacity for metasurfaces to play a significant role in future optoelectronic systems.

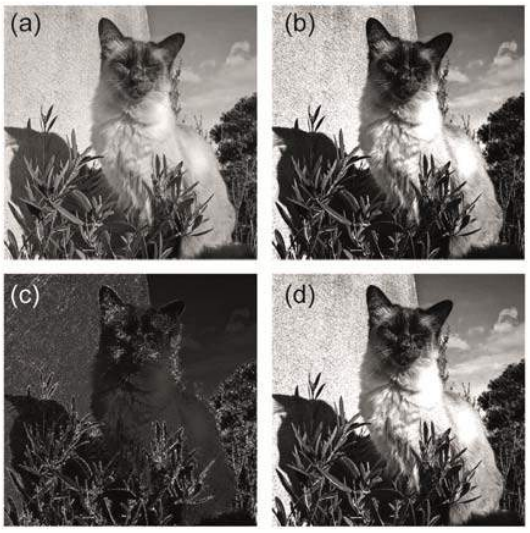


Figure 1: Simulated edge enhancement of amplitude object using a Salisbury screen. Image (a) is reflected from a metal-insulator-metal structure at wavelengths (b) 580 nm; (c) 666 nm and (d) 750 nm. Image size 200 μm.=

2.1. Metasurfaces, thin films and spatial filtering

There have been several recent demonstrations of the use of metasurfaces and plasmonic thin films to perform mathematical operation [1,2]. In one category of configuration, a metasurface can be used as a tailorable spatial filter in a conventional optical spatial filtering system. Optical differentiation or integration can be performed using independent tuning of the amplitude and

phase of scattered light at different points on the filter [1]. On the other hand, the angular sensitivity of certain plasmonic resonances permits direct access to the Fourier (or angular) spectrum of a reflected or transmitted field establishing the possibility of ultra-compact approaches to optical information processing. Zhu et al. [3] used the angular dependence of prism coupling to surface plasmons on a thin metal to demonstrate differentiation of both amplitude and phase objects. The measurement of phase differences [4] and othe Laplacian [5] of an optical field using the cross-polarized component of light transmitted through a metasurface consisting of 'dolmen' structures has also been demonstrated. Here we will discuss the use of 'Salisbury' screen absorbers and subradiant modes of metasurfaces to perform processing of optical information.

As an example, Fig. 1 shows the variation in an amplitude image reflected from a metal-insulator-metal structure (40 nm Au on 165 nm of silica (index 1.5) supported by a Au mirror). This thin film structure shows very strong absorption of normally incident plane waves at 666 nm. This means that at this wavelength, low-angle Fourier components of the angular spectrum of the image of Fig. 1(a) are absorbed, producing the simulated edge enhanced image of Fig. 1(c). At shorter wavelengths (e.g. 580 nm shown in Fig. 1(b) and 750 nm shown in Fig. 1(d)), the image is reflected with high fidelity.

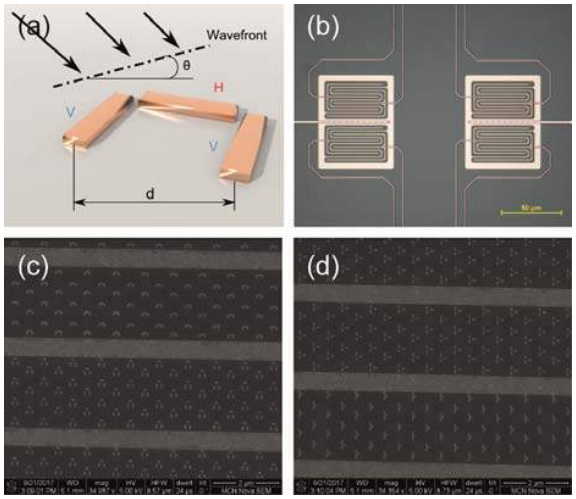


Figure 2: Dolmen structure (a) sensitive to phase differences in an incident plane wave; (b) architecture of the differential angle-sensitive photodetector. SEMs showing photodetectors sensitive to wavefront tilt in the (c) horizontal and (d) vertical directions for vertically polarized light. Scale bar in (b) is 50 μm, and 2 μm (c) and (d)=

2.2. Functional photodetectors

The use of planar information processing structures permits their inclusion into photodetectors compatible with conventional CMOS fabrication techniques [6]. We have fabricated an angle sensitive photodetector based on the dolmen structure of [4] (Fig. 2(a)) and using the metal-semiconductor-metal (MSM) differential approach of [6] (Fig. 2(b)). Each of the photodetector channels consists of two coupled MSM photodiodes. Different 'probe' and 'reference' antenna arrays are placed in the active regions of these diodes. Each metasurface consists of plasmonic dolmen nanoantenna structures (Fig 2(c) and (d)). In the case of the 'probe' metasurface, the horizontal nanoantenna is near-field coupled to the vertical rods. The excitation of this nanoantenna is, therefore, proportional to the phase difference between the vertical arms. In the case of the 'reference' metasurfaces, however, the horizontal nanoantenna is decoupled from the vertical rods so only one metasurfaces is sensitive to the local phase gradient while other remains insensitive. The photocurrent difference between these two detectors is proportional to the wavefront tilt along a specific direction. Furthermore, the utilization of differential detection method increases the robustness of the photodetector to noise [6].

3. Conclusions

We have shown that it is possible to perform optical information processing using thin metal films and metasurfaces composed of nanoscale optical antennas. Furthermore, these structures can be incorporated into photodetectors creating a new class of functional devices laying the foundation for ultracompact approaches to integrated optical information processing.

Acknowledgements

This work was performed in part at the Melbourne Centre for Nanofabrication (MCN) in the Victorian Node of the Australian National Fabrication Facility (ANFF). This research was also supported under the Australian Research Council's Discovery Projects funding scheme project number DP160100983 and the Future Fellowships (FT140100514).

References

[1] A. Silva, F. Monticone, G. Castaldi, V. Galdi, A. Alù, N. Engheta, Performing Mathematical Operations with Metamaterials, *Science* 343:160-163 (2014).

[2] A. Pors, M. G. Nielsen, and S. I. Bozhevolnyi, Analog Computing Using Reflective Plasmonic Metasurfaces, *Nano Lett.*, 15: 791-797 (2015).

[3] T. Zhu, Y. Zhou, Y. Lou, H. Ye, M. Qiu, Z. Ruan and S. Fan, Plasmonic computing of spatial differentiation, *Nat. Commun.*, 8: 15391 (2017).

[4] F. Eftekhari, D. E. Gómez, and T. J. Davis, Measuring subwavelength phase differences with a plasmonic circuit—an example of nanoscale optical signal processing, *Opt. Lett.* 39: 2994-2997 (2014).

[5] Y. Hwang and T.J. Davis, Optical metasurfaces for subwavelength difference operations, *Appl. Phys. Lett.* 109: 181101 (2016).

[6] E. Panchenko, J. J. Cadusch, T. D. James, and A. Roberts, Plasmonic Metasurface-Enabled Differential Photodetectors for Broadband Optical Polarization Characterization, *ACS Photonics*, 3: 1833–1839 (2016).

Lasing at K-point in plasmonic honeycomb lattice

Rui Guo, Marek Nečada, Aaro Väkeväinen, Tommi Hakala, and Päivi Törmä*

Department of Applied Physics, Aalto University School of Science, P.O.Box 15100, FI-00076 Aalto, Finland
*corresponding author, E-mail: paivi.torma@aalto.fi

Abstract

We experimentally demonstrate Bose-Einstein condensation of surface plasmon polaritons in lattice modes of a metal nanoparticle array interactiong with a room-temperature bath of dye molecules which enables thermalisation and condensation in picoseconds. In another recent experiment, we observe lasing action at K-points in an active golden nanoparticle array with honeycomb geometry. By thorough analysis of the polarisation properties of the observed emission in both real and reciprocal space and with the help of group theory, we get the microscopical characterisation of the lasing mode. The utilised methods provide prospects for studies of topological systems obtained by breaking symmetries.

1. Introduction

Thanks to their ability to confine electromagnetic radiation below the diffraction limit and couple it to quantum emitters, and also their broad tunability via their geometry, periodic plasmonic nanostructures provide an excellent platform for studying coherence phenomena in interacting light and matter. We present some of our recent studies of lasing action and Bose-Einstein condensation in such systems.

2. Bose-Einstein condensate

Bose–Einstein condensation is a remarkable manifestation of quantum statistics and macroscopic quantum coherence. We demonstrate a non-equilibrium Bose–Einstein condensate (BEC) of surface plasmon polaritons in lattice modes of a metal nanoparticle array. [1] Interaction of the nanoscale-confined surface plasmons with a room-temperature bath of dye molecules enables thermalization and condensation in picoseconds. The ultrafast thermalization and condensation dynamics are revealed by an experiment that exploits thermalization under propagation and the open cavity character of the system. A crossover from BEC to usual lasing is realized by tailoring the band structure. This new condensate of surface plasmon lattice excitations has promise for future technologies due to its ultrafast, room-temperature and on-chip nature.

3. K-point lasing

Plasmonic nanoparticle arrays can serve as a distributed feedback (DFB)-providing basis for highly tunable nanolasers. [2] The lasing action happens at band edges where the group velocity is zero. Previous experimental studies showed lasing at the band edges at the Γ point of the plasmonic lattices, typically leading to the emitted radiation escaping in the normal direction from the array. However, lasing might be possible also in the other high-symmetry points of the Brillouin zone—such as the K-points in a hexagonal lattice, as we demonstrate here. K-point lasing in such systems provides prospects for topological studies by breaking symmetries of the lattices and subsequent splitting of the degenerate states into modes with nontrivial topological characteristics [3].

3.1. Experiment

We fabricate and measure arrays of gold nanodisks on glass substrate arranged in honeycomb lattice geometry, covered by a fluorescent dye gain medium and immersed into an index-matching liquid. We pump the system from an oblique angle using a femtosecond pulse laser. Focusing the image and back-focal planes onto CCD cameras, we obtain respectively real-space and quasimomentum space images of the emitted radiation. We map the whole first Brillouin zone. In particular, we can identify clear patterns in the real space images, which provide us precious information about the observed modes.

We observe lasing emission into both K and K' directions. Employing group theory we single out the microscopic character of the modes into which the system lases.

References

[1] T.K. Hakala, A.J. Moilanen, A.I. Väkeväinen, Rui Guo, J.-P. Martikainen, K.S. Daskalakis, H.T. Rekola, A. Julku, P. Törmä, Bose-Einstein Condensation in a Plasmonic Lattice, *arxiv:1706.01528* (2017).

[2] T.K. Hakala, H.T. Rekola, A.I. Väkeväinen, J.-P. Martikainen, M. Nečada, A.J. Moilanen, P. Törmä, Lasing in dark and bright modes of a finite-sized plasmonic lattice, *Nature Communications* **8**, 13487 (2017).

[3] Long-Hua Wu, Xiao Hu, Scheme for Achieving a Topological Photonic Crystal by Using Dielectric Material, *Physical Review Letters* **114,** 223901 (2015).

Mapping photoemission and hot-electron emisssion from plasmonic nanoantennas

Richard G. Hobbs[1], William P. Putnam[2,4,5], Arya Fallahi[3], Yujia Yang[4], Franz X. Kärtner[3,5], and Karl K. Berggren[4]

[1]School of Chemistry, Centre for Research on Adaptive Nanostructures and Nanodevices (CRANN) and Advanced Materials and Bio-Engineering Research Centre (AMBER), Trinity College Dublin, Dublin 2, Ireland
[2]Northrop Grumman Corporation, NG Next, 1 Space Park Blvd., Redondo Beach, CA 90278, USA
[3]Center for Free-Electron Laser Science, Deutsches Elektronen-Synchrotron, Notkestraße 85, 22607 Hamburg, Germany
[4]Department of Electrical Engineering and Computer Science and Research Laboratory of Electronics, Massachusetts Institute of Technology, 77 Massachusetts Ave., Cambridge, MA 02139, USA
[5]Physics Dept., University of Hamburg and the Hamburg Center for Ultrafast Imaging, Luruper Chaussee 149, 22761 Hamburg, Germany
*corresponding author, E-mail: hobbsr@tcd.ie

Abstract

Understanding plasmon-driven electron emission and energy transfer on the nanometer length scale is critical to controlling light-matter interactions at nanoscale dimensions. In photoresist and electron-beam resist materials, electron emission and energy transfer lead to chemical transformations. In this work, we employ such chemical transformations in two different high-resolution electron-beam lithography resists, poly(methyl methacrylate) (PMMA) and hydrogen silsesquioxane (HSQ), to map local electron emission and energy transfer with nanometer resolution from plasmonic nanoantennas excited by femtosecond laser pulses.

Results and discussion

Measurement and control of hot carriers derived from surface plasmons may provide a route to guide photochemical reactions,[1]–[4] drive local heating on the nanoscale,[5]–[7] and harvest energy from light.[2] Direct observation of the spatial extent of hot-carrier-mediated chemical processes in materials near the surface of plasmonic nanoparticles will be key to engineering plasmonic structures for hot-carrier driven reactions. Moreover, identifying and differentiating between different electronic processes occurring within individual plasmonic nanoparticles will allow for greater control of reaction pathways enabled by these plasmonic nanoparticles. In this work, we take steps toward addressing these issues by taking advantage of two common electron-beam lithography resists poly(methyl methacrylate) (PMMA) and hydrogen silsesquioxane (HSQ), to image electron emission from plasmonic nanoantennas excited at resonant frequencies.[8]

We have previously characterized electron emission from plasmonic nanoantennas illuminated by intense femtosecond pulses of near-infrared light. In these recent studies we have observed signatures of optical-field-dependent emission that are consistent with an emission mechanism based on strong-field tunneling.[9], [10] In this work, as shown in figure 1b, we observed that the distribution of exposed PMMA on arrays of plasmonic nanoantennas illuminated by intense (~10 $GWcm^{-2}$ peak intensity) femtosecond laser pulses followed the near-field intensity distribution. Moreover, the estimated electron dose received by PMMA in the near-field is comparable to that used in previous reports for low-energy electron-beam lithography using a scanning probe,[11] while also being in agreement with simulated electron emission yields calculated using a model based on strong-field tunneling emission.

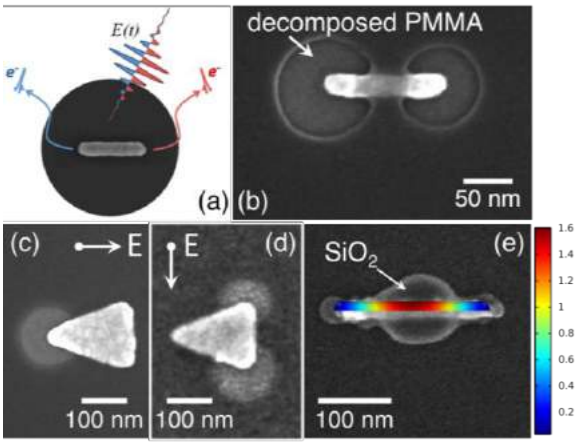


Figure 1. Imaging photoemission and hot-electron emission in lithographic materials. (a) Plasmonic nanoantennas excited by femtosecond laser pulses can emit electron pulses that are strongly localized in both space and time. (b) SEM micrograph of a nanorod antenna showing regions where PMMA was exposed due to electron emission at the antenna poles where the near-

field is most intense. (c,d) SEM micrographs of exposed PMMA around nanotriangles illuminated with linearly polarized such that the optical field is aligned parallel to (c), and orthogonal to (d), the long axis of the nanotriangle antennas. (e) SEM micrograph of Au nanoantenna after HSQ exposure and development showing cross-linked HSQ (SiO_2) at the centre of the nanorod. A colour map of the simulated resistive-losses in the nanoantenna is overlaid on the micrograph. Colour scale represents resistive losses in units of mW/nm^3. Resistive losses lead to the generation of hot electrons at the centre of the nanorod that may subsequently expose HSQ.

Investigations using HSQ as an imaging layer suggest that we may spatially distinguish between electrons emitted due to optical-field emission at nanorod poles and hot electrons generated at the center of the nanorods due to resistive losses. Figure 1e shows a SEM micrograph of a HSQ-coated antenna following exposure with the femtosecond laser source and development of unexposed HSQ. A colour map of the simulated magnitude of resistive losses in such a nanorod antenna is overlaid on the SEM micrograph. The figure shows that HSQ cross-links forming SiO_2 at the centre of the antenna where resistive losses are strongest. On the timescale of the laser pulse the energy dissipated due to resistive losses is carried by electrons in the antenna leading to production of hot electrons ~1-1.5 eV above the Fermi level. These hot electrons could drive the cross-linking of HSQ by inducing water dissociation at the metal surface leading to hydrolysis of HSQ. As such, this work suggests that lithographic materials may provide a number of opportunities to study the role of plasmons in energy transfer at the nanometer length scale and femtosecond timescale.

Acknowledgements

R.G.H., Y.Y., and K.K.B. would like to also acknowledge support from the Gordon and Betty Moore Foundation for support of simulations of energy deposition. R.G.H. was supported for work in the fabrication of structures, metrology, and data analysis by the Center for Excitonics, an Energy Frontier Research Center funded by the U.S. Department of Energy, Office of Science, Office of Basic Energy Sciences, under award no. DE-SC0001088. R.G.H. also acknowledges support from the Royal Society-Science Foundation Ireland University Research Fellowship. We thank James Daley and Mark Mondol for assistance with nanofabrication of gold nanoantennas. A. F and F.X.K. have been supported by the European Research Council under the European Union's Seventh Framework Programme (FP7/2007-2013) through the Synergy Grant AXSIS (609920) and the excellence cluster "The Hamburg Center for Ultrafast Imaging – Structure, Dynamics and Control of Matter at the Atomic Scale" (CUI, DFG-EXC1074) of the Deutsche Forschungsgemeinschaft and the accelerator on a chip program (ACHIP) funded by the Gordon and Betty Moore foundation (GBMF4744).

References

[1] S. Linic, U. Aslam, C. Boerigter, and M. Morabito, "Photochemical transformations on plasmonic metal nanoparticles," *Nat. Mater.*, vol. 14, pp. 567–576, 2015.

[2] S. Linic, P. Christopher, and D. B. Ingram, "Plasmonic-metal nanostructures for efficient conversion of solar to chemical energy," *Nat. Mater.*, vol. 10, pp. 911–921, 2011.

[3] S. Mukherjee, F. Libisch, N. Large, O. Neumann, L. V Brown, J. Cheng, J. B. Lassiter, E. A. Carter, P. Nordlander, and N. J. Halas, "Hot Electrons do the Impossible: Plasmon-Induced Dissociation of H2 on Au," *Nano Lett.*, vol. 13, pp. 240–247, 2013.

[4] C. Clavero, "Plasmon-induced hot-electron generation at nanoparticle/metal-oxide interfaces for photovoltaic and photocatalytic devices," *Nat. Photonics*, vol. 8, pp. 95–103, 2014.

[5] S. Lal, S. E. Clare, and N. J. Halas, "Nanoshell-enabled photothermal cancer therapy: Impending clinical impact," *Acc. Chem. Res.*, vol. 41, pp. 1842–1851, 2008.

[6] D. Zhu, M. Bosman, and J. K. W. Yang, "A circuit model for plasmonic resonators," *Opt. Express*, vol. 22, pp. 9809–9819, 2014.

[7] G. Baffou, C. Girard, and R. Quidant, "Mapping heat origin in plasmonic structures," *Phys. Rev. Lett.*, vol. 104, p. 136805, 2010.

[8] R. G. Hobbs, W. P. Putnam, A. Fallahi, Y. Yang, F. X. Kartner, and K. K. Berggren, "Mapping Photoemission and Hot-Electron Emission from Plasmonic Nanoantennas," *Nano Lett.*, vol. 17, pp. 6069–6076, 2017.

[9] R. G. Hobbs, Y. Yang, A. Fallahi, P. D. Keathley, E. De Leo, W. S. Graves, and K. K. Berggren, "High-Yield, Ultrafast, Surface Plasmon-Enhanced , Au Nanorod Optical Field Electron Emitter Arrays," *ACS Nano*, vol. 8, pp. 11474–11482, 2014.

[10] W. P. Putnam, R. G. Hobbs, P. D. Keathley, K. K. Berggren, and F. X. Kärtner, "Optical-field-controlled photoemission from plasmonic nanoparticles," *Nat. Phys.*, vol. 13, pp. 335–337, 2017.

[11] M. A. McCord and R. F. W. Pease, "Lift-off metallization using poly(methyl methacrylate) exposed with a scanning tunneling microscope," *J. Vac. Sci. Technol. B*, vol. 6, pp. 293–296, 1988.

Emerging materials for plasmonics

Jérôme Plain

Light, Nanomaterials and Nanotechnology, Charles Delaunay Institute, CNRS and TU Troyes, Troyes, France

*corresponding author, E-mail: jerome.plain@utt.fr

Abstract

We report on the fabrication of nanoobjects or nanostructures made from new materials. Moreover, we demonstrate the possibility to tune and control the plasmon resonance of Ni-Au nanoparticles using magnetic field or temperature.

1. Introduction

Over the past two decades, noble metal nanoparticles have attracted an increasing interest because of their varied and complex optical properties. These properties are mainly governed by the collective oscillations of conduction electrons called "plasmons". In particular, the excitation of the latter by optical fields leads to a local exaltation of the electromagnetic field on the surface of the nanoparticle. This very intense nanosource makes it possible to envisage nanometric optical concepts by controlling, manipulating and amplifying light at this scale. Very recently, new metals have been proposed as suitable plasmonic materials to tackle emerging applications of plasmonics, e.g. high-temperature applications, nanochemistry, sensing, or active plasmonics where gold and silver do not possess all the required properties, such as high-temperature sustainability, or catalytic activity. For these reasons, gold and silver are currently reducing their predominance in plasmonics to the benefit of other metals, metal oxides and alloys that constitute a new emerging branch of research. Following this burgeoning variety of plasmonic materials, it becomes useful to conduct a comprehensive and comparative study in order to clearly establish the relative efficiencies of these new plasmonic materials. In this context, I will discuss on the emerging materials and try to present the advantages of different materials like aluminum, nickel, nitrides or bimetallic.

2. Metal Oxides

We developed new processes in order to synthesize nanoparticles of Al@Al_2O_3 and Ni@NiO [1-2]. Both nanostructures present a plasmon resonance in the UV region as shown on figure 1 for aluminium. For aluminium, we report on three different technique allowing us to synthesize Al nanoparticles. The obtained nanoparticles show diameters ranging from 2 to 15 nm. Aluminum nanoparticles exhibit well-defined localized surface plasmon resonances in the ultraviolet range as revealed by extinction measurements and confirmed by Mie theory.

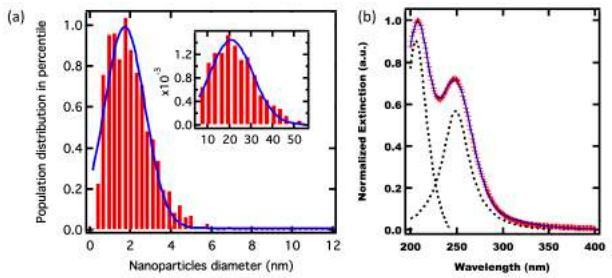


Figure 1: (a) Size distribution for Al nanoparticles obtained by chemical synthesis. Note that two families of nanoparticles are present (2-3nm and 20nm). (b) Normalized extinction spectrum for the corresponding solution. The blue line is a fit for eye.

We report on Ni nanoparticles via thin film thermal annealing. The as prepared particles exhibit a tunable average diameter ranging from 13 nm to 44 nm depending on the initial deposited film thickness and are covered with a stable NiOx shell. This technique is suitable for large scale fabrication of Ni nanoparticles onto substrates. The study of the magnetic and optical properties of these nanostructures revealed a ferromagnetic behaviour at room temperature and a localized surface plasmon resonance in the UV-range, promoting Ni nanoparticles as a suitable material for UV-plasmonic applications. The coupling between plasmon and interband transitions have also been studied.

3. Bimetallic nanoparticles

In recent years, a new challenge is the control and manipulation of optical properties of nanoparticles using an external stimulus.

In this context, we developed Ni-Au plasmonic nanoantennas which exhibit an optical response that can be modulated either by the application of an external magnetic field or by a change in temperature. Thus, we are able to control the plasmon resonance of such individual nanoobjects over several tens of nanometers as shown in figure 2.

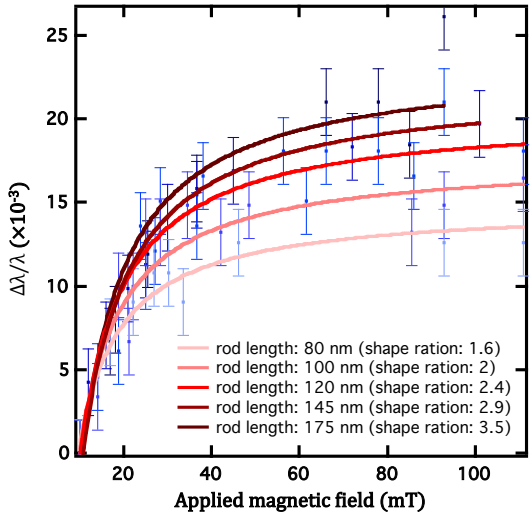


Figure 2: Relative shift of the plasmon resonance as a function of the applied magnetic field.

4. Conclusions

We demonstrate the possibility to use new materials for various applications based on plasmon properties of nanoparticles. Moreover, we demonstrate the possibility to tune under control the spectral response of the plasmon resonance.

Acknowledgements

The author thanks the Nano'mat platform, the LABEX ACTION and the SMFLUONA project. JP thanks Silvère Schuermans, Julien Proust, Thomas Maurer, Jérôme Martin and Davy Gérard.

References

[1] Martin, J., Proust, J., Gerard, D. & Plain, J. Localized surface plasmon resonances in the ultraviolet from large scale nanostructured aluminum films. *Opt. Mater. Express* **3,** 954, 2013.

[2] Schuermans, S., Maurer, T., Martin, J., Moussy, J.-B. & Plain, J. Plasmon / interband transitions coupling in the UV from large scale nanostructured Ni films. *Opt. Mater. Express* **7,** 1787–7 (2017).

Modulation of chiral optical responses in hybrid nanostructures

Wei Zhang[1]

[1] Institute of Applied Physics and Computational Mathematics, P. O. Box 8009(28), 100088 Beijing, P. R. China
*corresponding author, E-mail: zhang_wei@iapcm.ac.cn

Abstract

We discuss the modulation of chiral optical responses in hybrid nanostructures by geometric conformation and by external magnetic field. Our studies show the existence of both structural chirality and induced chirality in nanostructure AuNR@AuNPs (Au nanoparticles (AuNPs) in helical arrangement around a center Au nanorod (AuNR)). Distinct magnetic circular dichroism (MCD) responses of AuNR can be modulated by external magnetic field and geometric configuration (aspect ratio of AuNR, end-to-end and side-by-side assembly configurations).

1. Introduction

The study of chiral optical response, the different optical response to left/right circularly polarized light, is of great scientific and technological importance. The hybrid nanostructures provide much more opportunities for exploring the chiral optical responses due to their variable tunabilities[1-5].

In this presentation, I will present our recent studies of chiral optical responses at nanometer scale, due to the breaking of mirror symmetry either by spatial structure or by magnetic field. We show the existence of both structural chirality and induced chirality in nanostructure AuNR@AuNPs (Au nanoparticles (AuNPs) in helical arrangement around a center Au nanorod (AuNR)), thus clarifying the roles of different mechanisms of optical activities. Moreover, we have found that magnetic circular dichroism (MCD) responses of AuNR can be modulated by external magnetic field and geometric configuration.

2. Structural chirality and induced chirality

In principle, the optical chirality is due to the breaking of mirror symmetry. The optical activity can be generated in a chiral structure with broken mirror symmetry (such as helical structure), which we call structural chirality. An achiral object can also obtain induced chirality by interacting with another chiral structure. With the help of DNA origami, various hybrid nanostructures can be fabricated and their chiral optical responses can be explored. We study the chiral optical responses of AuNR@AuNPs, in which AuNPs form a helical structure and are around a center AuNR. It is known that the AuNP helix shows chiral optical responses. The key mechanism of our system is the interaction between the chiral AuNP helix and achiral AuNR, which induces new plasmonic CD of NR. Thus, we develop a simplified model to reveal the main picture. In our model, the optical response of AuNP helix is described by the effective polarizability α_1^L / α_1^R for left/right circularly polarized light, the optical response of the AuNR is described by the polarizability α_2 . $\alpha_2 \propto \frac{\varepsilon_1 - \varepsilon_0}{\varepsilon_0 + L \cdot (\varepsilon_1 - \varepsilon_0)}$, where L is the geometric factor. The geometric factor $L = \frac{1-e^2}{e^2}\left(\frac{1}{2e}\ln\left(\frac{1+e}{1-e}\right)-1\right)$, $e = \sqrt{1-1/AR^2}$, AR is the aspect ratio. ε_1 , ε_0 are the dielectric constants of bulk Au, and the background medium, respectively. Based on the effective dipole interaction, it can be shown that the coupling between the plasmon in the chiral AuNP helix and that in achiral AuNR leads to the strong optical activity of AuNR (at the its plasmon resonance) . Therefore, we see both structural chirality and induced chirality.

3. Geometry Modulated Magnetoplasmonic Optical Activity

Magnetic field is an effective route in inducing and manipulating the optical activity. We study the magnetic circular dichroism (MCD) responses of AuNR with different aspect ratios and assembly configurations. The polarizability of a AuNR is calculated based on the formula $\hat{\alpha} = V(\hat{\varepsilon} - \varepsilon_m \hat{I})[\hat{L}\hat{\varepsilon} + \varepsilon_m(\hat{I} - \hat{L})\hat{I}]^{-1}$, where V is the volume of AuNR, ε_m , ε denote the dielectric constant of the medium and the dielectric tensor of Au respectively. $\hat{L} = diag(L_{x,} L_y)$ the geometric factor tensor (with L_x and L_y stand for the geometry factors for the longitudinal and

transverse directions), $\hat{I}$ identity matrix. After some calculation, we obtain MCD and anisotropic factor g as

$$MCD = -\frac{4\varepsilon_m \omega V}{L_x L_y} \mathrm{Im}\frac{f(\omega)}{\Delta_0} \quad , \quad g = MCD / Absorption \quad ,(1)$$

$$f(\omega) = A(\omega)\frac{\omega_c}{\omega + i\gamma} \quad , \quad A(\omega) = \frac{\omega_p^2}{\omega(\omega + i\gamma)} \quad , \quad \omega_c = \frac{eB}{m} \quad ,$$

$$\Delta_0 = (\varepsilon_{xx} + \frac{1-L_x}{L_x}\varepsilon_m)\cdot(\varepsilon_{yy} + \frac{1-L_y}{L_y}\varepsilon_m) - f^2(\omega)$$

.

For AuNRs with large AR, the anisotropic factor at longitudinal surface plasmon resonance (LSPR) is:

$$g \propto \frac{L_x^2}{L_y - L_x}\lambda^3 . \qquad (2)$$

For the parameter range considered here, it is seen that MCD is proportional to the strength of the external magnetic field. Moreover, as clearly seen in equations (1) and (2) , the MCD spectra can be effectively tuned by the geometric parameters of AuNR. In addition, the MCD spectra can also be tuned by the assembly configurations (end-to-end and side-by-side assembly configurations).

4. Conclusions

Here we have shown that the chiral optical responses of hybrid nanostructures can be of different nature, i.e., the structural chirality and the induced chirality. The optical responses can be effectively modulated by external magnetic field and geometric configuration (the aspect ratio, the assembly configuration).

Acknowledgements

I acknowledge the collaboration of Zhiyong Tang, Qiangbin Wang, Bing Han, Xiaoqing Gao, Lin Shi, Yonglong Zheng, Ke Hou, Jiawei Lv, Jun Guo, Chenqi Shen, Xiang Lan, Chenggan Zhu, Leyu Wang, and the support from National Key Research and Development Program of China (2017YFA0303400), National Natural Science Foundation of China (11774036,11374039).

References

[1] B. Han, Z. Zhu, Z. Li , W. Zhang*, and Z. Tang*, Conformation Modulated Optical Activity Enhancement in Chiral Cysteine and Au Nanorod Assemblies, *J. Am. Chem. Soc.*, 136:16104-16107, 2014.

[2] Z. Y. Bao, W. Zhang, Y.-L. Zhang, J. He, J. Dai, C.-T. Yeung, G.-L. Law, D. Y. Lei, Interband Absorption Enhanced Optical Activity in Discrete Au@Ag Core-shell Nanocuboids: Probing Extended Helical Conformation of Chemisorbed Cysteine Molecules, *Angew. Chem. Int. Ed.,* 56:1283-1288 , 2017.

[3] C. Rao, Z.-G. Wang, N. Li, W. Zhang,* X. Xu* and B. Ding*, Tunable optical activity of plasmonic dimers assembled by DNA origami, *Nanoscale* 7: 9147-9152, 2015.

[4] C. Shen, X. Lan, C. Zhu, W. Zhang, L. Wang, and Q. Wang, Spiral Patterning of Au Nanoparticles on Au Nanorod Surface to Form Chiral AuNR@AuNP Helical Superstructures Templated by DNA Origami, *Adv. Mater. ,* 29: 1606533, 2017.

[5] B. Han, X. Gao, L. Shi, Y. Zheng, K. Hou, J. Lv, J. Guo, W. Zhang*, and Z. Tang*, Geometry-Modulated Magnetoplasmonic Optical Activity of Au Nanorod-Based Nanostructures, *Nano Lett.*, 17:6083-6089, 2017.

Surface-enhanced Circular Dichroism in the Nanostructure/chiral Medium Hybrid System

SeokJae Yoo[1,2,*], and Q-Han Park[1]

[1]Department of Physics, Korea University, Seoul, Korea
[2]Department of Physics, University of California, Berkeley, Berkeley, USA
*corresponding author, E-mail: seokjaeyoo.nano@gmail.com

Abstract

We present a theory of the microscopic origins of the surface-enhanced circular dichroism (CD) in the nanostructure/chiral medium hybrid system. The recent surge of interest in the surface-enhanced CD spectroscopy has been inspired by the enhancement of the inherent molecular CD, but our work shows that the induced CD in nanostructure can dominate the total CD of the hybrid system. We also provide design principles for metamaterial-based CD sensors.

1. Introduction

Circular dichroism (CD) spectroscopy is one of the optical methods to study the stereochemical information of chiral molecules. Circular dichroism (CD) signals, the difference in absorption for two opposite circularly polarized light, of chiral molecules are extremely weaker than absorption; CD magnitudes of molecules are typically the order of 10^{-6} to 10^{-2} in comparison to their ordinary absorption [1]. The inherent weakness of molecular CD signals is originated from their structural smallness. Sizes of chiral molecules are much smaller than the wavelength of light, and thus they are poor scatterer and absorber of light [1–4].

To overcome the weakness of CD signals, hybrid systems of resonant nanostructures and chiral molecules have been used for CD spectroscopy. Resonant nanostructures and metamaterials have significantly high scattering and absorption efficiency [2,5], and the hybridization of such nanostructures and chiral molecules can enhance inherently weak molecular CD signals [1,2,4,6–9]. However, it is hard to predict the amplified CD signals in the hybrid system because the interaction mechanism in the hybrid system has not been fully explained [4]. Many studies also reported huge mismatch between theoretically predicted CD magnitudes and experimentally measured CD signals [8,9].

Here, we present a theory to predict CD signals of the chiral molecule/nanostructure hybrid systems [7]. Using the Poynting theorem adapted for chiral media, we can calculate local absorption of light energy by the hybrid system whose optical response is dependent on polarization of probe light. We find that there are two distinct origins of CD signals. First, the inherent CD of chiral molecules can be enhanced by strong local fields induced by resonant nanostructures. Second, the induced CD is originated from back action of chiral molecules on the nanostructure, resulting in the chiral response of resonant nanostructure. We also find that the induced CD occurs for the hybrid system of chiral molecules and the achiral nanostructures as a result of the back action of chiral molecules.

2. Surface-enhanced Circular Dichroism in the Hybrid System

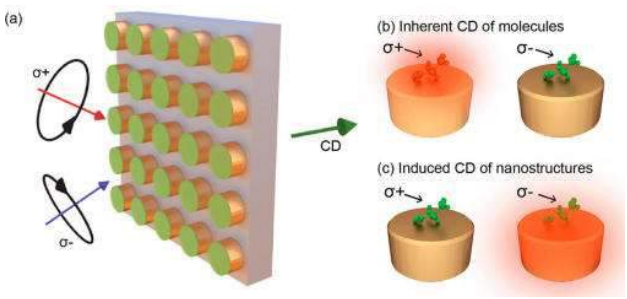


Figure 1: Schematic of (a) the surface-enhanced CD spectroscopy. Chiral molecules (green film) are adsorbed on the nanostructures (gold disks). Two origins of CD signals: (b) the inherent CD of molecules and (c) the induced CD of nanostructures.

The Poynting's theorem describes the energy dissipation in a volume V filled with a lossy medium; $P_{abs} = (\omega/2)\int_V \left(\tilde{\mathbf{E}}\cdot\tilde{\mathbf{D}}^* - \tilde{\mathbf{B}}\cdot\tilde{\mathbf{H}}^*\right)dV'$ for the harmonic fields $\tilde{\mathbf{E}}$ and $\tilde{\mathbf{H}}$ with the angular frequency ω. $\tilde{\mathbf{D}}$ and $\tilde{\mathbf{B}}$ are determined by the electromagnetic constitutive relations of the characteristics of medium. Electromagnetic constitutive relations of the chiral media are given by $\tilde{\mathbf{D}} = \varepsilon\tilde{\mathbf{E}} + i\kappa\tilde{\mathbf{H}}$ and $\tilde{\mathbf{B}} = \mu\tilde{\mathbf{H}} - i\kappa\tilde{\mathbf{E}}$, where ε, μ, and κ are the electric

permittivity, the magnetic permeability, and the chirality parameter of the chiral medium, respectively. The real and imaginary parts of the chirality parameter κ represent the optical rotatory dispersion (ORD) and the CD, respectively [3]. The energy dissipation $P_{abs}\left(\tilde{\mathbf{E}},\tilde{\mathbf{H}}\right)$ can be decomposed into three terms:

$$\begin{aligned} P_{abs,\mathrm{E}}\left(\tilde{\mathbf{E}}\right) &\equiv \left(\omega/2\right)\int_V \mathrm{Im}\left(\varepsilon\right)\left|\tilde{\mathbf{E}}\right|^2 dV' \\ &= \omega\int_V \left\{\mathrm{Im}\left(\varepsilon\right)/\mathrm{Re}\left(\varepsilon\right)\right\} u_E\left(\tilde{\mathbf{E}}\right) dV' \end{aligned}, \quad (1)$$

$$\begin{aligned} P_{abs,M}\left(\tilde{\mathbf{H}}\right) &\equiv \left(\omega/2\right)\int_V \mathrm{Im}\left(\mu\right)\left|\tilde{\mathbf{H}}\right|^2 dV' \\ &= \omega\int_V \left\{\mathrm{Im}\left(\mu\right)/\mathrm{Re}\left(\mu\right)\right\} u_M\left(\tilde{\mathbf{H}}\right) dV' \end{aligned}, \quad (2)$$

$$\begin{aligned} P_{abs,C}\left(\tilde{\mathbf{E}},\tilde{\mathbf{H}}\right) &\equiv \omega\int_V \mathrm{Im}\left(\kappa\right)\mathrm{Im}\left(\tilde{\mathbf{E}}\cdot\tilde{\mathbf{H}}^*\right) dV' \\ &= 2\omega^2 c^2 \int_V \mathrm{Im}\left(\kappa\right) h\left(\tilde{\mathbf{E}},\tilde{\mathbf{H}}\right) dV' \end{aligned}, \quad (3)$$

where $P_{abs,\mathrm{E}}\left(\tilde{\mathbf{E}}\right)$, $P_{abs,M}\left(\tilde{\mathbf{H}}\right)$, and $P_{abs,C}\left(\tilde{\mathbf{E}},\tilde{\mathbf{H}}\right)$ are the electric, magnetic, and chiral parts of the dissipation, respectively. The energy densities are respectively defined by $u_E\left(\tilde{\mathbf{E}}\right) = \mathrm{Re}\left(\varepsilon\right)\left|\tilde{\mathbf{E}}\right|^2/2$ and $u_M\left(\tilde{\mathbf{H}}\right) = \mathrm{Re}\left(\mu\right)\left|\tilde{\mathbf{H}}\right|^2/2$. $h\left(\tilde{\mathbf{E}},\tilde{\mathbf{H}}\right) = \left(1/2\omega c^2\right)\mathrm{Im}\left(\tilde{\mathbf{E}}\cdot\tilde{\mathbf{H}}^*\right)$ is the optical helicity density, where c is the speed of light in vacuum. Local electric fields $\tilde{\mathbf{E}}^{\pm}$ and magnetic fields $\tilde{\mathbf{H}}^{\pm}$ are induced differently inside the lossy materials according to the handedness of the excitation light. Therefore, the CD signals of the chiral molecule/nanostructure coupled system, $\Delta P_{abs} \equiv P_{abs}\left(\tilde{\mathbf{E}}^+,\tilde{\mathbf{H}}^+\right) - P_{abs}\left(\tilde{\mathbf{E}}^-,\tilde{\mathbf{H}}^-\right)$, can also be decomposed to three components: the electrically induced CD $\Delta P_{abs,E}$, the magnetically induced CD $\Delta P_{abs,M}$, and the inherent CD $\Delta P_{abs,C}$ given by

$$\begin{aligned} \Delta P_{abs,\mathrm{E}} &\equiv P_{abs,E}\left(\tilde{\mathbf{E}}^+\right) - P_{abs,E}\left(\tilde{\mathbf{E}}^-\right), \\ \Delta P_{abs,M} &\equiv P_{abs,M}\left(\tilde{\mathbf{H}}^+\right) - P_{abs,M}\left(\tilde{\mathbf{H}}^-\right), \\ \Delta P_{abs,C} &\equiv P_{abs,C}\left(\tilde{\mathbf{E}}^+,\tilde{\mathbf{H}}^+\right) - P_{abs,C}\left(\tilde{\mathbf{E}}^-,\tilde{\mathbf{H}}^-\right). \end{aligned} \quad (4)$$

For the chiral molecule/nanostructure hybrid systems, CD signals result from both the absorptive chiral molecule and the lossy nanostructure. Eq. (4) shows that the inherent CD alone cannot fully explain the total CD signals of the chiral molecule/nanostructure coupled system.

For example in Figure 2, CD signals in the chiral molecule gold nanodisk hybrid system can be analyzed by three contributions: the inherent molecular CD (green line), the induced CD in molecules (blue line) and gold disks (red line). The inherent molecular CD at the molecular absorption wavelength (500 nm) can be dominant, but the induced CD in gold disks is dominant at the plasmon resonance wavelength (650 nm).

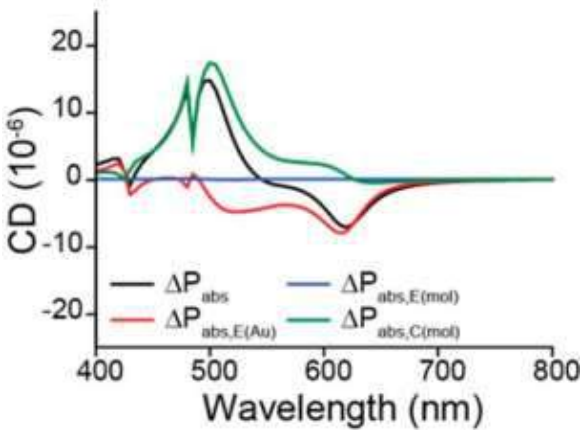


Figure 2: CD signals of the gold nanodisk/chiral molecule hybrid system.

3. Conclusions

In this work, we analytically describe the mechanism behind the CD signals of the nanostructure/chiral medium hybrid system. We expect that our theory reveals the microscopic origin of CD signals in the hybrid system, and it resolves the mismatch between conventional theory and experiment.

Acknowledgements

SeokJae Yoo was supported by Basic Science Research Program through the National Research Foundation of Korea (NRF) funded by the Ministry of Science, ICT & Future Planning (2017R1A6A3A11034238).

References

[1] S. Yoo, M. Cho, and Q.-H. Park, Phys. Rev. B **89**, 161405(R) (2014).

[2] S. Yoo and Q.-H. Park, Sci. Rep. **5**, 14463 (2015).

[3] L. D. Barron, *Molecular Light Scattering and Optical Activity* (Cambridge University Press, Cambridge, England, 2004).

[4] M. Hentschel, M. Schäferling, X. Duan, H. Giessen, and N. Liu, Sci. Adv. **3**, e1602735 (2017).

[5] L. Novotny and B. Hecht, *Principles of Nano-Optics* (Cambridge University Press, Cambridge, England, 2012).

[6] S. Yoo and Q.-H. Park, Phys. Rev. Lett. **114**, 203003 (2015).

[7] S. Lee, S. Yoo, and Q.-H. Park, ACS Photonics **4**, 2047 (2017).

[8] E. Hendry, R. V Mikhaylovskiy, L. D. Barron, M. Kadodwala, and T. J. Davis, Nano Lett. **12**, 3640 (2012).

[9] E. Hendry, T. Carpy, J. Johnston, M. Popland, R. V Mikhaylovskiy, A. J. Lapthorn, S. M. Kelly, L. D. Barron, N. Gadegaard, and M. Kadodwala, Nat. Nanotechnol. **5**, 783 (2010).

Driving Plasmonic Nanocircuits With Antenna-coupled Tunnel Junctions

Surya Prakash Gurunarayanan[*1,3], Jente Vandersmissen[2,3], Marc Heyns[3,1], Iuliana P. Radu[3], Pol Van Dorpe[3,2] and Niels Verellen[3,2]

[1]Department of Materials Engineering, KU Leuven, B-3001 Leuven, Belgium
[2]Department of Physics and Astronomy, KU Leuven, Celestijnenlaan 200D, B-3001 Leuven, Belgium
[3]IMEC, Kapeldreef 75, B-3001 Leuven, Belgium
*corresponding author, E-mail: surya.gurunarayanan@imec.be

Abstract

Electrically driven optical nanoantennas based on quantum mechanical tunneling of electrons recently gained much interest due to their on-chip electronic-photonic transducing properties. These antenna-coupled tunnel junctions can provide full control over light emission including the directionality. In this talk, we show that by carefully engineering the modes of the metallic nanoantenna, unidirectional light emission can be achieved. Moreover, we also show that these directional antennas can readily couple to plasmonic waveguides thereby injecting propagating modes.

1. Introduction

Metallic nanoantennas support collective oscillation of their free electrons (Surface Plasmon Polaritons, SPPs) thereby feature enhanced local density of optical states. Through Purcell effect, nanoantennas strongly modify and control the emission from local emitters. Such antenna-coupled emitter systems can feature spontaneous emission rates comparable to or even faster than that of stimulated emission systems such as a laser [1].

As optical circuits approach the nanoscale, it becomes increasingly important to direct all available energy into propagating waveguide modes. Electrically driven directional nanoantennas, that emit electromagnetic radiation in a predesigned spatial direction, constitute an important missing block that will enable on-chip nanoscale optical circuits. To this end, we experimentally demonstrate unidirectional light emission from antenna-coupled tunnel junctions (ACTJs) [2]. We also show that these unidirectional antennas enable efficient coupling to plasmonic waveguide modes. We finally discuss our recent experimental results on ACTJ-driven plasmonic nanocircuits. Numerical finite difference time domain (FDTD) simulations are used to support our experimental findings.

2. Discussion

Developments in the area of ACTJs gained a lot of momentum in the recent past. Lateral tunnel junctions coupled to two wire antenna geometries have been used to demonstrate spontaneous light emission. Full active (using DC voltage) and passive (using the antenna geometry) control over the properties of light emission- spectrum, polarization and direction have been demonstrated [3]. Spontaneous light emission was also demonstrated using more stable devices utilizing stacks of Metal-Insulator-Metal (MIM) tunnel junctions[4]. In all these works, the emission from the tunnel junction is modified by the antenna to give rise to a bidirectional emission pattern, similar to that of a dipole emitter.

In our approach, we create a nanoscale tunnel junction precisely at the feed point of the V-shaped nanoantenna using a controlled electromigration procedure at room temperature and ambient conditions. This allows tunneling electrons to couple to the plasmonic modes of the antenna. Reducing the symmetry of the two-wire geometry and forming the V-shaped antenna gives rise to a fundamental asymmetric quadrupole-like mode. The uncoupled emission from the tunnel junction interferes with the antenna mode constructively in the $+x$ direction and destructive in the $-x$ direction leading to a highly unidirectional emission pattern [5]. This mechanism is schematically illustrated in Figure 1.

With the rapid development of electrically driven nanoscale light sources, it is imminent that these sources will be used to drive nanoscale, subwavelength optical circuits. Such circuits utilizing propagating plasmon polaritons, can carry information at speeds exceeding 100 THz showing tremendous potential for ultra-fast on-chip optical communication. Electrically driven nanoscale optical circuitry was initially demonstrated using metal-clad nano-LEDs coupled to slot waveguides [6]. The metal-clad nano-LED though serves as a fast spontaneous emitter, its maximum operating speed is still fundamentally limited by the recombination rate of the electron-hole pairs in the semiconductor ($\sim$ ns). Here, we couple our electrically driven V-antennas to plasmonic waveguides and show that propagating waveguide modes could be injected. We also show that essential circuit elements such as gratings, bends and splitters can be easily implemented.

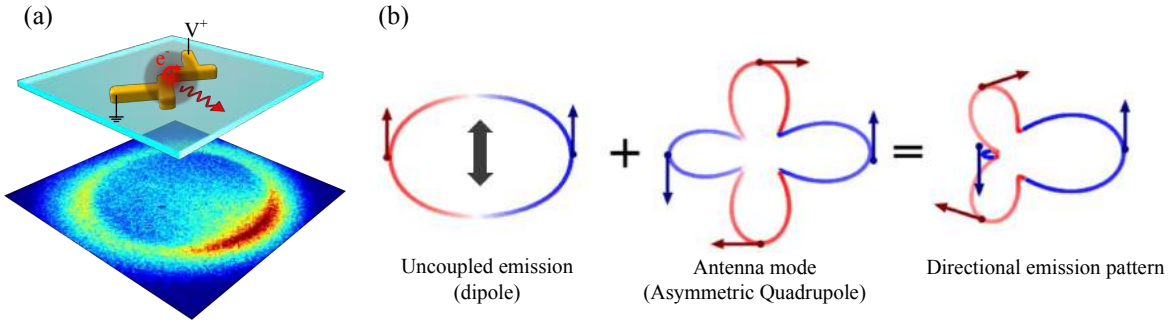


Figure 1: (a) Schematic of the electrically connected asymmetric V-shaped antenna-coupled tunnel junction (ACTJ). Experimental broadband back focal plane (BFP) image showing highly directional light emission. (b) Illustration of the mechanism behind directionality.

3. Conclusion

We experimentally demonstrate for the first time, unidirectional light emission from asymmetric V-shaped ACTJs. We also showed that these unidirectional antennas can easily excite propagating waveguide modes. Our work demonstrates the potential of driving integrated on-chip nanocircuits using ultra-fast electrically driven tunnel junctions.

Acknowledgement

The work was supported by Methusalem funding of the Flemish government and the Flemish Science Foundation (FWO). N.V. also acknowledges the Flemish Science Foundation (FWO-Vl) for financial support. The authors thank Johan Vandamme (KUL) and Joris van Laer (imec) for assistance in the electrical setup. The authors thank Dennis Lin (imec) for valuable discussions.

References

[1] M.S. Eggleston, K. Messer, L. Zhang, E. Yablonovitch, M.C. Wu, Optical antenna enhanced spontaneous emission, *Proc. Natl. Acad. Sci. USA* 112, 6, pp.1704-1709, 2015

[2] S.P. Gurunarayanan, N. Verellen, V.S. Zharinov, F. James Shirley, V.V. Moshchalkov, M. Heyns, J. Van de Vondel, I.P. Radu, P. Van Dorpe, Electrically Driven Unidirectional Optical Nanoantennas, *Nano Lett.* 17, pp. 7433-7439, 2017.

[3] J. Kern, R. Kullock, J. Prangsma, M. Emmerling, M. Kamp, B. Hecht, Electrically driven optical antennas *Nat. Photonics* 9, pp. 582586, 2015.

[4] M. Parzefall, P. Bharadwaj, A. Jain, T. Taniguchi, K. Watanabe and L. Novotny, Antenna-coupled photon emission from hexagonal boron nitride tunnel junctions, *Nat. Nanotech.* 10, pp. 1058106, 2015.

[5] D. Vercruysse, X. Zheng, Y. Sonnefraud, N. Verellen, G. Di Martino, L. Lagae, G.A.E. Vandenbosch, V.V. Moshchalkov, S.A. Maier, P. Van Dorpe, Directional Fluorescence Emission by Individual V-Antennas Explained by Mode Expansion, *ACS Nano* 8, pp. 82328241, 2014.

[6] K.C.Y. Huang, M.-K. Seo, T. Sarmiento, Y. Huo, J.S. Harris, M.L. Brongersma, Electrically driven subwavelength optical nanocircuits, *Nat. Photon.* 8, pp. 244249, 2014.

Shaping Light with an Inclusion: Contribution of Multipoles in Scattering Effect on Waveguide

Alina Karabchevsky[1,2,3*], **Yuriy A Artemyev**[1,2,3,4], **Nikita Volsky**[1,2,3,5], **Alexey A Basharin**[5], **Alexander S Shalin**[4]

[1]Electrooptical Engineering Unit, Ben-Gurion University, Israel
[2]Ilse Katz Institute for Nanoscale Science & Technology, Ben-Gurion University, Israel
[3]Center for Quantum Information Science and Technology, Ben-Gurion University, Israel
[4]ITMO University, Kronversky Prospekt 49, 197101 St. Petersburg, Russia
[5]National University of Science and Technology (MISiS), The Laboratory of Superconducting metamaterials, 119049 Moscow, Russia
*corresponding author, E-mail: alinak@bgu.ac.il

Abstract

Spectral multipole resonances of cylindrical inclusion embedded in a waveguide core and excited by guided optical mode are numerically explored. Here, we show that the scattered light can be shaped by means of the cylindrical inclusion filled with air in optical waveguide. A numerical FDTD method is applied for the calculations of the scattering cross sections. The contribution of multipole moments to the scattering effect is analyzed using our reformulation of the semi-analytical multipole decomposition approach.

1. Introduction

The phenomenon of light scattering by small particles is ubiquitous and central to many science and engineering disciplines [1]. Scattering depends largely on the size, shape [2, 3], and refractive index of the particles [4]. Therefore, understanding the electromagnetic scattering is important for characterizing the optical properties of the particle in numerous fields, including terrestrial and planetary remote sensing, biomedicine, engineering, and astrophysics [5]. Despite the fact that scattering effect is widely explored when a particle is illuminated by a plane wave in vacuum, the scattering from the particle when it is illuminated by the guided mode in a waveguide is somehow overlooked. Here, we explore the scattering from the inclusion (particle, index of 1) of cylindrical shape in waveguide core. Figure 1 shows the schematics of the explored system.

2. Light scattered by a particle or inclusion on waveguide

When the particle is illuminated by electromagnetic wave it can be decomposed to mutlipoles and the contribution of multipoles to scattering cross-section can be explored. However, when the particle is replaced by inclusion filled with air and placed on optical waveguide, the currents are not enclosed in the physical boundary of the inclusion anymore. Such a problem can be solved by the Babinet's principle, however here, we followed the classical multipole decomposition formalism and propose the amendments to multipole decomposition which allow us to reformulate the scattering cross-section. Any electric and magnetic fields are represented by six quantities. However, only four of them are independent. For this reason, we can describe electric and magnetic fields using four quantities: the scalar and vector potentials. After the derivations we obtain the relation for scattered light intensity (I):

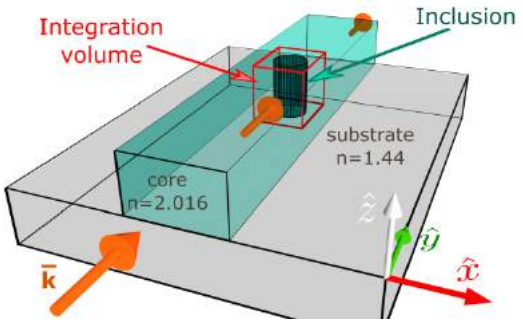


Figure 1: Schematics of the ridge waveguide structure with inclusion of cylindrical shape as deep as the guiding layer and the integration volume of parallelepiped-like shape. Waveguide core index is 2.016 and the substrate index is 1.44.

$$
\begin{aligned}
I = {} & \frac{k^4}{12\pi\, v\, \mu\mu_0\, \varepsilon^2\varepsilon_0^2}|\boldsymbol{d}|^2 + \frac{k^2}{12\pi\, v\, \varepsilon^2\varepsilon_0^2}|\boldsymbol{U}|^2 \\
& + \frac{k^6}{32\pi\, v\, \mu\mu_0\, \varepsilon^2\varepsilon_0^2}\left(\frac{1}{5}Q_{ij}Q_{ij}^* - \frac{1}{15}Q_{ii}Q_{jj}^*\right) + \\
& + \frac{k^4}{12\pi\, v\, \varepsilon\varepsilon_0}|\boldsymbol{m}|^2 + \frac{k^4}{32\pi\, v\, \varepsilon\varepsilon_0}\left(\frac{1}{5}U'_{ij}U'^*_{ij} - \frac{1}{15}U'_{ii}U'^*_{jj}\right) + \\
& + \frac{k^8}{288\pi\, v\, \mu\mu_0\, \varepsilon^2\varepsilon_0^2}\left(\frac{8}{105}O_{ijk}O^*_{ijk} - \frac{2}{105}O_{ijj}O^*_{ikk}\right) + \\
& + \frac{k^6}{32\pi\, v\, \varepsilon\varepsilon_0}\left(\frac{1}{5}M_{ij}M^*_{ij} - \frac{1}{15}M_{ii}M^*_{jj}\right) + \\
& + \frac{k^6}{288\pi\, v\, \varepsilon\varepsilon_0}\left(\frac{8}{105}U''_{ijk}U''^*_{ijk} - \frac{2}{105}U''_{ijj}U''^*_{ikk}\right) \qquad (1)
\end{aligned}
$$

k is the wave vector in medium ϵ, v is the speed of light in vacuum, μ and μ_0 are magnetic permeabilities in medium and vacuum respectively, ϵ and ϵ_0 are electric permittivities in medium and vacuum respectively, $\boldsymbol{d}$ is the electric dipole, $\boldsymbol{m}$ is the magnetic dipole, U is the first amendment, U' is the second amendment and U'' is the third amendment. Q is the electric quadrupole and O is electric octupole. M is magnetic quadrupole.

3. Results and discussion

Figure 2a shows the inclusion of cylindrical shape embedded in waveguide core and enclosed in Integration volume (red box), extracted from the FDTD model. Figure 2b shows the contribution of multipoles to the scattering cross-section. It appears that the first amendment U' and magnetic dipole $\boldsymbol{m}$ have major contributions to the scattering cross-section. However, the electric dipole, electric quadrupole, electric octupole, second amendment, and third amendment have negligible contribution to the scattering cross-section. In addition, we analyzed the scattering diagrams shown in Figure 3. We observed that for the wavelength of $\lambda = 2\mu m$ the light is predominantly scattered in the forward direction, suppressed in backward direction and also scattered toward the substrate and the superstrate three times stronger compared to the scattering effect at wavelength of of $\lambda = 2.4\mu m$. At wavelength of $\lambda = 3\mu m$ the scattered light is suppressed order of magnitude in direction of the substrate and superstrate, and in direction of the waveguide width.

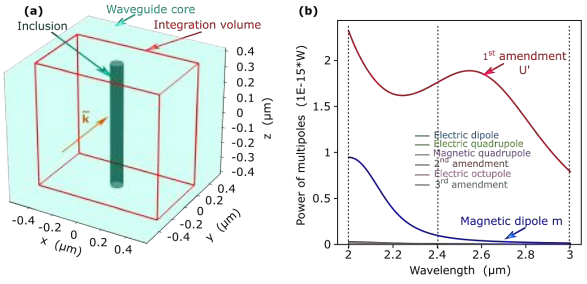


Figure 2: (a) Integration volume (red box) in the waveguide core with the inclusion of cylindrical shape, direction of illumination is indicated by k vector; (b) Contribution of multipoles to the scattering cross-section. Wavelength of $\lambda = 2\mu m, \lambda = 2.4\mu m$ and $\lambda = 3\mu m$ are indicated by the dashed lines.

4. Conclusions

We reformulated the scattering corss-section by introducing amendments. We showed that the scattered light can be shaped by means of the cylindrical inclusion made of air on optical waveguide. Scattering diagrams show that for the wavelength of $\lambda = 2\mu m$ the light is predominantly scattered in the forward direction, suppressed in the backward direction. At wavelength of $\lambda = 2.4\mu m$, the light is scattered toward the substrate and the superstrate thrice stronger compared to the scattering effect at wavelength of $\lambda = 2\mu m$. At wavelength of $\lambda = 3\mu m$ the scattered light is order of magnitude suppressed in direction of the substrate, superstrate and in waveguide width.

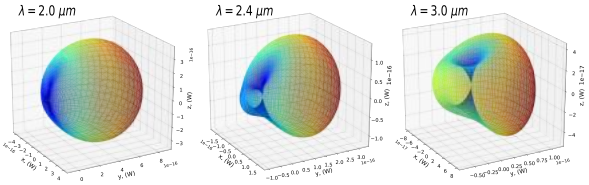


Figure 3: Calculated scattering diagrams for the wavelengths of λ =2 μm, λ =2.4 μm, and λ =3μm from the inclusion in the waveguide core as shown in Figure 1.

Acknowledgment

The work was supported by the Israel Innovation Authority Kamin Program (Grant No. 96717).

References

[1] J. W. S. B. Rayleigh, *Scientific papers*. University Press, 1899, vol. 1.

[2] P. D. Terekhov, K. V. Baryshnikova, Y. A. Artemyev, A. Karabchevsky, A. S. Shalin, and A. B. Evlyukhin, "Multipolar response of nonspherical silicon nanoparticles in the visible and near-infrared spectral ranges," *Physical Review B*, vol. 96, no. 3, p. 035443, 2017.

[3] P. D. Terekhov, K. V. Baryshnikova, A. S. Shalin, A. Karabchevsky, and A. B. Evlyukhin, "Resonant forward scattering of light by high-refractive-index dielectric nanoparticles with toroidal dipole contribution," *Optics Letters*, vol. 42, no. 4, pp. 835–838, 2017.

[4] A. K. Ospanova and A. A. Basharin, "Metamaterials with broken symmetry: general approach, experiment and multipolar decomposition," in *Book of abstracts*, 2017, p. 201.

[5] M. I. Mishchenko, L. D. Travis, and A. A. Lacis, *Scattering, absorption, and emission of light by small particles*. Cambridge university press, 2002.

Shaping Light Using Photonic Integrated Devices

A phase-shifted Solc-type filter based on periodically poled lithium niobate in a reflective geometry

Tingting Ding[1,2], Yuanlin Zheng[1,2], and Xianfeng Chen[1,2,*]

[1]State Key Laboratory of Advanced Optical Communication Systems and Networks,
School of Physics and Astronomy, Shanghai Jiao Tong University, Shanghai 200240, China
[2]Key Laboratory for Laser plasmas (Ministry of Education), Collaborative Innovation Center of IFSA (CICIFSA),
Shanghai Jiao Tong University, Shanghai 200240, China
*corresponding author, E-mail: xfchen@sjtu.edu.cn

Abstract

We observe the transmission of electromagnetic induction transparent (EIT)-like effect in periodically poled lithium niobate (PPLN) based on transverse electro-optic (EO) effect. The configuration can be dynamically tuned or switched on/off by the applied electric filed. The mechanism features a tunable center wavelength in a wide range with respect to temperature and controllable optical delay by the external electrical field, which may offer new way for optical tunable filters or delay lines.

1. Introduction

Electromagnetically induced transparency (EIT) is the quantum interference effect that renders a narrow transparent window in the absorption of a medium. In the transparent window, EIT produces a sharp dispersion and a large nonlinear susceptibility, which has great applications in slow light, optical switching and processing, and nonlinear optics. However, conditions for implementing EIT are difficult to achieve. People are looking for new methods to realize their equivalent phenomenon in classical optics, such as phase shifted Bragg gratings, photonic crystals, coupled microresonators. They exhibit EIT-like transmission spectra either by introducing a defect mode in the bandgap or by interfering two closely located optical resonances.

Lithium niobate (LN) crystal is a multi-functional material with the best overall performance. Besides, with the state-of-the-art poling and micro-fabrication techniques, complex domain structures can be fabricated precisely. PPLN with a defect has also been proposed to realize optical diodes. Similar to the configuration in phase shifted Bragg gratings, PPLN with an embedded defect placed in between two orthogonal polarizers has been predicted to manifest an EIT-like transmission spectrum via transverse electro-optic (EO) coupling. For electro-optic effects, there is also a high demand to achieve low voltage drive by using thinned crystals or waveguide structures.

Here, Solc-type filtering based on polarization coupling in a thinned PPLN crystal is experimentally investigated. With only 0.3 mm in thickness, the half-wave voltage is reduced to below 100 V. Analogy of EIT transmission spectrum (dual-wavelength resonances) in the PPLN based Solc-type filter in a reflective geometry is observed. The mechanism features tunable center wavelength in a wide range with respect to temperature and controllable optical delay by the applied external electrical field. By using a long PPLN crystal, we observed a 0.7-nm width transparent window in a 1.4-nm transmission dip. The operational wavelength can be tuned in a wide range using temperature control. The transmission (and dispersion) can be controlled by the applied external electric field. By using this configuration, a 6.0-ps tunable delay was measured by an applied voltage of 63 V. The device is dynamically addressed to obtain different tunable group velocity with near unity of transmission. The proposed scheme represents a significant step towards reconfigurable optical delay line for optical communications, processing and computing technology.

2. Theory

The polarization evolution of light in PPLN under transverse electro-optic effect can be modelled using Jones matrix. Define the light propagates along the X axis, an electric filed is applied along the Y axis, and Z axis is the optical axis (c axis). The transfer matrix of the *i*-th domain is expressed as

$$M_i = R(\theta) W_i R(-\theta) = \begin{bmatrix} \cos\theta & \sin\theta \\ -\sin\theta & \cos\theta \end{bmatrix} \begin{bmatrix} \exp(-i\delta\phi/2) & 0 \\ 0 & \exp(-i\delta\phi/2) \end{bmatrix} \begin{bmatrix} \cos\theta & -\sin\theta \\ \sin\theta & \cos\theta \end{bmatrix}. \quad (1)$$

Here, θ is the rotation angle of the optical axis about the X axis, and $\theta \approx \gamma_{51} E / \left(1/n_e^2 - 1/n_o^2\right)$, where E is the external transverse electric field intensity, γ_{51} is the EO coefficient of the crystal, and n_e, n_o are the extraordinary and ordinary refractive indices, respectively. For positive and negative domains, there is a sign flip in θ due to the modulation of EO coefficient. $\delta\phi = 2\pi\left(\mathrm{n_e} - n_o\right) d/\lambda$ is the phase retard in one domain, where d is the domain length and λ is the wavelength. The system transmittance matrix is given by

$$\mathrm{T} = \prod_{i=1}^{N} M_i \quad (2)$$

where N is the number of domains that optical waves propagates through. The transmission coefficient for

ordinary wave is $T_{21}(\lambda)$. And the corresponding phase shift is $\phi = \arg(T_{21})$.

3. Experiment and results

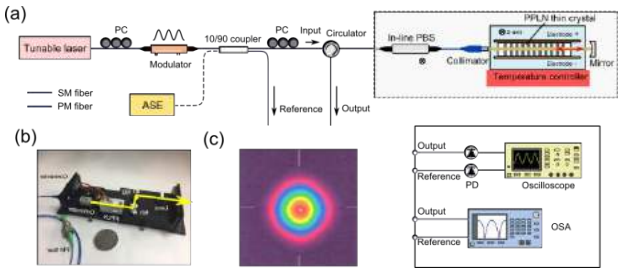


Figure 1: Phase-shifted Solc-type filter based on PPLN in a reflective geometry. (a) Schematic of the experimental setup. (b) Photograph of the device components. (c) Beam profile after passing the PPLN in the far field.

The experimental setup is depicted in Fig. 1. The dimension of the PPLN sample in our experiment is $25(L)\times 0.3(W)\times 1.0(T)$ mm^3. The temperature of the sample is controlled in an accuracy of 0.1℃. The poling period is 20.6 um, corresponding to the QPM wavelength of 1550 nm at 20 degree. The domain number is approximately 2500 in the single pass forward direction and doubled in the reflective geometry. The device is composed of the PPLN and an in-line polarization beam splitter (PBS), as marked by the dashed rectangle. A segment of polarization maintaining fiber is used in between the two components.

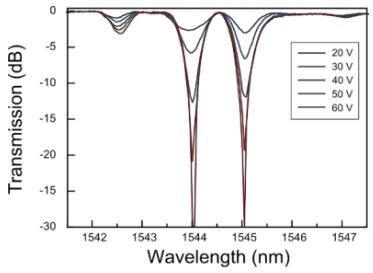


Figure 2: The EIT-like transmission spectra of PPLN in the reflective geometry at the different applied voltages.

In the reflective geometry, the light passing through the PPLN is reflected back by a concave mirror, passes the PPLN a second time, and coupled back to the in-line PBS. Thus, the input and output light has the same polarization. A π phase-shift is induced during the propagation. It is equivalent to a *2L*-long PPLN sample with a defect in the middle of twice the length of the domain unit. The phase shift during the polarization coupling opens a narrow window at the central wavelength. Due to the normal dispersion in this passband, it exhibits group delay with high transmission.

Figure 2 shows the measured spectra of the device at different applied voltages. The full-width at half-maximum (FWHM) of the transmission widow is ~0.5 nm, wider than 20 GHz. The tunable transmission spectrum means that its dispersion can be tuned, i.e., tunable group delay can be obtained by applying different voltages. The center wavelength of the EIT-like spectrum was tuned by the operational temperature in a wide range of over 30 nm at a sensitivity of -0.76 nm/℃.

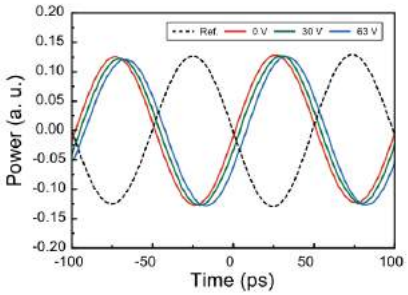


Figure 3: Experimentally measured temporal delay in PPLN in reflective geometry controlled by external voltage.

As the analysis predicted, the dispersion is also tailored via the transverse electro-optic effect. The effect can be turned on and off just by switching the applied voltage. This is an advantage in applications. Figure 3 shows the variation of group delay with respect to the electric field at the center wavelength. Tunable group delay time versus various applied voltages was not recorded due to the resolution limit of the electric circuit, but the group delay is apparent. It is worth mentioning that these characteristics have been investigated using both polarization, showing the same features.

4. Conclusions

In summary, we presented a phase-shifted Solc-type filter based on PPLN in a reflective geometry. EIT-like transmission spectrum was observed. The mechanism features tunable center wavelength in a wide range with respect to temperature and controllable optical delay by the applied external electrical field.

Acknowledgements

National Natural Science Foundation of China (11604206, 61235009, 61590934); Shanghai Education Development Foundation and Shanghai Municipal Education Commission (16CG08); National Key R&D Program of China (2017YFA0303700).

References

[1] I. Mhaouech, V. Coda, G. Montemezzani, M. Chauvet, and L. Guilbert, Low drive voltage electro-optic Bragg deflector using a periodically poled lithium niobate planar waveguide, *Opt. Lett.* 41, 4174-4177, 2016.

[2] X. S. Song, F. Xu, and Y. Q. Lu, Electromagnetically induced transparency-like transmission in periodically poled lithium niobate with a defect, *Opt. Lett.* 36, 4434-4436, 2011.

Optical Vortices Generation with Metallic Nano-Slit

Xue Feng, Xuesi Zhao, and Yidong Huang

Department of Electronic Engineering,
Tsinghua National Laboratory for Information Science and Technology,
Tsinghua University, Beijing 100084, China
x-feng@tsinghua.edu.cn

Introduced by Allen et al., it has been realized that light can carry orbital angular momentum (OAM) in addition to the spin angular momentum (SAM). Independent of the polarization state, light with an azimuthal phase dependence of $\exp(il\varphi)$ has OAM $l\hbar$ per photon. The value of l (the topological charge), as a new dimensionality, can be valued with any integer. Having l spiral phase fronts and a transverse component of the Poynting vector perpendicular to the propagating direction, such kind of light is also known as optical vortex.

As a fundamental tool for light-matter interactions, plasmonic vortex (PV) is extremely attractive due to its unique near field properties. However, it is hard to dynamically and continuously tune the OAM carried by PVs and the properties of fractional PVs are still not well investigated. We have proposed a novel method of utilizing the propagation induced radial phase gradient of incident Laguerre-Gaussian (LG) beam to sculpture PVs from integer to fractional OAM dynamically. Furthermore, a series of plasmonic devices are proposed to generate multi-patterned and two-dimensional optical lattice with helicity or not. Due to spin-orbit coupling, both the spin and orbital angular momentum of incident beam as well as the excited polygonal plasmonic mode contribute to the formation of optical lattice. With the compactness and flexible tunability, we believe that this work would facilitate the utilization of optical lattice in various on-chip applications.

Nonlinear Metasurface for Simultaneous Control of Spin and Orbital Angular Momentum

Guixin Li

Department of Materials Science and Engineering, Shenzhen Institute for Quantum Science and Engineering, Southern University of Science and Technology, Shenzhen, 518055, China.

Email: ligx@sustc.edu.cn

The spin and orbital angular momentum (SAM and OAM) of light is providing a new gateway towards high capacity and robust optical communications. While the generation of light with angular momentum is well studied in linear optics, its further integration into nonlinear optical devices will open new avenues for increasing the capacity of optical communications through additional information channels at new frequencies. However, it has been challenging to manipulate the both SAM and OAM of nonlinear signals in harmonic generation processes with conventional nonlinear materials. Here, we report the generation of spin controlled OAM of light in harmonic generations by using ultrathin photonic metasurfaces. The spin manipulation of OAM mode of harmonic waves is experimentally verified by using second harmonic generation (SHG) from gold meta-atom with three-fold rotational symmetry. By introducing nonlinear phase singularity into the metasurface devices, we successfully generate and measure the topological charges of spin-controlled OAM mode of SHG through an on-chip metasurface interferometer. The nonlinear photonic metasurface proposed in this work not only opens new avenues for manipulating the OAM of nonlinear optical signals, but also benefits the understanding of the nonlinear spin-orbit interaction of light in nanoscale devices.

The far field imaging of SHG radiations is characterized at the fundamental wavelength of 1100 nm for all the C3 metasurfaces (Figure 1). The SHG beams are collected by a second objective lens with N. A. = 0.3, with its Fourier plane imaged onto a charge coupled device camera after filtering out the FW by using band-pass filters As shown in **Figure 2**, SHG beams with RCP SAM state have donut shapes while the ones with LCP state have very low intensity, which is close to the background noise. We also proposed a different approach and used the co-axis metasurface interferometry. For linear polarized FW with both LCP and RCP components, the topological charge of SHG vortex beams radiated from the C3 nonlinear metasurfaces should be l and $-l$, respectively. The SAM states of the SHG vortexes are RCP and LCP, which are opposite to those of the FW. By choosing the linear polarized components from the two SHG vortices, we are able to observe the interference patterns of the two counter-handed OAM modes with topological charge: $\pm l$. The interference pattern is expected to be the Hermite-Gaussian (HG) mode of light with a petal number of $2l$. In this way, one can quantify the topological charge of the OAM mode of SHG wave. As shown in third and fourth rows of Figure 3, the petal number of the HG modes for the three nonlinear metasurfaces equals to $2l = 2$, 4 and 6. Thus we can experimentally retrieve the topological charge of the OAM of SHG vortices with $l = \pm\sigma, \pm 2\sigma$ and $\pm 3\sigma$. We also performed numerical calculations of the SHG radiations to verify our experimental observations.

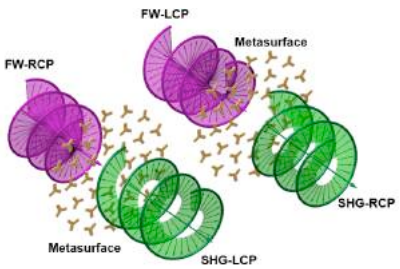


Figure 1. Schematic of spin controlled generation of OAM of SHG by using nonlinear photonic metasurface. The metasurface consists of C3 plasmonic meta-atoms with three-fold symmetry. For a fundamental wave (FW) with two spin states (LCP and RCP) normally incident onto the nonlinear photonic metasurface with C3 symmetry, generation of SHG waves with opposite handiness to that of FW are allowed. By encoding the phase singularity into the metasurfaces, the SHG vortex beams with spin controlled topological charges are generated.

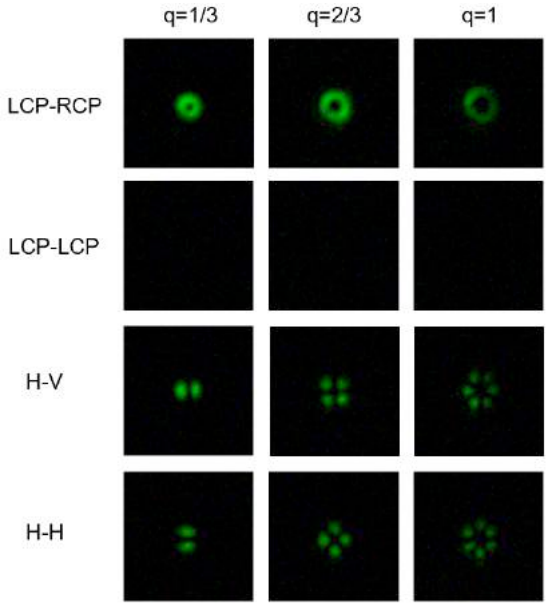


Figure 2. Measurement intensity distributions of SHG from metasurfaces with q=1/3, 2/3 and 1. Under pumping of left circularly polarized FW, the SHG radiation with RCP- and LCP- components (first and second rows) are measured in the far field. For the LCP(FW)-RCP(SHG) measurement, SHG vortex beams with increasing radiuses are observed. In comparison, no obvious SHG signals are found for LCP(FW)-LCP(SHG) measurement. The third and fourth rows show the results for FW with horizontal polarization (H), the SHG signals with horizontal (H) and vertical (V) polarizations were recorded by using CCD camera. From the petal numbers of SHG interference pattern, the absolute value of the topological charge of SHG vortex can be identified.

REFERENCES

(1) Pancharatnam, S. *Proc. Indian Acad. Sci. Sect. A* **1956**, *44*, 247–262.
(2) Berry, M. V. *Proc. R. Soc. London Ser. A* **1984**, *392*, 45–57.
(3) Chen, S. M.; Li, G. X.; Zeuner, F.; Wong, W. H.; Pun, E. Y. B.; Zentgraf, T.; Cheah, K. W.; Zhang, S. *Phys. Rev. Lett.* **2014**, *113*, 033901.
(4) Li, G.; Chen, S. M.; Pholchai, N.; Reinehe, B.; Wong, P. W. H.; Pun, E. Y. B.; Cheah, K. W.; Zentgraf, T.; Zhang, S. *Nat. Mater.* **2015**, *14*, 607–612).

Integrated OAM Laser at Telecom Wavelengths

Changzheng Sun[1], Juan Zhang[1], Bing Xiong[1], Jian Wang[1], Zhibiao Hao[1], Lai Wang[1], Yanjun Han[1], Hongtao Li[1], Yi Luo[1], Takuo Tanemura[2], Yoshiaki Nakano[2], Xinlun Cai[3], Siyuan Yu[3]

[1]Tsinghua National Laboratory for Information Science and Technology, State Key Lab on Integrated Optoelectronics, Department of Electronic Engineering, Tsinghua University, Beijing 100084, China
[2]Integrated Photonics Laboratory, Department of Electrical Engineering and Information Systems, Graduate School of Engineering, the University of Tokyo, Tokyo 113-8656, Japan
[3]State Key Laboratory of Optoelectronic Materials and Technologies, School of Physics and Engineering, Sun Yat-sen University, Guangzhou 510275, China
*corresponding author, E-mail: czsun@tsinghua.edu.cn

Abstract

An integrated OAM laser operating at telecom wavelengths will be presented. Vortex beam is generated by monolithically integrating an optical vortex emitter with a distributed feedback (DFB) laser on the same InGaAsP/InP epitaxial wafer. The device is believed to have promising potential for applications in fiber communications and quantum optics.

1. Introduction

Optical vortex beams with helical wave front carry orbital angular momentum (OAM) [1-3], and have attracted substantial attention due to their potentials in fiber and free-space communications [4, 5], quantum key distribution, and quantum information [6, 7]. Silicon-based devices for OAM beam generation have been demonstrated [8, 9]. However, the indirect bandgap of silicon requires external lasers to excite the OAM emitter, thus making monolithically integrated OAM emitters impossible.

By monolithically integrating an optical vortex emitter with a distributed feedback (DFB) laser on the same InGaAsP/InP epitaxial wafer, we demonstrate the first electrically pumped OAM laser operating at telecom wavelengths.

2. Device Design and Fabrication

Shown in Fig. 1 is the schematic of our integrated OAM laser, which consists of a DFB laser and a microring-based optical vortex emitter monolithically integrated on the same InP substrate. The DFB laser adopts the standard ridge waveguide structure, while a deeply-etched ridge waveguide structure is employed for the microring-based vortex emitter to reduce the bending loss. Specially designed top gratings are formed on top of the ring waveguide, so as to extract phase-coherent beam from the whispering-gallery-mode (WGM) in the microring. A pulley coupling structure is adopted to ensure sufficient coupling between the microring and the bus waveguide. When the wavelength of the DFB laser is on resonance with the microring, OAM-carrying beam will be emitted vertically by the vortex emitter.

The integrated OAM laser is realized by the identical active layer integration scheme [10], whereby the DFB laser and the vortex emitter are formed on the same InGaAsP multiple quantum well (MQW) active layer. A single-step dry etching process is developed to complete the deeply-etched microring with the shallow-etched top gratings. The process takes advantage of the lag effect, i.e. the etch rate is dependent on the mask opening. By optimizing the etch conditions, the MQW layer beneath the top gratings remains intact, thus ensuring low transmission loss in the microring resonator.

3. Device Performance

Figure 2 shows the L-I characteristics of the integrated OAM laser. The insets illustrate the near-field patterns of the OAM laser at pump currents near and above the threshold. The concentric annular pattern with a dark centre is characteristic of an OAM-carrying beam.

To determine the topological order of the laser emission, a spatial light modulator (SLM) encoded with different orders of helical phase is employed to analyze the emitted OAM beam [11]. According to the measurement results shown in Fig. 3, the l value of this OAM laser is found to be +4, and the mode purity of the right-hand circularly polarized (RHCP) and the left-hand circularly polarized (LHCP) components are determined to be 0.76 and 0.85, respectively.

4. Conclusions

An integrated OAM laser operating at telecom wavelengths is demonstrated for the first time. A single-step dry etching process is employed to complete the specially designed top gratings. The topological order as well as the OAM mode purity of the OAM laser is characterized. The integrated OAM laser has great potential for applications in communication systems and quantum domain.

Acknowledgements

This research was sponsored in part by National Basic Research Program of China (2014CB340002); National Natural Science Foundation of China (61621064, 61307024, 61574082, 51561165012); Tsinghua University Initiative Scientific Research Program (20131089364, 20161080068, 20161080062); and Open Fund of State Key Laboratory on Integrated Optoelectronics (IOSKL2014KF09).

References

[1] L. Allen, M. W. Beijersbergen, R. J. C. Spreeuw, *et al.*, Orbital angular momentum of light and the transformation of Laguerre-Gaussian laser modes, *Phys. Rev. A* 45: 8185-8190, 1992.

[2] A. M. Yao and M. J. Padgett, Orbital angular momentum: origins, behavior and applications, *Adv. Opt. Photonics* 3: 161-204, 2011.

[3] G. Molina-Terriza, J. P. Torres, and L. Torner. Twisted photons, *Nat. Physics* 3: 305-310, 2007.

[4] J. Wang, J. Y. Yang, I. M. Fazal, *et al.*, Terabit free-space data transmission employing orbital angular momentum multiplexing, *Nat. Photonics* 6: 488-496, 2012.

[5] A. E. Willner, H. Huang, Y. Yan, *et al.*, Optical communications using orbital angular momentum beams, *Adv. Opt. Photonics* 7: 66-106, 2015.

[6] A. Mair, A. Vaziri, G. Weihs, *et al.*, Entanglement of the orbital angular momentum states of photons, *Nature* 412: 313-316, 2001.

[7] S. Franke-Arnold, L. Allen, and M. Padgett, Advances in optical angular momentum, *Laser Photonics Rev.* 2: 299-313, 2008.

[8] X. Cai, J. Wang, M. J. Strain, *et al.*, Integrated compact optical vortex beam emitters, *Science* 338: 363-366, 2012.

[9] C. R. Doerr and L. L. Buhl, Circular grating coupler for creating focused azimuthally and radially polarized beams, Opt. Lett. 36: 1209-1211, 2011.

[10] C. Sun, B. Xiong, J. Wang, *et al.*, Fabrication and packaging of 40-Gb/s AlGaInAs multiple-quantum-well electro-absorption modulated lasers based on identical epitaxial layer scheme, *J. Lightwave Technol.* 26: 1464-1471, 2008.

[11] Strain, M. J. X. Cai, J. Wang, *et al.*, Fast electrical switching of orbital angular momentum modes using ultra-compact integrated vortex emitters. *Nat. Commun.* 5: 4856, 2014.

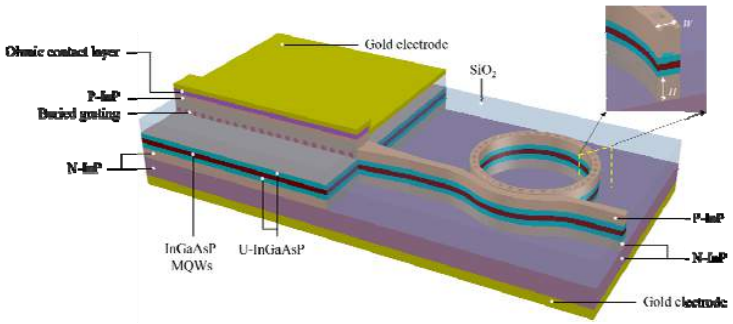


Figure 1: Schematic of the integrated OAM laser.

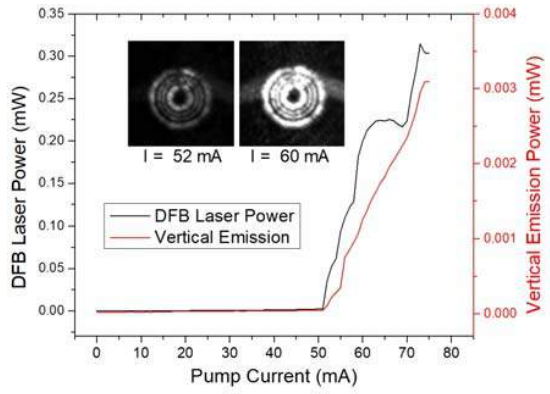


Figure 2: L-I characteristics of the integrated OAM laser. Inset : Near-field patterns at different pumping currents.

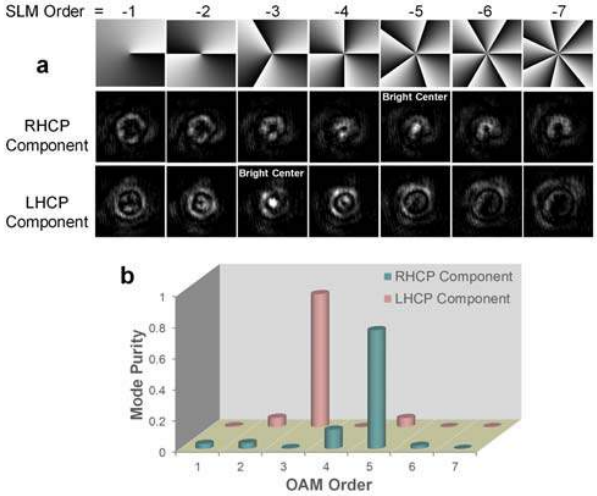


Figure 3: (a) OAM emission modulated by SLM. (b) Mode purities of the RHCP and LHCP components.

Light wavefront manipulation using dielectric metasurfaces

Yan Li[1]*, Bo Wang[1], Qitong Li[1], Dong Yang[1], Hang Feng[1], Qihuang Gong[1], Fengliang Dong[2], Weiguo Chu[2]

[1]State Key Laboratory for Mesoscopic Physics, Department of Physics, Peking University and Collaborative Innovation Center of Quantum Matter, Beijing 100871, China

[2]Nanofabrication Laboratory, CAS Key Laboratory for Nanosystems and Hierarchical Fabrication, CAS Center for Excellence in Nanoscience, National Center for Nanoscience and Technology, Beijing 100190, China

*corresponding author, E-mail: li@pku.edu.cn

Abstract

Light wavefront manipulation using dielectric metasurfaces was demonstrated. By spin manipulation and wavelength multiplexing, we can change the color of, not only the entire holographic image reconstructed from a silicon-on-insulator metasurface hologram, but also of defined parts of it. We design and fabricate the Rochon-prism-like planar circularly polarized beam splitters based on silicon metasurfaces by simultaneously controlling the geometric phase and the propagation phase via manipulation of the orientations and the sizes of the constituent silicon nanoblocks.

1. Introduction

Recently, dielectric metasurfaces consisting of sub-wavelegth Mie scatters of high refractive indexes have been used to manipulate light wavefronts [1,2]. Vivid images can be created with metasurface color holograms by configuring their subwavelength planar structures. However, it is a challenge to arbitrarily tune the colors of the images after the metasurfaces have been fabricated. The common method of balancing the incident intensities of individual wavelengths directly or indirectly does not change the relative brightness/color of different parts of the image. Here, we use spin manipulation and wavelength multiplexing to change the color of, not only the entire holographic image, but also of defined parts of it [3]. This is achieved by designing polarization-dependent dual images for each primary color. This work demonstrates potential for exploiting dielectric metasurfaces to reconstruct colorful images, which is highly desired in the holographic display industry.

By applying geometric Pancharatnam-Berry (PB) phase, single-layer ultrathin planar circularly polarized beam splitters (CPBSs) can symmetrically split the right-circularly polarized (RCP) and the left circularly polarized (LCP)] light as the Wollaston prism does for linearly polarized light. Unfortunately, the Rochon (Sénarmont) prism-like CPBS based on metasurfaces has not been realized yet. It has been demonstrated very recently that one can engineer the wavefront of both circular polarizations independently and arbitrarily by combination of PB phase and propagation phase in a metasurface, making metasurfaces a uniquely powerful platform for polarization optics. Here, we design and fabricate the Rochon-prism-like planar CPBSs based on dielectric metasurfaces by simultaneously controlling the geometric phase and the propagation phase via manipulation of the orientations and the sizes of the constituent silicon nanoblocks [4]. The special splitters deviate only one of the circular polarizations while leave the other undeviated, acting like a Rochon prism for linearly polarized light, and their efficiencies can be as high as 66.7% with an extinction ratio of 27. The mechanism makes it possible to fabricate metasurface holograms that can only be reconstructed by either of two circular polarizations while hidden from the other.

.

2. Results and Discussion

The photon spin-controlled color-tunable holograms using silicon-on-insulator metasurfaces were realized by reconstruction of dual holographic images. With this approach, each photon spin (RCP or LCP) for each primary color reconstructs purposefully designed spin-controlled dual holographic images based on holographic multiplexing or shared-aperture technique, which is different from the previous spin-controlled holograms with single reconstructed image or multiple uncoupled images. Any other incident polarization, consisting of the RCP and LCP components with certain intensity ratio, reconstructs the twin images whose intensities vary according to the ratio, resulting in tunable colors by color mixing.

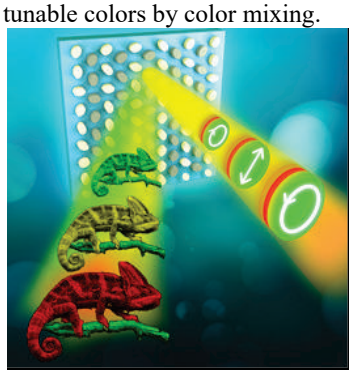


Figure 1: Illustration of the polarization controlled color hologram.

We have successfully modulated the color of not only the entire holographic image but also its definite part by using two kinds of silicon nanoblocks to encode the wavefronts of two primary colors (red and green) by the PB phase, as shown in Fig.1. By continually changing the incident polarization state from RCP to linear to LCP, the chameleon changes its color from green to yellow to red while the tree branch is always green. This approach is further extended to tuning the colors of holographic images using three primary colors by multiplexing three kinds of Si nanoblocks. The combination of the dielectric metasurface color holograms and the holographic multiplexing is expected to play a critical role in holographic display industry by providing an effective pathway of tuning the color of holographic images and enlarging the information capacity of metasurfaces at multi-wavelengths.

When an LCP or RCP incident beam impinges onto a metasurface consisting of inclusions of identical size but spatially distributed orientations θ, the transmitted RCP or LCP beam is imparted with the PB phase $\phi_{RCP\to LCP}(x,y) = -\phi_{LCP\to RCP}(x,y) = -2\theta(x,y)$. The geometric PB phase metasurfaces inevitably manipulate the wavefronts of both LCP and RCP light and the deflection angles are constrained to be equal and opposite.

By spatially varying the sizes of inclusions to induce additional propagation phase $\varphi(x,y) = 2\theta(x,y)$, we have $\phi_{LCP\to RCP}(x,y) = 0$ and $\phi_{RCP\to LCP}(x,y) = 4\theta(x,y)$. Therefore, an LCP incident beam can transmit without wavefront change but an RCP incident beam can be manipulated by properly designed metasurfaces, as shown in Fig. 2. With this, we have also designed a metasurface hologram which can only be reconstructed with RCP light whereas hidden from LCP light without wavefront change.

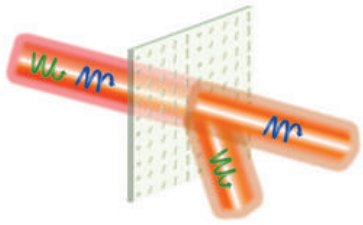


Figure 2: A Rochon-prism-like planar CPBS that only deflects the RCP light.

3. Conclusions

We have demonstrated dielectric metasurface color holograms with polarization-controlled tunable colors by integrating space, polarization and wavelength multiplexings. With the PB phase to manipulate the wavefronts of two wavelengths, high quality color holograms are successfully reconstructed and their colors can be changed entirely or in specific parts of the image by varying the polarization of the incident beams. Furthermore, this approach is extended to the full color tuning for three primary colors and multiple images by multiplexing three kinds of Si nanoblocks to form a meta-molecule. The combination of the color holograms and the holographic multiplexing for dielectric metasurfaces not only provides an effective way to continually tune the color of holographic images but increases the information capacity at multi-wavelengths, which renders dielectric metasurfaces very promising in both holographic display industry and information processing. In addition, we have designed and fabricated the Rochon-prism-like planar CPBSs by simultaneously controlling the PB phase and the propagation phase. The RCP light undergoes space variant phase and refracts, but the LCP light experiences identical phase change and passes through undeviated. With this, we have also designed a metasurface hologram which can only be reconstructed with RCP light whereas hidden from LCP light without wavefront change. The concept of this type of device is expected to play an important role in miniaturized polarizing optical systems and information security and processing.

Acknowledgements

This work was partly supported by the following grants: The National Natural Science Foundation of China under Grant Nos. 61590933, 11474010 and 11627803; Youth Innovation Promotion Association CAS under Grant No. 2015030; CAS Key Technology Talent Program and Key Research Program of Frontier Sciences, CAS (No. QYZDB-SSW-SYS031).

References

[1] D. Lin, P. Fan, E. Hasman, and M. L. Brongersma, Dielectric gradient metasurface optical elements *Science* 345: 298-302 (2014).

[2] J.B. Mueller, N. A.Rubin, R. C Devlin, B. Groever, F. Capasso, Metasurface polarization optics: Independent phase control of arbitrary orthogonal states of polarization. *Phys. Rev. Lett*. 118: 113901 (2017).

[3] Bo Wang, Fengliang Dong, Dong Yang, Zhiwei Song, Lihua Xu, Weiguo Chu, Qihuang Gong, Yan Li, Polarization-controlled color-tunable holograms with dielectric metasurface, *Optica* 4: 1368-1371 (2017).

[4] B. Wang, F. Dong, H. Feng, D. Yang, Z. Song, L. Xu, W. Chu, Q. Gong, Y. Li. Rochon-prism-like planar circularly polarized beam splitters based on dielectric metasurfaces, *ACS Photonics*, DOI: 10.1021/acsphotonics.7b01191 (2018).

Advances in Shaping Light Using Photonic Metasurfaces

(Invited Talk)

Jian Wang

Wuhan National Laboratory for Optoelectronics, School of Optical and Electronic Information, Huazhong University of Science and Technology, Wuhan 430074, Hubei, China
*Corresponding author, E-mail: jwang@hust.edu.cn

Abstract

In the past few years, photonic metasurfaces (meta-structures) and structured light have both attracted increasing interest in many emerging applications. Here, we will talk about very recent advances in flexible structured light manipulation using photonic metasurfaces. Shaping light with plasmonic and dielectric metasurfaces on a diversity of platforms such as metal film, silica, silicon and fiber will be presented. Future challenges and perspectives will be also discussed in the end.

Brief Summary

Shaping the spatial structure of lightwaves enables the flexible manipulation of various special light beams, such as Hermite-Gaussian/Laguerre-Gaussian/Bessel beams, twisted light beams with helical phasefront carrying orbital angular momentum (OAM), and radially/azimuthally polarized vector beams. These special light beams are also known as structured light, tailored light, shaped light, sculpted light or custom light. Structured light with spatially variant amplitude/phase/polarization has given rise to many developments in optical manipulation, microscopy, imaging, metrology, sensing, quantum information processing and optical communications [1-10].

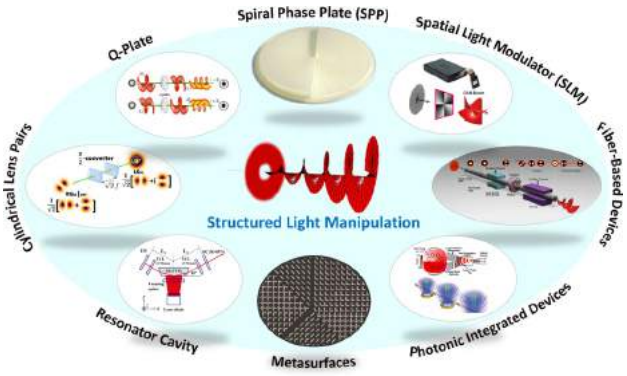


Figure 1: A brief summary of flexible structured light manipulation by different schemes.

As summarized in Fig. 1, many schemes have been demonstrated for flexible structured light manipulation, such as laser in resonator cavity, cylindrical lens pairs as mode converter, Q-plate, spiral phase plate, spatial light modulator (SLM), fiber-based devices and photonic integrated devices. Very recently, metasurfaces provide an alternative approach to flexibly manipulate the structured light [11-15].

Metasurfaces, the 2D equivalent of metamaterials, are periodic arrays of sub-wavelength engineered structures with each unit cell tailoring a local amplitude/phase/polarization, resulting in structured light manipulation over a sub-wavelength thickness.

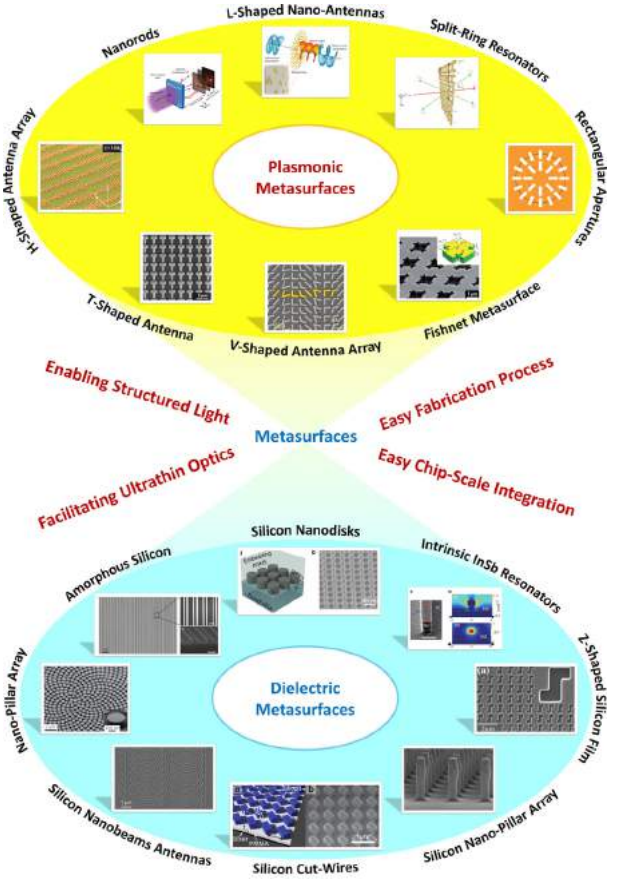


Figure 2: Advances of metasurfaces and a brief summary of different approaches of plasmonic and dielectric metasurfaces.

As summarized in Fig. 3, metasurfaces feature several distinct advances, e.g. enabling structured light manipulation, facilitating ultrathin (sub-wavelength scale) optics applications, easy fabrication process compared to 3D metamaterials, and easy chip-scale integration with nanophotonic devices. Most of the metasurfaces can be divided into two categories by the material type of unit cell, i.e. plasmonic metasurfaces relying on plasmon resonances and dielectric metasurfaces based on electric/magnetic dipole (Mie resonances). Typical examples of plasmonic metasurfaces include the use of V-shaped antenna array to generate OAM-carrying twisted light, T-shaped antenna for broadband polarization conversion, H-shaped antenna array as a bridge linking propagating waves and surface waves, nanorods for 3D optical holography, L-shaped nano-antennas to generate OAM at visible wavelengths, split-ring resonator for controlling light by nonlinearity, rectangular apertures to generate twisted vector field, and fishnet structures for tailoring dispersion. Typical examples dielectric metasurfaces include the use of silicon cut-wires for linear polarization conversion and optical vortex generation, silicon nanobeams antennas to generate Bessel beams, nano-pillar array for enhanced omnidirectional light extraction, amorphous silicon for high angle steering at visible wavelengths, silicon nanodisks to achieve full phase control with high transmission, intrinsic InSb resonators on heavily n-doped InSb films to construct reconfigurable optical antenna, Z-shaped silicon film to enable circular dichroism waveplate, and silicon nano-pillar array to realize micro-lenses. Plasmonic and dielectric metasurfaces have seen wide emerging applications in flat optics, such as anomalous reflection/refraction, holography, filtering, wave plates, lens, polarimetry, and optical vortex generation with impressive performance.

In this invited talk, we will show some of our recent research works in shaping light using various photonic metasurfaces on different platforms (metal film, silica, silicon, fiber) [16]. Structured light manipulation based on plasmonic metasurfaces, reflection-enhanced plasmonic metasurfaces, metasurfaces on fiber facet, dielectric metasurfaces, and sub-wavelength structures on silicon will be compresensively introduced [17-19]. Finally, we will also discuss the future challenges and perspectives of shaping light using photonic metasurfaces (from static to dyanic, from passive to active).

Acknowledgements

This work was supported by the National Natural Science Foundation of China (NSFC) (11574001, 11774116, 61761130082, 11274131), the National Basic Research Program of China (973 Program) (2014CB340004), the Royal Society-Newton Advanced Fellowship, the National Program for Support of Top-notch Young Professionals, and the Program for HUST Academic Frontier Youth Team.

References

[1] H. Rubinsztein-Dunlop et al. “Roadmap on structured light,” *J. Opt.* 19, 013001 (2016).

[2] R. Won, “Structured light spiralling up,” *Nature Photon.* 11, 613 (2017).

[3] S. Franke-Arnold, L. Allen, and M. Padgett, “Advances in optical angular momentum,” *Laser Photon. Rev.* 2, 299 (2008).

[4] Q. Zhang, “Cylindrical vector beams from mathematical concepts to applications,” *Adv. Opt. Photon.* 1, 1 (2009).

[5] A. Yao and M. J. Padgett, “Orbital angular momentum: origins, behavior and applications,” *Adv. Opt. Photon.* 3, 161 (2011).

[6] J. Geng, “Structured-light 3D surface imaging: a tutorial,” *Adv. Opt. Photon.* 3, 128 (2011).

[7] A. E. Willner, H. Huang, Y. Yan, Y. Ren, N. Ahmed, G. Xie, C. Bao, L. Li, Y. Cao, Z. Zhao, Jian Wang, M. P. J. Lavery, M. Tur, S. Ramachandran, A. F. Molisch, N. Ashrafi, and S. Ashrafi, “Optical communications using orbital angular momentum beams,” *Adv. Opt. Photon.* 7, 66 (2015).

[8] J. Wang, “Advances in communications using optical vortices,” *Photon. Res.* 4, B14 (2016).

[9] M. J. Padgett, “Orbital angular momentum 25 years on,” *Opt. Express* 25, 11265 (2017).

[10] J. Wang, “Data information transfer using complex optical fields: a review and perspective,” *Chin. Opt. Lett.* 15, 030005 (2017).

[11] N. Yu, P. Genevet, M. A. Kats, F. Aieta, J. P. Tetienne, F. Capasso, and Z. Gaburro, “Light propagation with phase discontinuities: generalized laws of reflection and refraction,” *Science* 334, 333 (2011).

[12] N. I. Zheludev, “A roadmap for metamaterials,” *Opt. Photon. News* 22, 30 (2011).

[13] N. Meinzer, W. L. Barnes, and I. R. Hooper, “Plasmonic meta-atoms and metasurfaces,” *Nature Photon.* 8, 889 (2014).

[14] S. Jahani and Z. Jacob, “All-dielectric metamaterials,” *Nature Nanotech.* 11, 23 (2016).

[15] A. M. Urbas et al., “Roadmap on optical metamaterials,” *J. Opt.* 18, 093005 (2016).

[16] J. Wang, “Metasurfaces enabling structured light manipulation: advances and perspectives,” accepted to be published on *Chin. Opt. Lett.*, 2018.

[17] Z. Zhao, J. Wang, S. Li, and A. E. Willner, “Metamaterials-based broadband generation of orbital angular momentum carrying vector beams,” *Opt. Lett.* 38, 932 (2013).

[18] J. Du and J. Wang, “Design of on-chip N-fold orbital angular momentum multicasting using V-shaped antenna array,” *Sci. Rep.* 5, 9662 (2015).

[19] J. Du and J. Wang, “Chip-scale optical vortex lattice generator on silicon platform,” *Opt. Lett.* 42, 5054 (2017).

Flexibly Tunable Valley Polarized Exciton-Plasmon Polaritons in 2-dimensional Semiconductors

Boyang Ding[1], Zhepeng Zhang[2], Yu-Hui Chen[1], Yanfeng Zhang[2], Richard J. Blaikie[1], and Min Qiu[3]

[1]MacDiarmid Institute for Advanced Materials and Nanotechnology, Dodd-Walls Centre for Photonic and Quantum Technologies, Department of Physics, University of Otago, PO Box 56, Dunedin 9016, New Zealand
[2]Department of Materials Science and Engineering, College of Engineering, Center for Nanochemistry (CNC), College of Chemistry and Molecular Engineering, Academy for Advanced Interdisciplinary Studies, Peking University, Beijing 100871, People's Republic of China
[3]State Key Laboratory of Modern Optical Instrumentation, Department of Optical Engineering, Zhejiang University, Hangzhou 310027, China
*corresponding author, E-mail: boyang.ding@otago.ac.nz

Abstract

We report the room temperature valley-polarized photoluminescence from a WS_2 monolayer that is deposited on a self-assembled plasmonic crystal. More importantly we find that the degree of valley-polarization is highly dependent on excitation angles of the pump beam. This flexibly tunable valley polarization is possibly due to the angle-dependent dispersive properties of polaritons as the result of strong coupling between excitons in WS_2 monolayers and lattice plasmon modes in plasmonic crystals.

1. Introduction

2-dimensional (2D) transition metal dichalcogenide (TMD), such as MoS_2 and WS_2 monolayers, are atomically thin semiconductors that have been viewed as a promising material system for optoelectronic devices. Together with the absence of inversion symmetry, the 2D TMDs' direct band gap at both K and K' valleys of the Brillouin zone lead to the emission of polarized photoluminescence (PL) after excitation with circularly polarized light.[1–3] This property provides the initialization and readout of so-called valley-polarization, opening up possibilities for electronics and computation based on the valley degree of freedom.

The valley-polarized PL is pronounced at cryogenic temperature but almost unobservable at room temperature. Various methods, such as electrical tuning, mechanical tuning and magnetic tuning, have been attempted to overcome such temperature dependence. Recently two groups have discovered that the valley-polarized PL can be observed at room temperature if the 2D TMDs are strongly coupled with an optical micro-cavity[4,5].

Here we report that a WS_2 monolayer that is strongly coupled with a self-assembled plasmonic crystal also shows the valley-polarized photoluminescence emission at room temperature. In addition, the valley-polarization degree can be flexibly tuned by adjusting the excitation angle of the pump beam. To the best of our knowledge, we are the first to report this excitation angle dependent valley-polarized PL in 2-dimensional TMD semiconductors.

2. Experimental

A hexagonally packed monolayer of silica spheres was deposited on a quartz substrate using self-assembly technique, followed by being evaporated with a 40 nm thick silver film. The metal film acquires the shape of caps on top of the spheres as shown in Figure 1a, forming a 2D periodic array of semishells with a hexagonal lattice, i.e. a plasmonic crystal (PC) structure. The chemical vapor deposition grown WS_2 monolayer was transferred onto the PC surface by using the polymethyl methacrylate nano-transfer method.

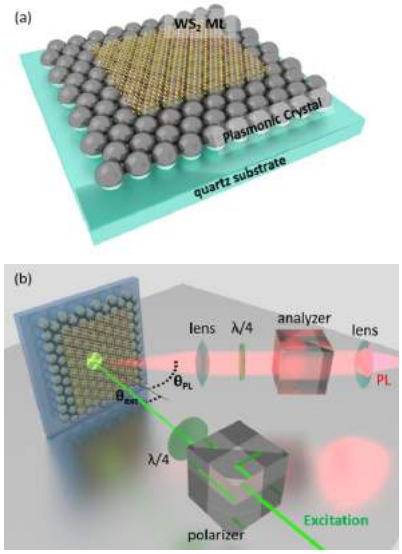


Figure 1: (a) schematic of plasmonic crystals (PC) coated with WS_2 monolayer; (b) schematic of angle-resolved photoluminescence (PL) measurement pumped by circularly polarized laser excitation.

As shown in Figure 1(b), a λ/4 waveplate (QWP) together with a linear polarizer (LP) are used to convert the continuous-wave laser (532 nm) to a circularly polarized beam. Under the polarized illumination, photoluminescence of WS_2 is excited and then collected by lenses. The PL helicity σ+ refers to the same circular polarization as the excitation beam while σ- refers to the different circular polarization as the excitation beam, which are resolved with the QWP-LP analyzer in the PL collecting optics. Both the excitation angle (θ_{exc}) and the PL angle (θ_{PL}) can be flexibly tuned. All measurements were undertaken at room temperature ($\boldsymbol{T}$ = 300 K).

3. Discussion

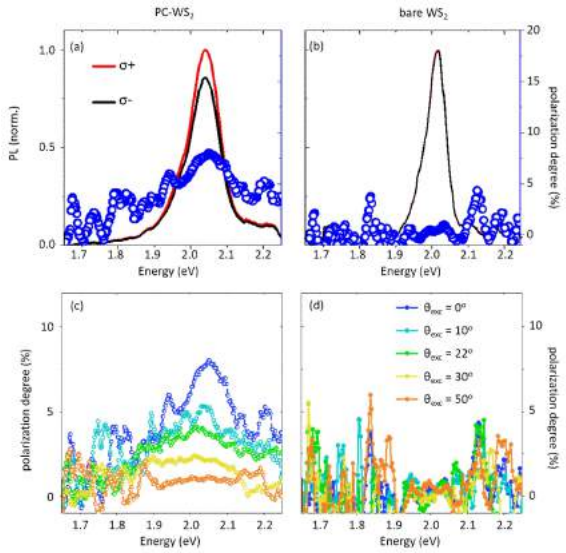


Figure 2: PL spectra at θ_{exc} = 0° and θ_{PL} = 20° with different helicity: σ+ (red line) and σ- (black line) and polarization degree (blue circles) for the (a) PC-WS_2 and (b) bare WS_2. Polarization degree for the (c) PC-WS_2 and (d) bare WS_2 samples under different θ_{exc}.

As shown in Figure 2(a), when the PC-WS_2 sample is excited at θ_{exc} = 0°, the σ+ PL (red curve) collected at θ_{PL} = 20° acquires higher intensity than the σ- polarized PL (black curve). This is a typical valley-polarized PL feature of WS_2 monolayer, i.e. the PL signal is preferably larger to σ+ polarized excitation. In contrast, the PL signal (Figure 2b) of the bare WS_2 monolayer shows almost no difference between σ+ and σ- polarized PL. To quantify this difference, the polarization $\boldsymbol{P}$ of PL is defined as：

$$P = \frac{I_{\sigma+} - I_{\sigma-}}{I_{\sigma+} + I_{\sigma-}} \qquad (1)$$

where $I_{\sigma+}$ and $I_{\sigma-}$ refer to the helicity resolved PL intensity.

The polarization spectrum (blue circles in Figure 2a) for the PC-WS_2 peaks at E = 2.06 eV with a maximum value of $\boldsymbol{P}$ = 8.5%, while the bare WS_2 sample shows ~0 polarization degree within the main PL spectral range, indicating that the PL of PC-WS_2 shows valley-polarized properties at room temperature.

More interestingly, the valley-polarized PL of PC-WS_2 sample can be flexibly adjusted by changing the excitation angle θ_{exc}. For example, as demonstrated in Figure 2c, increasing θ_{exc} of the excitation beam for the PC-WS_2 sample results in a significant reduction of the polarization degree. When θ_{exc} = 50°, the polarization degree approaches to zero. On the other hand, the polarization spectra for the bare WS_2 sample remain almost unchanged at $\boldsymbol{P} \approx 0\%$ irrespective of the excitation angles (Figure 2d).

According to previous reports[4,5] and our transmission /reflection measurements for PC-WS_2 and WS_2 samples (not shown here), the valley-polarized PL in PC supported 2D semiconductors is induced by the strong coupling between lattice plasmon modes in the plasmonic crystal and exciton A in the WS_2 monolayer. With coupling strength of ~160 meV, this exciton-plasmon coupling forms half-light half-matter polaritons in the PC-WS_2 sample, preserving the valley polarization at room temperature.

The excitation angle sensitivity of the valley polarization in PC-WS_2 samples is still unclear. One possible reason could be the highly angle-dependent dispersive properties of the exciton-plasmon polaritons, which are inherited from the lattice plasmon modes. Specifically, at low excitation angles, the pump energy (2.33 eV or 532 nm) overlaps with the highest polariton state, which may facilitate the formation of excitons at higher energy levels, preserving the valley-polarization of PL. While at high θ_{exc}, the pump energy runs far away from the polariton branch, the pumped excitons quickly scatter into the lowest exciton-plasmon polariton state, resulting in the reduction of PL valley polarization.

4. Conclusions

Valley-polarized PL from 2D TMDs that are strongly coupled with a plasmonic crystal have been observed. In addition, the PL valley-polarization is highly dependent on the excitation angle, which has been attributed to the highly dispersive properties of the exciton-plasmon ploaritons.

References

1. Zeng, H., Dai, J., Yao, W., Xiao, D. & Cui, X. Valley polarization in MoS 2 monolayers by optical pumping. *Nat. Nanotechnol.* **7,** 490–493 (2012).
2. Cao, T. *et al*. Valley-selective circular dichroism of monolayer molybdenum disulphide. *Nat. Commun.* **3,** 885–887 (2012).
3. Mak, K. F., He, K., Shan, J. & Heinz, T. F. Control of valley polarization in monolayer MoS2by optical helicity. *Nat. Nanotechnol.* **7,** 494–498 (2012).
4. Dufferwiel, S. *et al*. Valley addressable exciton-polaritons in atomically thin semiconductors. *Nat. Photonics* **11,** 497–501 (2017).
5. Chen, Y.-J., Cain, J. D., Stanev, T. K., Dravid, V. P. & Stern, N. P. Valley-Polarized Exciton-Polaritons in a Monolayer Semiconductor. *Nat. Photonics* **11,** 1–6 (2017).

3D Printing for Photonics, Metamaterials, and Energy Applications

Three-Dimensional Photonic Devices Functionalized With CdS Quantum Dots

Ioanna Sakellari[1], Elmina Kabouraki[1], Dimitris Karanikolopoulos[1], Sotiris Droulias[1], David Gray[1], Panagiotis Loukakos[1], Maria Vamvakaki[1], and Maria Farsari[1]

[1]Institute of Electronic Structure and Laser, Foundation for Research and Technology, Heraklion, Greece
*corresponding author, E-mail: isakel@iesl.forth.gr

Abstract

The fabrication of three-dimensional high-resolution woodpile photonic crystals containing an organic-inorganic silicon-zirconium composite and cadmium sulfide (CdS) quantum dots is presented. The structures are fabricated by combining direct laser writing by two-photon absorption and in-situ synthesis of CdS nanoparticles onto the photonic matrix. The novel composite material exhibits a high nonlinear refractive index measured by means of Z-scan method. Woodpile structures with inlayer periodicity down to 500nm show clear photonic stop-bands in the Vis-NIR wavelength region.

1. Introduction

Design of stimulus-responsive materials for dynamic tuning of photonic properties has been the subject of intense research in the last decade because of possible applications for all optical switching devices in active photonic integrated circuits. A significant modification of light-matter interactions can be achieved, for example, by the incorporation of quantum dot (QD) semiconductor nanocrystals in a photonic polymer matrix, since the energy of band-to-band transitions in semiconductor nanoparticles (NPs) embedded can overlap with the photonic band-gap region. Several efforts have been made up to date for the fabrication of 3D photonic devices using multiphoton lithography containing non-linear chromophores [1], metallic nanoparticles [2], as well as, QDs [5]. Usually, QDs are combined either with pure organic materials that suffer structuring efficiency due to shrinkage or NPs are dispersed in commercially available photoresists that provide no proof of washing off during the development process. In this work, we combine 3D direct laser writing (DLW) by two-photon absorption and in-situ synthesis of CdS NPs in order to fabricate high resolution 3D woodpile photonic devices exhibiting high $\chi^{(3)}$ nonlinearity.

2. Materials

The materials employed in the present research are photo-structurable organic-inorganic hybrid materials synthesized using the sol-gel process. This versatile technique has been exploited for the incorporation of inorganic networks into polymer matrices using as monomers molecules that carry an inorganic part, which serves as the precursor to the inorganic network, and a polymerizable organic group, which acts as the precursor to the organic polymer. The sol-gel technique is a simple and cost effective process for the synthesis of the photosensitive materials giving the advantage of altering the materials properties by manipulating the enormous variety of precursor molecules that are applicable for this technique. The precursors used in the present work are depicted in Figure 1.

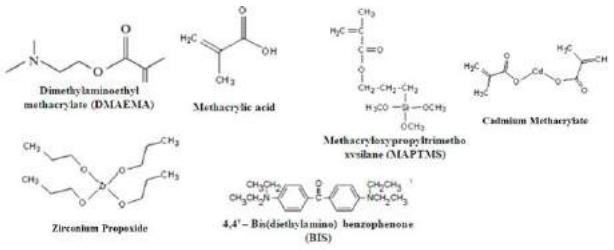


Figure 1: Precursor molecules used for the synthesis of the hybrid inorganic-organic composite material.

3. Discussion

In 2012, a new route for resolution improvement in direct laser written structures was presented by exploiting the diffusion of a mobile quenching molecule in the scanned area [3]. The material employed for the preparation of the photonic templates is an organic-inorganic zirconium-silicon composite doped with the quencher 2-(dimethylamino) ethyl methacrylate. The quencher proposed is also a photo-polymerizable monomer that increases the resolution without compromising the mechanical stability of the structures as it can freely diffuse in the scanned area, while becomes part of the polymer backbone only upon irradiation. By employing diffusion-assisted DLW, woodpile photonic crystals with inlayer periodicity as low as 400nm were successfully fabricated.
In the present work, the combination of diffusion-assisted DLW and in-situ synthesis of CdS NPs has enabled the fabrication of active woodpile photonic devices with varying inlayer periodicity from 600nm to 500nm. In Figure

2, a woodpile photonic crystal with 500nm inlayer periodicity is depicted.

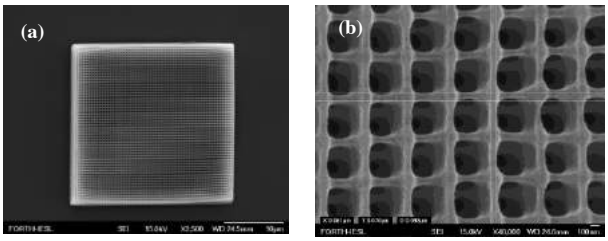


Figure 2: A woodpile photonic structure with 500nm inlayer periodicity: a) top view, b) top view at higher magnification.

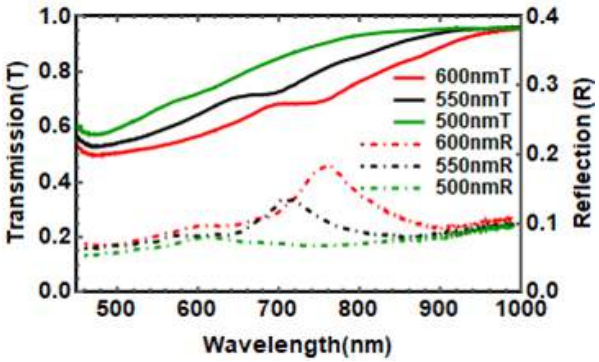


Figure 3: Transmission (solid line) and reflection (dashed-dot line) spectra of photonic crystal structures with varying inlayer periodicity from 600nm to 500nm fabricated using the material containing the diffusive quenchers.

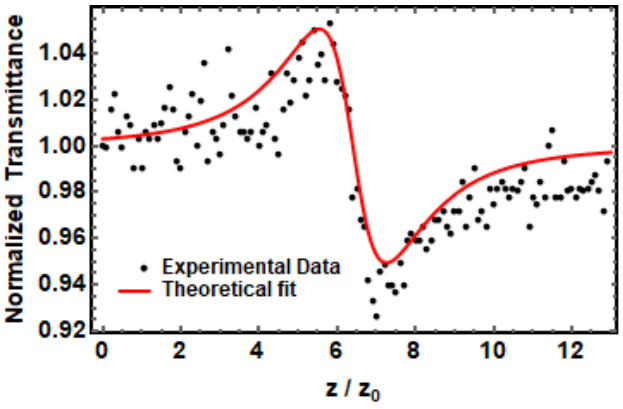


Figure 4: Z-scan measurement of the quantum dot containing material.

By means of FTIR spectroscopy, the optical properties of the fabricated photonic devices are measured demonstrating clear photonic stop bands in the Vis-NIR region as shown in Figure 3. In particular, the central wavelength of the first order stop band for the woodpile structures with 600nm, 550nm and 500nm inlayer periodicity is located at 760nm, 710nm and 620nm respectively. In situ synthesis of CdS on the polymer matrix takes place via sodium sulphide treatment. The incorporation of CdS NPs is confirmed by XRD measurements performed in a thin film of the QD containing material, while EDX measurements taken from the functionalized woodpile structures reveal the cadmium and sulfur elements. This novel composite material exhibits a high nonlinear refractive index value of $n_2 = 185.7 \times 10^{-15}$ (cm^2/W) measured by means of Z-scan method [4]. The corresponding Z-scan measurements performed in a thin film of the QD containing material are shown in Figure 4. Similar large nonlinearities have been previously reported in analogous experiments involving QD doped nanocomposites [5].

4. Conclusions

3D high-resolution woodpile photonic devices are successfully fabricated containing an organic-inorganic silicon-zirconium composite and CdS QDs. The structures are fabricated by the combination of diffusion-assisted 3D DLW by two-photon absorption and in-situ synthesis of CdS NPs. The novel composite material exhibits a high nonlinear refractive index value measured by means of Z-scan method. The fabricated woodpile structures show clear photonic stop bands in the ViS-NIR wavelength region.

Acknowledgements

The research leading to these results has received funding from LASERLAB-EUROPE (grant agreement no. 654148, European Union's Horizon 2020 research and innovation programme). I.S. thanks Stavros Niarchos Foundation for financial support.

References

[1] M. Farsari, A. Ovsianikov, M. Vamvakaki, I. Sakellari, D. Gray, B. N. Chichkov, and C. Fotakis, Fabrication of three-dimensional photonic crystal structures containing an active nonlinear optical chromophore, *Appl Phys A* 93: 11-15, 2008.

[2] X. M. Duan, H. B. Sun, K. Kaneko, and S. Kawata, Two-photon polymerization of metal ions doped acrylate monomers and oligomers for three-dimensional structure fabrication, *Thin Solid Films* 453: 518-521, 2004.

[3] I. Sakellari, E. Kabouraki, D. Gray, V. Purlys, C. Fotakis, A. Pikulin, N. Bityurin, M. Vamvakaki, and M. Farsari, Diffusion-assisted high-resolution direct femtosecond laser writing, *ACS Nano* 6: 2302-2311, 2012.

[4] M. Sheik-Bahae, A. A. Said, T. H. Wei, D. J. Hagan, and E. W. Van Stryland, Sensitive Measurement of Optical Nonlinearities Using a Single Beam, *IEEE J Quantum Electron* 26: 760–769, 1990.

[5] B. Jia, D. Buso, J. Embden, J. Li, and M. Gu, Highly Non-Linear Quantum Dot Doped Nanocomposites for Functional Three-Dimensional Structures Generated by Two-Photon Polymerization, *Adv Mater* 22: 2463-2467, 2010

Nonlinear Metasurfaces and Plasmonics

Second harmonic generation enhancement by Mie resonances in individual barium titanate nanoparticles

Churong Ma[1*], Jiahao Yan[1], Yingcong Huang[1], Guowei Yang[1]

[1]School of Materials Science and Engineering, Sun Yat-Sen University, Guangzhou, China
*corresponding author, E-mail: machr@mail2.sysu.edu.cn

Abstract

All-dielectric materials (ADMs) offer new ways to generate nonlinear optical (NLO) behavior at subwavelength scales. Herein, we report enhancement in the tunable second harmonic generation (SHG) reflected from individual mid-refractive ADM nanoparticles, $BaTiO_3$ nanoparticles (BTO NPs). Multipole decomposition, as observed in the linear spectra, demonstrated that the SHG enhancement originated from an overlap between the magnetic dipole or quadrupole resonance and the SH wavelength of the pump source.

1. Introduction

Nonlinear optics have been greatly developed and applied in the past half-century after the discovery of laser. Nanostructures including photonic crystals, plasmonic materials, and metamaterials have been studied in optical non-linearity. Metal plasmonic nanostructures can exhibit strong electric field enhancements but they suffer from confined volumes, high optical losses and high price[1].

ADMs are emerging as a promising alternative to plasmonic nanostructures for nanophotonic applications[2]. They exhibit strong interactions with light due to excitation of the Mie-type resonances. Compared to the electric mode appears in plasmonics, the magnetic Mie mode of the same order appears in ADM has a larger mode volume, which renders much higher overall NLO conversion efficiency. As a mid-refractive ADM, BTO has excellent properties, such as piezoelectric and photorefractive effects, and it has been widely used in capacitors, electromechanical transducers, and switches. In addition, BTO with a tetragonal structure possesses effective second-order nonlinear coefficients, which makes it promising in vivo imaging in biomedicine.

In this study[3], we reported the linear and nonlinear optical processes of BTO NPs, ranging from 100 to 300 nm in diameter, and revealed the relationship between them. We measured the SHG response and linear scattering spectra of individual BTO NPs with various sizes. Multipole decomposition observed in the scattering spectra indicates that the magnetic dipole and quadrupole resonances have a great influence on the SHG process. When the SH wavelength of the pump matches that of the magnetic dipole or quadrupole resonance, the SHG response is significantly enhanced. Moreover, the SHG responses of the BTO NPs display broad spectral tunability.

2. Results and Discussion

The typical morphology and structural characterization of the BTO NPs prepared using LAL are shown in Fig. 1. It suggests that the BTO NPs are spherical and have a tetragonal structure.

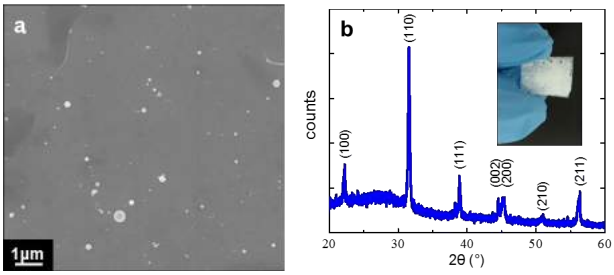


Figure 1: The typical morphology and structure characterization results obtained for the BTO NPs prepared using laser ablation in liquid (LAL). (a) The SEM image. (b) The XRD pattern. The inset is an image of the BTO NPs (white powders) dispersed on an ITO substrate.

We measured the SHG response and linear scattering spectra of individual BTO NPs with various sizes. In the NLO measurements, two BTO NPs (d = 151.0 and 224.9 nm) were subjected to fs pulses from a Ti:sapphire fs laser and what we detected were the reflected signals. At an average pump power of 15 mW, the tunable SHG spectra of these two BTO NPs are shown in Fig. 2(a) and 2(b), respectively.

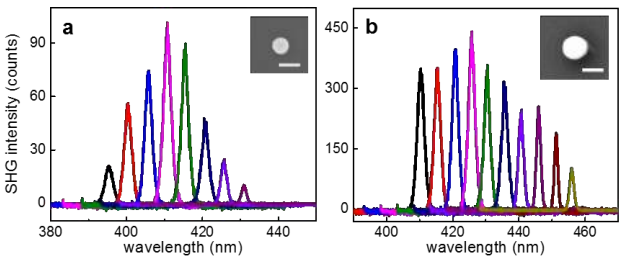


Figure 2: Tunable SHG spectrum of the individual BTO NPs. (a) d = 151.0 nm. (b) d = 224.9 nm. Scale bar, 200 nm.

3. Discussion

It has been proven that NLO processes are associated with linear spectra. Our linear scattering experiments and finite difference time-domain (FDTD) simulations provide evidence for this opinion. The total scattering spectra of an individual BTO NPs and the contributions from the electric and magnetic dipole and quadrupole resonances are shown in Fig. 3. For a BTO NP (d = 151.0 nm), the peak around 415 nm was dominated by the MD resonance while EQ and MQ were so small they could be disregarded. For another BTO NP (d = 224.9 nm), MQ resonance around 431 nm plays an important role in its scattering spectrum. Combining the tunable SHG responses (Fig. 2) with linear spectra (Fig. 3), a conclusion was drawn that the SHG response enhanced in the vicinity of the magnetic resonances, including the MD and MQ resonances. In fact, at the resonant regions, the electric field can be strongly enhanced, which directly results in the SHG enhancements.

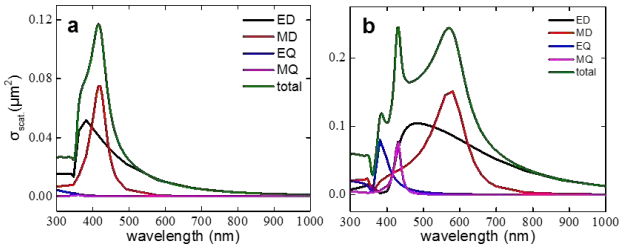


Figure 3: The contributions of the electric dipole (ED), magnetic dipole (MD), electric quadrupole (EQ), and magnetic quadrupole (MQ) to the scattering cross-section in an individual BTO NP with a diameter of (a) 151.0 nm and (b) 224.9 nm.

4. Conclusions

In summary, we demonstrated the enhanced SHG response pumped by the fs laser pulses in individual BTO NPs fabricated using fs LAL. The relationship between the linear scattering spectra and NLO response showed that the magnetic resonances, including MD and MQ resonances, drive the SHG enhancement.

Acknowledgements

The National Basic Research Program of China (2014CB931700), National Natural Science Foundation of China (91233203), Natural Science Foundation of Guangdong Province (2016A030313339), and State Key Laboratory of Optoelectronic Materials and Technologies supported this work.

References

[1] M. Kauranen, A. V. Zayats, Nonlinear plasmonics, *Nat. Photonics* 6: 737-748, 2012.

[2] S. Jahani, Z. Jacob, All-dielectric metamaterials, *Nat. Nanotechnol*. 11: 23-36, 2016.

[3] C. R. Ma, J. H. Yan, Y. M. Wei, P, Liu, G. W. Yang, Enhanced second harmonic generation in individual barium titanate nanoparticles driven by Mie resonances, *J. Mater. Chem. C* 5: 4810-4819, 2017.

Broadband Achromatic Optical Metasurface Devices

Shuming Wang[1,5*†], Pin Chieh Wu[2,3*], Vin-Cent Su[4*], Yi-Chieh Lai[6], Cheng Hung Chu[2], Jia-Wern Chen[3], Shen-Hung Lu[4], Ji Chen[1,5], Beibei Xu[1,5], Chieh-Hsiung Kuan[4], Tao Li[1,5†], Shining Zhu[1,5†], and Din Ping Tsai[2,3†]

[1]*National Laboratory of Solid State Microstructures, School of Physics, College of Engineering and Applied Sciences, Nanjing University, Nanjing, 210093, China*
[2]*Research Center for Applied Sciences, Academia Sinica, Taipei 11529, Taiwan*
[3]*Department of Physics, National Taiwan University, Taipei 10617, Taiwan*
[4]*Department of Electrical Engineering and Graduate Institute of Electronics Engineering, National Taiwan University, Taipei 10617, Taiwan*
[5]*Collaborative Innovation Center of Advanced Microstructures, Nanjing 210093, China*
[6]*Department of Photonics and Advanced Optoelectronic Technology Center, National Cheng Kung University, Tainan 70101, Taiwan*
*These authors contributed equally to this work.
†Corresponding authors: wangshuming@nju.edu.cn; taoli@nju.edu.cn; zhusn@nju.edu.cn; dptsai@phys.ntu.edu.tw

Abstract

Flat optics enables the miniaturization of optical systems that is highly desired in photonic applications. Among various flat optical devices, metasurfaces have presented their great ability in efficient manipulation of light fields and have been proposed for variety of devices with specific functionalities. However, due to the high phase dispersion of their building blocks, metasurfaces significantly suffer from large chromatic aberration, which greatly limits their applications. Here, for the first time, we design achromatic metasurface devices which successfully eliminate the chromatic aberration over a continuous wavelength region from 1200 nm to 1680 nm (~33.3% of the central wavelength) in a reflection scheme. The required phase compensation is achieved through exploiting the specially designed integrated-resonant unit elements. For the proof-of-concept, we demonstrate broadband achromatic metalenses that are capable of focusing light with arbitrary wavelength at the same focal plane. A broadband achromatic gradient metasurface is also implemented, which is able to deflect wide-band light by the same angle. Through this approach, various flat achromatic devices that are previously impossible can be realized, which will greatly innovate the flat photonic components and systems to the full-color detection and imaging.

Nonlinear Spin-Orbital Angular Momentum Interaction in Plasmonic Nanostructures

Xiaoyan Y. Z. Xiong[1], Li-Jun Jiang[1*], Wei E. I. Sha[2], Ahmed Al-Jarro[3], Nicolae C. Panoiu[3], and Weng Cho Chew[1,4,5]

[1]Dept. of Electrical and Electronic Engineering, The University of Hong Kong, Hong Kong
[2]College of Information Science and Electronic Engineering, Zhejiang University, Hangzhou 310027, China
[3]Dept. of Electronic and Electrical Engineering, University College London, Torrington Place, London WC1E 7JE, United Kingdom
[4]Dept. of Electrical and Computer Engineering, University of Illinois at Urbana-Champaign, Urbana, IL 61801 USA
[5]School of Electrical and Computer Engineering, Purdue University, West Lafayette, IN 47907, USA
*corresponding author, E-mail: jianglj@hku.hk

Abstract

Second-harmonic generation in plasmonic nanostructures has attracted significant attentions in nonlinear optics field due to unique properties of surface-sensitive and plasmon-enhancement effects. In this work, a rigorous self-consistent surface integral equation method has been developed for studying nonlinear spin-orbital angular momentum coupling induced by second-harmonic generation in plasmonic nanostructures. A general angular momenta conservation law is formulated for describing the nonlinear spin-orbital interaction process.

1. Introduction

Plasmonic nanostructures that support localized surface plasmon-polaritons (SPPs) find pervasive use in nonlinear optical devices, chiefly because plasmon-enhanced optical near-fields allow nonlinear optical processes that ordinarily are weak to be significantly enhanced [1]. The process of the second-harmonic (SH) generation (SHG) , where two photons are converted into one photon at the doubled frequency, is the most studied nonlinear process due to the relative simplicity of its experimental implementation. As an even-order nonlinear process, SHG strongly depends on the symmetry of both the material being used and the structure being studied. SHG is forbidden in the bulk of centrosymmetric media within the electric dipole approximation. However, the breaking of inversion symmetry at their surfaces results in the generation of SH waves [2]. Unique combination of surface-sensitive SHG and strong field enhancement in plasmonic nanostructures has opened up new possibilities in ultrasensitive shape characterization, nonlinear plasmonic sensing, biomedicine, and nanotechnology applications [3, 4].

As a parametric nonlinear process, SHG is governed by fundamental conservation laws including charge, energy, angular momentum and parity. In this work, inspired by energy conservation, a first-principle, self-consistent surface integral equation (SIE) method, which considers the depletion of pump waves, is developed for evaluating SH radiation generated from metal nanoparticles. The mutual coupling between fundamental and second harmonic field is captured in this method. Based on this method, we present a theoretical study of the characteristics of the nonlinear spin-orbital interaction induced by SHG in plasmonic chiral nanostructures. The doubling of total optical angular momentum as well as frequency during the second-harmonic nonlinear spin orbital interaction process has been demonstrated.

2. Method

SHG can be described by the two coupled wave equations

$$\nabla^2\mathbf{E}^{(\omega)} + {k^{(\omega)}}^2\mathbf{E}^{(\omega)} = -\frac{\omega^2}{\varepsilon_0 c^2}\mathbf{P}_S^{(\omega)} - \frac{i\omega}{\varepsilon_0 c^2}\mathbf{J}_{\text{pump}}^{(\omega)} \quad (1)$$

$$\nabla^2\mathbf{E}^{(\Omega)} + {k^{(\Omega)}}^2\mathbf{E}^{(\Omega)} = -\frac{\Omega^2}{\varepsilon_0 c^2}\mathbf{P}_S^{(\Omega)} \quad (2)$$

where $\mathbf{J}_{\text{pump}}^{(\omega)}$ is a pump source. The nonlinear polarizations $\mathbf{P}_S^{(\omega)} = \varepsilon_0\overline{\overline{\chi}}_s^{(2)} : \mathbf{E}^{(\Omega)}\mathbf{E}^{(\omega)*}$ and $\mathbf{P}_S^{(\Omega)} = \varepsilon_0\overline{\overline{\chi}}_s^{(2)} : \mathbf{E}^{(\omega)}\mathbf{E}^{(\omega)}$ are the nonlinear source terms for the fundamental and SH fields ($\Omega = 2\omega$). Here, $\overline{\overline{\chi}}_s^{(2)}$ is the surface second-order susceptibility tensor and $\mathbf{E}^{(\omega)}$ and $\mathbf{E}^{(\Omega)}$ denote the fundamental and SH electric fields, respectively. $k^{(\omega)}$ and $k^{(\Omega)}$ are the corresponding wave numbers. To fully capture the cross couplings between the fundamental and SH fields, Equations (1) and (2) are solved self-consistently by a SIE method with an initial condition $\mathbf{P}_S^{(\omega)} = 0$.

By invoking the Love's equivalence principle, the field can be calculated from the equivalent currents ($\mathbf{J}_\ell^{(\nu)}$, $\mathbf{M}_\ell^{(\nu)}$) placed on the outer ($\ell = e$) and inner ($\ell = i$) sides of the surface of a nanostructure. A matrix system is then constructed by exploiting the Galerkin testing procedure [5]:

$$C^{(\nu)}x^{(\nu)} = y^{(\nu)}, \quad (3)$$

with the impedance matrix

$$C^{(\nu)} = \begin{bmatrix} \mathcal{L}_e^{(\nu)} & \mathcal{K}_e^{'(\nu)} & -\mathcal{L}_i^{(\nu)} & -\mathcal{K}_i^{'(\nu)} \\ -\mathcal{K}_e^{'(\nu)} & \eta_e^{-2}\mathcal{L}_e^{(\nu)} & \mathcal{K}_i^{'(\nu)} & -\eta_i^{-2}\mathcal{L}_i^{(\nu)} \\ \mathcal{I} & 0 & \mathcal{I} & 0 \\ 0 & \mathcal{I} & 0 & \mathcal{I} \end{bmatrix}$$

where $\overline{\mathbf{G}}^{(\nu)}(\mathbf{r},\mathbf{r}') = (\bar{\mathbf{I}} + {k^{(\nu)}}^{-2}\nabla\nabla)\exp(ik^{(\nu)}R)/4\pi R$ is the dyadic Green's function, $\nu = \omega, \Omega$ denote the fundamental and SH frequencies, respectively. Operator $\mathcal{L}_\ell^{(\nu)} = i\nu\mu_\ell\overline{\mathbf{G}}^{(\nu)}$ and operator $\mathcal{K}_\ell^{'(\nu)}$ is the principal value part of the $\mathcal{K}_\ell^{(\nu)}$ operator with $\mathcal{K}_\ell^{(\nu)} = -\nabla\times\overline{\mathbf{G}}^{(\nu)}$. The vector of unknowns $x^{(\nu)}$ and the excitation $y^{(\nu)}$ are

$$x^{(\nu)} = \begin{bmatrix} \mathbf{J}_e^{(\nu)} \\ \mathbf{M}_e^{(\nu)} \\ \mathbf{J}_i^{(\nu)} \\ \mathbf{M}_i^{(\nu)} \end{bmatrix}, \qquad y^{(\nu)} = \begin{bmatrix} \frac{1}{2}\mathbf{n}\times\mathbf{M}_0^{(\nu)} \\ -\frac{1}{2}\mathbf{n}\times\mathbf{J}_0^{(\nu)} \\ \mathbf{J}_0^{(\nu)} \\ \mathbf{M}_0^{(\nu)} \end{bmatrix}$$

By using the boundary conditions, we have

$$\begin{cases} \mathbf{J}_0^{(\nu)} = \mathbf{n}\times\mathbf{H}^{(\nu,inc)} - i\nu\mathbf{P}_{St}^{(\nu)} \\ \mathbf{M}_0^{(\nu)} = -\mathbf{n}\times\mathbf{E}^{(\nu,inc)} + \frac{1}{\epsilon'}\mathbf{n}\times\nabla_S P_{Sn}^{(\nu)} \end{cases} \tag{4}$$

Equation (3) can be used to solve both the fundamental and SH fields by setting $\nu = \omega\,, \Omega$, respectively. In this work we consider gold material and surface nonlinear susceptibility data is taken from [6].

3. Results and discussions

We study the linear and nonlinear light scattering from a chiral cluster of 10 identical nanospheres arranged in an Archimedes-like spiral configuration with N-fold rotation symmetry. The chiral cluster is irradiated by a circularly polarized Laguerre-Gaussian (LG) beam [Fig.1(a)]. For the nanostructures with N-fold rotational symmetry, the incident beam with well-defined angular momentum can only scatter into a set of modes with specific values of the total angular momentum. In order to describe how nanostructures with N-fold rotational symmetry affect the transfer of angular momentum from the incident field to the scattered field during both linear and nonlinear interaction processes, we formulate a general angular momentum conservation law.

$$j_{sca} = s(l+\sigma) + qN, \tag{5}$$

where l and σ are the orbital and spin angular momentum numbers of the incident beam, respectively, s and N denote the order of harmonic generation and rotational symmetry, q is an integer and j_{sca} is the total angular momentum. To validate this angular momentum conservation law, the total angular momentum of the scattered fundamental and SH fields are analyzed by the multipole expansion method. As presented in Fig.1(b) and (c), the predictions based on the proposed conservation law, agree well with the multipole decomposition weights.

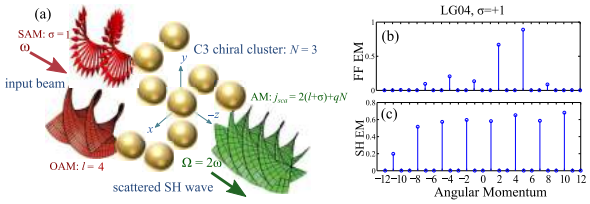


Figure 1: (a) Schematic of the spin-orbital angular momentum coupling induced by SHG in a chiral cluster with N-fold rotation symmetry. Electric multipole (EM) decompositions of the fundamental (b) and SH (c) scattered waves.

4. Conclusions

In summary, we have developed a SIE formulation for solving SH scattering generated from nanostructures. The mutual coupling between fundamental and second harmonic field is captured. We formulate a general angular momenta conservation law, including the quasi-angular-momentum of chiral nanostructures with N-fold rotational symmetry, to describe the angular momenta transfer in linear and nonlinear spin-orbital interaction processes.

Acknowledgement

This work was supported in part by the Research Grants Council of Hong Kong (GRF 17207114 and GRF 17210815), AOARD FA2386-17-1-0010, NSFC 61271158 and 61701424, and Hong Kong UGC AoE/P–04/08.

References

[1] M. Kauranen, and A. V. Zayats, Nonlinear plasmonics, *Nat. Photonics* 6, 737 (2012).

[2] J. E. Sipe, V. C. Y. So, M. Fukui, and G. I. Stegeman, Analysis of second-harmonic generation at metal surfaces, *Phys. Rev. B* **21**, 4389 (1980).

[3] J. Butet, K. Thyagarajan, and O. J. F. Martin, Ultrasensitive Optical Shape Characterization of Gold Nanoantennas Using Second Harmonic Generation, *Nano Lett.* 13, 1787 (2013).

[4] G. Bautista, M. J. Huttunen, J. Makitalo, J. M. Kontio, J. Simonen, and M. Kauranen, Second-Harmonic Generation Imaging of Metal Nano-Objects with Cylindrical Vector Beams, *Nano. Lett.* 12, 3207 (2012).

[5] A. Ern, J. L. Guermond, *Theory and Practice of Finite Elements* (Springer, New York, 2004).

[6] D. Krause, C. W. Teplin, and C. T. Rogers, Optical surface second harmonic measurements of isotropic thin-film metals: gold, silver, copper, aluminum, and tantalum, *J. Appl. Phys.* 96(7), 3626–3634 (2004).

Giant Optical Chirality in a Quasi-3D Meta-structure

Jiafang Li,* Ximin Tian, and Zhiguang Liu

Institute of Physics, Beijing National Laboratory for Condensed Matter Physics, Chinese Academy of Sciences
Beijing 100190, China
*corresponding author, Email: jiafangli@aphy.iphy.ac.cn

Abstract

Here we report the studies on two kinds of quasi-3D meta-structures with reduced fabrication complexity and enhanced interaction with the magnetic component of incident light, which result in giant optical chirality.

1. Introduction

Compared with three-dimensional (3D) optical meta-materilas that face the fabrication challenges, two-dimensional (2D) metasurfaces simplifie the fabrication requirements by employing the ultra-thin planar designs. However, the bypass of structural configuration in the third dimension resulted in the less interaction with the magnetic component of the incident light in most planar designs. As a result, some unique photonic properties related with the interaction with both electric and magnetic components of incident light, such as intrinsic optical chirality, is relatively weak or absent in the 2D designs. Here we report the studies on two kinds of quasi-3D meta-structures with reduced fabrication complexity and enhanced interaction with the magnetic component of incident light, which result in giant optical chirality.

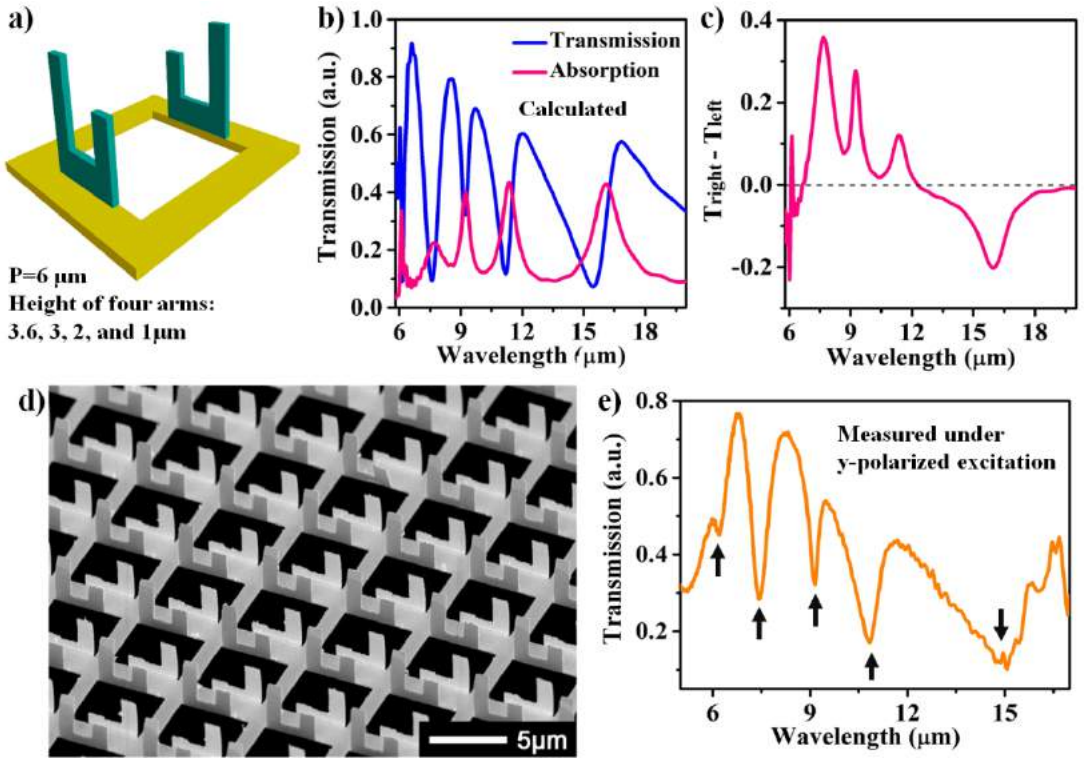


Figure 1: (a) Schematic illustration and (d) SEM image of the double split-ring resonators (DSRR) based quasi-3D meta-structures. (b) Simulated and (e) measured transmission spectra of the DSRR-based meta-structures under normal incidence with the electric field polarized along y-direction. (c) Simulated circular dichroism (T_{right} -T_{left}) of the DSRR-based meta-structures.

2. Results

The first structures we propose is a double split-ring resonators (DSRR) based quasi-3D meta-structure (Fig. 1a), in which the double SRRs standing along a planar air hole array with extraordinary optical transmission (EOT). Figure 1d shows the scanning electron microscope (SEM) image of the proposed DSRR-based structure, which was readily fabricated by employing the focused-ion-beam irradiation-induced folding technique applied in a freely suspended gold thin metal film [1-3]. Figures 1b and 1e plot the consistently calculated and measured transmission spectra under y-polarized light excitations (i.e., the incident light with the electric field polarized perpendicular to the SRR planes). One can clearly see the pronounced multiple Fano-type asymmetric resonances, which have not been achieved in such a simple configuration as far as we know. Due to the deliberately design, the unequal "arms" standing on the two sides of air hole array break the mirror and rotational symmetry. These artificially engineered asymmetric factors could inherently lead to pronounced chiroptical effects of the proposed nanostructures, as shown in Fig. 1c.

By further improving the fabrication technique, as well as the structural designs, another type of quasi-3D meta-structures with enhanced optical chirality is obtained (results not shown here), of which the operating wavelengths could be pushed to telecommunication wavelength region.

3. Conclusions

In conclusion, by employing focused-ion-beam irradiation-based techniques, we have developed two kinds of quasi-3D meta-structures with reduced fabrication complexity and enhanced interaction with the magnetic component of incident light, which result in giant optical chirality [4].

Acknowledgements

The authors thank Laboratory of Microfabrication, Institute of Physics, Chinese Academy of Sciences for assistance in FIB facilities and useful discussions.

References

[1] A. J. Cui, Z. Liu, J. F. Li, T. H. H. Shen, X. X. Xia, Z. Y. Li, Z. J. Gong, H. Q. Li, B. L. Wang, J. J. Li, H. F. Yang, W. X. Li, and C. Z. Gu, "Directly patterned substrate-free plasmonic "nanograter" structures with unusual Fano resonances," Light: Science & Applications 4, e308 (2015).

[2] Z. G. Liu, Z. Liu, J. F. Li, W. X. Li, J. J. Li, C. Z. Gu, and Z. Y. Li, "3D conductive coupling for efficient generation of prominent Fano resonances in metamaterials," Sci Rep-Uk 6, 27817 (2016).

[3] Z. G. Liu, J. F. Li, Z. Liu, W. X. Li, J. J. Li, C. Z. Gu, and Z. Y. Li, "Fano resonance Rabi splitting of surface plasmons", Sci Rep-Uk 7, 8010 (2017).

[4] J. F. Li, *et al.*, under submission.

Phase control of second harmonic generation from metasurfaces composed of complementary split ring resonators

Xin Yang[1], Zhuo Chen[1,2], and Zhenlin Wang[1,2,*]

[1] School of Physics and National Laboratory of Solid State Microstructures, Nanjing University, Nanjing 210093 China
[2]Collaborative Innovation Center of Advanced Microstructures, Nanjing University, Nanjing 210093, China
*corresponding author, E-mail: zlwang@nju.edu.cn

Abstract

We demonstrate that a complementary split-ring resonator (CSRR) is able to generate second harmonic (SH) currents that are mostly parallel to the incident polarization and asymmetric with respect to its base, and thus allowing for imposing a 180-degree-phase shift on the SH radiation by reversing the orientation of the CSRR. By simultaneously adjusting the geometrical parameters and reversing the orientation of the CSRR, we further demonstrate the realization of a continuous control over the phase change from 0 to 360 degrees for SH radiation.

1. Introduction

Recently, the concept of phased metasurfaces has been extended to the nonlinear regime to enable both coherent generation and manipulation. For example, a π phase shift can be imposed on the local second harmonic generation (SHG) nonlinearity by simply inverting the orientation of the metallic split ring resonator (SRR) [1]. For more complex beam manipulation in nonlinear processes, a continuous and spatially varying phase manipulation is highly desirable. The recent realization of the geometric Berry phase in nonlinear metasurfaces enabled a continuous control over the nonlinear phase change from 0 to 2π by simply rotating the meta-atoms with respect to the laboratory frame [2]. Although the concept of the nonlinear Berry phase provides a simple route for better manipulation of the beam profile of the nonlinear radiation, it requires circularly polarized fundamental wave (FW) and only generates circularly polarized harmonic generation.

Here, by theoretically investigating the SH response from the CSRRs-based metasurfaces excited under normal incidence at the fundamental resonance, we are able to demonstrate that the generated SH currents are mostly parallel to the incident polarization and asymmetric with respect to the base of the CSRRs. These features enable the possibility to impose the phase change of π on the SH currents and the locally generated SH radiation by mirroring the CSRR with respect to its base. Furthermore, we demonstrate that by finely adjusting the structural parameters of the CSRRs, the resultant spectral shift between the resonances in the CSRRs and the fundamental wave can introduce a local nonlinear phase with continuous tuning range exceeding π into the SHG processes for linearly polarized excitation. The nonlinear phase tuning range can be further extended to cover the entire 2π range by reversing the orientation of the CSRRs.

2. Results and Discussions

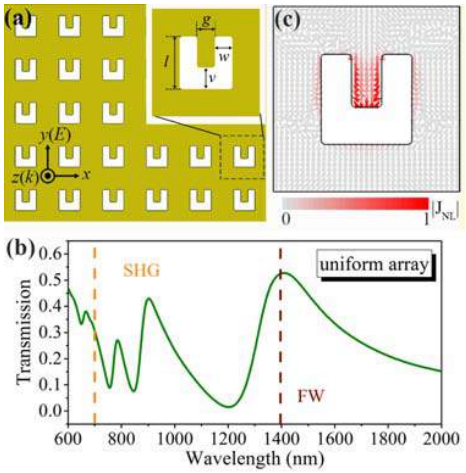


Figure 1: (a) Schematic of a uniform CSRR array. (b) Calculated normal incidence transmittance spectrum of the uniform CSRR array. The wine and orange dashed lines indicate the fundamental and SHG wavelengths, respectively. (c) Normalized SH surface currents at the top surface of the CSRR.

Figure 1(a) schematically depicts the gold CSRR element serving as the building block of the nonlinear metasurface. Each CSRR element is characterized by a set of structural parameters l (the arm length), w (the arm width), g (the width of the central metal patch) and t (the thickness of the gold film). Figure 1(b) shows the linear transmission spectrum of the CSRRs square array with the period of a = 400 nm calculated for normal incidence of light polarized along the CSRR arm. As expected, the transmittance through the CSRRs are interchanged with the reflectance of the corresponding SRRs [3], which ensures transmittance maxima at the fundamental resonance for the CSRRs rather than transmittance minima for the SRRs. In order to investigate the SHG from the CSRRs, a hydrodynamic model of the free electron dynamics [4] is employed here. The resultant SH surface currents of the CSRR excited by a

normally incident fundamental wave (λ_{FW} = 1400 nm, corresponding to the fundamental resonance) polarized along the CSRR arm are shown in Fig. 1(c), in which the SH surface currents are found to be concentrated at the surface of the central metal patch. Figure 1(c) also shows that the SH currents are mostly parallel to the polarization of the fundamental wave and more importantly are asymmetric with respect to the base of the CSRR. Therefore, a mirror inversion of the CSRR with respect to its base is able to reverse the direction of the generated SH currents, and consequently impose a π phase shift on the SH currents.

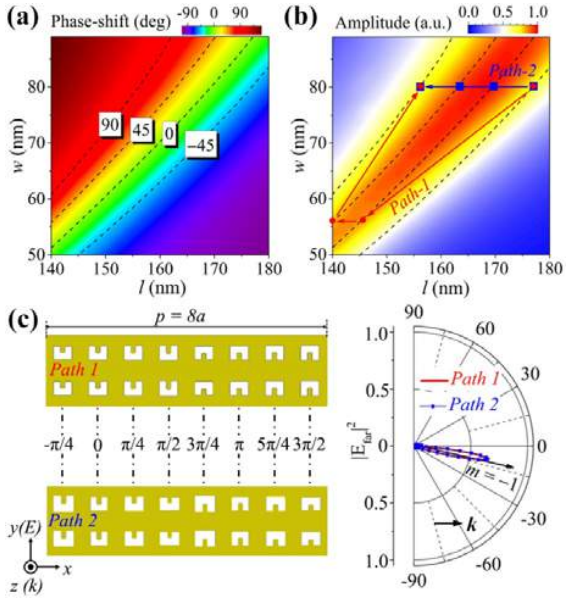


Figure 2: The maps of SHG phase shift (a) and amplitude (b) calculated at a given fundamental wavelength λ_{FW} = 1400 nm as functions of the arm length and width. (c) Left panel: schematic view of eight-resonator super-unit cells with a phase gradient of π/4. One super-unit is created from the CSRRs in the path-1, the other is from the CSRRs in the path-2. Right panel: far-field SHG intensity from the metasurfaces consisting of the super-unit cells presented in the left panel.

In the following, we demonstrate that a continuous control over the phase change from 0 to 2π could be achieved by simultaneously adjusting the geometrical parameters and reversing the orientation of the CSRR. Figures 2(a) and 2(b) show the maps of the calculated phase shift and amplitude of the SHG at a given FW wavelength λ_{FW} = 1400 nm, respectively, as functions of the arm length and width, which actually provide guidance for choosing the CSRRs with appropriate structural parameters to create a metasurface with a given phase gradient. For example, to obtain a π/4 phase gradient, the phase shift contours −45°, 0°, 45°, and 90° are first determined and outlined by dashed lines in Fig. 2(a). Then, the contour lines are superimposed to the colour map of the SHG amplitude in Fig. 2(b). Along each contour line, the phase shift of the SHG could remain the same, while its amplitude can be changed by selecting the CSRRs with different combinations of the arm length and width. By simply mirroring the CSRR with respect to its base, one creates an inverted CSRR whose locally generated SHG radiation has an additional π phase shift, which equivalently extends the nonlinear phase coverage shown in Fig. 2(a) by π. As schematically shown in Fig. 2(c), two eight-resonator unit cells with the same incremental phase shift of $\Delta\varphi = \pi/4$ (along the $+x$ direction) are thus created from the initial four CSRRs located in the path-1 or path-2 and the corresponding four inverted-CSRRs. The far-field SHG emission of the metasurfaces constructed from the above two super-cells excited by a normally incident fundamental wave (λ_{FW} = 1400 nm) polarized along the y-direction are calculated and shown in Fig. 2(c). Although the SHG amplitude ratio of the CSRRs along the path-1 (1.1:1.3:1.2:1) and path-2 (1.1:1.5:1.4:1) is different, the SHG radiation patterns of the metasurfaces constructed from these two sets of CSRRs are found to be almost the same. In each case, the SHG could be radiated into the backward hemisphere ($90° < \theta < 270°$, corresponding to the substrate side) and the forward hemisphere ($0° < \theta < 90°$ and $270° < \theta < 360°$, corresponding to the air side) at the emission angles of 192.4° and 347.4° (or equivalently −12.6°), respectively.

3. Conclusions

In conclusion, we demonstrate that the SH currents generated in the CSRRs are mostly concentrated in the central patch of metal, parallel to the CSRR arms, and asymmetric with respect to the CSRR base. This allows for imposing the phase change of π on the locally generated SH radiation by mirroring the CSRR with respect to its base. We also demonstrate that the adjustment of the geometrical parameters, such as the arm length and width, coupled with the mirror inversion of the CSRRs enable a continuous control over the phase change from zero to 2π for the locally generated SHG upon illumination by linearly polarized FW. By further designing a nonlinear metasurface consisting of eight-CSRR supercells with a phase gradient of $\Delta\varphi = \pi/4$, SHG beam bending behavior is demonstrated.

Acknowledgements

The authors thank the support by the National Nature Science Foundation of China (NSFC) under Grant Nos. 11674168, 91221206, 11474215, 11274160 and 51271092.

References

[1] N. Segal, S. Keren-Zur, N. Hendler, T. Ellenbogen, Controlling light with metamaterial-based nonlinear photonic crystals, Nat. Photonics 9, 180–184, 2015.

[2] G. Li, S. Chen, N. Pholchai, B. Reineke, P. W. H. Wong, E. Y. B. Pun, K. W. Cheah, T. Zentgraf, S. Zhang, Continuous control of the nonlinearity phase for harmonic generations, Nat. Mater. 14, 607–612, 2015.

[3] N. Feth et al., Second-harmonic generation from complementary split-ring resonators, Opt. Lett. 33, 1975-1977, 2008.

[4] C. Ciracì, E. Poutrina, M. Scalora, Phys. Rev. B 85, 201403, 2012.

Hide and Seek in the Polarization Profile of a Laser Beam

Xianzhong Chen[1*], Fuyong Yue[1], Shuang Zhang[2]

[1]School of Engineering and Physical Sciences, Heriot-Watt University, Edinburgh, UK
[2]School of Physics and Astronomy, University of Birmingham, Birmingham, UK
*corresponding author, E-mail: x.chen@hw.ac.uk

Abstract

Hide-and-seek is a popular children's game in which some players conceal themselves in the environment, to be found by seekers. We propose and experimentally demonstrate a metasurface approach to hide a high-resolution grayscale image in the polarization profile of a laser beam. An image with a pixel size of 300 nm by 300 nm is encoded into the spatially variant polarization states of the laser beam and revealed by using a linear polarizer.

1. Introduction

Images are usually optical patterns with spatially varying intensity or color profiles, which can be perceived by human eyes or recorded by cameras. Besides intensity and color, the information of an image can also be encoded in a spatially varying distribution of phase or polarization state. However, such images may not be viewed directly by human eyes or cameras as they may exhibit highly uniform intensity profiles. Here we propose and experimentally demonstrate an approach to hide a high-resolution grayscale image in a square laser beam with a size less than half a millimeter. Unlike optical holograms, where the information is encoded in the phase profile of the light beam, the image here is hidden in its polarization profile. This unique technology in hidden grayscale image and polarization manipulation renders new opportunities for a diverse range of applications including encryption, imaging, optical communications, quantum science, and fundamental physics.

2. Results

Metasurfaces have enabled us to engineer the spatial distribution of amplitude, phase and polarization response at subwavelength resolution, allowing us to develop a plethora of ultrathin devices with unusual properties [1]. Figure 1a shows the schematic of our approach for hiding an image. A grayscale image is hidden in the structured beam with a spatially variant polarization profile and uniform intensity profile [2], which is realized by a reflective metasurface illuminated by a laser beam at normal incidence. According to Malus' Law, when a linearly polarized light beam passes through an analyzer (linear polarizer), the intensity of the light transmitted by the analyzer is directly proportional to the square of the cosine of angle between the transmission axes of the analyzer and the polarizer. An analyzer (linear polarizer) is used to reveal the hidden image in the generated structured beam. In memory of the milestone work of James Clerk Maxwell in electromagnetics, we take one of his grayscale portraits as the hidden image. The resultant beam has a dimension of 390 μm by 390 μm since each pixel has a size of 300 nm by 300 nm, exhibiting the subwavelength resolution. The desired light beam with an inhomogeneous linear polarization profile is generated by the superposition of two circularly polarized beams with equal components and opposite handedness [3].

We do not directly observe the spatially-variant polarization profile of the laser beam but rather indirectly confirm its existence through the intensity profile (grayscale image) behind the analyzer. In comparison with the uniform intensity (no image), the hidden image is clearly observed with the analyzer (Figure 1b), which unambiguously shows the image-hidden functionality of the developed devices.

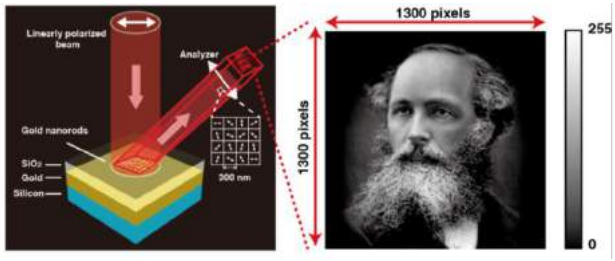


Figure 1 Schematic for hiding an image.

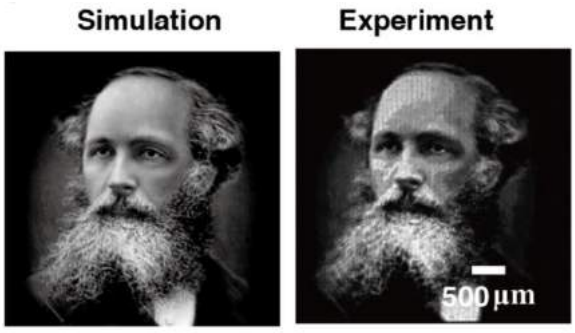


Figure 2 Simulation and experimental result.

3. Discussion

Benefiting from the broadband nature of the geometric metasurface, the developed device can operate in a broad wavelength range. Images at different wavelengths are also captured. The uniqueness of our approach lies in the encoding process of a high-resolution grayscale image onto the polarization profile of the laser beam. The obtained image shows how the electric field is oriented in the beam profile of the laser beam. These hidden images demonstrate the rich polarization structure that a light beam can possess at subwavelength scales.

4. Conclusions

Our approach provides a novel route to hide a high-resolution grayscale image in the polarization topology of a laser beam that has not previously been reported in the literature. The results are relevant to fundamental study of physics and light-matter interactions. The uniqueness of our approach in image hidden and precise polarization manipulation and high performance in resolution, bandwidth, and compactness renders this technology very attractive for diverse applications such as encryption, imaging, anti-counterfeiting, optical communications, quantum science, and fundamental physics.

Acknowledgements

This work is supported by the Engineering and Physical Sciences Research Council of the United Kingdom (Grant Ref: EP/M003175/1) .

References

[1] D. Wen, F. Yue, G. Li, G. Zheng, K. Chan, S. Chen, M. Chen, K. F. Li, P. W. Wong, K. W. Cheah, E. Yue Bun Pun, S. Zhang, X. Chen, Helicity multiplexed broadband metasurface holograms. *Nat. Commun.* 6, 8241, 2015.

[2] F. Yue, C. Zhang, X. Zang, D. Wen, B. D. Gerardot, S. Zhang, X. Chen, High-resolution grayscale image hidden in a laser beam, *Light: Sci. Appl.*, 7, 17129, 2018.

[3] F. Yue, D. Wen, C. Zhang, B. D. Gerardot, W. Wang, S. Zhang, X. Chen, Multichannel polarization-controllable superpositions of orbital angular momentum states, *Adv. Mater.*, 29, 1603838, 2017.

Fano resonance enhancement using fishnet metamaterials

Jiaxin Bao[1], Libang Mao[1], and Tun Cao[1,] *

[1]Department of Biomedical Engineering Faculty of Electronic information and Electrical Engineering , Dalian University of Technology, Dalian, China
*corresponding author, E-mail: caotun1806@dlut.edu.cn

Abstract

Fano resonance (FR) is routinely observed in three dimensional(3D) symmetric metamaterials(MMs) consisting of elliptical nanoholes array (ENA) embedding through metal/dielectric/metal (MDM) multilayers. It is shown theoretically that a square periodic ENA perforating through MDM layers produces a FR response in the near infrared (NIR) regime.This FR response is attributed to the interplay between the bright modes and dark modes, where the bright modes originate from the electric resonance(localized surface plasmon resonance) caused by the ENA and the dark modes are due to the magnetic resonance(inductive-capacitive resonance) induced by the MDM multilayers. Notably, one can achieve a narrower FR when the elliptical nanoholes occupy the sites of a rectangular lattice, owing to the interaction of the magnetic resonances with the enhanced electric resonances. Moreover, a higher varying degree of the lattice constant along the horizontal direction allows for a FR with a higher value of the quality factor and the tuning of the amplitude and the resonant frequency of the transparency window. Such a FR created by the interference among the magnetic and electric dipolar resonances opens up an alternative way of forming a sharp FR in the symmetric multilayer MMs, and could be exploited for sensing.

1. Introduction

Multilayer 3D MMs possessing a strong magnetic activity is thought to be a natural step in improving FRs. In 3D MMs based on the MDM multilayer, magnetic dipolar resonances are excited when displacement current (JD) forms a closed loop inside the dielectric interlayer[1-2]. A well known application of this phenomenon is to take advantage of the overlap of the electric and magnetic resonant moments to achieve the double negative index MMs [37]. Quite recently, several groups utilize the strong magnetic activity to achieve a sharp FR response in various multilayer MMs such as double layer electric ring resonators at GHz regime[3] and multilayer half elliptical hole resonators at THz regime[4]. However, limited attempts were made to obtain a FR in the near infrared (NIR) region through an intrinsically symmetric multilayer 3D MMs.

In the present work, we numerically study FR response in MMs consisting of the periodic elliptical nanoholes array (ENA) embedding through metal-dielectric-metal films in the NIR regime. The results suggest that a FR can be excited in the symmetric MDM-ENA when the bright mode and dark mode appear in the same spectral region, where the bright mode is generated through the ENA electric resonance(localized surface plasmon resonance) and the dark mode is due to the magnetic resonance(inductive-capacitive resonance) induced by the MDM multilayers. This indicates that structural symmetry-breaking may not be necessary to give rise to a FR. Moreover, it is shown that the MDM-ENA with rectangular lattice can increase the electric resonance at the same frequency where a strong magnetic resonance occurs thus inducing a significant interference among the electric and magnetic resonances, which enhances the FR accordingly. Our proposed structure has a simple design ideally suitable for the existing manufacturing nanotechnologies.

2. Results and discussions

The parameters in the present work are chosen to closely match those of technologically feasible physical systems. The MDM films consist of two 30nm thick Au separated by a dielectric interlayer of 60nm thick Al_2O_3. Here, we simulate two sets of structures starting from the square periodic ENA in which the elliptical holes are exactly at the sites of the square lattice (see figure 1(a)), the unit cell is shown in figure 1(b) where the horizontal lattice constant (L_x) and vertical lattice constant (L_y) is 400nm (L_x= L_y =400nm), the long diameter of the elliptical hole is 260nm (d_1=260nm), the short diameter of the elliptical hole is 160nm (d_2=160nm). Under the normal incident light shown in figure 1, MDM multilayers serve as the magnetic resonance to excite the dark modes and the ENA electric resonance generates the bright mode. The interaction of the bright modes with the dark modes creates a FR response. We then change L_x from 400nm to 500nm ,while keeping L_y fixed at 400nm, in order to create a rectangular periodic ENA, where the elliptical holes (d_1=260nm, d_2=160nm) are occupying the sites of the rectangular lattice (see figure 1(c)-(d)). At this case, a different FR spectrum emerges. To be specific: the MDM-ENA with a rectangular lattice can strongly

interact with the normally incident plane wave and thus enhancing the bright mode resonance, about which a more detailed discussion will be said later. For both of the structures, *βa*s a cross-section plane of the structure, and the elliptical holes are periodically arranged in both the *x* and *y* directions. The two structures are both suspended in a vacuum. Au is selected as the metal due to its stability and low ohmic losses. The structures are simulated using a commercial software '3D EM Explorer Studio', based on the finite difference time domain (FDTD) method. In the simulation, The dielectric properties of Au as given by Johnson & Christy are used. A plane wave source is simulated at the normal incidence to the structure with the electric field direction along the small axis of the elliptical hole. The computational domain (400nm × 800nm × 1000nm) has perfectly match layer (PML), absorbing boundaries, in the z direction and periodic boundaries in the *x*-*y* plane. A uniform FDTD mesh size is adopted, the mesh size is the same along all Cartesian axes: $\Delta x=\Delta y=\Delta z$=2nm, which is sufficient to minimize the numerical errors arising from the FDTD method.

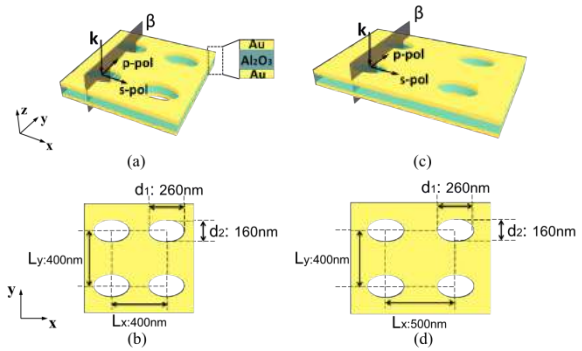


Fig. 1. (a) Schematic of the symmetric MDM structure consisting of a 60nm thick Al_2O_3 dielectric layer between two 30nm thick Au films perforated with a square array of elliptical holes suspended in a vacuum. (b) Illustration of the element of ENA, the horizontal lattice constant (L_x) and vertical lattice constant (L_y) is 400nm (L_x= L_y =400nm) and hole diameters are d_1=260nm, d_2=160nm. (c) Schematic of the symmetric MDM structure consisting of a 60nm thick Al_2O_3 dielectric layer between two 30nm thick Au films perforated with a rectangular array of elliptical holes suspended in a vacuum. (d) Illustration of the element of ENA, the lattice constants are L_x=500nm, L_y =400nm, hole diameters are d_1=260nm, d_2=160nm.

Figure 2 shows the simulated transmission (*T*) of both square periodic MDM ENA (L_x= L_y =400nm) and rectangular periodic MDM-ENA (L_x=500nm, L_y =400nm) respectively. As can be seen, the square periodic MDM ENA exhibits a FR at the wavelength of 1284nm with a transmission peak of 0.28 and a spectral width of 70nm, resulting in a *Q* factor of 23. As modifying the square lattice to the rectangular lattice, the FR blueshifts to the wavelength of 1270nm with the narrower spectral width of 44nm and higher *Q* factor of 31. Meanwhile, we observe a decreasing of the transmission peak at 0.25 owing to an increment on the impedance mismatching to vacuum for the rectangular periodic MDM-ENA.

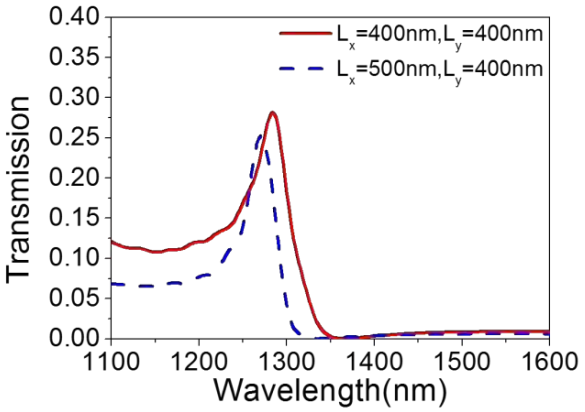


Fig. 2. 3D FDTD simulation of spectrum of transmission of both square periodic MDM ENA (Lx= Ly =400nm) and rectangular periodic MDM-ENA(Lx=500nm, Ly =400nm), for p polarization at normal incidence.

3. Conclusions

In summary, a FR in the NIR region is observed in the MMs consisting of rectangular periodic elliptical nanoholes array penetrating through Au/Al_2O_3/Au layers. It is shown that a strong interference between the electric and magnetic resonances can be induced by modifying the square periodic MDM-ENA to the rectangular periodic MDM-ENA, thus enhancing the FR in the symmetric MDM-ENA. Moreover, a higher varying degree of the L_x of the periodic ENA allows for a higher Q factor, and the tuning of the amplitude and resonant frequency. This design has the potential for sensing application in the NIR region.

Acknowledgements

We acknowledge the financial support from National Natural Science Foundation of China (Grant No. 61172059 and 51302026)

References

[1] T. Cao and M. J. Cryan, "Study of incident angle dependence for dual-band double negative-index material using elliptical nanohole arrays," J. Opt. Soc. Am. A vol. 29, pp. 209-215, 2012.

[2] Y. G. Ma, L. Zhao, P. Wang, and C. K. Ong, "Fabrication of negative index materials using dielectric and metallic composite route," Appl. Phys. Lett. vol. 93, pp. 184103, 2008.

[3] B. Seo, K. Kim, S. G. Kim, A. Kim, H. Cho, and E. M. Choi, "Observation of trapped-modes excited in double-layered symmetric electric ring resonators," J. Appl. Phys. vol. 111, pp. 113106, 2012.

[4] N. Soltani, É. Lheurette, and D. Lippens, "Wood anomaly transmission enhancement in fishnet-based metamaterials at terahertz frequencies," J. Appl. Phys. vol. 112, pp. 124509, 2012.

Magnetic Hyperbolic Metasurface

Yihao Yang, Peifei Qin, Bin Zheng, Huaping Wang, Lian Shen, Hongsheng Chen
The Electromagnetics Academy at Zhejiang University, Zhejiang University, Hangzhou 310027, China
*Email: hansomchen@zju.edu.cn

Abstract

A fundamental cornerstone in nanophotonics is the ability to achieve hyperbolic dispersion of surface plasmons, which shows great potentials in many unique applications, such as near-field heat transport, planar hyperlens, and strong enhanced spontaneous emission. The hyperbolic metasurfaces with such ability, however, are currently restricted to electric hyperbolic metasurface paradigm, showing inherently significant radiation losses. As the radiation loss of the magnetic dipole is substantially lower than that of its electric counterparts with similar size, to overcome the above challenge, we hereby proposed, designed, and fabricated magnetic hyperbolic metasurfaces on which magnetic surface plasmons (MSPs) travel in a convergent manner. We experimentally observed diffraction-free propagation, anomalous diffraction, negative refraction, and frequency-dependent strong spatial distributions of the MSPs on the metasurface in the hyperbolic regime at microwave frequencies. Our findings can be applied to manipulate MSPs and design planarized devices for near-field focusing, imaging, and spatial multiplexers without significant radiation losses. This concept can also be applied to terahertz and optical frequencies to produce novel quantum optical apparatuses with strong magnetic light-matter interactions.

Plasmonic enhancement and manipulation of optical nonlinearity in monolayer WS_2

Jinwei Shi[1,2,3], Wei-Yun Liang[1], Hyeyoung Ahn[1], Soniya S. Raja[4], Yungang Sang[3], Xin-Quan Zhang[5], Chun-An Chen[5], Yanrong Wang[3], Xinyue Yang[3], Yi-Hsien Lee[5], and Shangjr Gwo[2,4,6]

[1]Department of Photonics, National Chiao-Tung University, Hsinchu 30010, Taiwan
[2]Department of Physics, National Tsing-Hua University, Hsinchu 30013, Taiwan
[3]Department of Physics and Applied Optics Beijing Area Major Laboratory, Beijing Normal University, Beijing 100875, P.R.C.
[4]Institute of NanoEngineering and MicroSystems, National Tsing-Hua University, Hsinchu 30010, Taiwan
[5]Department of Materials Science and Engineering, National Tsing-Hua University, Hsinchu 30013, Taiwan
[6]National Synchrotron Radiation Research Center, Hsinchu 30076, Taiwan
*corresponding author, E-mail: shijinwei@bnu.edu.cn

Abstract

Two-dimensional transition metal dichalcogenides have giant second order nonlinearity. However, the sub-nanometer thickness of monolayer limits the conversion efficiency. Here, we experimentally show that the second-harmonic generation of WS2 can be enhanced by integrating it on a plasmonic metasurface. The direct enhancement factor of 400 can be realized due to the strong field confinement of the plasmonic dark mode. Meanwhile, the polarization dependence of SHG can also be controlled by the plasmonic mode.

1. Introduction

Atomically thin two-dimensional (2D) transition metal dichalcogenide (TMDC) monolayers possess many novel optoelectronic properties, which have made them enabling materials for ultracompact photonic devices. Owing to the broken crystal inversion symmetry in monolayer TMDCs, optical nonlinear processes, such as second-harmonic generation (SHG), are greatly enhanced as compared with their bulk counterparts. However, the nonlinear conversion efficiencies in monolayer TMDCs are still limited by their atomic thickness. Recently, much effort has been directed to enhance second-harmonic (SH) emission intensity from TMDCs by utilizing optical microcavities and waveguides, but usually only relatively small enhancement factors (EFs) have been achieved in most of these works (~5–10), resulting from the weak enhancement of the resonant field.

In this work, we report on 2D plasmonic enhancement and manipulation of SHG by surface plasmon polariton (SPP) modes confined in planar plasmonic resonators comprised of 2D nanogroove gratings with subwavelength pitch on atomically smooth Ag plates. Using efficient in-plane coupling of monolayer TMDC with SPP resonator mode, we demonstrate a 2D frequency-doubling coherent light source and a 400-fold SHG enhancement from monolayer tungsten disulfide (WS_2). Furthermore, the polarization-resolved SHG emission pattern is modified from a six-fold symmetry for monolayer WS_2 on the unpatterned region of Ag plate to a two-fold symmetry for monolayer WS_2 on the Ag nanogroove grating, which is controlled by the nanogroove plasmonic mode. These results reveal the immense potential of TMDC–plasmonic metasurface hybrid structures for further exploration in on-chip nonlinear photonics and plasmonics, as well as fundamental studies in quantum optics.

2. Page layout and style

In Fig. 1a, we show the schematic of the TMDC–plasmonic metasurface hybrid structure for 2D plasmonic enhancement and manipulation of optical nonlinearity in monolayer TMDC. To date, large discrepancies can be found in reported effective second-order susceptibilities ($\chi^{(2)}$) and conversion efficiencies for monolayer TMDCs. These discrepancies could be associated with multiple origins, such as the sample preparation method, resonant SHG at excitonic resonances in monolayer TMDCs, and polarization with respect to the monolayer crystal orientation,. To quantitatively and reliably demonstrate the plasmonic enhancement effects, we adopt a large-area triangular monolayer WS_2 flake grown by CVD to measure the EF, defined solidly by SHG intensity ratio of patterned to unpatterned regions covered by the **same** WS_2 flake with well-defined crystallographic orientation, at the same excitonic resonance (*C* exciton), and under the identical optical setup.

Our plasmonic resonator includes a large-area triangular WS_2 flake on a 5-nm alumina (Al_2O_3)-layer-protected Ag plasmonic metasurface consisting of V-shaped nanogroove gratings with a subwavelength pitch (~200 nm). As shown in Fig. 1a, both monolayer WS_2 and Ag nanogroove grating can generate SH emission15,28;

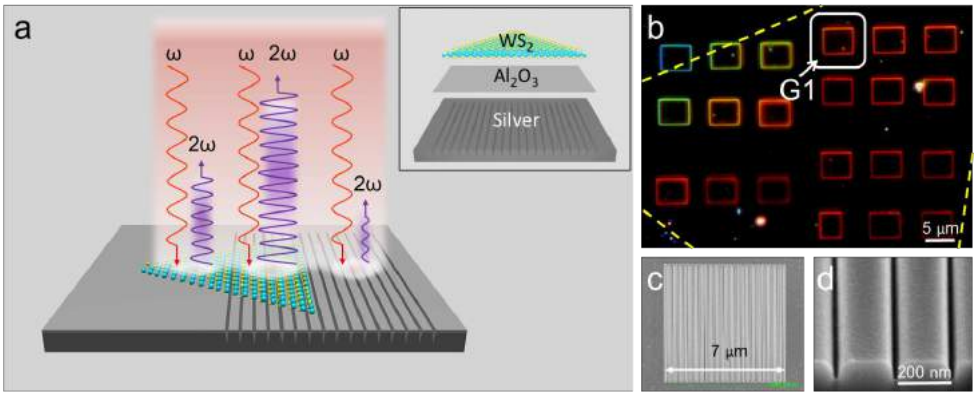


Figure 1: Illustration of plasmonic SHG enhancement of monolayer WS_2.

however, the individual SHG conversion efficiency suffers from either a low effective second-order susceptibility (Ag) or an atomically thin layer thickness (WS_2). In contrast, in the case of hybrid structure, the total SHG intensity can be far greater than the sum of the two, because the SHG from the WS_2 monolayer is strongly enhanced by coupling with the in-plane electric field of nanogroove plasmonic mode.

The resonant electric field within the nanogroove is at *C* exciton resonance and parallel to the Ag plate surface, making it ideal for strong nonlinear light–matter interaction between incident light and monolayer TMDC. Figure 1 also shows the optical dark-field image (panel b) and scanning electron microscope (SEM) images (panels c and d) of the fabricated Ag gratings. Figure 1b clearly shows that nanogroove gratings with a subwavelength pitch are optically dark. Among the 20 Ag gratings shown in Fig. 1b with varying groove depths, we present the measurement results taken for gratings G1 at the *C* exciton resonance wavelength (430 nm, on-resonance) and G2 at 445 nm (near-resonance) for the detailed investigation of linear and nonlinear optical properties at or near the *C*-exciton resonance.

Both experimental characterization and simulation indicate that the efficient SHG enhancement from WS_2 monolayer is achieved via coupling with the localized plasmons in nanogrooves. In principle, both the plasmonic resonances at fundamental and SH frequencies can be utilized to enhance the SHG conversion efficiency. However, the enhancement of fundamental wave can easily destroy the monolayer TMDC due to an intense pump laser field. Therefore, we designed the nanogroove structure with single resonance at the SH frequency. The EFs defined above are measured to be 400 (G1) and 100 (G2) respectively. The SHG conversion efficiency measured in our experiment is ~2×10 (860 nm), which is the best result reported for monolayer TMDCs and also much better (3-5 orders of magnitude) than reported results for nonlinear metasurfaces.

We also measured the polarization dependence of the enhanced SHG intensity and found that it is modified from the six-fold symmetry pattern to a two-fold symmetry pattern, which can be understood by an analytic mode. This property can be utilized for optical information encoding.

3. Discussion

The enhancement is strongly dependent on the localized plasmon resonance mode. However, the mode can be shifted easily by the environment index. Therefore, tunable and broadband resonant device need to be designed. We have made some progress in this field, and further work is still ongoing.

4. Conclusions

In conclusion, we show that the SHG from monolayer TMDCs can be dramatically enhanced by integrating it onto plasmonic metasurfaces. A giant EF of 400 and a surprisingly large conversion efficiency of ~2×10^{-5} is are realized using a simple 2D resonator design. The polarization dependence of SHG can also be manipulated by the plasmonic mode. Our results suggest that the planar hybrid structures comprised of monolayer TMDCs and plasmonic metasurfaces are very promising for the development of on-chip nonlinear photonics and plasmonics.

Acknowledgements

The authors acknowledge financial support from the Ministry of Science and Technology (MOST) in Taiwan (MOST 105-2112-M-007-011-MY3, MOST 104-2112-M-009-007-MY3, MOST-105-2112-M-007-032-MY3, MOST-105-2119-M-007-027, and MOST-105-2633-M-007-003). Y.-H.L. acknowledges financial supports from the AOARD grant FA2386-16-1-4009 (co-funded with ONRG), and the Academia Sinica Research Program on Nanoscience and Nanotechnology. J.S. thanks the NSFC for financial support (11374037, 11674032, and 11774035). This work was partially sponsored by Beijing Cooperative Construction Project.

Enhancement of nonlinearity at interfaces with discontinuous second-order susceptibility

Yuanlin Zheng[1,2], Xiaohui Zhao[1,2], and Xianfeng Chen[1,2,*]

[1]State Key Laboratory of Advanced Optical Communication Systems and Networks,
School of Physics and Astronomy, Shanghai Jiao Tong University, Shanghai 200240, China
[2]Key Laboratory for Laser plasmas (Ministry of Education), Collaborative Innovation Center of IFSA (CICIFSA),
Shanghai Jiao Tong University, Shanghai 200240, China
*corresponding author, E-mail: xfchen@sjtu.edu.cn

Abstract

We discuss the nonlinear response at the interface of two media with sharply discontinuous second-order susceptibilities. The enhancement of nonlinear Cerenkov radiation was theoretically predicted and experimentally observed. In our experiment, there was one order of magnitude enhancement in the conversion efficiency at the nonlinear interfaces as compared to the crystal boundary. The result suggests potential applications for efficient frequency conversion, and the scheme can also be useful in the UV or even EUV generation.

1. Introduction

Recent theoretical and experimental studies have showed that nonlinear Cerenkov radiation (NCR) can be enhanced at crystal boundaries by a sharp spatial modulation of $\chi^{(2)}$ from 1 to 0. However, for most nonlinear media, especially UV-transparent crystals, the efficiency at the boundary is not high since their nonlinear coefficient is typically small. Besides, the limitation of birefringent phase matching (BPM) and quasi-phase matching (QPM) is severe at short range of UV or EUV. We theoretically predicted that NCR can be enhanced at the interface as a result of sharper $\chi^{(2)}$ modulation, if the vacuum on the one side of the boundary is substituted by a nonlinear crystal with a much larger $\chi^{(2)}$. This scenario, where NCR is generated at an interface between two different quadratic crystals, has not been fully discussed until our investigation. The method exploits total internal reflection and has no limit for wavelength, which is promising for tunable frequency conversion to the UV range.

2. Theoretical modelling

To analyze the second harmonic (SH) generated at the nonlinear interface, e.g. BBO and lithium niobate (LN), we analytically solve the coupled wave equation under the slow varying envelop approximation. Considering a nonlinear interface along the *y* axis and the fundamental was propagating in the *x* direction. The intensity of SH is deduced to be:

$$I_2(k_x, y) = \left(\frac{k_2}{2n_2^2}\right)^2 I_1^2 y^2 \operatorname{sinc}\left[\frac{\left(\Delta k - k_x / 2k_2\right) y}{2}\right]$$
$$\left|\left(\chi_1^{(2)} + \chi_2^{(2)}\right)\sqrt{\frac{\pi}{8}} a \exp\left(-\frac{a^2 k_x^2}{8}\right) + i\left(\chi_1^{(2)} - \chi_2^{(2)}\right) aD\left(\frac{ak_x}{2\sqrt{2}}\right)\right|^2, \quad (1)$$

where k_x is the components of k_2 in the *x* direction, n_2 is the refractive index of SH, I_1 denotes the intensity of the Gaussian fundament wave (FW) with a beam diameter of a. And $D\left(ak_x / 2\sqrt{2}\right)$ denotes the Dowson function. From Eq. (1), one can find that the SH intensity I_2 is closely related to the absolute value of $\left|\chi_1^{(2)} - \chi_2^{(2)}\right|$. If the nonlinear coefficient of the second medium is large enough that the relation $\left|\chi_1^{(2)} - \chi_2^{(2)}\right| > \left|\chi_1^{(2)}\right|$ is satisfied, the SH intensity is thus enhanced theoretically.

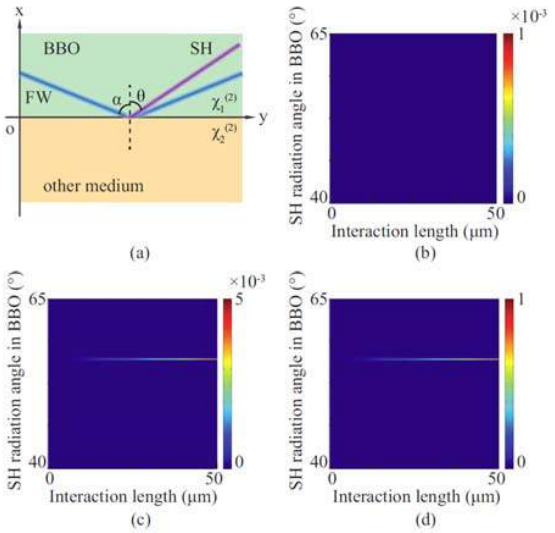


Figure 1: (a) Diagram of SH generated at the interface. (b) No SH emission in a homogeneous nonlinearity. (c) and (d) SH generated at the BBO boundary and that of BBO and LN, respectively.

The simulation result is given in Fig. 1, assuming with the FW wavelength of 650 nm and the incident angle $\alpha = 60^{\circ}$ in the BBO crystal. Both FW and SH waves are o-polarized. It is worth noting that the radiation angle in BBO is kept the same with or without presence of the other medium. Hence, the radiation of SH in the BBO will not be effected by the absorption of LN. It also indicates that one can employ a medium with a larger nonlinear coefficient to enhance the SH generated in UV-/EUV-transparent crystals no matter it is transparent or not.

3. Experiments and Discussion

For demonstrate, two different nonlinear crystals, BBO and lithium niobate (LN), bonded together under high pressure were used to achieve an artificially fabricated interface with a with a larger value of $\left|\chi_1^{(2)} - \chi_2^{(2)}\right|$ in our experiment. Figure 2 shows the experimental configuration and results conducted using a femtosecond (fs) laser source at the wavelength of 800 nm. The NCR generated at the BBO-LN interface is enhanced by a factor in the range of 4 to 10, as compared with that at the boundary of BBO crystal. The enhancement of SH in BBO induced by the presence of LN is obvious.

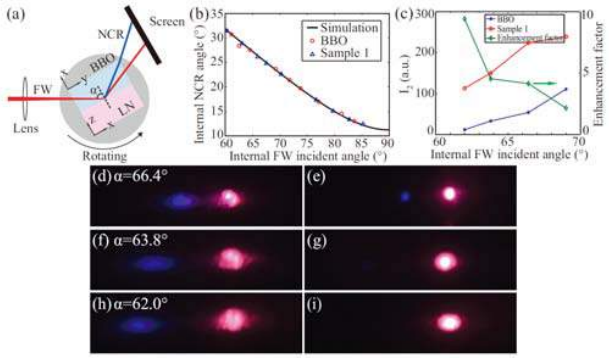


Figure 2: (a) Experimental setup. (b) Internal NCR angle versus FW incident angle. (c) Measured intensity and enhancement factor of SH generated at the BBO-LN interface and the boundary of BBO. (d), (f) and (h) are the emission patterns at the BBO-LN interface. (e), (g) and (i) are the emission patterns at the BBO crystal boundary.

A more convincing demonstration is presented using a shorter FW wavelength of 650 nm (the source was an optical parametric amplifier pumped by the fs laser), whose SH is in the absorption range of LN. The wavelength spectra of SH with respect to FW incident angles at the BBO-LN interface are shown in Fig. 3(a). For comparison, the SH generated on the boundary of single BBO sample was also recorded at the same incident and measurement conditions. It's obvious that the intensity of SH generated at the interface of BBO-LN was much higher than that generated at the BBO boundary for the same incident angle. The enhancement factor of SH intensity introduced by LN was in the range from 5 to 13.

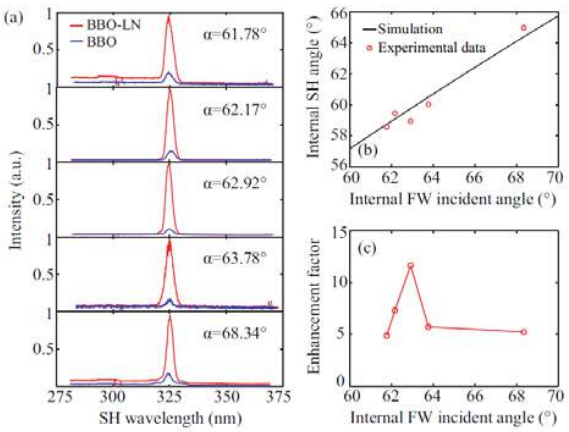


Figure 3: (a) Spectra of SH generated on BBO boundary and interface of BBO-LN. (b) Internal radiation angle of SH vs. internal FW incident angle. (c) Measured enhancement factor of SH generated at the BBO-LN interface.

In microcosmic perspective, the nonlinear polarization wave excited by FW and propagating along the interface can be viewed as an oscillation array of electric dipoles. The mechanism can be attributed to that the oscillating electric dipoles in BBO is enhanced by those in the LN. In the BBO side, the oscillating electric dipoles radiate enhanced SH at the phase-matching angle, although the SH at 325 nm is highly absorptive in LN.

4. Conclusions

In conclusion, the SH generated at a crystal boundary can be enhanced by another medium with a larger nonlinear coefficient, even though it is non-transparent at the SH wavelength. The emission angle of SH in the crystal will not be effect by the dispersion of that medium. Our results suggest potential applications in the frequency conversion for UV even EUV spectral emission.

Acknowledgements

The National Basic Research Program 973 of China (No. 2011CB808101), the National Natural Science Foundation of China (Nos. 61125503, 61235009, 61205110, 61505189 and 11604318)

References

[1] Xiaohui Zhao, Yuanlin Zheng, Huaijin Ren, Xuewei Deng, and Xianfeng Chen, Enhancement of UV second-harmonic radiation at nonlinear interfaces with discontinuous second-order susceptibilities, arXiv: 1612.05376, 2016.

[2] Xiaohui Zhao, Yuanlin Zheng, Huaijin Ren, Ning An, Xuewei Deng, and Xianfeng Chen, Nonlinear Cherenkov radiation at the interface of two different nonlinear media, Opt. Express, 24(12), pp. 12825-12830, 2016.

Active Plasmonics Based on Liquid Crystals

Yan Jun Liu[1]*, Shengtao Yin[1,2], Dong Xiao[1], Guixin Li[3], Dan Luo[1], Wei Ji[2], Shouzhen Jiang[4], and Xiao Wei Sun[1]

[1]Department of Electrical and Electronic Engineering, Southern University of Science and Technology, Shenzhen 518055, China.
[2]School of Information Science and Engineering, Shandong University, Jinan 250000, China.
[3]Department of Materials Science and Engieering, Southern University of Science and Technology, Shenzhen 518055, China.
[4]School of Physics and Electronics, Shandong Normal University, Jinan 250014, China.
*corresponding author, E-mail: yjliu@sustc.edu.cn

Abstract

As a unique material from nature, liquid crystals possess the smallest elastic constants and the largest birefringence among all known materials. Liquid crystals also have a large working window that spans the entire visible-infrared spectrum and beyond. Moreover, they can be manufactured and processed on a very large scale; they are also compatible with almost all optoelectronic materials. The alignment of liquid crystals can be easily controlled by many means, such as electricity, light, and acoustic waves, thus making them an excellent candidate for development of active nanophotonics. Here, we summarize our recent research on the liquid crystal based active plasmonics. Various active plasmonic devices are demonstrated, such as switches, modulators, and filters. These active plasmonic devices are potentially useful for future development of nanophotonic circuits, light sources, imaging and displays.

1. Introduction

Plasmonics opens a new platform to both control and manipulate optical signals by coupling light to coherent electronic excitations in deep sub-wavelength metallic nanostructures and hence merges photonics and electronics at nanoscale [1–3]. This has led to rapid development of a variety of sub-wavelength photonic components that are capable of manipulating plasmonic signals, such as waveguides, filters, lenses, and spasers. One of the most important yet challenging requirements for real applications is to introduce a means to reversibly control the optical properties of plasmonic devices, so called "active plasmonics".

Many active mediums have been exploited to construct active plasmonic devices, including liquid crystals, molecular machines, elastic polymers, and chemical reactions. Among them, liquid crystal stands out from all the rest because of its large birefringence on refractive index, low threshold on transition among different states, fluid nature for easy integration, and versatile driven methods to cause the transitions. Here, we will review our recent research progress on the liquid crystal based active plasmonics including filters, modulators, and switches. These active plasmonic devices are potentially useful for future development of nanophotonic circuits, light sources, and imaging.

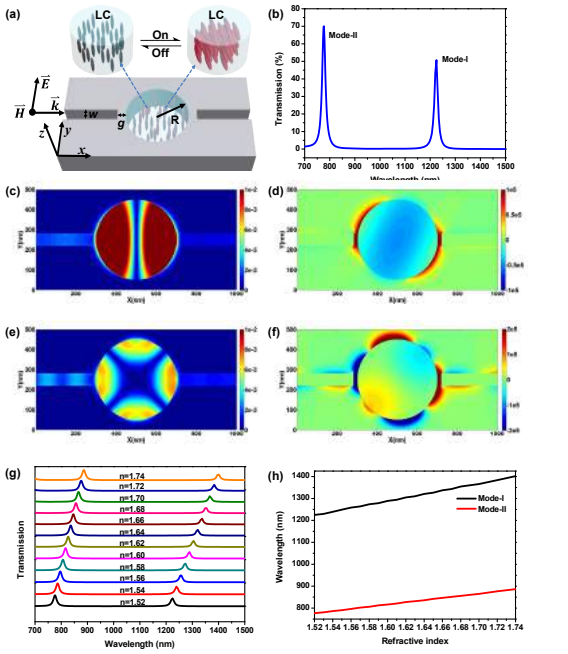


Figure 1. (a) Schematic diagram of the plasmonic waveguide filter structure composed of two slits, two semi-infinite metallic claddings, and a LC-filled nanocavity resonator in the middle of the MIM structure. (b) Simulated transmission spectrum of the plasmonic waveguide filter. The refractive index of the LC-filled nanocavity is 1.52. Simulated magnetic-field (c, e) and corresponding charge (d, f) distributions at the peak positions of Mode-I (c, d) and Mode-II (e, f), respectively. (g) Transmission spectra of the plasmonic waveguide filter with different refractive indices of the LC-filled nanocavity. (h) The evolution of the peak positions of Mode-I and Mode-II as a function of the refractive index of the LC-filled nanocavity.

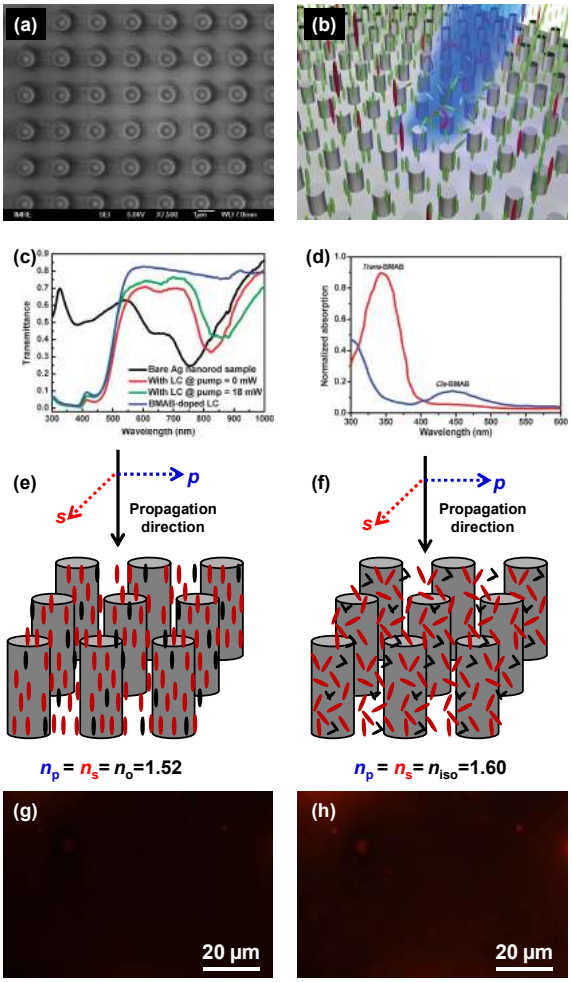


Figure 2. (a) Typical SEM image showing the top-view of a fabricated silver nanorod array. (b) Schematic demonstration of the hybrid system that integrates a silver nanorod array with photoresponsive liquid crystals. The silver nanorod array enables homeotropic alignment of the liquid crystal molecules, which makes the optical tuning polarization-insensitive under the UV light pump. (c) Measured transmittance of the bare sample before and after LC infiltration, with the UV light pump. (d) The trans – cis isomerization of BMAB under the UV fl ood exposure. The proposed model for the alignment of LC molecules inside the Ag nanorod array before (e) and after (f) the UV light pump. The observed optical images before (g) and after (h) light pump between two crossed polarizers under the polarized optical microscope.

2. Active Control

2.1. Electric control

Electric fields have very strong impact on the dipole-like liquid crystal molecules, whose properties are determined by its rod shape structure. Under an electric field, the director of the liquid crystal molecules will be re-oriented when an external electric field is applied to the liquid crystal. We propose a liquid-crystal-based tunable plasmonic waveguide filter that consists of a metal-insulator-metal waveguide with a nanocavity resonator [4], as shown in Figure 1. By filling the nanocavity with birefringent LCs, we could then vary the effective refractive index of the nanocavity by controlling the alignment of the liquid crystal molecules, hence making the filter tunable. The compact design of our proposed plasmonic filters is especially favorable for integration, and such filters could find many important potential applications in high-density plasmonic integration circuits.

2.2. Optical control

All-optical tuning is another promising method since it has many advantages such as non-contact tuning, low power consumption, and friendly integration. As compared to the electrical tuning method, light driven method requires: (1) no conductive substrate, (2) low power consumption, (3) large operation windows covering from UV to mid-IR. Here, we demonstrate the all-optical, polarization-insensitive tunable manipulation of a hybrid system that integrates a silver nanorod array with photoresponsive liquid crystals [5], as shown in Figure 2. The silver nanorod array also enables the homeotropic alignment of the liquid crystals, which makes the all-optical tuning behavior polarization-insensitive. With its advantages of cost-effective fabrication, easy integration, all-optical control, and polarization-insensitivity, the hybrid system could be valuable in many nanophotonic applications.

3. Summary

In summary, we have described our recent research progress on liquid crystal based active plasmonic devices. These results have clearly shown that LCs are a promising candidate for active plasmonics due to their unique properties. We anticipate that the optical performance of such devices could be further improved in terms of operating thresholds (either voltage or light power) and response time by carefully selecting other liquid crystals and engineering the plasmonic nanostructures.

Acknowledgements

We acknowledge the financial support from the Natural Science Foundation of Guangdong Province (Grant No. 2017A030313034), the Shenzhen Science and Technology Innovation Council (Grant No. KQTD2016030111203005), and the start-up fund provided by Southern University of Science and Technology (SUSTech).

References

[1] T.W. Ebbesen, *et al. Nature* 391: 667−669, 1998.

[2] A.V. Zayats, *et al. Phys. Rep*. 408: 131−314, 2005.

[3] S.I. Bozhevolnyi, *Plasmonic Nanoguides and Circuits*, Pan Stanford Publishing Pte. Ltd., Singapore, 2009.

[4] S. T. Yin, *et al.* Manuscript in submission.

[5] G. Y. Si, *et al. Phys. Chem. Chem. Phys.* 17:13223−13227, 2015.

Guide Mode Enhanced Third Harmonic Generation in Silicon Metasurfaces

Shumei Chen1[1,*], Mohsen Rahmani[2], King Fai Li[3], Andrey Miroshnichenko[4], Thomas Zentgraf [5], Guixin Li[3] , Dragomir Neshev[2] and Shuang Zhang[1]

[1]School of Physics and Astronomy, University of Birmingham, Birmingham, B15 2TT, UK
[2]Nonlinear Physics Centre, Research School of Physics and Engineering, The Australian National University, Canberra, ACT 2601, Australia
[3]Department of Materials Science and Engineering, Southern University of Science and Technology, Shenzhen, 518055, China
[4]School of Engineering and Information Technology, University of New South Wales - Canberra, Northcott Drive, Campbell, ACT 2600, Australia
[5]Department of Physics, University of Paderborn, Warburger Strasse 100, D-33098 Paderborn, Germany
*corresponding author, E-mail: s.chen.7@bham.ac.uk

Abstract

We propose to enhance the efficiency of the third harmonic generation (THG) in a complementary silicon nonlinear metasurface, consisting of cross nanoapertures in the silicon film. By exploiting its guided mode resonance, the measured THG efficiency from the silicon metasurface is 100 times higher than that from a planar silicon film of the same thickness.

1. Introduction

Silicon photonic circuits, which are compatible with mature CMOS technologies, show great potential for on-chip information processing and thus have attracted attention from both academic and industry communities.[1] In particular third order susceptibility of silicon plays a very important role in frequency conversion, light amplification based on Raman scattering, four wave mixing and all-optical de-multiplexing. [2, 3] However, one of the key obstacles that limits the applications of nonlinear silicon device is its low NLO efficiency. Unfortunately, both metal and metal-silicon hybrid plasmonic devices inherit some intrinsic disadvantages of noble metals, i.e. high loss and low damage threshold. In comparison, silicon nano-structures are exempt from these problems. In this work we propose a new scheme for achieving strong third harmonic nonlinear conversion in a metasurface featuring an extended mode volume that greatly facilitates the nonlinear interaction of light.

2. Results and Discussions

Here, we adopt a complementary silicon metasurface, which consists of a 2D periodic array of nanoapertures, as schematically shown in Figure 1. Such nanostructure was introduced in the concept of all-dielectric metasurfaces and was shown to exhibit a rich variety of modes, including leaky guided mode, dark and bright multipolar modes.[4] When the fundamental wave (FW) is normally incident onto the metasurface, the hole-array can couple the incident wave into different multipolar modes. The interference between the guided and localized modes in the structure results in Fano-type spectral resonant features, where the near field are strongly enhanced, allowing to dramatically increase the THG by the metasurface. The proposed silicon metasurface represents a facile approach towards highly efficient THG sources.

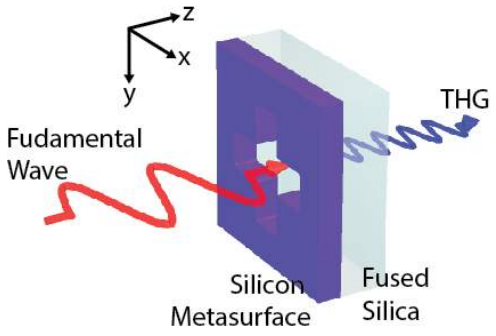


Figure 1: Schematic view of a single silicon nanoaperture. The nanoaperture is milled into 205 nm thick silicon thin film using electron beam lithography and dry etching methods. The geometry parameters of the nanoaperture are w = 120 nm, h = 300 nm. The period of the nanoaperture array is 600 nm.

2.1. Linear optical properties of the silicon metasurface

The calculated transmittance spectrum is shown in Figure 2 with red line and closed squires. The simulations match the resonance behaviour reasonably well, where the resonant mode appears at a wavelength around 1296 nm. We then characterize the linear optical properties of the silicon planar thin film and metasurface by using Fourier transformation infrared spectrometry. As shown in Figure 2, in the measured transmittance spectrum (open red circles) we observe a clear transmission dip at a wavelength of 1281 nm, which is a result of excitation of resonant modes in the complementary silicon structure. The discrepancies between

the measurement and simulation is due to the imperfection of nanofabrication and the large numerical aperture (N.A. = 0.36) objective lens used for the transmission measurement.

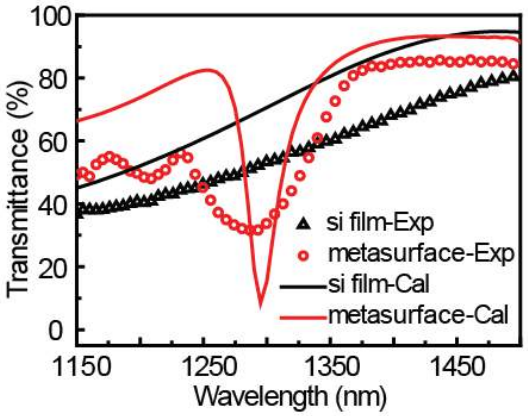


Figure 2: Simulated ('Cal') and measured ('Exp') transmission spectra of the Silicon metasurface (red curves) and Silicon thin film (black curves). The measured transmission dip of the metasurface is around 1287 nm.

In Figure 3 we shows the calculated field distributions of |Ex| and |Hy| at resonant (1296 nm) and non-resonant wavelengths (1260 nm and 1338 nm). As expected, the fundamental wave is strongly localized inside silicon when the guided mode is excited.

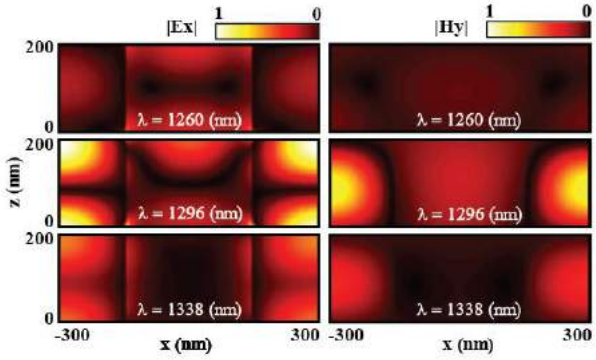


Figure 3: Calculated field distribution of fundamental wave in silicon metasurface. For linear (H-) polarized fundamental wave at wavelength of 1260 nm, 1295 nm and 1338 nm, the absolute values of electric field |Ex| and magnetic field |Hy| are plotted in X-Z plane of silicon metasurface.

2.2. THG from the silicon metasurface

The measured THG efficiency from silicon metasurface (Figure 4 solid squares) exhibits an enhancement factor up to 100 with respect to that from the planar silicon film (solid triangles). This observed strong enhancement of the THG signal arises from both the strong field enhancement inside the silicon metasurface, and the large third nonlinear polarizability of amorphous silicon. This is experimentally confirmed by the peak THG efficiency at waveguide resonant wavelength of 1280 nm. The maximum efficiency of the THG with a value of 1.76×10^{-7} is obtained from the experiment.

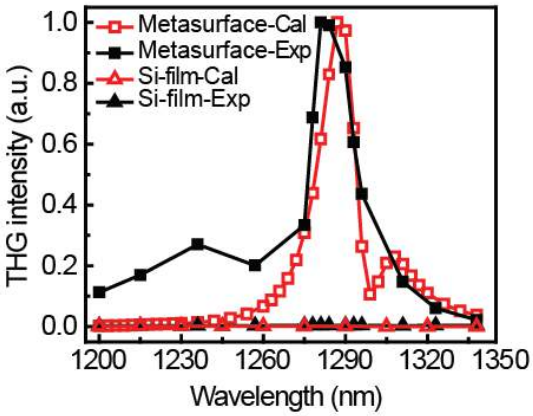


Figure 4: Measured ('Exp') THG spectra agree well with and calculated ('Cal') ones for both silicon planar film and metasurface. The giant THG enhancement occurs at wavelength of 1280 nm, which corresponds to the strong localization of fundamental wave due to waveguide mode in the silicon metasurface.

Conclusions

We have shown that the guided mode in silicon metasurface can be utilized to greatly enhance the THG efficiency. The concept of THG enhancement in this work can be used to design various nonlinear functional silicon photonic circuits.

Acknowledgements

Shumei Chen is supported by the Marie Curie Individual Fellowship (H2020-MSCA-IF-703803-NonlinearMeta).

References

[1] F. Priolo, T. Gregorkiewicz, M. Galli, T. F. Krauss, Silicon nanostructures for photonics and photovoltaics, *Nat. Photon.* 9, 19-32, 2014.

[2] J. Leuthold, C. Koos, W. Freude, Nonlinear silicon photonics, *Nat. Photon.* 4, 535-544, 2010.

[3] Boyd, R. W. *Nonlinear Optics*, Academic Press, San Diego, USA 2008.

[4] A. Jain, P. Moitra, T. Koschny, J. Valentine, C. M. Soukoulis, Electric and Magnetic Response in Dielectric Dark States for Low Loss Subwavelength Optical Meta Atoms, *Adv. Opt. Mater.* 3, 1431-1438, 2005.

External control of multipolar third harmonic generation from arrays of dielectric-metal core-shell resonators

Xin Yang,[1] Chi Zhang,[1] Lina Qian,[1] Zhi-Qin Li,[1] Ping Gu,[1] Zhuo Chen,[1,2,*] and Zhenlin Wang[1,2]

[1]School of Physics and National Laboratory of Solid State Microstructures, Nanjing University, Nanjing 210093, China
[2]Collaborative Innovation Center of Advanced Microstructures, Nanjing University, Nanjing 210093, China
*corresponding author, E-mail: zchen@nju.edu.cn

Abstract

We demonstrate that the dielectric-metal core-shell resonators (DMCSRs) in the array are acting as a set of phase-coherent sources of THG emission and their interference in the far-field region leads to the spatially tailored nonlinear radiation. By selectively matching fundamental wave to different cavity plasmons, the THG emission from the single DMCSR element can be redirected in different radiation patterns, and thus the ratio between the THG intensities into the first and zeroth order diffraction can be modified accordingly.

1. Introduction

Metallic nanostructures are capable of supporting collective electron excitations, known as surface plasmons (SPs). Associated with the excitations of surface plasmon resonances (SPRs), light can be concentrated into subwavelength volumes, producing a large local field enhancement [1, 2]. Recent work has shown that SHG and THG from periodically patterned metallic nanostructures can be diffracted into discrete directions that are determined by the momentum matching conditions between the fundamental and harmonic waves [3-5], thus providing a possible way to direct the nonlinear beam. More recently, it has been demonstrated that a mirror inversion of the split ring resonator (SRR) with respect to its base is capable of inducing a π phase shift on the locally generated SHG [6]. Based on this mechanism, the SRR and its inverted structure are arranged appropriately to construct metamaterials with nonlinear phase control over each element, thus enabling the engineered diffraction, intense focusing and polarization control of the output nonlinear signals [6, 7].

In this work, instead of varying the element phase across the array, we report on theoretically realization of an active control of THG far-field radiation from periodically arranged dielectric-metal core-shell resonators (DMCSRs) by shaping the THG radiation pattern of the single DMCSR element. We demonstrate that the THG emission from each DMCSR element can be coherently superimposed in the array of DMCSRs, leading to the observation of nonlinear diffraction patterns in the far-field region. By selectively matching fundamental wave on or off the cavity plasmon resonances supported by the DMCSRs, the THG emission from the single DMCSR can be redirected in different radiation patterns, and thus the ratio between the THG intensities into the first-order and zeroth-order diffraction from the array of DMCSRs can be tuned accordingly. Furthermore, we also demonstrate that the THG emission from the single DMCSR exhibit strong azimuthal anisotropy, and as a result, the THG intensities delivered into the first-order diffraction from the array of DMCSRs can be externally controlled by the incident electric field orientation angle. Our experimental well validate and an excellent agreement with theoretical calculations, and offer an extra degree of freedom in the control of nonlinear far-field radiation.

2. Discussion

Our previous experimental and theoretical studies have demonstrated that the excitations of the cavity plasmon resonances in the array of the DMCSRs are independent of the electric field orientations due to the spherical symmetry of the DMCSRs [8]. However, THG emissions from the individual DMCSRs are found to have relatively high intensities within a small range of azimuth angles that are very closed to the k-E plane and become quite weak at radiation azimuth angles approaching to the k-H plane, which clearly demonstrates that the cavity plasmon induced THG emission is azimuthally anisotropic and highly dependent on the electric field orientation. This provides us an opportunity to control the THG intensities into the first-order diffraction by varying the electric field orientation of the fundamental wave. Figure 1(a) shows the k-space image of the emitted THG from the array of DMCSRs with a 1.0-μm-diameter PS core [Fig. 1(a)] recorded at the fundamental wavelength of λ_{FW} = 1400 nm under the x-axis polarization (α = 0°). For the electric field orientation angle of α = 0°. In this case, the first-order (m = 0, n = ±1) THG diffraction with the azimuth angles φ = 90° and 270° are located in the k-H plane where the THG emission from the individual DMCSR achieve the minimum intensities, and as a result these two first-order (m = 0, n = ±1) diffraction spots almost disappear, as indicated by dashed-line circles in Fig. 1(a). Similarly, when the electric field is rotated to the specific orientation angles of α = 60° and 120°, the first-order (m = ±1, n = 0) THG diffraction with the azimuth

angles φ = 150° and 330° [Fig. 1(b)] and the first-order (m = 1, n = 1; m = -1, n = -1) THG diffraction with the azimuth angles φ = 30° and 210° [Fig. 1(c)] are respectively located in the k-H plane and found to have near-zero intensities. These results experimentally confirm the azimuthal anisotropy of the cavity plasmon induced THG emission from the individual DMCSRs.

To further demonstrate the controllability of the first order THG diffraction, the THG intensity ratios I0,1/I0,0 from the array of DMCSRs with a 1.0-μm-diameter PS core are measured at the fundamental wavelength of λ_{FW} = 1400 nm under different electric field orientations. Figure 1(d) shows that when the electric field is rotated from the x-axis direction (α = 0°) to the y-axis direction (α = 90°), the THG ratio is gradually increased from a near-zero minimum to a maximum value. After that, the THG ratio is found to drop back to the minimum value with further increasing the electric field orientation angle from α = 90° to α = 180°. The THG ratios that obtained from the THG radiation patterns calculated at the predicted electric quadrupolar cavity plasmonic resonance wavelength of 1370 nm for different electric field orientation angles are plotted in Fig. 1(e), which reproduces well the experimentally observed periodic variation in the THG intensity ratio with electric field rotation [Fig. 1(d)], confirming that the intensity of the first-order THG diffraction from the array of the DMCSRs can be externally controlled by rotating the electric field of the fundamental wave.

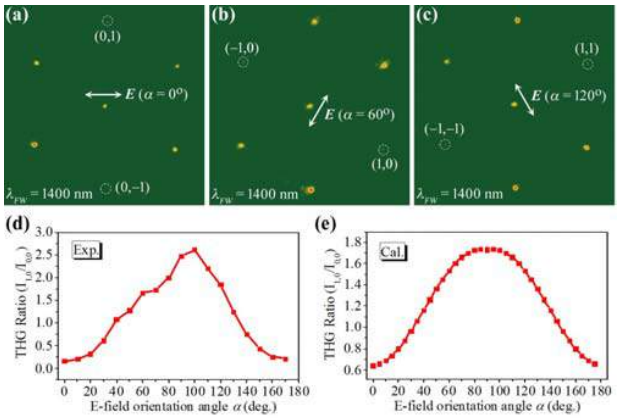


Fig. 1. (a)-(c) k-space images of the emitted THG from the array of DMCSRs with a 1.0-μm-diameter PS core recorded at the fundamental wavelength of λ_{FW} = 1400 nm for three different electric field orientation angles of α = 0°, 60° and 120°, respectively. The dashed-line circles in these figures indicate the first order THG diffraction that almost disappears. (d) and (e) Measured and calculated THG intensity ratios I0,1/I0,0 from the array of DMCSRs with a 1.0-μm-diameter PS core at the electric quadrupolar cavity plasmon resonance wavelength as a function of the electric field orientation angle, respectively.

3. Conclusions

In conclusion, we experimentally observe spatially tailored THG diffraction from the HCP array of DMCSRs that support multipolar electric and magnetic-based cavity plasmon resonances. We demonstrate that the THG emission from the single DMCSR element can be redirected in different radiation patterns at different cavity plasmon resonances, thus the THG intensities into the first and zeroth order diffraction can be dramatically modified by selectively matching the fundamental wave to different cavity plasmon resonances. In addition, we also demonstrate that the THG emission from the individual DMCSR exhibit a strong azimuthal anisotropy, making it possible to externally control the THG intensities into the first-order diffraction by varying the electric field orientation. Our experimental findings are supported by good agreement with theoretical calculations, which offer an extra degree of freedom in the control of nonlinear far-field radiation and may find useful applications in nonlinear optical routers and switches.

Acknowledgements

The authors thank the support by the State Key Program for Basic Research of China (SKPBRC) under Grant Nos. 2012CB921501 and 2013CB632703, and the National Nature Science Foundation of China (NSFC) under Grant Nos. 11174137, 91221206, 11274160, 11321063, and 51271092..

References

[1] W. L. Barnes, A. Dereux, and T. W. Ebbesen, Nature 424, 824 (2003).

[2] J. A. Schuller, E. S. Barnard, W. Cai, Y. C. Jun, J. S. White, and M. L. Brongersma, Nature Mater. 9, 193 (2010).

[3] A. V. Andreev, A. A. Korneev, L. S. Mukina, M. M. Nazarov, I. R. Prudnikov, and A. P. Shkurinov, Phys. Rev. B 74, 235421 (2006).

[4] T. Xu, X. Jiao, and S. Blair, Opt. Express 17, 23582 (2009).

[5] G. X. Li, T. Li, H. Liu, K. F. Li, S. M. Wang, S. N. Zhu, and K. W. Cheah, Appl. Phys. Lett. 98, 261909 (2011).

[6] N. Segal, S. Keren-Zur, N. Hendler, and T. Ellenbogen, Nature Photon. 9, 180 (2015).

[7] Wolf, S. Campione, A. Benz, A. P. Ravikumar, S. Liu, T. S. Luk, E. A. Kadlec, E. A. Shaner, John F. Klem, M. B. Sinclair, and I. Brener, Nature Communications 6, 7667 (2015).

[8] P. Gu, M. Wan, Q. Shen, X. He, Z. Chen, P. Zhan, and Z. Wang, Appl. Phys. Lett. 107, 141908 (2015).

Optimal double resonant condition in metallic core-shell nanocavity for third harmonic generation

Wenbo Zang [1], Lingling Fan [1], Guangxu Su [1], Xin Yang [1], Mingyu Ma [1], Peng Zhan [1,2], Zhuo Chen[1,2,*] and Zhenlin Wang [1,2]

[1]School of Physics and National Laboratory of Solid State Microstructures, Nanjing University, Nanjing 210093 China.
[2]Collaborative Innovation Center of Advanced Microstructures, Nanjing University, Nanjing 210093, China.
*corresponding author, E-mail: zchen@nju.edu.cn

1. Abstract

Numerical simulations show that the third harmonic generation (THG) intensity in the far field can be enhanced when the pump light and the THG signal are both coupled to spherical cavity modes. And it is optimum on double resonant conditions coupling two modes with the same order, up to 3 magnitudes. Subsequent theoretical analysis indicates that changing third-order nonlinear susceptibility of the metal shell while keeping that of the core fixed has almost no effect on THG efficiency.

2. Introduction

It is acknowledged that when a local surface plasmon resonance (LSPR) of metal particles is excited, a strong enhancement of optical near-field can be observed [1]. Since the generation efficiency of nonlinear signals is positively related with the high order of electric field intensity excited by pump light, orders of magnitude enhancement of nonlinear effects can be achieved [2]. Though there are many works devoted to the enhancement of nonlinear harmonic generation in recent years, most of them concentrated on the optical response of nanostructures on single resonant situation [3], in which a cavity mode of the nanostructure is excited by the pump light. In order to achieve stronger nonlinear signals, a few people pay attention to double resonant conditions that the nanostructure resonates at the fundamental frequency and the triple (or double) frequency simultaneously [4]. Rarely do works explore mechanism of double resonance's influence on nonlinear harmonic generation and how to achieve optimal results thoroughly.

In this letter, we simulated THG intensity on different double resonance situations in a metallic core-shell nanostructure whose core material has a high third order nonlinear susceptibility. There are lots of cavity modes ranging from visible area to near infrared can be excited efficiently in core-shell nanospheres and the corresponding resonant wavelength can be tuned easily by various methods. So it is convenient to acquire a double resonant situation which means the pump light and the THG signal both can be coupled to some cavity modes. Numerical simulations show that the THG intensity in the far field can be enhanced remarkably when the THG signal also couples well with the high order cavity mode. Also, the coupling efficiency depends on the multipolar moment of the THG signal which is governed by the resonant symmetry at the pump wavelength. Thus the symmetry matching of the involved cavity modes may heavily affect the THG efficiency. It is calculated that when double resonant situation occurs the THG intensity is greatly enhanced, compared to single resonant situation. Further, when the two cavity modes involved match well with each other, namely with the same multipolar moment, the final THG efficiency will display a dramatic enhancement up to 3 magnitudes. Subsequent theoretical analysis indicates that changing third-order nonlinear susceptibility of the metal shell while keeping that of the core constant has almost no effect on THG efficiency.

3. Calculation results and discussion

As a result of phase delay, the nanospheres have lots of plasmonic cavity modes ranging from visible area to near infrared in dielectric-metal core-shell nanocavity while the cavity modes all have narrow line width and different resonant frequencies, which can be adjusted easily by changing nanostructures' geometric parameters. In this letter, our research object is a single dielectric-metal core-shell nanosphere in air. The dielectric core's refractive index is 1.59 with a radius of 500nm and the metal shell is silver with a thickness of 50nm. Fig. 1(a) is total linear absorption spectrum numerically simulated by COMSOL Multiphysics and the inset is the structure schematic diagram. The pump light propagates along the z axis and its electric field polarizes along the x axis. We choose 1390nm, the resonant wavelength of TM21 in near infared, as pump wavelength in the next nonlinear simulation. And in the corresponding triple frequency range, five high order cavity modes, TM_{52}, TE_{13}, TM_{23} , TE_{61} and TE_{32}, are used to achieve double resonant conditions later.

For nonlinear simulations, third-harmonic fields are calculated by assuming that the fundamental fields are negligibly affected, undepleted pump approximation. Here we take the high core's and ignored shell's third order nonlinear susceptibility. To explore the influence of double resonance on THG, we simulated the THG intensity from this nanosphere cavity excited by pump wavelength changed from 1350nm to 1520nm in near infrared, shown as Fig. 1(b). We can conclude that both plasmonic cavity resonance excited by pump light and THG signal can enhance the THG intensity in far field.

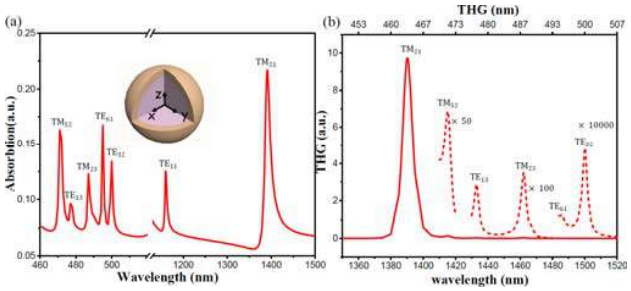


Figure 1: Linear and nonlinear response of the plasmonic dielectric-metal core-shell nanocavity excited by plane wave.

To achieve double resonant conditions, we tune the refractive index of dielectric in visible range to an appropriate value which makes the resonant wavelength of a high order cavity be a third of pump wavelength. The THG intensity when different high-order modes coupled with TM_{21} are shown in Fig. 2(a). Comparing Fig. 1(b) and Fig. 2(a), THG intensity emitted from the nanosphere on double resonant conditions is more significantly improved than that on not only single pump resonant situation but also single THG resonant situation. And the THG intensity on the double resonant condition that TM_{21} is coupled well with TM_{23} displays a dramatic magnification up to 3 magnitudes. It is obvious that the double resonant condition achieved by the coupling of two cavity modes in the same order can lead to the most efficient enhancement of THG. We can arrive the same conclusion when TE_{11} is coupled with the five modes respectively, shown as Fig. 2(b).

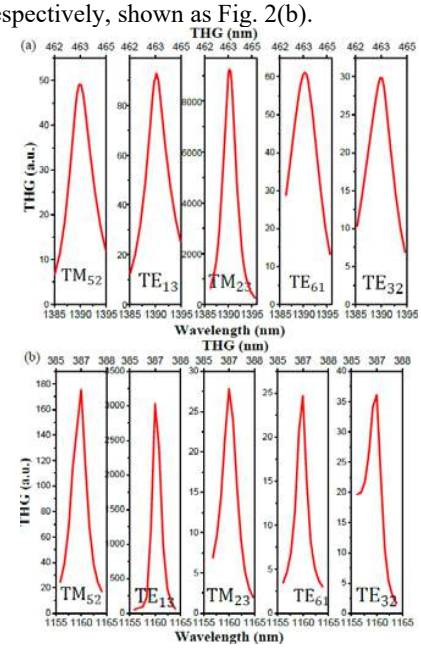


Figure 2: THG intensity at the pump wavelength of (a) 1390nm(TM_{21}) and 1161nm(TE_{11})in different 5 double resonant situations.

We infer that the good overlap of electric field distribution between same-order pump and THG modes results a stronger nonlinear source and the THG is enhanced in generation process. Beyond that, the highest coincidence of symmetry between the two modes with the same angular momentum lead to the strongest THG emitted from the sphere cavity. And subsequent theoretical analysis indicates that changing third-order nonlinear susceptibility of the metal shell while keeping that of the core constant has almost no effect on THG efficiency, shown as Fig. 3.

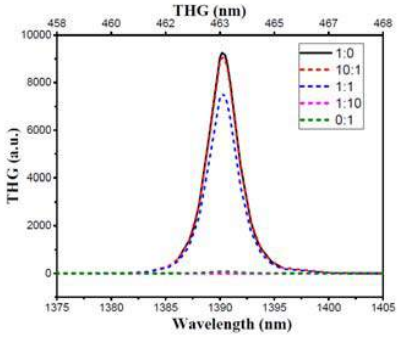


Figure 3: THG intensity with different third-order nonlinear susceptibility ratio between the core's and the shell's.

4. Conclusions

Numerical simulations show that the THG intensity in the far field from a metallic core-shell nanostructure can be enhanced remarkably while the THG signal couples well with the high order cavity mode. And the coupling efficiency depends on the multipolar moment of the THG signal which is governed by the resonant symmetry at the pump wavelength. Thus the symmetry matching of the involved cavity modes may greatly affect the THG efficiency. It is calculated that when double resonant situation occurs, the THG intensity is enhanced more than single resonant situation. And when the two cavity modes involved match well with each other, the final THG intensity will engage a dramatic enhancement up to 3 magnitudes. Subsequent theoretical analysis indicates that varying third-order nonlinear susceptibility of the metal shell and fixing that of the core have almost no effect on THG. It is worth mentioning that, the resonance positions can be easily changed by separating the shell's center to the core's or changing its geometric parameters in the core-shell structure.

References

[1] Hillenbrand R, Taubner T, Keilmann F. Phonon-enhanced light matter interaction at the nanometre scale. Nature 418, 159-162(2002).

[2] Klein M W, Enkrich C, Wegener M, et al. Second-harmonic generation from magnetic metamaterials. Science 313, 502-504(2006).

[3] Pu Y, Grange R, Hsieh C L, et al. Nonlinear optical properties of core-shell nanocavities for enhanced second-harmonic generation. Phys. Rev. Lett. 104, 207402(2010).

[4] Farnesi D, Barucci A, Righini G C, et al. Optical frequency conversion in silica-whispering-gallery-mode microspherical resonators. Phys. Rev. Lett. 112, 093901(2014).

Engineering optical responses of plasmonic objects with a hyperbolic coating

Pan Wang[1,*], Alexey V. Krasavin[1], Francesco N. Viscomi[2], Ali M. Adawi[2], Jean-Sebastien Bouillard[2], Diane J. Roth[1], Giovanni Sartorello[1], and Anatoly V. Zayats[1]

[1]Department of Physics, King's College London, Strand, London WC2R 2LS, UK
[2]School of Mathematics and Physical Sciences, University of Hull, Cottingham Road, Hull, HU6 7RX, UK
*corresponding author, E-mail: pan.wang@kcl.ac.uk

Abstract

We report the engineering of optical responses of plasmonic objects by coating them with a layer of anisotropic metamaterial, which displays a hyperbolic dispersion and allows the design of refractive index on demand. This is experimentally demonstrated by coating Au nanospheres with alternating SiO_2 and Au multishells, which creates rich plasmonic modal structures with high tuneability and produces highly enhanced local fields.

1. Introduction

The ability to engineer the optical response of a plasmonic object is highly desired to achieve better control over light-matter interactions. Due to the sensitivity of plasmon resonances to the surrounding media, isotropic dielectric coating is a straightforward way to modify the optical properties of a plasmonic object. However, the provided tuneability is limited by the range of refractive indices of available materials [1]. Here, we show that coating of plasmonic objects with an anisotropic hyperbolic metamaterial, which allows the design of refractive index on demand, provides greater flexibility to engineer their interaction with light.

2. Results

The most common realizations of hyperbolic metamaterials are metallic nanorod arrays [2] or layered metal-dielectric structures [3,4]. The latter method is particularly convenient for fabricating hyperbolic materials on various nanoscale objects. The hyperbolic coating of colloidal metallic nanoparticles can be realized by coating them with alternating metal-dielectric multishells using a wet chemical method.

2.1. Realization of hyperbolic coating

To experimentally demonstrate the feasibility of such method, we coated 62-nm diameter Au nanospheres (Fig. 1a) with alternating SiO_2 and Au shells (plasmonic nano-onions). The SiO_2 shells were fabricated by the hydrolysis of tetraethylorthosilicate onto an Au surface, while the Au shells were fabricated using seed-mediated reduction of Au ions onto a SiO_2 surface. Figure 1b-1d present the TEM images of the resulting onion-like plasmonic nanoparticles with 1, 2, and 3 pairs of SiO_2/Au shells, where the core and individual shells can be clearly identified. The thickness of each SiO_2 shell is about 10 nm, while the thickness of each Au shell is about 20 nm.

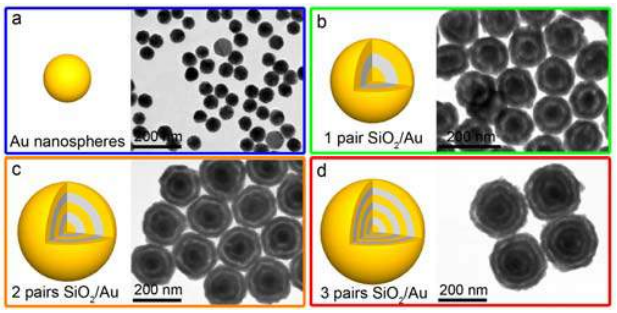


Figure 1: TEM images of plasmonic nano-onions with an increasing number of SiO_2/Au pairs. (a) Au nanospheres with 62-nm diameter. (b-c) Nano-onions with 1, 2 and 3 pairs of SiO_2/Au shells, respectively.

2.2. Optical properties of plasmonic nano-onions

In contrast to uncoated Au nanospheres, Au nanospheres coated with SiO_2/Au multishells, present a rich, broadband and highly tuneable plasmonic modal structure. With an increasing number of SiO_2/Au pairs, the optical properties of plasmonic nano-onions change dramatically. The extinction spectrum of nanoparticles changed from having one resonance peak at 534 nm for uncoated Au nanospheres (Fig. 2a) to having two resonance peaks at 572 and 787 nm (Fig. 2b) when the first pair of SiO_2/Au shells was coated. After the adding of the second pair of SiO_2/Au shells, an additional resonance appears around 1208 nm (Fig. 2c). Finally, when the third pair of SiO_2/Au shells was added, the extinction spectrum of nano-onions shows four resonance peaks around 614, 751, 875 and 1171 nm, respectively, as shown in Fig. 2d.

To get an insight into the experimental observations, finite element numerical simulations of scattering of an electromagnetic wave on plasmonic nano-onions was

performed, and the corresponding optical cross-sections were calculated.

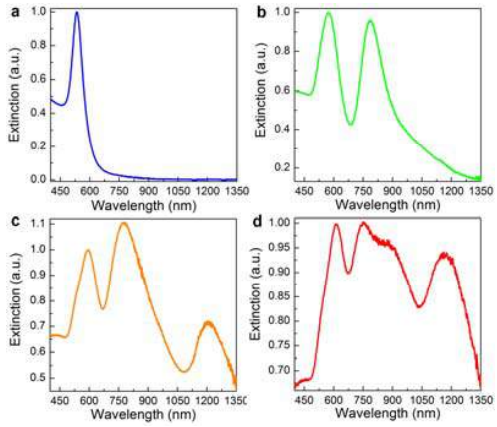


Figure 2: Extinction spectra of (a) uncoated Au nanospheres and nano-onions with (b) 1, (c) 2 and (d) 3 pairs of SiO_2/Au shells, respectively.

3. Conclusions

In conclusion, we have investigated the coating of a plasmonic object with an anisotropic hyperbolic metamaterial. The proposed approach provides an attractive way for designing an optical response of a plasmonic object with great flexibility and broadband response, and is extremely interesting for a wide range of applications such as plasmon-enhanced spectroscopy, nonlinear optics, nanoscale lasing, hot-electron effects, and optical sensing.

Acknowledgements

This work has been funded in part by the Engineering and Physical Sciences Research Council (UK) and the European Research Council iPLASMM project (321268). A.V.Z. acknowledges support from the Royal Society and the Wolfson Foundation.

References

[1] I. Pastoriza-Santos, J. Pérez-Juste, L. M. Liz-Marzán, Silica-coating and hydrophobation of CTAB-stabilized gold nanorods. *Chem. Mater.* 18: 2465–2467, 2006.

[2] L. H. Nicholls *et al.,* Ultrafast synthesis and switching of light polarization in nonlinear anisotropic metamaterials. *Nat. Photon.* 11: 628–633, 2017.

[3] X. D. Yang, J. Yao, J. Rho, X. B. Yin, X. Zhang, Experimental realization of the three-dimensional indefinite cavities at the nanoscale with anomalous scaling laws. *Nat. Photon.* 6: 450–454, 2012.

[4] D. Lu, J. J. Kan, E. E. Fullerton, Z. W. Liu, Enhancing spontaneous emission rates of molecules using nanopatterned multilayer hyperbolic metamaterials. *Nat. Nanotechnol.* 9: 48–53, 2014.

All-optical dynamic metasurface for terahertz wave-front modulation

Yan Zhang*, Jingying Guo, Teng Wang, and Xinke Wang

Department of Physics, Capital Normal University, Beijing Key Lab for Metamaterials and Devices,
Key Lab of Terahertz Optoelectronics, Ministry of Education, and Beijing Advanced Innovation Center for Imaging Technology, Beijing 100048, China
*corresponding author, E-mail: yzhang@cnu.edu.cn

Abstract

A novel configuration for active modulation of terahertz (THz) wave-front which is based on the all-optical dynamic metasurface is proposed. The dielectric metasurface is generated by pumping a thin silicon wafer with structured femtosecond light. Arbitrary pure phase modulation for THz radiation can be achieved. Several devices based on this technology, such as focal length tunable lens and dynamic holograms, have been experimentally demonstrated. This approach may pave the avenue of dynamic modulation of wave-front for THz imaging and communications.

1. Introduction

Terahertz (THz) radiation, which is sandwiched between the infrared and microwave in the electromagnetic spectrum, has many potential applications, especially in THz imaging and communications [1, 2]. However, due to the long wavelength property of the THz radiation, the devices which are used to modulate the wave-front are quite large, which blocks the integration of the THz system. There are no suitable materials to record the wave-front information of THz light, let alone to display a complex THz wave field. Therefore, THz wave-front devices are quite necessary.

Metasurfaces, a kind of ultrathin planar surfaces made of subwavelength metallic or dielectric antennas, have shown the capability to arbitrarily modulate the frequency, amplitude, phase as well as polarization of light. The ultrathin planar lenses, vortex beam generator, spin selected lens and metasurface holograms have already been demonstrated in the THz range [3-5]. The thickness of these merasurfaces is only 1/4000 of the working wavelength. Furthermore, the subwavelength antenna cell of the metasurface provide unprecedented spatial resolution which allows high precision and low noise in the modulation of wave-front. However, the function of the devices is fixed once they were fabricated. Many efforts have been made to exploit tunable and switchable metasurfaces using thermal-sensitive phase change materials [6], vanadium dioxide [7], and graphene [8], however, achieving dynamic devices with pixel-level reconfigurable metasurface is still a challenge. Using the electrical diode, 1-bit coding metasurfaces has been demonstrated in the microwave range, but this method cannot be applied in the THz range since the diode is too large for the THz radiation, furthermore, 1-bit modulation is not enough for precise control of wave-front.

In this presentation, we will propose a new approach to implement dynamic metasurface for THz wave-front modulation. Pure phase modulation is achieved and several functional devices are generated using this technology. Experimental results demonstrate the validity of the approach.

2. Basic idea

We propose an all-optical controllable pure phase spatial terahertz modulator, which is structure free, high resolution and broadband, to actively manipulate the THz wave front. The key component of this modulator is a thin silicon wafer which is illuminated by a structured control beam. The control beam modulated by a conventional digital micromirror device (DMD) illuminates the surface of the thin silicon wafer to produce the corresponding pattern of photo-generated carriers. The unit cell of the projected pattern is a bar structure with different rotation angle, thus a dielectric bar antenna is generated in the wafer. When this photo-generated antenna is illuminated by a left circularly polarized (LCP) or right circularly polarized (RCP) THz light, the light with opposite helicity (RCP or LCP) will be excited and imprinted with a Pancharatnam-Berry (PB) phase. The PB phase is related to the orientation angle of the antenna by $\emptyset(x,y) = 2\sigma_{\pm}\theta(x,y)$, where $\sigma_{\pm} = \pm 1$ is determined by the helicity of the incident and excited THz light and $\theta(x,y)$ is the rotation angle of the bar. The amplitude of generated cross polarization light is kept as a constant since the size of the bar antennas is the same. Since the rotation of each bar antenna can be controlled by the DMD independently, this device has a subwavelength resolution. The cross polarization light with preset phase modulation will generate the desired intensity distribution.

3. Experimental results

The dynamic metasurface is validated by proof-of concept experiments. The light generated by a 3 mJ amplifier is divided into three beams, one is control beam to generate the photo-generated antenna array in the silicon wafer via a DMD, another beam is used to generate THz radiation and the third one is employed to detect THz wave-front. A home built focal plane imaging system is combined with the control

beam to measure the modulated wave-front. The dynamic metasurface array contains 30*30 antennas. The pure phase holograms which can generate the letters “C”, “N”, and “U” are calculated with the simulated anneal algorithm, respectively, then the corresponding antennas array is designed and projected on the silicon wafer. The experimental results are shown in Figure 1. The up line presents the theoretical expectations and the bottom line displays the results obtained in the experiment. Good agreement between the theoretical expectations and experimental results can be found.

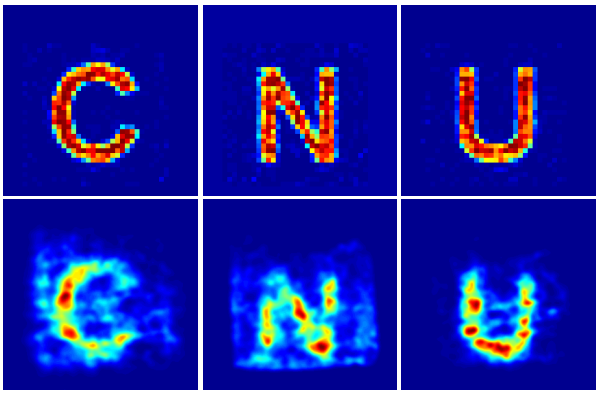


Figure 1: THz field distribution generated by the pure phase hologram. Up line, theoretical expectation and bottom line, experimental results.

4. Conclusions

In conclusion, we have proposed a new configuration for dynamical modulation of THz wave-front. A spatial light modulator is use to project a special pattern on a thin silicon ware, a dielectric metasurface will be generated. The phase of the THz radiation can be modulated by this dielectric metasurface. Several functional devices have been implemented using this technology. Experimental results demonstrate the validity of this technology. Other parameters of the THz wave-front can also be modulated by tuning the shape and size of antenna.

Acknowledgements

This work was supported by the 973 Program of China (grant no. 2013CBA01702) and the National Natural Science Foundation of China (grant nos. 11404224, 1174243, and 11774246).

References

[1] M. Tonouchi, Cutting-edge terahertz technology. *Nat. Photonics* 1: 97–105, 2007.

[2] T. Nagatsuma, G. Ducournau, C. C. Renaud, Advances in terahertz communications accelerated by photonics. *Nat. Photonics*, 10: 371–379, 2016.

[3] D. Hu, X. K. Wang, S. F. Feng, J. S. Ye, W. F. Sun, Q. Kan, P. J. Klar, and Y. Zhang, Ultrathin terahertz planar elements, *Adv. Opt. Mat.*, 1: 186-193, 2013.

[4] J. W. He, X. K. Wang, D. Hu, J. S. Ye, S. F. Feng, Q. Kan, and Y. Zhang, Generation and evolution of the terahertz vortex beam, *Opt. Express* 21 20230-20239, 2013.

[5] S. Wang, F. Zhao, X. K. Wang, S. L. Qu, and Y. Zhang, Comprehensive imaging of terahertz surface plasmon polaritons, *Opt. Express* 22: 16916-16924, 2014.

[6] Q. Wang, E. T. F. Rogers, B. Gholipour, C.-M. Wang, G. H. Yuan, J. H. Teng, and N. I. Zheludev, Optically reconfigurable metasurfaces and photonic devices based on phase change materials. *Nat. Photonics* 10: 60–65, 2015.

[7] G. Kaplan, K. Aydin, and J. Scheuer, Dynamically controlled plasmonic nano-antenna phased array utilizing vanadium dioxide, *Opt. Mater. Express* 5: 2513, 2015.3

[8] Y.-W. Huang, H. W. Lee, R. Sokhoyan, R. A. Pala, K. Thyagarajan, S. Han, D. P. Tsai, and H. A. Atwater, Gate-tunable conducting oxide metasurfaces, *Nano Lett.* 16: 5319–5325, 2016.3

[9] L. L. Li, T. J. Cui, W. Ji, S. Liu, J. Ding, X. Wan, Y. B. Li, M. H. Jiang, C.-W. Qiu, and S. Zhang, Electromagnetic reprogrammable coding-metasurface holograms, *Nat. Commun.* 8:197 2017.

Metasurface-assisted plasmonic wavefront modulation with incident polarization

Luping Du*, Chonglei Zhang, Jiao Lin and Xiaocong Yuan

Nanophotonics Research Centre, Shenzhen University, Shenzhen, 518060, China.
*corresponding author, E-mail: lpdu@szu.edu.cn

Abstract

I will introduce our recent work on manipulating and harnessing surface plasmon polaritons (SPPs) with incident polarization. A pair of rectangular-shaped nano-grooves as a meta-atom is employed for launching the SPPs. This kind of novel structured surfaces provides us more degrees of freedom on manipulating the SPPs, yielding many attractive techniques such as super-resolved imaging, on-chip nano-devices, etc.

1. Introduction

Surface plasmon polaritons (SPPs) are propagating surface waves confined at the interface between a dielectric and a conductor, which enable a variety of applications owing to their 2D-wave nature [1]. In order to harness SPPs for modern nanophotonic techniques, the manipulation of SPPs in a desired way is a crucial issue. Metasurfaces [2], which consist of assemblies of nanoscatterers with feature sizes reaching into the sub-wavelength scale, have rapidly gained profile in recent years owing to their flexibility and effectiveness in shaping the wavefront of a beam. The interaction of light with structured surfaces accompanies pronounced coupling between polarization and phase, which are normally two relatively independent properties of light showing little interplaying during propagation in free space. The remarkable polarization-phase coupling induced by metasurfaces leads to various applications in optics, physics, nanoscience, etc.

The nano-scatterers that form the metasurfaces are often polarization-selective. This anisotropic response of nano-scatterers limits the polarization as a degree of freedom for modulating the wavefront. Here we demonstrate that it is possible to dynamically control a plasmonic wavefront with incident polarization, using a pair of rectangular-shaped nano-grooves as a meta-atom [3, 4]. The initial phase of an SPP emitted from the metasurface is linked to the elliptical polarization state of the incident beam. This enables continuous and linear control of the wavefront of the SPP without affecting its amplitude. This type of optical modulation enables the dynamic control of the wavefront, which is useful for applications like plasmonic waveguides, structured-light illumination microscopy (SIM), and on-chip spin devices. As practical example, we built a plasmonic meta-SIM configuration, where the near-field SPP standing-wave is shifted linearly by changing the incident polarization, which improves both reliability and stability substantially as compared to the former pSIM configurations. The use of metasurfaces for SIM will increase the degrees of freedom such as polarization and aid the development of future SIM technology.

2. Results

A schematic illustration of the metasurface is shown in Fig. 1.The metasurface consists of a pair of vertical arrays of nano-apertures in a gold film, which are rectangular shaped and perpendicular to each other. The distances between the nano-apertures are t and d along the x and y directions, respectively. The metasurface is illuminated with an elliptically-polarized light, emitting SPPs at the air-gold interface.

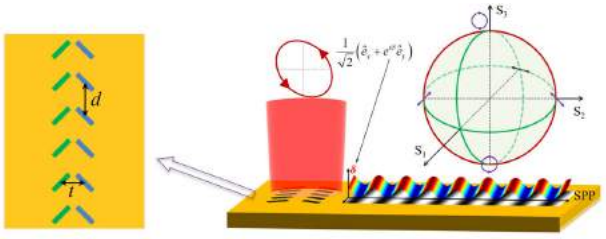


Figure 1: Schematic illustration of the configuration, where the wavefront of SPP emitted from the metasurface can be modulated continuously and linearly by polarization.

The simulation results with finite-difference time-domain (FDTD) method are shown in Fig.2, where, from top to bottom, the near field patterns of SPPs are shown. They are emitted from the metasurface with incident polarizations of right-handed circular polarization (RCP), linear polarization oriented 45º (LP45), left-handed circular polarization (LCP) and linear polarization oriented 135º (LP135), respectively. We can clearly see that, by tuning the incident polarization along the longitude line, as marked with red at the Poincare sphere (Fig. 1), we can achieve a linear phase-shift of the SPP wavefront.

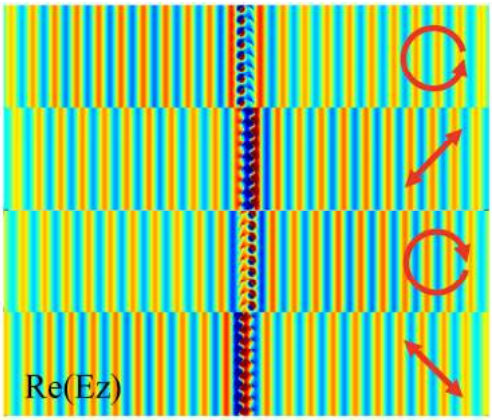


Figure 2: Numerical study of SPP wavefront modulation by polarization with FDTD

3. Conclusions

In conclusion, using a suitably designed metasurface, we accomplished dynamic control of a SPP wavefront using incident polarization. We studied the relationship between the polarization state of incident beam and the phase of the SPP. For this we applied a rigorous analytical analysis and a numerical simulation with FDTD. This type of optical modulation enables dynamic control of the wavefront which is useful for applications like plasmonic waveguides, structured-light illumination microscopy (SIM), on-chip spin devices, etc.

Acknowledgements

This work was supported by the National Natural Science Foundation of China under Grant Nos. 61490712, 61622504, 11504244; and the Science and Technology Innovation Commission of Shenzhen under grant Nos. KQTD2015071016560101, ZDSYS201703031605029.

References

[1] Barnes, W. L., Dereux, A. & Ebbesen, T. W. Surface plasmon subwavelength optics. *Nature* 424: 824–830, 2003.

[2] Yu, N. F. & Capasso, F. Flat optics with designer metasurfaces. *Nat. Mater* 13: 139–150, 2014.

[3] Lin, J. et al. Polarization-controlled tunable directional coupling of surface plasmon polaritons. *Science* 340: 331–334, 2013.

[4] L. P. Du, S. S. Kou, E. Balaur, J. Cadusch, A. Roberts, B. Abbey, X. C. Yuan, D. Y. Tang, and J. Lin, *Nat. Commun* 6: 10051, 2015.

Wavefront engineering based on complex amplitude modulation with metasurfaces

Lingling Huang[1,2], Song Xu[1], Ruizhe Zhao[1],Yongtian Wang[1], Thomas Zentgraf[2]

[1]School of Optics and Photonics, Beijing Institute of Technology, Beijing, 100081, China
[2]Department of Physics, University of Paderborn, Warburger Straße 100, Paderborn, 33098, Germany
*corresponding author, E-mail: huanglingling@bit.edu.cn

Abstract

Metasurfaces have attracted extensive interests due to their ability to locally manipulate optical parameters of light and easy integration to complex optical systems. Here, we propose and experimentally demonstrate novel methods for either generating independently selective diffraction orders or near-field plasmonic beam shaping based on complex amplitude modulation with metasurfaces, respectively. Our developed method with metasurfaces can provide an attractive platform for applications both in near- and far-field wavefront engineering.

1. Introduction

Metasurfaces have attracted great interests as novel kinds of flat artificial electromagnetic functional devices due to their unusual physical properties. By patterning judiciously designed subwavelength nanoantennas or resonator along an optical surface, strong light interaction and local optical response modulation can be achieved. In contrast to conventional methods that utilize phase accumulations along optical paths, the abrupt phase shift can be realized within an extremely thin layer compared to the wavelength of light. Besides, the other local optical parameters, such as amplitude, polarization state, angular momentum or wave vector, can also be abruptly changed by metasurfaces, which make it possible to modulate a set of optical properties directly on the surface and in the scattered far-field. As a burgeoning research field, metasurfaces have shown great promise for novel design in a great number of device applications such as flat lenses, wave plates, beam deflectors, switchable surface plasmon polariton couplers, and high resolution three-dimensional holography.

Specially, geometric metasurfaces, based on a Pancharatnam-Berry (PB) phase principle, are one of the most exciting recent progress in metasurfaces due to their capability of transferring the field of the emerging beams into demanded profiles based on optical spin-orbit interactions, with which phase profiles can be directly encoded by the azimuthal orientation of meta-atoms. Furthermore, by simultaneously tuning the geometry parameter of each meta-atom, the amplitudes can be readily modulated, which allows the complex amplitude modulation.

Here, we propose and experimentally demonstrate both far-field and near-field wavefront engineering based on the complex amplitude modulation with metasurfaces. As proofs of concept, *out-of-plane* two-dimensional (2D) independently selective diffraction orders and *in-plane* Airy plasmons are generated based on the same principle but totally different metasurfaces are demonstrated, respectively. We show the universalities and flexibilities of our method, which can be utilized in various wavefront engineering applications.

2. Selective diffraction orders generation with dielectric metasurfaces

A novel approach for the generation of two-dimensional selective diffraction orders based on tailored dielectric metasurfaces with complex amplitude modulation is demonstrated. By positioning the azimuthal angles of dielectric nanofins and simultaneously tuning the geometry parameters (length and width) of each nanofin, the generated phase and amplitude can be directly modulated. Such dielectric nanofins can generate different dynamic phase delays for different geometry parameters even with the same orientation angle. Therefore, each nanofin has its own initial transmission phase change, which will be combined with the PB phase that results from the azimuthal angle to achieve the final desired local phase modulation.

Figure 1 schematically illustrates the generation and reconstruction procedure of 2D selective diffraction orders based on our proposed dielectric metasurface [1]. Silicon nanofins are arranged on a glass substrate with the same lattice constants in both directions. For experimental validation of the proposed concept, we designed and fabricated a sample for which the selected diffraction orders form a pattern with the word “META” while all other diffraction orders are simultaneously suppressed. The desired diffraction orders can be expressed as the superposition of Fourier expansion. In our experiment, we analyzed the distribution uniformity and angles of the diffraction orders and compared them with a phase-only design. The simulation results and the experimental far-field images are well consistent with each other, confirming the

possibility to achieve selective diffraction with dielectric metasurfaces.

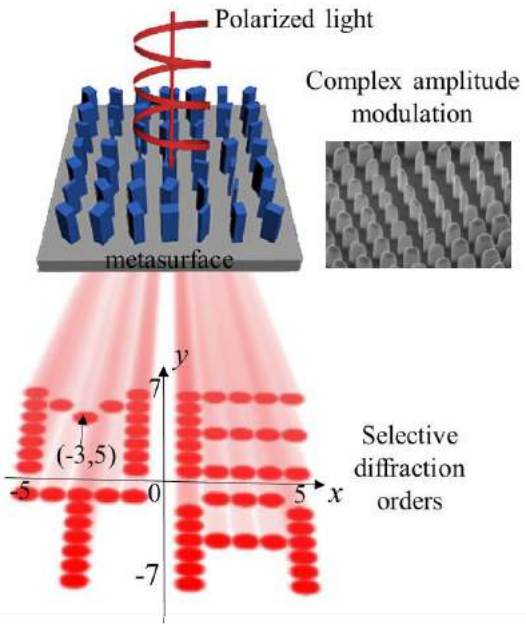


Figure 1: Schematic illustration of the complex amplitude modulation for selective diffraction with a dielectric metasurface. The diffractions orders are chosen to show a pattern of the word "META". The SEM image shows a typical example of a dielectric metasurface made of silicon nanofins.

3. Near-field surface plasmon manipulation with palsmonic metasurfaces

So far, most studies on metasurfaces have focused on the manipulation of propagating waves. Very recently, a few of studies have employed metasurfaces for manipulating SPPs in near field. Actually, with the ability of modulating local optical properties pixel by pixel, metasurfaces provide a convenient and flexible way for the controlling of SPP fields.

The metasurfaces for the generation of SPP fields by complex amplitude modulation as well as result detection is schematically shown in Figure 2 [2]. Subwavelength scale nano apertures are etched on a 40 nm thick gold film which is deposited on a glass substrate. The nano apertures are arranged with constant periods along both the horizontal axis (*x*-axis) and the longitudinal axis (*y*-axis), respectively. With a constant width, each nano aperture has its characteristic length and orientation angle, thus permitting the manipulation of both amplitude and phase of SPPs. The nano aperture arrays are fabricated with a focused ion beam so that the metal is completely removed in the corresponding regions. With the normal incidence of CP light, SPPs can launch from the nano aperture arrays and propagate on the air-gold interface. In order to verify the complex amplitude modulation with metasurfaces, a plasmonic Airy beam is generated as an example to manipulate SPP profiles. The field intensity distribution of propagation is measured by scanning near-field optical microscope (SNOM). This approach for SPPs modulation promise a variety of functionalities and applications, such as on-chip spectroscopy, plasmonic detectors and integrated plasmonic circuit.

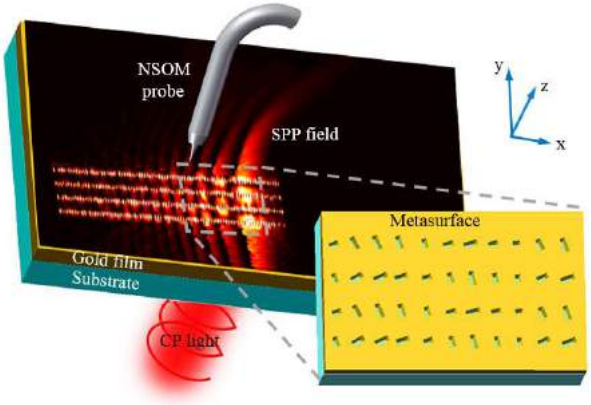


Figure 2: Schematic illustration of the proposed complex SPP fields manipulation based on metasurface composed of nano aperture arrays.

4. Conclusions

The above two demonstrations of complex amplitude manipulation with either dielectric or plasmoinc metasurfaces are based on the same PB phase principle, together with the combination of dynamic phase modulation as well as independent amplitude modulation. We show the universalities and flexibilities of our method. Such complex amplitude manipulation with metasurfaces can be used for potential applications in free-space/plasmonic beam shaping, integrated optoelectronic systems and holography.

Acknowledgements

The authors acknowledge the funding provided by the National Natural Science Foundation of China (No. 61775019, 61505007) program and Beijing Municipal Natural Science Foundation (No. 4172057). L.H. acknowledge the support from Beijing Nova Program (No. Z171100001117047) and Young Elite Scientists Sponsorship Program by CAST (No. 2016QNRC001).

References

[1] Song, X., Huang, L., Tang, C., Li, J., Li, X., Liu, J., Wang, Y., Zentgraf, T. Selective diffraction with complex amplitude modulation by dielectric metasurfaces. *Advanced Optical Materials*. 1701181 (2018).

[2] Song, X., Huang, L., Sun, L., Zhang, X., Zhao, R., Li, X., Wang, J., Bai, B., Wang, Y. Near-field plasmonic beam engineering with complex amplitude modulation based on metasurface. *Applied Physics Letters* (2018).

Highly uniform and controllable metasurface structures fabricated by shaped femtosecond laser: Fundamentals and Applications

Xiaowei Li

School of Mechanical Engineering, Beijing Institute of Technology, Beijing ,China

*corresponding author, E-mail: lixiaowei@bit.edu.cn

Abstract

Femtosecond lasers have been proven to be a powerful tool for micro- and nanoscale fabrication. Compared with traditional laser fabrication techniques that use longer pulse, femtosecond laser fabrication offers several key advantages due to its unique characteristics of ultrashort pulse width and extremely high peak intensity. In this study, the formation principle of surface structures by laser direct writing is intensively investigated, which reveals the fabrication rule and modulation mechanism. Several flexible and efficient approaches have been proposed to fabricate highly uniform and controllable metasuface structures by shaping femtosecond laser pulse in temporal or spatial domains. The flexible and high efficiency of this structuring strategy should facilitate applications in numerous fields, including metamaterials, nanoplasmonics, nanoelectronics, and mechatronics.

1. Introduction

Highly uniform surface micro/nano-structures on bulk solids with controllable morphologies and arrangements have been attracting great attention due to their scientific and technological properties in controlling optical, mechanical, wetting, and other properties. Significant effort has been devoted to the exploration of effective approaches for realizing various controllable surface patterning. Laser treatment is one of the main techniques for designing nano- and microstructures due to its excellent controllability of the surface micro/nanostructures compared to other processes. Especially in recent years, femtosecond (fs) laser surface micro/nanostructuring has been demonstrated as a versatile technology for producing a large variety of micro/nanostructured materials suitable for a wide range of applications.However, the lack of systematic mechanism support for the laser interaction mechanism and the fabricated material evolution property limits the controllable fabrication of surface micro/nano- structures and the development of its practical application.

The overcome of these difficulties relies on the further research on the modulation and interaction mechanism of locallized transient materials properties during fs laser irradiation. Professor Jiang et al. proposed the core idea of electrons dynamics control (EDC) based on the temporally and spatially pulse shaping. By shaping the fs laser pulse in temporal and spatial domain, we are able to control the localized transient electron dynamics, and then to modify localized transient materials properties, and finally to finish the optimization of the fabrication structures. The laser and material are the vital factors during the fabrication process.

In this study, the fs laser-induced micro/nano-structures are developed from two perspectives in laser parameter and material property. Firstly, the formation fundamental principle of surface structures is intensively investigated, which reveals the fabrication rule and modulation mechanism. And on this basis, we propose the temporal fs laser pulse shaping method to control the morphology of surface structures. Secondly, Two novel fs laser spatial pulse shaping method are proposed based on the Fresnel diffraction effect of squared hole and dual color dispersion effect, by which the morphology and arrangement of surface micro/nano- structures and the plasmonic nano-structures can be effectively modulated. Finally, a flexible and efficient approach is proposed to fabricate highly uniform and controllable nanograting structures through chemical-etching-assisted femtosecond laser modification. The potential applications in structural color and wetting ability of these fabricated surface structures are also discussed.

2. Fs laser induced periodic surface structures based on the temporally and spatially pulse shaping

Based on the surface plasmon polariton (SPP) excitation, propagation mechanism and property, a grating aided coupling and directional scattering mechanism is proposed. Continuous modulation of the polarization-dependent fs laser induced periodic surface structures (also termed as ripples) can be achieved based on the control of SPP dynamics. The geometrical evolution of surface micro/nano- structures, which determined by the irradiated pulse energy is investigated. And it demonstrates the different role of SPP excitation and scattering effect with different surface micro/nano- structures. Furthermore, double fs laser pulse train is adoped to modulate the morphology of ripple structures. By controlling the pulse delay between the double pulse train, we can control the free electrons generation and recombination, and then to

control the SPP excitation and scattering, and finally achieve the arbitrary modulation on the anisotropic geometrical morphologies of ripple structures. Based on the geometrical morphology modulation of ripple structures, we can further modulate the scanned ripple line widths and the anisotropy of its formation and continuity, which provide technical support for the large-area uniform fabrication of ripple structures, and improve the fabrication efficiency.

Based on the Fresnel diffraction effect of squared hole, a novel spatial fs laser pulse shaping method is proposed aided by squared grids, the novel method enables the programmable modulation of the surface micro/nano-structure's geometrical morphology and its arrangement. The morphology can be modulated based on the threshold effect of the surface micro/nano- structure formation. And the formation mechanism of striped ripple lines induced by the squared grids-aided fs laser is investigated based on the SPP excitation and scattering effect. For the dynamic scanning situation, morphology control of the surface micro/nano- structures based on the scanning speed is deeply investigated experimentally. Especially, the abnormal abltion enhancement effect and polarization-sensitive ablation effect is also investigated theoretically and experimentally.

Based on the focusing aberration and dispersion effect with different wavelength, another novel spatial fs laser pulse shaping method via the square grids is proposed for the modulation of the surface micro/nano- structures fabrication. And the implementation principle and property are investigated theoretically and experimentally. Based on this novel method, we can fabricated a concentric micro-structure on metallic films, on which the SPP excitation, propagation, and focusing are investigated experimentally and theoretically. Furthermore, we promote this method for the fabrication of semiconductor/metallic plasmonic nano-structures. The control of the irradiated parameter and film thickness enables the morphology modulation of the plasmonic nano-structures, and their optical properties are also investigated.

3. Highly uniform and controllable surface structures through chemical-etching-assisted fs laser modification

A flexible and efficient approach has been proposed to fabricate highly uniform and controllable surface structures through chemical-etching-assisted femtosecond laser modification. Through precisely controlling laser-material interaction process, alternating amorphous and crystalline nanograting structures can be fabricated by femtosecond laser interaction, with almost no material removal. Subsequently, assisted chemical etching, highly uniform nanograting structures would be processed on the silicon surface, due to the different etching rate of amorphous silicon and crystalline silicon in KOH solution. In addition, the height of the nanograting structures formed after chemical etching could be precisely controlled by controlling the etching process.

The structural color of the Si surface with 2D nanograting structures fabricated by this approach was investigated. When the viewing angle was gradually changed, colors of the visible spectrum from red to purple were observed due to the chromatic dispersion, and the nanograting structures fabricated in this approach exhibit more favorable structural color characteristics. Furthermore, this approach has the ability to fabricate any complex pattern with remarkable structural color characteristics in silicon.

Acknowledgements

The authors acknowledge the funding provided by the National Natural Science Foundation of China (No. 51675049) program, Beijing Municipal Natural Science Foundation (No. 3172027), and Young Elite Scientists Sponsorship Program by CAST (No. 2016QNRC001).

References

[1] Wang A., Jiang L., Li X., et al., Nanoscale material redistribution induced by spatially modulated femtosecond laser pulses for flexible high-efficiency surface patterning, *Optics Express* 25, 31431(2017).

[2] Han W., Jiang L., Li X., et al., Controllable Plasmonic Nanostructures induced by Dual-wavelength Femtosecond Laser Irradiation, *Scientific Reports* 7 (1), 17333(2017)

[3] Li X., Xie Q., Jiang L., Controllable Si (100) micro/nanostructures by chemical-etching-assisted femtosecond laser single-pulse irradiation, *Applied Physics Letters* 110, 181907(2017)

[4] Wang A., Jiang L., Li X., et al., Low-adhesive superhydrophobic surface-enhanced Raman spectroscopy substrate fabricated by femtosecond laser ablation for ultratrace molecular detection, *Journal of Materials Chemistry B* 5 (4), 777-784(2017)

[5] Han W., Jiang L., Li X., et al., Femtosecond laser induced tunable surface transformations on (111) Si aided by square grids diffraction, *Applied Physics Letters* 107, 251601(2015)

[6] Wang A., Jiang L., Li X., et al., Mask‐Free Patterning of High‐Conductivity Metal Nanowires in Open Air by Spatially Modulated Femtosecond Laser Pulses, *Advanced Materials* 27, 6238-6243(2015)

Controlling Light by Metasurfaces in the Linear and Nonlinear Regimes

Mengxin Ren[1], Di Zhang[1], Ninghui Gao[1], Wei Wu[1], Jingjun Xu[1]
[1]The Key Laboratory of Weak-Light Nonlinear Photonics, Ministry of Education, School of Physics and TEDA Institute of Applied Physics, Nankai University, Tianjin 300071, P.R. China
* corresponding author, E-mail: ren_mengxin@nankai.edu.cn

Abstract

Manipulation of light−matter interactions by tailored artificial microstructures is a key aspect of optics. During past decades, the developments of metamaterials or metasurfaces have provided a range of possibilities, for example nano-focusing, ultra-compact wave-plates, and low threshold optical switching, and so forth. In this talk we will give introductions to our recent works about controlling light in the matters of linear and nonlinear interactions in plasmonic metasurfaces, including light polarization control, beam splitting, and chromatic beam dispersing.

1. Introduction

Plasmonic metamaterials have opened up opportunities for tailoring the light−matter interactions. The localization of electromagnetic fields allows boosting linear/nonlinear processes in subwavelength dimensions, and various new type of components have been realized, for example ultrathin lenses, nano wave-plates, nonlinear optical elements, and so forth.[1-3] In this talk we will give introductions to our works about using the linear and nonlinear interactions in plasmonic metasurfaces to control light, including nonlinear light polarization control, beam splitting, and chromatic beam dispersing.

2. Light polarization control by nonlinear metasurfaces

Polarization of the electromagnetic wave has wide applications in areas extending from optical displaying, telecommunications, spectroscopic techniques, and so forth. Achieving control of light polarization on nanoscales is highly demanded for miniaturizing photonic devices. The current methods are mainly based on the electro-optic, and magneto-optic effects, which need conversion between optical and electronic signals. In order to realize the all-optical information processing, the polarization control in all-optical manner is highly desired.

In this talk we will review our works on nonlinear polarization control based on metasurfaces frameworks. In our paradigm, we combine the metallic nanostructure layer with a nonlinear switching layer and achieve more than 20° nonlinear optical polarization modulation under excitation of just a few milliwatts (Figure 1). Such components open the gateway towards the creation of various photonic functions, including novel displaying, optical computations, sensing, novel quantum optics devices, and real-time holograms.[4]

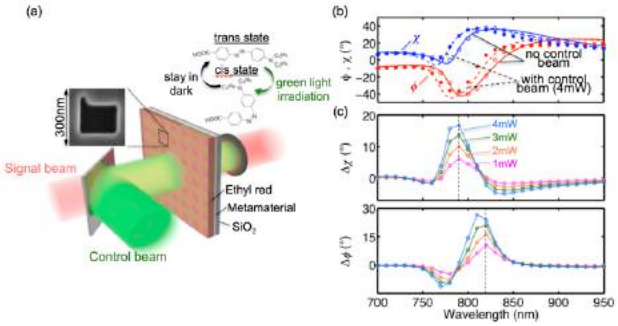


Figure 1: The nonlinear polarization control based on the hybrid metasurfaces. (a) The schematic of the hybrid metasurfaces. (b) Spectral dependence of the polarization changes by the nanostructure in terms of polarization azimuth rotation ϕ and ellipticity angle χ. (c) Measured nonlinear changes in the polarization parameters for various control light powers.

3. Beam splitting by ultrathin metasurfaces

Metasurfaces are proved to be able to steer incoming wave on demands by interactions between the light and the phase gradient at the interface. We realized a new type of ultrathin beam splitter based on metasurfaces. A beam splitter is an optical device that splits a beam of light into two or more directions. It is the crucial part of optics and photonics. Different types of beam splitters exist, but normally, traditional beam splitters are bulky sized. Beam splitters with nanoscale dimensions could be important for miniaturizing the components for integrated optical circuits.

We use the lithium niobate (LN) nano-cylinder arrays on fused quartz substrate as building blocks, which introduce 2π range tunable phase retardations to the transmitted light, with a broad transparency window covering the visible to infrared ranges. Two cylinder rows with reversed spatial radius gradient provides opposite phase gradients, thus refract the light into two different directions [Figure 2(a)]. Two dominant refracted components (T_+ and T_-) appears at the angle θ of 12.17º and -12.17º for the wavelength of 800nm determined by the generalized Snell's law.[5]

Variation of split ratios can be achieved by selectively increasing the loss of the first row of cylinders in each unit cell, while maintaining the second row unchanged. Hence the refracted light along the k_- direction would be decreased and split ratio between T_+ and T_- increases. As the imaginary part of refractive index κ increases from 0 to 1.0, the split ratio is effectively increased from 50:50 to 80:20 at 700nm [Figure 2(b)].

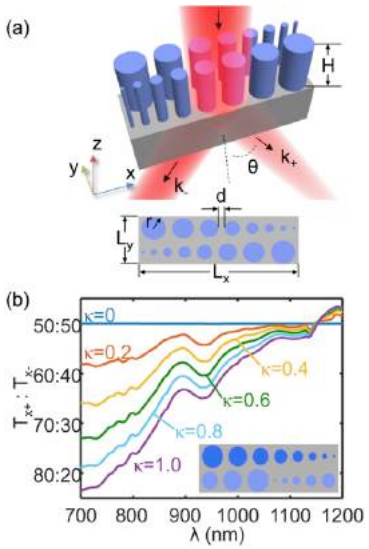


Fig. 1 The design of nano beam splitter based on LN metasurfaces. (a) The structure of a unit cell of LN beam splitting metasurface on a fused quartz substrate. It provides two opposite space-variant phase gradients to the incident light and cause the refraction in two directions (k_+ and k_-). (b) The tunability of split ratio of the LN nano beam splitter.

4. Meta-gratings with hyper-high dispersion

The phase gradients on metasurfaces provide an equivalent local momentum to the incident photon and lead to anomalous refraction (or reflection) along the angle determined by the ratio between local momentum and total photon momentum. It was observed that the anomalous refraction (or reflection) from metasurfaces is able to disperse incident light. However, the step of the phase discontinuity between neighboring sub-cells is not large in order to maintain the continuity of the output wavefronts. In this way, the anomalous refraction angle is small, which would limit the angular dispersion.

Here we will present a new type of grating design based on metasurface showing a hyper large angular dispersion. The idea is based on increasing the transmitted angle from metasurface by combining both the momenta provided by the phase gradient and sub-cell periodicity. We used the spatial variant geometric phase metasurfaces under illumination of circularly polarized light. The light diffraction angle could achieve more than 80° centered at 783nm. The angular dispersion can achieve about 0.5°/nm, which is more than 4 times larger than the conventional Littrow grating having the same period as the size of the sub-cell of the metasurface.[6]

Acknowledgements

This work was supported by National key R&D Program of China (2017YFA0305100, 2017YFA0303800); National Natural Science Foundation of China (61775106, 11711530205, 11374006, 11774185, 91750204); 111 Project (B07013); PCSIRT (IRT_13R29); Fundamental Research Funds for the Central Universities.

References

[1] N. Meinzer, W. L. Barnes and I. R. Hooper, Plasmonic meta-atoms and metasurfaces, Nat. Photon. 8, 889-898 (2014).

[2] M. Kauranen and A. V. Zayats, Nonlinear plasmonics, Nat. Photon. 6, 737-748 (2012).

[3] G. Li, S. Zhang and T. Zentgraf, Nonlinear photonic metasurfaces, Nat. Rev. Mater. 2, 17010 (2017).

[4] M. Ren, W. Wu, W. Cai, B. Pi, X. Zhang and J. Xu, Reconfigurable metasurfaces that enable light polarization control by light, Light: Sci. & Appl. 6, e16254 (2017).

[5] D. Zhang, M. Ren, W. Wu, N. Gao, X. Yu, W. Cai, X. Zhang and J. Xu, Nanoscale beam splitters based on gradient metasurfaces, Opt. Lett. 43, 267-270 (2018).

[6] N. Gao, D. Zhang, M. Ren, Wu, N. W. Cai, X. Zhang and J. Xu, To be submitted, (2018).

Unidirectional Second-Harmonic Generation with Plasmonic Nanoresonator Dimers

Shao-Ding Liu[1,2], and Dangyuan Lei[3]

[1]Key Lab of Advanced Transducers and Intelligent Control System of Ministry of Education, Taiyuan University of Technology, Taiyuan 030024, P. R. China
[2] Department of Physics and Optoelectronics, Taiyuan University of Technology, Taiyuan 030024, P. R. China
[3] Department of Applied Physics, The Hong Kong Polytechnic University, Hong Kong, China
*corresponding author, E-mail: liushaoding@tyut.edu.cn; dylei@polyu.edu.hk

Abstract

We propose and show that the second-harmonic generation of a single gold split-ring resonator dimer is strongly enhanced with the mode-matching condition. At the same time, the coupling between the two split-ring resonators results in constructive and destructive interferences on the two opposite emission directions, thereby leading to unidirectional second-harmonic generation. The simultaneously realization of enhanced and unidirectional second-harmonic generation makes the split-ring resonator dimer an excellent platform for realizing compact and on-chip ultrafast nonlinear optoelectronic devices.

1. Introduction

Nanoantennas composed of metallic nanoparticles (NPs) are key elements to devise functional subwavelength devices such as transmitters, receivers, and sensors, and the realization of directional scattering is important to improve the efficiency of on-chip nanodevices.[1] To obtain directional scattering, coherent coupling between two or more resonances (or resonators) is required to achieve constructive and destructive interferences.[2,3] Compared with its linear counterparts, directional second-harmonic (SH) emission is even more important to achieve compact and ultrafast nonlinear optoelectronic devices since the emission intensity is much weaker.[4,5] However, unidirectional SH emission with single plasmonic nanostructures is seldom reported. The main obstacle is that the SH emission cross section is orders weaker than that of the linear scattering, and SH emission would be too weak to be detected when the incidence is away for LSPRs. As a result, it is important to achieve enhanced and unidirectional SH emissions simultaneously for practical applications. In this study, we show that SHG of a single gold split-ring resonator (SRR) dimer is strongly enhanced with the mode-matching condition. At the same time, the coupling between the two SRRs results in constructive and destructive interferences on the two opposite emission directions, thereby leading to unidirectional SHG.

2. SH Emission with single SRRs

The magnetic dipole (MD) mode for a SRR can be excited when the incident polarization is along the split gap of a SRR. On the other hand, the electric dipole (ED) can be excited when the polarization is perpendicular to the split gap, and it is around the SH wavelength of the MD mode. The mode-matching condition for SHG, that is, the amplified nonlinear source with the MD mode and the amplified scattering with the ED mode, can be achieved with the SRR, thereby leading to enhanced SH emission.

3. Unidirectional SH Emission with SRR dimers

Since the SH emission with a single SRR can be treated as an oscillating electric dipole, far-field interferences may occur when two SRRs are coupling with each other, and it is possible to achieve unidirectional SH emission with a SRR dimer. For the incidences away from the bonding MD mode of the SRR dimer (the 1st and 5th panels, Figure 1a), there are obvious emission lobes at both positive and negative *y*-directions, and the emission intensity at the positive *y*-direction is only slightly weaker than that of the opposite direction. For the incidence matches with the silenced SHG (the 3rd panel, Figure 1a), the emission lobe at the positive *y*-direction is suppressed, but it is still relatively strong compared with that of the opposite emission lobe. When the incidence is at the SH emission peaks (the 2nd and 4th panels, Figure 9a), the emission lobe at the positive *y*-direction is almost eliminated, indicating the realization of unidirectional SH emission.

4. Conclusions

In conclusion, enhanced and unidirectional SH emissions with a plasmonic SRR dimer are investigated in this study, where one can get relatively strong (conversion efficiency ~ 1.31×10^{-9}) and directional (directivity > 17 dB) SH emissions around broad spectral ranges. The simultaneously realization of enhanced and unidirectional SH emissions provides us with important implications for realizing compact and on-chip ultrafast nonlinear optoelectronic devices.

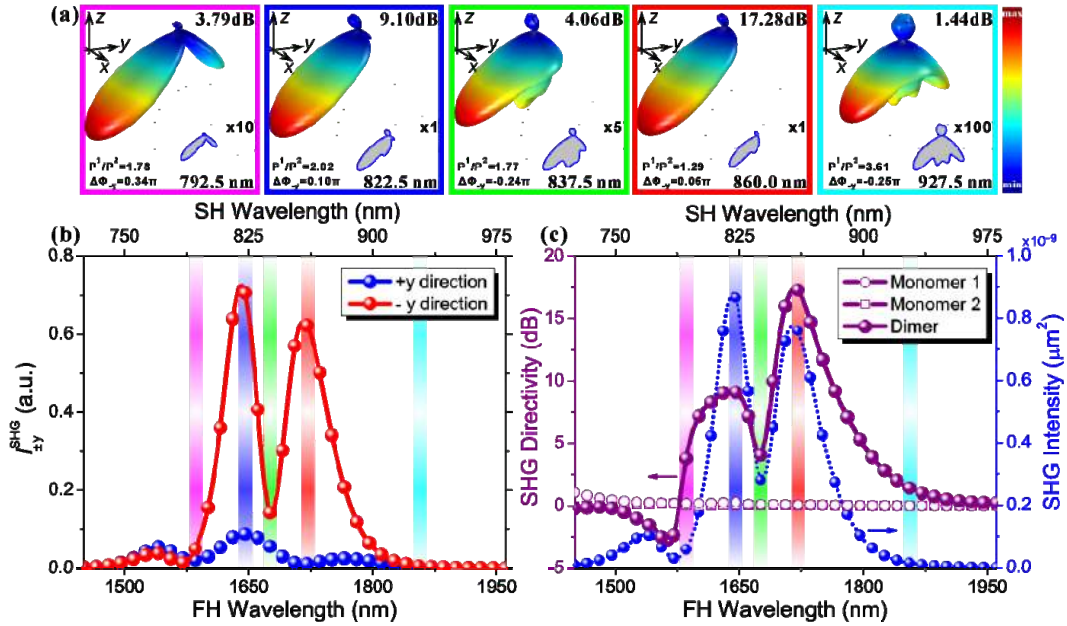


Figure 1: SHG unidirectional emission with the SRR dimer. (a) SH far-field emission patterns, the insets show the angular plots in the *yz*-plane, and the scaled factors are represented on the upper-right corners. (b) SHG emission intensities scattered in the positive and negative *y*-directions. (c) SHG emission directivity of the SRR dimer (the solid purple points) and the two monomers (the open purple points), and the SHG spectrum is represented for comparison (the dotted line).

Acknowledgements

This work was supported by National Natural Science Foundation of China (NSFC) (11574228, 61471254, and 11304219), the Natural Science Foundation of Shanxi Province (201601D021005), the Hong Kong Polytechnic University (Grant No. 1-ZVAW) and the Hong Kong Research Grants Council (ECS Grant No. 509513).

References

[1] Curto, A. G.; Volpe, G.; Taminiau, T. H.; Kreuzer, M. P.; Quidant, R.; van Hulst, N. F. Unidirectional Emission of a Quantum Dot Coupled to a Nanoantenna. *Science* **2010,** *329* (5994), 930-933.

[2] Vercruysse, D.; Sonnefraud, Y.; Verellen, N.; Fuchs, F. B.; Di Martino, G.; Lagae, L.; Moshchalkov, V. V.; Maier, S. A.; Van Dorpe, P. Unidirectional Side Scattering of Light by a Single-Element Nanoantenna. *Nano Lett.* **2013,** *13* (8), 3843-3849.

[3] Tanaka, Y. Y.; Shimura, T. Tridirectional Polarization Routing of Light by a Single Triangular Plasmonic Nanoparticle. *Nano Lett.* **2017,** *17* (5), 3165-3170.

[4] Yang, K.-Y.; Verre, R.; Butet, J.; Yan, C.; Antosiewicz, T. J.; Käll, M.; Martin, O. J. F. Wavevector-Selective Nonlinear Plasmonic Metasurfaces. *Nano Lett.* **2017,** *17* (9), 5258-5263.

[5] Liu, S.-D.; Leong, E. S. P.; Li, G.-C.; Hou, Y.; Deng, J.; Teng, J. H.; Ong, H. C.; Lei, D. Y. Polarization-Independent Multiple Fano Resonances in Plasmonic Nonamers for Multimode-Matching Enhanced Multiband Second-Harmonic Generation. *ACS Nano* **2016,** *10* (1), 1442-1453.

Refractometric Sensing Using Gradient Plasmonic Nanostructures: Mapping Spectral Information to Spatial Patterns

Wen-Di Li[1*], Siyi Min[1], Shijie Li[1], Zhouyang Zhu[1], Chuwei Liang[1], Jingxuan Cai[1]

[1]Department of Mechanical Engineering, The University of Hong Kong, Pokfulam, Hong Kong, China
*corresponding author, E-mail: liwd@hku.hk

Abstract

We report a spectrometer-free, pattern-based refractometric sensing scheme. This new detection scheme uses gradient plasmonic nanostructures to map spectral information to spatial locations and then use commercial imaging sensors, rather then spectrometers, to detect pattern change induced by local refractive index change due to adsorbed analyte molecules. Our preliminary results show the sensitivity performance of this new method can be comparable to conventional spectrometer-based methods, but with much more compact and cost-effective setup.

1. Introduction

Detection and identification of small amount of gas molecules, biomarkers, bacteria, and other chemicals is of great importance in our daily life for environmental monitoring, early disease detection, food safety inspection, just to name a few. Many detection schemes have been developed towards these applications. Thanks to the fast development of nanofabrication techniques in the past decade, plasmonic nanostructures with well-defined dimensions and geometries have received intensive attention for this purpose. Collective resonance of electrons in plasmonic nanostructures selectively scatters incident light at fingerprint wavelengths and such scattering behavior highly depends on the dimensions, geometries, and local refractive index. Therefore, if the target substance to be detected is locally adsorbed or attached to the plasmonic nanostructure, spectral change in the reflected or transmitted light will be induced and can be used as an indicator for detection and identification of the target substances.

Conventional substance detection scheme based on spectral change on plasmonic nanostructures relies on direct spectroscopy measurement of the reflected and transmitted light using spectrometers and collection optics. Although great effort has been devoted in developing low-cost and portable spectrometers for consumer applications, there is still no mature and affordable consumer-level spectrometers available in the market, keeping the plasmonic refractometric sensing based chemical detection tools out of reach for daily applications.

Our work aims to explore a novel scheme for detecting the refractive index induced spectral change in light scattered from plasmonic nanostructures using image acquisition and recognition method instead of direct spectroscopy characterization. We will map spectral information to spatial patterns by using gradient plasmonic nanostructures deterministically fabricated over centimeter-scale area. The gradient plasmonic nanostructures have key dimensions, such as the diameter of pillars or holes, continuously varying with spatial position. Instead of using a spectrometer to obtain scattered spectra, we use a low-cost camera to take images of light transmitted through the sample. When the environmental refractive index is slightly changed, the image of the reflected light will exhibit changed patterns. We will develop corresponding image processing algorithm to extract useful information from the obtained image and detect substances adsorbed or attached on the sensing structures. Our approach provides a low-cost and high-sensitivity alternative method for refractometric sensing based substance detection and has great potential to be implemented in consumer applications.

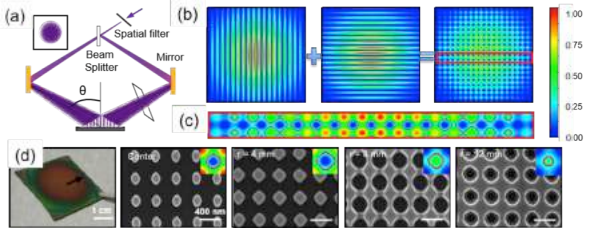


Fig. 1. Interference lithography fabrication process for spatially varying gradient nanostructures. (a) Schematic representation; (b) numerical simulation of double exposure for two-dimensional dots and holes with gradient sizes; (c) zoomed-in view of the numerical simulation of the red box region in (b); and (d) preliminary fabrication results showing the gradient feature sizes on 370-nm-period two-dimensional structures.

2. Fabrication of Gradient Plasmonic Structures

Gradient plasmonic nanostructures in our work are fabricated using interference lithography (IL). Conventional IL emphasizes pattern uniformity; therefore, uniform exposure intensity over the patterning area is desired. To fabricate spatially varying structures, we intentionally utilize the non-uniform Gaussian-shaped intensity distribution of the two coherent beams to realize spatially varying patterns (Fig. 1).

As shown in Fig. 1d, we successfully fabricated spatially varying two-dimensional nanostructures with circular symmetry. Exposed patterns on the positive-tone photoresist show pillars at the center, where the Gaussian beam has the maximum intensity. The diameter of pillars increases with the distance from the center. Nearby pillars start to merge and the overall pattern evolves into a hole array with the diameter of holes reducing when the distance from the center is further increased. We also use the IL system to make nanoimprint templates with the gradient structures and then, use NIL and other nanofabrication processing, including reactive ion etching and e-beam evaporation, to fabricate different types of gradient plasmonic structures for various sensing demonstrations.

3. Experimental Results

We carry out a series of experimental demonstrations and compare the performance of our new sensing scheme with existing spectrometer-based refractometric sensing methods. A schematic of our sensing setup is illustrated in Fig. 2a. A camera is used to record the transmitted intensity pattern on the gradient plasmonic sensing chip. Before and after exposing the sensing chip to analyte substances, two transmitted images are taken and compared. An image processing algorithm is developed to retrieve the change in the patterns to detect the existence of analyte substances.

We have performed preliminary experiment on hydrogen gas sensing by using a silver gradient plasmonic structure

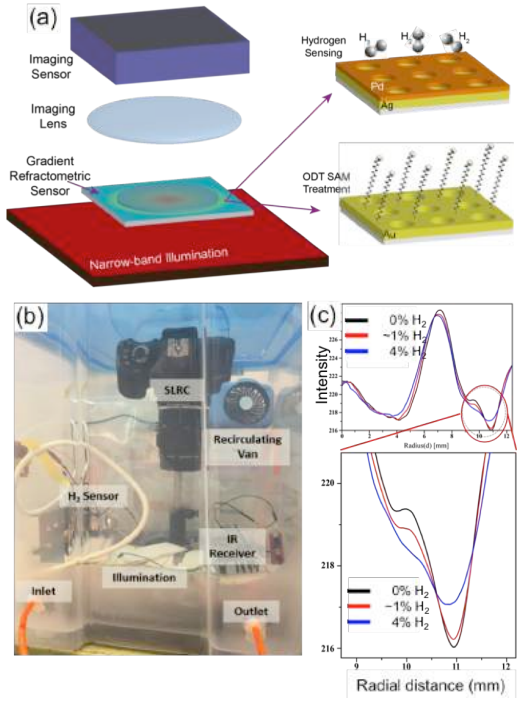


Fig. 2. (a) Schematic of the sensing setup for hydrogen sensing and a self-assembled monolayer, with future potential for biosensing applications; (b) hydrogen sensing setup; and (c) preliminary result showing that less than 1% hydrogen can be detected using the proposed pattern-based sensing.

with 20-nm-thick palladium deposited as the hydrogen-responsive layer [1-3]. The sensing platform is shown in Fig. 2b, which uses an LED source with a center wavelength of 635 nm and a bandwidth of 20 nm, and a Canon EOS 550D camera as the image sensor. A plastic enclosure is used as the gas sensing chamber with the inlet connected to a H_2/N_2 forming gas cylinder. A commercial hydrogen gas sensor is installed in the chamber to monitor the real-time hydrogen concentration. Our preliminary testing result (Fig. 2c) shows that hydrogen gas with 1% and 4% concentrations can induce a clearly resolvable intensity pattern change, which is comparable to many published plasmonic refractometric hydrogen sensing results [3-5]. We believe that there is considerable room for improvement of the sensing performance of our gradient plasmonic sensors and will explore its ultimate limitations in the subsequent investigation.

4. Conclusions

We report an innovative spectrometer-free, pattern-based refractometric sensing scheme. Our research covers novel fabrication methods, numerical modeling and image processing algorithm, and experimental prototype demonstration of gradient plasmonic structures for refractometric sensing. Our preliminary results show the sensitivity performance of this new method can be comparable or even superior to conventional spectrometer-based plasmonic refractometric sensing methods, but with much more compact and cost-effective setup. This work will potentially open a new avenue towards the development of consumer-level sensing solutions in biomedical and other areas.

Acknowledgements

Research Grants Council of Hong Kong (Grant No. 27205515 and 17246116) and the University of Hong Kong (Grant No. 201611160057 and 201511159175).

References

1. B. Sutapun, M. Tabib-Azar, and A. Kazemi, Pd-coated elastooptic fiber optic Bragg grating sensors for multiplexed hydrogen sensing, *Sensors and Actuators B-Chemical* **60**: 27-34, 1999.
2. Y. G. Sun and H.H. Wang, High-performance, flexible hydrogen sensors that use carbon nanotubes decorated with palladium nanoparticles, *Advanced Materials* **19**: 2818, 2007.
3. N. Liu et al., Nanoantenna-enhanced gas sensing in a single tailored nanofocus, *Nature Materials* **10**: 631-636, 2011.
4. A. Tittl et al., Palladium-Based Plasmonic Perfect Absorber in the Visible Wavelength Range and Its Application to Hydrogen Sensing, *Nano Letters* **11**: 4366-4369, 2011.
5. C. Wadell, S. Syrenova, and C. Langhammer, Plasmonic Hydrogen Sensing with Nanostructured Metal Hydridese, *ACS Nano* **8**: 11925-11940, 2014.

Interfacial Solar Steam Generations: Materials, Structures and Applications

Jia Zhu[1]

[1]College of Engineering and Applied Sciences
Nanjing University, Nanjing, China
*corresponding author, E-mail: jiazhu@nju.edu.cn

Abstract

Water scarcity is one of the most pressing global challenges. Nanomaterials with carefully tailored properties can be used to manipulate the flow of phonons, electrons and photons, to enable unconventional solution to addressing this issue. In this talk, I will present our recent progress in solar steam generation for water treatment.

We report a plasmon-enhanced solar desalination device. This most efficient and broad-band plasmonic absorber is fabricated through self-assembly of metallic nanoparticles onto a nanoporous template by one step deposition process. Because of its efficient light absorption and strong field enhancement, it can enable very efficient and effective solar desalination by using low cost aluminum nanoparticles.

Inspired by the transpiration process in plants, we report an artificial transpiration device with a unique design of two dimensional water path. With efficient two dimensional water supply and suppressed heat loss, it can enables an efficient (80% under one-sun illumination) and effective (four orders salinity decrement) solar desalination device. More strikingly, the energy transfer efficiency of this artificial transpiration device is independent of water quantity and can be achieved without extra optical or thermal supporting systems, therefore significantly improve the scalability and feasibility of this technology.

References

1. Ning Xu, Xiaozhen Hu, Weichao Xu, Xiuqiang Li, Lin Zhou, Shining Zhu and Jia Zhu*. Advanced Materials, 29, 1606762 (2017)
2. Xiuqiang Li, Renxing Lin, George Ni, Ning Xu, Xiaozhen Hu, Bin Zhu, Guangxin Lv, Jinlei Li, Shining Zhu and Jia Zhu*. Natl Sci Rev, 5, 70 (2018)
3. Lin Zhou, Shendong Zhuang, Chengyu He, Yingling Tan, Zhenlin Wang and Jia Zhu*. Nano Energy,32,195–200(2017)
4. Xiaozhen Hu, Weichao Xu, Lin Zhou, Yingling Tan, Yang Wang, Shining Zhu and Jia Zhu. Advanced Materials, 29, 1604031 (2017)
5. Xiuqiang Li,Weichao Xu,Mingyao Tanga,Lin Zhoua,Bin Zhu,Shining Zhu and Jia Zhu*. PNAS 113, 13953 (2016)
6. Lin Zhou , Yingling Tan , Jingyang Wang , Weichao Xu , Ye Yuan , Wenshan Cai , Shining Zhu,and Jia Zhu*. Nature Photonics 10, 393-398 (2016)
7. Lin Zhou, Yingling Tan, Dengxin Ji, Bin Zhu, Pei Zhang, Jun Xu, Qiaoqiang Gan, Zongfu Yu, Jia Zhu. Science Advances 2：e1501227 (2016)

Linear frequency conversion via sudden merging of resonances in time-variant metasurfaces

Kanghee Lee[1], Jaehyeon Son[1], Jagang Park[1], Byungsoo Kang[1], Wonju Jeon[1], Fabian Rotermund[2], and Bumki Min[1]

[1]Mechanical Engineering, Korea Advanced Institute of Science and Technology (KAIST), Daejeon, Republic of Korea
[2]Department of Physics, Korea Advanced Institute of Science and Technology (KAIST), Daejeon, Republic of Korea
*corresponding author, E-mail: bmin@kaist.ac.kr

Abstract

Here, we propose rapidly time-variant metasurfaces as a frequency-conversion platform and experimentally demonstrate their efficacy at THz frequencies. The proposed metasurface is designed for the sudden merging of two distinct resonances into a single resonance upon ultrafast optical excitation. From this spectrally-engineered temporal boundary onward, the merged-resonance frequency component is radiated.

1. Introduction

In 1958, Morgenthaler contemplated an interesting route towards the conversion of light frequency via temporal variations of permittivity and/or permeability of the media [1]. Although not much attention has been given to this seminal work relative to that given to nonlinear frequency conversion, continual theoretical efforts have been made to understand this linear frequency conversion. In line with these theoretical speculations, experimental verifications have followed in the field of plasma physics [2] and semiconductors [3], and chip-scale dynamic photonic structures [4], micro-ring resonators [5], and waveguides [6]. One lesson from previous studies is that it is necessary to make a large temporal change in the properties of media, through which light is transmitted, to maximize the frequency shift. Additionally, the introduction of a proper resonance structure enables miniaturization of the device, which in turn provides the additional benefit of maximizing temporal variation. For that reason, active resonant metamaterials [7], in which the resonating meta-atoms are hybridized with electrically or optically reconfigurable natural materials, can be thought of as an optimal platform that can be spatiotemporally rearranged.

2. Experimental Results

The proposed metasurface, shown in Fig. 1, consists of an array of two concentric SRRs patterned on a semi-insulating GaAs substrate and exhibit two fundamental LC resonances, both of which are designed to be merged into a completely different resonance mode when the conductivity of the area between the two SRRs is suddenly increased. The outer and inner SRRs in the unit cell were designed to exhibit fundamental resonance frequencies of $\omega_1/2\pi$ = 0.62 THz and $\omega_2/2\pi$ = 1.24 THz, respectively. The resonance frequency of the merged mode, ω_m, falls between those of the original SRRs (0.92 THz at 10 μJ/cm^2). Multiple dielectric layers were deposited on top of the patterned surface and etched selectively to expose only the area between the two SRRs (coloured in dark grey in Fig. 1); the dielectric layers left behind by the etching were designed to reflect pump pulses centred at 800 nm, enabling the pump pulses to reach only the exposed area. As a result, the exposed GaAs area becomes conductive due to the pump-induced photocarrier generation. The conductivity change occurs within hundreds of femtoseconds and the changed conductivity is maintained over several tens of picoseconds. Therefore, the temporal conductivity variation can be approximated with a step function. In all the subsequent experiments, incident THz and optical pump pulses propagate collinearly and enter the fabricated metasurface with a variable time delay, t_d.

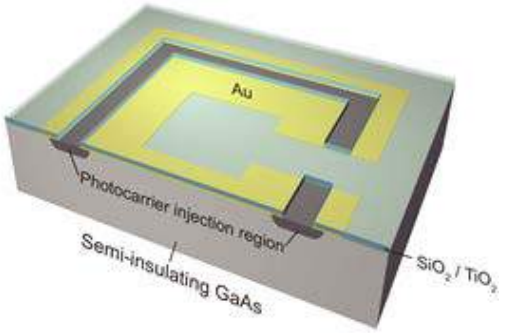


Figure 1: Schematic illustration of the metasurface structure. Photo-carrier injection occurs only in the dark grey region as the other area is screened from pump pulses by the patterned SiO_2/TiO_2 multilayer.

To experimentally confirm the frequency conversion, we first measured the amplitude transmission spectra of the metasurface as a function of the time delay t_d between a sub-cycle THz input pulse and a pump pulse of 10 μJ/cm^2. Here, the transmission amplitudes are obtained by dividing the transmitted signal through the metasurface by that measured through a reference sample, which consists of an unpatterned GaAs substrate and multiple dielectric layers. The measured delay-dependent spectra are shown in Fig. 2a for time delays between -4.4 ps and 15.6 ps. The observed spectra show the presence of two original fundamental modes for an approximate range of $t_d > 10$ ps and the merged mode for $t_d < 0$ ps, corresponding to the steady-state responses of two time-invariant metasurfaces. However, for an intermediate time delay of approximately $t_d = 2$ ps, where the original oscillating modes are disturbed by the temporal boundary, an amplitude transmission greater than unity is observed at ω_m. To clearly visualize each of these situations, transmission snapshots at time delays of -4 ps (black), 2 ps (red), and 15 ps (blue) are shown in Fig. 2b. A plot of the transmission as a function of the time delay at the merged frequency (Fig. 2c) reveals another notable feature related to the coherence in the frequency conversion; more specifically, the delay-dependent oscillation in the transmission is clearly noticeable in the plot (see also the inset of Fig. 2c for the expanded view). The origin of the transmission oscillation is the delay-dependent interference between the incident and the converted field at the merged frequency. The calculation is also plotted with a dotted line in Fig. 2c and exhibits a similar behavior to the measured data. The sudden approximation is validated by the analytical plot calculated using the experimental transfer function, and the correlation between the measured and semi-analytical formulae is shown to be reasonably high. The measured data are also in excellent agreement with the full numerical simulations.

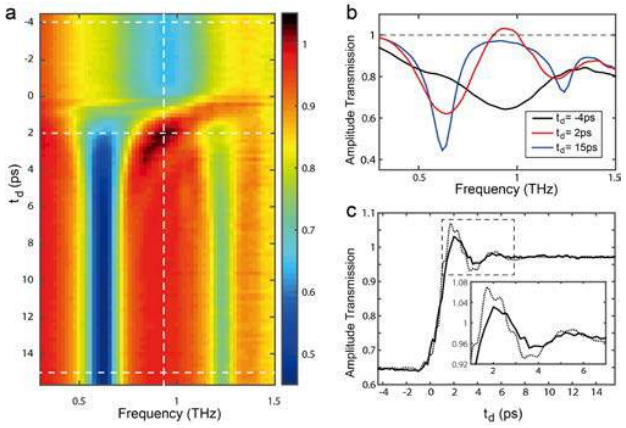


Figure 2: (a) Amplitude transmission spectra of the metasurface as a function of time delay. (b) Amplitude transmission spectra for three distinct time delays at $t_d = -4$ ps (black), $t_d = 2$ ps (red), and $t_d = 15$ ps (blue). (c) Amplitude transmission at ω_m (0.92 THz) as a function of time delay. The inset shows the expanded view between $t_d = 1$ ps and $t_d = 7$ ps.

3. Conclusions

Since our proposed conversion scheme does not rely on the nonlinearity of the constituent materials, the conversion efficiency is invariant with respect to the intensity of an input THz pulse. Therefore, this method is expected to be particularly beneficial for the frequency conversion of waves with weak intensities, which is distinct from the case of frequency conversion in nonlinear materials27 or nonlinear metamaterials28-30. Furthermore, the frequency of a converted wave and its efficiency is tailorable to a large degree because the conversion process does not require energy conservation between participating waves and because the metasurface can be reconfigured to exhibit temporally distinct dispersive responses. This type of engineering degree of freedom was not achievable in previous plasma-based apparatus or photonic crystal devices. Although the current demonstration was limited to the case of a step-like temporal variation, further sophistication could be achieved with other types of temporal variations, such as Dirac delta or sinusoidal functions.

References

[1] Morgenthaler, F. R. Velocity modulation of electromagnetic waves. IRE Trans. Microwave Theory Tech. 6, 167-171 (1958).

[2] Yablonovitch, E. Spectral Broadening in the Light Transmitted through a rapidly growing plasma. Phys. Rev. Lett. 31, 877-879 (1973).

[3] Nishida, A. et al. Experimental observation of frequency up-conversion by flash ionization. Appl. Phys. Lett. 101, 161118 (2012).

[4] Notomi, M. & Mitsugi, S. Wavelength conversion via dynamic refractive index tuning of a cavity. Phys. Rev. A 73 05180 (2006).

[5] Preble, S. F., Xu, Q. & Lipson, M. Changing the colour of light in a silicon resonator. Nature Photon. 1, 293-296 (2007).

[6] Fan, L. et al. Integrated optomechanical single-photon frequency shifter. Nature Photon. 10, 766-770 (2016).

[7] Chen, H. T. et al. Active terahertz metamaterial devices. Nature 444, 597-600 (2006).

Lock-in study of acoustic waves through a lead phononic plate

Cesar Alejandro Torres-Torres[1], Carlos Roberto Santillán-Rodríguez[1], Renee Joselin Sáenz-Hernández[1], María Eugenia Botello-Zubiate[1], María Cristina Grijalva-Castillo[1], José Andrés Matutes-Aquino[1*]

[1]Centro de Investigación en Materiales Avanzados, S.C., Chihuahua, Chih., México
*corresponding author, E-mail: jose.matutes@cimav.edu.mx

Abstract

A plate-shaped phononic crystal for preventing the propagation of acoustic waves in a frequency range from 45 to 73 kHz was simulated, constructed and tested. The structural elements of the phonon crystal were made up of a periodic arrangement of air holes in a lead metal plate. The band gap was experimentally determined with a lock-in amplifier. The experimentally determined band gap coincides with the simulated one by the finite elements method.

1. Introduction

A photonic (phononic) crystal creates forbidden bands (band gaps) in certain frequency ranges to the propagation of electromagnetic (acoustic) waves, as it also occurs in electron band theory. The Bragg scattering is the physical phenomenon behind the formation of these forbidden bands. A metallic plate, appropriately designed, can function as a phonon crystal to block the passage of acoustic waves over a range of frequencies. Besides that, in a metallic plate, stationary waves are established at certain frequencies (eigenmodes) that are a function of its finite dimensions and wavelengths. The detection of acoustic wave propagation is further complicated by acoustic noise generated by grain boundary scattering and other defects. As a result of all this, the signal to be detected is accompanied by an intense background. Lock-in amplification makes possible to extract the useful signal from the intense background of signals thanks to its phase-sensitive detection principle.

2. Results

The geometrical dimensions of a lead plate of 140 mm x 32 mm x 4 mm, with a periodic arrangement of 7.68 mm diameter air holes separated a distance of 8 mm were calculated by finite elements method with software COMSOL MULTIPHYSICS to work as a phononic crystal, so as to prevent transmission of acoustic waves in a frequency range from 45 to 73 kHz. Fig. 1 shows the unit cell formed by lead and an air hole. To simplify the calculations Bloch periodic boundary conditions, also known as Floquet boundary conditions for 1D, were applied.

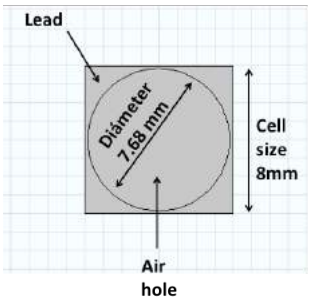


Figure 1: Unit cell formed by lead and an air hole.

Fig. 2 shows the band structure with allowed and forbidden bands for this phononic crystal.

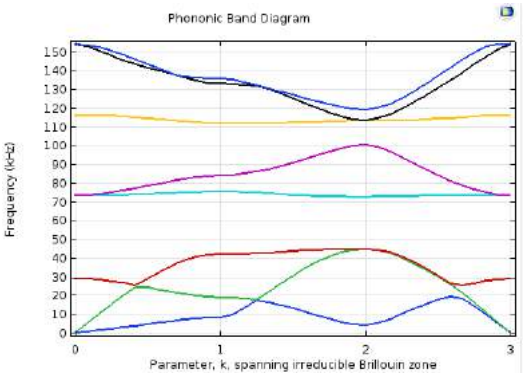


Figure 2: Calculated band structure for the phononic crystal.

The plate was built by melting lead into a mold and later the air holes were drilled. A pair of commercial piezoelectric elements from PI Piezo Technology were attached to the ends of the plate, one as wave source and the other as wave detector. To the piezoelectric-source, sinusoidal signals of 5 and 10 V were applied with a function generator, and the response signal, attenuated and directly proportional to the applied signal, was measured with the piezoelectric-detector,

first in the lead plate that served as reference, and later in the phononic plate, that is, in the lead plate with the periodic arrangement of air holes. Measurements were carried out with a lock-in amplifier from Stanford Research System, model SR830, which generates frequencies in the range from 1 mHz to 102.4 kHz, have a 256 kHz front-end sampling rate and a dynamic reserve > 100 dB (5 ppm/C stability). Fig. 3 shows the phononic plate.

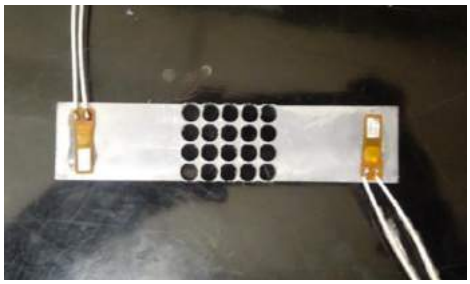


Figure 3: Phononic plate with holes and piezoelectric elements.

3. Discussion

The lead plate showed a characteristic pattern of peaks corresponding to its eigenmodes. On the other hand, the phononic plate showed, beside its eigenmodes, a strong signal attenuation in a frequency range, that matches with the band gap calculated by the finite elements method.

Fig. 3 compares the signal transmitted by the plate without air holes, with that transmitted by phononic plate that reveals a clear attenuation in the frequency range of the band gap.

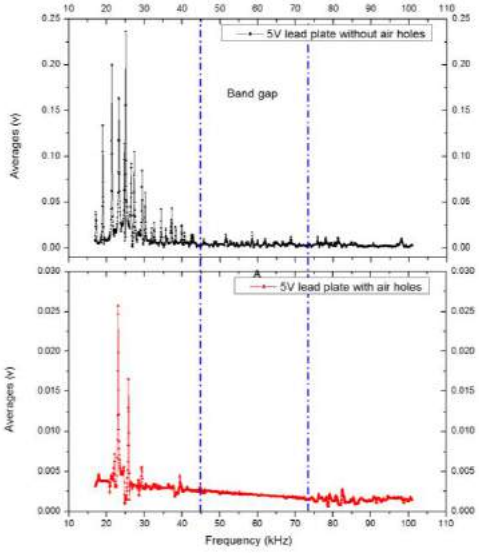


Figure 3: Transmitted voltage signal by the lead plate without air holes (above) and by the phononic plate (below) for an incoming signal 5V in amplitude.

4. Conclusions

Geometric dimensions of a phononic plate of lead with air holes were calculated by finite elements using COMSOL Mulphysics in order to obtain a band gap for the propagation of elastic waves in the frequency range from 35 to 73 kHz.

The forbidden band for the propagation of ultrasonic elastic waves, experimentally determined, coincides with the calculated band gap by the finite elements method.

It is worth noting that this band gap is effective, both for the longitudinal and transverse waves that propagate within a solid body.

A large number of eigenmodes were observed in the lead plate with their origin in the finite linear dimensions of the plate.

The attenuation of acoustic waves could be explained by true absorption inside the material, as well as by the scattering phenomenon in grains boundaries and other possible defects inside the material.

Measurement of wave propagation using lock-in amplifier is much less noisy when compared with measurement made with an amplifier followed by a passband Butterworth filter used by other authors in [1].

This phononic plates could have potential and interesting application to prevent noises propagation into edifications and other constructions.

References

[1] Design, fabrication and characterization of phononic crystals in macro and micro scale. Mohammadhosein G. Badoly. 2016.The University of New Mexico. Albuquerque, New Mexico.

[2] Acoustic Metamaterials and Phononic Crystals. Editor Pierre A. Deymier.Springer 2013.

[3] Plate-type elastic metamaterials for low-frequency broadband elas c wave a enua on. Li, Yinggang, Ling Zhu, and Tianning Chen.Ultrasonics 73 (2017) 34-42.

Electrically Small Resonators-Based Infrared Imaging Pixel Configuration

Mohammed R. AlShareef[1], Mohamed Ramy Abdel-Rahman[2]

[1]National Center for MEMS Technology, King Abdulaziz City for Science and Technology, Riyadh, Saudi Arabia
[2]Electrical Engineering Department, College of Engineering, King Saud University, Riyadh, Saudi Arabia
*corresponding author E-mail: alshareef@kacst.edu.sa

Abstract

In this work, an electrically small resonator-based infrared imaging pixel configuration is presented, designed and simulated. Split ring resonators (SRRs) are configured in an array arrangement where the absorbed power is coupled to a resistive sheet, resembling a microbolometer, via a microstrip (MS) line. The proposed structure shows an ability to absorb incident infrared radiation in the 8-14 μm band.

1. Introduction

Antenna-coupled microbolometers have been proposed and used extensively for long wave infrared (8-14 μm) detection mainly for imaging applications. [1, 2, 3] In antenna-coupled microbolometer structure, an antenna receives the incident infrared radiation and the antenna resonant currents are then dissipated in an impedance matched microbolometer causing a change in its temperature and a resultant resistance change that can be readout by an electronic circuit. Electrically small resonators are sub wavelength-sized structures having diameters that are less than $\lambda_o/21$. Electrically small resonators were investigated in array configurations for microwave and terahertz energy harvesting yielding absorption efficiencies that are higher than 80% [4, 5, 6]. Electrically small resonators can present an alternative to antennas in antenna-coupled microbolometer configurations potentially leading to higher detection efficiencies. In this paper, we propose an electrically small resonator-based infrared imaging pixel configuration. A square split ring resonator (SRR) array coupled, via a microstrip line (MS), to a resistive sheet shown in Fig. 1 is designed and simulated. Scattering parameters and power absorption efficiencies are analyzed, in the long wave infrared band, for different resistive loads.

2. Geometrical Configuration

An array of six SRRs is proposed, Fig. 1. The overall array dimension is 9 μm by 12 μm. This structure utilizes a silicon dioxide (SiO_2) layer with thickness (h= 2 μm) and dielectric constant (ϵ_r= 4.84 + j0.097) with an underlying layer of gold (Au) (simulated with a conductivity $\sigma = 2.8 \times 10^6$ S/m, as measured in [7]) having a thickness of 150 nm. However, the structure is to be fabricated on top of a silicon (Si) substrate. The outer (S) and inner (C) arm lengths of the SRR are 2 μm and 1.45 μm, respectively.

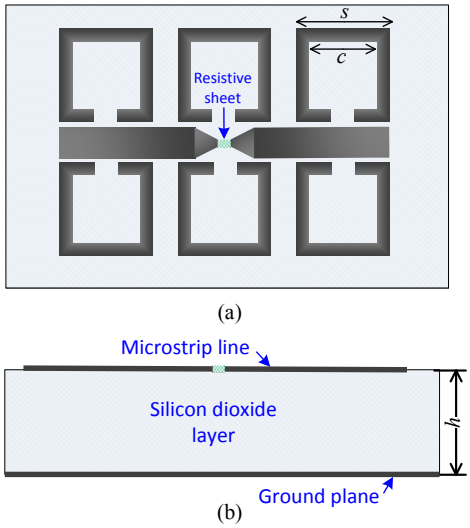


Figure 1: Layout of the infrared wave bolometer structure, (a) top and (b) side view.

The electric fields developed at the open ends of the SRRs are coupled to the MS resident in proximity. The MS acts to deliver the resonant currents to its inner two ends which are tapered in a semi-triangle shape. At the end of the two tips, there is a gap where a resistive sheet, representing the microbolometer, is placed across. The resistance of the resistive sheet can be varied during the simulation to determine the optimum resistance where impedance matching between the MS and the resistive sheet is achieved. In a focal plane array configuration, the microstrip line present in each individual pixel can be connected to an underlying readout integrated circuit for the purpose of microbolometer bias and signal readout. For the purpose of measuring the performance of a single element detector, the MSs may be extended and connected to a large area bias and signal readout pads lying on the top of the SiO_2 layer.

3. Discussion and Results

When the whole structure is excited by a wide band plane wave, the six SRRs greatly interacted with the impinging waves specifically from 24-30 THz. Fig. 2 shows that the structure can absorb more than 60% of the incident power at such high and lossy frequency, where both the transmission

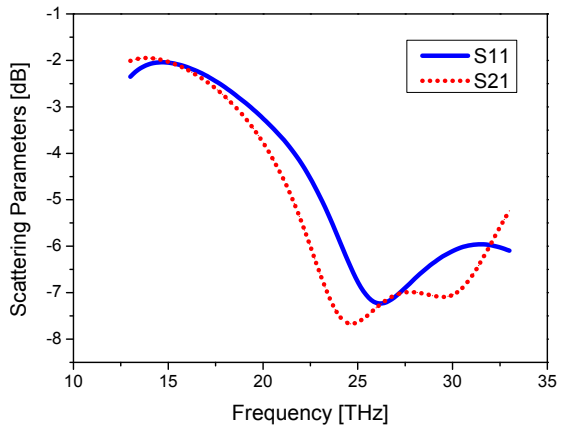


Figure 2: Simulated scattering parameters of the infrared bolometer structure

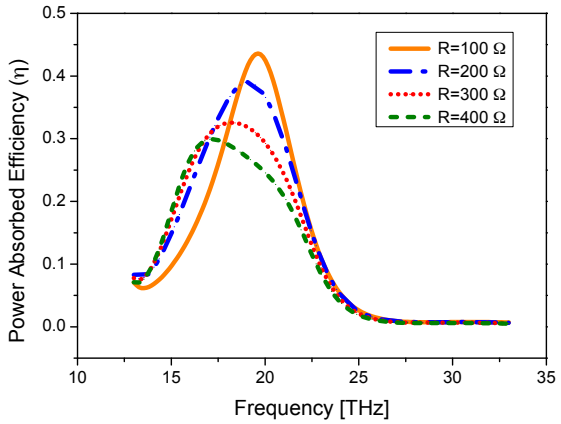


Figure 3: Calculated power absorption efficiency of the structure

and reflection are minimum at 26 THz frequency. The positive interaction between the SRRs and the incident wave induces a strong electric field across their gaps, which in turns couple to the microstrip line sitting in the middle of the arrangement. The two tapered ends of the MS allow an induced current to move along the strip and be consumed at the resistive sheet placed across the gap. Fig. 3 illustrates the power absorption across the gap at different resistive values. It is found that 100 Ω resistive value yields 44% power absorption efficiency, while 400 Ω achieves only 30% owing to impedance mismatching. One can say that the absorption is quite low and that may be attributed to the lossy gold at such high frequency as well as the mismatching issue.

4. Conclusion

We deigned and simulated a resonator-based infrared imaging pixel configuration to act as a microbolometer. Frequency dispersion effect is taken into consideration in the numerical calculations. As 44% power absorption efficiency is achieved utilizing the proposed structure, employing this configuration in infrared imaging applications is highly promising. Validating numerical results experimentally will be considered for future work.

Acknowledgement

This work was supported by King Abdulaziz City for Science and Technology.

References

[1] F. Gonzalez, B. Ilic, G. Boreman, Antenna-coupled microbolometers on a silicon nitride membrane, *Microw. Opt. Techn. Let.* 47: 546-548, 2005.

[2] F.J. Gonzalez, M.A. Abdel-Rahman, G.D. Boreman, Antenna-coupled VOx thin film microbolometer array, *Microw. Opt. Technol. Lett.* 38: 235237, 2003.

[3] H.-H. Yang G.M. Rebeiz, Micromachined Room-Temperature Air-Suspended Ni/Cr Nanobolometer, *IEEE T. on Microw. Theory* 63: 3760-3767, 2015.

[4] Mohammed R. AlShareef and O. Ramahi, Electrically small resonators for energy harvesting in the infrared regime, *Journal of Applied Physics* vol. 114, no. 22, pp. 223101-6, 2013.

[5] Mohammed R. AlShareef and O. Ramahi, Electrically small particles combining even- and odd-mode currents for microwave energy harvesting, *Applied Physics Letters* vol. 104, no. 25, pp. 253906-5, 2014

[6] Mohammed R. AlShareef and O. Ramahi, Electrically small particles for harvesting and channeling infrared energy, in *Antenna Technology and Applied Electromagnetics (ANTEM), 2014 16th International Symposium*, pp. 1-2, July 2014.

[7] D. Shelton, et al., Antenna-coupled microbolometers on a silicon nitride membrane, *J. Appl. Phys.* 104: 103514, 2008.

Generation and Enhancement of UV-Harmonic Wave at Nonlinear Interfaces

Xiaohui Zhao,[1,2,3] Yuanlin Zheng,[2,3] Yanqi Gao,[1] Yong Cui,[1] Daxing Rao,[1] and Xianfeng Chen[2,3,*]

[1]Shanghai Institute of Laser Plasma, China Academy of Engineering Physics, Shanghai, 201800 China
[2]School of Physics and Astronomy, Shanghai Jiao Tong University, Shanghai 200240, China
[3]Key Laboratory for Laser plasma (Ministry of Education), Collaborative Innovation Center of IFSA (CICIFSA), Shanghai Jiao Tong University, Shanghai 200240, China
*corresponding author, E-mail: xfchen@sjtu.edu.cn

Abstract

We investigate the enhancement of ultraviolet second-harmonic radiation at a nonlinear interface with large disparity in second-order susceptibility. The intensity of second harmonic wave generated at the nonlinear interface was up to 11.6 times at the crystal boundary.

1. Introduction

Coherent light at ultraviolet (UV) and vacuum ultraviolet (VUV) delivered by all solid-state laser systems is highly demanded due to numerous practical applications [1,2] in lithography, photoelectron spectroscopy, micro-machining and semiconductor processing, high-density optical storage and so on. Seeking for suitable transparent nonlinear media for UV and VUV harmonic wave generation has attracted great interest over past decades, for example, KBe2BO3F2 (KBBF) crystal, which has a cutoff wavelength in the UV region of 153 nm [3]. However, the layered structure is a big limitation of KBBF, which restricts the crystal size, cutting angles and so on. Efficient frequency conversion processes taking advantage of tunable and flexible phase matching methods can find a way out [4]. In this paper, we report on an automatic non-collinear phase matching method, which has no limit for wavelength. The second harmonic (SH) radiation was enhanced at the nonlinear interface with large disparity in $\chi^{(2)}$, which was formed by adhering another UV non-transparent crystal with higher $\chi^{(2)}$. And the added crystal doesn't change the properties of SH radiation, for example the emission angle.

2. The coupled wave equation

To analyze the properties of SH generated at the nonlinear interface with large disparity in $\chi^{(2)}$, a general situation was considered: x=0 plane is an interface with nonlinear coefficient $\chi_1^{(2)}$ and another medium with $\chi_2^{(2)}$ [see Fig. 1(a)]. The coupled wave equation of this nonlinear process was solved using the Fourier transform [5], and the intensity of SH I_2 can be expressed as

$$I_2(k_x,y)=\left(\frac{k_2}{2n_2^2}\right)^2 I_1^2 y^2 sinc^2\left[(\Delta k-k_x/2k_2)\frac{y}{2}\right]\left|[\chi_1^{(2)}+\chi_2^{(2)}]\sqrt{\frac{\pi}{8}}ae^{-\frac{a^2k_x^2}{8}}+i[\chi_1^{(2)}-\chi_2^{(2)}]\frac{\sqrt{\pi}}{2}aD\left(\frac{ak_x}{2\sqrt{2}}\right)\right|^2 \quad (1)$$

where k_x is the components of k_2 in x directions, n_2 is the refractive index of the SH, I_1 denotes the intensity of the gauss-type FW with beam width a. The phase mis-matching is $\Delta k=k_2-2k_y$, and $D(ak_y/2\sqrt{2})$ denotes the Dowson function.

According to Eq. (1), one can find that I_2 will have a maximum when the phase-matching condition $\Delta k=k_x/2k_2$ is satisfied. The radiation angle of SH can be derived as $k_2\sin\theta = 2k_1\sin\alpha$, which is exactly the longitudinal phase-matching condition. Since this is an automatic and tunable phase-matching process, one can always find suitable incident angles for SH radiation without wavelength limitation. The absolute value $\left|\chi_1^{(2)}-\chi_2^{(2)}\right|$ directly affects the SH intensity, since the term containing $\exp(-a^2k_y^2/8)$ decreases sharply with the increasing of the absolute value of k_x. When $\chi_2^{(2)}$ equals to 0, representing the condition of the boundary of crystal. If the nonlinear coefficient is large enough that the relation $\left|\chi_1^{(2)}-\chi_2^{(2)}\right|>\left|\chi_1^{(2)}\right|$ is satisfied, the SH intensity is thus enhanced theoretically.

3. Experiment results and discussion

To degenerate the theoretical prediction, at first, a x-cut β−BaB_2O_4 (BBO) sample (absorption edge is 189 nm, d_{11}=2.26 pm/V) of the size of 5 mm(x)×10 mm(y)×10 mm(z) was employed as the transparent nonlinear medium to generated the UV SH wave. The light source we used was an optical parametric amplifier (TOPAS, Coherent Inc.), producing 80 femtosecond pulses (1000 Hz rep. rate) at the variable wavelengths from 280 nm to 2600 nm. The FW was adjusted to be ordinary polarized with the wavelength of 650 nm and loosely focused by a 100-mm focal length lens to a beam waist of 50 μm. In experiment, we observed SH generated at the BBO boundary and the spectrum was shown in Fig. 1(b). As a comparison, a z-cut periodically poled 5 mol% MgO:$LiNbO_3$ (LN) sample with the size of 10 mm(x)×10 mm(y)×5 mm(z) was employed to repeat the above

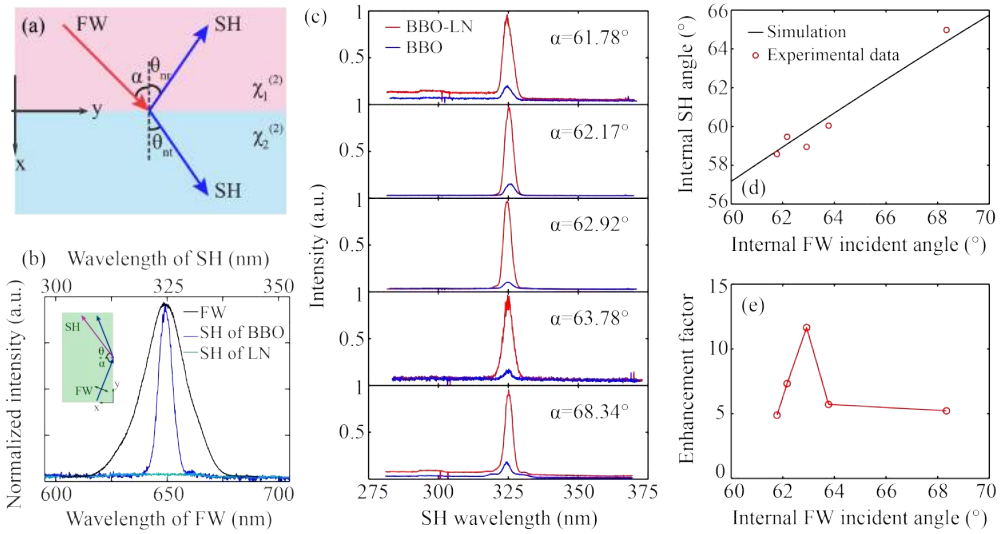


Figure 1: (a) Diagram of SH generated at the interface with large disparity in $\chi^{(2)}$. (b) Spectrum of the FW and harmonic wave generated at the boundary of BBO and LN. (c) Spectrum of SH generated on BBO boundary (blue) and interface of BBO-LN (red) with a set of FW incident angles. (d) Internal radiation angle of SH θ versus internal FW incident angle α. Theoretical prediction (solid curve) and experimental results (symbols) are in good agreement. (e) Measured enhancement factor of SH generated at the BBO-LN interface and boundary of BBO crystal.

experiment. Although the second-order nonlinear coefficient of LN sample is significantly higher than that of BBO, the SH was completely absorbed as the cutoff wavelength is 380 nm in LN.

Then the BBO sample and the LN sample was tightly abutted upon each other under high pressure. Similar to the above experiment, o-polarized FW with the center wavelength at 650 nm was obliquely incident onto BBO crystal and reflected at the BBO-LN interface with an angle α. The wavelength spectrum of SH with varying FW incident angles at the BBO-LN interface were measured by a fiber optic spectrometer, as shown in Fig. 1(c). For comparison, the SH generated on the boundary of single BBO sample was detected by the spectrometer with a same distance and angle at corresponding angles of incident FW. At the same α, the intensity of SH generated at the interface of BBO-LN was much higher than that generated at the BBO boundary. It verifies from the coupled wave equation.

Figure 1(d) shows the relationship of the measured SH radiation angle θ versus FW incident angle α, which agrees well with theoretical prediction. It demonstrates the attached LN sample doesn't change the phase-matching condition. The enhancement factor of SH intensity introduced by LN was from 5 to 13 in our experiment [Fig. 1(e)] smaller than the theoretical prediction. The FW refraction from BBO to LN reduces the bump energy of this nonlinear process. Using direct bonding or crystal growth techniques, a direct interface of two crystals may be fabricated to generate enhanced SH radiation at required wavelength region.

4. Conclusions

In conclusion, the SH generated on a crystal boundary under an automatic and tunable phase matching method can be enhanced by another medium with larger nonlinear coefficient even though it is non-transparency at the SH wavelength. The intensity of SH generated on this artificially fabricated interface was about 5 to 15 times of that on single crystal boundary in our experiment. The radiation direction of SH will not be effect by the pressed crystal. It suggests potential applications in the UV even vacuum-UV spectral region.

Acknowledgements

This work is supported in part by the National Natural Science Foundation of China (11604318)

References

[1] Kiss, T. et al. Photoemission spectroscopic evidence of gap anisotropy in an f-electron superconductor. Phys. Rev. Lett. 94, 057001 (2005).

[2] Okazaki, K. et al. Octet-line node structure of superconducting order parameter in KFe_2As2. Sci. 337, 1314–1317 (2012).

[3] Chen, C. et al. New development of nonlinear optical crystals for the ultraviolet region with molecular engineering approach. J. Appl. Phys. 77, 2268–2272 (1995).

[4] Ren, H., Deng, X., Zheng, Y., An, N. and Chen, X. Surface phase-matched harmonic enhancement in a bulk anomalous dispersion medium. Appl. Phys. Lett. 103, 021110 (2013).

[5] Zhao, X. et al. Nonlinear Cherenkov radiation at the interface of two different nonlinear media. Opt. Express 24, 12825–12830 (2016).

Direct visualization of momentum conversation through second harmonic Fourier image in 1D waveguide

Junjun Shi[1], Yang Li[2], Meng Kang[2], Shunping Zhang*[,2], and Hongxing Xu*[,1,2]

[1]The Institute for Advanced Studies, Wuhan University, Wuhan 430072, China
[2]School of Physics and Technology, Center for Nanoscience and Nanotechnology, and Key Laboratory of Artificial Micro- and Nano-structures of Ministry of Education, Wuhan University, Wuhan 430072, China.
*corresponding author, E-mail: spzhang@whu.edu.cn, hxxu@whu.edu.cn

Abstract

Coherently adding up signal wave from different locations are a prerequisite for realizing efficient nonlinear optical processes in traditional optical configurations. Here we present the experiment observation of momentum conversed coherent SHG in a 1D plasmonic nanowire (NW) waveguide and identify distinctive features that are inherent to the 1D system.[1] Periodic second harmonic signals are measured in a semiconductor nanowire through second harmonic Fourier image.

1. Introduction

Phase match in second harmonic generation (SHG), which means that the second harmonic wave vector has to be close to an integer multiple of the fundamental input wavevector, is necessary to optimize nonlinear efficiency and thus obtain powerful nanoscale devices. The overlap of the two oppositely propagating fields will give rise to a nonlinear polarization source at the sum frequency.[2] However, achieving collimated beaming in lower dimension systems are more appealing to take full advantage of the field confinement. In this study, we have demonstrated the transversely divergent coherent SHG from counterpropagating SPPs on 1D plasmonic waveguide. The SH photons are collimated perpendicular to the nanowire axis but are divergent within the perpendicular plane. The collimation (divergence) is inversely proportional to the length of the active region (lateral confinement of the SPPs). In addition, the SH emission pattern resembles that of an aligned dipole chain on top of the substrate with an emission peak at the critical angle.

2. Experiment results

2.1. 1D system of Ag NW-monolayer MoS_2 hybrids

To realize and characterize our setup we drop casted and dried Ag NWs onto the monolayer MoS_2 and used a femtosecond laser beam (central wavelength 796 nm, pulse duration ~20 fs) focused on one end of the Ag NW through an objective (Figure 1).

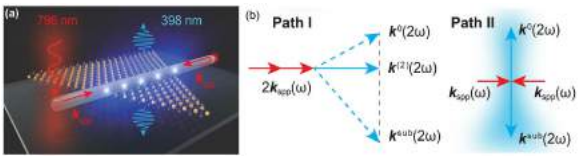


Figure 1. (a) Schematic of the remotely excited SHG from a Ag NW deposited on a monolayer MoS_2 sheet. (b) Schematic drawing of momentum conservation in SHG by the co-propagating (Path I) or counter-propagating SPPs (Path II).Reprinted with permission from ref 1. Copyright 2017 American Chemical Society.

There are two distinct processes of coherent SHG by SPPs, which can be understood based on the energy and momentum conservation (Figure 1b). In path I, the SH photons are generated by copropagating SPPs and leak away from the Ag NW. This process is inefficient because the phase-matched conditions cannot be satisfied because the momentums of bound SPPs are larger than those of photons in air or in the substrate. In path II, the SH photons are generated by counter-propagating SPPs, so that the relationship $k^{(2)}(2\omega) = k_{spp}(\omega) - k_{spp}(\omega) = 0$ holds. The vanishing parallel momentum indicates that the generated coherent SH signals will emit only in the direction perpendicular to the Ag NW (Figure 1d).However, this momentum conservation relation has no restriction on the directionality of the SHG in the perpendicular plane. Therefore, the SH photons are collimated perpendicular to the nanowire axis but are divergent within the perpendicular plane. The emission pattern of SHG and its dependence on the structural parameters are the major subject in the following.

To obtain information about the wavevector distribution hidden in the real plane SHG image, we recorded the Fourier/real image plane by the same CCD camera by flipping up/down a lens.The SH Fourier plane images obtained with the different α are shown in Figure 2b–d. In the Fourier image, we see the angular distribution of the SH emission is dominant for ϕ = 90°, which means that the direction of the SHG is perpendicular to the Ag NW. This is a direct consequence of the momentum conservation condition between counter-propagating SPPs. The

experimental measurements also show that the emission pattern of the SHG depends on α. We also prove the far field SH Fourier images $I(\theta,\varphi) \propto \cos^2(\varphi - 3\alpha + 2\theta_c)$ present a periodical change of 60° to the angle α.

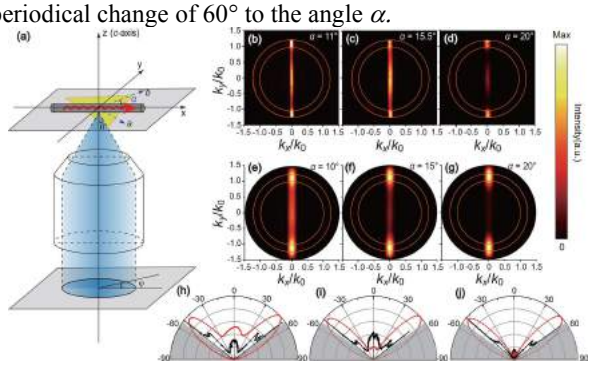


Figure 2. (a) Schematic of our Fourier imaging microscopy collecting signals with an oil objective. (b−d) Normalized experimental SH Fourier plane images obtained for different angle between the Ag NW and the monolayer MoS_2. (e − g) Normalized simulated Fourier image with the different angle between the Ag NW and the monolayer MoS_2, corresponding to (b − d). (h − j) Comparison between the angular distribution of the SH emission in experiments (b − d) and simulations (e − g) at ϕ = 90°. Reprinted with permission from ref 1. Copyright 2017 American Chemical Society.

2.2. 1D system of a tapered semiconductor nanowire

Experiments were performed on single-crystalline CdSe NWs grown mostly along the c axis that were dispersed onto SiO_2 substrate. In order to excite SHG, the supercontinuum laser light of 800 nm wavelength was focused onto the end of the CdSe nanowire with the electric field polarized along the c axis (transverse magnetic, TM). The second harmonic photons emitted from the structure were collected by the same objective through switching the filters into the collection light path. In figure 3a, the periodic second harmonic image of the wire are observed. We found that the SH emission is along with the perpendicular direction to the sample plane in figure 3b. It is approved that counter-propagating wave generated the second harmonic signal with momentum conservation.

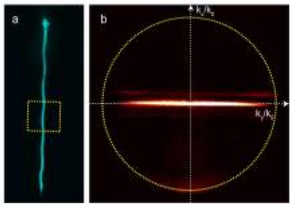


Figure 3: (a) Second harmonic image of the sample with the laser (800nm) focused on the top end of the nanowire . (b) Fourier image from SH image in (a).

3. Conclusions

In conclusion, we have presented SH image and its Fourier image to visualize the momentum conservation in 1D waveguide. As a consequence of the translation symmetry along the waveguide, SH photons are collimated perpendicular to the waveguide axis due to the coherent superposition.

References:

[1]. Li, Y., et al., Transversely Divergent Second Harmonic Generation by Surface Plasmon Polaritons on Single Metallic Nanowires. Nano Letters, 2017. 17(12): p. 7803-7808.

[2]. Chen, C.K., A. Castro and Y.R. Shen, Coherent second-harmonic generation by counterpropagating surface plasmons.

Transformation Optics and Other Waves: Novel Physics and Practical Applications

Magnetic invisible cloak without superconductor

Wei Jiang, Jiangfei Zhu and Yungui Ma*

State Key Lab of Modern Optical Instrumentation, Centre for Optical and Electromagnetic Research, College of Optical Science and Engineering, Zhejiang University, Hangzhou 310058, China

*Corresponding author: yungui@zju.edu.cn

Invisible cloaks designed by the general transformation optics scheme require the materials with strong inhomogeneous anisotropic electromagnetic parameters which seriously limits their applications. The requirement could be helpfully released when only considering the effect at ultralow frequencies. At the limit of quasi-static situation, Laplacian equation can be used to describe the system, which largely eases the fabrication. The bilayer approach consisting of superconductor SC and ferromagnetic shells has been employed to build a quasi-static magnetic cloak [1,2]. However, the usage of SC component is not suitable for general situations. In this work, we first show that the diamagnetic response could be electromagnetically realized by a thin metallic shell and its proper combination with the FM shell will give rise to a good dynamic magnetic cloaking effect without SC at frequency > 5 KHz [3]. At lower or strictly zero frequency, the metallic approach mimicking a diamagnetic sphere will fail to work. But in this case, we show that an active metamaterial approach could be adopted to replace the SC's position with a current surface. By this method, we also achieved good magnetic cloaking effect at zero frequency at room temperature.

References

[1] F. Gömöry, M. Solovyov, J. Šouc, C. Navau, J. Prat-Camps, and A. Sanchez, Science **335**, 1466 (2012).
[2] J. Zhu, W. Jiang, Y. Liu, G. Yin, J. Yuan, S. He, and Y. Ma, Nature Commun **6**, 8931 (2015).
[3] W. Jiang, Y. Ma, J. Zhu, G. Yin, Y. Liu, J. Yuan, and S. He, NPG Asia Mater **9**, e341 (2017)

Optical Spacetime in Self-Assembled Hyperbolic Metamaterials

Igor I. Smolyaninov[1,2], Vera N. Smolyaninova[3]

[1]Department of Electrical and Computer Engineering, University of Maryland, College Park, MD 20742, USA
[2]Saltenna LLC, 1751 Pinnacle Drive, McLean, VA 22102,USA
[3]Department of Physics Astronomy and Geosciences, Towson University,
8000 York Rd., Towson, MD 21252, USA
*corresponding author, E-mail: smoly@umd.edu

Abstract

Ferrofluid in the presence of magnetic field forms a hyperbolic metamaterial, which may be described via an effective "optical spacetime". If the magnetic field is reduced, this effective Minkowski spacetime gradually melts under the influence of thermal fluctuations. On the other hand, it may restore itself if the magnetic field is increased back to its original value. Microscopic visualization of such a spacetime melting/crystallization is presented, which is similar to hypothesized formation of the Minkowski spacetime in loop quantum cosmology.

1. Introduction

Very recently magnetic ferrofluids subjected to external magnetic field have emerged as an interesting example of a self-assembled hyperbolic metamaterial, which exhibits gravity-like nonlinear optical interactions, and which may be described by an emergent effective optical Minkowski spacetime [1-3]. By looking at this system we may better understand how macroscopic effective gravity may arise from the well-known microscopic degrees of freedom.

Propagation of monochromatic extraordinary photons inside the ferrofluid is described by the wave equation, which is formally equivalent to a 3D Klein-Gordon equation for a massive field $\varphi_\omega = E_z$ in a 3D Minkowski spacetime:

$$-\frac{\partial^2 \varphi_\omega}{\varepsilon_1 \partial z^2} + \frac{1}{(-\varepsilon_2)}\left(\frac{\partial^2 \varphi_\omega}{\partial x^2} + \frac{\partial^2 \varphi_\omega}{\partial y^2}\right) = \frac{{\omega_0}^2}{c^2}\varphi_\omega \qquad (1)$$

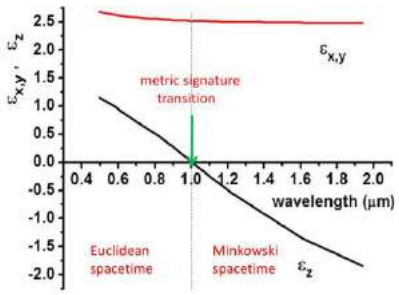
in which the spatial coordinate z behaves as a timelike variable, and E_z is the z-component of electric field in the wave [4,5]. Eq.(1) exhibits effective Lorentz invariance under the coordinate transformation:

$$z' = \frac{1}{\sqrt{1-\frac{\varepsilon_1}{(-\varepsilon_2)}\beta}}(z-\beta x) \qquad x' = \frac{1}{\sqrt{1-\frac{\varepsilon_1}{(-\varepsilon_2)}\beta}}\left(x-\beta\frac{\varepsilon_1}{(-\varepsilon_2)}z\right) \qquad (2)$$

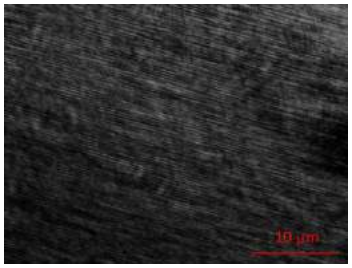
where β is the effective boost. Similar to our own Minkowski spacetime, the effective Lorentz transformations in the *xz* and *yz* planes form the Poincare group together with translations along *x, y*, and *z* axis, and rotations in the *xy* plane. Thus, the wave equation (1) describes world lines of massive particles which propagate in an effective 2+1 dimensional optical Minkowski spacetime. Components of the metamaterial dielectric tensor define the effective metric coefficients g_{ik} of this spacetime: $g_{00}=-\varepsilon_1$ and $g_{11}=g_{22}=-\varepsilon_2$. Nonlinear optical Kerr effect bends this spacetime resulting in the effective gravitational interaction between extraordinary photons [2]. Thus, transition to a hyperbolic state in the ferrofluid, which is described by Eqs.(1,2), may be understood as transition of the effective "optical spacetime" from Euclidean to Minkowski state. This transition may be driven by either temperature or external magnetic field. Since both parameters may experience variations across the volume of the ferrofluid, it is natural to expect that near the transition the ferrofluid separates into large number of individual Minkowski and Euclidean domains, leading to the notion of "metamaterial multiverse" [1].

2. Discussion

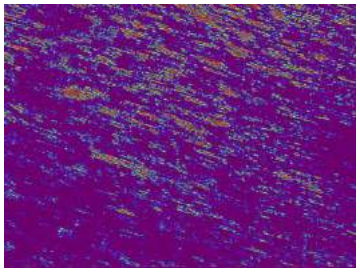
Our experiments use the cobalt magnetic fluid 27-0001 from Strem Chemicals, which is composed of 10 nm cobalt nanoparticles in kerosene coated with sodium dioctylsulfosuccinate and a monolayer of LP4 fatty acid condensation polymer. The average volume fraction of cobalt nanoparticles in this ferrofluid is p = 8.2%. Magnetic nanoparticles in a ferrofluid are known to form nanocolumns aligned along the external magnetic field [6]. In addition, depending on the magnetic field magnitude, solvent used, and the nanoparticle concentration, the ferrofluid undergoes phase separation into nanoparticle rich and nanoparticle poor phases [6]. The typical spatial scale of phase separation is 0.1-1 μm. Therefore, the microscopic structure of the ferrofluid may be visualized directly using an optical microscope.



(a)



(b)



(c)

Figure 1: (a) Wavelength dependencies of the real parts of $\varepsilon_z = \varepsilon_2$ and $\varepsilon_{x,y} = \varepsilon_1$ for a cobalt nanoparticle-based ferrofluid at 8.2% volume fraction of nanoparticles. While ε_x and ε_y stay positive and almost constant, ε_z changes sign to negative around $\lambda = 1\mu m$. (b) Microscopic image of cobalt nanoparticle-based ferrofluid in external magnetic field reveals nanoparticle alignment along the field direction. (c) Image of the stripe contrast in (b). This numeric procedure emphasizes ferrofluid regions having larger volume fractions of nanoparticles aligned into the nanochains. According to Eqs.(1,2), these regions behave as "Minkowski domains" separated by regions of Euclidean spacetime.

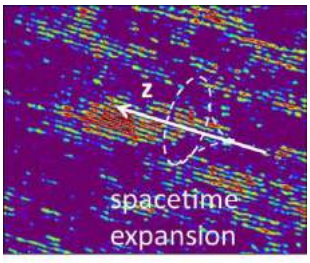


Figure 2: Magnified image of one of the Minkowski domains from Fig.1(c) illustrates inflation-like expansion of the effective spacetime near the domain wall.

As illustrated in Fig.1(c), our microscopic studies of the ferrofluid performed in varying magnetic field clearly reveal multiple Minkowski and Euclidean domains inside the ferrofluid. Fig.1(c) is obtained from the experimental image of light intensity *I(r)* in Fig.1(b) by numeric differentiation $\left|I(\vec{r}) - I(\vec{r} + \vec{d}/2)\right|$, where *d* is the periodicity of stripes visible in Fig.1(b). This numeric procedure reveals the stripe contrast, and emphasizes ferrofluid regions having larger volume fractions of nanoparticles aligned into the nanochains. According to Eqs.(1,2), these regions behave as "Minkowski domains" separated by regions of Euclidean spacetime, leading to a picture of "metamaterial multiverse". The experimentally measured image contrast in Fig.1(c) is proportional to the scale factor $(-\varepsilon_2)$ of the effective spacetime within the Minkowski domain. As illustrated in Fig.2, the effective spacetime exhibits very fast "expansion" along the arrow indicating the effective time direction near the Minkowski domain wall

3. Conclusions

In conclusion, we have presented direct microscopic visualization of optical spacetime domains, which describe extraordinary light propagation in cobalt-based self-assembled hyperbolic metamaterials. As was pointed out recently by Mielczarek and Bojowald [7], the properties of such self-assembled hyperbolic metamaterials exhibit strong similarities with the properties of such microscopic quantum gravity models as loop quantum cosmology.

References

[1] I.I. Smolyaninov, B. Yost, E. Bates, V.N. Smolyaninova, Experimental demonstration of metamaterial "multiverse" in a ferrofluid, *Optics Express* 21: 14918-14925, 2013.

[2] I.I. Smolyaninov, Analogue gravity in hyperbolic metamaterials, *Phys. Rev. A* 88: 033843, 2013.

[3] I.I. Smolyaninov, Holographic duality in nonlinear hyperbolic metamaterials, *Journal of Optics* 16: 075101, 2014.

[4] I.I. Smolyaninov, E.E. Narimanov, Metric signature transitions in optical metamaterials, *Phys. Rev. Letters* 105: 067402, 2010.

[5] I.I. Smolyaninov, Y.J. Hung, Modeling of time with metamaterials, *JOSA B* 28: 1591-1595, 2011.

[6] V.N. Smolyaninova, B. Yost, D. Lahneman, E. Narimanov, I.I. Smolyaninov, Self-assembled tunable photonic hyper-crystals, *Scientific Reports* 4: 5706, 2014.

[7] M. Bojowald, J. Mielczarek, Some implications of signature-change in cosmological models of loop quantum gravity, *J. of Cosmology and Astroparticle Phys.* 08: 052, 2015.

Chirality and Cartan's torsion in transformation optics

Yongliang Zhang[1], Che Ting Chan[2] and Kin Hung Fung[1,*]

[1]Department of Applied Physics, The Hong Kong Polytechnic University, Hong Kong, China
[2]Department of Physics, The Hong Kong University of Science and Technology, Hong Kong, China
*corresponding author, E-mail: kin-hung.fung@polyu.edu.hk

Abstract

We generalize the geometry of transformation optics to effective Riemann-Cartan space carrying both metric and torsion. By relaxing the integrable condition of the coordinate transformation, chiral magneto-electric coupling term emerges as torsion in the transformed Maxwell's equations. As a result, it is shown that a chiral medium is equivalent to a Riemann-Cartan space. Our theory provides a differential geometry description of the chiral medium and a generalization of the covariant pre-metric electrodynamics to realistic, complex media.

1. Introduction

The analogy of electromagnetic waves in response to transparent medium and curved space-time is a matter of extensive interest for both fundamental and technological reasons. Notably, the recent discovery of transformation optics [1] sheds new light on this pursuit. It is generally accepted that the geometry/material correspondence of transformation optics only relies on the Riemannian metric structure of the physical space determined by the spatial coordinate transformations, which is analogous to the general relativistic description of gravity. This assumption is in accordance with the Kotteler's approach of premetric electrodynamics [2] where the excitations (**D**, **H**) are related with the electromagnetic field strengths (**E**, **B**) with the constituent tensor [3]:

$$\chi^{ijkl} = \lambda_0 \sqrt{g}\left(g^{ik}g^{jl} - g^{il}g^{jk}\right). \tag{1}$$

It is obvious that the constituent tensor is completely determined by the metric tensor. Specifically, no magneto-electric coupling terms exist for purely spatial curved space. So it is natural to ask if the complex electromagnetic medium with magneto-electric coupling has a geometric origin in the framework of covariant electrodynamics.

2. Theory

Here, we show that the chiral medium with antisymmetric magneto-electric coupling is equivalent with a Riemann-Cartan space where the chiral term can be interpreted as the torsion of the curved space. A Riemann-Cartan space is the simplest extension of Riemannian geometry which is feature with torsion tensor besides the metric. Physically, the metric, i.e. permittivity and permeability specified by coordinate transformation, determines the local optical length and fix the causal structure of the space-time. On the contrary, it is generally believed that torsion arise from the spin angular momentum of matter, and interact with the spin of test particles inside the space.

2.1. Geometry

In conventional transformation optics, the spatial coordinate transformation implies the integrable condition of the Jacobian matrix:

$$\partial_\alpha J^a_\beta - \partial_\beta J^a_\alpha = 0 \tag{2}$$

According to the Frobeius theorem, the Pfaffian form $\vartheta^\alpha = \sum J^\alpha_a dx^a$ is a total differential. By relaxing the integrable condition, we can introduce torsion according to

$$\Omega^\gamma{}_{\alpha\beta} = e_a{}^\gamma\left(\partial_\alpha e^a{}_\beta - \partial_\beta e^a{}_\alpha\right) \tag{3}$$

where $e_a{}^\gamma$ is the non-integrable transformation matrix. In the anholonomic basis, the curved space is characterized by both metric and torsion tensor. The affine connection is given by

$$\Gamma^\gamma{}_{\alpha\beta} = \begin{Bmatrix} \gamma \\ \alpha\beta \end{Bmatrix} + Q^\gamma{}_{\alpha\beta} \tag{4}$$

where the first term in the right handed side is the usual symmetric Christoffel symbol which is determined by the metric tensor; while the asymmetric second term is determined by the torsion tensor. Consequently, we can obtain an effective Riemann-Cartan geometry.

2.2. Geometry/medium correspondence

In a torsional space, the curl Maxwell's equations can be written as the following form:

$$\varepsilon^{\alpha\beta\gamma}\left[\partial_\beta E_\gamma + \Omega^\delta{}_{\beta\gamma}E_\delta\right] - i\omega \mathrm{B}^\alpha = 0 \tag{5a}$$

$$\varepsilon^{\alpha\beta\gamma}\left[\partial_\beta H_\gamma + \Omega^\delta{}_{\beta\gamma}H_\delta\right] + i\omega \mathrm{D}^\alpha = 0, \tag{5b}$$

After rearrangement of the additional terms, we find that the chiral term is related to the torsion by

$$\kappa^{\alpha\beta} = \frac{1}{\omega}\varepsilon^{\alpha\gamma\delta}\Omega^\beta{}_{\gamma\delta} \tag{6}$$

2.3. Topology

The most important of the consequences of the torsional space is that the infinitesimal parallelogram is failed to be closed. The closed failure is given by

$$b^a = \int_S \Omega^a{}_{\alpha\beta} d\sigma^{\alpha\beta} \quad (7)$$

where $d\sigma^{\alpha\beta}$ is the infinitesimal area element in the physical space. It is clear that Eq. (7) is reminiscent of those of Berry's curvature and Berry's phase.

3. Example

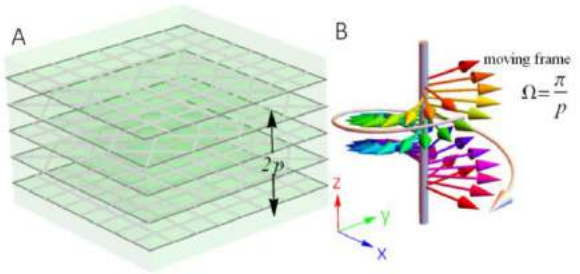


Figure 1: (A) Schematic of a helically twisted structure with a pitch distance p; (B) The twisted geometry defines a natural local frame rotating along z-axis.

We provide a realistic model for the above geometric theory based on helically twisted anisotropic medium (as shown in Fig. 1(A)). The intrinsic helical geometry defines a natural moving orthonormal frame rotating along z-axis. We calculate the associated torsion from the structural constant of the Lie bracket, and prove that torsion is equivalent to the chiral parameter of the effective medium in this model.

4. Conclusions

We demonstrate that the chiral medium can be interpreted as a Riemann-Cartan space with torsion tensor. Our theory provides a geometric interpretation of chiral magneto-electric coupling, extending the framework of transformation optics. It is expected that the generalized theory will find applications of manipulating the vectorial degree of freedom of light with complex electromagnetic media.

Acknowledgements

This work is supported by the Hong Kong Research Grants Council through grant No. 15300315, 15301917, AoE/P-02/12 and the Hong Kong Polytechnic University through grant No. G-UC70, G-YBPT and 1-ZVGH.

References

[1] J. B. Pendry, D. Schurig and D. R. Smith, Controlling electromagnetic fields, *Science* 312: 1780−1782, 2006.

[2] F. W. Hehl, Y. Itin and Y. N. Obukhov, *On Kottler's path: Origin and evolution of the premetric program in gravity and in electrodynamics*, Int. J. Mod. Phys. D 25: 1640016, 2016.

[3] E. J. Post, Formal Structure of Electromagnetics: General Covariance and Electromagnetics, Dover, 1997.

Controlling Surface Plasmons by Covariant Curved Spaces in One-dimensional Transformation Optical Nanostructures

Fan Zhong, [1] Jensen Li, [2] Hui Liu,*[1] and Shining Zhu[1]

Corresponding email: liuhui@nju.edu.cn

[1]*National Laboratory of Solid State Microstructures & School of Physics, Collaborative Innovation Center of Advanced Microstructures, Nanjing University, China*

[2]*School of Physics and Astronomy, University of Birmingham, UK*

General relativity uses curved space-time to describe accelerating frames. The movement of particles in different curved space-times can be regarded as equivalent physical processes based on the transformation between different metrics. In this work, we use one-dimensional transformation optical nanostructures to mimic accelerating particles in curved space-time. Using the covariant principle of general relativity, we can obtain different nanostructures designed from covariant space-times. Based on Lorentz covariance and conformal covariance, all these covariant structures can produce the same surface plasmon field when excited by polarized photons. Furthermore, using gauge (conformal) transformations between metrics, we can obtain more general covariant curved space-times and novel equivalent plasmonic structures.

Optical orbital angular momentum generated in a metamaterial ring by transformation optics

Mu Wang*, Hongwei Wu, Renhao Fan, and Ruwen Peng

National Laboratory of Solid State Microstructures, School of Physics, and Collaborative Innovation Center of Advanced Microstructures, Nanjing University, Nanjing 210093, China
*corresponding author, E-mail: muwang@nju.edu.cn

Abstract

Optical angular momentum plays a key role in many fundamental and applied researches [1-3]. In this work, we propose a scheme for the generation of transverse orbital angular momentum of light in metamaterial ring based on transformation optics. The metamaterial ring is designed to transform the straight trajectory of light into the circulating one by enlarging the azimuthal angle, effectively generating transverse orbital angular momentum of light. The simulation results confirm the theoretical predictions, which state that the magnitude of the transverse orbital angular momentum of light not only depends on the frequency of the incident light, but also depends on the transformation scale of the azimuthal angle. Because energy dissipation inevitably destroys the orbital angular momentum of light that exists in the metamaterial ring, the confined electromagnetic energy and the quality factor of the modes inside the ring are also studied in order to evaluate the stability of the orbital angular momentum of light. The results show that the metamaterial ring can effectively confine light with a high quality factor and maintain steady generation of the orbital angular momentum of light, even if the dimension of the ring is much smaller than the wavelength of the incident light. This technique for exploiting transverse orbital angular momentum of light provides a unique platform for applications related to optical micromanipulation.

References:

1. A. Bekshaev, K. Bliokh, and M. Soskin, “Internal flows and energy circulation light beams,” J. Opt. 13(5), 053001 (2011).
2. M. Mansuripur, “Spin and orbital angular momenta of electromagnetic waves in free space,” Phys. Rev. A 84(3), 033838 (2011).
3. H. W. Wu, F. Wang, Y. Q. Dong, F. Z. Shu, K. Zhang, R. W. Peng, X. Xiong, and Mu Wang, “Cavity modes with optical orbital angular momentum in a metamaterial ring based on transformation optics”, Optics Express (2015) 23, 32087.

Definite Light Deflection of Cosmic Topological Defects Mimicked By Rotational Metasurfaces

Chong Sheng[1], Ying Chen[2], Zhiwei Yan[1], Lin Xu[2], Xiangyang Wang[1], Qing Huo Liu[3], Shining Zhu[1], Huanyang Chen[2], Hui Liu[1]*

[1]National Laboratory of Solid State Microstructures and School of Physics,
Collaborative Innovation Center of Advanced Microstructures, Nanjing University, Nanjing, Jiangsu 210093, China
[2]Institute of Electromagnetics and Acoustics and Department of Electronic Science, Xiamen University, Xiamen, China
[3]Department of Electrical & Computer Engineering,Duke University, Box 90291,Durham, NC 27708-0291
*corresponding author, E-mail: liuhui@nju.edu.cn

Abstract

The existence of cosmic string, one-dimensional topological defect formed during a symmetry breaking phase transition in the early university, was predicted in the 1970s. However, thus far there is no direct astronomical observation. Here, by using rotational metasurfaces in an artificial waveguide, gravitational lensing caused by nontrivial spacetime of cosmic string is experimentally emulated. Our technique is a brand-new way to manipulate photons on chip using metasurfaces, and may be widely used in transformation optical devices in geometrical optics.

1. Introduction

Topology is playing a very important role in the frontiers of modern physics. It is well known that topological properties have been widely reported in condensed matters. Especially, theorists predicted that some topological defects may have formed during a symmetry breaking phase transition in the early universe when the topology of the vacuum manifold associated to this symmetry breaking was not simply connected[1] such as monopoles and cosmic strings. The experimental observation of these topological defects in astrophysics would revolutionize the vision of the cosmos. However, to the best of our knowledge, thus far there is no direct evidence to observe these topological defects in astrophysics. Fortunately, analog models, in various systems under the laboratory environment, have been motivated by the possibility of investigating phenomena not readily accessible in their cosmological counterparts. Recently, the ongoing revolution in transformation optics[2,3] based on metamaterials with manipulating permittivity and permeability profiles, can be extensively investigated to design artificial materials to mimick general relativity phenomena. In this work, we experimentally demonstrate that cosmic string (see Fig. 1(a)), which is a one-dimensional topological defect assumed to be long lived as phase transition in the early universe, can be emulated by steering a transformation optical waveguide using rotational metasurfaces (see Fig.1(b)-(d)).

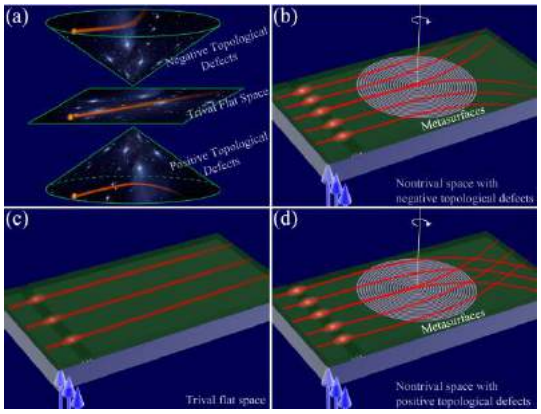


Figure 1: (a) Description of gravitational lensing caused by cosmic string: the trajectory of light move toward (away from) to the origin of the string with positive (negative) curvature, compare to the case that light propagates in a straight line without topological defect. (b-d) Schematic view of the fabricated artificial optical waveguide using meatasurfaces respectively mimicking topological defects with negative curvature at the origin, trivial flat space and topological defects with positive curvature at the origin.

2. Results

2.1. The electromagnetic parameter

We start with a spacetime metric for a static cylindrically symmetric cosmic string with straight and infinite long length:

$$ds^2 = dt^2 - dr^2 - \alpha^2 r^2 d\theta^2 - dz^2 \quad (1)$$

were $\alpha = 1 - 4G\mu$, G is the gravitational constant, μ is the linear mass density of the string along the rotation axis, and the nature units have been adopted. The corresponding Riemann curvature is given by $R_{12}^{12} = 2\pi(1-\alpha)\delta^{(2)}(r)/\alpha$ where $\delta^{(2)}(r)$ is the 2D Dirac delta function in the plane. According to Riemann curvature, if the mass density of the string $\mu > 0$, it carries positive curvature at the origin; on

the other hand, it carries negative curvature with a negative mass density ($\mu < 0$). It is well known that the motion of photon follows the null geodesic of the curved space, thus the trajectory of light moves toward (away from) the origin of the string with positive (negative) curvature, as shown in Fig. 1 (b)-(d). According to the correspondence between material electromagnetic parameters and the metric of spacetime in general relativity based on transformation optics. After calculations, the material parameter tensors required by cosmic string have their principal values along r , θ and z directions:

$$\varepsilon_r = \mu_r = \alpha,\ \varepsilon_\theta = \mu_\theta = 1/\alpha,\ \varepsilon_z = \mu_z = \alpha \qquad (2)$$

2.2. The Rotational Metasurfaces Design

In order to obtain anisotropic parameter in the slab waveguide, the metasurfaces which consists subwavelength grating, can be considered to weakly disturb the slab modes, which resulting in elliptical dispersion. The slab waveguide with metasurfaces has two principle values n_e and n_o as shown in Fig.2 (d), whose effective index distribution is similar to that of a uniaxial crystal. In order to rotate optical axis, a circular type grating instead of linear type grating (see Fig. 2(b), (c)), and the effective parameter distribution

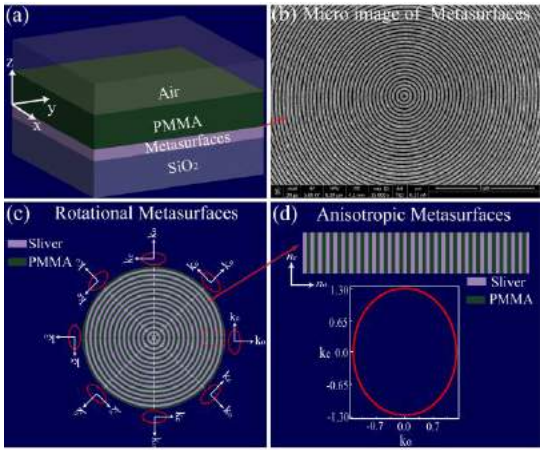


Figure 2. (a) A step-index planar waveguide consisting air/PMMA/metasurfaces/sliver multilayer. (b) The fabricated metasurfaces with a set of periodic circular grating in experimental sample using focused ion beam. (c) The anisotropic metasurfaces with rotating optical axis. (d) The contour of effective index in artificial optical waveguide using metasurfaces, and the iso-frequency curve becomes elliptical.

with a tensor is described as: $\varepsilon = R^{-1}(\theta)\begin{bmatrix} n_e^2 & 0 \\ 0 & n_o^2 \end{bmatrix} R(\theta)$,

where n_o and n_e are waveguide effective index along radial and azimuthal direction, $R(\theta)$ is rotational matrix. Comparing to expression formula in Equation (2), the effective parameters in a structured waveguide using metasurfaces as the circular type grating have a good correspondence to that required by cosmic string.

2.3. The Experimental Results

In experiments, the metasurface with a set of periodic subwavelength circular grating (a bull's eye structure, as shown in Fig.2(b)) was fabricated by focused ion beam (FEI Strata FIB 201, 30keV, 7.7pA) milling on a 250-nm-thickness sliver film, which has been initially deposited on a silica substrate (SiO_2). Then a polymethylmethacrylate (PMMA) resist mixed with oil-soluble PbS quantum dots was deposited on the silver film using a spin-coating process (as shown in Fig. 2(a)). Fig. 2(a) shows the SiO2/Sliver/Metasurfaces/PMMA/Air multilayer structure. Fig. 2(c) is the schematic plot of the bull's eye structure, which are locally periodic gratings along the r direction, as shown in Fig. 2(d). Fig.3 shows the gravitational lensing of cosmic string with positive and negative curvature at the origin respectively emulated with rotational metasurfaces waveguide.

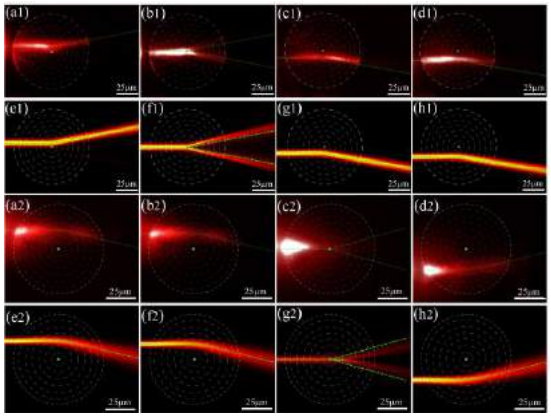


Figure3. (a1-h1) The experimental realization of mimicking gravitational lensing of cosmic string with positive curvature at the origin. (a1-d1) are experimental results; (e1-h1) are the corresponding simulation results. (a2-h2) The experimental realization of mimicking gravitational lensing with negative curvature at the origin. (a2-d2) are experimental results; (e2-h2) are the corresponding simulation results

3. Conclusions

In conclusion, we have experimentally demonstrated an optical analogy of topological defects in cosmology using meatasurfaces in an artificial waveguide. The gravitational lensing of cosmic string, one-dimensional topological defect, can be experimentally mimicked by steering the dispersion contour in the artificial waveguide. And the motion of photon in the nontrivial spacetime caused by cosmic string is clearly exhibited in our experiments.

References

[1] Kibble, T. W. B. Topology of Cosmic Domains and Strings. *J. Phy. A.* **9**, 1387-1398 (1976).

[2] Pendry, J. B., Schurig, D. & Smith, D. R. Controlling electromagnetic fields. *Science* **312**, 1780-1782 (2006).

[3] Leonhardt, U. Optical conformal mapping. *Science* **312**, 1777-1780 (2006).

Lightcone fluctuations in a metamaterial that mimics a cosmic string

Jiawei Hu[1] **and Hongwei Yu**[1,*]

[1]Department of Physics and Synergetic Innovation Center for Quantum Effects and Applications, Hunan Normal University, Changsha 410081, China
*corresponding author, E-mail: hwyu@hunnu.edu.cn

Abstract

We study the flight time fluctuations in an anisotropic medium that mimics a cosmic string with an effective fluctuating refractive index caused by fluctuating background vacuum electric fields, which are analogous to the lightcone fluctuations due to a fluctuating spacetime metric when gravity is quantized. For a probe light propagating close to the analogue string, the flight time fluctuations can be amplified compared with those in a normal homogeneous and isotropic medium. We argue that it seems possible to fabricate a metamaterial so that a currently observable flight time variance might be achieved in laboratory.

1. Introduction

In quantum gravity, lightcones, the boundaries between spacelike and timelike regions, are no longer fixed, but smeared out due to the quantum fluctuations of spacetime metric as necessitated by the uncertainty principle. A direct result of lightcone fluctuations is that the flight time of a probe light signal from its source to a detector spreads about the classical value in both directions [1, 2]. These flight time fluctuations are in principle observable but are extremely small in general and seem to be undetectable in experiment in the foreseeable future. Therefore, it is of interest to resort to analogue systems to see whether some basic predictions of quantum gravity can be analogously verified there. Recently, Ford *et al*. proposed that, in a nonlinear medium, the flight time of a probe light fluctuates due to a fluctuating effective refractive index when the medium is subjected to a fluctuating background field, which is analogous to the lightcone fluctuation when gravity is quantized [3, 4].

In this paper, we study the flight time fluctuation of certain probe light pulses that arises from a fluctuating refractive index due to electromagnetic vacuum fluctuations in an anisotropic medium that mimics a cosmic string in terms of the classical propagation of light. In particular, we demonstrate that the flight time fluctuations can be amplified compared with those in a normal medium by manipulating the electric permittivity and magnetic permeability of the analogue medium, and remarkably, a currently experimentally observable flight time variance would be obtained if an analogue cosmic string with a large enough ν could be fabricated in laboratory. The Lorentz-Heaviside units with $\hbar = c = 1$ are used in this paper unless specified.

2. Lightcone fluctuations in an analogue cosmic string spacetime

The total electric field E^i can be written as a sum of a background field $E_0^i(\omega_0)$ and a probe field $E_1^i(\omega_1)$. In the absence of the probe field E_1^i, the medium the background field E_0^i propagates in can be treated as a linear medium characterized by a dielectric tensor ε_{ij} such that $D^i = \varepsilon^{ij}E_j$ [4]. The line element of a static, straight cosmic string spacetime takes the form

$$ds^2 = dt^2 - d\rho^2 - \frac{\rho^2}{\nu^2}d\phi^2 - dz^2 \,. \tag{1}$$

Here $\nu = (1-4G\mu)^{-1}$, with μ the mass per unit length of the string, and G the Newtonian constant of gravitation. In the framework of transformation optics [5, 6], the electric permittivity and magnetic permeability tensors of a medium that mimics the cosmic string spacetime take the form

$$\varepsilon^{ij} = \mu^{ij} = n_B \begin{pmatrix} 1 & 0 & 0 \\ 0 & \dfrac{\nu^2}{\rho^2} & 0 \\ 0 & 0 & 1 \end{pmatrix} . \tag{2}$$

In such a medium, the electromagnetic wave equation for the background field E_0 takes the same form as that in the cosmic string spacetime with an effective speed of light $v_B = 1/n_B$. Consider a probe light E_1^i, which is much smaller than the background field E_0^i, while its frequency ω_1 is much larger than that of the background field ω_0 [3, 4], and assume that its the second order susceptibility tensor $\chi^{(2)}_{ijk}$ is nonnegligible. If the probe field is propagating in the z-direction and is polarized in the ρ-direction, i.e. $E_1^i = \delta^{i\rho}E_1(t,z)$, the wave equation for E_1 takes the form

$$-\frac{\partial^2 E_1}{\partial z^2} + \frac{1}{v_P^2}\left[1 + \frac{1}{n_P^2}\left(\chi^{(2)}_{\rho\rho j} + \chi^{(2)}_{\rho j\rho}\right)E_0^j\right]\frac{\partial^2 E_1}{\partial t^2} = 0 \,, \tag{3}$$

where $n_P = 1/v_P$.

Suppose that the probe light propagates through the metamaterial of an analogue cosmic string located at the z-axis, from (t_1, ρ, ϕ, z_1) to (t_2, ρ, ϕ, z_2), with $d = z_2 - z_1$ the thickness of the material. The relative flight time variance can be written as [3, 4]

$$\begin{aligned}\delta^2 \;=\; & \frac{1}{4n_P^4 d^2}\int_{z_1}^{z_2} dz \int_{z_1}^{z_2} dz' \left(\chi^{(2)}_{\rho\rho i} + \chi^{(2)}_{\rho i\rho}\right) \\ & \times \left(\chi^{(2)}_{\rho\rho j} + \chi^{(2)}_{\rho j\rho}\right)\langle E_0^i(t,\vec{x})E_0^j(t',\vec{x}')\rangle \,. \end{aligned} \tag{4}$$

Here the two point function of the electric field can be obtained by appealing to the existing result in the cosmic string spacetime [7, 8]. Note that the two point function is a summation over the contributions of vacuum field modes in all frequencies, while the derivation of the wave equation (3) is based on the assumption that the frequency of the background field is much smaller than that of the probe field. Interestingly, the contributions from high frequency modes of the background field can be suppressed by engineering a smoothly varying second order susceptibility in the frequency regime of the probe light in the direction parallel to the analogue string. To see this, let us take $\chi^{(2)}$ to be a function of z, for example, in the following Lorentzian form

$$\chi^{(2)}(z) = \frac{d^2}{\pi(z^2+d^2)}\chi_0^{(2)} \ , \tag{5}$$

where $\chi_0^{(2)}$ is the averaged second order susceptibility along the z-axis, then Eq. (4) can be re-expressed as

$$\delta^2 \propto \left\langle 0 \right| \int_{-\infty}^{\infty} d\omega e^{-|\omega|\tau} E^i(\omega) \int_{-\infty}^{\infty} d\omega' e^{-|\omega'|\tau} E^j(\omega') \left| 0 \right\rangle \ ,$$

where $\tau = n_P\, d$. Therefore, it is clear that contributions from vacuum modes whose wavelengths are shorter than the thickness of the medium are suppressed.

Computing Eq. (4) and expanding the result in a series of ρ/d, one obtains, when the trajectory of the probe light is close to the analogue string, i.e. $\rho/d \ll 1$, the following flight time fluctuations

$$\delta^2 \approx \frac{\nu\, n_B\, (\chi_0^{(2)})^2}{16\pi^2(n_P^2-n_B^2)^2 n_P^4 d^4} \ . \tag{6}$$

The result shows that, in principle, an observable light cone fluctuation within the current experiment precision would be obtained if the analogue cosmic string could be fabricated with a large enough ν in laboratory.

Now an important question is how large the factor ν could be. Recall that ν is related to the anisotropy of the medium. For a class of dielectrics with extreme optical anisotropy, ν can be extremely large [9]. Such a medium can be realized with artificial metamaterials [10, 11, 12]. For an order of magnitude estimation, we find that ν can be of the order of 10 or larger if we assume that the wavelength of the probe light λ_P is of the order of $\sim 1\ \mu$m, and the thickness of the metamaterial d is of the order of $\sim 10\ \mu$m. Therefore, it seems possible to fabricate a metamaterial that mimics a cosmic string with a large ν in laboratory.

3. Conclusions

In this paper, we have investigated the lightcone fluctuations in an anisotropic metamaterial of an analogue cosmic string. For a probe light close to the analogue string, it has been shown that the flight time fluctuations of the probe light can be amplified compared with those in a normal medium and become observable if an analogue cosmic string with a large enough ν could be fabricated in laboratory. So, our study here may seem to offer a possible way to manipulate lightcone fluctuations, presumably the most direct effect of quantum gravity, in analogue systems, and make it potentially observable.

Acknowledgement

This work was supported in part by the NSFC under Grants No. 11435006, No. 11690034, No. 11375092, and No. 11447022; the Zhejiang Provincial Natural Science Foundation of China under Grant No. LQ15A050001.

References

[1] L.H. Ford, Gravitons and light cone fluctuations, *Phys. Rev. D* 51: 1692, 1995.

[2] H. Yu and L.H. Ford, Light-cone fluctuations in flat spacetimes with nontrivial topology, *Phys. Rev. D* 60: 084023, 1999.

[3] L.H. Ford, V.A. De Lorenci, G. Menezesc, N.F. Svaiter, An analog model for quantum lightcone fluctuations in nonlinear optics, *Ann. Phys. (N.Y.)* 329: 80-92, 2013.

[4] C.H.G. Bessa, V.A. De Lorenci, L.H. Ford, N.F. Svaiter, Vacuum lightcone fluctuations in a dielectric, *Ann. Phys. (N.Y.)* 361: 293-302, 2015.

[5] U. Leonhardt, Optical Conformal Mapping, *Science* 312: 1777-1780, 2006.

[6] J.B. Pendry, D. Schurig, and D.R. Smith, Controlling Electromagnetic Fields, *Science* 312: 1780-1782, 2006.

[7] V.D. Skarzhinsky, D.D. Harari, and U. Jasper, Quantum electrodynamics in the gravitational field of a cosmic string, *Phys. Rev. D* 49: 755, 1994.

[8] H. Cai, H. Yu, and W. Zhou, Spontaneous excitation of a static atom in a thermal bath in cosmic string spacetime, *Phys. Rev. D* 92: 084062, 2015.

[9] F. Capolino, editor, *Applications of Metamaterials*, CRC Press, Boca Raton, FL, 2009.

[10] P.A. Belov, R. Marqués, S.I. Maslovski, I.S. Nefedov, M. Silveirinha, C.R. Simovski, and S.A. Tretyakov, Strong spatial dispersion in wire media in the very large wavelength limit, *Phys. Rev. B* 67: 113103, 2003.

[11] Mário G. Silveirinha, Nonlocal homogenization model for a periodic array of ϵ-negative rods, *Phys. Rev. E* 73: 046612, 2006.

[12] P.A. Belov and Y. Hao, Subwavelength imaging at optical frequencies using a transmission device formed by a periodic layered metal-dielectric structure operating in the canalization regime, *Phys. Rev. B* 73: 113110, 2006.

Light in Transformed Spaces: Optical Black Holes and Nanofocusing Lenses

Alexander V. Kildishev[1], Lian Shen[1,2,3], Hongsheng Chen[2,3], and Ludmila J. Prokopeva[1]

[1]Birck Nanotechnology Center and Purdue Quantum Center, School of ECE, Purdue University, W. Lafayette, USA
[2]State Key Laboratory of Modern Optical Instrumentation, Zhejiang University, Hangzhou 310027, China.
[3]The Electromagnetics Academy at Zhejiang University, Zhejiang University, Hangzhou 310027, China
*corresponding author, E-mail: kildishev@purdue.edu

Abstract

We use the formalism of transformed optical spaces to design omnidirectional concentrators and nanofocusing lenses employing manufacturable layered approximations in their designs. We show that accurate theoretical analyses and an improved effective medium theory allow to estimate and drastically improve the performance metrics of the proposed metadevices by reducing the number of approximating layers. We successfully verify the proposed theoretical design rules vs. full-wave numerical simulations.

1. Introduction

Transforming coordinate space equivalently to the distribution of electromagnetic material tensors, $\boldsymbol{\varepsilon}$ and $\boldsymbol{\mu}$, is a known technique for solving electromagnetic problems, see [1-3] and references within. This formalism also provides an elegant way to formulate design rules when constructing the optical metamaterial spaces with the desired properties, for metadevices including for example omnidirectional concentrators ("black holes") or nanofocusing lenses. Not only space transformations help to derive the required distribution of the material parameters for an ideal continuous device, but they also offer accurate design rules for the realistic lamellar structures that take into account the Jacobian of the exact transformation. The latter helps to avoid additional distortions from an approximate layered structure vs. the ideal continuous profile and significantly reduces the number of required layers, hence improving manufacturability of a given device.

In this talk, we review our previous results on designing optical black holes (section 2) and nanofocusing devices (section 3), where we briefly comment on the derivations of both design steps: (1) the exact ideal analytical distribution of the material tensors and (2) accurate approximation of the ideal device with a layered design that has a minimal number of layers. Finally, we validate the suggested designs with simulations that confirm exceptional performance of omnidirectional concentrators and nanofocusing devices with the minimal number of layers.

2. Optical black holes

The optical black hole (OBH) is an *omnidirectional* light concentrator and absorber that can be used for example in energy harvesting applications as a 'drop-and-forget' device since the tracking of the sun is not needed in this case. The founding theoretical works on the physical modelling of black holes were done in acoustics, e.g. [4] and then rediscovered in optics. The theory of a circular OBH was previously developed by us in [5,6], and then experimentally demonstrated at the microwave [7], and optical spectral bands [8], and then again in acoustics [9].

Recently, we have introduced a new elliptically flattened design, which could have elliptic cylinder, oblate or prolate spheroidal profiles [10]. This brings flexibility to the shape of the absorber, which can be flattened to a thin strip (elliptic cylinder), thin disk (oblate spheroid) or a thin wire (prolate spheroid). The new flattened designs of the absorber are suitable for existing semiconductor-based technologies that can be used in actual fabrication.

The key designing rule of an ideal OBH is to generate a quadratic fall of the permittivity in the trapping shell that creates a potential well for the optical beam (figure 1) and guides it to the absorbing core for any angle of incidence, while ensuring impedance matching on the interfaces,

$$\varepsilon(u) = \begin{cases} \varepsilon_0, & u > u_0 \\ \varepsilon_0 \left(\sinh u_0 / \sinh u \right)^2, & u_1 < u \le u_0 \\ \varepsilon_1 + i\gamma_1, & u \le u_1 \end{cases}. \quad (1)$$

Here u is the elliptic coordinate (in circular case, $u = r$ and $\sinh(u)$ gets replaced with just r).

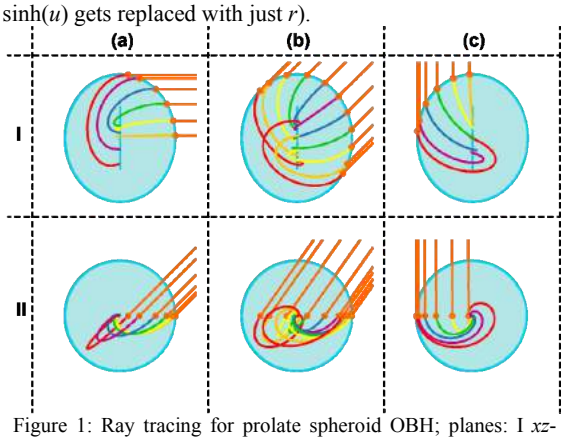


Figure 1: Ray tracing for prolate spheroid OBH; planes: I *xz*-plane, II *yz*-plane; angles of incidence: (a) 0°, (b) 45°, (c) 90°.

Then with full-wave simulations (figure 2) we derive a theoretical estimation for the absorbing performance and we study the performance of the layered designs.

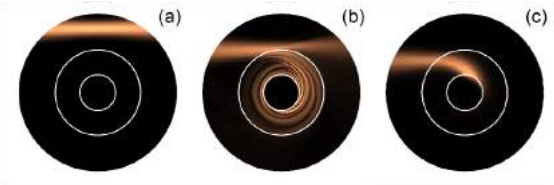


Figure 2: Full wave simulation of a Gaussian beam incident to an ideal circular black hole (eq. (1)) at different angles (a) $y_0 = 1.5R$; (b) $y_0 = R$; (c) $y_0 = 0.75R$.

3. Nanofocusing lenses

Extreme nanofocusing is now recognized as a scientifically interesting method of generating intense optical fields confined to the smallest possible sub-wavelength volume, finding applications in sensing, nonlinear optics, sub-wavelength optical lithography.

Most of the existing approaches sacrifice industrial scalability for the sake of core metrics such as throughput and focusing performance. In this work, we exploit hyperbolic dispersion that can be achieved with existing nanofabrication techniques using conventional metal and dielectric materials [11]. With hyperbolic dispersion we break the diffraction limit thus allowing deep subwavelength focusing, and we preserve the simplicity of fabrication at the same time. We show that with an accurate multi-layer design well-performing nanofocusing lens can be arranged with just 5 metal-dielectric pairs of layers, see figure 3.

Specifically, to design an ideal lens, we use a cubic scaling transformation that makes matching the impedances at the input and output interfaces possible, providing a theoretical foundation for the significant throughput enhancement. Then we use zeroth-order *Cylindrical* Effective Media Theory (EMT) (as opposed to conventional *Planar* EMT) that allows us to enable the practical realization of the layered designs with real-life metals and dielectrics.

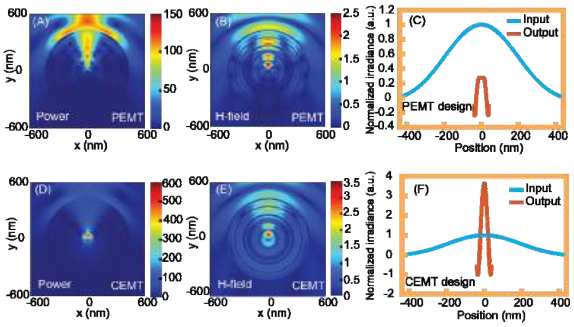


Figure 3: Full-wave simulation of the nanofocusing device with 5 pairs of binary metal-dielectric layers. Planar EMT (PEMT) design (A-C) fails with focusing performance, while accurate cylindrical EMT (PEMT) design (D-F) provides good nanofocusing.

4. Conclusions

Transformation optics is an important instrument for accurate multi-layer optic designs suitable for realistic nanofabrication. We use the formalism of transformed space for both stages – to design an ideal device and to construct accurate multi-layer approximation.

In this work, we presented realistic designs of omnidirectional light concentrators, with circular and flattened elliptic form factor, and we designed a nanofocusing hyperbolic lens that can be fabricated only with 5 pairs of metal-dielectric layers, provided that (1) high order (cubic) transformation is used and (2) improved cylindrical EMT is used for the layered design. Rigorous full wave simulations are used to verify our theoretical fundamentals.

Acknowledgements

AVK and LJP acknowledge the financial support by DARPA/DSO Extreme Optics and Imaging (EXTREME) Program, Award HR00111720032.

References

[1] L. S. Dolin, To the possibility of comparison of three-dimensional electromagnetic systems with non-uniform anisotropic filling, *Izvestiya Vysshikh Uchebnykh Zavedenii. Radiofizika* 4(5): 964−967, 1961.

[2] A. J. Ward and J. B. Pendry, Refraction and geometry in Maxwell's equations, *J. Mod. Opt.* 43(4): 773−793, 1996.

[3] H. Chen, J. B. Pendry and D. R. Smith, Special issue on transformation optics, *J. Opt.* 18: 040201, 2016.

[4] M. Visser, Acoustic black holes: horizons, ergospheres and Hawking radiation, *Class. Quantum Grav.* 15(6): 1767, 1998.

[5] E. E. Narimanov and A. V. Kildishev, Optical black hole: Broadband omnidirectional light absorber, *Appl. Phys. Lett.* 95: 041106, 2009.

[6] A. V. Kildishev, L. J. Prokopeva, and E. E. Narimanov, Cylinder light concentrator and absorber: theoretical description *Opt. Express* 18: 16646, 2010.

[7] Q. Cheng et al., An omnidirectional electromagnetic absorber made of metamaterials, *New J. Phys.* 12: 063006, 2010.

[8] C. Sheng et al., Trapping light by mimicking gravitational lensing, *Nat. Photonics* 7: 902 - 906, 2013.

[9] O. Umnova, A. S. Elliott, and R. Venegas, Omnidirectional acoustic absorber with a porous core – theory and measurements, *Proc. of Meetings on Acoustics* 19: 065018, 2013.

[10] L. J. Prokopeva and A. V. Kildishev, Expanding the theory of circular omnidirectional light concentrators to elliptic and spheroidal designs, *J. Opt.* 18(4): 044014, 2016.

[11] L. Shen, L. J. Prokopeva, H. Chen, and A.V. Kildishev, Designing optimal nanofocusing with a gradient hyperlens, *Nanophotonics* 7(2): 479−487, 2017.

A phase space plot of resonances in transformation cavities

Inbo Kim[1], Jinhang Cho[1], Yushin Kim[2], Sang-Jun Park[1], Bumki Min[2], and Muhan Choi[1,*]

[1]School of Electronics Engineering, Kyungpook National University, Daegu 41566, South Korea
[2]Department of Mechanical Engineering, Korea Advanced Institute of Science and Technology, Daejeon 34141, South Korea
*corresponding author, E-mail: mhchoi@ee.knu.ac.kr

Abstract

Gradient index cavities designed by conformal transformation optics enable directional whispering gallery modes (WGMs). For the inhomogeneous cavities, Husimi function, one of the widely used phase space representations for resonant modes can be obtained using the conventional Husimi functions for uniform index cavities through a fictitious space. As an illustration, we calculated Husimi function of a bidirectional WGM, which agrees well with the directionality of far-field of the WGM.

1. Transformation cavities

Recently, applying the transformation optics (TO) [1] to the design of optical dielectric resonators, Kim *et al.* have reported 2-dimensional (2D) gradient index dielectric cavities called transformation cavities by using conformal TO where directional WGMs are possible [2].

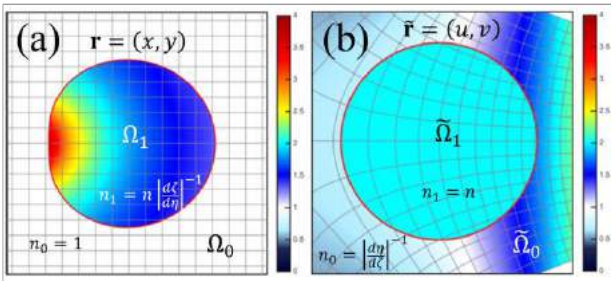


Figure 1: (a) a limaçon-shaped transformation cavity in the physical space, (b) the corresponding unit disk cavity in the associated reciprocal virtual (RV) space.

By an optical conformal mapping from the inside region of an uniform index unit disk cavity in an original virtual (OV) space with coordinates (u, v, w) to the physical space with coordinates (x, y, z), a realizable 2D gradient index cavity model, called as 'transformation cavities' can be built: w-axis and z-axis are taken along the axis of each infinite cylindrical cavity. The conformal mapping from the OV space to the physical space is given by an analytic function $\zeta = f(\eta) = x(u,v) + iy(u,v)$ of the OV space complex variable $\eta = u + iv$. Resonant modes in a transformation cavity are found by solving the following 2D wave equation,

$$\left[\Delta + n^2(\mathbf{r})k^2\right]\psi(\mathbf{r}) = 0\,, \tag{1}$$

; $\Delta \equiv \partial_x^2 + \partial_y^2$, $\mathbf{r} = (x,y)$ and the refractive index is given by

$$n(\mathbf{r}) = \begin{cases} n\left|\frac{d\zeta}{d\eta}\right|^{-1}, & \mathbf{r}\in\Omega_1 \ \text{(interior)} \\ 1, & \mathbf{r}\in\Omega_0 \ \text{(exterior)} \end{cases}, \tag{2}$$

The complex wave function $\psi(\mathbf{r})$ represents E_z and H_z components corresponding to the transverse magnetic (TM) and the transverse electric (TE) resonant modes, respectively with the following boundary conditions at the cavity–air interface,

$$\psi_1 = \psi_0\,, \quad \partial_\perp\psi_1 = \partial_\perp\psi_0 \qquad \text{for TM modes} \tag{3a}$$

$$\psi_1 = \psi_0\,, \quad \frac{\partial_\perp\psi_1}{n_1^2} = \partial_\perp\psi_0 \qquad \text{for TE modes}\,, \tag{3b}$$

where ψ_j are wave functions on the cavity boundary from the interior region ($j=1$) and the exterior region ($j=0$) and $\partial_\perp\psi_j$ are their normal derivatives, respectively; $\partial_\perp \equiv \mathbf{p}(\mathbf{r})\cdot\nabla|_{\mathbf{r}}$ and $\mathbf{p}(\mathbf{r})$ is the outward normal unit vector on the cavity boundary curve Γ at point $\mathbf{r}$ and n_1 is the refractive index along the boundary, i.e., $n_1 = n\left|d\zeta/d\eta\right|^{-1}$ evaluated at the boundary. The resonant modes are obtained under the outgoing-wave condition which leads to solutions exponentially decaying in time with discrete complex wavenumber k with $\mathrm{Im}[k] < 0$.

2. Husimi function at transformation cavities

For the case of 2D uniform index dielectric cavities, Hentschel *et al.* have derived four different Husimi functions in a reduced phase space, i.e., on the Poincaré surface of section (PSOS) at the dielectric interfaces [3]. Their Husimi functions can still be useful for optical modes supported in transformation cavities if we construct a virtual space which we call a reciprocal virtual (RV) space, through the inverse conformal mapping. Under the mapping, the wave equation (1) is transformed to

$$\left[\tilde{\Delta} + \tilde{n}^2(\tilde{\mathbf{r}})k^2\right]\tilde{\psi}(\tilde{\mathbf{r}}) = 0\,, \tag{4}$$

where $\tilde{\Delta} \equiv \partial_u^2 + \partial_v^2$, $\tilde{\mathbf{r}} = (u, v)$, and refractive index is given by

$$\tilde{n}(\tilde{\mathbf{r}}) = \begin{cases} n, & \tilde{\mathbf{r}} \in \tilde{\Omega}_1 \quad \text{(interior)} \\ \left|\frac{d\eta}{d\zeta}\right|^{-1}, & \tilde{\mathbf{r}} \in \tilde{\Omega}_0 \quad \text{(exterior)} \end{cases} . \qquad (5)$$

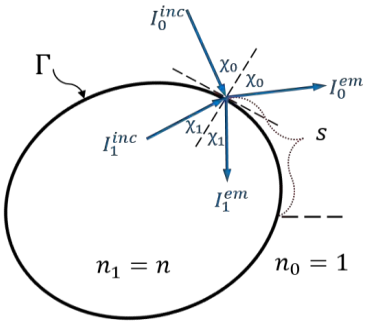


Figure 2: Incident and emerging rays at a dielectric interface with uniform refractive indices.

In the RV space, the Husimi function for the incident waves in the unit disk cavity with uniform index n can be written as

$$H_1^{inc}(\tilde{s}, \sin\tilde{\chi}_1) = \frac{k_1}{2\pi}\left|\mathcal{F}_1 h_1(\tilde{s}, \sin\tilde{\chi}_1) - \frac{in}{k_1 \mathcal{F}_1} h_1'(\tilde{s}, \sin\tilde{\chi}_1)\right|^2 \qquad (6)$$

with a weighting factor $\mathcal{F}_1 = \sqrt{n\cos\tilde{\chi}_1}$ and the functions h_1, h_1' given by overlap integrals

$$h_1(\tilde{s}, \sin\tilde{\chi}_1) = \oint_{\tilde{\Gamma}} d\tilde{s}'\, \tilde{\psi}_1(\tilde{s}')\, \xi(\tilde{s}'; \tilde{s}, \sin\tilde{\chi}_1), \qquad (7a)$$

$$h_1'(\tilde{s}, \sin\tilde{\chi}_1) = \oint_{\tilde{\Gamma}} d\tilde{s}'\, \tilde{\partial}_\perp \tilde{\psi}_1(\tilde{s}')\, \xi(\tilde{s}'; \tilde{s}, \sin\tilde{\chi}_1), \qquad (7b)$$

of the wave function $\tilde{\psi}$ and its normal derivative $\tilde{\partial}_\perp \tilde{\psi}$, taken on the inside ($j = 1$) of the unit disk at arc length $\tilde{s}'$ along the boundary $\tilde{\Gamma}$ in the RV space, with the minimum-uncertainty wave packet,

$$\xi(\tilde{s}'; \tilde{s}, \sin\tilde{\chi}_1) = \frac{1}{\sqrt[4]{\sigma\pi}} \sum_{l\in\mathbb{Z}} \exp\left[\begin{matrix} -\dfrac{(\tilde{s}' - \tilde{s} + 2\pi l)^2}{2\sigma} \\ -ik_1 \sin\tilde{\chi}_1 (\tilde{s}' + 2\pi l) \end{matrix}\right], \qquad (8)$$

which is periodic in $\tilde{s}'$ and centered around $(\tilde{s}, \sin\tilde{\chi}_1)$; the parameter $\sigma = \sqrt{2}/k_1$ determines the uncertainty in $\tilde{s}$ and $\sin\tilde{\chi}_1$. For a resonant mode, $k_1 = n\,\mathrm{Re}[k]$ where k is a complex wave number of the resonant mode.

3. An illustrative example

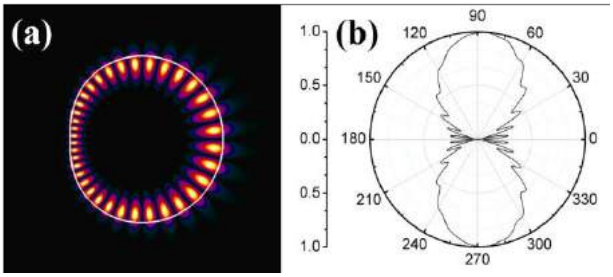


Figure 3: A bidirectional WGM in a limaçon-shaped transformation cavity (k =12.2333–i0.0022) (a) the near-field pattern, (b) the far-field intensity distribution.

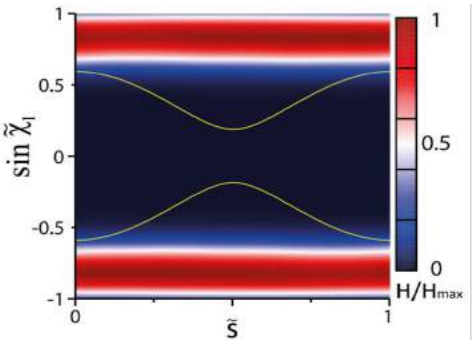


Figure 4: Husimi plot for incident waves of the bidirectional WGM in the RV space; two yellow solid curves are critical lines of total internal reflection.

4. Conclusions

Husimi representation for the internal waves on the boundary of a transformation cavity was presented by constructing a virtual space *via* inverse conformal mapping. Husimi plot of the corresponding modes in the virtual space explains well the far-field directionality of the resonant modes of a transformation cavity.

Acknowledgements

NRF grant funded by the Korea government (MSIP) (No. 2017R1A2B4012045 and No. 2017R1A4A1015565); CAMM funded by Korea Government (MSIP) as Global Frontier Project (CAMM 2014M3A6B3063709)

References

[1] J. B. Pendry, D. Schurig, and D. R. Smith, Controlling electromagnetic fields, *Science* 312; 1780–1782, 2006.

[2] Y. Kim, S. H. Lee, J. W. Ryu, I. Kim, J. H. Han, H. S. Tae, M. Choi, and B. Min, Designing whispering gallery modes via transformation optics, *Nat. Photonics* 10; 647–652, 2016.

[3] M. Hentschel, H. Schomerus, and R. Schubert, Husimi functions at dielectric interfaces: Inside-outside duality for optical systems and beyond, *Europhys. Lett.* 62; 636–642, 2003.

Quantum Nanophotonics for Applications in Quantum Information Science

Near-optimal entangled-photon sources in the solid state?

Fei Ding

[1] Institut für Festkörperphysik, Leibniz Universität Hannover, Appelstraße 2, 30167 Hannover, Germany
[2] Institute for Integrative Nanosciences, IFW Dresden, Helmholtzstraße 20, 01069 Dresden, Germany
E-mail: f.ding@fkp.uni-hannover.de

Abstract

How far are we away from an optimal entangled photon Source? This is a difficult question, and the answer depends, of course, on the specific applications. For optical quantum communications, the high repetition rate, photon indistinguishability, entanglement fidelity and brightness are required for a useful polarization entangled photon source. The aim of our works is to gather the above-mentioned features in a solid state source based on single semiconductor quantum dots.

1. Introduction

SPDC-based entangled photon sources play a crucial role in the development of quantum information sciences. However, these sources have several intrinsic problems, such as the low brightness and the lack of electric injection for practical applications. It is anticipated that semiconductor quantum dots (QDs) have strong potential to address these problems, as they can produce high quality entangled photon pairs on demand. However, due to the random growth nature of the quantum dots, several critical challenges need to be addressed. Despite the great efforts, the community has not yet reached the "*Eureka*!" moment for QD-based entangled photon sources. In the following we discuss the recent progress on improving the performances of these solid state sources.

2. Results

We can imagine an optical quantum communication network as a complex architecture of photons, a geographically distributed system for joining rapidly multiple quantum nodes with high scalability and for exchanging information with high fidelity.

2.1. Wavelength tunability

No two snowflakes are alike. The same is true for two QDs, which becomes a critical problem when "joining" two or more QDs in a quantum photonic network. For SPDC sources this so-called scalability is not an issue, as their wavelength tunability can be easily achieved by using identical bandpass filters. It is estimated that the probability to perform entanglement swapping between two different QDs is less than 10^{-13}. We developed a novel on-chip strain tuning platform and successfully demonstrated the spectral resonance of different QDs.[1] This work removes a major road-block in nesting multiple QD sources.

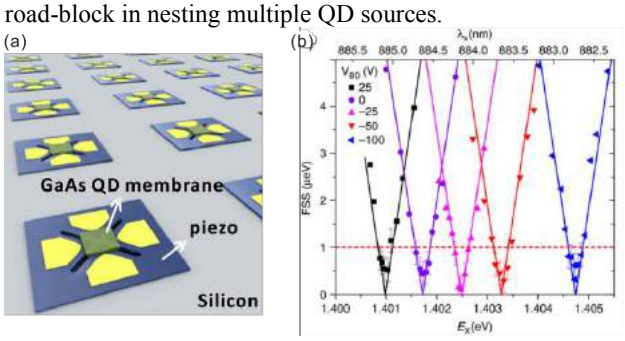


Figure 1 (a) On-chip strain tuning platform used to achieve the wavelength tunability of QD-based entangled photon sources. (b) Fine-structure-splitting (FSS) as a function of the exciton emission energy, measured at different stress conditions.

2.2. Photon indistinguishability

For "exchanging" information with the so-called entanglement protocol, it is also required that the photons emitted consecutively from the same QDs are highly indistinguishable. The GaAs/AlGaAs QDs grown by droplet etching and nanohole infilling [2] were investigated by resonance fluorescence spectroscopy, and it was shown that photons with Fourier-limited linewidth are emitted from these QDs. [3]

2.3. Entanglement fidelity

The entanglement fidelity provides a measure of how well the entanglement between two photons in a pair is preserved in a quantum process. To avoid too much multiphoton noise, single photon pairs in a SPDC source can only be produced at a low rate (p), typically $p < 0.1$ per excitation pulse. When the source efficiency is pushed towards 0.1, the entanglement fidelity degrades quickly to below 0.9. For QD-based sources, their fidelities have long been limited to below 0.75. We have demonstrated a source with entanglement fidelity of over 0.9, which is on par with the traditional SPDC sources. The improved fidelity may be attributed to the different spin-nuclear interaction mechanism in the new samples.[4, 5]

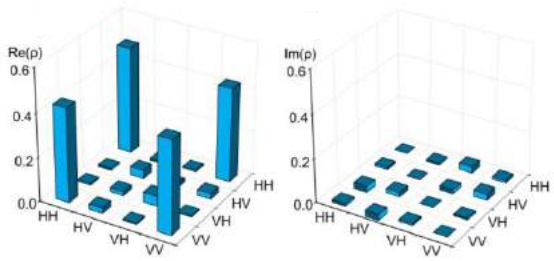


Figure 2 Representative two-photon density matrix for a QD-based polarization entangled photon source, showing an entanglement fidelity of about 0.9.

2.4. Electroluminescence

Electrically pumped entangled photon sources are very attractive for practical applications. After the first report in Nature, 465, 594 (2010), no second group was able to reproduce the result. This is mainly due to the extremely low yield (<1%) to cherry-pick a suitable QD. By combining our strain-tuning technology with electrical pumping, a high yield of 30% has been demonstrated. This value remains a record to date. The repetition rate for this electrically pumped entangled photon source is up to 400 MHz.[6]

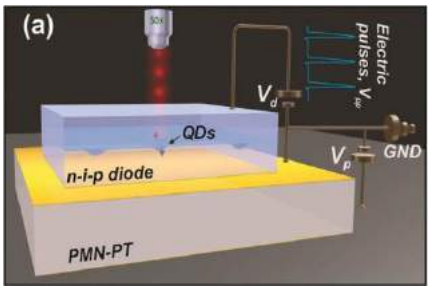


Figure 3 An electrically pumped entangled photon source with a repetition rate of up to 400 MHz and a yield of 30%.

2.5. Source brightness

To join remote quantum nodes "rapidly", it is required that the entangled photon sources can be operated at high repetition rates and have high brightness. Due to the short exciton lifetime (1 ns or less), it is possible to obtain GHz operation rate for semiconductor QDs. Unfortunately, the high refractive index of the host material limits the extraction efficiency of the photons and hence the source brightness. The record pair rate of 0.12 was obtained by using a double micropillar structure. We are employing a solid immersion lens based approach to improve the brightness further. Some recent results will be presented and discussed.

3. Conclusions

SPDC sources have been used as the main working horse in the quantum optics field for decades. However, further improvements in their performances are seriously limited. Here we show that the QDs have the potential to overcome the shortness of SPDC sources and are of particular interest in quantum communication, quantum metrology or quantum imaging.

Acknowledgements

The results presented here would not have been possible without the contributions from J.X. Zhang, B. Hoefer, Y. Chen, M. Zopf, R. Keil. Y. Zhang and many of our former members (E. Zallo, P. Atkinson, Y. Huo, J. Plumhof, S. Kumar, R. Trotta). I personally acknowledge A. Rastelli and V. Zwiller for their early guidance.

These works have been strongly supported over the past years by O. G. Schmidt and by many institutions, most importantly, BMBF (QuaHL-Rep, Q.Com-H), ERC Starting Grant (No. 715770, QD-NOMS), European Union Seventh Framework Programme 209 (FP7/2007–2013, HANAS), and IFW Excellence program.

References

[1] Y. Chen et al., Wavelength-tunable entangled photons from silicon-integrated III-V quantum dots, *Nature Communications* 7, 10387 (2016)

[2] Y. Huo et al., A light-hole exciton in a quantum dot, *Nature Physics* 10, 46 (2014)

[3] J.P. Jahn et al., An artificial Rb atom in a semiconductor with lifetime-limited linewidth, *Phys. Rev. B* 92, 245439 (2015)

[4] R. Keil et al., Solid-state ensemble of highly entangled photon sources at rubidium atomic transitions, *Nature Communications* 8, 15501 (2017)

[5] E. Chekhovich et al., Measurement of the spin temperature of optically cooled nuclei and GaAs hyperfine constants in GaAs/AlGaAs quantum dots, *Nature Materials* 16, 982 (2017)

[6] J.X. Zhang et al., High yield and ultrafast sources of electrically triggered entangled-photon pairs based on strain-tunable quantum dots, *Nature Communications* 6, 10067 (2015)

Nonlinear AlGaAs nanodisks as sources of sum-frequency light and entangled photons

Giuseppe Marino[1,2,3,*], Alexander S. Solntsev[1,4], Lei Xu[1], Valerio F. Gili[2], Luca Carletti[5], Alexander N. Poddubny[1,6,7], Mohsen Rahmani[1], Daria Smirnova[1], Haitao Chen[1], Guoquan Zhang[8], Anatoly V. Zayats[3], Costantino De Angelis[5], Giuseppe Leo[2], Yuri S. Kivshar[1], Andrey A. Sukhorukov[1], and Dragomir N. Neshev[1]

[1]Nonlinear Physics Centre, Research School of Physics and Engineering, Australian National University, Canberra ACT 2601, Australia
[2]Matériaux et Phénoménes Quantiques, Université Paris Diderot-CNRS, 10 rue Alice Domon et Lonie Duquet, F-75013 Paris, France
[3]Department of Physics, King's College London, Strand, London WC2R 2LS, UK
[4]School of Mathematical and Physical Sciences, University of Technology Sydney, 15 Broadway, Ultimo NSW 2007, Australia
[5]Dept. of Information Engineering, University of Brescia, Via Branze 38, 25123 Brescia, Italy
[6]ITMO University, 49 Kronverksky Pr., Saint Petersburg 197101, Russia
[7]Ioffe Physical-Technical Institute, Saint Petersburg 194021, Russia
[8]The MOE Key Laboratory of Weak Light Nonlinear Photonics, School of Physics, Nankai University, Tianjin, China
*Corresponding author, E-mail: giuseppe.marino@univ-paris-diderot.fr

Abstract

We demonstrate experimentally the generation of heralded photons with non-classical correlations via spontaneous parametric down-conversion in AlGaAs nanodisks. A quantum-classical correspondence establishes the AlGaAs nanoresonators as nanoscale nonlinear sources of efficient sum-frequency and difference frequency conversion.

1. Introduction

Nanoscale nonlinear sources have recently attracted enormous interest for classical and quantum applications due to the possibility of efficient wavelength mixing at the nano-scale [1]. In this context, an important role is played by all-dielectric and semiconductor resonant nonlinear nanophotonics, where efficient optical interactions between magnetic and electric resonances at the subwavelength scale, enable high figures of merit due to low losses and high directionality [1, 2]. It was shown that AlGaAs nanodisks can provide high efficiency of the second-harmonic generation (SHG) of the order of 10^{-4} [2]. This record-high efficiency opens a wide range of possible applications, including nonlinear imaging and holography [3]. In this work, we show experimentally that the strong quadratic nonlinearity in AlGaAs nanodisks allows for efficient sum-frequency generation (SFG) with nontrivial polarization dependencies, and high biphoton generation rate with strong non-classical polarization and angular correlations. By using the classical-quantum analogy between SFG and spontaneous parametric down-conversion (SPDC) [4], the experimental rate can be compared with predictions.

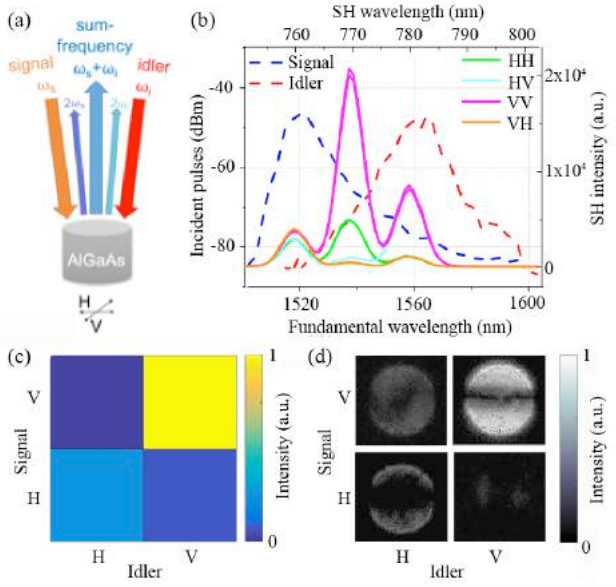


Figure 1: Experimental observation of SFG. (a) Scheme of SFG with signal and idler beams in an [100] AlGaAs nano-resonator. The horizontal (H) and vertical (V) polarization axes are parallel to the crystalline axes of the AlGaAs lattice. (b) AlGaAs nano-resonator SFG reflection spectra at 770 nm and signal / idler SHG spectra at 760 / 780 nm; the plot shows 4 combinations of H and V polarizations of signal and idler beams, respectively. (c) Color map of H-polarized SFG at 770 nm for the polarization combinations shown in (b). (d) SFG directionality diagrams for the polarization combinations shown in (b).

2. Sum-Frequency Generation

SFG is measured from an [100] AlGaAs-on-oxide monolithic nanoscale resonator [5], as shown in Fig. 1(a). A complete set of the experimental spectra are shown in Fig. 1(b). Dashed lines show the incident pulses, namely the signal and the idler with central wavelength of 1520 and 1560 nm, respectively, while solid lines show the three nonlinear parametric wave-mixing spectra, namely SFG at 770 nm, and signal and idler SHG at 760 nm and 780 nm, respectively. With the use of half-wave plates we control the polarizations of the two incident pulses onto the single AlGaAs nanodisk resonator. The resulting SFG-signal counts at 770 nm are shown in Fig. 1(c) for different states of polarization of the two incident pulses. The corresponding SFG radiation patterns measured with a camera and a Fourier imaging system are, instead, depicted in Fig. 1(d). The SFG radiation patterns strongly depend on signal/idler polarization combinations, with the highest measured SFG conversion efficiency being over 10^{-6}. We observe a good agreement between the experimental data and numerical simulations obtained by the COMSOL finite-element method.

3. Spontaneous Parametric Down-Conversion

Next, we measure the integrated generation of entangled photon pairs through SPDC and observe the photon-pair rate in the range of 200 Hz [see Fig. 2(b)]. This leads to figures of merit for SPDC efficiency that include the generation volume, being 600 times higher compared to leading parametric down-conversion on-chip sources [6]. The analysis based on the established proportionality to the SFG amplitude of classical signal and idler waves, propagating in the opposite direction [4], indicates that by utilising better designed structures, the SPDC rate can be dramatically improved. We predict that a sub-wavelength AlGaAs nano-resonator can generate over 10^4 photon pairs per second, which is comparable with some established bulk photon-pair sources and suggests that nonlinearity on the nanoscale can be employed for efficient generation of quantum states.

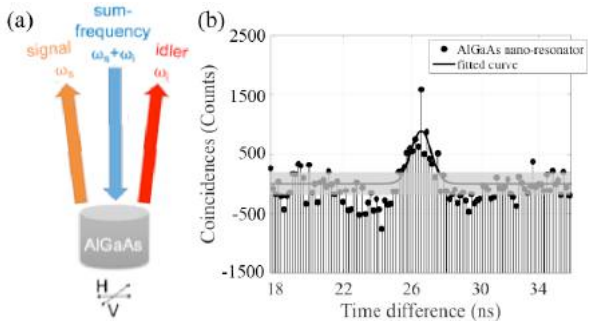


Figure 2: (a) Schematic of SPDC with signal and idler beams in an [100] AlGaAs nano-resonator. (b) Coincidence rate of the photon pairs generated via SPDC vs the time difference between the arrival of signal and idler photons to the single-photon detectors.

4. Conclusions

In summary, we have measured the first heralded photon source at the nanoscale with a bi-photon rate higher than 100 Hz. The source estimated fabrication and characterization flexibility gives also the potentials to compete with established bulk quantum sources.

References

[1] A.I.,Kuznetsov, A.E. Miroshnichenko, M.L. Brongersma, Y.S. Kivshar, B. Luk'yanchuk, Optically resonant dielectric nanostructures, *Science* 354.6314: aag2472, 2016.

[2] R. Camacho-Morales, M. Rahmani, S. Kruk, L. Wang, L. Xu, D.A. Smirnova, A.S. Solntsev, A. Miroshnichenko, H.H. Tan, F. Karouta, S. Naureen, K. Vora, L. Carletti, C. De Angelis, C. Jagadish, Y.S. Kivshar, D.N. Neshev, Nonlinear generation of vector beams from AlGaAs nanoantennas, *Nano Letters* 16.11: 7191-7197, 2016.

[3] L. Carletti, D. Rocco, A. Locatelli, C. De Angelis, V. Gili, M. Ravaro, I. Favero, G. Leo, M. Finazzi, L. Ghirardini, M. Celebrano, G. Marino, A. Zayats, Controlling second-harmonic generation at the nanoscale with monolithic AlGaAs-on-AlOx antennas, *Nanotechnology* 28.11: 114005, 2017.

[4] A.N. Poddubny, I.V. Iorsh, A.A. Sukhorukov, Generation of photon-plasmon quantum states in nonlinear hyperbolic metamaterials, *Physical Review Letters* 117.12: 123901, 2016.

[5] V. Gili, L. Carletti, A. Locatelli, D. Rocco, M. Finazzi, L. Ghirardini, I. Favero, C. Gomez, A. Lemaître, M. Celebrano, C. De Angelis, G. Leo, Monolithic AlGaAs second-harmonic nanoantennas, *Optics Express* 24.14: 15965-15971, 2016.

[6] X. Guo, C. l. Zou, C. Schuck, H. Jung, R. Cheng, and H. X. Tang, Parametric down-conversion photon-pair source on a nanophotonic chip, *Light: Science & Applications* 6.5: e16249, 2017.

In(Ga)As quantum dots at the telecom wavelength: single and entangled photons emission

Simone L. Portalupi*, Fabian Olbrich, Marc Sartison, Stephan Hepp, Cornelius Nawrath, Sascha Kolatschek, Michael Jetter and Peter Michler

Institut für Halbleiteroptik und Funktionelle Grenzflächen Center for Integrated Quantum Science and Technology (IQST) and SCoPE
University of Stuttgart,
*corresponding author, E-mail: s.portalupi@ihfg.uni-stuttgart.de

Abstract

In the present work we describe different techniques for the growth of single In(Ga)As quantum dots (QDs) emitting in the telecom regime. Single and entangled photon emission is demonstrated.

1. Introduction: fiber networks

Long distance telecommunication relies nowadays on optical fibers, which can cover distances among cities and among continents. In the realization of quantum networks it would be ideal to rely on such a very developed technology. While propagating into single mode fibers, two wavelength ranges are of interest: the so-called O-band (around 1310 nm) and the so-called C-band (around 1550 nm). The first represents the region of absolute minimal wavepacket dispersion while the latter covers the region of absolute minimum absorption. These properties make the aforementioned wavelength very interesting for quantum optics applications. Long distance quantum communications particularly require that the single photon wavepacket propagates with minimal losses and dispersion. Ideally, the information codified into single photons should arrive non-attenuated and with no dispersion: if on the one hand, losing photons means losing information, on the other hand a modification of the wavepacket will result into a lower capability of the single photons to interfere (then introducing errors in the computation). The choice of wavelength is then mainly determined by the photon property that must be mainly conserved.

2. Single quantum dots

Semiconductor quantum dots are currently considered as one of the main players in the generation of non-classical light. Since the first demonstration of single photon emission [1] they emerged as very bright sources of single and indistinguishable photons [2]. State-of-the-art performances are currently reached using InAs nanostructures grown on GaAs substrate. On the other hand, these quantum dots naturally emit in the NIR region (around 900 nm), far from being ideal for fiber-based applications. An alternative is based on the growth of InAs QDs on InP substrates [3, 4]. It has been demonstrated the possibility to reach the telecom C-band but the growth is complex and the emitter density is high compared to GaAs-based emitters. In addition to that, InP-based QDs lack of efficient Bragg mirrors which limits the choice of available resonators.
Here we show which techniques can be employed to utilize standard GaAs-substrates for growing QDs emitting up to the telecom C-band.

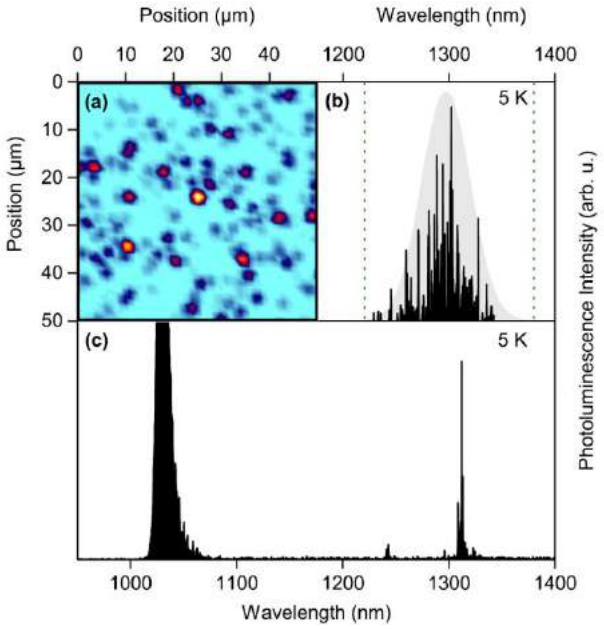


Figure 1: (a) Micro-PL map showing isolated QDs. (b) Quasi ensemble spectrum around 1300 nm. (c) Wide range micro-PL spectrum showing QDs and wetting layer emission. [5]

The most appealing perspective is that, in principle, the same state-of-the-art performances achieved in the NIR regime could be reached in the telecom bands. Here we utilized the strain-reduced layer approach to extend the growth of In(Ga)As quantum dots up to the telecom O-band

[5]. Single and cascaded photon emission is demonstrated [6]. Purity, in particular, is shown to be stable (i.e. below 0.5) up to nitrogen temperature [7]. It is also shown how to utilize strain tuning techniques to modify the QD emission wavelength and to reduce its fine structure splitting [8].
With a slightly different approach, i.e. using a metamorphic buffer, the emission wavelength can be extended up to the telecom C-band [9]. Here, on-demand emission of single photon is demonstrated and, for the first time, also the generation of polarization entangled photons [10].

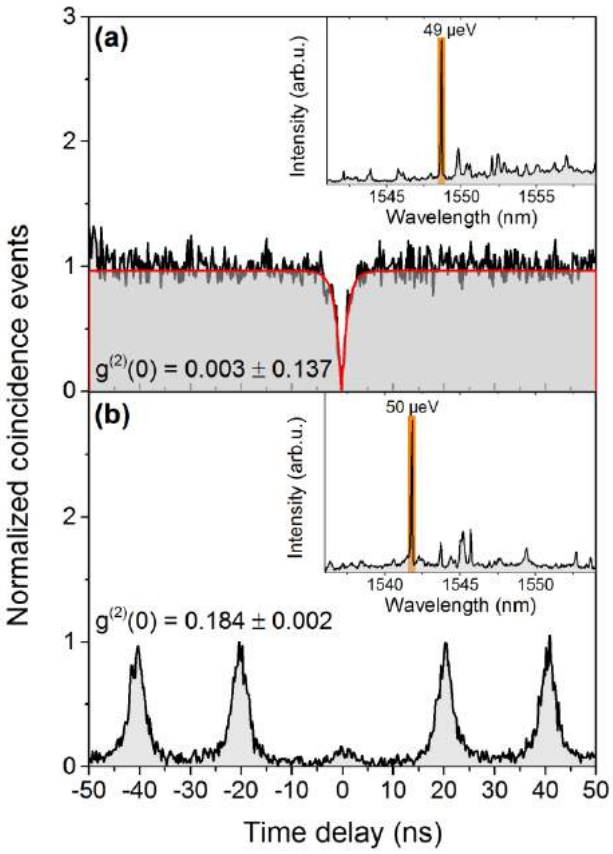


Figure 2: Autocorrelation measurements for the lines shown in the insets. (a) CW excitation. (b) pulsed excitation. [9]

3. Conclusions

Two complementary approaches have been utilized to grow InAs QDs emitting in the telecom regime. A strain reducing layer was used to reach the telecom O-band while a metamorphic buffer approach allowed emission in the telecom C-band. While in both cases single photon emission is achieved, in the case of C-band photons, polarization entanglement is also demonstrated.

Acknowledgements

The authors gratefully acknowledge funding by the Federal Ministry of Education and Research (BMBF), in particular, for the project Q.com-H (16KIS0115). SLP acknowledges the IQST via the project "QUDOSI".

References

[1] P. Michler, A. Kiraz, C. Becher, W. V. Schoenfeld, P. M. Petroff, L. Zhang, E. Hu, and A. Imamoglu, Science 290, 2282 (2000).

[2] P. Michler, ed., Quantum Dots for Quantum Information Technologies (Springer International Publishing, 2017).

[3] S. Fafard, Z. Wasilewski, J. McCaffrey, S. Raymond, and S. Charbonneau, Appl. Phys. Lett. 68, 991 (1996).

[4] R. Leonelli, C. Tran, J. Brebner, J. Graham, R. Tabti, R. Masut, and S. Charbonneau, Phys. Rev. B 48, 11135 (1993)

[5] M. Paul, J. Kettler, K. Zeuner, C. Clausen, M. Jetter and P. Michler Appl. Phys. Lett. 106, 122105 (2015)

[6] J. Kettler, M. Paul, F. Olbrich, K. Zeuner, M. Jetter, P. Michler Appl. Phys. B (2016) 122:48, DOI 10.1007/s00340-015-6280

[7] F. Olbrich, J. Kettler, M. Bayerbach, M. Paul, J. Höschele, S. L. Portalupi, M. Jetter, and P. Michler, J. Appl. Phys. 121, 184302 (2017).

[8] B. Höfer, F. Olbrich, J. Kettler, M. Paul, J. Höschele, M. Jetter, S. L. Portalupi, F. Ding, P. Michler and O. G. Schmidt, *submitted*

[9] M. Paul, F. Olbrich, J. Höschele, S. Schreier, J. Kettler, S. L. Portalupi, M. Jetter, and P. Michler, Appl. Phys. Lett. 111, 33102 (2017).

[10] F. Olbrich, J. Höschele, M. Müller, J. Kettler, S. L. Portalupi, M. Paul, M. Jetter, and P. Michler, Appl. Phys. Lett. 111, 133106 (2017).

Combining Laser 3D Printing with Self-Assembly

Maria Farsari[1*], Argyro Klini[1], Argyro N. Giakoumaki[1], George Kenanakis[1]

[1]IESL-FORTH, Heraklion, Greece*
*corresponding author, E-mail: mfarsari@iesl.forth.gr

Abstract

We report on a new method for preparing fully three-dimensional ZnO nanorod structures based on a combination of two laser techniques and low temperature hydrothermal growth. 3D structures are firstly fabricated employing Multiphoton Lithography. They are subsequently covered by a Zinc layer using Pulsed Laser Deposition; this layer acts as a seed for the growth of ZnO nanorods by Aqueous Chemical Growth. The resulting structures are covered uniformly by nanorods and are electrically conductive.

1. Introduction

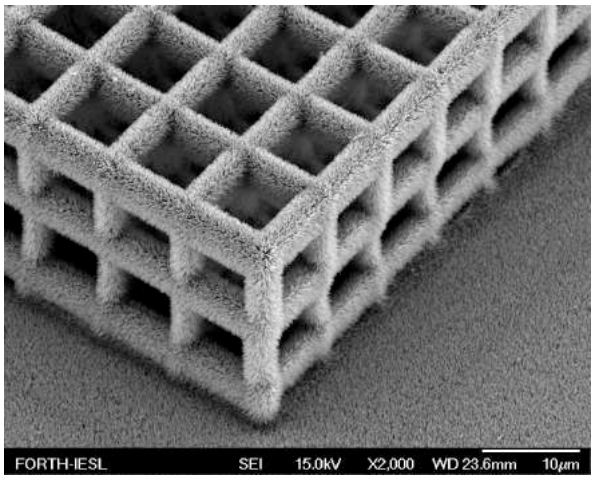
Zinc Oxide (ZnO) nanostructures have been the subject of intense research interest in recent years. Several applications have been proposed, such as gas sensors [1], phototocatalysts [2], and nanolasers [3]. Moreover, pure and doped ZnO has attracted attention to substitute noble metals such as gold and silver as the primary plasmonic building blocks of plasmonic metamaterials [4].

Different chemical and physical methods have been used for creating pure and doped ZnO nanostructures. For instance, Chemical Vapor Deposition (CVD) [5], Thermal Evaporation [6], electrochemical deposition in porous membranes [7], and Aqueous Chemical Growth (ACG)[8] have been reported amongst other techniques. Glass, Si wafers, flexible organic films, and wires have been used as substrates. In all cases, however, the ZnO nanorod patterning has been done on flat surfaces and in the form of films, and the 3D deposition has been limited to horizontal, vertical, or flower-like geometries, [9] or even nanobelts and nanosprings. [10]

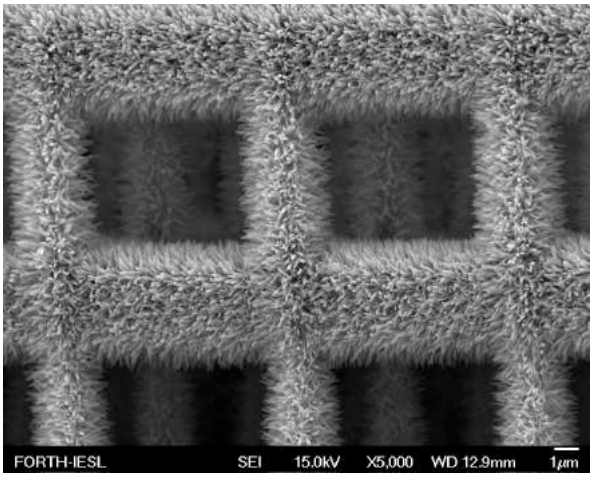
Here, we demonstrate a method of fabricating conducting, fully three-dimensional (3D) ZnO nanorod structures based on a combination of two laser techniques and low temperature hydrothermal growth. The first step is the fabrication of a 3D nano-scaffold using Multi-Photon Lithography (MPP) of an organic-inorganic hybrid material. [11] MPP is a laser-based Additive Manufacturing technique, which allows the fabrication of fully 3D microstructures with high resolution. Once the nano-scaffold is prepared, then it is subsequently covered with a thin film of zinc, by Pulsed Laser Deposition (PLD) [12]. This thin layer of Zinc acts as a seed layer for the growth of ZnO nanorods using ACG. This low-temperature hydrothermal method is ideal for this application, as it is simple to execute, low cost, easy to scale up, and also can be used to grow the nanostructures on non-flat surfaces. It addition, it is possible to control the morphology, geometry and properties of the nanorods by varying the different growth conditions (temperature, growth time, solvent, precursor concentration, and growth solution pH value). Last but not least, the hydrothermal growth can be easily modified to incorporate more chemical elements and grow doped or functionalised ZnO nanorods. [13]

2. Experimental

Figure 1(a) shows a Scanning Electron Microscope (SEM) picture of a 3D structure, after it has been built using MPL, covered with zinc using PLD, and decorated with ZnO nanorods using ACG. It can be seen that the nanorod coverage is uniform and has reached all visible surfaces. This can be visualized well in Figure 1 (b) where the coverage of the side columns can be seen, and also of the ones behind them. It is clear that the ZnO nanorod coverage is uniform, even at the interior of the structure. Figure 1(c) show details of the nanorod growth.



(a)



(b)

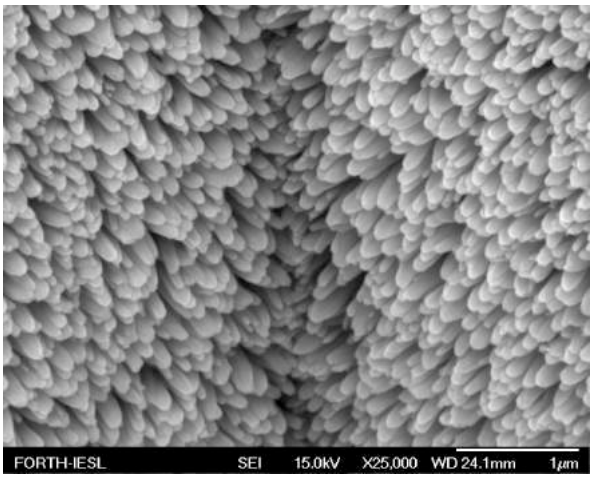


Figure 1: View of a 3D structure made with MPL and subsequently covered with ordered ZnO nanorods.

(c)

Low frequency (f = 18.33 Hz) impedance measurements were carried out on flat samples with nanorods grown on them. The ac conductivity was then extracted. Taking into account the thickness of our samples (~1 μm), we have calculated that the conductivity of the ZnO nanostructured samples is ~0.217 S/m. This metallic behaviour is most likely due to the presence of defects, oxygen vacancies as well as structural defects due to size, shape, and surface effects (polar surfaces causing charge transfer effects)[14]. Also, it should be made clear that the conductivity will change as the sample thickness change, and this depends on the nanorod growth conditions.

3. Conclusions

To conclude, we have developed a new method for constructing 3D ZnO structures, based on a direct laser writing technology, a laser deposition technique and a low-temperature hydrothermal method. This method can be modified for the deposition of other materials and for different ZnO and doped ZnO geometries, with potential applications in a variety of fields.

Acknowledgements

The authors acknowledge financial support from the ERA.Net RUS Plus project "EXODIAGNOS" – RUSPLUS_INNO_FULL-110.

References

[1] M. Konstantaki, A. Klini, D. Anglos *et al.*, "An ethanol vapor detection probe based on a ZnO nanorod coated optical fiber long period grating," *Opt. Exp.,* vol. 20, no. 8, pp. 8472-8484, Apr, 2012.

[2] P. V. Kamat, R. Huehn, and R. Nicolaescu, "A "sense and shoot" approach for photocatalytic degradation of organic contaminants in water," *J. Phys. Chem. B,* vol. 106, no. 4, pp. 788-794, Jan, 2002.

[3] M. H. Huang, S. Mao, H. Feick *et al.*, "Room-temperature ultraviolet nanowire nanolasers," *Science,* vol. 292, no. 5523, pp. 1897-1899, Jun, 2001.

[4] G. V. Naik, J. J. Liu, A. V. Kildishev *et al.*, "Demonstration of Al:ZnO as a plasmonic component for near-infrared metamaterials," *PNAS,* vol. 109, no. 23, pp. 8834-8838, Jun, 2012.

[5] J. J. Wu, and S. C. Liu, "Low-temperature growth of well-aligned ZnO nanorods by chemical vapor deposition," *Advanced Materials,* vol. 14, no. 3, pp. 215-218, Feb, 2002.

[6] Z. R. Dai, Z. W. Pan, and Z. L. Wang, "Novel nanostructures of functional oxides synthesized by thermal evaporation," *Adv. Funct. Mater.,* vol. 13, no. 1, pp. 9-24, Jan, 2003.

[7] C. H. Liu, J. A. Zapien, Y. Yao *et al.*, "High-density, ordered ultraviolet light-emitting ZnO nanowire arrays," *Adv. Mater.,* vol. 15, no. 10, pp. 838-+, May, 2003.

[8] L. Vayssieres, "Growth of arrayed nanorods and nanowires of ZnO from aqueous solutions," *Advanced Materials,* vol. 15, no. 5, pp. 464-466, Mar, 2003.

[9] D. Vernardou, G. Kenanakis, S. Couris *et al.*, "PH effect on the morphology of ZnO nanostructures grown with aqueous chemical growth," *Thin Solid Films,* vol. 515, no. 24, pp. 8764-8767, Oct, 2007.

[10] Z. L. Wang, "Nanostructures of zinc oxide," *Materials Today,* vol. 7, no. 6, pp. 26-33, Jun, 2004.

[11] M. Malinauskas, M. Farsari, A. Piskarskas *et al.*, "Ultrafast laser nanostructuring of photopolymers: A decade of advances," *Physics Reports,* vol. 533, pp. 1- 31, 2013.

[12] D. B. Chrisey, A. Piqué, R. A. McGill *et al.*, "Laser Deposition of Polymer and Biomaterial Films," *Chem. Rev.,* vol. 103, no. 2, pp. 553-576, 2003/02/01, 2003.

[13] C. O. Chey, O. Nur, and M. Willander, "Low temperature aqueous chemical growth, structural, and optical properties of Mn-doped ZnO nanowires," *J. Crystal Growth,* vol. 375, no. 0, pp. 125-130, 7/15/, 2013.

[14] K. Mun Wong, S. M. Alay-e-Abbas, Y. Fang *et al.*, "Spatial distribution of neutral oxygen vacancies on ZnO nanowire surfaces: An investigation combining confocal microscopy and first principles calculations," *J. Appl. Phys.,* vol. 114, no. 3, pp. 034901, 2013.

A Bright Triggered Twin-Photon Source in the Solid State

Tobias Heindel[1,*], Alexander Thoma[1], Martin von Helversen[1], Marco Schmidt[1,2], Alexander Schlehahn[1], Manuel Gschrey[1], Peter Schnauber[1], Jan-Hindrik Schulze[1], André Strittmatter[1,4], Jörn Beyer[2], Sven Rodt[1], Alexander Carmele[3], Andreas Knorr[3], and Stephan Reitzenstein[1]

[1]Institut für Festkörperphysik, Technische Universität Berlin, Hardenbergstraße 36, 10623 Berlin, Germany
[2]Physikalisch-Technische Bundesanstalt, Abbestraße 2-12, 10587 Berlin, Germany
[3]Institut für Theoretische Physik, Technische Universität Berlin, Hardenbergstraße 36, 10623 Berlin, Germany
[4]Present address: Institut für Experimentelle Physik, Otto-von-Guericke Universität Magdeburg, 39106 Magdeburg, Germany
*corresponding author, E-mail: tobias.heindel@tu-berlin.de

Abstract (70/80 Words)

We propose and experimentally demonstrate the efficient, triggered generation of photon twins using the energy-degenerate biexciton–exciton radiative cascade of semiconductor quantum dots. Deterministically integrated within a microlens, these nanostructures emit highly correlated photon pairs, degenerate in energy and polarization. We analyze the generated light states via polarization-resolved photon-correlation experiments and directly observe the twin-photon states by employing photon-number-resolving detectors, enabling the reconstruction of the emitted photon number distribution.

1. Introduction

The realization of integrated light sources capable of emitting non-classical multi-photon states, is a fascinating, yet equally challenging task at the heart of quantum optics.

Here we propose and experimentally demonstrate an integrated source of photon twins, that is pairs of photons with identical energy and polarization, highly correlated in time. For this purpose, we select semiconductor quantum dots (QDs) exhibiting a spectrally degenerate biexciton–exciton (XX-X) radiative cascade. To enhance the photon collection efficiency, the QDs are deterministically integrated within monolithic microlenses fabricated by three-dimensional (3D) in-situ electron-beam lithography [1].

2. Experimental Results

Polarization-resolved photoluminescence spectra of an ordinary QD are displayed in Fig. 1(a). Here, the emission of exciton and biexciton state is well separated due to a biexciton binding energy $E_{\mathrm{bin}}^{\mathrm{XX}}$ on the order of ~1 meV. Moreover, polarized doublets with a splitting on the order of ~10 µeV are visible for the emission of exciton and biexciton, which results from anisotropic electron-hole exchange leading to a fine structure splitting ΔE_{FSS} of the exciton state. In such ordinary cases, the emitted exciton-

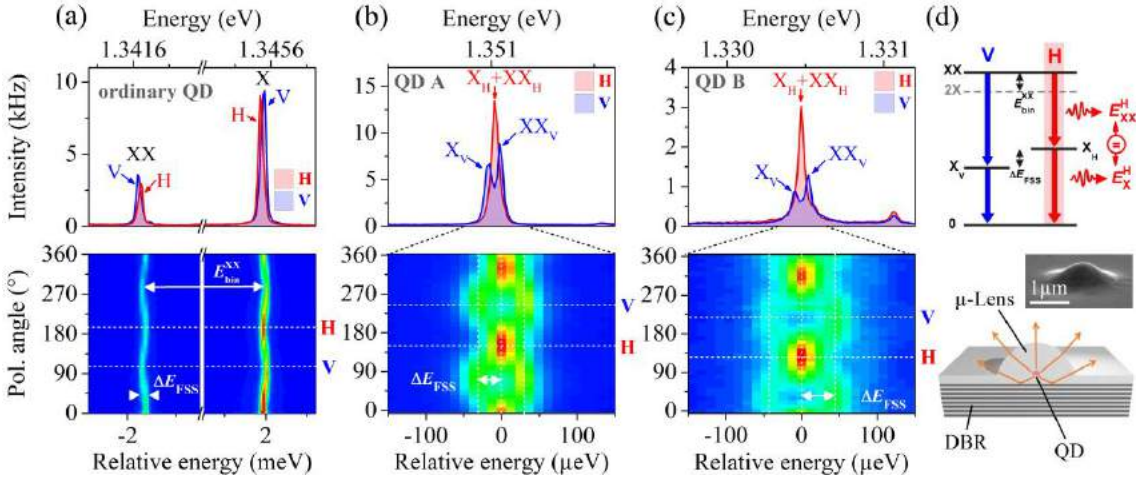


Figure 1: Polarization-resolved photoluminescence spectra for (a) an ordinary QD with $E_{\mathrm{bin}}^{\mathrm{XX}} >> \Delta E_{\mathrm{FSS}}$ and (b), (c) QDs capable for twin-photon generation featuring $E_{\mathrm{X}}^{\mathrm{H}} = E_{\mathrm{XX}}^{\mathrm{H}}$. (d) Schematic of the XX-X energy level scheme and the deterministic QD microlens device used for the experiments. Inset: Scanning electron microscopy image of a microlens.

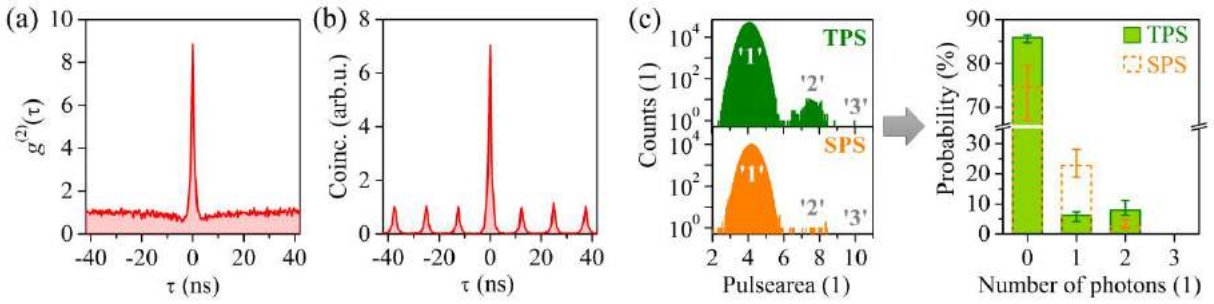


Figure 2: Photon-autocorrelation measurement on the twin-photon emission of the H-polarized decay channel of QD B under (a) continuous and (b) pulsed excitation. (c) Measured photon number distributions of the twin-photon source (TPS) and a single-photon source (SPS), serving as reference. The utilized photon-number-resolving detector is based on a transition edge sensor and allows for the clear discrimination between single- ('1') and twin- ('2') photon events.

and biexciton-photons are spectrally distinguishable in both possible decay channels (for H- and V-polarization).

For the generation of photon twins demonstrated in the following, we select QDs featuring a radiative cascade with $\Delta E_{\mathrm{FSS}} = |E_{\mathrm{bin}}^{\mathrm{XX}}|$, which results in $E_{\mathrm{X}}^{\mathrm{H}} = E_{\mathrm{XX}}^{\mathrm{H}}$ (cf. Fig. 1d). For this particular energy-level alignment, one decay channel of the biexciton–exciton cascade reveals the emission of photon twins—a non-classical light state constituted of two temporally correlated photons with identical emission energy and polarization. To enhance the photon collection efficiency, the QDs are deterministically integrated within monolithic microlenses (cf. Fig. 1(d)) by means of 3D in-situ electron-beam lithography [1]. Fig. 1(b) and (c) display the spectral signatures of two different QDs both featuring a twin-photon cascade. Here, the emission of exciton and biexciton become superimposed for H-polarization while it remains spectrally distinguishable for V-polarization, enabling the polarization-selective distillation of photon twins. A quantitative analysis of the spectra yields $\Delta E_{\mathrm{FSS}} = |E_{\mathrm{bin}}^{\mathrm{XX}}| = (30 \pm 5)$ µeV for QD A and $\Delta E_{\mathrm{FSS}} = |E_{\mathrm{bin}}^{\mathrm{XX}}| = (51 \pm 6)$ µeV for QD B. The fact that we observe antibinding biexciton states ($E_{\mathrm{XX}}^{\mathrm{V}} > E_{\mathrm{X}}^{\mathrm{V}}$) in both cases, is indicative for a relatively small QD size.

The dynamics of this unique four-level system are studied via photon auto-correlation measurements. For this purpose, the H-polarized twin-photon emission of QD B is spectrally filtered using a grating spectrometer and coupled to a fiber-based Hanbury-Brown and Twiss setup with silicon-based single-photon counting modules acting as detectors. Fig. 2(a) and (b) present the measured coincidence histograms under continuous as well as pulsed optical excitation, respectively. Both measurements reveal a prominent bunching signature at zero delay, proving the presence of strong temporal two-photon correlations in this unique biexciton–exciton radiative cascade. Moreover, we simultaneously detect clear antibunching at finite delay times, signifying the non-classicality of the emitted light state. A detailed study presented in Ref. [2] reveals, that this device produces photon twins at a rate of (234 ± 4) kHz collected via the microscope objective of our setup, which represents a significant improvement (by a factor of 5) compared with photon twins generated with atoms [3].

For a direct observation of the twin-photon state, we employ a photon-number-resolving detection system based on a transition edge sensor operated at a temperature of 150 mK. The analysis of the recorded time traces clearly reveals the single- and twin-photon events (Fig 2(c)), left panel) and we detect a total of 215 photon twins within a measurement period of 4.5 hours. For clarity, the results obtained for our twin-photon source (TPS) are also compared with a QD-based single-photon source (SPS), serving as reference. Finally, accounting for the losses of our experimental setup, we are able to reconstruct the photon number distribution of both quantum light source (see Fig. 2(c), right panel).

3. Conclusions

In conclusion, the twin-photon source presented in this work is an attractive type of integrated quantum light source, which might be exploited in emerging research fields, such as quantum-optical spectroscopy or quantum biology benefiting from multi-photon excitation schemes.

Acknowledgements

We acknowledge support from the German Research Foundation (DFG) via the SFB 787 and Grant RE2974/9-1, the German Federal Ministry of Education and Research (BMBF) via the VIP-project QSOURCE (Grant Number 03V0630). Parts of the results in this paper come from the project EMPIR 14IND05 MIQC2. A.C. gratefully acknowledges support from the SFB 910: 'Control of self-organizing nonlinear systems'. We thank A.E. Lita and S.W. Nam for providing the TES detector chips, and R. Schmidt, E. Schlottmann, F. Gericke and M. Schlösinger for technical assistance.

References

[1] M. Gschrey et al., Nat. Commun. 6, 7662 (2015).

[2] T. Heindel et al., Nat. Commun. 8, 14870 (2017).

[3] J. K. Thompson et al., Science 313, 74–77 (2006).

Quantum Dots in Nanowires Tuned to Atomic Transitions

Nika Akopain[1]

[1] DTU Fotonik, Technical University of Denmark, 2800 Kongens Lyngby, Denmark
E-mail: nikaak@fotonik.dtu.dk

Abstract

Hybrid semiconductor-atomic systems are promising building blocks for quantum photonic communication technologies. Here we show such a system, where we combine semiconductor nanowire quantum dots with an atomic vapor. We demonstrate: (1) a controlled growth of GaAs quantum dots in AlGaAs nanowires, (2) their excellent optical properties, and (3) tuning of their emission frequency to the optical transitions of Rb atoms.

1. Summary

Quantum dots tuned to atomic transitions represent an emerging field of hybrid quantum systems where the advantages of quantum dots and natural atoms can be combined [1,2]. Embedding quantum dots in nanowires boosts this hybrid system with a set of powerful possibilities, such as precise positioning of the emitters, excellent photon extraction efficiency and direct electrical contacting of quantum dots.

In this talk I will present a controllably grown nanowire-quantum-dot system frequency tuned to atomic transitions [3]. We grow GaAs quantum dots in AlGaAs nanowires with pure crystal structure around quantum dots and excellent optical properties. We precisely control the dimensions of quantum dots and their position inside nanowires, and demonstrate that the emission wavelength can be engineered over the range of a few tens on nm around 780 nm. We then apply an external magnetic field to tune the emission frequency of nanowire quantum dots to the D2 transition of 87Rb. Moreover, we use the Rb transitions to precisely measure the actual spectral linewidth of the photons emitted from a nanowire quantum dot to be smaller than 10 μeV, beyond the limit of a high-resolution spectrometer.

Our work, therefore, brings highly desirable functionalities to quantum technologies, enabling, for instance, a realization of an arbitrary number of nanowire single-photon sources, all operating at the same frequency of an atomic transition.

References

[1] Akopian, N., Wang, L., Rastelli, A., Schmidt, O. G. & Zwiller, V. Hybrid semiconductor-atomic interface: slowing down single photons from a quantum dot. *Nat. Photonics* **5,** 230–233 (2011).

[2] Meyer, H. M., Stockill, R., Steiner, M., Le Gall, C., Matthiesen, C., Clarke, E., Ludwig, A., Reichel, J., Atatüre, M. & Köhl, M. Direct photonic coupling of a semiconductor quantum dot and a trapped ion. *Phys. Rev. Lett.* **114,** 123001 (2015).

[3] Leandro, L., Gunnarsson, C. P., Reznik, R., Jöns, K. D., Shtrom, I., Khrebtov, A., Kasama, T., Zwiller, V., Cirlin, G. & Akopian, N. Nanowire quantum dots tuned to atomic resonances. *Submitted* (2018).

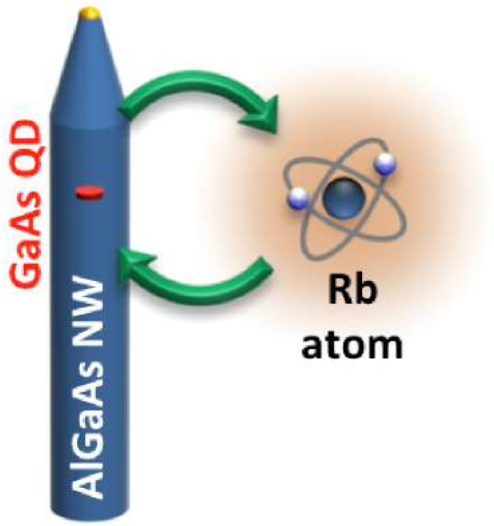


Figure 1: Schematics of GaAs quantum dot (QD) in AlGaAs nanowire (NW) coupled to Rb atom.

Towards practical single-photon sources at telecom wavelengths with GaAs-based deterministic QD-mesas

Anna Musiał[1,*], Łukasz Dusanowski[1,4], Paweł Holewa[1], Paweł Mrowiński[1], Aleksander Maryński[1], Krzysztof Gawarecki[2], Tobias Heuser[3], Nicole Srocka[3], David Quandt[3], André Strittmatter[3,5], Sven Rodt[3], Stephan Reitzenstein[3] and Grzegorz Sęk[1]

[1]Laboratory for Optical Spectroscopy of Nanostructures, Department of Experimental Physics, Faculty of Fundamental Problems of Technology, Wrocław University of Science and Technology, Wrocław, Poland
[2]Department of Theoretical Physics, Faculty of Fundamental Problems of Technology, Wrocław University of Science and Technology, Wrocław, Poland
[3]Institute of Solid State Physics, Technical University of Berlin, Berlin, Germany
*corresponding author, E-mail: anna.musial@pwr.edu.pl

Abstract

Hereby, we present a comprehensive combined experimental and theoretical study of band structure and optical properties of strain-engineered InGaAs quantum dots (QDs) emitting at telecom O-band (1.3 μm). The main focus is on generation and purity of single-photons from QDs integrated into photonic nanostructures - mesas defined by means of electron-beam lithography. The proposed approach enabled us to realize quasi-resonantly-driven efficient QD-based single-photon sources with high photon purity (as measured $g^{(2)}(0) = 0.03$) emitting at the second telecom window. Temperature dependence of the $g^{(2)}(0)$ has also been investigated.

1. Introduction

Semiconductor nanostructures have become a powerful and flexible solid-state platform to study quantum optics phenomena [1]. They are sources of light states which are truly quantum in their nature (as compared to probabilistic ones [2-4]) and offer vast engineering opportunities with respect to their electronic structure and optical properties and they are compatible with solid-state platform, in principle scalable and integrable with the existing optoelectronics and electronics systems within well-developed mature semiconductor technology. They enabled the realization of multiple proof-of-principle experiments at wavelengths below 1 μm exhibiting the high potential of epitaxial quantum dots (QDs) for applications in photonic quantum technologies, i.e., by demonstration of sources of triggered single, indistinguishable and entangled photons with high extraction efficiencies and repetition rates under optical or electrical excitation [1]. The next step in development of QD-based non-classical light sources is to target the telecommunication spectral range and realize more practical, i.e, compact, cryogenic-free quantum devices [5] that operate at telecom wavelengths. In this contribution we evaluate the potential of strain-engineered epitaxially-grown InGaAs/GaAs QDs with this regard [6].

2. Methods

2.1. Experimental

2.1.1. Investigated QD-structure

Investigated QD-structure contain a single layer of epitaxial MOCVD-grown self-assembled Stranski-Krastanow QDs in $In_{0.75}Ga_{0.25}As/In_{0.2}Ga_{0.8}As/GaAs$ material system and a bottom distributed Bragg reflector (DBR) to enhance the extraction efficiency of emitted photons from the structure. A mesa structures have been realized using electron beam lithography to increase the spatial resolution and further boost the extraction efficiency [7].

2.1.2. Hanbury Brown and Twiss interferometer

In order to prove single photon character of emission we measured second order correlation function $g^{(2)}(\tau)$ in Hanbury Brown and Twiss configuration. The signal was equally split into two spectral filters (0.32 m focal length monochromators) and detected using pair of superconducting single-photon counting detectors (NbN) and further time-correlations were measured resulting in histogram of coincidences. For pre-characterization of the QD emission in terms of power-, temperature- and polarization-dependent measurements a liquid nitrogen-cooled InGaAs multichannel linear detector was used.

2.2. Theoretical model

The electronic structure of the investigated QDs has been modelled using 8-band k·p calculations combined with the configuration interaction method for excitonic states (using 40 electron and hole states basis and realistic In distribution within the QD volume and QD size of 30 nm times 6 nm).

3. Discussion

The driving force of the emission redshift for this kind of GaAs-based QDs to telecom wavelengths is the adjacent strain-reducing layer. This results in ground state energy emission at the O-band fiber transmission window and relatively strong quantization with higher excitonic states

[4]currently at: Technical Physics, University of Würzburg and Wilhelm-Conrad-Röntgen-Research Center for Complex Material Systems, Würzburg, Germany
[5]currently at: Institute of Experimental Physics, Otto von Guericke University Magdeburg, Magdeburg, Germany

separated by 67 meV (so called s-p splitting) and 135 meV (d-shell) from the ground state and typical inhomogeneous broadening of the QD ensemble of 35 meV – Figure 1 [8].

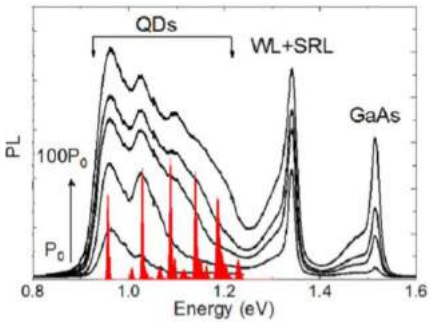


Figure 1: Excitation power-dependent photoluminescence (PL) spectra (black solid lines) of the emission from QD ensemble (T=5K) with calculated excitonic spectrum (red) [8].

To reach high-purity single-photon emission different excitation schemes were utilized to minimize the effect of background emission related mostly to neighboring QDs. Under nonresonant excitation and quasi-resonant excitation into the wetting layer we obtained a clear photon antibunching with as measured values of $g^{(2)}(0) = 0.19$ (λ_{exc}=787 nm) and $g^{(2)}(0) = 0.15$ (λ_{exc}=850 nm), respectively. In both cases non-classical character of emission was proven, but the probability of multiphoton events was relatively high: nonselective excitation results in a large number of carriers generated in the structure and therefore a significant background emission. To minimize this effect, the first excited state (p-shell) of the selected bright QD was identified in microphotoluminescence (μPL) excitation spectroscopy experiment to be at 1256 nm corresponding to s-p splitting of 67 meV (in agreement with high-excitation PL measurements on the QD ensemble and the performed calculations). Applying quasi-resonant pulsed excitation (Ti:Sapphire laser with 2 ps pulses at 76 MHz repetition rate) into the p-shell we obtained as measured single-photon emission in the telecom O-band from a single QD: as measured $g_{(2)}(0) = 0.03$ and background corrected value of 0.005 at $\lambda = 1.35$ μm (Figure 2). Additionally, $g_{(2)}(0)$ as a function of temperature has been investigated.

4. Conclusions

Investigated strain-engineered GaAs-based QDs are good candidates for practical single-photon sources (see also: [10,11]). High-purity triggered emission of single-photons at 5 K has been demonstrated. It was possible to lower the $g^{(2)}(0)$ significantly, down to the level of 0.01 a smeasured and 0.005 background-corrected, in a quasi-resonant excitation scheme with laser energy tuned to the first higher energy excitonic state.

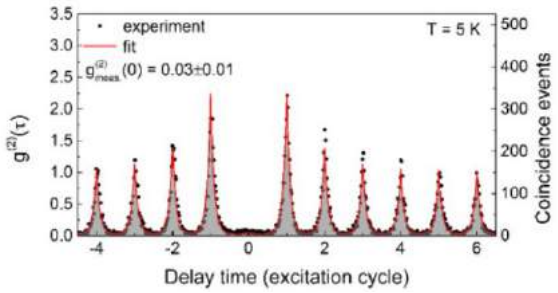


Figure 2: Second order autocorrelation function under quasi-resonant (p-shell) pulsed excitation [9].

Acknowledgements

We acknowledge financial support via the FI-SEQUR project jointly financed by the European Regional Development Fund (EFRE) of the European Union in the framework of the programme to promote research, innovation and technologies (Pro FIT) in Germany, and the National Centre for Research and Development in Poland within the 2nd Poland-Berlin Photonics Programme, grant No. 2/POLBER-2/2016 (project value 2 089 498 PLN), and the German Science Foundation via CRC787.

References

[1] F. Jahnke (ed.), *Quantum Optics with Semiconductor Nanostructures*, Woodhead Publishing Series in Electronic and Optical Materials, Science Direct, 2012.

[2] J. -W. Pan et al., *Phys. Rev. Lett.* 80:3891, 1998.

[3] N. Bruno et al., *Opt. Express* 22:17246, 2014.

[4] M. Patel et al., *New. J. Phys.* 16:043019, 2014.

[5] A. Schlehahn et al., *Rev. Sci. Instrum.* 86:013113, 2015.

[6] F. Guffarth et al., *Phys. Rev. B* 64:085305, 2001.

[7] M. Gschrey et al., *Nature Commun.* 6:7662, 2015.

[8] A. Maryński et al., *Acta Phys. Pol. A* 132:386, 2017.

[9] Ł. Dusanowski et al., *Opt. Express* 25: 31122, 2017.

[10] J. Kettler et al., *Appl. Phys. B* 122:48, 2016.

[11] F. Olbrich et al., *J. Appl. Phys*. 121:184302, 2017.

Advanced Numerical and Theoretical Tools as Applied to Materials for Photonics

Effective-Medium Permittivity of Planar One-Dimensional Gratings of Vertically Invariant and Laterally Arbitrary Permittivity Distribution

Lifeng Li

Department of Precision Instrument, Tsinghua University, Beijing 100084, China
E-mail: lifengli@mail.tsinghua.edu.cn

Abstract

Subwavelength periodic gratings can be considered as one of the most basic forms of meta-surfaces. When the period-to-wavelength ratio is very small, the meta-surface is characterized by the grating's effective-medium permittivity. An explicit formula of effective-medium permittivity accurate to the second order in the above ratio for gratings of vertically invariant and laterally arbitrary permittivity distribution in oblique incidence and TM polarization is rigorously derived. The derived formula will be compared with previously published results.

1. Introduction

Subwavelength periodic gratings can be considered as one of the most basic forms of meta-surfaces. They have been used as antireflection surfaces, solar absorbers, polarizers, and wave plates, etc. for several decades. When the period d of a grating is much smaller than the wavelength λ of the incident light the grating layer behaves like a homogeneous anisotropic thin film characterized by its effective-medium permittivities. Given a planar grating the need to calculate its effective-medium permittivities gives rise to the topic of effective medium theory as a subject of the modern electromagnetic theory of gratings.

The first closed-form expressions of effective-medium permittivities of lamellar gratings in TE (electric field vector parallel to the grooves) and TM (magnetic field vector parallel to the grooves) polarizations accurate to the second order in d/λ were derived by Rytov in the 1950s [1] for normal incident light. In 1982 McPhedran et al [2] presented an in-depth study of lossy lamellar gratings in the quasi-static limit ($d/\lambda \to 0$). In the same year Bell et al [3] derived an expression of the second-order effective permittivity in TE polarization and normal incidence for surface-relief gratings of arbitrary but symmetric profiles. In 1996 Lalanne and Lemercier-Lalanne [4] published a paper on the effective medium theory of gratings of both one and two directions of periodicities. In the one-dimensional grating part of the paper they present formulas of the second-order effective permittivities in both polarizations for gratings of vertically invariant and laterally arbitrary permittivity distribution in normal incidence. Their approach is based on the Fourier modal method (or the RCWA) and the results are given in terms of Fourier coefficients of the grating's permittivity function. Two years later Lalanne and Hugonin [5] treated the same type of gratings in oblique incidence using an integral form of the successive approximation approach.

2. The present work

In this work I derive an explicit formula of effective-medium permittivity accurate in the second order in d/λ for gratings of vertically invariant and laterally arbitrary permittivity distribution in TM polarization oblique incidence. The adopted method is based on the Fourier modal method, similar to the original work of Lalanne and Lemercier-Lalanne in [4], but the mathematical derivation is made fully rigorous with the relevant convergence issues [6] properly taken into account. The derived formula will be compared with those in [4] and [5].

References

[1] S. M. Rytov, Electromagnetic properties of a finely stratified medium, *Sov. Phys. JETP* 2: 466−475, 1956.

[2] R. C. McPhedran, L. C. Botten, M. S. Craig, M. Nevière, and D. Maystre, Lossy lamellar gratings in the quasistatic limit, *Optica Acta* 29: 289−312, 1982.

[3] J. M. Bell, G. H. Derrick, and R. C. McPhedran, Diffraction gratings in the quasi-static limit, *Optica Acta* 29: 1475−1489, 1982.

[4] Ph. Lalanne and D. Lemercier-Lalanne, On the effective medium theory of subwavelength periodic structures, *J. Mod. Opt.* 43: 2063−2085, 1996.

[5] Ph. Lalanne and J.-P. Hugonin, High-order effective-medium theory of subwavelength gratings in classical mounting: application to volume holograms, *J. Opt. Soc. Am. A* 15: 1843−1851, 1998.

[6] L. Li, Justification of matrix truncation in the modal methods of diffraction gratings, *J. Opt. A: Pure Appl. Opt.* 1: 531−536, 1999.

Novel Guided Wave Configurations with Nanostructures for Emerging Applications

Si Nanostrip Optical Waveguide for Molecular Overtone Spectroscopy

Aviad Katiyi* **and Alina Karabchevsky**

Electro-optical Engineering Unit, Ben-Gurion University, Israel
Ilse Katz Institute for Nanoscale Science & Technology, Ben-Gurion University, Israel
Center for Quantum Information Science and Technology, Ben-Gurion University, Israel
*corresponding author, E-mail: akatiyi@gmail.com

Abstract

The ability to probe the molecular fundamental or overtone vibrations is central to modern health-care monitoring techniques because it provides an information about the molecular structure. However, since the absorption cross-section of molecular vibrations overtones is much smaller compared to the absorption of the fundamental vibrations, their detection is challenging. Here, a silicon rib waveguide structure is proposed for label-free on-chip overtone spectroscopy in near-infrared. Our spectrometer distinguished several organic liquids such as N-methylaniline and aniline without any surface modification.

1. Introduction

Silicon photonic devices are made using existing semiconductor fabrication techniques. Since silicon is already used as the substrate for most integrated circuits, it is beneficial to study the guided light and matter interaction with Silicon-On-Insulator waveguides which are operating in near-infrared (near-IR).

It has been shown experimentally[1] and validated theoretically[2] that a waveguide scheme can be efficiently utilized for detection of molecular overtones. Therefore, despite the fact that the cross section of vibrational transitions overtones are few orders of magnitude smaller than that of the fundamental transitions which correspond to the same degree of freedom, overtones and combination modes can be studied on waveguides in near-IR absorption bands and enables identification of multiple bonds in the analyte. Although sophisticated on-chip spectrometers have been demonstrated in mid-IR and near-IR, broadband near-IR spectrometers have never been shown for detection of molecular vibrations overtones with silicon nanostrip. We present a chip-scale photonic device that utilizes near-IR absorption by molecular overtones vibrations for label-free chemical sensing. We designed a multimode silicon nanostrip rib waveguide in such a way that launching the high-order modes improves the sensitivity of the chip-scale device for broadband detection.

2. Results and Discussion

Figure 1 shows the energy levels calculated by Morse potential function for the anharmonic oscillator where ν_f is the fundamental frequency.

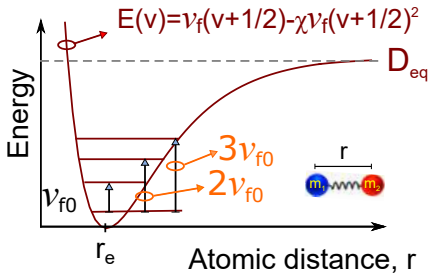


Figure 1: Diagram of an oscillator mechanism described by the energy levels for anharmonic vibration.

The proposed structure, shown in Figure 2, is a nanostrip rib waveguide made of silicon on silica substrate, a height of 2 μm and strip height of 400 nm.

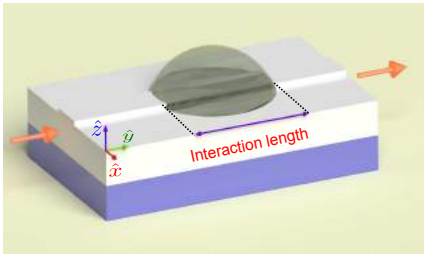


Figure 2: Illustration of the Si nanostrip rib waveguide.

Using Lumerical FDTD, we studied the modes and their absorption for rib waveguide at wavelength of 1.5 μm. Higher order modes have greater absorption in this wavelength due to the strong evanescent field. It is important to understand the evolution of the modes due to the abrupt discontinuity in the medium where the nanostrip is embedded.

Figure 3 shows the cross-sectional colormaps of the evolution of normalized mode profiles exhibiting interference and guidance in the interaction length of the designed waveguide (Figure 2b).

We performed a systematic experimental study where we utilize the enhanced interaction of multimode SOI (Silicon-On-Insulator) rib waveguides with molecular media. We illuminate the waveguides with broadband source butt-coupled to the facet. A pure probe molecules and dilutions with hexane are dripped onto the waveguide surface.

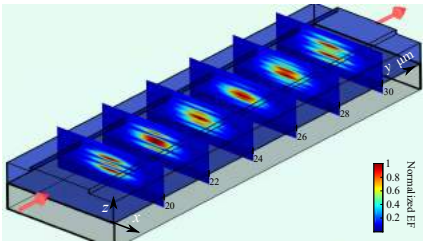


Figure 3: Evolution of the interfered guided modes in the interaction length with the analyte.

Differential transmittance is evaluated from the collected signals, then analyzed and compared to literature values.

Figure 4 shows the experimental results performed on silicon nanostrip rib waveguides.

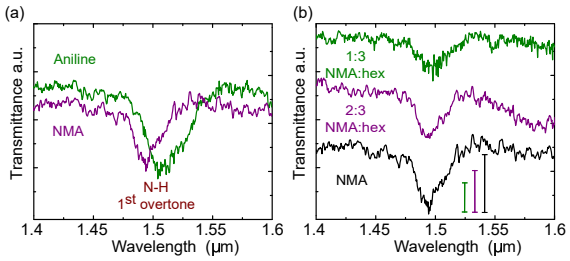


Figure 4: (a) Transmittance spectra of N-methylaniline and aniline. (b) Transmittance spectra of pure N-methylaniline molecule and mixture ratios of 1:3 and 2:3 of N-methylaniline in hexane.

Figure 4a clearly shows the waveguide's ability to distinguish between N-methylaniline and aniline. It shows the absorption of the first overtone of N-H bond of N-methylaniline and aniline around 1.5 μm. In addition, we observed the blue shift in the absorption band between the molecules and the broadening in the N-H first overtone absorption on aniline. Figure 4b shows the transmittance for different mixtures of N-methylaniline and hexane. A lower concentration of N-methylaniline in the sample decreases the absorption, allowing distinguishing between the concentration.

The molecular fingerprints of probe molecules from their overtone absorption spectra were successfully demonstrated with silicon waveguides in near-infrared. This is surprising, since at normal incidence, considering the same interaction length and longer the molecule and their mixtures were not detected. The coupling efficiencies (from fiber to waveguides) including the insertion and propagation losses are -30 dB. Even obtaining such a high loss, the molecular signatures overtones were detected.

3. Conclusions

In conclusion, we proposed a silicon nanostrip rib-waveguide structure for label-free on-chip overtone spectroscopy in near-IR. We show that utilizing the large refractive index contrast ($\Delta n > 2$) between the Si core of the waveguide and the SiO_2 substrate, a broadband near-IR lightwave can be efficiently guided. In addition, we show that the sensitivity for chemical detection is increased by more than 3 orders of magnitude when compared to the evanescent-wave sensing predicted by the numerical model. Our on-chip spectrometer distinguishes between several common organic liquids such as N-Methylaniline and Aniline precisely without any surface modification through the spectral scanning over the absorption dips in the near-IR transmission spectra. The planar near-IR silicon nanostrip waveguide is a compact sensor which can provide a platform for accurate chemical detection. Our near-IR silicon nanostrip rib waveguide device can enable the development of sensors for remote on-site chemical monitoring.

Acknowledgment

The work was supported by the Multidisciplinary Program Health-Engineering Sciences by the Ben-Gurion University of the Negev.

References

[1] A. Karabchevsky and A. V. Kavokin. Giant absorption of light by molecular vibrations on a chip, *Scientific reports* 6 (2016).

[2] A. Katiyi and A. Karabchevsky, Figure of merit of all-dielectric waveguide structures for absorption overtone spectroscopy, *Journal of Lightwave Technology* 35.14 (2017): 2902-2908.

Metamaterial substrates for optomechanical applications

Aliaksandra Ivinskaya[1], Natalia Kostina[1], Mihail I. Petrov[1], Andrey A. Bogdanov[1], Sergei Sukhov[2], Pavel Ginzburg[3], and Alexander S. Shalin[1,*]

[1]"Nano-Optomechanics" Laboratory, Department of Nanophotonics and Metamaterials, ITMO University, Birzhevaja line, 14, 199034, St. Petersburg, Russia
[2]CREOL, The College of Optics and Photonics, University of Central Florida, Orlando, Florida, USA.
[3]School of Electrical Engineering, Tel Aviv University, Ramat Aviv, Tel Aviv 69978.

*corresponding author, E-mail: alexandesh@gmail.com

Abstract

The optical force acting on a nanoparticle near a planar substrate is governed by incident light and excitation of surface and volume modes of the substrate. We study system configurations leading to significant enhancement of optical forces, for example, plane wave results in pulling forces towards the source for certain types of anisotropic substrates.

1. Introduction

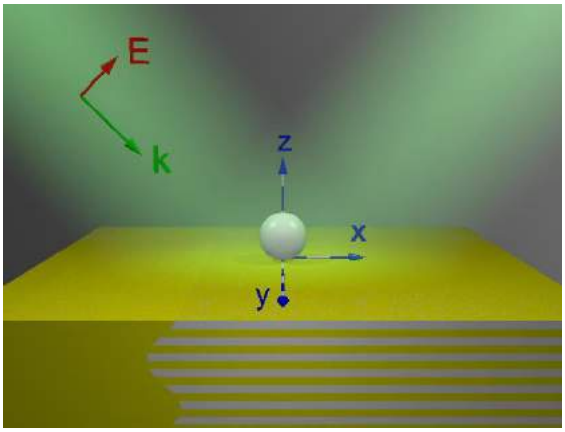


Figure 1. Optomechanically manipulated subwavelength dielectric particle ($\varepsilon = 3$, $R = 15$ nm, $z = 15$ nm) next to anisotropic (hyperbolic) metasurface. Plane wave of *p*-polarization is incident at 35°.

Optomechanics is a powerful tool at nanoscale relying on unique properties of light to manipulate matter non-invasively. Biological samples and nanoparticles can be arranged according predefined pattern what is very important for nanophotonics, chemistry, biology and other scientific directions. The ways to control spatial position of particles range from free-space optics to utilization of auxiliary nanostructures for field and force shaping. While nanostructures localize particles at particular positions, i.e. at hot spots of high field intensity, very simple planar substrate can serve as a platform for divers operations with nanoobjects. Here we are interested in the direction and strength of optical force when substrate is made of arbitrary anisotropic (i.e. hyperbolic) metamaterial.

Recent progress in metamaterials span over fascinating applications relying on the control over the flow of light with transformation optics [1], spin Hall effect [2], subdiffraction resolution [3], surface waves at metasurfaces [4], [5], ect., what strongly motivates their application in the field of optomechanics.

2. Theoretical formalism

The force on a dipole particle with polarizability α near semi-infinite substrate can be written as [6]

$$F_x = \frac{1}{2}\mathrm{Re}(\alpha \mathbf{E}^{tot}\partial_x \mathbf{E}^{0*}) + \frac{1}{2}|\alpha|^2\,\omega^2\mu_1\mu_0\,\mathrm{Im}(\mathrm{E}_x^{tot}\mathrm{E}_z^{tot*})\,\mathrm{Im}(\partial_x \mathrm{G}_{xz}), \quad (1)$$

where $\mathbf{E}^{\mathrm{tot}}$ is a local field at the particle location, $\mathbf{E}^0$ is incident field, $\mathbf{G}$ is Green's function. Green's function defines structure response to incident field and enters both expression for total field $\mathbf{E}^{\mathrm{tot}}$ and the force $\vec{\mathbf{F}}$.

3. Discussion

The force map is built as a function of real parts of dielectric permittivities along the two main axes $\varepsilon_x = \varepsilon_x' + i\varepsilon_x''$ and $\varepsilon_z = \varepsilon_z' + i\varepsilon_z''$ of the crystal. Regions of positive and negative values are displayed with grey and color legends respectively.

4. Conclusions

Auxiliary metasurfaces introduce additional degree of freedom into optomechanical manipulation schemes. Here, optical forces, mediated by hyperbolic metamaterials, interfacing dielectric homogeneous spaces (e.g. air or water, in the case of fluidic applications) were investigated. Strong optical pulling forces were obtained over the broad spectral range and this new effect is attributed to the hyperbolic type of dispersion of electromagnetic modes. Analytical

formalism of the phenomenon was developed and it relies on the self-consistent expressions for the total field at the particle location, given with the help of electromagnetic Green's function. Spectral decomposition of the Green function enabled identifying contributions of different interaction channels into the total optical force. In particular, surface plasmon polaritons, having strongly resonant behavior, were separated from the hyperbolic bulk modes for the case of homogeneous hyperbolic material. Hyperbolic modes, having high density of electromagnetic states over a broad spectral range, are the preferable channel for scattering. It was shown that the hyperbolicity of the substrate plays the key role in delivering the overall effect in the broad spectral range. Nevertheless, for multilayered realization top metal layer interfacing the air, introduces an important contribution to the value of the pulling force. The broadband property and tunability have an additional key advantage over a single metal layer – optical attraction can be achieved at the infrared spectral range, which is highly important to many optomechanical applications. Metasurfaces, designed to control near-field interactions, open a venue for flexible optomechanical manipulation schemes. While the effect of optical attraction was demonstrated here, other important fundamental effects and applications, such as optical binding, sorting, trapping, to name just few, can be enabled by carefully designed optomechanical metasurfaces.

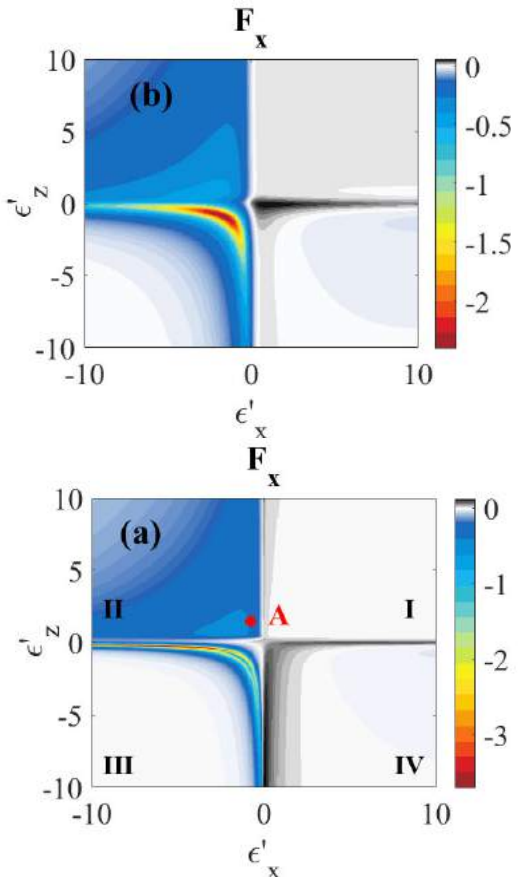


Figure 2. Colour maps of optical forces (in fN $mW^{-1}\mu m^2$) acting on a particle (ε=3, R=15 nm, z=15 nm) above an anisotropic material, as the function of substrate tensor parametrs $\varepsilon_x', \varepsilon_z'$. Material losses are set to (a) $\varepsilon_x'', \varepsilon_z'' = 0.05$, (b) $\varepsilon_x'', \varepsilon_z'' = 0.3$. Plane wave is incident at 35°, λ = 450 nm.

Acknowledgements

This work has been supported by the Russian Fund for Basic Research within the project 18-02-00414. A.S.S acknowledges the support of the Ministry of Education and Science of the Russian Federation (GOSZADANIE, Grant No. 3.4982.2017/6.7)

References

[1] A. V Novitsky, "Scattered field generation and optical forces in transformation optics," *J. Opt.*, vol. 18, p. 44021, 2016.

[2] P. V Kapitanova, P. Ginzburg, F. J. Rodríguez-Fortuño, D. S. Filonov, P. M. Voroshilov, P. A. Belov, A. N. Poddubny, Y. S. Kivshar, G. A. Wurtz, and A. V Zayats, Photonic spin Hall effect in hyperbolic metamaterials for polarization-controlled routing of subwavelength modes, *Nat. Commun.*, vol. 5, p. 3226, 2014.

[3] X. Zhang and Z. Liu, Superlenses to overcome the diffraction limit, *Nat. Mater.*, vol. 7, pp. 435–441, 2008.

[4] O. Y. Yermakov, A. I. Ovcharenko, M. Song, A. A. Bogdanov, I. V. Iorsh, and Y. S. Kivshar, Hybrid waves localized at hyperbolic metasurfaces, *Phys. Rev. B*, vol. 91, no. 23, pp. 1–7, 2015.

[5] A. A. High, R. C. Devlin, A. Dibos, M. Polking, D. S. Wild, J. Perczel, N. P. de Leon, M. D. Lukin, and H. Park, Visible-frequency hyperbolic metasurface, *Nature*, vol. 522, pp. 192–196, 2015.

[6] L. Novotny and B. Hecht, *Principles of Nano-Optics*, 2nd ed. Cambridge University Press, 2012.

Low-contrast photonic hook manipulator for cellular differentiation

Angeleene S. Ang[1,2,3,4*], Igor V. Minin[5], Oleg V. Minin[5], Sergey V. Sukhov[6,7], Alexander S. Shalin[4], and Alina Karabchevsky[1,2,3]

[1]Electrooptical Engineering Unit, Ben-Gurion University, Israel
[2]Ilse Katz Institute for Nanoscale Science & Technology, Ben-Gurion University, Israel
[3]Center for Quantum Information Science and Technology, Ben-Gurion University, Israel
[4]"Nanooptomechanics" Laboratory, ITMO University, Russia
[5]Federal State Unitary Enterprise "Siberian Scientific Research Institute of Metrology", Novosibirsk, Russia
[6]CREOL, The College of Optics and Photonics, University of Central Florida, USA
[7]Kotel'nikov Institute of Radio Engineering and Electronics of Russian Academy of Sciences S (Ulyanovsk branch), Russia
*corresponding author, E-mail: angeleene.ang@gmail.com

Abstract

By illuminating an asymmetric cuboid, the photonic hook is generated, a specialized curved photonic jet. In this work, we numerically explored the optical forces generated by the photonic hook's field, and found that the cuboid system can move large objects along a curved trajectory. We considered the interaction of this cuboid in the presence of a backing substrate, as our system is simple enough to be embedded in a 'lab-on-a-chip' platform, and possible applications for cellular differentiation.

1. Introduction

It is known that electromagnetic radiation can produce mechanical action on particles[1]. Through the use of auxiliary structures, it is possible to generate specialized fields, and these fields allow more varied kinds of optical manipulation beyond trapping. On the other hand, it is also known that dielectric microparticles (usually spheres) with a certain refractive index generate a photonic nanojet - a highly-localized, subwavelength, low-divergence beam - while being illuminated. This can be used for optical manipulation, with applications toward high-resolution microscopy, biology, etc.

In this work, we use the photonic hook[2] - a curved photonic nanojet - as a structured field formed by an asymmetric dielectric particle for generating optical forces to move large objects along curved trajectories. This photonic hook field combines the construction simplicity of the photonic nanojet, as well as the curvature produced by Airy and other self-accelerating beams. We note that other curved beams, such as the Airy beam, require the use of complicated and expensive optical elements that make these beams unsuitable for particular applications, such as embedding the system shown in Fig. 1, to generate the beams. Here we show that our photonic hook system can be used for manipulation of large objects with low-contrast between the probe and the background. This manipulation can be implemented for a variety of applications such as cellular differentiation in a lab-on-a-chip platform.

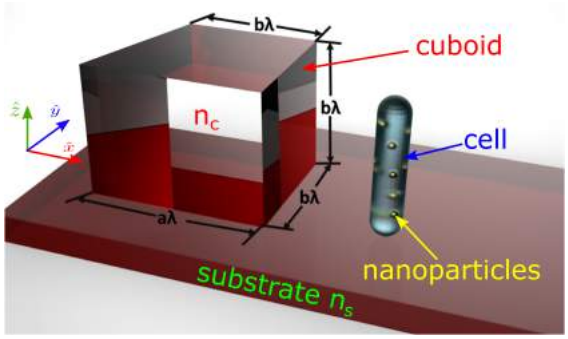


Figure 1: Illustration of the cuboid-substrate system. The E-field is polarized along the y axis, propagating along x.

2. Optical Forces

Mathematically, the forces acting on an arbitrary object can be obtained through the integration of the Maxwell stress tensor over a surface around the object[1]. Despite its accuracy, this process is computationally consuming. For the case of Rayleigh particles (where the particle size is much smaller compared to the incident wavelength), we can simplify the process and approximate the forces by assuming that the object is an electric dipole. In this case, the force in the electric dipole approximation becomes[1]

$$\langle F_i \rangle = \frac{1}{2}\mathrm{Re}\left(\alpha \mathbf{E} \cdot \frac{\partial \mathbf{E}^*}{\partial x_i}\right), \tag{1}$$

where x_i indicates the spatial coordinate, α indicates the particle's complex polarizability, and $\mathbf{E}$ is the incident electric field.

Using the equation Eq. (1), we investigate the forces produced by the photonic hook system: we consider the cuboid geometry shown in Fig. (1). To simplify the calculations, we initially neglect the substrate contribution to the fields, while the cuboid parameters are considered as $a = 4$ and $b = 3$. The cuboid is considered as made of glass ($n_c = 1.46$, in the optical frequencies), illuminated by

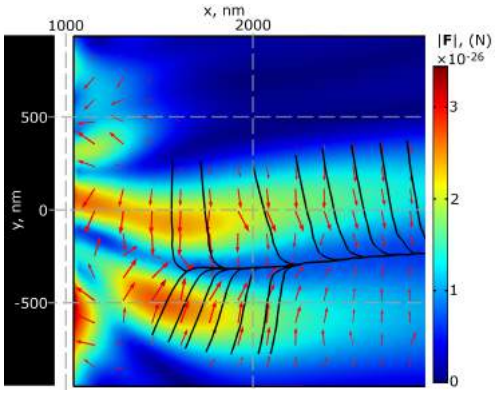


Figure 2: Force magnitude (colormap) and direction (arrow field, streamlines) of the cuboid obtained using the dipolar approximation method.

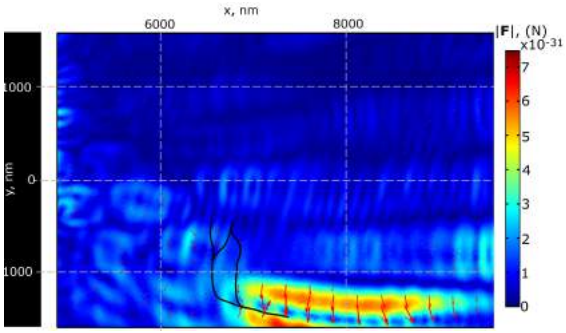


Figure 3: Force magnitude (colormap) and direction (arrow field, streamlines) of the cuboid placed atop a substrate.

a plane wave with wavelength of $625\,nm$, with propagation and polarization along the x and y axes, respectively. The entire system is embedded in air; the probe particle in this case is a gold sphere with radius of $0.03\,\mu m$ and complex dielectric permittivity $\epsilon = -11.208 + 1.3184i$. The calculation result of the forces are shown in Fig. (2). Fig. (2) shows that the trajectory produced by the photonic hook is curved. A related work[3] has shown that the forces acting on a dipolar probe particle are nearly identical with the forces obtained by integrating the Maxwell stress tensor.

3. Substrate contribution to the effect

A factor to consider in the system presented in the previous section is that the background of the cuboid is air. In a realistic system, the cuboid would need to be in contact with another larger substrate. However, this substrate generates its own scattered field, which interferes with the photonic hook field. Our approach to reduce this interference would be to add, for example, a index-matching liquid background to the whole system, as shown in Fig. (3). For this figure, the incident wavelength remains the same, however, the cuboid parameters are changed to $a = 7$ and $b = 5$, the cuboid material was changed from fused silica to zirconia of $n_c = 2.15$. In addition, the backing substrate has refractive index $n_s = 1.52$ (corresponding to borosilicate), and the index-matched background has $n = 1.47$ (glycerol). We emphasize that viscous forces were not considered in the force calculations.

4. Cellular Differentiation

One possible method of using this system in in-vitro application would be using it to guide the cells in a curved trajectory, in order to differentiate between them. However, the equation of the forces in Eq. (1), has a dependence on the polarizability α, which can be expressed as

$$\alpha = 4\pi r^3 \frac{\epsilon_p - \epsilon_a}{\epsilon_p + 2\epsilon_a} \tag{2}$$

and we note that the force becomes dependent on the permittivity contrast between the probe particle and the environment. If we were to consider guiding the cells without any modification, the force acting on these cells would be nearly negligible, as the index contrast is low. To address this challenge, we introduce gold nanoparticles using cellular uptake to serve as 'handles' to provide the needed material contrast.

Acknowledgement

This work has been supported by the Russian Fund for Basic Research within the project 18-02-00414, and the Multidisciplinary Program Health-Engineering Sciences by the Ben-Gurion University of the Negev. A.S.S acknowledges the support of Ministry of Education and Science of the Russian Federation (GOSZADANIE, Grant No. 3.4982.2017/6.7). The results leading to this manuscript were obtained during a joint PhD program between BGU (under supervision of Alina Karabchevsky) and ITMO (under supervision of Alexander S. Shalin).

References

[1] L. Novotny and B. Hecht, *Principles of Nano-Optics*. United Kingdom: Cambridge University Press, 2006.

[2] I. V. Minin and O. V. Minin, *Diffractive Optics and Nanophotonics*. Cham: Springer International Publishing, 2016.

[3] A. S. Ang, A. Karabchevsky, I. V. Minin, O. V. Minin, S. V. Sukhov, and A. S. Shalin, Photonic Hook based optomechanical nanoparticle manipulator, *Scientific Reports*, vol. 8, no. 1, p. 2029, Feb. 2018.

Coupling of Phononic Cavities in a Corrugated Nanobeam and Control of Transmission

A.V. Korovin[1], Y. Pennec[1] and B. Djafari Rouhani[1]

[1]IEMN, UMR CNRS 8520, University of Lille, 59652 Villeneuve d'Ascq, France
*corresponding author, E-mail: bahram.djafari-rouhani@univ-lille1.fr

Abstract

We study theoretically the acoustic wave propagation in a corrugated nanobeam structure containing two coupled phononic cavities. The coupling of their localized modes can be used for the modulation of the frequency and the quality factors of the cavity modes and their contribution to transmission. Additionally, when a phonon source is inserted in each cavity (potentially by optomechanical effect), the emission of phonons to the nanobeam waveguide can be tuned and become different towards the left or the right.

Recently, phononic and photonic properties have been combined into a single platform, then providing a new tool to control light and sound simultaneously. Such artificial materials are termed phoXonic crystals [1]. While canonical cavity optomechanical devices have seen significant development, recent interest now turns to engineering more complex on-chip phonon networks utilizing guided mechanical waves to connect optomechanical systems [2]. Realizing on-chip phonon networks requires engineering the phonon modes and the coupling of these modes to each other in a controllable way. We propose here to study theoretically the coupling of two phononic cavities and their interfacing through a phononic waveguide for coherent control of the elastic waves. The dual phononic/photonic structure is constituted (see figure 1) by a periodical array of holes and stubs along a nanobeam waveguide where the holes and stubs respectively bring the main contribution to the opening of the photonic and phononic band gaps [3]. Two cavities are created inside two such phoxonic crystals. The phononic cavities are coupled together in two ways, namely a direct link of both phononic crystals (Fig. 1(a)) or a coupling through a straight phononic waveguide (Fig. 1(b)). For each geometry, we study the interaction of the two cavity modes, first by using a simple equivalent multilayer method and then extended to real three-dimensional structures with the help of finite element method [4]. We show that the overlapping of two closely spaced phononic cavity modes leads to the formation of symmetric and antisymmetric modes, which can be used for the modulation of the frequency and the quality factors of the propagating cavity modes. In addition, the efficient coupling of cavity modes with the modes of a phononic waveguide connected between the two phononic cavities has been demonstrated (see Fig. 2). We show that such coupling can be used to route, control and modulate phononic cavity modes over large distances between cavities.

In a next step, we assume that each cavity is activated by an external phonon source, potentially by optomechanical effect. By playing with the relative phase and amplitude of both sources, as well as the possibility of acoustic loss in each cavity, it becomes possible tuning the relative transmission of the cavities towards the left or towards the right of the phoxonic crystals, thus creating the possibility of no reciprocal emission of the waves.

These demonstrations pave the way to engineering complex on-chip phonons networks utilizing mechanical waves to connect quantum systems as phononic or optomechanical cavities.

Acknowledgements

This work was supported by the European Commission H2020 project PHENOMEN, under Grant Agreement No. 713450

References

[1] Y. Pennec, V. Laude, N. Papanikolaou, B. Djafari-Rouhani, M.Oudich, S. E. Jallal, J. C. Beugnot, J. M. Escalante, and A. Martínez, Modeling light-sound interaction in nanoscale cavities and waveguides, *Nanophotonics* 3: 413, 2014.

[2] K. Fang, M. H Matheny, X.Luan, and O. Painter, Optical transduction and routing of microwave phonons in cavity-optomechanical circuits, *Nature Photonics* 10: 489, 2016.

[3] B. Djafari-Rouhani, S. El-Jallal, and Y. Pennec, Phoxonic crystals and cavity optomechanics, *C. R. Phys*. 17 : 555, 2016.

[4] A.V. Korovin, Y, Pennec and B. Djafari Rouhani, Strong coupling of phononic cavity modes in one-dimensional corrugated nanobeam structure, *Phys. Rev. B* 96: 184302, 2017.

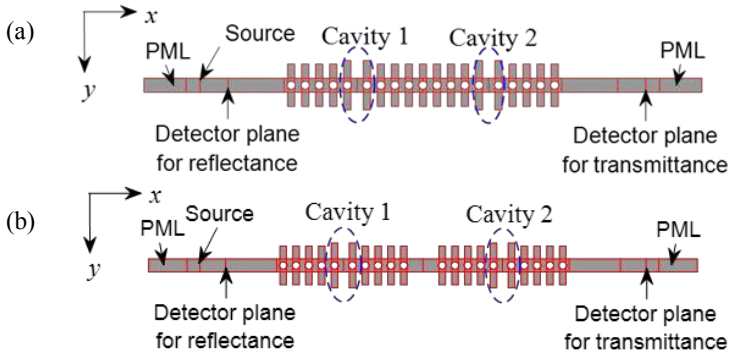


Figure 1: Schematic presentation of the phononic nanobeam consisting of a periodic array of holes and stubs along a waveguide. Two cavities are inserted in the structure by changing the geometrical parameters of the perfect unit cell. The cavities are coupled in two ways: (a) direct link through the nanobeam structure with the representation "- $o^4xo^Nxo^4$-" where "o" means a unit cell of the crystal and the numbers indicate the number of unit cells on each side of the cavity. (b) coupling through a waveguide between the two phononic crystals with the representation "-o4xo4--o4xo4-".

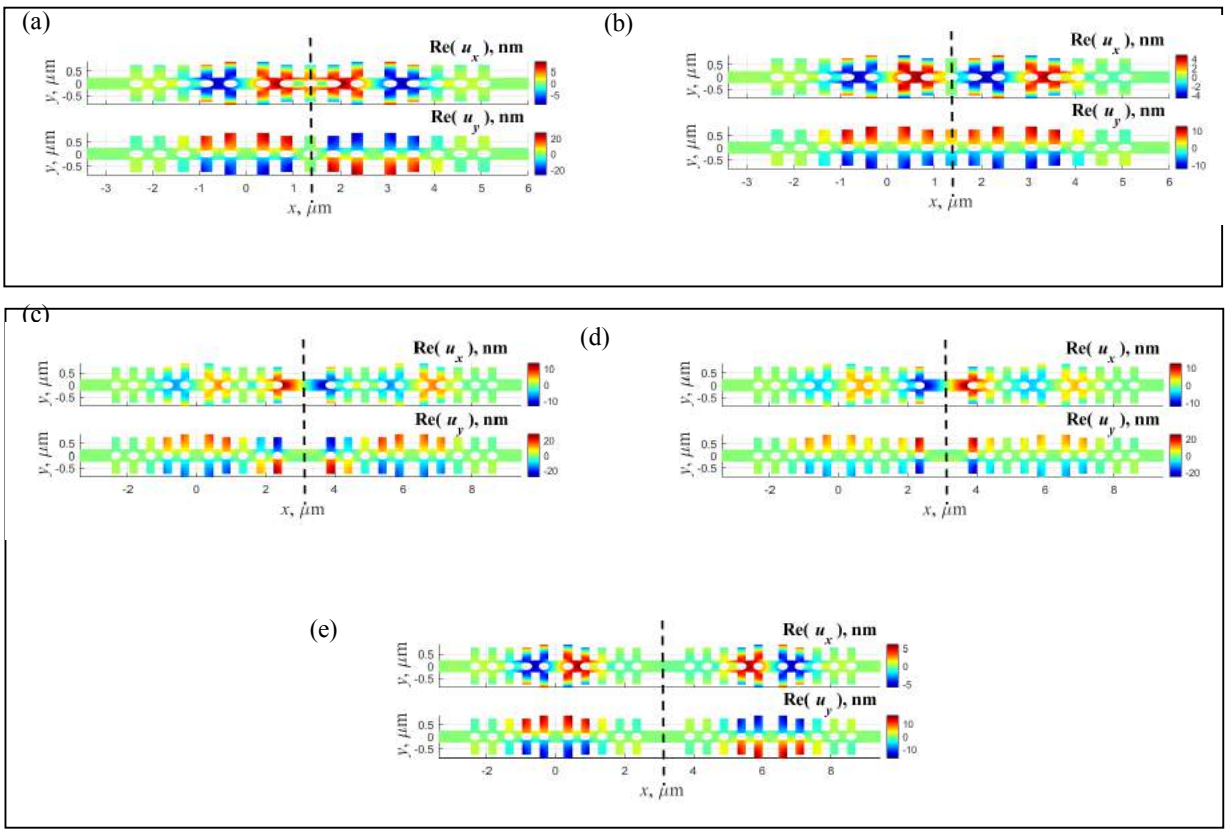


Figure 2: Illustrations of the displacement fields associated to two coupled cavities. (a, b) Spatial distribution of the longitudinal (u_x) and transverse (u_y) displacement components at the frequencies f_A = 2.042 GHz and f_B = 2.062 GHz, when the two cavity modes are directly coupled as shown in Fig. 1(a). (c, d, e) Spatial distribution of the longitudinal (u_x) and transverse (u_y) displacement components at the frequencies f_C = 2.049 GHz, f_D = 2.058 GHz, and f_E = 2.052 GHz when the two cavity modes are coupled through the straight phononic waveguide of length D = 1.04 μm as shown in Fig. 1(b).

Residue Number System Arithmetic based on Integrated Nanophotonics

Jiaxin Peng[1], Shuai Sun[1], Vikram K. Narayana[1,2], Volker J. Sorger[1], and Tarek El-Ghazawi[1]

[1]Department of Electrical and Computer Engineering, The George Washington University, Washington D.C., USA
[2]Intel Corporation, Santa Clara, USA
*corresponding author, E-mail: sorger@gwu.edu

Abstract

Residue number system (RNS) enables dimensionality reduction of an arithmetic problem by representing a large number as a set of smaller integers. Here we show an optical RNS adder and multiplier based on integrated nanophotonic in digit-wise shifting, expressed as spatial routing of an optical signal in 2×2 hybrid photonic-plasmonic switches. Our photonic arithmetic processor reaches 10's ps computational execution time given by the optical propagation delay through integrated nanophotonic router. Furthermore, we show how photonic processing in-the-network leverages the natural parallelism of optics such as wavelength-division-multiplexing in this RNS processor.

1. Introduction

Residue number system (RNS) in the field of digital computer arithmetic has been proven to have advantages in decomposing the larger integers into a set of smaller integers in calculation independently and in parallel, which is suitable for high-performance computing [1]. An integer number is represented as a set of residues obtained a set of moduli in RNS, resulting to high efficiency [2]. Also, RNS operations execute without digit-carry propagation. With a suitable number encoding scheme, these sub-operations can be realized by bit shifts, thereby making RNS computation amenable to optical realization. Fundamentally, adapting photonics into the RNS arithmetic for signal process could benefit from: (1) the fast execution time which is given by the photon's time-of-flight through the structure, (2) the nature of light that a photon always has to propagate with a momentum which in other words, an operation could be computed while switching and (3) In addition, the wavelength division multiplexing (WDM) capable of RNS computing units achieve highly instruction level parallelism with broadband nanophotonic devices. Optical communication scales more favorably than electronics in signaling distance in terms of data bandwidth and delay, due to the lack of capacitive parasitics [3]. However, the promise of optical computing has not delivered compute engines that outperform electronics when considering bandwidth, energy-per-bit, system size, and cost.

2. Method

Here we discuss a hybrid photonic-plasmonic (HPP) RNS adder with all-to-all sparse directional (ASD) structure, based on cascaded HPP 2×2 switches forming a crossbar with broad spectrum operating bandwidth. The conceptual idea of RNS computing modules based on 2×2 optical

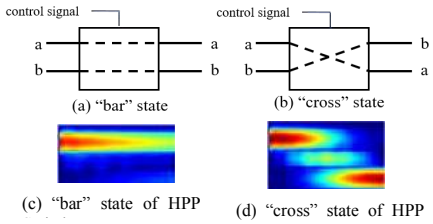


Figure 1: Two States of a 2×2 Switch. (a) and (b): the conceptual schematic of two states in a 2×2 switch. (c) and (d): the top view of the FDTD simulation results of two states in our Hybrid Photonic-Plasmonic switch. [5]

switches have been proposed based on a mesh grid of switches based on one-hot-end coding [4]. By converting the two input numbers of a RNS operations into optical and electrical signal separately, the results are obtained via bits-shifting. However, mesh schematic RNS computing units are high-power consumption and requires large footprints. Therefore, we proposed an ASD design based on a 2×2 HPP ITO switch discussed before [5]. The essential component of the RNS adder is the 2×2 optical switch with two states, which features a bar and cross state. In bar state, input light will go straight respectively; in cross state, the input lights will go cross each other (Figure 1). Our proposed Modulo-5 ASD RNS adder/multiplier are based on a HPP switch (Figure 2). Each switch has its own control signal. This complicated control circuit provides the possibility of fewer optical switches requirement, although a look-up table (LUT) is necessary to store the states of all the optical

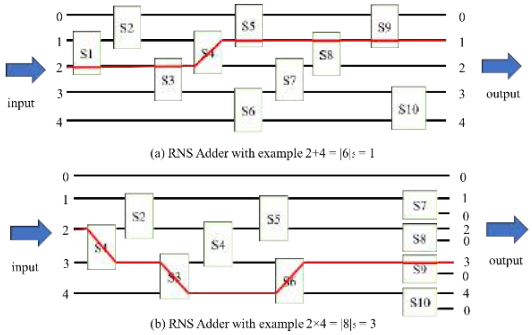


Figure 2: Modulo-5 RNS Adder (a) and Multiplier (b) with Examples. Red lines show the light path with specific example.

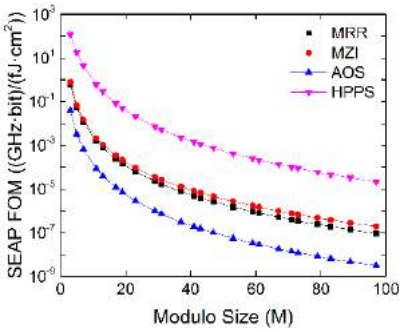


Figure 3: Speed (Energy Efficiency) (Area Efficiency) Product of the mesh RNS model and the ASD RNS model different types of switch as building blocks.

switches. Our RNS adder requires two more ((M-1)2/2+2) optical switches (M>2) to ensure strict non-blocking communication. Two summands are translated to optical light source and electrical control signal. The light could propagate as desired path by changing control signal after searching the LUT. Once the states of all the switches are set up, no matter what another summand is, the input light beam will propagate through the desired path. Finally, photodetector translates the result of an operation based on position. The overall design has a huge advantage in terms of area and energy.

3. Results and Discussion

Focusing on the Speed-Energy-Area Product (SEAP) FOM, ASD RNS schematic with HPP SEAP FOM performs 100 times better than MRR [6] and MZI [7] do (Figure 3). Although all-optical-switch (AOS) [8] performs very well in terms of speed, the high-energy consumption imposes the bad performance in SEAP FOM. Our design requires less area and less energy with higher speed, reaching around 10ps response time. As the modulo size increase, overall performance decreases. Since we have more components, the size and power requirement should increase as well. We keep our advantage when compared to other switches with the mesh schematic RNS adder. To the best of our knowledge, existing optical RNS adder design calculate only one operation at a time. Our proposed HPP device has a further feature that it is WDM capable. Here, we

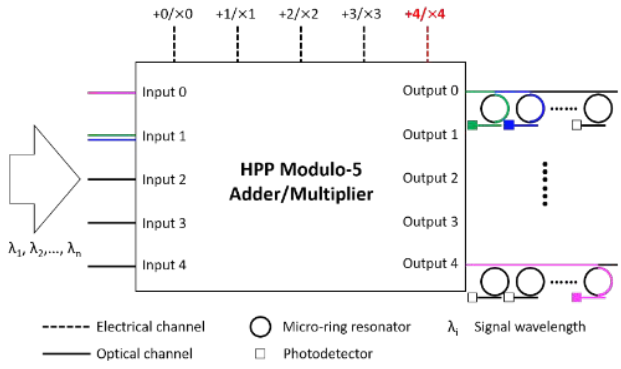


Figure 4: Schematic of WDM Modulo-5 RNS Computation Unit.

implemented a new design for RNS adder and multiplier, with additional ring resonators and photo-detectors at the end of outputs (Figure 4), allowing multiple operations to perform simultaneously. For example, if one of the summand is 4, the other summands are (1) same input with different wavelength – λ_1 and λ_2 (green and blue). (2) different input summand - λ_n (purple). A few operations could be executed at the same time, which is ideal method for convolutional neural network due to the feature of MAC operations require one of constant input (weight matrix). Our proposed design requires one-time setup and gains benefit of the speed of light.

4. Conclusions

Here we show a photonic residue number system (RNS) adder and multiplier based on an all-to-all, non-blocking, sparse directional crossbar. The RNS arithmetic is implemented by spatial routing of light using nanophotonic 2×2 switching building blocks, enabling a highly parallel compute engine. This programmable photonic processor utilized an extremely short execution time, only limited by the picosecond short time-of-flight through the 10's of micrometer compact optical router. This photonic RNS engine is well suited for convolutional neural networks by transferring the weighted matrix into the switch states.

References

[1] H.Garner, The residue number system,*IRE Transactions on Electronic Computers,* pp. 140–147, 1959.

[2] D. Psaltis and D. Casasent, Optical residue arithmetic: a correlation approach, *Applied Optics*, pp.163–171 ,1979

[3] S. Sun, A.-H. A. Badawy, V. Narayana, T. El-Ghazawi, and V. J. Sorger, "The case for hybrid photonic plasmonic interconnects (hyppis): Lowlatency energy-and-area-efficient on-chip interconnects," *IEEE Photonics Journal* 7(6), pp. 1–14, 2015.

[4] A. Tai, I. Cindrich, J. R. Fienup, and C. Aleksoff, Optical residue arithmetic computer with programmable computation modules, *Applied optics 18*(16), pp. 2812–2823, 1979.

[5] S.Sun, V.Narayana, I.Sarpkaya, J.Crandall, R.A.Soref, H.Dalir, T.ElGhazawi, and V. J. Sorger, Hybrid photonic-plasmonic non-blocking broadband 5×5 router for optical networks, *IEEE Photonics Journal*, 2017

[6] T. Baba, S. Akiyama, M. Imai, N. Hirayama, H. Takahashi, Y. Noguchi, T. Horikawa, and T. Usuki, 50-gb/s ring-resonator-based silicon modulator, *Optics express 21*, pp. 11869–11876, 2013.

[7] C. Haffner, W. Heni, Y. Fedoryshyn, J. Niegemann, A. Melikyan, D. Elder, B. Baeuerle, Y. Salamin, A. Josten, U. Koch et al., All-plasmonic mach–zehnder modulator enabling optical high-speed communication at the microscale, *Nature Photonics 9*, pp. 525–528, 2015.

[8] C. Min, P. Wang, C. Chen, Y. Deng, Y. Lu, H. Ming, T. Ning, et al. "All-optical switching in subwavelength metallic grating structure containing nonlinear optical materials, *Optics letters* (33), pp. 869–871, 2008.

Giant subradiance, strong interactions and positional disorder in metamaterials

Stewart D. Jenkins[1], Nikitas Papasimakis[2], Salvatore Savo[2,3], Nikolay I. Zheludev[2,4], Janne Ruostekoski[1,5*]

[1]Mathematical Sciences and Centre for Photonic Metamaterials, University of Southampton, Southampton SO17 1BJ, United Kingdom
[2]Optoelectronics Research Centre and Centre for Photonic Metamaterials, University of Southampton Southampton SO17 1BJ, United Kingdom
[3]TetraScience Inc., 114 Western Ave, Boston, MA, 02134
[4]Centre for Disruptive Photonic Technologies School of Physical and Mathematical Sciences and The Photonics Institute, Nanyang Technological University, Singapore 637378, Singapore
[5]Department of Physics, Lancaster University, Lancaster, LA1 4YB, United Kingdom
*corresponding author, E-mail: j.ruostekoski@lancaster.ac.uk

Abstract

We consider metamaterials consisting of strongly interacting resonators for regular and disordered positions and show how to engineer massive coherently driven classical subradiance in planar metamaterial arrays as a spatially extended eigenmode comprising over 1000 metamolecules. Disorder can be employed to control the electromagnetic response of metamaterial arrays. Our systematic analysis reveals how the response of disordered arrays with strong field-mediated interactions is inherently linked to their cooperative response to electromagnetic waves where the multiple scattering induces strong correlations between the excitations of individual resonators. For example, a gradual increase of the positional disorder rapidly leads to a spatial localization of the excitation profile of the spatially-extended collective subradiant eigenmode and the effects of disorder and cooperative interactions are mapped onto the transmission resonance in the far field spectrum.

1. Introduction

According to conventional wisdom, disorder and interactions are undesired phenomena with deleterious effects on the design and development of electromagnetic (EM) devices and functionalities. They lead to uncontrolled coupling between radiation and matter, resonance broadening, shifts and dephasing, thus limiting the potential of devices for practical applications, such as sensing and telecommunications. Strong field-mediated interactions can have a dramatic effects on the response. The classic example of neutrons and magnetic dipole radiation by Dicke over 60 years ago describes the collective super-radiant and subradiant response of emitters at high density. Super-radiance, where the emission is enhanced due to constructive interference, has been experimentally observed in a variety of systems. Subradiant excitations, however, have posed a long-standing challenge in physics owing to their weak radiative coupling to environment. Although they have been in recent years realized, e.g., in several few-resonator systems, utilization of massive many-particle subradiance has been lacking. Here we provide strong evidence on the observation of subradiance in far field resonance features in the reflection spectra corresponding to the excitation of a single subradiant eigenmode [1]. This mode in a regular array spatially extends over the entire metamaterial lattice of over 1000 unit-cell resonators, or metamolecules. Adding disorder to the positions of the resonators modifies this response. Due to the strong *collective* response of the metamaterial, we find that the effects of disorder are much more dramatic than one would surmise based on the disciplined and more predictable responses of regular arrays. In order to overcome the deleterious and unwanted effects of disorder and actually to benefit from them, we will here develop a systematic framework for analyzing the interplay between strong radiation-mediated interactions between unit-cell resonators and their positional disorder. Modifying the collective interaction phenomena in a controlled way then provides a platform for harnessing and engineering complex disorder-dependent EM-field response for the design of metamaterial-based devices with prescribed functionalities.

2. Regular arrays

We consider metamaterial planar arrays consisting of asymmetric split ring (ASR) metamolecules formed by two discrete circular arcs [2]. In Fig. 2(a) we show a side-by-side comparison for the far-field measurements and numerical calculations of the reflected field intensity spectrum in a narrow cone in the back direction. The spectral response of the metamaterials exhibits a narrow Fano resonance associated with the magnetic dipole excitation of the metamolecules. Numerical calculations are in good qualitative agreement with the experimental observations, indicating that the model captures well the multiple scattering phenomena between the resonators. Although an isolated ASR metamolecule exhibits no sharp resonance, the large array of interacting metamolecules displays a high-quality *col-*

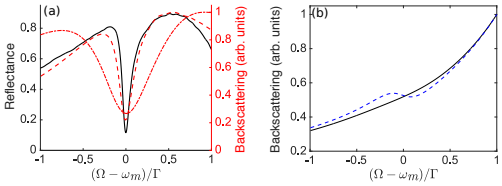


Figure 1: (a) Experimentally measured reflectance (black line) and numerically calculated back-scattered intensity (red dashed line) spectra from a 30×36 ASR microwave metamaterial array with a lattice spacing of $a = 0.28\lambda$. We also show calculated spectra (red dash-dot line) for arrays of plasmonic resonators ($a = 0.2\lambda$). (b) Calculated spectra from microwave arrays of noninteracting metamolecules (black line), and arrays with a large lattice spacing of $a = 1.9\lambda$ (dashed blue line) and thus weakened interactions. The frequencies are in the units of the single arc decay rate Γ.

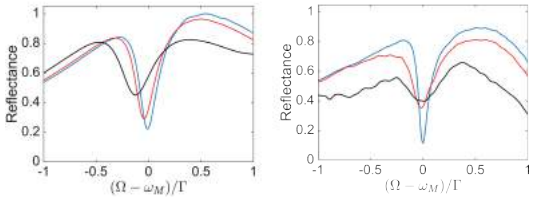


Figure 2: Far field spectrum of microwave and optical plasmonic arrays with varying degree of disorder. The backscattered intensity from the microwave array (a) as calculated by the theoretical model and (b) measured in the experiments. The blue lines represent scattering from ordered arrays ($D = 0$), and the red (black) lines represent scattering from arrays with disorder parameter $D = 0.22a$ ($D = 0.44a$).

lective resonance. The resonance results entirely from interactions between the metamolecules that are mediated by the scattered fields. This is illustrated in Fig. 2(b), where we show the calculated spectra of weakly and noninteracting metamolecules of the same array, illustrating how an increased spatial separation leads to a substantially less pronounced, broader resonance.

The origin of these resonances can be traced to collective phenomena. Numerical results indicate that a uniform incident field normal to the lattice plane couple most strongly to collective modes where metamolecules oscillate in phase, which is the case for a pure phase-coherent electric (PE) and a pure phase-coherent magnetic (PM) dipole mode. PM mode excitation is dominant at the resonance and rapidly decays outside of it. PE excitation is notable only outside of the resonance. The Fano resonance results from the interference between the collective subradiant PM mode with an extremely narrow radiative linewidth and the superradiant PE mode. We find that the steady-state excitation at the Fano resonance is overwhelmingly dominated (close to 70% of the total excitation) by a subradiant eigenmode with the decay rate of $\gamma_{\rm sub} \simeq 0.21\Gamma$. Remarkably, this subradiant excitation is a correlated many-body excitation between a large number of metamolecules and extends over the entire metamaterial lattice.

3. Disordered arrays

We find that the spatial disorder manifests itself in the collective radiative excitation eigenmodes that are responsible for the transmission resonances of the system. Even small changes in the positions of the resonators dramatically alter the spatial profiles of the relevant eigenmodes, which in turn has a profound effect on the EM response of the array. In Fig. 2 we show the far field spectrum for different values of disorder. The contrast, width, and shift of the resonance vary from sample to sample, and in our numerical simulations we found that this variance increases with the degree of positional disorder in the array. This variation is a manifestation of the dependence of interactions on the relative positions of the resonators, and shows how the fluctuations of the positions are mapped onto the fluctuations of the transmission and reflection resonance properties of the fields.

In the near field, disorder manifests itself in localized excitations with greatly enhanced Purcell factors, making it increasingly likely to find collective excitation eigenmodes with very high Purcell factors.

4. Conclusions

We have demonstrated the realization of massive many-particle subradiance, where most of the excitation is transferred into a single subradiant eigenmode of over 1000 resonators. Moreover, we have shown the effects of cooperative responses are even more dramatic in the presence of spatial disorder. Our analysis in terms of collective eigenmodes paves a way for controlled engineering of macroscopic electromagnetic functionalities in strongly interacting metamaterial arrays that could be utilized in the material design.

Acknowledgement

We acknowledge financial support from the EPSRC, the Leverhulme Trust, the Royal Society, and the MOE Singapore Grant No. MOE2011-T3-1-005.

References

[1] S. D. Jenkins *et al.*, Many-body subradiant excitations in metamaterial arrays: Experiment and theory, Phys. Rev. Lett. **119**, 053901 (2017).

[2] V. A. Fedotov *et al.*, Sharp trapped-mode resonances in planar metamaterials with a broken structural symmetry, Phys. Rev. Lett. **99**, 147401 (2007).

Bio-Engineered Metamaterials and Plasmonics

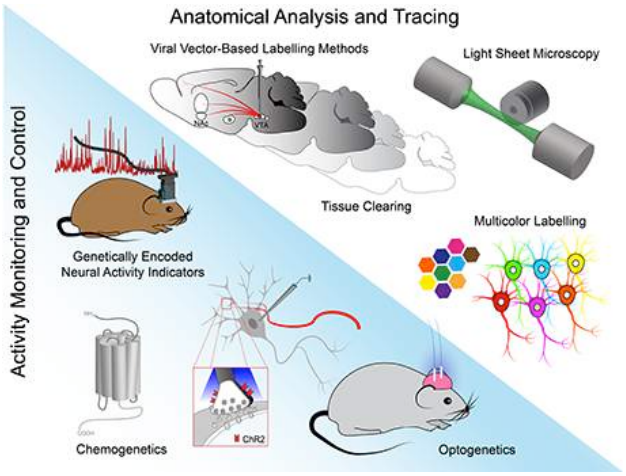
Optogenetic, tissue clearing, and viral vector approaches to understand and influence whole-animal physiology and behavior

Viviana Gradinaru

California Institute of Technology, Pasadena, California, USA
E-mail: viviana@caltech.edu

Abstract

Our research group at Caltech develops and employs optogenetics (control of neuronal circuits with light), tissue clearing for optical access into deep tissue, and viral vectors to gain new insights on circuits underlying locomotion, reward, and sleep. In addition to control of neuronal activity we need feedback on how exactly the tissue is responding to modulation. We have worked on two related topics: optical voltage sensors and imaging of single molecule RNA in cleared tissue.



Introduction

Our research group at Caltech develops and employs optogenetics, tissue clearing, and viral vectors to gain new insights on circuits underlying locomotion, reward, and sleep. We showed how bidirectional manipulation of mesopontine cholinergic cell bodies exerted opposing effects on locomotor behavior and reinforcement learning and how these effects were separable via limiting photostimulation to PPN cholinergic terminals in the ventral substantia nigra pars compacta or to the ventral tegmental area, respectively [1]. In most recent work [2], the group has delineated novel arousal-promotingdopaminergic circuits that might be at the root of sleep disturbances common to numerous neuropsychiatric disorders. Genetically encoded tools that can be used to visualize, monitor, and modulate mammalian neurons are revolutionizing neuroscience. However, use of genetic tools in non-transgenic animals is often hindered by the lack of vectors capable of safe, efficient, and specific delivery to the desired cellular targets. To begin to address these challenges, we have developed an in vivo Cre-based selection platform (CREATE) for identifying adeno-associated viruses (AAVs) that more efficiently transduce genetically defined cell populations [3]. As a first test of the CREATE platform, we selected for viruses that transduced the brain after intravascular delivery and found a novel vector, AAV-PHP.B, that transduces most neuronal types and glia across the brain. We also demonstrate how whole-body tissue clearing can facilitate transduction maps of systemically delivered genes [4,5] and how non-invasive delivery vectors can be used to achieve dense to sparse labeling to enable morphology tracing in both the central and peripheral nervous systems [6]**.** Since CNS disorders are notoriously challenging due to the restrictive nature of the blood brain barrier, the recombinant vectors engineered to overcome this barrier can enable potential future use of exciting advances in gene editing via the CRISPR-Cas, RNA interference and gene replacement strategies to restore diseased CNS circuits. In addition to control of neuronal activity we need feedback on how exactly the tissue is responding to modulation. We have worked on two related topics: optical voltage sensors and imaging of single molecule RNA in cleared tissue. We used directed evolution of opsins to make them better at reporting action potentials [7]. Changes in RNA transcripts can also report on activity history of brain circuits. Preserving spatial relationships while accessing the transcriptome

of selected cells is a crucial feature for advancing many biological areas, from developmental biology to neuroscience. Collaborators and us recently reported on methods for multi-color, multi-RNA, imaging in deep tissues. By using single-molecule hybridization chain reaction (smHCR), PACT tissue hydrogel embedding and clearing and light-sheet microscopy we detected single-molecule mRNAs in ~mm-thick brain tissue samples [8] and by rRNA labeling we mapped the identity and growth rate of pathogens in clinical samples [9]. Together these technologies can enable high content anatomical and functional mapping to define changes that affect cell function and health body-wide.

References

[1] Xiao C, Cho JR, Zhou C, Treweek JB, Chan K, McKinney SL, Yang B, Gradinaru V. Cholinergic Mesopontine Signals Govern Locomotion and Reward through Dissociable Midbrain Pathways. *Neuron* 90(2): 333-347, 2016

[2] Cho JR, Treweek JB, Robinson JE, Xiao C, Bremner LR, Greenbaum A, Gradinaru V. Dorsal Raphe Dopamine Neurons Modulate Arousal and Promote Wakefulness by Salient Stimuli. *Neuron* 94(6):1205-1219, 2017.

[3] Deverman BE, Pravdo PL, Simpson BP, Kumar SR, Chan KY, Banerjee A, Wu WL, Yang B, Huber N, Pasca SP, Gradinaru V. Cre-dependent selection yields AAV variants for widespread gene transfer to the adult brain. *Nat Biotechnol.* 34(2):204-209, 2016.

[4] Yang B, Treweek JB, Kulkarni RP, Deverman BE, Chen CK, Lubeck E, Shah S, Cai L, Gradinaru V. Single-cell phenotyping within transparent intact tissue through whole-body clearing. *Cell* 158(4):945-958, 2014.

[5] Treweek JB, Chan KY, Flytzanis NC, Yang B, Deverman BE, Greenbaum A, Lignell A, Xiao C, Cai L, Ladinsky MS, Bjorkman PJ, Fowlkes CC, Gradinaru V. Whole-body tissue stabilization and selective extractions via tissue-hydrogel hybrids for high-resolution intact circuit mapping and phenotyping. *Nat Protoco.* 10(11):1860-1896, 2015.

[6] Chan KY, Jang MJ, Yoo BB, Greenbaum A, Ravi N, Wu WL, Sánchez-Guardado L, Lois C, Mazmanian SK, Deverman BE, Gradinaru V. Engineered AAVs for efficient noninvasive gene delivery to the central and peripheral nervous systems. *Nat Neurosci.* 20(8):1172-1179, 2017.

[7] Flytzanis NC, Bedbrook CN, Chiu H, Engqvist MK, Xiao C, Chan KY, Sternberg PW, Arnold FH, Gradinaru V. Archaerhodopsin variants with enhanced voltage-sensitive fluorescence in mammalian and Caenorhabditis elegans neurons. *Nat Commun.* 5:4894, 2014.

[8] Shah S, Lubeck E, Schwarzkopf M, He TF, Greenbaum A, Sohn CH, Lignell A, Choi HM, Gradinaru V, Pierce NA, Cai L. Single-molecule RNA detection at depth by hybridization chain reaction and tissue hydrogel embedding and clearing. *Development* 143(15):2862-2867, 2016.

[9] DePas WH, Starwalt-Lee R, Van Sambeek L, Ravindra Kumar S, Gradinaru V, Newman DK. Exposing the Three-Dimensional Biogeography and Metabolic States of Pathogens in Cystic Fibrosis Sputum via Hydrogel Embedding, Clearing, and rRNA Labeling. *MBio* 7(5)796-816, 2016.

Utilising Nature's Biological Toolkit to Control the Enhancement of Raman Scattering through DNA Hybridisation

Jennifer Gracie[1], Karen Faulds[1], Duncan Graham[1]*

[1]Pure & Applied Chemistry, University of Strathclyde, Glasgow, Scotland, UK
*corresponding author, E-mail: duncan.graham@strath.ac.uk

Abstract

Plasmonic nanoparticle assemblies can be meticulously engineered to give greater control of the surface enhanced Raman scattering (SERS) effect. Nanoparticle hot-spots can be purposely formed by exploiting the specificity of biological molecules such as DNA, this increases the SERS intensity observed. Bacterial and viral infections, and even genetic mutations, can be accurately diagnosed through the symbiotic interplay between noble metal nanoparticles and specific sequences of DNA. Herein, key examples of biological nanoparticle assemblies from our research group will be discussed.

1. Introduction[1]

The ability to produce nanoparticle assemblies in solution has led to the improved control of hot-spot architecture, this achievement has massively contributed to the exploitation of the SERS effect in detecting an array of chemical and biological targets.

Molecules that have the ability to scatter light inelastically (Raman scattering) will experience an enhancement several orders of magnitude higher than that of isolated nanoparticles, if they are positioned in between nanoparticle surfaces. This phenomenon arises from the coupling of plasmons of nearby nanoparticles resulting in large localized electromagnetic field enhancement at the inter-particle junctions.

This comparison of isolated to 'aggregated' nanoparticles can be conveyed as a switch. Whereby, the isolated nanoparticles give a low signal and are considered 'off'. Then with the addition of a biological molecule, the nanoparticle interaction changes and causes them to aggregate; resulting in a very large SERS signal which can be considered as 'on'. The controlled aggregation of neighbouring nanoparticles can be through DNA-DNA, DNA-RNA, DNA-Protein, Peptide-Protein, Ligand-Protein or Ligand-Metal Ion interactions, which all force the nanoparticles closer together.

2. Discussion

2.1 DNA Hybridisation[2]

Our philosophy was to control the aggregation state of the nanoparticles by using DNA hybridisations. Figure 1 illustrates the concept.

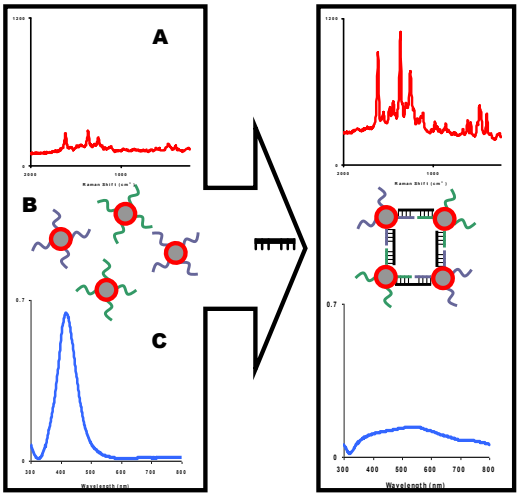


Figure 1: Schematic to illustrate the enhancement effect of DNA hybridisation. This specific interaction induces the controlled nanoparticle aggregation.

Silver nanoparticles were functionalised with specific DNA sequences (indicated by the blue and green strands). A Raman reporter (a molecule which expresses a unique fingerprint spectrum) was also included on the nanoparticle surface. On the left hand side, a low vibrational spectrum is observed as the monodispersed nanoparticles are repelled by the negatively charged DNA backbone. The corresponding extinction spectrum sits below, showing a sharp, narrow plasmon band.

Addition of the complementary DNA sequence induces aggregation of the nanoparticles as the DNA hybridisation

occurs, bridging between the blue and green DNA sequences. As a result, a large enhancement of the Raman signal intensity can be observed in the top right spectrum. The broad extinction spectrum seen after the addition of the target DNA supports the idea of controlled aggregation. This change in the vibrational spectroscopy is a direct consequence of the biological interaction taking place.

2.2 Distance Dependent DNA Sequences[3]

The capabilities of DNA hybridisation was further investigated by altering the base sequence length of the DNA strands. In this system we exploited the ability of DNA to form triplex assemblies. The design included dye-labelled silver nanoparticles with two different oligonucleotide probes on the surface. These has affinity to different regions of a complementary bridging dsDNA sequence, which allowed for the head-to-head nanoparticle triplex formation. The presence of additional non-complementary bases in the bridging dsDNA would force the nanoparticles in the assembly further apart from each other. As the complementary dsDNA sequences lengthened, and consequently the nanoparticles got further apart in the assembly, the SERS response followed a decreasing trend. This can be seen in Figure 2, where the SERS response drops in intensity as more bases are added to the dsDNA. It was also found that the shorter the complementary sequence, the faster the rate of nanoparticle aggregation.

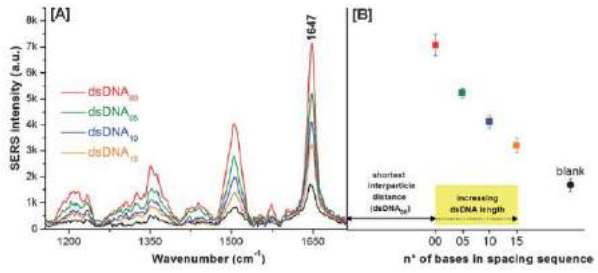


Figure 2: [A] SERS spectra of nanoparticle assemblies after adding the complementary dsDNA target. [B] Plot of maximum SERS intensity of the band at 1647 cm^{-1} for each spectrum vs number of additional non-complementary base pairs in the target dsDNA.

This example shows a correlation between biological function, structure and SERS intensity. This is a crucial step towards hybrid biological-inorganic systems with programmable properties.

2.3 Magnetic Nanoparticle Assay[4]

This work showcased a novel multi-target diagnostic assay which united a positive target recognition with the ability to magnetically capture. The addition of magnetic nanoparticles allows for sample clean-up and sample concentration, allowing for even lower detection limits. Figure 3 below summarises the assay design.

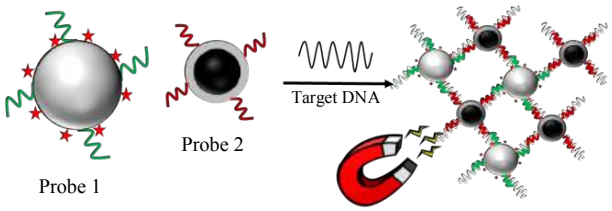


Figure 3: Schematic illustrating the dual nanoparticle magnetic assay.

Probe 1 consisted of silver nanoparticles functionalised with a DNA sequence and Raman reporter. Probe 2 consisted of silver coated magnetic nanoparticles conjugated to a different DNA sequence. Using this assay the sensitive detection of two different synthetic DNA sequences was demonstrated, both individually and in a duplex form. The robust target recognition of the sandwich assay shows the potential for the design to be used for detection within a complex clinical sample matrix.

3. Conclusions

The ability to modify the DNA functionalised nanoparticle probes has opened a whole new chapter of molecular and disease detection using SERS as the focal analysis tool. We have shown the ability to control the fabrication of assemblies and the ability to detect multiple targets in one sample matrix. This fundamental work in the nanoparticle probe design paves the way for future applications, in which biological-nanoparticle assays could become routine for a plethora of detection applications.

Acknowledgements

We wish to thank Luca Guerrini, Fiona McKenzie, Tara Donnelly, David G. Thompson, Alastair W. Wark and W. Ewen Smith for their contribution to this ongoing research.

References

1 L. Guerrini and D. Graham, *Chem. Soc. Rev.*, 2012, **41**, 7085.

2 D. Graham, D. G. Thompson, W. E. Smith and K. Faulds, *Nat. Nanotechnol.*, 2008, **3**, 548–551.

3 L. Guerrini, F. McKenzie, A. W. Wark, K. Faulds and D. Graham, *Chem. Sci.*, 2012, **3**, 2262.

4 T. Donnelly, W. E. Smith, K. Faulds and D. Graham, *Chem. Commun.*, 2014, **50**, 12907–12910.

Surface Enhanced Raman Scattering-Active Nanoparticle Assemblies for the Probing of Protein-Carbohydrate Interactions and their Applications

Craig Ward[1], Karen Faulds[1], Daniel Bracewell[2], and Duncan Graham[1]*

[1]Centre for Molecular Nanometrology, Department of Pure and Applied Chemistry, University of Strathclyde, Glasgow, UK
[2]Department of Biochemical Engineering, University College London, London, UK
*corresponding author, E-mail: duncan.graham@strath.ac.uk

Abstract

Protein-Carbohydrate interactions are prevalent in biological systems, and are known to be vitally important for various processes, including cellular recognition, and host-pathogen interactions. Here, we have taken advantage of these processes to, first of all, probe the interactions between carbohydrates and lectins, using assemblies of surface enhanced Raman scattering (SERS)-active nanoparticles. We have then moved on to disease detection and biopharmaceutical glycosylation analysis using similar assembly processes, monitored by localized surface plasmon resonance (LSPR) shifts in extinction spectroscopy, and SERS.

1. Introduction

The importance of protein-carbohydrate interactions in nature has led to a wealth of research in this area, and has provided valuable insights in to numerous biological processes. This includes furthering understanding of viral and bacterial interactions, cell differentiation, cell-to-cell adhesion, and cancer metastasis as examples. One particular class of proteins of particular interest are lectins, which bind to certain carbohydrates with high specificity. In our research, we have investigated the use of SERS to probe these protein-carbohydrate interactions, and used them to our advantage in detection assays. SERS often makes use of metallic nanoparticles to provide the enhancement of molecularly specific spectra of species bound to the metal surface. This takes place through controlled assembly of the nanoparticles, causing the formation of "hot-spots" of increased electromagnetic activity due to plasmonic coupling between the particles. Studies have been conducted where nanoparticle assemblies have been shown to provide SERS enhancements to probe DNA hybridisation and DNA-protein interactions. We have adopted a similar approach in the use of a lectin to induce assembly of silver glyconanoparticles which has provided reproducible SERS responses in relation to the lectin concentration, with limits of detection at picomolar level.[1]

Subsequent to this research, we have looked to applications of nanoparticle assemblies induced by protein-carbohydrate interactions. One such area of interest is disease detection, since host-pathogen relationships are often the result of these interactions. We have conducted a study in to the detection of the cholera toxin B-subunit (CTB), again using glyconanoparticles which form a SERS-active assembly when the toxin is present. This allows the CTB concentration to be quantified with limits of detection of 1 nM.[2]

We have also currently been developing an assay for biopharmaceutical glycosylation analysis using a similar approach. In this case we have used lectin-coated nanoparticles to detect bound oligosaccharides on protein surfaces. This has involved solution LSPR analysis, and the use of paper-based assays to provide a support for creating SERS-active assemblies upon glycoprotein detection.

2. Discussion

2.1. Probing protein-carbohydrate interactions[1]

Metallic nanoparticle assemblies have the potential for enhancing the Raman spectrum of a molecule bound to the metal surface, which means that they lend themselves well to SERS detection assays with high sensitivity. Therefore, they can be used to evaluate the binding of carbohydrates to lectins. We investigated these interactions by using glyconanoparticles. These were synthesised using silver nanoparticles which were functionalised with a mixed monolayer, consisting of a Raman reporter molecule and carbohydrate bound by a thiolated linker. (Fig. 1A) We chose to investigate the binding abilities of concanavalin A (Con A) as a model, which is known to specifically target α-D-glucose. The addition of Con A to the glyconanoparticles caused the particles to assemble in to aggregates (Fig. 1B) which could be followed by extinction spectroscopy (Fig. 1C) and SERS. (Fig. 1D) We have shown that the detection of Con A could be quantified to picomolar levels using SERS. Following on from this, we could then use these interactions in application-based SERS assays.

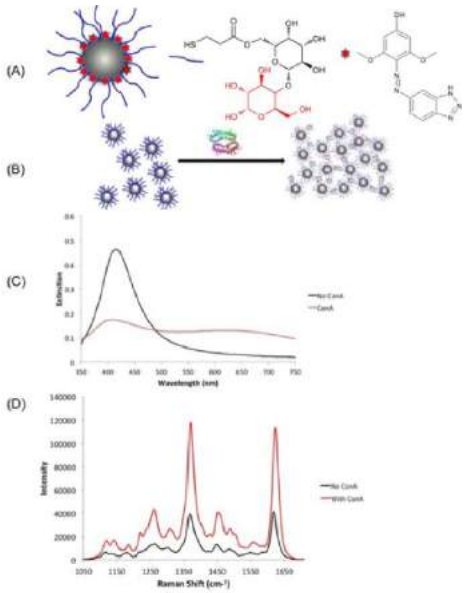


Figure 1: (A) Formation of glyconanoparticles via a mixed monolayer approach (B) Formation of aggregate structures as a result of ConA interaction with the glyconanoparticles (C) Extinction spectra and (D) SERS spectra before and after the addition of ConA.

2.2. CTB detection using nanoparticle assemblies[2]

Since host-pathogen interactions often rely on the binding of proteins to sugars, we decided to further investigate the capabilities of our nanoparticle assemblies in disease detection. CTB was selected as the target in this research. It is known that the cholera bacteria express lectins as toxins which play a vital role in the establishment and subsequent infection of the bacteria. CTB is one such toxin, and is known to bind to both the galactose and sialic moieties expressed on the surface of intestinal cells. Since protein-carbohydrate interactions are individually weak, the multivalency of CTB strengthens the binding to the cells. This property proved key to the detection using SERS-active nanoparticle assemblies. We explored the use of carbohydrate-functionalised nanoparticles as in previous research, but realised that mixed carbohydrate monolayers were much more sensitive to the presence of the CTB. The multivalent binding of the mixed monolayer nanoparticles proved to be much more effective in generating a quantifiable SERS response, (Fig. 2) allowing detection down to 1 nM of CTB.

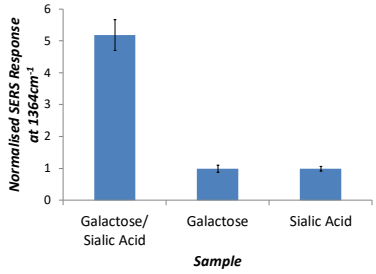


Figure 2: Normalised SERS response for mixed or single carbohydrate-coated nanoparticles after addition of 80 nM CTB.

2.3. Biopharmaceutical glycosylation analysis

The success of SERS-active assemblies in this research drove us to investigate another avenue of detection by exploiting these protein-carbohydrate interactions. In the biopharmaceutical industry, many patents are due to expire, meaning biosimilars are becoming more common. Since the majority of biopharmaceuticals are glycoproteins, it would be advantageous to have rapid and cost-effective methods to determine their glycosylation states, since this property can affect the structure, efficacy, and safety of the drug molecule. We have been using lectin-coated gold nanoparticles here and tracking detection of the glycoprotein using extinction spectroscopy in solution. We have also explored the use of paper-based assays to provide a support for our nanoparticle assemblies to generate a SERS response. (Fig. 3)

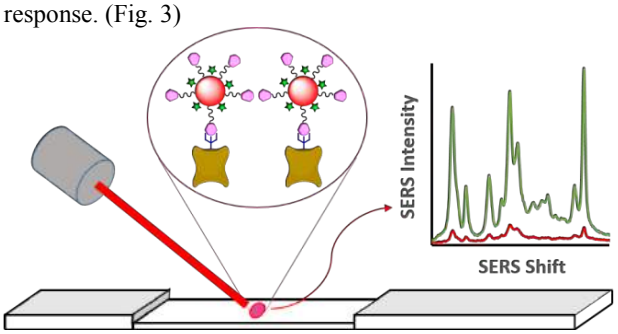


Figure 3: Lateral flow assay diagram showing the binding of the lectin-functionalised gold nanoparticles to the glycoprotein analyte spot, and the generated SERS response.

3. Conclusions

We have shown that by selectively inducing the assembly of nanoparticles we can created sensitive SERS assays to quantifiably assess protein-carbohydrate interactions to picomolar levels. This has been applied to disease detection, with respect to CTB, giving limits of detection of 1 nM. We have also been using paper-based assays to provide a support for nanoparticle assemblies to obtain SERS responses upon detection of protein glycosylation.

Acknowledgements

We would like to thank Dr. Derek Craig, and Dr. Jonathan Simpson for their contributions to this research.

References

1 D. Craig, J. Simpson, K. Faulds and D. Graham, *Chem. Commun.*, 2013, **49**, 30–32.

2 J. Simpson, D. Craig, K. Faulds and D. Graham, *Nanoscale Horiz.*, 2016, **1**, 60–63.

Fluorous directed facial selectivity of DNA origami structures on surfaces for the assembly of plasmonic nanoparticles

Sarah Henry[1], Gabriella Flynn[1], Andrea Taladriz-Sender[2], Jamie Withers [2], Nadia Chaher [1], Glenn Burley[2] and Alasdair Clark[1*].

[1]Biomedical Engineering, School of Engineering, University of Glasgow, U.K.
[2]Department of Pure and Applied Chemistry, University of Strathclyde, Glasgow U.K.
*corresponding author, E-mail: Alasdair.Clark@glasgow.ac.uk

Abstract

Facial selectivity of DNA structures is key for the creation of effective self-assembling building platforms. Typically, DNA nanostructures are made in liquid and deposition onto surfaces occurs in random orientation. In this work we functionalised one face of a DNA origami structure with fluorous labelled DNA strands to control the orientation of the structure on a surface.

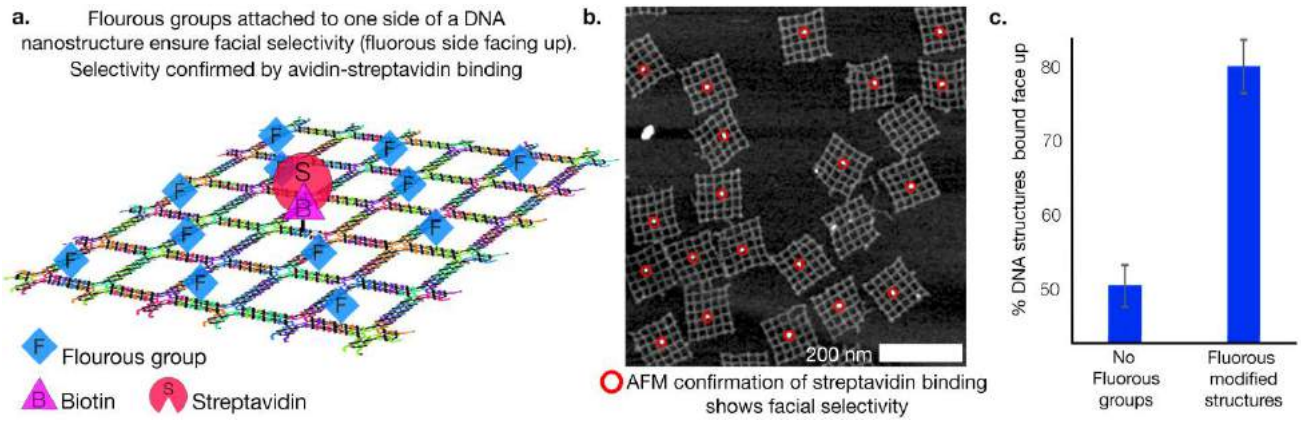
1. Introduction

Structural DNA nanotechnology allows for the rapid self-assembly of precise, programmable construction of complex structures which can easily be decorated with additional components to make functioning devices. The programmability of DNA structures is due to the strict Watson-Crick base-pairing and are constructed by folding short DNA 'staples' into desired conformations either to form small, repeating tiles which self-assemble into a larger unit, or with a plasmid DNA as scaffold in a process known as DNA origami[1]. Square, flat DNA structures were designed with twelve fluorous labelled staples on one side plus a biotin-streptavidin protein as a marker to visualise the orientation of the DNA structure on the surface by AFM. Fluorous labelled DNA staples directed the DNA structure to selectively deposit on the surface with the fluorous side of the DNA structure uppermost. Additionally, DNA structures were made with biotin and fluorous staples on opposing sides of the DNA structure which further confirmed that fluorous staples were able to control the orientation of the DNA structures. The functionality of the fluorous remains intact and able to capture DNA functionalized metal nanoparticles via the fluorous effect. This constitutes a new technique to use fluorous groups to control the orientation of DNA structures on surfaces as well as an integral component to attach other components, such as nanoparticles or proteins, with nanoscale precision.

Figure 1a Schematic showing position of 12 fluorous groups and one central biotin on DNA origami structure. DNA structures were incubated with streptavidin, which is easily visible by AFM (b) and an characterise the orientation of the DNA structure on the surface. (c) DNA structures with streptavidin uppermost were counted and compared to DNA structures without fluorous groups. DNA structures functionalized with 12 fluorous staples showed 80% uppermost orientation compared to 50% for the structures without fluorous.

References

[1] P. W. K. Rothemund. Folding DNA to create nanoscale shapes and patterns. *Nature* 440 297-302. 2006



Functional Materials and Devices for Lighting and Display

Control Photon Dynamics in Circuit Quantum Electrodynamics by Manipulating Qubits through a Phonon Bath

Fulu Zheng[1,2], Yuyu Zhang[3], Lu Wang[2,4], Yadong Wei[2], Yang Zhao[1]

[1]School of Materials Science and Engineering, Nanyang Technological University, Singapore, Singapore
[2]School of Physics and Energy, Shenzhen University, Shenzhen, China
[3]Department of Physics, Chongqing University, Chongqing, China
[4]School of Science, Inner Mongolia University of Science and Technology, Baotou, China
*corresponding author, E-mail: yzhao@ntu.edu.sg

Abstract

Bath induced effects on a circuit quantum electrodynamics (QED) system are investigated with the Dirac-Frenkel time-dependent variational principle combined with the multiple Davydov D_2 ansatze. The target system is a Rabi dimer with the qubits coupled to a phonon bath. It is found that the photon dynamics can be controlled by tuning the qubit-bath coupling strength. The QED device proposed here is experimentally feasible and can be applied for the studies of fundamental quantum physics.

1. Introduction

In circuit quantum electrodynamics (QED) systems, superconducting qubits are strongly coupled with microwave photons in resonators or transmission lines [1, 2]. Recently dissipation induced classical to quantum transition of photons has been observed experiment using transmon qubits and two coupled transmission-line resonators [3]. Theoretical studies model the tunnel-coupled resonators each containing a qubit as a Jaynes-Cumming (JC) dimer [1, 3] or a Rabi dimer [2]. The Markovian Lindblad master equation has been applied to describe the photon and qubit dynamics in these systems with the photon decay and the qubit decoherence taken into consideration [1, 3, 2]. The interplay between the QED devices and their surroundings is overlooked in these studies.

The time-dependent variational principle (TDVP) with the Davydov ansatze can capture simultaneously the system and the bath dynamics [4]. By employing the TDVP combined with the multiple Davydov D_2 ansatze, we present a comprehensive study of the bath induced effects on the dynamical behavior of a Rabi dimer. The environmental influences are modeled by coupling the qubits to a phonon bath.

2. Hamiltonian and Methodology

2.1. Hamiltonian of the hybrid system

As illustrated in Fig. 1, the total Hamiltonian for the complete system is composed of three terms

$$H = H_{\rm RD} + H_{\rm B} + H_{\rm BQ}. \quad (1)$$

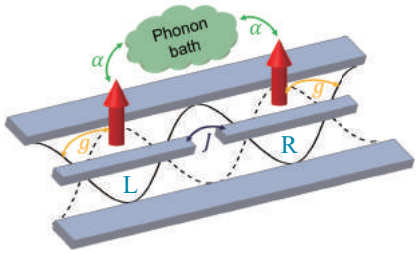


Figure 1: Schematic of the bath coupled circuit QED system studied in this work.

Here

$$H_{\rm RD} = H_{{\rm Rabi},L} + H_{{\rm Rabi},R} - J(a_L^\dagger a_R + a_R^\dagger a_L), \quad (2)$$

with J being the photon tunneling amplitude and $H_{{\rm Rabi},i}$ being the Hamiltonian of the ith Rabi system

$$H_{{\rm Rabi},i=L/R} = \frac{\Delta_i}{2}\sigma_z^i + \omega_i a_i^\dagger a_i - g_i(a_i^\dagger + a_i)\sigma_x^i. \quad (3)$$

Δ_i and ω_i are the energy spacing of the qubits and the frequency of the photon mode. σ_x^i and σ_z^i are the usual Pauli matrices, and a_i ($a_i^\dagger$) is the annihilation (creation) operator of the ith photon mode. g_i characterizes the coupling strength between the qubits and the photons. In this study, two Rabi sites are assumed to be identical, i.e., $\Delta_L = \Delta_R = \Delta$, $\omega_L = \omega_R = \omega_0$, and $g_L = g_R = g$.

The environmental effects on the Rabi dimer are modeled by coupling two qubits to a common phonon bath

$$H_{\rm B} = \sum_k \omega_k b_k^\dagger b_k \quad (4)$$

with an interaction Hamiltonian

$$H_{\rm BQ} = \sum_k \phi_k (b_k^\dagger + b_k)(\sigma_z^L + \sigma_z^R) \quad (5)$$

where b_k ($b_k^\dagger$) is the annihilation (creation) operator of the kth bath mode with frequency ω_k, and ϕ_k is the coupling strength between the kth mode and the qubits. The qubit-bath coupling is characterized by the spectral function,

$$J(\omega) = \sum_k \phi_k^2 \delta(\omega - \omega_k) = 2\alpha\omega_c^{1-s}\omega^s e^{-\omega/\omega_c}, \quad (6)$$

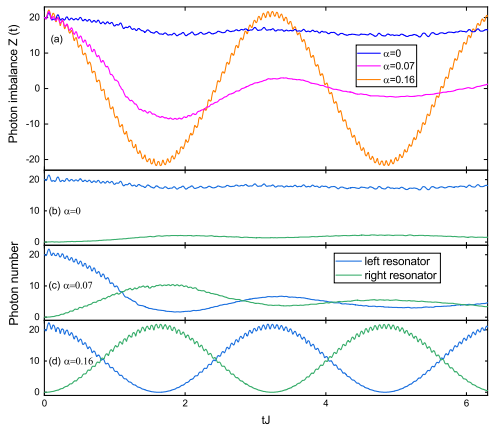


Figure 2: (a) Effects of the qubit-bath coupling α on the time evolution of the photon imbalance. (b)-(d) Time evolution of the photon numbers in the left and right resonators with different qubit-bath coupling α. The qubit-photon coupling is $g = 0.3\,\omega_0$ and the inter-resonator photon hopping rate is $J = 0.02\,\omega_0$. Sixty phonon modes are considered in the calculations.

with ω_c being the cut-off frequency and the dimensionless parameter α quantifying the qubit-bath coupling strength.

2.2. The Multiple Davydov D_2 ansatz

The multiple Davydov D_2 ansatz is employed to probe the time-evolution of the composite system described by Hamiltonian (1)

$$|\mathrm{D}_2^M(t)\rangle = \sum_{n=1}^{M}\Big[A_n(t)|\uparrow\uparrow\rangle + B_n(t)|\uparrow\downarrow\rangle + C_n(t)|\downarrow\uparrow\rangle + D_n(t)|\downarrow\downarrow\rangle\Big]\bigotimes|\mu_n\rangle_L|\nu_n\rangle_R|\eta_n\rangle_B, \quad (7)$$

where $|\uparrow\downarrow\rangle = |\uparrow\rangle_L \otimes |\downarrow\rangle_R$ with $\uparrow$ ($\downarrow$) indicating the up (down) state of the qubits. $|\mu_n\rangle_L$ and $|\nu_n\rangle_R$ are coherent states of the photon modes, and $|\eta_n\rangle_B$ is the coherent state of the phonon bath. In the ansatz, $A_n(t)$, $B_n(t)$, $C_n(t)$, $D_n(t)$, $\mu_n(t)$, $\nu_n(t)$, and $\eta_{nk}(t)$ are time-dependent variational parameters to be determined via the TDVP.

Initially, $N(0) = 20$ photons are pumped into the left resonator while keeping the right one in empty. Two qubits start to propagate from their down states. The phonon bath initiated from a vacuum state. The photon tunneling amplitude J is set to $0.02\,\omega_0$ and the qubit-photon coupling strength $g = 0.3\,\omega_0$.

3. Results and Discussions

The photon dynamics are presented in Fig. 2. In this parameter regime, the photons are localized in the left resonator of a bare Rabi dimer ($\alpha = 0$). Once the dissipation is taken into account by switching on the qubit-bath coupling α, the photons are no longer localized in the initial resonator.

For a qubit-bath coupling strength of $\alpha = 0.07$, the photons escape from the left resonator through two channels. On one hand, the photons tunnel to the right resonator at short times. On the other hand, some photons are dissipated due to the coupling to the phonon bath via the qubits, producing a gradually decreasing total photon number. At long times, only a small portion of photons are conserved and delocalized in two resonators. Therefore, the photon imbalance oscillates around zero with small amplitudes as time evolves. With stronger coupling, i.e., $\alpha = 0.16$, the photons are surprisingly delocalized over two resonators without any reduction of the total photon number. Comparing the photon localization for $\alpha = 0$ and the photon delocalization for $\alpha = 0.16$, we find that the photon confinement due to the qubit-photon coupling g can be eliminated by a strong qubit-bath coupling strength α. The photon dynamics can be controlled by tuning the qubit-bath coupling strength α. For instance, photon delocalization can be achieved from localized photons by coupling the qubits to a phonon bath strongly.

4. Conclusions

Equipped with the multiple Davydov D_2 ansatz, the time-dependent variational principle is applied to investigate the bath induced effects on the dynamics of a Rabi dimer by coupling the qubits to a common phonon bath. It is found that the photon dynamics can be tuned by controlling the qubit states via the qubit-bath coupling. With a moderate qubit-bath coupling strength, the bath induced dissipation is transferred to the photon modes, reducing the total photon number. Increasing α further, the qubit flipping is suppressed, breaking the indirect photon-phonon coupling.

Acknowledgement

This work is supported by Singapore National Research Foundation under Project No. NRF-CRP5-2009-04 and the Singapore Ministry of Education Academic Research Fund Tier 1 (Grant No. RG106/15).

References

[1] S. Schmidt, D. Gerace, A. A. Houck, G. Blatter, and H. E. Türeci, "Nonequilibrium delocalization-localization transition of photons in circuit quantum electrodynamics," *Phys. Rev. B*, vol. 82, p. 100507(R), 2010.

[2] M. J. Hwang, M. S. Kim, and M. S. Choi, "Recurrent delocalization and quasiequilibration of photons in coupled systems in circuit quantum electrodynamics," *Phys. Rev. Lett.*, vol. 116, p. 153601, 2016.

[3] J. Raftery, D. Sadri, S. Schmidt, H. E. Tureci, and A. A. Houck, "Observation of a dissipation-induced classical to quantum transition," *Phys. Rev. X*, vol. 4, p. 031043, 2014.

[4] Y. Zhao, B. Luo, Y. Zhang, and J. Ye, "Dynamics of a Holstein polaron with off-diagonal coupling," *J. Chem. Phys.*, vol. 137, p. 084113, 2012.

Ultra-high sensitive distributed acoustic sensor (DAS) based on distributed micro-structured optical fiber (DMOF)

Qizhen Sun, Fan Ai, Zhijun Yan, Wei Zhang, Hao Li, Deming Liu

School of Optical and Electronic Information, and National Engineering Laboratory for Next Generation Internet Access System , Huazhong University of Science and Technology, Wuhan 430074, Hubei, P. R. China;

*corresponding author, E-mail: qzsun@mail.hust.edu.cn

Short Abstract

Acoustical signal is one of the major information sources in our natural world, and acoustical sensing has been proved to have great importance in modern society. Fiber distributed acoustic sensor (DAS) has a wide range of application aspects of seismic wave recording, oil exploration, structural health monitoring and underwater acoustical sensing for high robustness in harsh environments. However, the low signal to noise ratio (SNR) of Rayleigh back scattered light and interference sensing mechanism of traditional DAS system severely limit the detection performance especially in the low frequency band.

In this talk, I will present a novel DAS with ultra-high sensitivity and broad bandwidth, to record the true acoustic signal continuously along the path of long-distance sensing fiber. Through designing and fabricating the DMOF with successive longitudinal microstructures along the fiber axial direction, the signal-to-noise ratio of the backscattered light modulated by the acoustic signal is significantly improved more than 30dB compared with the standard optical fiber. Meanwhile, the optical time domain reflectometer technique (OTDR) combined with the optical coherent detection are applied to realize the weak signal demodulation. As a result, the performance of the DAS system is greatly promoted through double-denoising mechanism, achieving the minimum detectable strain down to 20nε at the frequency of 0.01Hz, as well as the ultimate detection limit of 0.02nε over 10Hz, which is higher than the reported results to the best of our knowledge.

This non-power-driven fiber sensing probe enables monitoring in a wide area and extreme environment, having great potential in the fields of resources exploration, earthquake monitoring, pipeline safety, major engineering structure health monitoring and etc.

Dynamically encircling an exceptional point in voltage-controlled LRC resonator circuits

Youngsun Choi,[1] Jong Kyun Hong,[1] Yeonghwa Ryu,[1] Jae Woong Yoon,[1,2] and Seok Ho Song[1*]
[1] Department of Physics, Hanyang University, Seoul, Korea
[2]Electronics and Telecommunications Research Institute (ETRI), Daejeon, Korea

Abstract- We discuss time-resolved measurements on encircling an exceptional point parametric evolution in electrically tunable LRC resonator circuits.

Recently, exceptional points (EP) and associated dynamics have attracted significant attention due to the topologically robust chirality. When a non-Hermitian system slowly changes to encircle an EP in its parameter space, the dynamics state undergoes time-asymmetric evolution generating two orthogonal final states depending on the encircling direction. This chiral property is robust to the parametric-path change as long as it encircles an EP. Dynamically encircling an EP have been experimentally demonstrated in the metallic waveguides and opto-mechanical systems showing unidirectional state exchange and energy transfer and their robustness as a result of encircling EP[1, 2].

In this paper, we experimentally demonstrate dynamically encircling an EP (EEP) and consequent temporal dynamics in electrically tunable LRC resonator circuits. The circuit structure consists of two parallel LRC resonators connected through varactor diode providing voltage-controlled capacitance. One of the LRC resonators contains another varactor diode to control the resonance frequency detuning between two LRC resonators. With the varactor diodes and applied voltage, coupling strength and frequency detuning of the coupled resonator are precisely modulated to encircles an EP in the 2-dimensional parameter space [$V_{detuning}$, $V_{coupling}$]. In our experimental setup, the decay rate of an LRC resonator is conveniently tuned using negative-resistors in order to prevent sufficient loss of dynamic states. During the temporal modulation, the dynamics state in coupled resonator is estimated by measuring voltages across two LRC resonators. Importantly, this time-resolved measurements on dynamic state provide not only consequent final states but also entire evolution processes including geometric phase changes, adiabatic state evolution, and anti-adiabatic state jumps on the complex-eigenvalue sheets in the parameter space. These results may enhance understandings on the time-varying non-Hermitian systems associated with EP. Additionally, we discuss experimental feasibility on exploring temporal dynamics around high-order or multiple Eps with the voltage-controlled LRC circuits.

Acknowledgements, This research was supported in part by the Global Frontier Program through the National Research Foundation of Korea funded by the Ministry of Science, ICT & Future Planning (NRF-2014M3A6B3063708), the Basic Science Research Program (NRF-2015R1A2A2A01007553), and the Presidential Post-Doc Fellowship Program (NRF-2017R1A6A3A04011896).

REFERENCES

[1] J. Doppler *et al.*, "Dynamically encircling exceptional points in a waveguide: asymmetric mode switching from the breakdown of adiabaticity," *Nature*, vol. 537, pp. 76–79, 2016.
[2] H. Xu, D. Mason, L. Jiang, and J. G. E. Harris, "Topological energy transfer in an optomechanical system with exceptional points," *Nature*, vol. 537, pp. 1–28, 2016.

Substrate engineering for super-resolution tip-enhanced Raman spectroscopic imaging

Evgeniya Sheremet[1], Ashutosh Mukherjee[2], Vladimir Kolchuzhin[2], Alexander Milekhin[3], Ekaterina Rodyakina[3], Dietrich R.T. Zahn[2], and Raul D. Rodriguez[1]

[1]Tomsk Polytechnic University, Lenina ave. 30, 634034, Tomsk, Russia
[2]Chemnitz University of Technology, 09107 Chemnitz, Germany
[3]A.V. Rzhanov Institute of Semiconductor Physics, 630090 Novosibirsk, Russia
*corresponding author, E-mail: esheremet@tpu.ru

Abstract

We present an overview of published and unpublished work on the effects of the substrate optical properties on micro-Raman and tip-enhanced Raman spectroscopy (TERS) signal intensity. The investigation of a range of substrates and the two approaches provides a systematic understanding of the substrate effects in hyperspectral imaging methods. The key novel result concerns the substrates with interference effects, and their combination with near-field amplification in resonantly-excited plasmonic nanoantenna in surface-enhanced (SERS) and TERS regimes.

1. Introduction

Raman spectroscopic imaging provides a full set of chemical information at each point of the investigated sample area. But Raman spectroscopy tends to have low sensitivity due to low efficiency of inelastic scattering process. The Raman signal amplification is commonly tackled by using resonant Raman spectroscopy. But substrate engineering can be also very efficient for signal enhancement. A less common approach uses interference effects in the substrate to enhance the Raman signal. Surface-enhanced Raman spectroscopy (SERS) achieves single-molecule sensitivity and employs a substrate supporting localized surface plasmons (LSPs). Tip-enhanced Raman spectroscopy (TERS, nano-Raman), uses a single controlled metallic nanoparticle to achieve spatial resolution well below the diffraction limit of light [1].

2. Experimental

We present results obtained through a combination of experimental and theoretical approaches.
The Raman experiments were performed using a LabRam HR800 spectrometer with the excitation wavelengths 514.5 and 632.8 nm. The tip-enhanced Raman spectroscopy experiments were performed using two devices, a home-made coupled AFM/Raman system using an Agilent 5420 AFM and LabRam, and the other one a dedicated TERS system AIST-NT/XploRA from Horiba. Signal enhancement was achieved using fully metallic home-made golden tips [2].
Silicon was used as the typical semiconducting substrate. Golden films and nanoclusters were deposited using electron-beam lithography described previously [3].
Interference-enhanced effects are studied using an AFM calibration sample with SiO_2 grating of 119 nm thickness from MikroMesch and SiO_2 wedges on Si prepared by gradual HF etching of the SiO_2 film to obtain the gradual change of thickness.
Complementary numerical simulations of electric field enhancement for plasmonic TERS nanoantenna and interference effects have been performed with finite element calculations using COMSOL Multiphysics.

3. Results and Discussion

In this contribution, the approaches to the substrate engineering both in micro- and nano-Raman imaging regimes are considered.

3.1. Micro-Raman

By adjusting the substrate optical properties one can enhance the signal intensity. Practically relevant signal enhancement is achieved for metallic films [4] or coatings fulfilling interference conditions [5]. Signal enhancement by plasmonic nanostructures supporting localized surface plasmons (LSPs) is referred to as SERS. In our experiments, we observe $10^3 – 10^4$ times stronger signal as compared to Si for organic and inorganic compounds [3,6] depending on the efficiency of electric field enhancement due to LSP resonance in metallic nanostructures. The simultaneous matching of interference conditions in the substrate coating and resonance in the plasmonic nanoantenna opens new opportunities for the signal manipulation in SERS [7].

3.2. Nano-Raman

In the nano-Raman (TERS) imaging, the substrate has several effects since it determines the enhancement of electromagnetic field, its confinement and thus the achieved spatial resolution, and the near-field polarization of electromagnetic field. The strength of the effect depends on the strength of the image dipole determined by the substrate

optical properties. We present here TERS signal enhancement in several confisgurations: on silicon and gold-coated substrates, on curved surface, and on a surface with coating fulfilling interference conditions that was not considered until now. It produces subdiffraction spatial resolution for the Raman signal far below the near-field region of the TERS plasmonic nanoantenna (Figure 1). We also consider the resonant effects by investigating the enhancement depending on the excitation wavelength and the thickness of the interference coating.

4. Conclusions

The substrate effects including interference in the substrate coating, the optical properties of the substrate and the plasmonic contribution and their combinations in micro- and nano-Raman imaging. It gives a guide to optimizing the experimental approaches to imaging a range of samples with different experimental requirements and gives a tool for accessing near-field and far-field contributions for fundamental studies of the optical effects.

Acknowledgements

The research is carried out at Tomsk Polytechnic University within the framework of Competitiveness Enhancement Program. This work was performed in the context of the EU COST Action MP1302 Nanospectroscopy.

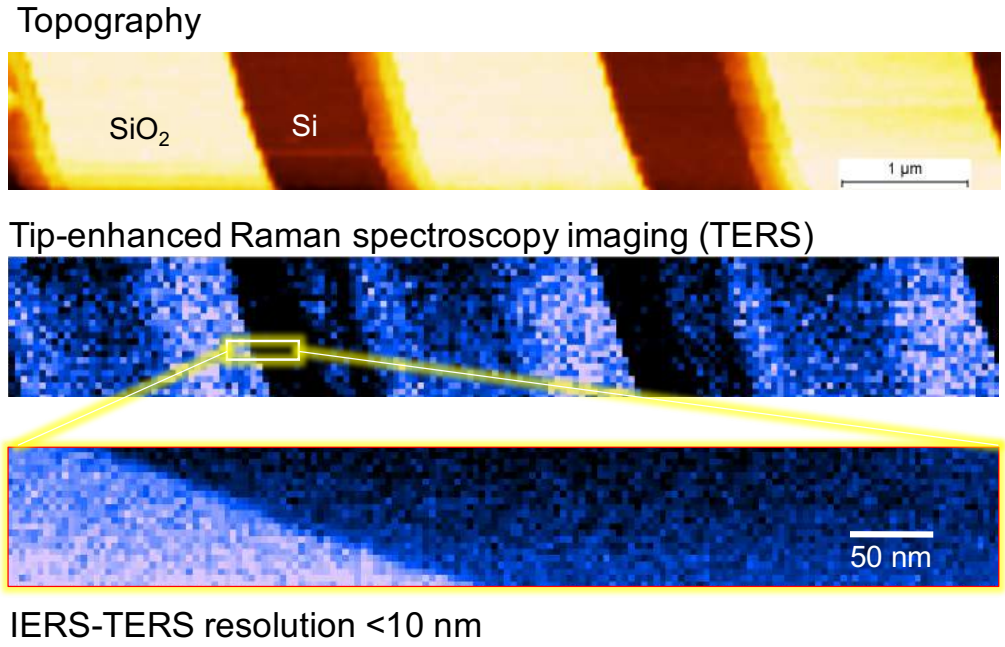


Figure 1: (Top) Topographic image of the AFM test grating with SiO_2 lines of 119 nm thickness on Si. (Middle) TERS image obtained by color-coding the Raman signal of Si substrate placed beneath the SiO_2 lines. (Bottom) Inset illustrating obtained TERS resolution below 10 nm.

References

[1] Sheremet, E.; Rodriguez, R. D.; Agapov, A. L.; Sokolov, A. P.; Hietschold, M.; Zahn, D. R. T. Carbon 2016, 96, 588-593.

[2] Kolchuzhin, V. A.; Sheremet, E.; Bhattacharya, K.; Rodriguez, R. D.; Paul, S. D.; Mehner, J.; Hietschold, M.; Zahn, D. R. Mechatronics 2016.

[3] Sheremet, E.; Milekhin, A.; Rodriguez, R. D.; Weiss, T.; Nesterov, M.; Rodyakina, E.; Gordan, O.; Sveshnikova, L.; Duda, T.; Gridchin, V. Physical Chemistry Chemical Physics 2015.

[4] Lina Mikoliunaite, Raul D. Rodriguez, Evgeniya Sheremet, Vladimir Kolchuzhin, Jan Mehner, Arunas Ramanavicius & Dietrich R.T. Zahn. Sci. Rep. 2015, 5.

[5] Milekhin, A. G.; Yeryukov, N. A.; Sveshnikova, L. L.; Duda, T. A.; Rodyakina, E. E.; Gridchin, V. A.; Sheremet, E. S.; Zahn, D. R. Beilstein journal of nanotechnology 2015, 6 (1), 749-754.

[6] Sheremet, E.; Rodriguez, R. D.; Zahn, D. R.; Milekhin, A. G.; Rodyakina, E. E.; Latyshev, A. V. Journal of Vacuum Science & Technology B 2014, 32 (4), 04E110.

[7] Milekhin, A. G.; Yeryukov, N. A.; Sveshnikova, L. L.; Duda, T. A.; Rodyakina, E. E.; Gridchin, V. A.; Sheremet, E. S.; Zahn, D. R. Beilstein journal of nanotechnology 2015, 6 (1), 749-754.

Plasmon-Induced Hot Carrier: Fundamentals and Applications

Broadband hot-electron photodetection based on hotspots-enriched disordered nanosystem

Qin Chen*, Long Wen

Guangdong Provincial Key Laboratory of Optical Fiber Sensing and Communications, Institute of Nanophotonics, Jinan University, Guangzhou, China
*corresponding author, E-mail: cq_qin@163.com

Abstract

The ability of plasmonic nanostructures to harvest photons beyond the band-to-band photovoltaic conversion has stimulated intensive research activities in hot electron. Here an approach for near-infrared photodetection by combining randomly and densely packed photonic nanostructures with plasmonic nanocoatings was demonstrated with a photoresponsivity around 1.5-13 mA/W at wavelengths ranging from 1100 to 1500 nm. Different loss mechanisms were described quantitatively and a large improvement potential of internal quantum efficiency above 20% was identified in the proposed hot electron harvesting platform.

1. Introduction

The photovoltaic (PV) effect driven by valence-to-conduction band transition of carriers sets the physical foundation for the current mainstream of energy-harvesting or photodetection devices. However, the applicable semiconductor materials are limited by their band gaps. For example, silicon cannot be used for photodetection below 1.1eV. Alternatively, important breakthroughs enabling photon-to-electricity conversion were achieved very recently via ejection of hot electrons at the plasmonic metals-semiconductor (MS) or –insulator-metals (MIM) interfaces [1]. The spectral response of such a photoelectric effect depends on the barrier height that energetic electrons should overcome rather than on the band-to-band transition of a semiconductor. There are two critical issues that determine the conversion efficiency of hot electron devices, i.e. the optical absorption and the internal quantum efficiency (IQE). Plasmonics is an emerging technique to harvest light and provide multifunctions [2]. In this paper, we present our recent work addressing these two issues by combining both optical and electrical perspectives into the design of plasmonic photodetectors on silicon platform [3,4].

2. Fabrication and Characterization

The hot electron device we proposed herein consists of a structured Si substrate with closely packed random SiNHs and an ultrathin conformal gold film coating, as shown schematically in Figure 1. The thin plasmonic absorber also serves as an anode as it forms Schottky contact with n-type Si. For the worm-like Au/SiNHs (inset, Figure 1b) which contain close-packed nanoscale features are characterized by the coexistence of spatially localized and delocalized modes over the entire structure. The presence of large number of hot spots at random nano-void and tips of this structure as shown in Figure 1a leads to the pronounced and broad-band plasmonic absorption enhancement, as verified by its absorption spectra shown in Figure 1b.

The device photoelectric responsivities of the ultrathin Au/SiNH device operating at two different illumination modes were measured as summarized in Figure 2. As expected, the back illumination mode exhibits much higher responsivity against the front illumination mode. The enhancement of responsivity of the back illumination mode cannot be solely attributed to its higher absorption. For example, at the wavelength of 1400nm, the back illumination mode has 6-fold enhancement on responsivity over the front illumination mode, but the absorption is only 4-fold. Consequently, it elucidates that the back

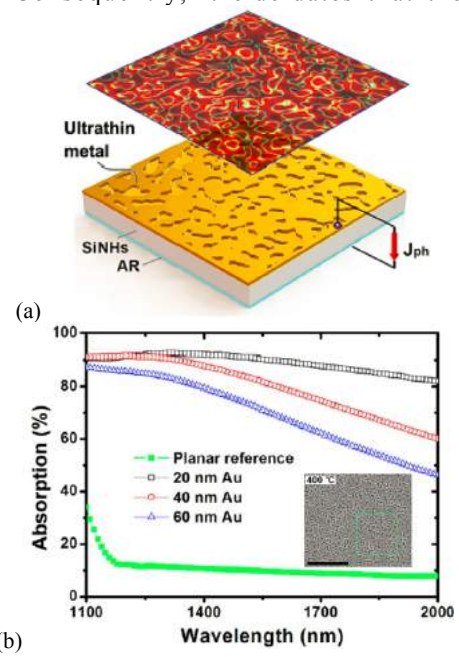


Figure 1: (a) Schematic of the proposed plasmonic hot electron photodetector and (b) the absorption spectra. The simulated field distribution with the profile of SiNHs from the SEM image in the inset of (b) are also shown.

illumination mode also yields a substantial improvement in its electrical aspects. In accordance with our previous statements, the back-illumnation mode with localized absorption adjacent to the M-S junction has higher IQE and therefore the more efficient hot electron photodetection.

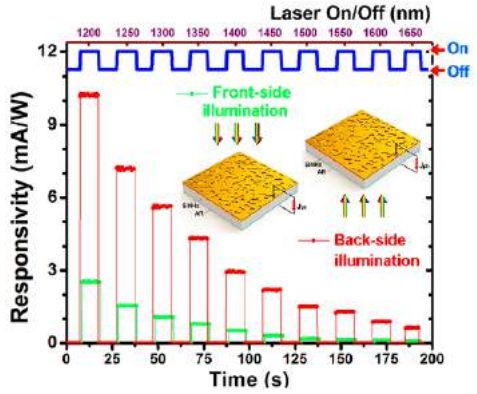


Figure 2: Time-dependent photoelectric responses of the optimized devices operating at two illumination modes.

The time-dependent current changes as a function of the applied voltage bias under intermittent irradiation are presented in Figure 3. There are large variations in the amplitude, sign and transient dynamic of the photonresponse at different bias conditions. For a negative bias, a rapid initial rise/fall of the photocurrent magnitude is observed as the light is switched on/off. This fast dynamic of response is associated with the photoelectric mechanism of hot electron. Under a negative bias of 0.5 V, a remarkable enhancement of the hot electron mediated current (I_{HE}) can be observed compared to the case in absence of external bias. With further increasing in the negative bias, I_{HE} increases gently but apparently tends to retard at large bias. With the continuous irradiation, the fast response characteristic of reverse biased device is followed by a slow photocurrent response, which increases with time and reaches a saturation stage in several tens of second.

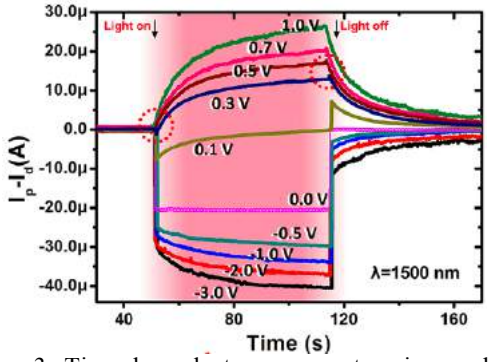


Figure 3: Time-dependent response at various voltage bias conditions. The incident laser was fixed to 1500 nm, with a power around 13.3 mW.

Similarly, when radiation is switched off, the amplitude of the current drops immediately and then a slow recovery process takes over to reach initial dark values. Under the reverse bias conditions, the fast response and slow response have the same polarity therefore are superimposed to give rise to an enhanced photocurrent of the devices.

As demonstrated in Fig. 4, constructing an M-S junction device with lower barrier height dramatically improve the theoretical IQE up to 36% for the wavelength of 1100 nm, as deduced from the t=8 nm case but with a much smaller barrier of 0.2 eV. It can be foreseen a boost for IQE by fabrication of the proposed random Au/SiNH devices with a p-type Si substrate instead of the n-type used herein. However, the decrease in barrier height raises some critical requirements for the detector, e.g. ultra-low series resistance or ultra-low temperature operation.

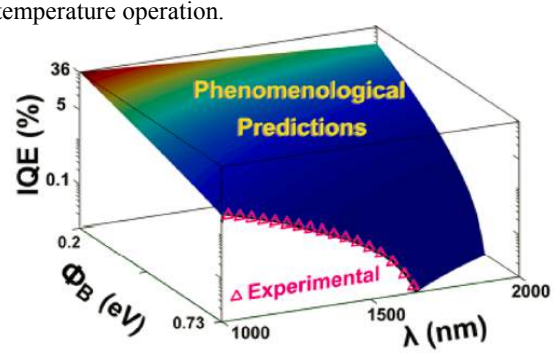


Figure 4: Calculated IQE by the phenomenological model based on the experimental results.

3. Conclusions

Realization of broad-band absorption and photon-to-electricity conversion from the hotspots-enriched disordered nano-system offers advantages in terms of simple, high-throughput, and low-cost fabrication, and in turn opens the door to future implementation of the metallic photon harvesting mechanism in NIR photodetector, bolometer, SERS and photocatalysis.

References

[1] M. L. Brongersma, N. J. Halas, P. Nordlander, Plasmon-Induced Hot Carrier Science and Technology *Nat Nanotechnol.* 10:25-34, 2015.

[2] L. Wen, Y.-F. Chen, L. Liang, Q. Chen, Hot electron harvesting via photoelectric ejection and photothermal heat relaxation in hotspots-enriched plasmonic/photonic disordered nano-composites, *ACS Photon.* 10.1021/acsphotonics.7b01156, 2017.

[3] L. Wen, Y.-F. Chen, W. Liu, Q. Su, Z. Qi, Q. Wang, Q. Chen, Enhanced Photoelectric and Photothermal Responses on Silicon Platform by Plasmonic Absorber and Omni-Schottky Junction, *Laser & Photon. Rev.* 11: 1700059, 2017.

[4] L. Wen, Q. Chen, X. Hu, H. Wang, L. Jin, Q. Su, Multifunctional silicon optoelectronics integrated with plasmonic scattering color, *ACS Nano* 10:11076-11086, 2016.

Low Cost Silicon-Based Hot-Electron Photodetector in the Near-Infrared Regime

Yupei Li[1], Yusheng Zhai[1], Guangdian Chen[1], Zhiyang Qi[1], Qilong Wang[1,*]

[1]Joint International Research Laboratory of Information Display and Visualization, School of Electronic Science and Engineering, Southeast University, Nanjing 210096, China
*corresponding author, E-mail: northrockwql@seu.edu.cn

Abstract

In this study, we propose a low-cost broadband near infrared light (NIR) photodetector fabricated by coating a thin layer of Au film onto a pyramidally textured silicon (Si) wafer. This structure utilizes the internal photoemission effect (IPE) through an Au/Si Schottky junction. The responsibility of the silicon pyramid photodetector exhibited up to 10-times increase compared with a control Schottky photodetector with a flat Au/Si surface. Large-area and lithography-free fabrication makes these devices suitable for low-cost NIR detection applications.

1. Introduction

Near infrared (NIR) photodetection is of great interest for night surveillance, telecommunication and various military applications. Si technologies provide a prominent platform to accomplish microsystems where photonic and microelectronic are monolithically integrated on a chip. However, for traditional silicon photodector, it is usually impossible to take advantage of the photovoltaic (PV) effect driven by valence-to-conduction band transition of carriers to operate in the NIR regime (>1200 nm) due to relatively huge energy bandgap (1.12eV) of Si. Thus, the CMOS-compatible NIR Si photodetectors have attracted largish research attention [1, 2]. Comparatively, a very promising approach is the internal photoemission effect which exploits photon-assisted transmission of hot electrons across a Schottky junction at metal-semiconductor (M/S) interfaces. Surface plasmons (SPs), which are excited with electromagnetic waves by means of coherent oscillations of free electrons in metals, play an important role in guiding and routing light at micro- or nano-scale[3, 4]. Following absorption and excitation, surface plasmons may non-radiatively delay into energetic electrons (hot electrons). Hot electrons can be transmitted to the M/S interface before thermalization and overcome the Schottky barrier, whose barrier height is lower than the photon energy of NIR light, resulting in photocurrent [5]. Figure 1 provides a schematic diagram of the energy band of an Au/Si interface. There are three significant steps that determine responsibility of hot electron devices, that is, optical absorption, electrical transmission and injection process of hot electrons [6]. Aiming at increasing conversion efficiency, a variety of plasmon nanostructures have been demonstrated, including nanowires [7], nanopillars [8], and metal gratings. However, very expensive precision lithography techniques are in need and it is not practical for the large scale and low cost manufacturing. In this work, we experimentally propose a lithography-free broadband silicon pyramid NIR Schottky photodetector [9], which takes both optical and electrical perspectives into consideration.

2. Fabrication

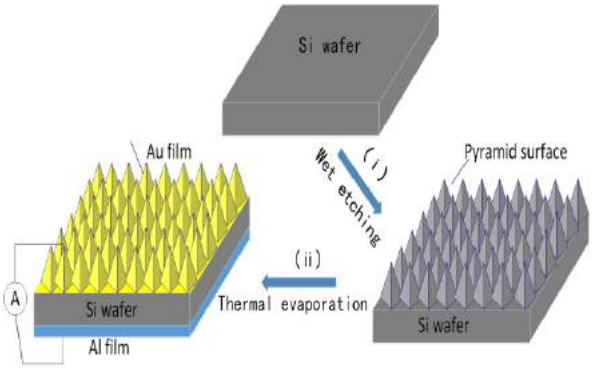


Figure 1: Fabrication procedure for our Au/Si Pyramid hot electrons photodetectors.

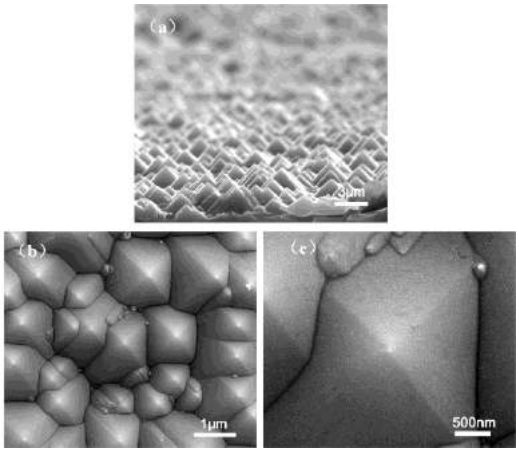


Figure 2: Si pyramid SEM images of (a) 25 min etching cross-section view (b) (c) top-side view with 30 nm Au films.Results and Discussion

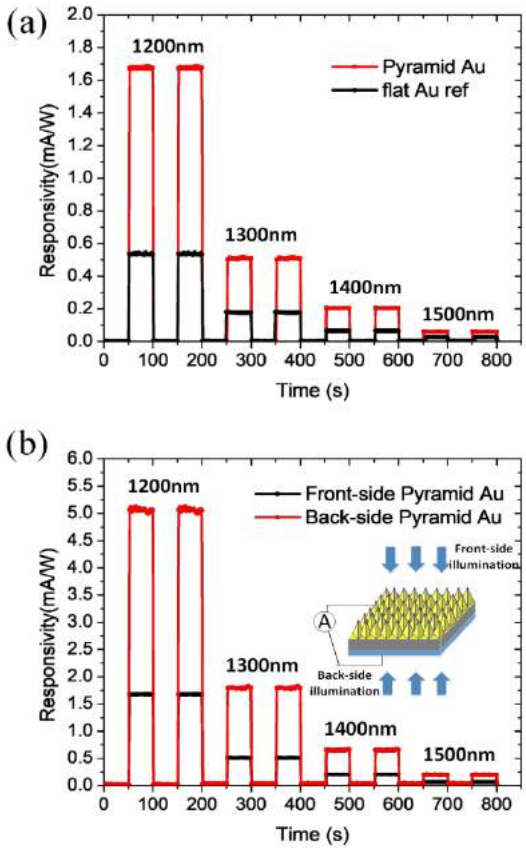


Figure 3: Time-dependent photoresponsivity of the samples for different wavelengths (1200~1500nm) at zero bias voltage. (a) pyramid-Si sample with Au films and flat Si reference with Au films operating at front-side illumination. (b) pyramid-Si sample with Au films operating at two illumination modes.

3. Conclusions

We have experimentally fabricated a low cost silicon-based hot-electron photodetector with broadband plasmonic absorption in the near-infrared regime without using any high resolution lithography or high temperature epitaxial growth technique. The analysis on the I-V curves estimated that Schottky junction was indeed formed at Au/Si interfaces that ensured NIR photodetection at zero bias voltage. Owing to the use of ultra-thin Au films coated and approximately periodic pyramid-Si plasmonic structures, the responsivity of optimum-designed sample was in the range of 5.2~0.3mA/W at the wavelength from 1200 to 1500nm without any external bias, presented around 10-times increase compared with a reference with an unstructured flat surface. In addition, we demonstrated that the responsivity of hot electron mediated photodetectors can be improved from not only optical absorption aspect, but also some electrical perspectives. Controlling the position where hot electrons were generated may shorten the mean transmission distance, then increases hot electron ejection probability. In summary, the lithography-free and large-area preparation processes and monolithic integration capability with CMOS electronics make the device suitable for low-cost NIR photodetectors and telecommunication industry. To further extend the detectable wavelength and enhance NIR responsivity, multiple sizes of pyramids and diversified thickness of metal absorbers will be necessary to study.

Acknowledgements

This work is supported by Postgraduate Research&Practice Innovation Program of Jiangsu Province (SJCX17_0020). the National Natural Science Foundation of China (61372030, 91333118, 51120125001, 61571124), the NSAF (U1730113), the Natural Science Foundation of Jiangsu Province (BK20171365),

References

[1] Knight M W, Sobhani H, Nordlander P, et al. Photodetection with active optical antennas. *Science*, 332(6030): 702-704, 2011.

[2] Sobhani A, Knight M W, Wang Y, et al. Narrowband photodetection in the near-infrared with a plasmon-induced hot electron device. *Nature Communications*, 4, 2013.

[3] Clavero C. Plasmon-induced hot-electron generation at nanoparticle/metal-oxide interfaces for photovoltaic and photocatalytic devices. *Nature Photonics*, 8(2): 95-103, 2014.

[4] Neumann O, Urban A S, Day J, et al. Solar vapor generation enabled by nanoparticles. *Acs Nano*, 7(1): 42-49, 2013.

[5] Hogan N J, Urban A S, Ayala-Orozco C, et al. Nanoparticles Heat through Light Localization. *Nano Letters*, 14(8): 4640-4645, 2014.

[6] Li W, Valentine J. Metamaterial perfect absorber based hot electron photodetection. *Nano letters*, 4(6): 3510-3514, 2014.

[7] Qin L, Zhang C, Li R, et al. Silicon-gold core-shell nanowire array for an optically and electrically characterized refractive index sensor based on plasmonic resonance and Schottky junction. *Optics letters*, 42(7): 1225-1228, 2017.

[8] Ajiki Y, Kan T, Yahiro M, et al. Silicon based near infrared photodetector using self-assembled organic crystalline nano-pillars. *Applied Physics Letters*, 108(15): 151102, 2016.

[9] Zhiyang Q, Yusheng Z, Long W, et al. Au nanoparticle-decorated silicon pyramids for plasmon-enhanced hot electron near-infrared photodetection. *Nanotechnology*, 28(27): 275202, 2017.

Electrical generation of hot electrons in plasmonic nanorod metamaterials

Pan Wang*, Alexey V. Krasavin, Mazhar E. Nasir, Wayne Dickson, and Anatoly V. Zayats

Department of Physics, King's College London, Strand, London WC2R 2LS, UK
*corresponding author, E-mail: pan.wang@kcl.ac.uk

Abstract

We report electrical generation of hot electrons and plasmons in plasmonic nanorod metamaterials by electron tunnelling. The large flux of hot electrons makes the tunnel junctions highly reactive, facilitating strongly confined chemical reactions in the junctions which results in dramatic changes in tunnelling current and light emission (radiative decay of tunnelling-induced plasmons).

1. Introduction

Nonequilibrium hot carriers formed near the interfaces of semiconductors or metals play an important role in chemical catalysis and optoelectronic processes [1]. In addition to excitation by optical illumination, such hot carriers can also be created by electron tunnelling, a quantum-mechanical effect which allows the transport of electrons across a nanometer scale junction between two conducting electrodes. Here we study electron tunnelling effects in electrically-driven plasmonic nanorod metamaterials containing up to 10^{11} tunnel junctions and show that the generation of hot electrons makes the tunnel junctions highly reactive, facilitating strongly confined chemical reactions which can in turn modulate the tunnelling processes [2].

2. Results

Plasmonic nanorod metamaterial is an array of electromagnetically coupled nanorods electrochemically grown in a substrate-supported, thin-film porous aluminum oxide template [3]. The typical nanorod areal densities are as high as 10^{10} to 10^{11} cm^{-2}, while the metamaterials can cover macroscopic areas due to the scalable electrochemical fabrication technique. In the metamaterial, each nanorod can functions both as a tunnel tip and as an optical antenna, providing an ideal platform for the exploitation of tunnelling effects.

2.1. Design of tunnel junctions

To form nanometer scale gaps for electron tunneling, an overgrown plasmonic nanorod metamaterial was first ion-milled at an oblique angle (75º with respect to the normal to the sample surface) to make the embedded gold nanorods approximately 1 nm shorter than the surrounding aluminum oxide. Then, a droplet of eutectic gallium and indium (EGaIn) was added onto the surface of sample working as an upper electrode, forming billions of ~1-nm metal-air-metal tunnel junctions between the Au nanorod tips and the EGaIn (Fig. 1) [2].

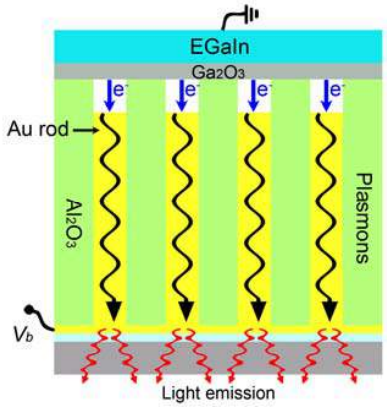


Figure 1: Schematic diagram of the device configuration.

2.2. Plasmon excitation

When a low voltage (2.5 V) was applied between the gold nanorods and the EGaIn, as shown in Fig. 2, a strong light emission (~ 4 mm^2 in size) was observed from the substrate side of the metamaterial due to the radiative decay of plasmonic modes excited in the nanorod metamaterial by inelastic tunnelling electrons [4,5,6]. With an increasing applied bias, the intensity of emission light increases gradually, and is accompanied by a blue-shift of the cutoff wavelength. This is because the energies of the emitted photons are always less than the energy of tunnelling electrons [4].

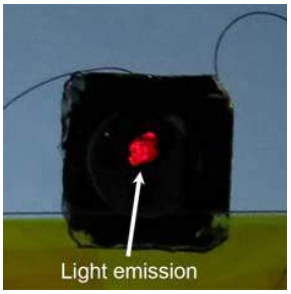


Figure 2: Photograph of an electrically-driven plasmonic nanorod metamaterial when a bias of 2.5 V is applied.

2.3. Hot-electron-activated tunnel junctions

Apart from the excitation of plasmons and photons by the inelastic tunnelling electrons, hot electrons are generated simultaneously in the tips of gold nanorods by the elastic tunnelling electrons while leaving hot holes in the EGaIn. To make use of the hot electrons for chemical reactions, metal‑polymer‑metal tunnel junctions [2] were constructed allowing access to the tunnelling region instead of the closed meta‑air‑metal tunnel junctions. The large flux of energetic hot electrons makes the otherwise inert tunnel junctions highly reactive, facilitating highly confined oxidation and reduction reactions in the junctions involving O_2 and H_2 molecules, respectively [2]. These reactions are monitored either optically by changes in the intensity of light emission (~50%) resulting from the radiative decay of tunnelling-generated surface plasmons, or electrically via tunnelling current variations (~10%).

3. Conclusions

In conclusion, we have demonstrated the electrical generation of hot electrons and plasmons by electron tunnelling. Electrically-driven plasmonic nanorod metamaterial with reactive tunnel junctions comprises a fertile platform merging photonics, electronics and chemistry at the nanoscale, opening up opportunities for developing electron tunnelling-based devices, such as sensors, nanoreactors, lab-on-a-chips and nanoscale light sources.

Acknowledgements

This work has been funded in part by the Engineering and Physical Sciences Research Council (UK) and the European Research Council iPLASMM project (321268). A.V.Z. acknowledges support from the Royal Society and the Wolfson Foundation.

References

[1] M. L. Brongersma, N. J. Halas, P. Nordlander, Plasmon-induced hot carrier science and technology. *Nat. Nanotech.* 10: 25‑34, 2015.

[2] P. Wang, A. V. Krasavin, M. E. Nasir, W. Dickson, A. V. Zayats, Reactive tunnel junctions in electrically driven plasmonic nanorod metamaterials. *Nat. Nanotechnol.* https://doi.org/10.1038/s41565-017-0017-7, 2017.

[3] P. Evans *et al.*, Growth and properties of gold and nickel nanorods in thin film alumina. *Nanotechnology* 17: 5746–5753, 2006.

[4] J. Lambe, S. L. McCarthy, Light emission from inelastic electron tunneling. *Phys. Rev. Lett.* 37: 923‑925, 1976.

[5] M. Parzefall *et al.*, Antenna-coupled photon emission from hexagonal boron nitride tunnel junctions. *Nat. Nanotechnol.* 10: 1058–1063, 2015.

[6] J. Kern *et al.*, Electrically driven optical antennas. *Nat. Photon.* 9: 582–586, 2015.

Anisotropic Pt-Au Nanostructure with Plasmonic Hot Electron Transfer for Hydrogen Generation Studied at Single-Particle Level

Zaizhu Lou[1*]

[1]Institute of Nanophotonics, Jinan University, Guangzhou, 511443, China
Osaka University, Japan
*corresponding author, E-mail: zzlou@jnu.edu.cn

Abstract

In recent years, SPR-induced hot electrons was used for hydrogen generation from water splitting. For traditional plasmonic photocatalysts metal/semiconductor composites, rapid recombination of plasmon-induced carriers results in low efficiency in photocatalysis. Based on fast transfer of electron between metals, we developed metal/metal composites plasmonic photocatalysts Pt-Au with various nanostructures including Pt-edged, Pt-covered, Pt-tipped Au triangular nanoprisms and Pt-edged Au nanodisks for hydrogen generation. Plasmon-induced hot electrons transfer between Au and Pt was studied and demonstrated by single-particle photoluminescence spectroscopy.

.

1. Introduction

Surface plasmonic resonance (SPR) is one unique physical phenomenon of electron oscillation occurring on surface of noble metal nanoparticle and has been applied in various fields including environmental, biology, medical and sensor. Under light irradiation, SPR can induce hot electrons which is used for hydrogen generation in photocatalysis by water splitting. However, due to fast recombination of plasmon-induced hot carriers, traditional plasmonic photocatalysts metal/semiconductors exhibited low efficiency in water splitting.[1] New system of plasmonic photocatalysts metal/metal were developed due to fast transfer of hot electrons between different metals[2]. Among various Au nanostructures including nanorods, nanocages, nanodisks, nanoprisms, etc., two-dimensional Au triangular nanoprisms [3] (TNPs) have various modes of SPR including in-plane dipole surface plasmon resonance (DSPR), multipole surface plasmon resonance (MSPR), and out-of-plane SPR in visible- NIR region and is a promising photocatalyst. Moreover, compared to NRs, TNPs with edges, tips and surface have more anisotropic bimetallic nanostructures as efficient photocatalyts for H_2 generation.

In this summary, three anisotropic Pt-tipped, Pt-edged, and Pt covered Au TNPs were prepared as photocatalyts for H_2 generation under visible-NIR light irradiation. Pt-edged Au TNPs with strong electric field and more interface for the hot electron transfer exhibited higher activity than both Pt-tipped and Pt-covered Au TNPs for H_2 generation. Single-particle PL spectra and simulations of finite-difference-time-domain (FDTD) was used to demonstrate that the DSPR of Au TNPs is the dominant channel for the hot electron transfer from Au to Pt.[5]

2. Discussion

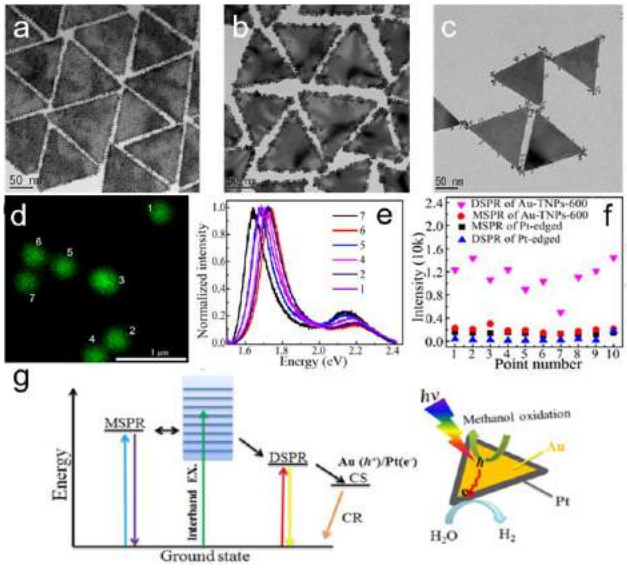


Figure 1. TEM images of Pt-covered (a), Pt-edged (e) and Pt-tipped Au-TNPs; Single-particle PL images (d) and spectra (e) of Au-TNPs(80 nm); PL intensity of ten Au-TNPs particles before and after Pt-loading; Mechanism of plasmon-induced hot electron transfer and decay (g, left), and photocatalytic hydrogen generation (g, right).[5]

Au TNPs with average length of 141 nm and uniform morphology were prepared.[5,6] After purification, Au TNPs covered by cetyltrimethylammonium chloride (CTAC) were used as precursors for Pt loading. With the absence of KI, Pt NPs grew randomly on the surface of TNPs to form Pt-covered Au TNPs which were observed in TEM (Figures 1a). With addition of KI (60 μL, 10 mM), Pt NPs grew only on the tips of Au TNPs as shown clearly in Figures 1c. For detailed synthetic process, see Experimental Section of reference X. The growth mechanism of Pt-tipped Au TNPs was investigated by tuning concentration of KI. As iodide ion was increased, the growth sites of Pt moved from the surface to edges and then to corners of Au TNPs. However, it is difficult to obtain pure Pt-edged Au TNPs in this case. A possible mechanism for Pt-tipped Au TNPs is that iodide

ions absorbed on Au(111) facets bind Ag^+ to form AgI on the surface of Au TNPs, limiting the seeding of Pt NPs. However, the corners of Au TNPs with high surface energy provide active sites for seeding and subsequently growth of Pt NPs. Finally, the dendritic structure of Pt NPs is formed on the corners under the effect of KI. For the overgrowth of Pt on edges of Au TNPs, CTAC was replaced by cetyltrimethylammonium bromide (CTAB). With addition of KI (60 μL, 10 mM), Pt NPs grew only on edges of Au TNPs to form Pt-edged Au TNPs (Figures 1b). The growth mechanism of Pt-edged Au TNPs was explained based on the transfer of electrons.

Under visible-NIR light irradiation using a 300-W xenon lamp equipped with 420 nm cutoff filter, the H_2 generation rate increased in the order of Pt-covered, Pt-tipped, and Pt-edged Au TNPs. The H_2 generation rate of Pt-edged Au TNPs was 0.167 μmol h^{-1} which is 5 and 3 times higher than that of Pt-covered (0.031 μmol h^{-1}) and tipped Au TNPs (0.048 μmol h^{-1}). Considering the great different area of the surface, edge, and tip of Au TNPs, the H_2 generation rate of three Pt-loaded Au TNPs was normalized by the actual Pt amount. Pt-tipped Au TNPs showed more than 7 times higher activity than that of Pt-covered Au TNPs. Pt-edged Au TNPs with part Pt loaded on corners exhibited a little difference with Pt-tipped Au TNPs in H_2 generation. Therefore, Pt loading on the corners of Au TNPs plays the main role on H_2 generation.

To clarify the detailed mechanism of photocatalytic reaction by Pt-loaded Au-TNPs, single-particle spectroscopy was used to study the hot electron transfer in individual Pt-edged Au TNPs. Figure 1d showed a typical single-particle PL image of individual Au-TNPs. The single-particle PL spectra of individual Au-TNPs are shown in Figure 1e. The peak in low energy region corresponds to in-plane DSPR, while the other does to in-plane MSPR of Au-TNPs. Peak position of the PL spectra depends on the ratio of length/thickness of Au TNPs. PL intensities of DSPR and MSPR are summarized for 10 individual Au-TNPs and 10 individual Pt-edged Au-TNPs particles as shown in Figure 1f. The DSPR PL intensity of Au-TNPs decreases significantly when Pt is edged, while the MSPR PL intensity is similar for both Au-TNPs and Pt-edged Au-TNPs. This proves that the DSPR PL is quenched by the Pt edged on Au-TNPs. PL of Au TNPs is attributed to the radiative decay from MSPR and DSPR, and the latter is the dominant channel for the decay. In single-particle PL experiment, 405 nm laser light excited d-sp interband transition of Au TNPs to generate electron-hole pairs (green line in Figure 1g left). Due to rapid interconversion between electron−hole pairs and MSPR, radiatively decay (purple line) occurs to generate short wavelength peak in PL spectrum. Meanwhile, in the electron−hole pairs, the energy transfer occurs from MSPR to DSPR. In addition, excitons of d−sp interbands transfer directly to DSPR by the nonradiative energy loss, which induces a radiative decay with emitting a photon leading to a PL peak in low energy level (yellow line). When Pt is edged on Au TNPs, the hot electron transfer from Au to Pt competes with the DSPR radiative decay. Our single-particle experiment proved the hot electrons transfer from Au to Pt. Under visible-NIR light irradiation, the excited hot electrons including d-sp interband excitation and MSPR/DSPR excitation transfer from Au to Pt and react with H^+ to generate H_2. Since electron transfer generates a charge separation (CS) state, the holes stay on Au to oxidize methanol.

3. Conclusions

Three anisotropic Pt-loaded Au TNPs nanostructures such as Pt-covered, Pt-edged, and Pt-tipped Au TNPs were successfully prepared as plasmonic photocatalyts. Pt-edged Au TNPs exhibited 3 and 5 times higher activity than Pt-tipped and Pt-covered ones in the photocatalytic H_2 generation under visible-NIR light irradiation. Single-particle PL spectra and FDTD simulations prove that the hot electrons can transfer from Au to Pt and Pt-edged Au TNPs have strong electric field and interaction between Au and Pt, resulting in the efficient charge separation and H2 generation.

Acknowledgements

This work was supported by the National Natural Science Foundation of China (Nos. 21703083), the Natural Science Foundation of Guangdong Province (No. 2017A030313026), and the Fundamental Research Funds for the Central Universities (No. 21617334).

References

[1] Zheng, Z. K.; Tachikawa, T.; Majima, T. Single-Particle Study of Pt-Modified Au Nanorods for Plasmon-Enhanced Hydrogen Generation in Visible to Near-Infrared Region. *J. Am. Chem. Soc.* 136: 6870−6873, **2014**.

[2] Lou, Z. Z.; Kim, S.; Zhang, P.; Shi, X. W.; Fujitsuka, M.; Majima, T. In Situ Observation of Single Au Triangular Nanoprism Etching to Various Shapes for Plasmonic Photocatalytic Hydrogen Generation. *ACS Nano* 11:968−974, **2017**.

[3] Scarabelli, L.; Puchau, M. C.; Giner-casares, J. J.; Langer, J.; Liz-Marzan, L. M. Monodisperse Gold Nanotriangles: Size Control, Large-Scale Self-Assembly, and Performance in Surface-Enhanced Raman, Scattering. *ACS Nano* 8: 5833−5842, **2014**.

[4] Lou, Z. Z.; Fujitsuka, M.; Majima, T. Pt-Au Triangular Nanoprisms with Strong Dipole Plasmon Resonance for Hydrogen Generation Studied by Single-Particle Spectroscopy. *ACS Nano* 10:6299−6305, **2016**.

[5] Lou, Z. Z.; Fujitsuka, M.; Majima, T. Two-Dimensional Au-Nanoprism/Reduced Graphene Oxide/Pt-Nanoframe as Plasmonic Photocatalysts with Multiplasmon Modes Boosting Hot Electron Transfer for Hydrogen Generation. *J. Phys. Chem. Lett.* 8:844−849, **2017**.

Plasmon-based nanohybrid structures for SERS and temperature sensing

Hongxiang Lei*

State Key Laboratory of Optoelectronic Materials and Technologies, School of Materials Science and Engineering, Sun Yat-Sen University, Guangzhou 510275, China
*corresponding author, E-mail: leihx@mail.sysu.edu.cn

Abstract

Developing plasmon-based nanohybrid structures with peculiar photoresponsive behaviors is critical and highly desired for the practical applications in surface enhancement Raman scattering (SERS) and temperature sensing. Here, a SERS-active substrate was fabricated by decorating a MoS_2 monolayer with Ag Nanowire (NW)-Nanoparticle (NP) structures, which exhibited an ultrasensitive ability, reliable reproducibility and good stability. Another nanohybrid structure was achieved by covering upconversion nanoparticles (UCNPs) on the surface of an Au-nanofilm-coated microfiber, which can be applied in temperature sensing.

1. Introduction

Plasmonic nanostructures, including Metallic nanoparticles (NP), nanowires (NW) and nanofilm (NF), are extremely important for nanoscience and nanotechnology [1,2]. Especially, plasmon-based nanohybrid structures with high performance have attracted great interest to researchers and become a research hotspot in the intersectional field of multi-subjects such as physics, chemistry, biology, material and so on. The nanohybrid structures not only have the original physical and chemical properties of single components, but also exhibit peculiar photoresponsive behaviors through the interaction among the components of the hybrid structures.

To obtain better surface enhancement Raman scattering (SERS) effect of Molybdenum disulfide (MoS_2) monolayer, a nanohybrid structure has been proposed by decorating the MoS_2 monolayer with metal NP, which make it possible to take advantages of both plasmonic metals and MoS_2 monolayer substrates [3,4]. However, this method requires the incident light is polarized and parallel to the NP dimer axis. It is difficult to estimate the direction of the dimer axis because of the diffraction limit of optical microscope. The metal NW-NP structures provide a straightforward way to figure out the problem. In this work, a SERS-active substrate was constructed by decorating the MoS2 monolayer with Ag NW-NP structures [5].

To enhance the efficiency of upconversion luminescence (UCL) for Lanthanide (Ln)-doped upconversion nanoparticles (UCNPs) as well as improve multiple peaks in the emission spectra, which greatly limit the applications of the UCNPs, a nanohybrid structure has been proposed by covering upconversion nanoparticles (UCNPs) on the surface of an Au-nanofilm-coated microfiber. The structure can selectively enhance the UCL and be applied in temperature sensing with excellent performance [6].

2. Results and Discussion

2.1. Plasmon-based nanohybrid structure for SERS

Figure 1a shows a schematic illustration of Raman signal detection of the R6G molecules deposited on the hybrid structure. The incident laser light at 633 nm was focused onto the "hotspot" formed between the AgNW-AgNP structure and the MoS_2 monolayer while the emitted Raman signal was detected from the same spot. The laser light was polarized perpendicular to the AgNW axis, and its polarization direction was controlled using a halfwave plate. For comparison, Figure 1b shows the Raman spectra on the different substrates under the identical experimental conditions. For the SiO_2 substrate, no Raman vibration mode was observed except the strong fluorescent signal (black curve). Weak Raman signal with partial peaks and lower fluorescent background was detected for the MoS_2 monolayer (pink curve). Obvious signals were detected for the AgNW-AgNW-MoS_2 (purple curve) and AgNP-AgNP-MoS_2 hybrid structures (green curve) due to the "hotspots" formed by the crossed AgNWs and AgNP dimers. Compared with the above structures, the AgNW-AgNP-MoS2 hybrid structure exhibits distinct peaks, strong intensity, and low fluorescent background (red curve). Particularly, for the small vibration mode at 1231 cm^{-1} (indicated by a pentagram), which was difficult to be observed using other SERS substrates, can be clearly observed. This indicates the Raman signals are significantly enhanced on the hybrid structure. The calculated enhancement factor value ranges from 1.4×10^6 to 5.6×10^6, which is higher than that of 8×10^5 observed on the reported AuNPs-MoS_2 hybrid structure [4].The fabricated structure was further demonstrated to exhibit an ultrasensitive ability with a detection limit of 10^{-11} M, reliable reproducibility and good stability.

2.2. Plasmon-based nanohybrid structure for temperature sensing

Figure 2a shows the schematic of the nanohybrid structure for selective enhancement the UCL and temperature sensing.

A 980 nm-wavelength laser beam was launched into the microfiber to excite the plasma in the Au nanofilm. This resulted in a large enhancement of the local electric field for the incident light and a higher utilization efficiency of the pump energy for light emission, whereby the upconversion efficiency could be enhanced. Moreover, with an increasing laser power, a strong plasmon-induced thermal effect upon the UCNPs next to the Au nanofilm could also be achieved. The increasing temperature induced a thermally-driven population increase of the $2H^{11/2}$ level and thus the emission intensity at 523 nm was selectively enhanced. The result indicates that the green emission at 523 nm was enhanced 36-fold over that of the UCNPs (Fig. 2b). Moreover, with increasing pump power, the increasing plasmon-induced thermal effect can enhance the intensity ratio (IR) of the $2H^{11/2}\rightarrow 4I^{15/2}$ (523 nm) and $4S^{3/2}\rightarrow 4I^{15/2}$ (545 nm) transition emissions, which can be used for temperature sensing and detection. Figure 2c shows the IR (I_{523}/I_{545}) as a function of temperature (taking the concentration of 0.02, 0.05 and 0.2 mg/mL as examples). For the three samples, ΔT was 125 K (341–466 K), 315 K (325–640 K) and 478 K (333–811 K), respectively, indicating the ΔT increases with the increasing of the UCNPs concentration. The relative sensitivity (S) decreases with an increasing temperature and the maximum sensitivity (S_m) was 1.35% K^{-1} at 325 K, 1.0% K^{-1} at 341 K and 1.46% K^{-1} at 333 K (Fig. 2d), and the temperature resolutions were calculated as 0.035–0.046, 1.3–1.6 and 2.9–3.0 K, respectively.

3. Conclusions

In summary, a SERS-active substrate was fabricated simply by decorating the MoS2 monolayer with the Ag NW-NP structures. The as-fabricated nanohybrid structure was experimentally demonstrated to provide strong Raman signal enhancement of 10^6 for the R6G molecules. Furthermore, the structure presents reliable reproducibility, good photostability, and a superior detection sensitivity of 10^{-11} M. In addition, a nanohybrid structure by covering upconversion nanoparticles (UCNPs) on the surface of an Au-nanofilm-coated microfiber was fabricated for selectively-enhanced UCL and temperature sensing. By controlling the pump power and the UCNP concentration, a wide temperature detection range of 486 K (325–811 K) and a high temperature resolution of 0.035–0.046 K were achieved.

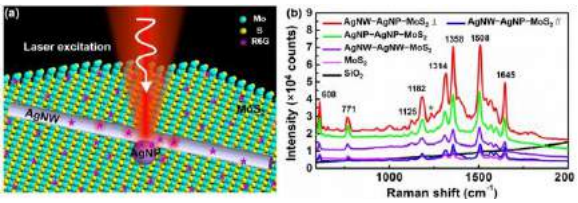


Figure 1: (a) Schematic illustration of SERS detection on the AgNW-AgNP-MoS_2 hybrid structure. (b) The Raman spectra with the polarization of laser perpendicular (red) and parallel (blue) to the AgNW axis, AgNW-AgNW-MoS_2 hybrid structure (purple), AgNP-AgNP-MoS_2 hybrid structure (green), MoS_2 (pink), and SiO_2 (black) substrates.

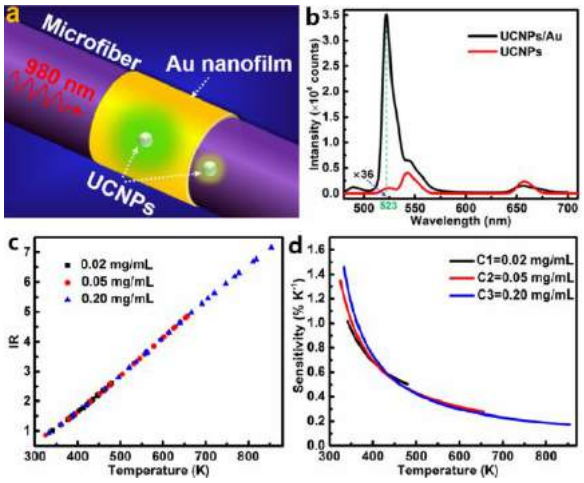


Figure 2: (a) Schematic of the hybrid structure. (b) UCL spectra of the hybrid structure and UCNPs. (c) IR and (d) relative sensitivity as a function of temperature with UCNPs concentrations of 0.02, 0.05 and 0.2 mg/mL.

Acknowledgements

This work was supported by the National Natural Science Foundation of China (Nos. 61205165 and 11274395), and the Open Fund of the Guangdong Provincial Key Laboratory of Optical Fiber Sensing and Communications (Jinan University).

References

[1] X. H. Xu, C. Cheng, Y. Zhang, H. X. Lei, and B. J. Li, Scattering and extinction torques: How plasmon resonances affect the orientation behavior of a nanorod in linearly polarized light, *J. Phys. Chem. Lett.*, 7:314–319, 2016.

[2] C. Cheng, X. H. Xu, H. X. Lei, and B. J. Li, Plasmon-assisted trapping of nanoparticles using a silver-nanowire-embedded PMMA nanofiber, *Sci. Rep.*, 6:20433, 2016.

[3] J. P. Lu, J. H. Lu, H. W. Liu, B. Liu, L. L. Gong, E. S. Tok, K. P. Loh, C. H. Sow, Microlandscaping of Au Nanoparticles on Few-Layer MoS_2 Films for Chemical Sensing. *Small*, 11:1792–18002015.

[4] S. Su, C. Zhang, L. H. Yuwen, J. Chao, X. L. Zuo, X. F. Liu, C. Y. Song, C. H. Fan, L. H. Wang, Creating SERS hot spots on MoS2 nanosheets with in situ grown gold nanoparticles. *ACS Appl. Mater. Interfaces*, 6:18735–18741, 2014.

[5] J. Li, W. N. Zhang, H. X. Lei, and B. J. Li, Ag nanowire/nanoparticle-decorated MoS_2 monolayers for surface-enhanced Raman scattering applications, *Nano Research*, https://doi.org/10.1007/s12274-017-1836-4, 2018.

[6] W. N. Zhang, J. Li, H. X. Lei, and B. J. Li, Plasmon-induced selective enhancement of green emission in Lanthanide-doped nanoparticles, *ACS Appl. Mater. Interfaces*, 9: 42935–42942, 2017.

Plasmon-enhanced electron emission in nano-metallic/semiconductor composites

Qilong Wang*, Zhiyang Qi, Yupei Li, Yusheng Zhai

Joint International Research Laboratory of Information Display and Visualization,
School of Electronic Science and Engineering, Southeast University, Nanjing 210096, China

*corresponding author, E-mail: northrockwql@seu.edu.cn

Abstract

Duo to the excellent optical properties, plasmonics nanostructures have been applied to many fields, Here, we present two aspects of works about the localized surface plasmon(LSPR) induced light trapping and hot electron in the application of photocathodes and photodetectors, respectively. Both experimental results indicate that the Au film or nanoparticles can improve the quantum yield and responsivity of the photocathodes and photodetectors, respectively.

1. Introduction

The excellent light-trapping and electromagnetic-field-concentrating properties of surface plasmons open up a widespread range of applications in the field of plasmonics . Localized surface plasmon resonance (LSPR) can occur in properly designed nanostructures in which confined free electrons oscillate with the same frequency as the incident radiation and eventually enter resonance, giving rise to intense, highly localized electromagnetic fields. Consequently, such nanostructures have been proposed as efficient light-trapping components that can be integrated in photovoltaic cells or photodetectors to increase the efficiency of conventional architectures considerably[1,2]. . However, recent investigations have shown that plasmonic nanostructures can also directly convert the collected light into electrical energy by generating hot electrons[3,4].

In this talk, I will introduce the plasmon-enhanced electron emission in nano-metallic/semiconductor composites. Two aspects of works about the LSPR induced light trapping and hot electron in photocathodes and photodetectors are presented, respectively. Firstly, the plasmon-enhanced photoemission based on Au nanoparticles (NPs) and cesiated surfaces is presented. Using the continuous laser and linearly polarized picosecond pulsed laser with 532nm wavelength, the electron emission performance is recorded under a low bias voltage. The experiment results indicate that the improvement of quantum efficiency is attributed to the plasmon-enhanced light absorption and localized electric field. With the increase of laser intensity, the electron emission mechanism is transmitted from photon absorption mechanism to strong-field tunneling emission. Second, We propose a low-cost broadband near infrared light (NIR) photodetector fabricated by coating a thin layer of Au film or Au nanoparticle onto a pyramidally textured silicon (Si) wafer. This structure utilizes the internal photoemission effect (IPE) through an Au/Si Schottky junction. The responsibility of the silicon pyramid photodetector exhibited up to 10-times increase compared with a control Schottky photodetector with a flat Au/Si surface. Large-area and lithography-free fabrication makes these devices suitable for low-cost NIR detection applications.

2. Result and Discussion

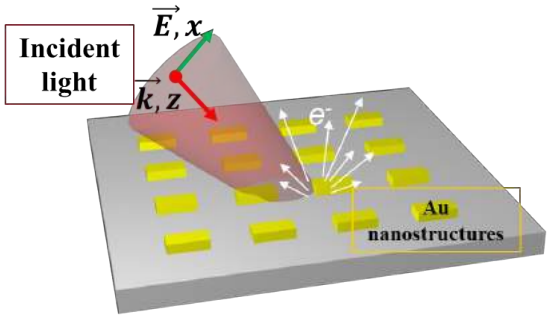


Figure 1: Scheme of photoemission from plasmonic nanostructures.

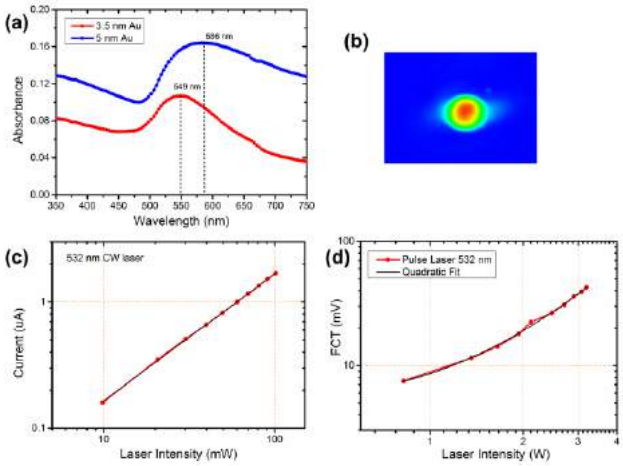


Figure 2: (a) Measured absorption spectra of the 3.5 nm and 5 nm Au samples. (b) The image of electron beam spot which is recorded using a YAG screen. The photoemitted

electron yield as a function of incident laser energy under the CW laser incidence (c) and the ps pulse laser incidence (d).

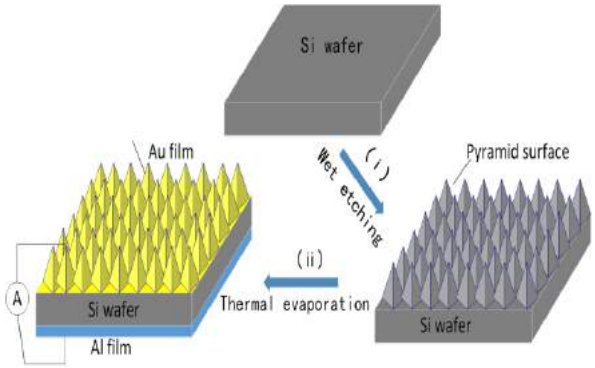


Figure 3: Fabrication procedure for our Au/Si Pyramid hot electrons photodetectors.

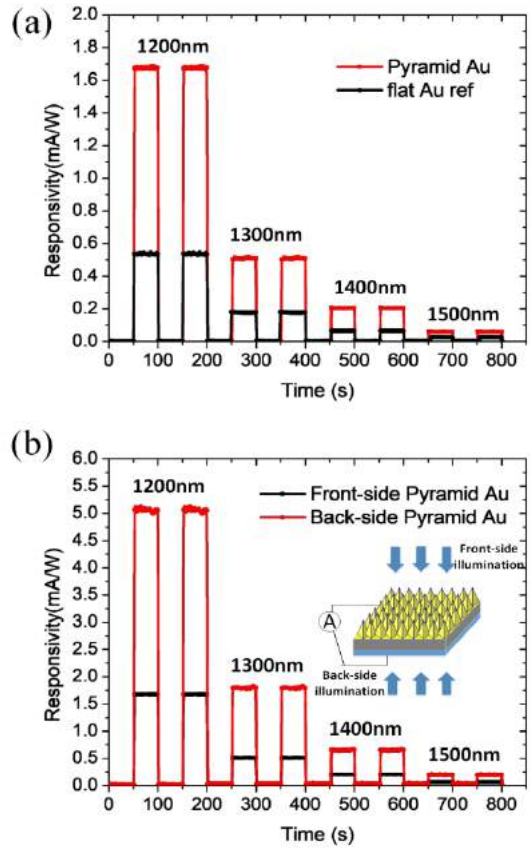


Figure 4: Time-dependent photoresponsivity of the samples for different wavelengths (1200~1500nm) at zero bias voltage. (a) pyramid-Si sample with Au films and flat Si reference with Au films operating at front-side illumination. (b) pyramid-Si sample with Au films operating at two illumination modes.

3. Conclusions

Here, we present two aspects of works about the localized surface plasmon(LSPR) induced light trapping and hot electron in the application of photocathodes and photodetectors, respectively. Both experimental results indicate that the Au film or nanoparticle can improve the quantum yield and responsivity of the photocathode and photodetector, respectively. We believe that through the delicate design and fabrication, the plasmon nanostructures will can be applied to more fields.

Acknowledgements

This work is supported by the National Natural Science Foundation of China (61372030, 91333118, 51120125001, 61571124), the NSAF (U1730113), the Natural Science Foundation of Jiangsu Province (BK20171365), and Fundamental Research Funds for the Central Universities and Graduate Innovation Program of Jiangsu Province (KYLX16_0214).

References

[1] Mendes, M. J., Luque, A., Tobías, I. & Martí, A. Plasmonic light enhancement in the near-field of metallic nanospheroids for application in intermediate band solar cells. Appl. Phys. Lett. 95, 071105 (2009).
[2] Atwater, H. A. & Polman, A. Plasmonics for improved photovoltaic devices. Nature Mater. 9, 205–213 (2010).
[3] Knight, M. W. et al. Embedding plasmonic nanostructure diodes enhances hot electron emission. Nano Lett. 13, 1687–1692 (2013).
[4] Mubeen, S. et al. An autonomous photosynthetic device in which all charge carriers derive from surface plasmons. Nature Nanotechnol. 8, 247–251 (2013).

Hot-electron generation in plasmonic nanostructures with hot spots: Quantum mechanisms

Alexander O. Govorov, Lucas V. Besteiro and Xiang-Tian Kong

Department of Physics and Astronomy, Ohio University, Athens, OH, 45701
govorov@ohio.edu

Generation of energetic (hot) electrons is an intrinsic property of any plasmonic nanostructure under illumination. Simultaneously, a striking advantage of metal nanocrystals over semiconductors lies in their very large absorption cross sections. Therefore, metal nanostructures with strong and tailored plasmonic resonances are very attractive for photocatalytic applications in which excited electrons play an important role. However, the central question in this problem is to quantify the number of hot electrons in a nanocrystal. Here we develop a theory describing the energy distributions of hot electrons in nanocrystals with various geometries [1-6]. In particular, we show that nanostructures with strong plasmonic hot spots generate unusually large numbers of hot electrons, which can be observed using ultra-fast spectroscopy [2,4], and photochemistry [6].

[1] A.O. Govorov, H. Zhang, V. Demir, and Y. K. Gun'ko, *Nano Today* 9, 85 (2014).
[2] H. Harutyunyan, et al., Nat. Nanotech. (2015).
[3] L.V. Besteiro, X.-T. Kong, Z. Wang, G. V. Hartland, A.O. Govorov, *ACS Photonics*, DOI: 10.1021/acsphotonics.7b00751 (2017).
[4] M. E. Sykes, J. W. Stewart, G. M. Akselrod, X.-T. Kong, Z. Wang, D. J. Gosztola, A.B.F. Martinson, D. Rosenmann, M. H. Mikkelsen, A. O. Govorov, G. P. Wiederrecht, *Nat. Commun*. 8, 986 (2017).
[5] G.V. Hartland, L. Besteiro, P. Johns, A.O.Govorov, Perspective paper*: What's so Hot about Electrons in Metal Nanoparticles?*, *ACS Energy Letters* 2, 1641 (2017).
[6] Y. Negrín-Montecelo, M. Comesaña-Hermo, X.-T. Kong, B. Rodríguez-González, Z. Wang, M. Pérez-Lorenzo, A.O. Govorov, and M. A. Correa-Duarte, *Traveling hot-spots in plasmonic photocatalysis: Manipulating interparticle spacing for real-time control of electron injection. ChemCatChem.*, doi:10.1002/cctc.201702053

Harnessing Acoustic and Elastic Waves via New Materials and Advanced Technologies

Accidental acoustic double Dirac degeneracy emerged by rotating scatterers and the corresponding topological transitions

Xiang Xie[1], Honglang Li[2], Qiuyun Fu[1], Xuefeng Zhu[3], Degang Zhao[3,*], and Wei Luo[1,*]

[1] School of Optical and Electronic Information, Engineering Research Center for Functional Ceramics of the Ministry of Education, Huazhong University of Science and Technology, Wuhan 430074, P. R. China
[2]Institute of Acoustics, Chinese Academy of Sciences No. 21, Bei-Si-huan-Xi Road, Beijing 100190, China
[3]Innovation Institute, Huazhong University of Science and Technology, Wuhan, Hubei 430074, People's Republic of China
*corresponding author, E-mail: hustluowei@gmail.com, dgzhao@hust.edu.cn; Tel. 027-87545167

Abstract

The specific two-dimensional phononic crystal (PC) consists of hexagonal steel plates with fan-like holes positioned in a triangular-lattice. Mutual evolution between deterministic Dirac degeneracy and accidental Dirac degeneracy was realized at the corner of the first Brillouin zone (FBZ). This provides multiple choice to achieve topological transition in acoustics. The associated valley–protected backscattering suppression around the curved interface channel was further demonstrated.

1. Introduction

Dirac point, the unique linear dispersion relations at the corner of the Brillouin zone (BZ) have attracted wide attention since the successful manufacture of the monolayer graphene. The conic dispersion originally proposed in quantum systems is also found in two-dimensional (2D) artificial crystals (ACs) including photonic and phononic crystals. In classical wave system, the linear dispersion relations at high symmetry points in the BZ are usually divided into three categories. The first type is the single Dirac cone located at the corner of the BZ, which is induced through a double degeneracy. The second type is the Dirac-like cone induced through an accidental degeneracy of a double-degenerate state and a single state. The third type is called the double Dirac cone which consists of a pair of two identical and overlapping Dirac cones and possesses four degeneracy modes correspondingly. Again, all these Dirac cones can be classified into two kinds. One is generated deterministically, and the other is generated accidentally.

Recently, with the advent of topological machanics, exploration of the topological properties in the classical wave field has been an active research area. Compared to condensed matter systems, in classical systems whether the spatial symmetry of the crystal or the scattering strength among the scatterers can be customized precisely. This makes two-dimensional artificial crystals, such as photonic crystal and phononic crystal, etc, a very suitable platform to study topologically protected edge wave propagation.

2. Methods and results

In this work, the physic structure of the acoustic system consists of hexagonal steel plates with fan-like holes positioned in a triangular-lattice, as shown in Fig. 1(a). The structural geometry can be described by the lattice constant a, the blade width l, the modulation parameter ht and the angle α indicating the orientation of the scatterer with respect to the horizontal axis. The material parameters of the steel are chosen as follows: the longitudinal wave velocity c_p=6010 m/s, the shear wave velocity c_s=3320 m/s, and the mass density ρ=7760 kg/m^3. In Fig. 1(b), the black solid lines show the band structure for the SC with an angle α = 0° and the colored dashed lines show the band structure for the SC with an angle α = 3°, both with a specific modulation parameter ht=2.4.

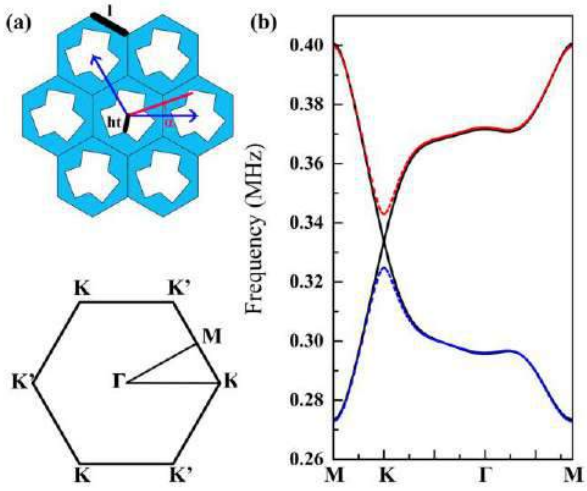


Fig. 1. (a) The SC (upper panel) consisting of hexagonal steel plates with fan-like holes positioned in a triangular-lattice with lattice vectors a1 and a2. The rotation angle α indicates the orientation of the scatterer with respect to a1. Bottom panel: the corresponding first Brillouin zone (FBZ). (b) The band structure for the SC with an angle α = 0° (black solid lines) and that for the SC with a rotation angle of 3 degrees (color dashed lines).

As the acatterers were rotated, the accidental double Dirac degeneracy occurred four times when α was equal to -41.07°, -18.93°, 18.93° or 41.07° (Within an angular period of 120°, shown in Fig. 2).

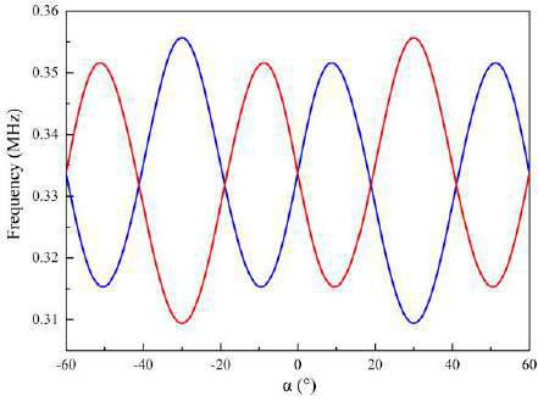


Fig. 2 Inversion of the band-edge frequencies of the bandgap with different α values within an angular period of 120°.

In order to verify the acoustic valley Hall phase transition in the above picture (Fig. 2), two kinds of Ⅰ - Ⅱ - Ⅰ superlattice structure were constructed. One was constructed by the SCs with α = 10° (Ⅰ) and 50° (Ⅱ), and the other was constructed by the SCs with α = 10° (Ⅰ) and 30° (Ⅱ). As shown in Fig. 3, for the former one, the edge spectrum is completely gapped since the two SCs possess the same topological charge; however, a pair of counter-propagated valley-chiral edge states arised in the band structure of the latter.

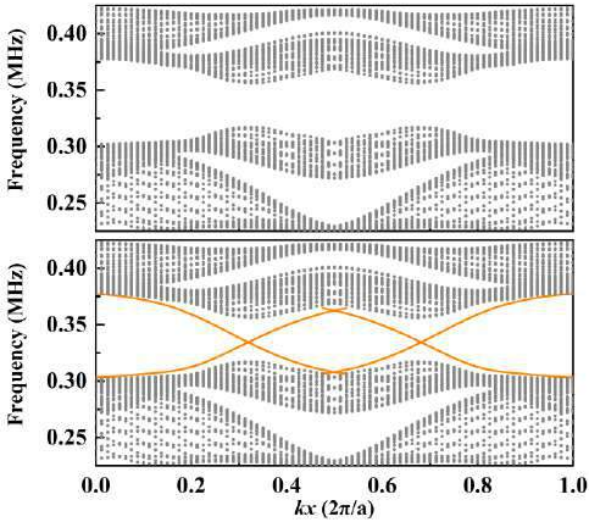


Fig. 3 Comparative dispersions for the SC interfaces separating two topologically distinct (α = 10° and 30°) and separating two topologically identical (α = 10° and 50°) acoustic valley Hall (AHV) insulating phases, where the green lines correspond to interface dispersions and the gray dots correspond to bulk dispersions.

In order to demonstrate the valley-protected backscattering suppression, an arch bridge-shaped waveguide was designed. The results of our simulation confirmed that elastic wave can propagate along the constructed edge with negligible loss.

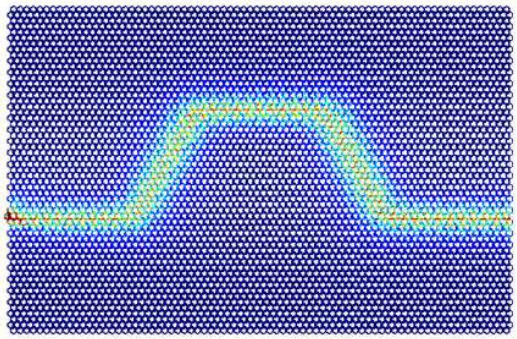


Fig. 4 elastic wave can propagate along the constructed edge with negligible loss.

3. Discussion and Conclusions

In summary, a new structured phononic crystal for elastic waves was presented and its band structure was obtained. The existence of the topological transition was confirmed. A new way to realize acoustic double Dirac degeneracy and the evolution between two kinds of Dirac cones has been proposed afterwards. The existence of edge states was demonstrated and valley-protected backscattering suppression of elastic waves propagating along the curved waveguide was achieved ulteriorly.

4. Acknowledgements

This work was supported by the National Natural Science Foundation of China under Grant No. 11574106, No. 61106081 and No. 51635007, the Fundamental Research Projects of Shenzhen City: JCYJ20150831202835225.

References

[1] Jiu-Yang Lu, Chun-Yin Qiu, *et al*. Dirac cones in two-dimensional artificial crystals. Phys. Rev. B 89, 134302, 2014.

[2] Yu-Gui Peng, Ya-Xi Shen, De-Gang Zhao, Xue-Feng Zhu., et al. Experimental demonstration of anomalous Floquet topological insulator for sound. Nat. Commun.7, 13368, 2016.

[3] Xiao-Dong Chen, Jian-Wen Dong. Valley-protected backscattering suppression in silicon photonic graphene. arXiv:1602.03352, 2016.

[4] Jiu-Yang Lu, Chun-Yin Qiu, *et al*. Observation of topological valley transport of sound in sonic crystals. Nat. Phys. 13, 369–374, 2016.

Handed walk of sound in periodically driven systems

Xue-Feng Zhu[1], Jie Zhu[2], Yu-Gui Peng[1], Ya-Xi Shen[1]

[1]School of Physics and Innovation Institute, Huazhong University of Science and Technology, Wuhan, 430074, P. R. China
[2]Department of Mechanical Engineering, the Hong Kong Polytechnic University, Hung Hom, Kowloon, Hong Kong SAR, P. R. China

*corresponding author, E-mail: xfzhu@hust.edu.cn

Abstract

Topological insulator provides intriguing properties such as spin-momentum locking that allows symmetry protected surface states with robustness against local defects. Here, we report the pseudo-spin free topological transport of sound in a periodically driven waveguides system with periodical modulations along three spatial dimensions, where acoustic waves propagating along the tightly coupled waveguides experience four different hopping patterns in one periodically driven cycle and follow a handed walk with chirality and topological protection.

1. Introduction

Topological insulator is a significant discovery in condensed-matter physics [1]. It has many intriguing properties such as spin-momentum locking, which allows symmetry protected surface states with robustness against local perturbations. The new concept of this novel class of condensed matters has been extended into classical wave systems as well. The past decade witnessed tremendous progresses in topological photonics [2], mechanics [3], and acoustics [4] studies, leading to the realization of various topologically protected wave-steering effects in artificial structures, such as unidirectional and backscattering-free wave transport. For acoustic wave, due to its 'spinless' nature, the analog of spin-momentum locking is implemented through judiciously constructing pseudo-spins, giving rise to the acoustic version of spin/valley Hall topological insulators. However, the previously reported pseudo-spin dependent acoustic topological insulators are still not strictly robust in one-way topological transport, since the bosonic-like time-reversal symmetry in linear and static acoustic system does not allow any Kramers doublet. As a result, the pseudo-spin of acoustic topological states could be reversed by certain impurities, leading to the emergence of backscattering.

In this work, the pseudo-spin independent topological chiral transport of sound, in stark contrast to previous pseudo-spin dependent realizations, is presented in a periodically driven waveguides system. Sound propagation in the system experiences four different waveguides coupling processes in each period cycle. We experimentally demonstrated the chiral transport of 'spinless' sound on the surface without employing external intervention. Such chiral transport is further shown to be topologically protected, while the number of chiral edge states equals to the topological invariant of winding number. In addition, the proposed periodically driven topological insulator also bears the unique advantages of low loss, broad operation band, small fingerprint, and simple design.

2. Theory and Experiment

The proposed periodically driven acoustic system can be realized through periodically arranging waveguides in parallel to form a two-dimensional array, while intentionally introducing periodical modulation and chiral coupling between the waveguides along the third dimension. As shown in Fig. 1(a), our actual waveguides array is arranged in an 8×8 fashion in the *x*-*y* plane. Along the *z* axis, *viz*., the direction of sound propagation inside the waveguides, the sample consists of multiple period cycles. All period cycles are divided into four sections (or driven evolution steps) numbered from 1 to 4. Each of the four sections has its own unique coupling patterns between waveguides, with the cross sections visually displayed in Fig. 1(b). When sound propagates along *z* direction, the four different coupling patterns are activated sequentially and periodically.

In our experiments, sound signals are firstly sent into the system at the waveguide sites (1, 1), (4, 7), and (8, 3), as shown in Fig. 2. The sound intensities for all waveguides are measured at incident side z=0 cm, then 8 cm, 16 cm, 24 cm, 32 cm, 40 cm, 48 cm, 56 cm, and 64 cm, corresponding to the ends of the eight sections. Together, the nine sound intensity maps presented in Fig. 2 visually display the dynamic transport of sound signals through two complete evolution cycles. For the edge excitations, unidirectional transport of sound in clockwise direction can be clearly observed. More specifically, for the incident signal at the edge site (8, 3), it travels along the route (8, 3)→(8, 2)→(8, 1)→(7, 1)→(6, 1), as marked by the cyan arrows. In our closed system without local resonances, the propagation attenuation is low for the chiral transport of sound, with the transmission coefficient measured at site (6, 1) on the output facet (z=64 cm) above 0.85. For the incidence at the

internal site (4, 7), sound signal experiences two anticlockwise closed loop walks [(4, 7)→(4, 6)→(5, 6)→(5, 7)→(4, 7), as marked by the lime arrows]. The measured transmission coefficient can also reach 0.7 at site (4, 7) on the output facet.

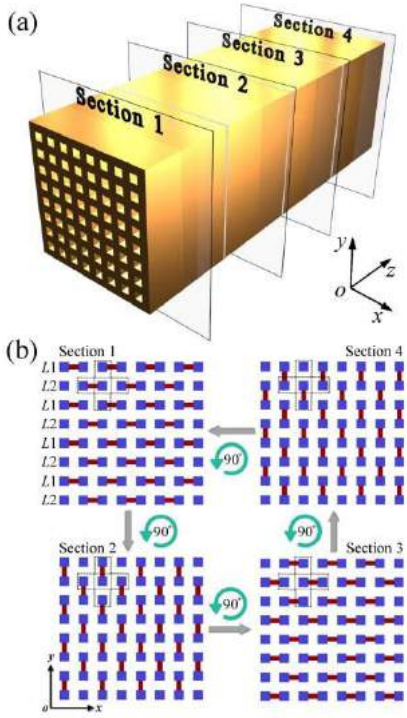


Figure 1: (a) The schematics of one period cycle of a periodically driven waveguides system, comprising 4 sections along z direction segregated by the solid gray lines. Each of the section has its own unique coupling pattern. (b) The cross sections of the 4 sectional cutting planes shown the schematics of the four different coupling patterns in sections 1, 2, 3, and 4. Through rotating the waveguides coupling pattern of section 1 by 90º in anticlockwise at a time, we can successively obtain the corresponding arrangements for section 2, section 3, and section 4. The blue blocks refer to waveguide sites in the 8×8 array, while the red ones are coupling tunnels connecting different waveguides.

This phenomenon takes a striking resemblance to the cyclotron motion of electrons under a static magnetic field (*viz.*, quantum Hall effect). While electrons forming spin-independent chiral currents at the boundary of quantum Hall insulators do not scatter at the edge defects, the chiral transport of sound in our periodically driven waveguides system is also topologically protected from the defects, such as rugged boundaries and sharp corners. To verify this property, we purposely introduced a defect by blocking the waveguide located at site (1, 3) of the upper edge. When sound incidence is excited at site (1, 1), it evidently travels along the route (1, 1)→(1, 2)→(2, 2)→(2, 3)→(2, 4)→(1, 4), as marked by the magenta arrows, bypassing the defect with little reflection.

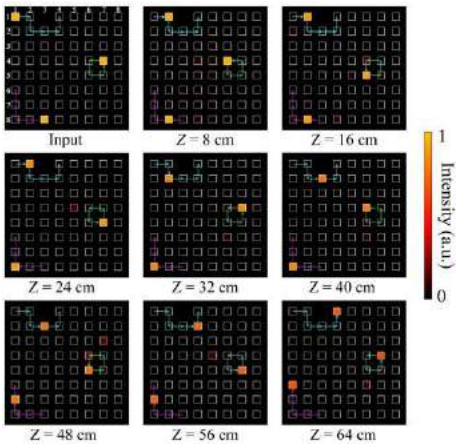


Figure 2: The measured sound intensity maps at z=0 cm, 8 cm, 16 cm, 24 cm, 32 cm, 40 cm, 48 cm, 56 cm, and 64 cm, which shows the chiral transport of sound signal in two complete evolution cycles. Acoustic waves are launched at three different sites (1, 1), (4, 7), and (8, 3) on the input facet, travelling along the routes marked by arrows.

3. Conclusions

In this work, we demonstrate the topological chiral transport of sound in a periodically driven waveguides system. The robustness of chiral transport of 'spinless' sound is protected by the artificial gauge field that originates from the periodical evolution of coupling patterns along the waveguides. Sound propagation in the nontrivial topological phase is shown to be pseudo-spin independent. With the measured sound intensity field evolution along the waveguides, we vividly show the cyclotron orbiting of sound in the bulk as well as topologically protected chiral transport at the edges, for directly mimicking the 2D quantum Hall effect.

Acknowledgements

This work was supported by National Natural Science Foundation of China (Grant Nos. 11674119, 11690030, 11690032, 11404125). J. Z. acknowledges the support from the Early Career Scheme (ECS) of Hong Kong RGC (Grant No. 25208115).

References

[1] D. J. Thouless, M. Kohmoto, M. P. Nightingale, M. den Nijs, Quantized Hall Conductance in a Two-Dimensional Periodic Potential, *Phys. Rev. Lett.* 49: 405, 1982.

[2] G. Q. Liang, Y. D. Chong, Optical Resonator Analog of a Two-Dimensional Topological Insulator, *Phys. Rev. Lett.* 110: 203904, 2013.

[3] R. Süsstrunk, S. D. Huber, Observation of phononic helical edge states in a mechanical topological insulator, *Science*, 349: 47, 2015.

[4] Y. G. Peng, C. Z. Qin, D. G. Zhao, *et. al.*, Experimental demonstration of anomalous Floquet topological insulator for sound, *Nat. Commun.*, 7, 13368, 2016.

A Design of Transparent Anisotropic metamaterial for airborne sound

Weiwei Kan, Menping Guo

School of Science, Nanjing University of Science and Technology, Nanjing 210094, P. R. China
*corresponding author, E-mail: Kan@njust.edu.cn

Abstract

We present a design of transparent anisotropic media based on transformation acoustics. The effective acoustic parameters of the structures, constructed by periodically arranging subwavelength objects in acoustic chambers, are studied in the quasi-static limit. By properly tuning the corresponding parameters, the acoustic parameters can be modulated independently, thereby the realizable ranges of these effective parameters can be broadened. The transparent feature of the designed structure is verified in broadband. The scheme will provide feasibility in versatile acoustic manipulation with metamaterials.

1. Introduction

The recent advances in artificial materials have remarkably enhanced the ability to manipulate acoustic wave, giving rise to many novel wave-manipulation designs [1-5]. Among various methods developed for designing metamaterial devices, the technique of coordinate transformation is a commonly used as well as powerful one. By transforming the coordinate according to the physical fields, the required material parameters for such device can be obtained. But the parameters are often inhomogeneous, anisotropic, or of extreme values that do not exist in nature. Such media that perfectly meet the requirement of the coordinate transformation are difficult to construct.

We present the method to address the abovementioned problem in the existing designs of acoustic metafluids [3, 4] that are formed by periodically arranging subwavelength elastic structures and can be characterized by anisotropic dynamic effective mass density, allowing for broadband manipulation of acoustic wave. Although such kinds of metamaterials have already shown great potentials for various wave-steering purposes such as invisibility cloaks[4-7], waveguides [8] and so on, perfect impedance match is still hard to achieve with them. Here we propose to realize independent modulation of effective mass density and bulk modulus of the metafluid by tuning the geometry parameter and the temperature of air, thereby broadening the range of achievable effective parameters. As a result of avoiding adopting reduced parameters in the previous metafluid designs, the associated impedance mismatch between the proposed metafluid and air is virtually suppressed, leading to a vanishing reflection of acoustic energy when passing the structures. We verify our design idea by numerically demonstrating a metamaterial based waveguide that allows for high efficiency transmission of airborne sound within a broad frequency band.

2. Theory and results

Suppose a bending waveguide is only filled with air, sound wave would be reflected with the wavefront distorted near the bending part. In order to eliminate the reflection and restore the field, the required distribution of effective parameters in the bending part can be designed with coordinate transformation. For a straight waveguide, the sound wave will travel through it with no reflection, which can be regarded as target space as shown in Fig. 1.

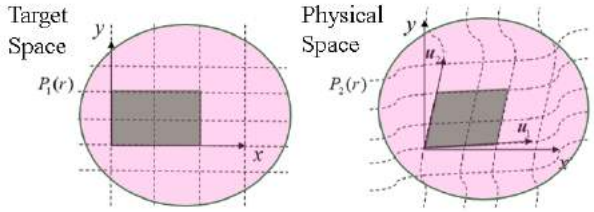


Figure 1: Schematic illustration of the coordinate transformation for the bending waveguide.

According to the well-established theory of transformation acoustics[9], by choosing a special coordinate in the bending area (physical space in Fig. 1), we can rewrite the pressure field, and in this way link the target sound field with this field: although there should be two different acoustic systems in Fig. 1, it is possible to make the mathematical form of these two systems the same by properly implementing the coordinate transformation [9]. The target bending waveguide with the corresponding geometric configurations is shown in Fig. 2. The width of the waveguide is 1 cm, and the bending angle is about 20°. Here, according to the geometric relation, the required new coordinate can be obtained, and the desired density is anisotropic, taking the form of a tensor. In order to realize the effective parameters, we periodically arrange the subwavelength structures designed by the effective medium theory (EMT). The anisotropic unit cells are simply sound-hard thin slabs inserted at each lattice point. Considering the requirement of EMT, the dimension of the unit cell is chosen as 0.5 cm, small enough compared with the

wavelength for the frequency of 3.4 kHz. The desired density anisotropy can be obtained by tuning the geometry parameters of the slab: the anisotropy of density will increase monotonously with the increase of the anisotropy of the slab geometry, while the bulk modulus keep constant. At the same time, the absolute value of the density tensor can be modulated by increasing the temperature in the chamber. Notice that the desired effective bulk modulus is the same with the air. In order to keep the bulk modulus unchanged, we have to compensate the volume occupied by the slabs, by increasing the height of the quasi-two-dimensional chamber as 0.51 cm.

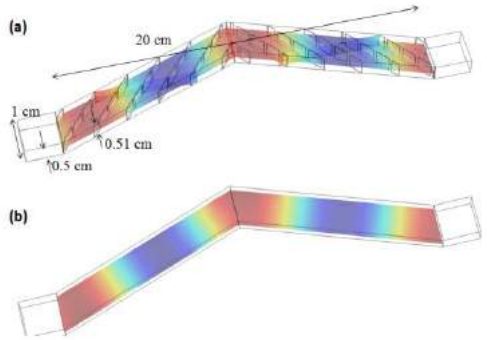


Figure 2 : (a) The illustration of the device in the numerical simulations. (b) The bending waveguide only filled with air.

As shown in Fig. 2(a). In Fig. 2(b) we present the pressure field when the 3.4 kHz plane wave travels through an ordinary bending waveguide filled with air. Without manipulation of the acoustic field by metamaterial, the resulting wave field is distorted and reflected as expected. The wave vector and the phase velocity are along the direction parallel to the sound hard wall of the waveguide. By periodically arranging the designed structure inside the bending part of the original waveguide, the device is obtained as shown in Fig. 2(a), where the good performance of the low-reflection is clearly demonstrated with the wavefront not disturbed. The wavefront manipulated by the metafluid still keep parallel to the y axis in the bending part, where the sound hard walls of the bending waveguide do not extend along the x axis though. In this special medium, the wave vector and the phase velocity remain the same with the case in the background medium, while the direction of group velocity and the flow of acoustic energy are along the direction parallel to the sound hard wall of the waveguide.

3. Discussion

The broadband performance of the device is characterized by reflection coefficient of the waveguide, showing the device work quite well in the designed frequency region from 2 kHz to 6 kHz, where the reflection coefficient remains a small value. The metafluid still work well at a comparatively high frequency beyond 6 kHz, where the effective parameters have deviated from the ideal value. The operating frequency band of metafluid in this scheme has no lower limit, and at the upper limit the wavelength is only about 5 times the dimension of the unit cell, in order to meet the requirement of EMT. In theory this upper limit can be further increased by decreasing the size of the unit structure.

4. Conclusions

A method for designing transparent metamaterial is proposed. The effective acoustic parameters of the units, constructed by periodically arranging anisotropic subwavelength objects in quasi-two-dimensional chambers, are studied in the quasi-static limit. By tuning the geometry parameters, the chamber volume and the temperature in the chamber, the anisotropic effective mass density and bulk modulus can be modulated independently, thereby the realizable ranges of these effective parameters can be broadened according to the requirement of the waveguide design. The performance of the designed structure is verified in broadband, with the reflected wave nearly cancelled and the wavefront undistorted. The proposed scheme shows potential versatile acoustic manipulation with metamaterials.

Acknowledgements

This work was supported by National Natural Science Foundation of China (Grant Nos. 11634006, 11604153, 81127901, and 11274168), Natural Science Foundation of Jiangsu Province (No. BK20160818).

References

[1] Jiang X, Li Y, Liang B, Cheng JC, Zhang L. Convert Acoustic Resonances to Orbital Angular Momentum. Phys Rev Lett. 117:034301, 2016.

[2] Zhu X. Acoustic waves switch based on meta-fluid phononic crystals. J. Appl. Phys. 112: 044509, 2012.

[3] Norris AN. Acoustic metafluids. J Acoust Soc Am. 125(2):839-49, 2009.

[4] Pendry JB, Li J. An acoustic metafluid: realizing a broadband acoustic cloak. New Journal of Physics. 10(11):115032, 2008.

[5] Kan W, Liang B, Zhu X, Li R, Zou X, Wu H, et al. Acoustic illusion near boundaries of arbitrary curved geometry. Scientific reports, 3:1427, 2013.

[6] Zigoneanu L, Popa BI, Cummer SA. Three-dimensional broadband omnidirectional acoustic ground cloak. Nat Mater. 13(4):352-5, 2014.

[7] Kan W, García-Chocano VM, Cervera F, Liang B, Zou X-y, Yin L-l, et al. Broadband Acoustic Cloaking within an Arbitrary Hard Cavity. Physical Review Applied,3:064019, 2015.

[8] Kan W, Liang B, Cheng J. A broadband low-reflection bending waveguide for airborne sound, Applied Physics Letters, 110:253502 , 2017.

[9] Kan W, Shen Z. Ultra-transparent media with anisotropic mass density for broadband acoustic invisibility, Applied Physics Letters, 111: 223501, 2017.

Observation of the Weyl points and Fermi arcs in a chiral phononic crystal

Feng Li [1], Xueqin Huang [1], Jiuyang Lu [1,3], Jiahong Ma [3], Zhengyou Liu [1,2,3]

[1] School of Physics and Optoelectronic Technology, South China University of Technology, Guangzhou, China
[2] Key Laboratory of Artificial Micro- and Nanostructures of Ministry of Education and School of Physics and Technology, Wuhan University, Wuhan, China
[3] Institute for Advanced Studies, Wuhan University, Wuhan 430072, China
*corresponding author, E-mail: zyliu@whu.edu.cn

Abstract

The discovery of Weyl semimetals extends not only semimetals beyond the Dirac type but also topological matters beyond topological insulators. Weyl points have also been found for classical waves in artificial periodic structures, for example, for electromagnetic waves in photonic crystals and for acoustic waves in phononic crystals. Here, we experimentally realize Weyl points in a chiral phononic crystal system, and we demonstrate the topological one-way propagation of the surface states associated with the Weyl points.

1. Introduction

Recently, interest in Weyl semimetals has been growing [1-3]. Weyl semimetals are materials in which the electrons have linear dispersions in all directions while being doubly degenerate at a single point, called the Weyl point, near the Fermi surface in three-dimensional (3D) momentum space. The Weyl point and the associated topological invariants enable Weyl semimetal to exhibit a variety of unusual properties, including robust surface waves (SWs) and chiral anomaly. In addition to the standard Weyl points possessing a point-like Fermi surface (referred to as type-I), another type of Weyl point was more recently recognized, which has a conical Fermi surface (referred to as type-II).

Since the Weyl point or Weyl cone in Weyl semimetals represents a special dispersion of electrons moving in periodic potentials, the question naturally arises as to whether a similar dispersion or the Weyl point for classical waves propagating in artificial periodic structures exists. Lu et al. were the first to report the existence of Weyl points and the associated one-way SWs in photonic crystals based on double-gyroid structures. Following the developments of the Weyl photonic crystals, Weyl phononic crystals (PCs) with Weyl points for acoustic waves have also been proposed in graphene-based structures with coupled cavities or coupled plane waveguides [4]. To date, the search for Weyl points in PCs has been a theoretical effort, and the realization of Weyl PCs in practice is therefore necessary.

In this work, we report for the first time the experimental observation of Weyl points in a 3D chiral PC [5]. Since the time-reversal symmetry is preserved in the design, the Weyl points come out of the breaking of the inversion symmetry. Weyl points in the first Brillouin zone (BZ) are determined by measuring and Fourier transforming the field distributions of the bulk waves; the Fermi-arc dispersions of the SWs are similarly obtained by measuring and Fourier transforming the surface acoustic fields. All observations are in agreement with the theoretical predictions.

2. Acoustic Weyl point and Fermi Arcs

The Weyl PC is fabricated based on a layer-stacking strategy. Figure 1a provides a photo of our sample. Portions of the front and back surfaces of the structured plate together with a schematic of the outlined unit cells are shown in Figs. 1b and 1c, respectively. In the unit cell, a = 7.0 mm, r_0 = 2.6 mm, h = 6.1 mm, r_1 = 2.9 mm, r_2 = 5.5 mm, d = 1 mm. All holes twist at an angle of 90 degrees in a spiral manner, such that the unit cell on the back surface appears as shown in Fig. 1c. The sample has a total height of 21 layers along the z direction and dimensions of 31 and 30 unit cells in the x and y directions, respectively. The hexagonal first BZ of the sample is shown in Fig. 1d.

Theoretical studies have shown that there are two pairs of Weyl points for the structure distributed on the $k_z=0$ and $k_z=\pi/c$ planes in the first BZ, as shown in Fig. 1d. To confirm the existence of the Weyl points on the two planes, we measure the 2D band structures by fixing $k_z=0$ and $k_z=\pi/c$. Figure 2a (2c) shows the measured and calculated 2D band structures on $k_z=0$ ($k_z=\pi/c$) plane along the ΓK and KM (AH and HL) directions in the first BZ for the two lowest-order acoustic modes. The color maps represent the experimental dispersions obtained by Fourier transforming the measured pressure fields inside the sample, and the white circles denote the calculated values obtained from full wave simulations. Double degeneracy and linear dispersions at the K (H) point are clearly observed at approximately 15.0 kHz (16.0 kHz) in Fig. 2a (2c) on plane $k_z=0$ ($k_z=\pi/c$). However, a gap of approximately 2.0 kHz opens at K point

on plane $k_z=0.5\pi/c$, the halfway point between $k_z=0$ and $k_z=\pi/c$, as shown in Fig. 2b, which can be attributed to the breaking of the time-reversal symmetry due to the effective gauge flux arising from the nonzero k_z. In all cases, the experimental results are in agreement with the numerical simulations.

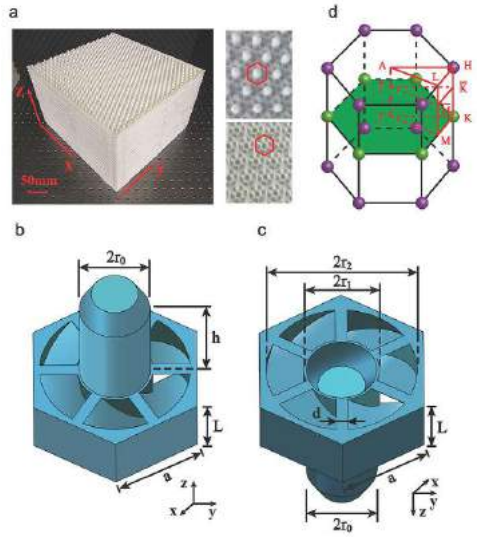


Figure 1: Illustration of the unit cell of the phononic crystal.

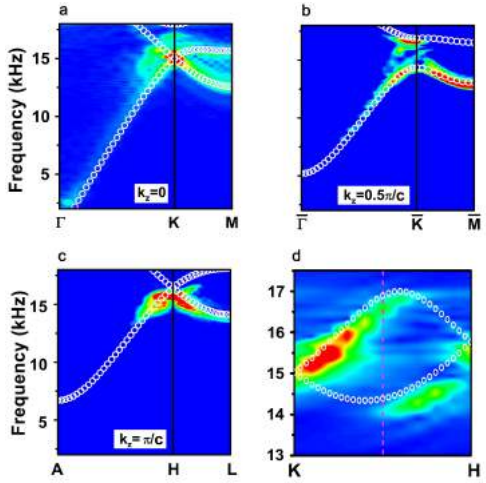


Figure 2: Bulk bands of the two lowest modes.

By Fourier transforming the measured fields, we can arrive at the dispersion surface of the surface states or the Fermi arcs at the working frequency. Figure 3 left shows the Fermi arcs of the surface states on the XZ surface and projections of the bulk Weyl points H (H') and K (K') in the 2D momentum space of the XZ surface. The color map shows the experimental results, and the white solid lines represent the calculated values. For comparison, we also show the calculated Fermi arcs of the surface states on the opposite XZ surface as white dashed lines. Vertical black lines mark the boundaries of the first BZ of the XZ surface. Clearly, the Fermi arc starts from the projection of K. However, it does not end at the projection of H but somewhere on the equi-frequency surface (purple curves) of the working frequency around the projection of H because the Weyl points H and K have different frequencies, and at the working frequency, i.e., the frequency of point K, a spherical equi-frequency surface surrounds the H point. Similarly, we show the measured and calculated Fermi arcs for the edge states on YZ surfaces in Fig. 3 right. However, in this case, the projection of K coincides with that of K', and the projection of H coincides with that of H'.

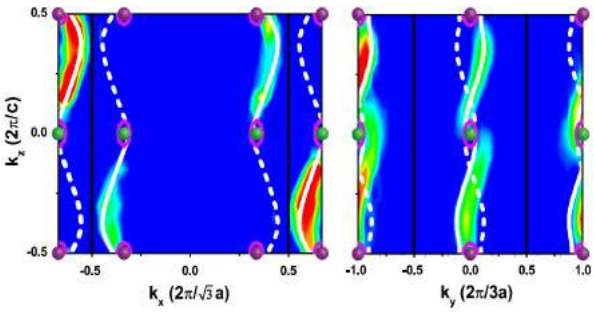


Figure 3: The dispersions of surface waves.

3. Conclusions

The Weyl points for acoustic waves observed in our experiment open the door to 3D topological acoustics, in addition to the 2D topological acoustics, recently implemented in acoustic topological insulators and valley acoustics. Near the Weyl-point frequency, Weyl phononic crystals provide directional selectivity for filtering sound incident from any direction and enable the pseudo-diffusive transport of sound. The unique Berry curvature field associated with the Weyl points can lead to the weak localization of sound against disorder in Weyl acoustic materials. The topological surfaces may lead to potential applications of Weyl PCs in innovative acoustic devices.

Acknowledgements

This work is supported by the National Basic Research Program of China (Grant No. 2015CB755500), the National Natural Science Foundation of China (Grant Nos. 61271139, 11572318, 11604102, and 11374233).

References

[1] Soluyanov, A. A. et al. Type-II Weyl semimetals. *Nature* 527, 495–498 (2015).

[2] Xu, S.-Y. et al. Discovery of a Weyl fermion semimetal and topological Fermi arcs. *Science* 349, 613-617 (2015).

[3] Wan, X., Turner, A. M., Vishwanath, A. & Savrasov, S. Y. Topological semimetal and Fermi-arc surface states in the electronic structure of pyrochlore iridates. *Phys. Rev. B* 83, 205101 (2011).

[4] Xiao, M. et al. Synthetic gauge flux and Weyl points in acoustic systems. *Nature Phys.* 11, 920-924 (2015).

[5] Li, F. et al. Weyl points and Fermi arcs in a chiral phononic crystal. *Nature Phys.* 14, 30-34 (2018).

Valley States and Valley Edge States in Phononic Crystals

Jiuyang Lu[1]*, Chunyin Qiu[2], Zhengyou Liu[1,2],

[1] Department of Physics, South China University of Technology, Guangzhou, Guangdong, China.
[2] Key Laboratory of Artificial Micro- and Nanostructures of Ministry of Education and School of Physics and Technology, Wuhan University, Wuhan, Hubei, China
*corresponding author, E-mail: phjylu@scut.edu.cn

Abstract

The valley pseudospin is now serving as a new approach to manipulate sonic and elastic waves in artificially designed phononic crystals (PCs). Here we review the valley states with intrinsic vortex features in PC. Topological index nominated as valley Chern number can be introduced to describe the valley material and distinguish the PCs into different valley Hall phases (VHPs). The valley edge states are expected on the domain walls between PCs with distinct VHPs.

1. Introduction

The striking conduction of topological electronic material has stimulated a pursuit of topologically protected acoustic wave that is immune to imperfections and disorders. Such a robust acoustic transport can be used in improved ultrasonic devices, communications, and information-processing systems. Recently, airborne acoustic topological insulators was realized as an analogy to the quantum spin Hall effect. Besides spin, the valley pseudospin provide an additional degree of freedom for sound manipulation.

2. Results

Here we review the discovery of acoustic valley states in PCs and the observation of the valley edge states in the domain walls [1, 2]. The concept of valley pseudospin, originating from the electron behavior in atomic crystals, labels electron quantum states of energy extremes in momentum space, which is attracting attention for its potential as a new type of information carrier. Inspired by the recent valley related phenomenon in election systems, the acoustic version of valley states in PCs is studied.

2.1. The valley vortex states

The valley states are usually constructed in hexagonal lattice by destroying Dirac cones locating at the first Brillouin zone corners. The Dirac cones in two dimensions are protected the C_{3v} symmetry of the corner points. The valley states can be obtained by breaking the mirror symmetry, i.e. reducing the symmetry to C_3. A practical realization of valley states in PC is shown in Fig. 1. The PC consists of a hexagonal array of regular triangular steel rods immersed in water. With uniform nonzero rotation angle of scatterer, the crystal presents a pair of valley states K or K' points, which are separated by an omnidirectional band gap. The most significant feature of the acoustic valley states is the vortex distribution in the high symmetry point shown in Fig 1(b).

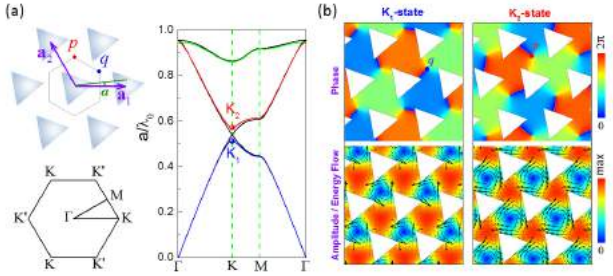


Figure 1: (a) PCs possessing valley states by breaking mirror symmetry of the K point. (b) The vortex feature of the valley states.

In contrast with atomic crystals, the purely polarized acoustic valley states can be directly excited by external sound incidence and detected directly from the field distributions inside and outside the PCs [1, 3]. As shown in Fig. 2, the pressure is generated by a Gaussian beam incident onto a finite PC obliquely, where the inset enlarges a vortex inside the SC. The right panel displays the corresponding Fourier spectra in momentum space, where only the K valley state is excited. The excitation of acoustic valley states enables us to produce a compact array of acoustic vortices with a controllable chirality [1]. In addition to the usual momentum matching mechanism, an azimuthal rule for selectively exciting valley states is established based on the rotational symmetry of a crystal.

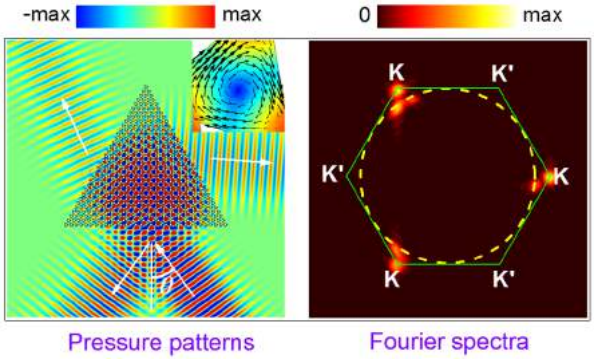


Figure 2: Selection exictation of the valley state. Acoustic pressure distribution and its Fourier spectra.

The valley-momentum lock wave behavior is further proposed in this system [1,3]. In Fig. 3, the acoustic beams carrying opposite chirality split and transforms along opposite direction. In addition, considering the interaction with matter, the vortex array can be used to pattern and rotate micro-particles without contact [1], which may lead to new applications.

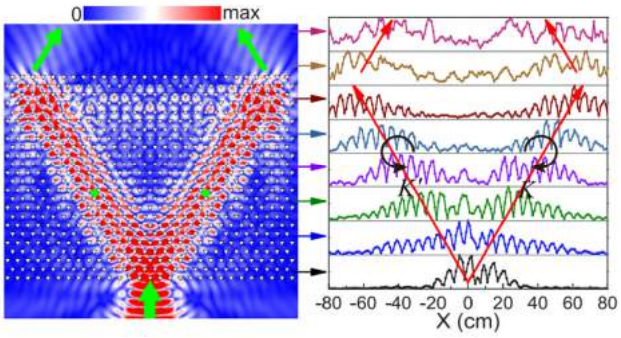


Figure 3: A demonstration of the valley-momentum lock wave behavior. The sonic crystals is stimultated by a narrow Gaussian beam incident normally from the bottom.

2.2. The valley projected edge states

We observe the valley projected edge transport of sound in PCs [2]. The PCs belong to distinct VHPs by opposite rotation of the regular triangular rods. The VHP transition happens when the omnidirectional band gap closes and reopen shown in Fig. 4(a). A rotation angle dependent continuum Hamiltonian is adopted to describe the phase transition and to predict the valley projected edge transport. The acoustic valley transport is confined in the domain walls of PCs with the dispersions depicted as green lines in Fig 4(b).

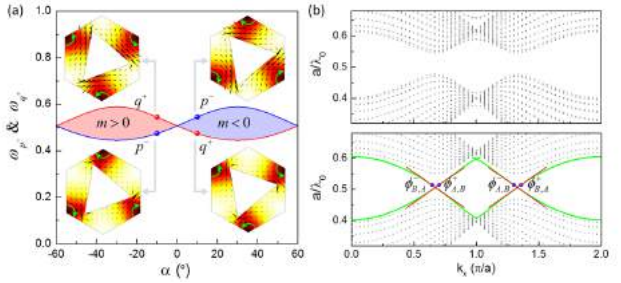


Figure 4: (a) Phase diagram revealed by the order of band-edge frequencies locked with specific vortex features (insets). (b) Comparative dispersions for the PC interfaces separating two topologically identical and separating two topologically distinct AVH insulating phases.

Because of the inter-valley decoupling, the fascinating transport phenomena, such as the angularly selective excitation by external sound and negligible backscattering to the interface corners, are observed and discussed. Demonstrated in Fig. 5, both systems show nearly perfect sound transmissions through the multi-corners, associated with the power reflection less than 0.1% overall in the bulk gap frequency. The acoustic valley transport of sound, strikingly different from that in traditional sound waveguides, may serve as the basis for designing devices with unconventional functions.

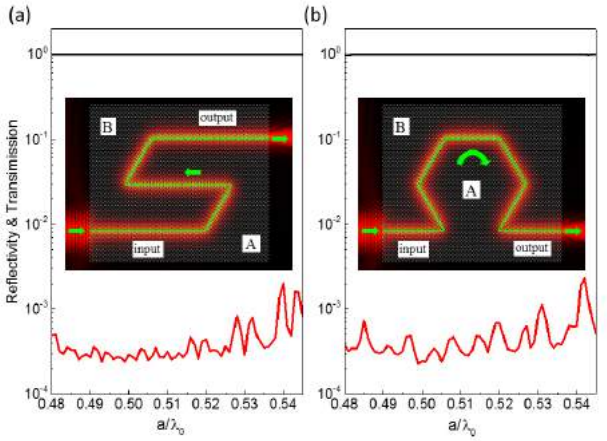


Figure 5: Reflection immunity from the multi-corners of the PC interfaces. (a) S-type and (b) Ω-type interfaces.

3. Conclusions

We have introduced the concept of valleytronics to PCs, and revealed the vortex nature of valley states. Interestingly, the acoustic valley states can be stimulated directly by external sound, and detected through the field distributions inside and outside the crystal. The vortex chirality-locked valley transport enables a novel manipulation of sound. In addition, we find that there exist two kinds of topologically distinct acoustic valley Hall phases, and an interface separating them can host topologically-protected edge states, associated with many exotic transport properties such as antireflection in bent corners.

Acknowledgements

This work is supported by the National Postdoctoral Program for Innovative Talents (Grant No. BX201600054); China Postdoctoral Science Foundation (Grant Nos. 2017M610518); Fundamental Research Funds for the Central Universities (Grant Nos. 2017BQ039).

References

[1] J. Lu, C. Qiu, M. Ke, and Z. Liu, *Valley vortex states in sonic crystals*, Phys. Rev. Lett. 116(9), 093901 (2016).

[2] J. Lu, C. Qiu, L. Ye, X. Fan, M. Ke, F. Zhang and Z. Liu, *Observation of topological valley transport of sound in sonic crystals*, Nat. Phys. 13(4) (2017).

[3] L. Ye, C. Qiu, J. Lu, X. Wen, Y. Shen, M. Ke, Fan, Z, and Z. Liu, *Observation of acoustic valley vortex states and valley-chirality locked beam splitting*, Phys. Rev. B 95(17) (2017).

[4] J. Lu, C. Qiu, S. Xu, Y. Ye, M. Ke, and Z. Liu, *Dirac cones in two-dimensional artificial crystals for classical waves*, Phys. Rev. B, 89(13), 134302 (2014).

Soft Metasurface with Gradient Acoustic Index

Yabin Jin[1,*], Raj Kumar[2], Olivier Poncelet[1], Olivier Mondain-Monval[2], Thomas Brunet[1]

[1]Université de Bordeaux - CNRS - Bordeaux INP, I2M, Talence, France
[2] Université de Bordeaux - CNRS, CRPP, Pessac, France
*corresponding authors, E-mail: yabin.jin@u-bordeaux.fr

Abstract

In this talk, we will report a new class of gradient index (GRIN) acoustic metasurface with a wide range of refractive index range for water-bone waves focusing, with subwavelength thickness. The GRIN metasurface is fabricated via an emulsion templating method, locally controlling the random distribution of air cavities (only several micrometres in size) along 2mm-thickness metasurface, so that it realizes gradient index profile as design. We experimentally and numerically study a rectangular and a circular metasurfaces for 2D and 3D focusing, respectively, with excellent quantitative agreements. Our GRIN metasurfaces permit portable, low-cost and efficient applications.

Introduction

The generation of acoustic focusing is demanded in diverse fields such as imaging, detection and matter control, boosting both fundamental multidiscipline study and industry/defense applications. In the past two decades, the emergences of phononic crystals, acoustic metamaterials and acoustic metasurface boost the development of acoustic focusing from the properties of intrinsic structure rather than the shape of aperture with the following ways: i) negative refractive index of phononic crystals [1] and acoustic metamaterials [2]. Waves from a point source locating at one side of such negative refractive lens will be focused at the other side of lens. ii) gradient index(GRIN) phononic crystals [3]. The local varied refractive indices in a lens will allow wave propagation following specific trajectories as design, resulting in focusing effect; iii) subwavelength acoustic metasurface [4,5] with coiling space to locally control the reflected/transmitted wave phase, which is designed to meet the generalized Snell's law for wavefront steering, such as focusing effect. However, the first two ways normally needs the total thickness of a lens much larger than the working wavelength; the third way only works for single frequency sonic wave in air.

Result

We use emulsion-templating method [6] to fabricate air-filled porous silicone rubber. The sound speed can decrease two-order-of-magnitude [7] with the increasing porosity, from km/s to tens of m/s, resulting in varying the relative acoustic refractive index within a large range. Then we fabricated a rectangular and a circular GRIN metasurface with 2mm-thickness for 2D and 3D focusing, respectively, by locally controlling the porosity [8]. The acoustic fields are experimentally measured by directly attaching the metasurface to the surface of piezoelectric ultrasonic transducers (rectangular surface for 2D focusing sample and circular surface for 3D focusing sample) in the water tank. Excellent agreements are found between the experiment and the simulation for the pressure distributions along the propagating direction and its vertical direction crossing the focusing spot. The proposed metasurface bonds the capabilities of the conventional space-coiling metasurface and gradient index phononic crystals to realize a compact focusing spot for acoustic wave in liquid with subwavelength in entire sample's thickness. It also shows dramatically impact in diverse applications in imaging, non-destructive detecting, micro-particles controlling, et al.

Acknowledgements

This work was funded and performed within the framework of the Labex AMADEUS ANR-10-LABEX-0042-AMADEUS with the help of the French state Initiative d'Excellence IdEx ANR-10-IDEX-003-02. This work was also supported by Agence Nationale pour la Recherche, and the Cluster Aerospace Valley (Grant ANR-15-CE08-0024 BRENNUS).

References

[1] S. Yang, *et al.* Focusing of sound in a 3D phononic crystal. *Physical Review Letters* 93, 024301, 2004.

[2] S. Zhang, L. Yin, & N. Fang. Focusing ultrasound with an acoustic metamaterial network. *Physical Review Letters* 102, 194301, 2009.

[3] A. Climent, D. Torrent, J. Sanchez-Dehesa. Sound focusing by gradient index sonic lenses. *Applied Physics Letters* 97, 104203, 2010.

[4] Y. Li, *et al*. Experimental realization of full control of reflected waves with subwavelength acoustic metasurfaces. *Physical Review Applied* 2, 064002, 2014.

[5] G. Memoli, *et al*. Metamaterial bricks and quantization of meta-surfaces. *Nature Communication* 8, 14608, 2017.

[6] A. Kovalenko, *et al*. Tuning the sound speed in macroporous polymers with a hard or soft matrix. *Soft Matter* 13, 4526-4532, 2017.

[7] A. Ba, *et al*. Soft porous silicone rubbers with ultra-low sound speeds in acoustic metamaterials. *Scientific Reports* 7, 40106, 2017.

[8] Y. Jin, R. Kumar, O. Poncelet, O. Mondain-Monval, and T. Brunet, *to be submitted*.

Current Advances in Frequency Selective Surfaces and Metasurfaces

Learning from Nature: Bio-inspired Metasurface Microwave Absorber

Shubo Wang[1*], C. T. Chan[2]

[1]Department of Physics, City University of Hong Kong, Hong Kong, China
[2]Department of Physics, The Hong Kong University of Science and Technology, Hong Kong, China
*corresponding author, E-mail: shubwang@cityu.edu.hk

Abstract

Recent advances in metasurfaces have given rise to the designs of electromagnetic wave absorber with unprecedented performance. We show that a bio-inspired design of metasurface composed of logarithmic spiral resonators can achieve >95% absorption of incident microwave within the frequency range of 7.7 GHz – 37 GHz. The near-perfect absorption, subwavelength and broadband properties are attributed to the impedance matching of the magnetic resonance modes, space coiling, and the self-similarity of the logarithmic structure.

A metasurface is a thin-layer metamaterial composed of subwavelength elements that are periodically patterned on a substrate. The development of metasurfaces has given rise to novel devices and applications such as ultrathin invisibility cloak [1] and flat lenses [2]. Recently, electromagnetic wave absorbers based on metasurfaces attract considerable attention [3-5]. Such absorbers have the advantages of being geometrically thin and capable of achieving high absorption. However, due to the intrinsic resonance nature of the subwavelength elements, metasurface absorbers normally suffer from narrow band problem. A remedy is to employ multipole resonances arising from structures of different dimensions, such as the pyramid structure in Refs. [3-4]. From a different perspective and by learning from nature, we designed a thin metasurface which can achieve broadband near-perfect absorption. We show that the superior performance of the metasurface arises from a combination of several interesting physical mechanisms including impedance-matched resonance modes, space coiling, and self-similarity.

We consider a logarithmic spiral unit shown by the inset of Fig. 1. The spiral is made of copper and filled with absorptive dielectric material. Such a structure can be viewed as transformed from a parallel plate waveguide through space coiling. Under TM polarization, the spiral supports multipole magnetic resonances, and the corresponding modes' impedance matches with vacuum impedance well. We found that, at the resonance frequencies, the absorption cross section of the spiral resonator can easily beat the theoretical upper bound of single channel resonance, as shown in Fig. 1 for different absorption δ. Due to the self-similarity of the spiral shape, such a large absorption cross section exists in a wide range of frequencies.

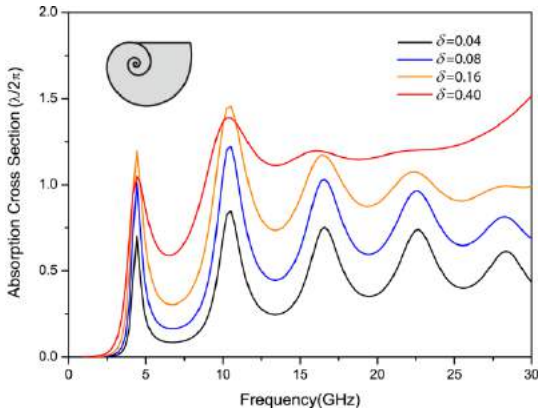


Figure 1: Absorption cross section of the logarithmic-spiral resonator, i.e., metasurface building block, as a function of frequency for different loss δ.

By arranging the spiral resonators into a one-dimensional periodic structure on a metallic surface, we arrive at a design of metasurface which can almost perfectly (>95%) absorb the normally incident microwave within the frequency range of 7.7 GHz – 37 GHz [6]. The high absorption is attributed to the large absorption cross section of individual spirals. The thickness of the metasurface is about 1/8 of the maximum wavelength with >95% absorption. We also calculated the absorption spectrum of the metasurface with different incident angles, and found that near-perfect absorption can be achieved for incident angle within -30 to 30 degrees [6].

The design can also be extended to three dimensions to achieve broadband absorption for both TE and TM polarizations. To this end, we arranged two spiral resonators in one unit cell, and their axes are perpendicular to each other. Our numerical results (data not shown) show that such a metasurface can absorb over 90% energy of incident microwave. The performance of the metasurface for oblique incidence is similar to that of the two-dimensional case.

In summary, we presented a design of metasurface formed of logarithmic spiral resonators. The self-similarity of the spiral leads to broadband performance of the metasurface. The high absorption is enabled by the magnetic resonance modes whose impedance match that of vacuum. The subwavelength feature of the metasurface is attributed to the space-coiling structure of the spiral. Similar absorption performance is achieve for both two-dimensional and three-dimensional systems.

Acknowledgements

This work was supported by AoE/P-02/12 and a grant from City University of Hong Kong (Project No. 9610388). We thank Prof. Z. Q. Zhang for valuable comments and suggestions.

References

[1] X. Ni, Z. J. Wong, M. Mrejen, Y. Wang, & X. Zhang, An ultrathin invisibility skin cloak for visible light. *Science*, 349: 1310-1314, 2015.

[2] N. Yu & F. Capasso, Flat optics with designer metasurfaces. *Nat*. *Mater*., 13: 139-150, 2014.

[3] Y. Cui, K. H. Fung, J. Xu, H. Ma, Y. Jin, S. He, & N. X. Fang, Ultrabroadband light absorption by a sawtooth anisotropic metamaterial slab. *Nano Lett*., 12: 1443-1447, 2012.

[4] F. Ding, Y. Cui, X. Ge, Y. Jin, & S. He, Ultra-broadband microwave metamaterial absorber. *Appl*. *Phys*. *Lett*., 100: 103506, 2012.

[5] Y. Ra'Di, C. R. Simovski, & S. A. Tretyakov, Thin perfect absorbers for electromagnetic waves: theory, design, and realizations. *Phys*. *Rev*. *Applied*, 3: 037001, 2015.

[6] S. Wang and C. T. Chan, Logarithmic spiral metasurface as a broadband microwave absorber, *under preparation*.

Plasmonic components towards photonic-nose

Yoshiaki Nishijima[1], Armandas Balčytis[2,3], Gediminas Seniutinas[2,4], Saulius Juodkazis[2]

[1]Department of Physics, Electrical and Computer Engineering, Graduate School of Engineering, Yokohama National University, 79-5 Tokiwadai, Hodogaya-ku, Yokohama 240-8501, Japan
[2]Centre for Micro-Photonics, Faculty of Science, Engineering and Technology, Swinburne University of Technology, Hawthorn, Vic 3122, Australia
[3]Center for Physical Sciences and Technology, A. Goštauto 9, LT-01108 Vilnius, Lithuania
[4]Current adress, Paul Scherrer Institute, Villigen CH-5232, Switzerland
*corresponding author, E-mail: nishijima-yoshiaki-sp@ynu.ac.jp

Abstract

We demonstrate the frequency selective plasmonic metamaterials in mid infrared (MIR) wavelengths range. Such components can be applied for a plasmonic smell sensor (photonic nose) applicaiton, which detects a small amount of specific molecules in air. Plasmonic materials can be used not only for signal enhancement by surface enhanced infrared absorption, but also for thermal radiation light sources and photo detectors. We also discuss the possibility of on-chip integration.

1. Introduction

Detection of small amount of molecules in air is a technology required for advancment towards a safer and more secure society. It is of paramounf importance to develop a capability to detect explosive or/and hazardous materials, illegal drugs and substances at harbors, stations and airports. Detecting people burried under rubble of collapsed buildings in zones of natural disasters. Also, a daily monitoring of health by, e.g, analyzing breath is evolving to become a wide spread technology in the future health care system. The concept of electronic nose (E-nose) is expected to be soon realized with a functionality of the natural dog's nose senstivity [1, 2]. Requirements for sensitivity is increasingly high. Sensors should provide a high selectivity, at low consumption of energy, low production/maintainance costs, be portable or wearable devices, a long lifetime and accessible via a smart phone to connect the internet world as shown schematically in Fig. 1.

Typical E-nose consist of semiconductor nanoparticles and their surface reactivity or electrical conductivity change due to presence of target molecules. These devices are highly sensitive, low cost, and can be wearable. However, they still have problems with stability and selectivity.

We are aim to realize an E-nose by a MIR nanophotonics approach using frequency selective plasmonic metamaterials (photonic-nose). MIR photonic-nose makes it possible to analyze data qualitatively and quantitatively due to the molecular fingerprinting character at MIR wavelengths. A high sensitivity down to part per billion (ppb) level is accessible. Photonic system required light source, sample chamber, detector and electric circuitry, i.e., it is a relatively more complex system than a typical e-nose. Plasmonic materials can help with sensitivity and be used for realisation of optical components with a strong electro-magnetic field enhancement. Here we demonstrate the plasmonic materials for the photonic-nose applications.

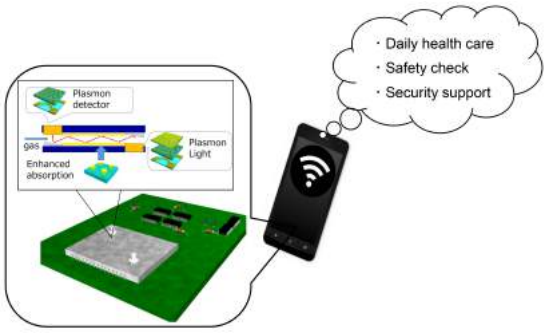


Figure 1: Concept of the photonic nose by plasmonic components integrated on a small chip. This chip communicates via a smartphone to the internet.

2. Experiments

Since the sub-micrometer to micrometer size is required, MIR plasmonic materials can be fabricated by the conventional photolithography techniques, which are well established and common use even far beyond a dedicated semiconductor technology [3, 4]. Around 10 μm wavelength, we used contact photo-lithography while for 3-4 μm wavelengths a stepper was deployed. This size reduction projection lithography technique is useful to fabricate resist pattern with further size reduction by a factor of four [5]. Non-doped, both side polished silicon was used for substrate of plasmonic materials. All optical characterization has been carried out with a Fourier transform infrared (FT-IR) spectroscopy system.

3. Results and discussions

3.1. Transmission plasmonic materials

A metal hole array frequency selective surface is one of the transmission type of plasmonic materials, which can be used for the optical windows and enhancement of absorption via the surface enhanced IR absorption (SEIRA). Wavelength selection for detection of particular molecular fingetrinting region can be done using narrow or broad band pass filters from thermal light source. We have demonstrated selective signal enhancement at the transmission peak of the plasmon resonance [3]. When multiple plasmonic materials, e.g., metal hole arrays (MHA), are used on the path from light to detector, it is possible to further enhance signal to noise ratio. We have constructed and carried out proof-of-the-concept experiments for gas sensing with MHA window [4]. Compared to a single MHA window, two substrates with MHAs can increase sensitivity down to single to sub-ppm levels of a gas concentration. When the internal wall of gas cell was covered by the scattering plasmonic materials (rough surface of gold films), a further signal enhancement was obtained [4, 5].

3.2. Absorption control by plasmonic materials

Absorption by designed plasmonic materials - a plasmonic perfect absorber (PPA) - can be used for both, for the light source and detector due to reciprocity defined by the Kirchhoff's law of thermal radiation at the spectral region of interest at MIR[7, 8]. We have fabricated different PPAs with different metal and insulator combinations to tailor their optical properties. By heating the PPAs around 300°C, an effective radiation at plasmon wavelengths was obtained. By shining the MIR light onto the PPA, we have realized more than 50% absorption with only a 10 nm thin insulator layer. Due to stability to the oxidation at the used comparatively low temperature, we measured the thermal radiation with Au based PPAs. The obtained emissivity have a good correlation with absorbance of the structures. Using same structures, we have measured the MIR absorption and thermal generation effect using the Seebeck devices. When absorption was strong, generation of the thermal radiation was observed. Therefore, PPAs can be used for both: a light source and a photo detector at MIR wavelength.

4. Conclusion

We have succesfully performed an initial stage experiments with designed and fabricated plasmonic components. This leads towards realisation of the photonic-nose. Optimisation of the structures for stronger IR absorption is required. The efficiency of thermal radiation and photo-thermal generation requires optimisation together with development of a low-price simplification of the entire fabrication process. Integrating plasmonic components onto a micro-chip using CMOS-MEMS technology, it shold be possible to realize the photonic nose.

Acknowledgement

Authors are grateful for Tokyo Ohka Kogyo Co. Ltd for their support of reduction exposure lithography to produce resist pattern for PPA structures.

References

[1] A. T. Güntner, V. Koren, K. Chikkadi, M. Righettoni, and S. E. Pratsinis, E-Nose sensing of low-ppb formaldehyde in gas mixtures at high relative humidity for breath screening of lung cancer, *ACS Sens.*, 1, 528-535 (2016).

[2] S. Maruyama, T. Hizawa, K. Takahashi, and K. Sawada, Optical-Interferometry-Based CMOS-MEMS Sensor Transduced by Stress-Induced Nanomechanical Deflection, *Sensors* 18: 138 (2018).

[3] Y. Nishijima, H. Nigorinuma, L. Rosa, and S. Juodkazis, Selective enhancement of infrared absorption with metal hole allays, *Opt. Mat. Express* 2: 1367–1377, (2012).

[4] Y. Nishijima, Y. Adachi, L. Rosa, and S. Juodkazis, Augmented sensitivity of an IR-absorption gas sensor employing a metal hole array, *Opt. Mat. Express* 3: 968–976, 2013.

[5] Y. Nishijima, A. Balčytis, G. Seniutinas, S. Juodkazis, T. Arakawa, S. Okazaki, and R. Petruskevicius Plasmonic hydrogen sensor at infrared wavelength, *Sens. Mater.* 29: 1269–1274 2017.

[6] Y. Nishijima, S. Suda, G. Seniutinas, A. Balčytis, and S. Juodkazis Plasmonic sensor: towards parts-per-billion level sensitivity, *Sens. Mater.* 29: 1253–1258, 2017.

[7] H. T. Miyazaki, T. Kasaya, M. Iwanaga, B. Choi, Y. Sugimoto, K. Sakoda, Dual-band infrared metasurface thermal emitter for CO_2 sensing. *Appl. Phys. Lett.* 105: 121107-1, 2014.

[8] K. Ikeda, H. T. Miyazaki, T. Kasaya, K. Yamamoto, Y. Inoue, K. Fujimura, T. Kanakugi, M. Okada, K. Hatade, S. Kitagawa, Controlled thermal emission of polarized infrared waves from arrayed plasmon nanocavities. *Appl. Phys. Lett.* 92: 021117-1, 2008.

Optical Metasurfaces for Simultaneous Control of Holograms and Twisted Light Beams

Xianzhong Chen*, Chunmei Zhang, Wei Wang

School of Engineering and Physical Sciences, Heriot-Watt University, Edinburgh, UK
*corresponding author, E-mail: x.chen@hw.ac.uk

Abstract

An optical device with multiple functionalities is desirable for device miniaturization and system integration. We experimentally demonstrate an optical device that can simultaneously realize polarization-controllable hologram and superposition of orbital angular momentum (OAM) in multiple channels. By continuously controlling the polarization state of the incident light, the polarization-dependent holographic images in two channels along the horizontal direction and the continuous control of OAM superposition in two channels along the vertical direction are realized.

1. Introduction

To meet the growing requirement of system integration, it is of great importance and interest to develop ultrathin optical devices that integrate multiple functionalities into one device while preserving their independent functionalities. Optical metasurfaces, or planar metamaterials with subwavelength thickness, have aroused considerable interest due to their capability of arbitrary control of light propagation. Unlike spin angular momentum (SAM), a twisted light beam with an OAM has a helical phase structure, which has attracted much attention due to its promising applications in particle trapping, optical communication, quantum science and metrology. Recently, an efficient approach to generate multiple OAM light beams and arbitrarily control their superpositions was experimentally demonstrated [1]. The advance in polarization-sensitive metasurface holograms [2] and polarization-controllable OAM superposition provides a new approach to realize a multi-channel device with tunable functionalities.

2. Results

Figure 1 shows the schematic of experimental setup and expected results based on the designed metasurface device that can simultaneously control the holographic images and the OAM superposition [3]. The arbitrary control of the superpositions of various light beams with OAM and polarization-controllable holograms can be realized in two vertical channels and two horizontal channels, respectively. Two separate holographic images and two OAM light beams with a topological charge 1 (or -1) are predicted when a metasurface device is illuminated with an input light beam with pure circular polarization, i.e., right circular polarization (RCP) or left circular polarization (LCP).

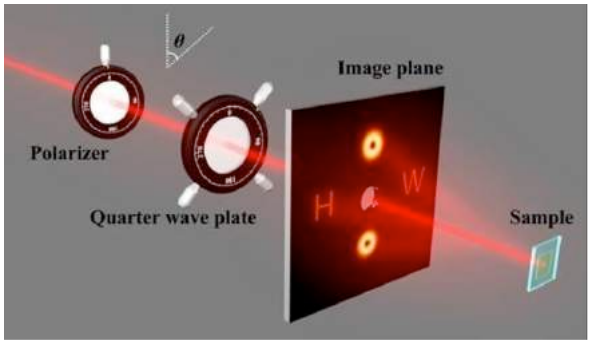


Figure 1 Schematic illustration of simultaneous control of hologram and superposition of orbital angular momentum (OAM).

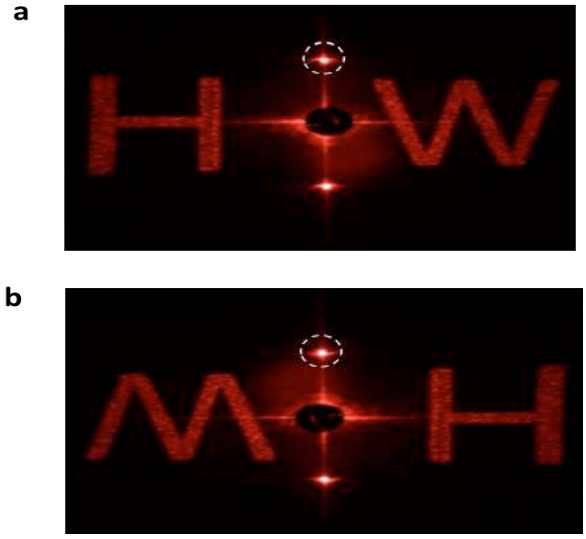


Figure 2 Experimentally obtained images for the incident light with (a) LCP and (b) RCP.

In order to reconstruct two symmetrically distributed off-axis holographic images along the horizontal direction, Gerchberg−Saxton algorithm is adopted to generate the required phase profile. The combination of two OAM beams with opposite topological charges ±1 and with equal power can generate a radially polarized vector beam, which is characterized by passing through a rotating polarizer. To

realize the tunable multi-channel optical device with different functionalities, two metasurfaces (one for two holographic images along the horizontal direction and one for two OAM beams along vertical direction) are designed to operate with opposite incident helicities and merged together with a displacement vector of (d/2, d/2). Where d is the distance between neighboring nanorods with a value of 424 nm along both x and y directions.

To experimentally verify the proposed device, we fabricate the design reflective-type metasurface consisting of nanorods with spatially varying orientation. Upon the illumination of pure LCP light, two separate holographic images of 'H' pattern on the left and the 'W' pattern on the right of the screen along the horizontal direction are clearly observed when viewed from the sample, while the two 'donut'-shaped OAM patterns are symmetrically located along the y direction, as shown in Figure 1. The incident light impinges normally onto the metasurface and the reconstructed images are projected onto the image plane. Figure 2 shows the measured experimental results upon the illumination of incident light with LCP and RCP. When the linearly polarized (LP) light is incident onto the metasurface, the resultant output beam is a radially polarized vector beam. Figure 3 shows the schematic of radially polarized light beam and the experimental result after the beam passes through a linear polarizer.

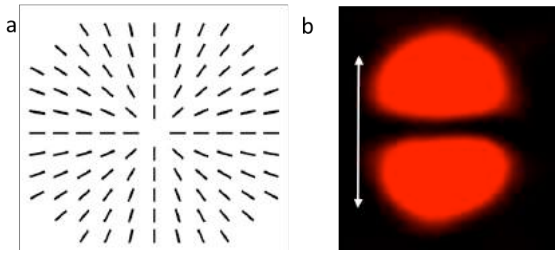


Figure 3 (a) Schematic of radially polarized light beam and (b) experimental result after passing through a polarizer

3. Discussion

The uniqueness of our design lies in the design combination of multiple functionalities and multiple channels to experimentally realize the polarization-controlled OAM superposition and hologram on a single metasurface device. The alliance between functionality and channel can dramatically increase the density of functionality and shrink the size of the device, which can push the limit of device miniaturization and system integration. The developed device here provides a unique method to integrate different tunable functionalities into a single nanodevice. This approach possesses several practical and technical advantages over conventional methods. Without the metasurface device designed here, to realize the simultaneous control of hologram and superposition of OAM states of different topological charge, one must rely on a complicated experimental setup consisting of beam-splitters, prisms, mirrors etc. Here, only a single device can easily complete the complicated task, which avoids the technical hassles (e.g., misalignment) caused by the conventional optical systems.

4. Conclusions

In summary, we experimentally demonstrate a metasurface device that can realize polarization-dependent hologram and continuously control the superposition of orbital angular momentum in multiple channels. By controlling the polarization state of incident light, different superpositions of OAM states and holographic images are realized. Good agreement between the simulated and experimental measured results is found. The developed device provides a new tool to modify the polarization and phase simultaneously. The alliance between multiple functionalities and multiple channels dramatically increases the density of functionalities, which can further push the limit of device miniaturization and system integration.

Acknowledgements

This work is supported by the Engineering and Physical Sciences Research Council of the United Kingdom (Grant Ref: EP/M003175/1).

References

[1] D. Wen, F. Yue, G. Li, G. Zheng, K. Chan, S. Chen, M. Chen, K. F. Li, P. W. Wong, K. W. Cheah, E. Yue Bun Pun, S. Zhang, X. Chen, Helicity multiplexed broadband metasurface holograms. *Nat. Commun.* **6**, 8241, 2015.

[2] F. Yue, D. Wen, C. Zhang, B. D. Gerardot, W. Wang, S. Zhang, X. Chen, Multichannel polarization-controllable superpositions of orbital angular momentum states, *Adv. Mater.*, 29, 1603838, 2017.

[3] F. Yue, C. Zhang, X. Zang, D. Wen, B. D. Gerardot, S. Zhang, X. Chen, High-resolution grayscale image hidden in a laser beam, *Light: Sci. Appl.*, 7, 17129, 2018.

Surface Acoustic Wave Manipulation by a Phononic Crystal Made of Multilayered Ridges or Pillars

M. Oudich[1], Y. Jin[2], E.H. El Boudouti[3], B. Bonello[4], Y. Pennec[5], F. Sarry[1] and B. Djafari Rouhani[5]

[1]Institut Jean Lamour, Université de Lorraine, UMR 7198, 54506 Vandoeuvre-lès-Nancy, France
[2]Institut de Mécanique et d'Ingénierie (I2M-APY), CNRS UMR 5295, Université de Bordeaux, 33405 Talence, France
[3]LPMR, Département de Physique, Faculté des Sciences, Oujda, Morocco
[4]Sorbonne Universités, UPMC Université Paris 06, INSP UMR CNRS 7588, 4 Place Jussieu, 75005 Paris, France
[5]IEMN, UMR CNRS 8520, University of Lille, 59652 Villeneuve d'Ascq, France
*corresponding author, E-mail: bahram.djafari-rouhani@univ-lille1.fr

Abstract

After reviewing our recent works on band structure and possibility of very confined modes in pillared phononic crystals, we focus on pillars made of periodic multilayered materials. Each pillar behaves itself like of a 1D phononic crystal exhibiting band gaps where very localized modes can be found either at the upper or lower edge, or inside a cavity. We study the scattering of Rayleigh waves by such modes and evidence very narrow Fano and Acoustic Induced Transparency resonances.

Phononic crystals made of pillars on a membrane or on a substrate know a growing interest due to their possibility of exhibiting both Bragg and hybridization gaps and a variety of local resonances. In some recent works, we have studied the resonances of the pillars as a function of their shapes and constituting materials. In particular we have shown the possibility of very confined modes by considering hollow pillars that can exhibit whispering gallery modes (WGM) inside the band gap of the phononic crystal without the hollows [1]. Such modes can exist both in the Bragg and in the low frequency gaps. They open new perspectives for functionalities such as filtering and multiplexing by the introduction of waveguides and cavities in the phononic crystal. We have further proposed a new type of phononic crystal plate consisting of hollow pillars on a bar-connected plate, whose Bragg band gap can be tuned to be much wider and extended to sub-wavelength region whereas the low frequency gap can be moved to extreme low frequency range. Such a structure can generate quadrupolar, hexapolar and octopolar WGMs inside the band gaps with very high confinement [2]. Additionally, we have shown that filling the hollow parts with a fluid gives rise to new localized modes, which can be actively controlled and tuned by several parameters, such as the physical properties of liquid, liquid's height or the temperature [3].

In another set of investigations, we have studied the scattering properties of an incident Lamb wave with a single or a line of pillars deposited on a plate [4]. The pillars can exhibit both compressional (monopolar) and bending (dipolar) resonances, which are sensitive to the geometric parameters of the pillars. The amplitude and phase of the displacement fields are calculated both on top of the pillars and in the far-field. It is shown that the pillars act as acoustic sources emitting either monopolar or dipolar waves when the frequency of the exciting wave is close respectively to a compressional or to a bending resonance of the pillars. The emitted wave is out of phase with respect to the incident wave. This produces large dips in the transmission spectrum of the line of pillars when the bending and compressional resonances are separated from each other. When the geometrical parameters are chosen in such a way as to superpose the two resonances, the amplitude of the out of phase emitted wave exceeds the amplitude of the incident wave, thus allowing a new transmission channel. All the results are in agreement with experimental measurements of vertical vibrations at the top of the pillars and on the plate.

Very recently, we have focused on another type of pillar structures exhibiting very confined modes, namely pillars (or ridges in the case of 1D geometry) that are constituted by a periodic multilayer structure [5,6]. A schematic picture is given in Figure 1. Indeed, the pillar behaves itself like a one-dimensional phononic crystal exhibiting band gaps. Therefore, highly localized modes associated to the top surface of the pillar, or to a cavity inserted in the pillar or to the interface of the pillar with the substrate, can be found in such gaps. We have calculated the scattering of Rayleigh surface acoustic waves (SAW) with these modes and evidenced the possibility of both Fano and Acoustic Induced transparency resonances in the transmission spectra. For instance, we show that SAW interaction with localized modes at the top surface or in a cavity gives rise to sharp attenuation in the SAW transmission, while the modes confined at the interface cause broad band attenuations of SAW. Furthermore, we demonstrate that the coupling between the two kinds of modes within the band gap gives high SAW transmission amplitude in the form of Fano like peaks with high quality

factor. An example is illustrated in Figure 2 where the SAW scatter an array of three multilayered ridges where each ridge is constituted by a periodic repetition of Si and W layers. The broad attenuation bands A and B are associated with the modes confined in the bottom Si/W layers of the ridges. The modes T1 and T2 are associated with the flexural and compressional motions at the top surface of the ridges. Depending on the relative positions of T1 and T2 with respect to the attenuation bands A-B, the transmission of SAW exhibits Fano shape and AIT shape resonances.

The structure proposed here could provide an efficient solution for accurate SAW control for sensing and optomechanic applications for instance.

References

[1] Yabin Jin, Nicolas Fernez, Yan Pennec, Bernard Bonello, Rayisa P. Moiseyenko, Stéphanie Hémon, Yongdong Pan and Bahram Djafari-Rouhani, Tunable waveguide and cavity in a phononic crystal plate by controlling whispering-gallery modes in hollow pillars, *Phys. Rev. B* 93: 054109, 2016.

[2] Yabin Jin, Yan Pennec, Yongdong Pan, and Bahram Djafari-Rouhani, Phononic crystal plate with hollow pillars connected by thin bars, *J. Phys. D: Appl. Phys.* 50: 035301, 2017.

[3] Y. Jin, Y. Pennec Y, Y. Pan and B. Djafari-Rouhani, *Crystals* 6 **:** 64, 2016.

[4] Yabin Jin,Bernard Bonello, Rayisa P. Moiseyenko, Yan Pennec, Olga Boyko and Bahram Djafari-Rouhani, Pillar-type acoustic metasurface, *Phys. Rev. B* 96: 104311 (2017).

[5] M. Oudich, B. Djafari-Rouhani, B. Bonello, Y. Pennec and F. Sarry, Phononic crystal made of multilayered ridges on a substrate for Rayleigh waves manipulation, *Crystals* 7: 372, 2017.

[6] M. Oudich , B. Djafari-Rouhani, B. Bonello, Y. Pennec, S. Hemaidia, F. Sarry and D. Beyssen, Rayleigh waves in phononic crystal made of multilayered pillars: confined modes, Fano resonances and Acoustic Induced Transparency, Submitted to *Phys. Rev. Appl.*

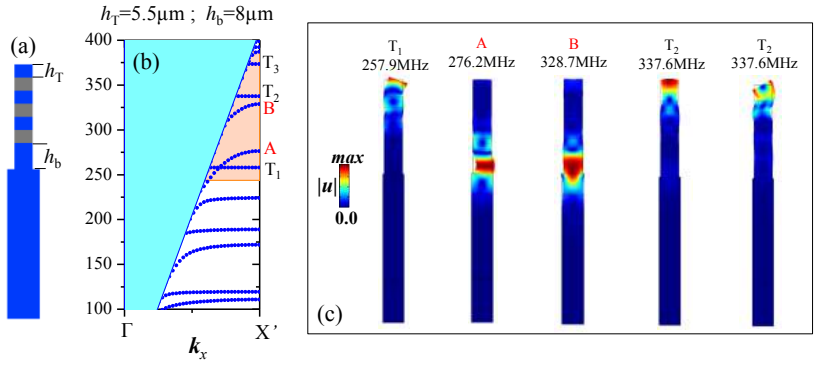


Figure 1: (a) Schematic of the Si/W multilayer ridge deposited on a Si substrate. The figure shows the unit cell of the phononic crystal (PC) with the thicknesses: bottom Si layer h_b= 8µm, top Si layer h_T = 5.5µm, normal layers h_{Si} = h_W =3.5 µm, width of the ridge D=6 µm and period of the PC a= 7 µm. (b) Band structure of the PC where we represent the dispersion curves of the surface acoustic modes below the sound line of the substrate. The orange shaded region corresponds to the band gap of the multilayer phononic ridge. (c) Total displacement field amplitude ***lul*** for the confined modes inside the band gaps.

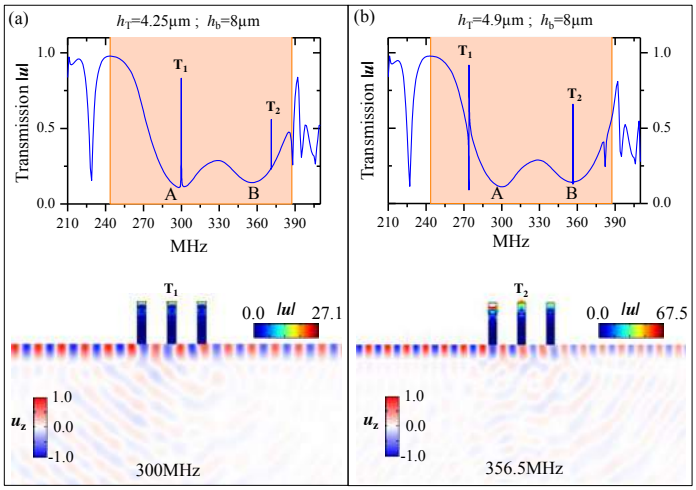


Figure 2: Upper panel: Transmission spectra of SAW for (a) h_T = 4.25µm and (b) h_T = 4.9µm. The thickness of the bottom Si layer is fixed to h_b = 8µm. Bottom panel: displacement field of (a) T_1 mode; (b) T_2 mode.

Metasurfaces: from fundamental ideas of polarization conversion, broadband Huygens' surfaces and topological photonics to applications in magnetic resonance imaging

Stanislav B. Glybovski[1], Alena V. Shchelokova[1], Irina V. Melchakova[1], Alexey P. Slobozhanyuk[1], Pavel A. Belov[1,*]

[1]Department of Nanophotonics and Metamaterials, ITMO University, St. Petersburg, Russia
*corresponding author, E-mail: belov@metalab.ifmo.ru

Abstract

Metasurfaces have become a new paradigm in the studies of artificial subwavelength structures due to their potential to overcome many challenges typically associated with metamaterials. In this contribution, recent advances in the field of microwave metasurfaces are described with the focus on novel fundamental ideas of polarization conversion, broadband Huygens' surfaces and two-dimensional topologically protected structures as well as on applications in the field of medical imaging.

1. Introduction

Metasurfaces [1] are artificial subwavelength patterned structures representing an ultrathin planar realization of the metamaterial concept [2]. An essential advantage of metasurfaces over metamaterials is their simplicity of manufacturing and ability to control reflected and transmitted waves, as well as to specifically sculpt the near-field patterns over a frequency range from radio to optical [3]. Structural elements of metasurfaces can be made from different metallic, plasmonic, or low-loss dielectric materials, while their geometrical dimensions and element separations are essentially subwavelength. In this way, homogeneous or nearly homogeneous metasurfaces reflect and transmit plane waves as infinitely thin sheets, supporting both electric and magnetic currents [3]. Here, we will review our recent results in the field of microwave metasurfaces starting from fundamental ideas and novel physics to real applications in magnetic resonance imaging (MRI).

2. Polarization conversion and broadband Huygens' surfaces

First, we study novel linear-to-circular polarizers based on a self-complementary metasurface composed of zigzag-shaped metal strips printed on a dielectric substrate, which may be used as components of circularly polarized antennas. The term self-complementary indicates that the structure is identical to its complement, except for some translation smaller than the periodicity. This property together with the nonresonant response of the unit cells ensures broadband conversion from linear polarization to circular polarization. Although we have experimentally achieved a relative 3-dB-axial-ratio (AR) bandwidth (BW) of 53%, in principle, it could reach up to 70.5%. Moreover, the studied metasurface has a very small periodicity, which avoids any higher order grating lobes and provides angular stability of the phenomenon. In fact, the relative 3-dB-AR BW obtained in experiments stays always above 40% for incidence angles within ±30°. An excellent agreement was achieved among theory, simulations, and experiments [4].

Next, a broadband Huygens' metasurface composed of paired and overlapped split-ring resonators is introduced. Excitation of degenerate eigenmodes in the coupled resonator pair allows to reach high broadband transmission for both polarizations of the incident wave introducing a phase shift between them. We show, that under certain condition the metasurfaces can operate as a linear-to-circular polarizer as a twist polarizers keeping low reflection coefficient in a broad band.

3. All-dielectric topologically protected metasurfaces

Here, we demonstrate that degeneracy between electric and magnetic modes also can be employed in construction of topologically protected metasurfaces. The structure that we study represents a dielectric metasurface formed as a triangular array of dielectric disks with their dimensions tuned such that the array supports two doubly degenerate Dirac cones at K and K' points of the Brillouin zone. The band structure reveals two pairs of Dirac bands, stemming from electric and magnetic dipolar modes of the disks, respectively, and their degeneracy effectively restores the dual symmetry responsible for the topological properties we exploit here [5]. The double degeneracy between electric and magnetic dipolar modes enables emulating the spin degree of freedom of topological insulators. On the other hand, coupling between electric and magnetic modes, referred to as magneto-electric coupling (or bianisotropic response), allows emulating coupling of spin and orbital degrees of freedom, essentially the spin-orbit interaction of light [5]. To induce such coupling, we use the fact that

electric and magnetic modes have different parity in the out-of-plane direction, and break this symmetry by introducing a circular notch on one of the flat faces of the cylinders. This gives rise to hybridization of electric and magnetic dipolar modes and opening a complete photonic band gap [6]. The proposed structure was fabricated using high index (ϵ=39) ceramic discs. Based on this platform, we demonstrate topologically robust photonic transport, and directly visualize the robustness of topological edge states and their spin-locking properties by near field microwave spectroscopy [6].

4. Metasurfaces for MRI

Recently, we have proposed a novel concept showing that a metasurface composed of resonant wires can substantially increase the signal-to-noise ratio (SNR) of an MRI machine due to the spatial redistribution of the radiofrequency electromagnetic field through the resonant excitation of a metasurface eigenmode [7]. More explicitly, the length of each wire was tuned in order to approximately match the half wavelength resonance condition at 63.62 MHz (the operational frequency of a 1.5 T MRI). The placement of the metasurface in a close proximity of the studied object inside the MRI machine improves the sensitivity of the receiving radiofrequency coil and thus increases the SNR. Here, we will present a novel hybrid tunable metasurface capable to enhance substantially the MR-image quality, allowing to resolve smaller features of images, e.g. tumours, much faster and more efficiently [8].

5. Conclusions

We propose and study a set of microwave metasurfaces with different functionalities starting from novel ideas for polarization conversion, the realization of broadband Huygens' surfaces, topologically protected structures to real applications in MRI.

Acknowledgements

We thank our numerous colleagues and coauthors for many useful discussions and very fruitful collaboration, especially Alexander Khanikaev, Juan Baena, Andrea Alù, Andrew Webb and Yuri Kivshar. The part of this work was supported by the Russian Science Foundation (grant no.16-19-10538) and by Ministry of Education and Science of the Russian Federation (Zadanie No. 3.2465.2017/4.6).

References

[1] C. Holloway, E. F. Kuester, J. Gordon, J. O'Hara, J. Booth, and D. Smith, An overview of the theory and applications of metasurfaces: The two-dimensional equivalents of metamaterials, *IEEE Trans. Antennas Propag*. 54: 10, 2012.

[2] N. Engheta and R.W. Ziolkowski, *Metamaterials: Physics and Engineering Explorations*, Wiley-IEEE Press, Hoboken, 2006.

[3] S. B. Glybovski, S. A. Tretyakov, P. A. Belov, Y. S. Kivshar, and C. R. Simovski, *Metasurfaces: From microwaves to visible*, Phys. Rep.: 634, 1, 2016.

[4] J. D. Baena, S. B. Glybovski, J. P. del Risco, A. P. Slobozhanyuk, P. A. Belov, Broadband and Thin Linear-to-Circular Polarizers Based on Self-Complementary Zigzag Metasurfaces, *IEEE Trans. Antennas Propag*. 65: 8, 4124-4133, 2017.

[5] A. B. Khanikaev, S. H. Mousavi, W. K. Tse, M. Kargarian, A. H. MacDonald and G. Shvets, Photonic topological insulators, Nat. Mater. 12: 233, 2013.

[6] A. P. Slobozhanyuk, A. V. Shchelokova, X. Ni, S. H. Mousavi, D. A. Smirnova, P. A. Belov, A. Alù, Y. S. Kivshar, A. B. Khanikaev, Near-field imaging of spin-locked edge states in an all-dielectric topological metasurface, arXiv:1705.07841.

[7] A. P. Slobozhanyuk, A. N. Poddubny, A. J. E. Raaijmakers, C. A. T. van den Berg, A. V. Kozachenko, I. A. Dubrovina, I. V. Melchakova, Y. S. Kivshar, and P. A. Belov, Enhancement of magnetic resonance imaging, Adv. Mater *Adv. Mater*.: 28, 1832, 2016.

[8] A. V. Shchelokova, A. P. Slobozhanyuk, I. V. Melchakova, S. B. Glybovski, A. G. Webb, Y. S. Kivshar, and P. A. Belov, Locally enhanced image quality with tunable hybrid metasurfaces, *Phys. Rev. Appl*. 9: 014020, 2018.

Wideband Metamaterial Absorber Made of Composite Materials

Olivier Rance[1], Anne Claire Lepage[1], Xavier Begaud[1], Michel Soiron[2], André Barka[3], and Patrick Parneix[4]

[1]LTCI, Télécom ParisTech, Université Paris-Saclay, France
[2]SART, France
[3]ONERA – The French Aerospace Lab, France
[4]Naval Group, France
*corresponding author, E-mail: olivier.rance@telecom-paristech.fr

Abstract

The dielectric layers of a metamaterial absorber initially designed for RF materials are replaced with fiber-reinforced composite materials. The thickness of the dielectric layers is optimized again. The absorber achieves a reflection coefficient below -14 dB within the band 4.6 GHz-17.2 GHz, for a total thickness of 8.9 mm.

1. Introduction

Radar absorbing materials (RAM) have been traditionally used for stealth purposes in the military domain. Lately they have become of great interest also for solving interference problems in aerospace and civil domains.

At the same time, the use of fiber-reinforced composites as structural materials has known a substantial growth due to their better mechanical behavior compared to bulk materials. The possibility to use structural composite materials for the realization of electromagnetic absorbers is appealing as it would allow combining both functionalities in a unique material, reducing both cost and weight of the global structure.

In this paper, we consider a wideband absorber which has been designed with RF materials and we replace the dielectric layers by classical composite materials. The thicknesses of the layers are optimized again in order to evaluate the performances that can be obtained with these new materials. This work is a part of the development of an ultra-wide bandwidth absorber of low thickness realized within the framework of the SAFASNAV project (Self-complementary surface with low signature for naval applications).

2. Absorber

The absorber under study has been designed in the frame work of a previous study called SAFAS [1, 2]. It is composed of three dielectric layers separated by two High Impedance Surfaces (HIS), all lying on a ground plane (Fig.1-a). The bottom part includes a dielectric substrate and a self-complementary structure (checkerboard), which

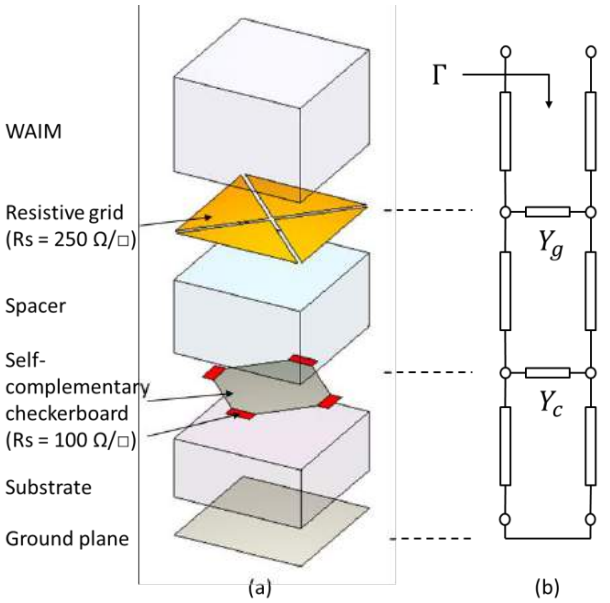


Figure 1: (a) Geometry and (b) equivalent circuit of the EM absorber.

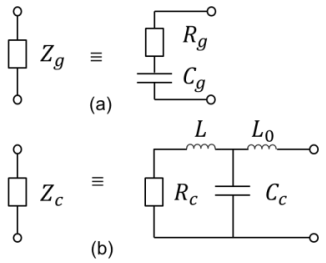


Figure 2: (a) Equivalent circuit of the resistive grid.
(b) Equivalent circuit of the auto-complementary checker.

is intrinsically wideband. The metallic parts of the checkerboard are loaded with resistive elements to improve the absorption. In order to extend the bandwidth of the structure a second capacitive layer (resistive grid) has been added. Finally, a Wide Angle Impedance Matching (WAIM)

layer has been used to improve the behavior of the structure with respect to the angle of incidence.

This absorber can be modeled by an equivalent circuit which is represented in Fig.1-b [3]. The dielectric layers (WAIM, Spacer, Substrate) are replaced by structural composite materials. Each dielectric layer is associated to a transmission line section and the thin HIS are associated to their admittances. The equivalent circuits of the resistive grid and of the self-complementary checkerboard are given in Fig.2-a, and Fig.2-b respectively. The cascading of the ABCD matrices of each layer allows calculating in a very efficient manner the reflection coefficient of the whole structure [4]. The equivalent model is used to rapidly analyze and optimize the absorber with calculation tools like Matlab. The optimized result is checked against Full-Wave simulations (CST Microwave studio) in a second steps.

3. Re – Optimization with structural composite materials

Three composite laminates of different permittivity are considered. The composition of the laminates and the associated EM characteristics are given in table 1. The optimization results obtained after replacement of the dielectrics by the structural materials are presented Fig.3.

Table 1: EM characteristics of composite layers

Layer	WAIM	Spacer	Substrate
Reinforcement	Quartz	S-glass	E-glass
Resin	Vinylester	Vinylester	Polyester
Permittivity	3.1	4	4.7
Loss tangent	0.02	0.02	0.02

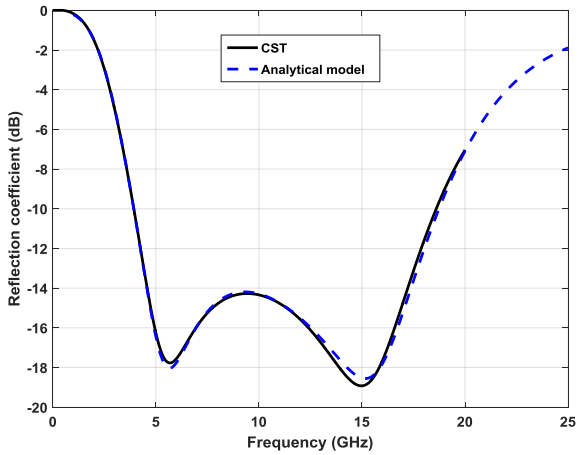


Figure 3: Reflection coefficient obtained after optimization of the dielectric composites thicknesses. The analytical model is compared to CST simulations (Frequency domain solver, infinite array, normal incidence).

The total thickness of the absorber is 8.9 mm. The reflection coefficient is less than -14 dB in the band 4.6 GHz -17.2 GHz. The analytical model is in very good agreement with the full wave simulation.

4. Conclusions

A metamaterial absorber initially designed for RF materials has been successfully optimized with composite materials. The magnitude of the reflection coefficient is below -14 dB within the frequency band going from 4.6 GHz to 17.2 GHz. This study shows that fiber-reinforced composite materials used in combination with high impedance surfaces can be employed to design structural absorbing materials.

Acknowledgments

The research leading to these results has received funding by French Ministry of Defense (DGA), through the French National Research Agency (ANR) and Astrid Program in the framework of SAFASNAV project.

References

[1] X. Begaud, S. Varault, A-C. Lepage, M. Soiron, A. Barka, Design of a Thin Ultra Wideband Metamaterial Absorber, *Proc. ICEAA17*, Verona, Italy, 2017.

[2] S. Varault, M. Soiron, A. Barka, A-C. Lepage, X. Begaud, RCS reduction with a Dual Polarized Self-Complementary Connected Array Antenna, IEEE Transactions on Antennas and Propagation, vol. 65, no. 2, pp. 567-575, Dec. 2016.

[3] S. Varault, A-C. Lepage, M. Soiron and X. Begaud, Equivalent Circuit Model of a Self-Complementary Connected Array Antenna, *European Conference on Antennas and Propagation*, EuCAP 2014.

[4] X. Begaud, F. Linot , M. Soiron, C. Renard, Analytical model of a self-complementary connected antenna array on high impedance surface, *Applied Physics A*, May 2014, Volume 115, Issue 2, pp 517-522.

Advances in Textile (Knitted) Frequency Selective Surfaces (FSS) and Meta-Surfaces

Alan Tennant[1], Xiaobin Jia[1], William Hurley[2] and Tilak Dias[2]

[1]Department of Electronic and Electrical Engineering, University of Sheffield, United Kingdom
[2]Advanced Textiles Research Group, School of Art and Design, Nottingham Trent University United Kingdom
*corresponding author, E-mail: a.tennant@shef.ac.uk

Abstract

We report a commercially attractive approach to manufacturing conducting textile meta-surfaces which is based on computerised flat-bed knitting technology using conducting yarns. We examine how flat-bed knitting can be used to manufacture large area samples of functional electromagnetic structures such as frequency selective surfaces (FSS) and high impedance surfaces (HIS). In addition we show how the knitting process can be adapted to allow the integration of conducting vias into a 3-D knitted spacer structure to form an electromagnetic high impedance surface (HIS).

1. Introduction

Passive and active electromagnetic surfaces are traditionally manufactured from sheet metal or using lithographic techniques for printed circuit boards. However, over the past decade new materials and manufacturing techniques have been developed that permit the creation of electromagnetic structures, such as antennas and transmission-lines using conducting textiles [1,2].

Electromagnetic structures based on conducting textiles have certain advantages over equivalent structures constructed from conventional materials. Textile structures offer advantages such as light weight, flexibility, softness, and high-strength-to-weight ratios. A unique advantage of electromagnetic structures based on textiles is that they can be integrated into clothing to provide functions such as on-body and off-body communications. Functional conducting textiles may also be integrated into composite structures where they provide a light weight and flexible alternative to conventional structures based on circuit-board technology. Advanced textile manufacturing techniques, such as computerised flat-bed knitting, can also be used to create a variety of 3-D and conformal structures to prescribed geometries [3]

Much of the previously published work on conducting textiles at RF frequencies considers structures constructed from combinations of traditional (non-conducting textiles) with commercially available conducting textiles, such as Zelt to form hybrid structures [4]. The disadvantage of this approach, particularly when applied to complex structures such as Frequency selective surfaces (FSS), is that the conducting textile needs to be "cut-to- shape" and then attached to the non-conducting textile substrate using adhesive or some other means. This is obviously a time consuming process that is not amenable to mass manufacturing and alternatives are sought. One alternative technique that has been investigated is the use of computerised embroidery in which a conducting yarn is used to embroider conducting features, such as a patch antenna, onto a non-conducting textile base, or substrate, layer [5]. Although, computerised embroidery is a step forward with regard to efficient manufacturing, it is still a relatively slow process and the conducting surfaces created often suffer from poor continuous conductivity.

In this contribution we investigate the use of another textile manufacturing process – knitting – to fabricate conducting textile structures. Knitting is a very old and traditional process that has been revolutionised over the past few decades to allow the efficient, commercial manufacture of a wide variety of textile products using advanced, large-scale, flat-bed knitting machines under computer control and driven by advanced CAD software interfaces [6]. The computerised flat-bed knitting process can easily be used to manufacture of large area textile structures with repeated patterns and is therefore ideally suited to the manufacture of periodic structures such as FSS and meta-material surfaces.

2. Textile meta-surfaces

In this section, we present some examples of knitted meta-surfaces and give both simulated and experimental results.

2.1. Knitted textile FSS

A knitting process was used to manufacture a typical inductive FFS and consists of a square conducing grid of side length equal to approximately 8mm. The FSS structure was knitted using a Shima Seiki SWG091N (gauge 15) computerised flat-bed knitting machine. The non-conducting base yarn was polyester and the conducting yarn (≈4Ωcm-1) was formed by embedding silver nano particles on the surface of a 235 Denier 34 filament Polyamide 6.6 yarn. The sample size of e FSS was approximately 300mm by 300mm and a photograph of a section of the surface is shown in figure 1.



Fig. 1 *Example sections a knitted, conducting textile FSS. The white area is knitted from polyester yarn and the dark regions are knitted from conducting yarn.*

The normal incidence, free-space reflectivity (S11) characteristics of the textile FSS were measured in a fully calibrated NRL arch using an automated measurement system employing an Agilent 8510B Vector Network Analyser. The reference, calibration standard was a flat aluminium plate of equivalent size (30cm by 30cm). The measurements were performed in a dedicated anechoic chamber and a standard time-domain gating procedure was used to remove any spurious returns. Figure 2 shows the reflectivity response of the single layer knitted textile with the conducting diamond grid pattern. The response is typical of an inductive FSS and is strongly reflective at lower frequencies and non-reflecting (indicating transmission) at higher frequencies.

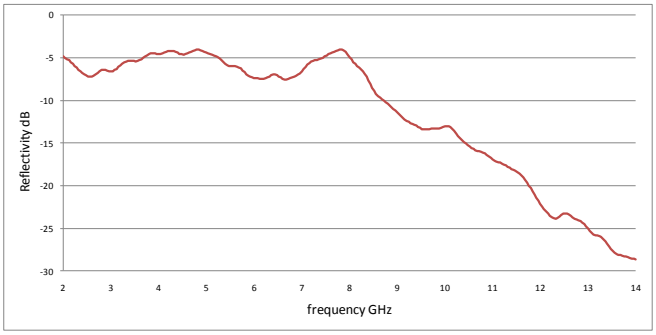


Fig. 2 *Reflectivity response of the conducting grid knitted FSS measured at normal incidence.*

2.2. Knitted textile HIS

A typical HIS design of consists of a two-dimensional, planar grid of periodically arranged conducting patches separated from a conducting ground-plane by a dielectric substrate material. Additionally, in many HIS designs the conducting patches on the top surface are electrically connected to the ground-pane by conducting pins, or vias. This type of HIS design is particularly useful for suppressing electromagnetic surface, or creeping wave, propagation and is exemplified by the classic Sievenpiper "mushroom" HIS [6]. However, the manufacture of mushroom type HIS employing conducting vias is a non-trivial process and typically requires many holes to be drilled through the HIS structure and conducting pins to be inserted and soldered to form the electrical connections between the patch elements of the top layer and the ground-plane. It is in the creation of conducting vias between the conducting surface elements and the ground-plane of a HIS that the proposed manufacturing process based on flat-bed knitting excels. In particular the flat-bed knitting process is used to create such a structure in one continuous process which is highly efficient in terms of manufacturing cost and time.

Variations of HIS are also known as artificial magnetic conductors (AMCs) and electromagnetic band gap (EBG) structures and applications include: AMC ground-planes which permit the design of efficient low-profile planar antennas that can be placed in close contact to electrically conducting surfaces; the suppression of surface wave transmission to reduce inter-element coupling in array antennas and the use of EBGs to design of various microwave components and structures. In this section of the paper we report experimental details of a unique knitted HIS which incorporates integrated conducting vias and present

results of reflectivity phase and surface wave transmission measurements.

Flatbed knitting machines consist of two needle beds positioned opposite to each other and set at an angle of between 90 ^{o} to 104^{o} giving the appearance of an inverted V. Each bed has a set number of knitting needles which actively form the knitted loops with yarn that is introduced during the knitting process. In flat-bed knitting, a single feed of yarn can be progressively fed from one needle to the next in a continuous process which binds the knit loops together thus creating the fabric [6]. During this knitting process it is possible to selectively choose which needles are knitted and also to control the choice of fibre used. Of all methods of knit manufacturing computerised flat-bed knitting is the most versatile with the potential to develop complex 3D structures which can have embedded, at predetermined areas, yarns and structures with different core properties and functionalities [6]. Flat-bed knitting is a proven industrial technology capable of producing complex fabrics over 2 meters wide in a continuous roll.

The HIS structure was knitted as a spacer material (Fig.1) with a conductive ground plane using a Shima Seiki SWG091N (gauge 15) computerised flat-bed knitting machine. The non-conducting spacer yarn was polyester and the conducting yarn (≈4Ωcm-1) was formed by embedding silver nano particles on the surface of a 235 Denier 34 filament Polyamide 6.6 yarn [8]. To create the conductive patches on the front of the structure the nonconductive polyester was selectively knitted to create the negative shape of the conductive patch which was then filled by using the conductive yarn from the back (ground plane) and knitting it on the front (non-conductive layer). By moving the yarn from the back layer to the front a via was created connecting the front conductive patches to the ground plane layer as illustrated by figure 3. The top surface of the knitted HIS is shown in figure 4.



Fig. 3 *Example 3 D spacer fabric with 2 knit layers interconnected by spacer material*

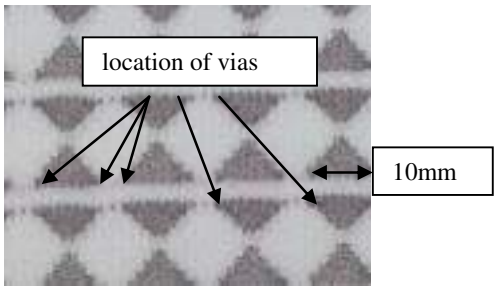


Fig. 4 *Top surface of the conducting textile HIS. The white area is knitted from polyester yarn and the dark regions are knitted from conducting yarn. Integrated vias connect the top conducting surface to the ground plane at the base corners of the triangular patches.*

To characterise the properties of the knitted textile HIS, two separate types of measurement were made: a free-pace reflectivity phase measurement and a surface wave propagation measurement. The free-space reflectivity phase measurement was made in an anechoic chamber using a fully calibrated NRL arch system employing an Agilent 8510B Vector Network Analyser. The reference calibration standard was a flat aluminium plate of equivalent size to that of the HIS (36cm by 36cm). The measurement was made for illumination at normal incidence and a standard time-domain gating procedure was used to remove any spurious returns. The surface wave propagation measurements were made using a test rig based on the system described in [6]. Surface waves are launched and received using broadband conical monopole antennas (TM mode). The test rig was used in conjunction with an Agilent E5071 network analyser. A “thru” (S21) calibration was made using the uncovered, conducting surface (Aluminium) of the test rig as the reference standard. The conducting surface of the test rig was then replaced by the knitted HIS surface and the resulting S21 data were recorded. Both the reflection phase and the surface wave propagation measurements were made over a frequency band between 2GHz and 6GHzFigures

Results: The free-space reflection phase measured from the knitted HIS for normally incident illumination is shown in figure 5a. The surface exhibits the classic band-gap reflection phase response with zero phase reversal at approximately 4.7GHz and with a +/-90^{o} band-gap of approximately 750MHz. The measured surface wave propagation properties of the textile HIS are shown in figure 6, where it is observed that the HIS shows a distinct, sharp propagation cut off at around 4GHz and a band-gap between approximately 4GHz and 5GHz.

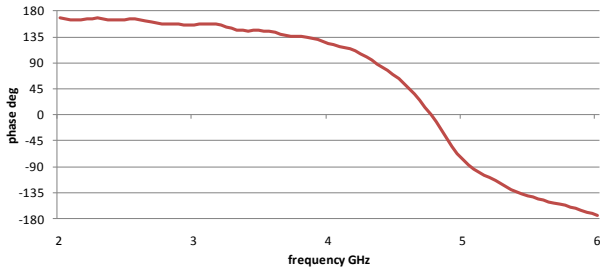


Fig. 5 *Measured reflection phase response of the knitted HIS at normal incidence.*

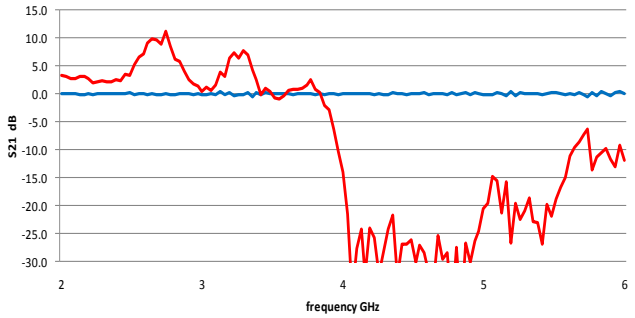


Fig. 6 *Measured S21 surface propagation (TM mode) response of the knitted HIS and reference conducting surface.*

3. Conclusions

Several examples of textile metamaterial surfaces knitted from conducting yarn on a computerised flat-bed knitting machine have been presented. Measured data shows that the knitted textile FSS exhibit the fundamental characteristics of capacitive and inductive FSS designs. No simulated data is presented in this Letter as, of yet, we do not have any accurate models to describe the highly complex interactions and contact processes between the individual conducting yarns in the knitted structure (particularly at microwave frequencies) and this is an area for future research. Other microwave components have been fabricated using the flat-bed knitting process, including 3-D structures, and these will be reported at a later date.

References

[1] Cottet D, Grzyb J, Kirstein T and Troster G, "Electrical characterization of textile transmission lines," Advanced Packaging, IEEE Transactions on, vol. 26, pp. 182-190, 2003.

[2] Kennedy, T.F.; Fink, P.W.; Chu, A.W.; Champagne, N.J.; Lin, G.Y.; Khayat, M.A.; , "Body-Worn E-Textile Antennas: The Good, the Low-Mass, and the Conformal," Antennas and Propagation, IEEE Transactions on , vol.57, no.4, pp.910-918, April 2009

[3] Dias T., Hurley W., Monaralgala R. and Wijeyesiriwardana R., "Development of Electrically active knitted textiles", Advances in Science & Technology, vol. 60, pp 74-84, 2008.

[4] Locher I, Klemm M, Kirstein T, and Tröster G, "Design and characterization of purely textile patch antennas, IEEE Transactions on advanced packaging, vol. 29, No. 4, pp 777-788 2006

[5] T. Acti, S. Zhang, A. Chauraya, W. G. Whittow, R. Seager, T. Dias, and Y. Vardaxoglou, "High Performance Flexible Fabric Electronics for Megahertz Frequency Communications," presented at 2011 Loughborough Antennas & Propagation Conference (LAPC), Loughborough, UK, 2011

[6] Dias, T., Knitting seamless 3D shell structures, Textile Technology International 2001, ISBN 185938, pp 57-61, 2002

Plasmonics and Nanophotonics

Optical metasurface based holographic stereogram

Yun-Seok Choi[1*], Joo-Yun Jung[2] and Min-Kyo Seo[1]

[1]Department of Physics and Institute for the NanoCentury, Korea Advanced Institute of Science and Technology, Daejeon, Rep. of Korea
[2]Department of Nano Manufacturing Technology, Korea Institute of Machinery and Materials, Daejeon, Rep. of Korea
*corresponding author, E-mail: yunseok@kaist.ac.kr

Abstract

Holographic stereogram displays a fully three-dimensional image by generating different two-dimensional holograms depending on the direction of viewpoint. Conventional holographic stereograms by micrometer-scale pixels suffer from multiple diffraction orders and narrow viewing angle. We demonstrate optical metasurface based holographic stereogram with a wide viewing angle of 60 degrees. The metasurface consists of several phase-only hologram sub-metasurfaces producing different directional holograms at specific angles. We combine a spatial Fourier filter with the Gerchberg-Saxton algorithm to calculate phase distributions for directional holograms.

1. Introduction

In recent decades, there have been a large number of researches on three-dimensional (3D) holographic image generation.[1] Especially, holographic stereogram is one of the efficient methods to visualize 3D images by generating a sequence of different two-dimensional (2D) holograms depending on the direction of viewpoint.[2] However, conventional holographic stereogram recorded on a flat medium with micrometer-scale pixels suffers from multiple diffraction orders which results in a narrow viewing angle of only a few degree (Fig. 1(a)). To enlarge the narrow viewing angle of the conventional holographic stereogram, additional optical elements, such as a lens array, are required.[3] On the other hand, optical metasurfaces consisting of sub-wavelength-scale meta-atoms can support a wide viewing angle without multiple diffraction orders as well as display high-precision holographic images.[4] Recently, optical metasurfaces have been employed to realize not only high-performance 3D holograms [5,6] but also angle-dependent multiplexing[7].

In this research, we demonstrate optical metasurface based holographic stereogram which displays a number of different 2D holograms over a wide viewing angle without multiple diffraction orders (Fig. 1(b)). The optical metasurface consists of several sub-metasurfaces for phase-only holograms. Each sub-metasurface produces a holographic wavefront which propagates directionally at the desired angle without disturbing the hologram image in the other direction. The sub-wavelength-scale arrangement of meta-atoms enables the directionally propagating hologram even at a large diffraction angle of >30 degrees. Finally, the assembly of the directionally propagating holographic wavefronts completes an entire holographic stereogram.

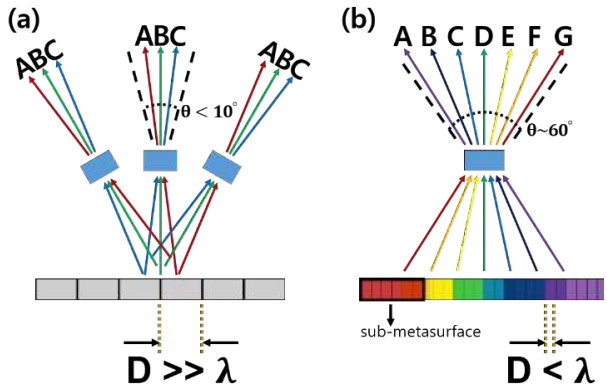


Figure 1: Comparison of the holographic stereograms generated by (a) conventional micrometer-scale hologram pixel and (b) optical metasurface pixel. D and λ are the size of the phase control pixel and the wavelength of light, respectively. θ represents the viewing angle of holographic stereogram.

2. Method and Result

2.1. Modified Gerchberg-Saxton algorithm

The Gerchberg-Saxton (GS) algorithm is one of the most famous methods to generate either phase- or amplitude-only holograms. Direct application of the raw GS algorithm to the metasurface with a sub-wavelength-scale arrangement of meta-atoms produces a hologram which spreads over a very wide angle. To calculate the phase distribution of meta-atoms for the directionally propagating holographic wavefront, we developed a modified GS algorithm which employs a spatial Fourier filter in the iteration loop. The spatial Fourier filter enables to control not only the propagation direction but also the divergence angle of the holographic wavefront.

2.2. Design and fabrication of metasurface

We designed seven hologram sub-metasurfaces of which the phase distributions are calculated to display alphabets from 'A' to 'G' at the different angles from -30 to +30 degree with a step of 10 degrees. The size of the sub-metasurface is 50×50 μm^2, and the reconstructed alphabet characters appear in an area of 40×40 μm^2 at the height of 50 μm above the metasurface. The pixel size of the phase distribution is 250×250 nm^2 small enough to support a wide viewing angle at the wavelength of 675 nm. Overlapped each other partially and arranged in an area of 107×50 μm^2, the seven sub-metasurfaces constructs the entire metasurface for holographic stereogram. In the overlapping region, the phase of the metasurface is defined as the sum of the phases of the two sub-metasurfaces.

We employed the inverted V-shaped nanoantennas as sub-wavelength phase-control pixels of the metasurface. The metasurface is fabricated in the gold film with a thickness of 30 nm on the glass substrate. Figures 2(a) and 2(b) show the optical and scanning electron microscope images of the fabricated metasurface. The inverted V-shaped nanoantenna enables to control the phase of the transmitted light, of which the polarization state is orthogonal to the incident light, depending on its shape and orientation [8]. We employed eight different inverted V-shaped nanoantennas to support the phase shifts over 2π radians with a step of $\pi/4$.

2.3. Holographic stereogram generation

Figures 2(c) and 2(D) show the theoretical and experimental results of the holographic stereogram generation by the optical metasurface. The different alphabets from 'A' to 'G' are clearly reconstructed at the different angles of viewpoint from -30 to +30 degrees. The reconstructed alphabet images appear at the same position from the metasurface and thus result in a holographic stereogram. Regardless of the angle of viewpoint, the reconstructed holograms have almost similar brightness, which is one of the advantages of employing the sub-wavelength-scale meta-atoms. We note that the quality of hologram image can be further improved by controlling the amplitude distribution of the pixels simultaneously.

3. Conclusions

We demonstrate a novel holographic stereogram based on the optical metasurface, which consists of the phase-only hologram sub-metasurfaces to generate different holograms at different angles of viewpoint. The modified GS algorithm employing a spatial Fourier filter successfully provides the phase distribution required for the directionally propagating holographic wavefront. We expect that our metasurface based holographic stereogram, combining with the depth-resolved hologram generation, will pave the way to display genuinely full-3D images.

Acknowledgements

M.-K.S. acknowledges support for this work by the National Research Foundation of Korea (NRF) (2017R1A2B2009117, 2017M3C1A3013923, 2014M3A6B3063709, and 2017R1A4A1015426).

References

[1] N. S. Holliman, N. A. Dodgson, G. E. Favalora, and L. Pockett, *IEEE Trans. Broadcast.* 57, 362 (2011).

[2] M. Yamaguchi, *J. Opt. Soc. Am. A* 33, 2348 (2016).

[3] K. Choi, J. Kim, Y. Lim, and B. Lee, *Opt. Express* 13, 10494 (2005).

[4] A. Arbabi, Y. Horie, M. Bagheri, and A. Faraon, *Nat. Nanotechnol.* 10, (2015).

[5] G. Zheng, H. Mühlenbernd, M. Kenney, G. Li, T. Zentgraf, and S. Zhang, *Nat. Nanotechnol.* 10, 308 (2015).

[6] L. Huang, X. Chen, H. Mühlenbernd, H. Zhang, S. Chen, B. Bai, Q. Tan, G. Jin, K.-W. Cheah, C.-W. Qiu, J. Li, T. Zentgraf, and S. Zhang, *Nat. Commun*. 4, 2808 (2013).

[7] S. M. Kamali, E. Arbabi, A. Arbabi, Y. Horie, M. Faraji-Dana, and A. Faraon, *Phys. Rev. X* 7, 41056 (2017).

[8] X. Ni, A. V. Kildishev, and V. M. Shalaev, *Nat. Commun.* 4, 1 (2013).

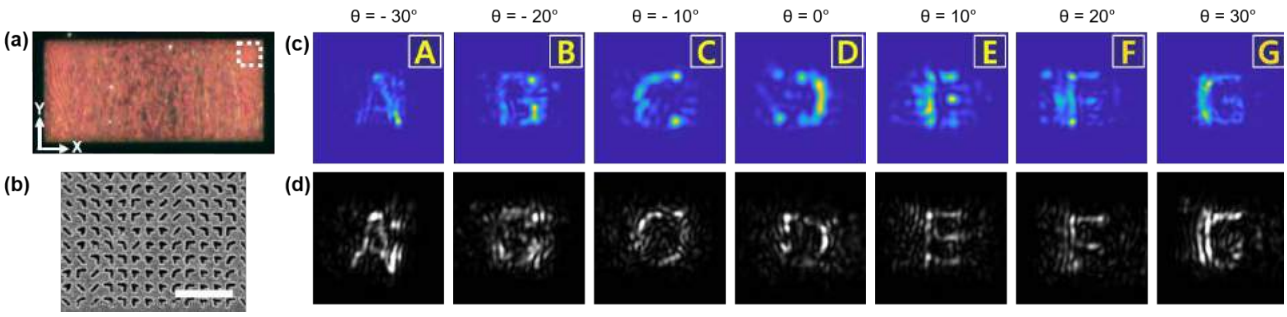


Figure 2: Optical metasurface based holographic stereogram. (a) Optical and (b) scanning electron microscope images of the fabricated metasurface. The area of the SEM image corresponds to that of the white dashed-square in Fig. 2(a). Scale bar, 1 um. (c) Simulated and (d) measured holographic images depending on the directions of the viewpoints in the range from -30 to +30 degree.

Optical properties and mid infrared applications of plasmon perfect absorber metasurfaces

Yoshiaki Nishijima[1], Armandas Balčytis[2,3], Gediminas Seniutinas[2,4], Saulius Juodkazis[2]

[1]Department of Physics, Electrical and Computer Engineering, Graduate School of Engineering, Yokohama National University, 79-5 Tokiwadai, Hodogaya-ku, Yokohama 240-8501, Japan
[2]Centre for Micro-Photonics, Faculty of Science, Engineering and Technology, Swinburne University of Technology, Hawthorn, Vic 3122, Australia
[3]Center for Physical Sciences and Technology, A. Goštauto 9, LT-01108 Vilnius, Lithuania
[4]Current adress, Paul Scherrer Institute, Villigen CH-5232, Switzerland
*corresponding author, E-mail: nishijima-yoshiaki-sp@ynu.ac.jp

Abstract

We demonstrate the optical properties of a plasmonic perfect absorber (PPA) in mid-infrared (IR) wavelength region with a layered structure: the bottom metal layer, insulator, and top nano-structures. Thickness was optimised for the perfect absorption at mid-IR wavelengths. We have fabricated PPA structures with various combinations of metal and insulator layers. The experimentally measured optical properties were compared with simulations by Finite-difference time-domain calculations. Also, we demonstrate applications of these structures for the plasmonic IR-light sources and detectors.

1. Introduction

Plasmon perfect absorbers (PPAs) are plasmonic metasurface structures which consist of the thick metal film, insulator layer, and plasmonic nanostructures. The metasurfaces made from plasmonic perfect absorbers (PPAs) realize the perfect absorption (simultaneous zero-transmission and reflection) at a specific resonance wavelength. The simple configuration of the metal-insulator-metal(MIM) are easy to design and to make by a well-established semiconductor nanofabrication processes or self assembly of nano particles.

We focused on PPA structures as the photo-thermal light emitter and detector in mid-infrared (IR) wavelengths for constructing plasmonic non-dispersive infrared (ND-IR) gas sensors [1, 2]. The Kirchhoff's law of the thermal radiation defines the absorption and emission efficiencies being equal to each other. Therefore PPAs are expected for good performance as light emitters [3, 4]. When material absorbs the light at the plasmon resonance, free electron oscillation generates heat. This heat generation can be used for the thermal bolometric detector.

In this study, we performed experiments with a wide set of parameters of MIM structures. The PPAs consist of the bottom layer (Au and Ag), insulator layer (SiO_2 with refractive index $n \sim 1.4$), ZnO ($n \sim 2.0$), or Si ($n \sim 3.4$)), and metal nanostructures (Au, Ag, Cu and Pd), respectively. The nanodisc and metal-hole-array (NDA and MHA) of plasmonic patterns were compared. We also demonstrate thermo-optical absorption vs emission (input vs output) properties of PPAs.

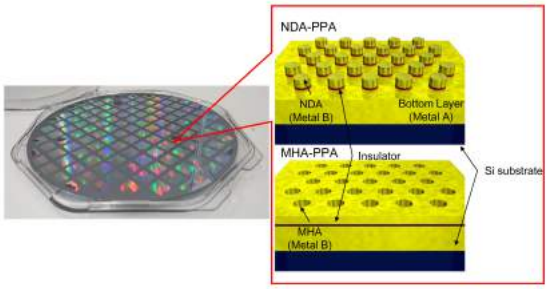


Figure 1: Photograph of a reduction projection resist pattern on the 8-inch Si wafer made by reduction projection and schematic illustrations of NDA and MHA PPAs.

2. Experiments

Sub-micrometer structure dimensions are required for the MIM structures functional at the IR wavelength range. Therefore, the reduction projection photolithography is more suitable than the electron beam lithography for the future applications, large area, and mass production of devises. The NDA/MHA PPAs nanostructures were fabricated on a double-side polished 8-inch silicon wafer, which had a 200 nm Au film on top, using the i-line stepper (NSR205-i14E, NIKON Co.). The positive tone (TLOR-P003 HP, Tokyo Ohka Kogyo Co.) and negative tone (TLOR-N001 PM, Tokyo Ohka Kogyo Co.) photo-resists were used for the NDA and MHA fabrication as shown in Fig. 1. Then, 10 nm of insulator and 50 nm of metal were deposited by magnetron sputtering using a 3 nm Ti adhesion layer between the insulator and metals over the developed resist pattern (AXXIS, JKLesker). After deposition, a lift-off was perfromed in an organic solvent to obtain final PPA structures.

Optical reflection spectroscopy has been performed

with the combination of the FT-IR (FT-IR 4200, JASCO CO.) and microscope unit (IRT-1000). As a reference for the reflectance spectra, a Au mirror with the 98% absolute reflectance has been used.

For the thermal radiation spectroscopy, specially modified FT-IR system was implemeted. The light from the outside was coupled into the FT-IR setup from an optical side port. The light passed through the interferometer and directed to the HgCdTe(MCT) detector. The PPA substrates were contacted to the ceramic heaters on a Al plate.

Photo-thermal conversion has been measured using the Seebeck effect. A tungsten-based thermal radiation emitter was used for the IR-light source. Sample was put on the Seebeck cell on the Al cover to prevent a heat generation form the other parts of setup. The output voltage was measured with a multimeter.

3. Results and discussions

Fabricated structure has a good uniformity over the 1×1 cm^2 region. Plasmon resonance appeared from 2 to 6 μm and had a 45% reflection (a 55% absorption) at the minimum. This was obtained with Ag (nanostructure) - Si - Au (bottom layer) system. The thickness of insulator layer was only 10 nm. Therefore, the interaction between the two metals was increasing an impedance of the system. An optimization of the insulator thickness had to be carried out to improve the absorption.

For thermal radiation, to prevent the oxidization of the metal, Au nanostructure and bottom layer were used. For comparison, Si and SiO_2 insulators with NDA and MHA were tested. For these four different structures, the absorption was in the following order: NDA-Si, NDA-SiO_2, MHA-Si, MHA-SiO_2 as shown in Fig. 2. The span of values from $\sim$ 50% of absorption (NDA Si insulator) to 10% (MHA SiO_2 insulator) was obtained.

When sample was heated up from 100 to 300°C, we observed the thermal emission at the plasmon resonance. Emissivity related to the black body paint ($\sim$ 95% radiation) is almost same as the absorption ($\sim$50% with NDA-Si, $\sim$10% with MHA-SiO_2).

When these structures were used for photo-thermal generation, by illuminating broad infrared light, the NDA-Si PPAs had a 2.5 times larger output than MHA-SiO_2. The output voltage was also ordered similarly to the absorption of the structures. This is due to the broadband illumination. By using a narrow band light illumination with quantum cascade laser or through a band pass filter, a more clear difference would be expected.

4. Conclusions

In this study, we have demonstrated the optical absorption properties of various kinds of PPAs in mid-IR wavelengths. Even in a thin insulator layer, 55% of absorption is realized. Using this Au PPAs, we also obtained the thermal radiation and photo-thermal generation which well agreed with the optical absorption. After optimization of the other parameters (i.e. thickness of metal and insulator), it should become possible to realize perfect absorber and efficient radiation emitter.

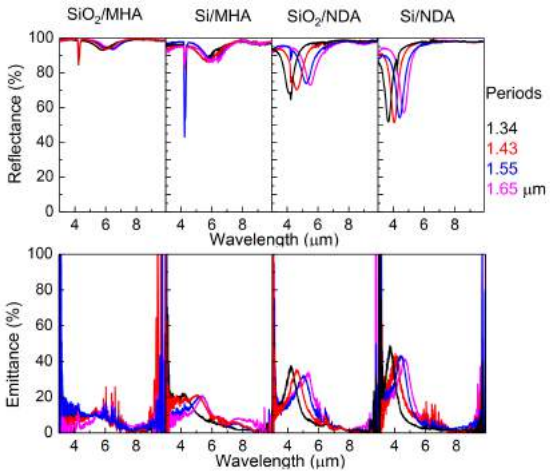


Figure 2: Optical reflection spectra of NDA / MHA PPAs and their thermal radiation spectra.

Acknowledgement

Authors are grateful for Tokyo Ohka Kogyo Co. Ltd for their support of reduction exposure lithography to produce NDA and MHA PPAs. YN is thank to Dr. H. T. Miyazaki, National institute for materials science (NIMS), Wako Japan for his kind advise for thermal radiation measurements.

References

[1] Y. Nishijima, Y. Adachi, L. Rosa, and S. Juodkazis, Augmented sensitivity of an IR-absorption gas sensor employing a metal hole array, *Opt. Mat. Express* 3: 968–976, 2013.

[2] Y. Nishijima, S. Suda, G. Seniutinas, A. Balcytis, and S. Juodkazis Plasmonic sensor: towards parts-per-billion level sensitivity, *Sens. Mater.* 29: 1253–1258, 2017.

[3] H. T. Miyazaki, T. Kasaya, M. Iwanaga, B. Choi, Y. Sugimoto, K. Sakoda, Dual-band infrared metasurface thermal emitter for CO_2 sensing. *Appl. Phys. Lett.* 105: 121107-1, 2014.

[4] K. Ikeda, H. T. Miyazaki, T. Kasaya, K. Yamamoto, Y. Inoue, K. Fujimura, T. Kanakugi, M. Okada, K. Hatade, S. Kitagawa, Controlled thermal emission of polarized infrared waves from arrayed plasmon nanocavities. *Appl. Phys. Lett.* 92: 021117-1, 2008.

Frequency discrete diffraction control by photonic gauge potentials

Chengzhi Qin[1], Bing Wang[1], Peixiang Lu[1,2]

[1]Wuhan National Laboratory for Optoelectronics and School of Physics, Huazhong University of Science and Technology, Wuhan, 430074, China

[2]Laboratory for Optical Information Technology, Wuhan Institute of Technology, Wuhan, 430205, China

*corresponding author, E-mail: wangbing@hust.edu.cn

Abstract

We demonstrate theoretically and experimentally photonic gauge potential in synthetic frequency dimension. The gauge potential is realized by controlling the modulation phase in optical phase modulators. We experimentally achieve a 50 GHz frequency shift and three-fold expansion of an impinging comb and frequency analogues of refraction phenomena, including negative refraction and perfect focusing in the frequency domain, both for discrete and continuous incident spectra. Our study paves a way towards versatile frequency management for optical communications and signal processing.

1. Introduction

Controlling the spectrum of light is important in exploring both fundamental physics and for practical applications. Traditional methods for frequency conversion rely on nonlinear optical effects, which are limited by low efficiency and high pump power. Recent efforts have shifted from nonlinear effects to the dynamic modulation. The phase of dynamic modulation corresponds to an effective gauge potential for photons [1, 2], which is a direct analogue of vector potential for electrons. The gauge potential can be used to realize Aharnov-Bohm effect [1], photonic quantum Hall effect [2]. So it is ready to introduce photonic gauge potential to the frequency space to control the spectrum evolution of light.

2. Photonic gauge potential in frequency space

Consider a travelling-wave $LiNbO_3$ phase modulator (PM) with a dynamic refractive index modulation $n(z, t) = n_0 + \Delta n\cdot\cos(\Omega t - qz + \phi)$. Here n_0, Δn, Ω, q and ϕ are background index, modulation amplitude, frequency, wave vector, and initial phase, respectively. The modulation induces photonic intraband transitions between the modes with frequency $\omega_n = \omega_0 + n\Omega$ and wave vector $\beta_n = \beta_0 + nq$ ($n = 0, \pm1, \pm2,\ldots$). Considering the phase-matching condition of $\Omega/q = c/n_0$, we can obtain the coupled-mode equation [3]

$$i\frac{\partial a_n(z)}{\partial z} = C\left(e^{i\phi}a_{n-1}(z) + e^{-i\phi}a_{n+1}(z)\right), \qquad (1)$$

where $C = \Delta n k_0/2$ is the coupling strength between adjacent order modes with k_0 being the vacuum wave number. There is nonreciprocal phase shift of $\pm\phi$ accompanying photonic transitions. This phase shift is a photonic analogue of Peierls phase, which corresponds to an effective gauge potential in the frequency dimension

$$\int_{\omega_n}^{\omega_{n+1}} A_{eff}\, d\omega = \phi, \qquad (2)$$

from which we find $A_{eff} = \phi/\Omega$.

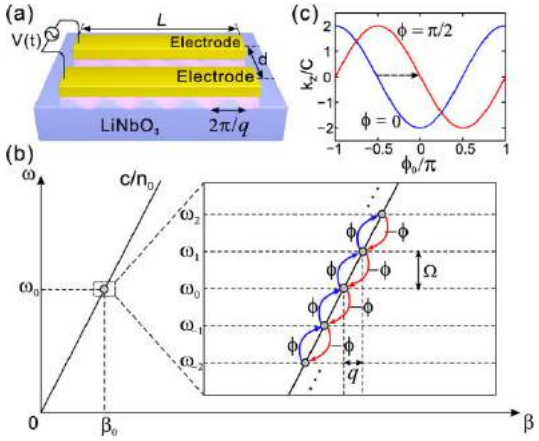


Figure 1. (a) Schematic of phase modulator (PM). Schematic of photonic intraband transitions. (c) Band structure of frequency comb for $\phi = 0$ and $\phi = \pi/2$.

The frequency dimension can support Bloch mode with $a_n(z) = a_0\exp(in\phi_0)\exp(ik_z z)$, where a_0, ϕ_0 and k_z are the mode amplitude, Bloch momentum and propagation constant. Combined with Eq. (1), we can obtain the band structure

$$k_z(k_\omega) = -2C\cos((k_\omega - A_{eff})\Omega), \qquad (3)$$

where we denote $\phi_0 = k_\omega\Omega$, the gauge potential can induce a band structure shift in momentum space. For a finite-width frequency comb with center Bloch momentum ϕ_0, the group velocity in the frequency dimension is $v_{g,\omega} = -\partial k_z/\partial k_\omega = -2C\Omega\sin(\phi_0 - \phi)$, leading to a frequency shift $\Delta\omega(z) = \int_0^z v_{g,\omega}dz'$. For one PM with length L, the phase modulation depth is $m_\varphi = \Delta n k_0 L = 2CL$. So the total accumulated frequency shift is

$$\Delta\omega = -m_\varphi\Omega\sin(\phi_0 - \phi), \qquad (4)$$

The finite-width frequency comb also experiences a spectral expansion, which is described by the diffraction coefficient

$$D = \partial^2 k_z/\partial k_\omega^2 = 2C\Omega^2\cos(\phi_0 - \phi), \qquad (5)$$

So we have $|\Delta\omega|_{max} = m_\varphi\Omega$ and $|D|_{min} = 0$ for $\phi_0 - \phi = \pm\pi/2$, and $|\Delta\omega|_{min} = 0$ and $|D|_{max} = 2C\Omega^2$ for $\phi_0 - \phi = 0$ or π. By cascading two PMs with distinct modulation phases ϕ_1 and ϕ_2, the frequency comb will exhibit a refraction at the boundary of two PMs, with a relative refractive index

$$n_{12}(\phi_0) = \cos(\phi_0 - \phi_1)/\cos(\phi_0 - \phi_2), \qquad (6)$$

So we can impart arbitrary refraction phenomena for input

frequency combs, such as realizing positive, negative refraction and spectral compression.

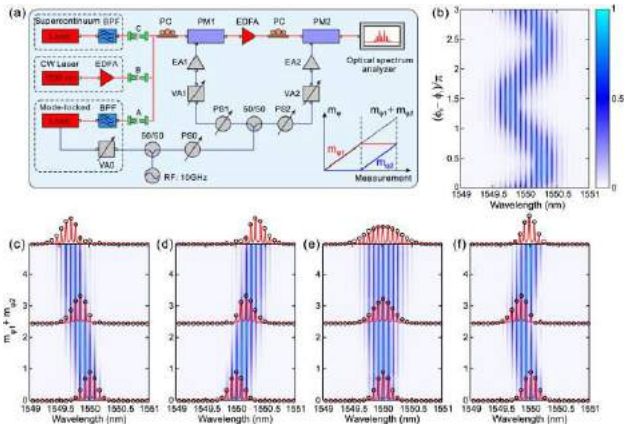


Figure 2. (a) Experimental set-up. PS: phase shifter, EA: electrical amplifier, VA: variable attenuator, BPF: band-pass filter, PC: polarizer controller, EDFA: erbium-doped fiber amplifier. (b) Output frequency spectrum as $\phi_0 - \phi_1$ varies for $m_{\varphi 1} = m_{\varphi 2}$. (c)-(e) Frequency comb evolution as $\phi_0 - \phi_1 = -\pi/2$, $\pi/2$, and 0 for $\phi_1 = \phi_2$. (f) Frequency comb evolutions for $\phi_0 - \phi_1 = -\pi/2$ and $\phi_0 - \phi_2 = \pi/2$.

In experiment, the frequency comb is generated by a mode-locked laser, which is synchronized with the two PMs. Firstly, we keep two PMs modulated in phase ($\phi_1 = \phi_2$) and fix $m_{\varphi 1} = m_{\varphi 2}$, the frequency envelope exhibits a sinusoidal variation as $\phi_0 - \phi_1$ varies, which agrees well with Eq.(4). In Figs. 2(c) and 2(d), the spectral width remains constant and the comb center manifests linear blue and red shifts for $\phi_0 - \phi_1 = -\pi/2$ and $\pi/2$, respectively. The maximum frequency shift is ~ 50 GHz (~ 0.4 nm) which spans up to five comb lines. For $\phi_0 - \phi_1 = 0$ in Fig. 2(e), the spectral center is not affected and bandwidth is broadened by three folds from 0.18 to ~ 0.6 nm. By choosing $\phi_0 - \phi_1 = -\pi/2$ and $\phi_0 - \phi_2 = \pi/2$ shown In Fig. 2(f), the frequency comb undergoes a "negative refraction" between the two PMs.

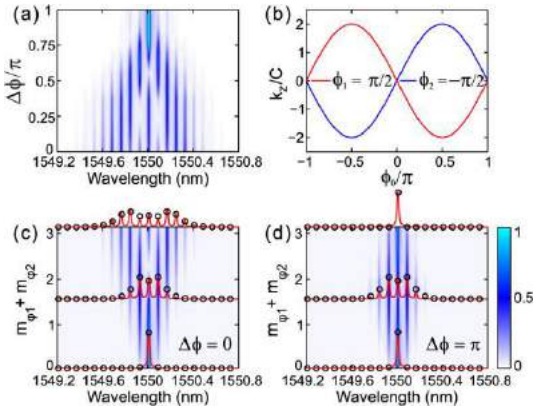


Figure 3. (a) Output frequency spectrum versus $\Delta\phi$ for $m_{\varphi 1} = m_{\varphi 2}$. (b) Band structures of the two PMs for $\phi_1 = -\pi/2$ and $\phi_2 = \pi/2$. Frequency evolutions: (c) $\Delta\phi = 0$. (d) $\Delta\phi = \pi$.

For a single frequency input under $m_{\varphi 1} = m_{\varphi 2}$, the out spectrum is $|a_n| = a_0|J_n(2m_{\varphi 1}\cos(\Delta\phi/2))|$. We experimentally input a continous-wave laser. Firstly, we keep $m_{\varphi 1} = m_{\varphi 2}$ and vary $\Delta\phi = \phi_2 - \phi_1$ from 0 to π shown in Fig. 3(a), the output spectrum is squeezed from maximum to a single frequency. The band structures of the two PMs are shown in Fig. 3(b) as $\phi_1 = \pi/2$, $\phi_2 = -\pi/2$. For in-phase modulation $\Delta\phi = 0$ shown in Fig. 3(c), $|a_n| = a_0|J_n(m_{\varphi 1} + m_{\varphi 2})|$, which exhibits constructive interference of frequency comb generation in the two PMs. For out-of-phase modulation $\Delta\phi = \pi$ shown in Fig. 3(d), $|a_n| = a_0|J_n(m_{\varphi 1} - m_{\varphi 2})|$, manifesting destructive interference of comb generation in two PMs. Interestingly as $m_{\varphi 1} = m_{\varphi 2}$, the spectrum restores to the single-frequency, manifesting the effect of "frequency perfect imaging". The effect can be applicable to arbitarily input spectra, including both dicrete and continous ones, as shown in Fig. 4.

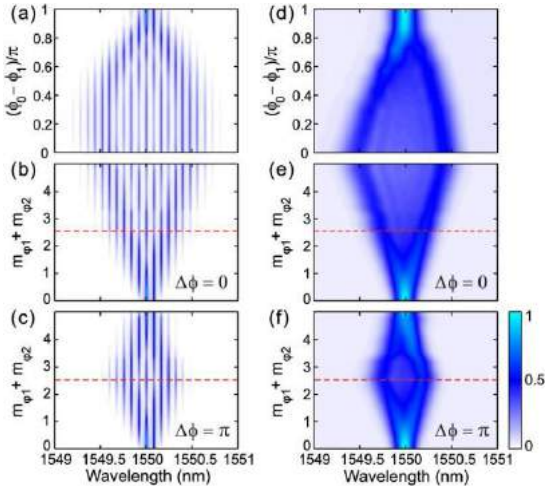


Figure 4. (a) Two continuous-wave laser evolution versus $\Delta\phi$ for $m_{\varphi 1} = m_{\varphi 2}$. Output spectral evolutions: (b) $\Delta\phi = 0$. (c) $\Delta\phi = \pi$. (d) Supercontinuum evolution versus $\Delta\phi$ for $m_{\varphi 1} = m_{\varphi 2}$. Supercontinuum evolutions: (e) $\Delta\phi = 0$. (f) $\Delta\phi = \pi$.

3. Conclusions

In summary, we realize frequency shift up to 50 GHz and bandwidth expansion up to three-folds for frequency combs by using distinct gauge potentials. We also realize negative refraction for frequency combs and perfect imaging for arbitrary spectra. Our study may find applications in signal reshaping, spectral imaging, and secure communications.

Acknowledgements

The work is supported by the 973 Program (No. 2014CB 921301), the National Natural Science Foundation of China (No. 11304108, 11674117, 61622502).

References

[1] K. Fang, Z. Yu, and S. Fan, Photonic Aharnov-Bohm Effect Based on Dynamic Modulation. Phys. Rev. Lett. **108**, 153901, 2012.

[2] K. Fang, Z. Yu, and S. Fan, Realizing effective magnetic field for photons by controlling the phase of dynamic modulation. Nature. Photon. **6**, 782-787, 2012.

[3] C. Qin, F. Zhou, Y. Peng, H. Chen, X. Zhu, B. Wang, J. Dong, X. Zhang, and P. Lu, Frequency manipulation of light by photonic gauge potentials, arXiv:1705.07296.

Active controlled scattering from dielectric nanoantennas in the visible range

Jiahao Yan[1], Churong Ma[1], Yingcong Huang[1], and Guowei Yang[1]

[1]State Key Laboratory of Optoelectronic Materials and Technologies, Nanotechnology Research Center, School of Materials Science and Engineering, Sun Yat-sen University, Guangzhou 510275, Guangdong, People's Republic of China
*corresponding author, E-mail: stsygw@mail.sysu.edu.cn

Abstract

Dielectric nanoantennas and metasurfaces with low-loss feature and strong magnetic dipole responses offer a brand new mechanism to tailor and modulate the electromagnetic waves. The ability to dynamically modulate plasmon resonances or Mie resonances shows a practical approach to build nanophotonic devices. However, how to actively modulate the resonant peaks in dielectric structures especially at visible wavelengths still needs to be answered. Here, we realize the spectral tailoring of an individual silicon nanoparticle and an individual vanadium dioxide (VO_2) nanostripe.

1. Introduction

The ability to dynamically modulate plasmon resonances or Mie resonances brings some advantages such as adjusting the operating wavelength and modulating the optical signals.[1] Electrically tuning as one of the most effective active tuning methods can realize high switching speed and large tuning ranges.[2] Recently, electrically tuning plasmonic metamaterials have been widely investigated where the modulation is realized through semiconductor layers,[3] graphene,[4] or electromechanical deformation.

Noted that, there are much few works about the electrically tuning on single nanoparticle level up to now, which is important for building nanoscale functional devices. Silicon as a kind of high-index dielectric materials has shown promising applications in metasurfaces,[5] optical nonlinearity,[6] and sensors.[7] The magnetic resonant modes in silicon nanocavities can be modulated through changing the sizes or crystallographic phases. However, how to realize active control of the magnetic responses in silicon nanocavities has not been studied yet.

Here, first, we demonstrate the electrically tunable scattering of a single silicon NP in the visible range. We found the scattering from silicon NPs exhibits blueshift and obvious intensity attenuation when increasing the applied voltage from 0 to 1.5 V. Schottky junctions can be formed at Au−SiO_2−Si interfaces, so the amount of free carriers decreases due to the existence of depletion region without applied voltage. Once the bias voltage is increased, the inversion and accumulation effect would produce much more free carriers at interfaces and then change the permittivity. In theory, the Drude model was used to explain how free carriers influence the permittivity of silicon NPs under inversion and accumulation situations.

Second, we proposed the other strategy to realize the active control. VO_2 nanostripes are treated as all-dielectric nanoantennas directly. When changing the environment temperature or applied voltage, reversible phase change in VO_2 nanostripes can lead to significant spectral modulation. The large intensity contrast between metallic and insulator states at specific wavelengths make it possible to realize directivity radiation and adjustable photoluminescence (PL).

2. Results

2.1. Electrically controlled scattering of silicon nanoparticles

- For isolated silicon nanoparticles, the resonant modes depend on particle sizes and particle numbers. For Au electrode-loaded silicon NPs, the interaction between silicon NPs and Au electrodes also needs to be considered. All these factors make hybrid nanoantennas exhibit different scattering spectra in the visible range. In general, the scattering peaks are generated from the interaction between the Mie magnetic dipole mode and the LSPRs at Au−Si interfaces.

- First, whether different applied voltages can change the optical properties of silicon nanoantennas was studied in theory. As the schematic diagram shown in Figure 1a, the band bends upward at interfaces when no voltage applies. Depletion region can be formed near the surface, which means free carriers are driven away from surface. Once applying voltage, built-infield and surface potential on both sides becomes larger. The energy band near the interface with gold under lower potential was bent downward, which gives rise to an enhanced carrier concentration and accumulation of electrons. The other junction with gold under higher potential forms an inversion layer when energy bands bend upward and the intrinsic energy level E_i at the surface crosses over the Fermi level. As a result, holes

are much more than electrons and then inversion happens. Considering such high voltage crosses the thin insulator, the carrier densities can be increased by more than 3 orders of magnitude within 5nm accumulation or inversion layers width. During the measurement process, the scattering spectra under different voltages (0, 0.3, 0.6, 0.9, 1.2, and 1.5 V) were all collected within one measurement process in 1 min to minimize anyfluctuations as shown in Fig. 1b. For this 180 nm silicon nanoantenna, we can observe the suppression of hybrid plasmon-Mie resonant peaks when increasing the voltages. The MD peak was dominated when no voltage applies, however, the ED peak at shorter wavelength becomes the more prominent one when applied voltage equals to 1.5 V.

- Different applied voltages result in different free carrier concentrations of silicon NPs. How free carriers contribute to the refractive index change at interfaces can be described by the Drude model. After combining the initial dielectric function of silicon and the variation contributed by free carriers injection, the changes of the real part of permittivity can be obtained. Using the obtained dielectric functions under a series of carrier concentrations into numerical simulation, we can explain the variation trend of scattering spectra under different applied voltages in Figure 1c. The variation trend is consistent with the experimental results.

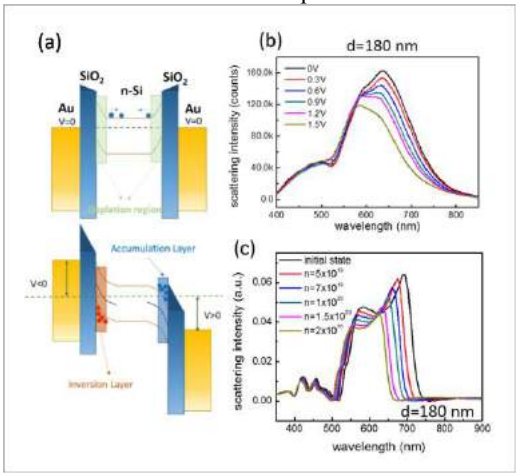


Figure 1. (a) Band diagram (top) revealing the depletion region without applied voltage. Band diagram (bottom) revealing the accumulation and inversion situations when applying voltages. Experimental (b) and simulated (c) scattering spectra when applying voltages.

2.2. Tunable scattering from VO_2 nanostripes

Using pulsed laser deposition and focused ion beam milling technique, VO_2 nanostripes with widths from 500nm to 1um were fabricated on the Al_2O_3 substrate. Under linear polarized incident light perpendicular to nanostripes. VO_2 nanostripes can be regarded as Mie resonators. When heating or applying voltages along the nanostripe, it will change from insulator to metallic state. Meanwhile, the backward scattering intensity decreases dramatically especially above 700 nm (see Fig. 2). We are also trying to use this feature to dynamically modulate the PL signals from 2D materials or some other excitons.

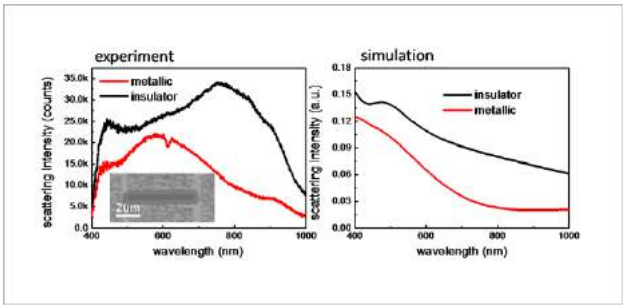


Figure 2. Scattering spectra from VO_2 nanostrips.

3. Conclusions

In conclusion, we have demonstrated the electrically controlled scattering of individual silicon NPs and VO_2 nanostripes. These structures give us an opportunity to collect the electrically controlled scattering spectra on single-particle level. In the emerging applications based on high-index dielectric nanostructures, our findings provide an important and feasible method to build photoelectricity functional devices that can transfer electrical signal to optical signal.

Acknowledgements

The National Basic Research Program of China (2014CB931700), the National Natural Science Foundation of China (91233203), and State Key Laboratory of Optoelectronic Materials and Technologies supported this work

References

[1] S. H. Lee *et al*, Switching terahertz waves with gate-controlled active graphene metamaterials, *Nature Mater*. 11: 936–941, 2012.

[2] J. Kern *et al*, Electrically driven optical antennas, *Nature Photon*. 9: 582-586, 2015.

[3] H.-T. Chen *et al*, Active terahertz metamaterial devices, *Nature* 444: 597-600, 2006.

[4] N. K. Emani *et al*. Electrical Modulation of Fano Resonance in Plasmonic Nanostructures Using Graphene. *Nano Lett*. 14: 78-82, 2014.

[5] J. Yan *et al*. Generating scattering dark states through the Fano interference between excitons and an individual silicon nanogroove. *Light: Sci.& Appl*. 6:e16197, 2017.

[6] C. R. Ma *et al*. Second harmonic generation from an individual all-dielectric nanoparticle: resonance enhancement versus particle geometry. *J. Mater. Chem. C* 5: 4810-4819, 2017.

[7] J. Yan *et al*. New type high-index dielectric nanosensors based on the scattering intensity shift. *Nanoscale* 8: 5996, 2016.

Realizing Scattering Dark State in a Hybrid System of Germanium Nanogroove and Molecular Excitons

Yingcong Huang[1], Churong Ma[1], Jiahao Yan[1], Guowei Yang[1,*]

[1]State Key Laboratory of Optoelectronic Materials and Technologies, Nanotechnology Research Center, School of Materials Science & Engineering, Sun Yat-sen University, Guangzhou, China
*corresponding author, E-mail: stsygw@mail.sysu.edu.cn

Abstract

Coupling between light and matter gives rise to many infusive physical effects and potential applications. However, the Joule heating losses at the optical frequencies makes plasmonic nanostructures not suitable to interact with molecular excitons. Here, we demonstrated germanium nanogroove as a new all-dielectric metasurface building block for the Kerker effect with molecular excitons. A significant dip was observed in the backward scattering spectra because of the cavity magnetic resonance mode, which is benefit from the refractive index of germanium.

1. Introduction

Strong light-matter interactions are not only important for fundamental quantum optics study, but also interesting in designing and fabricating nanophotonics devices for potential applications [1]. A common way to trap light at subwavelength scales and enhance the electromagnetic field is to use noble metallic nanomaterials. Unfortunately, plasmonic nanostructures are always associated with high level of Joule heating losses at the optical frequencies [2], which will limit the efficiency of the coupling systems and the whole system will become unstable.

On the other hand, loss-less all-dielectric materials which can manipulate light at subwavelength scales like metallic materials have been widely studied [3]. Therefore, they may be an alternative route towards addressing the problems facing in the plexcitonic coupling systems.

In this work, significant dips can be observed in the backward scattering spectra of the hybrid systems composed of germanium nanogrooves and J-aggregates molecules, which is caused by their destructive interference in the far-field [4]. Germanium nanogrooves can offer a considerable magnetic field enhancement, which originates from the cavity magnetic resonant mode rather than the leaky magnetic resonant mode excited in silicon nanogrooves [5].

2. Results and discussion

2.1. Prepartion of samples

Germanium nanogrooves were fabricated using focused ion beam milling technology and J-aggregates molecules were spun coated onto its surface as shown in Fig. 1. Considering the difficulty about putting J-aggregates molecules into the grooves, the groove width we chose to study in this work was about 100 nm. However, the depth of the grooves varied from 100 nm to 500 nm could finely tune the resonant mode of the germanium nanogrooves.

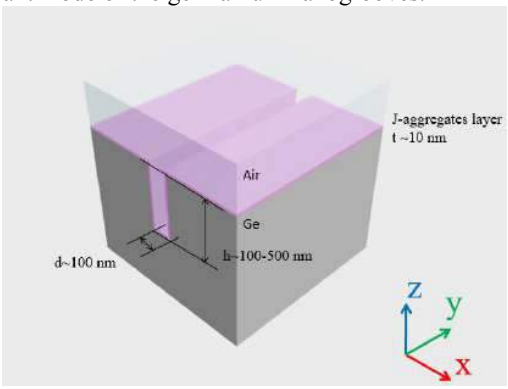


Figure 1: Hybrid system composed of a germanium nanogroove and a thin layer of J- aggregates molecules.

2.2. Far-field scattering spectra

The backward scattering spectra of germanium nanogrooves without and with J-aggregates molecules are shown in Fig. 2. The spectra from top to down represent the nanogrooves with a depth of 100 nm, 200 nm, 300nm, 400 nm and 500 nm respectively. All the backward scattering spectra of the individual germanium nanogroove have a similar wide line shape with a resonant peak approximately at λ = 550 nm. In addition, the magnetic resonant mode can be considered to dominate the scattering spectra. After adding J-aggregates molecules into the germanium nanogrooves, the scattering spectra of such hybrid system with different depth exhibit a dip at λ = 587 nm with varying degree.

Thinking about the magnetic spheres that has been discussed by Kerker in 1983, the backward scattering gain can be expressed as below form.

$$G(180^\circ) = (4/\alpha^2)\left|\sum_{n=1}^{\infty}(n+1/2)(-1)^n(b_n - a_n)\right|^2, \quad (1)$$

where a_n are the electric scattering coefficients and b_n are the magnetic scattering coefficients. If we neglect the multipole moment and a_1=b_1, than the backward scattering

gain G(180^{O})=0. As for our case, the J-aggregates molecules can be treat as the electric dipole moments and interact with the magnetic resonant mode of the germanium nanogrooves. The overlap between these two modes will lead to the destructive interference of their backward independent responses, and thus there will be significant dips on the backward scattering spectra.

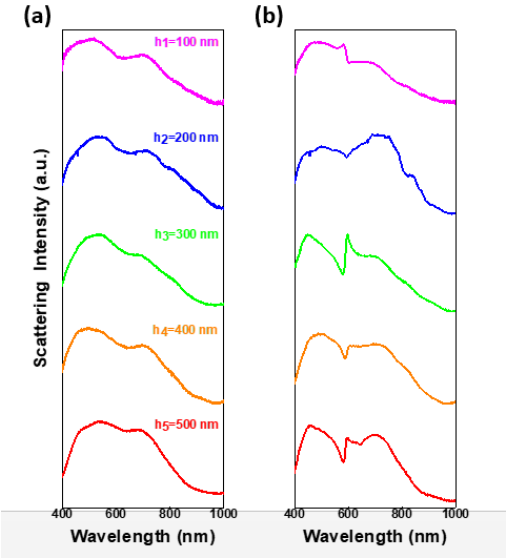


Figure 2: Experimental backward scattering spectra of an individual germanium nanogroove (a) without and (b) with J-aggregates molecules.

2.3. Near-field electromagnetic enhancement

Unlike the leaky magnetic resonant mode in silicon nanogrooves, this cavity magnetic resonant mode in germanium nanogrooves arises from the direct confinement of the incident light. When the incident light illuminates a germanium nanogroove, it will be trapped in the groove directly, which can enhance the electromagnetic field in the groove like plasmonic gap. This cavity magnetic resonant mode benefits from a large real part of the refractive index of germanium and would be not influenced by the increasing imaginary part.

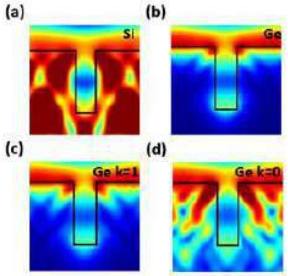


Figure 3: Simulated magnetic field distribution images of an individual 300-nm-deep dielectric nanogroove. (a) Silicon. (b) Germanium. (c) Germanium with fixed real part of the refractive index and an imaginary part k=1. (d) k=0.

3. Conclusions

In summary, we introduced a new hybrid system consisting of an individual germanium nanogroove and J-aggregates molecules showing the Kerker effect experimentally. It is the cavity magnetic resonant mode that interrelated with the electric dipole moments of molecular excitions, which is benefit from the refractive index of germanium. These findings pave a way for germanium to be used in nanophotonics devices based on its unique optic properties.

Acknowledgements

The National Basic Research Program of China (2014CB931700), The Natural Science Foundation of Guangdong Province (2016A030313339) and State Key Laboratory of Optoelectronic Materials and Technologies supported this work.

References

[1] R. Chikkaraddy, B. de Nijs, F. Benz, S. J. Barrow, O. A. Scherman, E. Rosta, A. Demetriadou, P. Fox, O. Hess, J.J. Baumberg, Single-molecule strong coupling at room temperature in plasmonic nanocavities, *Nature* 535: 127-130, 2016.

[2] S. Jahani, Z. Jacob, All-dielectric metamaterials, *Nat. Nanotechnol*. 11: 23-36, 2016.

[3] Y. Kivshar, A. Miroshnichenko, Meta-Optics with Mie Resonances, *Opt. Photonics News* 28: 24-31, 2017.

[4] Y. Huang, C. Ma, J. Yan, G. Yang, An All-dielectric Metasurface Building Block for the Kerker Effect between Excitons and Nanocavities: Germanium nanogroove, *in press*.

[5] J. Yan, C. Ma, C. Wang, G. Yang, Generating scattering dark states through the Fano interference between excitons and an individual silicon nanogroove, *Light: Sci. Appl*. 6: e16197, 2017.

Inelastic Relaxation and Thermal Properties in Strongly Coupled Plasmon-Exciton Hybrid Nano Structures

Martin Wersäll[1], Gülis Zengin[1], Jorge Cuadra[1], Tomasz J. Antosiewicz[1,2], Mikael Käll[1] and Timur Shegai[1]

[1]Department of Physics, Chalmers University of Technology, 412 96 Göteborg, Sweden
[2]Centre of New Technologies, University of Warsaw, Banacha 2c, 02 -097 Warsaw, Poland

Abstract

Nano scale light-matter interactions are an interesting topic for numerous reasons, including realization of future quantum optics/plasmonics. Recent studies have demonstrated single-particle strong coupling at ambient conditions by investigating formation of hybrid states in optical scattering spectra [1]. However, these works lack signatures of spectral hybridization in photoluminescence (PL), yet another important signature of strong coupling dynamics. Here we demonstrate mode hybridization in PL from a nanoscale system comprised by single plasmonic silver prisms embedded in layers of J-aggregated TDBC dye molecules [2].

1. Introduction

Light-matter interactions at the nanoscale play a crucial role in several spectroscopic applications. In the case of plasmon-exciton interactions, various prominent phenomena such as plasmon-mediated fluorescence, nanoscale lasing, and strong coupling are made possible which opens up new routes for further scientific development. For example, strong coupling may be useful for future single-photon nonlinearities and quantum information processing networks, which have a potential to revolutionize our present way of performing computations and data processing etc. The phenomenon of strong coupling arises when a quantum emitter strongly interacts with a resonant cavity. This strong interaction in turn leads to formation of hybrid polariton states and vacuum Rabi splitting. The notion of Rabi splitting relates to the frequency on which the cavity and emitter coherently exchange energies. It is in the limit when this frequency overcomes the rates of any other dissipation/decoherence that the system is considered to be in the strong coupling regime.

In recent years, light-matter interactions in nanoscale plasmon-exciton systems have been studied thoroughly by mainly investigating the elastic photo response. This is to determine the interaction strength via the vacuum Rabi splitting etc. Dark-field scattering enables several crucial parameters to be extracted, but to get a deeper understanding of the intrinsic dynamics of a hybrid plasmon-exciton system, the inelastic photo-response properties are vital. In order to achieve strong plasmon-exciton coupling, certain conditions need to be fulfilled. Firstly, the mode volume of the plasmonic field needs to be small. Secondly, the transition dipole moment between ground- and excited states of the matter-excitation (exciton) needs to be large.

To realize this, a thin (~ 10 nm) single crystalline silver nanoprism was chosen as a plasmonic cavity together with J-aggregated TDBC molecules as quantum emitters. Since the coupling-to-damping ratio between the cavity and emitter scales linearly with the quality factor (Q) of the cavity the single-crystallinity of the silver particles minimizes the dissipation and hence increases the quality factor. The J-aggregates are chosen since they possess a very high transition dipole moment (~ 20 Debye) together with a very narrow spectral resonance peak even at room temperature. Since the spectral resonance of the J-aggregates are positioned at 588 nm, the side length (L ~ 70 nm) of the silver nanoprisms are tuned so that the plasmon and molecular exciton resonances coincides.

To verify strong plasmon-exciton coupling on a single particle level at ambient conditions, dark-field scattering data from numerous individual hybrid structures were collected and analyzed (see Figure 1). Due to the optical diffraction limit, all particles were further studied in SEM in order to ensure that the signal actually originated from a single nanoprism. In addition, to study photoluminescence and dark-field at low temperatures the sample with hybrid structures needs to reside in a cryo-chamber under high vacuum. The system was cooled down to 4 K by utilizing vapor from liquid Helium, and both dark-field scattering and photoluminescence were studied for multitudinous single hybrid systems (see Figure 2). All data were later compared to the values acquired at room temperature in order to study the effect of environmental conditions.

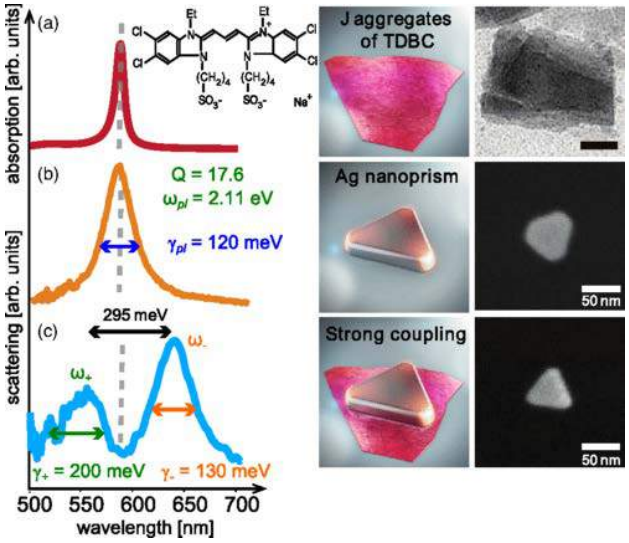


Figure 1: (a) Absorption spectrum of uncoupled J-aggregates, with depicted molecular structure of a TDBC monomer. The right columns show graphic sketch and cryo-TEM image of the molecular flakes. (b) Dark-field scattering spectrum of uncoupled plasmon resonance, together with values of quality factor (Q), resonance energy (ω_{pl}) and damping (γ_{pl}). The right columns show sketch and SEM image of corresponding plasmonic Ag nanoprisms. (c) Dark-field scattering spectrum of a strong coupled plasmon-exciton system together with values of Rabi splitting and polariton decay rates ($\gamma_{\pm}$). The right columns show a sketch of the plasmonic particle on top of the molecular sheet and a SEM image of the corresponding nanoscale system.

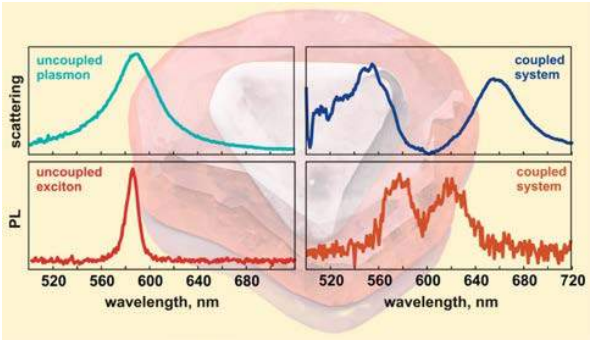


Figure 2: Dark-field scattering spectra of uncoupled (upper left) and coupled (upper right) systems, together with photoluminescence from uncoupled (lower left) and coupled (lower right) systems. The background displays a graphic sketch of the plasmonic nanoparticle embedded in a thick shell of J-aggregates.

2. Discussion

To begin with, we may discuss the data shown in Figure 1. The spectral resonance position of the exciton and plasmon is almost identical which makes the energy transfer very efficient. The resulting hybrid spectrum displays a vacuum Rabi splitting of 295 meV which exceeds both plasmon and exciton dissipation rates. Hence this data highly supports that strong plasmon-exciton coupling on a single-particle level at ambient conditions is realized in our nanostructures. The response in photoluminescence was not thoroughly studied in the work related to Figure 1. In Figure 2 a similar microscopic plasmon-exciton system (with vacuum Rabi splitting up to ~ 400 meV) displays mode hybridization both in dark-field scattering and photoluminescence. Note that the lowest energy peak corresponds to emission from the lower polariton whereas the peak highest in energy corresponds to light emitted by molecules weakly coupled to the resonant cavity. These results supports that the system can no longer be treated as neither plasmonic nor excitonic, but a mixture of both – i.e. a polaritonic system. From Figure 2 it is moreover obvious that the position of the lower polariton in photoluminescence occurs at higher energies than in dark-field scattering, which is supported by theoretical FDTD calculations.

3. Conclusions

In conclusion, our works have demonstrated strong plasmon-exciton coupling on a single particle level in both ambient and low-temperature experiments. These claims are based not only on immense vacuum Rabi splitting (~ 400 meV) extracted from dark-field scattering data, but also from formation of hybrid states in photoluminescence at cryogenic temperatures (~ 4 K). Moreover we show that photoluminescence from hybrid system exhibit significant temperature dependence. The systems under study were various sized single crystalline silver nanoprisms covered in shells of J-aggregated TDBC molecules.
These results indicate that single particle plasmon-exciton systems may play a vital role in future quantum optics operating at room temperature. In addition, the results give a more profound understanding of the intrinsic dynamics of plasmon-exciton hybrid systems.

Acknowledgements

We acknowledge financial support from the Swedish Research Council and from the Knut & Alice Wallenberg Foundation.

References

[1] G. Zengin, M. Wersäll, S. Nilsson, T.J. Antosiewicz, M. Käll, and T. Shegai. Realizing Strong Light-Matter Interactions between Single-Nanoparticle Plasmon and Molecular at Ambient Conditions, *Phys. Rev. Lett.* 114 (15): 157401, 2015.

[2] M. Wersäll, J. Cuadra, T.J. Antosiewicz, S. Balci, and T. Shegai. Observation of Mode Splitting in Photoluminescence of Individual Plasmonic Nanoparticles Strongly Coupled to Molecular Excitons, *Nano. Lett.* 17 (1): 551-558, 2016.

Local polarization of nano rectangle ring and the spontaneous emission enhancement of a circularly polarized emitter

Fan Zhang[1], Juanjuan Ren[1], Zhao Chen[1], Xueke Duan[1], He hao[1], Ying Gu[1,2], and Qihuang Gong[1,2]

[1]State Key Laboratory for Mesoscopic Physics, Collaborative Innovation Center of Quantum Matter, Department of Physics, Peking University, Beijing 100871, China
[2]Collaborative Innovation Center of Extreme Optics, Shanxi University, Taiyuan, Shanxi 030006, China
*corresponding author, E-mail: 1401110180@pku.edu.cn

Abstract

We have illustrated the electric field and local polarization of various symmetry nanostructures excited by right- and left-handed circularly polarized light. For nano rectangle ring, we find that the polarization character performs opposite corresponding to adjacent modes because of the mode coupling in it. The spontaneous emission rate of a circularly polarized emitter has a 6069-fold enhancement by the nano-ring than that in the vacuum.

1. Introduction

The enhancement of spontaneous emission at a subwavelength scale plays an important role in quantum information process such as single photon sources, nanolasers and on-chip photonic circuit. The spontaneous emission of an emitter can be modified by the local electromagnetic density of states around it [1]. In the previous works, various methods have been used to enhance spontaneous emission of a linear polarized emitter, including increasing the quality factors of photonic crystal nanocavities, using the highly localized electric field of plasmonic nanoparticles, and in the coupled plasmonic nanostructures [2, 3]. However, the modification of spontaneous emission of a circularly polarized emitter has mainly been studied in the photonic crystal. In this case, the spontaneous emission rate of a circularity polarized emitter can be enhanced by several tens of times [4], which is restrained by large mode volume of the photonic crystal. In this work, we explore the spontaneous emission enhancement of a circularly polarized emitter by various symmetry nanostructures.

The chirality of metallic nanostructures with different symmetry have been studied recently [5]. These works reveal the further applications for modifying the emission of incoherent quantum sources and chiral biophotonics sensors. Here, we focus on the Local polarization of various nano rectangle ring which have center symmetry, namely, the near-field of these nanostructures is right- or left-handed polarized when a circularly polarized light is performed to excite them. We find that, different from sphere or circle plate nanostructures, the polarization of rectangle ring is totally opposite for adjacent modes because of the mode coupling in it. Besides, the radiative spontaneous emission rate of a circularly polarized emitter is enhanced as a factor of 6069 by placing the emitter 5 nm away from the nano-ring.

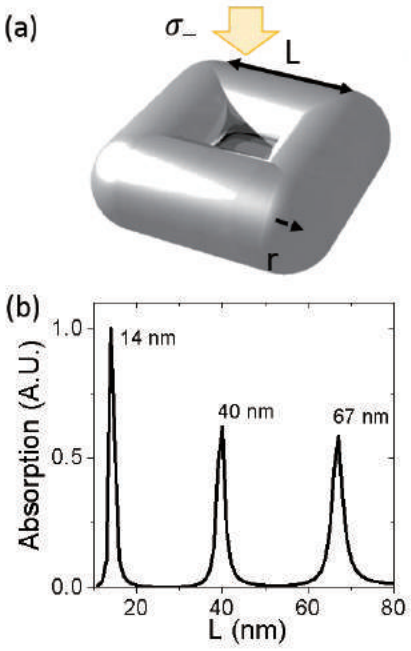


Figure 1: (a) Schematic diagram of a silver nano-rectangle ring. A clockwise polarized light in yz-plane is performed to excite it. (b) The absorption spectrum of a silver nano-rectangle ring with radius r of 5 nm.

2. Results

As shown in Fig. 1(a), the silver nano-ring is a union of four identical rod with radius r of 5 nm and length L, excited by a right handed light. The modes of the nano-ring are depicted in Fig. 1(b). We can see that the resonant length L is 14 nm, 40 nm, and 67 nm for n=1 to 3 modes.

The electric field and local polarization (defined by helicity) have been plotted in Figs. 2(a)-(d). We find that the electric field of the nano-ring is located in the corner for both n=1 and 2 modes. However, the local helicity of these two modes in vicinity of the nano-ring are different because

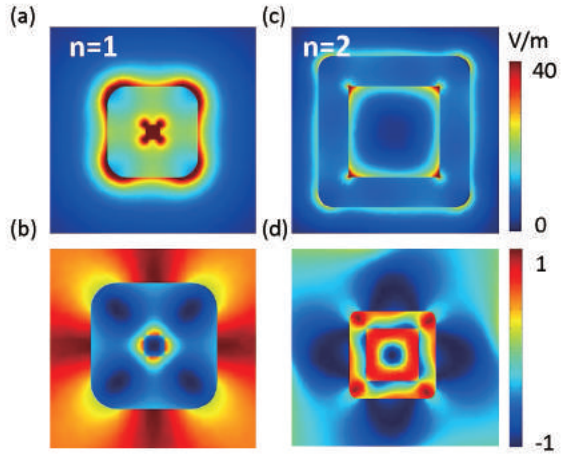


Figure 2: The electric field (a) and local polarization (b) distributions of a nano-ring for n=1 mode. The electric field (c) and local polarization (d) distributions of a nano-ring for n=2 mode. The local polarization arround the nano-ring of these two modes are different.

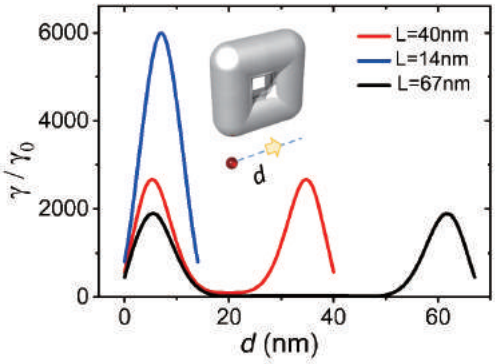


Figure 3: The spontaneous emission rate enhancement of a σ_- emitter as a function of distance L. The emitter is placed 5 nm away from the nano-ring.

of the mode coupling. The helicity of the higher mode has the same chirality with the excited field while the n=1 mode has opposite chirality.

Further, we calculate the spontaneous emission rate enhancement of a σ_- emitter as a function of distance d for various modes. The distance between the emitter and the surface of the nano-ring is 5 nm. As seen in Fig. 3, the spontaneous emission rate when the emitter in vicinity of a nano-ring with n=1-3 mode is 6069, 2747, and 2004 times larger than that in the vacuum. The positions of maximal enhancement is near the corners of the nano-ring because of the maximal localized electric field.

3. Conclusions

We have illustrated the electric field and local polarization of various symmetry nanostructures excited by right- and left-handed circularly polarized light. For nano rectangle ring, we find that the local polarization is opposite for adjacent modes because of the mode coupling. The spontaneous emission rate of a circularly polarized emitter has a 6069-fold enhancement by the nano-ring than that in the vacuum.

Acknowledgement

This work was supported by the National Natural Science

Foundation of China (NSFC) under Grants No. 11525414, No. 11734001, No. 11704013 and by China Postdoctoral Science Foundation under Grant No. 2017M620493.

References

[1] E.M. Purcell, Spontaneous emission probabilities at radio frequencies Phys. Rev. 69, pp. 681, 1946.

[2] M. Ringler, A. Schwemer, M. Wunderlich, A. Nichtl, K. Krzinger, T.A. Klar and J. Feldmann, Shaping emission spectra of fluorescent molecules with single plasmonic nanoresonators, Phys. Rev. Lett. 100, 203002, 2008.

[3] H. Lian, Y. Gu, J. Ren, F. Zhang, L. Wang and Q. Gong, Efficient single photon emission and collection based on excitation of gap surface plasmons, Phys. Rev. Lett. 114, 193002, 2015.

[4] M. Sahand, P-N. Kasper, S. Immo, S. Søren, Engineering chiral lightCmatter interaction in photonic crystal waveguides with slow light, Opt. Mater. Express 7, 43 2017.

[5] B. Hopkins, A. N. Poddubny, A. E. Miroshnichenko, and Y. S. Kivshar, Circular dichroism induced by Fano resonances in planar chiral oligomers, Laser Photonics Rev. 10, 137, 2016.

Surface electromagnetic waves in a semiconductor with strong magnetic field

Igor Bychkov[1,2], Dmitry Kuzmin[1,2], Valentin Tolkachev[1], Vladimir Shavrov[3] and Vasily Temnov[4,5]

[1]Chelyabinsk State University, 129 Br. Kashirinykh Str., Chelyabinsk 454001, Russian Federation
[2]South Ural State University (National Research University), 76 Lenina Ave., Chelyabinsk 454080, Russian Federation
[3]Kotelnikov Institute of Radio-Engineering and Electronics of RAS, 11/7 Mokhovaya Str., Moscow 125009, Russian Federation
[4]Institut des Molécules et Matériaux du Mans, CNRS UMR 6283, Université du Maine, 72085 Le Mans Cedex, France
[5]Groupe d'Etude de la Matiere Condensée (GEMaC), Université de Versailles-Saint Quentin en Yvelines, CNRS UMR 8635, Université Paris-Sacley, 45 avenue des Etats-Unis, 78035 Versailles Cedex, France
*corresponding author, E-mail: bychkov@csu.ru

Abstract

The propagation of surface electromagnetic waves along the surface of semiconductor in strong magnetic fields (so-called surface helicons) is studied. Conditions for the existence of surface helicons at the vacuum - semiconductor boundary are obtained. Dependence of the refractive index and the damping coefficients of surface helicon on the angle between the direction of propagation of the wave and the magnetic field is calculated.

1. Introduction

Semiconductors have unique properties due to the existence in them of the electronic and dipole subsystems. Many of these properties can be used and implemented in practice: the creation of different systems of information processing, delay lines, filters, new element base of micro and nanoelectronics, plasmonic and spintronics. In semiconductors there are quasiparticles of a new type, there is a phase separation in the ground state, the special properties exhibit magnetoresistance, etc. When creating microstructures on their base the important role played by physical processes occurring on the surface. These include effects associated with the peculiarities of excitation and propagation of surface electromagnetic waves.

In this paper, we investigate the propagation of surface electromagnetic waves along the surface of the magnetic semiconductor in strong magnetic fields, the so-called surface helicons. Here we obtain conditions of the existence of the surface helicons at the vacuum – semiconductor interface. Dependence of the refractive index and attenuation coefficients of surface helicons on the angle between the direction of wave propagation and the magnetic field has been calculated.

1. Theory

We investigate the propagation of surface electromagnetic waves in the XZ plane in the structure of the vacuum – semiconductor interface, which is shown in Figure.1. The external magnetic field **H** is directed along the **z** -axis, θ is the angle between the magnetic field and wave vector of the surface waves **k**. In this geometry, the tensors of permittivity and permeability have the following form:

$$\hat{\varepsilon} = \begin{pmatrix} \varepsilon_{\perp} & i\varepsilon_a & 0 \\ -i\varepsilon_a & \varepsilon_{\perp} & 0 \\ 0 & 0 & \varepsilon_{\parallel} \end{pmatrix}, \quad (1)$$

$$\hat{\mu} = \begin{pmatrix} \mu_{\perp} & i\mu_a & 0 \\ -i\mu_a & \mu_{\perp} & 0 \\ 0 & 0 & \mu_{\parallel} \end{pmatrix}, \quad (2)$$

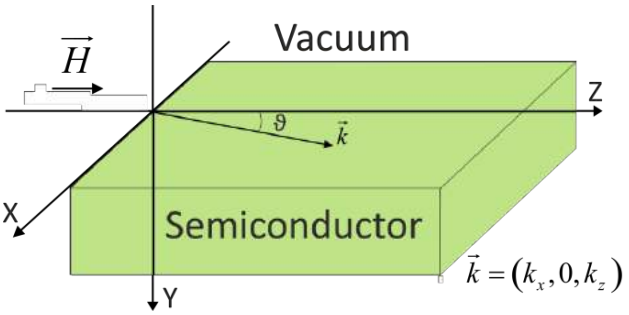


Figure 1: Geometry of the problem.

Here we have taken into account the tensor of magnetic permeability for a more general solution of the problem and a more precise modelling of the magnetic semiconductor properties. Solution of the system of Maxwell's equations for surface waves in the geometry given by Figure 1 shows that the along the semiconductor-vacuum interface two surface electromagnetic waves of different polarization can propagate, with the same propagation constant but different localization parameters γ_1, γ_2 which are determined by the equation:

$$\left(n_x^2 + a_e n_z^2 - b_e - \gamma^2\right)\left(n_x^2 + a_m n_z^2 - b_m - \gamma^2\right) - \\ -c_e c_m n_z^2 = 0 \quad (3)$$

where

$n_x = k_x/k_0 = n\sin\theta$, $n_z = k_z/k_0 = n\cos\theta$, $k_0 = \omega/c$, $a_e = \varepsilon_{\|}/\varepsilon_{\perp}$, $b_e = \varepsilon_{\|}/\mu_{\perp}$, $a_m = \mu_{\|}/\mu_{\perp}$, $b_m = \mu_{\|}/\varepsilon_{\perp}$, $c_e = \mu_{\|}\left(\varepsilon_a/\varepsilon_{\perp} + \mu_a/\mu_{\perp}\right)$, $c_m = \varepsilon_{\|}\left(\varepsilon_a/\varepsilon_{\perp} + \mu_a/\mu_{\perp}\right)$, $\varepsilon_{\perp} = \varepsilon_0 - \omega_p^2/\left(\omega^2 - \omega_H^2\right)$, $\varepsilon_a = -\omega_p^2\omega_H/\omega\left(\omega^2 - \omega_H^2\right)$, $\varepsilon_{\|} = \varepsilon_0 - \omega_p^2/\omega^2$, $\mu_{\perp} = 1 + \omega_g\omega_M/\left(\omega_g^2 - \omega^2\right)$, $\mu_{\|} = 1$, $\mu_a = \omega\omega_M/\left(\omega_g^2 - \omega^2\right)$, $\omega_p = \sqrt{4\pi Ne^2/m_e}$, $\omega_H = eH/m_e c$, $\omega_g = g\left(H + \beta M\right)$, $\omega_M = 4\pi gM$. Where ε_0 is a lattice dielectric constant, ω is the angular frequency, c is speed of light in vacuum, ω_p is the plasma frequency, ω_H is the cyclotron frequency, ω_M is the magnetostatic frequency, ω_g is the frequency of spin waves, g is the gyromagnetic ratio, M is the magnetization, β is an anisotropy constant, m_e is an electron mass, N is the carriers concentration.

Solving the system of Maxwell equations and boundary conditions, we obtain a dispersion equation for surface electromagnetic waves at the vacuum-semiconductor interface. For the polarization of a wave with H_z=0, the dispersion equation has the form

$$\mu_{\|} n_z^2 \left[\begin{array}{l} n_x\varepsilon_{\perp} - \gamma_0\left(\varepsilon_{\perp}\mu_a + \mu_{\perp}\varepsilon_a\right) - \\ -n_x\mu_{\perp}\left(\varepsilon_{\perp}^2 - \varepsilon_a^2\right) \end{array}\right] + \\ + \varepsilon_{\perp} n_x \left[\begin{array}{l} \left(\mu_{\perp}^2 - \mu_a^2\right)\left(\varepsilon_{\|}\gamma_0 + \gamma_1 + \gamma_2\right)\gamma_0 + \\ +\mu_{\perp}\gamma_1\gamma_2 \end{array}\right] + \\ + \varepsilon_{\perp} n_x^3\left[\mu_{\perp} - \varepsilon_{\|}\left(\mu_{\perp}^2 - \mu_a^2\right)\right] + \\ + \varepsilon_{\perp}\mu_a n_x^2(\gamma_1 + \gamma_2) = 0 \quad (4)$$

where $\gamma_0 = \sqrt{n^2 - 1}$ describes localization of electromagnetic wave in a vacuum.

To obtain the dispersion equation for a wave with polarization E_z=0, it is necessary to make the substitution $\mu \to \varepsilon, \varepsilon \to \mu$ in equation. (4). From equations (3) and (4) with known parameters of the material (semiconductor), it is possible to determine the conditions for the existence of surface electromagnetic waves, their spectrum, propagation constants and attenuation coefficients, and other wave parameters.

In earlier work [1] conducted the study of surface helicons in semiconductors, some results were obtained for low frequencies. We study a higher frequency region and larger fields. Let us consider not a magnetic semiconductor, i.e. we put $\mu_{ij} = \delta_{ij}$. The conditions for the existence of surface helicons have the form $\left|\varepsilon_{\|}\right| >> \left|\varepsilon_a\right| >> \left|\varepsilon_{\perp}\right|$, $\left|\varepsilon_{\|}\varepsilon_{\perp}\right| >> \left|\varepsilon_a^2\right|$, $\omega << \omega_H << \omega_p$.

The study of the propagation of surface helicons at the vacuum semiconductor boundary is carried out, the spectrum of surface helicons is investigated as a function of the magnitude of the external magnetic field, the frequency, and the angle between the magnetic field and the wave vector of the wave. The characteristics of the surface wave for various semiconductors are also calculated (depending on the effective mass of the charge carriers). As an example let us model the propagation of surface helicons in a semiconductor InSb with ε_0 = 16, carrier concentration N=5 10^{14} см$^{-3}$. From the joint solution of equations (3) and (4), angular dependences of the propagation constants of surface helicons are obtained Figure 2. It can be seen from the graphs that helicons with different polarization of the electromagnetic field can propagate only at certain angles to the magnetic field.

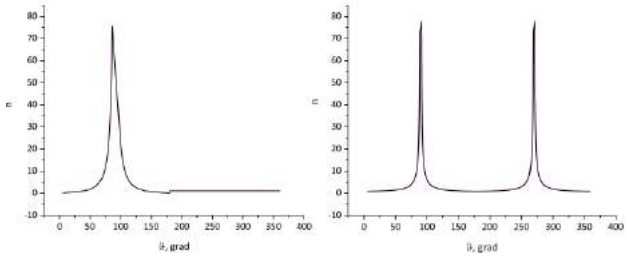


Figure 2: Dependence of the wave propagation constant on the angle between **k** and **H** for the polarizations of waves with E_z=0 (left panel) and with H_z=0 (right panel). H=5·10^{4}Oe, ω=10^{11}s^{-1}.

2. Conclusions

The dispersion equation for surface helicons is obtained in the case of an arbitrary direction of the wave vector in the wave propagation plane. The spectrum of surface helicons, the values of the propagation constants and localization coefficients are calculated as a function of the angle between the direction of propagation of the wave and the magnetic field. It is determined that surface helicons can propagate near the $\theta = \pi/2$ angle for waves with polarization at $E_z = 0$ and near the angles $\theta = \pi/2$ and $\theta = (3/2)\pi$ for waves with $H_z = 0$.

Acknowledgements

The work was financially supported in part by RFBR (16-07-00751, 16-29-14045, 17-57-150001), RScF (14-22-00279), Grant of the President of the RF (MK-1653.2017.2), Act 211 Government of the Russian Federation (contract № 02.A03.21.0011), Stratégie international NNN-Telecom de la Région Pays de La Loire, PRC CNRS-RFBR "Acousto-magneto-plasmonics".

References

[1] V.L. Fal'ko, S.I. Khankina, V.M. Yakovenko, Surface magnetoplasma waves in a ferromagnetic semiconductor and their excitation by a magnetic dipole, Semiconductors 34: 680 – 685, 2000.

Large Enhancement of the Goos-Hänchen shift and Fragmentation of the Reflected Beam due to the Excitation of Surface Plasmons

Sangbum Kim and Kihong Kim*

Department of Energy Systems Research and Department of Physics, Ajou University, Suwon, Korea
*corresponding author, E-mail: khkim@ajou.ac.kr

Abstract

It is shown theoretically that, when a p wave Gaussian beam is incident on a metal-dielectric boundary and excites surface plasmons, the Goos-Hänchen shift can be enhanced greatly. The maximum size of the negative Goos-Hänchen shift is shown to decrease as the beam width decreases. The spatial distribution of the field intensity associated with the reflected beam shows that there appears a fragmentation of the reflected beam when the width of the incident beam is sufficiently small.

1. Introduction

It has been shown previously that when surface plasmon polaritons are excited, the Goos-Hänchen shift Δ of an incident p wave beam, which is the lateral shift of the reflected beam along the interface with respect to the incident beam, can take extremely large values [1–3]. This result was obtained using the Artmann formula

$$\Delta = -\frac{d\Phi}{dq}, \tag{1}$$

where q is the component of the wave vector along the interface and Φ is the phase of the reflection coefficient for incident plane waves. In this paper, we revisit this problem and calculate the Goos-Hänchen shift directly for a Gaussian slab beam with a finite width using the invariant imbedding method, but without using the Artmann formula. We find that the Goos-Hänchen shift at the incident angle where surface plasmons are excited remains extremely large for reasonable values of the beam width. In addition, we find that when the width of the incident beam is sufficiently small, the reflected beam shows a fragmentation into two.

2. Method

We consider a p wave Gaussian (slab) beam with a finite half-width W propagating in the xz plane. The amplitude of the y component of the magnetic field associated with the incident beam, $H_y^{(i)}$, is written as

$$H_y^{(i)}(x,z) = H_0 \exp\left[-\frac{x^2}{W_x^2} + i\left(k_z z + k_x x\right)\right], \tag{2}$$

where W_x $(= W\sec\theta)$ is the half-width in the x direction and θ is the incident angle. This field is transformed into a k-space by taking a Fourier transform:

$$\widetilde{H}_y = \frac{1}{\sqrt{2\pi}} \int H_y^{(i)}(x,z) \exp\left[-i\left(k_z z + k_x x\right)\right] dx, \tag{3}$$

where $k_x = k\sin\theta$. The center of the incident Gaussian beam is at $x = 0$ in the $z = 0$ plane. The amplitude of the reflected field is given by

$$H_y^{(r)}(x,z) = \frac{1}{\sqrt{2\pi}} \int r(k_x)\widetilde{H}_y(k_x) \exp\left(-ik_z z + ik_x x\right) dk_x, \tag{4}$$

where the reflection coefficient $r(k_x)$ is obtained for incident plane waves as a function of θ. In order to obtain the spatial profile of the reflected beam, we need to calculate the reflection coefficients corresponding to all values of k_x using the invariant imbedding method described in detail in [2,4] and perform a numerical integration.

The Goos-Hänchen shift for the reflected beam is obtained by

$$\Delta = \frac{\int x \left|H_y^{(r)}(x,z)\right|^2 dx}{\int \left|H_y^{(r)}(x,z)\right|^2 dx}. \tag{5}$$

The spatial profile of the reflected beam will be modified when the half-width of the incident beam is sufficiently

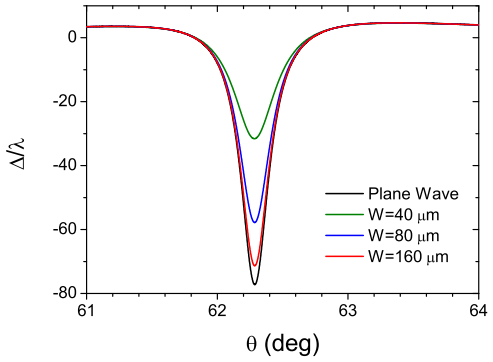


Figure 1: Goos-Hänchen shift for the reflected beam versus incident angle for several values of the half-width of the incident beam. The black line is the Goos-Hänchen shift for a plane wave.

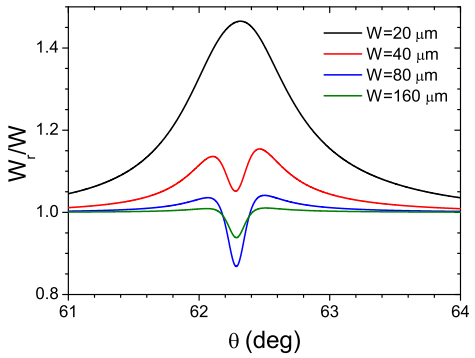


Figure 2: Ratio of the half-widths of the reflected beam and the incident beam versus incident angle for several values of the half-width of the incident beam.

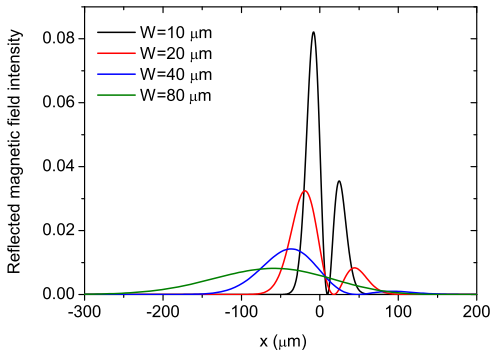


Figure 3: Spatial profile of the magnetic field intensity associated with the reflected beam at $\theta \approx 62.3^\circ$ for several values of the half-width of the incident beam.

small. This effect can be measured by calculating the second moment of the field amplitude defined by

$$\beta = \frac{4\int (x-\Delta)^2 \left|H_y^{(r)}(x)\right|^2 dx}{\int \left|H_y^{(r)}(x)\right|^2 dx}. \quad (6)$$

The half-width of the reflected beam can be written as

$$W_r = \sqrt{\beta}\cos\theta. \quad (7)$$

3. Results

In the numerical calculation, we consider the Otto configuration studied previously in [2]. The beam is incident from a prism onto a dielectric-metal bilayer which lies on a dielectric substrate. The refractive indices of the prism and the dielectric layer are 1.77 and 1.46 respectively. The dielectric constant of the metal layer at 633 nm wavelength is assumed to be $-16+i$, which is the value for silver. The refractive index of the substrate is assumed to be equal to 1.77. The thicknesses of the dielectric and metal layers are 320 nm and 50 nm respectively.

In Fig. 1, we plot the Goos-Hänchen shift for the reflected beam as a function of the incident angle for several values of the half-width of the incident beam. We find that for reasonable values of W, the size of the negative lateral shift at the incident angle $\theta \approx 62.3^\circ$ where surface plasmons are excited remains to be much larger than the wavelength. It decreases as the beam width decreases. This result confirms that the negative Goos-Hänchen shift for a realistic beam can be as large as $80\lambda \approx 50$ μm.

In Fig. 2, we plot the ratio of the half-widths of the reflected beam and the incident beam versus incident angle for several values of the half-width of the incident beam. We observe that at $\theta \approx 62.3^\circ$, this ratio can be bigger or smaller than 1 and shows a non-monotonic dependence on W.

In Fig. 3, we show the spatial distribution of the magnetic field intensity associated with the reflected beam at $\theta \approx 62.3^\circ$ for several values of the half-width of the incident beam. We find that when the half-width of the incident beam is smaller than about 40 μm, the reflected beam is fragmented into two parts. The fragmentation disappears as the half-width of the incident beam increases.

4. Conclusion

Using the invariant imbedding method, we have studied theoretically the Goos-Hänchen shift of a p wave Gaussian slab beam incident on a metal-dielectric boundary. At the incident angle where surface plasmons are excited, we have found that the Goos-Hänchen shift can be enhanced greatly. We have also found that the reflected beam shows a fragmentation into two parts when the width of the incident beam is sufficiently small. An experimental confirmation of the presented results will be of great interest.

References

[1] L. Chen, Z. Cao, F. Ou, H. Li, Q. Shen, H. Qiao, Observation of large positive and negative lateral shifts of a reflected beam from symmetrical metal-cladding waveguides, *Opt. Lett.* 32: 1432–1434 (2007).

[2] K. Kim, D.K. Phung, F. Rotermund, H. Lim, Strong influence of nonlinearity and surface plasmon excitations on the lateral shift, *Opt. Express* 16: 15506–15513, 2008.

[3] K. Kim, Large enhancement of nonlinear Goos-Hänchen shifts and optical bistability due to surface plasmon excitations, *J. Korean Phys. Soc.* 67: 2092–2095 (2015).

[4] K. Kim, D.K. Phung, F. Rotermund, H. Lim, Propagation of electromagnetic waves in stratified media with nonlinearity in both dielectric and magnetic responses, *Opt. Express* 16: 1150–1164 (2008).

Near-field coupling and mode competition in anapole system

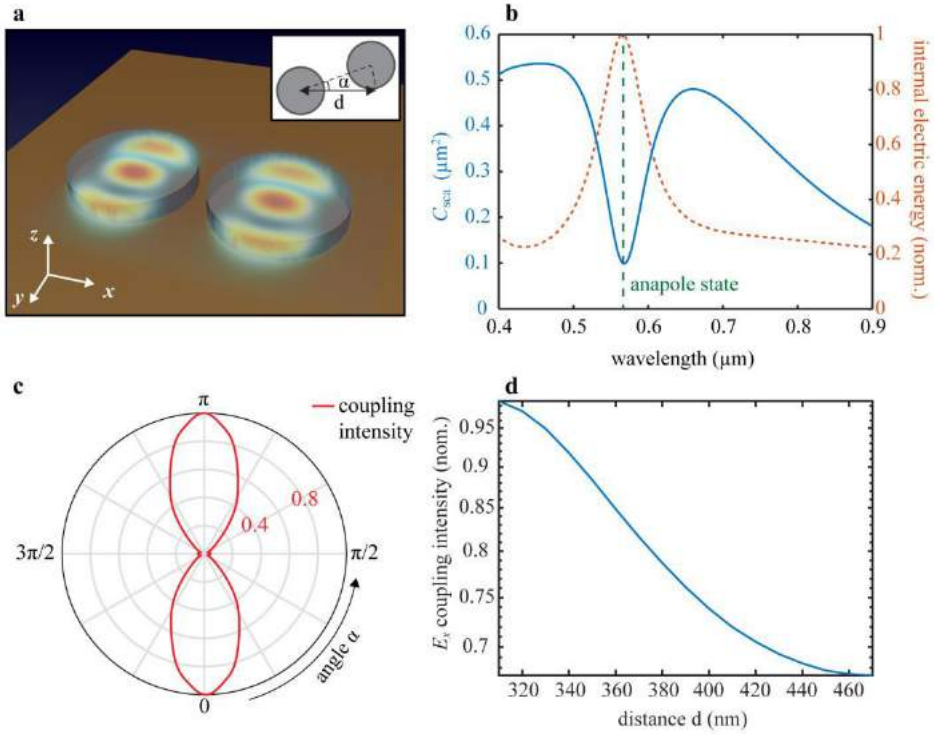
V. Mazzone[1], J. S. Totero[1*], and A. Fratalocchi[1]

[1]PRIMALIGHT, Faculty of Electrical Engineering; Applied Mathematics and Computational Science, King Abdullah University of Science and Technology, Thuwal 23955-6900, Saudi Arabia

*Correspondence: andrea.fratalocchi@kaust.edu.sa

Abstract- Inspired by recent progress in the development of an integrated near-field based laser source, we designed a new scheme for optical guiding at the nanoscale. Our approach leverages the near-field and the scattering-free nature of anapole-state to exploit an effective waveguide functionality. In principle, should not be possible to transfer an anapole state among different subwavelength nanoparticles. However, our results show how, exploiting the interference nature of anapoles, it is possible to couple light in an effective and robust fashion.

The simplest system able to exhibits anapole mode at optical frequency are high-refractive index subwavelength nanoparticles. By precisely adjusting the material and the shape of the nanostructures is possible to obtain advanced functionalities such as anti-reflective surfaces or integrated waveguides made by nanoparticles chains. Recently the study of multiple system of anapoles and their interaction have unclosed the possibility to fabricate nanoscale laser, exploiting the near-filed properties of the anapole mode [1]. Regardless of the many schemes proposed for the manipulation of light at the nanoscale, the effectively coupling of light through optical structures is still a crucial challenge. The interaction and the coupling along a chain of anapole nanoparticle is still to be explored. Guiding properties have been showed to be reasonable in plasmonic nanochains [2,3]. However, the presence in these systems of metals have moved the attention of researchers to all dielectric solutions based on high-refractive index nanoparticles [4]. In principle anapoles states should not couple to each other, due to their non-resonant nature. Recently anapole states have been re-explained as a Fano interference between resonant states in the proximity of the anapole wavelength [5]. In this work, we show how an anapole state can be effectively transferred among distinct nanoparticles. Our results play a key role in the development of integrated optical circuitry based on non-radiating states (e.g., anapole-based wave-guides). Waveguides based on these scattering free states are extremely robust against physical bending and splitting, opening to the realization of high-density optical circuitry based on silicon.



Mutual coupling of non-radiating anapole states. **a** Near-field coupling between two silicon nanodisks (n = 3.5) excited at the anapole wavelength λ_{an} = 568 nm. (inset) The dielectric resonators are mutually displaced by a centre-to-centre distance d and by an angle α. **b** Scattering cross-section C_{sca} (blue line) and internal electric energy (orange dotted line) as a function of the incident wavelength λ. The anapole state (green-dashed line) is characterized by the simultaneous suppression of the scattering cross-section and by a strong enhancement of the internal field intensity. **c** Coupled electric energy as a function of the rotation angle α (d = 450 nm). The mutual coupling is maximum at $\alpha = 0, \pi$ and negligible at $\alpha = \pi/2, 3\pi/2$. **d** Coupled electric energy as a function of the mutual distance d. The results correspond to the angular condition of maximum scattering $\alpha = 2\pi$.

REFERENCES

1. Totero Gongora, J.S.; Miroshnichenko, A.E.; Kivshar, Y.S.; Fratalocchi, A. Anapole nanolasers for mode-locking and ultrafast pulse generation. Nat. Commun. **2017**.
2. Brongersma, M.L.; Hartman, J.W.; Atwater, H.A. Electromagnetic energy transfer and switching in nanoparticle chain arrays below the diffraction limit. Phys. Rev. B **2000**, 62, R16356–R16359.
3. Totero Gongora, J.S.; Fratalocchi, A. Harnessing Disorder at the Nanoscale. In Encyclopedia of Nanotechnology; Bhushan, B., Ed.; Springer Netherlands: Heidelberg, Germany, 2015; pp. 1–13.
4. Bakker, R.M.; Yu, Y.F.; Paniagua-Domínguez, R.; Luk'yanchuk, B.; Kuznetsov, A. Silicon Nanoparticles for Waveguiding. Frontiers in Optics; Optical Society of America: Washington, DC, USA, 2015; p. FM1B.2.
5. Gongora, J.S.T.; Favraud, G.; Fratalocchi, A. Fundamental and high-order anapoles in all-dielectric metamaterials via Fano–Feshbach modes competition. Nanotechnology **2017**, 28, 104001.

Holographic tracking for real-time spectroscopy of moving nanoparticles

Minh-Chau Nguyen [1,2], Pascal Berto[1], Fabrice Valentino [1], Catherine Combellas[2], Frédéric Kanoufi[2], and Gilles Tessier[1,3*]

[1] Sorbonne Paris Cité, Université Paris Descartes, Neurophotonics Laboratory, CNRS UMR 8250, Paris, France
[2] Sorbonne Paris Cité, Université Paris Diderot, ITODYS Laboratory, CNRS UMR 7086, Paris, France
[3] Sorbonne Université, CNRS, Institut de la Vision, Paris, France
*corresponding author, E-mail: gilles.tessier@parisdescartes.fr

Abstract

The scattering spectrum of nanoparticles can reveal their behavior as well as their chemical and physical properties. However, the spectral study of an individual NP in solution is extremely difficult due to its Brownian motion. Here, we present a system based on digital holographic microscopy which localizes a moving nanoparticle with sub-diffraction accuracy in real-time and uses its localization to drive an adaptive optical system and redirect the light scattered by the moving nano-object towards the spectrometer.

1. Introduction

Because of their high reactivity, metal NanoParticles (**NPs**) provide various promising applications such as catalysis, cancer treatment,... Many of their properties depend on their electrochemical behavior. At the macroscopic scale, nanoparticle properties are averages over many individual NPs, which can actually differ strongly. Studying electrochemistry at the single particle scale is therefore crucial, as well as challenging. Since the beginning of 21st century, by reducing the electrode size, electrochemists managed to observe an electron transfer between a single NP and an electrode [1]. However, this electrochemical signal does not provide sufficient information about the physical behavior of individual NPs. Consequently, other observations are needed to obtain a more profound understanding of the electrochemical properties of NP, for example, optical observation [2, 3].

The light scattered by a white light illuminated NP can reveal valuable information since its spectrum is driven by the particle size, morphology and composition, but also by the nature of its surrounding medium. Unfortunately, spectral studies of single NPs in situ are extremely difficult due to their Browian motion. We have developed a **3D spectro-electrochemistry nanoscope** which adds spectral observation to (electro)chemical reaction monitoring. We can now track a single gold NP in real time, and measure its spectrum. As a result, the interaction between a single NP and its environment can be detected *in situ*.

2. Experiment Setup - Development

To measure the spectrum of an individual NP, we need to collect light over one small zone in the object plane while rejecting other regions. For this reason, we use an optical fiber to collect the signal for the spectrometer. However, in the case of a moving NP, the position varies during the experiment, which forbids spectral information collection. We have designed an adaptive optical system which allows to redirect the light scattered from NP toward the spectrometer wherever it is located in the field of view. Our adaptive optical system contains 2 galvanometric mirrors for the correction of lateral displacement and a dynamic lens having a variable focal length for the correction of axial displacement.

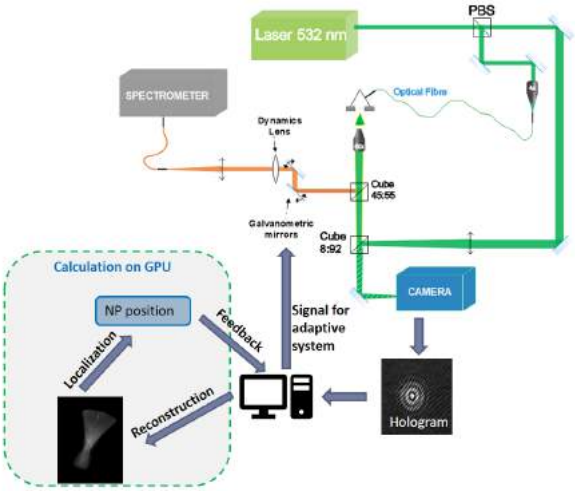


Figure 1: **Experimental setup:** A hologram is acquired from a basic setup of digital holographic microscopy. From the CPU, the hologram is transfered to GPU for the digital analysis in order to localize the NP. Its position is used as a feedback for the adaptive optical system.

Using **digital holographic microscopy (DHM)**, we are able to reconstruct in 3D the electromagnetic field scattered by single nano-objects. From this reconstruction, NPs can be localized in real time with sub-diffraction precision (up to 3x3x10 nm^3 with a SNR of 70). The numerical analysis of the hologram, that consists of several 2D Fourier transformations of images 512x512 and an algorithm of localisation, can be determined in 200ms on a CPU. By transfering the calculation on a Graphics Processing Unit (GPU), we can now reduce the calculation

time to 10ms which allows us to track a NP in real-time.

From the position of the NP, the electrical signals applied to the adaptive optical system are obtained using a matrix of transformation calculated by the linear least squares regression, and are sent to the mirrors and dynamic lens (**Figure 1**). In real-time, even if the particle moves, the light scattered by the NP is redirected to a fixed position where it can be collected by a spectrometer.

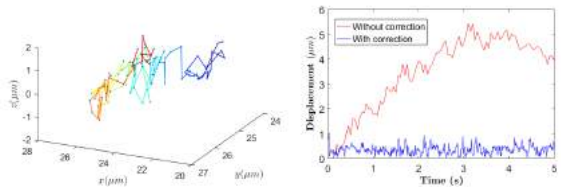
3. Results – Discussion

3.1. Validation of the adaptive optical system

We prepared a solution of 100nm gold NP (Sigma Aldrich) and glycerol at 3:1 volume fraction to obtain a solution of gold NPs with viscosity of 2cP.

To validate the tracking system, a camera was installed in the image plane of the particle, after the adaptive optics. The 3D tracking of a moving NP is illustrated in **Figure 2a**. The position of the particle is shown in **Figure 2b** with or without tracking : the particle remains in focus and centered on the camera with $\pm 0.5 \mu m$, but drifts and defocuses when the tracking is off.

This proves that our adaptive optical system is able to follow and redirect the light scattered by a moving NP toward a defined position, where the optical fiber is installed.



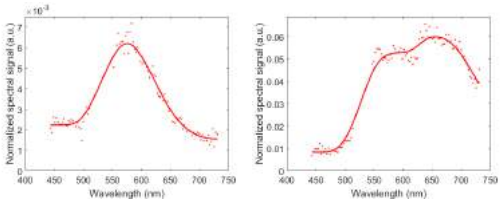
(a) (b)

Figure 2: **(a)** 3D tracking of a 100nm NP in solution **(b)** The displacement of the NP in the plane of the camera without correction(red line), and with correction by the adaptive optical system(blue line,)

3.2. Real-time spectroscopy

Having validated the tracking and adaptive optics, we acquired the spectrum and the 3D position of NPs. In **Figure 3**, we show the spectra of two systems. In the **Figure 3a**, the spectrum show a NP resonance at about 580nm which corresponds to the localized surface plasmon resonance band of the 100nm gold NP. Mean square displacement analysis provides the hydrodynamic diameter of NP about 110nm which corresponds to an individual NP in solution.

In the other spectrum (**Figure 3b**), another band appears at about 660nm. In addition, the light scattered from this nano-object is more intense than the one in Figure 3a, and a size of about 220nm is deduced from the mean squared displacement, reveals : the particle is most likely an aggregate.



(a) (b)

Figure 3: The spectra was recorded while the particle was in Brownian motion. **(a)** Spectrum of a 100nm gold NP **(b)** Spectrum of an aggregate

The matching of the 3D tracking and the spectrum of NP has proved our system's ability to track and acquire the spectrum of moving NPs.

4. Conclusions

In this paper, we demonstrate a system able to track and measure the spectrum of single moving NPs in real-time. The spectral information brings another observation in order to understand the behavior of an individual NP in solution. This work opens a path to the long acquisition of small effects (e.g. NP enhanced SERS). It should find applications in cases where either the properties of the NP, or of its environment, need to be monitored, e.g. in chemistry or biology. Associated to nanometer precision tracking, it will soon be able to reveal ultralocal chemical properties.

Acknowledgement

This work was supported by "Agence Nationale de la Recherche" (NEOCASTIP ANR-CE09-0015-01). M.C.N thanks Université Paris Sorbonne Cité for funding.

References

[1] X. Xiao and A. J. Bard, "Observing single nanoparticle collisions at an ultramicroelectrode by electrocatalytic amplification," *Journal of the American Chemical Society*, vol. 129, no. 31, pp. 9610–9612, 2007. PMID: 17630740.

[2] V. Brasiliense, A. N. Patel, A. Martinez-Marrades, J. Shi, Y. Chen, C. Combellas, G. Tessier, and F. Kanoufi, "Correlated electrochemical and optical detection reveals the chemical reactivity of individual silver nanoparticles," *Journal of the American Chemical Society*, vol. 138, no. 10, pp. 3478–3483, 2016. PMID: 26900633.

[3] C. Batchelor-McAuley, A. Martinez-Marrades, K. Tschulik, A. N. Patel, C. Combellas, F. Kanoufi, G. Tessier, and R. G. Compton, "Simultaneous electrochemical and 3d optical imaging of silver nanoparticle oxidation," *Chemical Physics Letters*, vol. 597, pp. 20 – 25, 2014.

Full control of near-field dipolar coupling beyond spin-momentum locking

Michela F. Picardi, Lei Wei, Jack J. Kingsley-Smith, Anatoly V. Zayats, and Francisco J. Rodríguez-Fortuño*

[1]Department of Physics, King's College London. The Strand. WC2R 2LS, London, United Kingdom
*corresponding author, E-mail: francisco.rodriguez_fortuno@kcl.ac.uk

Abstract

Unidirectional coupling of circularly polarized dipoles into photonic structures has opened the way to the design of novel devices such as polarization-based nano-routers, integrated Stokes nano-polarimeters, and non-reciprocal optical devices. Here we propose an extension to the directionality of dipolar near-fields, uncovering novel directional sources that exhibit distinct symmetries and behaviors. We provide a complete analytical theory of dipolar near-field directionality in planar slabs.

1. Introduction

Unidirectional scattering from circularly polarized dipolar nanoscale sources has been recently achieved experimentally in near-field optics. The phenomenon is based on spin-momentum locking involving circularly polarised electric or magnetic dipoles [1], [2]. It is a robust and broadband phenomenon which has enabled fascinating applications such as quantum spin state readout [3], optical nano-routers [1], [4], nano-polarimeters [5]–[7] and non-reciprocal optical devices [8], [9].

Spin-momentum locking is a manifestation of the quantum spin-Hall effect of light [10]. It applies to near-field evanescent waves, showing that their transverse spin polarization is locked to their propagation direction. This locking of spin and momentum dictates that a circularly polarized dipole emitter will scatter directionally into a nearby waveguide [11].

Experimentally, dipolar sources can be realized via nanoscale emitters (e.g. quantum dots), or via illuminated atoms, molecules or nanoparticles with strong dipole-like scattering. In particular, nanoparticle scatterers can be realized with strongly resonant plasmonic or high-index dielectric nanoparticles, supporting electric and/or magnetic dipolar resonances.

The above phenomena and applications were realized via circularly polarized electrical or magnetic dipoles. These rely on the phase and amplitude relation between different components of the electric or magnetic fields of waveguide modes: however, the relative phase and amplitude relation between electric and magnetic fields in near fields can be exploited further, so that near-field dipolar directionality can be achieved beyond spin-momentum locking, via the appropriate use of combined electric and magnetic dipoles. In this work we explore this possibility and arrive at a general theory of dipolar sources exhibiting near-field directionality for planar geometries, uncovering novel types of directional dipoles with unique symmetries, very different to those of circularly polarized sources, opening up new avenues for near-field directionality.

2. Elemental directional dipole sources

All possible directional near field sources (i.e. sources which can scatter directionally into nearby waveguides) in a planar geometry can be written as linear superpositions of three simple cases. The behavior of these three elemental dipoles for near-field directionality is shown in Fig. 1. The first one, Fig 1(a), is the well-known circular electric or magnetic dipole, exciting modes unidirectionally thanks to spin-momentum locking of near fields. The second one, Fig 1(b), is the Huygens dipole, a combination of orthogonal electric and magnetic dipoles with a ratio of $p = m/c$ in their amplitudes (where c is the speed of light). This dipole source is well known to radiate directionally in the far-field, due to it being associated with a directional Poynting vector, but it also appears as one of the fundamental elemental dipoles in near-field directionality. The third case, Fig 1(c), is similar to the Huygens dipole, but its electric and magnetic moments are in quadrature phase to each other. This means that, instead of producing a well-defined direction in the time-averaged Poynting vector, it produces a well-defined direction of the imaginary component of the complex Poynting vector, i.e. the reactive power flow. This source will only couple to waveguides modes whose reactive power directions matches that of the source. It couples to the waveguide placed on one side, while showing no coupling to the one on the other side; top or bottom waveguides in Fig 1(c). We label this source Janus dipole due to this unique face-dependent behavior. Flipping the sign of one of the components of the Janus dipole changes the coupling side.

Each dipolar source has a unique symmetry (mirror and rotational symmetries, as well as time-reversal and parity-reversal symmetries). The three sources arise as elemental solutions to a single equation of dipolar near-field coupling, as discussed below.

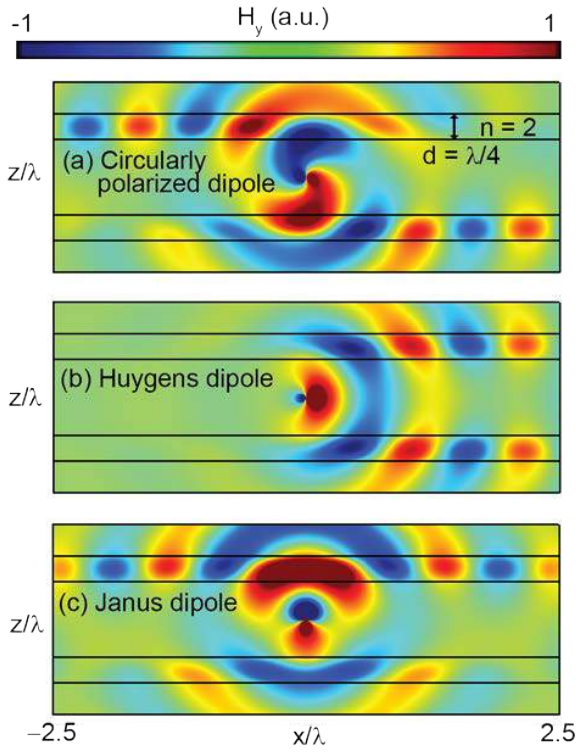


Figure 1: Comsol simulation of the three elemental dipolar sources placed between two dielectric slabs with refractive index $n = 2$ and quarter wavelength thickness. (a) Circularly polarized dipole $\mathbf{p} = \mathbf{x} + i\mathbf{z}$ and $\mathbf{m} = 0$; (b) Huygens dipole $\mathbf{p} = \mathbf{z}$ and $\mathbf{m} = c\mathbf{y}$; (c) Janus dipole $\mathbf{p} = \mathbf{x}$ and $\mathbf{m} = -ic\mathbf{y}$; where $\mathbf{x}$, $\mathbf{y}$ and $\mathbf{z}$ are the cartesian unit vectors, i is the imaginary unit and c is the speed of light.

3. Theory

The Fermi Golden rule states that the amount of coupling between an electric/magnetic dipole ($\mathbf{p}$ and $\mathbf{m}$) and a waveguide mode with fields $\mathbf{E}$ and $\mathbf{B}$ is proportional to $|\mathbf{p}\cdot\mathbf{E}^* + \mathbf{m}\cdot\mathbf{B}^*|$. If we wish to study dipolar sources with near-field directionality, we can demand this coupling to be exactly zero for a certain mode/direction:

$$\mathbf{p}\cdot\mathbf{E}^* + \mathbf{m}\cdot\mathbf{B}^* = 0 \qquad (1)$$

This is a homogeneous linear equation which we solve using standard linear algebra. In a simple 2D case considering only transverse magnetic modes as in Fig. 1, all solutions to this equation are mathematically given by a superposition of the three elemental dipoles discussed above. The study of transverse electric modes gives analogous results, with differently oriented dipoles [12]. Finally, the theory can be easily extended into three dimensions.

4. Conclusions

A general analytical theory of dipolar near-field directionality near planar geometries can easily be obtained from Fermi's Golden rule. The theory can be easily extended into more general three-dimensional waveguides. With this work we show that going beyond the usual linearly polarized electric dipoles opens unexpected opportunities for electromagnetic designs.

Acknowledgements

This work was supported by European Research Council Starting Grant ERC-2016-STG-714151-PSINFONI and EPSRC (UK). A.Z. acknowledges support from the Royal Society and the Wolfson Foundation.

References

[1] F. J. Rodriguez-Fortuno *et al.*, "Near-Field Interference for the Unidirectional Excitation of Electromagnetic Guided Modes," *Science*, vol. 340, no. 6130, pp. 328–330, Apr. 2013.

[2] A. Aiello, P. Banzer, M. Neugebauer, and G. Leuchs, "From transverse angular momentum to photonic wheels," *Nat. Photonics*, vol. 9, no. 12, pp. 789–795, Nov. 2015.

[3] R. Mitsch, C. Sayrin, B. Albrecht, P. Schneeweiss, and A. Rauschenbeutel, "Quantum state-controlled directional spontaneous emission of photons into a nanophotonic waveguide," *Nat. Commun.*, vol. 5, p. 5713, Dec. 2014.

[4] D. O'Connor, P. Ginzburg, F. J. Rodríguez-Fortuño, G. A. Wurtz, and A. V. Zayats, "Spin-orbit coupling in surface plasmon scattering by nanostructures," *Nat. Commun.*, vol. 5, 2014.

[5] F. J. Rodríguez-Fortuño, I. Barber-Sanz, D. Puerto, A. Griol, and A. Martínez, "Resolving Light Handedness with an on-Chip Silicon Microdisk," *ACS Photonics*, vol. 1, no. 9, 2014.

[6] F. J. Rodríguez-Fortuño, D. Puerto, A. Griol, L. Bellieres, J. Martí, and A. Martínez, "Sorting linearly polarized photons with a single scatterer," *Opt. Lett.*, vol. 39, no. 6, 2014.

[7] A. Espinosa-Soria, F. J. Rodríguez-Fortuño, A. Griol, and A. Martínez, "On-Chip Optimal Stokes Nanopolarimetry Based on Spin-Orbit Interaction of Light," *Nano Lett.*, vol. 17, no. 5, 2017.

[8] C. Sayrin *et al.*, "Nanophotonic Optical Isolator Controlled by the Internal State of Cold Atoms," *Phys. Rev. X*, vol. 5, no. 4, p. 41036, Dec. 2015.

[9] J. Ma, X. Xi, Z. Yu, and X. Sun, "Hybrid graphene/silicon integrated optical isolators with photonic spin–orbit interaction," *Appl. Phys. Lett.*, vol. 108, no. 15, p. 151103, Apr. 2016.

[10] K. Y. Bliokh, D. Smirnova, and F. Nori, "Quantum spin Hall effect of light," *Science*, vol. 348, no. 6242, pp. 1448–1451, Jun. 2015.

[11] K. Y. Bliokh, F. J. Rodríguez-Fortuño, F. Nori, and A. V. Zayats, "Spin-orbit interactions of light," *Nat. Photonics*, vol. 9, no. 12, 2015.

[12] M. F. Picardi, A. V. Zayats, and F. J. Rodríguez-Fortuño, "Janus and Huygens' dipolar sources for near-field directionality," *ArXiv*, Aug. 2017.

Probing and Controlling Negative Photoconductivity of Plasmonic Nanowire

Jihye Lee[1,2], Jiyoung Yoon[3], Sang-Heon Park[1,2], and Jong-Souk Yeo[1,2*]
[1] School of Integrated Technology, Yonsei University, Incheon, Republic of Korea
[2] Yonsei Institute of Convergence Technology, Yonsei University, Incheon, Republic of Korea
[3] Nano Science and Engineering, Yonsei University, Incheon, 406-840, Republic of Korea
[*]corresponding author: jongsoukyeo@yonsei.ac.kr

Abstract

Here, we investigate the photoresponsivity by changing the wavelength of incident light on plasmonic nanowires with their resonant scattering colors in visible wavelength. By varying the wavelength of light and its coherency, we probe and control the negative photoconductivity of gold nanowire based on localized surface plasmon resonance (LSPR), surface plasmon polariton (SPP), and perturbation related damping mechanisms.

1. Introduction

Metal nanoplasmonics have been considered for practical applications in optoelectronics, photovoltaics, optical nanocircuits, displays and sensing [1-2]. These applications have been developed by merging photonics and electronics in nanoscale dimensions by controlling photoconductive properties of plasmonic nanostructures. When the plasmonic nanostructure goes into the resonance condition in the vicinity of active materials, they provide hot electrons. This can lead to the generation of a photon-excited electrical current, thus a positive photoconductance [3-4].

Other researches focused on the thermoplasmonics where absorption of light on metal nanostructure results in a significant local heating in the nanostructure, thus providing a negative photoconductance [5]. These photoconductance changes can be analyzed by Landau damping theory. The Landau damping occurs in electron-electron scattering, electron-phonon scattering, and phonon-phonon scattering within ~1 fs to 10 ns. When the nanoparticle, nanorod, and bow-tie antenna structure interact with incident light, they are strongly coupled to the electromagnetic field of light and exert an effective restoring force within a confined and curved surface of the particles so that their photoconductance can be explained by LSPR based Landau damping process. However, for the nanowires, which has hundreds of nanometers in width and micro-scale length, their photoconductivity cannot be fully explained by LSPR based damping process alone.

In this paper, we fabricate the different width of gold nanowires (NWs) and investigate the photoconductivity by the excitation of LSPR and SPP along the NW using different properties of light such as changing the wavelength, coherency, and on/off resonance conditions of the light sources.

2. Result and Discussion

We fabricated the blue, green, and red scattered gold nanowire arrays which have 94, 178, 265 nm width in average and 160 μm in length as shown in Fig. 1. The peak resonance wavelength on each nanowire is 464 nm, 574 nm, and 601 nm, respectively. By comparing the wavelength of peak resonance in each nanowire with incident light sources (325 nm He-Cd laser, 532 nm Nd:YAG, 633 nm He-Ne laser, and 785 nm diode laser), we define the on- and off-resonance conditions. When the wavelength of peak resonance in the nanowire is close to the wavelength of laser light, it is called on-resonance condition but other conditions are called off-resonance. Interestingly, the on-resonance condition matches the LSPR excitation along the width direction of nanowire. This negative photoconductivity ($-\Delta G(S)$) is largest compared to the SPP related photoconductance and other UV and infrared excited photoconductance as shown in Fig. 2. In SPP related region which is excited by visible light sources, the photoconductance has higher value than UV and infrared excited photoconductance. This is because visible wavelength randomly excites SPP along the nanowire so that the longitudinal direction of nanowire also experiences carrier relaxation and thermal dissipation by SPP. In UV and infrared excited condition, all nanowires show similar photoconductances which stem from the electronic and lattice absorption, and vibration respectively.

3. Conclusions

By using different wavelength and coherency of incident light, we investigated and analyzed the LSPR, SPP, and perturbation related (electronic and lattice absorption) photoconductance changes on gold nanowires. The different mechanism of inducing a photoconductance can control the optoelectrical property of simple plasmonic metal nanostructure, thus enabling the integration between the nano-electronic circuits, photons and plasmons for future devices and sensing applications.

Acknowledgements

This research was supported by the MSIT (Ministry of Science and ICT), Korea, under the ICT Consilience Creative program (IITP-2017-2017-0-01015) supervised by the IITP (Institute for Information & communications

Technology Promotion) and also under the "Mid-career Researcher Program" (NRF-2016R1A2B2014612) supervised by the NRF (National Research Foundation).

References

[1] E. Ozbay, Plasmonics: Merging photonics and electronics at nanoscale dimensions, *Science* 311: 189-193, 2006.

[2] J. Lee, J. Y. Lee and J. S. Yeo, Optimally functionalized adhesion for contact transfer printing of plasmonic nanostructures on flexible substrate, *ACS Appl. Mater. Interfaces*, 9: 3251-3259, 2017.

[3] F. Wang and N. A. Melosh, Power-independent wavelength determination by hot carrier collection in metal-insulator-metal devices, *Nat. Commun.* 4: 1711, 2013.

[4] M. L. Brongersma, N. J. Halas, and P. Nordlander, Plasmon-induced hot carrier science and technology, 10: 25-34, 2015.

[5] J. H. Kim and J. S. Yeo, Enhanced detection of broadband incoherent light with nanoridge plasmonics, *Nano Lett*, 15: 2291-2297, 2015.

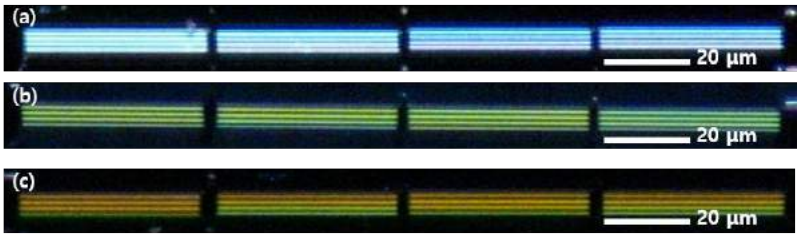


Fig. 1. Different scattering colors in the nanowire structure arrays fabricated by focused ion beam process. The average width of each nanowire is (a) 94 (b) 178, and (c) 265 nm, respectively. The total length of the nanowire is 160 μm. All colors are measured by dark-field microscope using the incoherent halogen lamp as a light source.

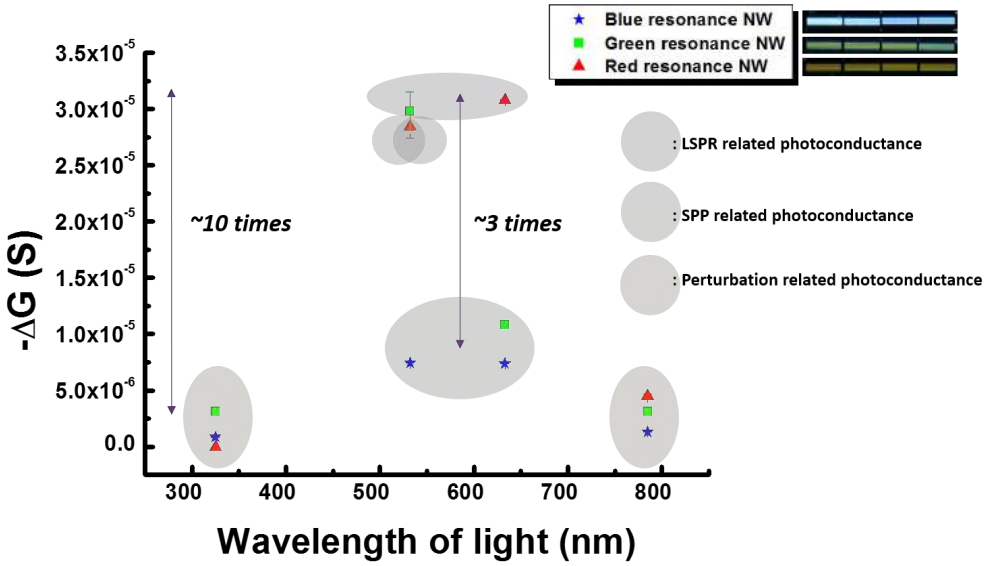


Fig. 2. Photoconductance (ΔG) change depending on the wavelength of incident light sources. All the photoconductances were measured by a probe station and calculated using the equation ($\Delta G=\Delta I_{pc}/V_{dc}$, ΔI_{pc} is photocurrent and V_{dc} is bias voltage). Violet, green, and yellow region in the plot can be explained by LPSR related, SPP related, and perturbation related photoconductance changes, respectively.

Probing Spin-Orbit Interaction via Fano Interference.

Rajesh Desapogu[1], Dima Cheskis[2], Shmuel Shternklar[3] & Yuri Gorodetski[1,3]

[1]Ariel University, Electrical Engineering & Electronics department, Ariel, 40700, Israel
[2]Ariel University, Physics department, Ariel, 40700, Israel
[3]Ariel University, Mechanical Engineering & Mechatronics department, Ariel, 40700, Israel
*corresponding author, E-mail: yurig@ariel.ac.il

Abstract

We experimentally present a novel plasmonic phenomenon of Fano interference in plasmonic wavefront excitation by a nanoscale structure wich is strongly affected by the spin-orbit interaction. This effect allows to directly probe the helical phase arising in the plasmon coupling process.

1. Summary

Surface plasmons (SP) – the collective oscillation of the bound charges in the vicinity of the conducting surface are crucial in various nanophotonic applications due to their surface confinement and relative long-range propagation [1, 2]. Often a subwavelength scatterer is used to excite a point-like source of SPs. In this case, the coupling efficiency is considered to by only a function of the scatterer shape and the illumination uniformity [3, 4]. Nevertheless, here we show that Fano interference effect modulated by the helical phase arising due to the plasmonic spin-orbit interaction [5, 6] (P-SOI) can significantly modify the SP excitation and even cause its total suppression. This Fano effect is experimentally studied in this paper and is shown to be a considerable parameter in plasmonic system design.

Fano interference is a very general physical phenomenon arising from the interaction of two oscillating systems one of which has a discrete resonant behavior while the other one is characterized by a broadband response [7, 8, 9]. Such an effect can be observed in atomic physics [10, 11], quantum [12] and classical mechanics [13] and in optics [9, 14]. The main characteristic of the Fano resonance is its asymmetric shape with the respect of the driving force frequency [8, 13]. Moreover, under some conditions an anti-resonant behavior can be observed due to the destructive interference of the participating systems' responses [15]. Recently a lot of attention was devoted to the Fano effect as its various implementations were demonstrated in a variety of physical systems [16, 12]. In photonics a special interest is attracted to the systems involving scattering [17, 14] and plasmonic excitations[18, 19]. Specifically, the interaction of a resonant surface plasmon waves with a spatially broadband background scattering may lead to a characteristic Fano-shaped resonance [20, 21, 22]. Here, the coupling of the two systems is simply represented by the interference strength due to the intensity ratio and the relative phase of the the continuum and the discrete function. Again the variation of this coupling factor can drive the interfering systems into an anti-resonance state where the total response will be completely suppressed [18, 23]. In this sense the plasmonic wave excitation becomes strongly sensitive to the phase lag and some unexpected asymmetry can arise in the wavefront propagation [24, 25].

Here we experimentally demonstrate a Fano lineshape tuning by the plasmonic spin-orbit interaction in circularly symmetric nanostructures. We use circularly polarized light impinging on a subwavelength nanoscale sphere to excite a radially propagating plasmonic wave. Despite a full rotational symmetry the resulting wavefront exhibits a strong azimuthal variation in the k-space (see the Fig. 1). Moreover, by interchanging the handedness of the illumination the intensity distribution can be reversed. We attribute this effect to the Fano-induced resonance asymmetry due to the azimuthal phase variation arising in the P-SOI. We analyze the phenomenon using basic theory and show the dependence of the the plasmonic resonant shape on this phase. Finally we show the general character of the effect by demonstrating the Fano-shape resonance in the plasmonic signal scattered by other circularly symmetric objects. In some cases we obtain a full extinction of SP wave at a certain angle due to the appearance of the anti-resonance.

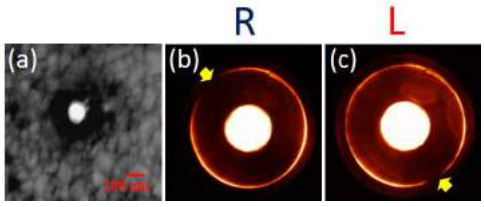


Figure 1: Scattering by a nanoparticle. (a) - SEM picture of the gold nanoparticle fabricated on top of the gold film; (b) and (c) k-space intensity distribution for the RCP and LCP illumination, respectively.

References

[1] W. L. Barnes, A. Dereux, and T. W. Ebbesen, "Surface plasmon subwavelength optics," *nature*, vol. 424, no. 6950, p. 824, 2003.

[2] S. A. Maier, *Plasmonics: fundamentals and applications*. Springer Science & Business Media, 2007.

[3] A. Zharov and N. Zharova, "Control of surface plasmon excitation via the scattering of light by a nanoparticle," *Journal of Experimental and Theoretical Physics*, vol. 123, no. 1, pp. 17–26, 2016.

[4] C. Genet and T. Ebbesen, "Light in tiny holes," *Nature*, vol. 445, no. 7123, p. 39, 2007.

[5] Y. Gorodetski, A. Niv, V. Kleiner, and E. Hasman, "Observation of the spin-based plasmonic effect in nanoscale structures," *Physical review letters*, vol. 101, no. 4, p. 043903, 2008.

[6] K. Y. Bliokh, F. Rodríguez-Fortuño, F. Nori, and A. V. Zayats, "Spin–orbit interactions of light," *Nature Photonics*, vol. 9, no. 12, p. 796, 2015.

[7] U. Fano, "Sullo spettro di assorbimento dei gas nobili presso il limite dello spettro darco," *Il Nuovo Cimento (1924-1942)*, vol. 12, no. 3, pp. 154–161, 1935.

[8] A. E. Miroshnichenko, S. Flach, and Y. S. Kivshar, "Fano resonances in nanoscale structures," *Reviews of Modern Physics*, vol. 82, no. 3, p. 2257, 2010.

[9] C. Ott, A. Kaldun, P. Raith, K. Meyer, M. Laux, J. Evers, C. H. Keitel, C. H. Greene, and T. Pfeifer, "Lorentz meets fano in spectral line shapes: a universal phase and its laser control," *Science*, vol. 340, no. 6133, pp. 716–720, 2013.

[10] H. Feshbach, "Unified theory of nuclear reactions," *Annals of Physics*, vol. 5, no. 4, pp. 357–390, 1958.

[11] I. Bloch, J. Dalibard, and W. Zwerger, "Many-body physics with ultracold gases," *Reviews of modern physics*, vol. 80, no. 3, p. 885, 2008.

[12] K. Kobayashi, H. Aikawa, S. Katsumoto, and Y. Iye, "Tuning of the fano effect through a quantum dot in an aharonov-bohm interferometer," *Physical review letters*, vol. 88, no. 25, p. 256806, 2002.

[13] Y. S. Joe, A. M. Satanin, and C. S. Kim, "Classical analogy of fano resonances," *Physica Scripta*, vol. 74, no. 2, p. 259, 2006.

[14] M. F. Limonov, M. V. Rybin, A. N. Poddubny, and Y. S. Kivshar, "Fano resonances in photonics," *Nature Photonics*, vol. 11, no. 9, p. 543, 2017.

[15] A. Nitzan, "Photon absorption and scattering in fano anti-resonances," *Molecular Physics*, vol. 27, no. 1, p. 65, 1974.

[16] E. H. Hasdeo, A. R. Nugraha, M. S. Dresselhaus, and R. Saito, "Breit-wigner-fano line shapes in raman spectra of graphene," *Physical Review B*, vol. 90, no. 24, p. 245140, 2014.

[17] M. I. Tribelsky and B. S. Lukyanchuk, "Anomalous light scattering by small particles," *Physical review letters*, vol. 97, no. 26, p. 263902, 2006.

[18] M. V. Rybin, D. S. Filonov, P. A. Belov, Y. S. Kivshar, and M. F. Limonov, "Switching from visibility to invisibility via fano resonances: theory and experiment," *Scientific reports*, vol. 5, p. 8774, 2015.

[19] Q. Wang, Y. Huang, Z. Yao, and X. Xu, "Analysis of transition from lorentz resonance to fano resonance in plasmon and metamaterial systems," *Optical and Quantum Electronics*, vol. 48, no. 2, p. 83, 2016.

[20] B. Gallinet and O. J. Martin, "Influence of electromagnetic interactions on the line shape of plasmonic fano resonances," *ACS nano*, vol. 5, no. 11, pp. 8999–9008, 2011.

[21] B. Stein, J.-Y. Laluet, E. Devaux, C. Genet, and T. W. Ebbesen, "Fano resonances and leakage radiation for high-resolution plasmonic sensing," *The Journal of Physical Chemistry C*, vol. 116, no. 10, p. 6092, 2012.

[22] J.-Y. Laluet, A. Drezet, C. Genet, and T. W. Ebbesen, "Generation of surface plasmons at single subwavelength slits: from slit to ridge plasmon," *New Journal of Physics*, vol. 10, no. 10, p. 105014, 2008.

[23] A. Lovera, B. Gallinet, P. Nordlander, and O. J. Martin, "Mechanisms of fano resonances in coupled plasmonic systems," *Acs Nano*, vol. 7, no. 5, pp. 4527–4536, 2013.

[24] K. Kobayashi, H. Aikawa, S. Katsumoto, and Y. Iye, "Mesoscopic fano effect in a quantum dot embedded in an aharonov-bohm ring," *Physical Review B*, vol. 68, no. 23, p. 235304, 2003.

[25] O. V. Misochko, M. Hase, K. Ishioka, and M. Kitajima, "Fano interference with the alternating asymmetry parameter in time-domain experiments," *Journal of Experimental and Theoretical Physics Letters*, vol. 82, no. 7, pp. 426–430, 2005.

Oscillatory Plasmon-Exciton Coupling and Non-Traditional Plasmonics

Matthew S. Kirschner[1], Wendu Ding[1], Xiao-Min Lin[2], Lin X. Chen[1,3], George C. Schatz[1], Richard D. Schaller[1,2]*

[1]Department of Chemistry, Northwestern University, Evanston, IL 60208, USA
[2]Center for Nanoscale Materials, Argonne National Laboratory, Lemont, IL 60439, USA
[3]Chemical Science and Engineering, Argonne National Laboratory, Lemont, IL 60439, USA
*corresponding author, E-mail: schaller@northwestern.edu

Abstract

We report oscillatory plasmon exciton coupling in colloidally suspended nanoparticles. Coherent acoustic phonons derived from plasmonic nanoparticles are examined for modulation of electronic interactions with proximal excitonic molecular species. Gold bipyramids with varied aspect ratios and localized surface plasmon resonance energies, functionalized with J-aggregate thiacarbocyanine dye molecules, produce distinct hybridized states that exhibit clear coupling. For such coupled systems, these photo-generated oscillations alter the metal nanoparticle energetic contribution to the hybridized system and, as a result, transiently change the coupling between the plasmon and exciton in oscillatory manner.

1. Introduction

Several preceding studies of nanomaterials present time-dependent characterization of transient geometric changes induced by coherent acoustic phonons generated following photoexcitation.[1-5] In such studies, changes in particle geometry can result in discernible modifications of optical properties such as localized surface plasmon resonance (LSPR) energy, which permits the characterization of the phonon modes that alter such resonances. Size dispersion in an ensemble of measurement generally leads to a spread of phonon frequencies that can result in significant inhomogeneous dephasing. This dephasing can be circumvented through the use of single particle measurements or relatively monodisperse ensembles. Taken as a whole, these studies have provided insights into the nature of phonon-induced geometrical distortion of nanoparticles as well as phonon-solvent coupling.

The same acoustic phonons that cause oscillations following photoexcitation potentially can transiently alter the electronic coupling between an LSPR and a molecular electronic transition. Similar systems that take advantage of the coupling of plasmonic nanomaterials have gained interest and shown potential in an array of applications.[6] In this way, we probe molecular sensitivity to the vibrational mode of an inorganic solid undergoing acoustic deformation.

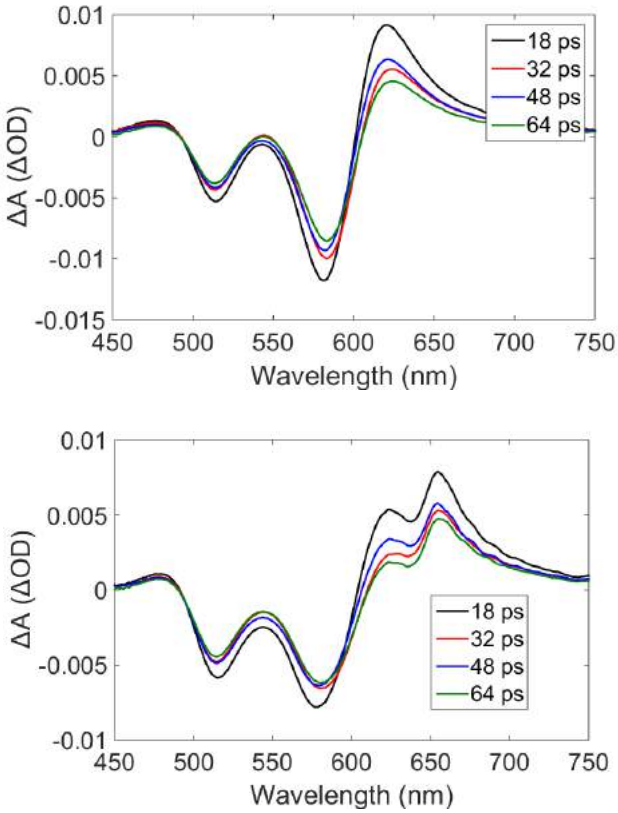


Figure 1: (top) Transient spectra at indicated times for unfunctionalized gold bipyramids in water following optical excitation. (bottom) J-aggregate functionalized gold bipyramids that exhibit hybridized resonances.

.

2. Results and Discussion

We produced and examined a series of different highly monodisperse gold bipyramid samples (AuBPs) with and without thiacarbocyanine dye, 2,2'-dimethyl-8-phenyl-5,6,5',6'-dibenzothiacarbocyanine chloride (TCC) molecules deposited on the AuBP surface, to achieve time-dependent ensemble characterization of the phonon-induced energetic modulation. Previous reports have shown that TCC can successfully attach to gold nanostructures and couple to the particle electronically resulting in a plexcitonic

system with plasmon-exciton hybridized states. We characterize the static properties of several different AuBPs, with corresponding LSPR energies, functionalized with TCC, then analyze the ultrafast dynamics of these systems to determine the effects coherent acoustic phonons on the electronic transitions.We offer a qualitative explanation for the direction and magnitude of the observed changes in coupling. The resulting paradigm, represents a model system in the development of photochemistry facilitated by vibrational modes as well as provide fundamental insight into plexcitonic systems or enable new applications owing to the inherent fine-tuning of the plasmonic resonance.

3. Conclusions

In conclusion, we successfully functionalize AuBPs with j-aggregates to form oscillatory plasmonic-exciton systems with hybridized states that are modulated by the coherent acoustic phonons of AuBPs. These changes are rationalized in the context of the static coupling between these two species. The existence of this new class of nanomaterials is promising in a number of contexts. The fine-tuning of the hybridization of such coupled systems could improve existing applications of plexcitonic materials. Further, such systems could serve as a developmental testbed for the utilization of vibrational modes in controlling electronic interactions.

Acknowledgements

We acknowledge support from the Ultrafast Initiative of the U. S. Department of Energy, Office of Science, Office of Basic Energy Sciences. Use of the Center for Nanoscale Materials, an Office of Science user facility, was supported by the U. S. Department of Energy, Office of Science, Office of Basic Energy Sciences, under Contract No. DE-AC02-06CH11357.

References

[1] Hartland, G.V. *Chem. Rev*., **2011**, *111*, 3858-3887.
[2] Pelton, M.; Sader, J. E.; Burgin, J.; Liu, M.; Guyot-Sionnest, P.; Gosztola, D. *Nat. Nano.* **2009**, *4*, 492-495.
[3] Ruijgrok, P. V.; Zijlstra, P.; Tchebotareva, A. L.; Orrit, M. *Nano Lett.* **2012**, *12*, 1063-1069.
[4] Soavi, G.; Tempra, I.; Pantano, M. F.; Cattoni, A.; Collin, S.; Biagoni, P.; Pugno, N. M.; Cerullo, G. *ACS Nano* **2016**, *10*, 2251-2258.
[5] Kirschner, M. S.; Letheic, C. M.; Lin, X. M.; Schatz, G. C.; Chen, L. X.; Schaller, R. D. *ACS Photon*. **2016**, *3*, 758-763.
[6] Fofang, N. T.; Park, T.-H.; Neumann, O.; Mirin, N. A.; Nordlander, P.; Halas, N. J. *Nano Lett.* **2008**, *8*, 3481-3487.
[7] M.S. Kirschner, W. Ding, Y. Li, C.T. Chapman, A. Lei, X.-M. Lin, L.X. Chen, G.C. Schatz, R.D. Schaller "Phonon-Driven Oscillatory Plasmonic Excitonic Nanomaterials" *Nano Lett.* **2018**, *18*, 442-8.

Tuning propagation of surface plasmon polariton by geometric phases

Feng Lin[1]

[1]State Key Lab for Mesoscopic Physics, School of Physics, Peking University, Beijing 100871, China

*corresponding author, E-mail: linf@pku.edu.cn

Abstract

We used a scanning near-field optical microscope (SNOM) to observe the near-field distribution of surface plasmon polaritons (SPPs) from a ring-shaped metasurface under illumination of circularly polarized light. It was found that with an additional degree of freedom of the geometric phase provided by the regularly arranged metamolecules, control over the near-field interference of the SPPs can be achieved, which is governed by the metasurface geometric symmetry that can be tuned by its topological charge. Meanwhile, the planar chiral character of the metamolecules exerts a deep influence on the near-field interference patterns. Our results can pave the way for active control of SPP propagation in near fields, and have potential applications in highly integrated optical communication systems.

1. Introduction

Metasurfaces are made of two-dimensional arrays of subwavelength nanostructures that form a spatially varying optical response, to control the wave fronts of optical waves. As the feature size of its constituent materials is nanoscale, investigation of the light-nanostructure interactions in the near-field is critical for understanding the novel properties of metasurfaces.[1-10] In this work, regularly arranged nanoslits (also called metamolecules) on Au films, forming a ring-shaped metasurface, generate different topological charges (q-values) that add a geometric phase in the surface plasmon polariton (SPP) near-field under the illumination of circularly polarized light. The scanning near-field optical microscope (SNOM) measurements and theoretical simulations show that with an additional degree of freedom of geometric phases, the excited SPP field modes are tunable by q-values and have an electromagnetic structural character that coincides with the metasurface geometry. Meanwhile, planar chiral features of the nanoslits also greatly affect the SPP near-field.

2. Results and discussion

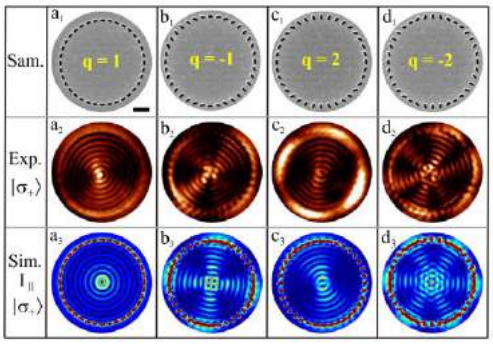


Figure 1. (a_1, b_1, c_1, d_1) Scanning electron microscope images of ring-shaped metasurfaces made of bar-type metamolecules for topological charges q = 1, -1, 2, -2, respectively. The radius of the ring is 2.6 μm and the number of metamolecules within the circumference is 36. Under the illumination of $|\sigma_+\rangle$, the excited SPP distribution ($I_{||} = |E_{||}|^2$) for various topological charges measured by SNOM (a_2, b_2, c_2, d_2) and simulated by FDTD (a_3, b_3, c_3, d_3). The bar at the bottom-right corner of (a_1) represents 1 μm, which is applicable to the rest of the frames.

The experimental results of bar-type metasurfaces with different q-values under the illumination of $|\sigma_+\rangle$ were presented in Figure 1. The scanning electron microscope (SEM) images in Figure 1(a_1), (b_1), (c_1), and (d_1) show the metasurface structures of q = 1, -1, 2, -2, corresponding to the exp(jα), exp(-jα), exp(2jα), and exp(-2jα) geometric phases of SPP, respectively. Here, the ring radius of 2.6 μm and 36 metamolecules were chosen. Due to the rotation of each metamolecule, the metasurface structures changed from circular symmetry (q = 1) to square- (q = -1), line- (q = 2), and hexagon-symmetry (q = -2). When analyzing the near-field intensity in Figure 1(a_2), (b_2), (c_2), and (d_2), different SPP modes within the rings can be achieved. Specific near-field interference patterns are circular, square, line, and hexagonal symmetries, arising from the metasurface structural features induced by the q-values. The simulation results [Figure 1(a_3), (b_3), (c_3), and (d_3)] are in good

agreement with the SNOM measurements. Previous works show that in the metasurface structure of circular slits, the appearance of the geometric phase of SPPs arises from the phase delay, when circularly polarized light rotates around the structure. This is similar to our case where q = 1. In contrast to the circular slit structure, we can obtain any topological charge q-values as the metamolecules rotate, so that the excited SPPs geometric phase is tunable. Therefore, different SPP propagation modes can be artificially controlled. When the incident light was changed to $|\sigma_-\rangle$, the near-field interference patterns are exactly the same as for $|\sigma_+\rangle$ illumination, which indicates that the achiral structure of the bar-type nanoslits cannot distinguish the helicity of light.

3. Conclusions

In this work, we have established a tunable topological charge on a ring-shaped metasurface, which facilitates significant control over the propagation modes of excited SPPs under the illumination of circularly polarized light. This is due to the fact that, at the nanoscale, regularly arranged metamolecules introduce additional geometric phases in the SPP field, which creates a field exhibiting apparent geometric structural character in accordance with metasurface structures.

References

[1] Yu, N. F.; Capasso, F. Flat optics with designer metasurfaces. *Nature Mater.* 13: 2014 , 139-150.

[2] Lin, J.; Balthasar Mueller, J. P.; Wang, Q.; Yuan, G. H.; Antoniou, N.; Yuan, X. C.; Capasso, F. Polarization-controlled tunable directional coupling of surface plasmon polaritons. *Nature* 340: 2013, 331-334.

[3] Kang, M.; Chen, J.; Wang, X. L.; Wang, H. T. Twisted vector field from an inhomogeneous and anisotropic metamaterial. *J. Opt. Soc. Am. B* 29: 2012, 572-576.

[4] Zhang, L.; Mei, S.; Huang, K.; Qiu, C.-W. Advances in full control of electromagnetic waves with metasurfaces. Adv. *Opt. Mater.* 4: 2016, 818-833.

[5] Jahani, S.; Jacob, Z. All-dielectric matamaterials. *Nat. Nanotech.* 11: 2016, 23-36.

[6] Aieta, F.; Genevet, P.; Kats, M. A.; Yu, N.; Blanchard, R.; Gaburro, Z.; Capasso, F. Aberration-Free Ultrathin Flat Lenses and Axicons at Telecom Wavelengths Based on Plasmonic Metasurfaces. *Nano Lett.* 12: 2012, 4932-4936.

[7] Kim, H.; Park, J. H.; Cho, S. W.; Lee, S. Y.; Kang, M. S.; Lee, B. H. Synthesis and dynamic switching of surface plasmon vortices with plasmonic vortex lens, *Nano Lett.* 10: 2010, 529-536.

[8] Ee, H. S.; Agarwal, R. Tunable metasurface and flat optical zoom lens on a stretchable substrate. *Nano Lett.* 16, 2016, 2818-2823.

[9] Yu, N.; Aieta, F.; Genevet, P.; Kats, M. A.; Gaburro, Z.; Capasso, F. A Broadband, Background-Free Quarter-Wave Plate Based on Plasmonic Metasurfaces. *Nano Lett.* 12: 2012, 6328-6333.

[10] Grady, N. K.; Heyes, J. E.; Chowdhury, D. R.; Zeng, Y.; Reiten, M. T.; Azad, A. K.; Taylor, A. J.; Dalvit, D. R.; Chen, H.-T. Terahertz metamaterials for linear polarization conversion and anomalous refraction, *Science* : 340: 2013, 1304-1307.

Acknowledgements

The authors gratefully acknowledge The National Key Research and Development Program of China (No. 2017YFA0205700 and 2015CB932403)

Phase resonances in all dielectric compound silicon gratings

Jian Qiang Liu[1],Yu Xiu Zhou[1], and Guang Hou Sun[1], Xia Qin Zeng[1]

[1]Key laboratory of Jiangxi microstructure functional materials and school of Science, Jiujiang University, Jiujiang 332005, People's Republic of China
*corresponding author, E-mail: ljqjju@126.com

Abstract

We theoretically demonstrate phase resonance occurs at all dielectric compound silicon gratings with three identical silicon pillars in each unit cell. It is shown that phase resonance characterized by out-phase magnetic field distributions within the silicon pillars appear at certain wavelength in this compound silicon gratings. Unlike the counterparts of compound metallic gratings, phase resonance mainly appear at the first order of Mie resonances of Si gratings. The second order Mie resonances only show phase resonances at oblique incidence. This feature indicate the resonance behaviors of all dielectric gratings can be controlled with compound structure, which is helpful to nanophotonic devices such as filter etc

1. Introduction

Phase resonance is a resonance mechanism that appears as a sharp dip in the transmission of transverse magnetic polarized light through so-called compound grating structures[1, 2], i.e., gratings comprised of multiple elements in each unit cell. In the present letter, we demonstrate that phase resonances are still observed in a compound silicon gratings with three silicon pillars in each unit cell even at normal incidence of light. And the simulated results show that phase resonances in this Mie resonant based all dielectric gratings is very different from those metallic compound gratings. We attribute this difference to the weak near field coupling between Mie resonance modes.

2. Theory model and method

In Figure 1, the schematic view of the simulated compound silicon gratings is demonstrated. Here, we assume the geometry parameters are the followings: periodicity $p = 1.5um$, the thickness of silicon pillar h =258 nm, the width of silicon pillar $w = 300$ nm. It should be note that the basic conclusions and phenomenon are independent on these chosen geometry parameters. The spacer between silicon pillars in each unit cell is denoted as d. Finite element method (FEM)[3] based of COMSOL multiphysics is used to simulate the electromagnetic response of considered compound gratings.

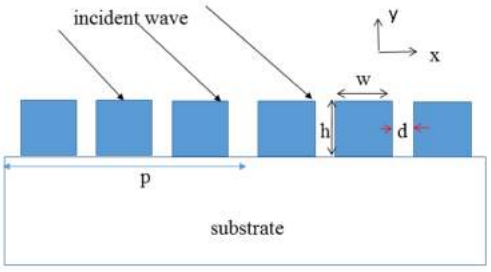


Figure 1: The illustration of compound silicon gratings with periodicity p. The width of silicon pillar is $w = 300$nm and its height is h =258 nm. The distance between silicon pillar in each unit cell is denoted as d.

3. Results

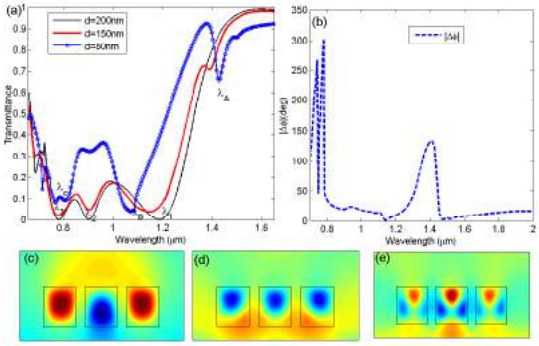


Figure 2: (a)Transmission spectra for the compound silicon gratings show in Fig. 1(a) with difference spacer d. (b)The phase difference between the central and adjacent silicon pillars at wavelength λ_A =1410 nm. Panels (c), (d), and (e) correspond to the snapshots of magnetic field distributions for wavelengths $\lambda_A, \lambda_B, \lambda_C$.

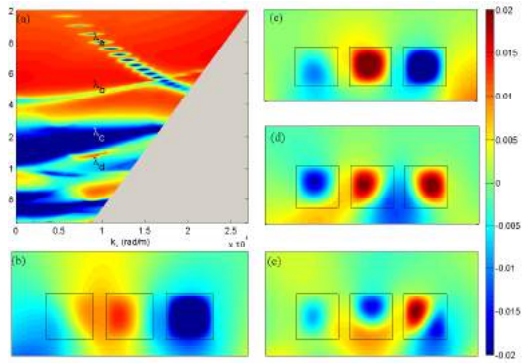


Figure 3: (a) The dispersion of resonant modes for compound silicon gratings under p-polarized incidence. (b)-(e) denote the snapshots of magnetic field distributions at wavlengths $\lambda_a, \lambda_b, \lambda_c, \lambda_d$ with incidence angle $\theta = 30^o$.

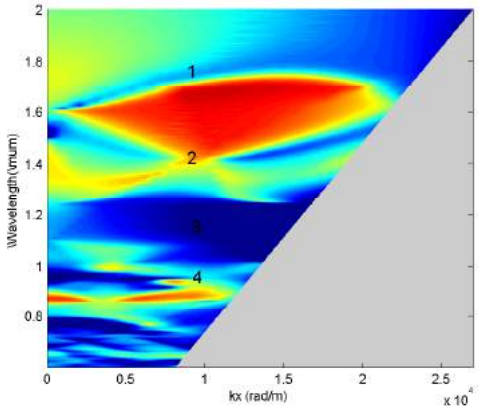


Figure 4: Dispersion of resonant modes for TE-polarized incidence wave.

4. Conclusions

In summary, we have theoretically demonstrated phase resonances in a compound silicon grating consisting of three silicon pillars in each unit cell. At normal incidence, phase resonance mode with out-phase configuration is observed in the first order Mie resonance and electric resonance modes. When at oblique incidence, the second resonance shows phase resonance due to the induced phase difference in each unit cell. The investigated model could be fabricated by the current nano-fabrication technology. The obtained result is helpful to understand the coupling behavior of Mie resonance in compound all dielectric gratings, which is of importance to the design nanophotonic devices such as filter in the near infrared region.

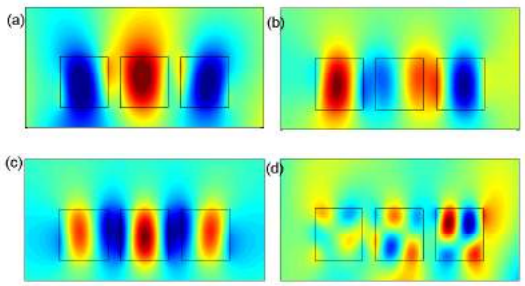


Figure 5: Magnetic field distributions correspond to the resonant wavelengths $\lambda_1, \lambda_2, \lambda_3, \lambda_4$ shown in Fig. 4 at incidence angle 30^o.

Acknowledgement

This work was supported by the Natural Science Foundation of Jiangxi Province, China(Grant No. 20161BAB201002, 20151BAB207056) and the Key Program for Scientific Research of Jiujiang University(2014KJZD005).

References

[1] D. C. Skigin, and R. A. Depine,Transmission Resonances of Metallic Compound Gratings with Subwavelength Slits, *Phys. Rev. Lett.* 95: 217402, 2005.

[2] D. C. Skigin, and R. A. Depine, Bandwidth control of forbidden transmission gaps in compound structures with subwavelength slits, *Phys. Rev. E* 74:046606, 2006

[3] COMSOL 4.4, http://www.comsol.com/

Nanonewton Plasmonic Forces from a 3D Coaxial Nanopillar

Brandon Terranova[1] and Adam K. Fontecchio[1]

[1]Drexel University, Department of Electrical and Computer Engineering, Philadelphia, PA, USA
*corresponding author, E-mail: bbt25@drexel.edu

1. Introduction

Electromagnetic (EM) fields can provide trapping forces that can be used for the localization and manipulation of subwavelength particles similar to how classical trapping experiments take advantage of the EM gradient force around a diffraction-limited focus. In this paper, we numerically investigate the forces available for plasmonic trapping due to resonances in a coaxial nanopillar (CNP) nanostructure. We show here results of finite-difference time-domain (FDTD) calculations which solve the Maxwell stress tensor (MST) in a volume surrounding a dielectric test particle suspended above the channel of the CNP, and find forces exceeding a magnitude of 10.5 nN in the z-direction on a 10 nm diameter test sphere in vacuum 10 nm above the surface of the CNP under 100 mW illumination at 626 nm. All FDTD results are obtained using Lumerical's FDTD Solutions software. Comparable trapping forces have been realized using a double pillar structure ($F_{\text{trap}} \sim 2$ nN on 1μm diameter polystyrene ($n = 1.6$) microspheres in oil ($n = 1.5$) @ 440 mW incident laser power) [1], and anti-reflection coated titania microspheres ($F_{\text{trap}} \sim 1.2$ nN on 1μm diameter coated ($n_{core} = 2.3$/ $n_{shell} = 1.78$) microspheres in water ($n = 1.33$) @ 1.1 W) [2].

The system presented in this work utilizes a reflective substrate. Systems such as this can take advantage of out-of-plane interactions, which have been shown to exist in other 3D plasmonic nanostructure systems as well [3,4]. This out-of-plane interaction can be tuned similar to how other parameters (gap size, incident beam power, incident beam angle, polarization, etc.) can be tuned to control the electric field enhancement in plasmonic nanostructures.

2. Methods

In this study, full three-dimensional FDTD simulations are conducted to model the plasmonic forces on a test particle above the upper surface of the CNP, pictured in Figure 1. The key results presented in this work are obtained from a CNP metamolecule with an outer radius $r = 140$ nm, height $h = 210$ nm, and a channel gap width $g = 25$ nm centered 50 nm radially away from the center of the upper surface of the CNP with a channel depth $d = 50$ nm. The gold CNP is located on a gold substrate, whose material properties are modeled on the anisotropic permittivity results obtained by Johnson and Christy [5], with background medium vacuum ($n = 1$). Using Lumerical's multi-coefficient model, a dielectric nanosphere is modeled as having a refractive index $n = 2$, and is evaluated for various diameters and distances above the CNP. In the presented results, force is calculated as the surface integration of the MST $\overleftrightarrow{T}_{ij}$ around a virtual rectangular volume surrounding the test nanosphere.

Experimental configuration of the dielectric sphere in relation to the CNP gap is shown in Figure 2. For all simulations, the center of the plasmonic trap is located 45 nm radially away from the center of the CNP, due to the fact that the center of the resonant channel plasmon above the CNP is shifted slightly toward the center of the CNP.

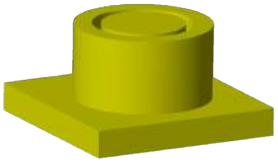


Figure 1: CNP geometry.

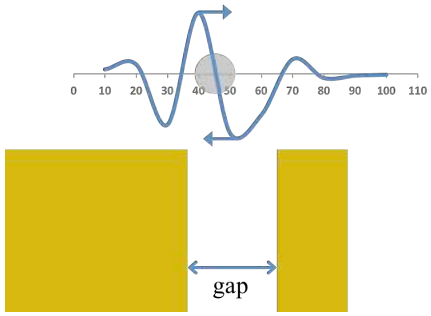


Figure 2: Experimental configuration with inset graph illustrating the stabilizing radial forces on the test sphere.

3. Results

Considering an infinite coaxial cylinder, $\overleftrightarrow{T}_{ij}$ can be written down exactly. For transverse magnetic (TM) plasmonic modes in the cavity of an infinite coaxial cylinder, there are electric field components in the z and ρ directions of typical cylindrical coordinates, and a magnetic field component in

the ϕ direction only. For waveguided EM waves, $\varepsilon E^2 = \mu H^2$, so for a TM wave the MST in the cylindrical channel of the coaxial cable is:

$$\overleftrightarrow{T}_{ch} = \begin{bmatrix} 0 & 0 & \varepsilon E_\rho E_z \\ 0 & 0 & 0 \\ \varepsilon E_\rho E_z & 0 & -\varepsilon E^2 \end{bmatrix}. \quad (1)$$

The diagonal terms in Equation 1 represent *pressures*, and the off-diagonal terms represent *shears*, so there is a momentum flux generating a pressure-like force proportional to εE^2 in the longitudinal direction, and a momentum flux generating a shear-like force with components in the radial and longitudinal directions.

The total time-averaged force associated with the EM field confined in the channel of the infinite coaxial cable is thus:

$$\boldsymbol{F}_{ch} = \oint \overleftrightarrow{T}_{ch} \cdot \hat{n}\, d\boldsymbol{a} = \varepsilon \oint \left[(E_\rho E_z)\hat{\rho} + (E_\rho E_z - E^2)\hat{z} \right] \cdot \hat{n}\, d\boldsymbol{a}, \quad (2)$$

where the surface of integration has its normal in the longitudinal direction for the z-components, and along the radius for the ρ-components. This expression shows which fields contribute to the forces experienced in the channel of the infinite coaxial cable.

We expect the fields to behave similarly for the case of the finite CNP. The out-of-plane coupling from the reflective substrate will affect the magnitude of the resulting field, as the channel plasmon will interfere with the time-retarded plasmon.

The electric field distribution on the top of the CNP which gives rise to the forces on the test sphere can be seen in Figure 3. The E-field distribution in the *XY* plane at the top of the CNP under normally incident, linearly polarized light shows the dipolar nature of the channel plasmons. Overlaid on the image is the surface charge distribution as determined using the plasmon hybridization method [6]. The color bar shows the magnitude of the E-field enhancement compared to the initial field. The two hot spots in the gap arise due to the linear polarization of the excitation beam. Under circularly polarized incidence, the hot spots circulate within the cavity in whispering gallery modes.

The *x*-components in these simulations correspond to a radial component in a cylindrical coordinate system. When the test particle is above the hot spot, the x-component of the force is zero, as illustrated in the inset graph of Figure 2. There exist restoring forces on either side of the center of the hot spot, creating a plasmonic trap.

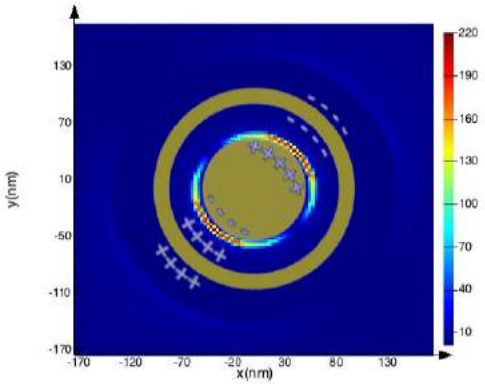


Figure 3: E-field distribution above the CNP showing charge distribution and field enhancement.

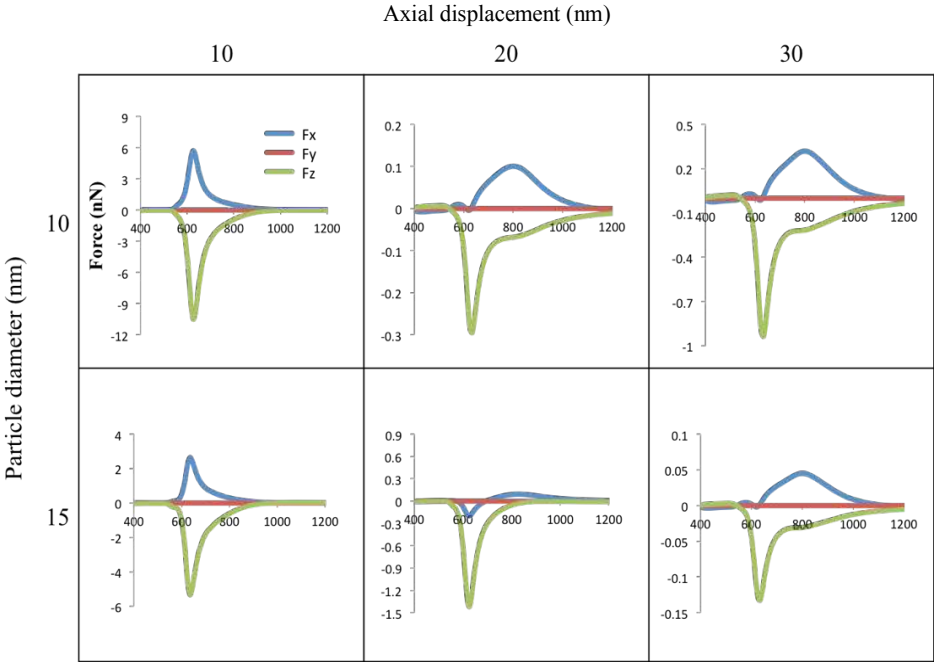


Figure 4: All force components on the test sphere for different conditions 40 nm radially away from the center of the CNP.

To study the forces on the test sphere, two different diameter test spheres were considered under various axial displacements from the upper surface of the CNP. The plots displayed in Figure 4 show a series of results of the MST computation on the test sphere, where the force is calculated using 100 mW incident excitation beam power—which is a typical laser power used for traditional optical tweezers. For each simulation, the test sphere was located 40 nm radially away from the center of the CNP to ensure the x-components would have non-zero values. Each simulation is run with at least two mesh points (calculation nodes) within the sphere and between sphere and the CNP upper surface. Convergence testing was done to ensure the physical validity of this mesh resolution. The results in Figure 4 show that at a 10 nm distance from the CNP gap, FDTD simulated fields predict forces greater than 10.5 nN on a 10 nm diameter test sphere. It is also observed that with the exception of the 20 nm axial displacement results for the 10 nm diameter particle, force on the test sphere generally falls off quickly with distance from the CNP upper surface as expected.

To further highlight the capabilities of this system, a 1 nm diameter sphere was tested, and the forces were calculated as shown in Figure 5. In the longitudinal direction, a force greater than 500 pN was calculated on the 1 nm sphere. The magnitude of this force is again obtained using a 100 mW excitation beam.

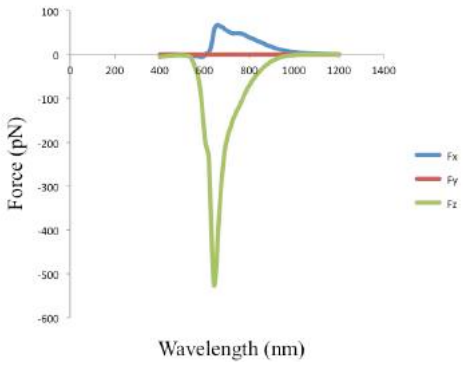


Figure 5: Force components on a 1 nm diameter test sphere.

4. Discussion

The nanostructure investigated in this paper utilizes resonant plasmonic fields in a coaxial cylinder on a reflective substrate to create stable trapping regions in the region above the CNP gap. This strong resonance can be used for sensing and trapping applications. The simulation results indicate this system is capable of producing nanonewton scale forces, and the analysis of the radial forces show that stable trapping regions exist above the upper surface of the CNP upon illumination.

We can see from the plots in Figure 4 that for each simulation, there is a field in the *x* and *z*-components generating the forces presented at 626 nm, and the *y*-components are zero across all wavelengths for each simulation as well, consistent with what was expected in the analysis of the infinite coaxial cylinder.

3D nanostructures such as the CNP can utilize design elements such as the reflective plasmonic coupling, to increase field enhancement and provide strong forces on this scale. The channel plasmons in the system investigated can reflect off of the substrate, leading to time-dependent phase matching conditions which create large resonance behavior in the system.

5. Conclusions

In this study it is shown that minor modifications to plasmonic nanostructures can create large field enhancements that generate strong forces on nearby dielectric particles. It is demonstrated that 3D nanostructures with cavities with subwavelength dimensions are able to support surface plasmons and can be used for local field enhancements capable of generating nanonewton forces. These results provide evidence that through plasmonic nanostructure design, plasmon resonances can be engineered that enable the nanostructure to perform as a force transducer capable of supporting stable trapping regions utilizing nanonewton forces.

References

[1] A. N. Grigorenko, N.W.R., M. R. Dickinson, Y. Zhang, *Nanometric optical tweezers based on nanostructured substrates.* Nature Photonics, 2008. **2**: p. 6.

[2] Anita Jannasch, A.F.M., Peter D. J. van Oostrum, Alfons van Blaaderen, Erik Schaffer, *Nanonewton optical force trap employing anti-reflection coated, high-refractive-index titania microspheres.* Nature Photonics, 2012. **6**: p. 5.

[3] Wei Zhou, T.W.O., *Tunable subradiant lattice plasmons by out-of-plane dipolar interactions.* Nat Nanotechnol, 2011. **6**(7): p. 5.

[4] Shunping Zhang, K.B., Naomi J. Halas, Hongxing Xu, Peter Nordlander, *Substrate-induced Fano resonances of a plasmonic nanocube: a route to increased-sensitivity localized surface plasmon resonance sensors revealed.* Nano Lett, 2011. **11**(4): p. 7

[5] P. B. Johnson, R.W.C., *Optical constants of the noble metals.* Physical Review B, 1972. **6**(12): p. 10.

[6] E. Prodan, C.R., N. J. Halas, P. Nordlander, *A hybridization model for the plasmon response of complex nanostructures.* Science, 2003. **302**(5644): p. 5.

Metamaterials and Negative Index Materials

Analysis of solitonic pulse propagation in metamaterials implemented in photonic crystals

Michelle Savescu [1], Kaisar Khan [2‡]

[1] Department of Mathematics, Kuztown University of Pennsylvania,
15200 Kutztown Road, Kuztown, PA-19530, USA
[2] Department of Electrical Engineering, McNeese State University,
Lake Charles, LA, 70605, USA

Abstract

In this paper we present the theoretical study of soliton pulse propagation in photonic crystal metamaterials. The traveling wave model for short pulse propagation through waveguides implemented in photonic crystals reveals constraint conditions related to wavelength dependent dispersion in negative refraction cases. Earlier simulations show that at certain wavelengths the optical wave guided in photonic crystals can get negative refraction if the holes are filled with metals. Current analysis also considers the unavoidable larger losses of the waveguides.

1 Introduction

Photonic crystals have drawn attention to the researchers mainly due to their capability to engineer dispersion in order to obtain metamaterials which are not present in nature [1-2]. Optical waveguides implemented in photonic crystals reveal that the light can be either slowed down, or it can get negative refraction, either by altering the geometry or by inserting metals in the holes, instead of air [1-2]. However, short duration pulses propagating through these waveguides depend on the wavelength due to the dispersion-wavelength dependency relation [1-4]. One potential issue with these waveguides is caused by the higher losses due to more interaction with the metamaterials, and that must be considered in the mathematical model. This paper will treat the cases of soliton propagation in optical metamaterials with negative refraction and high losses by providing the analytical formulation of the processes. Earlier simulations using commercial software (Crystalwave from Photondesign Inc.) show negative refraction at certain wavelengths. We use the traveling wave method to model the short pulse propagation and evaluate constraint conditions due to different signs of the group velocity of the metamaterial, conditions that are necessary to support the existence of soliton waves[1-4].

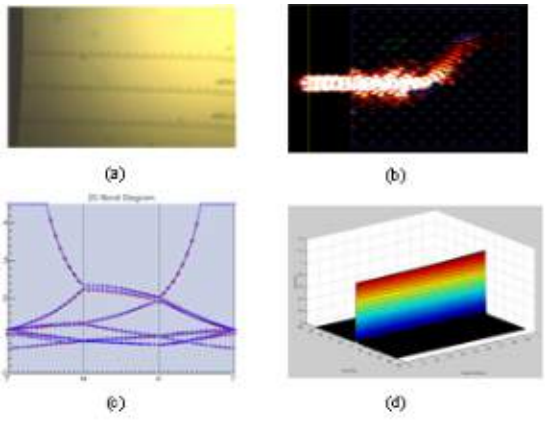


Figure 1: Bended optical waveguide implemented in a photonic crystal with gold filled holes a) magnified image of a fabricated photonic crystal b) simulated CW wave propagated through bent waveguide in photonic crystal c) evaluated band diagram d) optical soliton propagation

*Corresponding author at: Dept of Electrical Engineering,
†McNeese State University, Lake Charles, LA, 70605, USA
‡E-mail address mkhan@mcneese.edu

2 Mathematical Model

The equation governing the process of the propagation of solitons is

$$\frac{\partial A_1}{\partial z}+\left(\frac{\alpha}{2}\right)A_1+\beta_1\frac{\partial A_1}{\partial t}+i\frac{\beta_2}{2}\frac{\partial^2 A_1}{\partial t^2}+i\gamma|A_1|^2A_1=0 \quad (1)$$

The traveling wave hypothesis method is applied to determine the bright soliton solutions to the model. The starting hypothesis is

$$A_1(z,t)=g(s)e^{i\phi(z,t)} \quad (2)$$

where g(s) represents the shape of the pulse, and s = z - vt; the phase is $\phi(z,t)$ = - ωz + κt, z is the distance, t is the time, ω is the frequency, and κ is the wave number. Two cases are analyzed, Case 1 for β_1 a negative real number, and Case 2 when β_1 is a complex number.

2.1 Case 1

In this case we consider β_1 a negative real number and analyze the model for negative refractive metamaterials.

Using the traveling wave hypothesis we obtain the solution $A_1(z,t)$ as follows

$$A_1(z,t)=\sqrt{\frac{2\omega+\beta_2\kappa^2-2\beta_1\kappa}{\gamma}}csch[$$

$$\sqrt{\frac{2\omega+\beta_2\kappa^2-2\beta_1\kappa}{\beta_2}}\frac{(vt-z)}{v}]e^{i\phi} \quad (3)$$

The following constraint conditions are necessary for the existence of the solution $A_1(z,t)$

$$\gamma(2\omega+\beta_2\kappa^2-2\beta_1\kappa)>0 \quad (4)$$

$$\beta_2(2\omega+\beta_2\kappa^2-2\beta_1\kappa)>0 \quad (5)$$

$$\boldsymbol{\beta_1<0} \quad (6)$$

2.2 Case 2

In this case we consider β_1 a complex number and analyze the model for higher losses metamaterials. Replacing $\beta_1=C+iD$ in equation (3) we obtain the solution

$$g(z,t)=Mcsch[\frac{N(vt-z)}{v}] \quad (7)$$

where

M = $\sqrt{\frac{(2\omega-2C\kappa+\beta_2\kappa^2)(1-Cv+\beta_2v\kappa)+Dv(2D\kappa-\alpha)}{\gamma(1-Cv+v\beta_2\kappa)}}$

N = $\sqrt{\frac{(2\omega-2C\kappa+\beta_2\kappa^2)(1-Cv+\beta_2v\kappa)+Dv(2D\kappa-\alpha)}{\beta_2(1-Cv+v\beta_2\kappa)}}$

The following constraint conditions are derived for the existence of the soliton solutions

$$\gamma[(2\omega-2C\kappa+\beta_2\kappa^2)(1-Cv+\beta_2v\kappa)$$
$$+Dv(2D\kappa-\alpha)](1-Cv+v\beta_2\kappa)>0 \quad (8)$$

$$\beta_2[(2\omega-2C\kappa+\beta_2\kappa^2)(1-Cv+\beta_2v\kappa)$$
$$+Dv(2D\kappa-\alpha)](1-Cv+v\beta_2\kappa)>0 \quad (9)$$

We will distinguish between the following two cases for different types of materials

$$C<0,D>0 \quad (10)$$

$$C>0,D>0 \quad (11)$$

where (10) pertains to DNG materials, and (11) to regular metamaterials.

3 Conclusions

In the current paper we proposed an analytical model, and obtained soliton solutions to the model along with constraint conditions for short soliton pulse propagation through photonic crystal metamaterials with negative refraction and higher losses. The model carefully considers refraction and loss properties observed in earlier simulations and experimental results.

4 References

[1] Kaisar Khan, M. Mahmood, Anjan Biswas,Milivoj Belic, "Nonlinear pulse propagation in optical metamaterials". *Journal of Computational and Theoretical Nanoscience.* Volume 12, 4837-4841. (2015.

[2] Kaisar Khan, Khaled Mnaymneh, Hazem Awad, Imad Hasan, Trevor Hall, "Optical waves in photonic crystal metamaterials". *Journal of Applied Physics A*, 117(2), 629-634, (2014).

[3] Yanan Xu, Michelle Savescu, Kaisar R. Khan, Mohammad F. Mahmood, Anjan Biswas, Milivoj Belic, "Soliton propagation through nanoscale waveguides in optical metamaterials" *Optics and Laser Technology* 77, 177–186, (2016) (invited paper)

[4] Yanan Xu, Qin Zhoub, Ali H. Bhrawy,Kaisar R. Khan, M. Mahmood, Anjan Biswas, Milivoj Belic ," Bright solitons in optical metamaterials by traveling wave hypothesis", *Optoelectronics And Advanced Materials – Rapid Communications*, Vol. 9, No.3-4, 384 - 387, (2015).

Multiple toroidal Resonances in Folded Metamaterials

Shengyan Yang[1,3], Zhe Liu[1], Ling Jin[1], Wuxia Li[1], Shuang Zhang[2], Junjie Li[1,3], and Changzhi Gu[1,3*]

[1] Beijing National Laboratory for Condensed Matter Physics, Institute of Physics, Chinese Academy of Sciences, Beijing 100190, China

[2] School of Physics and Astronomy, University of Birmingham, Birmingham B15 2TT, United Kingdom

[3] School of Physical Sciences, CAS Key Laboratory of Vacuum Physics, University of Chinese Academy of Sciences, Beijing 100190, China

[*]corresponding author: czgu@iphy.ac.cn

Abstract- We demonstrate the excitation of multiple high-Q-factor toroidal resonances in folded metamaterials, which were fabricated by focused-ion-beam induced deformation technique. The field distributions clearly show the generation of toroidal mode with tightly restrained magnetic vortex in the subwavelength structures. It is shown that the toroidal resonances can be controlled by the geometry of the metamaterial and the angle of incident light. The folded metamaterial exhibiting toroidal resonances holds potential for applications in lasing spaser, nonlinear processing, and sensing.

Toroidal dipole is a fundamental electromagnetic excitation distinct from the magnetic and electric dipoles. Such excitation have been held responsible for parity violation in nuclear and particle physics, and provide important contributions to the basic physical properties of matters[1-3]. The exploitation of toroidal excitations may have significant implications for the fields of photonics, plasmonics, chemical/biological sensing, information and energy[2]. Specifically, metamaterials supporting toroidal resonance have been predicted to be a promising candidate for lasing spaser, dichroism and non-reciprocal refraction of light, which is well worth studying in high frequency region. However, as the resonant frequency approaching infrared and visible regime, the implementation of a toroidal resonance in true 3D sophisticated metamaterials becomes extremely difficult due to the limitations of fabrication, which makes it very difficult to experimentally study the elusive optical phenomena involving the toroidal dipole. Moreover, almost all of the preceding studies have exclusively focused on a single toroidal dipolar resonance, while simultaneous excitation of multiple toroidal dipolar resonances still remains formidable task[2].

In this paper, we experimentally demonstrate novel folded metamaterials that support multiple high-Q-factor toroidal resonances at infrared region. The folded metamaterial consist of an array of subwavelength joint double split ring resonators (JDSRRs) and square holes arranged in a square lattice geometry. The metamaterial samples were fabricated using focused-ion-beam induced deformation technique on gold nano-films[4-6], and the transmission spectra were measured utilizing a Fourier transform infrared (FTIR) spectrometer. The experimental results indicate that double sharp toroidal resonances with Q factor exceeding 23 are achieved. The toroidal resonances are induced by the strong coupling between the bright surface-plasmon-polariton mode supported by the in-plane hole array and dark inductive-capacitive modes of the vertical JDSRRs. The lateral coupling between adjacent unit-cells give rise to an otherwise inaccessible hybridized toroidal dipolar resonance. By tailoring the geometrical parameters of the folded metamaterials or the angle of incident light, both the toroidal resonance can be modulated.

Moreover, the folded metamaterials, exhibiting sharp toroidal resonances with unique topology of electromagnetic field, provide a unique platform for tailoring the electromagnetic distribution of complex topology for light confinement, energy trapping and sensor applications, and may promote the understanding of the quantum mechanism of inter-molecular interactions involving toroidal molecular structures, which are widespread in nature.

Acknowledgements: This work is supported by the National Key Research and Development Program of China under Grant No. 2016YFA0200400, and No. 2016YFA0200800; the National Natural Science Foundation of China under Grants Nos. 91323304, 11674387, 11504414, 11574369, 11574385, 11574368, and 61390503; Trategic Priority Research Program and Key Research Program of Frontier Sciences, CAS, Grant No.XDB07020200 and No.QYZDJ-SSW-SLH042; European Research Council Consolidator Grant (TOPOLOGICAL).

REFERENCES

1. Kaelberer, T., Fedotov, V. A., Papasimakis, N., Tsai, D. P. and Zheludev, N. I. "Toroidal dipolar response in a metamaterial," *Science*, Vol. 330, 1510-1512, 2010.
2. Papasimakis, N., Fedotov, V. A., Savinov, V., Raybould, T. A., Zheludev, N. I., "Electromagnetic toroidal excitations in matter and free space," *Nat. Mater.*, Vol. 15, 263−271, 2016.
3. Fan, Y., Wei, Z., Li, H., Chen, H. and Soukoulis, C. M., "Low-loss and high-Q planar metamaterial with toroidal moment," *Phys. Rev. B*, Vol. 87, 115417, 2013.
4. Liu, Z., Du, S., Cui, A. J., Li, Z. C., Fan, Y. C., Chen, S.Q., Li,W. X., Li, J. J. and Gu, C. Z., "High-quality-factor mid-infrared toroidal excitation in folded 3D metamaterials,"*Adv. Mater.*, Vol. 29, 1606298, 2017.
5. Yang, S. Y., Liu, Z., Jin, L., Li, W. X., Zhang, S., Li, J. J., and Gu, C. Z., "Surface plasmon polariton mediated multiple toroidal resonances in 3D folding metamaterials," *ACS Photonics*, Vol. 4, 2650-2658, 2017.
6. Cui A. J., et al, "Directly patterned substrate-free plasmonic 'nanograter' structures with unusual Fano resonances," *Light: Science & Applications*, Vol. 4, e308, 2015.

Shear Horizontal Wave Propagation in Magnetoelastic Multilayered Plates with Negative-Indexed Piezomagnetic Materials

Yongqiang Guo[1], and Liangteng Guo[1]

[1]School of Civil Engineering and Mechanics, Lanzhou University, and Key Laboratory of Mechanics on Disaster and Environment in Western China, Ministry of Education, Lanzhou 730000, China
*corresponding author, E-mail: guoyq@lzu.edu.cn

Abstract

The method of reverberation-ray matrix (MRRM) is introduced to analyze the dispersion curves of SH waves in magnetoelastic multilayered plates consisting of piezomagnetic and elastic laminates. Any piezomagnetic layer can be negative-indexed magnetic material with part or all of its permeabilities being negative. Novel dispersions of SH waves in magnetoelastic multilayered plates with this left-handed piezomagnetic materials are studied. The effects of the magnitude of negative permeabilities and of the overlaid elastic layers on these new properties are discussed.

1. Introduction

In the study of waves in the magnetoelastic waveguides, the permeability is one of the critical characteristic parameters that determine the dispersion properties of wave propagation. When the permeability and permittivity become negative, the electromagnetic material will have many novel properties including the anomalous refraction, the reversal of the Doppler shift and the reversed Cherenkov radiation, some of which have been predicted previously by Veselago [1] with theoretical model. This kind of negative-indexed material has been realized in practice and some researchers [2,3] have observed the novel phenomena in experiments.

Inspired by the concept of left-handed electromagnetic material, we introduce the negative permeabilities, by employing piezomagnetic layers with some or all parts of the permeabilities being negative, into the study of guided SH waves in magnetoelastic multilayered plates to search for new dispersion properties.

2. The formulation of MRRM

2.1. Model description

Consider a general magnetoelastic multilayered plate with n layers unbounded in the layering plane. Each layer is assumed as either piezomagnetic or elastic material with monoclinic anisotropy of 2 point group polarized in y direction and arbitrary thickness, in which the out-of-plane SH wave are decoupled from the in-plane P-SV waves. Here SH wave polarized in y and propagating in x directions is studied.

2.2. Governing equations and their solutions

The generalized strain-displacement relations, the constitutive relations, and the dynamic equations for mechanical field and the Gauss's law of magnetostatics for magnetic field are

$$\boldsymbol{\varepsilon} = \mathbf{L}^{\mathrm{T}}\mathbf{u}\,,\ \mathbf{H} = -\nabla\psi \tag{1}$$

$$\boldsymbol{\sigma} = \mathbf{c}\boldsymbol{\varepsilon} - \mathbf{q}^{\mathrm{T}}\mathbf{H}\,,\ \mathbf{B} = \mathbf{q}\boldsymbol{\varepsilon} + \boldsymbol{\mu}\mathbf{H} \tag{2}$$

$$\mathbf{L}\boldsymbol{\sigma} = \rho\frac{\partial^2\mathbf{u}}{\partial t^2}\,,\ \nabla\cdot\mathbf{B} = 0 \tag{3}$$

where $\mathbf{u}$, $\boldsymbol{\varepsilon}$, $\boldsymbol{\sigma}$, $\mathbf{H}$ and $\mathbf{B}$ only contain the components related to the considered SH wave.

The solutions to these governing equations can be obtained by assuming the harmonic plane-wave forms and using the state-space formalism.

$$\begin{Bmatrix}\hat{\mathbf{v}}_u(z)\\ \hat{\mathbf{v}}_\sigma(z)\end{Bmatrix} = \begin{bmatrix}\boldsymbol{\Phi}_{u-} & \boldsymbol{\Phi}_{u+}\\ \boldsymbol{\Phi}_{\sigma-} & \boldsymbol{\Phi}_{\sigma+}\end{bmatrix}\begin{bmatrix}\exp(\boldsymbol{\Lambda}_- z) & \mathbf{0}\\ \mathbf{0} & \exp(\boldsymbol{\Lambda}_+ z)\end{bmatrix}\begin{Bmatrix}\mathbf{a}\\ \mathbf{d}\end{Bmatrix} \tag{4}$$

where $\hat{\mathbf{v}}_u = \left[\hat{v}, \hat{\psi}\right]^{\mathrm{T}}$ and $\hat{\mathbf{v}}_\sigma = \left[\hat{\tau}_{zy}, \hat{B}_z\right]^{\mathrm{T}}$ are the involved state variables in generalized displacements and stresses, respectively.

2.3. The MRRM for the calculation of dispersion curves

Within the framework of MRRM, the phase relations in the laminates and the scattering relations on the surfaces/interfaces can be obtained:

$$\mathbf{a}_G = \mathbf{P}\mathbf{U}\mathbf{d}_G\,, \tag{5}$$

$$\mathbf{A}\mathbf{a}_G + \mathbf{D}\mathbf{d}_G = \mathbf{0}\,, \tag{6}$$

The system equations are deduced by eliminating the arriving wave amplitudes.

$$(\mathbf{A}\mathbf{P}\mathbf{U} + \mathbf{D})\mathbf{d}_G = \mathbf{0}\,, \tag{7}$$

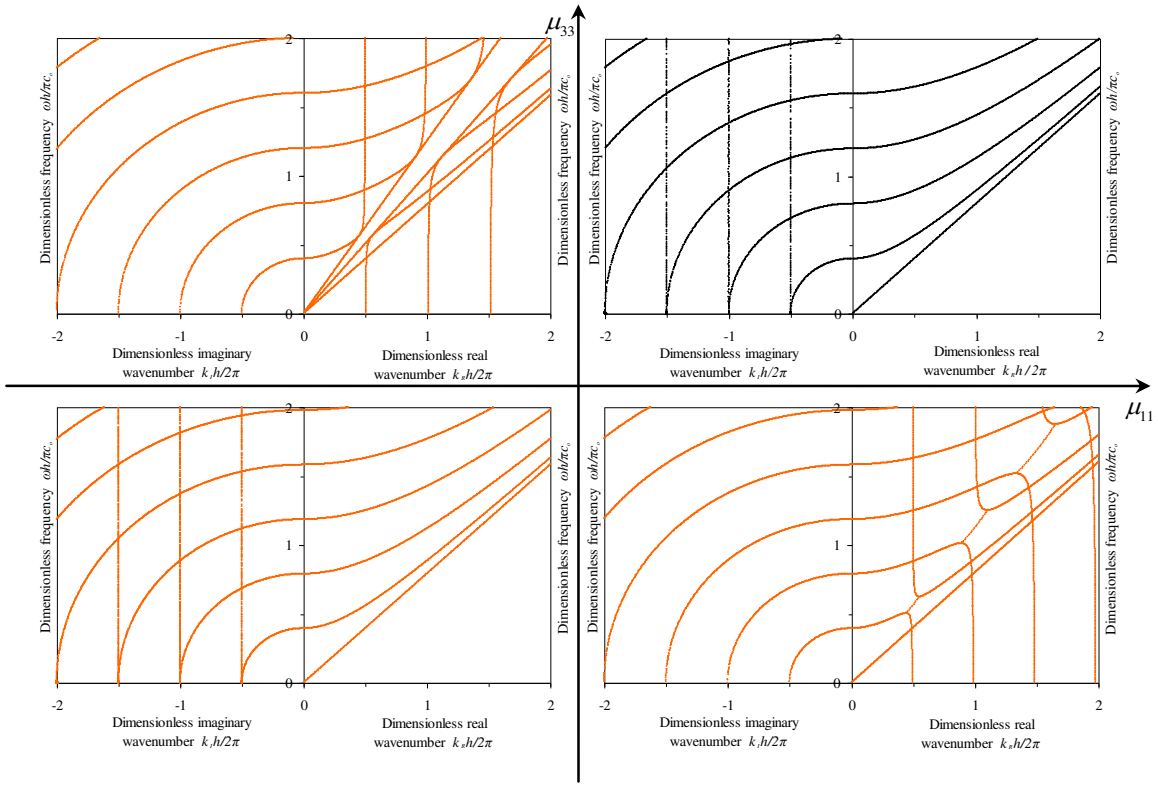


Figure 1: Wavenumber- frequency dispersion curves of a single $CoFe_2O_4$ layer with negative permeabilities.

For existing non-trivial solutions, the determinant of the system matrix needs to vanish.

$$\det\left[\mathbf{APU}+\mathbf{D}\right]=0\,, \tag{8}$$

which implies the dispersion relation among the circular frequency, the wavenumber and the phase velocity.

3. Numerical examples and discussions

Numerical examples are performed to verify the above proposed MRRM and to illustrate the effect of negative permeabilities on SH wave in magnetoelastic multilayered plates. Various dispersion curves are calculated for a single piezomagnetic $CoFe_2O_4$ layer with negative permeabilities, as shown in Fig. 1 for instance. As comparing the counterpart dispersion curves in the four quadrants, the mode transition phenomena can be easily discerned in cases of only one permeability being negative. The group velocity $c_g = \mathrm{d}\omega/\mathrm{d}k$ is pretty large when the transition happens.

The effects of the magnitude of negative permeabilities and of the overlaid elastic layers on the mode transition are also discussed. The change to the frequencies where the mode transition arises can be noticed, which may be used to control the mode transition phenomenon.

4. Conclusions

In summary, this paper extends the MRRM based on the state-space formalism for the analysis of the SH waves in magnetoelastic multilayered plates. The effect of negative permeabilities on the dispersion characteristics of SH wave are studied. Several numerical examples are provided for discussing the novel dispersion in various cases of negative permeabilities in constituent piezomagnetic materials. The mode transition phenomenon is observed in some cases of negative permeabilities in the magnetoelastic multilayered plates. The effects of the magnitude of negative permeabilities and of the overlaid elastic layers on the new mode transition phenomenon are discussed.

Acknowledgements

The work is supported by the National Natural Science Foundation of China (No. 11372119).

References

[1] V.G. Veselago, The electrodynamics of substances with simultaneously negative value of ε and μ, *Sov. Phys. Usp.* 10(4): 509−514, 1968.

[2] C.G. Parazzoli, R.B. Greego, K Li, B.E.C. Koltenbah, M. Tanielian, Experimental verification and simulation of negative index of refraction using Snell's law, *Phys. Rev. Lett.* 90(10): 107401, 2003.

[3] S. Xi, H.S. Chen, T. Jiang, L.X. Ran, J.T. Huangfu, B.-I. Wu, J. A. Kong, M. Chen, Experimental verification of reversed Cherenkov radiation in left-handed metamaterial. *Phys. Rev. Lett* 103(19): 194801, 2009.

Negative refraction and negative dispersion due to quadrupole response of finite size particles

E. Fourkal[1] and A. Smolyakov[2]*,

[1] UPMC Pinnacle, 4300 Londonderry Rd, Harrisburg, PA 17109
[2] University of Saskatchewan, Saskatoon SK, 116 Science Place, S7N 5E2 Canada
*corresponding author, E-mail: andrei.smolyakov@usask.ca

Abstract

The relation between magnetic response of the dispersive media, negative refraction and negative dispersion is discussed. Negative dispersion and refraction is demonstrated for longitudinal and transverse electromagnetic modes in the system of finite size charged clouds. It is also shown that a random set of non-magnetic metal spheres embedded in a dielectric host possesses additional longitudinal and transverse eigen-modes with negative dispersion due to the electric quadrupole coupling. In the region of negative refraction the calculated effective negative permittivity and permeability are also negative.

1. Magnetic response of the dispersive media.

Magnetic response is a common property of strongly dispersive materials, e.g. plasmas. This fact may have been obscured in part due to a commonly accepted in plasma physics approach which does not rely on the notion of magnetic permeability. As it was noted in [1], the notion of the magnetic permeability for high frequency phenomena is not directly related to the density of the magnetic moment of the material. For such cases, it is possible to write Maxwell equations with $\mathbf{B} = \mathbf{H}$ (i.e. $\mu = 1$) so that all currents (including bound currents, normally associated with magnetization) are assigned to the generalized polarization vector $\mathbf{P}$. In this, the so called three field ($\mathbf{E}$, $\mathbf{D}, \mathbf{B}$) model [2], the dielectric response becomes a tensor dependent on the wave vector $\widetilde{\varepsilon} = \varepsilon(\omega, \mathbf{k})$. For the isotropic medium, the most general form of such permittivity tensor is

$$\widetilde{\varepsilon}(\omega, \mathbf{k}) = \varepsilon_T(\omega, k)\left(\mathbf{I} - \frac{\mathbf{kk}}{k^2}\right) + \varepsilon_L(\omega, k)\frac{\mathbf{kk}}{k^2}, \qquad (1)$$

and the electric current is determined by $\mathbf{j} = -i\omega(\varepsilon(\omega, \mathbf{k}) - \mathbf{I}) \cdot \mathbf{E}/4\pi$. Alternatively, the dispersive medium characterized by the tensor (1) can be described by two tensor functions $\varepsilon(\omega, \mathbf{k})$ and $\mu(\omega, \mathbf{k})$ [2]. In such description, the electric current is,

$$\mathbf{j} = \frac{\partial \mathbf{P}}{\partial t} + c\nabla \times \mathbf{M}, \qquad (2)$$

where effective polarization vector $\mathbf{P}$ and magnetization vector $\mathbf{M}$ are defined by the expression

$$\begin{aligned} 4\pi\mathbf{P} &= [\varepsilon(\omega,\ \mathbf{k}) - \mathbf{I}]\,\mathbf{E}, \\ 4\pi\mathbf{M} &= \left[\mathbf{I} - \mu^{-1}(\omega,\ \mathbf{k})\right]\mathbf{B}. \end{aligned} \qquad (3)$$

Both approaches are equivalent and lead to the same physical conclusions. The transition from $\varepsilon(\omega, \mathbf{k})$ and $\mu(\omega, \mathbf{k})$ to $\widetilde{\varepsilon}(\omega, \mathbf{k})$ is unique, while the inverse transformation is not [3, 4]. However, in the limit of small wave numbers k, the inverse transformation $\widetilde{\varepsilon}(\omega, \mathbf{k})$ to $\varepsilon(\omega)$ and $\mu(\omega)$ is well defined [1]. Thus, magnetic response can be viewed merely as a manifestation of the spatial dispersion in the system, which in itself arises not only from the magnetic dipole (and higher order magnetic-type) moments, but also from those associated with the electric polarization currents. In this paper, we show how the magnetic response, in particular, negative permeabiloty and permittivity, arise due to the the electric quadrupole moments.

2. Negative permeability and negative refraction in systems of finite size charged clouds

Computer simulation of plasmas are often done by replacing real charged particles with the finite size charged clouds, Particle-in-Cell method [5]. In this approach, effects of the short range forces are not important and smeared out by spatial field averaging procedure. This averaging procedure is analogous to the averaging employed in the derivation of the macroscopic Maxwell equations and equivalent to the introduction of finite size particles. $\bar{\rho}(\mathbf{k}) = S(\mathbf{k})\rho(\mathbf{k})$.The averaging function $S(\mathbf{k})$ is a smooth localized function in space, which decays to zero at distances larger than the characteristic length scale a. The latter would be a characteristic size of the finite size object. A typical choice is the Gaussian test function, $S(k) \sim e^{-k^2a^2/2}$. The longitudinal and transverse dielectric response functions for the Maxwellian distribution of finite size particles are known[5]

$$\varepsilon_l(k, \omega) = 1 + S(k)^2\frac{k_D^2}{k^2}W\left(\frac{\omega}{kv_T}\right), \qquad (4)$$

$$\varepsilon_t(k, \omega) = 1 - S(k)^2\frac{\omega_p^2}{\omega^2}\left[1 - W\left(\frac{\omega}{kv_T}\right)\right]. \qquad (5)$$

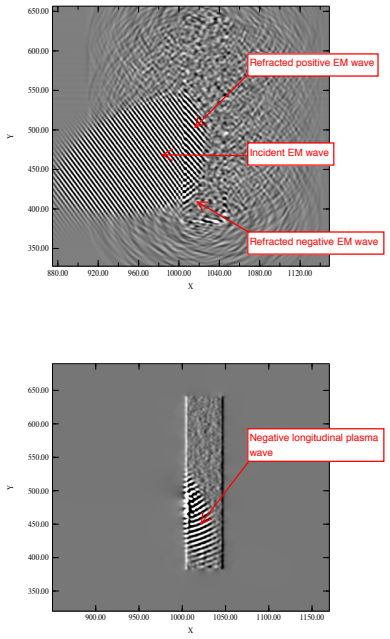


Figure 1: The 2D spatial distribution of the transverse magnetic field $B_z(x, y)$ (the upper picture) and longitudinal electric field $E_x(x, y)$ (the bottom picture) obtained from the PIC simulations.

The electromagnetic system described by Eqs (1) and (2) has strong dispersion for $ka \leq 1$. The negative dispersion and negative refraction has been observed in the PIC simulations of the laser pulse interaction with the cold plasma slab [6], shown in Figure 1 (the bottom picture). In this case, the incident laser pulse with the carrying frequency $\omega_0 < \omega_p$ directly excites the negative refractive plasma wave. Figure 2 (the top picture) shows the snapshot of the spatial distribution of the transverse magnetic field for the case when the laser pulse is incident on the plasma slab. One can clearly see two propagating branches inside the plasma, one of which has a positive dispersion and the other negative.

3. Negative permeabily and negative refraction in a system of of finite size conducting spheres.

Here, we directly calculate the $\varepsilon_l(k, \omega)$ and $\varepsilon_T(k, \omega)$ tensors for the collection of non-magnetic dielectric sphere of radius a and dielectric constant ε_1 embedded in the medium with dielectric constant ε_2 and magnetic permeability $\mu = 1$. External inhomogeneous electric field induces set of multipole moments on a sphere which in the lowest order, $a/\lambda < 1$, are given by

$$\mathbf{p} = \frac{1}{4\pi} \frac{\varepsilon_1 - \varepsilon_2}{\varepsilon_1 + 2\varepsilon_2} a^3 \mathbf{E}, \tag{6}$$

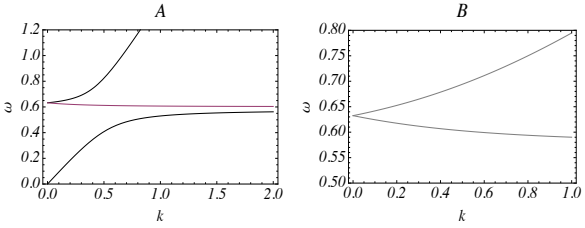


Figure 2: (A) Transverse modes with electric quadrupole and magnetic dipole corrections. Note the negative disp (B) Longitudinal modes with electric quadrupole corrections

$$q_{ij} = \frac{1}{4\pi} \frac{\varepsilon_1 - \varepsilon_2}{2\varepsilon_1 + 3\varepsilon_2} a^5 \left[\frac{1}{2} \left(\nabla_j E_i + \nabla_i E_j \right) - \frac{1}{3} \nabla \cdot \mathbf{E} \delta_{ij} \right], \tag{7}$$

$$\mathbf{m} = \frac{\omega^2 a^5}{30c^2} \left(\varepsilon_1 - \varepsilon_2 \right) \mathbf{B}. \tag{8}$$

One can calculate the transverse and longitudianl tensors, ε_T and ε_L defining propagating transverse and longitudinal electromagnetic modes, as shown in Fig. 2(A) and Fig. 2(B). In each case, there is one mode with negative dispersion. One can also show [6] that the effective electric permittivity $\varepsilon(\omega)$ and the magnetic permeability $\mu(\omega)$ are negative in the region of negative dispersion.

References

[1] L. D. Landau and E. M. Lifshitz. *Electrodynamics of Continuous Media*. Pergamon Press, second edition, 1984.

[2] V. M. Agranovich, Y. R. Shen, R. H. Baughman, and A. A. Zakhidov. Linear and nonlinear propagation in negative refraction metamaterials. *Phys. Rev. B*, 69:165112, 2004; V. M. Agranovich and Y. N. Gartstein. Spatial dispersion and negative refraction of light. *Physics-Uspekhi*, 49, 1029–1044, 2006.

[3] D. A. Kirzhnits. General properties of electromagnetic response functions. *Physics-Uspekhi*, 30:575–587, 1987.

[4] A. P. Vinogradov. On the form of constituitive equations in electrodynamics. *Physics-Uspekhi*, 45(3):331–338, 2002.

[5] C. K. Birdsall and A. B. Langdon. *Plasma Physics, via computer simulation*. Taylor and Francis group, LLC, 2005.

[6] A. Smolyakov and E. Fourkal, Negative permeability and negative refraction in composite systems with finite size inclusions. *Phys Rev A*, 87, 013817, 2013.

Plasmon resonances, extraordinary transmission and reflection-less absorption in overdense plasma-diffraction grating structures

A. Smolyakov[1]* and N. Sternberg

[1] Department of Physics and Engineering Physics, University of Saskatchewan, Saskatoon SK S7N 5E2, Canada
[2]Department of Mathematics and Computer Science, Clark University, Worcester, MA, USA
*corresponding author, E-mail: andrei.smolyakov@usask.ca

Abstract

Structure of resonances and coupling are studied in the overdense plasma slab configuration with a diffraction grating. Analytical criteria and exact expressions are obtained for resonance conditions for absolute transparency of the ideal over-dense plasma and reflectionless absorption in plasma slab with dissipation.

1. Introduction

The anomalous (up to 100%) energy transmission through an overdense plasma region with $\omega < \omega_{pe}$, $\varepsilon_p = 1 - \omega_{pe}^2/\omega^2 < 0$, where ω_{pe} is the electron plasma frequency, can be achieved via superposition of decaying and growing evanescent waves in the tunneling region [1, 2, 3]. The propagating vacuum mode can be coupled with a surface wave via zero-ε_{eff} structures [2, 5] with $\varepsilon_{eff} = \varepsilon_a a + \varepsilon_p a = 0$, where a is the width of the layer with $\varepsilon_a > 0$, and d is the width of the plasma layer with $\varepsilon_p < 0$. In another approach, the plasmon surface wave mode can be coupled with the vacuum wave via scattering on a periodic subwavelength structure [6]. Formally, the full solution of the transmission and/or reflection problem is straightforward linear problem for coupled equations for incident, reflected, and transmitted propagating waves, as well as for the standing and evanescent modes in different regions. However due to large number of unknowns, obtaining the solution is technically cumbersome and is often done numerically so that the nature of the involved resonance modes and their coupling is not easily understood. A phenomenological model, based on the idea of critical coupling in optical waveguides has been suggested for resonance coupling and conditions for transmission and absorption [1] in overdense plasmas. Here a simple framework based on the standard wave impedance concept is formulated that allows a compact description of the resonance coupling, mode amplification, transmission and absorption in overdense plasmas.

2. Basic model

We consider the electromagnetic wave incident on the plasma layer preceded by the diffraction grating which is placed at a distance a from the plasma boundary as shown in Fig. 1. The transverse magnetic TM or p-polarization is assumed, so that the electromagnetic field has the components $\mathbf{E} =(E_x, E_y, 0)$ and $\mathbf{B} =(0, 0, B_z)$. The magnetic field is described by the following equation

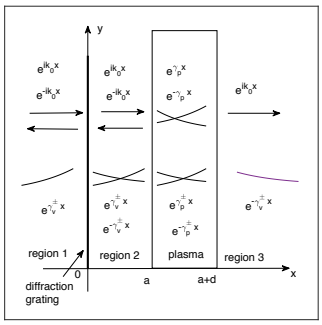


Figure 1: Geometry of the problem

$$\varepsilon \frac{\partial}{\partial x}\left(\frac{1}{\varepsilon}\frac{\partial B_z}{\partial x}\right) - k_y^2 B_z + \frac{\omega^2}{c^2}\varepsilon B_z + \frac{\omega^2}{c^2}\varepsilon_g h_g \left(\mu_0 + \mu_1 \cos\left(qy\right)\right)\delta\left(x\right) B_z = 0 \quad (1)$$

The last term here describes the diffraction grating at $x = 0$ with q as the wave vector of the grating. Here, similarly to other works we neglect the higher order side-bands and consider the analytical solution as a sum of the principal $B^0\left(x\right)e^{ik_y y}$, and two sideband $B^{\pm}\left(x\right)e^{i(k_y \pm q)y}$ harmonics. After some algebra one formulates the matching condition at the diffraction grating in the impedance form

$$\left(Z_2^0\left(0\right) - Z_1{}^0\left(0\right) - \frac{ik_{g0}c}{\omega}\right) \times \left(Z_2^+\left(0\right) - Z_1{}^+\left(0\right) - \frac{ik_{g0}c}{\omega}\right) = -\frac{k_{g1}^2 c^2}{2\omega^2}. \quad (2)$$

3. Surface wave resonance and reflectionless transmission

Absolute transparency (100%) of an overdense plasma layer has been demonstrated in complex multi-layer structures where it can be supported by surface wave resonances as well as by standing wave (Fabry-Perot type) resonances [2]. Additional resonances caused by standing waves can also be supported by the additional modes which exist in

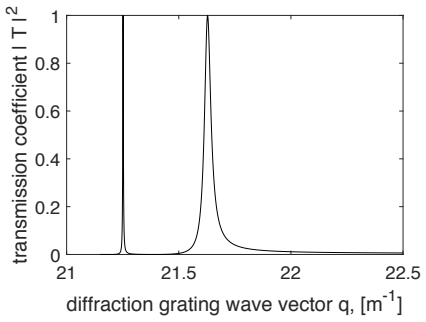


Figure 2: Transmission, $|T|^2$, coefficient versus diffraction grating wave vector, q.

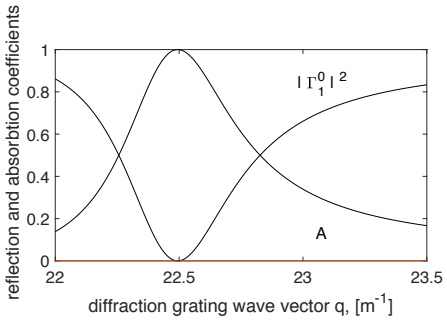


Figure 3: Reflection and absorption coefficients, $|\Gamma_1^0|^2$ and A, versus diffraction grating wave vector, q.

warm plasmas [3]. It was proposed BliokhRMP2008 that two diffraction gratings on both sides of a plasma layer are required to realize the absolute (100%) transparency. Here, we show that full transparency can be achieved with a single grating. We have derived the following conditions for absolute transparency

$$1 = Z_2^0(0) - \frac{k_{g1}^2 c^2}{2\omega^2} \frac{1}{Z_2^+(0) + \kappa_v^+}. \qquad (3)$$

We show that this equation reduces to two analytical conditions, one of which is equivalent to the dispersion relation for the coupeld surface modes in a finite width slab and another condition defines the distance between diffraction grating and plasma. Both conditions have to be satisfied simultaneously for absolute (100%) transmission with $T = 1$. A numerical example for the transmission coefficients as a function of the diffraction grating wave vector is shown in Fig.2.

4. Reflection-less absorption in the dissipative plasma layer

The plasmon resonances are sensitive to dissipation. They are however are responsible for the reflectionless absorption of the electromagnetic wave. This has been demonstrated experimentally in Ref. [4]. Here we derive the exact analytical condition that emphasizes the role of the plasmon resonance and fully determines the exact conditions on the values of a (width of the vacuum region) and q (diffraction grating wave vector) for reflectionless absorption, when the energy of the incident electromagnetic wave is fully absorbed in the plasma, $T = 0$, $\Gamma_1^0 = 0$, as illustrated in Fig. 3.

5. Summary

We have shown that the extraordinary transmission also exists in the configuration with single diffraction graying, in addition to the two gratings scheme (on both sides of the plasma layer) as proposed in Ref. [1]. We have determined analytically the resonance values of the width of the vacuum region for the full transmission and reflectionless absorption problems.

This work was supported in part by AFOSR #FA9550-07-1-0415 and #FA9550-15-1-0226.

References

[1] K. Y. Bliokh, Y. P. Bliokh, V. Freilikher, S. Savel'ev, and F. Nori. *Reviews of Modern Physics*, 80(4):1201–1213, 2008; Y. P. Bliokh. *Optics Communications*, 259(2):436–444, 2006.

[2] A. I. Smolyakov, E. Fourkal, S. I. Krasheninnikov, and N. Sternberg, *Progress in Electromagnetics Research-Pier*, 107:293–314, 2010.

[3] E. Fourkal, I. Velchev, C. M. Ma, and A. Smolyakov, *Physics of Plasmas*, 13(9):092113, 2006.

[4] Y. P. Bliokh, J. Felsteiner, and Y. Z. Slutsker, *Physical Review Letters*, 95(16):165003, 2005.

[5] A. Alu and N. Engheta, *Ieee Transactions on Antennas and Propagation*, 51(10):2558–2571, 2003.

[6] A. M. Dykhne, A. K. Sarychev, and V. M. Shalaev, *Physical Review B*, 67(19):195402, 2003.

Polaritonic light-matter interaction in van der Waals heterostructures

Itai Epstein

ICFO, Spain
*corresponding author, E-mail: Itai.Epstein@icfo.eu

Abstract

Van der Waals heterostructures of two-dimensional (2D) materials have become a key enabler for revealing and tailoring electronic, optical and opto-electronic properties (1). These heterostructures are constructed by vertically stacking atomically thin 2D materials, selected from a rich palette of multiple materials, such as graphene (semi-metal), hexagonal-boron-nitride (hBN ,dielectric) and transition-metal-dichalcogenides (TMD, semiconductors) (2). The most common heterostructure - graphene encapsulated by hBN, has also recently emerged as a platform for polaritonics (3, 4), revealing unique properties of both plasmons in graphene and excitons in TMDs. In this talk I will present our recent research relating to plasmonic and excitonic light-matter interaction in Van der Waals heterostructures: We show that heterostructures of graphene, h-BN, and metals support highly confined and slow plasmons, at 300 times the fraction of the speed of light, where nonlocal effects can be probed (5). We also investigate the limits of (out-of-plane) confinement of plasmons down to the ultimate physical boundary of one atom-thick layer. We find that propagating graphene plasmons can be confined down to 0.3 nm and drive a low-loss nonlocal metal response, with mode volume confinement of about 10-9 (6). In addition, I will discuss new possibilities for increased light matter interaction in excitonic Van der Waals heterostructures.

References

1. K. Novoselov et al, Science 353 (2016).
2. A. K. Geim et al, Nature 499, 419 (2013).
3. T. Low et al., Nature materials 16, 182 (2017).
4. D. Basov et al, Science 354 (2016).
5. M. B. Lundeberg, et al., Science 357, 187 (2017).
6. D. Alcaraz et al, accepted to Science (2018).

Double-Epsilon-Near-Zero and Resonant Gain Metal/Dielectric Multilayers

Vincenzo Caligiuri[1], Milan Palei [1,2], Muhammad Imran [1,2], Liberato Manna[1], and Roman Krahne[1]

[1] Nanochemistry Department, Istituto Italiano di Tecnologia, Via Morego 30, 16163 Genova, Italy
[2] Dipartimento di Chimica e Chimica Industriale, Università degli Studi di Genova, Via Dodecaneso, 31, 16146 Genova, Italy

*Vincenzo Caligiuri, E-mail: vincenzo.caligiuri@iit.it

Abstract

Here we investigate the possibility to weakly-couple a $CsPbBr_3$ perovskite dye with a "double-epsilon-near-zero" planar plasmonic nanoresonator in order to obtain a noticeable enhancement of its spontaneous emission, quantum efficiency and decay rate. Furthermore, we illustrate the possibility to reach the so-called "Resonant Gain dielectric singularity" propagation regime, in which remarkable amplification and canalization of the emitted light are possible, constituting a very promising starting point for nanoscale lasing effects and amplified perfect lensing.

1. Introduction

One of the most versatile platforms to engineer and study the ENZ response of matter is constituted by multilayered metamaterials made of alternated pairs of metal and dielectric films.[1,2] A nanometric MIM capacitor can manifest volume plasmons called *Gap Plasmon Polaritons* (GPPs) able to effectively confine light inside the internal dielectric. When stacking multiple MIM capacitors, their plasmonic response hybridizes giving rise to BPPs.[3,4] Here, we demonstrate via direct spectroscopic ellipsometric analysis the ENZ nature of the BPPs rising from the strong coupling between two MIM nanocavities that constitute a MIMIM structure. The associated two BPPs are engineered such that the higher energy BPP is tuned with the absorbance of $CsPbBr_3$ perovskite nanocrystal layer, and the lower energy BPP to its emission. We demonstrate that the weak coupling between the selected fluorophore and the MIMIM allows the Surface Plasmon Enhanced Absorption (SPEA) and Surface Plasmon Coupled Emission (SPCE) phenomena to occur, inducing a remarkable enhancement of the spontaneous emission, decay rate and quantum efficiency of the fluorophore. Furthermore, we theoretically investigate a second architecture in which the fluorophore is directly embedded in the metal/dielectric multilayer.[5] Such a structure, falls in the field of the so called *Hyperbolic Metamaterials*.[6–8] We demonstrate how this structure can manifest a special dispersion resonance known as *Resonant-Gain Dielectric Singularity*, by virtue of which remarkable light confinement and amplification is obtainable. This structure constitutes also a very promising candidate for plasmonic nano-LASER devices and self-amplified nano-imaging.

2. Discussion

A MIMIM structure made of Ag (20 nm) and Al_2O_3 (80 nm) has been realized whose BPPs resonances have been found at 373 nm and 510 nm, respectively (see Figure 1a). The MIMIM structure has been engineered and fabricated such that the two BPPs are tuned with the absorbance and emission of a $CsPbBr_3$ perovskite nanocrystal (see inset of figure 1b) placed on the top of it, separated from the MIMIM by a 50 nm thick alumina layer.

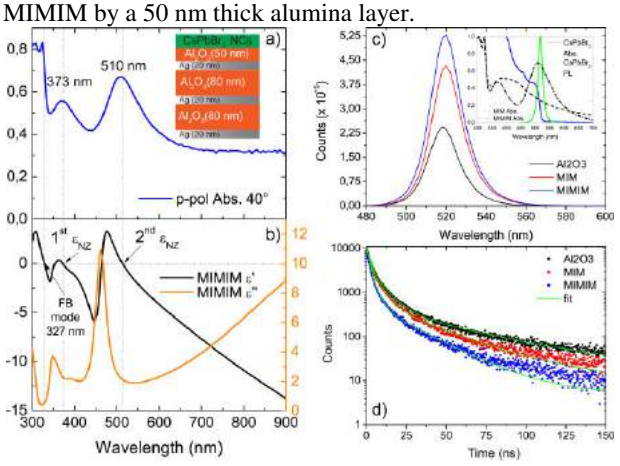


Figure 1: (a) Absorbance and (b) ellipsometric analysis of the MIMIM structure. (c) PL and (d) decay rate of the fluorophore placed on Al_2O_3, MIM and MIMIM structure.

Spectroscopic ellipsometry allows for a direct measure of the ENZ nature of the BPPs present in the MIMIM structure (Figure 1b). When placed on the top of the MIMIM multilayer, a remarkable enhancement of the spontaneous emission (Figure 1c) and of the decay rate (Figure 1d) is found with respect to the cases in which the fluorophore is in contact with a bare Al_2O_3 layer or a MIM system. Noteworthy, in the case of the MIMIM system, an enhancement of the quantum yield is found with respect to the Al_2O_3 , while a decrease is found in the case of the MIM system. This demonstrate how the combination of the SPEA

and SPCE effects leads to an effective enhancement of the quantum efficiency of the system. On the other hand, a second scenario is theoretically analyzed here, in which the dye is placed inside the multilayers. When considering a sufficiently high number of metal/dielectric multilayers, the optical response of the full *metamaterial* becomes extremely anisotropic giving rise to two permittivities, one parallel ($\tilde{\varepsilon}_{\parallel}$) and one perpendicular ($\tilde{\varepsilon}_{\perp}$) to the surface plane of the multilayer, whose expression can be approximated in the framework of the effective medium theory. If the signs of the two permittivities are opposite, the dispersion relation of the metamaterial is hyperbolic and, therefore, these materials take the name of *Hyperbolic Metamaterials* (HMM). Straightforwardly, here we demonstrate that $\tilde{\varepsilon}_{\parallel}$ and $\tilde{\varepsilon}_{\perp}$ can manifest respectively a zero and a pole at the same wavelength if

$$t_d = t_m,\ \varepsilon'_m = -\varepsilon'_d \text{ and } \varepsilon''_m = -\varepsilon''_d;$$

(see Figure 2a). When such a condition is satisfied the HMM respects the *Resonant Gain* (RG) conditions and, when a suitable number of bilayers is chosen (see Figure 2b), extremely subwavelength canalization together with a huge amplification of the radiation inside the HMM are possible (see Figure 2c).

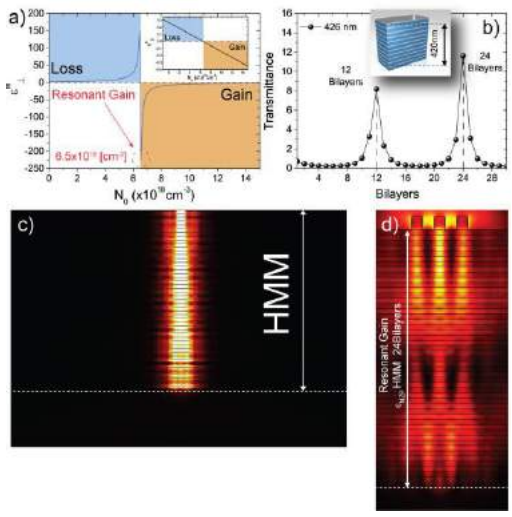


Figure 2:(a) EMT design of the Resonant Gain condition, (b) suitable number of bilayers. Extreme light confinement (c) and Amplified Perfect Imaging (d).

Moreover, thanks to the noticeable light confinement reached in this configuration, the RG-HMM can be used a near-field planar amplifying perfect lens with a resolution close to λ/d, where d is the periodicity of the HMM, as demonstrated in Figure 2d. This system is also a very promising candidate for plasmonic nano-LASER applications.

3. Conclusions

In conclusion, we illustrate our recent findings in light-matter interaction involving exotic plasmonic nanoresonators. In the first case, the weak coupling between a perovskite and a *double-epsilon-near-zero* nanostructure is explored, demonstrating a noticeable enhancement of the spontaneous emission, decay rate and quantum yield. In the second case, a complete HMM multilayer embedding a dye is theoretically analyzed, working at the so-called *Resonant Gain* condition in which strong amplification and canalization of light inside the HMM is demonstrated. The structures we propose here are appealing for a variety of applications, ranging from sensing, low-threshold amplified spontaneous emission, nano-LASER and self-amplified super-resolution nano imaging.

4. Acknowledgment

The research leading to these results has received funding from the European Union 7th Framework Programme under Grant Agreement No. 614897 (ERC Consolidator Grant "TRANS-NANO") and from Horizon 2020 under the Marie Skłodowska-Curie Grant Agreement COMPASS No. 691185.

References

[1] S. Savoia, G. Castaldi, V. Galdi, A. Alù, N. Engheta, PT -symmetry-induced wave confinement and guiding in ε -near-zero metamaterials, *Phys. Rev. B - Condens. Matter Mater. Phys.*, *91*, 2015.

[2] M. G. Silveirinha, N. Engheta, Theory of supercoupling , squeezing wave energy , and field confinement in narrow channels and tight bends using ε near-zero metamaterials, *Phys. Rev. B - Condens. Matter Mater. Phys.*, *76*, 245109, 2007.

[3] I. Avrutsky, I. Salakhutdinov, J. Elser, V. Podolskiy, Highly confined optical modes in nanoscale metal-dielectric multilayers, *Phys. Rev. B - Condens. Matter Mater. Phys.*, *75*, 241402, 2007.

[4] S. A. Maier, *Plasmonics: Fundamentals and Applications*.

[5] V. Caligiuri, L. Pezzi, A. Veltri, A. De Luca, Resonant Gain Singularities in 1D and 3D Metal-Dielectric Multilayered Nanostructures *ACS Nano*, *11*, 1012, 2017.

[6] V. Caligiuri, R. Dhama, K. V Sreekanth, G. Strangi, A. De Luca, Dielectric singularity in hyperbolic metamaterials: the inversion point of coexisting anisotropies, *Sci. Rep.*, *6*, 20002, 2016.

[7] V. Caligiuri, A. De Luca, Metal-semiconductor-oxide extreme hyperbolic metamaterials for selectable canalization wavelength, *J. Phys. D Appl. Phys.*, *49*, 08LT01, 2016.

[8] V. Caligiuri, R. Lento, L. Ricciardi, R. Termine, M. La Deda, S. Siprova, A. Golemme, A. De Luca, Environmental Control of the Topological Transition in Metal/Photoemissive-Blend Metamaterials, *Adv. Opt. Mater.*, *6*, 1, 2018.

Investigation on the optimization of the coding matrix based on the tailor scattering properties of the coding metamaterials

Shuai Yang[1], Qun Wu[1,*], Yuming Wu[2], Xumin Ding[1], and Kuang Zhang[1]

[1]School of Electronic & Information Engineering, Harbin Institute of Technology, Harbin, China
[2]School of Information and Electronics, Beijing Insititute of Technology, Beijing
*corresponding author, E-mail: qwu@hit.edu.cn

Abstract

Diverse electromagnetic(EM) responses of coding metamaterials have been investigated, and the general research method is to use full-wave simulation. But if we only care its scattering properties, it is not necessary to perform full-wave simulation. Based on metamaterial particle that has multiple response and genetic algorithm which is coupled with the scattering pattern analysis, we can optimize the coding matrix quickly to tailor the scattering properties without using full-wave simulation every time. Since the coding matrix control of each particle allow modulation of EM wave, various EM phenomena can be achieved easier. In this article, We proposed two reflective unitcells with different reflection phase, then build a semianalytical model for unitcells. To tailor the scattering properties, genetic algorithm which normally based on binary coding, is coupled with the scattering pattern analysis in order to optimize the coding matrix. Finally we compared the simulation results with the semianalytical calculation results and we found that the simulation results agrees very well with the theoretical values.

1. Introduction

Metamaterials, normally composed by artificially periodic structures with sub-wavelegth scales, made it possible to design multifunction coding metamaterials[1][2][3].Various of extraordinary EM phenomena have been found in microwave, terahertz and optical fields[4][5][6][7]. Consequently, coding metamaterials have tremendous application potentials, numerous devices like invisibility cloak, planar lens, and perfect absorber were made by using metamaterials[8][9][10]. Most of aforementioned metamaterials have a certain function, consequently the manipulation of EM wave is fixed once the design is completed. In recent years, much attention has been paid on coding metamaterials whose EM response can be dynamically controled[11] [12]. While a variety of functionalities have been successfully present with different metamaterials, the way to get coding matrix and simultaneous demonstration of different functionalities on a certain metamaterial has not been fully reported.

The present study focuses on the optimization of the coding matrix and the effect of different coding matrix on its scattering properties. Initially, we present a design of metamaterial particles with dynamic mutlti-functional properties and we simulated the reflection performances using full-wave simulation software. Subsequently we arranged the metamaterial particles periodically to construct a metasurface. Finally we get certain scattering properties by programming a coding matrix with the aid of genetic algorithm(GA)[11].Fig. 1 illustrates the flowchart of the GA-Based optimization.

2. Semianalytical Modeling

In what follows, we study the scattering properties of our coding metamaterials for plane-wave illumination. As a meaningful observable to quantify the scattering properties, we consider the bistatic RCS:

$$\sigma(\theta,\phi) = \lim_{x\to\infty} 4\pi r^2 \frac{|E_s|^2}{|E_i|^2} \tag{1}$$

Accordingly, we define the RCS tatio

$$\gamma = \frac{\max\limits_{\theta,\phi} \sigma_{MM}(\theta,\phi)}{\max\limits_{\theta,\phi} \sigma_{PEC}(\theta,\phi)} \tag{2}$$

Where E_i and E_s denote the incident and scattered electric fields respectively, (θ,ϕ) denote the observation direction in the far fields, and the subscripts "MM" and "PEC" indetify the metamaterials and PEC targets. In Equation (2) requires the full-wave numerical solution of two 3D scattering problems. Nevertheless, the Semianalytical approximation that was developed in ref. [1]. And the directivity of metamaterials can be described as

$$D(\theta,\phi) = \frac{4\pi|f(\theta,\phi)|^2|F(ksin\theta cos\phi, ksin\theta sin\phi)|^2}{\int_0^{2\pi} d\phi \int_0^{\frac{\pi}{2}} d\theta |f(\theta,\phi)|^2|F(ksin\theta cos\phi, ksin\theta sin\phi)|^2} \tag{3}$$

The expression in Equation (3) closely resembles the directivity of antenna arrays. So we considered every unitcell as an antenna. Then we identify the "antenna

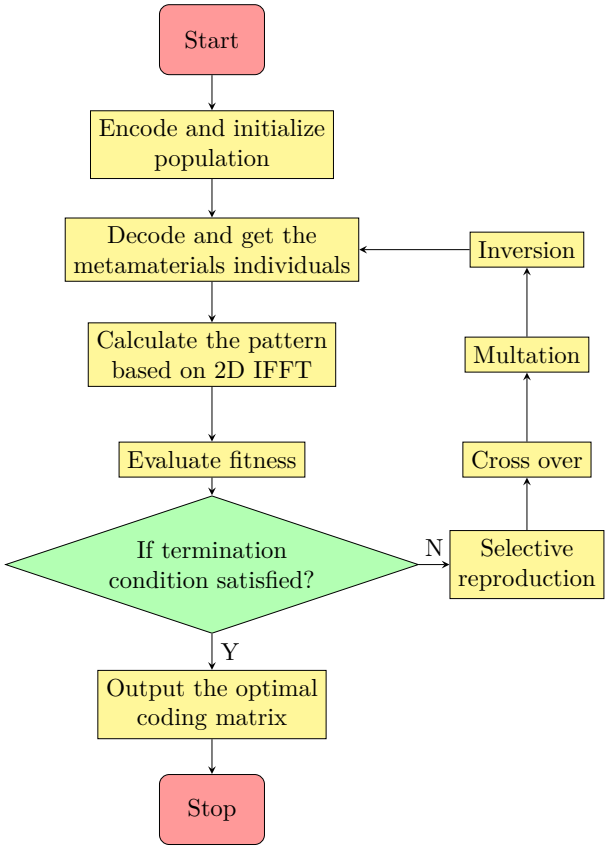


Figure 1: Flowchart of genetic algorithm(GA) based optimization for various functions.

factor"

$$f(\theta,\phi) = (\vec{y}cos\theta - \vec{z}sin\theta sin\phi) \times sinc(\frac{kdsin\theta cos\phi}{2})sinc(\frac{kdsin\theta sin\phi}{2}) \quad (4)$$

and the "array factor"

$$F(k_x,k_\gamma) = \sum_{n,l=0}^{N-1} \Gamma_{nl} exp[-id(nk_x + lk_\gamma)] \quad (5)$$

with $\vec{x}$ denoting an x directed unit vector, $sinc(x) \equiv sin(x)/x$, $k = 2\pi/\lambda$ the vacuum wavenumber, N the number of unitcell per linear dimension, Γ_{nl} the reflection coefficient associated with the generic unitcell and k_x and k_γ the x-domain and γ-domain wavenumbers.

The equations (3)-(5) show an semianalytical working model without full-wave numerical simulations. Furthermore, we designed the unitcell which reflection phase 0 and π as "0" and "1" lattices. The total number of the lateeices is depended on the size of matematerials, and the number of lattices "0" and "1" is chosens accroding to the information entropy theoty. For controlling the reflective scattering beam, a coding matrix T has been introduced to describe a metamaterial with $M \times N$ array.

$$T = \begin{bmatrix} t_{1,1} & \cdots & t_{1,n} & \cdots & t_{1,N} \\ \vdots & \ddots & \vdots & \ddots & \vdots \\ t_{m,1} & \cdots & t_{m,n} & \cdots & t_{m,N} \\ \vdots & \ddots & \vdots & \ddots & \vdots \\ t_{M,1} & \cdots & t_{M,n} & \cdots & t_{M,N} \end{bmatrix}, t_{i,j} \in [0or1] \quad (6)$$

In the coding matrix T, $t_{m,n}$ is either "0" or "1". According to the information entropy theory, the metamaterial can be described as

$$X = \begin{bmatrix} x_1 & x_2 \\ p_1 & p_2 \end{bmatrix} = \begin{bmatrix} 0 & 1 \\ p & 1-p \end{bmatrix} \quad (7)$$

where p_i is the probability of X takes x_i, The information entropy can be calculated by

$$\begin{aligned} H(X) = H(p_1,p_2) &= -\sum_{i=1}^{2} p_i log p_i \\ &= -plogp - (1-p)log(1-p) \end{aligned} \quad (8)$$

According to the equation (8), the information entropy H is a function of the prior probability p. Fig. 2 shows the relationship between p and H. We can see that H achieves maximum value when $p = 0.5$. So the numbers of unitcell "0" should be equal to the numbers of unitcell "1".

3. Optimized Coding Matrix

After analysis by semianalytical model, we designed the unitcells to verify the model. The unitcells are composed of three-layer dielectric substrate with double metallic split-rings structure and full copper ground plane on the bottom. The dielectric substrate can be described as $\varepsilon_r = 2.65, tan\delta = 0.001$, the radius of each ring are $2.5mm, 3.8mm, 4.1mm, 4.6mm$, respectively. The phase differences are approximation equal to π from 6GHz-18GHz as shown in Fig.3(d). So we can use the unitcells to build a metamaterial accroding to the coding matrix T as shown in Equation (6).

In order to achieve the various functionalities, we used genetic algorithm (GA) that shown in Fig. 1 to

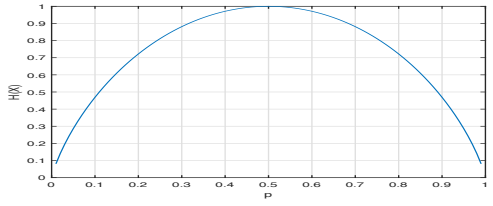


Figure 2: Information entropy H of the coding matrix

optimeze the coding matrix. We combined the scattering properties of unit cell and the semianalytical modeling, and get the relationship between scattering properties and coding matrix without using full-wave simulation.

For a reflective matematerial with 8×8 lattices, each lattice has 2×2 unitcells, the different coding matrices with different information entropy and different corresponding scattering patterns are shown in Fig.4. First we define the coding matrix T as:

$$T_1 = \begin{bmatrix} 0 & 0 & 0 & 0 & 0 & 0 & 1 & 1 \\ 0 & 0 & 0 & 0 & 0 & 0 & 1 & 1 \\ 0 & 0 & 0 & 0 & 0 & 0 & 1 & 1 \\ 0 & 0 & 0 & 0 & 0 & 0 & 1 & 1 \\ 0 & 0 & 0 & 0 & 0 & 0 & 1 & 1 \\ 0 & 0 & 0 & 0 & 0 & 0 & 1 & 1 \\ 0 & 0 & 0 & 0 & 0 & 0 & 1 & 1 \\ 0 & 0 & 0 & 0 & 0 & 0 & 1 & 1 \end{bmatrix} \tag{9}$$

It's corresponding scattering pattern shown as Fig.4 a . And it's information entropy is $H(X) = 0.8113$, we can found that the reflection of EM wave gather in one direction.

Then we try to get the maximum of information entropy.Thus, T_2:

$$T_2 = \begin{bmatrix} 0 & 0 & 1 & 1 & 0 & 0 & 1 & 1 \\ 0 & 0 & 1 & 1 & 0 & 0 & 1 & 1 \\ 0 & 0 & 1 & 1 & 0 & 0 & 1 & 1 \\ 0 & 0 & 1 & 1 & 0 & 0 & 1 & 1 \\ 0 & 0 & 1 & 1 & 0 & 0 & 1 & 1 \\ 0 & 0 & 1 & 1 & 0 & 0 & 1 & 1 \\ 0 & 0 & 1 & 1 & 0 & 0 & 1 & 1 \\ 0 & 0 & 1 & 1 & 0 & 0 & 1 & 1 \end{bmatrix} \tag{10}$$

In T_2 the prior probability of "0" equals to the prior probability of "1"($p = 0.5$), So the information entropy $H(X) = 1$, and it's corresponding scattering pattern shown as Fig.4(b), we can found that the beam of reflection divided into three direction. In other words, while the larger information entropy, the smaller radar cross section.

Furthermore by using GA to optimeze the coding matrix, the coding matrix staggered alone the x-direction,Then we get the third coding matrix:

$$T_3 = \begin{bmatrix} 0 & 1 & 0 & 1 & 0 & 1 & 0 & 1 \\ 0 & 1 & 0 & 1 & 0 & 1 & 0 & 1 \\ 0 & 1 & 0 & 1 & 0 & 1 & 0 & 1 \\ 0 & 1 & 0 & 1 & 0 & 1 & 0 & 1 \\ 0 & 1 & 0 & 1 & 0 & 1 & 0 & 1 \\ 0 & 1 & 0 & 1 & 0 & 1 & 0 & 1 \\ 0 & 1 & 0 & 1 & 0 & 1 & 0 & 1 \\ 0 & 1 & 0 & 1 & 0 & 1 & 0 & 1 \end{bmatrix} \tag{11}$$

it's corresponding scattering pattern shown as Fig.4(c),the number of "0" lattice in T_2 is same as in T_3, So the information entropy also get the maximum

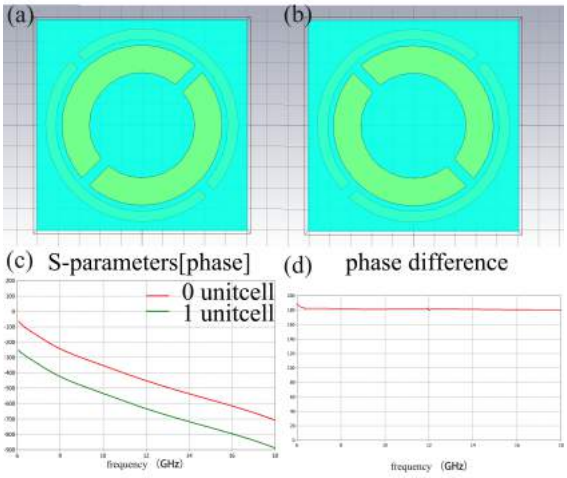


Figure 3: Geometry of the unitcells and their reflective parameters.(a) Geometry of "0" lattice; (b) Geometry of "1" lattice; (c) S-parameters of unitcells; (d) phase difference between "0" and "1" unitcells

value, the only difference is that the reflection is more similar to diffuse reflection in x-direction.

Finally, we optimized the coding matrix in both x-direction and y-direction, and we got the fourth coding matrix:

$$T_4 = \begin{bmatrix} 1 & 0 & 1 & 0 & 1 & 0 & 1 & 0 \\ 0 & 1 & 0 & 1 & 0 & 1 & 0 & 1 \\ 1 & 0 & 1 & 0 & 1 & 0 & 1 & 0 \\ 0 & 1 & 0 & 1 & 0 & 1 & 0 & 1 \\ 1 & 0 & 1 & 0 & 1 & 0 & 1 & 0 \\ 0 & 1 & 0 & 1 & 0 & 1 & 0 & 1 \\ 1 & 0 & 1 & 0 & 1 & 0 & 1 & 0 \\ 0 & 1 & 0 & 1 & 0 & 1 & 0 & 1 \end{bmatrix} \tag{12}$$

it's corresponding scattering pattern shown as Fig.4(d), compared to the results above, we can found that is a metamaterial with diffuse scattering. By using GA, we encode and initialize a population, and calculated it's information entropy and calculated the pattern based on the semianalytical model. Compared to the full-wave numerical simulation, the semianalytical method is faster.

4. Conclusions

A multifunction coding metamaterials can be relized to demonstrate the dynamic manipulation of EM wave. Utilizing 1-bit unit cell and binary coding matrix which had been optimized by genetic algorithm, reconfigurable metamaterials can obtain various scattering properties. In conclusion, we have investigated the design of coding metamaterials for tailor sacattering properties by optimizing the coding matrix. The above results and predictions rely on semianalytical modeling and full-wave numerical simulations. They provide

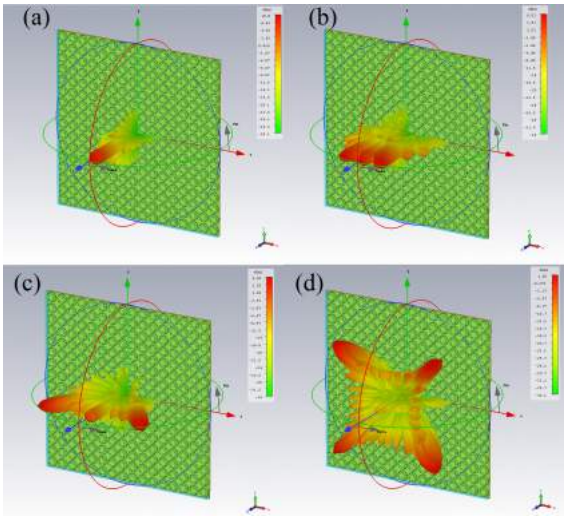


Figure 4: Simulated scattering pattern of different coding matrices

a way to design multifunction coding metamaterials, this may enable to approach the absolute lower RCS or shaping the EM wave. In this paper, the information entropy theory and genetic optimization algorithm were used for optimized the numbers and combinational format of unitcells. From the comparison, we can tailor sacattering properties by coding matrix. In addition to the reduction of RCS this method may also find more general applications to complex field.

References

[1] T. J. Cui, M. Q. Qi, X. Wan, J. Zhao, and Q. Cheng, "Coding metamaterials, digital metamaterials and programmable metamaterials," Light: Science & Applications, vol. 3, no. 10, p. e218, 2014.

[2] Q. Zheng, Y. Li, J. Zhang, H. Ma, J. Wang, Y. Pang, Y. Han, S. Sui, Y. Shen, H. Chen, and S. Qu, "Wideband, wide-angle coding phase gradient metasurfaces based on pancharatnam-berry phase," Scientific Reports, vol. 7, 2017.

[3] Q. Zhang, X. Wan, S. Liu, J. Y. Yin, L. Zhang, and T. J. Cui, "Shaping electromagnetic waves using software-automatically-designed metasurfaces," Scientific Reports, vol. 7, 2017.

[4] H. T. Wu, S. Liu, X. Wan, L. Zhang, D. Wang, L. L. Li, and T. J. Cui, "Controlling energy radiations of electromagnetic waves via frequency coding metamaterials," Advanced Science, vol. 4, no. 9, p. 12, 2017.

[5] J. Su, Y. Lu, H. Zhang, Z. Li, Y. Yang, Y. Che, and K. Qi, "Ultra-wideband, wide angle and polarization-insensitive specular reflection reduction by metasurface based on parameter-adjustable meta-atoms," Scientific Reports, vol. 7, 2017.

[6] Y. Shen, J. Zhang, Y. Pang, Y. Li, Q. Zheng, J. Wang, H. Ma, and S. Qu, "Broadband reflectionless metamaterials with customizable absorption-transmission-integrated performance," Applied Physics a-Materials Science & Processing, vol. 123, no. 8, 2017.

[7] M. Moccia, S. Liu, R. Y. Wu, G. Castaldi, A. Andreone, T. J. Cui, and V. Galdi, "Coding metasurfaces for diffuse scattering: Scaling laws, bounds, and suboptimal design," Advanced Optical Materials, vol. 5, no. 19, 2017.

[8] T. J. Cui, S. Liu, and L. Zhang, "Information metamaterials and metasurfaces," Journal of Materials Chemistry C, vol. 5, no. 15, pp. 3644–3668, 2017.

[9] K. Chen, Y. Feng, F. Monticone, J. Zhao, B. Zhu, T. Jiang, L. Zhang, Y. Kim, X. Ding, S. Zhang, A. Alu, and C.-W. Qiu, "A reconfigurable active huygens' metalens," Advanced Materials, vol. 29, no. 17, 2017.

[10] K. Chen, L. Cui, Y. Feng, J. Zhao, T. Jiang, and B. Zhu, "Coding metasurface for broadband microwave scattering reduction with optical transparency," Optics Express, vol. 25, no. 5, pp. 5571–5579, 2017.

[11] H. Yang, X. Cao, F. Yang, J. Gao, S. Xu, M. Li, X. Chen, Y. Zhao, Y. Zheng, and S. Li, "A programmable metasurface with dynamic polarization, scattering and focusing control," Scientific reports, vol. 6, p. 35692, 2016.

[12] C. Huang, W. Pan, X. Ma, and X. Luo, "Multi-spectral metasurface for different functional control of reflection waves," Scientific Reports, vol. 6, 2016.

[13] K. Chen, Y. Feng, Z. Yang, L. Cui, J. Zhao, B. Zhu, and T. Jiang, "Geometric phase coded metasurface: from polarization dependent directive electromagnetic wave scattering to diffusion-like scattering," Scientific reports, vol. 6, p. 35968, 2016.

[14] C. Qu, S. Ma, J. Hao, M. Qiu, X. Li, S. Xiao, Z. Miao, N. Dai, Q. He, and S. Sun, "Tailor the functionalities of metasurfaces based on a complete phase diagram," Physical review letters, vol. 115, no. 23, p. 235503, 2015.

Photonic Crystals, Laser and Cavities

Standing waves with infinite group velocity in temporal photonic crystals

J. Sabino Martínez-Romero* **and P. Halevi**

Instituto Nacional de Astrofísica y Electrónica, Tonantzintla, Puebla, México.
*corresponding author, E-mail: jsmr8812@me.com

Abstract

We extend our studies of a medium whose permittivity and/or permeability are modulated periodically in time, namely temporal photonic crystals (TPCs). When the frequency of the wave w is equal to $1/2, 3/2, ...$ of the modulation frequency, we find that the fields in a TPC slab (as well as in a boundless TPC) are standing waves. Interestingly, at these values of w the group velocity is infinite. Such behavior strongly differs from that of an ordinary photonic crystal.

1. Introduction

Recently we studied a modulated magneto-dielectric medium whose permittivity $\varepsilon(t)$ and/or permeabilty $\mu(t)$ are periodic functions of time [1]. Such a temporal photonic crystal (TPC) is periodic in the wave frequency ω, with the period equal to the modulation frequency Ω. Its most outstanding characteristic are bands of the wave vector k, separated by k-gaps (rather than ω-gaps, as for a spatially periodic medium). We have indeed verified experimentally that such gaps exist for a transmission line with periodically modulated capacitances $C(t)$, known to play a role analogous to the permittivity [2]. Indeed, the effective medium model for the transmission line behaves similarly to the corresponding TPC.

2. Boundless TPC medium

We assume that our infinite medium is spatially uniform, with harmonic models for the relative permittivity and permeability:

$$\varepsilon_r(t) = \bar{\varepsilon}_r[1 + m_\varepsilon \sin(\Omega t)], \tag{1a}$$

$$\mu_r(t) = \bar{\mu}_r[1 + m_\mu \sin(\Omega t + \theta)]. \tag{1b}$$

Here, $\bar{\varepsilon}$ and $\bar{\mu}$ are the average permittivity and permeability and m_ε and m_μ are the corresponding modulations. The angle θ takes into account a possible phase difference between the two modulations. The electric field contributed by a single band p $(= 1, 2, ...)$ is a superposition of plane waves with different frequencies $(\omega - n\Omega)$, $n = 0, \pm1, \pm2, ...$ (the "harmonics") [1]:

$$E_p(x,t) = e^{ik_p(\omega)x} \sum_n e_{pn}(\omega) e^{-i(\omega - n\Omega)t} \tag{2}$$

In addition to this exact field, it is also instructive to consider the weak modulation approximation $m_\varepsilon \ll 1$, $m_\mu \ll 1$. In this case it is sufficient to limit the summation in eq.(2) to the terms $n = 0$ and $n = 1$ and only the first two bands $(p = 1, 2)$ are important. For the frequency of our interest $\omega = \frac{1}{2}\Omega$, namely the border of the first *temporal* Brillouin zone, we get

$$E_p(x,t) = e^{ik_p x}[e_{p1} e^{i\Omega t/2} + e_{p0} e^{-i\Omega t/2}], \;\; p = 1, 2. \tag{3}$$

The eigenvectors e_{p0} and e_{p1} are equal in magnitude and differ only in sign for the two bands. Taking $e_{p0} = 1$, the real electric field is

$$Re[E_p(x,t)] \cong \cos\left(k_p x - \frac{\Omega}{2}t\right) \pm \cos\left(k_p x + \frac{\Omega}{2}t + \psi\right) \tag{4}$$

This equation describes two counterpropagating waves with the same frequency $(\Omega/2)$, same wave vector (k_p), same amplitude, and a phase difference (ψ). Then it follows that the approximate fields for the two bands are

$$Re[E_1(x,t)] = 2\cos\left(k_1 x + \frac{1}{2}\psi\right)\cos\left(\frac{1}{2}\Omega t + \frac{1}{2}\psi\right) \tag{5a}$$

$$Re[E_2(x,t)] = 2\sin\left(k_2 x + \frac{1}{2}\psi\right)\sin\left(\frac{1}{2}\Omega t + \frac{1}{2}\psi\right) \tag{5b}$$

We see that, for both bands, the spatial and temporal oscillations are independent of each other, namely, these are standing waves. In Fig.1 we compare the approximate (5) and exact (2) solutions for the two bands at $\omega = \frac{\Omega}{2}$, with no magnetic modulation present $(m_\mu = 0)$. It is seen that the approximation works very well for the weak modulation $(m_\varepsilon = 0.1)$, but rather poorly for the strong modulation $(m_\varepsilon = 0.5)$. While this has been plotted for the time $t = 0$, the field vanishes for all times at the nodal points (marked by dots), even for the exact fields. Comparing with ordinary (spatial) photonic crystals, there at the edge of the Brillouin zone $(k = \pi/a)$ one also has standing waves, however the group velocity vanishes, while it is infinite for TPCs at $\omega = \frac{1}{2}\Omega$ [1].

3. Temporal photonic crystal slab

In a TPC slab, eq.(2) must be generalized to allow for waves propagating in the negative direction and the total field is now a superposition ot the partial fields due to all the p bands:

$$E_{sl}(x,t) = \sum_{n=-\infty}^{\infty}\sum_{p=1}^{\infty}(A_p e^{ik_p(\omega)x} + B_p e^{-ik_p(\omega)x}) \times e_{pn}(\omega) e^{-i(\omega - n\Omega)t}. \tag{6}$$

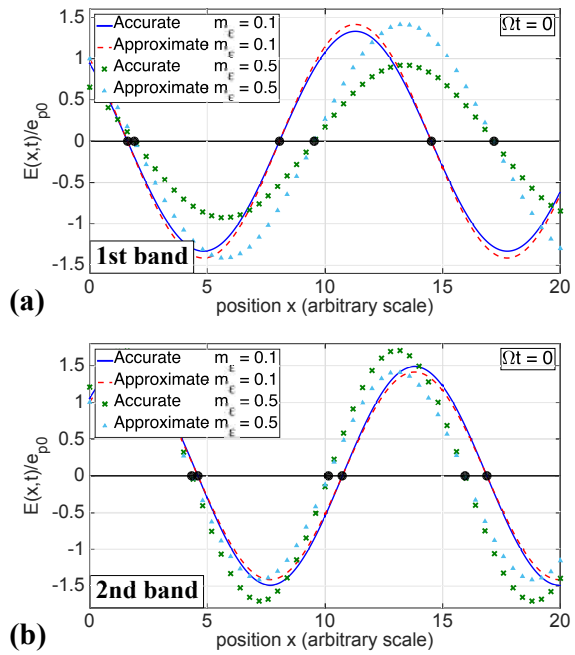


Figure 1: Normalized electric fields for the band $p = 1$ (a) and $p = 2$ (b) in an unbounded TPC.

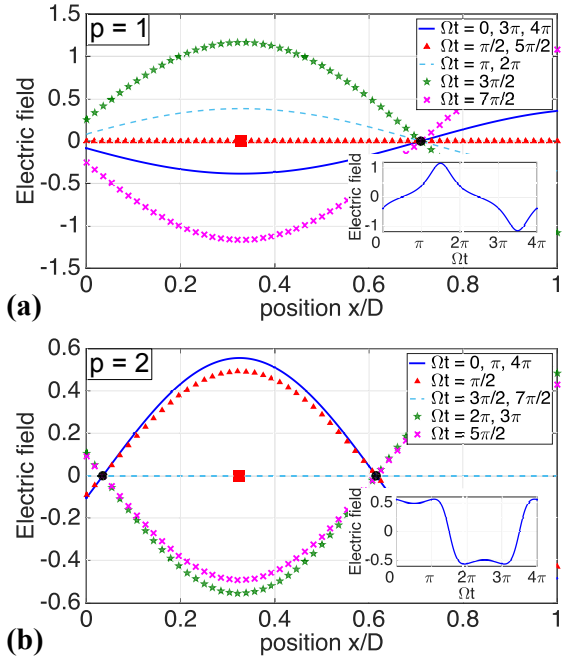


Figure 2: Standing waves $Re[E(x,t)]$ in a TPC plate ($m_\varepsilon = 0.5$) for the first two bands. Here, $\bar{\varepsilon}_r = \bar{\mu}_r = 5.25$, $\omega = \Omega/2$ and $\bar{k}D = 5$, where D is the plate thickness.

The weak modulation approximation now gives a solution of the form $Re[E(x,t)] = F_1(x)\cos(\Omega t/2 + \psi/2) + F_2(x)\sin(\Omega t/2 + \psi/2)$. Thus, again, each band contributes a standing wave. The electric field vanishes at fixed nodal points that are separated at distances $\Delta x = \pi/k_p = \lambda_p/2$. It also vanishes at fixed times t separated by a modulation period $2\pi/\Omega$.

Returning to the exact solution, eq.(6), the amplitudes A_p and B_p can be determined from the continuities of the electric and magnetic fields at the boundaries of the slab. The real electric fields inside the slab are plotted in Fig.2 for the first two bands and $\omega = \frac{1}{2}\Omega$, with strong electric modulation ($m_\varepsilon = 0.5$) and, again, no magnetic modulation. This is shown for five different instants of time, the nodal points (dots) emphasizing that a TPC slab, as well as an unbounded medium, supports standing waves. However, the nodal points do not coincide with the boundaries. The insets provide the behavior in time at a selected position (red square).

We confirmed the standing wave behavior for higher bands ($p = 3$ and 4) as well and for arbitrarily strong modulations. Moreover, for equal modulations ($m_\varepsilon = m_\mu$) the fields are standing waves for both out-of-phase modulations ($\theta = \pi$) and in-phase modulations ($\theta = 0$, where there are no band gaps [1]). In all these cases, with the exception of $m_\varepsilon = m_\mu$ with $\theta = 0$, $d\omega/dk = \infty$ at $\omega = \frac{1}{2}\Omega$ for all the p-bands.

4. Conclusions

We demonstrated that the fields of a TPC (boundless or bounded) are standing waves if the wave frequency ω is one-half of the modulation frequency Ω. Here $\frac{1}{2}\Omega = \pi/T$ is the border of the first *temporal* Brillouin zone. At this frequency the group velocity is infinite for all bands. This contrasts with (spatial) photonic crystals where for $k = \pi/a$ the fields are also standing waves, however the group velocity vanishes for all non-degenerate bands. Finally we note that with allowance for losses (non-vanishing Im ε and/or Im μ) the standing wave property does not hold up accurately.

Acknowledgement

J.S.M.-R. and P.H. wish to acknowledge CONACyT Grants No. 377286 and No. 103644-F, respectively.

References

[1] J. S. Martínez-Romero, O. M. Becerra-Fuentes, and P. Halevi, Phys. Rev. A **93**, 063813 (2016).

[2] J. R. Reyes-Ayona and P. Halevi, Appl. Phys. Lett. **107**, 074101 (2015); IEEE Trans. Microw. Theory Techn. **64**, 3449 (2016).

Ultralow-threshold continuous-wave lasing assisted by a metallic optofluidic resonantor

Bei Jiang[1,2], Hailang Dai[1,2], and Xianfeng Chen[1,2]

[1]State Key Laboratory of Advanced Optical Communication Systems and Networks, School of Physics and Astronomy, Shanghai Jiao Tong University, Shanghai 200240, China
[2]Key Laboratory for Laser plasma (Ministry of Education), Collaborative Innovation Center of IFSA (CICIFSA), Shanghai Jiao Tong University, Shanghai 200240, China
*corresponding author, E-mail: xfchen@sjtu.edu.cn

Abstract

We report an ultralow-threshold continuous-wave lasing via a metallic optofluidic resonant cavity. The high quality factor Q and spontaneous emission coupling factor of the waveguide strengthen the interaction between the gain medium and the ultrahigh order modes (UOMs). Methylene blue with concentration of 2.57×10^{-13} mol/ml is chosen to verify the applicability of the proposed concept, and the narrow-band lasing can be effectively pumped from the chip surface by a continuous laser with the launched pump threshold as low as 2.1 μW/cm^2.

1. Introduction

Optical microcavities, which confine the resonant modes to very small volumes, figure prominently in research fields such as optics and solid-state physics[1]. The small cavity volume with high Q factor gives new avenues in the pursuit of efficient and compact laser source with low power dissipation[2]. Particularly, micro- or even nanocavity lasers are taking on increasing importance. This paper adopts a macroscale optofluidic waveguide cavity whose dimension is much larger than wavelength scale as a resonant cavity. The specific hollow-core metal-cladding waveguide (HCMW) structure is introduced to enhance the interaction between the gain medium and the resonant modes. Since the resonant cavity in the waveguide chip is millimeter scale, the ultrahigh order modes (UOMs) can exist in the guiding layer and result in high sensitivity, Q factor and power density. These provide far application potentials in biosensing, integrated optical components, etc. The intrinsic energy shift between adjacent modes in the HCMW can be explained by the inter-mode coupling effect[3]. In our experiment, the optofluidic resonator with Methylene Blue solution is pumped by a continuous laser and the threshold intensity is very low. In addition, our chip is easy to fabricate with low costs, and it is anticipated to open new avenues for lab-on-chip or optofluidic integration.

2. Metallic optofluidic resonantor

Our resonant cavitys Q factor is extremely high, which benefits from the millimeter-scale metal cladding optical waveguide structure. As figure 1(a) shows, the HCMW is composed by a silver coupling layer with thickness of 30 to 50 nm, a silver substrate with 300 nm and a guiding layer contains a 1.1 mm thick channel for dye solution. In figure 1(b), direct coupling from the free space without high refractive index prism becomes possible and no propagating plasmon wave is involved.

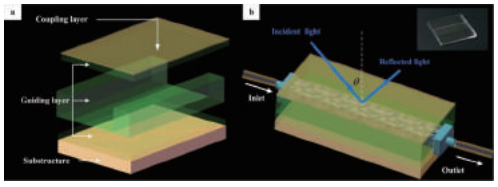


Figure 1: (a) Schematic diagram of the HCMW chip. (b) Excitation of UOMs via free space coupling technique. The right inset shows the image of the HMCW chip before vacuum evaporation.

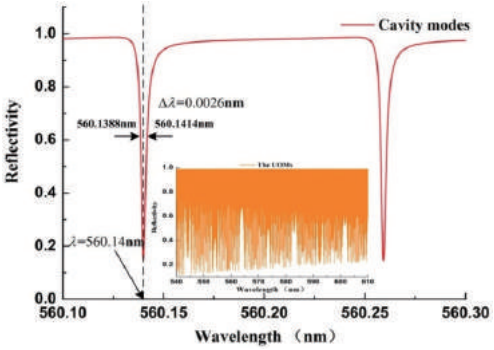


Figure 2: Numerical calculated reflection spectrum of the simplified HMCW structure.

2.1. High Q factor

The numerical calculated reflectivity is shown in figure 2 for the simplified model described above, where the FWHM of the extremely sharp resonant peak is about 0.0026 nm. It can be seen that the Q factor is about 2.15×10^4.

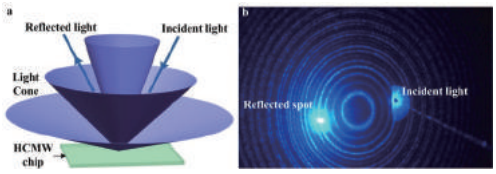


Figure 3: (a) Schematic diagram of the reflected light cones. (b) Image of the light cones on a screen, where a bright spot corresponds to the reflected beam can be found.

2.2. Model for the β Value

In our waveguide chip, the β value is also high. We calculate the volume of the guided mode and the expression for β could be proposed. Numerical simulations are carried out to calculate the β value for different mode orders. The β value is about 0.14, which does not vary too much as the mode order changes. As a contrast, the β value of a plane mirror Fabry-Perot configuration is about 0.1.

2.3. Mechanism of the Reflected Light Cones in HCMW

When the incident laser illuminates on the chip surface, the energy is coupled into the guided layer and stored as guided modes. Since the coupling metallic layer is relatively thin, all these UOMs are leaky modes. To each UOM with a fixed transverse wave vector, a concentric light cone can be observed as its energy converting back to free space through leakage radiation, as shown in figure 3(a). That is to say, after the incident light is coupled and stored in the guiding layer, leakage radiation take place via all UOMs channels, while each mode leakage produces a reflection cone. As figure 3(b) shows, a series of concentric cones were observed in our experiments.

3. Results and Discussion

3.1. Experimental Systems

The experimental setup to verify the above hypothesis is shown in figure 4(b). The pump was a DPSS CW laser of 15 mW at 473 nm wavelength. An optical fiber and a spectrometer were used to collect and measure the output emission, respectively. A $\theta/2\theta$ goniometer was used to adjust the incident angle for the investigation of the relation between lasing emission and UOMs coupling. Note that we do not need to consider the triplet state issue due to the extremely low concentration used in our experiments which is shown in figure 4(a).

3.2. Illustration via Methylene blue

The representative laser dye Methylene blue with a concentration of 2.579×10^{-13} mol/ml was used to verify the above hypothesis. Two emission peaks with very narrow bandwidth can be observed at the wavelength of 708.5 nm and 723.1 nm, respectively. Figure 5 shows the measured

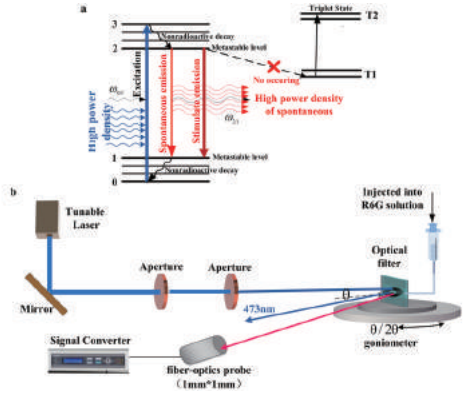


Figure 4: (a) Energy level diagram of R6G. (b) Schematic of the experimental setup of the optofluidic dye laser.

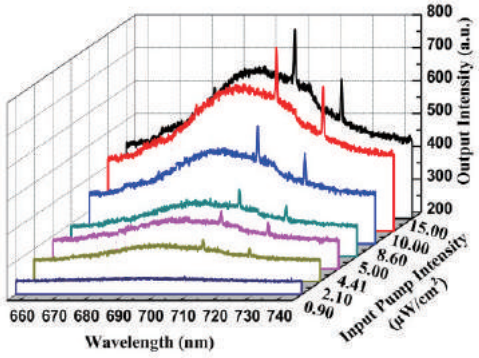


Figure 5: The threshold behavior of Methylene Blue dye laser.

output intensity as a function of excitation pump density. The lasing pump threshold for Methylene Blue is as low as 2.1 μW/cm^2.

4. Conclusion

Different from tranditional strategy of using micro- or nanocavity structure, a novel low threshold dye lasing based on a millimeter scale resonant cavity was proposed. Taking advantage of the high Q and β value of the HCMW structure, the experimental threshold was significantly reduced; Considering the attributes mentioned above, the HCMW is anticipated to open up new prospects for optofluidics and integration optics.

References

[1] K. -J. Vahala., Optical microcavities, *Nature* 424: 839, 2003.

[2] C. Walther, J. Faist, Microcavity laser oscillating in a circuit-based resonator, *Science* 327: 1495-7, 2010.

[3] P. Andrew, W. -L. Barnes, Energy transfer across a metal film mediated by surface plasmon polaritons, *Science* 306: 1002-5, 2004.

Lasing Cavity based on Defect Modes in 2D Groove Metal Array inside MIM Structure

Seong-Han Kim[1*] and Chul-Sik Kee[1]

[1]Integrated Optics Laboratory,Advanced Photonics Research Institute, GIST, Gwangju 61005, South Korea
*corresponding author, E-mail: topofuni@gmail.com

Abstract

We propose and numerically investigate a metallic resonant cavity for lasing infrared light based on guided spoof SPPs on 2D groove metal array. To design a resonant cavity, we demonstrate guiding modes on 2D groove metal array with a line defect inside metal-insulator-metal structure. Furthermore, we examine the lasing performance of the resonant cavity by introducing gain medium.

1. Introduction

Nanoscale lasers based on small metallic structure have attracted great interest for their fundamental and technological potential from spectroscopy, sensing, and integrated nanophotonic devices to quantum physics. Spoof surface plasmon polaritons (SPPs) on a structured metallic surface [1] have been widely applied for manipulating THz and GHz waves [2, 3, 4] in a deep subwavelength scale. To pursue the quest for coherent light sources at the nanoscale, the spoof SPPs would be a good candidate to localize infrared (IR) and visible waves at the nanoscale region. At visible and IR frequencies, however, it is still in question whether the spoof SPP modes shows still good performance due to a loss of metals.

Here, we propose and numerically investigate a small metallic resonant cavity with gain for lasing IR light based on guided spoof SPPs on 2D groove metal array(GMA). Firstly, we demonstrate guiding modes at IR frequencies in 2D GMA with a line defect inside a metal-insulator-metal (MIM) structure. Next, using the waveguide, we design a passive resonant cavity for lasing and investigate its optical responses. Lastly, we examine the performance of the cavity for lasing by introducing a gain medium.

2. Results

The idea of a waveguide in this study comes from defect modes inside a bandgap by breaking discrete translation symmetry in photonic crystal. Firstly, we consider a 2D GMA inside a MIM structure which is composed of two overlapping 1D groove metal arrays perpendicular to each other with the lattice constant a = 200 nm, width w = 0.4a and depth h = 150 nm. Next, To guide modes within a small area, the waveguide is formed by introducing a defect structure with defect depth h_d on 2D GMA as shown in the upper inset of Fig. 1.

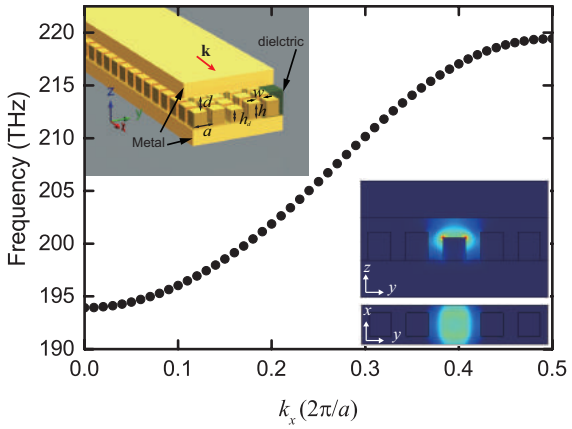


Figure 1: Dispersion relation of a line defect mode on a 2D GMA inside MIM structure. Upper inset shows schematic diagram of the waveguide with groove depth h, defect depth h_d, gap d, groove width w, and periodicity a. Lower inset shows electric field intensity of a guiding mode at k_x=$\frac{\pi}{a}$.

The optical response in this waveguide and following resonant cavities is modeled by solving 3D Maxwell equations via the finite element method. The permittivity of metal ϵ_m is expressed by Drude model with the plasma frequency $\omega_p = 2\pi \times 2.175 \times 10^{15}$rad/s^{-1} and the damping constant $\gamma = 2\pi \times 6.5 \times 10^{12}$rad/s^{-1}. The refractive index n_d of the dielectric material is 1.39. Figure 1 shows the dispersion relation of a guiding mode. As shown in the lower inset of Fig. 1, the distribution of electric fields clearly shows that the guiding modes are propagating along the defect site within the area in a subwavelength scale since the ratio a/λ is around 0.15 at the wavelength of 1364 nm.

Next step is to design a resonant cavity for lasing by using the waveguide. Since guiding mode exists only in the defect site, a resonant cavity can be formed by simply blocking the guiding mode at both sides. Figure. 2(a) shows a schematic diagram of an array in the y-direction of a resonant cavity with two defects which called D2 cavity. In this cavity, we use same parameters as in the waveguide, as depicted in Fig. 2(b,c).

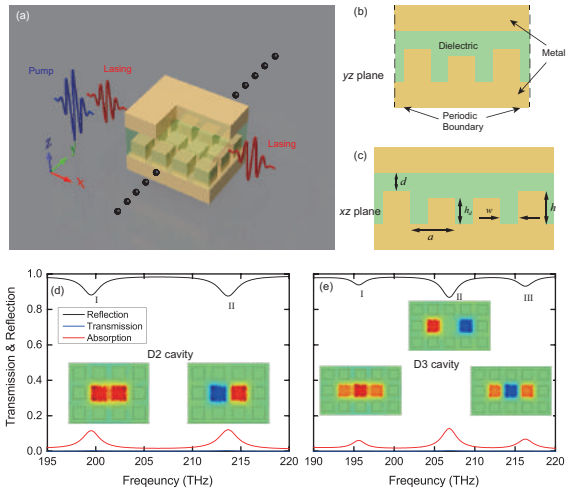


Figure 2: Schematic diagram of D2 resonant cavity. Cross section in the yz plane (b) and the xz plane (c) with parameters of the D2 cavity. Simulated spectra for D2 cavity (d) and D3 cavity (e). The inset shows the z-component of electric fields, where I, II, and III indicates the first, second, and third resonant mode, respectively.

Figure 2(e) and (d) show numerically simulated transmission, reflection, and absorption spectra for D2 and D3 cavities, respectively. The spectra for the D2 cavity show two resonances located at 199.5 and 213.7 THz, respectively, and the spectra for the D3 cavity show three resonances located at 195.6, 206.8, and 216.3 THz, respectively. Also, from the electric field distributions as shown in insets of Fig. 2(d,e), we can verify that the cavities have resonances in the form of the Fabry-Perot resonance.

To examine the performance of the lasing cavity, we place gain medium inside MIM structure by introducing gain coefficient, which is assumed to be independent of frequency, via imaginary part of the dielectric permittivity ϵ_i. The gain coefficient is defined as $\alpha = 2\pi/\lambda\sqrt{\epsilon_r + i\epsilon_i}$.

Figures 3(a,c) and (b,d) show how the transmittance and reflectance spectra of the D2 cavities vary as the gain coefficient α increases from 242 to 420 cm^{-1}, exhibit two phases of the spectral response. At first, an increase of the gain coefficient gives rise to an increase of transmittance and decrease of reflectance at both resonances. The resonant transmittance reaches unity,that is, the threshold at α_{th}^{I} = 295 cm^{-1} and α_{th}^{II} = 327 cm^{-1} respectively, while the reflectance drops to zero. At second, a more increase of gain results in a rapid increase of both reflectance and transmittance, which attain a maximum value of 26 dB at α = 312 cm^{-1} and 40 dB at α = 348 cm^{-1} for I and II resonances, respectively.

3. Conclusions

In summary, we have proposed and numerically studied the IR lasing cavity with the gain medium as a coherent light source. It has been shown that the resonant cavity has good

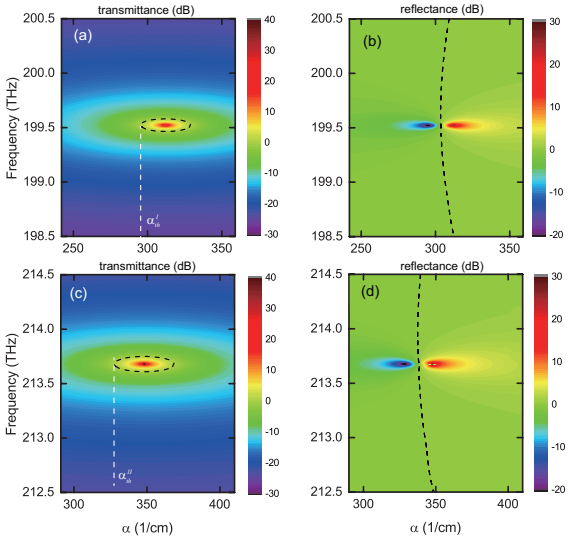


Figure 3: Panels (a,c) and (b, d) show transmission and reflection spectra for D2 cavity as a function of the gain coefficient α and in frequency regions around the resonant mode I (a, b) and the resonant mode II (c, d). The black dashed contours indicate the unity transmittance and reflectance, and α_{th}^{I} and α_{th}^{II} are threshold gain of I and II, respectively.

potential for lasing since it has around 300 cm^{-1} of threshold gain and 40 dB in maximum laser output at 350 cm^{-1}. These gain values can be easily provided by optically or electrically pumped gain medium such as quantum well, quantum dot and dye molecules.

Acknowledgement

This research was supported by the Basic Science Research Program through the National Research Foundation of Korea (No. NRF-2015R1D1A1A0160180) and by GIST Research Institute (GRI) grant in 2018.

References

[1] J. B. Pendry, L. Martin-Moreno, F. J. Garcia-Vidal, Mimicking Surface Plasmons with Structured Surfaces, Science 305: 847–848 ,2004.

[2] S. A. Maier, *et al.*, Terahertz Surface Plasmon-Polariton Propagation and Focusing on Periodically Corrugated Metal Wires, *Phys. Rev. Lett.* 97: 176805, 2006.

[3] S.-H. Kim ,*et al.* , Subwavelength localization and toroidal dipole moment of spoof surface plasmon polaritons, *Phys. Rev. B* 91: 035116, 2015.

[4] S.-H. Kim, *et al.*, Waveguiding of spoof surface plasmon polaritons, in *Proceedings of 2015 Conference on Lasers and Electro-Optics Pacific Rim,*, Busan, South Korea, 24-28 August 2015, 26P_78.

An angular study of the diffraction of light from one row of cylinders

J. D. Valenzuela-Sau[1*] and Raúl García-Llamas[2]

[1]Posgrado en Física, Departamento de Investigación en Física, Universidad de Sonora, Sonora, México
[2]Photonic Lab, Physic Research Department, Universidad de Sonora, Sonora, México
*corresponding author, E-mail: ragal@cifus.uson.mx

Abstract

The scattering of a Gaussian beam from a finite number of cylinders aligned in a row, is studied. The row is treated as an inhomogeneous periodic bounded medium and the magnetic field is expanded in terms of the eigenvector obtained by using the Plane Wave Method. The period a of the inhomogeneous periodic medium is much greater than the total length of the row. We focused in the angular behavior of the scattered light. We observed that the total integrated scattering in transmission (reflection) presents minima (maxima) and one of them can be explained as if the row of cylinders behaved as a photonic crystal.

1. Introduction

The study of the scattering from single particles or a bunch of particles has been issue of interest for decades [1-6]. In a recent paper [6], the diffraction of light from a row of cylinders with rectangular cross section was studied. The Total Integrated Scattering (TIS) in transmission and reflection was studied as a function of the number of cylinders in the row and some maxima (minima) were found. They were explained using the classical quarter wave formula from the thin film area. This was done for normal incidence. In this work the TIS is studied for several angles of incidence and a future work will be extended to study two rows of cylinders.

2. Theory and numerical results

A transverse magnetic (TM) (the magnetic field is perpendicular to the axis of the cylinders) Gaussian beam, of width w_g, is incident on a row of a finite number of square cross section cylinders. The angle of incidence is the arc subtended by the direction of propagation and a line normal to the row of cylinders. The interested reader can see the mathematical details in ref. [6].

In order to obtain numerical results, the infinite dimension of the scattering matrix equation was truncated and fixed to $2N = 2048$. The value of this parameter is good enough to reach the energy conservation within 0.1 % of variation.

There are until fifteen cylinders in the unit cell. The waist of the p-polarized non-diffracted Gaussian beam is fixed to $w_g = 32\lambda_0 = 25.6$ μm. The cylinders have square cross section with sides $w_x = w_y = 0.436\lambda_0 = 349$ nm. The material filling the cylinder has a dielectric constant $\varepsilon_c = 5.29$ (n_c=2.3) and it is surrounded by a medium (the envelope) with dielectric constant $\varepsilon_e = 1.0$. The distance between cylinders or the local period is $\lambda_0 = 0.8$ μm. The period a=128λ_0=102 μm.

In figure 1, the TIS (transmission and reflection) versus the energy for three angles of incidence is displayed. The number of cylinders is 15. The red, blue, magenta curves correspond to the TIS for θ_i=0°, 20° and 30° of incidence, respectively. Four minima (maxima) in the TIS-T (TIS-R) are observed at E_3=1.15 eV (λ_3=1,078.3 nm), E_4=1.56 eV (λ_4=794.9 nm), E_5=2.05 eV (λ_5=604.9 nm) and E_6=2.31 eV (λ_6=536.8 nm), for normal incidence. It must be noted that the energy of the third (E_5) minimum is almost double than the first (E_3) one. They are due to interference effects and its positions can be obtained with the classical quarter wave thickness equation $\lambda_k = 4n_c w_y/k$, with k=3, 4, 5 and 6.

The first maximum (minimum) is blue shift at the same time that its intensity decreased as the angle of incidence is increased. On the contrary, the fourth maximum (minimum) intensity is increased as the angle of incidence is increased.

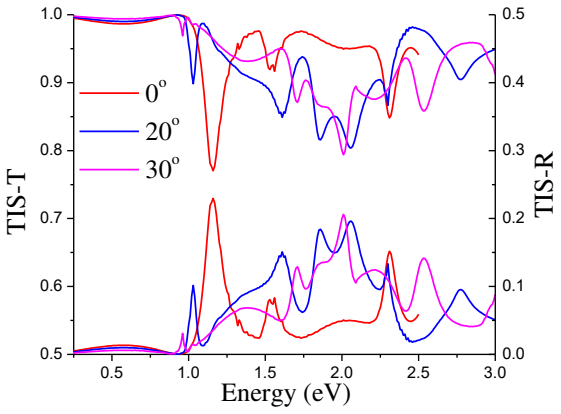


Figure 1: The total integrated scattering (transmission and reflection) versus the energy for three different angles of incidence is displayed. The left (right) scale is associated to TIS-T (TIS-R).

In figure 2, the TIS (transmission and reflection) as a function of the wavelength for oblique incidence (θ_i=30°) is displayed, for three different number of cylinders. The red, blue and magenta

curves correspond to the TIS from 5, 10 and 15 cylinders, respectively. Five minima (maxima) in the TIS-T (TIS-R) are observed at E_3=1.38 eV (λ_3=898.6 nm), E_4=1.71 eV (λ_4=725.1 nm), E_5=2.01 eV (λ_5=616.9 nm), E_6=2.22 eV (λ_6=558.6 nm) and E_7=2.53 eV (λ_5=490.1 nm), which decreased (increase) as the number of cylinder is augmented.
The intensity of the minima decreased almost linearly as a function of the number of cylinders.

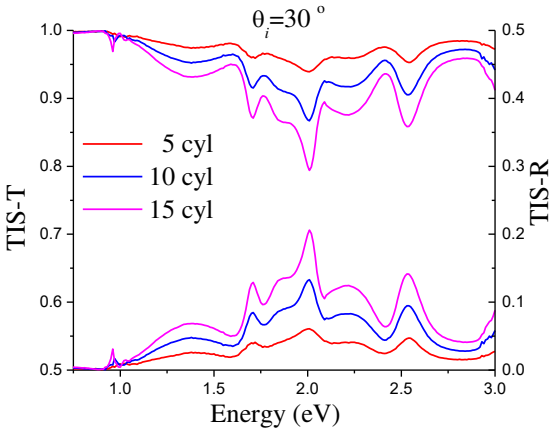


Figure 2: The total integrated scattering (transmission and reflection) as function of the energy (wavelength) for oblique incidence is displayed. The red, blue, magenta curves correspond to the TIS by 5, 10 and 15 cylinders.

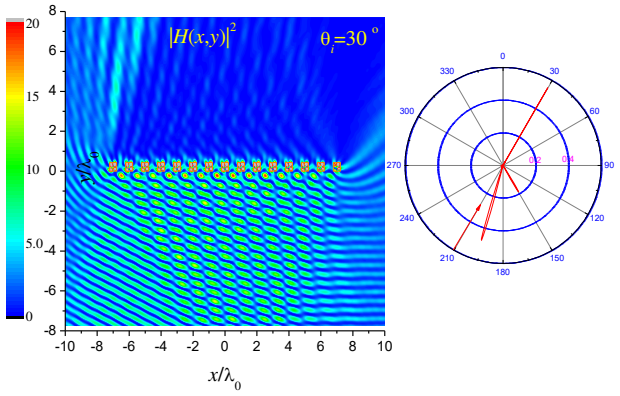


Figure 3: In the left, the square modulus of the magnetic field projected at the plane *x-y* is shown for a wavelength λ= 620.0 nm. The orange lines correspond to the limits of the cylinders. The maximum intensity of the magnetic field was very high and they are located inside of the cylinders, for this reason some points are dark gray colored. At the right, the angular distribution of the scattered energy is shown.

In figure 3, the projection of the square modulus of the magnetic field in the plane z=0 is shown for the maximum TIS-R (2.01 eV) for an incidence at 30°. It is possible to observe the incident field interfering with the specular one near to the cylinders. Part of the incident field surrounds the edge of the row. The maxima intensity of the field is reached in the cylinders (greys spots).
The transmission at 30 ° and the reflection at 150 ° are observed. The row of cylinders behaves like a grating, then the -1 order is also observed at 195 °. The signal, in the hemisphere of reflection, was multiplied by a factor of 30.

The band structure calculation, not shown here, of a 2D photonic crystal in square lattice of cylinders of squared cross section, shown that exist a band gap centered in about 2 eV and width 0.1 eV, when the parameters are equals to the ones used in this work. Thus, the row of cylinders has some photonic crystal-like properties.

3. Conclusions

In this paper, the diffraction of light from a row of a finite number of cylinders as a function of the angle of incidence was studied. We showed that it behaves like a photonic crystal.

Acknowledgements

J.D.V.S. acknowledge to National Council of Science and Technology of Mexico (CONACYT) for the scholarship.

References

[1] Lord Rayleigh "On the electromagnetic theory of the light," Phil. Mag. **12**, 81-101 (1881).

[2] W. von Ignatowsky, "Reflexion elektromagnetischer Wellen an einem Draht," Ann. Physik, **13**, 495-522 (1905)

[3] H.C., Van de Hulst, *Light scattering by small particles*, Dover Publication Inc., New York (1957). (p300-305).

[4] C. F. Bohren and D. R. Huffman, *Absorption and Scattering of Light by small particles*, (Wiley, 1983) p194-213

[5] G. O. Olaofe, "Scattering by an arbitrary configuration of parallel circular cylinders," J. Opt. Soc. Am. **60**, 1233 (1970)

[6] J. D. Valenzuela-Sau, R. Munguía-Arvayo, S. Gastélum-Acuña, J. Gaspar-Armenta, J. Nápoles-Duarte and R. García-Llamas, Scattering of a Gaussian beam from a row of cylinders with rectangular cross section, J. Opt. Soc. Am A. **34**, No. 8, 1369-1375, 2017.

Non-local effect on surface modes of non-reciprocal effective media

K. F. Lee [1], Raymond P. H. Wu [1], Yong-Liang Zhang [1], Wang Tat Yau [1], and Kin Hung Fung [1*]

[1] Department of Applied Physics, The Hong Kong Polytechnic University, Hong Kong, China
*corresponding author, E-mail: kin-hung.fung@polyu.edu.hk

Abstract

Recently, it has been shown theoretically that macroscopic Maxwell's equations support interesting surface magnetic mode having zero electric field and polarization field at an interface between two homogenous magnetic domains. We introduce inhomogeneous lattice to the magnetic domains and study its effect on the surface magnetic mode. We found the edge mode not only becoming repeating in Brillouin Zone but also has significant change in dispersive property. This change can be caused by non-local lattice effect.

1. Introduction

Non-reciprocity is an active area in photonics research [1-7]. A number of non-reciprocal edge modes were proposed in the interface consisted of two dimensional MOPCs based on topological band theory [1-4]. The topological band theory has provided a systematic way to predict the existence and the number of edge states which is called topological edge states. The topological band theory, though it is successful in predicting non-reciprocal edge states in lattice system, may have difficulty in explaining non-reciprocal edge states between continuous MO medium(s) which does(do) not have non-local effect [5-7]. The non-local effect introduced by the lattice in domains forming the interface seems to have significant influence on the edge modes.

Recently, non-reciprocal surface magnetic mode (SMM) with zero electric field and polarization was shown to exit between two continuous MO mediums subjecting to opposite magnetic field [8]. By effective medium theory [9, 10], a lattice of particles can be modelled as a continuous effective medium in a sense that they share similar dispersion relation (DR). It is therefore possible that this interesting non-reciprocal edge mode can have a mapped edge states sharing similar properties when non-local lattice effect is introduced in each domain. In this paper, we try to verify this possibility and study the influence of the non-local effect introduced by the lattice to this interesting magnetic edge mode.

2. Homogenization of lattice of gyromagnetic cylinder

We consider the system in Fig. 1a which is a square lattice of gyromagnetic cylinders divided equally into two domains by opposite biasing magnetic field. The radius of the cylinder and the lattice constant are denoted by r and a. The gyromagnetic property of cylinder was characterized by a constant scalar relative permittivity, ε_m and a frequency dependent relative permeability tensor, $\boldsymbol{\mu}_{\mathbf{m}}$ with forms as:

$$\boldsymbol{\mu}_{\mathbf{m}} = \begin{pmatrix} \mu_r & iq\Delta & 0 \\ -iq\Delta & \mu_r & 0 \\ 0 & 0 & 1 \end{pmatrix}, \quad \begin{cases} \mu_r = 1 + \dfrac{\omega_m \omega_h}{\omega_h^{\,2} - \omega^2} \\ \Delta = \dfrac{-\omega_m \omega}{\omega_h^{\,2} - \omega^2} \end{cases}, \qquad (1)$$

where $q = +1(-1)$ indicates the +z(-z)-direction biased magnetic field for the upper(lower) domain in Fig 1a. $\omega_h = \gamma H_o$ is the precession frequency, γ is the gyromagnetic ratio and H_o is the magnitude of the biased magnetic field. $\omega_m = \gamma M_s$ and M_s is the saturation magnetization[10]. We only focus on the TE mode $\left(\mathbf{E} = (0 \;\; 0 \;\; \mathrm{E_z}), \mathbf{H} = (\mathrm{H_x} \;\; \mathrm{H_y} \;\; 0)\right)$ which has in-plane magnetic field for exciting the gyromagnetic effect.

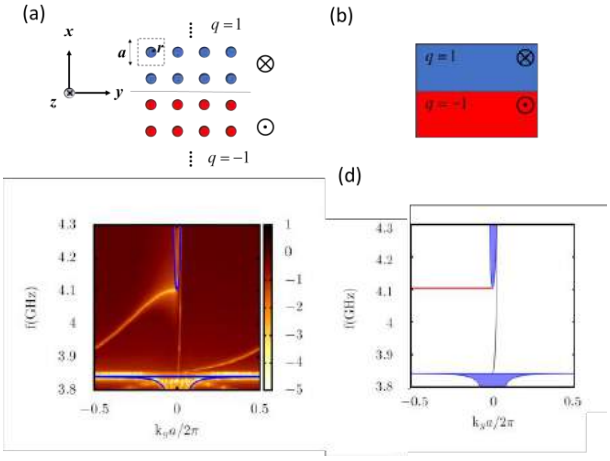


Figure 1: (a) the square lattice of gyromagnetic cylinder which is divided into two domains equally at x=0 by opposite biased magnetic field. (b) The effective system for Fig. 1a – continuous gyromagnetic medium divided into two domains by opposite biased magnetic field. (c) and (d) The bulk and edge DR for system in Fig. 1a and 1b

According to Wu [9], the square lattice of cylinder can be homogenized by the two dimensional Maxwell Garnett equation

$$\begin{aligned} \varepsilon_{eff} &= (1-f)\varepsilon_b + f\varepsilon_m \\ (\boldsymbol{\mu}_{\mathbf{eff}} - \mu_b \mathbf{I})(\boldsymbol{\mu}_{\mathbf{eff}} + \mu_b \mathbf{I})^{-1} &= f(\boldsymbol{\mu}_{\mathbf{m}} - \mu_b \mathbf{I})(\boldsymbol{\mu}_{\mathbf{m}} + \mu_b \mathbf{I})^{-1} \end{aligned}, \quad (2)$$

under the limits, $k_o a/\sqrt{\pi}$, $k_o r$, $k_s r \ll 1$ where k_o is the free space wavenumber, $k_c = k_o n_c$ is the wavenumber in the cylinder with refractive index, n_c. The effective medium calculated is again a gyromagnetic medium as characterized by Equation (1) with $\omega_m \to \omega_{m,eff} = f\omega_m$, $\omega_h \to \omega_{h,eff} = \omega_h + [(1-f)\omega_m]/2$ where f is the filling factor.

We consider the bulk DR for each magnetic domain in Fig. 1a. By checking the field pattern of the mode, we conclude that the yellow curves surrounded by blue curves in the density plot of Fig. 1c are the bulk band. The blue curve, in addition, matches with the bulk DR (blue area in Fig 1d) derived from the effective medium characterized by Equation (2) in the whole Brillouin Zone(BZ). We, therefore, propose that the system in Fig. 1b may have certain mapping with the system in Fig. 1a.

3. Influence of non-local lattice effect on SMM

From the effective system (Fig. 1b) proposed, there are two non-reciprocal edge modes and they are indicated by red and black curve in Fig. 1d. The edge modes after introduction of lattice effect (Fig. 1a) are still non-reciprocal because the symmetries breaking still preserves. The black curve can reconstruct the edge mode near the BZ center. On the other hand, the red edge state which is called the SMM in Ref. [8] can map to the edge mode in Fig. 1c that passes through the BZ boundary and reappear in the opposite boundary. It shows similarity only near the upper bound of the band gap and the BZ center and has completely different dispersive property beyond that region.

For better understanding, we adopted coupled dipole model to recalculate the DR of system in Fig. 1a. The main equation of this model is

$$\mathbf{m}^i = \boldsymbol{\alpha}_{\mathrm{m}} \mu_o \mathbf{H}_{ext} = \boldsymbol{\alpha}_{\mathrm{m}} \mu_o (\mathbf{H}_{applied}{}^i + \mathbf{H}_{dd}{}^i(\mathrm{k}, \mathrm{a}, \mathbf{m}^j)) \quad (3)$$

This model treated each cylinder as magnetic dipole with dipole moment, **m** (same consideration as in effective medium) and each dipole feel the applied field, $\mathbf{H}_{applied}{}^i$ and the field from dipole interaction, $\mathbf{H}_{dd}{}^i$. Both coupled dipole model and effective medium consider dipole interaction. The major difference between these two models is the non-local lattice effect (dependence of k in $\mathbf{H}_{dd}{}^i$, the Bloch wavenumber) which is neglected in the effective medium described in Equation (2). The DR by coupled dipole theory is shown in Fig. 2. The edge DR which map to SMM shows a close dispersive property as that in Fig. 1c. This implies that the non-local effect from the dipole interaction is the main cause for the significant change of the SMM upon the introducing lattice to magnetic domain.

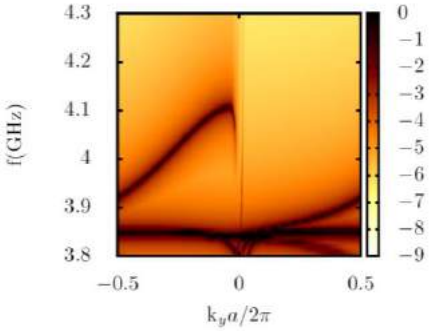


Figure 2: The DR of the system in Fig. 1a by coupled dipole theory.

4. Conclusions

In summary, we demonstrate the SMM flipped back in the opposite side of the BZ and had significant change in the dispersive properties upon introduction of non-local lattice effect. This significant change mainly concentrated in the BZ boundary.

References

[1] X. Ao, Z. Lin, and C. Chan, "One-way edge mode in a magneto-optical honeycomb photonic crystal," *Physical Review B,* vol. 80, p. 033105, 2009.

[2] S. Liu, W. Lu, Z. Lin, and S. Chui, "Magnetically controllable unidirectional electromagnetic waveguiding devices designed with metamaterials," *Applied Physics Letters,* vol. 97, p. 201113, 2010.

[3] Z. Wang, Y. Chong, J. D. Joannopoulos, and M. Soljačić, "Reflection-free one-way edge modes in a gyromagnetic photonic crystal," *Physical review letters,* vol. 100, p. 013905, 2008.

[4] Z. Yu, G. Veronis, Z. Wang, and S. Fan, "One-way electromagnetic waveguide formed at the interface between a plasmonic metal under a static magnetic field and a photonic crystal," *Physical review letters,* vol. 100, p. 023902, 2008.

[5] M. G. Silveirinha, "Chern invariants for continuous media," *Physical Review B,* vol. 92, p. 125153, 2015.

[6] M. G. Silveirinha, "Bulk-edge correspondence for topological photonic continua," *Physical Review B,* vol. 94, p. 205105, 2016.

[7] G. W. Hanson, S. Gangaraj, and A. Nemilentsau, "Notes on photonic topological insulators and scattering-protected edge states-a brief introduction," *arXiv preprint arXiv:1602.02425,* 2016.

[8] J. Wang, H. Y. Dong, C. W. Ling, C. T. Chan, and K. H. Fung, "Nonreciprocal μ-near-zero mode in PT-symmetric magnetic domains," *Physical Review B,* vol. 91, p. 235410, 2015.

[9] Y. Wu, J. Li, Z.-Q. Zhang, and C. Chan, "Effective medium theory for magnetodielectric composites: Beyond the long-wavelength limit," *Physical Review B,* vol. 74, p. 085111, 2006.

[10] J. Jin, S. Liu, Z. Lin, and S. Chui, "Effective-medium theory for anisotropic magnetic metamaterials," *Physical Review B,* vol. 80, p. 115101, 2009.

Acoustic Metamaterials

Acoustic Metasurface for Giant Transmission through Water-Air Interface

Eun Bok[1*], Jong Jin Park[2], Haejin Choi[1], Chung Kyu Han[1], Oliver B. Wright[3], and Sam H. Lee[1]

[1]Institute of Physics and Applied Physics, Yonsei University, Seoul 03722, Korea
[2]Reserch Department, Center for Advanced Meta-Materials, Daejeon, 34103, Korea
[3]Faculty of Engineering, Division of Applied Physics, Hokkaido University, Sapporo 060-8628, Japan
*corresponding author, E-mail: eunbok81@gmail.com

Abstract

Giant acoustic transmission through water-air interface lead to dramatic enhancement of the sensitivity of underwater sound detection. However, such transmission was never realized until recently, because of three orders of magnitude difference in acoustic impedance between water and air. Here, we present the new method that we first realized. We designed an acoustic metasurface for the giant transmission, and experimentally demonstrated that the metasurface increases the power transmission by 160 times of magnitude.

1. Introduction

Impedance matching between two media has been studied to develop a high efficiency acoustic device [1]. Effective water-to-air sound transmission would allow dramatically to enhance the sensitivity of underwater sound detection [1]. However, the giant transmission through water-air interface was never realized until recently, owing to the huge difference between two characteristic impedances of water and air [1]. In this case, a conventional method using a quarter-wavelength layer [2] suffers from the lack of suitable materials. In addition, the layer used for the method would be inconveniently thick for audible frequency applications.

A solution applicable to the problem is an acoustic metasurface, an artificial two-dimensional array of subwavelength sized unit cells containing resonators [3]. Here, we present the new method using acoustic metasurface for the giant transmission. We design the metasurface consisting of two dimensional array of unit cell based on taut membranes and an air-filled cavity. And we demonstrate that the metasurface placed between two media provides giant sound transmission in the extreme mismatch case: we experimentally demonstrate giant water-to-air sound transmission with a metasurface of thickness much smaller than the acoustic wavelength in air.

2. Design of metasurface

Metasurface is two dimensional array of the unit cells called meta-atoms, and therefore the properties of metasurface are determined by design of the meta-atom. The meta-atom consists of two parts, the effective mass element and the cylindrical cavity element, as shown in Figure 1. The effective mass element consists of a central membrane with a mass at the center and four identical separate peripheral membranes. The cylindrical cavity element is terminated by a circular separator membrane to prevent water entering the cavity and to allow the volume of the cavity to be accurately controlled (The circular membrane is in contact with water). The role of the element is to provide an air-filled space of suitable volume between water and the effective mass element. The metasurface consisting of square array of meta-atoms is represented in figure 2.

Considering a wave incident from water or air side, the wave is scattered by the metasurface. The scattered wave in the incident domain is a superposition of two waves reflected from the separator membrane of the cavity element and the effective mass element, respectively. Here, the amplitude and phase of the wave reflected from the effe-

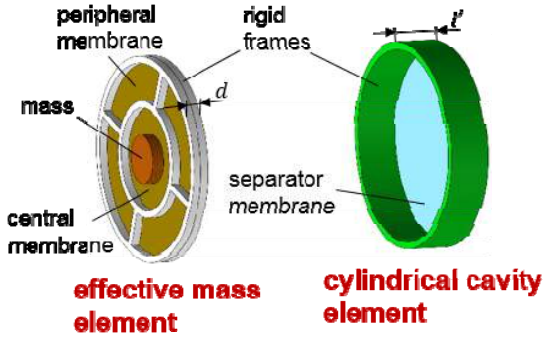


Figure 1: Structure of the meta-atom, shown in exploded view, composed of an effective mass element and a cylindrical cavity element.

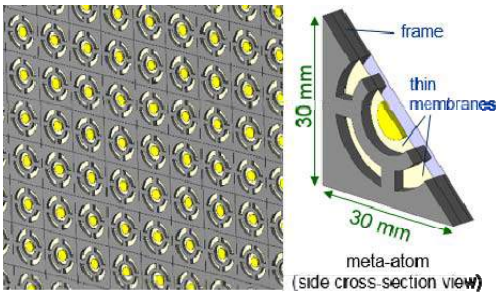


Figure 2: Diagram of the metasurface shown from the air side. Inset: Cross-section and side view of the meta-atom.

ctive mass element can be any value, because the element can effectively change the mass from $-\infty$ to ∞ by adjusting the tensions of the membranes and the weight of the center mass. In other word, the surface impedance on the metasurface can be the same value with the characteristic impedance of incident domain. The metasurface works as an acoustic impedance transformer between air and water.

3. Realization

The acoustic transmission and reflection properties of metasurface is the same with that of the meta-atom, except that the matching frequency is changed [1]. Therefore, we can demonstrate the metasurface by realizing the meta-atom. The meta-atom realized is shown in figure 3. All the membranes of the effective mass element are made of stretched latex rubber of thickness 57 μm, and are fixed to a rigid aluminum-alloy frame. The outer radius of the peripheral membranes and the radius of the element are 12 mm and 15 mm, respectively. The radius of the central membrane is 6 mm and the radius of the attached 60 mg epoxy mass is 3.5 mm. The total thickness *d* of the element is 4.1 mm. And the cylindrical cavity element is formed from a ring-type rigid frame made of acrylonitrile butadiene styrene, in which a thin polyethylene separator membrane of thickness 10 μm is fixed. The cavity length is 0.671 mm. Further details of realized specifications are referred to the reference [1].

The transmission loss spectrum measured by one dimensional waveguide system [1] is represented in Figure 4. The transmission loss spectrum in the presence of the meta-

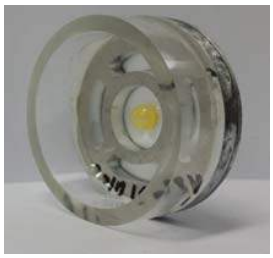


Figure 3: Photo image of the realized meta-atom with a short acrylic tube attached.

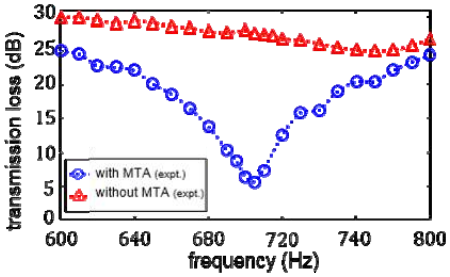


Figure 4: This is the figure caption. Color figures are acceptable.

atom are shown by the blue circles, indicating a minimum of 5.6 dB at 705 Hz. In contrast, we get the data shown by the red triangles for the case that the meta-atom is not installed. At 705 Hz, the meta-atom increases the power transmission by 160 times, equivalent to a 22 dB enhancement. This remarkable increase is achieved with a meta-atom of total thickness 4.8 mm that corresponds to the extremely small value $\sim\lambda/100$ in air (The wavelengths in air and water are, respectively, estimated as 491 and 2120 mm at 705 Hz).

4. Conclusion

We demonstrate experimentally a metasurface that works as an acoustic impedance transformer between air and water in spite of their huge impedance mismatch. With the metasurface of only $\sim\lambda/100$ thickness, we measure a transmission loss of 5.6 dB, corresponding to an intensity transmission of 160 times that of a bare air-water interface. The results are scalable, and arrays of our meta-atoms with different frequencies could be used to cover wide frequency ranges. Our system can be applied to sensitivity enhancing of every underwater measuring system important in marine biology, sonar, underwater communication, and positioning systems.

Acknowledgements

This work was supported by the Center for Advanced Meta-Materials (CAMM) funded by the Ministry of Science, ICT, and Future Planning as a Global Frontier Project (CAMM-2014M3A6B3063712) and by the National Research Foundation of Korea (NRF) Grant funded by the Korea government (MSIP) (No. 2015001948).

References

[1] E. Bok, J.J. Park, H. Choi, C.K. Han, O.B. Wright, S. H. Lee, Metasurface for Water-to-Air Sound Transmission, *Phys. Rev. Lett.* 120: 044302, 2018.

[2] T.G. Alvarez-Arenas, *IEEE Trans. Ultrason. Ferroelectr. Freq. Control* 51:624-633, 2004.

[3] N. Yu, P. Genevet, M. A. Kats, F. Aieta, J.-P. Tetienne, F.Capasso, Z. Gaburro, *Science* 334: 333-337, 2011.

Materials for Photonics (Graphene, MoS2, WS2, etc)

Engineering Photon Upconversion with an Optical Cavity

Ye Yu[1], Yejing Liu[2], Joel K. W. Yang[2], Tobias A. F. König[1,3], Andreas Fery[1,3,4]

[1]Leibniz-Institut für Polymerforschung Dresden e. V., 01069 Dresden, Germany
[2]Singapore University of Technology and Design, Somapah Road 8, 487372, Singapore
[2]Cluster of Excellence Centre for Advancing Electronics Dresden (cfaed), Technische Universitat Dresden, 01062 Dresden, Germany
[3]Department of Physical Chemistry of Polymeric Materials, Technische Universitat Dresden, Hohe Str. 6, 01069 Dresden, Germany
*corresponding author, E-mail: ye-yu@ipfdd.de

Abstract

In this poster we will show a strategy to manipulate the upconversion of photons using an optical cavity as the work horse. Instead of chemically re-designing the upconvertive nanomaterial to tune the upconversion process, an optical cavity can manipulate the effective excitation feature and hence engineer the photon upconversion pathways. As a result, the upconverted light intensity, lifetime, as well as emission ratio can be readily tuned.

1. Introduction

Photon upconvertive nanomaterials have gain much attention due to the possibility of converting multiple photons with lower energy to single photon with higher energy. This provides a possible path for better light harvesting, background-free deep imaging, and light-emitting diode devices with efficiency surpass the theoretic limitation. Yet the converting efficiency, especially for the nanometric materials, is still too low for the possibility of real-life application; and the upconversion mechanisms are, to this day, very much open to debate.

Numerous researchers had revealed the basic principles of upconverting photons. While highly efficient, most of them involve chemically designing and synthesizing the required nanomaterials. In order to understand the conversion mechanism in depth, an alternative approach is in need to provide a different perspective. Recently researchers had shown that introducing plasmonic and photonic components can usually provide brand new channels in the light-matter interaction. Yet not many had shown in the field of upconversion nanomaterials.

In this poster we will show the design and analysis of a simple planar optical cavity when the photoluminescence of the upconvertive material is in strong interaction with the cavity resonance. We systematically studied the photon upconversion dynamics when under the influence of optical cavity and further show the possibility of using such a simple cavity to engineer the upconverted light intensity, lifetime of the resulting photons, as well as the intensity ratio of the emission channels.

2. Results and Discussion

The optical cavity was constructed using two metallic mirrors separated by dielectric matrix. The cavity length was controlled by the thickness of the dielectric matrix while keeping the amount and position of upconverters constant.

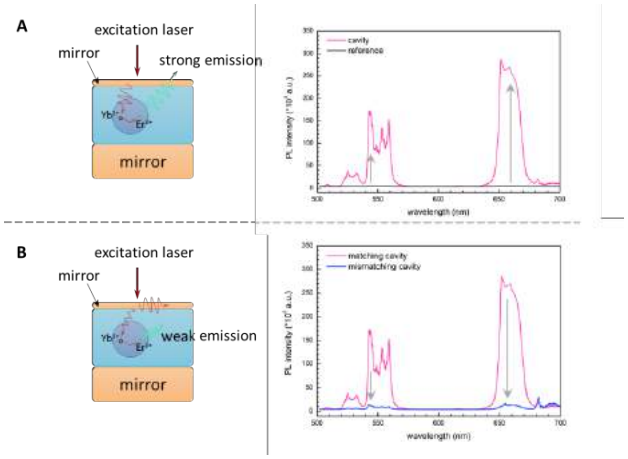


Figure 1: Illustration of the design of the Fabry-Perot cavity altering the photon upconversion process. Photoluminescence spectra on the right panel show the reinforcing (A) and suppressing (B) of the resulting upconverted photons.

It is obvious that the steady-state photoluminescence intensity of the upconvertive material shows strong dependency against the cavity length. Changing the cavity length can engineer the intensity of upconverted emission, lifetime of the emitted photons, as well as the intensity ratio of the as-shown two characteristic emission bands. We will show further detailed results in the poster.

Acknowledgements

This work is supported by the Alexander von Humboldt Foundation.
The authors would like to thank Dr. Petr Formanek for the support of TEM imaging; Dr. Vladimir Lesnyak for the advices in upconversion photoluminescence measurements.

References

[1] B. Zhou, B. Shi, D. Jin, X. Liu, Controlling upconversion nanocrystals for emerging applications. Nature Nanotech. 10: 924-936, 2015.

[2] D. Lien, J. S. Kang, M. Amani, K. Chen, M. Tosun, H. –P. Wang, T. Roy, M. S. Eggleston, M. C. Wu, M. Dubey, S. –C. Lee, J. –H. He, A. Javey, Engineering light outcoupling in 2D materials. *Nano Letters* 15: 1356-1361, 2015.

[3] J. Wirth, K. K. Green, M. O'Connor, S. F. Lim, Enhancement of upconverted fluorescence by interference layers. *Small* 13: 1602846(8), 2017.

Crystal Growth and optical properties of $BaMgF_4$ single crystal

Zhuo Wang[1,2], Junjie Chen[1,2], Yanzhi Ma[1,2], Yuanlin Zheng[1,2], and Xianfeng Chen[1,2]

[1]State Key Laboratory of Advanced Optical Communication Systems and Networks, School of Physics and Astronomy, Shanghai Jiao Tong University, Shanghai 200240, China
[2]Key Laboratory for Laser plasma (Ministry of Education), Collaborative Innovation Center of IFSA (CICIFSA), Shanghai Jiao Tong University, Shanghai 200240, China
*corresponding author, E-mail: xfchen@sjtu.edu.cn

Abstract

$BaMgF_4$ crystal is a very promising candidate for many applications in vacuum ultraviolet region. In our experiments, the $BaMgF_4$ single crystal is grown by temperature gradient technique and the short cut-off wavelength is determined to be 130 nm. The second- and third-order nonlinear optical coefficients are measured by Maker fringe and Z-scan technique, respectively. A considerable electro-optic coefficient is measured as well. At last, frequency conversion experiment is discussed.

1. Introduction

In the past decades, there is a strong demand for all solid-state lasers (ASSLs) working at vacuum ultraviolet (VUV) region for its promising applications in VUV lithography, micromachining and photoelectron spectroscopy[1]. Conventional nonlinear optical crystals such as $LiNbO_3$, BBO, and LBO cannot be used as the nonlinear medium in VUV ASSLs because of their rare transparency. To overcome the difficulty, a series of nonlinear fluoride crystals were found including $KBe_2BO_3F_2$ (KBBF)[2], $BaMgF_4$ (BMF), $SrAlF_5$ and so on. Among these crystals, BMF may be the most promising one for its widely transparency from 130 nm to 13 μm and ferroelectric property to realize quasi-phase-matching (QPM)[3]. In this letter, the second-, third-order nonlinear optical coefficients and electro-optic (EO) coefficient of BMF crystal are determined. Furthermore, sum frequency generation (SFG) from 1064 nm and 532 nm laser to 355 nm laser in BMF crystal is realized.

2. Experiments and discussions

The BMF single crystal was grown by temperature gradient technique (TGT) at the Institute of Ceramics, Shanghai, China. The raw materials were BaF_2 (99.99%), MgF_2 (99.99%) and PbF_2 (99%). In our case, 0.5 wt% PbF_2 was used as oxygen scavenger. Figure 1 shows as-grown BMF single crystal with the dimensions of 75 mm in diameter and 50 mm in height.

2.1. The short cut-off wavelength of BMF crystal

The transmission spectrum in the ultraviolet (UV) region of <0 0 1> orientation of BMF sample was measured by the UV spectrophotometer (Cary 500). Considering the strong absorption of air to the light with wavelength lower than 180 nm, the experiment was carried out in a vacuum cavity. The transmission spectrum is shown in figure 2. It can be seen that there is a monotonous decrease in transparent region without absorption peak towards the UV absorption edge which lies at 130 nm.



Figure 1: $BaMgF_4$ single crystal grown by temperature gradient technique.

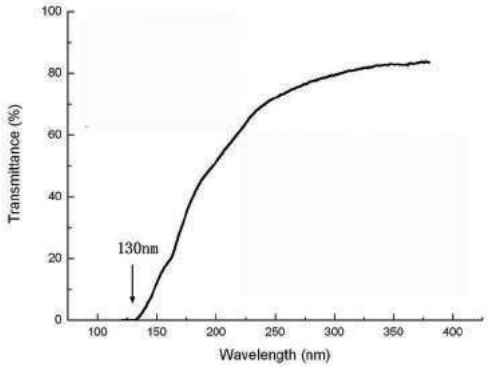


Figure 2: The transmission spectrum of $BaMgF_4$ single crystal.

2.2. The second-order nonlinear optical coefficients of BMF crystal

The standard Maker fringe experiment was performed to measure the nonlinear optical coefficients of BMF single crystal. From Table 1 we can see that, our measured results are about 1 order of magnitude larger than the previously reported results and consistent with our recent theoretical calculation.

Table 1: The measured, theoretical calculated (TC) and previously reported (PR) second-order nonlinear optical coefficients of $BaMgF_4$ crystal.

d	d_{ij} (pm/V) measured	d_{ij} (pm/V) TC	d_{ij} (pm/V) PR
d_{31}	0.15	0.103	0.0286
d_{32}	0.36	0.016	0.0022
d_{33}	0.12	0.091	0.0828

2.3. The third-order nonlinear optical coefficients of BMF crystal

The nonlinear refractive index (n_2) and nonlinear absorption coefficients (β_3) of BMF single crystal have been investigated using the Z-scan technique in the UV region with a pulsed laser at 400 nm with 1 ps pulse duration. Table 2 shows the results.

Table 2: Measured results of third order nonlinear optical parameters of the $BaMgF_4$ Crystal.

Axis	n_2 (10^{-19} m^2/W)	β_3 (10^{-29} m^3/W^2)
a	3.52	4.2
b	4.04	6.1
b	4.57	5.3

2.4. The EO coefficient of BMF crystal

The electro-optic coefficient of BMF single crystal was measured by means of a symmetric metal-cladding waveguide, in which the effect refractive index is very sensitive to the change of the refractive index of the guiding layer. In our experiments, we measured various external incidence angles when changing the applied voltages corresponding to the same guided mode. The EO coefficient γ_{13} = -36.2 pm/V is calculated by a linear fitting. Due to its sufficiently large EO coefficient, BMF can be used as one promising material for key technical realization, such as EO modulators, switches, and highly dense memories, especially in VUV region.

2.5. SFG in BMF crystal

The optical pumping was a Q-switched Nd:YAG laser (USA Continuum Company, Surelite), both 1064 nm and 532 nm lasers as the pump lasers were output simultaneously through adjusting Nd:YAG laser. The average power is 400 mW (1064 nm) and 89 mW (532 nm), respectively. Several 1064 nm and 532 nm holophotes were utilized to make the two pump lasers collinear before they were illuminated onto the BMF sample. After passing through the filter system, 355 nm wavelength signal was extracted from the beam and detected by the spectrometer (HR4000). The shortest coherent radiation is obtained in UV region at 355 nm in the BMF crystal by means of SFG method. The spectrum of 355 nm from SFG is shown in figure 3. The low conversion efficiency is mainly ascribed to phase-mismatching in the process of SFG.

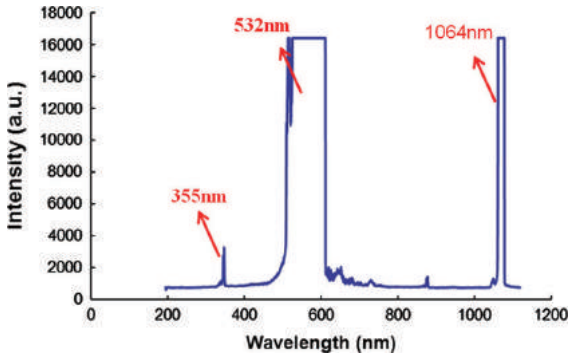


Figure 3: Spectrum of sum frequency generation of 355 nm wavelength laser from1064 nm and 532 nm wavelength laser in $BaMgF_4$ sample.

3. Conclusions

A study on BMF single crystal was demonstrated. The short cut-off wavelength was determined to be 130 nm. The second-, third-order nonlinear optical coefficients and EO coefficient are measured. Moreover, a 355 nm laser was obtained by means of SFG from 1064 nm and 532 nm lasers.

Acknowledgement

This work is supported in part by the National Natural Science Foundation of China under Grant No. 61235009.

References

[1] K. Shimamura and E. G. Víllora, Growth and characteristics of optical single crystals for UV/VUV applications, *J. Fluorine Chem.* 132(12): 1040-1046, 2011.

[2] C. Chen, Y. Wang, Y. Xia, B. Wu, D. Tang, K. Wu, Z. Wenrong, L. Yu, and L. Mei, New development of nonlinear optical crystals for the ultraviolet region with molecular engineering approach, *J. Appl. Phys.* 77(6): 268-2272, 1995.

[3] H. Zeng, K. Shimamura, C. Kannan, E. Villora, S. Takekawa, and K. Kitamura, Ferroelectric domain phenomena and microdomain engineering in $BaMgF_4$ single crystal, *Appl. Phys. A* 85(2): 173-176, 2006.

Laser-patterning of graphene oxide beyond the diffraction limit

Raul D. Rodriguez*[1], Ma Bing[1], Gennady Mustarov[1], Munis Khan[2], Ashutosh Mukherjee[2], Zoheb Khan[2], Suhail Shah[2], Alexey Ruban[1], Sergey Pavlov[1], Anna Lipovka[1], Ammar Al-Hamri[2], Olfa Kanoun[2], Varnika Prakash[3], Surinder K. Mehta[3], and Evgeniya Sheremet[1]

[1]Tomsk Polytechnic University, 30 Lenin Ave, 634050 Tomsk, Russia
[2]Chemnitz University of Technology, D-09107 Chemnitz, Germany
[3]Panjab University, Chandigarh, India
*corresponding author, E-mail: raulmet@gmail.com

Abstract

Graphene oxide (GO) offers excellent possibilities recently demonstrated in applications ranging from biological sensors to optoelectronic devices. Thermal annealing modifies GO by removing the oxygen-containing groups making GO more graphene-like. This thermal reduction can also be achieved by intense light. Here, we demonstrate a scalable and straightforward method based on laser-reduction to pattern graphene oxide films beyond the diffraction limit of light. The potential of this method is illustrated by the fabrication of different devices on flexible and transparent substrates.

1. Introduction

Similarly to graphene, graphene oxide (GO) is becoming a hot-topic material in the 2D materials community. Contrary to graphene, GO has low electrical conductivity. Its electrical conductivity as well as its chemical properties can be drastically modified by applying excess energy that removes the oxygen-containing groups. In this way, the sp^2 hybridization of graphene is partly restored making reduced graphene oxide (rGO) an electrical conductor. The light irradiation can be considered a form of thermal annealing, in particular when using a laser to generate laser-reduced graphene. Besides light, there are other ways to produce rGO from GO films, and these include using an electron beam or a heated atomic force microscopy (AFM) tip. In these latter cases, it is possible to obtain submicrometer-sized patterns of rGO that can be exploited in the fabrication of micro and nanosystems. However, patterning by an electron beam is not scalable or inexpensive. The same goes for patterning by AFM; it would be time-consuming and definitively non-scalable limiting the development of devices using this method. In this contribution to META 2018, we aim at developing and demonstrating an inexpensive, scalable, and fast way to produce rGO patterns of GO films deposited on any arbitrary surface. Our method shows the additional advantage of creating conductive patterns of rGO with spatial dimensions below the laser spot size.

2. Materials and Methods

Graphene oxide commercially available from "Graphenea" was used to obtain GO films deposited by drop-coating. Different substrates were used: a rigid substrate (glass slips) and two flexible ones (PDMS and cellophane).
Different laser irradiation systems were investigated to produce the rGO patterns in lines, as shown schematically in Figure 1. A CO_2 laser engraving machine with 1064 nm excitation using the following parameters: laser spot 80 µm, speed rate 400 mm/s, frequency 90 kHz, pulse duration 50 ns, 5% power. The second system was a portable laser engraving system with 1 W laser excitation output at 405 nm wavelength. The third method investigated involved two solid state lasers at 785 nm and 532 nm. The Raman spectroscopy experiments were performed in a DXR™2xi Raman Imaging Microscope in the backscattering geometry with a 532 nm laser focused on the sample by a 50x LWD objective. Current sensing atomic force microscopy was performed with a NTEGRA Prima SPM using fully metallic tips. The current maps and localized IV curves were obtained in contact mode. The macro-scale conductivity was evaluated using a home-made voltage-amperometer device. After contacting the ends of rGO lines the voltage-current characteristics were recorded for samples obtained under different irradiation conditions (see Figure 1).

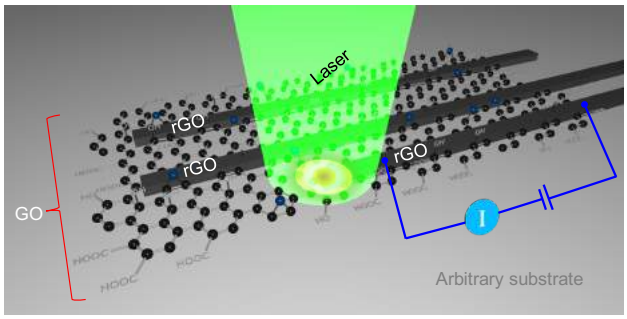


Figure 1: Schematics of the laser reduction of graphene oxide in patterned lines and the I-V characterization.

3. Results and Discussion

The direct observation by optical microscopy shows the different regions of interest on the sample. The Figure 2 shows the optical microscopy image of a few line patterns made on a GO film. The aluminum electrode for external contact is visible at the left side of the image. The right side of the optical image in Figure 2 corresponds to the GO on the plastic substrate. The optical contrast between the laser-irradiated region reveals the difference in materials. The light color in the middle of the line patterns is due to the reflectivity of the substrate. This observation indicates that the GO material under the laser was removed entirely. Therefore, we did not expect to be able to measure any current along these patterns, but we observed experimentally was different to our expectations.

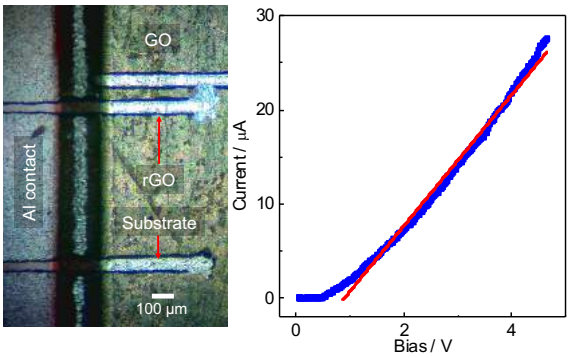


Figure 2: Top view optical microscopy image of a region of the patterned lines showing the different regions of the sample (left). IV characteristics of one of the rGO lines made by laser annealing (right).

The IV characteristics of such patterns, like the one shown at the right of Figure 2, indicates that charges are passing along the patterns. In several control samples, we systematically observed that: 1) there was no material remaining in the patterned lines, the laser ablated down to the plastic substrate, and 2) the patterned lines showed an unexpected high electrical conductivity. To reconcile this apparent contradiction, we took a closer look at the laser irradiated regions with Raman spectroscopy. The results shown in Figure 3 obtained from dozens of spectra measured in the lines and on the pristine GO films show spectral changes that can be attributed to a modification of the carbon at the edges of the film. Current sensing atomic force microscopy results allowed to spatially visualize the regions responsible for the conductivity of the patterns showing that the edges were responsible for that. This allowed us to conclude that by working in an extreme regime of high laser power, much higher than any reported until now in laser-reduced GO highly confined regions of rGO could be obtained. The creation of these highly conductive edges occurred at the interface between the ablated GO regions where only the bare substrate remains, and the pristine GO at the other side of the edge. It can also be seen from the optical microscopy image in Figure 2 that the laser spot size represented by the ablated area (bare substrate) is much wider in size than the thin darker edges made of rGO.

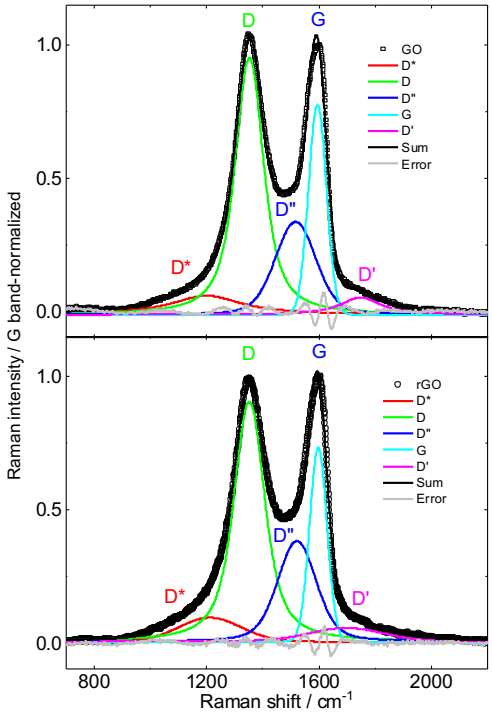


Figure 3: Raman spectroscopy analysis obtained by averaging over a dozen of spectra from the pristine GO film (top) and the rGO edges (bottom).

The generality and power of our method are demonstrated by the fabrication of different kinds of devices including flexible electrochemical sensors with plasmonic nanoparticles for dual-channel sensing, electronic circuits for lighting, and optical elements such as diffraction gratings and polarizers. Furthermore, this method opens the door to the creation of tunable optoelectronic devices by controlling the reversibility of the reduction process *via* an external bias. This latter is an exciting part of our ongoing research that will be briefly discussed as future perspective.

4. Conclusions

These results have tremendous implications in the inexpensive and large-scale fabrication of graphene-based optoelectronic devices with dimensions much smaller than the laser spot size circumventing the diffraction limit of light.

Acknowledgements

The research is carried out at Tomsk Polytechnic University within the framework of Competitiveness Enhancement Program. This work was performed in the context of the EU COST Action MP1302 Nanospectroscopy.

Dynamically Tunable Electromagnetically Induced Transparency in Graphene and Split-Ring Hybrid Metamaterial

Guangxu Su[1], Zhong Huang[1], Wenbo Zang[1], Peng Zhan[1,2,*], Zhenlin Wang[1,2]

[1]School of Physics and National Laboratory of Solid State Microstructures, Nanjing University, Nanjing 210093, China
[2]Collaborative Innovation Center of Advanced Microstructures,Nanjing 210093, China
*corresponding author, E-mail: zhanpeng@nju.edu.cn

Abstract

We proposed a novel hybrid metamaterial consisting of periodic array of graphene nano-patch and gold split-ring resonator to realize an active control of the EIT analog by tuning the Fermi energy of the graphene nano-patch through electric gating in the mid-infrared regime. A narrow transparency window occurs over a wide absorption band due to the coupling of the high-quality factor mode provided by graphene dipolar resonance and the low-quality factor mode of split-ring resonator magnetic resonance.

1. Introduction

Electromagnetically induced transparency (EIT), which is generated when a narrowband discrete state destructively interferes with a broadband continuum, is a quantum effect in atomic systems giving rise to a sharp peak within a broad transmittance dip [1]. In the past decade, various metallic plasmonic sub-wavelength microstructures have been employed to generate EIT-like effect in the visible and infrared regime because of its flexible design and easy implementation [2]. However, most of these metallic microstructures have to be tuned to work in different frequency regimes only by varying their geometrical parameters because the properties of the surface plasmon in metals are greatly limited by the difficulty or impossibility in dynamically tuning their plasma frequencies. Recently, two-dimensional (2D) materials such as graphene have received a great deal of attention due to their exceptional optical and electronic properties [3]. More importantly, graphene shows strong tunability of electromagnetic properties through manipulating its Fermi energy level by electrical gating or chemical doping [4], allowing it to be a good candidate for active tunable plasmonic nanostructures and their corresponding functionalized electro-optic devices. Herein, we purposed a graphene-gold complex metamaterial working at mid-infrared regime, which is a double-layer nanostructure with its unit cell consisting of a gold split-ring resonator (SRR) and a graphene rectangular resonator, separated by a dielectric layer. Graphene rectangular resonator used here works as a "dark" mode with high-quality factor (narrow linewidth), while the gold SRR works as a "bright" mode with low-quality factor (large linewidth). The induced surface charge distribution of the metamaterial at different wavelengths suggests that the EIT-like effect is obtained from the destructive interference between the narrowband graphene dipolar resonance and the broadband magnetic resonance of the SRR, resulting in transmitting spectra with an EIT-like window. The active control of the EITlike effect is demonstrated by tuning the Fermi energy of the graphene, the structure's geometrical parameters and the environmental dielectric constant.

2. Discussion

As is shown in Fig. 1a, the purposed double-layer metamaterial is constructed with a square array by a unit cell composed of upper layer of a gold SRR resonator and lower layer of a graphene resonator. As shown in the Fig. 1b and 1c, we define d =1 μm, h =30 nm, p =6 μm, l =3 μm, w =0.75 μm, w_g=0.65 μm. For monolayer graphene, the dielectric constant of the graphene ε_g can be derived from[5]: $\varepsilon_g = \varepsilon_0 + \frac{i\sigma_g}{\omega t_g}$.

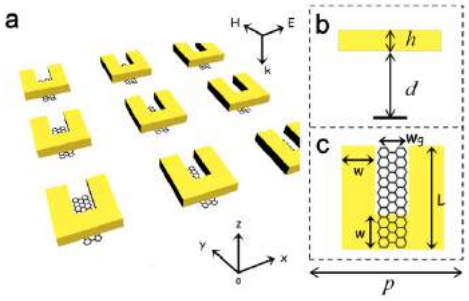


Fig. 1 a Three-dimensional schematic view of the hybrid structure, b the front view of a unit cell, and c the bottom view of a unit cell

To demonstrate the nature of the EIT-like effect clearly, we firstly study the transmission spectra under the normal incidence with TM polarization for the pure gold SRR array

with different l and the pure graphene rectangular nano-patch array with different w_g, as shown in Fig. 2a, c, respectively. While the parameters are used as mentioned above, a broad transmission dip centered at 15 μm is observed for the pure gold SRR array, which corresponds to an excitation of magnetic resonant mode as shown in Fig. 2b, and a narrow transmission dip centered at 15 μm is observed for the pure graphene, which corresponds to an excitation of electric dipole mode as shown in Fig. 2d.

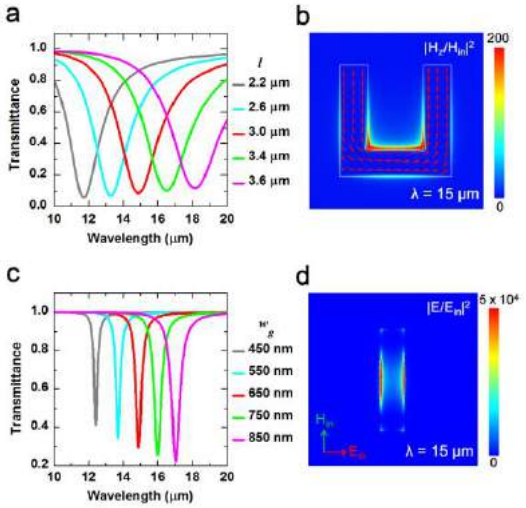


Fig. 2 a Transmittance of the pure gold SRR array for different l, b magnetic field distribution at the half-height plane of the SRR under 15 μm light illumination, c transmittance of the pure graphene resonator for different w_g and d electric field distribution of the graphene resonator under 15 μm light illumination.

When these two modes have near perfect spectral overlap with strong linewidths contrast and comparable resonant amplitudes, a conspicuous coupled resonant mode with Fano line-shape will be formed, creating a narrow transparency window in the wavelength center of the bright mode. As verified by the corresponding simulated transmission spectra in Fig. 3a, the interference of the resonant modes leads to an evident narrow transparency window with a transmission peak frequency at 15.1 μm and two dips at 14.2 μm and 15.9 μm. Complimentarily, the transmission phase data exhibits a typical anomalous dispersion associated with the Fano-resonance region, and an abrupt phase change of 0.975 rad is observed.

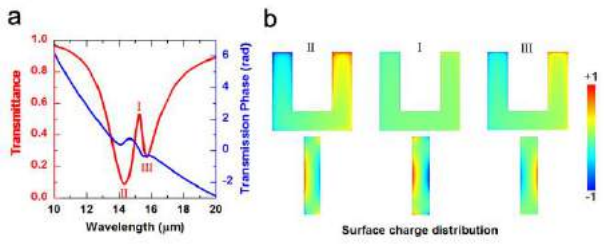


Fig. 3 a Transmittance andtransmission phase of the hybrid structure, the full wavelength of the transmission phase is shown in the inset, b the surface charge distribution at the half-height plane of the SRR and the surface of the graphene patch respectively

Furthermore, our proposed metamaterial shows great tunabilities to the transparency window by tuning the Fermi energy of the graphene nano-patch through electric gating and its electronic mobility without changing the geometric parameters as shown in Fig. 4.

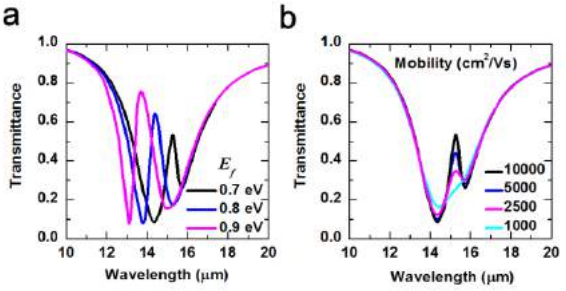


Fig. 4 a Transmittance for the hybrid metamaterial with different Fermi energy and b transmittance for the hybrid structure with different electronic mobility in the graphene patch.

3. Conclusions

In conclusion, we numerically proposed a novel electrically tunable EIT-like metamaterial consisting of top-layer gold SRR array and bottom-layer graphene nano-patch array. The destructive interference between the low-quality factor magnetic resonance of the SRR and the high-quality factor dipolar resonance of the graphene resonator, which can be both directly excited by the incident light, leads to the EIT-like effect. The related physical mechanism is studied by inspecting the phase change and induced surface charge distributions at different wavelengths within the transparency window. The transparency window of the metamaterial can be actively controlled by tuning the Fermi energy and the electron mobility of the graphene.

Acknowledgements

This work was supported by the State Key Program for Basic Research of China (Grant No. 2013CB632703), and by the National Nature Science Foundation of China (Grant Nos.11674166, 91221206, 51271092, and 11574270).

References

[1] Miroshnichenko AE, Flach S, Kivshar YS, Fano resonances in nanoscale structures. Rev Mod Phys 82:2257–2298, 2010.

[2] Gu J, Singh R, Liu X, Zhang X, Ma Y, Zhang S, Active control of electromagnetically induced transparency analogue in terahertz metamaterials. Nat Commun 3:1151, 2012.

[3] García de Abajo FJ, Graphene plasmonics: challenges and opportunities. ACS Photonics 1:135–152, 2014.

[4] Yu R, Pruneri V, García de Abajo FJ, Resonant visible light modulation with graphene. ACS Photonics 2:550–558, 2015.

[5] Jablan M, Buljan H, Soljačić M, Plasmonics in graphene at infrared frequencies. Phys Rev B 80:245435, 2009.

Highly confined biaxial hyperbolic phonon polaritons in van der Waals crystal of semiconducting transition metal oxides

Zebo Zheng, Huanjun Chen*

State Key Laboratory of Optoelectronic Materials and Technologies, Guangdong Province Key Lab of Display Material and Technology, School of Electronics and Information Technology, Sun Yat-sen University, Guangzhou 510275, China

*Corresponding author: chenhj8@mail.sysu.edu.cn; zhengzb2@mail2.sysu.edu.cn

Abstract- Here we report the study on the biaxial hyperbolic phonon polaritons (HPhPs) in a layered van der Waals transition metal oxide, orthogonal molybdenum trioxide (α-MoO_3). The ultra-confined infrared HPhPs waves resulted from the coupling of IR light and optical phonons of α-MoO_3 were launched, detected, and imaged in real space. Due to the low symmetric lattice structure, the HPhPs of α-MoO_3 exhibits a naturally biaxial hyperbolic dispersion. Our results suggest α-MoO_3 as a new platform for studying on novel regimes of light−matter interactions and the future nanophotonic devices.

Phonon polaritons (PhPs), quasiparticles induced by coupling of electromagnetic fields with optical phonons in polar crystals, can strongly confine the light field at deep subwavelength-scale. In comparison with the well-documented metallic plasmon polaritons, the PhPs can achieve improved light confinements, significantly reduced optical losses, and much higher quality factors. These characteristics enable a wealth of potential applications, such as sensing, thermal management, and ultramicroscopy, especially in the mid-infrared and terahertz spectral ranges where most of the plasmon polaritons cannot access. [1, 2]

In recent years, 2D vdW atomic crystals hexagonal boron nitride (h-BN) have been demonstrated as polaritonic material sustaining naturally hyperbolic phonon polaritons with ultra-high confinement due to the strong anisotropic lattice vibrations along the in- and out-of-plane directions of the crystals.[3] However, in comparison to the insulating and wide-band-gap h-BN, 2D materials with semiconducting characteristics are more preferred for practical optoelectronic device applications for their excellent electrical transportation characteristics, tunable optoelectronic properties upon doping, as well as high optical-to-electrical conversion efficacy. These properties can provide new opportunities for the PhPs in active applications of nanophotonics and optoelectronic devices.

As a typical vdW semiconductor, the lattice of the α-MoO_3 is composed of octahedron unit cells with nonequivalent Mo–O bonds along the three principal crystalline axes. Such a low-symmetry crystalline structure gives rise to asymmetric phonon modes that are infrared-active lead to the hyperbolic phonon polaritons similar to that in h-BN. In this study, by using scattering-type scanning near-field optical microscopy (s-SNOM), the ultra-confined HPhPs waves resulted from the coupling of IR light and optical phonons of the α-MoO_3 were launched, detected, and imaged in real space. Our results demonstrated that the α-MoO_3 exhibits natural biaxial hyperbolicity originates from the strong dielectric anisotropy, where the three principal permittivities have mixed signs, give rise to rich modes of deep subwavelength-scale hyperbolic phonon polaritons in three “reststrahlen” bands. Interestingly, the natural in-plane hyperbolic dispersion (where the two in-plane dielectric components

have opposite signs, that is, $\varepsilon_x < 0,\ \varepsilon_y > 0$ or $\varepsilon_x > 0,\ \varepsilon_y < 0$) can give rise to highly confined phonon polaritons propagating along the surface with concave wavefront. The highest electromagnetic confinement on one hand can reach ~ 10^{-2} λ_0 which is comparable to those in other materials such as graphene and hexagonal boron nitride, and on the other hand, can be tuned by altering the thickness of the α-MoO_3. We further experimentally demonstrated the active controlling of the propagation of HPhPs by applying the facile chemical doping manner. In this manner, metal atoms are intercalated into the gap between adjacent α-MoO_3 layers, resulting in a reversible lattice disorder, and therefore the annihilation of surface waves. [4]

In summary, we studied the biaxial hyperbolic phonon polaritons in the layered α-MoO_3 crystal using near-field optical microscopy. Our results suggest the natural biaxial hyperbolicity of the α-MoO_3 crystal originates from the strong dielectric anisotropy can produce deep subwavelenth-scale phonon polaritons with concave wavefront. We also demonstrated the tunable spatial confinement and active controlling of the HPhPs in the α-MoO_3. We believe that our results can on one hand provide new platform for studying novel regimes of light−matter interactions and the future nanophotonic devices, and on the other hand offer guidelines for exploring new 2D polaritonic materials.

REFERENCES

1. Basov. D. N., Fogler. M. M. and Garcia de Abajo. F. J. “Polaritons in van der Waals materials,” *Science*, Vol. 354, No. 6309, aag1992, 2016.
2. Low. T. et al. “Polaritons in layerd two-dimensional materials,” *Nat. Mater*, Vol. 34, No. 10, 1064–1076, 1986.
3. Dai. S., Fei. Z., Ma. Q. et al, “Tunable phonon polaritons in atomically thin van der Waals crystals of boron nitride,” Science, Vol. 343, No. 6175, 1125–1129, 2014.
4. Zheng. Z., Chen. J., Wang. Y. et al, “Highly confined and tunable hyperbolic phonon polaritons in van der Waals semiconducting transition metal oxides,” *Adv Mater*, 1705318, 2018. (DOI: 10.1002/adma.201705318)

High-efficiency sound collimation with an ultra-thin metastructure

Jie Hu[1,2,*], Bin Liang[1] and Xiao-jun Qiu[3]

[1] Key Laboratory of Modern Acoustics (MOE), Institute of Acoustics, Nanjing University, Nanjing, China
[2] College of information Science and Technology, Nanjing Forestry University, Nanjing, China
[3] Centre for Audio, Acoustics and Vibration, Faculty of Engineering and IT, University of Technology Sydney, Sydney, Australia
*corresponding author, E-mail: hujie@njfu.edu.cn

Abstract

We herein design an acoustic metastructure perforated with a single aperture much thinner than the working wavelength for realizing collimated sound beam with high efficiency. The aperture has a zigzag-shaped cross section for substantially increasing the propagation distance of incident acoustic wave and effectively enhancing the transmission efficiency of incident low-frequency waves. The surface of the proposed structure is decorated with subwavelength resonators for the reduction of diffraction effects, which enables directional emission of acoustic energy at the transmitted side. We use numerical simulations to verify the proposed mechanism and demonstrate the performance of the designed device with compact size to produce strong directivity for airborne sound at low frequency.

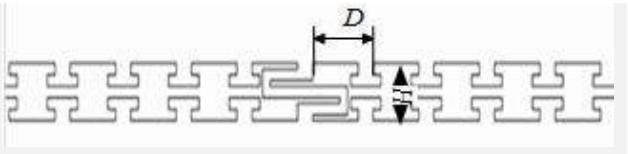
1. Introduction

How to focus and collimate sound energy in space with high efficiency is a fundamental problem in many branches of acoustics, with wide application potentials in various fields such as loudspeaker design and medical ultrasound imaging [1]. Considering importance of miniaturization of acoustic devices, it would be highly desirable to use compact structures to produce collimated beams for incident acoustic waves of long wavelength in practical situations. Recently, the emergence of acoustic artificial materials offer unconventional acoustical properties unattainable with natural materials and produce enabling various fascinating phenomena of acoustic manipulation [2,3] especially effective acoustic focusing and collimation with simple and low-cost passive structures [4-6] such as such as grooved plates [4, 5] and acoustic metasurfaces with subwavelength dimensions [6].

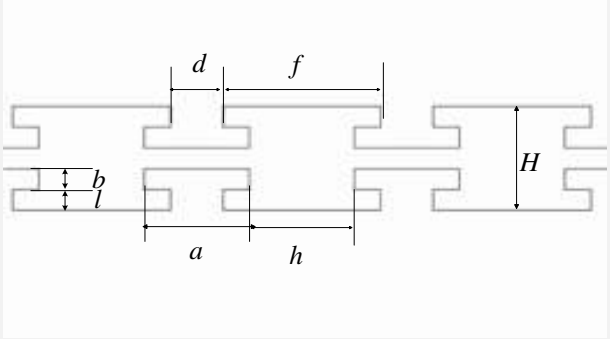
Here we propose to realize high efficiency collimation of sound beam by designing a planar plate with deep-subwavelength thickness, perforated with a single aperture much thinner than the working wavelength. We prove via numerical simulations that by rationally designing the surface of plate decorated with an array of subwavelength resonators, the raditation pattern on transmitted side can be effectivley modified due to the the interference between the scattered wave from resonators and the transmitted wave diffracted by the small aperture. This results in efficient elimination of high order diffracted waves and enables strong collimation of acoustic wave.

2. Metastructure design

For simplicity without losing generality, we consider two-dimensional case in the current study. Figure 1 schematically illustrates the proposed structure perforated with an aperture located in the center, which is inherently a zigzag-shaped channel for increasing the propagation distance of incident acoustic wave substantially. This central aperture are perforated by small Helmholtz resonators arranged in a finite arrays.



(a)



(b)

Figure 1. (a) Cross-section view of the proposed metastructure which has a folded slit in the center. (b) Zoom-in view of the metastructure with Helmholtz-shaped grooves in both sides.

In our design, the whole structure is made of steel, the numbers of resonators in each side is 20, the overall

thickness of the metastructure is H = 2.0mm, and the distance between neighboring resonators is D = 5 mm.
Hence the central aperture supports Fabry-Perot resonance at certain frequency whose wavelength is twice of the length of aperture, which also verified by Figure 2. In Figure 2, we change the size of aperture from 12 mm to 19.6 mm, each size is consistent with the half-length of Fabry-Perot resonant frequency. Here we choose the length of the aperture is 14.5 mm, which supports F-P resonance at frequency of approximately 11.8 kHz. Correspondingly, the structural parameters of an individual Helmholtz resonator is chosen as d = 0.025 mm, l = 0.4 mm, a = 3.4 mm, and b = 0.4mm such that it will resonate at frequency of 11.42 kHz as well.

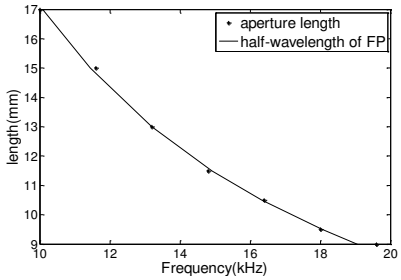


Figure 2. The aperture length (*) is consistent with the calculated half-wavelength of F-P resonance (-)

Here the F-P resonance in the aperture and the bilateral resonators will collectively help to eliminate the diffracted high order waves and generate the desired directivity of acoustic emission, as will be demonstrated in what follows.

3. Results and discussions

Consider a plane acoustic wave illuminates on the proposed metastructure normally. The driving frequency is chosen to be identical with both the F-P frequency in the central aperture and the resonant frequency of each of the Helmholtz resonators. Because of the coupling between F-P resonance in the central slit and the wave guide mode on the surfaces of the designed metastructure, the transmitted acoustic waves are not subject to strong diffraction effect and thereby show high directivity, as manifested by the numerical results shown in Fig. 3.

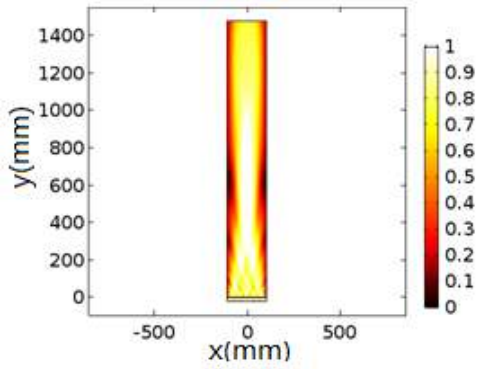


Figure 3. Sound intensity distribution of the transmitted sound beam

The results in Fig. 3 demonstrate the performance of the proposed structure of producing collimated beam for the incident acoustic waves travelling through the deep-subwavelength aperture, and the total propagation length of the generated beam exceeds 1400 mm which is equivalent to approximately 45 wavelength.

4. Conclusions

In conclusion, we demonstrate that with a rationally designed metastructure of deep-subwavelength thickness, high-efficiency directional emission of low-frequency sound energy can be realized for normal incidence planar wave. We prove that the designed structure allows the incident acoustic energy to pass through the central slit with deep-subwavelength width and physical thickness, and then effectively changes the radiation pattern in the transmitted side by suppressing the diffraction effect via the combination of resonances in the aperture and the cavities. The results clearly demonstrate the performance of the designed device to produce strong acoustic collimation at low frequency, resulting in a collimated sound beam that propagates for more than 45 wavelength. This would open route for the acoustic wave collimation with compact devices and may have deep implications in acoustics and relevant fields.

References

[1] B. Raeymaekers, C. Pantea, D. N. Sinha, Creating a collimated ultrasound beam in highly attenuating fluids. *Ultrasonics*. 52:564-570, 2012.

[2] N. Fang, D. Xi, J. Xu, M. Ambati, W. Srituravanich, C. Sun, X. Zhang, Ultrasonic metamaterials with negative modulus, *Nature Mat.* 5, 452 (2006).

[3] Z. Y. Liu, X. X. Zhang, Y. W. Mao, Y. Y. Zhu, Z. Y. Yang, C. T. Chan, P. Sheng, Locally Resonance Sonic Materials, *Science*, 289: 1734-1736, 2000.

[4] J. Christensen, A. I. Fernandez-Dominguez, F. de Leon-Perez, L. Martin-Moreno & F. J. Garcia-Vidal, Collimation of sound assisted by acoustic surface waves, *Nature Phys.* 3: 851–852, 2007.

[5] Y. Zhou, M. H. Lu, L. Feng, X. Ni, Y. F. Chen, Y. Y. Zhu, S. N. Zhu, N. B. Ming, Acoustic Surface Evanescent Wave and its Dominant Contribution to Extraordinary Acoustic Transmission and Collimation of Sound, Phys. Rev. Lett. 104: 164301, 2010.

[6] Y. Li, X. Jiang, R. Q. Li, B. Liang, Z. Y. Zou, L. L. Yin, J. C. Cheng, Experimental Realization of Full Control of Reflected Waves, *Phys. Rev. Appl.* 2: 064002, 2014.

Direct Observation of Semiconductor-Metal Phase Transition in Bilayer Tungsten Diselenide Induced by Potassium Surface Functionalization

Bo Lei[1,3,4†], Yuanyuan Pan[2,5†], Zehua Hu[1,3,4†], Jialin Zhang[3,6], Du Xiang[4,6], Yue Zheng[3,4], Rui Guo[6], Cheng Han[7], Lianhui Wang[8], Jing Lu[5], Li Yang[2*], Wei Chen[1,3,4,6*]

1National University of Singapore (Suzhou) Research Institute, 377 Lin Quan Street, Suzhou Industrial Park, Jiang Su 215123, China
2Department of Physics and Institute of Materials Science and Engineering, Washington University in St. Louis, St. Louis, Missouri 63130, United States
3Department of Physics, National University of Singapore, Singapore 117542, Singapore
4Centre for Advanced 2D Materials and Graphene Research Centre, National University of Singapore, 6 Science Drive 2, 117546, Singapore
5State Key Laboratory of Mesoscopic Physics and Department of Physics, Peking University, Beijing 100871, China
6Department of Chemistry, National University of Singapore, Singapore 117543, Singapore
7SZU-NUS Collaborative Innovation Center for Optoelectronic Science and Technology, Shenzhen University, Shenzhen 518060, China
8Key Laboratory for Organic Electronics & Information Displays (KLOEID), Institute of Advanced Materials (IAM), Jiangsu National Syngerstic Innovation Center for Advanced Materials (SICAM), Nanjing University of Posts &Telecommunications, 9 Wenyuan Road, Nanjing 210023, China
*corresponding author, E-mail: phycw@nus.edu.sg

Abstract

1. Structures determine properties of materials and controllable phase transitions are, therefore, highly desirable for exploring exotic physics and fabricating devices. We report a direct observation of a controllable semiconductor-metal phase transition in bilayer tungsten diselenide (WSe_2) with potassium (K) surface functionalization. Through the integration of in-situ field-effect-transistor (FET), X-ray photoelectron spectroscopy, ultraviolet photoelectron spectroscopy measurements and first-principles calculations, we identify that the electron doping from K adatoms drives bilayer WSe2 from a 2H-phase semiconductor to a 1T'-phase metal. The phase-transition mechanism is satisfactorily explained by the electronic structures and energy alignment of the 2H and 1T' phases. This explanation can be generally applied to understand doping induced phase transitions in two-dimensional (2D) structures. Finally, the associated dramatic changes of electronic structures and electrical conductance make this controllable semiconductor-metal phase transition of interest for 2D semiconductors based electronic and optoelectronic devices.

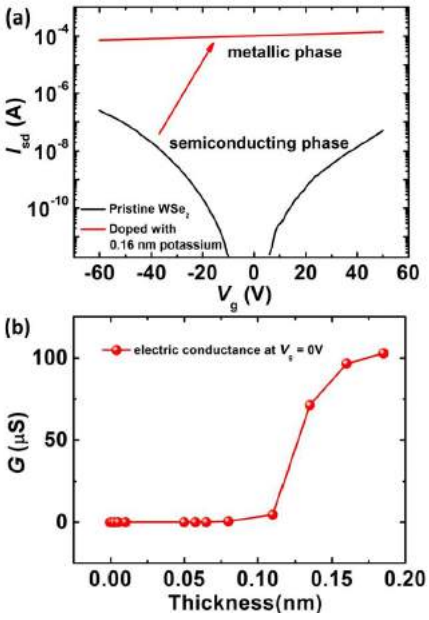


Figure 1. Electric characteristics evolution for potassium-modified WSe_2 field effect transistor. (a) Logarithmic scale transfer characteristics evolution for potassium-modified WSe_2 field effect transistor. (b) Electric conductance at V_g = 0 V of WSe_2 versus potassium thickness.

Chiral and Bianisotropic Materials

Metamaterial with magnetism and structural chirality in the deep UV region

Hiroyuki Kurosawa and Shin-ichiro Inoue

National Institute of Information and Communications Technology (NICT), Japan
*corresponding author, E-mail: kurosawa.hiroyuki@nict.go.jp

Abstract

This study theoretically and numerically investigates the magneto-chiral (MCh) effects in a metamaterial with magnetism and chirality. The MCh effect is modeled by a coupled oscillator, which is known as the Born-Kuhn model, subject to an external magnetic field. Solution of the coupled equation indicates that the MCh effect is realized even in the absence of an internal coupling between magnetism and chirality. The validity of the model is confirmed by numerical calculations. This study opens the door to realize the MCh effects in a metamaterial in the optical region.

1. Introduction

Controlling symmetry is a key to realize new functional devices. In a system with simultaneous breaking of space and time inversion symmetries, an absorption coefficient of a material for unpolarized light depends on the propagation direction of light. This is known as the magneto-chiral (MCh) effect. The MCh effect has attracted a considerable attention due to the potential that one-way mirror may be realized in a MCh media. Theoretical studies have also revealed that an artificial gauge filed for light is realized in the media [1, 2]. The MCh effect has been investigated in natural materials [3] so far, but it has been demonstrated only under unpreferable conditions for practical applications such as high external magnetic field and/or low temperature. Recently, a large MCh effect in a microwave region has been demonstrated in a metamaterial under low external magnetic fields and at room temperature [4, 5, 6]. However, as far as we know, such a large MCh response in an optical region has been missing up-to now.

In this study, we show that a large MCh effect is realized in a metamaterial in the optical region. Formulation of the MCh effects is presented based on a coupled oscillator subject to an external magnetic field, which indicates that a MCh effect is realized in the absence of an internal coupling between the magnetism and chirality. Following our theoretical results, we design a MCh metamaterial in the optical region and numerically show that a large MCh effect is realized in the deep ultraviolet (UV) region.

2. Born-Kuhn model under an external magnetic field

In order to describe the electrodynamics of a system without space and time inversion symmetries, let us start with the coupled oscillators subject to an external magnetic field

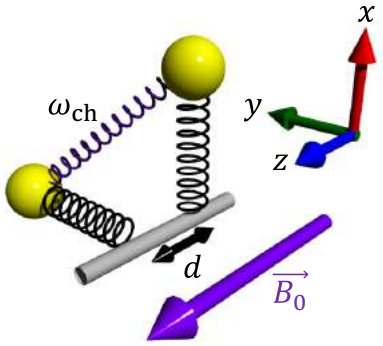


Figure 1: Schematic of two coupled oscillator. These oscillators separated by a distance d have a resonance frequency ω_0. An external magnetic field is applied in this system.

shown in Fig. 1. The two oscillators with resonance frequency ω_0 are directed orthogonal with each other and connected with a coupling constant ω_c. The distance between the oscillators is d. The equations of motion (EOM) for this coupled oscillators are described as follows:

$$\ddot{u}_x + \gamma\dot{u}_x + \omega_0^2 u_x + \omega_c^2 u_y = \frac{q}{m}\left(e_x + i\omega u_y B_0\right), \quad (1)$$

$$\ddot{u}_y + \gamma\dot{u}_y + \omega_0^2 u_y + \omega_c^2 u_x = \frac{q}{m}\left(e_y - i\omega u_x B_0\right), \quad (2)$$

where $\vec{u} = (u_x, u_y)$ is the displacement vector. Solving the EOM and taking volume average of the polarization vector $\vec{p} = q\vec{u}$, we obtain the macroscopic polarization $\vec{P}$. Therefore, the following constitutive equations are derived:

$$\vec{D} = \varepsilon_0\hat{\varepsilon}\vec{E} - i\xi\sqrt{\frac{\varepsilon_0}{\mu_0}}\vec{B} - 2\varepsilon_0\xi\frac{ck\Omega_c}{\Omega^2}\vec{E}, \quad (3)$$

$$\vec{H} = \mu_0^{-1}\vec{B} - i\xi\sqrt{\frac{\varepsilon_0}{\mu_0}}\vec{E}, \quad (4)$$

where $\hat{\varepsilon}$ is the permittivity tensor, ξ is so-called a chiral parameter, Ω_c is the cyclotron frequency defined as qB_0/m, k is the wavevector, and Ω is defined as $\sqrt{\omega_0^2 - \omega^2 - i\gamma\omega}$. These constitutive equations are well known except for the last term of Eq. (3), which consists of Ω_c characterizing the magnetims and ξ characterizing the chirality and is proportional to the wavevector k. Namely, the last term represents the MCh effects.

In the derivation of the MCh effects, we have not assumed an internal coupling between the magnetism and chi-

rality. We show that a MCh effect is realized even in the absence of the coupling.

3. Numerical calculation

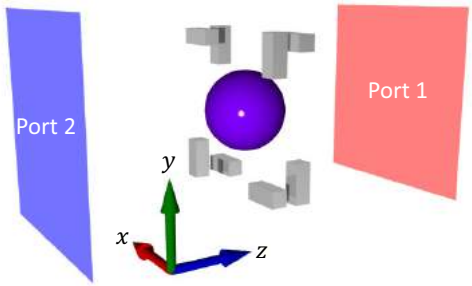


Figure 2: Schematic of the MCh metamatereial in the optical region.

Figure 2 depicts a MCh metamaterial, which consists of chiral and magnetic components (meta-atoms). The chiral meta-atom has two orthogonal aluminum rods, which is configured so that the system has the C_4 symmetry. The magnetic meta-atom is a magnetic nano-sphere with a radius of 100 nm. The diagonal and off-diagonal components of the permittivity of the sphere was set to be 2.6^2 and $0.2i$, respectively. The period of the metamaterial in the x and y directions are 500 nm. We introduced x polarized light to the metamaterial from the ports 1 and 2 and evaluated the S-parameters, S_{21} and S_{12}.

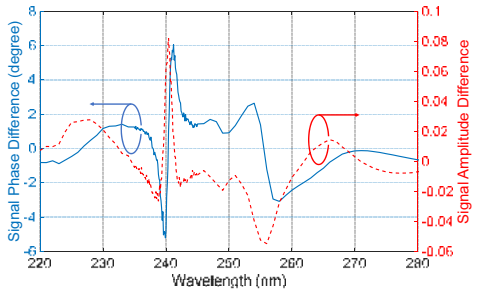


Figure 3: The phase (blue) and amplitude (red) difference spectra.

Figure 3 shows the phase and amplitude difference spectra of $S_{21}-S_{12}$. In this figure, there is a large difference in the spectra around the wavelength of 240 nm, where the phase and amplitude difference spectra respectively exhibit dispersive and peaky structures. The phase and amplitude differences are nearly 6 degree and 8% respectively. These values are two orders magnitude greater than those of previous studies. In order to clarify the eigenmode involving this resonance, we calculated the near field distribution pattern. The result is shown in Fig. 4. The cone and color indicate the electric field vector and its intensity at the peak of the amplitude difference (240.5 nm). The magnetic meta-atom has a characteristic of the Mie resonance, while the chiral meta-atoms has a vortex-like field distribution, indicating that the magnetic and chiral resonances are simultaneously excited. This field distribution indicates that combination of the chiral and magnetic resonances in each meta-atom gives rise to the large MCh response.

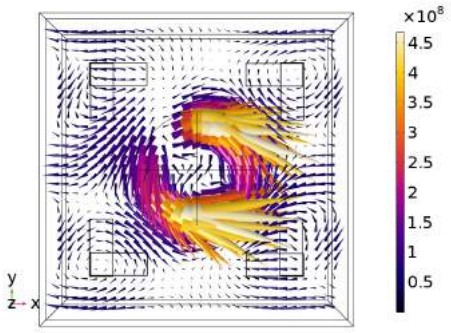


Figure 4: Electric field distribution at the maximum peak of the amplitude difference (at a wavelength of 240.5 nm).

4. Conclusions

We have investigated the MCh effect in a metamaterial with magnetism and structural chirality in the deep UV region. We have formulated the MCh effect based on the Born-Kuhn model under an external static magnetic field and revealed that the MCh effect is realized even in the absence of an internal coupling between magnetism and chirality. Following our theory, we have designed a MCh metamaterial, which exhibits a large MCh effect in the deep UV region.

References

[1] K. Sawada and N. Nagaosa, Lorentz force on light, Phys. Rev. Lett. **95**, 237402 (2005).

[2] H. Kurosawa and K. Sawada, Artificial gauge field for a light ray, Phys. Rev. A **95**, 063846 (2017).

[3] Rikken, G. L. J. A. and Raupach, E Observation of magneto-chiral dichroism, Nature **390**, 493-494 (1997).

[4] S. Tomita, K. Sawada, A. Porokhnyuk, and T. Ueda, Direct observation of magneto-chiral effect in a sigle meta-molecule, Phys. Rev. Lett. **113**, 235501 (2014).

[5] S. Tomita, H. Kurosawa, K. Sawada, and T. Ueda, Enhanced magneto-chiral effect, Phys. Rev. B **95**, 085402 (2017).

[6] S. Tomita, H. Kurosawa, T. Ueda, and K. Sawada, Metamaterial with magnetism and chirality, J. Phys. D: Appl. Phys. , in press.

Large Area Fabrication of 2D Chiral Plasmonic Nanoparticles

Vladimir E. Bochenkov

Lomonosov Moscow State University, Moscow 119991, Russia
E-mail: boch@kinet.chem.msu.ru

Abstract

Large-area arrays of substrate-supported chiral plasmonic gold particles with comma-like shape have been manufactured using a new colloidal lithography technique with in-situ formed silica resist layer and glancing angle evaporation. The structures support three localized plasmon resonance modes spanning from visible to near infrared spectral region and exhibit a pronounced circular dichroism.

1. Introduction

Chiral plasmonic nanostructures have a high potential for efficient enantioselective sensing of biomolecules [1]. A number of accurate top-down fabrication techniques exists that allow manufacturing chiral planar and 3D plasmonic structures with high precision. However, these approaches suffer from low throughput and high costs that determines the need for alternative fabrication methods suitable for practical applications of chiral nanostructures

2. Fabrication procedure

A good candidate for such a method is a self-assembly-based colloidal lithography. In this work, we used an In-situ Resist Colloidal Lithography (IRCL), our modification of sparse colloidal lithography [2], which has successfully been used for the fabrication of large area (few cm^2) arrays of gold rings and crescents [3].

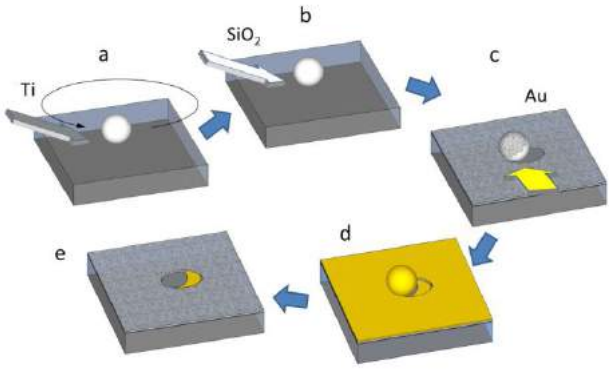


Figure 1: IRCL fabrication of 2D chiral crescent Gold nanoparticles.

The technique has been adjusted for the fabrication of chiral crescents and involved the following steps. First, 300 nm sulfate latex beads are electrostatically adsorbed from aqueous colloidal solution onto glass or Si substrates containing pre-deposited triple layer of polyelectrolytes. This procedure has been described in detail elsewhere [4].

The following vapor deposition steps, illustrated by Fig. 1, are carried out after 15 sec of oxygen plasma treatment. Stationary glancing angle deposition of 25 nm of silica at 30º to surface normal onto a substrate with adsorbed polystyrene particles and pre-deposited adhesion layer (2 nm Ti at 40º with rotation) leaves the area of elliptical shape under each particle unmasked. The subsequent deposition of 20 nm gold at 40º to substrate normal after turning the substrate by 60-90º, leads to formation of an asymmetric crescent structure inside the silica well. The polystyrene particles as well as the top layer of gold are then removed by repeated tape stripping. Asymmetric gold crescent particles remain at the bottom of the wells in silica layer.

3. Optical properties

Extinction (1-T) spectra of crescent particles contain three localized plasmonic resonance modes spanning from visible to near-IR region, which correspond to the low-energy fundamental dipolar mode and the two higher order modes, similar to symmetric crescents [3].

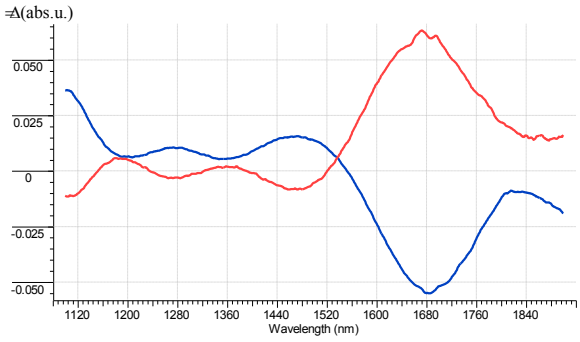


Figure 2: Circular dichroism ($\Delta=A_{RCP}-A_{LCP}$) spectra of 300 nm gold comma-like particles illuminated from the top (red line) and from the bottom (blue line) side (absorbance units)

For the asymmetric particles, studied here, a pronounced circular dichroism signal has been detected at the wavelength of the dipolar plasmon mode. The CD signal changed its sign when the sample was flipped over in the spectrometer (see Fig.2). Such behavior is different from intrinsically 3D structures, where the handedness cannot be altered by any rotation (such as a helix shape, which can be either left or right). That confirms the 2D chiral nature of these structures.

4. Conclusions

The IRCL-based fabrication procedure allows controlling the size of the particles and their shape by changing the diameter of the nanospheres used to form the mask as well as the deposition angles of silica and gold layers. Based on our results, we believe that such asymmetric plasmonic crescent particles can be useful for label-free enantioselective detection of chiral organic and biomolecules. Additionally, the resulting material has enhanced durability since plasmonic nanostructures are located at the bottom of the holes in silica layer, which protects them from scratching.

Acknowledgements

The work has been supported by the Russian Science Foundation grant № 17-13-01276.

References

[1] Hendry, E., Carpy, T., Johnston, J., Popland, M., Mikhaylovskiy, R. V., Lapthorn, A. J., Kelly, S. M., Barron, L. D., Gadegaard, N. and Kadodwala, M., "Ultrasensitive detection and characterization of biomolecules using superchiral fields", *Nature Nanotech*., Vol. 11, No. 5, 783–787, 2010.

[2] V. E.Bochenkov. In-situ resist colloidal lithography for affordable plasmonics. *AIP Conference Proceedings*, 2017, Vol. 1874, No. 1, paper no: 030004.

[3] Bochenkov V. E. and Sutherland D. S., "From rings to crescents: a novel fabrication technique uncovers the transition details," *Nano Letters*, Vol. 13, No. 3, 1216–1220, 2013.

[4] Hanarp, P., Sutherland, D. S., Gold, J. and Kasemo, B. "Control of nanoparticle film structure for colloidal lithography," *Coll. and Surf. A*, Vol. 214, No. 1-3, 23–36, 2003.

Broadband and high-efficiency wavefront manipulation based on chiral metamaterials

Chaoqun Fang[1,2], Chao Wu[1,2,3,*], Zhijie Gong[1,2], Song Zhao[1,2], Anqi Sun[1,2], Zeyong Wei[1,2,3] and Hongqiang Li[1,2,3]

[1]School of Physics Science and Engineering, Tongji University, Shanghai 200092, China
[2]Shanghai Key Laboratory of Special Artifcial Microstructure Materials and Technology, Tongji University, Shanghai 200092, China
[3]The Institute of Dongguan-Tongji University, Dongguan, Guangdong 523808, China
*Corresponding author: chaowu@tongji.edu.cn

Abstract

Wave front shaping devices based on Pancharatnam-Berry (PB) phase possess broadband manipulating range owing to its frequency-independent feature. Chiral metamaterials can achieve high-efficiency circular polarization regulation in a broadband frequency range. Combining with the frequency-independent PB phase, broadband and high-efficiency wave front shaping devices can be realized with chiral metamaterials.

1. Introduction

Wavefront shaping have inspired surge of interests among researchers for its freedom in designing spatial distribution of phase, amplitude and polarization, leading to many advances such as abnormal reflection and refraction [1], focusing [2], vortex beams [3, 4], etc. Wavefront shaping devices based on Pancharatnam-Berry (PB) phase [5, 6] possess a unique broadband circular polarization conversion feature, which can be used for designing user-friendly broadband devices. The PB phase, which is frequency independently introduced to circular polarization conversion components by the rotation of optical element, is an elegant solution to accurately introducing uniform abrupt phase changes through wide frequency range. In recent work, the high efficiency bandwidth is limited by the frequency dependence of the circular polarization conversion efficiency. Chiral metamaterials intrinsically can manipulate circular polarization in broadband frequency range [shown in Fig.1], which makes chiral metamaterials an excellent building block candidate for PB phase based wave front modulation devices. By using frequency-independent PB phase, chiral metamaterials can realize broadband and high-efficiency wave front modulation devices.

In this work, we propose a PB phase based wave front modulation device built with a hybrid helix array. This design demonstrates high-efficiency circular polarization conversion with polarization conversion efficiency above 92% in 8.1GHz-13GHz. By varying orientation angle rotational arrangement of hybrid helix array, broadband high-efficiency wave front shaping can be realized, such as beam bending, focusing, and vortex beam generation. For example, vortex beam generator with 65% efficiency in the relative bandwidth of 46.5% are shown in Fig.2.

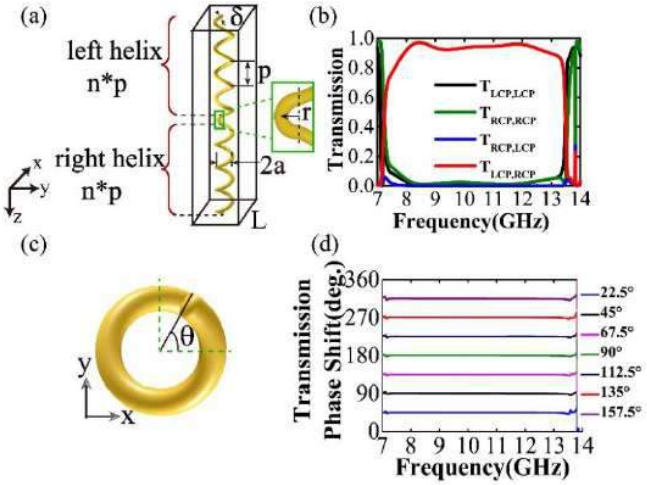


Figure 1: (a) Schematic diagram of hybrid helix. (b) transmission spectra. The first and the second subscripts of the transmission spectra refer to the polarized states of the transmitted and the incident waves, respectively. (c) The orientation angle is defined as the azimuthal angle of start point with respect to the helix axis. (d) transmission phase shift of RCP to LCP conversion component for arrays with orientation angle 22.5°, 45°, 67.5°, 90°, 112.5°, 135° and 157.5°, comparing to 0° array.

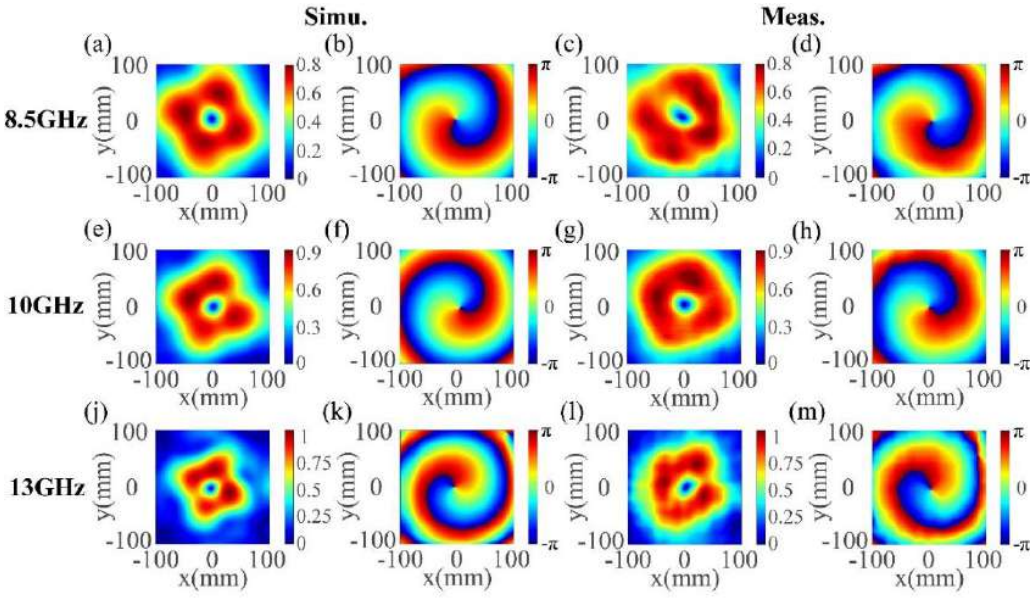


Fig. 2 The electric field amplitude and phase distribution of vortex beam with topological charge $l = 1$. Calculated and measured results are presented at the frequencies of (a)-(d) 8.5GHz, (e)-(h) 10GHz, and (i)-(l) 13GHz. The electric field distributions are normalized to the incident beam amplitude.

Acknowledgements

National Natural Science Foundation of China (11174221, 11204218, 11404213, 61205041, 11674248); China Postdoctoral Science Foundation (2013T60460, 2012M520922).

References

[1].N. K. E. Xingjie Ni, Alexander V. Kildishev, Alexandra Boltasseva, Vladimir M. Shalaev, "Broadband Light Bending with Plasmonic Nanoantennas," Science 335, 427 (2012).

[2].M. Khorasaninejad, W. T. Chen, R. C. Devlin, J. Oh, A. Y. Zhu, and F. Capasso, "Metalenses at visible wavelengths: Diffraction-limited focusing and subwavelength resolution imaging," Science 352, 1190-1194 (2016).

[3].P. Genevet, N. Yu, F. Aieta, J. Lin, M. A. Kats, R. Blanchard, M. O. Scully, Z. Gaburro, and F. Capasso, "Ultra-thin plasmonic optical vortex plate based on phase discontinuities," Applied Physics Letters 100, 013101 (2012).

[4].R. C. Devlin, A. Ambrosio, D. Wintz, S. L. Oscurato, A. Y. Zhu, M. Khorasaninejad, J. Oh, P. Maddalena, and F. Capasso, "Spin-to-orbital angular momentum conversion in dielectric metasurfaces," Opt Express 25, 377-393 (2017).

[5].S. Pancharatnam, "Generalized Theory of Interference and its Applications," Part I Coherent Pencils. Proc. Indian Acad. Sci. Sect. A 44, 247-262 (1956).

[6].M. V. Berry, "Quantal phase factors accompanying adiabatic changes," Proc. R. Soc. London A 392, 45-57 (1984).

Analytical study of the chiral optical potential for dielectric nano-objects

Hipólito A. Arredondo Champi, Rina H. Bustamante, Walter J. Salcedo,

Department of Electronic Systems, Polytechnic School of the University of São Paulo, São Paulo, Brazil
*corresponding author, E-mail: radeemdlb@usp.br

Abstract

We theoretically study the optimal conditions of an enantioselective optical process by means of the chiral optical potential which is created by a split-ring shaped plasmonic nano-aperture when it is illuminated with CP light. We introduce a dissymmetry factor that characterizes the degree of enantiomeric separation and we found that it depend mainly of the near-field *optical chirality* and the chirality parameter of the enantiomers. Our numerical and analytical results prove that an enatiomer pair of chiral spherical nano-objects with tunable chirality parameter between 0.1 and 0.4 can be optically separated for a wide range of material contrasts between the enantiomer and their environment. The contribution of the work could be useful in the efficient design of enantioselective plasmonic devices.

1. Introduction

Enantioselective passive processes of chiral molecules is one of the most important and challenging problems of the pharmaceutical industry that even the chemistry did not manage to solve. To date, analical methods such as chiral chromatographic and capillary electrophoresis continue to be widely used for their efficiency and high performance in the enantioselective recognition [1,2]. However, these chemical methods are mainly time-consumming and require expensive instrumentation which makes its use in the industry unviable. Therefore, there is a need to propose new simple and effective systems for the processes of chiral discrimination.

Recently, optical methods for chiral separation were proposed due to its easy handling, low cost and scalability, and is based mainly on the calculation of optical force [3-6] exerced on chiral nano-objects. Two different approaches include the use of light in free space such as circularly polarized light (CPL) [7,8], rotating electric fields [9] and Laguerre-Gaussian beams [10,11], and the use of the nanostructures as intermediary to intensify the optical force [12] and control to optical chirality [13-15]. For example, Zhao et al. [12] showed that using coaxial plasmonic apertures the chiral optical force allows capturing and repelled opposite enantiomers depending on whether the incident light is LPR or RCP demonstrating the selectivity of small chiral specimens based on their chiralities. However, many amino acids and proteins present weak chirality owing to the nature and the existing methods to date only managed to separate specimens with chirality of 0.5 and a specific solvent. In this sense it is a challenge to extend and improve the functionalities of optical methods based on plasmonic nanostructures that allows to separate chiral nano-objects with a chirality parameter of less than 0.5 in different solvents.

In our analysis we used an analytic approach of the chiral potential optical for small molecules in the dipolar approach [3-16]:

$$U^{\pm} = -\frac{\alpha}{4}\left|\mathbf{E}\right|^2 - \frac{\beta}{4}\left|\mathbf{H}\right|^2 \pm \frac{|\gamma|}{2}\left|\mathbf{E}\right|\left|\mathbf{H}\right|\cos(\theta) \qquad (1)$$

where U^+ (U^-) represents the optical potential for the enantiomer $S(R)$, $\mathbf{E}$ and $\mathbf{H}$ are the local near-fields created by some nanostructure when it interacts with circularly polarized (CP) light, θ is the angle between the vectors $i\mathbf{E}$ and $\mathbf{H}$ which measures the degree of chiral asymmetry of the field electromagnetic. The quantities α, β and γ represent the real part of the electric, magnetic and chiral polarizability, respectively, that for our case will be the polarizabilities of a spherical dipolar nano-object [17]:

$$\alpha = 3\epsilon_o\epsilon_{rm}V\left\{\frac{(\epsilon_r-1)(\mu_r+2)-\hat{\kappa}^2}{(\epsilon_r+2)(\mu_r+2)-\hat{\kappa}^2}\right\} \qquad (2)$$

$$\beta = 3\mu_o\mu_{rm}V\left\{\frac{(\mu_r-1)(\epsilon_r+2)-\hat{\kappa}^2}{(\epsilon_r+2)(\mu_r+2)-\hat{\kappa}^2}\right\} \qquad (3)$$

$$\gamma = \frac{9}{c}\sqrt{\epsilon_{rm}\mu_{rm}}V\left\{\frac{\hat{\kappa}}{(\epsilon_r+2)(\mu_r+2)-\hat{\kappa}^2}\right\} \qquad (4)$$

As usual, ϵ_o, μ_o, and c denote the permitivity and permeability and velocity of the light of free space, ϵ_{rm} and μ_{rm} denote the relative permitivity and permeability of the host medium, ϵ_r and μ_r denote the relative permitivity and permeability of the chiral nano-objects, V represent their volume and $\hat{\kappa}$ their chirality parameter which generally has a small value less than unity. In this case we will consider $\kappa > 0$ for S-enantiomer and $\kappa < 0$ for R-enantiomer.

It is well-known that the optical chirality [7,13,16,18] is defined as $\mathcal{C} = -\frac{\epsilon_m\mu_m\omega}{2}\mathrm{Im}\left\{\mathbf{H}\cdot\mathbf{E}^*\right\}$, but for our case it will be more convenient to define the normalized optical chirality as $\hat{\mathcal{C}}$ as:

$$\hat{\mathcal{C}}(\theta) = \frac{\mathcal{C}}{\left|\mathcal{C}_o^{\pm}\right|} = -I_{\mathbf{E}}I_{\mathbf{H}}\cos(\theta) \qquad (5)$$

where $I_{\mathbf{E}}$, $I_{\mathbf{H}}$ represent the intensifications of the electric and magnetic near-field, respectively, relative to an incident wave CPL in a vacuum with optical chirality $\mathcal{C}_o^{\pm} = \pm\frac{\epsilon\omega}{2c}\left|\mathbf{E}_o\right|^2$

where plut is used for RCP and minus for LCP and the vector $\mathbf{E}_o$ represent the incident electric field. The advantage of equation 5 is in fact that the optical chirality $\hat{\mathcal{C}}(\theta)$ is composed of three factors where the factor angular $\cos(\theta)$ will represent one more degree of freedom to intensify the optical chirality. This angular factor we will call it intrinsec optical chirality.

For CP light we define the local dissymmetry factor $\Delta(\hat{\kappa},\theta)$ as the differential optical potencial which is given by

$$\Delta(\hat{\kappa},\theta) = U^{+} - U^{-} = -\frac{1}{\eta_m}\left|\mathbf{E}_o\right|^2 \left|\gamma(\kappa)\right| \hat{\mathcal{C}}(\theta) \qquad (6)$$

wherein η_m is the impendade of the host medium and the sign of the $\Delta(\hat{\kappa},\theta)$ depends of the chirality of the CP light: Δ is positive (negative) if the incident light is LCP (RCP). It is noted from the equation 6 that $\Delta(\hat{\kappa},\theta)$ depends implicitly on the chirality parameter $\hat{\kappa}$ via magneto-electric polarizability and of the intrinsec optical chirality. This local dissymmetry factor characterizes the degree of enantiomeric separation of a racemic mixture.

2. Results and Discussion

In figure 1, we show the optical potential for LCP light as function of the local electric field intensification $I_{\mathbf{E}}$ for a chiral spherical nano-objetc (enantiomer R or S) with radius of 10 nm and several angles between the fields $i\mathbf{E}$ and $\mathbf{H}$ given by the $\cos(\theta_{i\mathbf{E},\mathbf{H}})$. For our case we have considered transparent enantiomers ($\epsilon_r = 1, \mu_r = 1$) in such a way that the polarizabilities of the enantiomer only dependent on its chirality parameter. We chose $\hat{\kappa} = \pm 0.2$ and Dichloromethane as solvent with $\epsilon_{rm} = 2$. The relationship between the $\mathbf{E}$ and $\mathbf{H}$ was fit using achiral plasmonic nanopertures [12,19,20].

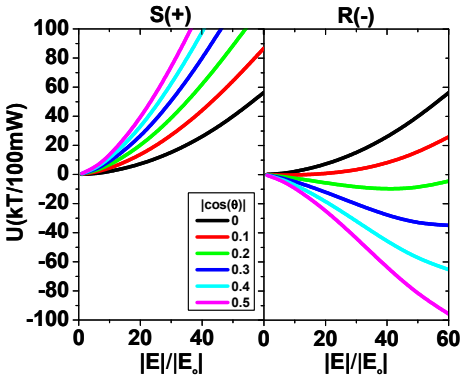


Figure 1: Optical potential as a funcion of $I_{\mathbf{E}}$ for transparents spherical enantiomers R and S with radius of 10 nm and several angles θ. The host medium is dichloromethane with $\epsilon_{rm} = 2$.

The curves of the optical potential for the enantiomer S reveal that these specimens experience a repulsion for all the angles considered (left side of figure 1). Since that the $\cos(\theta)$ measure the intrinsec optical chirality (for $\theta = 0$ the fields $\mathbf{E}$ and $\mathbf{H}$ are orthogonal leading thus to a maximum chirality and for $\theta = \pi/2$ the fields are parallels and lead to a minimum chirality) it's observed that for $\cos(\theta) \geq 0$ the repulsion is intensified. In the case of the R enantiomers (right side of figure 1), although they experience a repulsion for $\cos\theta \leq 0.2$ due to thermal fluctuations $\sim 10kT/100mW$ these enatiomers begin to be captured when the intrinsec optical chirality is intensified ($\cos\theta \geq 0.2$) and $I_{\mathbf{E}} \geq 20$. Under these conditions it is possible to obtain a stable trap for the enantiomer R. In other words, an intensification in the optical chirality leads to an increase in the depth of the optical potential and therefore a better efficiency in the trapping of the enaniomer R.

Now let's consider $I_{\mathbf{E}} = 30$ as it happens in metallic nanostructures [12,19,20]. The figure 2 shows the trapping optical potential for the enantiomers S and R described above but now as a function of its chirality parameter for several angles θ and both light LCP and RCP. It's observed that for light LCP the minimum of the optical potential U_{min} decreases as intrinsic optical chirality increases ($\cos\theta > 0$) and that happens for negative chirality parameters ($\hat{\kappa} < 0$) that makes it a stable trap for the enantiomer R. On the other hand, when light is RCP now the minimum optical potential decreases in the range of positive chirality parameters ($\hat{\kappa} > 0$) as the intrinsic optical chirality increases thus leading to a stable trap for enantiomer S. This property of symmetry that occurs when we exchange LCP for RCP and $\hat{\kappa}$ for $-\hat{\kappa}$ not altering the curves of the optical trap is valid only when it's considered non-chiral nanostructures which creates enantiomorphic plasmonic fields [21].

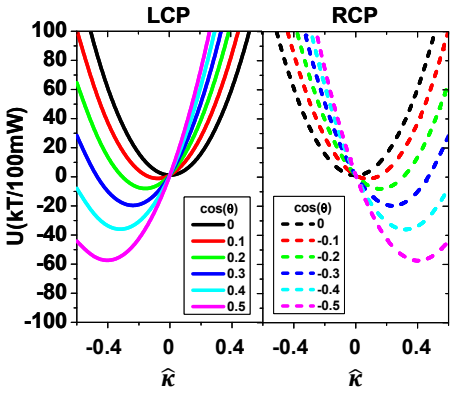


Figure 2: Trapping optical potential for $I_{\mathbf{E}} = 30$ as a funcion of $\hat{\kappa}$ and several angles θ when the incident light is LCP and RCP. The enantiomers are transparent with radius of 10 nm and are immersed in dichloromethane with $\epsilon_{rm} = 2$

It is also important to note from Figure 2 that it is possible to efficiently capture chiral nano-objects with a tunable chirality parameter between 0.1 and 0.4 for $\cos(\theta) \geq 0.4$ and the enantiomorphic symmetry of the electromagnetic fields

allows the use of light LCP or RCP to turn on or turn off the optical trap.

Figure 3 shows an enantioselective optical diagram (EOD) showing the effect of the permittivity contrast ϵ_r between the chiral nano-objects and the host medium (dichloromethane) and the effect of the intensification of intrinsec optical chirality on the trapping optical potential. In this EOD is shown the dissymmetry factor $\Delta(\theta)$ that depends on the angle θ and measures the distance between the potentials corresponding to the R and S enantiomers and keeping its chirality parameter constant. To build this EOD we have considered $I_{\mathbf{E}} = 30$, light LCP, a pair of enantiomers with $\hat{\kappa} = \pm 2$. Notice that in the range of material contrast $-0.97 \leq \epsilon_r \leq 1.08$ an enantiomeric separation process is observed for all values of θ considered, while the separation is more localized to $\cos(\theta) = 0.1$ a more modifiable enantioseparation with ϵ_r is reveled when $\cos(\theta) \geq 0.2$. So also according to equation 6 the dissymmetry factor $\Delta(\theta)$ that depends only on θ increases linearly with intrinsec optical chirality, thus leading to a better efficiency and tunability of the enantioselective optical process. As an immediate result of the previous analysis we can consider a racemica mixture composed of two types of enantiomers R and S en diclhoromethane and under the aforementioned optical conditions the racemate will undergo a highly efficient enatiomeric separation based on an optical trap where the R enantiomers will be trapped in a potential well (bottom of Figure 3) and the S enantiomers will experience a repulsion to a potential barrier (top of Figure 3).

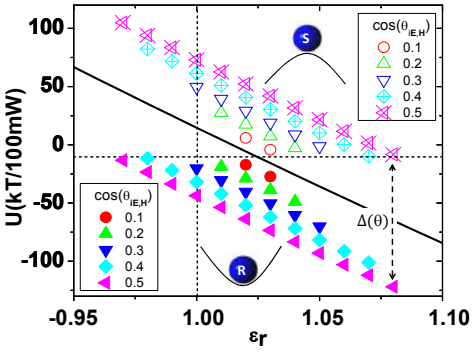


Figure 3: Enantioselective optical diagram for chiral nano-objects showing the effect of the permittivity contrast ϵ_r and the effect of the optical chirality on the optical potential when $I_{\mathbf{E}} = 30$ and the incident light is LCP.

Diagrams similar to figure 3 were obtained for different solvents (ar, water and benzene) showing slight differences in the slopes of the optical potential curves, but the conclusions are qualitatively similar. The solid black line that appears in the EOD is the optical potential for a chiral nano-object ($\hat{\kappa} \neq 0$) with linearly polarized incident light ($\Delta = 0$) or equivalently the optical potential for achiral nano-objects ($\hat{\kappa} = 0$) with light CP ($\Delta \neq 0$) which acts as a reference line for the enantioselective process; for $\epsilon_r < 1.025$ the nano-objecs are repeled while for $\epsilon_r > 1.025$ they are captured. Also note that the intensification of Δ allows you to capture transparent enantiomers R with $\epsilon_r < 1$ thus expanding the range of applicability in the processes of enantiomeric separation.

When a nanostructure interacts with light this creates collective oscillations of electrons on the metal-dielectric interface and depending on whether the incident light is LCP or RCP the local near-fields are also LCP or RCP, respectively, and that is valid for many achiral nanoapertures. In particular, coaxial plasmonic nanoapertures have been recently proposed to present high factors of intensification of the electric field and therefore intensify the optical gradient forces which allows to capturing nanometer-sided specimens [12], but still the challenge of designing nanoaperturas that intensify the intrinsic optical chirality. In this sense, we propose una split-ring shaped plasmonic nanoaperture (complementary split-ring) similar to a metalic split-ring shaped meta-atom used in optical metamaterials. In the inset of figure 4 the complementary split-ring is shown where the geometrical parameters were optimized to achieve a maximum optical chirality.

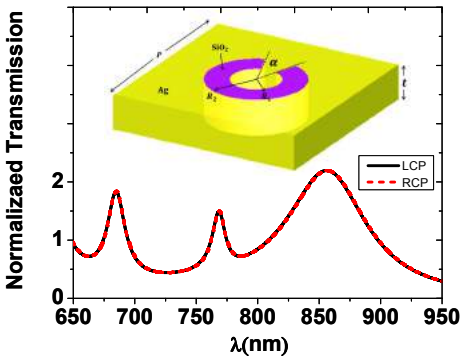


Figure 4: Transmission spectra normalized to the area of the complementary split-ring for LCP and RCP. The inset shows the unitary cell constituted for an split-ring shaped nanoaperture in 130 nm silver slab with internal and external radii of 50 nm and 100 nm, respectively, and $\alpha = 60^o$.

The unitary cell of the metasurface is constituted by a dielectric nanoperture with a split-ring shape in an Ag film. The thickness of the film is $t = 130$ nm and the periodicity of $P = 400$ nm. The internal and external radii of the complementary split ring are $R_1 = 50$nm and $R_2 = 100$nm, respectivamente, and a ring opening angle of $\alpha = 60^o$. These geometric values were chosen with the objective that the complementary meta-atom resonances appear in the visible and near infrared spectrum. We have considered a normal incident light on the complementary split ring to ensure that our meta-atom is achiral [20]. Unlike the coaxial plasmonic nanoapertures [12], the angular parameter α is the most important once it is related to the intensification of the optical chirality.

The normalized transmission spectra for incident light LCP and RCP of the complementary split-ring are shown in figure 4 and this exhibit three resonant peaks in the optical frequency range and near-infrared. These peaks correspond to non-propagating mode ($\lambda = 850$ nm), the fundamental plasmon mode ($\lambda = 768$ nm) and high order modes ($\lambda = 685$ nm) [20]. We observe that the spectra for LCP and RCP coincide ($T_{LCP} = T_{RCP}$) revealing no geometrical dissymmetry for the complemenatry meta-atom due to normal incidence. In what follows we will use the fundamental plasmon mode to intensify the opticl chirality. The figura 5 shows the intensification of the intrinsec optical chirality $\cos(\theta)$ and the normalized optical chirality $\hat{C}$ for the complementary split-ring (solid lines) and coaxial plasmonic nanoapertures (dashed lines) and several host medium [A:Air, W: Water, D: Diclhoromethane and B: Benzene] as a function of the distance to a transverse plane on the z axis taking as reference the top surface of the complementary split-ring. The origin of this intensification in both optical chirality is due to the breaking of symmetry in coaxial plasmonic nanoapertures that besides intensifying the electric field this allowed to increase the intrinsec optical chirality for a factor of 2 when $z = 5$ nm.

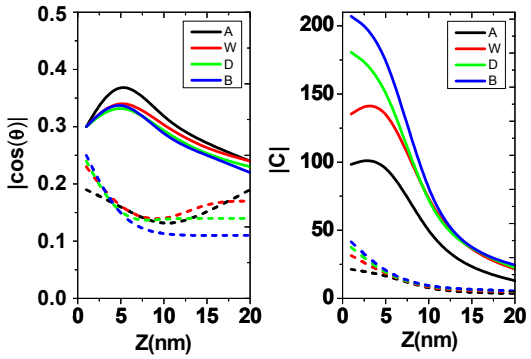


Figure 5: Local optical chirality for complementary split-ring (curvas solidas, $\alpha = 60^o$) and coaxial plasmonic nanoapertures (line dashed, $\alpha = 0$). Left side: Intensification of the intrinsec optical chirality. Right side: Intensification of optical chirality.

Knowing the optimal values of the local optical chirality of the complementary split-ring in figure 6 we show the EOD for chiral nano-objetcs caracterized by the dissymmetry factor $\Delta(\hat{\kappa})$. In this EOD we are shown the effect of permittivity contrast ϵ_r for several values of the chiralidade parameter of the enatiomeros keeping the intrinsec optical chirality constant. Similar to figure 3, the dissymmetry factor $\Delta(\hat{\kappa})$ that now depends on $\hat{\kappa}$ and characterizes the enantioselective process increases linearly with the $\hat{\kappa}$, that is, the greater the chirality parameter, the greater the dissymmetry factor will be and therefore the more efficient the enantioselective process becomes. Additionally, figure 6 reveals that it is possible to obtain an enantioselective process even for $\hat{\kappa} = 0.1$ where other enantioselctive processes fail [12]. On the right side of Figure 6 we show the transverse 3D optical potentials for the S and R enantiomers with $\hat{\kappa} = \pm 0.1$ created by the complementary split ring plasmonic meta-atom. It is observed that the S enantiomers are captured in regions near the angular opening of the ring with a potential of -30 kT/100mW enough to overcome any thermal fluctuation of repulsion experienced by the enantiomers. Already the S enantiomers experience a repulsion due to a potential barrier of 40 kT/100mW which leads to an acceleration of the particles which could be used for propulsion of nanopaticles. The relevance of our results shown in figure 6 is in the theoretical possibility of optically separating a racemate composed of chiral molecules with small chirality parameters ($|\hat{\kappa}| \leq 0.4$) and for a wide range of refractive index of enantiomer of 1.98 to 2.3 for dichloromethane and from 1.4 to 1.9 for water and benzene.

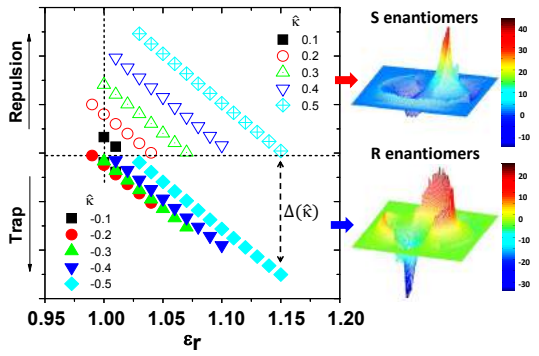


Figure 6: Enantioselective optical diagram for R and S enantiomers with $|\hat{\kappa}| \leq 0.4$ showing the effect of ϵ_r. Trapping optical potential in 3D for chiral molecules with $\hat{\kappa} = 0.1$ for the enantiomer S and with $\hat{\kappa} = -0.1$ for the enatiomer R.

3. Conclusions

In summary, We have theoretically studied the chiral optical potential and demonstrated that under certain values of field intensification and optical chirality an enantioselective passive optical process emerge for small chirality parameters. By introducing a parameter of dissymmetry which characterizes the efficiency of the enantioselective process we find that it depends linearly on the chirality parameter of the enantiomers and the optical chirality for a specific medium host. Finally, we have proposed a split-ring shaped plasmonic nanoaperture that on a normal illumination with CP this intensifies the optical chirality and therefore increases the depths of the chiral optical potentials desired to separate the enantiomers with small chirality parameter and for a wide range of indices of refraction of the solvent. Our contribution will allow us to efficiently design new enantioselective plasmonic devices.

Acknowledgement

We gratefully acknowledge CAPES and CNPq for financial support, as well as the Laboratory of Integrated Systems (LSI) from Polytechnic School of the University of São Paulo.

References

[1] T. J. Ward and B. Ann Baker, Chiral Separations, *Anal. Chem.* 80, 4363, 2008.

[2] L. N. Chennuru et al., Direct Separation of Pregabalin Enantiomers Using a Zwitterionic Chiral Selector by High Performance Liquid Chromatography Coupled to Mass Spectrometry and Ultraviolet Detection, *Molecules* 21, 1578, 2016.

[3] S.B. Wang 1 and C.T. Chan, Lateral optical force on chiral particles near a surface, *Nature Communications* 5, 3307, 2014.

[4] M. H. Alizadeh, and Bjorn M. Reinhard, Transverse Chiral Optical Forces by Chiral Surface Plasmon Polaritons, *ACS Photonics* 2, 1780, 2015.

[5] A. Hayat; J. P. Balthasar Muller; F. Capasso, Lateral chirality-sorting optical forces, *Proc. Natl. Acad. Sci. U. S. A.* 112, 13190, 2015.

[6] M. H. A Lizadeh and B. M. R Einhard, Dominant chiral optical forces in the vicinity of optical nanofibers, *Optics Letters* 41, 4735, 2016.

[7] Y. Tang and A. E. Cohen, Optical Chirality and Its Interaction with Matter, *Phys. Rev. Lett.* 104, 163901, 2010.

[8] G. Tkachenko and E. Brasselet, Optofluidic sorting of material chirality by chiral light, *Nature Communications* 5, 3577, 2014.

[9] J. B. Clemens, O. Kibar and M. Chachisvilis, A molecular propeller effect for chiral separation and analysis, *Nature Communications* 6, 7868, 2015.

[10] I. A. Vovk, Chiral nanoparticles in singular light fields, *Scientific Reports* 7, 45925, 2017.

[11] L. Carretero, P. Acebal, S. Blaya, Chiral Rayleigh particles discrimination in dynamic dual optical traps, *Journal of Quantitative Spectroscopy and Radiative Transfer.* 201, 209, 2017.

[12] Y. Zhao, Amr A. E. Saleh, and Jennifer A. Dionne, Enantioselective Optical Trapping of Chiral Nanoparticles with Plasmonic Tweezers, *ACS Photonics* 3, 304, 2016.

[13] C. Kramer, M. Schaferling, T. Weiss, H. Giessen, and T. Brixner, Analytic Optimization of Near-Field Optical Chirality Enhancement, *ACS Photonics* 4, 396, 2017.

[14] L. Kang, Q. Ren, and D. H. Werner, Leveraging Superchiral Light for Manipulation of Optical Chirality in the Near-Field of Plasmonic Metamaterials, *ACS Photonics* 4, 1298, 2017.

[15] C. Kelly etal., Controlling Metamaterial Transparency with Superchiral Fields, *ACS Photonics* 5, 535, 2018.

[16] A. García-Etxarri and J. A. Dionne, Surface-enhanced circular dichroism spectroscopy mediated by nonchiral nanoantennas, *Phys. Rev. B* 87, 235409, 2013.

[17] I. V. Lindell, A. H. Sihvola, S. A. Tretyakov and A. J. Viitanen, Electromagnetic Waves in Chiral and Bi-isitropic Media, *1 ed.; Artech House: London* 1994.

[18] I. Fernandez-Corbaton, M. Fruhnert and C. Rockstuhl, Objects of Maximum Electromagnetic Chirality, *Phys. Rev. X* 6, 031013, 2016.

[19] Amr A. E. Saleh and J. A. Dionne, Toward Efficient Optical Trapping of Sub-10-nm Particles with Coaxial Plasmonic Apertures, *Nano Lett.* 12, 5581, 2012.

[20] Y. Chen, J. Gao, and X. Yang, Chiral Metamaterials of Plasmonic Slanted Nanoapertures with Symmetry Breaking, *Nano Lett.* 18, 520, 2018.

[21] M. Schaferling, N. Engheta, H. Giessen and T. Weiss, Reducing the Complexity: Enantioselective Chiral Near-Fields by Diagonal Slit and Mirror Configuration, *ACS Photonics* 3, 1076, 2016.

Plasmonics-Based Devices

Photocurrent transient variation in IGZO phototransistors decorated with Au nanoparticles

Yusheng Zhai, Guangdian Chen, Yupei Li, Qilong Wang*,

Joint International Research Laboratory of Information Display and Visualization,
School of Electronic Science and Engineering, Southeast University, Nanjing 210096, China

*corresponding author, E-mail: northrockwql@seu.edu.cn

Abstract

Here, we decorated the channel of IGZO-TFT with the Au nanoparticles(AuNPs) by post-annealing the Au film and delicately investigate the photocurrent transient variation under different wavelength illumination(405nm, 532nm and 658nm). The AuNPs decorated devices show dramatic overshot photocurrent transient variation at wavelength of 658nm, which demonstrate the existence of the hot electron ejection into the IGZO channel. The FDTD method was employed to obtain the electromagnetic field distribution and explain the background mechanism. The hot electron ejection is strongly dependent on the field enhancement factor and the location of the field enhancement.

1. Introduction

Although, there are several papers have investigated the optoelectronic properties of the metallic nanoparticle decorated wide bandgap semiconductor, and they have found that the decoration can widen the responsivity spectra[1,2], which is attributed to the plasmon induced hot electron ejection into the semiconductor channel, they pay little attention to the ejection process, Besides, it is very difficult to measure the ultrafast hot electron ejection process, the timescale is about several tens of femtoseconds. In this paper, we decorated the channel of IGZO-thin film transistor(TFT) with the Au NPs by post-annealing the Au film and delicately investigate the photocurrent transient variation under different wavelength illumination. We indirect demonstrate the electron ejection process by the photocurrent transient curve and find that the electron ejection process strongly dependent on the Au NPs and the wavelength of the illumination wavelength.

2. Result and Discussion

Figure 1(a-d) show the SEM and AFM images of the bare IGZO film and the AuNPs-decorated IGZO film. From the Fig.1(d)and 1(e), we can find the bare IGZO film have a flat surface(roughness is about 1.5 nm), as for the Au NPs-decorated IGZO film(Figure 1a and 1b), the Au NPs are well dispersed on the IGZO film which suggest that the annealing process is an effective process to combine the metallic nanostructure with the semiconductor. Unlike the chemical synthesized nanoparticles, in this method, the metallic nanoparticles are directly contact with semiconductor film and without surface ligand on the nanoparticle surface to impede the hot electron ejection. The size distribution of the Au NPs is shown in Fig1(c),most of the size are concentrate at the 35nm.

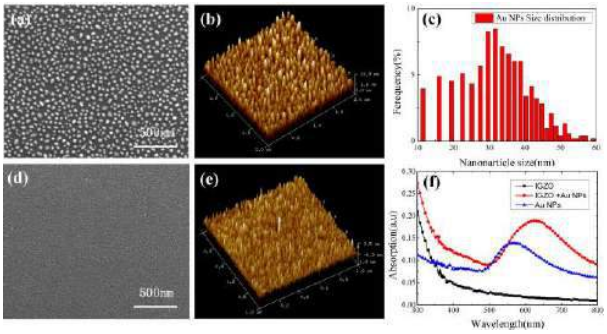


Fig.1 (a,b)The SEM and AFM image of the Au NPs decorated IGZO film and (d,e)the bare IGZO film, respectively. (c)The particle size distribution histogram of AuNPs on the IGZO film,(f)the absorption curve of the IGZO film , the AuNPs-decorated IGZO films and AuNPs on quartz substate.

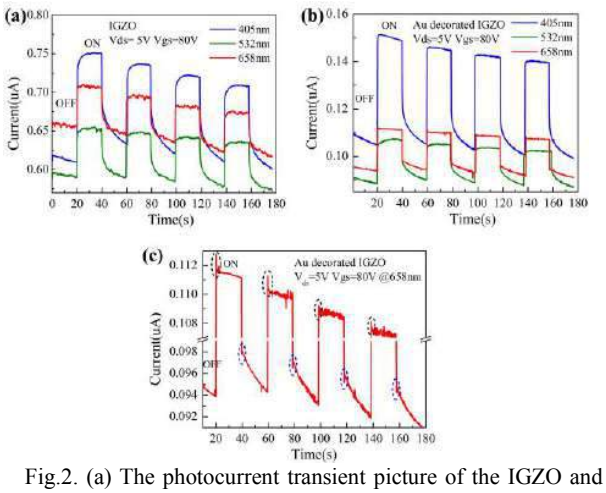


Fig.2. (a) The photocurrent transient picture of the IGZO and (b)Au-decorated IGZO under different wavelength light

illumination. (c) the enlarged curve of the photocurrent transient of Au-decorated IGZO under 658nm illumination.

To investigate the hot electron ejection behavior, the transient responses of IGZO and Au NPs/IGZO phototransistors were measured by periodic illumination with visible light, as shown in Fig.2 (λ=405 nm, 532 nm and 658 nm). The drain current Id was measured at V_{ds}=5 V and V_{gs} = 80 V under repeatedly switching laser diode light with an ON-OFF interval of 20 s, and the laser power density was fixed at 1 mW/cm^2.

For the bare IGZO TFT, once the device was exposed to the light (ON) with λ=405nm, 532nm or 658nm, Ids quickly increase and reach a steady level. After the light was turned off (OFF), Ids relaxes back to its original level. Multiple switching cycles of the repeated ON and OFF illumination were recorded. The photocurrent measurements were stable and reproducible. I_{ds} increases and remains at a steady value for the incident wavelength of 405 nm, 532 nm and 658 nm, as we have mentioned above the visible light response of the IGZO film is due to the defect level band.

The AuNPs decorated devices show the same photocurrent transient under 405 nm and 532 nm illumination(Fig.2b), the photocurrent measurements were stable and reproducible, Ids increased and remained at a steady value for the incident light. But when the incident light change to 658 nm, the devices show different photocurrent transient, when the light was turned on, Ids promptly increased and then promptly decreased to a steady state, which form a overshot peak at the rise edge of the photoresponse curve(Fig.2c). When the light was turned off, I_d promptly decreased and then promptly recovered to a steady state.

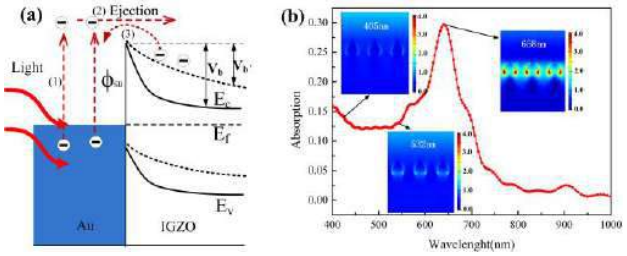


Fig.3. The simulated absorption curve of the AuNPs decorated IGZO film and the field distribution at different wavelength,(b) The mechanism schematic of the peak current overshot peak at the rising edge of the photocurrent transient variation.

This phenomenon looks like capacitive effects, which is not common in traditional photodiodes and photoconductors, however, in our devices it is reasonable and it demonstrates the existence of the electron transfer process at the interface between the AuNPs and the IGZO channel(Fig. 3a). In detail, before illumination the conductance of IGZO channel remains at a steady value. Right after illumination, the light induced the surface plasmon resonant of the Au NPs and the resonant decay into hot electrons(process 1), then the surface plasmon resoance-induced hot electrons transfer into the IGZO channel (process 2), resulting in the AuNPs become positively charged and increasing the conductivity of the IGZO channel. At the same time, the positive Au NPs and the electron are accumulating at the AuNPs and the IGZO channel, the potential barrier from the IGZO to the AuNPs is reduced from Vb to Vb', resulting the electron in the IGZO film transfer back more easily and the process 3 gradually play a leading role, after the initial increase, the conductance rapidly recovers to its initial value as the electrons are transmitted back to the AuNPs, which causes a decrease of the conductivity of the IGZO channel. Over a long illumination period, the two processes offset each other, thus resulting in an dynamic equilibrium state and a steady photocurrent. Turning the light off terminates the photo-induced hot-electron transfer. But the electrons are still being transfer back to the AuNPs(process 3) and promptly leads to a decreased conductance in IGZO film which is similar to process of the overshot raising of the current. At the end of both processes, the conductance approaches its initial value. The devices show an optically-induced gating effect under illumination and demonstrate the existence of the electron ejection between the interface of AuNPs and IGZO channel. To deeper understand the different transient photoresponse, we also utilized the FDTD method to calculate the absorption curve and the field distribution pattern of the Au-decorated IGZO at different wavelength, as shown in Fig.3b.

Conclusions

In summary, a photocurrent transient variation effect in an AuNPs decorated IGZO TFT was revealed. AuNPs are efficient light-harvesting centers that possess an extraordinary optical response and light absorption spectrum. The plamosn induce hot electron ejection process is strongly dependent on the absorption spectrum of the Au NPs, only the wavelength of the incident light include in the resonance band, does the incident light can induce the hot electron ejection. The integration of photosensitive AuNPs with wideband gap semiconductor TFT offers a new research platform for plasmon-induced hot-electron transfer and new type phototransistor to realize novel function such as polarimatric image if we design the Au NPs into polarized dependent array.

Acknowledgements

This work is supported by the National Natural Science Foundation of China (61372030, 91333118, 51120125001, 61571124), the NSAF (U1730113), the Natural Science Foundation of Jiangsu Province (BK20171365),

References

[1] F. Tan, T. Li, N. Wang, S.K. Lai, C.C. Tsoi, W. Yu, X. Zhang, Rough gold films as broadband absorbers for plasmonic enhancement of TiO2 photocurrent over 400-800 nm, Sci Rep, 6 (2016) 33049.

[2] Y. Lu, W. Dong, Z. Chen, A. Pors, Z. Wang, S.I. Bozhevolnyi, Gap-plasmon based broadband absorbers for enhanced hot-electron and photocurrent generation, Scientific Reports, 6 (2016): 30650.

Polarization-controlled tunable-focusing of surface plasmon polaritons with nanostructure array

Mingqian Zhang

Qian Xuesen Laboratory of Space Techonology, China Academy of Space Technology,Beijing, China
*corresponding author, E-mail: zhangmingqian@qxslab.cn

Abstract

Tunable plasmonic directing and focusing devices are highly demanded in various applications of nanophotonics for achieving controllable plasmonic signals coupling and multiplexing. Here, a tunable-focusing device with nanostructure array of V-shape slots is suggested. This device allows polarization-controlled tunable plasmonic directing and focusing on the two-dimensional metallic surface. The plamonic field regulation performance of this device was theoretically simulated with finite-difference time-domain method and experimentally measured with a self-constructed phase-resolved near-field microscopy. These results indicate that the focal position of the excited plasmon field can be flexibly tuned between two distinct positions just by manipulating the incident polarization state. We expect this may open new possibilities in the design of controllable plasmonic routers and demultiplexers.

Summery

Surface plasmon polariton (SPP) is a kind of electromagnetic surface wave that propagates along a metal-dielectric interface [1, 2]. Its tight spatial confinement and information processing speed has made it a promising candidate to realize ultra-high-density photonic integration and led to its advances in optical information technology recently [3]. For this purpose, tunable focusing is highly demanded for achieving controllable SPP signals coupling and multiplexing.

In this work, a nanostructure consisting an array of V-shape slots was proposed. Its nanosturctures were designed based on holographic principles to modulate the SPPs wavefront. The position of the focused plasmon field can be flexibly and dynamically tuned by adjusting the polarizer in an optical system to control the polarization direction of linearly polarized incident light. Hence, this device allows coupling light with different polarizations into distinct positions its field regulation performance was simulated using finite-difference time-domain method.

As a proof-of-concept, the designed V-shape slots array was fabricated with focused Ion beam method and its performance was experimentally measured using a self-constructed phase-resolved near-field microscopy. We directly characterized the distributions of optical field intensity and phase excited by incident light with different polarization states. Despite negligible differences, the results agree well with the desired ones. It shows that the incident beams with different polarization states are directed to their desired focal positions specified in the design. This validates the effectiveness of our approach. It indicates that this nanostructure allows coupling light with different polarizations into well-separated positions. The focal position of the excited plasmon field can be flexibly switched between two well-separated positions just by manipulating the incident polarization state.

Hence, this V-shape slots array can serve as controllable plasmonic routers and demultiplexers. On the other hand, it can also be used to analysis the incident polarizations effectively by detecting the focal position of the plasmon field. Therefore, this method may have promising applications not only in plasmonics but also in many other fields of optics.

References

[1] H. Raether, Surface plasmons on smooth surfaces, Springer, Berlin Heidelberg, 1988.

[2] S. A. Maier, Plasmonics: fundamentals and applications, Springer, Science & Business Media, 2007.

[3] M. LB. rongersma, V. M. Shalaev, The case for plasmonics, Science, Vol. 328, No. 5977, 440-441, 2010.

Plasmonic-coupled sensors: from multiphoton-assisted quantum coupling to graphene-coupled subwavelength resonant strain sensors

Morteza Aramesh[1], Raphael Tiefenauer[1] and János Vörös[1]

[1] Institute for Biomedical Engineering, Laboratory of Biosensors and Bioelectronics, ETH Zürich, Zurich, Switzerland
E-mail: maramesh@ethz.ch

Abstract

Plasmonic sensors enable ultrahigh speed information processing and are emerging as promising platform for future optoelectronic devices. For some practical applications, plasmonic materials need to be coupled to other materials - such as quantum emitters or 2D materials – to provide multi-functionalities. Despite their great importance, approaches towards scalable fabrication of hybrid plasmonic-coupled devices remain limited due to considerable technical challenges. Here, we present various techniques towards multiscale fabrication of plasmonic-coupled devices and investigate their potentials as sensors.

Introduction

Plasmonic nanomaterials can be combined with other materials (such as quantum emitters or 2D materials) to create hybrid plasmonic-coupled devices with enhanced functionalities which may not be achieved by the individual components. For example, quantum plasmonic circuits require coupling of quantum emitters – such as color centers in nanodiamonds – to plasmonic elements.[1-4] Moreover, coupling plasmonic structures with 2D materials (such as graphene and hBN) have shown great promise for some advanced analysis in molecular scales.[5-6] Despite such importance, scalable integration of hybrid plasmonic-coupled devices faces several technical challenges. In this presentation, we introduce novel techniques towards fabrication of hybrid plasmonic-coupled devices and explore their applications for sensing. First, we present the possibility of plasmonic-assisted excitation of quantum emitters by implementing multiphoton plasmonic coupling. Second, we introduce a strain sensor based on Raman shifts in a suspended single-layer graphene coupled with a subwavelength plasmonic array, using surface-enhanced Raman spectroscopy.

Results and Discussion

Multiphoton-assisted quantum coupling: In our first approach, by using DNA we bring together two important elements for a quantum-plasmonic circuit: (i) a quantum emitter and (ii) a plasmonic coupler. Nanodiamonds (< 15 nm in size) with single photon emitter centers are chosen as a quantum emitter element and gold nanoparticles (50 nm in size) as the plasmonic element. The surfaces of the nanoparticles were functionalized to allow covalent binding of single stranded DNA (ssDNA) to the particles. As it is schematically shown in Figure 1, addition of a complementary DNA to the system allows the particles to make coupled structures by hybridization. A large number of coupled particles (~ 10^{10} particles per mL of solution) can be obtained using this technique. Via a simple spin-coating, the particles can then settle on top of a substrate for further analysis. The influence of various parameters such as particle size and concentration on the coupling efficiency were studied.

To optically couple an NV center in nanodiamonds to a gold nanoparticle we implemented a new technique based on second harmonic excitation of plasmons. In this method, a multi-photon laser was used to excite the gold nanoparticles through second harmonic generation (SHG) of plasmons.[7] Upon excitation, the gold nanoparticles were able to emit green light, which was then used as an excitation source for the neighboring nanodiamond particles (with ~650 nm emission). We will discuss the mechanism of such coupling in our presentation. In this manner, we were able to demonstrate the possibility of coupling the SHG signal generated from gold nanoparticles to the optical centers in nanodiamond.

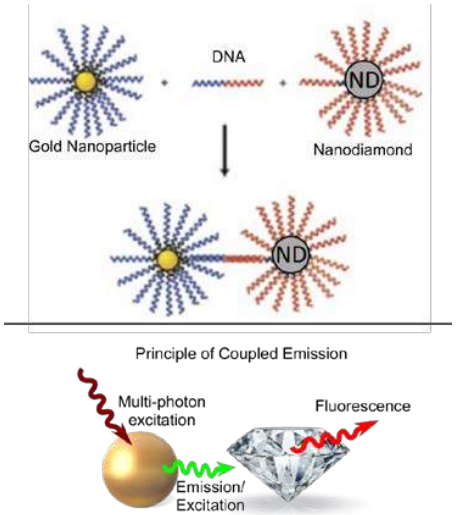


Figure 1. (Top) DNA hybridization technique was used to attach gold nanoparticles to nanodiamonds. (Bottom) shows the principle of plasmonic coupling between the two elements.

Graphene-coupled subwavelength resonant strain sensors: In our second approach towards fabrication of multiscale hybrid plasmonic sensors, we introduce a new stretchable plasmonic platform, which can be easily integrated with other 2D materials such as graphene (Figure 2). The plasmonic platform is composed of ordered arrays of gold nanowires on a flexible and stretchable substrate, such as rubber.[8] The thickness and spacing of the gold nanowires can be tuned precisely during the fabrication process and allow subwavelength spacing for resonant sensing through plasmonic coupling. This possibility is realized by transferring a single layer of graphene film on top of the structures, and by optically measuring the induced strains via plasmonic-enhanced resonant Raman signal of the graphene layer. The platform enables fast and sensitive measurement of strains on various conditions such as on curved surfaces and/or in liquid environment.

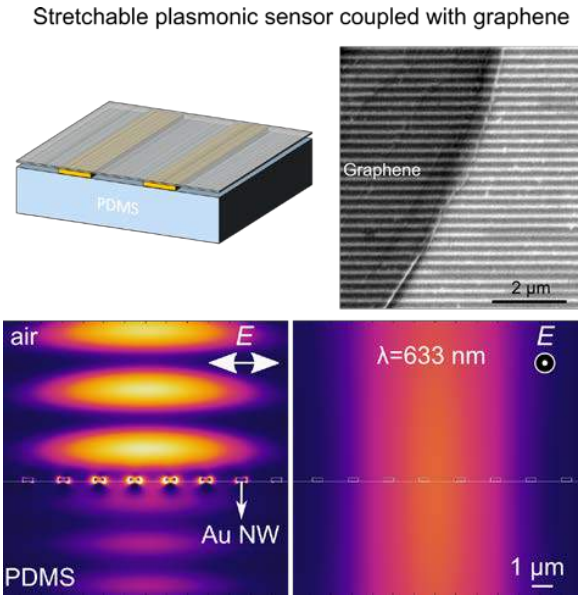


Figure 2. Schematic and SEM image of the stretchable plasmonic sensor coupled with graphene. The simulation shows polarization dependence of the field enhancement near the plasmonic structure upon illumination with a laser (Gaussian beam).

Conclusion

In this presentation, we introduce new techniques for fabrication of multiscale hybrid plasmonic-coupled structures. Realization of such hybrid components raises new possibilities for advanced applications, which were not possible to achieve before. In particular, we introduce new concepts for sensing applications that are developed based on these coupled elements.

References

1. Kolesov, R.; Grotz, B.; Balasubramanian, G.; Stöhr, R. J.; Nicolet, A. A.; Hemmer, P. R.; Jelezko, F.; Wrachtrup, J., Wave–particle duality of single surface plasmon polaritons. *Nature Physics* **2009,** *5* (7), 470.
2. Giovannetti, V.; Lloyd, S.; Maccone, L., Advances in quantum metrology. *Nature photonics* **2011,** *5* (4), 222.
3. Aramesh, M.; Cervenka, J.; Roberts, A.; Djalalian-Assl, A.; Rajasekharan, R.; Fang, J.; Ostrikov, K.; Prawer, S., Coupling of a single-photon emitter in nanodiamond to surface plasmons of a nanochannel-enclosed silver nanowire. *Optics express* **2014,** *22* (13), 15530-15541.
4. Al-Baiaty, Z.; Cumming, B. P.; Gan, X.; Gu, M., Detection of the ODMR signal of a nitrogen vacancy centre in nanodiamond in propagating surface plasmons. *Journal of Optics* **2018**.
5. Cai, T.; Dutta, S.; Aghaeimeibodi, S.; Yang, Z.; Nah, S.; Fourkas, J. T.; Waks, E., Coupling Emission from Single Localized Defects in Two-Dimensional Semiconductor to Surface Plasmon Polaritons. *Nano letters* **2017,** *17* (11), 6564-6568.
6. Rodrigo, D.; Limaj, O.; Janner, D.; Etezadi, D.; de Abajo, F. J. G.; Pruneri, V.; Altug, H., Mid-infrared plasmonic biosensing with graphene. *Science* **2015,** *349* (6244), 165-168.
7. Ramakrishna, G.; Varnavski, O.; Kim, J.; Lee, D.; Goodson, T., Quantum-sized gold clusters as efficient two-photon absorbers. *Journal of the American Chemical Society* **2008,** *130* (15), 5032-5033.
8. Raphael F. Tiefenauer, Klas Tybrandt, Morteza Aramesh and János Vörös, Fast and Versatile Multiscale Patterning by Combining Template-Stripping with Nanotransfer Printing ACS Nano, 2018, in press

Fabrication of plasmonic nanostructure for optical brain imaging

J. S. Kang[1], J. H. Kim[1], Z. Shoaib[1], and M. Y. Jeong[1*]
[1]Department of Cogno-Mechatronics Engineering, Pusan National University, Busan, Korea
[*]corresponding author: myjeong@pusan.ac.kr

Abstract- Recently, many researchers investigated human's brain and the optical brain imaging system was widely used. However, it had limitation of spatial resolution. To solve this problem and enhance contrast-to-noise ratio, noble plasmonic nanostructure was used. The interaction between light and plasmonic nanostructure was governed by surface plasmon polariton and it is used to concentrate and enhance optical signals. In this study, we design and fabricated plasmonic nanostructure for optical brain imaging application. Designed plasmonic nanostructure was based on dipole nanoantenna and grating theory and fabricated by imprint lithography. And we studied the key parameter which was important to fabricate plasmonic nanostructure by nanoimprint lithography.

The optical brain imaging system has been used for understanding human's brain system. The important part of research in relation with the optical brain imaging system was contrast-to-noise ratio(CNR). For enhancing CNR of optical brain imaging system, in this study, we proposed noble plasmonic nanostructures. Plasmonic nanostructures have been widely used to concentrate light for various applications, such as surface-enhanced spectroscopies, quantum optics and sensing.[1] Because of the interaction between light and surface plasmon polariton, the output optical signal could be enhanced by using plasmonic nanostructures.[2-4]

In this study, we design noble plasmonic nanostructure and fabricate these structures to enhance optical signal which are from optical brain imaging system. Design of the nanostructures are based on dipole nanoantenna and grating theory. Grating, array of dipole nanoantenna structure, was considered as it could enhance performance of dipole nanoantenna structure. Designed nanostructure was transferred on Si wafer by E-beam lithography, lift-off and etching process. And fabricated nanostructures on Si wafer are used as stamp for nanoimprint lithography. The nanostructures are imprinted on PMMA sheet under various process variables. Finally, we studied the key parameter in the fabrication process of imprinted plasmonic nanostructure and this parameter was evaluated by using SEM images of nanostructure. The proposed structure is expected to enhance optical signal and CNR and has a potential that adapt to optical brain imaging system.

REFERENCES

1. Bagheri, S., Weber, K., Gissibl, T., Weiss, T., Neubrech, F., & Giessen, H. "Fabrication of square-centimeter plasmonic nanoantenna arrays by femtosecond direct laser writing lithography: effects of collective excitations on SEIRA enhancement." *ACS Photonics*, *2*(6), 779-786.2015
2. Zhuo, X., Yip, H. K., Ruan, Q., Zhang, T., Zhu, X., Wang, J., & Yang, Z. "Broadside Nanoantennas Made of Single Silver Nanorods." *ACS NANO*, 2018.
3. Qi, J., Kaiser, T., Peuker, R., Pertsch, T., Lederer, F., & Rockstuhl, C. "Highly resonant and directional optical

nanoantennas.” *JOSA A*, *31*(2), 388-393.2014

4. Law, S., Podolskiy, V., & Wasserman, D. “Towards nano-scale photonics with micro-scale photons: the opportunities and challenges of mid-infrared plasmonics.” *Nanophotonics*, *2*(2), 103-130.2013

Metamaterial-based devices

Broadband enhancement of light absorption in energy harvesting systems by complex epsilon-near-zero materials

M. Bonifazi[1], **Y. Tian**[1], **A. Fratalocchi**[1]

[1]PRIMALIGHT, Faculty of Electrical Engineering; Applied Mathematics and Computational Science, King Abdullah University of Science and Technology (KAUST), Thuwal, Saudi Arabia
andrea.fratalocchi@kaust.edu.sa

Abstract— We create a new class of dispersionless composite metamaterials, engineered from suitably disordered metallic nanostructures. By means of Atomic-Force-Microscopy (AFM) and Photoluminescence (PLE) measurements we demonstrate that our ENZ dramatically increases the absorption in ultra-thin films, from UV to near-infrared wavelengths. Furthermore, a broadband enhancement of 170% in the external quantum efficiency (EQE) is observed when these materials are inserted in a working device. In addition, we developed a cost-effective fabrication process that make these materials suitable to large scale production.

1. INTRODUCTION

Recently, Colloidal quantum dots (CQD) revealed itself to be most valuable approach in enhancing the performances of light harvesting systems. In fact, CQDs are used in a wide range of energy harvesting applications, from photodetectors [1] to photovoltaic and photoJFET devices [2, 3] because they show a size-tunable optical bandgap and are extremely cost-effective. On the other hand, one of the biggest restraint with these materials is the compromise between the charge carrier extraction and the light absorption [4].
Different approaches have been proposed to overcome this limitation [5], but coupling light directly into the active layer by micro-structuring the substrate and introducing plasmonic nanostructures in CQD layer, seems to be the most effective [6]. The main drawback of this technology is that often most of the energy is localized inside the metal.

Here we present a new class of broadband epsilon-near zero (ENZ) materials based on disordered plasmonic nanostructures. These structures are able to localize broadband radiation within ultra-thin light harvesting films, greatly enhancing their absorption [7]. A theoretical investigation based on transformation optics allows us to obtain a material design effective for harvesting purposes. In fact, these ENZ materials slow down light on scale smaller than the charge diffusion length and dramatically enhance the absorption. in addition to that, an innovative fabrication process make it suitable for large scale production.

2. DISCUSSION

We developed a large scale process to fabricate suitable complex disordered ENZ metallic structures with completely controllable features. Figure 1a shows SEM cross sections of a fabricated sample, assembled by an electroplating process that grows a random networks of gold (Au) nanowires from a flat metallic Au substrates. When a thin layer of absorptive material is deposited on top of the ENZ nanostructures, incoming radiation gets trapped inside the ENZ material, originating a quasi-static field localized in areas of $10 - 100$ nm in proximity of the metal. In a series of AFM, Photoconductive AFM (PC-AFM) and Photoluminescence excitation (PLE) measurements, which are illustrated in Fig. 1b-c, we investigate the impact of ENZ nanostructures on the broadband absorption of an ultra-thin CQD film of $50 - 300$ nm thickness. Figure 1b reports the PC-AFM map of one region of a sample. The spatial current distribution is illustrated as a pseudocolor plot in Fig. 1b, and is superimposed on the surface topography of the sample, which is obtained by AFM. We observe a great current enhancement on the peak of the structures, where the ENZ regions are formed. To further prove that the electromagnetic localization happen proximity of the peaks of our nanostructures, figure 1c show a TEM image of our metasurface. It is clear that the light is concentrated in the bright areas near the tips and, in particular, it is shown that most of the radiation is collected in the active material side. Figure 1d, shows the results of PLE experiments, which measure the absorption increase in the CQD region for different electroplating times.

For CQD thicknesses between $50 - 300$ nm, we experimentally observed a dramatic absorption enhancement ($\approx$400%) when compared to the PLE signal from an equivalent planar configuration, which becomes completely flat in the visible and infrared regions.

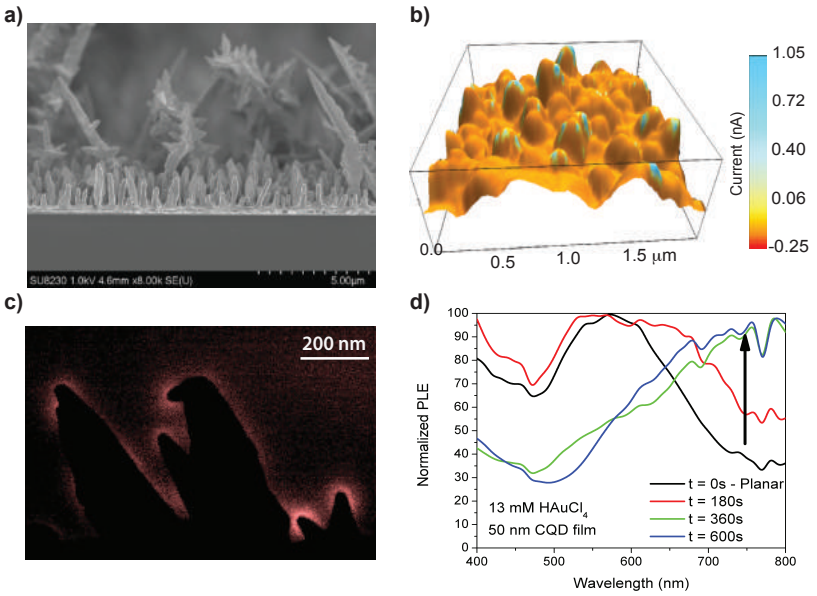


Figure 1: Light trapping in ENZ nanostructures: a) SEM cross section of a nanostructured sample. Photoconductive AFM and PLE measurements. b) Photocurrent distribution plotted over surface profile. c) PLE signals of 50-300 nm CQD film deposited on ENZ nanostructures, d) TEM measurements show a concentration of electromagnetic radiation near the tips of the nanostructures.

3. CONCLUSION

Exploiting complex metallic nanostructures we design an innovative light harvesting device based on ultra-broadband ENZ material. We verified our theoretical model trough different experimental measurements, such as AFM, PC-AFM,TEM and spatial photoluminescence efficiency measurements. As a result, it is shown that we efficiently localize white light within $10 - 100$ nm outside the metal, developing a material which can be easily combined with ultra-thin absorptive film, achieving very high efficiency in light absorption.

REFERENCES

1. Konstantatos, G., et al, "Ultrasensitive solution-cast quantum dot photodetectors", *Nature*, Vol. 442, 180-183, 2006.
2. Chuang, C.-H. M., et al, "Improved performance and stability in quantum dot solar cells through band alignment engineering", *Nat. Materials*, Vol. 13, 796-801, 2014.
3. Adinolfi, V., et al, "Photojunction field-effect transistor based on a colloidal quantum dot absorber channel layer", *ACS Nano*, Vol. 9, 356-362, 2015.
4. Labelle, A. J., et al, "Conformal fabrication of colloidal quantum dot solids for optically enhanced photovoltaics " *ACS Nano*, Vol. 9, 5447-5453, 2015.
5. Barkhouse, D. A. R., et al, "Depleted bulk heterojunction colloidal quantum dot photovoltaics" *Adv. Materials*, Vol. 23, 3134-3138, 2011.
6. Labelle, A. J., et al. "Colloidal quantum dot solar cells exploiting hierarchical structuring", *Nano Letters*, Vol. 15, 1101-1108, 2015.
7. Labelle, A. J, et al. "Broadband epsilon-near-zero reflectors enhance the quantum efficiency of thin solar cells at visible and infrared wavelengths", *ACS Applied Materials and Interfaces*, Vol. 9, 5556-5565, 2017.

Application of Semiconductor into Solar Cells using Lorentzian-Drude Model

Rifa J. El-Khozondar[1,*], Hala J. El-Khozondar [2], Mohammad M. Shabat[3]

[1]Physics Department, Al-Aqsa University, Gaza, Palestine
[2]Electrical Engineering Department, Islamic University, Gaza, Palestine
[3]Physics Department, Islamic University, Gaza, Palestine
*corresponding author, E-mail: hkhozondar@iugaza.edu

Abstract

In this work, a four layer solar cell is introduced. The active layer are nanoparticles (Ag) embedded in a dielectric media and semiconductor layer (Si) layer surrounded by air and glass layers. Hybrid transmission Matrix is used to find the average reflection and transmission power. Results are promising to solar cell designers.

1. Introduction

Photovoltaics are vital basis for unpolluted energy. The photovoltaic (PV) cell encompasses semiconductor materials, which can transform solar energy into electricity. Various semiconductor materials are used in solar cells such as silicon and its alloys. Silicon be able to have varied structures, extends from amorphous to polycrystalline, in addition to microcrystalline and nanocrystalline silicon. Nanocrystalline silicon has great short current density; therefore, it is potential for application in the lowermost unit of multiconnection solar cells [1].

A light trapping method based on using a rough back reflector having a high reflectivity leads to absorption rise; thus, a high short circuit current density is reached. Hence, the back reflector plays a critical issue in enhancing the efficiency of solar cells. A normally used back reflector involves a Ag stratum in order to reflect the light, which touches the substrate [2].

At optical wavelength, most semiconductors have a high index of refraction; therefore, a substantial amount of light is reflected from the film surface. This problem is solved by applying an anti-reflective covering layer sited above the absorber layer of the solar cell [3].

Unwanted reflection from optical surfaces is diminished by adding one-layer quarter wave coverings. However, their use is restricted by a small series of wavelength. To prolong this series over an expansive band of visible region spectrum, multilayers of thin films are used, even though, these multilayers have problem related to thermal misalliance and connection [4]. A rough configuration having a period longer than the wavelength of light is used to inhibit reflection. This configuration destroys the transferred wave for the reason that several reflection of incident light stops reflection by light trapping [5].

A subwavelength organized surface having a period lesser than the light wavelength acts as an antireflection outward. These surfaces are made of slight knobs groups with a period less than the apprehensive wavelength. Moreover, these surfaces are arranged on substrate to reduce external reflection [3].

2. Theoretical analysis

Fig. 1 presents the proposed solar structure consists of four layers. A dielectric media with embedded nanoparticles layer in top of a semiconductor layer. Both layers are sandwiched between air cladding and glass substrate. The semiconductor layer has a complex permittivity based on Lorentzian-Drude (LD) model as follows [6],

$$\varepsilon_2(\omega) = \varepsilon_\infty + \sum_m \frac{\sigma_m \omega_m^2}{\omega_m^2 - \omega^2 - i\omega\Gamma_m} \qquad (1)$$

$\varepsilon_\infty$is the instantaneous dielectric response (DC), Γ_m and ω_m are LD coefficient, and σ_m is a function of potion specifying the strength of the mth resonance. The dielectric with embedded nanoparticles has a permittivity defined by Maxwell-Garnett (MG) formula [7],

$$\bar{\varepsilon}_1 = \varepsilon_h \frac{\varepsilon_1(1+2f) + 2\varepsilon_h(1-f)}{\varepsilon_1(1-f) + \varepsilon_h(2+f)} \qquad (2)$$

where ε_1 is the permittivity of the nanoparticles, ε_h is the host permittivity, and f is the volume fraction of the embedded particles (silver Ag). Glass permittivity is ε_3 and air permittivity is ε_0. The average reflection power and transmission power are calculated using Hybrid Transfer Matrix Method (TMM) [8].

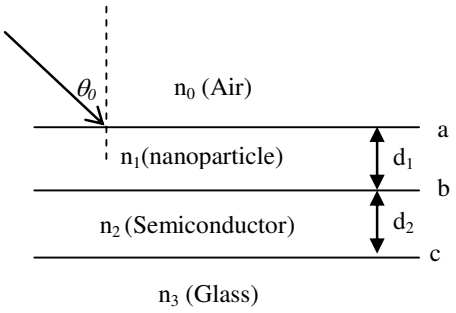


Figure 1: The proposed solar cell structure

3. Results and Discussion

In our calculations, we assumed normal incidence. The average reflection power (R) is plotted against the wavelength (nm) in Fig. 2. It can be notice that the reflection power is close to zero in the range between 500nm and 600nm and the minimum changes with the value of d_2.

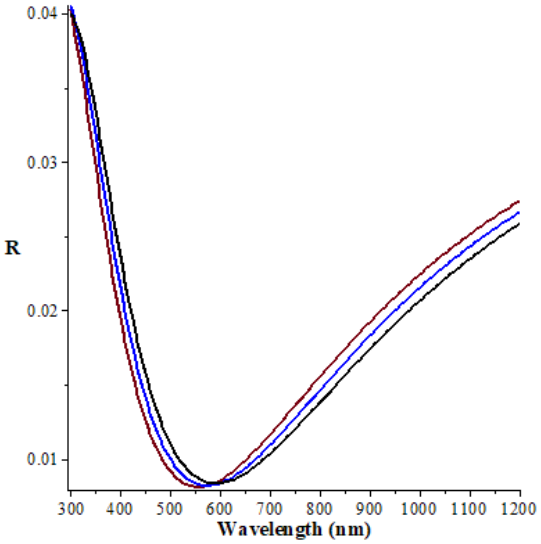


Figure 2: The reflection power as a function of wavelength. Red curve, blue curve and black curves are for d2=5nm, 10nm and 15nm.

Fig. 3 displays the relation between average Transmission power (T) and the wavelength (nm). It is observed from Fig. 3 that T is close to 1 in the range between 500 nm and 600 nm and the maximum changes with the value of d_2.

4. Conclusions

In the present work, we studied the reflection power and transmission power of semiconductor solar cell using Lorentzian-Drude model. The results are promising for solar cell industry.

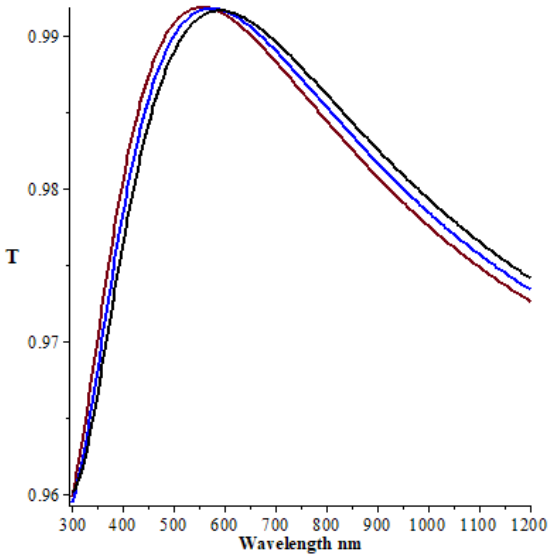


Figure 3: The transmission power as a function of wavelength. Red curve, blue curve and black curves are for d2=5nm, 10nm and 15nm.

References

[1] G. Yue, L. Sivec, J.M. Owens, B. Yan, J. Yang, S. Guha, Optimization of back reflector for high efficiency hydrogenated nanocrystalline silicon solar cells, *Applied Physics Letters* 95: 263501, 2009.

[2] W. Guang-Hong, Z. Lei, Y. Bao-Jun, C. Jing-Wei, W. Ge, D. Hong-Wei, W. Wen-Jing, The investigation of ZnO:Al2O3/metal composite back reflectors in amorphous silicon germanium thin film solar cells, *Chin. Phys. B* 22(6): 068102, 2013.

[3] D. Zhou, *Light-trapping enhancement in thin film solar cells with photonic crystals*, Retrospective Theses and Dissertations, Iowa State University, 2008.

[4] M.A. Green, J. Zhao, A. Wang, and S.R. Wenham, 45% efficient silicon photovoltaic cell under monochromatic light, *IEEE Electron. Device Lett*. 13: 317–318, 1992.

[5] A. Deinega, I. Valuev, B. Potapkin, Y. Lozovik, Minimizing light reflection from dielectric textured surfaces, *J. Opt. Soc. Am. A* 28(5): 770-777, 2011.

[6] A.D. Rakić, Aleksandra B. Djurišić, J.M. Elazar, M.L. Majewski, Optical properties of metallic films for vertical-cavity optoelectronic devices, *Applied Optics* 37(22): 5271-5283, 1998.

[7] R. Ruppin, Evaluation of extended Maxwell-Garnett theories, *Optics Communications* 182: 273-279, 2000.

[8] H. J. El-Khozondar, M. M. Shabat and A. N. AlShembari, Characteristics of Si-Solar Cell (PV) Waveguide Structure Using Transfer Matrix Method, IEEE 2017 International Conference on Promising Electronic Technologies (ICPET), Deir El-Balah, Palestine, 2017, pp. 99-102.

Quantum Searching with Metamaterials

Weixuan Zhang[1*], Kaiyang Cheng[2] Chao Wu[2], Yi Wang[2] Hongqiang Li[2], Xiangdong Zhang[1]

[1]School of Physics and Beijing Key Laboratory of Nanophotonics & Ultrafine Optoelectronic Systems, Beijing Institute of Technology, 100081, Beijing, China
[2] The Institute of Dongguan-Tongji University, Dongguan, Guangdong 523808
[*]corresponding author: 783923276@qq.com

Abstract

We designed and printed metamaterials to perform quantum search algorithm. The structures, comprising of an array of two-dimensional (2D) sub-wavelength air holes with different radii perforated on the dielectric layer, have been fabricated by using 3D printing technique. When an incident wave enters in the designed metamaterials, the profile of beam wavefront is processed iteratively as it propagates through the metamaterial periodically. After sqrt(N) roundtrips, precisely the same as the efficiency of quantum search algorithm, searched items will be found with the incident wave all focusing on the marked positions. Such a metamaterial-based quantum searching simulator may lead to remarkable achievements in wave-based signal processors.

1. Introduction

Metamaterials, artificially structured electromagnetic (EM) materials, have enabled the realization of many unconventional electromagnetic properties not found in nature, such as negative refractive index, magnetic response, invisibility cloaking and so on. Based on these man-made materials with novel EM properties, various devices have been designed and realized. However, quantum analog devices based on metamaterials have not been achieved so far. Here we designed and printed metamaterials to perform quantum search algorithm [1].

The general protocol is graphically shown in Fig. 1a with different colors being used to distinguish the structural regions that perform different functions. In this metamaterial-based searching protocol, the electric field amplitude of the incident microwave "$E(y)$" is recognized as the probability amplitude of the equivalent quantum state, spatial positions "y" are used to label the items in the database, and the maximum number of the database is fixed by the full width at half maximum (FWHM) "D" of the incident intensity profile with near-Gaussian distribution. The designed metamaterial is comprised of four cascaded subblocks: an oracle subblock (red area, U_m), two Fourier transform subblocks (green areas, F) and a phase plate subblock (blue area, U_0). The role of the oracle subblock is to mark the targeted item (red arrow) $|y=m\rangle$ by imprinting a spatially-dependent phase profile on the incident beam. A combination of two Fourier transform subblocks and the phase plate subblock can convert the phase difference marked by the oracle subblock into amplitude information by the sequences $\sim FU_0F$, which is similar to the "inversion-about-average" operation (*IAA*) of the original quantum search algorithm. Here, the Walsh-Hadamard transform is replaced by the Fourier transform. When two reflectors (R_1 and R_2) are fixed at both ends of the structure, the incident pulse will travel back and forth within the cavity, each roundtrip representing one iteration of the search algorithm. After a few iterations, the optical fields are completely concentrated on the searched positions and the marked items are proven to be found. The designed cascaded subblocks can be realized by drilling 2D sub-wavelength holes array with different radii on a single piece of dielectric layer based on the effective medium theory and it is fabricated with a resolution at 0.016 mm, i.e., ~one-thousand of operational wavelength, by using 3D-printing technology. Fig. 1b presents the photograph of the printed metamaterial.

In order to test the efficiency of the searching scheme, we perform full-wave numerical simulations using finite element method. In Fig. 1c and 1d, we plot the distribution of the wave intensity $|E(y)|^2$ at the output plane with 0.5- and 1.5-iterations, respectively. Here the input function is $E(y)=\exp(-y^2/20)$. In this case, the *FWHM* value of the incident intensity equals to D=5.26 cm. It is clearly shown that the output microwaves are nearly all concentrated on the marked positions after 1.5-iterations with the corresponding *FWHM* being d=1.4 cm. The ratio D/d can be interpreted as the size of the database (N) for a single item search. A straightforward calculation demonstrates that the number of iterations performed on the metamaterial is precisely consistent with the efficiency of the quantum search algorithm $\pi\sqrt{D/d}/4 \approx 1.5$, when the marked items are located.

To further validate our design, experimental measurements are carried out. The corresponding experimental results are shown in Fig. 1e and 1f. We can see that the experimental measured output profiles with 0.5- and 1.5-iterations are nearly consistent with the corresponding numerical simulations. The wider peak compared to the numerical solution is the result of the imperfect sample fabrication and minor variation for the incident wave profile compared to the ideal condition. The experimental demonstration indicates that the quantum search algorithm can be simulated successfully using the designed metamaterials.

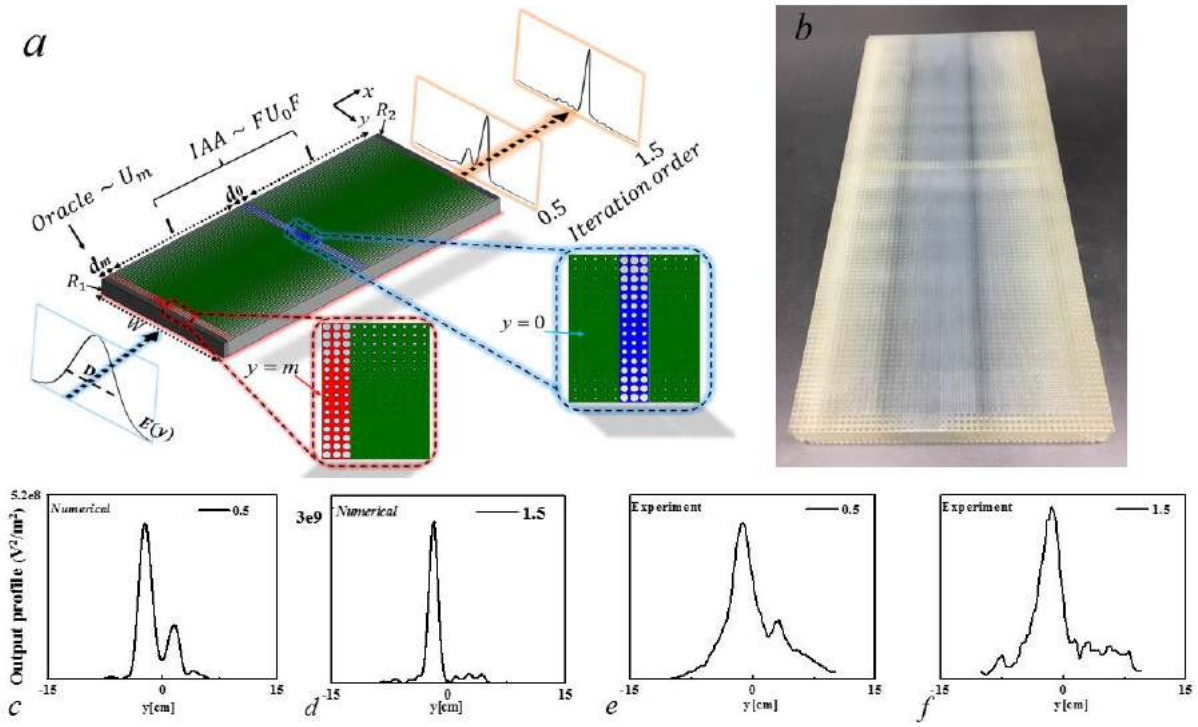


Figure 1: (a) The general protocol of simulating quantum searching arithmetic with metamaterial. (b) The photographs of the metamaterial sample fabricated by using 3D printing technology. (c), (d) Simulation results for the output intensity of the metamaterial with the incident wave propagating 0.5- and 1.5-roundtrips within the metamaterial, respectively. (e), (f) Experimental results for the profiles of the output intensity of the metamaterial with 0.5- and 1.5-iterations, respectively.

2. Conclusions

In summary, we have proposed and designed metamaterials to perform wave-based quantum search algorithm. Our numerical simulations and experiments clearly confirm that the searching efficiency, on such metamaterials fabricated by 3D printing technology, is the same as quantum computing. Moreover, the general design principle in our device can be applied, in principle, to any wavelength. Our metamaterial approach for an all-optical quantum searching simulator provides a new way to shed light on quantum analog behaviors, which may lead to remarkable achievements in wave-based signal processors.

Acknowledgements

This work was supported by the National Natural Science Foundation of China (Grant No. 11574031 and 61421001).

References

[1] W. X. Zhang, K. Y. Cheng, C. Wu, Y. Wang, H. Q. Li and X. D. Zhang, "Implementing Quantum Search Algorithm with Metamaterials," *Advanced Materials*, 30 (1), 1703986–20537, 2017.

Plasmonics for Highest-Speed

J. Leuthold[1]*, W. Heni[1], M. Ayata[1], C. Haffner[1], A. Messner[1], U. Koch[1], C. Hoessbacher[1], T. Watanabe[1], Y. Salamin[1], R. Bonjour[1], A. Josten[1], B. Baeuerle[1], A. Dorodny[1], P. Ma[1], Y. Fedoryshyn[1], M. Burla[1], D.L. Elder[2], L.R. Dalton[2]

[1]ETH Zurich, Institute of Electromagnetic Fields (IEF), 8092 Zurich, Switzerland
[2] University of Washington, Dept. of Chemistry, Seattle, WA, USA 98195-1700
*corresponding author, E-mail: JuergLeuthold@ethz.ch

Abstract

Plasmonics is emerging as a technology with a potential for components featuring ultrafast speed, energy efficiency and a most compact footprint. So for instance, novel plasmonic modulators, detectors and microwave components with bandwidths beyond 100 GHz have come into the spotlight of the communications community. More recently, plasmonic losses have been addressed with various measures. Here, we review the recent progress in the field.

1. Introduction

Plasmonics is the art of generating, processing, transmitting, detecting and sensing signals at optical frequencies along metallic surfaces. In plasmonics, the information is carried by surface plasmon polaritons (SPPs) instead of photons. Plasmonic wavelengths are much smaller than the corresponding wavelengths of photons. The small wavelength ultimately allows the fabrication of devices with footprints that are unmatched in the photonics world.

In this paper we review the progress in the field of ultra-fast plasmonic modulators and discuss recent advances in the field of plasmonic detectors. An emphasis will thereby be on the plasmonic organic hybrid (POH) and plasmonic ferroelectric platform – two platform that have been in the research focus of the authors.

2. Plasmonic Modulators

Modulators are key elements in an optical communications link. They are needed to encode electrical information onto an optical carrier. Traditionally, in fiber communications backbones $LiNbO_3$ modulators or electroabsorption modulators are employed to encode information onto an optical carrier. More recently, silicon photonic modulators are entering the market. Both technologies offer bandwidths up to 50 GHz. The former feature a length of centimeters, the later are millimeters in length.

In the past few years an increasing number of plasmonic switches and modulators has emerged. The operation principles of plasmonic modulators typically rely on metal-insulator-metal waveguides where the insulator is acting as a nonlinear element. They rely on different nonlinear effects such as the Pockels, the carrier dispersion, the thermal or electrochemical effect. In this review we cannot go into the details of the various nonlinear effects. However, a concise review can be found in Ref [1]. Our group has mostly focused on Pockels effect nonlinear modulators [2] where the nonlinear material is either an organic [3] or ferroelectric material [4]. Good reviews on the state-of-the art of nonlinear organic materials can be found in Refs. [3, 5-7].

2.1. Footprint

A recent plasmonic modulator is depicted in Fig. 1, see Ref. [8]. The modulator has been demonstrated to operate at 116 Gbit/s with as little as 25 fJ/bit. It features a record compact footprint of only 6 x 36 µm. On this space one can find metallic grating couplers that map the optical signals from the core of a multicore fiber to the modulators, there are a plasmonic splitter and combiner as well as two polarization rotators that convert the p-polarized SPPs into s-polarized slot modes. In the center of the modulator is the interferometric section where the phase is modulated by means of the Pockels-effect when a voltage is applied to the metallic island.
Similarly, plasmonic IQ-modulators with lengths below 80 µm have been presented [2].

Plasmonic devices can be very compact. The most compact optical switch ever published is a plasmonic switch with a 10 dB extinction ratio. It does not even require 10 nm in length and in fact has atomic scale [9].

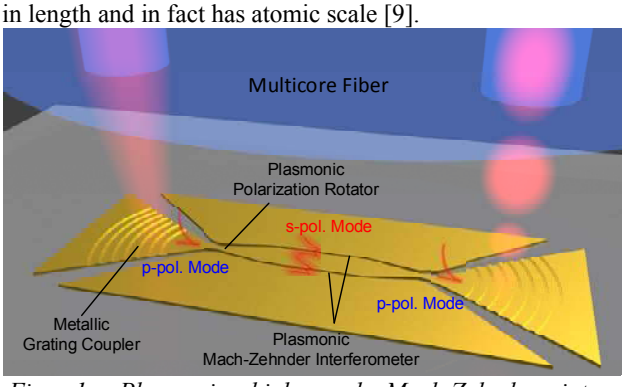


Fig. 1: Plasmonic high-speed Mach-Zehnder interferometer with metallic grating couplers, plasmonic polarization rotators and a plasmonic interferometer section. The modulator has been tested at 116 Gbit/s [8].

2.2. Speed, Bandwidth & Power Consumption

Plasmonic modulators feature a 1 dB frequency response way beyond 170 GHz [10]. They have already been tested for NRZ operation at 100 GBd with as little as 2.8 fJ/bit [11] or PAM4 at 116 or 120 Gbit/s [8, 10].

Plasmonic IQ-modulators so far have been tested with the QAM4 modulation formats at 200 Gbit/s or QAM16 at 128 Gbit/s [12]. Power consumptions of 78 fJ/bit and 27 fJ/bit have been reported for QPSK and 16-QAM modulation formats at 144 and 72 Gbit/s, respectively [2].

2.3. Plasmonic Losses

Unfortunately, the fast speed of plasmonics comes at the price of higher losses. In fact, plasmonic losses are in the order of 100 dB/mm – and thus would make plasmonics impractical if plasmonic devices were not much shorter. Typical high speed plasmonic devices feature lengths in the order of 5 to 10 µm [13]. Thanks to such small lengths the on-chip losses can be as small as 8 dB [13]. Unfortunately, this is still too much for many applications. Yet, new approaches show that losses can be cut by reaching out for materials with larger nonlinearities [14].

Most recently, it was shown that plasmonic losses can be bypassed by employing "resonant switching". More precisely, a ring modulator was shown in which light is only coupled to the lossy surface plasmon polaritons in the device's off-state (in resonance) where attenuation is desired. In the on state (out of resonance), light has been prevented from coupling to the lossy plasmonic section by destructive interference. In an experiment low on-chip optical losses of 2.5 dB, high-speed operation (>>100 GHz) with good energy efficiency (12.5 fJ/bit) was found [15].

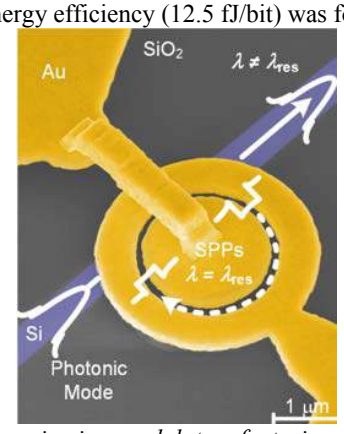


Fig. 2: Plasmonic ring modulator, featuring 2.5 dB device losses and a 100 GHz bandwidth. [15]

3. Plasmonic Photodetectors

Plasmonics photo detection is currently explored for two reasons [16, 17]. First, plasmonic metals can act as absorbers in hot-carrier devices [18, 19], and second, metals can provide enhancement of electromagnetic fields inside an absorber.

Ideally, photodetectors feature fast speed, a high responsitivity and low noise. So far only few demonstrations have surfaced. Some of these concepts will be discussed during the talk.

Acknowledgements

The authors acknowledge partial funding through the Swiss SNF Project Padamo, the EU project PLASILOR, the EU projects PlasmoFab and PlaCMOS, the US National Science Foundation (DMR-1303080) and the Air Force Office of Scientific Research (FA9550-15-1-0319).

References

[1] A. Emboras, C. Hoessbacher, C. Haffner, W. Heni, U. Koch, M. Ping, *et al.*, "Electrically controlled plasmonic switches and modulators," *IEEE Journal of Selected Topics in Quantum Electronics (JSTQE),* vol. 21, pp. 276-283, July/Aug. 2015.

[2] C. Haffner, W. Heni, Y. Fedoryshyn, A. Josten, B. Baeuerle, C. Hoessbacher, *et al.*, "Plasmonic Organic Hybrid Modulators – Scaling Highest-Speed Photonics to the Microscale," *IEEE Journal of Selected Topics in Quantum Electronics (JSTQE),* vol. 104, pp. 2362 - 2379, Dec. 2016.

[3] L. Dalton, P. Günter, M. Jazbinsek, O. P. Kwon, and P. A. Sullivan, *Organic Electro-Optics and Photonics*: Cambridge Univ. Press, 2015.

[4] A. Messner, F. Eltes, P. Ma, S. Abel, B. Baeuerle, A. Josten, *et al.*, "Integrated Ferroelectric Plasmonic Optical Modulator," in *Optical Fiber Communication Conference (OFC) Postdeadline Papers* Los Angeles, California, 2017, p. Th5C.7.

[5] D. L. Elder, L. E. Johnson, A. F. Tillack, B. H. Robinson, C. Haffner, W. Heni, *et al.*, "Multi-Scale, Theory-Assisted, Nano-Engineering of Plasmonic-Organic Hybrid Electro-Optic Device Peformance," in *Proc. SPIE* San Francisco, CA, 2018, pp. 10529-18.

[6] D. L. Elder, C. Haffner, W. Heni, Y. Fedoryshyn, K. E. Garrett, L. E. Johnson, *et al.*, "Effect of Rigid Bridge-Protection Units, Quadrupolar Interactions, and Blending in Organic Electro-Optic Chromophores," *Chemistry of Materials,* 2017/07/07 2017.

[7] W. Heni, Y. Kutuvantavida, C. Haffner, H. Zwickel, C. Kieninger, S. Wolf, *et al.*, "Silicon–Organic and Plasmonic–Organic Hybrid Photonics," *ACS Photonics,* vol. 4, pp. 1576-1590, 2017/07/19 2017.

[8] M. Ayata, Y. Fedoryshyn, W. Heni, B. Baeuerle, A. Josten, M. Zahner, *et al.*, "High-speed plasmonic modulator in a single metal layer," *Science,* vol. 358, pp. 630-632, 2017.

[9] A. Emboras, J. Niegemann, P. Ma, C. Haffner, A. Pedersen, M. Luisier, *et al.*, "Atomic Scale Plasmonic Switch," *Nano Letters,* vol. 16, pp. 709-714, Jan. 2016.

[10] C. Hoessbacher, A. Josten, B. Baeuerle, Y. Fedoryshyn, H. Hettrich, Y. Salamin, *et al.*, "Plasmonic modulator with >170 GHz bandwidth demonstrated at 100 GBd NRZ," *Optics Express,* vol. 25, pp. 1762-1768, Feb. 2017.

[11] B. Baeuerle, C. Hoessbacher, W. Heni, Y. Fedoryshyn, A. Josten, C. Haffner, *et al.*, "Driver-Less Sub 1 Vpp Operation of a Plasmonic-Organic Hybrid Modulator at 100 GBd NRZ," in *Optical Fiber Communications Conference (OFC)*, San Diego, 2018, p. M2I. 1.

[12] W. Heni, B. Baeuerle, Y. Fedoryshyn, A. Josten, C. Haffner, T. Watanabe, *et al.*, "100 GBd Plasmonic IQ Modulator," in *CLEO*, San Jose, USA, 2018.

[13] C. Haffner, W. Heni, Y. Fedoryshyn, J. Niegemann, A. Melikyan, D. L. Elder, *et al.*, "All-plasmonic Mach–Zehnder modulator enabling optical high-speed communication at the microscale," *Nature Photonics,* vol. 9, pp. 525-528, Aug. 2015.

[14] C. Haffner, W. Heni, D. L. Elder, Y. Fedoryshyn, N. Đorđević, D. Chelladurai, *et al.*, "Harnessing nonlinearities near material absorption resonances for reducing losses in plasmonic modulators," *Optical Materials Express,* vol. 7, pp. 2168-2181, July 2017.

[15] C. Haffner, D. Chelladurai, Y. Fedoryshyn, A. Josten, B. Baeuerle, W. Heni, *et al.*, "Low loss electro-optial plasmonic ring modulators " *Nature Photonics,* 2018.

[16] M. L. Brongersma, "Plasmonic Photodetectors, Photovoltaics, and Hot-Electron Devices," *Proceedings of the IEEE,* vol. 104, pp. 2349, 2016.

[17] A. Dorodnyy, J. V. Plestina, Y. Salamin, N. Lassaline, D. Mikulik, P. Romero-Gomez, *et al.*, "Plasmonic Photodetectors," *Submitted Invited Paper Publication,* 2018.

[18] A. Sobhani, M. W. Knight, Y. Wang, B. Zheng, N. S. King, L. V. Brown, *et al.*, "Narrowband photodetection in the near-infrared with a plasmon-induced hot electron device," *Nat Commun,* vol. 4, p. 1643, 03/27/online 2013.

[19] I. Goykhman, B. Desiatov, J. Khurgin, J. Shappir, and U. Levy, "Locally Oxidized Silicon Surface-Plasmon Schottky Detector for Telecom Regime," *Nano Letters,* vol. 11, pp. 2219-2224, May 2011.

Metamaterial based nanobiosensors, nanophotodetectors and perfect absorbers

Ekmel Ozbay

Nanotechnology Research Center, Bilkent University, Bilkent, 06800 Ankara, Turkey

Abstract

In this talk, we will present metamaterial based nanobiosensors, nanophotodetectors and perfect absorbers. We present a label-free, optical nano-biosensor based on the LSPR effect that is observed by using nano-cylinder arrays located periodically on a sapphire substrate by EBL. We will report on UV plasmonic antenna integrated MSM photodetectors based on GaN. We also report a lithography free, and large scale compatible fabrication route to fabricate ultra-broadband wide angle perfect absorber based on non-uniform texturing and disordered nano hole plasmonic patterns. Our findings show that the optimized design can retain light absorption above 90% over a wide range wavelength of 400 nm – 1490 nm.

In this talk, we will present metamaterial based nanobiosensors, nanophotodetectors and perfect absorbers. Our results show that a plasmonic structure can be successfully applied to bio-sensing applications and extended to the detection of specific bacteria species. A highly tunable design for obtaining double resonance substrates to be used in Surface Enhanced Raman Spectroscopy will also be presented. Surface Enhanced Raman Scattering experiments are conducted to compare the enhancements obtained from double resonance substrates to those obtained from single resonance gold truncated nano-cones. We will present a UV plasmonic antenna integrated metal semiconductor metal (MSM) photodetector based on GaN. We designed and fabricated Al grating structures. Well defined plasmonic resonances are measured in the reflectance spectra. Optimized grating structure integrated photodetectors exhibit more than eight-fold photocurrent enhancement. We also demonstrate a facile, lithography free, and large scale compatible fabrication route to fabricate ultra-broadband wide angle perfect absorber based on metal-insulator-metal-insulator (MIMI) stack design. 600 nm band-width (400 nm – 1000 nm) is attained utilizing this planar design. This design is later improved by introduction of non-uniform texturing and employing disordered nano hole plasmonic patterns where the overall process is large scale compatible and lithography free. Our findings show that the optimized design can retain light absorption above 90% over a wide range wavelength of 400 nm – 1490 nm. To the best of our knowledge, this bandwidth is the highest among other reported studies that employ such multilayer architectures.

Metasurfaces and Flat Optics

Generating of optical vortices by spiral metalenses

Victor Kotlyar[1], Anton Nalimov[2*]

[1]IPSI RAS – Branch of the FSRC "Crystallography and photonics" RAS, Samara, Russia
[2]Samara National Research University, Samara, Russia
*corresponding author, E-mail: anton@smr.ru

Abstract

It is demonstrated numerically and theoretically that in the intensity pattern of the resulting focal spot formed using a metalens there are local (symmetric and asymmetric) regions, which can be located both at its center or on the periphery, where the light energy flux has the opposite direction. The effect discovered can be utilized for moving a microparticle in the opposite direction to the beam propagation.

1. Introduction

The study of optical components with metarsurfaces was prompted by Refs. [1,2], which demonstrated that using nanostructures synthesized in thin metal or dielectric films, the amplitude, phase, and polarization of laser light can be simultaneously controlled in a local manner at each point of the beam cross-section. Vector optical vortices (VOV) have been generated using subwavelength rectangular apertures arranged along two concentric circles in a thin golden film for the incident laser wavelength of 1500 nm [3]. A review of photonic components with plasmonic and dielectric metasurfaces designed using both the PB method and Huygens method [4] was made in [5]. A review of recent advances in the design of plasmonic and dielectric metasurfaces can be found in [6]. In [7], an array of 410x175x466 nm nano-plates arranged with a 600-nm period and fabricated in amorphous silicon (refractive index n=3.9231+i0.1306 for 780 nm wavelength) were used as a quarter-wave plate, simultaneously converting the transmitted beam into several optical vortices with the topological charges m=2, 4, and 6 in different diffraction orders.

In this work, using a FDTD-based approach implemented in the Fullwave, spiral metalenses capable of simultaneously generating vector optical vortices with the topological charges m=1, 2, and 4 and a subwavelength focal spot or a doughnut intensity pattern are numerically simulated. The metalenses are illuminated by plane linearly polarized TE- or TM- waves and a beam with (left- and right-hand) circular polarization. Locally, the metalenses operate as half-wave plates. The said approach is novel because the metalenses are computed using an original authors' method proposed in [8], rather than using the PB and Huygens method.

2. Computing an optical surface of spiral metalenses

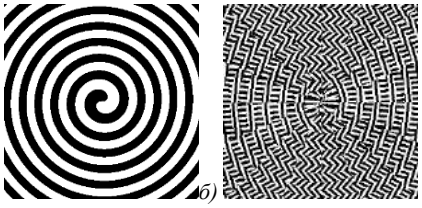
A method for designing photonic components with metasurfaces in a thin-film amorphous silicon for visible spectrum was proposed in [8]. The half-wave gratings rely in their operation for different effective refractive indices of two polarization vectors oriented along (TE-component) and across (TM-component) the grating lines [9]:

$$n_{eff}^{TE} = \sqrt{Qn_r^2 + (1-Q)n_m^2}\ ,$$

$$n_{eff}^{TM} = \left(Qn_r^{-2} + (1-Q)n_m^{-2}\right)^{-1/2}, \qquad (3)$$

where Q is the fill-factor (the ratio of the grating step width to its period), nr is the refractive index of the step material, and nm is the refractive index of the environment.

In this work, we designed spiral zone plates and corresponding metalenses with the topological charges m=1, 2, and 4.



a) *б)*

Fig. 1. Binary SZPs with the topological charge m: (a) 1, (c) 2, and (e) 4 and corresponding spiral metalenses with the topological charge m: (b) 1, (d) 2, and (f) 4.

Figure 1 depicts SZPs of the 1st, 2nd, and 4-th order (a, b, c) and corresponding metalenses (d, e, f). The calculation parameters for Fig. 1 were as follows: the SZP focal length- f=λ=633 nm, the metalens mask pixel- 22 nm, and the overall size of the element- 8x8 μm. The gratings in Fig. 1 were assumed to have a period of d=220 nm and a fill-factor of Q=0.5, meaning that the step and groove have a 110-nm width. All the gratings had a depth of H=120 nm. The refractive index of the thin-film amorphous silicon was defined as n=4.352+0.486i, with the substrate refractive index being n=1.5.

3. Computing the Poynting vector projection in the focus of a spiral metalens

For comparison, Fig. 2 shows z-projections Sz of the Poynting vector in the focus of the metalens of Fig. 1d (m=1), illuminated by a beam linearly polarized along the X- and Y-axis (Fig. 2*a*), and with right- and left-hand circular incident polarization (Fig. 2*b* and *c*).

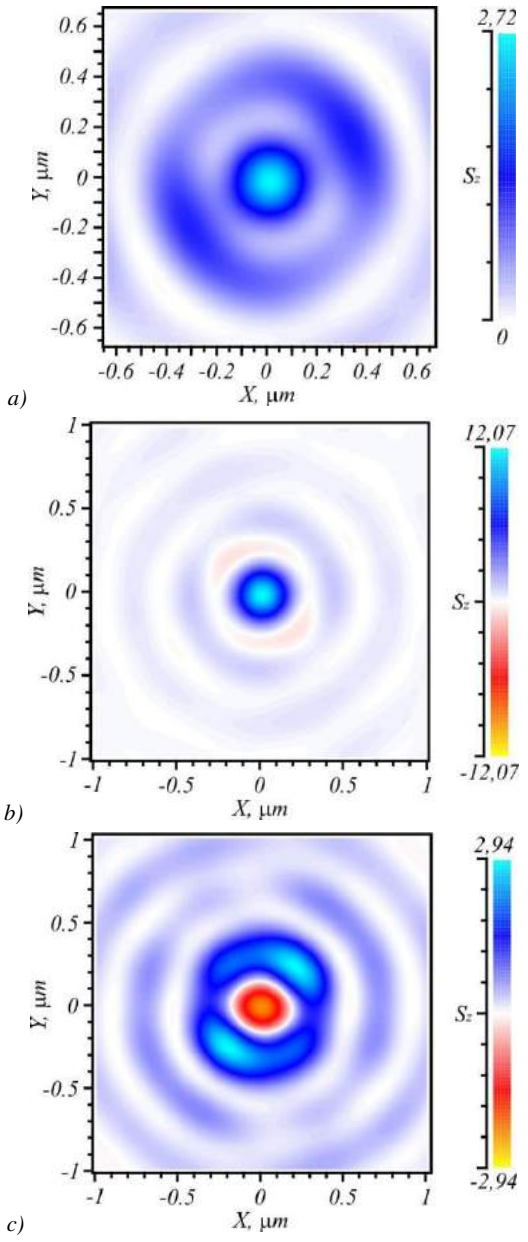


Fig. 2. 2D patterns of the projection Sz of the Poynting vector in the focus of a metalens with m=1 (Fig. 1) with the incident light linearly polarized along the (a) X-axis, as well as with (b) right- and (c) left-hand circular polarization.

As seen from Fig. 2, there are regions in the 2D pattern where the Poynting vector z-projections Sz are negative, which are found (a, b) near and (c) on the optical axis. The maximum on-axis value of Sz equals 2.72 (Fig. 2a), 12.0 (Fig. 2b), and -2.31 (Fig. 2c). Hence, we can infer that when illuminating the metalens with a linearly polarized beam (Fig. 2a), the near-axis energy flux in the positive direction approximately equals that propagating in the reverse direction for the left-hand circular polarization of the incident light (Fig. 2c).

4. Conclusions

We have shown by FDTD-simulation, that in the tight focal spot (NA≈1) generated by a spiral metalens for differently polarized homogeneous incident laser beams, there are local regions with the negative value of the Poynting vector projection, implying the reverse energy flux direction. Above, an 'optical tractor' phenomenon was mentioned, with the reverse energy flux shown to be capable of moving microparticles counter the laser beam propagation direction.

Acknowledgements

The work was partly funded by the Russian Science Foundation under grant # 17-19-01186.

References

[1] Litchinitser NM. Structured light meets structured matter. *Science* 337: 1054-1055, 2012.

[2] Kildishev AV, Boltasseva A, Shalaev VM. Planar photonics with metasurfaces. *Science,* 339: 1232009, 2013.

[3] Zhao Z, Wang J, Li S, Willner AE. Metamaterials-based broadband generation of orbital angular momentum carrying vector beams. *Opt. Lett.* 38: 932-934, 2013.

[4] Decker M, Staube I, Falkner M, Dominguez J, Neshev DN, Brener I, Pertsch T, Kivshar YS. High-Efficiency dielectric Huygens' surfaces. *Adv. Opt. Mat.* 3: 813-820, 2015.

[5] Chen H, Taylor AJ, Yu N. A review of metasurfaces; physics and applications. *Rep. Prog. Phys*.79: 076401, 2016.

[6] Genevet P, Capasso F, Avieta F, Khorasaninejad M, Devlin R. Recent advances in planar optics: from plasmonic to dielectric metasurfaces. *Optica,* 4: 139-152, 2017.

[7] Huang L, Song X, Reineke B, Li T, Li X, Liu J, Zhang S, Wang Y, Zentgraf T. Volumetric generation of optical vortices with metasurfaces. *ACS Phot*. 4: 338-346, 2017.

[8] Kotlyar VV, Nalimov AG, Stafeev SS, Hu C, O'Faolain L, Kotlyar MV, Gibson D, Song S. Thin high numerical aperture metalens. *Opt. Express* 25(7): 8158-67, 2017.

[9] Lalanne P, Lemercier-Lalanne D. On the effective medium theory of subwavelength periodic structures. *J. Mod. Opt.* 43: 2063–2085, 1996.

High Quality Factor Fano Resonances in All-Dielectric Metasurfaces

Tanchao Pu[1,2,3], Ziwei Liu[1,2,3], Jiebin Niu[1], Lina Shi[1,3,*] and Changqing Xie[1,3,*]

[1]Key Laboratory of Microelectronic Devices & Integrated Technology, Institute of Microelectronics, Chinese Academy of Sciences, Beijing, China
[2]University of Chinese Academy of Sciences, Beijing, China
[3]Jiangsu National Synergetic Innovation Center for Advanced Materials, Nanjing, China
*corresponding author, E-mail: shilina@ime.ac.cn; xiechangqing@ime.ac.cn

Abstract

We numerically demonstrated an all-dielectric metasurface with high quality factor Fano resonance. The metasurface comprises a two-dimensional array of amorphous Si hexamers. Numerical results show that both square and triangular lattices support the asymmetric Fano resonances. Especially, the quality factor of the triangle array can attain 836.1 for the closely packed case in the near infrared range. Such metasurfaces with Fano resonance are promising for practical applications, such as biosensor and optical filter.

Keywords: Fano resonance, all-dielectric, metasurface, high Q.

1. Introduction

In the past decades, metamaterials have stimulated intensive research worldwide since they can manipulate the light artificially with fancy properties, such as negative refractive index, which can't be found in natural bulk material [1,2]. However, metamaterial with novel optical properties usually need complex three-dimensional structures that are hard to fabricate by current technology. Therefore, two-dimensional metasurfaces, especially all-dielectric metasurfaces, are the promising structures to manipulate the light due to its compatibility with the mature complementary metal–oxide–semiconductor (CMOS) process. Additionally, all-dielectric metasurfaces have been demonstrated a promising path to achieve low-loss at optical wavelength where metal structures' performances are limited by its intrinsic loss [3,4]. However, high quality factor (Q) spectral features are still hard to obtain [5]. Thus, new designs based on high Q Fano resonance have been a promising strategy.

In this work, we present a new type of all-dielectric metasurface to achieve the high Q Fano resonance. The optical responses of the silicon metasufaces are investigated by the finite difference time domain (FDTD) method. It is found that the array of closely packed hexamers benefits a distinct Fano resonance. This facilitates its applications such as Raman spectroscopy, biosensor and optical switcher.

2. Fano resonance in closely packed metasurfaces

The metasurfaces we propose comprise a two-dimensional array of amorphous Si hexamers with radius R on a quartz substrate. The hexamer consists of six same cylinders with the diameter d=160 nm and the height 220 nm. Figure 1(a) and (b) respectively show the square and triangle arrays with periods Px and Py. The dielectric function of silicon in simulation was obtained from the ellipsometer's data by the measurement of the unpatterned Si on quartz grown by magnetron sputtering.

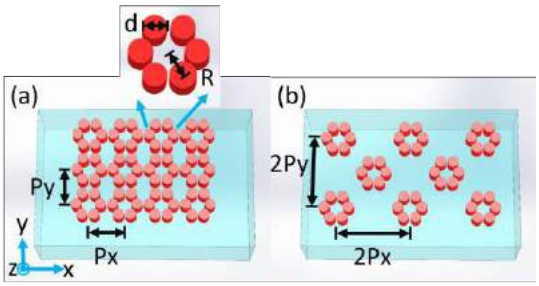


Figure 1: (a) and (b) are the metasurfaces comprise the square and triangle arrays of Si hexamers, respectively. Inset: the unit cell of arrays. R is the distance between the cylinder center and the unit cell center in the x-y plane. d is the diameter of the cylinder.

Firstly, we calculated the transmission spectra of two metasurfaces of square and triangle arrays with periods Px=540 nm and Py=491.76nm. The plane wave with polarization direction along x axis was normally incident on the sample. Figure 2 shows that both square and triangular lattices support the asymmetric Fano resonances with a lowest frequency narrow dip at 783.7 nm and 791.0 nm, respectively. And the corresponding quality factors are respectively $Q_{square} = 783.7/3.0 = 261.2$, and $Q_{triangle} = 791.0/3.4 = 232.6$, which is defined by $Q = \lambda_0 / \Delta\lambda$, here λ_0 is the resonance wavelength and $\Delta\lambda$ is the full width at half maximum (FWHM).

What's more important, Fig. 2 shows that the square array with closely packed hexamers obtains a distinct Fano resonance. In order to obtain the insight of the feature, we calculated the field distributions at the Fano dip wavelength. The electric field distribution of square array shows a circular displacement electric current distribution in each cylinder, which accounts for a magnetic dipole resonance.

The magnetic resonance contributes stronger field than other resonances. Whereas in the triangular lattice, a distinct circular magnetic field distribution between the cylinders shows electric dipole resonances dominates at this Fano dip.

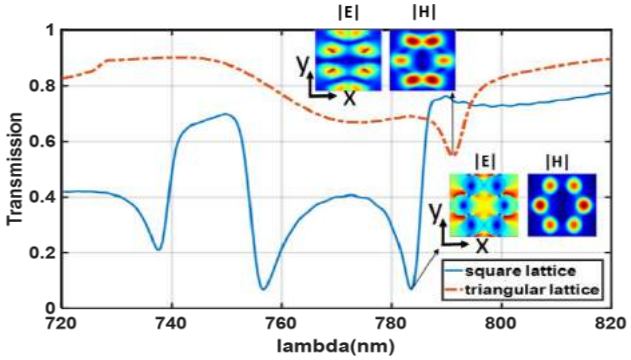


Figure 2: The transmission spectra of both square and triangle arrays with periods Px=Py=540 nm, respectively. Inset: the electric and magnetic field distributions in the x-y plane at the Fano resonance dip wavelength.

3. Discussions

Triggered by high Q Fano resonance resulted from the square array of closely packed Si hexamers, we consider the corresponding triangle array. The triangle array of the closely packed Si hexamers, as shown in the inset of Fig. 3(a), is obtained with periods Px=Py=350 nm. The transmission spectrum in Fig. 3(a) shows a narrow dip with FWHM equaling to 1.1 nm at the wavelength of 919.7 nm. Thus, the Q factor can attain 836.1, which is much higher than the square one. At the same time, Fig. 3(b) and (c) show a much higher enhancement of both electric and magnetic field in the gaps between Si hexamer cells. This is due to the smaller gap and diverse distances between cylinders, which enhances the near-field coupling between the nano cylinders. The circular magnetic field distribution that demonstrated the electric resonance dominates at the Fano dip for this case.

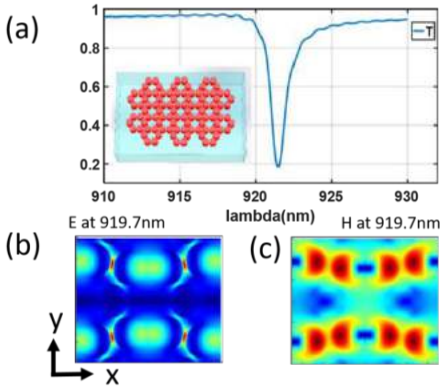


Figure 3: (a) Transmission and reflection spectra of the triangle array of the closely packed Si hexamers. (b) and (c) are the electric field and magnetic field distributions at the Fano resonance dip wavelength. Insets: The schematic of the triangle array of the closely packed Si hexamers.

4. Conclusions

We have demonstrated all-dielectric metasurfaces with high Q Fano resonance. Both metasurfaces with square and triangular lattice array support a sharp narrow dip in the transmission spectra. Especially, the Q factor of the Fano dip of the triangle array with closely packed Si hexamers can attain 836.1 in the near infrared range. Additionally, we also demonstrated that the Fano resonance of square and triangular lattice array were dominated by the induced magnetic and electric resonances, respectively. Accordingly, all-dielectric metasurfaces with Fano resonance would be suitable for various applications, including Raman spectroscopy, biosensor and optical switcher.

Acknowledgements

This work was partially supported by National Key Research and Development Program of China (2017YFA0206002), Major National Scientific Instruments Developed Special Project (2013YQ1508290602), National Natural Science Foundation of China (NSFC) (61107032, 61275170), Research and Development of Major Research Equipment of Chinese Academy of Sciences (YZ201446) and Opening Project of Key Laboratory of Microelectronic Devices and Integrated Technology, Institute of Microelectronics of Chinese Academy of Sciences.

References

[1] D. R. Smith, J. B. Pendry, M. C. Wiltshire, et al. Metamaterials and Negative Refractive Index. *Science*, 305: 788-792, 2004.

[2] N. Engheta, Circuits with Light at Nanoscales: Optical Nanocircuits Inspired by Metamaterials. *Science*, 317: 1698-1702, 2007.

[3] A. I. Kuznetsov, A. E. Miroshnichenko, M. L. Brongersma, Y. S. Kivshar, B. Luk'yanchuk, Optically Resonant Dielectric Nanostructures. *Science* 354: (6314), 2016.

[4] I. Staude, J. Schilling, Metamaterial-Inspired Silicon Nanophotonics. *Nat. Photonics*, 11 (5): 274–284, 2017.

[5] B. Luk'yanchuk, et al. The Fano resonance in plasmonic nanostructures and metamaterials. *Nat. Mater.*, 9, 707–715, 2010.

Correlations of cascaded photons: Two-photon processes in the Mollow regime

Alexander Carmele[1], Samir Bounouar[2], Max Strauß[2], Stephan Reitzenstein[2]

[1]Nichtlineare Optik und Quantenelektronik, Institut für Theoretische Physik, TU Berlin, Germany.
[2]Optoelektronik und Quantenbauelemente, Institut für Festkörperphysik, TU Berlin, Germany.
*corresponding author, E-mail: alex@itp.tu-berlin.de

Abstract

Mollow physics in the two-photon regime gives access to time-reordering of photon pairs, erasing the which-path information of the decay process. Here, we calculate the two-photon correlations $g^{(2)}(\tau)$, essential to discuss and study such phenomena in the resonant-driven dressed-state regime. Recent reported experiments agree with the presented theory and thereby it is shown that the resonant-driven four-level system is an interesting source for steerable quantum light in quantum cascade setups. We stress the unlikeliness to observe antibunching for the delay time $\tau = 0$ in the exciton-biexciton correlation functions in such experiments, since antibunching stems from a coherent and in-phase superposition of different photon emission events. Due to the occuring laser photon scattering, this coherent superposition state is easily disturbed and leads to correlation functions of $g^{(2)}(0) = 1$.

1. Introduction

Two-photon states are of particular interest to study nonlinear phenomena in quantum optics and lie at the heart of the pursuit to exploit nonlocal properties in quantum mechanics itself [1]. Progress in semiconductor nanotechnology allows to generate on demand two-photon states, e.g. in biexciton-exciton cascade processes [2, 3, 4]. They also gave rise to test the indistinguishability of such photons via Hong-Ou-Mandel type of experiments [5]. Two-photon signatures reveal the true quantum character as they exhibit interesting quantum interference phenomena (entanglement, indistinguishability, photon-heralding) in the regime of non-classical photon statistics (anti-bunching, squeezing).

Recently, a proposal has drawn interest, which allows one to coherently generate photon bundles in leap-frog processes [6]. This idea has been experimentally realized recently with a semiconductor quantum dot [3, 4, 2] . Here, the biexciton is coherently driven in a two-photon process and via only one of the two possible polarization transitions. In the strong driving regime, dressed state become visible and allow for frequency-selected photon-photon correlation measurements [2]. This way, path-controlled time-reordering of photon pairs can be steered. As a measure whether there is and there is no time-order, we use the correlation function and investigate whether the function is symmetric under sign exchange $g^{(2)}(\tau) = g^{(2)}(-\tau)$ or not.

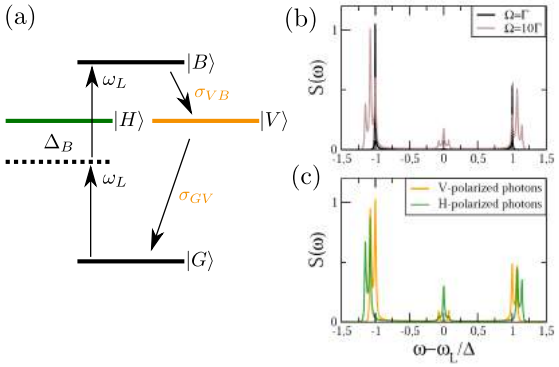


Figure 1: (a) The energy schema of the setup. The biexciton state is driven via a continuous two-photon, $H-$polarized excitation, while the exciton transitions are far detuned. (b) The power spectrum $S(\omega)$ of the full emission, including $H-$ and $V-$polarized photons for two excitation strengths. In the strong excitation limit (grey), triplets appear. (c) Differentiating the spectrum in the strong excitation limit between $H-$ (green,shaded) and $V-$ emission (orange, solid) events.

If the correlation function is symmetric, the time-order of the emission sequence is erased. Such a vanishing time-reordering is only possible, when the emitter is driven into a superposition state with long coherence times.

2. Model

The quantum dot is modelled as a four-level system consisting of a ground state $|G\rangle$, two excitonic states $|H\rangle, |V\rangle$ and a biexcitonic state $|B\rangle$. The ground state energy $\omega_G = 0$ is set to zero, cf. Fig. 1. Here, we focus on a driven experiment, where photon correlations in the Mollow regime are studied and the fine structure splitting is of minor importance. The biexciton shift is of particular interest, as only due to this shift it is possible to drive the biexciton population without driving necessarily at the same time the excitonic transitions: $\omega_B = \omega_H + \omega_V + 2\Delta_B = 2(\omega_X + \Delta_B)$. Here, the external laser field drives only the horizontal polarization with frequency ω_L and amplitude Ω_H, the full

Hamiltonian reads therefore ($\hbar = 1$) and $\sigma_{ij} := |i\rangle\langle j|$:

$$H = \omega_X (\sigma_{HH} + \sigma_{VV}) + 2(\omega_X + \Delta_B)\sigma_{BB} \quad (1)$$
$$+ \Omega \cos(\omega_L t)(\sigma_{GH} + \sigma_{HG} + \sigma_{BH} + \sigma_{HB}). \quad (2)$$

To allow for an adiabatic elimination of the excitonic states in case of biexciton shift in the regime $\Delta_B \gg \Omega_H$, the laser frequency is chosen to be in a two-photon resonance with the biexciton frequency, namely we set $\omega_L = \omega_H/2 + \omega_V/2 + \Delta_B$, cf. Fig. 1(a). We assume a radiative decay Γ of the electronic system via photon emission into a Markovian continuum to yield the following master equation:

$$\dot{\rho} = -i[H_R, \rho] + \Gamma \sum_{i=H,V} (\mathcal{D}[\sigma_{Gi}] + \mathcal{D}[\sigma_{iB}])\rho, \quad (3)$$

after assuming the biexciton decay to be double as fast as the exciton decay and using the standard Lindblad form $\mathcal{D}[J]\rho = 2J\rho J^\dagger - \{J^\dagger J, \rho\}$.

3. Results

To enable a vanishing time-ordering, a spectral selection of the photons is necessary. Basically, three photons with slightly different frequencies can be emitted from the exciton, as well as from the biexciton state. To unravel these three possibilities, it is necessary to change the basis of the theoretical description into the dressed state coordinates [6]. In the following, we calculate analytically the signal of the correlation functions, which exhibits in the strong driving limit such a vanishing time-reordering. The observable reads $i, j = G, V, H, B$:

$$g^{(2)}_{ijji}(\tau) = \lim_{t\to\infty} \frac{\langle c^\dagger_{ij}(t) c^\dagger_{ji}(t+\tau) c_{ij}(t+\tau) c_{ji}(t)\rangle}{\langle c^\dagger_{ij}(t) c_{ji}(t)\rangle \langle c^\dagger_{ji}(t) c_{ijV}(t)\rangle}. \quad (4)$$

In the experiment, the biexciton-exciton correlation is taken only partially (only signals far away from the laser frequency). The analytical solution of the biexciton-exciton detection sequence reads:

$$g^{(2)}_{\mathrm{EX,BX}}(\tau) = 3 + e^{-2\Gamma\tau} + 2\alpha e^{-\Gamma\tau}[1 + \cos(\Omega\tau)], \quad (5)$$

with $\alpha := \Gamma^2/\Omega^2$, and in a exciton-biexciton sequence, therefore,

$$g^{(2)}_{\mathrm{EX,XB}}(\tau) = 1 + e^{-2\Gamma\tau} - \frac{2\alpha\cos(\Omega\tau)}{1+2\alpha} e^{-\Gamma\tau}. \quad (6)$$

Both detection sequences show bunching. In Fig. 2(a), the bunching effect is shown in the experimental data for the strong (green) and weak driving regime (orange). For stronger excitation the detection around $\tau = 0$ symmetrizes, which signifies a superposition in detection events rendering the detection order partially indistinguishable. The analytical theory reproduces the effect well, cf. Fig. 2(b).

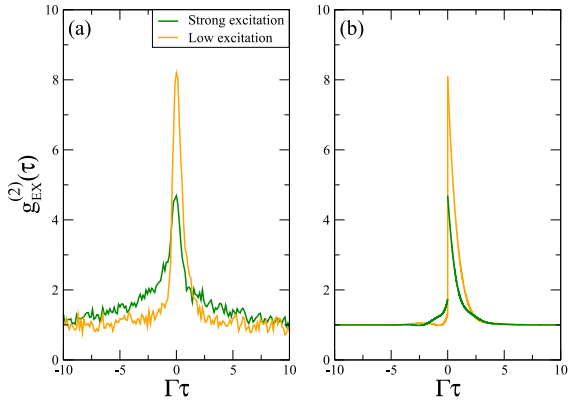


Figure 2: Comparison between experiment (a) and theory (b) for two low (30μW) and strong excitation (100μW) power and the exciton-biexciton photon-photon correlations without $|-\rangle$ state contributions. The qualitative agreement is very good. Both plots show the symmetrization of detection events for stronger excitation (green) in comparison to lower excitation (orange). The experimental data is shown with a substracted background, in particular for the lower excitation.

4. Conclusion

We have calculated analytically the two-time correlations of the exciton-biexciton cascade in the adiabatic limit, where the detuning between the laser and the excitonic transition is much larger than the driving amplitude. If the dressed states can spectrally be selected, it is possible to erase this time-ordering. Furthermore, we showed with our calculations the limits of the correlation functions, and why it is difficult to observe in such a system the antibunching effect.

References

[1] M.O. Scully and M.S. Zubairy. *Quantum Optics*. Cambridge University Press, 1997.

[2] S. Bounouar et al, *Physical Review Letters*, 118(23):233601, 2017.

[3] F. Hargart et al, *Physical Review B*, 93(11):115308, 2016.

[4] P.L. Ardelt et al, *Physical Review B*, 93(16):165305, 2016.

[5] A. Thoma et al, *Physical review letters*, 116(3):033601, 2016.

[6] C.S. Muñoz et al, *New Journal of Physics*, 17(12):123021, 2015.

Thin metalens based on subwavelength grating

S.S. Stafeev[1,2*], A.G. Nalimov[1,2], C. Hu[3], L. O'Faolain[4], M.V. Kotlyar[2], D. Gibson[3], S. Song[3], and V.V. Kotlyar[1,2]

[1]Image Processing Systems Institute – Branch of the Federal Scientific Research Centre "Crystallography and Photonics" of the Russian Academy of Sciences, Samara, Russia
[2]Samara National Research University, Samara, Russia
[3]SUPA, Institute of Thin Films, Sensors & Imaging, University of the West of Scotland, Paisley, United Kingdom
[4]Centre for Advanced Photonics and Process Analysis, Cork Institute of Technology, Cork, Ireland
*corresponding author, E-mail: sergey.stafeev@gmail.com

Abstract

We designed, fabricated, and characterized a thin metalens with diameter of 30 μm and focal length of 633 nm in an amorphous silicon film. The lens is capable of simultaneously manipulating the state of polarization and phase of incident light and converts a linearly polarized beam into radially polarized light, producing a subwavelength focus. Illuminated by a linearly polarized Gaussian beam, the lens produces a focal spot with diameters at full-width half-maximum of 0.49λ and 0.55λ (λ is incident wavelength). The experimental results are in good agreement with the numerical simulation, with the simulated focal spot measuring 0.46λ and 0.52λ.

1. Introduction

In recent years, optical researchers have been studying subwavelength-thick planar binary microoptics components in the form of metallic or semiconductor subwavelength element arrays (rods, slits, strips, and gratings) that can simultaneously modify the polarization, amplitude, and phase of an incident electromagnetic wave. Such photonic components are referred to as metasurface optical elements [1]. Of particular interest is the use of the metasurface optical elements as ultra-thin lenses [2, 3, 4].

In this paper we investigated a thin metalens in an amorphous silicon film, which is capable of simultaneously manipulating the state of polarization and phase of incident light. The lens produces a focal spot with diameters at full-width half-maximum of 0.49λ and 0.55λ (λ is incident wavelength). The experimental results are in good agreement with the numerical simulation, with the simulated focal spot measuring 0.46λ and 0.52λ [5].

2. Design and manufacturing

It is known that by converting a laser beam from the linear to radial polarization it is possible to obtain a circular subwavelength focal spot. In particular, radial polarization could be produced using a subwavelength grating [6]. The aim of our investigation is to design an element that combines a zone plate and a micropolarizer investigated in [6].

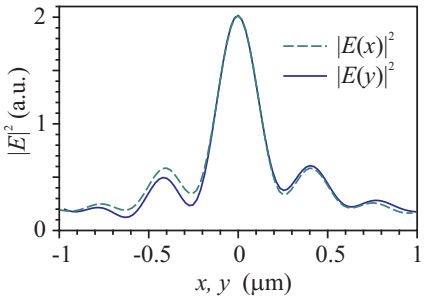


Figure 1: Intensity distribution at distance z = 0.391 μm. Dashed line – along the x-axis, solid line – along the y-axis.

The operation of the proposed metalens was simulated at the following parameters: wavelength λ = 633 nm, focal length f = 633 nm, microrelief height h = 0.24 μm, grating period T = 220 nm, refractive index of amorphous silicon n = 4.35 + i0.486. Shown in Fig. 1 is intensity profiles in the focal plane along the x- and y-axes.

A metalens with the relief depicted in Fig. 2 was fabricated using electron beam lithography. A 130-nm thick amorphous silicon (a-Si) film deposited on a transparent pyrex substrate (with refractive index n = 1.5) was coated with a 320-nm thick PMMA resist, which was baked at a temperature of 180 °C. The resist thickness of 320 nm was chosen to give both good etch resistance and high resolution patterning. To prevent charging, the surface was sputtered with a 15-nm thick gold layer. A binary template (Fig. 2) was transferred onto the resist surface using a 30-kV electron beam. The specimen was developed in the water blended with isopropanol in the ratio 3:7.

To account for fabrication errors when modelling the metalens, the microrelief characteristics measured by an atomic force microscope were used in the simulation. The focal spot size of the manufactured lens in simulation is FWHM$_x$ = 0.46λ and FWHM$_y$ = 0.52λ (across and along the polarization direction consequently). The focal length is z = 600 nm.

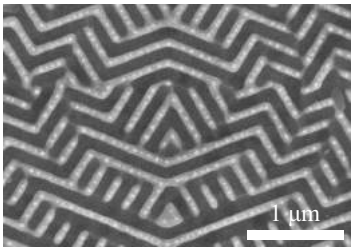


Figure 2: An electron microscope image of a central fragment of a metalens

3. Experiment

The focusing properties of the metalens were experimentally studied by means of near-field scanning optical microscopy (NSOM). In the experiment, a light beam from a He-Ne laser (wavelength 633 nm) was fed to the metalens under study, generating a subwavelength focal spot. The intensity in the focal spot was measured using a hollow metallized pyramid-shaped tip having a 100-nm pinhole in the vertex. The experimentally measured focal length of the metalens was $z = 0.6$ μm. Fig. 3 depicts the intensity profiles in the focal spot along the x- and y-axes. The maximal intensity in the focus was found to be 11 times that of the incident beam.

Experimentally measured size of the focal spot was $\mathrm{FWHM}_x = 0.49\lambda$ and $\mathrm{FWHM}_y = 0.55\lambda$. These values are just 8% different from those obtained via simulation ($\mathrm{FWHM}_x = 0.46\lambda$, $\mathrm{FWHM}_y = 0.52\lambda$) taking into account the metalens fabrication errors.

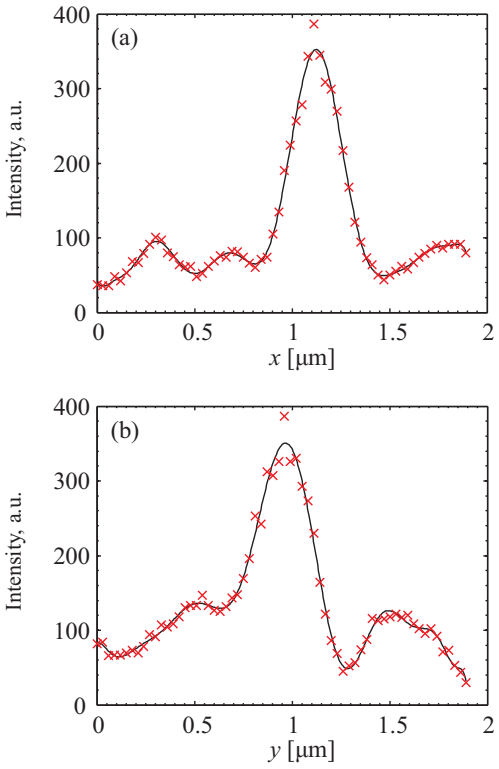


Figure 3: Measured intensity profiles of the focal spot along (a) x- and (b) y-axis. Red crosses mark experimental values and black curve presents a polynomial-based approximation.

4. Conclusions

We designed, fabricated, and characterized a thin metalens with diameter 30 μm and focal length 633 nm in an amorphous silicon film. The lens is capable of simultaneously manipulating the state of polarization and phase of incident light and converts a linearly polarized beam into radially polarized light, producing a subwavelength focus. Illuminated by a linearly polarized Gaussian beam, the lens produces a focal spot with diameters at full-width half-maximum of 0.49λ and 0.55λ (NSOM). The experimental results are in good agreement with the numerical simulation, with the simulated focal spot measuring 0.46λ and 0.52λ (FDTD).

Acknowledgement

The work was partially funded by the Federal Agency of Scientific Organizations (Agreement No 007-/3363/26) in part of numerical simulation, Russian Federation Ministry of Education and Science (grant No NSh-6307.2018.8), and Russian Foundation of Basic Research Grants RFBR (grants 18-07-01122, 18-07-01380, 17-47-630417, 17-47-630420, 17-42-630008, 16-47-630483, 15-47-02492, 15-07-01174) in part of fabrication and experiment.

References

[1] N. Yu, F. Capasso, Flat optics with designer metasurfaces, *Nat. Mater.* 13: 139-150, 2014.

[2] A. Arbabi, Y. Horie, M. barheri, A. Faraon, Dielectric metasurfaces for complete control of phase and polarization with subwavelength spatial resolution and high transmission, *Nat. Nanotech.* 10: 937–943, 2015.

[3] X. Ni, S. Ishii, A.V. Kildishev, V.M. Shalaev, Ultra-thin, planar, Babinet-inverted plasmonic metalenses, *Light Scien. Appl.* 2: e72, 2013.

[4] P.R. West, J.L. Steward, A.V. Kildishev, V.M. Shalaev, V.V. Shkunov, F. Strohkendl, Y.A. Zakharenkov, R.K. Dodds, R. Byren, All-dielectric subwavelength metasurface focusing lens, *Opt. Express* 22:, 26212–26221, 2014.

[5] V.V. Kotlyar, A.G. Nalimov, S.S. Stafeev, C. Hu, L. OFaolain, M.V. Kotlyar, D. Gibson, S. Song, Thin high numerical aperture metalens, *Opt. Express* 25: 8158-8167, 2017.

[6] S. Stafeev, L. OFaolain, V. Kotlyar, A. Nalimov, Tight focus of light using micropolarizer and microlens, *Applied Optics* 54: 4388–4394, 2015.

Active metasurface for terahertz beam steering

Sang-Hyeok Mun, Yong-Hoon Lee, Sang-Jun Park, Jinhang Cho, Inbo kim and Muhan Choi*

School of Electronics Engineering, Kyungpook National University, Daegu, South Korea
*Corresponding author, E-mail: mhchoi@ee.knu.ac.kr

Abstract

We have designed tunable meta-lens operating in Terahertz frequency regime. The meta-lens is composed of the metasurface blocks coupled with graphene layers in which gate voltage can be controlled individually. In order to achieve maximum phase shift, meta-atoms with strong capacitive coupling are employed.

Keywords: Meta-lens, Metasurface, Graphene, Terahertz, Ion-gel

The focal length of a conventional lens is determined by only its geometric structure. To realize a tunable lens without geometrical change, active metasurface technology for controlling path of light wave has been intensively studied.

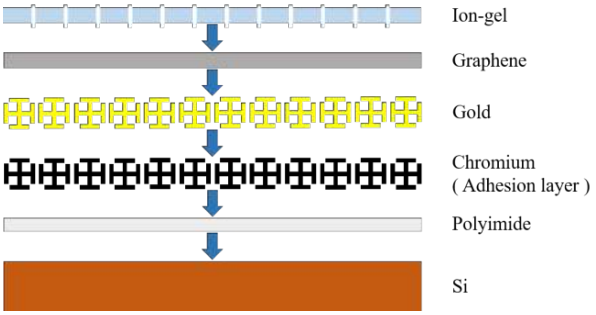


Figure 1. Fabrication process of the active metasurface

In this study, we have designed tunable meta-lens operating in Terahertz frequency regime. The meta-lens is composed of a lot of the meta-surface blocks coupled with graphene active layers [1]. The transmission properties of meta-surface blocks can be controlled by changing applied gated voltage to graphene layer[2,3,4]. We also design meta-atoms to have strong capacitive coupling to each other so as to achieve maximum phase shift [5].

We control the gate voltage of the each graphene layer block individually by using patterned the ion-gel [6]. The photo-lithography is performed for the high resolution patterning of graphene and a dry-transfer technique using polydimethylsiloxane (PDMS) stamp is used to achieve precise transfer of graphene on the substrate of the meta-lens.

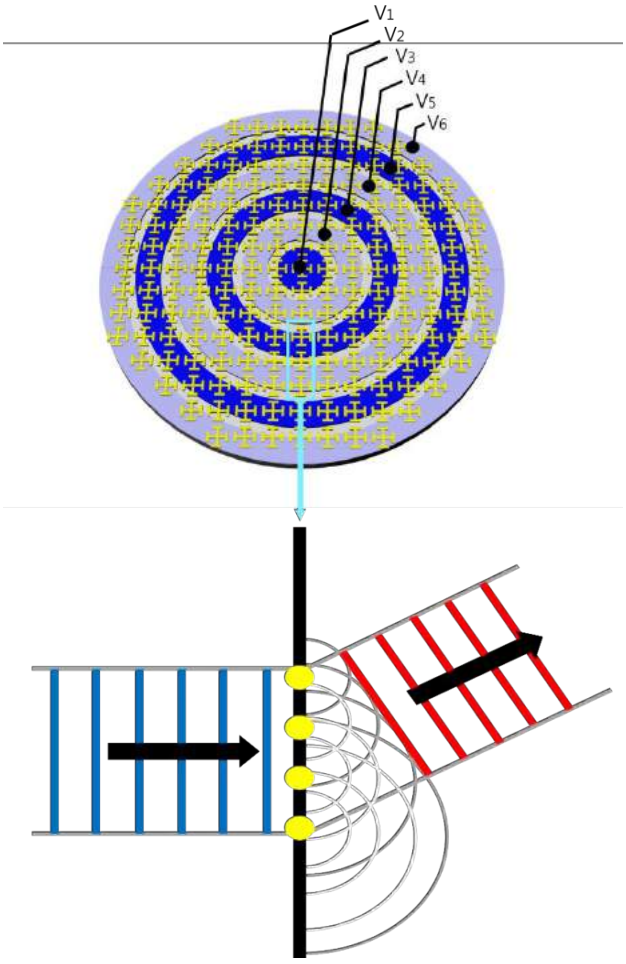


Figure 2. Schematic of the proposed tunable meta-lens

By virtue of polarization-independent characteristic of the meta-atom design, the meta-lens can operate regardless of the polarization of the incident wave. The metasurface shows various transmission phase shift spectrum according

to the applied gate voltage to graphene layer with high modulation speed as shown in Fig. 3.

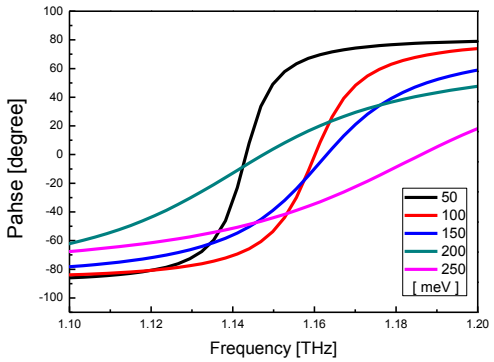


Figure 3. Phase shift spectrum between the transmitted and the incident wave according to the applied gate voltage to graphene layer

We expect that the tunable meta-lens with a graphene active layer will be applied to various applications in terahertz and mid-infrared range.

Acknowledgements

NRF grant funded by the Korea government (MSIP) (No. 2017R1A2B4012045 and No. 2017R1A4A1015565); CAMM funded by Korea Government (MSIP) as Global Frontier Project (CAMM 2014M3A6B3063709)

References

[1] Seong Hoon Lee, Muhan Choi, *et al.*, "Switching terahertz waves with gate-controlled active graphene metamaterials", *Nature Materials*, 11, 936. September 2012.S.V. Patankar, *Numerical Heat Transfer and Fluid Flow*, Hemisphere Publishers, New York, 1980.

[2] G. Hanson, "Dyadic Green's functions and guided surface waves for a surface conductivity model of graphene", *J. Appl. Phys.*, 103, 064302. March 2008.

[3] P. Gusynin *et al.*, "Magneto-optical conductivity in Graphene", *J. Phys: Condens. Matter*, 19, 026222. December 2006.

[4] Muhan Choi, Seong Hoon Lee, *et al.*, "A terahertz metamaterial with unnaturally high refractive index", *Nature*, 470, 369. February 2011.

[5] Nanfang Yu, Federico Capasso, *et al.*, *SCIENCE*, 334, October 2011.

3D nanostructuring of functional photopolymers for photonics and sensing

Safi Jradi[1*], Mélissa Merheb[1], Ali Issa[1], Ying Peng[1], Aurélien Bruyant[1], Xuan Quyen Dinh[2], Xiaowei Sun[2,3], Renaud Bachelot[1]

[1] Light, nanomaterials, nanotechnologies (L2n), Technological University of Troyes, France.
[2] Nanyang Technological University, Singapore
[3] Southern University of Science and Technology, China
*corresponding author, E-mail: safi.jradi@utt.fr

Abstract

Two-photon direct writing is a very promising technique for fabrication of arbitrary 3D structures for multiple applications including micro/nanophotonics, microfluidics, and microdevices. Most of the applications require functional photoresist with high spatial resolution, improved mechanical properties, and chemical compatibility with inorganic nanostructures.

In the presented work, 3D hybrid functional nanostructures are made by two-photon polymerization (TPP) of functionalized homemade photoresist. Photopolymer materials are formulated and functionalized in order to induce strong chemical non-linearity effect and to confine the writing volume into the nanoscale. The fabrication of complex and hybrid 3D structures with high spatial resolution for metamaterial, photonic and sensing applications will be demonstrated.

As example, functional IR light concentrators based on a thick layer of air polymer metamaterial (MM) with controlled pore size gradients are realized (Fig. 1). Infrared imaging of the structures reveals a tight focusing with a maximum local intensity increase by a factor of 2.5 for a concentrator volume of 1.5 λ^3 [1].

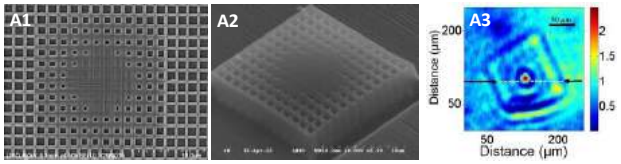


Figure 1. Examples of hybrid and functional 3D structures made by TTP. (A1) SEM top view of MM concentrator designed for 10.4 µm. (A2) SEM side view of the MM concentrator. (A3) IR CCD image of the MM concentrator at λ = 10.4 µm.

Furthermore, the capability to fabricate 3D fluorescent structures with 80 nm resolution is demonstrated. Blue, Green or Red emitting quantum dots (QDs) are grafted into acrylic monomers and then used as negative photoresist for TPP. 2D and 3D photoluminescent nanostructures containing Qds are realized by TPP. The photoluminescent images and emission spectra show strong local emission of blue, green and red light from the polymer micro and nanostructures (Fig. 2). The influence of Qds on the TPP at the nanoscale is investigated. It turns out that, the presence of QDs increases the lateral resolution where the feature size of polymer lines can reach 75 nm. This promising result paves the way for the integration of single nanoemitters with a fine control of their spatial positioning in some nanophotonic devices [2]. More particularly, this active photopolymer is investigated for the fabrication of new multifunctional and multicolor hybrid Nano-emitters.

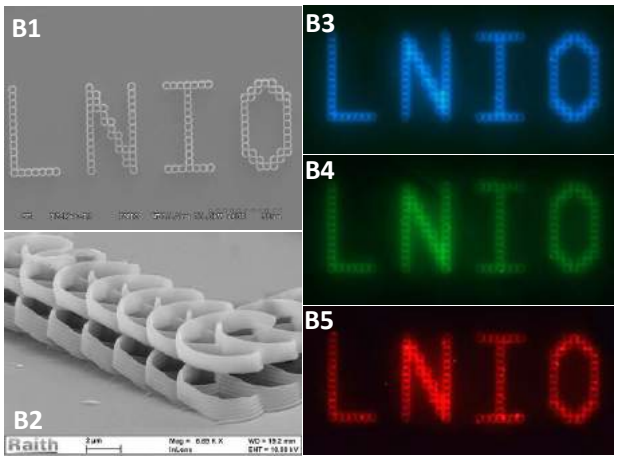


Figure 2. (B1 and B2) SEM images of 3D polymer microstructures fabricated by TPP Lithography using the QD-containing photoresist. (B3, B4, and B5) Fluorescence images of the QD-containing 3D microstructures showing emission of blue (B3), green (B4) and red (B5) light.

Finally, a general and original approach of 1D, 2D and 3D assembly of both organic and inorganic nanoparticles (NPs) within true complex polymer templates will be demonstrated. In this approach, TPP of a specific home-mode functional photopolymer is combined with colloidal deposition in order to assemble different kinds of NPs within 1D, 2D and even 3D complex micro templates.

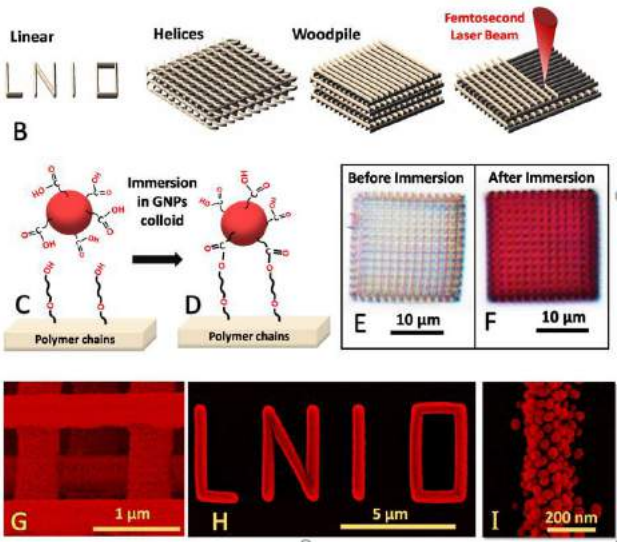


Figure 3. (B) Fabrication of linear and complex 3D structures by two-photon polymerization of the functionalized monomer using a femtosecond laser beam. (C) Scheme showing the functionalities on the polymer surface and on the GNPs that leads for (D) their assembly on the polymer surface during its immersion in GNPs colloid (~50 nm). (E) Optical microscope images of 3D woodpile structure before and (F) after immersion in GNPs colloid. (G) SEM image of the woodpile surface after immersion. (H) SEM image of linear assembly of GNPs on LNIO design structure; (I) Magnification of H

Thanks to the high density of chemical functions, colloidal NPs can penetrate inside a complex 3D microstructure that can be completely covered by Gold NPs (GNPs) providing thus an extremely large surface area where a huge number of hot spots can exist. SERS and LSPR measurements are performed on the 2D and 3D assembled GNPs. The influence of laser treatment parameters and thickness of assembled layers on the sensing performance is investigated. Femto-molar concentrations of bipyridine derivatives are detected.

Acknowledgements

Financial support of "Fonds Européen de Développement Régional" (Projet Nano-Assemblage 3D), the "Conseil Régional Champagne-Ardenne", (Projet Nanomatériaux 3D), NanoMat (www.nanomat.eu) by the "Ministère de l'enseignement supérieur et de la recherche" is acknowledged.

References

[1] J. Moughames, S. Jradi, T.M. Chan, S. Akil, Y. Battie, A. En Naciri, H. Ziad, S. Guenneau, S. Enoch, L. Joly, J. Cousin, and A. Bruyant, Wavelength-scale light concentrator made by direct 3D laser writing of polymer metamaterials" *Scientific Reports* 6, 33627 (2016)

[2] X. Zhou et al., Two-Color Single Hybrid Plasmonic Nanoemitters with Real Time Switchable Dominant Emission Wavelength, *Nano Lett.*, 15 (11), 7458–7466, 2015

Optical Antennas

Broadband Infrared Refractive Index Measurement Using Plasmonic Antenna Resonance

Hibiki Kagami[1], Tomohiro Amemiya[1, 2], Satoshi Yamasaki[1], Keisuke Masuda[1], Zhichen Gu[1], Nobuhiko Nishiyama[1, 2], and Shigehisa Arai[1, 2]

[1]Department of Electrical and Electronic Engineering, Tokyo Institute of Technology, Tokyo, Japan
[2]Institute of Innovative Research (IIR), Tokyo Institute of Technology, Tokyo, Japan
*corresponding author, E-mail: kagami.h.aa@m.titech.ac.jp

Abstract

We propose a novel method to measure broadband complex refractive indices of liquid materials using plasmonic antenna resonance. By applying this method to PMMA, we succeeded in obtaining high-precision infrared refractive index from 50 to 250 THz.

1. Introduction

'Infrared refractive index' is an indispensable parameter for various fields including infrared photonics [1, 2]. However, to date, there has been no method for measuring complex refractive index with high accuracy from near- to mid-infrared regions. Here we propose and demonstrate a plasmonic antenna method which can detect broadband and high-precision ($< 5\times10^{-3}$) complex refractive index using just a single droplet of liquid. By applying this method to polymethyl methacrylate (PMMA), we succeeded in obtaining infrared refractive index from 50 to 250 THz.

2. Concept of infrared refractive index measurement using plasmonic antenna resonance

In this study, we first prepare an infrared transparent Barium Fluoride (BaF_2) optical window with various plasmonic antenna arrays resonating at a specific frequency (Fig. 1). A procedure of the proposed measurement method using this chip is as follows:

A. Using a Fourier-transform infrared (FTIR) spectroscopy, we investigate the resonant frequency ω_1 of the antenna corresponding to the frequency at which the transmission intensity is minimum (upper Fig. 2(a)). From the results, a characteristic curve of the antenna (i.e. the refractive index around the antenna versus the resonant frequency) is calculated (lower Fig. 2(a)).

B. A liquid sample to be measured is dropped onto BaF_2 and similar measurement is performed to find the resonance frequency ω of the antenna (upper Fig. 2(b)). After that, by comparing the obtained resonance frequency ω with the characteristic curve derived in A,

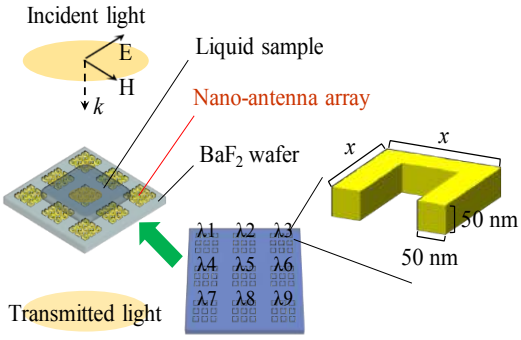


Fig. 1. Concept of infrared refractive index measurement using BaF_2 optical window with various plasmonic antenna arrays.

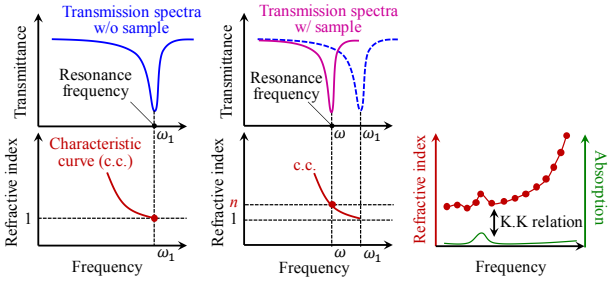


Fig. 2. Procedure of the proposed infrared refractive index measurement method. Transmittance spectrum and characteristic curve (a) w/o and (b) w/ sample to be measured. (c) Broadband infrared refractive index of the sample.

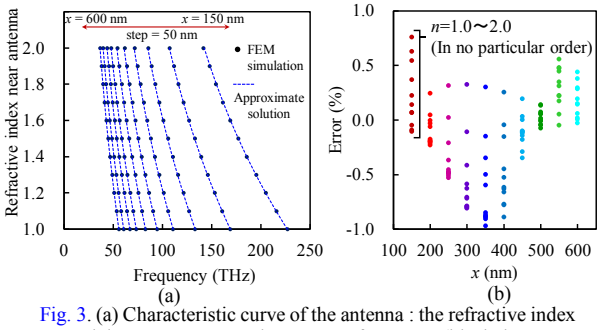


Fig. 3. (a) Characteristic curve of the antenna : the refractive index around the antenna versus the resonant frequency (black dot: FEM simulation results, blue curve: approximate solution). (b) Error of calculation results between FEM and approximate solution.

it is possible to estimate the refractive index of the sample at a specific frequency (lower Fig. 2(b)).

C. A broadband infrared refractive index of the sample can be obtained by repeating the procedures A and B for all antenna arrays (Fig. 2(c)). Finally, a broadband absorption coefficient can be derived by applying Kramers-Kronig relations to the obtained refractive index profile.

In the procedure A, it is necessary to derive an approximate equation $\omega(n)$—representing the characteristic curve of the plasmonic antenna—only with the resonance frequency ω_1 at $n = 1$. In this study, $\omega(n)$ was obtained as follows.

First, an accurate characteristic curve of the antenna was calculated from electromagnetic field analysis using the finite element method (FEM). In simulation, the arm length x of the antenna (see Fig. 1) was varied in the range of 150 to 600 nm (50 nm pitch). The calculation results are plotted in Fig. 3(a). Here, the vertical axis represents the refractive index around the antenna and is synonymous with the refractive index of the sample to be measured.

Next, we derived an approximate equation $\omega(n)$ that passes through all the plotted points shown in Fig. 3(a). When $\omega(n)$ is given by

$$\omega(n) = 1/\sqrt{f_1(\omega_1)n^2 + f_2(\omega_1)}, \quad (1)$$

$$f_1(\omega_1) = 0.01220{\omega_1}^{-1.887}, \; f_2(\omega_1) = 14.70{\omega_1}^{-2.104}, \quad (2)$$

it was found that errors were within 1% as compared with the accurate results calculated by FEM (Fig. 3b).

3. Evaluation of refractive index of PMMA using proposed method

In order to validate the proposed method, the experimental demonstration was performed by applying this method to PMMA. First, various plasmonic antenna arrays with different resonant frequencies were arranged on a BaF_2 optical window by using electron-beam lithography and lift-off process (Fig. 4). The arm length x of the antenna which is equal to the distance between the antennas was varied from 150 nm to 600 nm by 50 nm step for each array. In addition, the area size of each array was 100 μm square which is the same as the spot size of the FTIR used in this measurement.

One example of the transmission spectrum of the antenna array measured with the FTIR is shown in Fig. 5. When PMMA was coated to the BaF_2 substrate, the resonant frequency shift caused by the refractive index transition was confirmed. The approximate equation $\omega(n)$ representing the characteristic curve of the antenna was obtained by substituting the resonant frequency of the antenna w/o PMMA for ω_1 in Eq. (1). Subsequently, the refractive index of PMMA at an appropriate frequency was derived to be 1.404 by substituting the resonance frequency with PMMA for the left-hand side of Eq. (1).

Figure 6 shows the frequency dependence of the refractive index of PMMA obtained by performing the above measurement for all antenna arrays. The literature value of the refractive index of PMMA [4] and the absorption spectrum due to molecular vibration obtained by FTIR are also shown. In Fig. 6, we succeeded in obtaining infrared refractive index

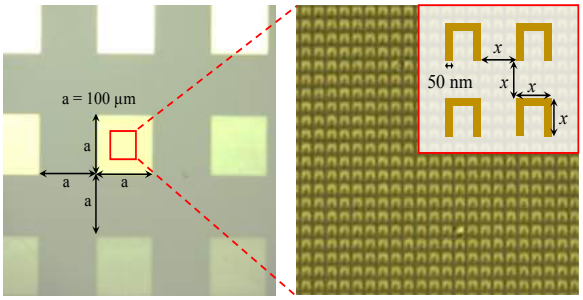


Fig. 4. Optical microscope image of fabricated BaF_2 optical window with various plasmonic antenna arrays.

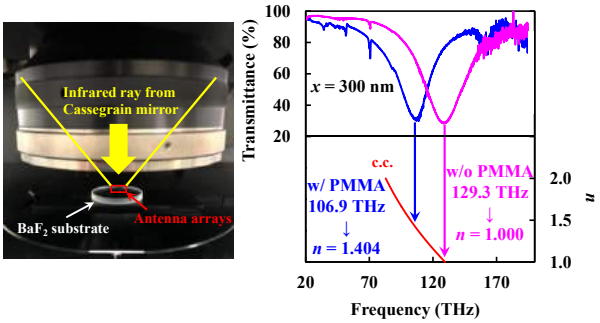


Fig. 5. One example of the transmission spectrum of the antenna array measured with the FTIR (Arm length x of the antenna is 300 nm).

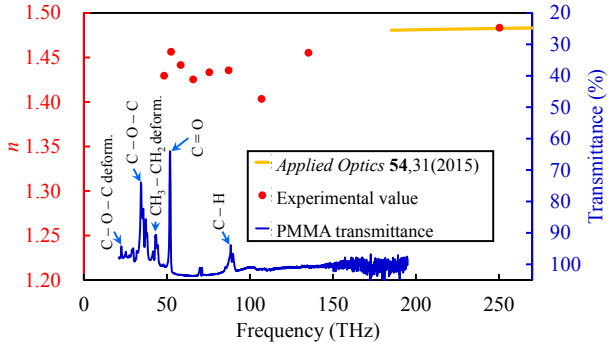


Fig. 6. frequency dependence of the refractive index of PMMA obtained by performing the proposed method for all antenna arrays.

of PMMA from 50 to 250 THz. The sensitivity of ~ 5×10^{-4} was achieved at around 250 THz compared to the literature value. Since it is expected that the refractive index fluctuates greatly in the absorption region accompanying the molecular vibration, the number of optical antenna arrays should be increased in the future work in order to improve the frequency resolution.

Acknowledgments

This research was financially supported by JST-CREST (JPMJCR15N6), and JSPS KAKENHI (#15H05763, #16H06082, #17H03247).

References

[1] R. Soref *et al., Nature Photon.* **4**, 495 (2010).
[2] B. Jalali, *Nature Photon.* **4**, 506 (2010).
[3] G. Beadie *et al., Applied Optics* **54**, 31 (2015).

Design of plasmonic grating nano structure for enhancing optical imaging system signal

J. H. Kim[1], J. S. Kang[1] , Z. Shoaib[1] and M. Y. Jeong[1*]
[1]Department of Cogno-Mechatronics Engineering, Pusan National University, Busan, Korea
[*]corresponding author: myjeong@pusan.ac.kr

Abstract- The metasurfaces have many unexpected properties including anti-refractivity, anti-doppler effect, and surface plasmon. Among these properties, surface plasmon effect was considered importantly because of the enhancement of optical signals. It is important to detect small optical signal in neuroscience and bio technology due to detect smaller image or signal. In this paper, we proposed the nano-micro patterned structure to detect small optical signal by using surface plasmon effect which can enhance electromagnetic field.

Nowdays, many researchers want to know about brain image and brain computer interface. The brain image and brain activity were detected many method including Electron Encephalography(EEG), magnetic Resonance Imaging(MRI), functional near-infrared Spectroscopy (fNIRS). These systems use electromagnetic wave to detect brain activity and brain imaging. For example, the fNIRS system uses a NIR laser to measure brain activation by measuring changes in hemoglobin and deoxyhemoglobin differences. But the contrast with hemoglobin and deoxyhemoglobin is too low to discriminate the smaller part of brain activity. [1-3]

Metasurfaces have many unexpected properties including anti-refractivity, anti-doppler effect, and surface plasmon. [4-6] Surface plasmon is most important part in biology and chemical field to detect more smaller molecules. Metasurface can make the surface plasmon which made by nano- micro structure. The structure can gather the electromagnetic field in one spot due to surface plasmon theory. [7-8]

In this paper, we proposed new nano-micro pattern structure to gather fNIRS optical signal. The new proposed nano structure can get the surface plasmon effect in one spot by using antenna theory and grating structure which can gather 700~900nm wavelength. These structures can detect more smaller difference between hemoglobin and deoxyhemoglobin to enhance electromagnetic field in one spots. The device based on optics and photonics have been developed rapidly for new optical bio imaging system and detect smaller biological cells. The enhancement of optical signal by using proposed surfaces can be embedded in certain part of bio imaging system.

REFERENCES

1. León-Carrión, José, and Umberto León-Domínguez. "Functional near-infrared spectroscopy (fNIRS): principles and neuroscientific applications." Neuroimaging-Methods. InTech, 2012.
2. Kidwell, Chelsea S., and Amie W. Hsia. "Imaging of the brain and cerebral vasculature in patients with suspected stroke: advantages and disadvantages of CT and MRI." Current neurology and neuroscience reports 6.1 (2006): 9-16.
3. Noachtar, Soheyl, and Jan Rémi. "The role of EEG in epilepsy: a critical review." Epilepsy & Behavior 15.1

(2009): 22-33.

4. Chen, H. T., Taylor, A. J., & Yu, N. “A review of metasurfaces: physics and applications.”, *Reports on Progress in Physics*, *79*(7), 07640, 2016
5. Kildishev, A. V., Boltasseva, A., & Shalaev, V. M. ” Planar photonics with metasurfaces.” *Science*, *339*(6125), 1232009, 2013
6. High, A. A., Devlin, R. C., Dibos, A., Polking, M., Wild, D. S., Perczel, J., ... & Park, H. “Visible-frequency hyperbolic metasurface.” *Nature*, *522*(7555), 192-196.2015
7. Nguyen, Thi Thanh Kieu, Quang Minh Ngo, and Truong Khang Nguyen. "Design, Modeling, and Numerical Characteristics of the Plasmonic Dipole Nano-Antennas for Maximum Field Enhancement." Applied Computational Electromagnetics Society Journal 32.7 (2017).
8. Piccoli, Riccardo, et al. "Terahertz Nanoantennas for Enhanced Spectroscopy." Terahertz Spectroscopy-A Cutting Edge Technology. InTech, 2017.

Silicon-based Nanoscale Plasmonic Bowtie Nanoantenna in the Mid-IR

Hosam Mekawey[1*], Yehea Ismail[1], Mohamed Swillam[2]

[1]School of Science and Engineering, Center of Nanoelectronics and Devices (CND), The American University in Cairo, Zewail City of Science and Technology, Egypt
[2]Department of Physics, School of Science and Engineering, The American University in Cairo, New Cairo, 11835, Egypt
*corresponding author, E-mail: hmekawey@aucegypt.edu

Abstract

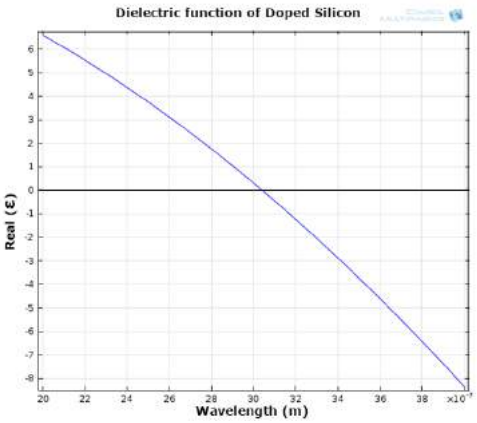
Much research was conducted on enhancing of the localized field through the Plasmon Resonance effect on metallic nanostructures. Here, we investigate replacing plasmonic metals such as silver with doped silicon for designing a bowtie nanoantenna operating in the mid-IR. The objective is to be able to integrate such nanoantenna into opto-electronic circuits manufactured using standard Complimentary-Metal-Oxide Semiconductor (CMOS) fabrication process. A study of the effect of manipulating the design parameters on the enhancement level and spectral range was also conducted.

1. Introduction

Significant research has been conducted in the last decade on exploiting the Localized Surface Plasmon Resonance (LSPR) effect in producing many order of magnitude enhancement in the localized field of plasmonic nanostructure when illuminated with an electromagnetic field. Such enhancement can be utilized in many applications that include sensing, spectroscopy, energy harvesting, and nonlinear optics [1-8]. It also enables building antenna operating in the visible spectral range [9]. Using plasmonic metals as the material of choice in building such nanoantenna produces enhanced field in the visible spectrum. By engineering the shape and geometrical attribute of a gold nanoantenna, it was shown that the spectral range of enhancement can be shifted to the near-IR [10], albeit on the expense of the simplicity of the geometry and its actual fabrication.

In this work, the first objective is to build nanoantenna that can provide enhancement in the localized field in the mid-IR for sensing applications in that regime. The second objective is that its fabrication should be compatible with the standard Complimentary Metal-Oxide Semiconductor (CMOS) fabrication process which is used for the low cost mass fabrication of modern electronics and integrated opto-electronics chips. Hence, based on the objectives mentioned above, silicon was used instead of the plasmonic metals usually employed in plasmonic nanoantenna, and by introducing a high concentration of excess carriers through doping, the plasma dispersion effect would alter the optical response of silicon allowing it to behave like metal in producing Plasmon resonance, however, it is expected based on the resultant dielectric function of an n-doped silicon with doping concentration as high as 5E+20 cm-3 that the surface plasmon resonance would occur in the mid-IR range instead of the visible range of plasmonic metals' resonance. This conforms to our goal of producing plasmonic enhancement in the mid-IR spectral range. The bowtie antenna design has been chosen due to the expectation of achieving a high localized field enhancement at the gap of the antenna.

(a)



(b)

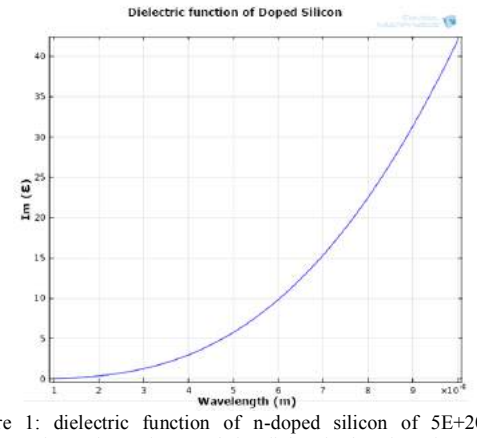
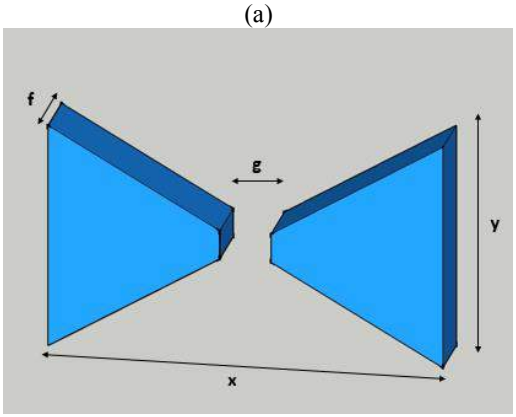


Figure 1: dielectric function of n-doped silicon of 5E+20 cm^{-3} concentration. The real part of the dielectric function shown in (a) possess negative values above 3 µm wavelength.

2. Results and Discussion

Upon introducing a phosphorus doping of 5E+20 cm^{-3} concentration into crystalline silicon, the plasma dispersion effect on the optical response of silicon shown in the dielectric function dispersion curves in figure 1 indicates that the dielectric function would possess negative values, mimicking the behavior of metal, around 3 micrometer wavelength. The resultant plasma frequency and collision frequency used in the Drude model representing the dielectric function has the values of 2.132E+15 rad/sec and 7.0316E+13 Hz respectively.

(a)



(b)

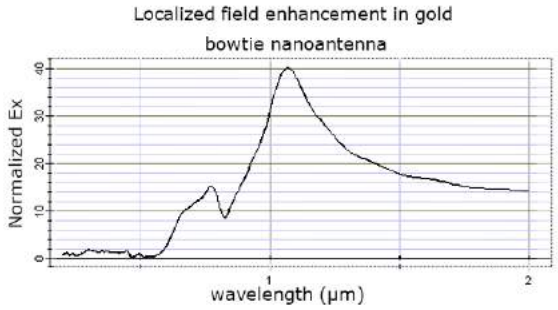


Figure 2: (a) Schematic diagram of the bowtie nanoantenna showing its design parameters. (b) Localized field enhancement around 1.1 μm wavelength in a gold bowtie nanoantenna with g=30 nm and x=y=475 nm.

The bow antenna design parameters are shown in figure 2.a below where g is the square gap dimension. X and y are the x extent and y extent of the nanoantenna respectively. Figure 2.b shows the enhancement in gold bowtie antenna with g = 30 nm and x=y = 475 nm. The bow tie antenna with gold material was able to show enhancement in the local field around 1.1 μm wavelength due to localized surface Plasmon resonance. By using doped silicon as the material of choice instead of gold, the enhanced field and plasmonic resonance is red shifted to mid-IR range at around 4 μm wavelength for the same dimensions used in the gold results as shown in figure 3. The effect of varying the geometrical design parameters of the nanoantenna on the enhancement is shown as well in figure 3. It shows that the enhancement increases as the gap size is reduced. As the x and y extent of the bowtie antenna increases, the enhancement peak is red shifted and widened while maintaining the same level of enhancement. The widening of the enhancement to become more broadband that confined to narrow spectral range has its benefit for building a broadband sensor or energy harvester in Mid-IR based on such plasmonic resonance.

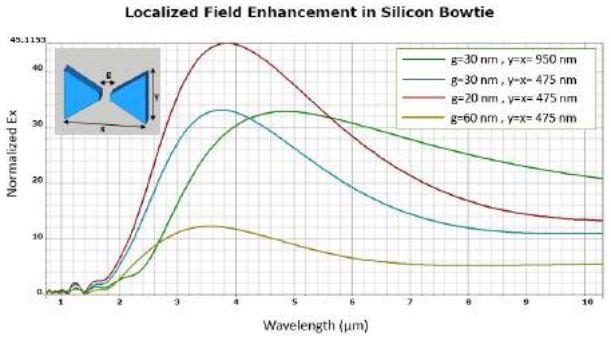


Figure 3:.Localized field enhancement in N-Doped silicon bowtie nanoantenna for different gap sizes and antenna dimensions.

3. Conclusions

A silicon-based bowtie nanoantenna is designed to provide localized field enhancement in the Mid-IR spectral range. A gold bowtie nanoantenna is found to provide enhancement due to localized surface plasmon resonance around 1.1 μm with a 40 folds enhancement. When using phosphorus doped silicon with 5E+20 cm^{-3} concentration, the enhancement reached 32 folds and red shifted to 4 μm. when the gap size of the bowtie is reduced in size, the enhancement increased to 45 folds for 20 nm gap size. Doupling the size of the nanoantenna causes a slight red shift as well as a broadening in enhancement peak, yet the same level of enhancement was maintained.

Acknowledgements

This research was partially funded by Zewail City of Science and Technology, AUC, STDF, Intel, Mentor Graphics, ITIDA, SRC, ASRT and MCIT.

References

1. L. Wang and X. Xu, "High transmission nanoscale bowtie-shaped aperture probe for near-field optical imaging," Appl. Phys. Lett. 90(26), 261105 (2007).
2. S. Aksu, A. A. Yanik, R. Adato, A. Artar, M. Huang, and H. Altug, "High-throughput nanofabrication of infrared plasmonic nanoantenna arrays for vibrational nanospectroscopy," Nano Lett. 10(7), 2511–2518 (2010).
3. F. Neubrech, A. Pucci, T. W. Cornelius, S. Karim, A. García-Etxarri, and J. Aizpurua, "Resonant plasmonic and vibrational coupling in a tailored nanoantenna for infrared detection," Phys. Rev. Lett. 101(15), 157403 (2008).
4. R. Adato, A. A. Yanik, J. J. Amsden, D. L. Kaplan, F. G. Omenetto, M. K. Hong, S. Erramilli, and H. Altug, "Ultra-sensitive vibrational spectroscopy of protein monolayers with

plasmonic nanoantenna arrays," Proc. Natl. Acad. Sci. U.S.A. 106(46), 19227–19232 (2009).
5. S. Kim, J. Jin, Y. J. Kim, I. Y. Park, Y. Kim, and S. W. Kim, "High-harmonic generation by resonant plasmon field enhancement," Nature 453(7196), 757–760 (2008).
6. N. Yu, E. Cubukcu, L. Diehl, D. Bour, S. Corzine, J. Zhu, G. Höfler, K. B. Crozier, and F. Capasso, "Bowtie plasmonic quantum cascade laser antenna," Opt. Express 15(20), 13272–13281 (2007).
7. K. D. Ko, A. Kumar, K. H. Fung, R. Ambekar, G. L. Liu, N. X. Fang, and K. C. Toussaint, Jr., "Nonlinear optical response from arrays of Au bowtie nanoantennas," Nano Lett. 11(1), 61–65 (2011).
8. E. J. Smythe, M. D. Dickey, J. Bao, G. M. Whitesides, and F. Capasso, "Optical antenna arrays on a fiber facet for in situ surface-enhanced raman scattering detection," Nano Lett., Vol. 9, 1132–1138, 2009.
9. P. Muhlschlegel, H.-J. Eisler, O. J. F. Martin, B. Hecht, and D. W. Pohl, "Resonant optical antennas," Science, Vol. 308, 1607–1608, 2005.
10. S. Sederberg and A. Y. Elezzabi, "Nanoscale plasmonic contour bowtie antenna operating in the mid-infrared," Opt. Express 19, 15532-15537 (2011).

Strong coupling at SWIR in Photocurrent of Quantum Cascade Infrared Photodetectors Coupled to Metamaterial Nano-antennas

Matias Katz[1], Ofir Sorias[1], Ben Dror[1], Nicolas Grandjean[2], Meir Orenstein[1] and Gad Bahir[1]

[1]*Department of Electrical Engineering, Technion-Israel Institute of Technology, Haifa 32000, Israel*
[2]*Institute of Condensed Matter Physics, Ecole Polytechnique Fédérale de Lausanne, Lausanne, Switzerland*
Author e-mail address: bahir@ee.technion.ac.il

Abstract: We present the design, realization, and characterization of room temperature optical and electrical strong light−matter coupling between intersubband transitions, at wavelength of 1.8 micron, in quantum cascade detector and planar metamaterials nano-cavity antenna.

1. Introduction

Intersubband (ISB) transitions constitute the backbone principle behind quantum cascade lasers and quantum well (QW) infrared detectors. Optical strong light−matter coupling describes the phenomenon of energy oscillating between an optical cavity and a two-level system at a rate that is faster than all loss mechanisms present in the system. This periodic energy exchange can be observed as a beating in the time domain of various observables such as reflectance or transmittance or in the frequency domain as a splitting of the single cavity resonance into two polariton branches. The characteristic frequency for this exchange is called the vacuum Rabi frequency.

Metamaterials are artificial structures consisting of individual sub-wavelength resonators where the electric and magnetic resonances are defined by the geometry of its constituents. These properties can be realized with a single layer of sub-wavelength resonators, often referred to as a meta-surface making metamaterials very interesting for experiments as the fabrication remains fully compatible with conventional planar processing. Furthermore, metamaterials allow for strong electric field confinement and enhancement in their vicinity making them well suited to couple incoming light to a detector medium. The optical properties of dipole transitions in semiconductor heterostructures can be engineered to a similar extent as the optical resonances in metamaterials using advanced epitaxial growth techniques. The optical transitions are now restricted to quantized states with discrete energies. The energy and the dipole matrix element of these intersubband transitions can be controlled by the width of the individual barriers and wells leading to advanced concepts for light detectors especially in SWIR, MID-IR and LW-IR spectral regions.

The basic idea of coupling mechanism is described schematically in Figure 1a. Short wave IR (SWIR) light is normally incident on the sample surface with the electric field vector parallel to the *x-axis*. The active QW is located beneath the meta-material antenna with its growth direction parallel to the *z-axis*. In this geometry, the incident SWIR light cannot directly couple to the ISBs transition due to the selection rules, but it can couple to the meta-material antenna. Most of the light (propagating along the z direction) is transferred into the z component of the electric field (E_z) in the vicinity of the metamaterial. Hence, the meta-material couples the incident in-plane field to the z field that is necessary to induce ISBs.

2. Experimental

A recent work by Benz et al [1] described optical (transmission measurement) strong coupling between near-infrared metamaterials and ISB transitions in III-nitride multi-quantum wells. In our work we demonstrate electrical (photocurrent measurement) strong coupling between shortwave- infrared (SWIR) metamaterials resonators and ISB transitions in III-nitride quantum cascade detector (QCD). Experimentally, we study strong light-matter interaction by performing optical transmission and electrical photocurrent measurements at normal incidence. The study was performed on the alloy-extractor QCD sample that described in Ref. 2. The sample consists of 40 active periods sandwiched between top and bottom Si doped $Al_{0.6}Ga_{0.4}N$ contact layers. The active QW consists of 8 ML thick GaN well lightly doped with Si and two AlN barriers and extraction region that formed by a non-intentionally-doped 15 nm thick $Al_{0.58}Ga_{0.42}N$ layer (Fig 2a). The devices was first processed in the form of 700x700 μm^2 mesas with Ti/Al/Ti/Au metallic layers to form the top and bottom contacts layers. The photo-response, measured at room temperature (RT) in wedge configuration, was peaked at 1.87 μm. Following full characterization, at different light coupling schemes, a second metallization deposition of metamaterial structures on the mesa top surface was implemented. For the experimental verification of the strong light-matter coupling, we fabricate "H" metamaterial nanocavities with different bare cavity resonances on top of the mesa structure (Fig. 1c and

Fig.2a). We used commercial finite-difference time–domain (FDTD) simulation package for the design of metamaterial structures (Figures 1bc). We model one unit cell with periodic boundary conditions that mimic the effect of two-dimensional metamaterial array in the real device. The metamaterial structures are define by electron-beam lithography, followed by an e-beam Ti/Au (5/50 nm) evaporation and lift-off. Eleven metamaterial structures with scaled geometric sizes (area of 100x120 μm^2) where define on the top surface of the QCD (Fig. 2b). We perform all measurements at room temperature using Bruker Equinox 55 FTIR equipped with a IR microscope objective to control the spot size of incident light (Fig.2e). As the bare metamaterial resonance frequency is varied across the intersubband resonance (as shown in Fig. 1c), a clear anti-crossing behavior is observed in the frequency domain both in transmission and photocurrent measurements (see Figures 2f and 2g). Using bound-to-bound transition in quantum cascade detector as a two-level system and metamaterial nano-cavities with deep sub-wavelength mode-volumes ($V_{eff} \approx 2x10^{-3}$ $(\lambda/n)^3$), we demonstrate room temperature strong coupling, in photo current measurement, with Rabi splitting on the order of 15% of the fundamental bare cavity frequency at short wave infrared spectral region of 1.8 micron (Fig.2g). By changing the metamaterial array period the photocurrent response changes from light-matter interaction that occurs at the single resonator level (Fig. 2g) to collective resonance phenomenon that enhances the photo-signal responsivity from 2.5 mA/W (Normal incident with MHA Ref. 2) to 15 mA/W (Fig. 2h), opening the possibility to fabricate enhanced normal incidence two dimensional multi-element planar detector.

The Authors acknowledge partial finance support by the EC FET OPEN "Unitride" Grant # 233950" and by the FTA program on Nanophotonics for Detection and Sensing.

3. References

[1] Benz et al "Strong coupling in the sub-wavelength limit using metamaterial nano-cavities", Nat. Commun. 4, 2882 (2013)
[2] Pesach et al "First demonstration of plasmonic GaN quantum cascade detectors with enhanced efficiency at normal incidence" Opt. Express. 22, 21069 (2014).

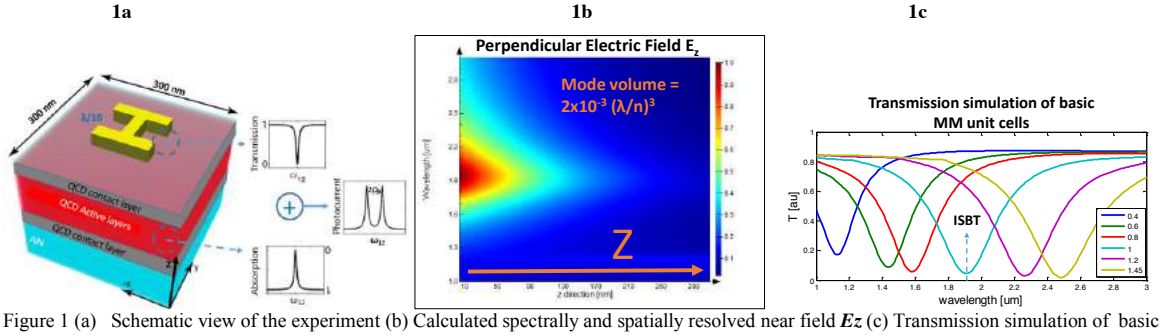


Figure 1 (a) Schematic view of the experiment (b) Calculated spectrally and spatially resolved near field ***Ez*** (c) Transmission simulation of basic metamaterial unit cells on bare sapphire/AlN template. The bare metamaterial resonance frequency is varied across the intersubband resonance.

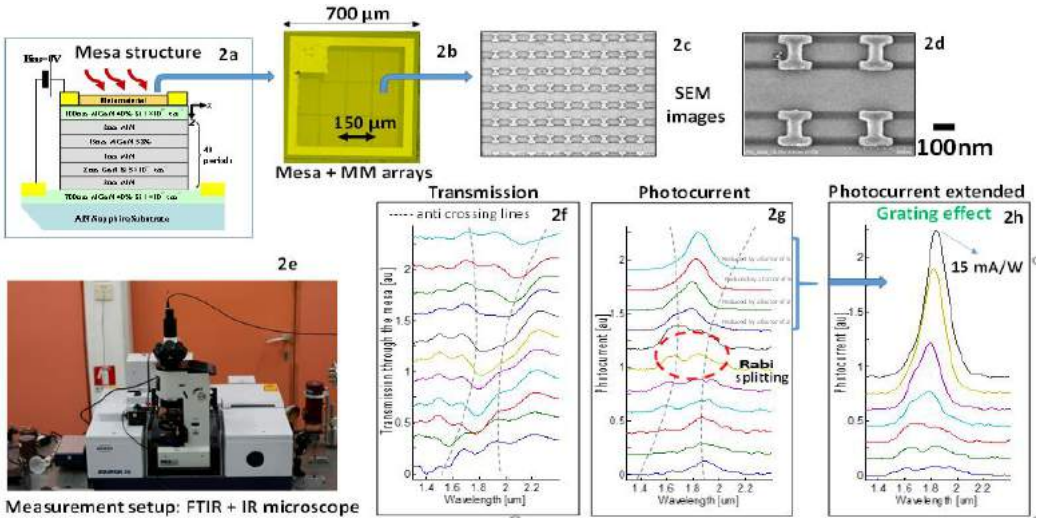


Fig. 2 (a) Device structure. (b) SEM image of mesa top surface. (c) - (d) SEM images of single metamaterial structure. (e) FTIR + IR microscope. (f) Details transmission plots for 11 different metamaterial nano-cavities corresponding to bare cavity frequencies shown in Fig. 1c. (g) Details Photocurrent plots for 11 different metamaterial nano-cavities. (h) Transition from strong coupling of single resonator to collective resonance phenomenon.

Photothermal and Photoelectric Nanophotonics

Biased-modulating photodetector using graphene embedded carbon film/n-Si heterojunction

Xi Zhang,[1] Luping Du[2*]

[1]Institute of Nanosurface Science and Engineering, Shenzhen University, Shenzhen, 518060, China
[2]Nanophotonics Research Center, Shenzhen University, Shenzhen, 518060, China
*corresponding author, E-mail: lpdu@szu.edu.cn

Abstract

We proposed a bias-modulating graphene embedded carbon (GEC) film/n-Si photodetector with electron trapping centers enabled by high-density edges of standing structured graphene-nanocrystallines. The bias-induced tunability of the relative positions of the Fermi levels that enables a high photocurrent responsivity of 0.35A/W. A fast response time of 2.2μs was also achieved.

1. Introduction

Combinations of carbon materials with semiconductors have attracted enormous attentions in photovoltaic applications. The amorphous carbon (a-C) film is the earliest carbon-based material applied in heterojunctions for photoelectric devices with the responsivity of 0.18A/W[1, 2]. Plane graphene-Si photoelectric devices were constructed by using chemical vapor deposited, reduced graphene oxide or mechanically exfoliated graphene, although it is difficult to obtain large-scale heterojunctions with low interface defect.

Here, we proposed a bias-modulating graphene embedded carbon (GEC) film photodetector with electron trapping centers enabled by high-density edges of standing structured graphene-nanocrystallines (GNs). The GEC film, prepared by electron cyclotron resonance (ECR) plasma technique,[3, 4] contains a large amount of graphene nanocrystallines (GNs) growing perpendicularly to the substrate. By virtue of its special structure, the GEC film has a high density of edges which is capable to trap itinerate electrons with unpaired spin[5] and induce a strong magnetism[3]. Hence, the high-density edges of GEC film can serve as trapping centers for photo-excited electrons in photovoltaic process.

2. Results and Discussion

2.1. Device Configuration

The GEC film (~70nm thickness) was deposited on a slightly n-doped silicon wafer (square resistance ~10Ω, 0.5mm thickness). Finger-type gold electrodes were deposit on top of GEC film using UV lithography technique. The GEC film/n-Si form a heterojunction and external bias (V) is applied on GNEC film against n-Si.

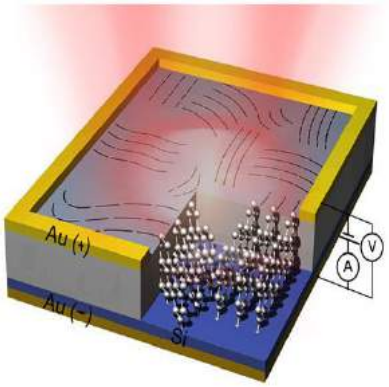


Figure 1: Schematic diagram of the GNEC film/n-Si devices.

2.2. I-V curves

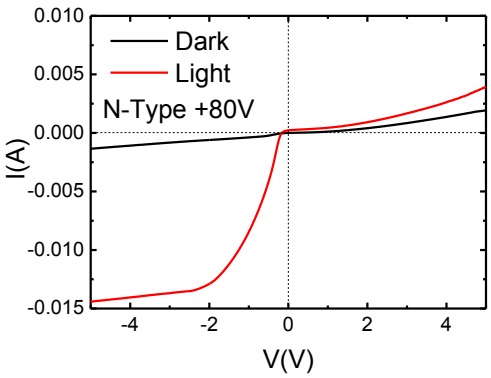


Figure 2: I-V curves of device in darkness and under illumination of 40mW 785nm laser.

Due to the unique electronic structure of graphene near its Fermi level (Dirac cone), a strong suppression of photocurrents occurs close to V = 0, and a sharp rise and rapid saturation of photocurrents at low reverse biases. An applied reverse bias can lift the Dirac point of GNs to

higher values, opening up a large number of accessible states for the holes to inject into and allowing a complete collection of the injected holes. As a result, at V=-5V, a high responsivity of 0.33A/W was achieved. The bias-induced tunability of the relative positions of the Fermi levels that enables a high photocurrent responsivity, and results in a tunable photocurrent ON/OFF ratio.

2.3. Spectral Response

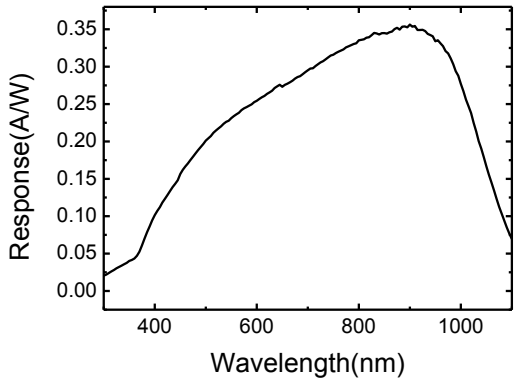


Figure 3: Spectral response of GEC film/n-Si photodetector.

The GEC film/n-Si photodetector show a broadband photo responsivity over the range from 350nm to 1100nm. The highest responsivity is 0.35A/W at 915nm in NIR region.

2.4. Time Response

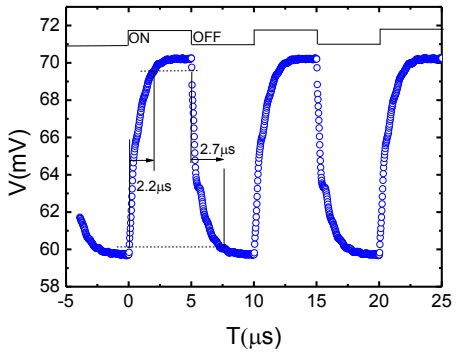


Figure 4: Time response of of GEC film/n-Si photodetector under 40mW 785nm laser.

Moreover, due to the standing structured GNs keeping the transport channels, a fast response time, τrise= 2.2μs was achieved, as shown in Figure 4.

3. Conclusions

A bias-modulating GEC film/n-Si photodetector was proposed with electron trapping centers enabled by high-density edges of standing structured graphene-nanocrystallines. A high photocurrent responsivity of 0.35A/W and a fast response time of 2.2μs were achieved. The GEC film/n-Si open a way to fabricate low-cost and highly sensitive photodiodes.

Acknowledgements

This work is supported by the National Nature Science Foundation of China (Nos 51605306), Guangdong Natural Science Foundation (Nos 2016A030310060) and Shenzhen foundation fund (No.JCYJ20160427105015701).

References

[1] K.M. Krishna, M. Umeno, Y. Nukaya, T. Soga, T. Jimbo Photovoltaic and spectral photoresponse characteristics of n-C/p-C solar cell on a p-silicon substrate *Appl. Phys. Lett.*, 77: 1472-1474, 2000.

[2] H.A. Yu, Y. Kaneko, S. Yoshimura, S. Otani Photovoltaic cell of carbonaceous film/n‐type silicon *Appl. Phys. Lett.*, 68: 547-549, 1996.

[3] C. Wang, X. Zhang, D. Diao Nanosized graphene crystallite induced strong magnetism in pure carbon films *Nanoscale*, 7: 4475-4481, 2015.

[4] W. Chen, X. Zhang, D. Diao Low-energy electron excitation effect on formation of graphene nanocrystallites during carbon film growth process *Appl. Phys. Lett.*, 111: 114105, 2017.

[5] X. Zhang, C. Wang, C.Q. Sun, D. Diao Magnetism induced by excess electrons trapped at diamagnetic edge-quantum well in multi-layer graphene *Appl. Phys. Lett.*, 105: 042402, 2014.

Plasmon-Enhanced Photovoltaics, Photocatalysis, and Solar Fuels

3D Multi-scale Nanostructured Plasmonic Materials for Record Efficient Hot-Carriers Based Photocatalysis

Yi Tian[1], Francisco Pelayo García de Arquer[2], Cao-Thang Dinh[2], Gael Favraud[1], Marcella Bonifazi[1], Min Liu[2], Sjoerd Hoogland[2], Edward H. Sargent[2*] and Andrea Fratalocchi[1*]

[1]Faculty of Electrical Engineering Applied Mathematics and Computational Science, King Abdullah University of Science and Technology, Thuwal 23955-6900, Saudi Arabia
[2]Department of Electrical Engineering and Computer Engineering University of Toronto, 35 St. George Street, Toronto, Ontario M5S 1A4, Canada
*Corresponding author, E-mail: andrea.fratalocchi@kaust.edu.sa

Abstract

By engineering metal epsilon-near-zero metamaterials, we demonstrate a new photocatalyst for hydrogen evolution. Electron energy loss spectroscopy is employed to illustrate hot carriers are excited in a broadband fashion within a 10-nm region. Finally, the resulting photocatalyst achieve a hydrogen production rate of 9.5-μmol $h^{-1}cm^{-2}$ that exceeds, by a factor of 3.2 that of the best previously reported plasmonic-based photocatalysts for the dissociation of H_2 with 50 h stable operation.

1. Introduction

Photocatalytic conversion of solar energy to chemical fuels or feedstock is considered as an attractive strategy to solve the increasing demand of renewable energy sources. Typically, in a solar-conversion-system, semiconductors serve as photoactive materials, which capture, absorb and then transfer photo-excited electrons to catalytic sites to enable proton reduction reaction [1-3]. Direct photo-excitation of metal has emerged in recent years as a new promising strategy applied in photochemistry. Plasmonics is capable to provide the ultimate spatial and temporal manipulation over light and photo-derived chemical reactions, with help of an exquisitely designed metallic nanostructure network can efficiently enclose electromagnetic irradiation within a nanometric region. Surface plasmons, that charge-density oscillation, consequently are excited at the metallic surface and decay by photons reemission or through the creation of energetic electrons and holes. These photo-excited energetic carriers can be leveraged to trigger efficient photo-derived fuels and chemicals production, such as hydrogen evolution [4].

2. Results

We illustrate a new strategy to achieve highly efficient Photocatalysis in a material based on 3D multi-scale epsilon-near-zero (ENZ) nanostructures. ENZ matematerials are structures whose optical properties appear as the refractive index of the structure close to zero. This extraordinary property can be leveraged to slow down the light significantly, focusing electromagnetic fields on nanometric regions. By using the electroplating that a large-scale fabrication technique to create disorder metallic nanostructured needles and combining with Pd/TiO_2/Pt heterojunction engineering, we realized designs of the broadband ENZ materials and photocatalysis devices.

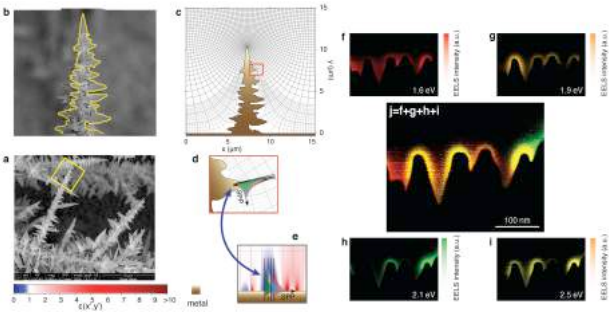


Figure 1: General idea, sample fabrication and EELS demonstration. (a)-(b) SEM images of metallic needle shape structures. (c) Equivalent structures of panel b, calculated by applying transformation optics. (d) Zoomed a local area of panel c, and shows the corresponding broadband squeezing of light in the points of positive curvatures of the material, where equivalent ENZ region exist in panel e. (e) Optical properties of the complex ENZ structure, showing the motion of SPP wave excited by incident light. (f)-(i) EELS plasmons mapping at various input energy of nanoscale features of the ENZ materials. (j) Overlap of EELE signals to illustrate the broadband ENZ effect.

The key to enhance the production of hot carriers in the

system is to maximize the confinement of electromagnetic field in each single region on the device surface. Fig.1a–Fig. 1e show the concept of the complex ENZ structures and theoretical study of interaction between ENZ materials and light. Fig. 1e shows a section of refractive index of the structure. The system is composed of a flat metallic surface covered by material with a permittivity $\varepsilon(x', y')$, characterized by a network of ENZ regions separated by high refractive index. Due to the permittivity $\varepsilon(x', y')$ does not change with frequencies, all surface plasmon polaritons (SPP) excited at various wavelengths propagate at the metal-dielectric interface, and are trapped when they encounter ENZ regions. Inside the ENZ volume, the strong quasi-static energy localization is generated. Due this effect, the electromagnetic field in ENZ regions become to super high, which favors the decay of broadband SPP waves into highly energetic carriers.

To experimentally demonstrate this effect, we employ a combination of STEM and electron energy loss spectroscopy. Fig.1f-I shows the measured EELS spectra from different excitation ranging between 1.6 eV and 2.5 eV. The morphological information of the sample is observed in the black regions under the colorful EELS signals. The Fig.1j is the sum of EELS signals at different wavelengths, which clearly demonstrate the broadband ENZ effect.

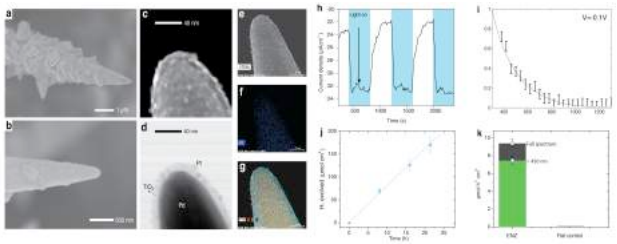


Figure 2: ENZ photocatalyst assembly and hydrogen generation performance. (a)-(g) The SEM and TEM image of ENZ Photocatalysis device, and the element mapping. (h) Current-time trace at -0.1V reversible hydrogen electrode potential. (i) Photoelectrochemical external quantum efficiency spectra characterization. (j) Amount of H_2 evolved at different times. (k) Comparison of H_2 generation rates for full-spectrum illumination with a control sample.

Fig. 2a-g shows the architecture of an ENZ photocatalyst, including Pd/TiO_2/Pt heterojunction. We confirmed the material composition of the ENZ catalyst by energy dispersive X-ray spectroscopy, specifically demonstrated by the Fig. 2e-g. Fig. 2h-k shows hydrogen production performance of ENZ photocatalysts. The evolution rate under one sun condition is 9.5-μmol $h^{-1}cm^{-2}$, corresponding to an average quantum yield over solar spectrum of 0.8%. The enhanced performance of this system is approximately one order of magnitude higher than the reported one.

3. Discussion

The broadband nature of ENZ matematerials demonstrated in this work is quite interesting to many applications in the photochemistry and hot-carriers chemistry, since it overcomes the limit of conventional plasmonic materials. With the advance and optimization of mechanisms of hot-carrier generation, extraction and transportation, the ENZ material can also open applications for efficient production of other chemical fuels in different metal-based redox reactions.

4. Conclusions

In this work, we design and fabricate the efficient photocatalyst for hydrogen production based on 3D ENZ materials. The broadband ENZ effect is clearly demonstrated by the application of electron energy loss spectroscopy.

Acknowledgements

The authors acknowledge the funding from KAUST (Award No. OSR-2016-CRG5-2995) and the Ontario Research Fund-Research Excellence Program, the Natural Sciences and Engineering Research Council (NSERC) of Canada, and the Connaught Global Challenges program of the University of Toronto.

References

[1] J. Liu, Y. Liu, N. Liu, Y. Han, X. Zhang, H. Huang, Y. Lifshitz, S. Lee, J. Zhang, Z. Kang, Water splitting Metal-free efficient photocatalyst for stable visible water splitting via a two-electron pathway, *Science*, *347*, 970, 2015.

[2] M. L. Brongersma, N. J. Halas, P. Nordlander, Plasmon-induced hot carrier science and technology, *Nat. Nanotechnol. 10*, 25, 2015.

[3] C. Clavero, Plamon-induced hot-electron generation at nanoparticle/metal-oxide interfaces for photovoltaic and Photocatalytic devices, *Nat. Photonics*, *8*, 95, 2014.

[4] S. Mubeen, J. Lee, N. Singh, S. Kramer, G. D. Stucky, M. Moskovits, An autonomous photosynthetic device in which all charge carriers derive from surface plasmons, *Nat. Nanotechnol.*, *8*, 247, 2013.

Partially-Embedded Plasmonic Nanoparticles within Semiconductors for Enhanced Hot Electrons Extraction

Charlene Ng[1,2,3], Peng Zeng[4], Julian Lloyd[3,5], Ann Roberts[6], Trevor A. Smith[4], Udo Bach[3,5], Timothy J. Davis[2,6], Andreas Fery[1], and Daniel E. Gómez[3,7*]

[1]Leibniz-Institut für Polymerforschung, Instituite of Physical Chemistry and Polymer Physics, Dresden, Germany
[2]CSIRO, Manufacturing Flagship, Private Bag 33, Clayton, VIC, 3168, Australia
[3]Melbourne Centre of Nanofabrication, Australian National Fabrication Facility, Clayton, VIC, 3168, Australia
[4]School of Chemistry, The University of Melbourne, VIC, 3800, Australia
[5]Department of Materials Science and Engineering, Monash University, Clayton, VIC, 3800, Australia
[6]School of Physics, The University of Melbourne, VIC, 3800, Australia
[7]RMIT University, Melbourne, VIC, 3000, Australia
*corresponding author, E-mail: daniel.gomez@rmit.edu.au

Abstract

When plasmonic nanoparticles are coupled with semiconductors, highly energetic hot carriers are extracted from the interface for various light-related applications. Here we demonstrate using visible pump, near-infrared probe transient-absorption spectroscopy, that increases in the contact area between metal and semiconductor leads to an increase in the quantum yield for hot electron injection. Further analysis of the experimental data suggests that the hot electrons are emitted across the interface via a surface photoemission mechanism, instead of a homogeneous energy–momentum distribution.

1. Introduction

When plasmonic metal nanostructures are in direct contact with a semiconductor, a Schottky barrier is formed at the metal-semiconductor interface.[1] Hot charge carriers due to the non-radiative Landau decay can be emitted across the Schottky interface resulting in photon-to-electron conversion that is beneficial for various applications such as photocatalysis, photovoltaics, photo-detection and sensing.[2,3] The geometry of individual plasmonic nanostructures determines the hot carrier generation process and plasmon resonance, while the partial embedding of plasmonic structures introduces more Schottky interfaces and allows thusly a larger percentage of excited hot electrons with appropriate wavevector to be transported across the barrier (Figure 1).[4] Therefore, approaches to enhance the hot carrier generation and extraction process include tailoring the geometry parameters of individual plasmonic nanostructures, and maximising the number of metal-semiconductor Schottky interfaces, which can be achieved by almost completely burying the metal nanostructures into the semiconductor. [4]

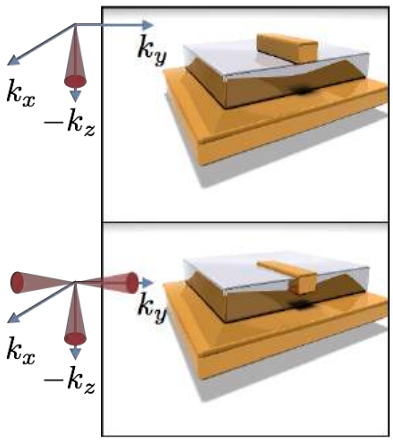


Figure 1: Schematic of the partially embedded plasmonic nanostructures to illustrate the increase in Schottky interfaces via partial embedding.

However, the precise control of the geometrical parameters of plasmonic nanoparticles in a large-scale manner is challenging. The use of complex tools such as reactive ion etching and lithography techniques also limits scalability and represent a bottleneck for the large scale fabrication of such promising structures. **To overcome these restrictions, we demonstrate a simple and cost effective strategy to partially embed colloidal-plasmonic nanoparticles within the semiconductor on a wafer-scale.** Well-defined plasmonic nanoparticles that are synthesized via a wet chemical method that is amendable to upscaling is utilized in this work. Furthermore, a novel nanofabrication concept is also developed to create these partially embedded structures over macroscopic areas at low costs and absence of complex tools. Using ultra-fast pump probe spectroscopy, we have demonstrated that this partial embedding strategy has led to

a much higher efficiency of hot electron injection into the semiconductor.

2. Results and Discussion

Large scale partial-embedding of plasmonic nanoparticles are achieved using physical vapour deposition and colloidal-based well-defined nanoparticles. The successful fabrication is further confirmed by the use of scanning electron microscopy and atomic force microscopy. Using a visible pump, near--infrared probe transient absorption spectroscopy, we demonstrate that the increase in contact area between metal and semiconductor using partially embedded plasmonic nanoparticles within semiconductors (TiO_2) leads to a ~3 times increase in hot electron injection efficiency. Although an enhancement was observed from the resulting structure, the enhancement is shown to be inconsistent, when a homogenous energy-momentum distribution is considered for the hot electron extraction process. Upon further analysis of the achieved experimental data, it is suggested that the highly energetic electrons are emitted across the interface via a surface photoemission mechanism, instead of the assumed homogenous energy-momentum distribution.

3. Conclusions

In summary, we have shown that the increase in metal–semiconductor contact area leads to a higher efficiency of hot–electron injection into the semiconductor. Detailed analysis of our data suggests that surface photoemission is likely to be the dominant mechanism for hot–electron injection. In order to increase the metal–semiconductor contact area, we have developed a fabrication process that only requires physical vapour deposition techniques and does not involve any complex processes such as electron beam lithography or reactive ion etching, making it highly attractive for large scale fabrication. In particular, we envisage that contrary to other approaches, our method can enable the construction of near–perfect absorbers of light that incorporate partially–buried metal nanostructures. We also envisage that important insights into the mechanism of electron emission in plasmonic hot carrier extraction process, a key area that impacts further development of such plasmon-based devices.

Acknowledgements

This work was performed in part at the Melbourne Centre for Nanofabrication (MCN) in the Victorian Node of the Australian National Fabrication Facility (ANFF). C. N. was supported by an OCE Fellowship from CSIRO. D.E.G. acknowledges the ARC for support through a Future Fellowship (FT140100514). D.E.G and U.B. acknowledge the ANFF for the MCN Technology Fellowships. The authors acknowledge use of facilities within the Monash Centre for Electron Microscopy A.R., T.J.D. & D.E.G. acknowledge the ARC for support through a Discovery Project (DP160100983). T.A.S., D.E.G. U.B. and J.E.S. also acknowledge support from the Australian Research Council Centre of Excellence in Exciton Science (CE170100026).

References

[1] Z. Zhang, J. T. Yates, Band Bending in Semiconductors: Chemical and Physical Consequences at Surfaces and Interfaces, *Chemical Reviews*, 112, 5520-5551, 2012

[2] C. Ng, L. W. Yap, W. Cheng, A. Roberts, D. E. Gomez, Black gold: Broadband, high absorption of visible light for photochemical systems, *Advanced Functional Materials*, 27, 2016

[3] C. Ng, J. Cadusch, S. Dligatch, A. Roberts, T. J. Davis, P. Mulvaney, D. E. Gomez, Hot Carrier Extraction with Plasmonic Broadband Absorbers, *ACS Nano*, 10, 4704-4711, 2016

[4] M. W. Knight, Y. Wang, A. S. Urban, A. Sobhani, B. Y. Zheng, P. Nordlander, N. J. Halas, Embedding Plasmonic Nanostructure Diodes Enhances Hot Electron Emission, *Nano Letters*, 13, 1687, 2013

Quantum Photonics

Some electronic transport properties of nanostructure HgTe/CdTe type III superlattice for mid infrared and terahertz detection

Nassima Benchtaber[1], Abdelhakim Nafidi[*1], Abderrazak Boutramine[1], Driss Barkissy[1], Rachid Ben Koujan[1], Fatiha Chibane[1], Es-saïd Es-Salhi[1]

Laboratory of Condensed Matter Physics & Nano-Re, University Ibn Zohr, 80000 Agadir, Morocco
[*]corresponding author: nafidi21@yahoo.fr

Abstract

We reported here bands structure and the effective mass, in the direction of growth and in plan of HgTe (d_1= 4.5 nm)/ CdTe(d_2=4.8 nm) superlattice performed in the envelope function formalism. We interpreted Hall Effect and calculated the density of states and the Fermi level as a function of temperature. The laters reveal that temperature induced transitions from p type to n type conductivity and quasi bidimensional (Q2D) to three dimensional (3D) holes and electrons, respectively. When T increases, E_g increases and the cut-off wavelength λ_c decreases, with 5.06 μm <λ_c< 6.3 μm and the cut-off frequency 47 THz < f_c < 59 THz. This sample can be used as a mid infrared terahertz detector. At 21.88 K, this superlattice is a stable alternative for application as infrared detector than the alloy $Hg_{0.72}Cd_{0.28}Te$. These results are as a guide for the design of infrared nanostructured detectors.

1. Introduction

It's well known that the reduction of the dimensionality of an electronic device, from three-dimensional (3D) to bidimensional (2D), yield to the energy bands quantification and the confinement of carriers charges in quantum wells and hetero structures like in superlattices.

The intersubband absorption in semiconductors superlattices is fundamental in the most high performance infrared detectors. Various materials are used for IR detection like superlattices: type I, type II and type III [1-2]. The objectif of this paper is the type III superlattices especially the HgTe/CdTe superllatice that have been proposed as materials for Infrared optoelectronic devices [3]. This superlattice is comprised of nanometer-thin alternating layers of the mercury telluride (HgTe) and cadmium telluride (CdTe) [4]. The combination of semimetal and wide-gap material creates a unique band structure with an effective band gap at infrared energies. It was first suggested by Schulman and MacGill in 1979 [5-6].

The level of development achieved in the growth technique and molecular beam epitaxy of semi-conductors has allowed the fabrication of different alloys, quantum wells and superlattices. The optoelectronic properties of the superlattice exhibit a number of distinct advantages over that of the alloy, particularly at LWIR and VLWIR wavelengths. The applications of this technology are in military, automobile, aircraft safety, medical diagnosis and in remote sensing systems [7].

The concept of band structures is very important, since it provides an understanding of many physical properties of these materials. This is useful in terms of explaining many electrical and optical properties [8].

In this paper we calculated the bands structure, the effective masse, the cut-off wavelength λ_c as function of temperature and d_1/d_2 in HgTe (d_1= 4.5 nm)/ CdTe(d_2=4.8 nm) superlattice. We interpreted the Hall Effect and calculated the density of states and the Fermi level as a function of temperature. Our results are a guide for the design of infrared nanostructured detectors and indicated that this sample can be used as a mid infrared terahertz detector.

2. Theory of structural bands and computational methods:

The general expression of the dispersion relation for light particles (electrons and light holes) and heavy holes sub-bands is given by [9,10]:

$$\cos = [k_z(d_1 + d_2)] = \cos(k_1 d_1)\cos(k_2 d_2) - \frac{1}{2}[(\xi + \frac{1}{\xi}) + \frac{k_p^2}{4k_1 k_2}(r + \frac{1}{r} - 2)]\sin(k_1 d_1)\sin(k_2 d_2) \quad (1)$$

Where 1 and 2 refer to HgTe and CdTe materials respectively, k_z the wave vector in the direction of growth and $k_p(k_x,k_y)$ in the plane of the superlattice. In this case, the energy E of light particles is given by:

$$\begin{cases} \frac{2}{3}p_1^2\hbar^2(k_1^2 + k_p^2) = (E - \Lambda)(E - \Lambda + |\varepsilon_1| & \text{for HgTe} \\ \frac{2}{3}p_2^2\hbar^2(k_2^2 + k_p^2) = E(E - \varepsilon_2) & \text{for CdTe} \end{cases}, \quad (2)$$

The expression of ξ and r in the Eq.(1) are:

$$\xi = \frac{k_1}{k_2}r \text{ and } r = \frac{m^*_{HH_2}}{m^*_{HH_1}}$$

P_i is the Kane matrix element calculated by the following formula [11,12]:

$$P_i^2 = \frac{E_{pi}}{2m_0}, \quad (3)$$

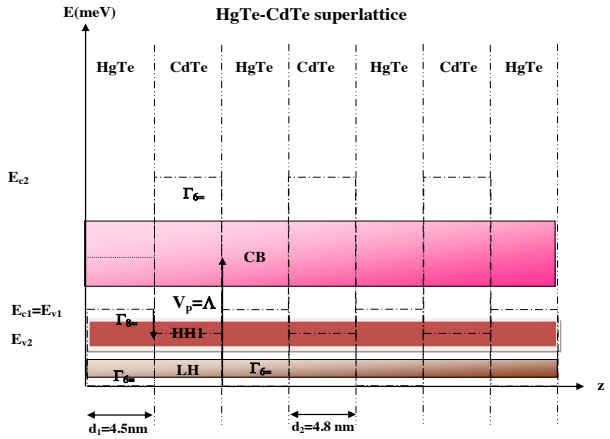


Figure 1: Schematic illustration of type III band alignment indicates the relative position of the HgTe/CdTe conduction and valence bands edges. Here, E_{c1} (E_{c2}) and E_{v1} (E_{v2}) are, respectively, the conduction and the valence bands of HgTe (CdTe). LH denotes the light holes and HH designates heavy holes. The valence band offset Λ act as the barriers for confining electrons and holes, respectively.

From the same equation (1), the superlattice heavy hole sub-bands are given by the following relations:

$$\begin{cases} -\dfrac{\hbar^2(k_1^2+k_p^2)}{2m_{HH}^*} = E-\Lambda & \text{for HgTe} \\ -\dfrac{\hbar^2(k_2^2+k_p^2)}{2m_{HH}^*} = E & \text{for CdTe} \end{cases}, \qquad (4)$$

Where m_{HH1}^*= 0.3 m_0 and m_{HH2}^*= 0.35 m_0, are the bulks heavy hole effective masses of HgTe and CdTe, respectively [13]. Fig. 1 shows the Schematic illustration of type III bands alignment.

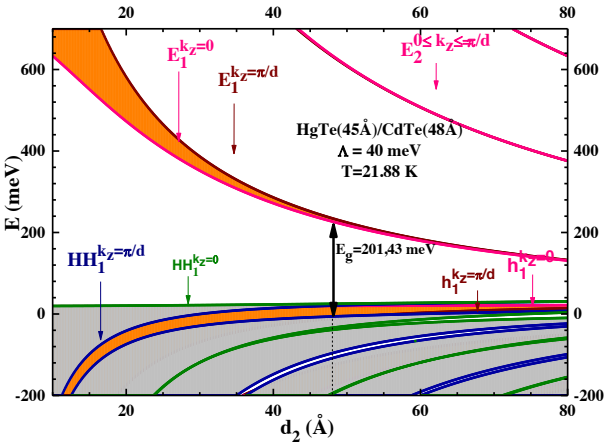


Figure 2: Energy position and width of the conduction (E_i), heavy-hole (HH_i), and light-hole (h_i) subbands calculated at 21.88 K, in the first Brillouin zone as a function of the d_2(CdTe) layer thickness.

The investigated sample is HgTe/CdTe with d_1(HgTe)= 45 Å and d_2(CdTe)= 48 Å. Consequently, d_2/d_1=1.07 and the superlattice period is d= d_1+d_2= 93 Å.

3. Theory results of structural bands:

3.1. Band gap calculation:

We show in the Fig. 2, the calculated spectra of energy E(d_2) with the energy position and width of the conduction (E_i), heavy-hole (HH_i) and light-hole (h_i) subbands calculated at 21.88 K for d_1= 0.937 d_2, in the first Brillouin zone as a function of the d_2(CdTe) layer thickness of the superlattice. That has been performed in the envelope function formalism with a valence band offset of 40 meV determinate from far-infrared magneto absorption measurements [14]. When d_2 increases the width of the bands and the band gap deceases. The well thickness of the studied sample is indicated by a vertical dashed line. The calculated band gap energy, from the bottom of the first conduction sub-band to the top of the first valence sub-band is E_g= E_1-HH_1= 201.43 meV.

The band gap energy E_g and the cut off wavelength λ_c as function of the temperature for various d_1/d_2 are shown in Fig. 3. For a given d_1/d_2, E_g increases with temperature. At fixed temperature, E_g increases when d_1/d_2 decreases and the cutoff wavelength λ_c decreases.

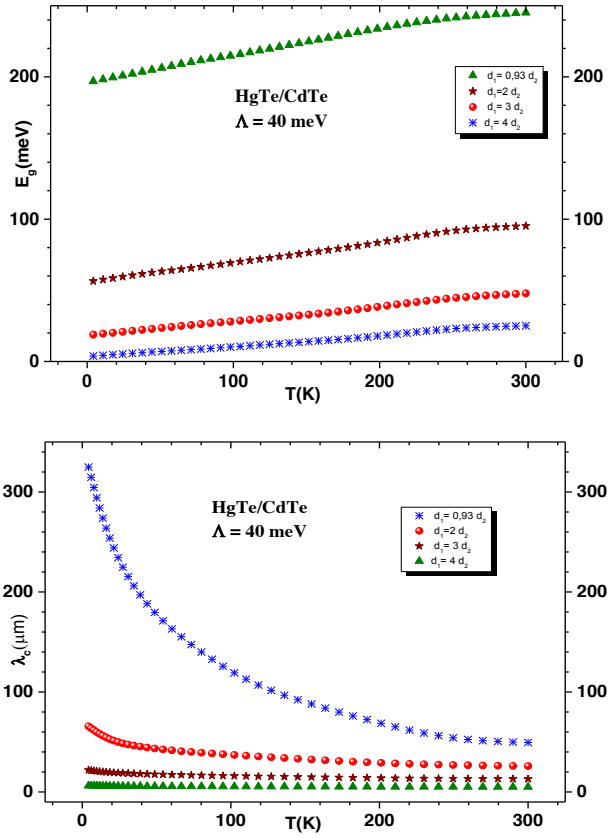


Figure 3: The band gap energy E_g and the cut-off wavelength λ_c as function of the temperature for various d_1/d, respectively.

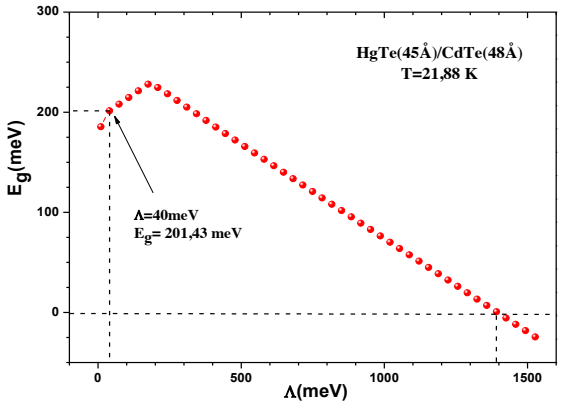


Figure 4 :The band gap, $E_g(\Gamma)$, as a function of valence band offset at 21.88 K, in the investigated HgTe/CdTe SL with d_1=45 Å / d_2=48 Å. The vertical dashed line indicates our chosen value of 40 meV.

We calculate the cut-off wavelength by the relation [15-16]:

$$\lambda_c(nm) = \frac{1240}{E_g(eV)}, \qquad (5)$$

In the investigated temperature range of 4.2 K to 300 K, 5060 nm ≤ λ_c ≤ 6300 nm, situates this sample in the mid infrared region.

Fig. 4 shows the band gap $E_g(\Gamma)$ at the center Γ of the first brillouin zone, as a function of valence band offset between heavy holes sub-bands edges of HgTe and CdTe, at 21.88 K. E_g=201.43 meV is the band gap energy for our investigated sample for the valence band offset Λ=40 meV. E_g increase to a maximum of 229 meV at Λ=179.4 meV and after it decease liniary. The transition from semiconductor to semimetal conductivity occur at Λ=1391 meV.

In figure 5, E_g of the investigated superlattice increases with temperature from 196.91 meV at 4.2 K to 245.15 meV at 300K. When the temperature increases the cut-off wavelength λ_c decreases.

We can see in figure 6.a, the bands structure along k_z and k_p (k_x,k_y) in the first Brillouin zone. Along k_p, the first

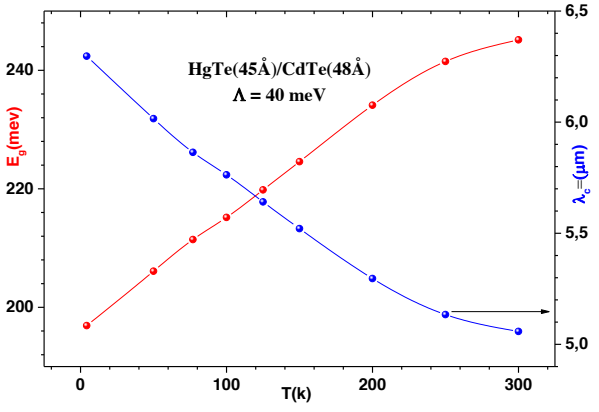


Figure 5: Band gap energy and cut-off wavelength λ_c as a function of temperature.

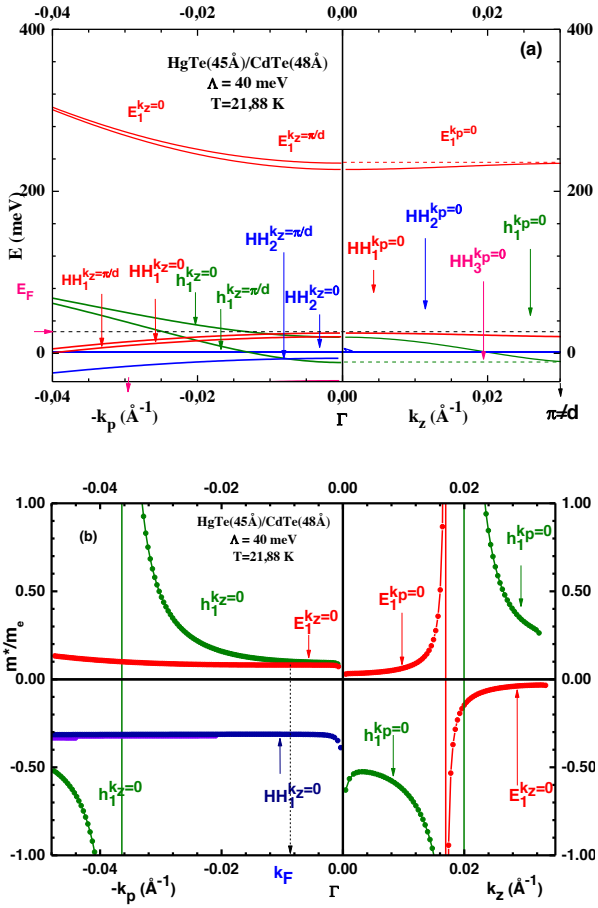


Figure 6: (a) The calculated bands structure, along k_z and k_p, (b): Carrier effective masses calculated along k_z and k_p, in the growth direction and in the plane of the investigated superlattice.

conduction sub-band E_1 and first light hole suband h_1 increases with k_p whereas HH_1 and HH_2 decreases. In addition, these dispersion curves show that, the electronic states are quantized and discrete along k_z direction and pseudo-continuous in the plane of the superlattice. Consequently, a weak coupled quantum wells HgTe can be distinguished. In this case, the electronic transport is dominated in the plane of the superlattice (parallel transport).

Carrier's effective mass of the first conduction and valence mini-bands for the in-plane motion and along growth direction $m^*(k_p,k_z)$ are shown In figure (6.b). The latter, is derived from Fig. 6. (a), by using following expression:

$$\left(\frac{1}{m^*}\right)_{ij} = \frac{1}{\hbar^2}\frac{\partial^2 E_{k_{ij}}}{\partial k_i \partial k_j}, \qquad (6)$$

Along k_p, the effective mass of heavy holes mass m^*_{HH1} is constant. Whereas, the effective mass of electrons m^*_{E1} increases and that of light holes m^*_{h1} increases and diverge at k_p=0.036 Å.

3.2. **Interpretation of Hall Effect:**

From the measurements of Hall constant R_H of H.S. Jung et al [17], we draw $\ln R_H$ as a function of $10^3/T$. At low temperature the sample is p type. When the temperature increases R_H decreases, vanishes at T= 84 K and becomes negative accusing n type conductivity.

In intrinsic regime, the law of mass action gives the concentration of electrons:

$$n = p = n_i = (N_c.N_v)^{1/2} e^{-E_g/2K_BT}, \quad (7)$$

The Hall constant is given by the relation

$$\left|R_H T^{3/2}\right| = (eA)^{-1}.\exp(E_g/2k_B), \quad (8)$$

The slope of $\ln(|R_H T^{3/2}|)$ as a function of $10^3/T$ allowed us to determine a gap E_g = 244.1 meV, which is in good agreement with our calculated band gap E_g(300 K) = 245.15 meV from Fig. 5. The corresponding detection wavelength is λ_c(300 K) = 6.3 μm. The sample is therefore a mid infrared detector.

The intercept of $\ln(|R_H T^{3/2}|)$ as a function of $10^3/T$ give us A and $(\frac{m^*_{E_1}}{m_0}\cdot\frac{m^*_{HH_1}}{m_0}) = 2.507.10^{-2}$ for a number of periods N=57. The later value is in agreement with $(\frac{m^*_{E_1}}{m_0}\cdot\frac{m^*_{HH_1}}{m_0}) = 2.510.10^{-2}$ obtained from $m^*/m_0(k_p=k_F)$ in Fig.6.b.

It is well know that in intrinsic regime, the mobility of electrons $\mu \approx T^{-3/2}$ the fitting of the Hall mobility μ_H, measured in [17], in logarithms scales gives us an agreement with $\mu \approx T^{-1.41}$. This indicated that when the temperature increased the mobility decreased linearly due to the interaction of electrons with phonons.

At weak field, the Hall constant in presence of electrons and holes is given from the transport theory of Boltzmann [19] by:

$$(R_H)_w = \frac{1}{|e|}\frac{p-nb^2}{(p+nb)^2} \text{ with } b = \frac{\mu_e}{\mu_h}, \quad (9)$$

n, p, μ_e and μ_h are, respectively, the concentrations and mobility of electrons and holes.

At low temperature in the saturation regime we have:

$$(R_H)_{sat} = \frac{1}{|e|p}, \quad (10)$$

Near of the intrinsic regime, the minimum of Hall constant is given from Eq (9) by:

$$(R_H)_{min} = \frac{(b-1)^2}{|e|4bp}, \quad (11)$$

This results in the ratio:

$$\frac{4(R_H)_{min}}{(R_H)sat} = \frac{(b-1)^2}{b} = \alpha, \quad (12)$$

This equation gives:

$$b^2 - b(2+\alpha) + 1 = 0,$$

$$\text{with } b = 2.81 \quad \text{and } b = 0.60, \quad (13)$$

Equation (9) implies for $R_H = 0$: $b^2 = \frac{p}{n}$

For T< 84 K, the sample is p-type with p > n and

$$b = \frac{\mu_e}{\mu_t} = \sqrt{\frac{p}{n}} = 2.81, \quad (14)$$

For T> 84 K, the sample is n-type with n > p and

$$b = \frac{\mu_e}{\mu_t} = \sqrt{\frac{p}{n}} = 0.6, \quad (15)$$

The equations (14) and (15) permit us to deduce the electronic characteristics of the sample in Tab.1. For example when the temperature increase, the mobility of electrons decreases whereas the mobility of holes decreases until the transition with μ_h= 3743 cm^2/Vs and after it decreases to 2522 cm^2/Vs.

3.3. **Density of state and Fermi Level**

For the superlattice i^{th} mini-band, with a finite energy width $\Delta E = E^i_{max} - E^i_{min}$, the density of states (DOS) can be expressed as [18]:

$$\rho^i_{DOS}(E) = \begin{cases} 0 & for \quad E^i_{min} > E > E^i_{max} \\ \frac{m^*}{\pi^2\hbar^2}k_z(E) & otherwise \end{cases} \quad (16)$$

The generalization of Eq.(16) required a sum over all mini-bands:

$$\rho_{DOS}(E) = \sum \rho^i_{DOS}(E), \quad (17)$$

Tab.1. Calculated electrons and holes concentrations n, p and mobility μ_e, μ_p. k_F, m^*/m_0 and E_F are the Fermi wave vector, the effective masse of electrons or holes and the Fermi level energy, respectively, as a function of temperature.

The carriers type	T(K)	$n*10^{14}$ (cm^{-3})	$p*10^{15}$ (cm^{-3})	k_F*10^{-5} (cm^{-1})	m^*/m_0	E_F (meV)	μ_e (cm^2/Vs)	μ_h (cm^2/Vs)
p- type (2D)	21.88	7.20	5.67	2.56	0.0704	24,669	12775.10	4546.3
	50	1.41	1.11	3.23	0.0742	24.669	5935.85	2112.40
	77	4.27	3.37	4.63	0.0750	24.669	2245.82	799.22
Transition	84	3.92	1.41	4.87	0.0756	24.669	2245.82	3743.30
n- type (3D)	237	1.24	4.46	7.45	0.0768	249.260	1867.29	3112.15
	300	2.46	8.87	8.10	0.0775	269.819	1513.29	2522.15

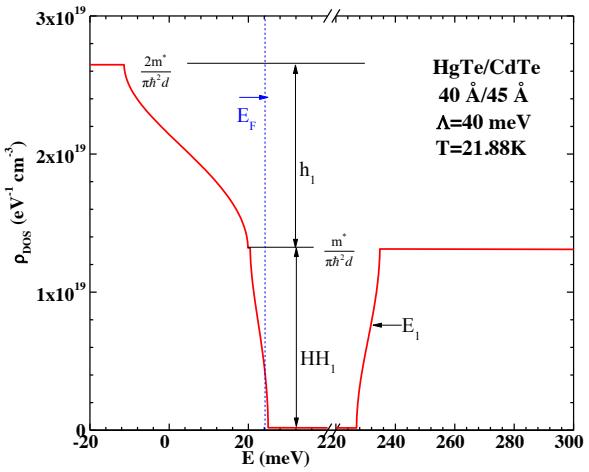


Figure 7: DOS of the investigated superlattice at T=21.88K.

The Figure 7 show the calculated density of state of bands E_1, HH_1 and h_1 from $E(k_z)$ in Fig. 6 (a). Once the electron and holes concentration are known in table 1, we calculated the energy E_F of Fermi level by:

$$\begin{cases} E_{HH1} - E_F = \dfrac{\hbar^2 k_{F2D}^2}{2m_{HH1}^*} \quad \text{with} \quad k_{F2D} = (2\pi p)^{1/2} \quad \text{for} \quad \text{p type} \\ E_F - E_1 = \dfrac{\hbar^2 k_{F3D}^2}{2m_{E1}^*} \quad \text{with} \quad k_{F3D} = (3\pi^2 n)^{1/3} \quad \text{for} \quad \text{n type} \end{cases} \quad ,(18)$$

where k_{F2D} and k_{F3D} are the bidimensional and tridimensional Fermi wave vector respectively. The position of the Fermi level energy E_F, indicating p type and quasi bidimentional (Q2D) holes gas at 21.9 K. A similar Figure, at 300 K, showed n type and 3D electrons gas in the investigated superlattice.

At T_{inv}= 84 K, the conductivity of this semiconductor sample change from p-type at low temperatures to n-type at high temperatures. Using the calculated effective mass and the concentrations of electrons and holes in table 1, the

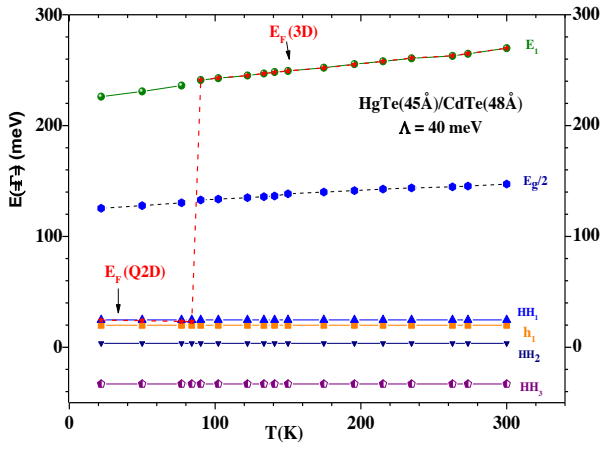


Figure 8: Temperature dependence of energy subbands and Fermi level transition from Q2D to 3D at the center Γ of the first Brillouin zone.

energy of Fermi level E_F is constant for $T < T_{inv}$ and increases linearly at high temperatures. These means a transition of the carriers charges from quasi bidimensional to three-dimensional as seen in Fig. 8.

4. Conclusion

In this paper, we reported the bands structure and the effective mass, in the direction of growth and in plan of a semiconductor HgTe/CdTe superlattice. We deduce the variation of the band gap and the cut-off wavelength as a function of the offset, d_1/d_2 and temperature. We interpreted Hall Effect and calculated the density of states and the Fermi level as a function of temperature. We demonstrated that the temperature induced transitions p type to n type conductivity and quasi bidimensional (Q2D) to three dimensional (3D) holes and electrons gas, respectively. In the investegated temperature range, the cut-off frequency 47 THz < f_c < 59 THz situated this sample as a mid infrared terahertz detector. The calculated band gap at 300K and the ratio of effective mass are in good agreement with the measurement of Hall Effect. At 21.88 K, this superlattice is a stable alternative for application as infrared detector than the alloy $Hg_{0.72}Cd_{0.28}Te$.

References

[1] M. Razeghi, B. Minh Nguyen, Advances in mid-infrared detection and imaging, *Rep. Prog. Phys.* 77: 082401, 2014.

[2] P. Norton, *Opto-Electronics Review* 10: 159, 2002.

[3] D. Perkowitz and D. RajavelI. K. SOU, J. Reno, and J. P. Faurie, far-infrared study of alloying in the HgTe-CdTe superlattice, *Appl. Phys. Lett* 49: 13, 1986.

[4] P. Martyniuk, M. Kopytko, A. Rogalski, *Opto-Electronics Rev.* 22: 127–146, 2014.

[5] J. N. Schulman and T. C. McGill, The CdTe/HgTe superlattice proposal for a new infrared materials, *Appl. Phys. Lett.* vol. 34: no. 10, 663-665, 1979.

[6] M. Z. Hasan and C. L. Kane, Topological insulators, *Rev. Mod. Phys* 82:3045, 2010.

[7] M. Razeghi, B. Minh Nguyen, HgCdTe infrared detector material: history, status and outlook , *Rep. Prog. Phys.* 68: 2267–2336, 2005.

[8] Z. Yang, Z. Yu, Y. Lansari, S. Hwang, J. W. Cook, Jr., and J. F. Schetzina, Optical properties of HgTe/CdTe superlattices in the normal, semimetallic and inverted-band regimes, *Physical Review B* 49:12, 1994.

[9] G. Bastard,Teoretical investigations of superlattice band structure in the envelope-function approximation , *Phys. Rev. B* 25:7584, 1982.

[10] D. Barkissy, A. Nafidi, A. Boutramine, H. Charifi, A. Elanique, M. Massaq, Electronic properties of GaAs/AlAs Nanostructure superlattice, *J. Low Temp. Phys.* 182-185, 2016.

[11] E. G .Novik, et al, Band structure of semimagnetic $Hg_{1-y}Mn_yTe$ quantum wells, *Phys. Rev. B* 72: 035321, 2005.

[12] P. Capper (Hrsg.). Properties of Narrow Gap Cadmium-based Compounds. Book, inspec publication, No 10, the Institution of Electrical Engineers, London XXI, 1994, DOI: 10.1002/crat.2170300311.

[13] S. Kasap, P. capper (Eds), Springer Handbook of electronic and photonic materials, Springer in volumes 2, LXVIII-1407, 2007,.

[14] Y. Guldner, G. Bastard, J. P. Vieren, M. Voos, J. P. Faurie et A. Million, Magneto-Optical Investigations of a Novel Superlattice: HgTe-CdTe, *Phys*. *Rev*. *Lett*. 51(10): 907, 1983.

[15] D. Barkissy, A. Nafidi, A. Boutramine, E. Y. El Yakoubi, H. Chaib, Investigations in electronic quantum transport of quasi two dimensional $In_xGa_{1-x}As$/InP nanostructure superlattice for infrared detection, *journal of Superlattices and Microstructures*, 2018. https://doi.org/10.1016/j.spmi.2018.03.016.

[16] A. Boutramine, A. Nafidi, D. Barkissy, M. Bellioua, A. Khalal, "Correlation between electronic bands structure and magneto-transport properties of nanostructure type II superlattice for terahertz detection", *Journal of Superlattices and Microstructures*, 2017. https://doi.org/10.1016/j.spmi.2017.12.036

[17] H.S. Jung, P. Boieriu, and C.H. Grein, p-Type HgTe/CdTe Superlattices for Very-Long Wavelength Infrared Detectors, *Journal of Electronic Materials* vol. 35: no. 6, 1341–1345, 2006.

[18] H.-S. Cho, Density of states of quasi two one and zero dimensional superlattice, *J*. *Vac*. *Sci*. *Technol*. *B* Microelectron. Nanom. Struct. 7: 13-63, 1989.

[19] P. K Seeger, Springer Handbook, Springer-Verlag Berlin Heidelberg, 2004.

Bands structure and electro-optical properties in ternary InAs/GaInSb type II superlattice for LWIR photodetection

Nassima Benchtaber[1], Abdelhakim Nafidi[*1], Driss Barkissy[1], Abderrazak Boutramine[1], Rachid Ben Koujan[1], Es-saïd Es-Salhi[1], Fatiha Chibane[1]

[1]Laboratory of Condensed Matter Physics and Nanomaterials for Renewable energy, University Ibn Zohr, 80000 Agadir, Morocco
*corresponding author, E-mail: nafidi21@yahoo.fr

Abstract

We have used the envelope function formalism to investigate the bands structure of LWIR type II SL InAs(d_1=2.18d_2)/$In_{0.25}Ga_{0.75}Sb$(d_2=21.5Å). Thus, we are able to extract optical and transport parameters as the band gap, cut off wavelength, careers effective mass, Fermi level and the density of state. Our results show that the higher optical cut-off wavelength can be achieved with smaller layer thicknesses. The semiconductor-semi metal transition was studied as a function of temperature. Our results permit us the interpretations of Hall and Shubnikov-de Haas effects. The agreement with experimental results is good and limited by the inevitable experimental uncertainty.

1. Introduction

There are a several efforts in developing infrared materials for Very Long Wavelength Infrared (VLWIR) photodetection with the optical cut-off wavelengths $\lambda_c \geq 14$ µm. Currently, InAs/$In_{1-x}Ga_xSb$ type-II superlattices (SLs) are still the most promising candidate. In this area, Smith and Maihiot [1] have shown that this material system provides distinctive advantages suitable for VLWIR photodetection.

The key lies in the fact that by increasing indium composition in $In_{1-x}Ga_xSb$ layer, the corresponding lattice constant increases. As a result, the tension in the InAs layer lowers the conduction subbands (E_i) whereas the compression in the $In_{1-x}Ga_xSb$ layer raises the heavy hole subband (HH_i). Therefore, a very smaller band gap can be optimized with a reasonably thinner period which is not possible in InAs/GaSb SL [2]. The most important advantage of this SL lies in the fact that the presence of strain within this SL layers reduces the Auger recombination process and improves significantly the carrier lifetime and many other electrical properties like detectivity [3]. We note that in the previous years, a very few works were reported to verify the theoretically performance of InAs/InGaSb SLs for LWIR and VLWIR photodetection. Owing to this lack of studies, we have investigated and exploited the bands structure of presented LWIR type II SL InAs(d_1=47Å)/$Ga_{0.75}In_{0.25}Sb$(d_2=21.5Å) to extract some useful electro-optical properties like the optical cut-off wavelength, the semiconductor (SC) to Semimetal (SM) transition and the effective mass of electrons and holes and many others parameters.

2. Theory

The general expression of dispersion relation of type-II SLs, within the envelope function formalism and effective mass approximation, is given by [4,5]:

$$\cos(k_z d) = \cos(k_1 d_1)\cos(k_2 d_2) - \frac{1}{2}\left[\left(\xi + \frac{1}{\xi}\right) + \frac{k_p^2}{4k_1 k_2}\left(r + \frac{1}{2} - 2\right)\right]\sin(k_1 d_1)\sin(k_2 d_2) \quad , \quad (1)$$

With k_z and $k_p(k_x,k_y)$ the wave vector in the growth direction and in-plane of the superlattice. The origin of the energy E has been chosen at the top of InAs valence band as shown in the Fig.1. In each host material and for a given energy, the two–band Kane model [6] gives the wave vector ($k_i^2+k_p^2$). Therefore, the energy E of the light particles (electron and light hole) is given by:

$$\begin{cases} \frac{2}{3}P_1^2\hbar^2\left(k_1^2 + k_p^2\right) = (E - \varepsilon_1)E \quad for\ InAs \\ \frac{2}{3}P_2^2\hbar^2\left(k_2^2 + k_p^2\right) = (E - \varepsilon_2 - \Lambda)(E - \Lambda) \quad for\ InGaSb \end{cases} \quad , \quad (2)$$

The expression of ξ and r in the Eq(1) are:

$$\xi = \frac{k_1}{k_2} r \text{ and } r = \frac{E - \Lambda - \varepsilon_2}{E - \varepsilon_1}$$

From the same equation (1), the superlattice heavy holes mini-bands can be calculated with the following relations:

$$\begin{cases} -\frac{1}{2}\frac{\hbar^2}{(m_{hh}^*)_1}\left(k_1^2 + k_p^2\right) = E \quad for\ InAs \\ -\frac{1}{2}\frac{\hbar^2}{(m_{hh}^*)_2}\left(k_2^2 + k_p^2\right) = (E - \Lambda) \quad for\ InGaSb \end{cases} \quad , \quad (3)$$

with $\xi = \frac{k_1}{k_2} r$ and $r = \frac{(m_{hh}^*)_2}{(m_{hh}^*)_1}$

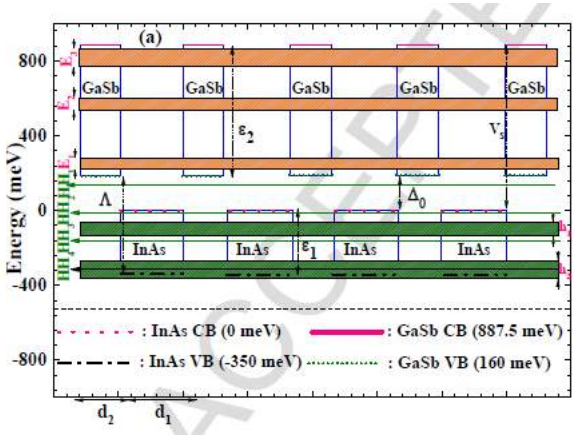


Figure 1: Illustration of InAs/GaSb SL band alignment.

The direct band gaps parameters ε_i (i= 1 and 2) used here, as a function of temperature, are given by the empirical expressions reported in [7,8]. P_i is the Kane matrix element.

The heavy holes effective masses of InAs and $In_{0.25}Ga_{0.75}Sb$ are, respectively, $(m^*_{hh})_1= 0.41m_0$ and $(m^*_{hh})_2= 0.42\ m_0$, as given in [9].

In this work, we have used the valence band offset Λ of 510 meV between heavy holes sub-bands edges of InAs and $In_{0.25}Ga_{0.75}Sb$ [10].

The computation of band structures consists of solving the general dispersion relation with the reported parameters. In the Eq. (1), state energy exists if the right-hand side lies in the range -1 to 1. In other words, $-1\leq \cos(k_z d)\leq 1$ which implies $-\pi/d \leq k_z \leq \pi/d$ in the first Brillouin zone, with $d=d_1+d_2$ is the superlattice period. In the study of energy E as a function of wave vector in the direction of growth k_z (k_p=0), the solving procedure consists of going with small steps of energy through the studied range. Then finding, for a given E, the value of k_z which is root of the dispersion relations. The same procedure is used for studying E versus the in-plane wave vector k_p (k_z=0 and $k_z= \pi/d$).

3. Results and discussions

3.1. Bands structures, band gap, cut off wavelength and carriers effective mass.

In the Fig. 2, we have plotted the energy of conduction (E_i), light-hole (h_i) and heavy-hole (HH_i) subbands at the center Γ(k_z= 0) and the limit ($k_z= \pi/d$) of the first Brillouin zone (FBZ) as a function of d_1= 2.18 d_2 at 1.2 K. These results show that when d_1 increases, the width of E_i and HH_i deceases. In addition, we can notice that the fundamental band gap energy $E_g(\Gamma)= E_1(\Gamma)-HH_1(\Gamma)$ decreases. Therefore, a crossover between E_1 and HH_1 takes place at the SC-SM transition point $T_c(d_{1c}= 115.43$ Å, $E_{1c}= HH_{1c}=$ 485.25 meV).

In fig. 3, at a given temperature the E_g decreases when the valence band offset Λ, between the top of the heavy hole bands in the two host materials, increases. The transition SC-SM occurs when E_g goes to zero. We choose for our calculations Λ =510 meV [10].

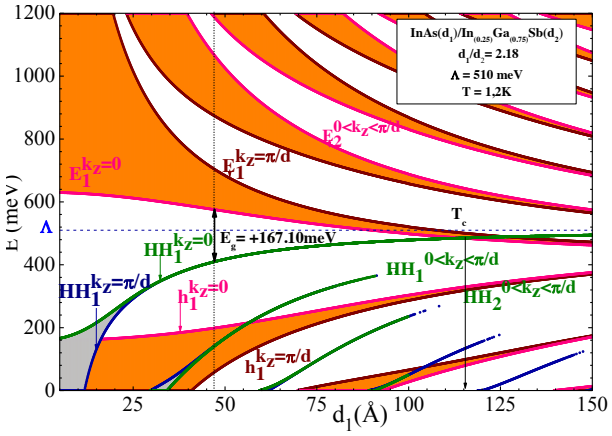


Figure 2: Energy position and width of E_i, HH_i and h_i subbands calculated at 1.2 K, in the FBZ as a function of d_1.

The evolution of the cut off wavelength $|\lambda_c|$ as a function of d_2 is shown in Fig. 4. These results were calculated by using the expression:

$$\lambda_c(\mu m)=\frac{1240}{E_g(meV)} \qquad (4)$$

The dependencies of $|\lambda_c(\Gamma)|$ on d_2 and temperature (T) are shown in Fig. 4. The figure divides itself into two regimes: **i)** For $d_2\leq d_{2c}$: for each T, $\lambda_c(\Gamma, d_2)$ increases significantly with increasing d_2. When d_2 exceeds the critical value of d_{2c}, E_1 is confounded with HH_1 at the SC-SM transition point where $\lambda_c(\Gamma, d_{2c})$ diverges. The critical d_{2c} decreases from 53.5 Å at 1.2 K to 37 Å at 300 K. Thus the SC-SM transition goes to lower d_1 when T increases. **ii)** For $d_2> d_{2c}$: E_1 falls completely below HH_1 and the SL shows an inverted bands structure with a SM conductivity. In this regime a reverse behavior was observed. The inset figure shows the sensitivity of E_g on T. This result shows that when T increases E_g shifts to lower energies with 0.21 meV/K. This is due to the fact that the thermal energy and electron-phonon interaction increase with T which lead to a reduction of the potential seen by electrons, leading to a reduced E_g.

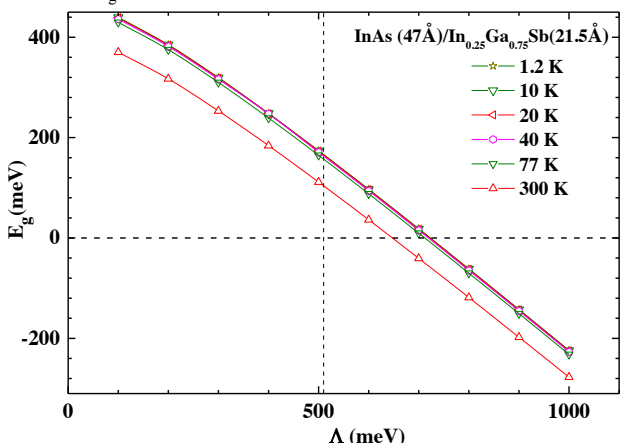


Figure 3: Band gap, E_g, as a function of the valence band offset at different temperatures in the investigated superlattice. The vertical dashed line indicates our chosen value of 510 meV.

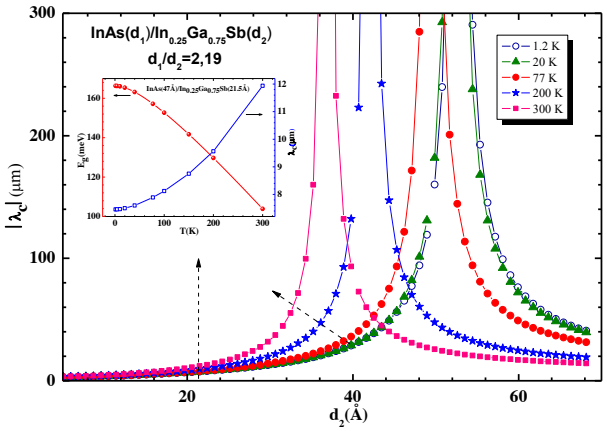


Figure 4: SL $|\lambda_c(\Gamma)|$ as a function of d_2 for various Temperatures.

The observed difference of 8.87 meV is due to the adopted input parameters here or to the fluctuations during the growth of SL which could affect E_g. In the investigated temperature range, the corresponding $7.46 \leq \lambda_c(\mu m) \leq 11.94$ situates this sample in the LWIR region.

The SL bands structure shown in Fig. 5 was computed at 1.2 K along k_z and k_p the growth and in-plan directions, respectively. Along k_z, the widths of E_1 and E_2, $|E_i(k_z=\pi/d)-E_i(k_z=0)|$, were found to be 129 and 193 meV, respectively. The presence of such dispersion indicates three dimensional like behavior of electrons which is in agreement with the reported results of Ref. [11].

The energy as a function of k_z^2 and k_p^2 at 1.2 K shows that: along k_z, the bands E_i and h_i of the light particles are non parabolic and the heavy holes bands HH_i are parabolic but along k_p, E_1 and HH_i are parabolic but h_1 is non parabolic.

The theoretical effective mass in general turns out to be a tensor with nine components defined as:

$$\frac{1}{m^*_{ij}} = \frac{1}{\hbar^2}\frac{\partial^2 E(k)}{\partial k_i \partial k_j} \qquad (5)$$

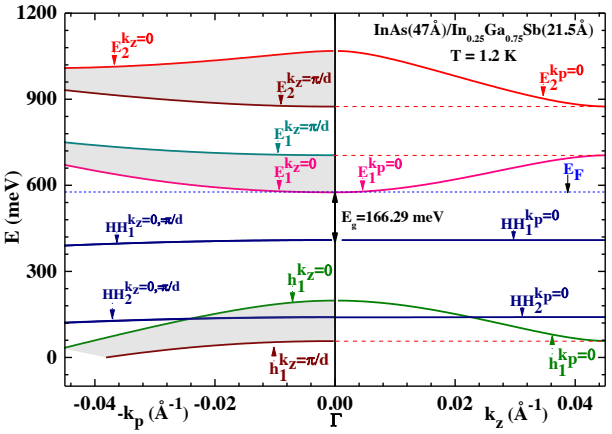


Figure 5: Band structures of the investigated SL along the k_z and k_p directions.

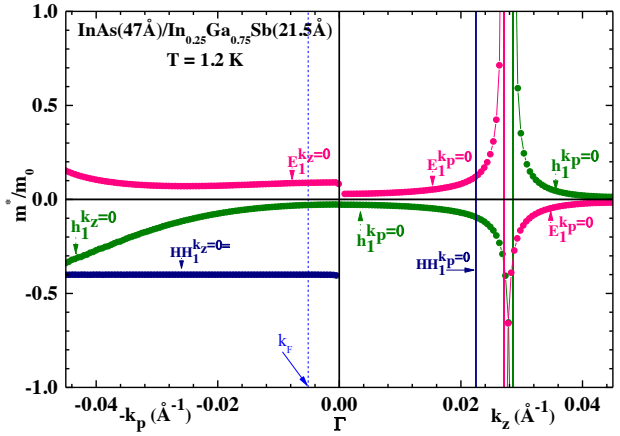


Figure 6: Calculated carriers effective mass, at Γ point, along the growth direction and in plan of the investigated SL.

The second derivative of E with respect to k is obtained directly from E(k) plotted in Fig. 5. The carriers' effective mass in both k_z and k_p directions for lowest CBs and the first highest light and heavy-hole VBs of this SL is shown in Fig. 6. This results shows that $m^*_{E1}(k_z)$ is a strongly varying function of k_z. Starting at Γ-point, diverges at $k_z = 4.9.10^{-3}$ Å^{-1} and decreases thereafter to 2.10^{-2} m_0 at $k_z = \pi/d$. The inflection point, where the effective mass changes its sign, in electron and light-hole bands, occurs at $k_z = 4.9.10^{-3}$ and $5.3.10^{-3}$ Å^{-1}, corresponding to relatively lower energies of 400 and 444 meV, respectively. This can be attributed to the fact that, because of the longer periodicity, the subbands in a SL are much narrower than that of bulk materials. Since there is no inflection point in k_p, $m^*_{HH1}(k_p)$ keep a negative constant value of -0.45 m_0, whereas $m^*_{E1}(k_p)$ becomes heavier as k_p increases.

3.2. Interpretation of the Hall Effect and the density of states

In order to determine the band gap with accuracy, we have used the carrier density measurements n of Ref. [12] with the inverse of the temperature $nT^{-3/2}$. This led to a band gap of E_g= 95 meV in the intrinsic domain, which is in agreement with 104 meV calculated at 300K. The observed difference of 8.87 meV is due to the input parameters considered here as well as fluctuations during the growth of SL which could affect E_g. Note that Szmulowicz et al. [13] have studied band structures of InAs(d_1=43.6)/$In_{0.23}Ga_{0.77}Sb$(d_2=17.3) and the origin of energy was taken at the bottom of the conduction of InAs. The InAs conduction band–GaSb valence-band overlap is taken to be 140 meV. The band gap in this structure was tailored to be 120 meV without mentioning the temperature. Whereas [11] gives E_g= 66.4 meV for the investigated SL here.

From carrier density versus inverse of temperature, we deduced the activation energy E_a-E_g=0.196 meV which is corresponding to the magnitude of thermal activation energy k_BT at 2.3 K.

The representation of mobility μ versus temperature in logarithmic scales shows that when T increases, μ decreases as $T^{-1.5}$ indicating the interaction of electrons with phonons in the intrinsic domain.

From the dispersion curves, we have derivate the SL density of states (DOS) of the two lowest conduction minibands E_i and the first valence subband HH_1. As seen in Fig 7, the DOS is quantized in term of $m^*/\pi\hbar^2 d$, with the presence of dispersion in E_i. This shows a significant interaction between wells d_1 justified by the ratio $d_1 = 2.18\ d_2$ in this sample. This indicated a tridimensional conduction behavior. Whereas the first valence subband HH_1 has a very narrow band width indicating 2D-like behavior. These results are in agreement with observations of [11].

Fig. 8 shows the energy bands of light (h_1), heavy (HH_1) holes, and E_1 electrons. As can be seen, the band gap decreases as the temperature increases. The Fermi level E_F(3D) decreases with E_1 when T increases. This is the behavior of a three-dimensional electron gas. For a two-dimensional electron gas the level of Fermi E_F(2D) is constant i.e. independent of temperature.

The position of Fermi level E_F indicates n type conductivity. These results are in agreement with the experimental observation of Mitchel et al. [12].

The conduction bands E_1 and E_2 width were $\Delta E_1 = E_1(k_z=\pi/d) - E_1(k_z=0) = 136.2$ meV and $\Delta E_2 = E_2(k_z=0) - E_2(k_z=\pi/d) = 183.3$ meV, respectively with a separation between them $\Delta E(k_z=\pi/d) = E_2 - E_1 = 232.5$ meV. The width of HH_1 was 0.01 meV along k_z.

Whereas at 1.2 K, our calculated bands structure indicated E_g=166.3 meV, ΔE_1=123 meV, ΔE_2=193 meV, and $\Delta E(k_z=\pi/d)$= 169.4 meV. The widths of HH_1 are 0.05 meV and 20.8 meV along k_z and k_p, respectively. These values are in the same range as those given by [12,13] except for the band gap given there without temperature. Our results combined to the calculated energy of Fermi level on the density of states indicated n type conductivity. So the electrons are confined to the conduction band E_1 at low temperature.

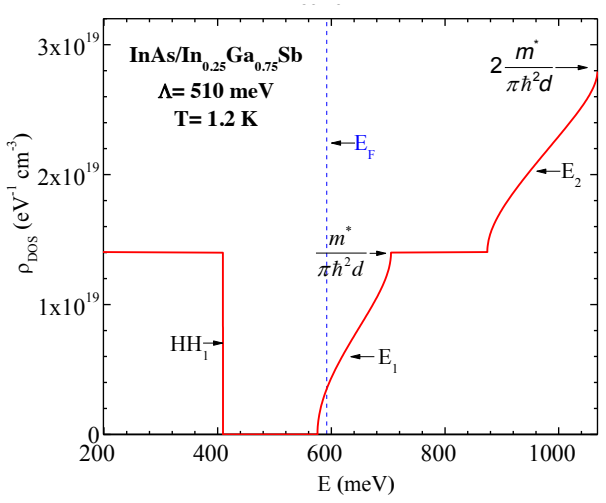


Figure 7: The SL DOS of the two lowest conduction subbands at 1.2 K. The vertical dashed line indicates the position of the Fermi level.

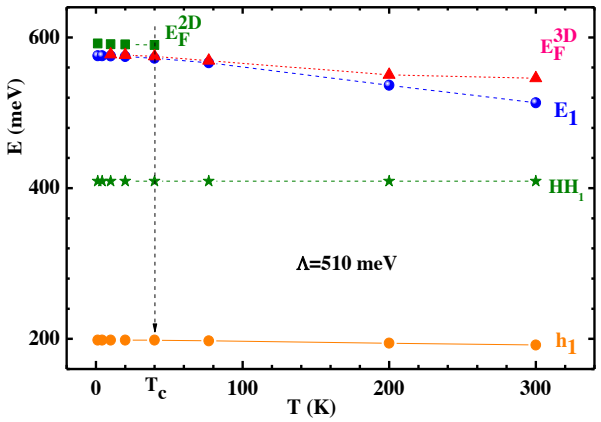


Figure 8: Energy of the first conduction (E_1), valence (HH_1 and h_1) subbands, two and three dimensional Fermi level energy (E_F) at different temperatures.

3.3. Interpretation of the Shubnikov-de Haas effect and the density of states with magnetic field B

We have calculated the Fermi level in this SL by using the magnetoresistance results reported in [11]. It is well known that, the oscillations of the magnetoresistance, due to the Shubnikov-de Haas effect (SdH), are periodic with respect to 1/B. The inverse of the minima $1/B_m$ as a function of the entire N is given by the formula:

$$\frac{1}{B_m} = \Delta\left(\frac{1}{B}\right)\left(N + \frac{1}{2}\right), \qquad (6)$$

The straight line slope of (6) gives the period, $\Delta(1/B) = 1.16\ T^{-1}$. The relation between $\Delta(1/B)$ and the electron concentration n_{3D} for a 3D system is given by:

$$n_{3D} = \left(\frac{2e}{\Delta_{1/B}\hbar\left(3\pi^2\right)^{\frac{2}{3}}}\right)^{\frac{3}{2}}, \qquad (7)$$

At T=1.2K the SL electron density is $n = 4.53\ 10^{15}\ cm^{-3}$. The later permits us to estimate the Fermi energy at 1.2 K:

$$\left|E_F - E_1\right| = \left|\frac{\hbar e}{m^*_{E1}.\Delta(1/B)}\right|, \qquad (8)$$

Here, $m^*_{E1} = 0.09\ m_0$ is the electron effective mass at the Fermi wave vector, extracted from Fig. 6. As seen in Fig. 5 and 7, E_F= 576.87 meV and the SL has an n type conductivity at 1.2 K.

In their work of InAs/InGaSb SL magnetotransport properties properties, Mitchel et al. [12] have shown that such SL shows Shubnikov-de Haas (SdH) effect. In the Fig. 8 we show the calculated Landau levels (LL) energies of E_1 in the investigated SL. These results are obtained by

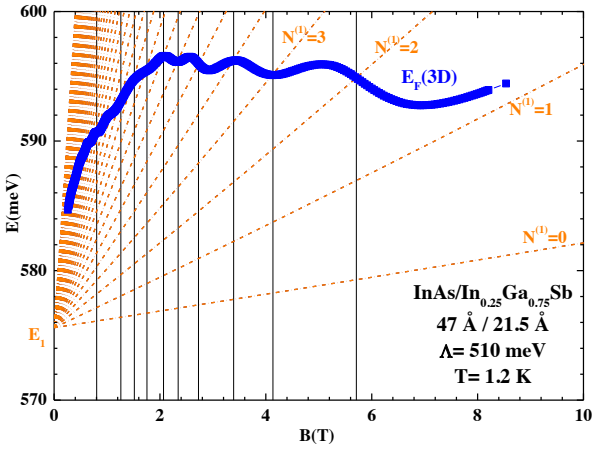


Figure 9: Calculated Landau levels as a function of the applied magnetic field in the investigated SL at 1.2 K. E_F is the Fermi level energy.

transposing the quantification rule of the wave vector in the plan of the SL in $E(k_p)$ plotted in Fig. 5:

$$k_p^2=(2N+1)\frac{eB}{\hbar}, \qquad (9)$$

With N the LL index.

The Fermi energy as a function of the applied magnetic field has been calculated by using formula (10) with N_{SL}=73 is the SL number of periods. Hall resistance has been

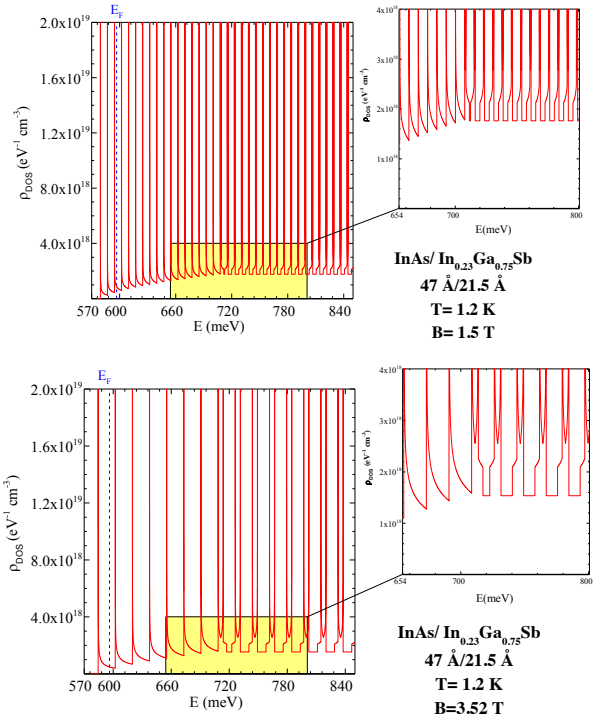


Figure 10: DOS of the first conduction subbands at 1.2 K in the presence of magnetic field B.

calculated with the following: $R_{xy}(\Omega)=h/\nu N_{SL}e^2$ and ν is the filling factor.

$$E_F=\frac{\hbar^2}{2m^*}\left(\frac{3\pi^2 B}{R_{xy}.e.N.(d_1+d_2)}\right)^{2/3}, \qquad (10)$$

In the Fig. 9,when the magnetic field increases, the crossover between

the calculated LL energy and the Fermi level gives the same minima (at B=5.71 T, 4.13 T, 3.40 T, 2.73 T and 2.34 T), of the Shubnikov-de Haas effect (SDH) oscillations of the transverse magneto-resistance measured by [12].

The Fig. 10 represents the computed density of states (DOS) of the first conduction mini-band of the investigated SL by using the following expression:

$$\rho_{DOS}^{3D}(E,B_z)=\frac{|e|B_z}{8\pi^2\hbar^2}\sqrt{2m^*}\sum_i\sum_{N^{(i)}=0}^{N_{max}^{(i)}}\frac{1}{\sqrt{E-\left(N^{(i)}+\frac{1}{2}\right)\hbar\omega_c}}, \qquad (11)$$

As can be seen in the figure the DOS is inversely proportional to the square root of total energy and the spacing between LL increases when the applied magnetic field decreases.

A condition for the observation of the SDH effect is that the separation $\hbar\omega_c$ (ω_c=eB/m^*_{E1} is the cyclotron pulsation) between LL must be superior to activation thermal energy k_BT. So here the magnetic field must be $B > k_B m^*_{E1} T/\hbar e$ = 0.9 T for T=1.2 K and m^*_{E1}=0.09 m_0. When B< 0.9 T, the LLs disappear and E_1 is a continuum. This condition of quantum limit agrees well with our calculated DOS (E_1, B) in Fig. 10.

We also calculated the transport scattering time $\tau_p=\mu_H m^*_{E1}/e$ =0.52 ps for Hall mobility μ_H=1.02 10^4 cm^2/Vs measured at 1.2 K by [12] and our m^*_{E1}=0.09 m_0. This value of τ_p can be compared to the quantum relaxation time τ_q= 0.5 ps and τ_p=2.34 ps measured in AlGaN/GaN two-dimensional electron gas [14].

4. Conclusion

Using the envelope function formalism, we have investigated the electronic and optical properties of LWIR InAs(d_1=2.18d2)/$In_{0.25}Ga_{0.75}Sb$ (d_2=21.5Å) type II SL. The dependencies of the band gap and the corresponding cut-off wavelength on layer's thicknesses and temperature was studied and interpreted. Our results show that a very smaller band gap can be achieved with reasonably thinner layers. The SC-SM transition was found to go to lower d_{1c} and/or d_{2c} when the temperature increases. Transport properties of this sample indicate a tridimensional conduction behavior. Whereas the first valence subband HH_1 shows 2D-like behavior. The densities of states without and as a function of magnetic field of the lowest subbands were computed at 1.2 K. The condition of quantum limit agrees well with our calculations. In the intrinsic regime, our results agree well with experimental observations of W. C. Mitchel et al.

References

[1] D. L. Smith and C. Mailhiot, Theory of semiconductor superlattice electronic structure, *Rev. Mod. Phys.* **62**: 173, 1990.

[2] A. Boutramine, A. Nafidi, D. Barkissy, E.-S. El-Frikhe, H. Charifi, A. Elanique, and H. Chaib, Electronic band structure and Shubnikov-de Haas effect in two-dimensional semimetallic InAs/GaSb nanostructure superlattice. *Appl. Phys. A Mater. Sci. Process*. 122 : 1 , 2016.

[3] C. H. Grein, W. H. Lau, T. L. Harbert, and M. E. Flatte, Modeling of very long infrared wavelength InAs/GaInSb strained layer superlattice detectors , *in edited by R. E. Longshore and S*. Sivananthan, p:39, 2002.

[4] G. Bastard, Theoretical investigations of superlattice band structure in the envelope-function approximation**,** *Phys. Rev. B* 25:7584, 1982.

[5] D. Barkissy, A. Nafidi, A. Boutramine, N. Benchtaber, A. Khalal, and T. El Gouti, Electronic transport and band structures of GaAs/AlAs nanostructures superlattices for near-infrared detection, *Appl. Phys. A* ,123: 61 , 2017.

[6] E. O. Kane, Band structure of indium antimonide, *J. Phys. Chem. Solids,* **1**:249,1957.

[7] F. Matossi and F. Stern, Temperature Dependence of Optical Absorption in p-Type Indium Arsenide, *Phys. Rev*. 111: 472, 1958.

[8] A. P. Roth, W. J. Keeler, and E. Fortin, Photovoltaic effect and temperature dependence of the energy gap in the $In_{1-x}Ga_xSb$ alloy system, *Can. J. Phys*. 58: 560, 1980.

[9] M. Levinshtein, S. Rumyantsev, and M. Shur, *Handbook Series on Semiconductor Parameters* (WORLD SCIENTIFIC, 1996).

[10] G. J. Gualtieri, G. P. Schwartz, R. G. Nuzzo, R. J. Malik, and J. F. Walker, Determination of the (100) InAs/GaSb heterojunction valence band discontinuity by Xray photoemission core level spectroscopy, *J. Appl. Phys*. 61:5337,1987.

[11] W. C. Mitchel, S. Elhamri, H. J. Haugan, G. J. Brown, S. Mou, and F. Szmulowicz, Shubnikov–de Haas Effect in InGaSb/InAs superlattices, *J. Appl. Phys*. 122: 185106, 2017.

[12] W. C. Mitchel, S. Elhamri, H. J. Haugan, G. J. Brown, S. Mou, and F. Szmulowicz, Multicarrier transport in InGaSb/InAs superlattice structures, *J. Appl. Phys*. 120: 175701, 2016.

[13] F. Szmulowicz, Numerically stable secular equation for superlattices via transfer-matrix formalism and application to $InAs/In_{0.23}Ga_{0.77}Sb$ and $InAs/In_{0.3}Ga_{0.7}Sb/GaSb$ superlattices, *Phys. Rev. B*, 57: 9081, 1998.

[14] A.Saxler, P. Debray, R. Perrin, et al, Electrical transport of an AlGaN/GaN two-dimensional electron gas, *Materials Research Society Internet Journal of Nitride Semiconductor Research,* Volume 5 Issue s1, 2014.

Biophotonics

On-Chip Sensing and Multiplexing Platform for miRNA in Cancer Cell based on Nanoplasmonics

Sang-Heon Park[1, 2], Jihye Lee[1, 2], and Jong-Souk Yeo[1, 2*]
[1] School of Integrated Technology, Yonsei University, Incheon, Republic of Korea
[2] Yonsei Institute of Convergence Technology, Yonsei University, Incheon, Republic of Korea
[*]corresponding author: jongsoukyeo@yonsei.ac.kr

Abstract

We demonstrate on-chip colorimetric sensing platform by using nanoplasmonics. By using an emitting and quenching characteristic of quantum dot and gold nanoparticle, we can distinguish the different type of miRNA in gastric cancer cell, thus enabling the multiplexing platform for maximizing the usefulness for clinical sensing applications.

1. Introduction

Recent evidences have shown that microRNAs (miRNAs) are promising biomarkers for cancer diagnosis.[1] Some of miRNAs showing abnormal concentration of ratio in patient serum and plasma can be used as potential biomarkers for clinical applications in a specific organ.[2] In order to detect these miRNA in cancer cell, our group has demonstrated the on-chip miRNA sensing platform using an optical and electrical characteristics of nanoplasmonics. One of the optical approaches for detecting a miRNA is plasmonic coupling method by hybridizing the target oligonucleotide on the gold nanoparticles. This coupling method can detect the miRNA-21 (miRNA in breast cancer cell) with 1 pM limit of detection (LOD) on on-chip glass sensing platform and with 10 fM LOD on a flexible substrate platform, especially using a side edge of the nanostructure on a substrate [3] [4]. These coupling methods are also applied to the gastric cancer cell detection. The miRNA-106a that is one of the biomarker in a gastric cancer cell is up-regulated marker. In order to detect this highly concentrated single marker, we demonstrated the colorimetric sensing approach using 50 nm and 30 nm gold nanoparticles (AuNPs). Other method based on electrical sensing using plasmonics has been demonstrated on the gold nanowire arrays. This electrical sensing utilized the negative photoconductivity of metal nanowires so that we can differentiate the small concentration of molecules with electrical signal [5]. However, all the methods so far only focused on a single strand of target miRNA and maximized the sensitivity and selectivity for detecting the single miRNA in breast and gastric cancer cell and further development is necessary to enable clinically meaningful technique.

In here, we demonstrate the multiplexing approach for detecting the different types of miRNAs in cancer cells. Using gold nanoparticles and quantum dota, we distinguish the different types of miRNAs by on chip sensing platform.

2. Result and Discussion

On the organosilane treated (APTES/OTMS = 3:1) quartz substrate, core AuNPs (diameter of 50 nm) which were functionalized with one probe (probe 1) were distributed in the optimal density showing green color. The satellite AuNPs (diameter of 30 nm) were pre-functionalized with another probe (probe 2). The probe 1 and probe 2 are 12 mer long oligonucleotide with the sequence complementary to both ends of target miRNA sequence. When the satellite AuNPs hybridized with the single core AuNPs mediated by miRNA, the core-satellite assemblies are made. These nanoscale assemblies lead to the colorimetric change, thus enabling the detection of miRNA corresponding to the miRNA concentration. While the single core AuNPs show green color with 550 nm wavelength, hybridized structure with the 10 μM concentration of miRNA is applied showing nearly 660 nm wavelength due to the plasmon coupling effect.

We develop a method further for detecting multiplexed miRNA signal with quantum dots (QDs) and AuNPs as a quencher. We used the glass substrate treated by O_2 plasma and organosilanes to make optimal density of AuNPs on the substrate. On the treated glass substrate, we dispersed AuNPs as a quencher.[6] The AuNPs are pre-functionalized with an oligonucleotide probes which are matched with one end of miRNA. Then, different kinds of QDs with various light emission frequency are pre-functionalized with the probes which are matched with the other end of miRNA. Functionalized QDs emit the light ordinarily, however when it binds with substrate functionalized with AuNPs, the emission is quenched by plasmon-resonance energy transfer (PRET). When circulating miRNA has sufficiently high concentration, the probes functionalized on QDs conjugate with miRNA by pairing complementary sequences. Thus, quenched QDs re-emit the light and we can detect the specific frequency of QDs recognizing which miRNA has abnormal concentration.

3. Conclusions

To make on-chip detection for point-of-care test (POCT) platform, we modified the substrate with self-assembled monolayers of organosilanes to achieve a density of AuNPs as a quencher. On a modified substrate, we have dispersed pre-functionalized QDs so that the light emission of QDs is

quenched by AuNPs. When, miRNA concentration is high enough to detect, QDs functionalized with the probes having complement sequences to the target miRNA break up with the quencher and conjugate with target miRNA by pairing a complementary sequence. Thus, QDs re-emit the inherent light frequency. We show the highly specific and sensitive optical detection by quenching and re-emitting the inherent light emission frequency of QDs as a label to detect multiplexed miRNA.

Acknowledgements

This research was supported by the MSIT (Ministry of Science and ICT), Korea, under the ICT Consilience Creative program (IITP-2017-2017-0-01015) supervised by the IITP (Institute for Information & communications Technology Promotion) and also under the "Mid-career Researcher Program" (NRF-2016R1A2B2014612) supervised by the NRF (National Research Foundation).

References

[1] T. Paranjape, F. Slack, J. Weidhaas, MicroRNAs: tools for cancer diagnostics, *Gut*, 58: 1546-54, 2009.
[2] E. Larrea, C. Sole, L. Manterola, I. Goicoechea, M. Armesto, M. Arestin, et al., New Concepts in Cancer Biomarkers: Circulating miRNAs in Liquid Biopsies, *Int. J. Mol. Sci.,* 17: 627, 2016.
[3] J. Lee, J. Park, J.Y. Lee, J.S. Yeo, Contact Transfer Printing of Side Edge Prefunctionalized Nanoplasmonic Arrays for Flexible microRNA Biosensor, *Adv. Sci*, 2: 201500121, 2015.
[4] J. Park, J.-S. Yeo, Colorimetric detection of microRNA miR-21 based on nanoplasmonic core–satellite assembly, *Chem. Comm*, 50: 1366-1368, 2014.
[5] J.-H. Kim, J.-S. Yeo, Enhanced detection of broadband incoherent light with nanoridge plasmonics, Nano letters, 15(2015) 2291-7.
[6] A. Samanta, Y. Zhou, S. Zou, H. Yan, Y. Liu, Fluorescence quenching of quantum dots by gold nanoparticles: a potential long range spectroscopic ruler, *Nano letters*, 14: 5052-5057, 2014.

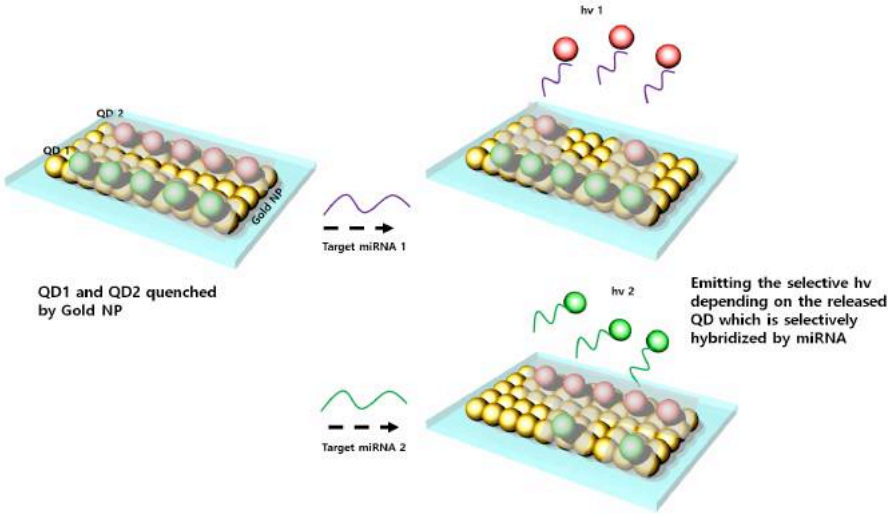


Fig. 1. Schematic of multiplexed miRNA optical sensing method. Different kinds of QDs which emit different frequency of light functionalized with probes which have complementary sequence with target miRNA. QDs are used as miRNA label. Pre-functionalized QDs are dispersed on AuNPs modified glass substrate. AuNPs on a substrate quenched the emission of QDs, so that prepared substrate does not emit any light. When miRNA concentration is high enough to bind with functionalized QDs, QDs break the binding with AuNPs and re-emit the inherent light.

Transformational Electromagnetics, Cloaking

Cloaking a magnetic sensor

Rosa Mach-Batlle*, Carles Navau, Alvar Sanchez

Departament de Fisica, Universitat Autonoma de Barcelona, 08193 Bellaterra, Barcelona, Spain
*corresponding author, E-mail: rosa.mach@uab.cat

Abstract

Magnetic sensors are employed in a wide range of technologies. Most sensors contain ferromagnetic materials because of the field attraction they provide. This limits the sensor applicability, because ferromagnets distort the probing field, which may be an issue in some applications. Here we present a novel strategy on how to make a three-dimensional sensor magnetically undetectable while maintaining its ability to sense.

1. Introduction

Static magnetic fields are essential for many technologies, including biomedical techniques, transportation, motors or generators. Fields are usually shaped with the use of magnetic materials, which depending on their permeability attract or repel the magnetic field lines. Magnetic metamaterials, which consist of tailored arrangements of natural materials, have allowed the development of novel ways of shaping static magnetic fields. For example, concentrators that enhance the magnetic field have been introduced as a way to enhance the sensitivity of a magnetic sensor [1, 2].

There are many types of sensors to measure static magnetic fields. Most of them make use of ferromagnetic materials because of their ability to attract magnetic field lines. This field attraction comes at the prize of making the sensor detectable. Based on the idea of cloaking a sensor by the scattering cancellation technique [3], we present a new strategy on how to cloak a magnetic sensor [4]. A practical realization will be devised using a metasurface composed of superconducting elements.

2. Invisible magnetic sensors

We assume that the distortion a magnetic sensor creates is due to its ferromagnetic components, which either intrinsically constitute the sensor or are used to enhance the sensor sensitivity. We thus model a sensor as a ferromagnetic material.

In Figure 1(a) we show how a ferromagnetic sphere distorts a uniform magnetic field. Following the recent advances in magnetic metamaterials, one could think of surrounding the sensor by a magnetic invisibility cloak to cancel its distortion [5, 6]. However, as shown in Figure 1(b), the use of a bilayer cloak [5] is not appropriate in this case, because the sensor would be completely isolated from its external surrounding and therefore unable to measure the external field.

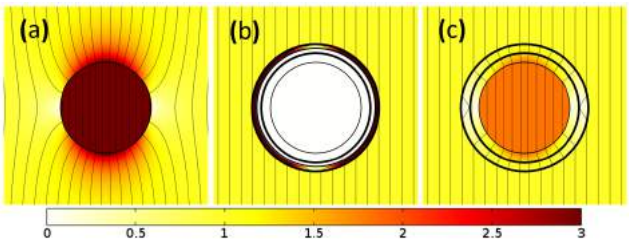


Figure 1: Modulus of the magnetic induction normalized to the applied magnetic field H_0, $B/(H_0\mu_0)$, and magnetic induction field lines for (a) a ferromagnetic sphere, (b) the sphere in (a) surrounded by a bilayer magnetic cloak and (c) the sphere in (a) surrounded by a cloaking device.

Our cloaking shell is different from the bilayer invisible cloak since it allows the sensor to receive magnetic field lines while being exactly undetectable [4]. This is achieved at the cost of reducing the sensor sensitivity because there are less magnetic field lines arriving to the ferromagnetic material [see Figure 1(c)].

We analytically demonstrate that spherical sensors in uniform applied magnetic fields, which only create a dipolar response, can be made exactly invisible by a single layer spherical shell. When the distortion the sensor creates is more complex, as for non-spherical objects and non-uniform applied fields, a single layer shell can also largely reduce the distortion the sensor creates. For sensors which create a multipolar field distortion, extra layers can be added to the shell to reduce not only the dipolar term of the distortion but also higher ones, as the quadrupolar or the sextupolar.

3. Discussion

The cloaking shell that cancels the distortion created by a ferromagnetic material is diamagnetic, since it has to repel the magnetic field lines to compensate for the attraction of the ferromagnet. Diamagnetic materials with intermediate values of the permeability may be hard to find in nature. A practical solution to obtain the required shell permeability is the use of metamaterials. One could construct, for example, a metasurface consisting of superconducting pieces, with permeability approximately zero, arranged to effectively yield the necessary intermediate permeability value.

4. Conclusions

We have presented a cloaking shell that cancels (or largely reduces) the field distortion a magnetic sensor creates without losing its ability to sense. The shell reduces the magnetic field lines the sensor receives by a factor that depends on its geometry, which can be calculated by the theory. Cloaking magnetic sensors can be advantageous for applications requiring non-invasive sensing.

Acknowledgement

We thank European Union Horizon 2020 Project FET-OPEN MaQSens (grant agreement 736943), and project MAT2016-79426-P (Agencia Estatal de Investigacion / Fondo Europeo de Desarrollo Regional) for financial support. A. S. acknowledges a grant from ICREA Academia, funded by the Generalitat de Catalunya.

References

[1] C. Navau, J. Prat-Camps, and A. Sanchez, Magnetic Energy Harvesting and Concentration at a Distance by Transformation Optics, *Phys. Rev. Lett.* 109: 263903, 2012.

[2] C. Navau, R. Mach-Batlle, A. Parra, J. Prat-Camps, S. Laut, N. Del-Valle and A. Sanchez, Enhancing the sensitivity of magnetic sensors by 3D metamaterial shells *Sci. Rep.* 7: 44762, 2017.

[3] A. Alu, and N. Engheta, Cloaking a sensor, *Phys. Rev. Lett.* 102: 233901, 2009.

[4] R. Mach-Batlle, C. Navau, and A. Sanchez, Invisible magnetic sensors, *preprint*.

[5] F. Gomory, M. Solovyov, J. Souc, C. Navau, J. Prat-Camps, and A. Sanchez, Experimental Realization of a Magnetic Cloak, *Science* 335: 1466, 2012.

[6] J. Prat-Camps, C. Navau, and A. Sanchez, A magnetic wormhole, *Sci. Rep.* 5:12488, 2015.

CMA-ES based topology optimization for external cloaks

Garuda Fujii[1]

[1]Institutute of Engineering, Shinshu University, Nagano, Japan
*corresponding author, E-mail: g_fujii@shinshu-u.ac.jp

Abstract

This paper presents topology optimization for external cloaks which can render a scattering object at a distance invisible. To design external cloaks, the intensity of the scattered electric field is minimized as the objective function and external cloaks are transformed in a fixed design domain which is set at a distance from a PEC scattering object. A level set method is used to express external cloaking structures made of dielectrics without any grayscales that are intermediate materials between air and dielectrics. Obtained optimal configurations prevent scattering caused by PEC.

1. Introduction

Optical invisibility [1, 2] has been actively studied in the past decade and spread, by analogies, to acoustic cloaks, thermal cloaks, direct current electric cloaks, and fluid flow cloaks. External cloaks [3, 4] are the optical devices that cloak a scattering object at a distance outside the cloaks by reproducing the electromagnetic field when no scattering object exists.

Topology optimizations are known as a powerful approaches to enhance the performance of devices in engineering. The design methodology provided optimal design of cloaking devices having superior performances and are applied to the designs of optical cloaks [5], carpet cloaks [6], thermal cloaks [7], and DC electric cloaks [8].

In this work, we presents topology optimization for external cloaks expressed by level set functions explored by covariance matrix adaptation evolution strategy (CMA-ES).

2. Topology optimization for external cloaks

The performance of external cloaks is evaluated by the amount of scattering caused by scattering objects. Then, the objective function Ψ is set to be integrated intensity of scattered electric field as

$$\Psi = \frac{1}{\Psi^{\mathrm{n}}} \int_{\Omega_{\mathrm{out}}} |E_{\mathrm{s}}|^2 \, d\Omega,$$

where E_{s} represents a scattered electric field, Ψ^{n} is the value for normalization of the objective function as

$$\Psi^{\mathrm{n}} = \int_{\Omega_{\mathrm{out}}} |E_{\mathrm{bare}}|^2 \, d\Omega,$$

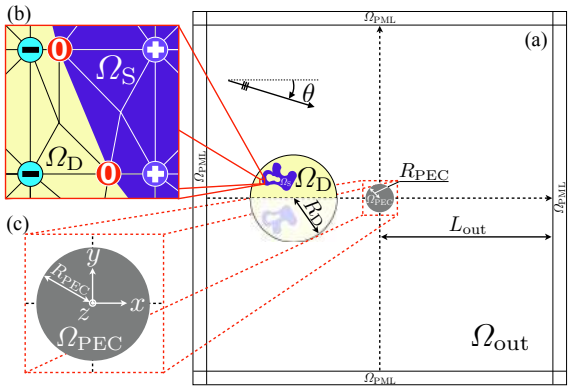


Figure 1: (a) Scheme of topology optimization for external cloaks. (b) Level set function and structural boundaries. (c) Cloaked PEC and each axis.

where E_{bare} represents a scattered electric field when the bare scattering object presents in the absence of cloak. The E_{s} follows Helmholtz equation as

$$\nabla^2 E_{\mathrm{s}} + \frac{\omega^2}{c^2}\epsilon(\mathbf{x})E_{\mathrm{s}} = -\frac{\omega^2}{c^2}[\epsilon(\mathbf{x}) - \epsilon_{\mathrm{air}}]E_{\mathrm{i}},$$

where E_{i} denotes the incident electric field satisfying $E_z = E_{\mathrm{s}} + E_{\mathrm{i}}$, ω the circular frequency of light, and c the velocity of light in vacuum.

Topology optimization is an ill-posed problem and the optimization must employ the relaxation of design space or the regularization by the geometrical constraint. In this study, we employ a perimeter constraint that is a kind of geometrical constraints and a minimize fitness as follows:

$$\inf_{\phi} \qquad F_{\mathrm{top}} = \Psi + \tau L_{\mathrm{p}},$$

where τ is regularization parameter, and L_{p} is the length of Γ_{S} which is the boundary between Ω_{S} and Ω_{D}.

With ϵ_{air} and ϵ_{S} denoting the relative permittivities of air and dielectric material of designed structures, respectively, the position-dependent relative permittivity $\epsilon(\mathbf{x})$ is defined as

$$\epsilon(\mathbf{x}) = \begin{cases} \epsilon_{\mathrm{air}} + \chi(\epsilon_{\mathrm{S}} - \epsilon_{\mathrm{air}}) & \mathbf{x} \in \Omega_{\mathrm{D}} \\ \epsilon_{\mathrm{air}} & \mathbf{x} \in \Omega_{\mathrm{out}} \end{cases},$$

where χ is the characteristic function,

$$\chi(\phi(\mathbf{x})) = \begin{cases} 1 & \text{if} \quad \mathbf{x} \in \Omega_{\mathrm{S}} \\ 0 & \text{if} \quad \mathbf{x} \in \Omega_{\mathrm{D}} \backslash \Omega_{\mathrm{S}} \end{cases},$$

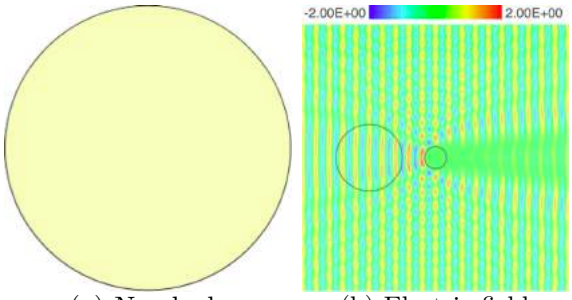
and $\phi(\mathbf{x})$ denotes a level-set function whose isosurfaces provide clear structural boundaries such that

$$\begin{cases} -1 \leq \phi(\mathbf{x}) < 0 & \forall \mathbf{x} \in \Omega_{\mathrm{D}} \backslash \Omega_{\mathrm{S}} \\ \phi(\mathbf{x}) = 0 & \forall \mathbf{x} \in \Gamma_{\mathrm{S}} \\ 0 < \phi(\mathbf{x}) \leq 1 & \forall \mathbf{x} \in \Omega_{\mathrm{S}} \backslash \Gamma_{\mathrm{S}} \, . \end{cases}$$

The level set function is discretized to the grid points as shown in Fig. 1(b) and is expressed as the vector $\boldsymbol{\phi} = \{\phi_1, \cdots \phi_j, \cdots \phi_N\}$ where N is the number of discretized level set functions. The optimal vector $\boldsymbol{\phi}$ minimizing F_{top} is explored by CMA-ES employing a box constraint [9].

2.1. Results

Figure 2(a) shows the fixed design domain Ω_{D} without cloaks and Fig. 2(b) shows light scattering caused by bare PEC. Light waves are scattered at the surface of the PEC and interference between incident and scattered waves are observed in Fig. 2(b).



(a) No cloak (b) Electric field

Figure 2: Fixed design domain without cloak and electric field scattered by PEC.

Figure 3(a) represents obtained optimal configuration under $\tau = 1 \times 10^{-3}$. The blue color represents the domains of dielectric material given by $\epsilon = 2.0$ and the light yellow represents air domains given by $\epsilon = 1.0$. Figure 3(b) shows the scattered light when the obtained optimal configurations exist at left side of the PEC domain. The light scattering is prevented by the designed external cloaks.

3. Conclusions

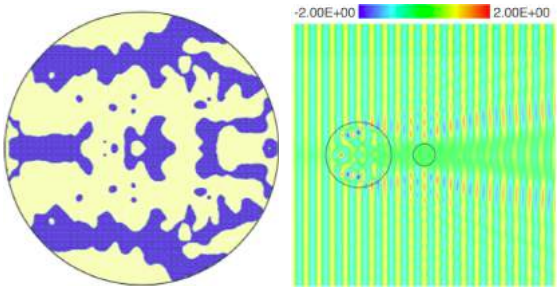
This paper presents optimal design of external cloaks obtained by topology optimization based on CMA-ES. Obtained optimal configuration present light scattering caused by PEC.

Acknowledgement

This work is supported by JSPS KAKENHI [Grant No. 17K17778].

References

[1] U. Leonhardt, Optical conformal mapping, *Science* 312: 1777–1780, 2006.



(a) Optimal configuration (b) Electric field

Figure 3: Result of topology optimization obtained under $\tau = 1 \times 10^{-3}$. The blue color represents the domains of dielectric material given by $\epsilon = 2.0$ and the light yellow represents air domains given by $\epsilon = 1.0$.

[2] J.-B. Pendry, D. Schurig and D.-R. Smith, Controlling Electromagnetic Field, *Science*, 312: 1780–1782, 2006.

[3] Y. Lai, H. Chen, Z.-Q. Zhang, and C. T. Chan, Complementary media invisibility cloak that cloaks objects at a distance outside the cloaking shell, *Phys. Rev. Lett.*, 102: 093901, 2009.

[4] T. Han, X. Tang, and F. Xiao, External cloak with homogeneous material, *J. Phys. D: Appl. Phys.*, 42(23): 235403, 2009.

[5] G. Fujii, H. Watanabe, T. Yamada, T. Ueta and M. Mizuno, Level set based topology optimization for optical cloaks, *Appl. Phys. Lett.* 102(25): 251106, 2013.

[6] G. Fujii and T. Ueta, Topology-optimized carpet cloaks based on a level-set boundary expression, *Phys. Rev. E*, 94(4): 043301, 2016.

[7] G. Fujii, Y. Akimoto, and M. Takahashi, Exploring optimal topology of thermal cloaks by CMA-ES, *Appl. Phys. Lett*, (accepted).

[8] G. Fujii, Y. Akimoto and M. Takahashi, Achieving direct current electric invisibility through a topology optimization based on CMA-ES, *J. Appl. Phys.*, (submitted).

[9] G. Fujii, M. Takahashi and Y. Akimoto, CMA-ES-based structural topology optimization using a level set boundary expression—Application to optical and carpet cloaks, *Computer Methods in Applied Mechanics and Engineering*, 332, 624 – 643, 2018, (submitted).

FSS, HIS and Extraordinary Transmission

Extraordinary Transmission in Mid-IR through a perforated doped silicon film

Hosam Mekawey[1*], Yehea Ismail[1], Mohamed Swillam[2]

[1]School of Science and Engineering, Center of Nanoelectronics and Devices (CND), The American University in Cairo, Zewail City of Science and Technology, Egypt
[2]Department of Physics, School of Science and Engineering, The American University in Cairo, New Cairo, 11835, Egypt
*corresponding author, E-mail: hmekawey@aucegypt.edu

Abstract

In this work, the plasma dispersion effect is introduced into silicon film with an array of sub-wavelength holes. The effect on the fundamental modes of the subwavelength rectangular hole and their dispersion is studied. The transmission through such subwavelength hole array is investigated showing an enhanced transmission mimicking the Extraordinary Transmission (EOT) phenomenon reported in real metallic films with array of subwavelength holes. In case of silicon with carrier concentration as the thin film material, the enhanced transmission is observed in the near and mid-IR spectral range instead of the visible range as in the case of metallic films. By tuning the excess carriers' concentration, the extraordinary transmission characteristics can be tuned and engineered.

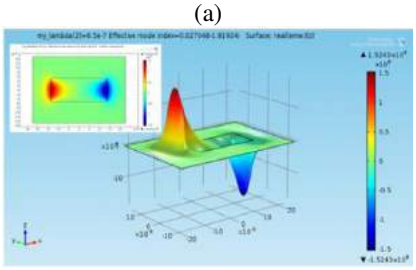
1. Introduction

Transmission through subwavelength holes in a perforated metal film was expected to be very poor according to Bethe theory of diffraction [1]. However, in 1998, experiments have shown an extraordinary transmission (EOT) through such sub-wavelength holes that was many orders of magnitude greater than what was expected by the tradition diffraction theory [2]. Such EOT can be exploited in applications like sensing, color filtering and metamaterials amongst other applications [3-8]. In this work, an investigation of the possibility of replacing the metallic material of the perforated film with a doped silicon in order to generate EOT at mid-IR instead of visible which is the case when using metals.

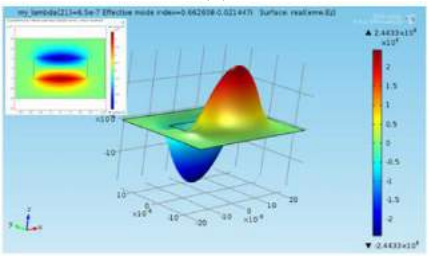
2. Results and discussion

The fundamental guided modes of light through a rectangular hole array have been studied extensively in [9]. It was found that the fundamental Vertical Odd (VO) and Horizontal Odd (HO) modes through a silver film with subwavelength rectangular hole array has the modal profile and dispersion shown in figure 1 below.

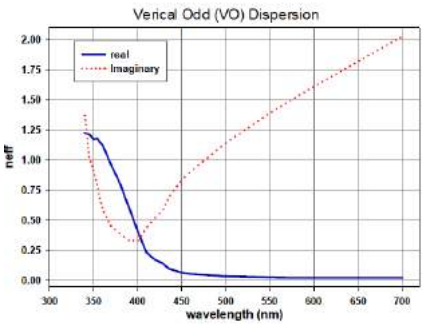
(a)



(b)



(c)



(d)

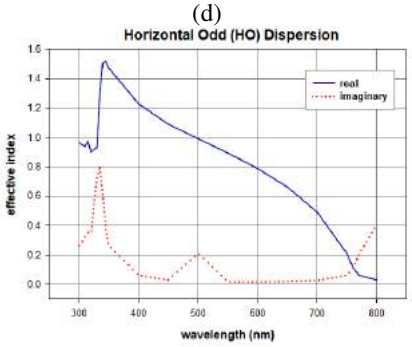


Figure 1: Modal profile for the fundamental VO and HO (a, and b). The dispersion relation for the VO and HO modes (c, and d) in a perforated silver film.

By using phosphorus-doped silicon with concentration of 1E+20 cm^{-3}, the cutoff wavelength in the dispersion curves of the VO and HO modes are red shifted when compared to the case of perforated silver film. VO and HO modal profile and dispersion are shown in figure 2.

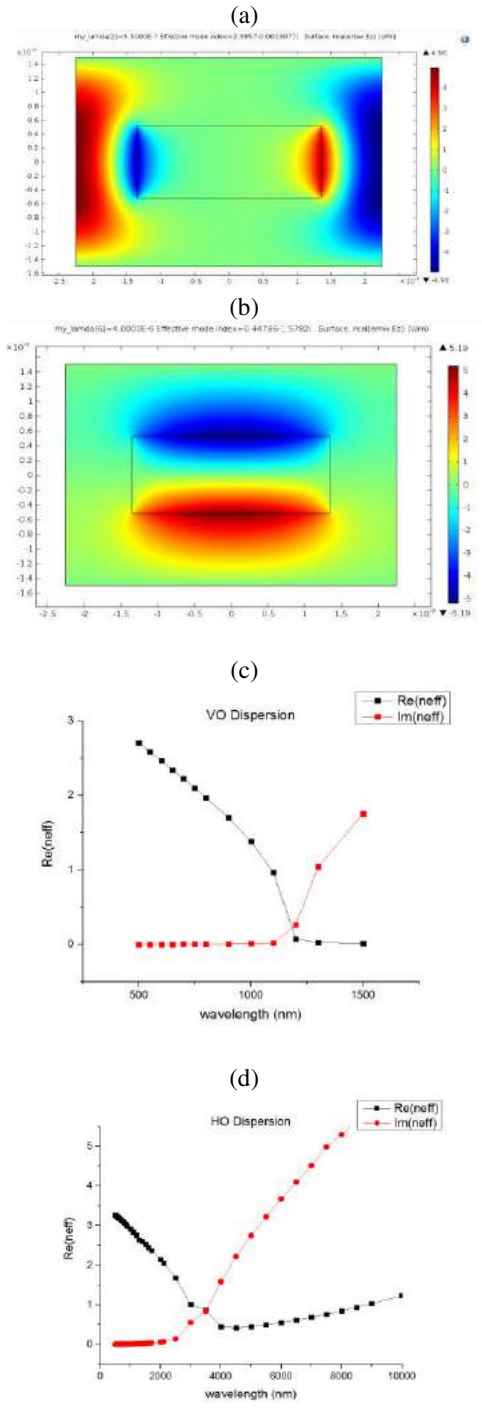


Figure 2: modal analysis and dispersion relation for the VO and HO modes in perforated doped silicon film.

The normalized-to-area transmission spectrum through a silver film perforated with 270x105 nm rectangular hole array is shown in figure 3.a. An extraordinary transmission (EOT) appears in the range from 680 nm to 850 nm. While the transmission through perforated doped Si film is shown in figure 3.b. The EOT in the case of perforated silicon film is red shifted to 2200 nm.

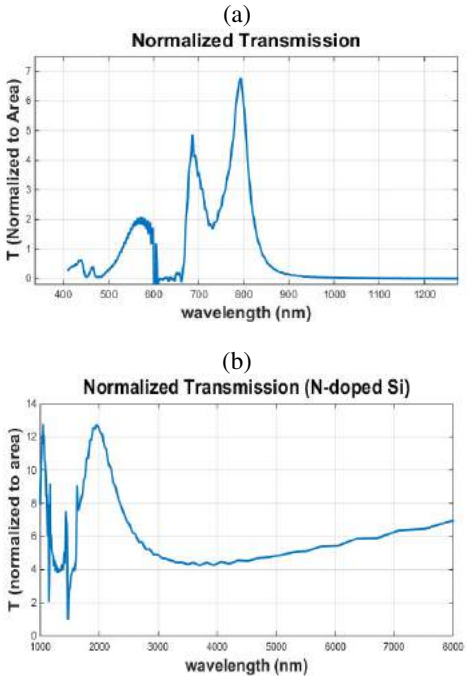


Figure 3: Normalized to area transmission in (a) perforated silver film and (b) perforated n-doped silicon film.

3. Conclusions

By replacing the silver with N-doped silicon with 1E+20 cm^{-3} concentration as the material of a thin film perforated with rectangular subwavelength hole array, a red shift in the cutoff of the fundamental VO and HO modes has been identified and by analyzing the transmission through such perforated film in both material cases, it is found that a EOT was successfully realized in the mid-IR when using the doped silicon. Hence successfully mimicking the behavior of metal in generating EOT, but in mid-IR instead of the visible spectral range. The enhancement has also increased in magnitude in the case of doped silicon, in comparison to the enhancement when using silver.

Acknowledgements

This research was partially funded by Zewail City of Science and Technology, AUC, STDF, Intel, Mentor Graphics, ITIDA, SRC, ASRT and MCIT.

References

[1] Bethe, H.A., Theory of Diffraction by Small Holes. Phys. Rev. Lett., 1944. 66: p. 163–182.S.V. Patankar, *Numerical Heat Transfer and Fluid Flow*, Hemisphere Publishers, New York, 1980.

[2] Ebbesen, T.W., et al., Extraordinary optical transmission through sub-wavelength hole arrays. Nature, 1998. 391(6668): p. 667-669.

[3] Escobedo, C., On-chip nanohole array based sensing: a review. Lab Chip, 2013. 13: p. 2445–2463.

[4] R. Gordon, D.S., K. L. Kavanagh, and A. G. Brolo, A new generation of sensors based on extraordinary optical transmission. Accounts Chem. Res., 2008. 41: p. 1049–1057.

[5] Brolo, A.G., Plasmonics for future biosensors. Nature Photonics, 2012. 6: p. 709-713.

[6] Dean, N., Colouring at the nanoscale. Nature Nanotechnol., 2015. 10(1): p. 15-16.

[7] Yan Yu, L.W., Shichao Song, and Qin Chen, Transmissive/Reflective Structural Color Filters: Theory and Applications. J. Nanomater., 2014. 2014(8): p. 1-17.

[8] Shuang Zhang, W.F., K. J. Malloy, S. R. J. Brueck, N. C. Panoiu, and R. M. Osgood, Near-infrared double negative metamaterials. Opt. Exp., 2005. 13: p. 4922.

[9] Mekawey, H., Ismail, Y., Swillam, M., "Dispersion analysis and engineering of 2D plasmonic waveguides," J. Opt. 17, 015003 (2015).

Modeling, Computational Techniques and Verification of Theory

2D–3D coupled spectral element method for modelling of guided waves propagation in a composite plate

Piotr Fiborek*, Paweł Kudela, and Wiesław Ostachowicz

Institute of Fluid–Flow Machinery Polish Academy of Sciences, Poland
*corresponding author, E-mail: pfiborek@imp.gda.pl

Abstract

Elastic waves are extensively used in Structural Health Monitoring for damage detection in the structures. In this paper, spectral element method with a various dimension of elements is used for modelling of the wave propagation in a composite plate. All components used in the simulation are decomposed from each other and connected by Lagrange multipliers. In this type of scheme elements with different dimension can be used for modelling of each component significant decreasing the time of the simulation.

1. Introduction

Among various techniques applied for advanced NDT and Structural Health Monitoring (SHM), the method based on Guided Waves (GW) has a great potential ([1]). Excitation and sensing of GW propagating in composite materials are usually realized by the piezoelectric (PZT) transducers ([2]). The transducers can be permanently surface bonded to the host structure by the adhesives. A thickness and mechanical properties of adhesive interface layer have a significant effect on a sensor signal [3].

To study the effects of the adhesive layer on the elastic waves propagation besides experimental and theoretical studies the following numerical models have been developed: the hybrid spectral element method [4], the finite element method (FEM) [5] and spectral element method (SEM) with two–dimensional (2D) elements coupled by Lagrange multipliers [6].

In this paper, numerical simulations of elastic waves propagating in the composite plate and excited by the PZT transducer adhesively bonded to the structure are presented. A novel scheme assumed to define all components independently by two types of spectral elements. Three–dimensional (3D) solid element ([7]) is used for modelling PZT transducer and the host structure while adhesive layer is modelled by the 2D shell element ([8]). The displacements coupling between the adjacent elements is forced by Lagrange multipliers. In practice, the thickness of adhesive layer is in a range from 1 up to 100 μm, therefore, modelling by the 3D elements of a very thin components can be very inefficient because a convergence of Central Difference Time Integration Method applied for solving equation of motion is strongly correlated with the size of the smallest element. The proposed model also takes into account material damping of the plate.

2. Time–domain spectral element method formulation

2.1. Spectral element method

In general, the idea of SEM has a lot in common with FEM. The domain of the modelled structure is divided into finite elements. The main difference between those methods is a distribution of nodes in elements and approximation function describing changes of displacements. The element nodes are non-uniformly distributed and their locations are obtained by finding the roots of Equations 1.

$$(1-\xi^2)P'_{p-1}(\xi)=0 \tag{1}$$

where $\xi \in [-1,1]$, P_{p-1} is Legendre polynomial of degree (p-1) and symbol $'$ denotes the first derivative. 3D shape function is constructed as a tensor product of the 1D shape functions $N_m(\xi)$, $N_n(\eta)$ and $N_l(\zeta)$ defined by the Lagrange interpolating polynomials of order $p-1$, $q-1$ and $r-1$ degree, respectively.

2.2. Substructures coupling by Lagrange Multipliers

The displacements coupling between substructures is realized by imposing traction forces represented by a vector of Lagrange multipliers. The compatibility of the substructure displacements u^s can be written as:

$$\sum_{s=1}^{n} = \mathbf{G}^s u^s = 0 \tag{2}$$

where n is the number of substructures and G^s is the matrix which localizes the interface degrees of freedom of the substructure.

2.3. Elementary governing equations of motion

The elementary governing equations of motion incorporating Lagrange multipliers can be written in the matrix form:

$$\begin{bmatrix} \mathbf{M}^e_{uu} & 0 & 0 \\ 0 & 0 & 0 \\ 0 & 0 & 0 \end{bmatrix} \begin{Bmatrix} \ddot{u}^e \\ \ddot{\phi}^e \\ 0 \end{Bmatrix} + \begin{bmatrix} \mathbf{C}^e_{uu} & 0 & 0 \\ 0 & 0 & 0 \\ 0 & 0 & 0 \end{bmatrix} \begin{Bmatrix} \dot{u}^e \\ \dot{\phi}^e \\ 0 \end{Bmatrix} + \\ + \begin{bmatrix} \mathbf{K}^e_{uu} & \mathbf{K}^e_{u\phi} & \mathbf{G}^{eT} \\ \mathbf{K}^e_{\phi u} & \mathbf{K}^e_{\phi\phi} & 0 \\ \mathbf{G}^e & 0 & 0 \end{bmatrix} \begin{Bmatrix} u^e \\ \phi^e \\ \lambda \end{Bmatrix} = \begin{Bmatrix} F^e \\ Q^e \\ 0 \end{Bmatrix} \tag{3}$$

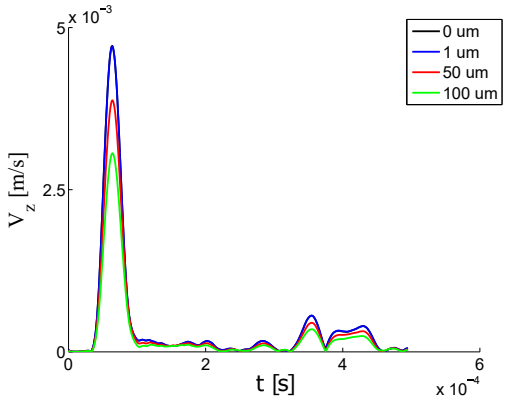


Figure 1: Simulated out of plane particle velocity for different thickness of the adhesive layer

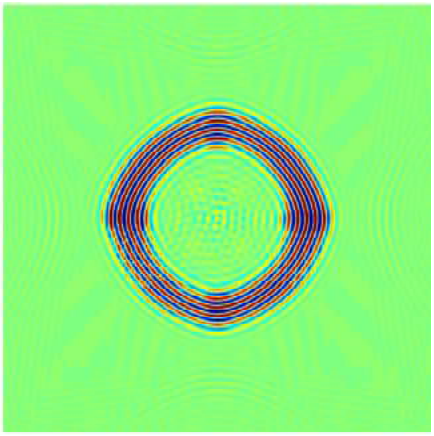


Figure 2: Front of the propagating guided wave in carbon fiber composite plate

where M^e_{uu}, C^e_{uu}, K^e_{uu} are structural mass, damping and stiffness matrices, respectively; $K^e_{\phi u} = {K^e_{u\phi}}^T$ are piezoelectric coupling matrix; $K^e_{\phi\phi}$ is the dielectric permittivity matrix, u^e is the nodal displacement and ϕ^e is the electric potential; F^e the nodal external force vector, Q^e is the nodal externally applied charge vector, λ is the vector of Lagrange multipliers and G^e is the matrix of Lagrange multipliers; $(\dot{}) = \frac{\partial}{\partial t}$.

Unknown vector λ_t is dependent on the load acting on the structure and it is calculated for every time step by imposing the constraint from Eq 2.

Structural damping C^e_{uu} is defined according to Rayleigh damping model:

$$\mathbf{C}^e_{uu} = \alpha_M \mathbf{M}^e_{uu} + \beta_K \mathbf{K}^e_{uu} \tag{4}$$

where α_M and β_K are the mass– and stiffness–proportionality coefficients. However, β_K is assumed to be zero. In this way, very efficient central difference scheme can be applied for solving the equation of motion 3 which leads to reduced computation time.

3. Conclusions

The effect of adhesive layer on guided waves propagation in carbon fiber composite plate was studied. The numerical simulations were performed for various parameters: thickness of the layer (Fig. 1), Young's modulus of the adhesive and the frequency of excitation signal.

On Fig 2 the wave field of propagating wave is presented and the results are in a good agreement with experimental measurements conducted by using Scanning Doppler Laser Vibrometer.

Acknowledgement

The research was funded by the Polish National Science Center under grant agreement no $DEC - 2013/10/A/ST8/00071$ in the frame of MAESTRO project entitled: Excitation and control of mechanical waves in nonlinear media.

References

[1] W. Ostachowicz, P. Kudela, M. Krawczuk, A. Żak, Guided Waves in Structures for SHM: The Time–domain Spectral Element Method. Wiley, Chichester, 2012.

[2] V. Giurgiutiu, S.E. Lyshevski, *Micromechatronics. Modeling, analysis and design with Matlab. Second Edition*. CRC Press, Boca Raton. 2009.

[3] E.F. Crawley, J. De Luis, Use of piezoelectric actuators as elements of intelligent structures. AIAA journal, 25: 1373–1385, 1987.

[4] S. Ha, F.–K. Chang, Adhesive interface layer effects in PZT–induced Lamb wave propagation. Smart Materials and Structures, 19: 025006. 2010.

[5] C. Willberg, S. Duczek, U. Gabbert, Increasing the scanning range of Lamb wave based SHM systems by optimizing the actuator–sensor design. CEAS Aeronautical Journal, 4: 87–98, 2013.

[6] U. Ashwin, S. Raja, C.N. Sathyanarayana, Formulation of 36–noded piezoelectric spectral finite element scheme with active/passive layers coupled by Lagrange multipliers. Smart Materials and Structures, 23: 085017, 2014.

[7] P. Kudela, W. Ostachowicz, 3D time–domain spectra elements for stress waves modelling. 7th International Conference on Modern Practice in Stress and Vibration Analysis, Journal of Physics: Conference Series 181: 012091, 2009.

[8] P. Kudela, A. Żak, M. Krawczuk, W. Ostachowicz, Modelling of wave propagation in composite plates using the time domain spectral element method. Journal of Sound and Vibration, 302: 728–745, 2007.

A Theoretical, Numerical and Experimental Analysis of Adhesive Bond Effect on Lamb Wave Propagation in Sandwich Structure

Shirsendu Sikdar[1], Wieslaw Ostachowicz[2]

[1,2]Institute of Fluid-Flow Machinery, Polish Academy of Sciences, 14, Fiszera Street, Gdansk 80-231, Poland
[2]Warsaw University of Technology, Faculty of Automotive and Construction Machinery, Narbutta 84, 02-524 Warsaw, Poland
*Shirsendu Sikdar, E-mail: ssikdar@imp.gda.pl

Abstract

A combined semi-analytical analysis, finite element simulation, and experimental investigation have been carried out in order to study the bond effect on the Lamb wave propagation in a jointed honeycomb sandwich structure. It is observed that the presence of adhesive bond significantly influences the propagating wave modes in terms of decrease in amplitude and propagation velocity. A good agreement is noticed among the theoretical, numerical, and experimental results, in all the cases studied.

1. Introduction

Honeycomb sandwich structures are often used in Aeronautic, Marine, and Automotive industries as lightweight construction material due to their high stiffness/weight ratio, acoustic insulation, and energy absorption capabilities [1]. Jointed sandwich structures are often used in some specialized applications and structural reasons, where multiple pre-fabricated honeycomb cores are bonded with adhesives [2]. The guided Lamb wave propagation based inspection techniques are suitable to monitor such complex and multi-layered structures owing to their long-distance propagation capacity with less attenuation and dispersion. Therefore, it is important to study such joint effects on the propagating Lamb wave signals. In this paper, the wave propagation is thoroughly studied for a 7 mm thick jointed sample 3D-core honeycomb sandwich structure (500 mm × 500 mm), using piezoelectric transducers (PZTs) as shown in Figure 1.

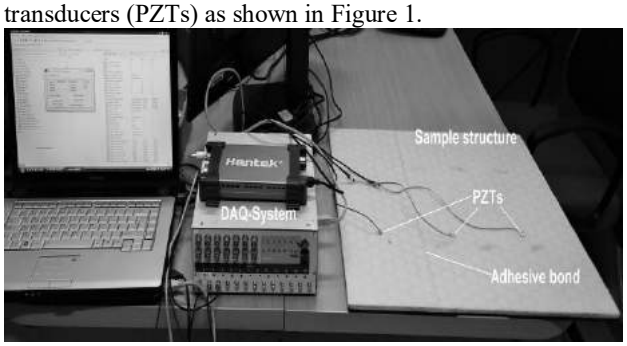


Figure 1: Laboratory experimental setup for the Lamb wave propagation based analysis of bond effects using PZTs.

In the process, a global matrix formulation based 2D (two dimensional) semi-analytical model is used to obtain the theoretical dispersion curve. A PZT actuation-reception based 3D finite element simulation of Lamb wave propagation in the jointed sample sandwich structure is carried out in ABAQUS (Figure 2). The simulation results are then successfully verified with the experiments conducted on the sample structure in the laboratory.

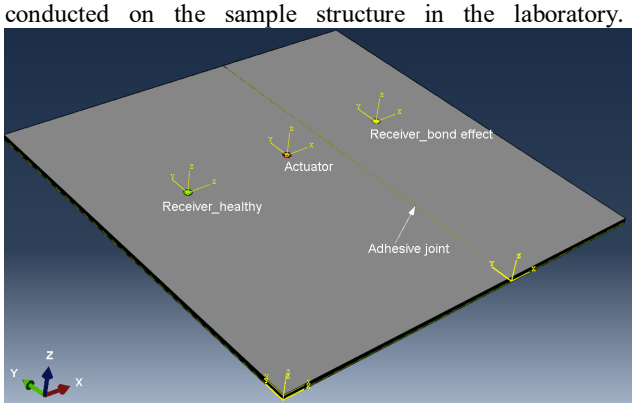


Figure 2: Numerical model of bonded sandwich structure.

2. Theoretical formulation

The phase-velocity dispersion curve for lamb wave propagation in the sample structure is obtained by using a global-matrix formulation based 2D semi-analytical model. The formulation of the 3-layer sandwich structure can be summarized in a global matrix form as-

$$\begin{bmatrix} \hat{Q}^1 & 0 & 0 \\ Q^1 & -Q^2 & 0 \\ 0 & Q'^2 & -Q^3 \\ 0 & 0 & \hat{Q}^3 \end{bmatrix}_{12x12} \begin{bmatrix} A^1 \\ A^2 \\ A^3 \end{bmatrix}_{12x1} = \begin{bmatrix} \vec{F} \\ 0 \\ 0 \\ 0 \end{bmatrix}_{12x1} \quad (1)$$

where the 'Q matrix' is the global matrix, the 'F-matrix' is the force matrix, and, the 'A-matrix' is the constant component matrix obtained from a complex matrix formulation as described in [3]. The dispersion condition can be obtained by solving the determinant of the formulated 12×12 global matrix as-

$$G(\xi, \omega) = 0 \quad (2)$$

The wavenumber, ξ_1 values can be determined for a range of frequency, ω and the corresponding frequency verses

phase-velocity, c dispersion plots can be obtained by using the following equation-

$$c = \frac{\omega}{\xi} \tag{3}$$

The real-roots of ξ are only considered to calculate the propagating wave modes [4]. Whereas, the complex-roots of ξ represents non-propagating Lamb wave modes.

3. Results and discussion

The phase velocity dispersion curve is theoretically obtained using Equation (3), which indicates the presence of three independent wave modes (A0, S0, and A1) at 100 kHz frequency.

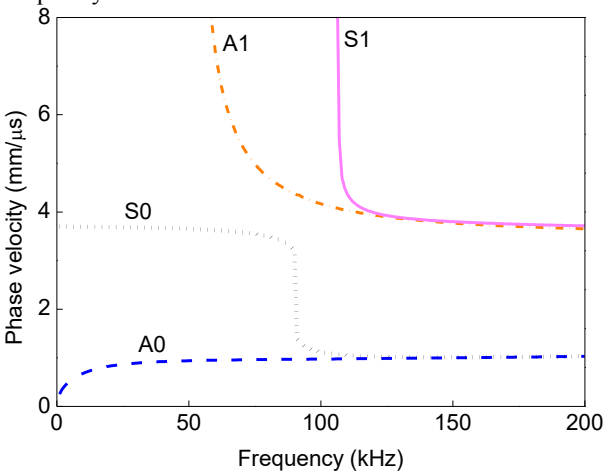


Figure 3: Theoretical dispersion curve for the sample sandwich structure.

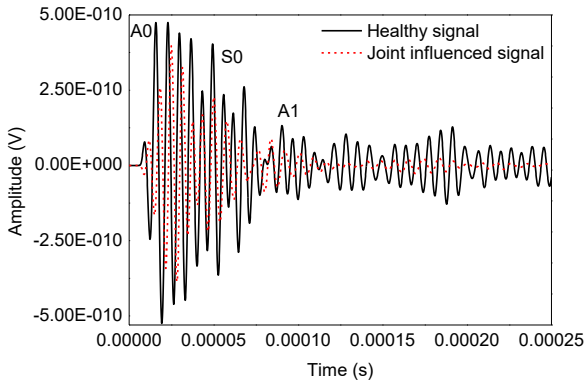


Figure 4: Comparison of numerical signals showing the bond effects on wave modes.

The numerical and experimental healthy and adhesive bond influenced signals are obtained for 100 kHz actuation frequency and compared, as shown in Figure 4 and Figure 5, respectively. All the signals clearly indicate the presence of three different Lamb wave modes as identified from the dispersion curve in Figure 3. It is also observed that the presence of adhesive bond substantially reduces the amplitudes and group velocities of the wave modes (Figure 4 and Figure 5).

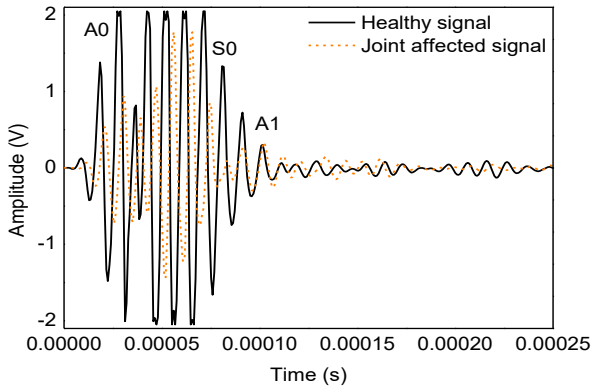


Figure 5: Comparison of experimental signals showing the bond effects on wave modes.

4. Discussion

The theoretical, numerical, and experimental study of the adhesive bond effect on the guided Lamb wave propagation in a jointed honeycomb sandwich structure have been carried out. It is observed that the presence of core joint significantly influences the propagating Lamb wave modes. A good agreement is noticed among the theoretical, numerical, and experimental results, in all the cases studied.

5. Conclusions

The presence of adhesive bond between cores in honeycomb sandwich composite structure reduces the modal amplitude and velocity of the propagating guided Lamb wave signals. Therefore, based on these changes in modal characteristics, efficient structural monitoring strategies can be developed for the sandwich structures.

Acknowledgements

The research work is funded by the Polish National Science Centre (NCN) under grant agreement number: UMO-2016/23/N/ST8/01326 in the frame of the PRELUDIUM12 project.

References

[1] D. Zenkert, *An introduction to sandwich construction*, EMAS Publishing: West Midlands, 1995.

[2] S. Sikdar, S. Banerjee, *Structural Health Monitoring of Advanced Composites Using Guided Waves*, LAP LAMBERT Academic Publishing, Saarbrücken, 2017.

[3] S. Banerjee, C.B. Pol, Theoretical modeling of guided wave propagation in a sandwich plate subjected to transient surface excitations. *Int. J. of Solids and Structures* 49(23): 3233-41, 2012.

[4] N. Vasudevan, A.K. Mal, Response of an elastic plate to localized transient sources. *ASME J. Appl. Mech.* 107: 356–362, 1985.

Near Optimal Freeform Inverse Design Approach For Future Metastructures

Mohammad Haghtalab[1,2], Federico Capasso[1], and Safieddin Safavi-Naeini[2]

[1]Harvard John A. Paulson School of Engineering and Applied Sciences, Harvard University, Cambridge, Massachusetts, USA
[2]The Centre for Intelligent Antennas and Radio Systems (CIARS), Department of Electrical and Computer Engineering University of Waterloo, Waterloo, ON, Canada
*corresponding author, E-mail: safavi@uwaterloo.ca

Abstract

Demands for highly efficient meta-structures require the employment of designs with high degrees of freedom in design parameters. Due to large number of variables, using the conventional global optimization methods is not efficient in such structures. To overcome this challenge, new approaches should be devised, allowing us to efficiently explore electrically large and geometrically complex structures. In this paper, we introduce a stochastic-based algorithm for this purpose.

1. Introduction and Summary

Metastructures have enabled unprecedented engineering of light-matter interaction through designs which are composed of arrays of sub-wavelength-scale scatterers. Not only have they been shown to be perfect alternatives to the conventional bulky optical devices [1], but also, new functionalities have been demonstrated [2-4], which are either impossible or difficult to achieve through conventional approaches. These breakthroughs are made possible by the ability to manipulate the phase and the amplitude of the field over each unit cell of the planar structures, known as metasurfaces, independently; thereby controlling the wavefront of the incident waves in desired manners. The proposed design approaches are based on engineering the interaction of incident fields with the coupled scattering elements within each unit cell and can be classified by the type of the elements utilized in the structure, namely resonant or non (weakly)-resonant elements. Depending on the type of the elements of choice, there are limitations in terms of the maximum efficiency which can be achieved for various design specifications. These limitations are imposed either due to the undesired inter-cell couplings throughout the structure or the intrinsic resonant characteristics of the resonating elements employed in the design. As such, new design approaches for designing metasurfaces with higher efficiencies have been proposed [5, 6].

Thus far, the most common type of the proposed metasurfaces operates based on introducing abrupt changes of optical/electromagnetic properties at an interface, utilizing dielectric or metallic nanostructures [7]. The collective effect of all unit cells leads to the desired functionalities, such as lensing, over a desired region in space. While the inter-cell coupling is not desired in these approaches and can cause significant drop in efficiency, the new proposed structures take advantage of strong inter-element couplings throughout the structure to alleviate the fundamental limitations of conventional designs. This approach requires the consideration and optimization of the coupling between large numbers of elements. Different methods have been utilized to overcome this challenge.

Recently, topology optimization approaches have been employed to optimize metalens structures with extremely large degrees of freedom. It is important to note that the optimization problem defined for such structures is not convex which typically means that there are several different local minima (maxima), or non-unique solutions. The reported topology optimization approaches are based on the method of gradient descent where initial solutions are iteratively optimized to obtain a local minimum (maximum). On the other hand, due to the large number of variables, most global optimization methods cannot handle this type of problems efficiently.

In this paper, we outline a new stochastic-based optimization approach, called Near Optimal Freeform Inverse Design (NOFID), which is capable to search for the global solutions based on defined constraints and design parameters. Our proposed approach, summarized in Fig. 1, is based on controlled iterative perturbations of solutions in solution space. Starting from an initial state (configuration), the primary solution undergoes probabilistic changes through an iterative approach. This process is controlled by defining different parameters which ultimately leads to the optimization of the defined cost function(s). These parameters include the critical threshold, updating multiplier, cross-over values, and iteration maximum numbers. In this paper, we are going to explain the steps and the parameters used in this optimization approach. As an example, we consider the problem of super-resolution in disordered dielectric metalenses. The results confirm the effectiveness of our method through comparison with periodic and totally random structures.

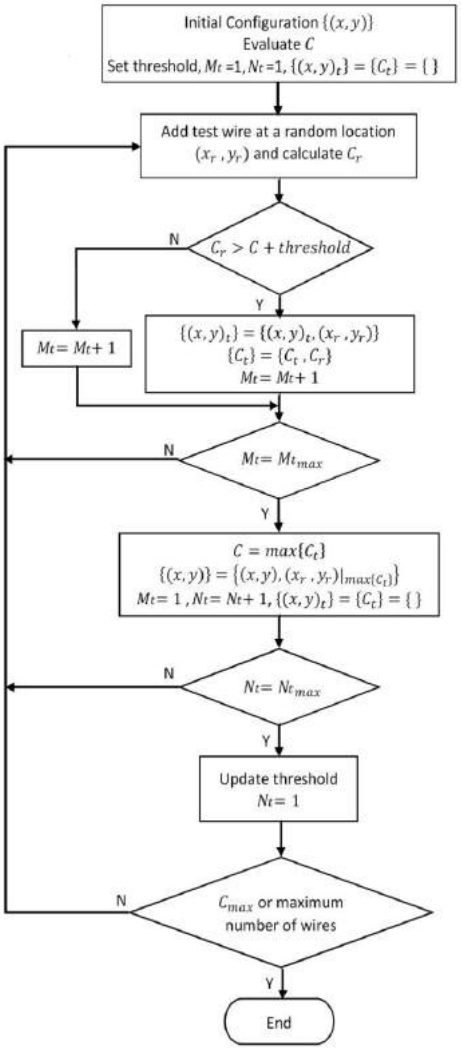


Figure 1 Flowchart of the proposed algorithm: NOFID

Acknowledgements

This work has been supported by the National Science and Engineering Research Council (NSERC) of Canada, and C-COM Satellite Systems.

References

[1] Mohammadreza Khorasaninejad, Wei Ting Chen, Robert C. Devlin, Jaewon Oh, Alexander Y. Zhu, and Federico Capasso. "Metalenses at visible wavelengths: Diffraction-limited focusing and subwavelength resolution imaging." *Science* 352, vol. 6290 1190-1194 (2016).

[2] Robert C. Devlin, Antonio Ambrosio, Noah A. Rubin, JP Balthasar Mueller, and Federico Capasso. "Arbitrary spin-to–orbital angular momentum conversion of light." *Science* 358, vol. 6365 896-901(2017).

[3] Mohammad Haghtalab, Reza Faraji-Dana, and Safieddin Safavi-Naeini. "Design and Analysis of Disordered Optical Nanoantenna Structures." *Journal of Lightwave Technology* 34, vol. 11 2838-2847 (2016).

[4] Mohammad Haghtalab, and Safieddin Safavi-Naeini. "Disordered Nanoantennas: A New Paradigm in Space-Division Multiplexing." In *CLEO: Science and Innovations*, pp. JTh2A-43. Optical Society of America, 2017.

[5] Jianji Yang , David Sell, and Jonathan A. Fan. "Freeform metagratings based on complex light scattering dynamics for extreme, high efficiency beam steering." *Annalen der Physik* (2017).

[6] Zin Lin, Benedikt Groever, Federico Capasso, Alejandro W. Rodriguez, and Marko Lončar. "Topology optimized multi-layered meta-optics." *arXiv:1706.06715* (2017).

[7] Nanfang Yu, and Federico Capasso. "Flat optics with designer metasurfaces." *Nature materials* 13, vol. 2 139-150 (2014).

An asynchronous FDTD solver for efficient simulations in nanophotonics

Sergei Belousov[1,2,4,*], Sergey Khilkov[2], Vadim Levchenko[3], Anastasia Perepelkina[3], and Ilya Valuev[2]

[1]Kintech Lab Ltd., Moscow, Russia
[2]HIPERCONE Ltd., Moscow, Russia
[3]Keldysh Institute of Applied Mathematics, Moscow, Russia
[4]National Research Centre "'Kurchatov Institute"', Moscow, Russia
*corresponding author, E-mail: belousov@kintechlab.com

Abstract

In this paper we introduce a novel full-wave electromagnetic solver based on the Finite-Difference Time Domain method, which is extremely efficient in terms of CPU and GPU performance and scalability (HIPERCONE FDTD). The use of asynchronous mesh updates, localization of data in the fast levels of computer memory, and parallelism at all levels including vectorization allows the HIPERCONE FDTD solver to achieve the performance up to 1–2 orders of magnitude higher than the traditional approaches. Unlike the traditional memory-bound electromagnetic solvers, the maximum performance rate of HIPERCONE FDTD in terms of mesh cell updates per second is reached for large meshes occupying or even exceeding the total available CPU RAM. Therefore, the HIPERCONE solver is especially advantageous in solving large-scale problems. Moreover, the asynchronous mesh update algorithm provides a natural framework for simulation of oblique plane wave incidence on periodic metamaterials. In this work we describe the algorithmic background of the simulation method and discuss applications which benefit from the solver's performance.

1. Introduction

Electromagnetic phenomena in metamaterials include intricate behavior of electromagnetic fields on a broad length scale ranging from nanometers up to microns and more. Therefore, full-wave electromagnetic simulations of metamaterials often require large meshes and are computationally expensive. Thus, for assessing metamaterial designs, a solver performance becomes the key feature [1].

According to the roofline model [2] the performance is limited either by the peak flop rate of the computer (compute-bound) or by the memory bandwidth (memory-bound). In most cases the algorithms for full-wave electromagnetic simulations, including the finite difference and finite element methods both for the time and frequency domains, are memory bound. In order to get faster code we have to increase the flop/byte ratio of our algorithm. Another problem is achieving scalability of the computation with the increase of the problem size. This requires efficient data transfers between computing units (parallel scalability) and efficient use of the computer memory hierarchy (memory scalability). We have developed an approach to constructing mesh update algorithms for the conventional explicit FDTD scheme which is both memory efficient, and highly scalable on all levels of computer parallelism including vectorization, multi-core and multi node levels.

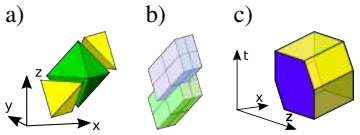


Figure 1: (a) Candy xyz projection decomposed into octahedron and two tetrahedrons; (b) candies xyz projections for H and E fields; (c) candy xzt projection.

2. Asynchronous mesh update algorithm

In the HIPERCONE FDTD code the updates of field values are performed according to the Maxwell equations in a Yee cell with a regular stencil of 2nd or 4th order in space and 2nd order in time. The stencil determines the dependency graph in 4D space-time domain. Each individual field update (an event in our model 4D space-time) depends only on the results of other events inside 4D hypercone domain of influence. Performing hypercone-based computation and keeping track of the 4D domains compact in computer memory allowed us to construct a class of asynchronous algorithms, which are called Locally Recursive non-Locally Asynchronous (LRnLA) algorithms [3]. Among the many possibilities, each type of 4D decomposition is more or less efficient depending on the computer architecture and the scheme stencil. Different 4D mesh decompositions (ConeFold, DiamondTorre) were successfully applied earlier to electromagnetic and acoustic FDTD simulations [4, 5] for multi-CPU and multi-GPU architectures.

Recently, a new LRnLA algorithm DiamondCandy was proposed [6]. It provides superior data access locality in 3D space and is suitable for building vectorized updates with tunable vector size. We use local vectorization approach where the components of the CPU or GPU vector corre-

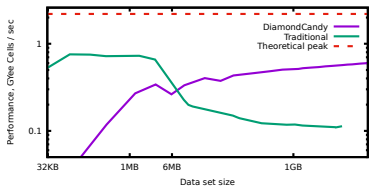


Figure 2: Performance test results for 4th order double-precision electromagnetic FDTD on Intel Core i5-6400 (4 cores with AVX2).

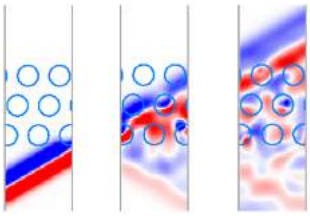


Figure 3: Asynchronous FDTD simulation of oblique incidence of a plane wave on a periodic structure. Note that the mesh is drawn at three time moments. This data never appears simultaneously in simulation, but restored from the recorded field evolution.

spond to positions adjacent in space. This requires some extra vector transformations in the updates, however increases the re-use of data and keeps the vector conformal to local material properties. This algorithm has been implemented into universal multi-purpose electromagnetic solver, based on the parallel EMTL library [7]. The library was designed for many-core CPUs and clusters and implements most of the state of the art FDTD techniques including dispersive media, subpixel smoothing, periodic and PML boundaries, near to far field transformation.

The efficiency of the new DiamondCandy algorithm for the FDTD simulation in HIPERCONE has been tested in CPU and GPU implementations. As an example we present a benchmark for the desktop computer with Intel Core i5-6400 (Fig. 2). We compare the traditional algorithm (not LRnLA, data synchronization takes place on each time step for the whole mesh) with the new DiamondCandy. The performance of the traditional algorithm drops when the data size exceeds L3 cache capacity (6MB). The use of DiamondCandy provides 6 times greater performance (0.6 GYeeCells/sec) for practically important large problem sizes. The achieved performance is 30% of the peak floating point rate for this processor.

For GPU implementation, the performance benchmarks have shown the rate of 9 GYeeCells/sec for a single state-of-the-art GPU card (Nvidia P-100), which is 15 times greater than the rate of the CPU version on Core i5-6400.

3. Discussion

The asynchronous mesh update in LRnLA algorithms provides a natural framework for oblique incidence simulations of surface periodic structures or metamaterials possessing 1D or 2D-periodicity. With the traditional synchronous FDTD it is impossible to implement time-delayed Bloch boundary conditions valid for all frequencies and angles of incidence in time domain (Fig.3). Therefore either multiple FDTD runs or boundary-matching iterations [7] are required to extract the frequency spectrum for a specific incidence angle. Using LRnLA it is possible to create the required time delay between periodic borders of the simulation cell. We show that it is possible to set up Bloch conditions for almost arbitrary range of incidence angles.

4. Conclusion

We present a new multipurpose FDTD solver HIPERCONE-FDTD, based on the highly efficient LRnLA algorithm DiamondCandy, which optimizes memory data locality and parallel scalability for the FDTD cross stencil, and uses all available methods of parallelism, including vectorization. The application of the solver to simulations of surface metamaterial structures at oblique incidence is discussed.

References

[1] A. Zakirov, S. Belousov, I. Valuev, V. Levchenko, A. Perepelkina, and Y. Zempo, "Using memory-efficient algorithm for large-scale time-domain modeling of surface plasmon polaritons propagation in organic light emitting diodes," *Journal of Physics: Conference Series*, vol. 905, no. 1, p. 012030, 2017.

[2] S. Williams, A. Waterman, and D. Patterson, "Roofline: an insightful visual performance model for multicore architectures," *Communications of the ACM*, vol. 52, no. 4, pp. 65–76, 2009.

[3] V. D. Levchenko, "Asynchronous parallel algorithms as a way to archive effective ness of computations (in Russian)," *J. of Inf. Tech. and Comp. Systems*, no. 1, p. 68, 2005.

[4] V. Levchenko, A. Perepelkina, and A. Zakirov, "DiamondTorre algorithm for high-performance wave modeling," *Computation*, vol. 4, no. 3, p. 29, 2016.

[5] A. Zakirov, V. Levchenko, A. Perepelkina, and Y. Zempo, "High performance FDTD algorithm for GPGPU supercomputers," in *Journal of Physics: Conference Series*, vol. 759, no. 1, 2016, p. 012100.

[6] A. Perepelkina and V. Levchenko, "The DiamondCandy algorithm for maximum performance vectorized cross-stencil computation," *to be published*.

[7] I. Valuev, A. Deinega, and S. Belousov, "Implementation of the iterative finite-difference time-domain technique for simulation of periodic structures at oblique incidence," *Comp. Phys. Commun.*, vol. 185, no. 4, p. 1273, 2014.

Modal Analysis of Cylindrical Waveguides with 2D Metamaterial Wall

Lucille Kuhler[1,2,3,*], Gwenn Le Fur[2], Luc Duchesne[3], Nathalie Raveu[1]

[1]University of Toulouse, INPT, CNRS, Laplace, 2 rue Charles Camichel, Toulouse, France
[2]CNES, antennas department, 18 avenue Edouard Belin, Toulouse, France
[3]MVG Industries, 17 avenue de Norvege, Villebon Sur Yvette, France
*corresponding author, E-mail: lucille.kuhler@laplace.univ-tlse.fr

Abstract

In this article the Modal Expansion Theory (MET) is developed for 2D metamaterial cylindrical waveguides. A new code based on 2D Finite Element Method (FEM) is implemented to compute conformal surface impedances. The MET using this FEM code is successfully applied to waveguides with different θ-invariant metamaterials. For such cases, computation time is at least 30 times faster than the commercial software HFSS.

1. Introduction

In the space industry, the launch cost of spacecraft is a constraint. In order to lower it, the size and the weight of the used devices are reduced. Metamaterials in waveguides or horn antennas could be used in this purpose [1] - [4]. Thanks to their structuration electromagnetic properties which are not available in natural materials, can be created [5]. With metamaterials, it is possible to obtain a relative permittivity and/or permeability lower than one or less than zero [6] - [8]. In research, metamaterials are mostly defined by characterizing both permittivity and permeability. However another method consists in computing their surface impedances at any given volume height [9].

In [10], metamaterials are characterized with a new method called the Modal Expansion Theory. This method aims at studying waveguides [10] - [12]. With the MET, it is possible to characterize the dispersion properties of rectangular or cylindrical waveguides with constant anisotropic surface impedances. In [13], a 2D FEM code has been added to the MET and allows the characterization of dispersion properties of rectangular waveguides with metamaterial walls. Surface impedances are defined at any given volume height and vary with the frequency and incidence angle of the electromagnetic wave.

In this article, 2D metamaterial waveguides are characterized with the cylindrical MET. Thanks to the θ-invariance of the structure, this new code is using a 2D FEM computation of the surface impedances deduced from the 3D FEM simplification. Conformal surface impedances are computed with this code. As in [13], the surface impedances are dependent on the frequency and incidence angle. The validation of the MET with this new 2D FEM code (for conformal impedances) is presented. Hence the MET is applied on three different 2D metamaterial waveguides to obtain their dispersion diagrams. Results are compared to the dispersion diagrams obtained with HFSS. By using the MET, the computation time is drastically reduced to obtain equivalent results.

2. Characterization principles

In this article, the MET [10] is proposed to characterize cylindrical waveguide with metamaterial walls. These waveguides are considered invariant along the z-axis, see Fig. 1. So electromagnetic fields have an $e^{-\gamma z}$ dependence, with γ the propagation constant along the z -axis. Furthermore the studied metamaterials are also invariant along the θ-axis.

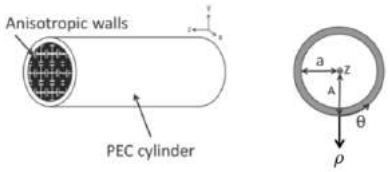


Figure 1: A cylindrical waveguide with anisotropic walls.

The metamaterial periodicity is supposed small compared to wavelength [6]. Therefore metamaterials are assumed to be equivalent to anisotropic surface impedances.

2.1. Modal Expansion Theory for cylindrical waveguides

In the cylindrical coordinate system, the surface impedance Z'_S is defined as follows:

$$\overrightarrow{E_T} = Z'_S\left(\overrightarrow{H_T} \times \vec{n}\right) \tag{1}$$

where $\overrightarrow{E_T}$ and $\overrightarrow{H_T}$ are the electric and magnetic fields tangent to the cylinder surface, $\vec{n}$ the normal unit vector to the cylinder surface. It leads to two impedance definitions:

$$Z'_T = -\left.\frac{E_\theta}{H_Z}\right|_{\rho=a}, \qquad Z'_Z = \left.\frac{E_Z}{H_\theta}\right|_{\rho=a} \tag{2}$$

The dispersion equation is determined in [11] from Helmholtz's equation and the anisotropic boundary conditions.

$$\frac{Z'_Z}{Z_0}\left(J'_m(u_a)\right)^2 - \frac{Z'_T}{Z_0}\left(\frac{k_c J_m(u_a)}{k_0}\right)^2 + \left(\frac{Z'_Z Z'_T}{Z_0^2}+1\right)\frac{k_c J_m(u_a) J'_m(u_a)}{jk_0} + \frac{Z'_Z}{Z_0}\left(\left(\frac{k_c}{k_0}\right)^2 - 1\right)\left(\frac{m J_m(u_a)}{u_a}\right)^2 = 0 \quad (3)$$

where a is the internal radius, $u_a = k_c a$, k_c the cutoff constant, k_0 the free space wavenumber, J_m the Bessel function of order m, J'_m the derivative of the Bessel function J_m and Z_0 the free space characteristic impedance .
In this article, cylindrical waveguides with 2D metamaterials due to an invariance along the θ-axis are of interest. Consequently only 0 order modes are studied. Metamaterials could be considered as anisotropic surface impedances but their shape should be undertaken. In [13] the MET with a 2D FEM code is successfully applied to rectangular waveguides with 2D metamaterials with invariance along the y-axis. In this article, the FEM is developed to cylindrical waveguides with 2D metamaterials with invariance along the θ-axis.
The equation (3) is simplified for 0 order modes [11] into:

$$\left[j\omega\mu_0 J'_0(u_a) + Z'_T k_c J_0(u_a)\right] \times \left[Z'_Z j\omega\epsilon_0 J'_0(u_a) + k_c J_0(u_a)\right] = 0 \quad (4)$$

where μ_0 is the free space permeability, ϵ_0 the free space permittivity and ω angular frequency (by using the convention of electromagnetic fields dependent on $e^{j\omega t}$).
From (4) TE_{0n} and TM_{0n} modes could be characterized separately, whatever n is. As a matter of fact in (4) either the first term is equal to zero or the second term. The first term with Z'_T will define TE_{0n} modes and the second term with Z'_Z will define TM_{0n} modes.

2.2. Characterization of conformal metamaterials

As the waveguide is θ-invariant, the 3D FEM code is simplified into a 2D FEM code. In any P plane of the cylindrical waveguide, a unit cell can be extracted, see Fig. 2.

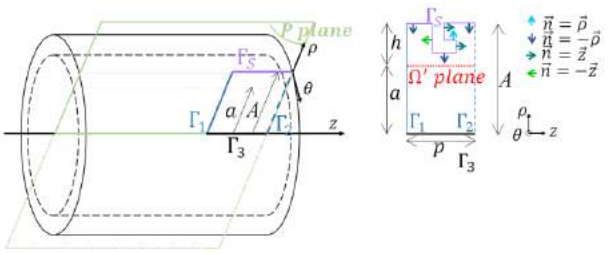


Figure 2: A cylindrical waveguide with an example of 2D metamaterial unit cell.

Γ_1 and Γ_2 are periodic boundaries, Γ_3 is the rotational axis and Γ_S is a boundary where the Z_S surface impedance (Z_T and Z_Z) is defined. Ω' is the plane where the Z'_S surface impedance (Z'_T and Z'_Z) is computed. A is the radius of the waveguide, h is the height of the metamaterial and p the distance between Γ_1 and Γ_2.
The Z'_S conformal surface impedance (Z'_T and Z'_Z) is computed with the 2D FEM code in the Ω' plane. Z'_Z defined in (2) is generated by H_θ, that is considered θ invariant; Z'_T defined in (2) is generated by E_θ , and considered θ invariant. This code is inserted in the MET solution of (3).

2.3. Recursive solution of dispersion equation

The Z'_S surface impedance (Z'_T and Z'_Z) depends on the φ incidence angle [13] which is deduced from β, the phase constant along the z-axis. The algorithm of Fig. 3 is implemented to compute the dispersion diagrams.

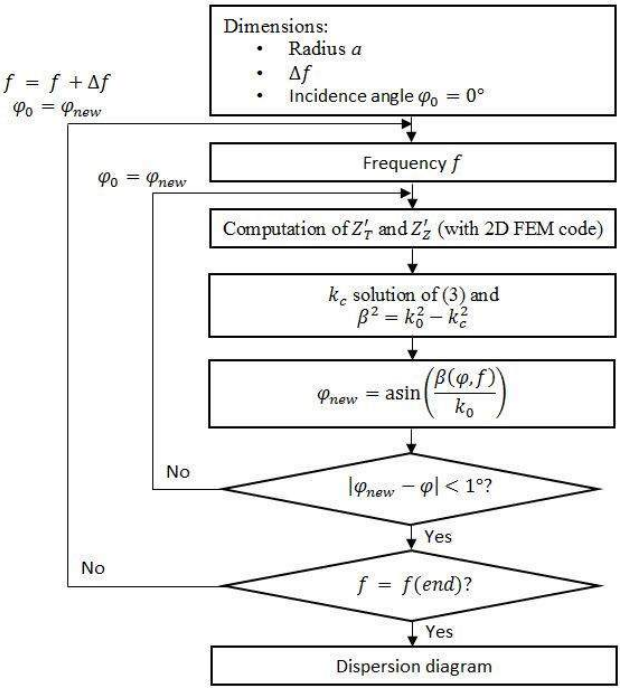


Figure 3: The MET algorithm to obtain β.

With this algorithm different 2D metamaterials (with a θ invariance) in cylindrical waveguides can be studied. A 3D FEM code is required to deal with 3D metamaterials or mode with angular dependency (m order different from 0).

3. Results

The method and the algorithm are validated in three different cases:

- firstly in a corrugated waveguide,
- subsequently the code is applied to a L-shape metamaterial,
- finally a stair-shape metamaterial is studied.

In all these cases, results are compared to HFSS solutions. To study these waveguides with HFSS, the same method as [11] is used. Dispersion diagrams are obtained from the volume of the section represented in Fig. 5, 11 and 14 with dashed lines and using periodic boundary conditions, see Fig. 4. The propagation constant is computed thanks to the phase delay between two periodic boundary conditions and the distance between them. By using the eigenmode solver in HFSS, the frequency of each solution is given. The complete dispersion diagram is obtained by varying the phase delay between the two periodic boundary conditions from 0° to 180°.

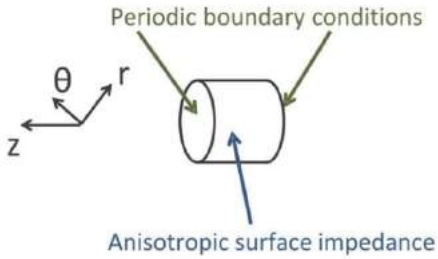


Figure 4: A cylindrical representation of a waveguide with periodic boundary conditions and anisotropic surface simulated in HFSS.

3.1. Corrugated cylindrical waveguide

A corrugation invariant in θ direction is considered. The studied waveguide is represented Fig. 5.

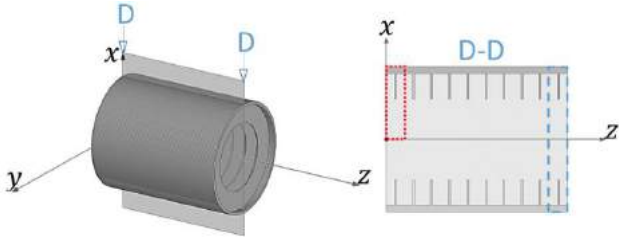


Figure 5: A corrugated waveguide. The blue dashed section is the section used in HFSS and the red doted one is used in the MET.

For the MET, the unit cell is created with the open source software Gmsh [14] and represented in Fig. 6.a.

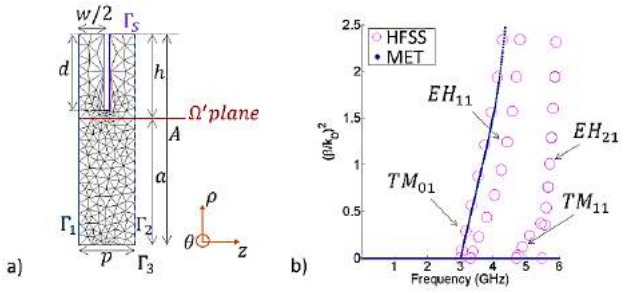


Figure 6: a) Unit cell mesh and dimensions: $A = 39.3\,mm$, $a = 23.58\,mm$, $d = 14.3\,mm$, $h = 15.72\,mm$, $p = 10.3\,mm$, and $w = 9.28\,mm$. b) Dispersion diagrams of the corrugated cylindrical waveguide obtained with MET (dots) and HFSS (circles).

Both simulations are made with the same computer (Intel (R) Xeon (R), 1.8 GHz 2 processors, 64 GB of RAM). The dispersion diagrams are represented Fig. 6.b, they perfectly coincide for 0 order modes. The dispersion diagrams are obtained in 622 minutes with HFSS while it requires only 18 minutes with MET. Consequently the MET code is 34 times faster.

Since only TM_{01} mode appears in this dispersion diagram, only Z'_Z is of interest. The figure 7 represents the Z'_Z surface impedance computed in the Ω' plane.

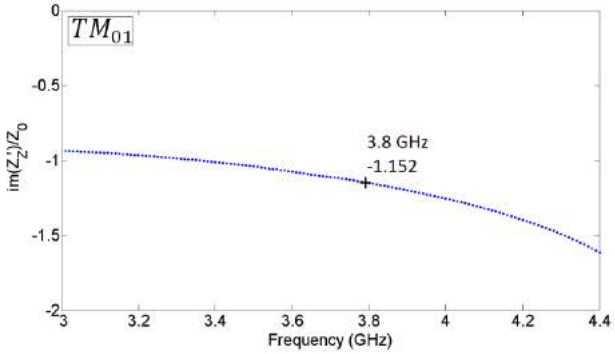


Figure 7: The Z'_Z surface impedance of the TM_{01} mode of Fig. 6.b.

While the Z_S surface impedance (Z_T and Z_Z) in Γ_S is null, Z'_Z in the Ω' plane change with frequencies. This Z'_Z impedance is computed with the algorithm of Fig. 3 which means that the φ incidence angle is different from one frequency to another.

In order to observe a TE_{0n} mode, the dispersion diagram of Fig. 6.b is studied up to 7 GHz and represented in the Fig. 8.

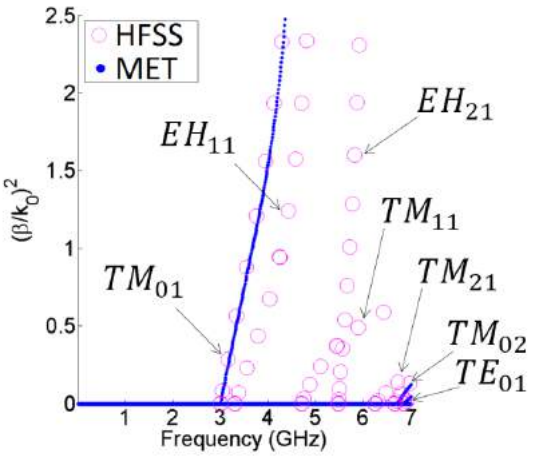


Figure 8: Dispersion diagrams of the corrugated cylindrical waveguide obtained with MET (dots) and HFSS (circles).

In this new dispersion diagram, two new 0 order modes are identified: the TM_{02} and the TE_{01} modes. Consequently Z'_Z is of interest for the TM_{02} mode and Z'_T is of interest for the TE_{01} mode as explained in (4). Figure 9 represents the Z'_Z surface impedance computed in the Ω' plane for the TM_{02} mode and figure 10 represents the Z'_T surface impedance for the TE_{01} mode.

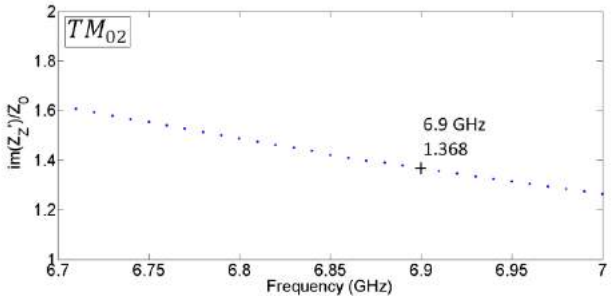


Figure 9: The Z_Z' surface impedance of the TM_{02} mode of Fig. 8.

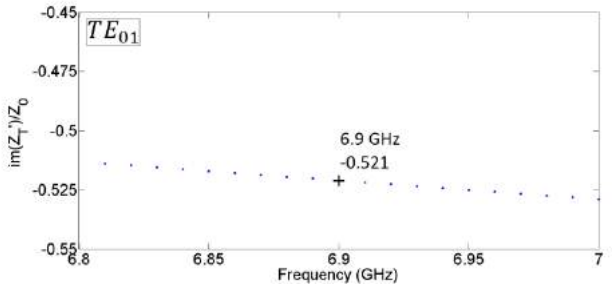


Figure 10: The Z_T' surface impedance of the TE_{01} mode of Fig. 8.

Both figures lead to the same conclusion as Fig. 7: the Z_S' surface impedance (Z_T' and Z_Z') in the Ω' plane changes with frequencies, with the φ incidence angle and also are dependent on the mode.

3.2. Cylindrical waveguide with L-shape metamaterial

The studied waveguide is presented in Fig. 11. The L-shape metamaterial is also invariant along the θ-axis.

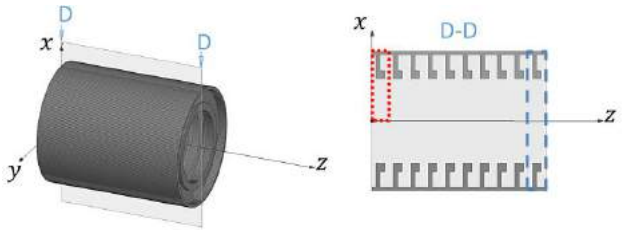


Figure 11: A cylindrical waveguide with a L-shape metamaterial. The blue dashed section is the section used in HFSS and the red doted one is used in the MET.

As in the previous case, the unit cell is created with Gmsh from the red doted section of Fig. 11. Figures 12 represent the unit cell mesh used and the dispersion diagrams obtained with the MET (dots) and with HFSS (circles).

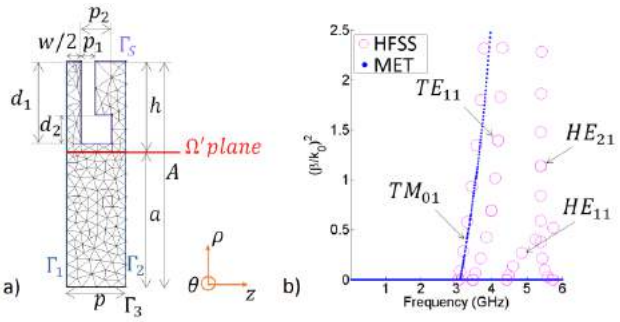


Figure 12: a) Unit cell mesh and dimensions: $A = 39.3\ mm$, $a = 23.58\ mm$, $d_1 = 14.3\ mm$, $d_2 = 2.5\ mm$, $h = 15.72\ mm$, $p = 10.3\ mm$, $p_1 = 2.5\ mm$, $p_2 = 5.3\ mm$, and $w = 5\ mm$. b) Dispersion diagrams of the corrugated cylindrical waveguide obtained with MET (dots) and HFSS (circles).

Both dispersion diagrams in Fig. 12.b perfectly coincide. Concerning the computation time with HFSS, the simulation lasts around 1032 minutes while this process takes only 20 minutes with the MET. Hence the time is divided by 51.

The L-shape metamaterial changes the propagation properties of the waveguide (different modes and different orders). Indeed the cutoff frequency of the TM_{01} mode is now $3.11\ GHz$, while it was $3\ GHz$ for the corrugated waveguide. Moreover the Z_Z' surface impedance for the TM_{01} mode is slightly different from the corrugation case see Fig. 13.

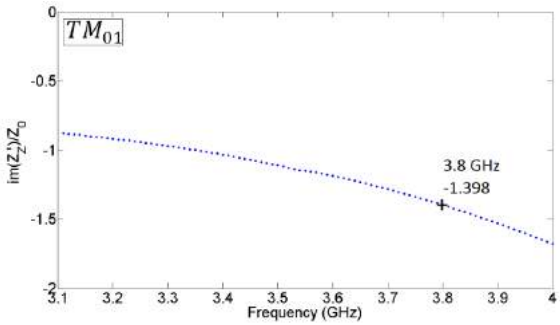


Figure 13: The Z_Z' surface impedance of the TM_{01} mode of Fig. 12.b.

3.3. Cylindrical waveguide with stair-shape metamaterial

The last waveguide studied is a waveguide with a stair-shape metamaterial θ-invariant, see Fig. 14.

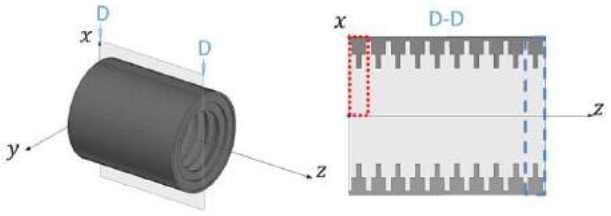


Figure 14: A cylindrical waveguide with a stair-shape metamaterial. The blue dashed section is the section used in HFSS and the red doted one is used in the MET.

Figures 15 represent the unit cell and the dispersion diagrams.

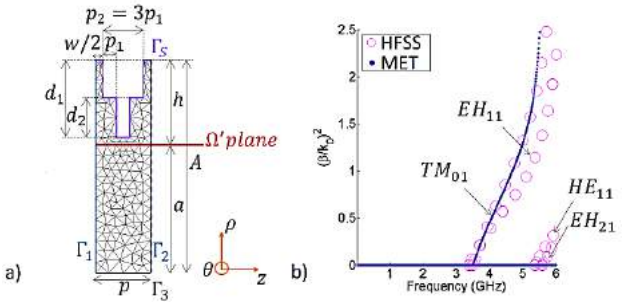


Figure 15: a) Unit cell mesh and dimensions: $A = 39.3\,mm$, $a = 23.58\,mm$, $d_1 = 14.3\,mm$, $d_2 = 7\,mm$, $h = 15.72\,mm$, $p = 10.3\,mm$, $p_1 = 2.5\,mm$, $p_2 = 7.5\,mm$, and $w = 5\,mm$. b) Dispersion diagrams of the corrugated cylindrical waveguide obtained with MET (dots) and HFSS (circles).

The dispersion diagrams are obtained with HFSS (circles in Fig. 15.b) in 1256 minutes and with the MET (dots in Fig. 15.b) it requires an eleven-minute computation times. The reduction time is around 114.

With this metamaterial the first mode is not the TM_{01} but the EH_{11} mode. Consequently the propagating modes and their cutoff frequencies change again with the shape of the metamaterial. In this case, the TM_{01} cutoff frequency is now $f_c = 3.49\,GHz$, while it was $3\,GHz$ for the corrugated waveguide. Moreover the Z'_Z surface impedance of the TM_{01} mode is divided by two at $3.8\,GHz$ compared to the previous cases, Fig. 16.

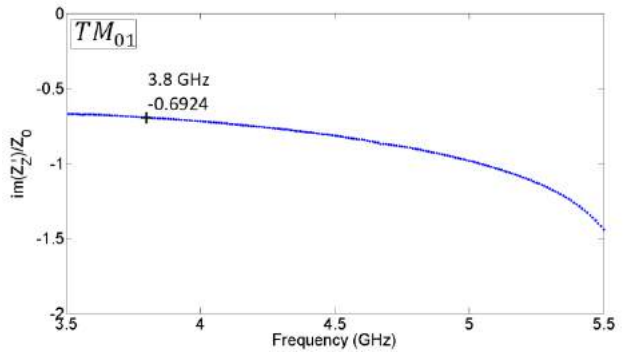


Figure 16: The Z'_Z surface impedance of the TM_{01} mode of Fig. 15.b.

4. Conclusion

The MET has been successfully applied to cylindrical waveguides with 2D metamaterial walls, for 0 order modes. The proposed method appears accurate and extremely faster than HFSS solution, at least 30 times faster. This method allows a comparison between the propagation characteristics of all kinds of θ-invariant metamaterials. In this article three different waveguides have been studied. It has been proved that the shape of the metamaterial can modify the propagation properties in the waveguide. Furthermore all metamaterials can be defined by using their surface impedance at any given volume height. In these three examples the surface impedances are computed at the same volume height h and are different. They depend on the frequencies, on the φ incidence angle, on the propagating mode and on the metamaterial shape.

An extension of the method to 3D metamaterials is now under process. As metamaterials could be θ-dependent, the 3D FEM code could no longer be reduced to a 2D FEM code. With this extension all kinds of metamaterial but also all the mode orders can be dealt with.

References

[1] J. G. Pollock and A. K. Iyer, "Below-Cutoff Propagation in Metamaterial-Lined Circular Waveguides," IEEE Transactions on Microwave Theory and Techniques, vol. 61, no. 9, pp. 3169-3178, September 2013.

[2] J. G. Pollock and A. K. Iyer, "Radiation Characteristics of Miniaturized Metamaterial-Lined Waveguide Probe Antennas," chez IEEE International Symposium on Antennas and Propagation USNC/URSI National Radio Science Meeting, Vancouver (Canada), July 2015.

[3] J. G. Pollock and A. K. Iyer, "Miniaturized Circular-Waveguide Probe Antennas using Metamaterial Liners," IEEE Transactions on Antennas Propagations, vol. 63, no. 1, pp. 428-433, January 2015.

[4] J. G. Pollock and A. K. Iyer, "Experimental Verification of Below-Cutoff Propagation in Miniaturized Circular Waveguides Using Anisotropic ENNZ Metamaterial Liners," IEEE Transactions on Microwave Theory and Techniques, vol. 64, no. 4, pp. 1297-1305, April 2016.

[5] R. A. Shelby, D. R. Smith and S. Schultz, "Experimental Verification of a Negative Index of Refraction," Science, vol. 292, pp. 77-79, april 2001.

[6] D. R. Smith, W. J. Padilla, D. C. Vier, S. C. Nemat-Nasser, and S. Schultz, "Composite Medium with Simultaneoustly Negative Permeability and Permittivity," Physical Review Letters, vol. 84, no. 18, pp. 4184-4187, May 2000.

[7] V. G. Veselago, "The Electrodynamics of Substances with Simultaneously Negative Values of ε and μ," Soviet Physics Upsekhi, vol. 10, no. 4, pp. 509-514, 1968.

[8] R. W. Ziolkowski and E. Heyman, "Wave Propagation in Media Having Negative Permittivity and Permeability," Physical Review E., vol. 64, n° 15, pp. 1-15, 2001.

[9] Q. Wu, M. D. Gregory, D. H. Werner, P. L. Werner and E. Lier, "Nature-Inspired Design of Soft, Hard and Hybrid Metasurfaces," chez 2010 IEEE Antennas and Propagation Society International Symposium (APSURSI), Toronto, Canada, July 2010.

[10] B. Byrne, Etude et Conception de Guides d'Onde et d'Antennes Cornets à Métamatériaux, Toulouse: Thèse en vue de l'obtention du Doctorat de l'université de Toulouse, 2016.

[11] N. Raveu, B. Byrne, L. Claudepierre and N. Capet, "Modal Theory for Waveguides with Anisotropic Surface Impedance Boundaries," IEEE Transactions On Microwave Theory And Techniques, vol. 64, no. 64 pp. 1153-1162, 2016.

[12] B. Byrne, N. Capet and N. Raveu, "Dispertion Properties of Corrugated Waveguides Based on the Modal Theory," EUCAP 2014: 8th EUropean Conference on Antennas and Propagation, The Hague, Netherland, 6-11 April 2014.

[13] B. Byrne, N. Raveu, N. Capet, G. Le Fur and L. Duchesne, "Modal analysis of Rectangular Waveguides with 2D Metamaterials," Progress In Electromagnetics Research C, vol. 70, pp. 165-173, 2016.

[14] C. Geuzaine, and J.-F. Remacle "Gmsh: A three-dimensional finite element mesh generator with built-in pre- and post-processing facilities," International Journal for Numerical Methods in Engineering, vol. 79, n° 111, pp. 1309-1331, 2009.

Emerging Applications

Artificial Intelligence Based Complex ENZ Network Nanomaterials for Large Scale Microprinting, Broadband Holograms and Bio-imaging

Gael Favraud, Marcella Bonifazi, Valerio Mazzone, Yi Tian, and Andrea Fratalocchi

PRIMALIGHT, King Abdullah University of Science and Technology, Thuwal 23955-6900, Saudi Arabia
www.primalight.org
E-mail: gael.favraud@kaust.edu.sa

Abstract

We present a complex Epsilon Near Zero Network material able to guide broadband light in 10 nm thick oxide layer. This material is designed thanks to swarm artificial intelligence methods. We discuss applications to micro-printing, bio-imaging, and broadband holograms.

1. Introduction

Over the past years Epsilon Near Zero (ENZ) materials stirred growing interest thanks to their many fascinating properties [1, 2]. In ENZ materials, light phase velocity diverges, resulting in the generation of quasi-static electromagnetic fields. This effect allows the possibility to squeeze light energy in extremely narrow spatial regions, opening remarkable results in several fields such as supercoupling or energy harvesting. However, many realizations of ENZ materials to date are based on compound materials that only manifest the ENZ property at specific frequencies or in narrow frequency bands.

Recently, a new class of material based on ENZ networks was proposed and experimentally fabricated [3, 4, 5]. It was shown that these materials can have important applications in photovoltaics, structural color generation and solar generation of clean chemical fuels by photocatalysis [4, 5]. Besides, these materials have the important advantage that their fabrication relies on inexpensive and scalable processes based on electroplating or dealloying.

In this contribution we introduce a new form of complex ENZ Network nanomaterial able to trap and guide light in few atomic layer (< 10 nm thick) of transparent oxides, releasing electromagnetic energy at will by simply removing the oxide layer.

2. Design and fabrication

The design of this material takes advantage of recent advances in artificial intelligence based on swarms [6]. Swarm intelligence relies on the iterative optimization of tentative solutions, called particles. These particles explore the multidimensionnal space of possible solutions and update their direction at each step by relying on memory and cooperation concepts.

The nanomaterials are fabricated through inexpensive and largely scalable electroplating from suitably engineered metallic substrates.

Experimental results show that the reflection of this material can be tuned from almost 0 to nearly 1 thanks to a mere modulation of the oxide layer that is deposited on the material.

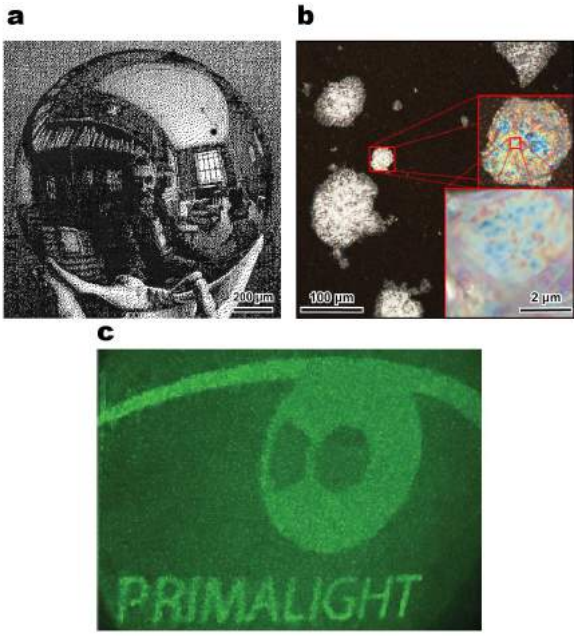


Figure 1: **ENZ network material applications.** (a) Black and white microprinted reproduction of one of Escher's piece. (b) Bright field images of embryonic stem cells deposited on an ENZ network membrane. (d) Binary amplitude hologram image using ENZ network material illuminated by a $\lambda = 532\,\mathrm{nm}$ laser.

3. Applications

We also present three applications of our material.

Genuine authentication and anti-counterfeiting technics based on microprinting can be implemented by using this material. Figure 1a, reproducing one of Escher's piece, shows a sample of such a microprint. As light is squeezed

in the 10 nm thick oxide layer, dark and white pixel can be microprinted depending on the presence or the absence of the oxide layer.

The unique light trapping properties of this material can also find applications in biological imaging with a new type of "rainbow" imaging. Figure 1b shows an image taken with this new technique which is able to use conventional bright field microscopy of stem cells deposited over our complex material. Even without the addition of colorant in the cells, the membrane naturally generate colors, which permits to achieve a fine resolution over the cell aggregates.

Eventually, we present an application of our material in the fabrication of cm-large scale broadband binary holograms, whose result is reproduced on Fig. 1c. These holograms can provide another scalable alternative for anti-counterfeiting technics.

References

[1] M. G. Silveirinha and N. Engheta, "Theory of supercoupling, squeezing wave energy, and field confinement in narrow channels and tight bends using ϵ near-zero metamaterials", *Phys. Rev. B* **76**, 245109 (2007).

[2] I. Liberal and N. Engheta, "Near-zero refractive index photonics", *Nat. Photon.* **11**, 149–158 (2017).

[3] H. Galinski *et al.*, "Scalable, ultra-resistant structural colors based on network metamaterials", *Light Sci. Appl.* **6**, e16233 (2017).

[4] A. J. Labelle *et al.*, "Broadband epsilon-near-zero reflectors enhance the quantum efficiency of thin solar cells at visible and infrared wavelengths", *ACS Appl. Mater. Interfaces* **9**, 5556–5565 (2017).

[5] Y. Tian *et al.*, "Enhanced solar-to-hydrogen generation with broadband epsilon-near-zero nanostructured photocatalysts", *Adv. Mater.* **29**, 1701165 (2017).

[6] J. Kennedy, R. C. Eberhart and Y. Shi, *Swarm Intelligence* (San Francisco, 2001).

Nanofabrication Technology

Spectroscopic Analysis of Structural Colour Reflectors of Helical nanostructures

Taewoo Ha[1*], Wongi Park[2], Teun-Teun Kim[1], Anna Zep[3], Hyungju Ahn[4], Tae Joo Shin[5], Damian Pociecha[3], Kyung Ik Sim[7], Taek Sun Jung[7], Jae Hoon Kim[7], Ewa Gorecka[3] and Dong Ki Yoon[2,6*]

[1]Center for Integrated Nanostructure Physics, Institute for Basic Science, Sungkyunkwan University, Suwon 16419, Republic of Korea
[2]Graduate School of Nanoscience and Technology, Korea Advanced Institute of Science and Technology, Daejeon 34141, Republic of Korea
[3]Department of Chemistry, University of Warsaw, Warsaw, 02-089, Poland
[4]Pohang Accelerator Laboratory, POSECH, Pohang 37673, Republic of Korea
[5]UNIST Central Research Facilities & School of Natural Science, UNIST, Ulsan 44919, Republic of Korea
[6]Department of Chemistry and KINC, Korea Advanced Institute of Science and Technology, Daejeon 34141, Republic of Korea
[7]Department of Physics, Yonsei University, Seoul 03722, Korea
*corresponding author, E-mail: bspha77@gmail.com

Abstract

We have measured polarized reflection of colour reflectors that are fabricated using hierarchical structure of liquid crystal (LC) material. Controlled pitch of nano-helix structure present angle dependent reflection color probed by polarized reflection measurement. Transverse electric (TE) and transvers magnetic (TM) modes can be clearly separated by numerical simulation. We demonstrated reflection characteristics of specific colour reflector produced by self-assembled nano-helix structure with unique resonance frequency as a short wavelength region in visible from green to blue.

1. Introduction

What makes nanostructure mechanically as using e-beam and photolithography that are conventional metamaterial fabricating method is not easy and efficient because of their multiple steps, which are very laborious and costly. That's why metamaterials and photonic crystals operating in visible region hinders its commercialization.

Recently, for three dimensional nano-helix structure using by self-assembly has been emerged for photonic crystals and metamaterials as forming a periodic structure with a specific unit structure [1]. However, still, the self-assembly based techniques are hard to realize practical colour applications because of limits in structural uniformity and surface roughness [2]. Many studies have been conducted for metamaterial produced by self-assembly, but not many mechanism-analysis have been done yet due to limitation of structural uniformity. In this research, we have focused on optical spectroscopic analysis and theoretical approach of ordered nano-helix structure.

We optically investigated structural colour reflectors with different pitch size nano-helix structures from 206 to 282.7 nm, which are named to D-5, D-7, D-9, D-11 as shown in Figure 1. The nano-helix structure is composed with azobenzene moiety containing helical nanofilaments phase, precisely structured bundles of twisted layers, ~ 40 nm in diameter and ~ 200nm in pitch, can be precisely controlled in the nanopores, like the spaghetti in a cylinder [3]. We carried out angle and polarization dependent optical spectroscopy of the colour reflectors using ellipsometry. This measurement gives us the amplitude ratio (ψ) and phase difference (Δ) between p- and s-wave that are changed from incident linear polarized light with 45° composed with p- and s-wave of same phase. An angle-dependent reflection and relative phase information can be obtained simultaneously and effective optical constant as complex refractive index and dielectric constant can be calculated.

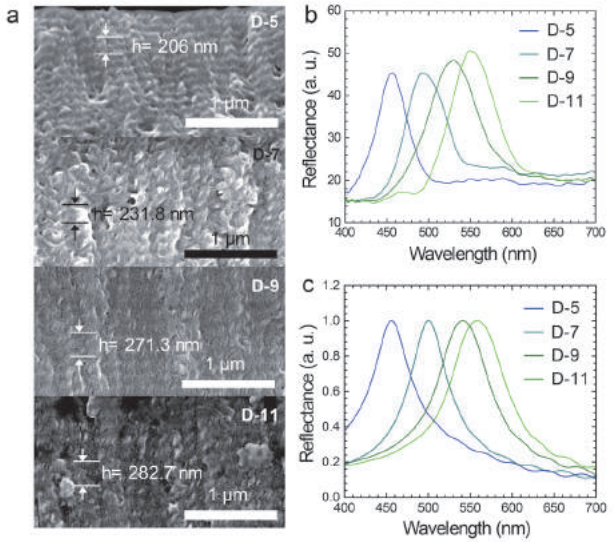


Figure 1 **a** Pitch control of nanohelix structure from 206 to 282.7 nm, named from D-5 to D-11, observed in side view SEM image. b Reflectance of nanohelix structure using unpolarized light with the range from 400 to 700 nm. c Corresponding numerical calculation of normalized reflectance.

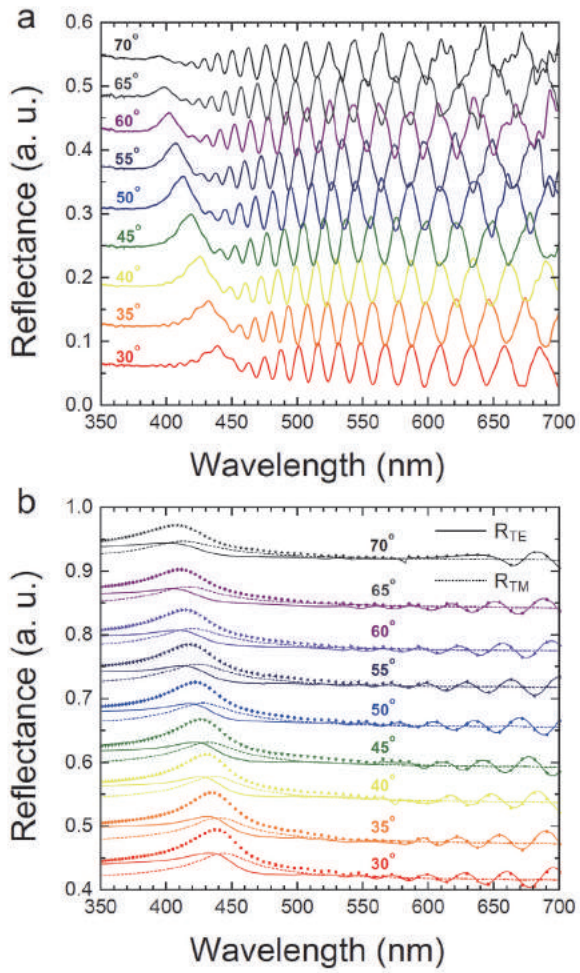


Figure 2 **a** Angle dependent relfection of unpolized light in D-5 nanohelix (pitch = 206 nm). **b** Numerical calculated reflectance of D-5 nanohelix with combination of transverse electric (TE) and transverse magnetic (TM) modes, which represent solid and dashed line, respectively. Unpolaized reflection measurement is marked in symbol with rainbow colors corresponding with each incident angle from 30º to 70º with 5º steps.

2. Discussion

Fig 1 a shows reflectance along normal direction of nano-helix structure. We identified that the specific resonance of each nano-helix structure systematically can be seen by pitch. Theoretical verification for interaction mechanism of light in the three-dimensional helical nanostructure will be tried on the basis of the theory related to photonic crystal and metamaterial. For numerical calculation, an exact refractive index of non-structured HNF thin film in the visible range should be measured primarily and we can obtain the optical response which is estimated by structural and measurement parameters. The results of numerical simulation give us quite consistent reflectance comparing with experimental data (Fig 1 b). Through a numerical calculation, as we had expected, we found that the pitch length is the most dominant component to change specific resonance efficiently. Fig 2 a shows the angle dependent reflectance of unpolarized light. The vivid interference phenomenon imply forming high quality surface and interface by the fringe pattern is the evidence of multiple reflection in both of bottom and top side. We can observe the shift of resonance with incidence angle caused by changing photonic band dispersion with each momentum. Theoretical analysis show that each of the angle dependent resonances consists of a transverse electric (TE) and transverse magnetic (TM) modes.

3. Conclusions

Three-dimensional helical nanostructure gives us a specific reflection resonance energy of light. The specific resonance can be modified not only by the structural parameters such as periodicity, pitch, lattice parameter, diameter of helix, and so on. The specific reflection energy with each radiation angle maybe determined due to changing band dispersion with k in a photonic band structure. The angle dependent reflectance compose the combination of TE and TM mode. The variability of our helix nano-structure makes the chiral photonic crystal that responds with unique resonance frequency as a short wavelength region in visible from green to blue. These results could provide a new way to study existing photonic crystals or materials that were very difficult to control.

Acknowledgements

This work was supported by IBS-R011-D1.

References

[1] Luca Passoni et al., Self-Assembled Hierarchical Nanostructures for High-Efficiency Porous Photonic Crystals, *ACS Nano* 8: 12167–12174, 2014.

[2] Lee, S. S. et al., Robust Microfluidic Encapsulation of Cholesteric Liquid Crystals Toward Photonic Ink Capsules. *Adv. Mater.* 27: 627-633, 2015

[3] Kim, H. et al., Multistep hierarchical self-assembly of chiral nanopore arrays. *Proc. Natl. Acad. Sci. U.S.A.* 111: 14342-14347, 2014